An Evaluation of Portable X-Ray Fluorescence on Applied Blue Faience Glazes: A Study Using Replicate Glazes of the Late, Ptolemaic and Roman Periods in Egypt

James Christopher Wilkins

ORCID ID:

A thesis submitted in partial fulfilment of the requirements for the degree of Doctor of Philosophy

Department of Archaeology and Conservation

Cardiff University

September 2018

File Name:

File Status: Submission

DECLARATION

This work has not been submitted in substance for any other degree or award at this or any other university or place of learning, nor is being submitted concurrently in candidature for any degree or other award.

Signed  (candidate) Date 11.09.2018

STATEMENT 1

This thesis is being submitted in partial fulfillment of the requirements for the degree of PhD.

Signed  (candidate) Date 11.09.2018

STATEMENT 2

This thesis is the result of my own independent work/investigation, except where otherwise stated, and the thesis has not been edited by a third party beyond what is permitted by Cardiff University's Policy on the Use of Third Party Editors by Research Degree Students. Other sources are acknowledged by explicit references. The views expressed are my own.

Signed  (candidate) Date 11.09.2018

STATEMENT 3

I hereby give consent for my thesis, if accepted, to be available online in the University's Open Access repository and for inter-library loan, and for the title and summary to be made available to outside organisations.

Signed  (candidate) Date 11.09.2018

STATEMENT 4: PREVIOUSLY APPROVED BAR ON ACCESS

I hereby give consent for my thesis, if accepted, to be available online in the University's Open Access repository and for inter-library loans **after expiry of a bar on access previously approved by the Academic Standards & Quality Committee.**

Signed  (candidate) Date 11.09.2018

This work is dedicated to my father: an historian, a soldier and a teacher.

I must study politiks and War, that my sons may have liberty to study Mathematicks and Philosophy - my sons ought to study Mathematicks and Philosophy, Geography, natural History and Naval Architecture, navigation, Commerce and Agriculture in order to give their Children a right to study Painting, Poetry, Musik, Architecture, Statuary, Tapestry and Porcelaine.

–John Adams, Letter to Abigail Adams (post - 12 May 1780).

[Spelling mistakes and grammatical errors are those of John Adams.]

Summary

This thesis presents a systematic evaluation of energy dispersive hand-held X-ray fluorescence (HH-XRF) on the semi-quantitative net peak analysis (NPA) of Late, Ptolemaic and Roman Period (644 BC to AD 395) faience from Egypt. The study develops a non-destructive protocol in the analysis of faience glazes using HH-XRF, a relatively recent technological innovation in cultural heritage. The benefits (e.g. portable, non-destructive, non-radiological source (i.e. X-ray tube)) and limitations (e.g. depth of analysis, layered analytes (i.e. glaze on body)) of HH-XRF are examined.

Replicated faience glazes were produced as a part of the HH-XRF evaluation. Glaze recipes were derived from the literature involving experimental archaeology and instrumental analysis. One body and three glaze batches were produced that were aesthetically and structurally similar to the archaeological material. The glaze batches were fired on raw and bisque-fired bodies in a raw and prefritted state to produce 30 replicated glaze samples.

The HH-XRF parameters (e.g. voltage, current, acquisition time) were evaluated using Corning Glass B as the known analyte. Optimum results were based on a compromise (bivariate coefficient) between high precision (C_v) and high signal-to-noise ratio (SNR).

Multivariate statistics were explored providing the optimal methods for data preparation and analysis using hierarchical cluster analysis, principle component analysis and K-means analysis. The HH-XRF (NPA) measurements for high (40 kV) and low (15 kV) voltages combined with multivariate statistics successfully discerned the three replicated faience glaze sets.

A small case study of faience glazed sherds from Saqqara were examined and analysed using the optimally determined settings to illustrate HH-XRF use on archaeological material. The results categorized the faience into 5 groupings (with subgroups) based on composition.

The project was designed to help field archaeologist and others responsible for the study and care of faience objects by providing steps that can be utilized in the field or in a laboratory setting using materials and tools that are readily accessible. This is especially useful in places like Egypt where there are on-going excavations but exportation of artefacts is difficult to impossible and importation of radiological sources is highly regulated.

Acknowledgements

Engaging with the work required to complete a PhD is surprisingly lonely and psychologically challenging. One often feels the whole world is composed of the four walls surrounding them, and it is usually around this time that a hand breaks through the fourth dimension to remind you that, while important, there actually is a whole world beyond the current project on which you are working. It is to these people that I would like to express my gratitude in their help for the accomplishments made in the pursuit of this PhD.

Firstly, I am indebted to my supervisors, Dr. Panagiota Manti and Dr. Paul T. Nicholson of Cardiff University: Dr. Manti for encouraging me, keeping me focused, and insisting on rigorous science, and Dr. Nicholson for calming me down, providing advice and introducing me to other scholars.

I am grateful to Phil Parkes for instructing me on how to maintain and service the SEM and HH-XRF when they start having issues, sometimes seemingly out of spite. I am thankful for the help provided by Dr. Eric Nordgren regarding the SEM, new software tools and generally answering my questions in the research laboratory. I am appreciative of the help provided by Dr. Mary Davis and Louise Mumford (National Museum of Wales) in locating and transferring the HH-XRF equipment between museum and university campus. I am grateful to Mike Dobby, Bruce Kaiser and Lee Drake (Bruker), Dr. Rebecca Scott (Leuven University) and Dr. Matt Nicholas for the help regarding HH-XRF, the Tracer Bruker III-SD and related software, and to Dr. Caroline Jackson (Sheffield University) for providing me with the NIST glass standards.

I am very thankful to Marie-Domonique Nenna (CNRS) for graciously providing advice and inviting me to a closed-door Faience round-table at the Louvre where I had the opportunity to meet other scholars in the field. I am also thankful to the Egyptian Exploration Society (c/o Paul Nicholson) for providing me with Saqqara faience sherds for SEM and HH-XRF analysis.

I acknowledge those who work behind the scenes at SHARE and who make the student experience much more enjoyable: I am grateful to Helen Szewczyk for handing the administrative details and communicating my deadlines, Sue Virgo in all her help at purchasing and disposing of chemicals (not the same ones), Rob Thomas and Aled

Cooke for IT support and hashing out computer software problems, and to the John Percival Porters, Paul and Keith, for helping me secure equipment in the evenings as they were prodding me to leave the building, then for all the conversations we had at the exit. I am also thankful to David McConnell and the assisting students at the Cardiff University Mathematics Support Service for their help and input with multivariate statistics.

I am indebted to my surrogate family, the conservation department faculty and those related not already mentioned including Jane Henderson (and family), Phil Parke's family Dr. Nicola Emmerson, David Watkinson and all the students who are currently present or have matriculated through the system, and also to fellow PhD students Vicki Kontogianni ,Ashley Lingle Meeklah (and Joshua, "Jesus!, …your moving again?"), Jerrod Seifert, Johanna Thunberg, Dr. Amber Lawson and Sam Johnson for griping sessions, drinking sessions, gaming sessions, Eurovision sessions, Great British Bake-off sessions and the Cretan sun.

Lastly, I thank my wife for letting me come to Cardiff the first time without her, insisting I do a PhD and accompanying me the second time, and my mother and father, neither of whom are around anymore to witness this accomplishment. In addition, I am thankful to all the others that I have invariably left off this list and of whom I will immediate think of after having submitted this work. …I love you all!

Contents

List of Figures

List of Tables

List of Equations

Acronyms and Initialisms

µA	Micro-Amps
AAS	Atomic Absorption Spectroscopy
Bi-Q	Bivariate Quotient
CLR	Centered Logratio
cps	Counts Per Second
CRAN	Comprehensive R Archive Network
Cv	Coefficience of Variance
C-XRF	Component X-Ray Fluorescence
ED-XRF	Energy Dispersive X-Ray Fluorescence
EPMA	Electron Probe Micro-Analyzer
FTIR	Ffourier-Transform Infrared Spectroscopy
FWHM	Full Width Half Maximum of Peak
HCA	Hierarchical Cluster Analysis
HH-XRF	Handheld X-Ray Fluorescence
IAL	Interaction Layer
ICP-AES	Inductively Coupled Plasma - Atomic Emission Spectroscopy
ICP-MS	Inductively Coupled Plasma - Mass Spectrometry
ICP-OES	Inductively Coupled Plasma - Optical Emission Spectroscopy
IDE	Integrated Development Environment
INAA	Instrumental Neutron Activation Analysis
IQR	Interquartile Region
keV	Kilo-electron Volts
kV	kilovolts
LA-ICP-MS	LASER Ablation Inductively Coupled Plasma Mass Spectroscopy
LDM	Limit of Determination of a Method
LOD	Limit of Detection
LOO	Leave-One-Out Method
LOQ	Limit of Quantification
MR	Multiplicative Replacement
MVS	Multivariate Statistics
NAA	Neutron Activation Analysis
NIST	National Institute of Standards and Technology
NPA	Net Peak Analysis
OES	Optical Emission Spectrometry
OM	Optical Microscopy
PCA	Principle Component Analysis
PET	Polyethylene Terephthalate
PIXE	Particle-Induced X-Ray Emission
ppm	Parts Per Million
pXRF	Portable X-Ray Fluorescence
RAE%	Relative Absolute Error Percent
RSD%	Relative Standard Deviation Percent
SEM-BSE	Scanning Electron Microscopy - Backscattered Electron Imagery
SEM-EDS	Scanning Electron Microscopy - Energy Dispersive Spectroscopy
SEM-SE	Scanning Electron Miscroscopy - Secondary Electron Imagery
Si-PIN	Silicon P-Type Semiconductor
SNR	Signal-to-Noise Ratio
WDS	Wavelength Dispersive Spectroscopy
WD-XRF	Wavelength Dispersive X-Ray Fluorescence
wt%	Weight Percent
XRF	X-Ray Flouresence
Z	Atomic Weight

Map 1: Map of modern Egypt exhibiting place names that are used in the text. Cairo is included for reference. Partitions (A-B) indicate areas covered by additional maps after this page.

Map 2: Map A of modern Lower Egypt exhibiting place names that are mentioned in the text. Blue markers are known workshops utilized at some point during the Late through Roman Periods. The single white marker (Wadi Natrun) exhibits the best known source for natron. The yellow markers indicate areas where sand samples were collected for analysis by various authors. Saqqara (red marker) is the site where the case study faience sherds were recovered.

Map 3: Map B exhibiting Middle and Upper Egypt and place names used in the text. This map exhibits the location of the one known faience workshop (Elephantine) utilized in Upper Egypt sometime during the Late through Roman Periods. The other markers exhibit areas where sand was collected for analysis by various authors.

Table P - 1: Egyptian Cultural (Shaw 2000) and Faience Technological Chronology (Kaczmarczyk and Vandiver 2008; Nicholson 2013; Nicholson and Peltenburg 2000; Vandiver 1982, Vandiver and Kingery 1986)

Egyptian Cultural and Faience Technological Chronology			
Period (Shaw 2000)	Body Manufacture	Glaze Process	Factory Evidence
PreDynastic (Before 3200 BC)	Core grinding, Surface grinding and Free-form modeling	Experimental Period: Efflorescence, cementation and application (?)	None
Early Dynastic / Archaic (3200 - 2686 BC) Old Kingdom (2686 - 2160 BC) and First Intermediate (2160 - 2055 BC)	Modeling, surface grinding, Painting with a slurry, Layering, Core forming, Marbleizing and possibly molding	Efflorescence	None Abydos (Old Kingdom and First Intermediate)
Middle Kingdom (2055 - 1650 BC) and Second Intermediate (1650 - 1550 BC)	Modeling, Form molding, Core forming, Marbleizing, Layering, Painting with a coloured quartz slurry, Incising, Inlaying, Resisting and Painting with a pigment wash	Efflorescence is primarily glazing technique Cementation and application also used	Lisht Kerma
New Kingdom (1550 - 1069 BC)	Molding on a form, open-faced molds molds, Core forming, Luting with quartz slurry, Layering, Incising, Inlaying with quartz slurry, Painting with pigment wash, Throwing (?)	Efflorescence, cementation and application Finely powdered glass added to body or inlay to extend colour range Introduction of cobalt ore used for dark blue Cobalt ore is high in alumina and magnesia	Amarna Lisht Malkata Qantir
Third Intermediate (1069 - 664 BC)	Same techniques as New Kingdom Natron is preferred or potash for alkali	Efflorescence, cementation and application Introduction of new cobalt ore to replace older ore Cobalt ore is high manganese and moderate in iron	
Late Period (664 - 332 BC)	Same techniques as New Kingdom	Efflorescence, cementation and application Introduction of new cobalt ore to replace older ore Cobalt ore is high in iron and low in manganese	Naucratis
Ptolemaic (Hellenistic) (332 - 30 BC)	Same techniques as New Kingdom plus stamping and addition of appliques Pottery techniques: bisque firing	Efflorescence, cementation and application Pottery techniques: glost firing	Memphis, Arthribis Alexandria (?) Schedia, Buto
Roman (30 BC - AD 395)	Same techniques as Ptolemaic plus larger vessels and standardization	Efflorescence, cementation and application Thicker glazes	Memphis, Buto Elephantine, Terenouthis

Chapter 1: Introduction

1.1 Introduction

This PhD research project is a response to the heavy adoption of handheld portable X-ray fluorescence (HH-XRF) by the cultural heritage sector including archaeologists, conservators and others charged with the care and understanding of our past through material science. Blue faience glazed objects from the Late, Ptolemaic and Roman Periods of Egypt are the subject of study. The composition of the glazes has changed as new sources for raw materials were used. Analysis of these glazes in the field and laboratory will be useful with on-going excavation strategies and may prove beneficial in the future for provenance studies of artefacts in making connections with specific raw material sources or workshops (far beyond the purview of this PhD thesis). The scope of the project is to determine what useful information HH-XRF can provide beyond the identification of the colourant used in the glaze.

The seemingly ambiguous term ‘faience’ has taken on three meanings in the last century: tin-glazed delftware (English and Dutch), more commonly Italian majolica from Faenza, and the vitreous glazed bodies of Egyptian origin which are sometimes called frit-ware but not without controversy because of confusion with glass manufacture (Lucas and Harris 1962:156; Nicholson and Peltenburg 2000:177; Tite 2009:2066; Tite and Shortland 2008:21). Egyptian faience indicates ancient Egyptian vitreous glazed ware and objects. For non-archaeological ceramicists, this term can be confused with Egyptian paste which refers strictly to the modern efflorescence glazed material (see Chapter 2) made in the style of Egyptian faience. For this work the term ‘faience’ or ‘Egyptian faience’ refers to the glazed non-clay powdered quartz bodied ceramic of Egyptian origin, the glazing of which can be by cementation, efflorescence or application, or any combination of the three methods.

Blue glazes from the Late through the Roman Periods (664 BC – AD 395) are the analytical study subjects of the research. These cultural periods have not had the same amount of study as the earlier pharaonic periods. This period marks a time when the position of Egypt in the ancient world changed from one of dominance in the Near East to one of foreign domination and incorporation into a wider Mediterranean world. Blue glazes represent the most abundant colour being produced during this period and

have thusly been selected for investigation. Isolating the study to a single colour removes the colourant as the variable with the highest variance, and therefore removing the colourant as the driving force of the post-data-collection analysis.

HH-XRF is becoming ubiquitous in archaeology and museum collection studies. HH-XRF provides museums and archaeologists with the potential of portable non-destructive analysis and the capability to conduct several measurements within a short period of time. Other benefits of HH-XRF include the use of an X-ray tube versus a radiological source, minimal sample preparation and relative low cost. However, an understanding of the limitations of HH-XRF are paramount for producing trusted results. These limitations include depth of measurement, unsuitable surface conditions, sample non-uniformity and detection of light elements. Benefits and limitations are covered in greater detail in Chapter 3.

Egyptian faience is composed of a glaze layer over a ground sand or quartz body. Depth of analysis in layered structures is a limitation with HH-XRF; the source depth of the detected X-rays (i.e. body or glaze) is determined by the thickness of the glaze, the voltage used during analysis and the specific elements detected. The study of faience glazes in the field or in museums would benefit from HH-XRF analysis if the technique reveals useful information beyond the glaze colourant used.

Field archaeology would benefit from HH-XRF analysis of faience glazes but traditional analytical methods require the results to be in wt% or ppm. The generation of wt% and ppm results require the analysis of 10-20 reference standards to represent the number and compositional ranges of glaze and glass elemental components. Reference standards are expensive and can be cost prohibitive for many users of HH-XRF. Alternatively, net peak area (NPA) can be used for sample categorization.

Drake (2014) states that all HH-XRF information is contained within the spectra; calibration adds no new information and is just a translation of the data into wt%. HH-XRF NPA analysis is a semi-quantitative method which, not being bound to calibration through reference standards, can still provide faience categorization based on ratios. Semi-quantitative analysis is the analysis conducted when conditions for quantitative analysis are not met (e.g. no reference standards) but qualitative analysis (spectra comparisons) is not enough to answer the questions on hand (Bruker 2018). The NPA results are in counts per second for each element. These results cannot be directly compared across the literature unless the same HH-XRF unit (because of intra-instrument detection variabilities) is used with the same analytical setup. However, glaze categories, like those produced from cluster analysis, can be compared across

the literature because the NPA are directly related to wt%. Thusly, although each HH-XRF unit may produce variations in NPA and wt%, the categorizations will be similar. In this way, HH-XRF can be useful for archaeological fieldwork with the caveat that NPA semi-quantitative analytical results cannot be directly compared.

Evaluations of HH-XRF have occurred for archaeological materials including obsidian (Forster and Grave 2012; Millhauser 2011; Nazaroff et al. 2010), unglazed pottery (Forster et al. 2011; Morgenstein and Redmount 2005; Speakman et al. 2011), glazed stoneware (Mitchell et al. 2012), and porcelain (Bezur and Casadio 2012; Domoney 2012). These have revealed HH-XRF as a valuable tool for the material-based researcher (see Chapter 3). Success of HH-XRF with obsidian sourcing has demonstrated the potential for faience chemical provenancing in archaeology. However, obsidian is a homogenous material with no chemically distinct layers (ignoring the effects of hydration). HH-XRF evaluations of layered glazed materials such as stoneware and porcelain have been examined but not to the same extent as obsidian. HH-XRF has been used on faience material (De Viguerie et al. 2009; Abe et al. 2012; Toffolo et al. 2013, Whisenant 2012) but a thorough evaluation for HH-XRF use on faience glazes is missing from the literature. This thesis is an extensive evaluation of the HH-XRF method on the analysis of faience glazes.

1.2 Rationale

HH-XRF is a relatively new analytical tool in the cultural heritage repertoire which is relatively cheap and easily transported across national borders but there have been systemic issues in analysis and in understanding the limitations of HH-XRF (Shugar and Mass 2012:19). Faience analysis would benefit from HH-XRF because of the quick analytical acquisition times and the ease of portability, be it in museums, the field or private collections, and across national boundaries where export of antiquities are forbidden (e.g. Egypt). However, faience characteristics (i.e. layered, heterogeneous, and often weathered) present a challenge for non-destructive quantitative analysis. HH-XRF can detect sodium[1] and higher Z (atomic weight) elements at various depths in a matrix depending on the voltage used, the specific element of interest and the density of the matrix. The quantification of HH-XRF measurements requires reliable calibrations based on several reference standards. However, semi-quantitative NPA could be a suitable alternative and is explored in this thesis. Appropriate HH-XRF

[1] Silicon drift detection (SDD) sensors combined with the use of a vacuum or helium flush can enable detection of sodium using the Bruker Tracer III-SD and the Spectra software (ver. 7.4) although experience of this author found that precision (C_V) is low resulting in a drop of the element for post-measurement statistical analysis.

parameters may provide the capability to determine faience production technology based on specimen characteristics such as colourants and trace elements, and could have greater consequences in the future on raw material sourcing and workshop determination.

Compositional analysis of faience glazes has been carried out using various analytical techniques including neutron activation analysis (NAA (e.g. Aspinall et al. 1972)), inductively coupled plasma-mass spectrometry (ICP-MS (e.g. Mangone et al. 2011)), scanning electron microscopy using secondary electron imagery and backscattered imagery (SEM-EDS, -BSE (e.g. Vandiver and Kaczmarczyk 1987)), atomic absorption spectrometry (AAS (e.g. Foster and Kaczmarczyk 1982)), and proton induced X-ray emission (PIXE (e.g. McGovern et al. 1993)). There are no comparisons of these techniques with HH-XRF on faience glazes[2]. However, a comparison of obsidian and glass HH-XRF results with other analytical techniques reveal that both discriminate to nearly the same level although these materials differ from faience glazes in that they represent homogenous single-layer matrices (Craig et al. 2007; Goodale et al. 2012; Nazaroff et al. 2009, 2010; Scott et al. 2012b; see Chapter 3). HH-XRF offers an added benefit to these other methods; the object does not require sampling and large objects are not subject to analyser chamber size restrictions. In other words, complete objects of any size larger than the HH-XRF analyser window can be non-destructively analysed but are still required to be thick enough to absorb 99% of the photon beam for semi-quantitative and quantitative analysis to be effective.

The main issue of HH-XRF analysis on faience glazes is the depth of detection and knowing the origin of the output information (i.e. body or glaze). The depth of penetration is dependent on the HH-XRF voltage and the composition of the substrate. Greater voltage will penetrate deeper into the glaze and possibly into the body and is required to fluoresce elements with higher ionization energy. This may result in certain elements being restricted from post-measurement glaze analysis (e.g. multivariate statistics) because the origin of the detected photons is below the depth of the glaze (e.g. tin and antimony with 40 kilo-volt (kV) measurements).

The capabilities of HH-XRF with the analysis of faience glazes were assessed through the measurement of faience glaze replications produced in the Cardiff University conservation science laboratory specifically for this project. The replicated faience glazes on bodies simulating the archaeological material will provide a layered material

[2] De Viguerie et al. (2009) found consistent results between a component XRF (C-XRF) system and PIXE of a New Kingdom faience pendent glaze. Giumlia-Mair and Soles (2013) found semi-consistent (±10 wt%) results between C-XRF and AAS of a Mycenaean faience necklace.

and substrate of known composition for analysis. HH-XRF analysis of these glazes will determine if the analytical technique is capable of differentiating between glaze batches (one copper and two cobalt glazes).

The results of the project will benefit the HH-XRF analysis of faience in the future whether it reveals appropriate avenues for analysis or paths that should not be followed in future evaluations. The analytical methodology for glazes is similar regardless if the substrate is composed of powdered quartz or wedged clay. The point is to analyse the glaze and not the substrate. However, most of the information provided from HH-XRF measurements will be from the glaze even if the substrate is detected. The methodology produced as a result of the project can be used on many glazed materials assuming the glaze density is similar.

1.3 Aims and Summary of Methods

The aim of this study is to evaluate the Bruker Tracer III-SD HH-XRF to determine its efficacy in the analysis of faience glazes and, if successful, to suggest a methodology for the analysis of archaeological faience. To achieve this, the project will include the analysis of 30 faience replicates, produced as part of this research, and 24 faience sherds attributed to the Late/Ptolemaic Period (712-332/332-30 BC) (Dayton 1981) as a case study using semi-quantitative HH-XRF and quantitative scanning electron microscopy with energy dispersive spectroscopy (SEM-EDS) of sample cross-sections. The glaze replicates were used to verify the methodology and validate the HH-XRF technique on faience through the clustering of the known groups. Archaeological faience glazes were analysed as a case study. Backscattered electron imagery (BSE) determined glaze depths and faience microstructures to help characterize the archaeological and replicated glazes.

Replications of application-glazed faience were produced to match the chemical, microstructural and aesthetical characteristics of copper and cobalt-coloured blue archaeological material from the end of the Late Period (Dynasties XXX-XXXI (380-332 BC)) through the Ptolemaic (332-30 BC) and Roman (30 BC - AD 395) Periods of Egypt. Replication experiments will enable the testing of fabrication materials versus composition, use of a range of application methods (i.e. dipping and painting) and firing parameters. The replicated material was used in the evaluation of HH-XRF for analysis of faience material from the archaeological record. Corning glass standards were used to determine optimized settings for the detection of the elements expected in the glazes; these settings are a compromise between highest precision and greatest signal-to-noise ratio (they often do not correspond; see Chapter 6). The faience glaze

replicates were analysed using these optimum settings because they provide a known layered material on a substrate and helped to examine the effects of a layered structure on the analytical results.

The archaeological sherds were recovered from disturbed zones at Saqqara and are associated with the 30th dynasty (Late Period) or to the early Ptolemaic Period, c. 355 BC (Dayton 1981:135). The glazes are mostly turquoise and ultra-marine blue, however purple, yellow and green glazed archaeological glazes are analysed to provide analytical contrast. The sherds are now a part of the Egyptian Exploration Society collection held at Cardiff University and have been kindly provided by Dr Paul Nicholson.

1.4 Chapter Layout

The background of faience including the technology, past compositional analysis and use of faience replicates are further explored in Chapter 2. HH-XRF benefits, limitations and the principles of X-ray fluorescence are discussed in Chapter 3. Case studies involving archaeological objects are covered to provide a foundation on which to base the current project parameters. Chapter 4 provides a methodology for the current project and discusses the selection of investigative techniques including instrumental and statistical analysis. The formation of replicated faience glaze batch recipes and the results of glazing and firing are covered in Chapter 5. The HH-XRF parameters are discussed and evaluated in Chapter 6 to determine the optimal setup conditions for the analysis of the replicated glazes and the faience material from Saqqara. Chapter 7 is a discussion on the macro-structures of the analogue and archaeological material and the microstructures as determined through SEM-BSE of object glaze profiles. Compositional profiles are generated and glaze depths are further explored. Chapter 8 provides the background and methodology for multivariate statistical analysis to determine faience clusters based on chemical composition of the glazes. One faience replicate dataset is thoroughly explored to determine optimal statistical methods for the analysis of all the replicated materials (Chapter 9) and archaeological materials from Saqqara (Chapter 10). Chapter 11 is a review of the findings and a proposed method for analysis of faience glazes in the field and suggestions for further research.

Chapter 2: Background: Faience Materials and Manufacture

2.1 Introduction

Faience glazes from the Late through Roman Periods (747 BC – AD 395) have not had the same amount of analytical attention as the earlier pharaonic glazes despite having undergone a conceptual change from association with stonework in the pharaonic periods to association with pottery, metalwork and glass in the later periods, the periods of this study (Nicholson 2012; 2013 148). Along with this cognitive change are the establishment of new workshops associated with the production of faience (e.g. Memphis, Terenouthis, Arthribis) and new sources for old colourants. Elemental analysis of the glazes will indicate categories that may be based on specific workshops and possibly raw material sources.

Egypt law 117 (2010 (most recent incarnation of 1983 law)) ended the practice of exporting 10% of finds generated by international excavations and generally states that no archaeological materials shall leave the country without the expressed written consent of the Egyptian Council of Antiquities. As with any bureaucracy, granting of permission can take time if given at all. This translates into difficulties with conducting analysis on recently excavated materials unless it occurs within Egypt. Two possible resolutions are the borrowing of pre-existing analytical equipment in-country or the importation of new equipment. Borrowing of hands-on time on pre-existing equipment introduces problems of scheduling, reliance on the host institution to honor that scheduling and vetting of the international users by the host to ensure safety of equipment and efficient time management practice. Importation of analytical equipment can be even more problematic in securing funds for equipment and transportation, safety while in transit and use, finding a host to house and power the equipment and potential local and international laws affecting the transportation of equipment across international borders (e.g. radiological sources).

With the recent development of HH-XRF units comes a potential resolution. Many units available today are relatively cheap compared to the cost of other equipment, contain X-ray tubes instead of radiological sources curtailing local and international laws restricting the transportation of radioactive sources, are small and easily handled and are battery operated and/or can be plugged into standard AC power outlets. HH-XRF allows the in situ analysis of recently excavated finds with immediate results.

However, HH-XRF analysis of faience has to be evaluated with the use of replicated and archaeological glazes to determine if the results actually have archaeological meaning. The problem does not lie with the analyte (subject of analysis) but with the analytical technique involved in its analysis. That is not to say that the analyte does not have characteristics that provide difficulties with some forms of analysis. Faience material is composed of a glaze layer on a body substrate. In addition, the glaze may contain partially or non-reacted materials resulting in a heterogeneous glaze (and body?) as the subject of analysis when HH-XRF analysis is best conducted with homogenous materials. As a result, the source (i.e. body or glaze) of the fluoresced X-rays is not known. Additionally, greater density particles in the glaze/body will provide greater information output which may not accurately reflect the network composition as a whole.

Production of replicated faience glazes for HH-XRF analysis provides a known material (both in physical (i.e. depth of glaze) and elemental characteristics). A sample set consisting of 30 individual samples divided between three batches (one copper colourant and two cobalt colourant glazes on a sufficient faience body) was produced for testing. Twenty-four archaeological faience sherds from Saqqara were also analyzed to evaluate HH-XRF use on archaeological material.

A review of faience technology is required to assist in the production of the replicate faience glazes and to inform on origin (intentional or inclusion) of possible elements encountered with HH-XRF analysis of archaeological material. This chapter provides a definition of the term ‘Egyptian faience’ and presents a cultural background spanning the period of interest in Egypt (Late, Ptolemaic and Roman Periods). The technological aspects of faience are covered including chemical components typically encountered during analysis and the forming, glazing and firing methods of Egyptian faience. The importance of analysis of faience and potential information uncovered is explored and the use of faience replication as a part of this analysis is discussed. The chapter following this

provides background information and more in-depth discussion on benefits and limitations of HH-XRF.

2.2 What is Egyptian Faience?

Egyptian Faience is a non-clay ceramic composed of a ground sand, or quartz, body with a soda-lime-silica glaze and was produced in Egypt from the 4th millennium BC through the end of the Roman Period (AD 395) (Kaczmarczyk and Vandiver 2008:58-60). It was initially produced possibly to imitate lapis lazuli and turquoise (Friedman 1998:15; Nicholson 2012; Vandiver 1983:A5) and early forms included beads and amulets. By the end of the Roman Period the faience objects included statues, tableware and many other forms. Faience has been described as the "first high-tech ceramic" implying that knowledge of the properties bestowed by the various elements were known and intentionally used by the crafters (Vandiver and Kingery 1986:19). Copper was the primary blue and green colourant for faience but other colourants were introduced during various periods (Kaczmarczyk and Vandiver 2008:72-73). For example, manganese was used for purple and black glazes from the archaic to the Late Period (ibid., p.76-77). Iron oxides (possibly Fe_3O_4) started replacing manganese for black glazes in the Late Period (ibid.). Cobalt produces a dark to ultra-marine blue and was introduced three times in the form of different ores (New Kingdom, Third Intermediate and Late Periods) (ibid., p.75). Lead antimonate was first used for green and yellow glazes in the New Kingdom Period (ibid., pp.78-79).

There are three reported glazing methods practiced in antiquity used on faience which vary by composition and process: efflorescence, cementation, and application (Vandiver 1982:168-169). All three methods were possibly used during the predynastic period but efflorescence was dominant from the Early Dynastic through the Second Intermediate Period (Kaczmarczyk and Vandiver 2008:58-59). By the New Kingdom the selection of glazing technique was determined by the object themselves; cementation for small beads and amulets, application for larger objects and efflorescence for small and large objects requiring complete glaze coverage (Kaczmarczyk and Vandiver 2008:5; Tite and Shortland 2008:208). The application method, used from the 4th millennium BC onward, was the primary means of applying glaze during the Late, Ptolemaic and Roman Periods (Nicholson 2013:19, Vandiver 1983:A4). Glass and glazes are composed of a variety of network former, network modifier and network stabilizer elements (Freestone 1991:39-40; Hodges 1976: 42 and 54; Kaiser and Shugar 2012:454). Elements important to glaze

structure (formers, modifiers and stabilisers) consist of the light elements silicon, sodium, potassium and calcium (Hodges 1976:55). Colourants are generally higher weight (Z) elements (e.g. cobalt, copper, iron, manganese and antimony). A typical blue faience glaze can contain between 10-20 elements including the major structural components (e.g. sodium, calcium and silicon), the unintentional inclusions (e.g. aluminium, iron and strontium) and the colourants (copper, cobalt) (Kaczmarczyk and Hedges 1983: Appendix C). All of these elements are easily detected by HH-XRF with the exceptions of sodium and magnesium which have an easily attenuated signal, the effects of which can be reduced with a vacuum or helium flush (Jenkins 1999:179; Potts and West 2008:8).

The use of material culture and technology is dependent on the social culture in which it is devised. The Egyptian world view before the first millennia BC held Egypt at the centre of civilization (Schneider 2010:156). This view was rattled during the first millennia BC which witnessed greater impact and dominance by outside forces including the Libyan (in the Third Intermediate Period), Kushite and Persian (in the Late Period) and Greek (Ptolemaic Period). The Libyan and Kushite dynasties could still be considered Egyptian because they appeared to adopt Egyptian culture along with its continued placement at the centre of their world (ibid.)[1]. This world view started to change in the seventh century in conjunction with increased Hellenization. Greeks were invited to settle in the area of Naucratis in the seventh century presumably to maintain an allied partnership with Greece against the Persians (Dodson 1996: 194; Thomas and Villing 2013: 83). Egypt continued to maintain its identity in the Late Period despite an influx of new ideas and a foreign dominance by Nubia, Persia and eventually Greece (Dodson 1995:175-203). The Late Period witnessed the last of the native rulers (ibid.) but an increasing presence in Mediterranean affairs (Berman 1999:390). Egyptian art flourished combining an emphasis on the past with the adoption of new techniques. Greek styles were becoming more infused into Egyptian art and sculpture (Berman 1999:391-392; Dodson 1995:199). Faience of this period exhibits a transition from Pharaonic to Ptolemaic in raw materials, colours and use of colours (Kaczmarczyk and Hedges 1983:265). Faience was treated as a pottery craft and considered less as worked malleable stone as it had been before the

[1] This is not without controversy. The Libyans did introduce a foreignness into Egyptian society by keeping their own titles, depicting Libyan functionaries with the Libyan symbolic feather and enforcing Libyan feudal state order centered on personalities rather than institutions (Schneider 2010:156). A similar argument could be made for the Kushite Dynasty.

Late Period (Nicholson 2012; 2013:148). This idea was certainly in place by the Ptolemaic Period (ibid.).

2.3 Egyptian Faience Chronology

A faience chronology is included to illustrate a change in cognition and technology of faience between the New Kingdom and the Ptolemaic Periods which will have a bearing on faience analysis. There is evidence of various faience production sites related to the Late through Roman Periods (see Maps 1, 2 and 3, and Table P-1 in the preface). Analytical faience clusters based on element/oxide components could represent workshops, the source of raw materials (e.g. sand and alkali) and processing used for production (e.g. addition of clay to facilitate forming).

Egyptians referred to faience as “tjehnet” (alt. spelling “thnet”) and less commonly “ḫsbḏ” (lapis lazuli), both words being related to scintillation and luminosity (Bianchi 1998:24; Nicholson 1993:9; Nolte 1969, cited in Nicholson and Peltenburg 2000:179). Stone was the first glazed Egyptian material (Nicholson 2012:12-13). Egyptian faience was possibly first constructed from the debitage of soft stone bead and amulet carving (Vandiver 1983:A6). Faience was considered a malleable stone that provided quick formation (moulding versus carving), the capability to produce large objects, and uniform production of multiple copies; characteristics lacking in carved stone (Nicholson 2012:15-16; Nicholson 2013:16). The production of faience was technologically conservative during the pharaonic periods; innovations (e.g. new colourants) and changes to production methods were slow to change in the 4,000+ years of its production (Vandiver and Kingery 1986:25, 31; see Table P-1 in preface). Faience of the Predynastic Period (prior to 3200 BC) consisted of blue and green copper coloured glazed beads and amulets (Kaczmarczyk and Vandiver 2008:58; Vandiver 1983:A11) (Fig. 2-1). Glazing technology could have consisted of application, cementation or efflorescence based on experimentation (ibid.). The Early Dynastic Period (3200-2686 BC) incorporated the same technology with an emphasis on efflorescence and with additional faience forms including figurines and small vessels (Kaczmarczyk and Vandiver 2008:58) (see Fig. 2-1). The Old Kingdom (2686-2160) and First Intermediate Period (2160-2055 BC) introduced turquoise copper blue glaze, manganese black and brown glaze and white as produced from the exposed faience body and the continued manufacture of beads, small vessels and figurines (ibid., p.59; Vandiver 1983:A11) (see Fig. 2-1). Core forming, luting and the use of kiln setters, calcium carbonate as a non-wetting kiln surface and all three glazing

Fig. 2-1: This is a representative selection of Predynastic Period (prior to 3200 BC), Early Dynastic Period (3200-2686 BC), Old Kingdom (2686-2160 BC) and First Intermediate Period (2160-2055 BC) faience. Objects A are two Predynastic Period blue-glazed non-descript faience fragments (UC73088). The blue glazed bowl (B) is attributed to the Early Dynastic Period (Dynasty 1; UC41282). The glassy glaze is patchy at best. These pieces were most likely glazed through efflorescence. Most of the colour on the small bowl is likely from the upper surface of the interaction layer (IAL). Object C is an Old Kingdom green-glazed barrel bead (Dynasty 6; UC20506). Object D is a First Intermediate Period small blue-glazed cosmetic vessel (Dynasty 11; UC41434) exhibiting a glassy glaze surface. The beaded collar (E; UC31716) is composed of blue faience cylinders in original ordering and show variation in blue-glazed copper-based colours. It is attributed to the First Intermediate Period (Dynasty 1). The large scale is associated with objects A-D. All photographs are licensed under a CC By-NC-SA license (A-E © 2018 UCL).

techniques is evident in the Middle Kingdom (2055-1650 BC) and Second Intermediate Period (1650-1550 BC) (Kaczmarczyk and Vandiver 2008:59). Hippos and hedgehogs were the dominate animal figurines produced (ibid.) (Fig. 2-2). The repertoire of colours and objects for faience multiplied during the New Kingdom (1550-1069 BC) (Fig. 2-3) just as Egyptian glass was introduced suggesting a close link between the crafts, possibly to economize on resources (Friedman 1998:17; Kaczmarczyk and Vandiver 2008:59-60; Nicholson 1993:17, 47; Vandiver 1983:A7). Red, yellow, opaque white and various shades of blues and greens were added to the existing blues, greens, black and brown colour palette (Petrie 1910; Tite and Shortland 2008:206; Vandiver 1983:A7).

Traditional raw material sources were no longer utilized during the Third Intermediate Period (1069-664 BC) (Fig. 2-4) and the faience colour palette was greatly reduced from what it was during the New Kingdom (Kaczmarczyk and Hedges 1983:260). The chemistry of Egyptian faience changes during this period as the use of cobalt (dark blue) and antimony (green) was greatly reduced (Kaczmarczyk and Hedges 1983:259; Nicholson 1993:37) resulting in a loss in colour variability (e.g. yellows and ultra-marine blues). Glass fell out of favour partly because of increased interest for glassy faience (Kaczmarczyk and Hedges 1983:260). Plaques, chalices and shabtis were the dominant forms.

The traditional Egyptian art genre was re-established during the Late Period (664-332 BC) and available colours increased with the inclusion of apple green, yellow, and other shades of green based on antimony and lead (Kaczmarczyk and Hedges 1983:265; Nicholson 1993:39). Bowls, vases and statuettes were produced in much greater quantities from the Late Period (Fig. 2-5) to the end of the Roman Period than in the preceding periods (Kaczmarczyk and Vandiver 2008:60). Application glazing was prominent but cementation and efflorescence glazing were still used and of high quality (Nicholson 1993:39). Black faience was formed more commonly through reduced firing conditions with iron, replacing manganese used in prior periods (Kaczmarczyk and Hedges 1983:269).

Vandiver (1983:A124) suggested the use of the wheel during the Late Period. Nicholson and Peltenburg (2000:185) suggest it was probably in conjunction with moulding to smooth the interiors of vessels; the thixotropic nature of the material would not lend itself to be free-thrown without binders (e.g. clay, resin) for which there is currently no evidence. Griffin (2002:332-333) found high levels of calcium in a finely carved Late Period shawabti

Fig. 2-2: This is a selection of Middle Kingdom (2055-1650 BC) and Second Intermediate Period (1650-1550 BC) faience. The blue-glazed carinated bowl sherd (A; UC45215) with purple-black hieroglyphic inscription is ascribed to the Middle Kingdom. The inscription is most likely imparted with manganese which can be used to produce purple and 'black' in faience glazes. The 'black' colour is actually a very deep hue of purple. The green-glazed hedgehog (B; EA22873) with black details and base edge is associated with the 12th Dynasty. The blue-glaze faience hedgehog (C; UC8661) with black-glazed dots in relief on body and a black-glazed base is associated with the Late Middle Kingdom. Some of the glaze has spalled revealing the body substrate below. The green-glazed (D; EA35004) and blue-glazed (E; EA59777) hippos both have black lotus patterns and are ascribed to the Middle Kingdom. Object F is a Second Intermediate Period blue-green glazed vessel (UC45068) with flared rim and rounded base. Object G is a blue-glazed vessel basal sherd (UC8498) with exterior darker blue triangles and is also attributed to the Second Intermediate Period. The large scale is associated with objects A-C and F-G. No scale was provided for objects D and E. All photographs are licensed under a CC By-NC-SA license (A, C, F-G © 2018 UCL; B, D and E © The Trustees of the British Museum).

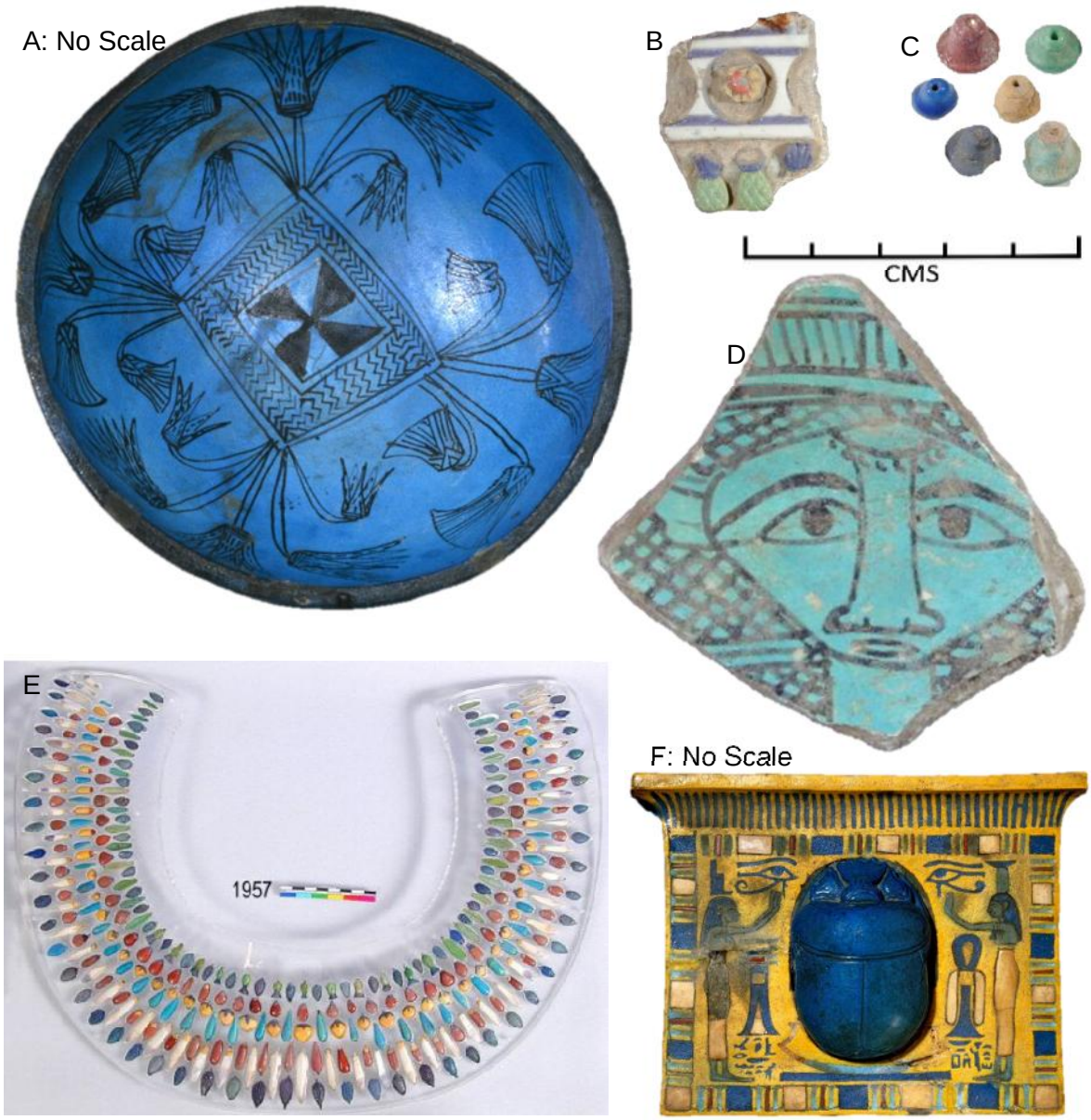

Fig. 2-3: This is a selection of New Kingdom (1550-1069 BC) faience. Object A is a blue glazed dish (18th Dynasty; EA4790) with manganese decoration showing lotus flowers surrounding a pool. The rim is coloured with manganese black. Object B is a faience bowl sherd (18th Dynasty; UC6777) with white background with a red-centred yellow rosette in a depression above three cornflowers with blue blossoms. The six faience beads (C; UC23723) of various glaze colour (red, yellow, purple, blue and two green) represent calyxes and are associated with the 18th Dynasty. Object D is a blue-glazed faience bowl sherd (UC38094) with face of Hathor in the interior. Object E is a reconstructed bead necklace (18th Dynasty; UC1957) consisting of 335 beads (83 grape bunches, 47 white petals, 57 red petals, 27 red dates, 30 yellow mandrakes, 13 yellow dates, 43 turquoise pendants, 12 green and blue corn flowers, 23 green palm leaves). Object F is a faience breast-plate (pectoral) with central heart scarab (19th Dynasty; EA7865). The large scale is associated with objects B-D. No scale was provided for objects A and F. E is provided with a scale. All photographs are licensed under a CC By-NC-SA license (B-E © 2018 UCL; A and F © The Trustees of the British Museum).

Fig. 2-4: This is a selection of Third Intermediate Period (1069-664 BC) faience vessels. Object A is a dark blue glazed faience bowl (22nd Dynasty; UC28740) decorated in black with three fish sharing a head. Object B is a blue-glazed chalice (21st Dynasty; EA26226) with bowl in the form of a lotus. Object C is a blue-glazed situla (21st Dynasty; EA17402) with dark blue painted registers. The scale applies to the bowl (A). No scale was provided for objects B and C. All photographs are licensed under a CC By-NC-SA license (A © 2018 UCL; B and C © The Trustees of the British Museum).

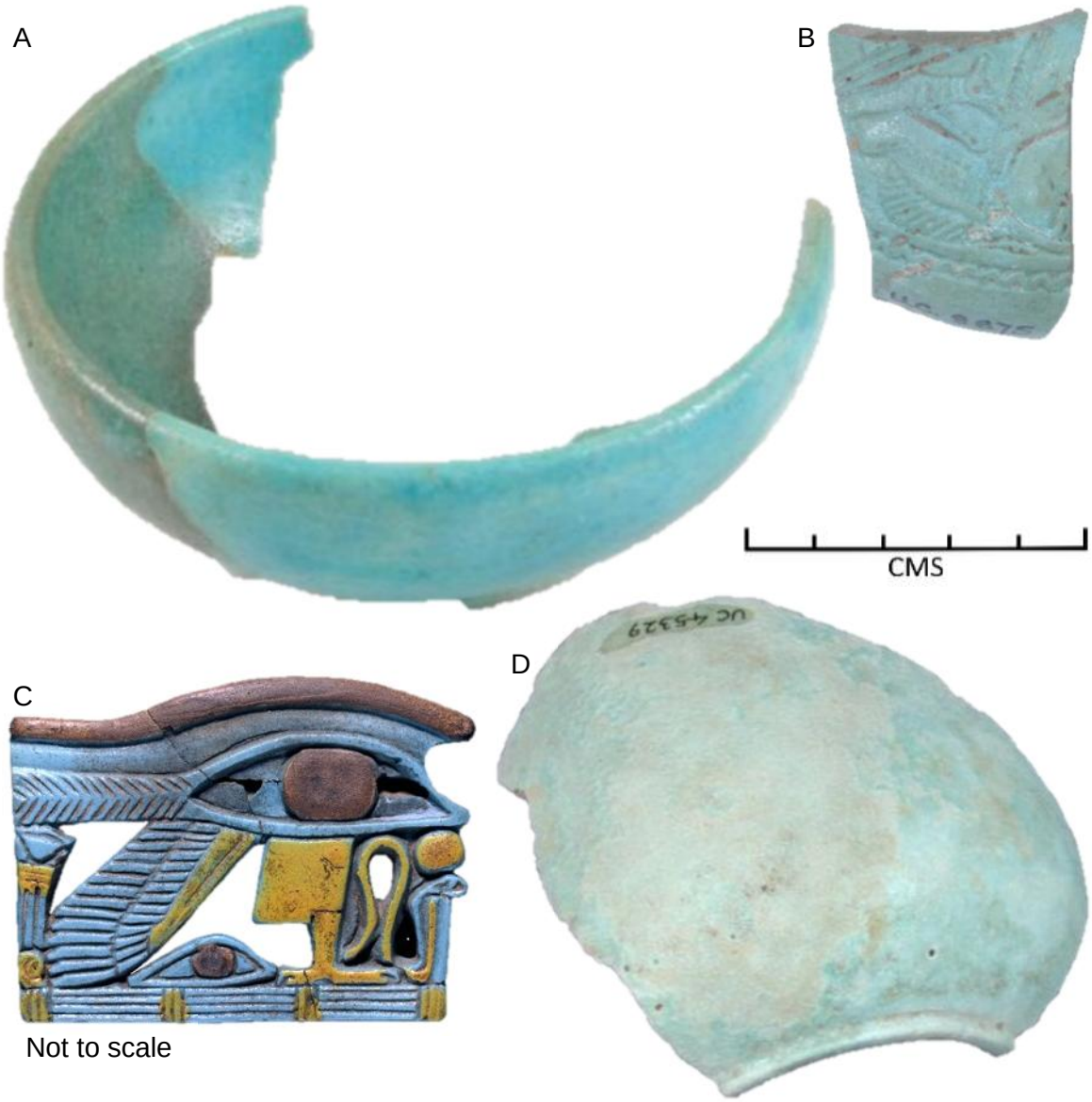

Fig. 2-5: This is a selection of Late Period (664-332 BC) faience objects. Object A is a partially reconstructed blue-glazed faience bowl (Dynasty 30; UC42841) consisting of three adhered sherds. Object B is a blue-glazed faience vessel sherd (26th Dynasty; UC8875) with a hunting scene in relief showing a dog attacking an oryx. Object C is a Wedjat eye amulet (26th Dynasty; EA29222) with pale turquoise blue with yellow and black glazed details. Object D is a wide-shouldered blue-glazed faience vessel sherd (UC45329). The scale is associated with objects A, B and D. No scale was provided for object C. All photographs are licensed under a CC By-NC-SA license (A, B and D © 2018 UCL; C © The Trustees of the British Museum).

and two fine vessels. The calcium may have been intentionally added to improve the prefired working qualities (ibid.).

Naucratis is the best known Late Period faience workshop site having first been identified by Petrie (1886:36) as a ‘scarab factory’ who found a great quantity of moulds and scarabs, tiles and vases. Pottery kilns were more recently uncovered at this poorly preserved site; two mounds, Kom Hadid and Kom Ge’if, were excavated between 1980 and 1984 (Coulson and Leonard 1981; Leonard 1998:1). Faience was recovered in small fragments and consisted of monochrome and polychrome white, blue and yellow tableware examples with some use of green and brown (Leonard 1998:195-201). Some sherds appear moulded.

The Ptolemaic Period (332-30 BC) witnessed a further ingress of Greek decorative sensibilities towards faience with appliques of satyrs, pillars and altars (Nenna and Seif el-Din 2000:19) but sometimes with subtle homage paid to the pharaonic period in the form of Bes appliques (Bianchi 1998:28) (Fig 2-6). Whereas in the past it was thought of as stone, faience was now treated more as a ceramic with the introduction of pottery techniques such as the use of saggars, high relief moulding, use of appliques and the abundant use of application glazing (Nenna and Seif el-Din 2000:20; Shortland and Tite 2005:31,38; Vandiver 1983:A11, 124). Colour variability of the glazes increased during the early Ptolemaic partly because of the reintroduction of cobalt and its associated blues and violets but became less diverse again during the late Ptolemaic and into the Roman Period (Nicholson 1993:41). The glaze colours were distinct from those use in the pharaonic periods and moulded vessels were generally monochromatic tones of blue or green, or two-toned polychromatic with lighter colours such as yellow on top to emphasize relief (Mao 2000:187, 196; Mao 2001; Shortland and Tite 2005:31, 38).

Memphis represents the most studied of the faience production sites during the Ptolemaic-Roman Periods (332 BC - AD 395). Petrie (1909;1911) was the first to associate Memphis with faience production having found kiln remains, wasters and kiln furniture. Further evidence was provided more recently with the recovery of additional materials from kilns (Nicholson 2002 and 2013). Saggars may have been devoted to biscuit or glost firings based on saggar diameter and the presence of glaze or lime (Nicholson 2013:80-81). Memphis is actually two sites, Kom Qalama and Kom Helul. Kom Qalama is associated with the Ptolemaic and Kom Helul was used throughout both periods (Nenna and Nicholson 2013:133). Other furnace sites of the period include Buto

Fig. 2-6: This is a selection of Ptolemaic Period (332-30 BC) faience objects. Object A is a blue-glazed faience bowl (UC64937). Object B is a blue-glaze oinochoe (wine container) with decoration in high relief (1856,1226.192). Object C is a blue-glazed faience sherd (UC2333) with decoration in high relief. Flowers located above the figure are composed of a lighter blue glaze. Object D is a blue and green glazed faience sherd (1910,116.17) with decoration in relief. Object E is a blue-glazed faience sherd (2001,0429.1) and a possible effigy adorno of Ptolemy IV. Object F is a green-glazed beaker (1888,0601.39) with decoration in low relief. The upper portion of the vessel has been conserved/restored. The scale is associated with objects A and C. No scale was provided for objects B and D-F. All photographs are licensed under a CC By-NC-SA license (A and C © 2018 UCL; B and D-F © The Trustees of the British Museum).

where two kilns were revealed, one of which was similar to the kilns at Memphis and may have been associated with faience vessel production (Charlesworth 1972:45). Wasters, cone setters, and a crucible containing copper traces, probably used as part of the glaze processing, were recovered (ibid.). Vessel fragments were found at the Ptolemaic site of Arthribis and there is evidence that amulets and statuettes were produced there as well (Mysliwiec 1996:35-36). A faience workshop is suggested by the presence of over-fired fragments, wasters and cone setters still attached to some of the vessel fragments (Welc 2011:248). An unglazed cracked bowl with cone setters still attached (Welc 2013:724-725 (Fig. 3)) is evidence of a 2 step firing process (bisque and glost firings). The finds were recovered in close proximity to pottery workshops and where coroplastic figures were worked (Nenna and Nicholson 2013:133).

Utilitarian ware and figurine production expanded as faience became more standardized during the Roman Period (30 BC – AD 395) (Nenna and Nicholson 2013: 133) (Fig. 2-7). Faience vessels were thicker and larger, bodies were less compact and friable and applied glazes were thicker (Nenna and Seif el-Din 2000:23, 25). Decoration, when used, was bolder than the material from the previous period and the selection of colours and creativity in decoration were reduced (Nicholson 1993:41; 2013:148; Shortland and Tite 2005:31). The significant use of the wheel, a production technique aligned with the pottery industry, has been suggested for this period (Nenna and Seif el-Din 2000:22) but actual evidence is still lacking (Nenna and Nicholson 2013:135, 138).

Terenouthis, an early Roman Period site, revealed two potential workshops (Nenna and Seif el-Din 2000:39-40). Artefacts include saggar fragments, statuette moulds, frit blocks, setters and clay rolls. Main products of the site are simple dishes and statuettes. Work at Elephantine (early Roman) revealed simple glazed bowls, plates, lids and statuettes (Rodziewicz 2005). Alexandria is mentioned by Vitruvius (Book VII, Chapter XI; see Morgan 1914:218-219) as the site of discovery for making Egyptian blue and faience objects have been found in the vicinity but there is no evidence of workshops to date (Nenna and Seif el-Din 2000:32-33, 40). Another site that may eventually reveal faience workshop evidence is Schedia, near Alexandria, where a craft quarter has been identified (Bergmann and Heinzelmann 2004:4).

Fig. 2-7: A selection of Roman Period (30 BC – AD 395) faience objects. Object A is a blue-glazed faience bowl (UC33515) with floral design in high relief. Object B is a blue faience vessel sherd (UC33452) with yellow and green details in relief. Object C is a blue-green glazed faience vase (EA62639) with decoration in relief. Object D is a blue glazed faience vase (EA24677) with decoration in low relief. The scale is associated with objects A and B. No scale was provided for objects C and D. All photographs are licensed under a CC By-NC-SA license (A and B © 2018 UCL; C and D © The Trustees of the British Museum).

2.4 Manufacture of Faience

In the simplest terms, the manufacture of faience is the production of a glaze-covered quartz body composed of an agglomeration of raw materials collected from various sources, formed, glazed and fired. It is important to understand the process and the materials used in the construction of faience. The process of making faience (Fig. 2-8) can be expanded to include choices in material for kiln production and the fuels that fire it, or on the series of various plants that can be used to determine an appropriate source of potash.

2.4.1 Faience Chemical Composition

Materials present in a faience glaze can provide information regarding source and production method. Knowledge of the elements of composition in a glaze is important when correlations occur between some elements. These correlations can indicate alkali, colourant and material source (e.g. ores) choices made by the craftsmen. The elements typically encountered with faience glazes and bodies represent the network former (silicon), network modifier (e.g. sodium and potassium), network stabilizer (calcium), colourant (e.g. copper and/or cobalt) and unintended inclusions (Table 2-1).

Glass and glaze are amorphous vitreous materials; they lack recurring structures that can be found in crystalline materials such as quartz or metal (Henderson 2000:24; 2013: 2). Silicon oxide (SiO_2) is the network former and, in a pure crystalline structure, the silicon combines with four oxygen atoms to form a tetrahedron ($(SiO_4)^{+4}$) (Henderson 2013:2). Soda is a network modifier and will ionically bond with network oxygen disrupting the bridging atoms and the crystalline network (Henderson 2000: 25; 2013: 3; Pollard and Heron 2008:150-1). Calcium oxide (CaO) is a network stabilizer, with a bonding strength much greater than sodium, which strengthens the glaze structure and reduces dissolution in water (Freestone 1991:40; Henderson 2013:3, 5). The colour is imparted by either transition metal ions or particulates that absorb and reflect specific frequencies of light providing the glaze with colour (Doremus 1994, cited in Henderson 2013:65).

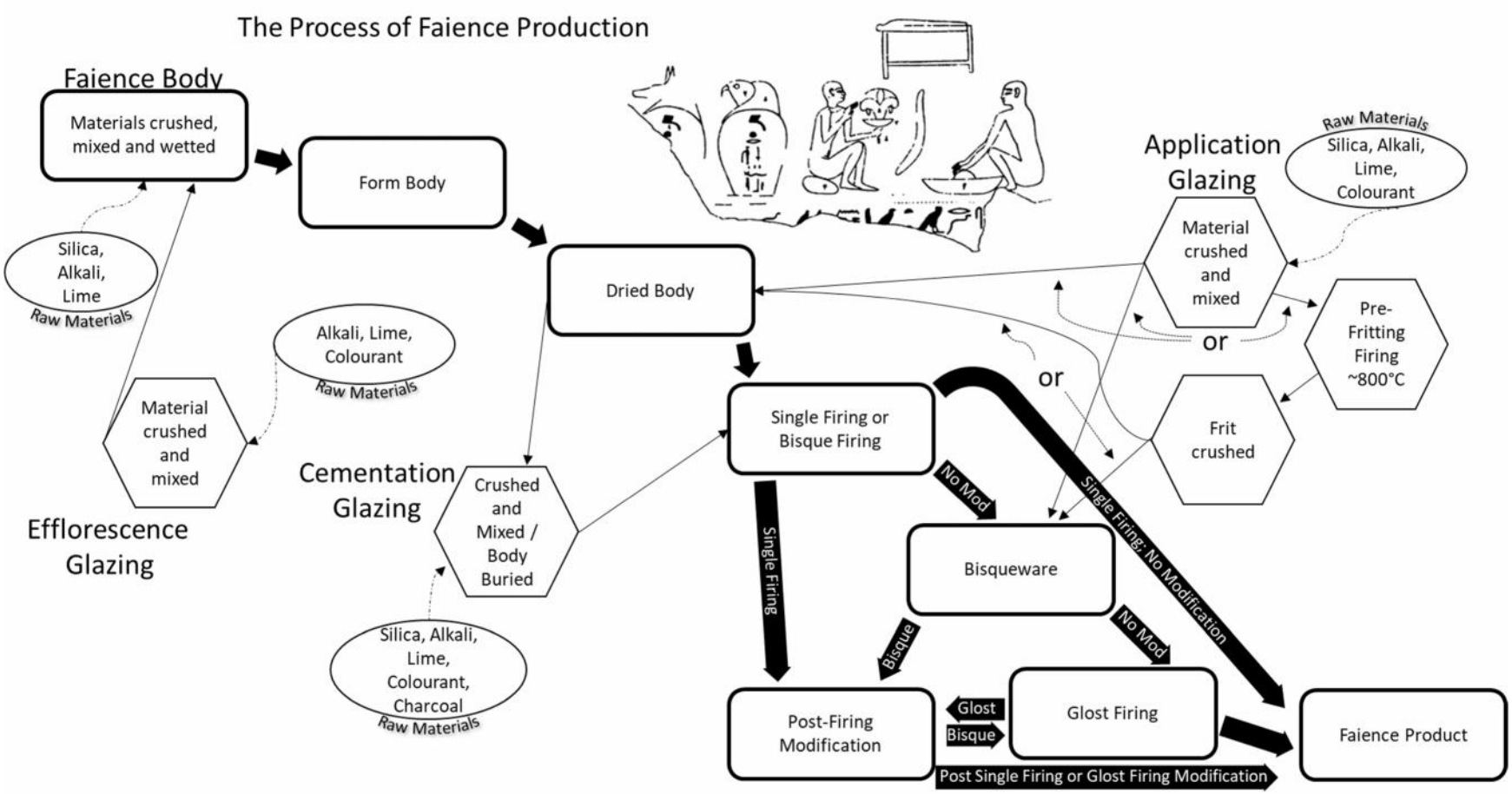

Fig. 2-8: The process of faience production exhibiting the three glazing techniques. The process can involve a single glazing technique or any combination. The glaze mixture is added directly to the wet body paste for efflorescence glazing. The unglazed dried body is immersed in a glaze mixture for cementation glazing. The application glazing mixture can be added to an unfired body or to a bisque ware body in either a raw state or as a prefritted glaze powder. Modification of the faience object occurs during initial forming of the body and after firing a bisque ware object or a fully glazed object such as a single fired glazed object or one that was produced through bisque and glost firings. Thick solid black arrows show the progress of the body through the production process. The thin black lines indicate glazing processes. The thin dashed lines indicate choices in the glazing process. The Egyptian scene, from the tomb of Aba (26th Dynasty; Davies 1902, Plate XXV), may show two craftsmen making faience.

Table 2-1: Elements and their possible sources detected in Egyptian faience from the New Kingdom and later periods.

Egyptian Faience Element Sources	
Aluminium	Sand (epidote ($Ca_2(Al,Fe)_3(SiO_4)_3OH$)), feldspars, clay, plant ash and New Kingdom cobalt ores.
Arsenic	Arseno-Sufide Ores containing Cobalt and antimony-arsenic ores (neither common post-New Kingdom).
Barium	Sodium-rich feldspars, calcium deposits, sand, clay, Nile alluvium and in ores (psilomelane ($Ba_2Mn_5O_{12}$).
Bismuth	Traces in copper sulfide ore (Cu_2S) and also occurs with antimony in bindhymite ($Pb_2Sb_2O_6(O, OH)$).
Bromine	Evaporites and carbonates
Calcium	Sand (epidote ($Ca_2(Al,Fe)_3(SiO_4)_3OH$) and calcite ($CaCO_3$)), shell, feldspars, bone, plant ash and dolomitic limestone (positive correlation with magnesium).
Cobalt	Mined Ores (cobalterferous alum (associated with Mn, Zn and Ni during New Kingdom, during Late - Roman Periods associated with Fe but not Mn, Zn nor Ni) and other ores (cobalite (sometimes associated with Zn)($Co_3(AsO_4)_2.8H_2O$, (CaAsS), skutterudite ((Co, Ni, Fe)As_3), bieberite ($CoSO_4 . 7H_2O$), trianite ($2Co_2O . CuO . 6H_2O$) and absolane (a mixture of Mn and heterogenite (CoOOH)).
Chromium	Sand (chromite ($FeCr_2O_4$))
Copper	Leaded Bronze (blue and green glazes), sand or copper tool contamination.
Iron	Sand (olivine (Mg, Fe2SiO4), chromite ($FeCr_2O_4$), epidote ($Ca_2(Al,Fe)_3(SiO_4)_3OH$) and ilmenite ($FeTiO_3$)), wood and plant ash, copper sulfides of Eastern Desert and ferruginous manganese ore.
Potassium	Wood and plant ash, sand
Magnesium	Sand (olivine (Mg, Fe_2SiO_4)), wood and plant ash
Manganese	Sand (pyrolusite (MnO2)), manganese ore (psilomelane (($Ba, H_2O)_2Mn_5O_{10}$)) and cobalterferous alums of New Kingdom
Sodium	Natron (Na_2SO_4) and plant ash
Nickel	Rare, Cobalterferous alums of New Kingdom
Lead	Leaded Bronze, sand and copper ores (prior to 19th Dyansty)
Phosphorus	Plant ash
Rubidium	Sand and potentially other sources
Sulfur	Natron (Na_2SO_4), plant ash and sulfide, copper-sulfide (Cu_2S) and lead sulfide (PbS) ores.
Antimony	Leaded Bronze, antimony ore (stibnite (Sb3S) and copper ores (prior to 19th Dynasty). Frequently associated with bismuth
Silicon	Sand, quartz, pebbles and plant ash
Tin	Bronze, impurity in some lead ores and copper ores (prior to 19th Dynasty)
Strontium	Shell, carbonates and plant ash
Titanium	Sand (ilmenite ($FeTiO_3$), sphene or titanite ($TiSiO_5$) and rutile (TiO_2)
Vanadium	Lithic fragments
Zirconium	Sand (zircon ($ZrSiO_4$)) and lithic fragments
Zinc	Sand, copper ores of the Eastern Desert and cobalterferous alums of New Kingdom

Table 2-2: Faience colours and associated colourants

Faience Colours and Associated Colourants	
Colour	Colourant
Metal Ion Based	Transition Metal Ions (M^{+2})
Blue	Copper*
Dark Blue	Cobalt*
Green	Copper (intentional or result of weathered blue)*, Lead antimonate ($Pb_2Sb_2O_7$) and copper***
Apple Green‡	Copper, with high levels of lead and tin**
Indigo/Violet‡	Cobalt, iron and copper**
Particulate Based	Particles
Purple	Manganese*; also iron and copper**
Black	Manganese oxide (MnO) or reduced iron oxide (Fe_3O_4)*
Red	Oxidized iron oxide (Fe_2O_3)*
Yellow	Lead antimonate ($Pb_2Sb_2O_7$)*
Brown	Weathered red, black or purple*; Manganese, iron and copper**
References: *Vandiver (1998: 43-45), **Nenna and Nicholson (2013: 135) and ***Kaczmarczyk and Vandiver (2008:78)	

The glaze colourant represents the widest variety of elements for a single purpose found in faience. Metal ions produce transparent glazes and particulates form opaque glazes (Vandiver 2008:43) (Table 2-2). Metal ions will chemically bond with other cations to form silicates or oxides in a glaze; the colour being dependant on the frequencies absorbed and those allowed to be reflected or to pass through a glaze. Particulates do not chemically bond with other cations but are held in suspension within the glaze and cause the light to be reflected and scattered. The majority of colours encountered as a part of this research are turquoise blue and ultra-marine blue, however purple, yellow and green glazed archaeological glazes were analysed to provide analytical contrast. Some information is provided for black, brown and red glazes but this work does not represent a comprehensive colourant treatise across all periods. Vandiver (2008) and Kaczmarczyk and Hedges (1983) provide discussion concerning all colours.

The colour characteristics of glaze depend on several factors: the glass batch, occurrence of colourants, kiln atmosphere, kiln heating cycle and peak temperature (Henderson 2013:66). The transition metal ions responsible for colour interact with several oxide ions forming either tetrahedral (acting as a network former) or octahedral (acting as network modifier) arrangements (Kaczmarczyk and Hedges 1983:140; Pollard and Heron 2008:159-162). The introduction of many other cations renders the

structure amorphous and influences the chemical environment changing the field strength of the colourant which affects the final colour (Kaczmarczyk and Hedges 1983:140; Henderson 2013:67; Pollard and Heron 2008:161). The energy shells of the transition metal colourants are partially filled allowing interaction with other ions (e.g. SiO^{+4}) that distort the chemical environment. In the presence of energy (i.e. light), the lower shell electrons absorb different wavelengths (i.e. energy) to fill the unoccupied higher energy shells thereby changing the frequency and thus the colour observed (Henderson 2013:67). Elevated temperatures favour formation of tetrahedrons and longer wave-lengths (Kaczmarczyk and Hedges 1983:141). Greater kiln temperatures and longer firings at high temperature allow gases to escape resulting in less porous glazes which will absorb light differently than porous glazes (Henderson 2013:68).

Silica forms the bulk of the body of faience and is derived from sands or ground quartz pebbles as indicated by its purity (i.e. pebbles tend to have less inclusions) (Shortland and Tite 2005:35; Vandiver 2008:37-38). The parent material of sand is stone and it is conceivable that, at some point in its history, some faience material was derived from the debitage of worked stone (Vandiver 1983:A6). Quartz-α is the main crystalline form of silica at room temperature but at 570°C transforms to its β form and increases in volume by 2% (Henderson 2000:133; 2013:56). Tridymite is a polymorph of silica that forms at temperatures between 870°C and 1470°C, and cristobalite is another polymorph of silica that forms above 1470°C (ibid.). The presence of various polymorphs can be used to determine temperatures obtained during the firing process. Toffolo et al. (2013:3631) determined that faience was fired to a temperature between 870°C and 1100°C due to the presence of tridymite and the lack of cristobalite as determined through Raman micro-spectrometry.

Silica procured from ground quartz pebbles exhibit greater purity than that from ground sand. The presence of iron, alumina, magnesia, potash, lime and titanium oxides in measurable amounts characterize the impurity of silica sands (Vandiver 2008:37; Brill 1999; Hatton 2005; Nicholson et al 2007; Turner 1956; Tite *et al*. 2008) (Tables 2-3 and 2-4). However, sands can be sifted and washed to remove the impurities (Kaczmarczyk and Hedges 1983:123). The colour of the body material is not a good indicator of the source material for this reason and because impurities can be introduced through other means (e.g. potash, grinding tools, moulds). Particle shape is not an indicator of pebble or sand origin as both would have to be ground to reach a fine particle size required for some of the faience encountered (Vandiver 2008:38).

Table 2-3: Chemical composition of Egyptian sands and pebbles (Parodi 1908:25-27 (cited in Lucas 1962:481); Brill 1999:474; Hatton 2005 (cited in Vandiver 2008:38); Shortland et al. 2007a:186; Turner 1956:281, 300 (cited in Lucas 1962:481 and Vandiver 2008:38). Totals are a mixture of normalized and raw data.

Chemical Composition of Egyptian Sands and Pebbles

Location	Code	Na_2O	MgO	SiO_2	Al_2O_3	P_2O_5	SO_3	Cl	K_2O	CaO	TiO_2	V_2O_5	MnO	FeO	CuO	ZnO	SrO	ZrO_2	Ag_2O	BaO	PbO	Fe-Al	Totals
Sands																							
Alexandria	Parodi 6		2.20	32.00						35.00												0.70	69.90
Amarna	AM43**	0.81	0.61	76.64	2.37				0.45	17.26	0.32			1.36									99.82
	AM44**	0.26	0.21	93.55	1.23				0.29	3.68	0.15			0.57									99.94
	Turner-1	0.30	0.80	60.50	2.30	0.10	0.10		0.70	18.90	0.40		tr	1.70									85.80
Aswan	Parodi 5		tr	93.80						0.70												3.60	98.10
	Turner-3(V)	bd	bd	95.65	3.66				na	0.68	na			na									99.99
Bacchias	Brill-321	0.51	0.45	84.10	3.15		0.01	0.03	0.72	4.81	0.40	0.01	0.03	1.68	0.00	0.01	0.01	0.05	0.00	0.01	0.01		95.97
Dakhia	H7*	0.02	0.06	98.11	0.39				0.08	1.01	0.03			0.30									100.00
Eshmunein	Parodi 3		0.60	96.70						1.90												0.60	99.80
Fayum	Parodi 2		0.10	95.20						1.90												1.90	99.10
	Turner-4		0.10	97.80	1.00					0.40	0.20		tr	0.30									99.80
Giza	Parodi 4		tr	82.40			0.20			8.40												1.50	92.50
	Turner-1(V)	0.21	bd	89.13	1.57					9.09													100.00
Karnak	Parodi 1		1.20	83.60						12.00												1.30	98.10
	Turner-2(V)	bd	1.25	85.17	1.34				na	12.23													99.99
Kharga	H8*	0.08	0.08	97.78	0.55				0.17	1.15	0.02			0.17									100.00
Luxor	Turner-2	1.20	2.40	72.70	8.20	0.10	0.10		1.10	4.90	1.20		0.10	5.60						0.20			97.80
Maadi	Turner-3			97.90	1.40					0.20				0.20									99.70
Sinai	9*	0.13	0.36	93.93	1.25				0.25	3.00	0.20			0.87									99.99
	11*	0.02	0.02	95.80	3.75				0.01	0.25	0.09			0.06									100.00
	14*	bd	0.06	97.80	0.42				0.02	1.38	0.03			0.29									100.00
	15s3*	0.01	0.01	99.77	0.13				0.01	0.02	0.01			0.04									100.00
	Turner-5			99.20	0.50					0.30				0.10									100.10
Wadi Natrun	WN31*	0.04	0.03	99.34	0.27				0.11	0.10	0.01			0.10									100.00
	WN38*	0.09	0.04	99.12	0.35				0.14	0.13	0.02			0.11									100.00
Pebbles																							0.00
Amarna	Brill-1298	0.05	0.01	99.83	0.05				bd	0.05	0.01			0.01									100.01
	Brill-1299	0.05	0.01	99.79	0.05				0.00	0.05	0.01			0.05									100.01
Sinai	H13*	bd	bd	99.90	0.03				0.01	0.04	bd			0.02									100.00

Note: Brill (1991), Parodi (1908), Turner (1952) as indicated. All others are Hatton (2005) as cited in *Vandiver 2008:37 and **Shortland 2007:186.

Table 2-4: Stone and Thomas (1956: Table III, p.65) Optical Emission Spectroscopy Results for Egyptian Sands.

Stone and Thomas (1956) Optical Emission Spectroscopy Results for Egyptian Sands																
Sample	Location	Na	K	Li	Ca	Sr	Pb	Cu	Mg	Fe	Mn	Al	Si	Ti	Ni	Sb
68	Amarna	3	4		3	4		5	4	3	5	4	1	4		
67	Cairo	4	4	5	1	3	5	4	3	3	4	2	1	3	5	5
69	Luxor	4	4	4	3	4	5	5	4	3	4	2	1	3	4	
70	Aswan	5	4		3	4		5	4	3	5	4	1	5	4	5
Key:																
1 = 100-10 wt%; 2 = 10-1 wt%; 3 = 1-0.1 wt%; 4 = 0.1-0.01 wt%; 5 = 0.01-0.001 wt%																

Sodium and potassium are alkali metals and the most common alkali components in a glaze. The alkali component acts as a flux to lower the melting point of silica (1710°C) resulting in sintered silica edges that melt together providing the body with cohesiveness after firing. The source of the alkali is natron, a natural evaporate composed of $NaHCO_3$ and Na_2CO_3, and/or soda-rich plant ashes (*Salicornia* or *Salsola*) (Kaczmarczyk and Hedges 1983:22; Rehren 2008; Shortland 2004; Tite et al. 2006). Both alkali sources introduce sodium as the major component (Vandiver 2008:38-41) and include potassium, calcium, magnesium, phosphorus, sulphur, chloride, silicon, aluminium and iron in various quantities (Table 2-5). Like sand, this is a source for trace elements in faience. Potassium is usually introduced into the glaze melt through alkali selection but it can be an impurity in the sand.

Calcium is a stabilizer and cements the prefired faience body so that it is easier to work and handle (Nicholson 1998:51). Griffin (2002: 332) found two Late Period faience objects of exquisite detail with calcium-rich consistencies (~6% compared to typical ~2%) in the body components indicating a possible intentional addition to increase workability. Ptolemaic glazes have greater concentrations of calcium and a narrower gap between mean and median indicating a controlled intentional addition of calcium (Kaczmarczyk and Hedges 1983:24). Replication performed by Griffin (2002:333) determined that the addition of 5 wt% quicklime to the body material resulted in a dried body that could be carved like steatite, and 10 wt% resulted in a dried faience body that could be handled with considerable force. Quicklime (CaO) is formed by burning lime ($CaCO_3$) thereby reducing the calcium carbonate to form calcium oxide and carbon dioxide.

Copper has been used as a blue-green colourant for Egyptian faience since the fourth millennia BC and provides a green hue when combined with greater amounts of potassium and chlorine, and blue when used alone (Kaczmarczyk and Hedges 1983:56-57; Vandiver 2008:44). Copper as a translucent green colourant exhibits a

Table 2-5: Chemical composition of selected alkali fluxes from natron recovered from tombs and plant material (species italicized) (from Brill 1999; Tite et al. 2006).

Chemical Composition of selected Alkali Fluxes					
(Normalized to 100%)		Egyptian Tombs			Taposiris Magna
	Barnug (Suaeda)	#1 (natron)	#2 (natron)	#3 (natron)	(*Anabasis articulata*)
Na_2O	43.40	51.30	61.64	67.13	48.95
MgO	3.90	0.39	0.61	0.74	2.00
SiO_2	5.10	0.51	2.89	3.23	0.80
Al_2O_3	1.50	0.10	0.88	0.76	0.50
P_2O_5	5.30				2.00
SO_3	8.20	7.21	10.64	10.75	4.20
Cl	20.00	39.49	21.51	15.36	34.93
K_2O	6.50	0.56	0.69	0.94	4.50
CaO	5.20	0.30	0.56	0.68	2.00
FeO	0.90	0.14	0.58	0.42	0.10

steady decline after the 18th dynasty; it is replaced by lead antimonate to produce an opaque green glaze (ibid.). Copper before the 19th dynasty came from local Egyptian copper ores which contained zinc, lead, arsenic, tin and antimony that can be used as markers to provenance the source. Copper is found in Egyptian sands at trace levels (Kaczmarczyk and Hedges 1983:56; Stone and Thomas 1956:65). Vitruvius states in Book VII of the *Ten Books on Architecture (Morgan 1914:219)* that copper was scraped from copper cores by using coarse files. El Goresy (2000) conducted analysis of pigments collected from well-dated provenances and found that arsenical copper scrap was used as a source of colourant between the 5th and early 18th dynasty, replaced for a short period with bronze scrap in the 19th dynasty which was replaced by leaded bronze scrap at the end of the 19th dynasty. Shortland and Tite (2005:35-36) conducted analysis of monochrome Ptolemaic/Roman faience and found low levels of tin (0.2-0.4% SnO_2) and lead (0.2-0.4% PbO) in ratios that matched the ratio of tin and lead used in contemporary leaded bronze objects supporting the hypothesis that scrap material was used as a source of colourant. Pliny the Elder in *Natural History* (34:26) (Bostock 1855) describes suspending copper over vinegar in a sealed cask and leaving it for several days. The scale that formed on the surface was scraped off and used as a colourant.

Chemically, the copper ions (Cu^{+2}) occupy octahedral sites which produce a turquoise blue (Vandiver 2008:44). A greener hue will result from the addition of potash and

chlorine, or the inclusion of ~1wt% of iron (ibid.). An increase in the copper content will shift the colour towards green (ibid.). Weathering can change the copper blue colour to green through the deposition of copper chloride or copper carbonate on the surface (ibid.). Schiegl et al. (1989:395) found copper carbonates on the surface of devitrified faience glaze of tiles from Saqqara which caused a loss in transparency and a shift from blue to green.

Cobalt is the strongest transition metal colourant (Henderson 2013:69). It is known as a blue, indigo and violet colourant starting in the New Kingdom Period (Kaczmarczyk and Hedges 1983:42). Cobalt is found in pre-New Kingdom Period glazes in small quantities but is assumed to be an impurity in copper ores (ibid., pp.42-43). A new cobalt source dominated by cobalterferous alum ($CoAl_2O_4$) associated with manganese, zinc, and nickel from the Western Desert was utilized during the New Kingdom Period (Kaczmarczyk 1986). The use of cobalt mostly disappears during the Third Intermediate Period but is reintroduced in the Late Period. However, the cobalt appears to be from a different source, possibly the Caucasus in present-day Iran, as the ore is less associated with aluminium and manganese, and more strongly associated with iron (Kaczmarczyk and Hedges 1983:47, 53, 267-8; Tite and Shortland 2008:206).

The occurrence of lead in faience glazes prior to the New Kingdom Period is sporadic. It is sourced from local galena (PbS) which contains sphalerite (ZnS) inclusions that can be used as a marker (Kaczmarczyk and Hedges 1983:110, 112). However, the presence of zinc is greatly reduced after the New Kingdom Period indicating a change in source for the ore (Kaczmarczyk and Hedges 1983:117-118). Lead was commonly added to faience glaze from the New Kingdom onward in the form of lead antimonate which gave the glaze a yellow to yellowish-green colour, or without antimonate which produced a red colour commonly used during the Roman Period (Kaczmarczyk and Hedges 1983:112, 115; Tite et al. 1998:114). Lead could enter the melt of blue and green glazes through the use of leaded bronze as the source of the copper colourant.

Kaczmarczyk and Hedges (1983:117) state that the levels of lead found in faience glazes for all periods are well below the quantities required to affect the mechanical properties of the glaze and they are insistent that lead was not introduced for this purpose. Mao (2000) found high quantities of lead in 20 Ptolemaic faience glazes that was not introduced as a colourant. Most of the consistencies are <5 wt% but much greater than the 0.05% figure indicated for post New Kingdom faience where the lead was incidental. Two glazes contained ~8 and 11 wt% lead coupled with low antimony. The antimony content in these were ~0.3%, much lower than the average 1.35% found

for Ptolemaic yellow glazes (Kaczmarczyk and Hedges 1983:97) indicating that the lead was not introduced as a typical colourant for these specific objects. Mao acknowledges that weathering depleted the alkali component leaving an artificially lead enriched glaze but the lead consistencies were too high for weathering to be fully responsible. Mao suggests the lead was intentionally added to the glaze to create a lead-alkaline glaze. The first recognized lead glazes in the Mediterranean region occur during the first century BC (Greene 2007:653-654). If these Ptolemaic glazes are lead-alkaline, they are the first reported lead glazes having occurred a few centuries before what is commonly accepted.

Antimony was an impurity in pre-New Kingdom faience that was probably introduced with copper. Its deliberate use in association with lead first occurs during the 18th dynasty (Kaczmarczyk and Hedges 1983:98). Use of antimony during the Third Intermediate Period greatly declined or was absent in the production of faience but reappears for use in yellows and greens during the Late Period (ibid., p.101).

Tin is considered an impurity associated with lead and sometimes copper in pre-New Kingdom Period glazes where it is rarely encountered (Kaczmarczyk and Hedges 1983:83). It was an intentional component in glazes after the New Kingdom Period where it appears in greater quantities associated with lead in yellows and greens, and copper in blues and greens (ibid., pp.84-94). The lead associations are probably due to a tin impurity in the lead source. The copper association is based on the use of bronze scrap as a colourant. For the blue and green glazes, a tin/copper ratio of 1-10% equates to bronze as being the source; tin >15% received a supplementary dose from some source, 10-15% and the precise origin of tin is unknown (Kaczmarczyk and Hedges 1983:91).

Manganese ions in an oxidized state (Mn+3) produced a purple coloured glaze (Vandiver 2008:44). Manganese is found in sand at 0.1% levels and less, and should not be considered intentional unless >0.1% (Kaczmarczyk and Hedges 1983:30). Manganese was associated with cobalt blue prior to the Third intermediate Period but was not a specific colourant until after the 20th dynasty. Manganese (0.06% - 0.42%) provides a reddish purple colour during the Ptolemaic and contains less than 0.02% cobalt oxide (ibid., pp. 31, 34).

Iron could be used as a colourant producing green-brown (Fe+3) or blue-green (Fe+2) as an ion or red and black as a particulate (Vandiver 2008:45). Iron-rich rock deposits in Egypt are extensive and its occurrence in sand derived from these rocks is understandable (Kaczmarczyk and Hedges 1983:35). It could also enter into the

faience glaze as an impurity in the sand or from the potash (ibid.). Iron impurities could produce changes to the colour of the glaze (e.g. blue to green) and it was in the interest of the faience worker to filter the iron out or use sources of purer silica when working with the susceptible colours (ibid.). Strong colourants such as cobalt will overpower the effects of iron.

Barium is associated with sand, limestone, Egyptian clays and alluvium, and manganese ores (Kaczmarczyk and Hedges 1983:106-107). The presence of barium in faience glazes can be attributed to sand impurities or contact with clay moulds. Detection of barium in faience glazes is uncommon but closely correlated with manganese. Therefore, glazes that contain manganese as a colourant are expected to have higher barium content. This is actually not the case with purple and violet glazes that incorporate cobalt and manganese indicating that these were added as a single ore and not as individual components (Kaczmarczyk and Hedges 1983:109).

There are other elements that play a minor role in the glaze structure but can still provide useful information. Titanium, in the form of rutile (TiO_2) and ilmenite ($FeTiO_3$), and vanadium are introduced into the glaze as sand inclusions (Kaczmarczyk and Hedges 1983:25). Ptolemaic Period glazes contained the most titanium and the least vanadium but this is probably because of the sand source and not technical considerations (ibid.). Chromium is one of the most abundant trace elements in Egyptian clay and chromite is a common mineral in steatite (Kaczmarczyk and Hedges 1983:29).The presence of chromium in faience glazes could be due to contamination with clay or steatite moulds in antiquity (ibid., p.29). Kaczmarczyk and Hedges (ibid.) suggest that any result >0.05% should be reanalysed, or considered a foreign import or fake. Nickel is uncommon in faience glazes unless associated with New Kingdom Period cobalt ore (Kaczmarczyk and Hedges 1983:55). Zinc can be an inclusion in sand at very low quantities (0.004%) but is more usually associated with copper ores of the eastern desert and lead ores of Egyptian or foreign sources which fell out of favour by the 20th dynasty having been replaced by low-zinc lead sources (Kaczmarczyk and Hedges 1983:64, 67). Strontium composes a very low percentage (~0.023%) as a sand inclusion. It is usually more associated with calcium in limestone deposits, calcareous sands and plant ash (Kaczmarczyk and Hedges 1983:75). Chloride and sulfur are major components of natron and potash and sulfur is found in galena (PbS) (Kaczmarczyk and Hedges 1983:125, 128). Aluminium and magnesium are impurities in the sand (Kaczmarczyk and Hedges 1983:136). Alumina quantities can be used to indicate source of quartz: <1% alumina suggests quartz pebbles whereas 1-2% suggest sand for body material (Shortland and Tite 2005:35). High

magnesia will indicate plant ash alkali source (Nicholson and Peltenburg 2000:187). Phosphorus is a common component of plant ash (Kaczmarczyk and Hedges 1983:137).

Sometimes other elements are detected that indicate possible usage and have little to do with the production of the faience. Silver has been found on faience seals that were probably mounted in silver, and the detection of gold on faience glazes is probably due to the object being partly covered in gold leaf (Kaczmarczyk and Hedges 1983:137).

2.4.2 Faience Forming Methods

The body of faience is composed of ground quartz sand or pebbles with a small amount of alkali flux and calcium to provide strength (Vandiver 1983:A18). Sometimes glazing mixture was added to the body to increase the amount of interparticle glass formed during firing (Griffin 2002:334; Vandiver 1983:A19). The particle size of the ground matrix has a direct influence on the paste during shaping and the final product (Griffin 2002:332); bodies with a fine paste will facilitate the imparting of more intricate details. The body particles of Roman faience are more course and less compact than Ptolemaic examples (Nenna and Seif el-Din 2000:17). An alkali is used as a flux to lower the melting point (1710 ºC) of the silica particles. The body only requires enough alkali to sinter the edges of the quartz grains so that they fuse together. The alkali is composed mostly of sodium with some potassium and other elements depending on source (see Section 2.4.4). It was introduced from evaporates such a natron or halophytic plant ash. Calcium stabilizes and increases the strength of the body after it has been fired. Some calcium is introduced with the sand but it is possible that calcium is intentionally introduced through other sources (e.g. limestone, crushed shell) (Griffin 2002:327, 332). The ingredients for the faience body were mixed together with water to form a paste. The amount of water is critical; too much water and the paste will slump, not enough and it will crack when pressure is applied (Vandiver 1983:A21). Vandiver (1982:167; 1983:A18) determined the average post-fired faience body to consist of 92-99% silica, 1-5% lime and 0.5-3% soda with small quantities of copper, aluminium, iron, magnesium, titanium and potassium oxides introduced as impurities.

The body was first worked while wet but could be re-worked in a partially dried state after the free water had evaporated. The shaping technology of faience evolved from scraping, grinding and modelling of the predynastic and Old Kingdom (2613-2181 BC), simple moulding and core forming of the Middle Kingdom (2040-1782 BC), to the use of complex moulds and possibly the potter's wheel during the Ptolemaic and Roman Periods (Vandiver 1983; Mao 2000, 2001; Nenna and Seif El-Din 2000:18-19). The

primary means of shaping in Memphis is free-hand forming and moulding (open and complex), sometimes in conjunction with luting individually moulded parts (Nicholson 2013:136). It has been suggested that clay or gum resin was added to the faience body to facilitate throwing on the potter's wheel, but there has yet to be archaeological evidence of the use of clays or other organic binders (i.e. gum arabic, resin) for this purpose (Griffin 2002:335; Kiefer and Allibert 1971:110-1; Mao 2001:20; Nicholson 2013:135; Tite et al. 1998:112; Vandiver 1983:A124). Throwing on a wheel without a binder is very difficult to impossible because of the thixotropic nature of unfired faience paste; it can be thick when static but becomes less viscous when agitated and can easily slump depending on the amount of water (Vandiver 1983:A21). The use of the potter's wheel is not unreasonable although its use would have probably been limited to delineating areas of decoration, creating simple lines or facilitating exterior moulding and allowing the jollying/smoothing of the interiors of open forms (Nicholson 1998:62; Nenna and Seif El-Din 2000:20).

2.4.3 Faience Glazing Methods

There are three main techniques for the glazing of faience: application, cementation, and efflorescence. Application glazing was used for the glazing of stone during the predynastic era (Beck 1932, cited in Vandiver 1983:A27). It is the assumed technique for all faience until efflorescence and cementation were proposed. Application glazing is used throughout all the periods and was the prominent method of glazing during the Late-Roman Periods although efflorescence was relatively common as well (Vandiver 1983:A4).The glazing material consists of the same material used in the production of the faience body but in different quantities and with a colourant added. For example, a typical post-fired blue copper glaze will contain 60-70% silica, 3-7% calcium oxide, and 1-5% copper oxide combined with 16-20% alkali (Shortland and Tite 2005:37; Stocks 1997:180). The glazing material can be raw or prefritted and applied as a powder or a powder/water suspension with which the object is dipped or painted (Vandiver 1983:A27). The colours of faience can be manipulated by the addition of minerals and pigments in various quantities in the glaze mixture (Kaczmarczyk and Hedges 1983; Tite el al. 1983; Shortland and Tite 2005; Tite et al. 2007).

The application technique is good for objects of all sizes and it offers more control over coverage than the other two methods. Application glazed objects may exhibit drip runs and distinct glaze lines form where it may have been dipped into the glaze suspension (Vandiver 1983:A27). These objects generally reveal little interparticle glass in the body and an ill-defined interaction layer.

The cementation process, also known as the Qom process, from whence it was first recorded by Wulff et al. (1968) in Iran, works best with smaller objects. Once formed and dried, the unglazed objects are embedded in the glazing mixture composed of silica, alkali, colourant, calcium and charcoal, and are fired beyond 900°C (Vandiver 1983:A34). During firing the alkalis melt relatively quickly, compared to the calcium and charcoal, and are drawn to the body surface and form a glaze (Kiefer and Allibert 1971:115-116; Vandiver 1983:A33-34). After firing unreacted glazing material will flake away from the glazed-coated object.

The advantage of cementation is the ability to conduct mass production of small objects, and the complete glaze coverage of each faience object (Vandiver 1983:A34; 2008:47). However, the objects have to be small (e.g. beads, amulets, rings) as slightly larger objects may have a thicker glaze on the bottom (as oriented during firing) and may have marks where the object came to rest in the mixture (Vandiver 1983:A35). Some of the unreacted glazing mixture may be embedded in the glaze. The cross section of a cementation-glazed object will exhibit a thick and well-defined interface between glaze and body, and the body will have little interparticle glass (Vandiver 1983:A38-39).

Binns et al. (1932) proposed efflorescence glazing after comparing contemporary faience beads with fragmented Egyptian rings and noting the similarities. Efflorescence glazing is compatible with objects 20-30 cm across (Vandiver 2008:54). The glazing material is mixed into the body paste before forming. The soluble alkaline salts, carbonates, sulphates and chlorides migrate through capillary action to precipitate on the surface of the object while drying (Vandiver 1983:A31-32). The copper ions also migrate to the surface where they interact with the other materials and melt to form the glaze during firing.

Efflorescence glazing is dependent on evaporation as a function of glaze deposition, therefore, where there is little to no evaporation, there is little to no glaze. The glaze will be thinner in areas where it was handled before firing and dry marks may still be evident (Vandiver 1983:A32-33). Internally there will be extensive interparticle glass compared to the other glazing methods. The body-glaze interaction zone characteristics are dependent on rate of drying, temperature and the amount of flux in the mixture (ibid.).

Macro and microscopic characteristics for each glazing technique are provided (see Tite 1987; Tite and Bimson 1986; Tite, Freestone and Bimson 1983; Tite et al. 1998; Vandiver 1983) but do not irrevocably determine the glazing technique as these can be

created through various means with the other glazing techniques as Vandiver (1998) has shown. It is possible that objects have been glazed using a combination of methods making more difficult still to differentiate glazing method.

2.4.4 Faience Firing Methods

Vandiver (1983:A10) states that most pharaonic faience was fired between 800 and 1000 °C[1] in a single step after it was formed and glazed. The two-step firing process comprising a biscuit and glost firing is common with glazed pottery but was not a technique commonly used with faience prior to the Ptolemaic Period (Nicholson 2013:149).

The presence of saggars, cones and other kiln furniture at faience workshops suggest that a two-step firing process (i.e. biscuit and glost) may have been used in the production of the faience (Nicholson 1993:40; 1998:62; 2013:93; Nenna and Seif El-Din 2000:26). Saggars are vessel in which other vessels are fired to protect them within the kiln. Saggars are stacked into a kiln in columns known as bungs. The saggars are separated from each other in a bung with a clay joiner. Clay rods are used to secure each bung to the kiln wall. Cones are clay wedges that separate individual vessels within a single saggar. Three pointed clay stands may have been used to lift the bottom saggar of each bung from the kiln floor to allow heated gases underneath the initial bung saggar (Nicholson 2013:100). Kiln furniture assemblages have been recovered from Memphis (Kom Helul and Kom Qalama) and Terenouthis (Petrie 1909:14-15; 1911; Nicholson 2013; Nenna and Seif El-Din 2000:39-40).

Two different size groups of saggars have been identified at Memphis in addition to cone setters, clay saggar joiners, clay rods and three pointed stands in the vicinity of faience kilns (Nicholson 2013:80, 100-104). The larger of the saggars (>40cm in diameter) are plain but have evidence of a lime powder layer in the bottom and the smaller (<40cm in diameter) are usually covered with glaze on the inner surface and the outer base but lack the lime powder residue (ibid., pp.81-82). These saggars are stacked in a kiln to form a bung, the base of the upper saggar acting as a lid for the lower saggar.

[1] Morey (1964: L133-L134, Fig. 20, Table 13) shows a eutectic point (or invariant point) of 725°C for a mixture of 21.9 wt% of soda, 5 wt% of calcium and 73.1 wt% of silicon which is very close the what is found with faience. Temperatures higher than 725°C will cause the glaze melt to become less viscous but the glaze melt may become too liquefied beyond 1000°C.

The larger saggars are hypothesized to be for the biscuit firing of faience bodies based on lack of glaze and presence of lime residue (Nicholson 2013:93, 104). Several unglazed vessels separated by cone setters would be placed into the saggar, the bottom-most resting in a bed of lime.

The small saggars are hypothesised to be for the glost firings of multiple vessels separated by cones (Nicholson 2013:101, 104). The glaze in the smaller saggars is not an intentional aspect of the saggar but is a result of small glaze particles coating the interior surfaces during firing. This would explain why it covers the interiors and only the bases of the exterior (base of upper saggar acted as a lid for lower saggar). Three pointed stands have been recovered and may represent supports for the bottom-most vessel in a saggar or used to separate saggars and allow hot gases to circulate through the bung (ibid.).

An application glaze could be applied to bisque ware as a slurry of raw materials or a slurry of ground prefritted raw material. Prefritting is the process of firing the glaze mixture to 700-800°C to remove carbon dioxide and other gases through the fractionation of carbonates, sulphates and hydroxides from the glaze melt before glaze application (Henderson 2000:88). The effect is a reduction in the porosity of the glaze caused by evolving gases. The kiln must reach at least 800°C to meet the minimum temperature for the calcium carbonate to fractionate to calcium oxide and carbon dioxide (Vandiver 1998:132). Sodium carbonate will fractionate at ~700°C to form sodium oxide and carbon dioxide. The prefritted glaze does not have to completely fuse into a glassy glaze for the gases to evolve and exit. The prefritted glaze is ground after firing and applied to the bisque ware as a powder or suspension to be fired again.

2.5 Past Analysis of Egyptian Faience

2.5.1 Historical Overview

Egyptian faience has been a subject of interest since the late 19th century. Lucas (Lucas and Harris 1962:474-475) cited several early elemental compositional analyses of faience bodies and glazes (Boccolari 1954, Burton 1912, Le Chatelier 1889, Franchet 1907, Hayes 1930, Hofmann 1885, and Lucas 1908). Results from the analyses of bodies were congruent with the average values (92-99% SiO_2, 1-5% CaO and 0.5-3% NaO) indicated by Vandiver (1982:167) based on work conducted by Lucas and Harris (1962), Kiefer and Allibert (1971), Noble (1969), Kuhne (1969) and Kaczmarczyk (1981). Stone and Thomas (1956) conducted optical emission spectrometry (OES) on faience from around the Mediterranean and Europe, and attempted to differentiate between faience of different periods based on trace

Table 2-6: Faience classification devised by Lucas and Harris (1962).

Lucas and Harris (1962: 161-166) Faience Variants		
Variate	Description	Criteria
Ordinary	Blue, Green, Violet, White, Yellow glazes or a combination of two or more. Bodies are white to gray or yellow to various shades of brown.	Catch-all
A	Faience with an Extra Layer	Technological
B	Black Faience	Colour
C	Red Faience	Colour
D	Faience with Hard Blue or Green Body	Colour
E	Glassy Faience	Technological
F	Lead Glazed Faience	Technological

elements. In 1983 Kaczmarczyk and Hedges published their tome on the X-ray fluorescence (XRF) analysis of over 1100 faience glazes from Egypt in an attempt to find characteristics diagnostic of the various time periods. Since then there have been many published articles and books on the subject covering specific periods and sites.

Lucas devised a series of categories (Table 2-6) to describe the various faience characteristics in the objects investigated (Lucas and Harris 1962:157-167). The criteria were not systematically based on stylistic or technological characteristics and can potentially obscure some variable relationships (Vandiver 1983:A20). Vandiver (2008:55) describes how the classification system can be misleading from a technological perspective. Variates B, C and D are based on colour of glaze or body but do not consider that black faience can be produced through the addition of manganese oxide or reduced iron oxides whereas the blue colour can be the result of either copper or cobalt. Vandiver (ibid.) states that all potential colour variability in faience is not included resulting in a classification system that lacks applicability and technological relevancy.

Vandiver (ibid.) recognizes that variates A and E do have technological relevancy and are generally applicable. Variate F is technological but is erroneous; lead was not being used in faience to enhance faience glazes other than as a yellow/green colourant in the form of lead antimonate or as a part of the leaded bronze used as a blue colourant.

The focus of classification techniques evolved from Lucas and Harris variants to the glazing methodology used on the faience objects (Tite 1987; Tite and Bimson 1986;

Tite et al. 1983; Vandiver 1983:A26-42). Vandiver (1998) argued against this and stated that glazing technologies were not useful for technological chronologies (ibid., p.137). Classifications of faience are now more commonly conducted through composition (e.g. colourants) (Vandiver 2008; Kaczmarczyk and Vandiver 2008), morphology (Nenna 2013; Nenna and Sief el-Din 2000, 2014) and styles (Berman and Bohac 1999; Friedman 1998; Nenna 2014).

Table 2-7 provides information pertaining to articles covering glazes of the Late – Roman Periods. Manti (2013) and Shortland and Tite (2005) conducted analyses on Memphis faience. The remainder of the analyses in this table were conducted on museum collection pieces with no reported archaeological provenance. The provenance listed for vessels and sherds in Griffin's (2002) analyses are Thebes, Luxor, Cairo, Mit Rahina, Tuna el Gebel or just Egypt. These are all pieces donated around 1912 to the Cleveland Museum of Art and probably represent towns and cities in which the pieces were bought.

SEM-EDS has been used for compositional analyses of Egyptian faience (Tite et al. 1983; Tite and Bimson 1986; Shortland 2000; Tite and Shortland 2003; Shortland and Tite 2005; and Tite et al. 2007). BSE imagery, in particular, has been used to determine thickness of the glaze and interaction layers, to characterize the transition between the layers and the body and to determine the amount of interparticle glass within the body (Tite and Bimson 1986; Tite et al. 1983; 1987; 2007:1570).

Vandiver's (1983) appendix in Kaczmarczyk and Hedges (1983) outlined production methods of different periods in Egypt using XRF. This production chronology addressed again in Vandiver and Kingery (1986) and in Nicholson and Peltenburg (2000), the latter updating earlier information and providing site specific evidence of faience production. Tite and Shortland (2008) along with other contributing authors provide information concerning many aspects of faience from around the Mediterranean.

A review of the literature (see Table 2-7) revealed the analysis of 67 blue (234 total measurements) faience glazed sherds from the Late to Roman periods (Abe et al. 2012; Griffin 2002; Kaczmarczyk and Hedges 1983; Manti 2013; Shortland and Tite 2005; Tite and Shortland 2003 and Tite et al 1983). The analyses were conducted using a variety of techniques including SEM-EDS, wave-dispersion spectroscopy (WDS), XRF and HH-XRF. Elements were divided into categories (i.e. major, minor and trace) based on reported mass fractions (wt%) (Table 2-8). All the elements typically found in blue faience glazes are discussed in detail in section 2.4.4.

Table 2-7: List of selected published results for elemental compositional analysis on faience of the Late Period and after. The total represents the number of analyses conducted on 67 sherds. Some published results are omitted because of lack of detail (e.g. Dayton 1981).

Analyses of Late, Ptolemaic and Roman Period Faience Application Glazes

Reference	Analytical Technique	Period	Color	Total
Abe et al. 2012	pXRF	Late	Blue	5
		Ptolemaic/Roman	Blue	1
			Subtotal	6
Griffin 2002	SEM-BSE, EDS; XRF	3rd Intermediate - Late	Blue	6
			Other	5
		Late	Other	33
		Ptolemaic	Dark Blue	1
			Other	13
		Roman	Blue	4
			Other	4
			Subtotal	66
Manti 2013	SEM-BSE, EDS	Ptolemaic/Roman	Light Blue	14
Mao 2000	SEM-BSE, EDS, WDS; XRF	Ptolemaic	Other	21
Shortland	SEM-BSE, EDS, WDS	Ptolemaic/Roman	Blue	7
and Tite 2005			Blue-Green	2
			Other	5
			Subtotal	14
Tite et al 1983	SEM-BSE, EDS	Late	Blue	1
Tite et al. 1998	SEM-BSE, EDS, WDS	Late	Other	1
Kaczmarczyk	XRF; AAS	Late	Blue	9
and Hedges 1983			Blue-Grey	1
			Blue-Deep Blue	1
			Blue-Green	2
			Dark Blue	2
			Violet Blue	1
			Violet Blue to Blue	2
			Violet Blue to Blue-Green	1
			Other	43
		Ptolemaic	Blue	3
			Blue-Green	2
			Blue-Grey	1
			Blue to Violet Blue	1
			Blue Grey to Pale Blue	1
			Blue Green to Dark Blue	1
			Dark Blue	3
			Dark Blue to Green	1
			Pale Blue	1
			Violet Blue	1
			Other	13
		Ptolemaic/Roman	Blue	8
			Blue-Green	1
			Blue to Pale Blue	1
			Dark Blue	2
			Pale Blue	1
			Other	5
		Roman	Other	2
			Subtotal	111
Grand Total				**234**

Blue Faience Glaze Element Abundance Classification		
Major	Minor	Trace
C > 10 wt%	C = 1-10 wt%	C < 1 wt%
Silicon	Aluminium	Magnesium
Sodium	Potassium	Manganese
	Calcium	Chromium
	Iron	Nickel
	Copper	Phosphorus
	Tin	Rubidium
	Cobalt	Strontium
	Lead	Titanium
	Barium	Vanadium
	Antimony	Zinc
	Sulfur	Zirconium

Table 2-8: Literature survey found 67 Late to Roman Period faience objects with blue glazes. The elements identified and quantified were categorized into major, minor and trace consistencies based on mass fractions (C).

The presence/absence or concentration of certain elements is useful to determine temporal placement in a chronology (e.g. cobalt and associated ore), presence of binders (e.g. clay (high concentration of aluminium), lime, alkali), and colourants (e.g. copper, cobalt, lead, antimony). These results can be used to identify raw material sources thereby providing information on trade and technology (far beyond the scope of this project). The element ratios can be used to identify groups that may belong to different regions and/or workshops and the type of alkali used (e.g. natron and plant ash) (Kaczmarczyk and Hedge 1983:280; Shortland and Tite 2005:66; Kaczmarczyk and Vandiver 2008:66-67). Compositional profiles of glaze can help to determine type of glazing. Tite (1991) writes of isotope analysis of metals to explain the metal trade (p.144), isotope analysis of bones in relation to past diets (p.148), and mentions the development of new isotope applications in geochemistry but does not go into detail. Since his writing, strontium, neodymium, oxygen and lead isotope analysis has been conducted on glass to determine source for silica, plant ashes and lime, and to determine possible workshops (Degryse et al. 2009; Freestone 2005; Freestone et al. 2003; Foster and Jackson 2009; Henderson et al. 2005; 2010). The success with glass prompted Hammerle (2012) to conduct partial thesis research on strontium isotope analysis of Egyptian faience. This project aims to add to these analyses and offer more understanding of the presence of elements, ratios of elements and where within the objects the elements can be detected.

2.5.2 Identification of glazing methods (compositional profiles)

Macroscopic and microscopic characteristics of glazes used to identify glazing method can be conflated by other production parameters (e.g. peak firing temperature and time). Compositional profiles of cross-sectioned samples can be used to further ascertain the glazing method. Copper, along with sodium, is known to migrate through the silica matrix (Kaczmarczyk and Hedges 1983:56, 61-62). Application glazes typically exhibit an even distribution through the glaze (Vandiver 1998:136) whereas self-glazing techniques tend to exhibit variation in distribution of these elements (Tite et al. 2007: 1571-2; Vandiver 2008:51).

In efflorescence glazed materials there is an increase in sodium and a decrease in potassium, magnesium and copper from the body to the glaze surface resulting in a sodium-rich glaze surface (Tite et al. 2007:1572; Vandiver 2008:51). This is because of the lower solubility of sodium carbonate in water compared to potassium carbonate which is hygroscopic and has higher solubility (Vandiver 1998:128; 2008:51). Insoluble particles are pulled to the surface through tension as the water evaporates. The extent of movement is dependent on the particle size and density (Vandiver 2008:51). Cementation glazed faience exhibits an increase of sodium and copper colourant from the body to the glaze surface (Tite et al 2007:1572; Vandiver 2008:53). The results for the copper component in the glaze profile offers another way of discerning between efflorescence and cementation glazing (Vandiver 1998:132).

Cementation and efflorescence glazing rely on migration to occur during the firing cycle. Application glaze relies more on the initial application of the glaze to the body but smaller scale migration of alkali will occur as the water content evaporates. The copper colourant of application glazes are expected to remain constant throughout the glaze profile (Vandiver 1998:136). Sodium may be slightly higher because it is precipitated out during evaporation. Weathered glazes, however, will exhibit changes in profile with perhaps the extreme concerning sodium and potassium as they are leached from the system. This will result in low sodium/potassium totals during analysis.

2.5.3 Alumina: Indication of the use of clay in the body/cobalt source for the glaze

Kaczmarczyk (1986) demonstrated a connection between cobalt and alumina in cobalt coloured glazes during the New Kingdom. These glazes are characterized by high alumina and magnesia with minor to trace amounts of manganese, zinc and nickel (Kaczmarczyk and Vandiver 2008:75). Cobalt was not used immediately after the New Kingdom but reappeared later during the Third Intermediate Period and is associated

with high manganese (~0.70%) and medium iron (~0.85%) (ibid.). This was replaced by iron-rich cobalt ores during the Late Period (Kaczmarczyk and Hedges 1983:42-43, 47, 53, 267-8) and is characterized by high iron content (~1.9-7.0%) and low manganese (<0.05%) (Kaczmarczyk and Vandiver 2008:75). These associations with cobalt can be used to infer period of manufacture of the faience glaze. This is an important aspect that has been investigated further in other published materials (Abe et al. 2012; Shortland et al. 2006b; Tite and Shortland 2008:206).

More relevant to the project and the period of interest is the potential use of clay in the body as a binder. Lucas and Harris (1962:175) explored the possibility of clay being added to the body to facilitate forming and state that the amount of alumina detected during analysis (averaging 1.2 wt%) is too low for added clay and is probably the result of impurities in the sand, alkali or some other source. Burton (1912, cited in Lucas and Harris 1962:175) tried to replicate faience by adding clay in quantities of ~1.2 wt% and determined that there was not enough to allow the use of pottery forming methods on the faience body, the assumption being made those methods at least partly refer to throwing. Griffin (2002:335-336) conducted investigations into the use of clay as a binder and found that a 3% addition facilitated moulding and 12% enabled free-throwing based on replication experiments. Kaczmarczyk and Hedges (1983:198) state that if clay were added, their analysis failed to reveal a significant change to alumina and magnesia levels when compared to those typically found in Egyptian sands (see Table 2-3). Nenna and Nicholson (2013:135) argue that clay was not required for forming during the previous 3000 years and that the addition of appropriate quantities for throwing would significantly change the colour of the faience core which has not been noted. Despite lack of evidence indicated by Vandiver (1983:A125), this idea is continually perpetuated without evidence. For instance, Kaczmarczyk and Vandiver (2008:60) suggest that clay “may” have been added to the faience body to facilitate throwing during the Ptolemaic/Roman Periods.

2.5.4 The use of natron or plant ash (via the soda, potash and magnesia content)

Potassium and magnesium are inclusions in sand but can potentially inform on the general source of the alkali component: natron or plant ash (see Table 2-4). Natron is an evaporate that is composed of $NaHCO_3$ and Na_2CO_3. Plant ash is another source of sodium and is associated with phosphorus and contains higher levels of magnesium, potassium and calcium than natron. The ability to differentiate between alkali sources can help to determine a chronological and/or regional origin of faience. Natron was the preferred flux for glass and faience from the Third Intermediate Period and afterwards (Freestone 1991:40; Kaczmarczyk and Hedges 1983:280; Kaczmarczyk and Vandiver

2008:67), however Kaczmarczyk and Hedges (ibid.) suggest plant ash (derived from halophytic plants) was seemingly preferred in Memphis during the Ptolemaic Period based on potassium levels ~1.6 wt%. This is possibly because of the abundance of grasses in the area and the cost of importing natron (Nenna and Nicholson 2013:134). Contrary to this, Shortland and Tite (2005:66, Table 4.1) conducted analysis of faience vessels from Memphis that reveal potassium quantities ~0.45 wt% and Na_2O/K_2O ratios ~35 indicating natron as the alkali source.

Sodium/potassium ratios may indicate the alkali flux source of a glaze; a ratio of ~2-6 suggests plant ash whereas a ratio >10 suggests natron based on compositional analysis of glazes from different periods containing the two oxides (Kaczmarczyk and Vandiver 2008:66-67, 71; Shortland and Tite 2005:35). High magnesia is an indicator of plant ash. Lilyquist and Brill (1993:56, Fig. 51) found that >2% MgO and K_2O indicates plant ash whereas <1.5% indicates natron for Egyptian glass. Kaczmarczyk and Vandiver's tables 4.1a-e (2008:66-67) do exhibit Memphis faience vessels containing ~0.5 wt% K_2O and ~1 wt% MgO whereas previous periods exhibit much greater K_2O and mixed MgO suggesting use of natron at Memphis; potassium is the better indicator for this data set. Unfortunately, Kaczmarczyk and Hedges (1983) did not have the capability to accurately detect sodium because they were conducting XRF analysis and no ratios can be provided from their data.

2.5.5 The use of leaded bronze as colourant

The source of the blue colourant in glazes was established as arsenical copper ore during the early Egyptian periods but the presence of lead in blue glazes was significantly increased during the New Kingdom (Kaczmarczyk and Hedges 1983: 56-57; El Goresy 2000). Lead was intentionally added as a colourant for yellows and greens in the form of lead antimonate during the New Kingdom and after (Kaczmarczyk and Hedges 1983:115), but the presence of lead in blue glazes represented a mystery and its usefulness as a flux, glaze modifier or unintentional inclusion was questioned. Kaczmarczyk and Hedges (1983:117) state that lead quantities in blue glazes across all periods in Egypt are too low to noticeably affect the faience glaze qualities indicating that the additional lead was not a function of glaze technology, but more probably the result of an inclusion. Brill (1970:120-123) noted the use of leaded bronze during the Late through Roman Periods as a colourant for contemporary glasses. Shortland and Tite (2005:35-36) found lead in copper blue glazes that were comparable to lead found in leaded bronze (5-10%). A Cu/Pb ratio of 5 to <10 could indicate leaded bronze as being the copper colourant, and therefore, a connection with metalworkers.

2.5.6 Identification of provenance and raw materials used (via trace element analysis)

Part of the scope of the project is identifying colourants and designating faience groups based on the occurrence of trace elements. Trace element analysis is typically used to differentiate between production regions and raw material sources. Stone and Thomas (1956:68) used OES for trace element analysis to determine if faience beads found in Britain were locally produced or imported by comparing results of beads from Egypt, Europe and Syria. This initial analysis was equivocal because of highly correlated variables and a lack of statistical methods to handle such data without loss of information. Newton and Renfrew (1970) re-examined the Stone and Thomas' (1956) OES results and applied multiple regression analysis to handle the highly correlated data (Newton and Renfrew 1970: 200-201). They determined that magnesium, aluminium and tin were the best discriminators but the application of NAA, with a lower detection limit, could reveal additional elemental discriminators (ibid., pp. 201-202). Aspinall et al. (1972) used NAA to reanalyse most of the samples originally analysed by Stone and Thomas (1956). NAA did reveal additional minor and trace elements. Results for magnesium and aluminium could not be obtained because of the analytical setup. Tin was confirmed as the best discriminator to determine that British faience beads were produced in the Britain and not imported (Aspinal et al. 1972:36, 38). The copper/tin ratio is 3:1, not 10:1 as would be expected when using bronze shavings as a colourant in the manufacture of the beads (ibid., p.38).

Trace elements (e.g. manganese, iron, nickel, copper, zinc, arsenic, antimony, lead) have assisted in the sourcing of cobalt used as a deep blue colourant in faience glazes (Kaczmarczyk 1986; Shortland et al. 2006). Traces of arsenic in the presence of lead antimonate can be used to source antimony (Shortland 2002). Traces of lead naturally associated with copper (lead <1.5% in copper is usually indicative of ore; lead between 5-10% is indicative of intentional leaded bronze; see section 2.5.4) can be used in conjunction with lead isotope analysis to identify the source of the copper ore (Gale and Stos-Gale 1982:13).

Non-volatile refractory elements are the most instructive for trace element analysis. Titanium, zirconium, yttrium, niobium, lanthanum, nickel and chromium are commonly used as compositional discriminants in igneous geochemistry because they are robust to low temperature alteration (i.e. temperatures lower than those associated with magma) and weathering. Strontium and barium can be useful but are more susceptible to alteration (Pearce and Cann 1973:294). These elements can enter the system as inclusions in sand and/or in the alkali source (Nicholson and Jackson 2013:98).

Differing ratios of non-fractionated elements indicate separate sources (Shortland et al. 2007b:787). Distinctiveness can be enhanced by combined ratio plotting (e.g. chromium/lanthanum and zirconium/titanium). Absolute differences should not be used because they are less indicative and suggest that elements were added in different ratios to the glaze batch (ibid.).

The presence of iron, alumina, magnesia, potash, lime and titanium oxides in measurable amounts characterize the impurity of silica processed from desert sands (Vandiver 2008:37). Analysis of the sands of Egypt (Brill 1999; Hatton 2005; Lucas and Harris 1962; Nicholson 2007; Vandiver 2008) exhibit local variation in these characteristics. This suggests that faience produced in different regions may exhibit a variation in trace elements. Provenancing using trace element analysis requires a robust identification of specific sources, geochemical correlations between elements and an understanding of how the elements react to processing (Rehren 2008:1346). Currently source material analysis may not have the robustness to define a production area but trace element variances in faience glazes should be adequate to define faience groups based on these differences. Provenancing of raw faience material is a possible future direction of HH-XRF but is currently outside of the scope of this project.

2.6 The Use of Faience Analogues

Replication is a tool that should be coupled with compositional and microscopic analysis to help interpret technology and manufacturing processes (Griffin 2002:326; Vandiver 2008:47). Published faience replication studies have previously been conducted to test composition, morphology, microstructure and firing temperatures. Cementation and efflorescence glazing techniques have been the subject of most studies with minor attention on application glazing (Table 2-9).

Binns (et al. 1932) tested efflorescent glazing techniques after examining a contemporarily produced faience bead and comparing it to fragmented archaeological Egyptian faience finger rings. The efflorescent glazing failed to produce the desired glaze but results were improved after applying a glaze mixture to the surface of a wet body. The ‘self-glazing’ mixture contained mostly alkali and colourant, and required the surface quartz of the objects to form a glaze. Although the publication is known for the self-glazing of faience, it represents one of the earliest published replication recipes in the modern era for an applied faience glaze.

Table 2-9: Published replication studies of faience based on body and glaze experiments.

Published Faience Replication Experimetation			
Glazing Technique	**Layer**	**Reference**	**Rationale (To test...)**
Application	**Body**	Binns et al. 1932	Composition
		Eccleston 2008	Firing Conditions
		Griffin 2002	Composition, Forming, Morphology
		Tite and Bimson 1986	Microstructure
	Glaze	Binns et al. 1932	Composition
		Eccleston 2008	Firing Conditions
		Griffin 2002	Composition, Forming, Morphology
		Tite and Bimson 1986	Microstructure
		Vandiver 1998[ŧ]	Composition, Microstructure and Morphology
Cementation	**Body**	Griffin 2002	Composition, Forming, Morphology
		Kiefer and Allibert 1971	Composition
		La Delfa et al. 2008	Practical and Chemical Aspects
		Matin et al. 2012	Composition
		Mesbahinia et al. 2014	Composition, Microstructure, Morphology
		Tite et al. 1983*	Composition and Microstructure
		Tite et al. 2007	Composition and Microstructure
	Glaze	Griffin 2002	Composition, Forming, Morphology
		Kiefer and Allibert 1971	Composition
		La Delfa et al. 2008	Composition and Process
		Manti 2004	Composition and Microstructure
		Matin et al. 2012	Composition
		Mesbahinia et al. 2014	Composition, Microstructure, Morphology
		Tite et al. 2007	Composition and Microstructure
		Vandiver 1998[ŧ]	Composition, Microstructure and Morphology
Effluorescence	**Body**	Binns et al. 1932	Composition
		Kiefer and Allibert 1971	Composition
	Glaze	Binns et al. 1932	Composition
		Eccleston 2008	Firing Conditions
		Griffin 2002	Composition, Forming, Morphology
		La Delfa et al. 2008	Composition and Process
		Manti 2004	Composition and Microstructure
		Noble 1969	Composition
		Riccardelli et al. 2002	Inlaying Techniques
		Tite et al. 1983	Composition and Microstructure
		Tite et al. 2007	Composition and Microstructure
		Vandiver 1998[ŧ]	Composition, Microstructure and Morphology

*Glazing mixture used but composition not provided

[ŧ]Body composition not provided

Note: Vandiver (1982) writes of producing faience replicates of the three glazing methods but did not provide compositions. The rationale was composition, microstructure and morphology.

Kiefer and Allibert (1971) tested glazing compositions using efflorescence, cementation and a combination of both. They also used a process that can loosely be considered application but is better described as a wet cementation process where the object is immersed in the 'pulp' (Kiefer and Allibert descriptor, p. 116) prior to firing. The object had to be freed of unreacted surrounding material after firing similar to the dry cementation process. The application techniques were similar to the 'self-glazing' methods tested by Binns. Microstructural characteristics of the three glazing techniques were examined by Tite and Bimson (1986) who expanded on previous work conducted by Vandiver (1983) and Tite (et al. 1983). They examined the microstructure of raw and prefritted application-glazed replications as part of the study. The replicated glazes contained SiO_2 and did not require the upper layers of quartz from the body to form a quartz-based glaze, thus departing from glazes replicated by Binns (1932) and Kiefer and Allibert (1971).

Vandiver (1998) used replicated glazes of the three glazing methods to illustrate that microstructural characteristics previously attributed to certain glazing techniques could be duplicated by changing the firing parameters. Vandiver indicated that the glaze mixtures contained SiO_2 but the recipes were vague and generalized and cannot be reproduced unless further information is provided. Griffin (2002) used a multi-faceted approach to characterize the faience collection of the Cleveland Museum of Art. Replications of the three glazing methods were conducted on various faience bodies to explain the technological complexity of production. One finding is the calcium component which Griffin conjectures is an intentional additive. It was tested and found to improve dry carving of the paste at higher concentrations before firing (ibid., p. 332). Griffin conducted investigations into the use of clay as a binder and found that a 3% addition facilitated moulding and 12% enabled free-throwing based on replication experiments (ibid., pp.335-336). Eccleston (2008) produced faience objects using efflorescence and application methods within a small bread oven kiln on the site of Amarna. The kiln reached temperatures in excess of 800 °C and was successful in producing fully glazed faience.

Many of the replication experiments were concerned with microstructural characteristics for the identification of glazing methods (Tite 1987; Tite and Bimson 1986; Tite et al. 1983; Vandiver 1983:A26-42). Vandiver (1998) argued, however, that microstructural characteristics could be influenced by several factors. This is covered in greater detail in the glazing methods section (see Section 2.4.3).

Fractionation (or decomposition) is the division of a mixture during a phase transition such as partial dissolution in a liquid or in a glass melt (Rehren 2008:1353). In regards

to glass and glaze, fractionation commonly occurs as carbon dioxide is evolved from carbonates or water from hydroxides. An accurate measure of evolved gases requires a gas bench with attached mass spectrometer for isotope analysis (Sharp et al. 2003:88). A less reliable method that will still provide a rough estimation uses a known input and output to determine values. Archaeological glazes do not provide a specific input and are impossible to calculate using this method but faience replicates are suitable for this calculation if starting values are recorded.

The compounds used for the replication of faience in this study include sodium carbonate, calcium carbonate, aluminium hydroxide, potassium carbonate and magnesium carbonate. The general reaction to produce an oxide from a carbonate through the application of heat is

$$M_2CO_2 \xrightarrow{\Delta} M_2O + CO_2 \qquad (2\text{-}1)$$

where M = metal (i.e. alkali metals, alkali earth metals, transition metals, basic metals and semimetals found on the periodic table). For aluminium hydroxide the reaction is

$$2A(O)_3 \xrightarrow{\Delta} A_2O_3 + 2(H_2O) \qquad (2\text{-}2)$$

The temperature of fractionation varies depending on the chemical environment. For example, any carbonate will require greater temperatures in a carbon dioxide-rich environment (e.g. kiln) for the CO_2 equilibrium pressure to exceed the atmospheric CO_2 pressure to off-gas. The decomposition of calcium carbonate occurs above 600°C (Escardino et al. 2010:1989, 1991; Vandiver 1998:132) although mass loss continues above 800°C and presumably at a faster rate unless capped by the CO_2 equilibrium pressure. Sodium carbonate will decompose above 700°C (Motzzfeldt 1955:142; Vandiver 1998:132). Aluminium hydroxide will start to decompose between 180-200°C (Hollingbery and Hull 2010:1, 8) and magnesium carbonate at 515 – 640°C (ibid., p.8). The evolution of gas and incomplete off-gassing of the glaze is evident by the formation of bubbles or pores with the glaze.

2.7 Discussion

2.7.1 Faience Glaze Replication Discussion

The replication of faience glazes was used as part of the evaluation of HH-XRF. It was important that the replicated blue faience glazes resemble the archaeological blue faience glazes as closely as reasonable (e.g. travel to Egypt to produce replicates is cost prohibitive) to have a greater understanding of HH-XRF analysis of archaeological

faience glazes. Several aspects of faience production were examined based on a review of the literature in this chapter.

Excavations and research into the production of faience during the Late to Roman Periods in Egypt shows evidence of a 2-phase (i.e. biscuit and glost) firing process across several sites. These were evinced by the presence of glazed and unglazed wasters, and two different sized saggars dedicated to biscuit and glost firings (see section 2.4.4). Pharaonic faience is believed to have been fired in a single step thus representing another change with greater Hellenization of Egypt during the Late and Ptolemaic Periods. The glaze could have been applied as a raw or prefritted powder or a water suspension. Additionally, Roman glazes were found to be thicker than Ptolemaic and earlier faience glazes. As a result, glaze replication experiments involved application of a raw and prefritted powder and water suspensions in different thicknesses to dried but unfired and fired bodies (see Chapter 5).

A firing temperature of between 800 and 1000ºC is required to form the oxides of calcium, silicon and sodium from the raw materials introduced to the glaze and body batches (Vandiver 1983:A10). The final colour and porosity, which influences colour, of the glaze is affected by the kiln temperature, atmosphere and heating cycle (Henderson 2013:66). Faience replications, as a single phase or glost phase, were fired at 800, 850 and 970ºC using heating cycles that produced the desired temperature at faster or slower rates to find the kiln parameters that resulted in a replicated analogue of the archaeological glazes (see Chapter 5).

2.7.2 Instrumental Analysis of Faience Discussion

Replicated and archaeological glazes were analyzed using HH-XRF (NPA), SEM-EDS (wt%) and BSE. The presence/absence and ratio of elements can be used as diagnostic for technology and chronology. This information can inform of possible binders, colourants and the alkali (i.e. natron or potash) used in the production of a faience body/glaze. In addition, compositional profiles provide evidence of type of glazing method.

Colourants are easily determined by colour of the glaze and qualitative HH-XRF analysis where presence/absence of peaks indicate the colorant. A clay binder in the body would be indicated by the presence of relatively high peaks for alumina and magnesia in a body spectra. Smaller peaks may still be visible for glaze spectra if using a higher kV setting for bulk analysis but it is not decisive and may only indicate a need for further investigation such as a measurement of the body.

Determining the type of alkali involves the ratio of sodium to potassium, a sodium/potassium ratio of ~2-6 indicating potash while >10 indicates natron. To produce these potential results, the ratio requires that the two variables be measured on the same scale negating the use of NPA. SEM-EDS wt% results were used for this determination due on the lack of required standards for HH-XRF wt% results.

Element associations with copper are diagnostic of Egyptian chronology. Arsenical copper was used as a pigment between the 5th and 18th Dynasty. The copper ore used to smelt copper during this period is associated with zinc, lead, arsenic, tin and antimony. Leaded bronze scrap was used after the 19th Dynasty. A copper/lead ratio of 5 to <10 indicated use of contemporary bronze scrap as a colourant and show a relationship between the crafts of faience and metalworking. Correlations of copper with zinc, lead, arsenic, tin and antimony would have indicated the faience was produced earlier than the 20th Dynasty but this was not the case (see Chapter 7).

Cobalt associations with elements are also diagnostic of chronology and raw material sourcing. Cobalt used during the New Kingdom is associated with high levels of alumina and magnesia and traces of manganese, zinc and nickel. Cobalt used during the late Third Intermediate Period is associated with high magnesia and moderate iron components. Cobalt used during the Late Period and later are associated with high iron and low manganese. These associations possibly represent three different raw material sources. HH-XRF and SEM-EDS were used to examine the cobalt relationships of the archaeological glazes and determine if they confirmed a Late or Ptolemaic Period association for the archaeological glazes.

The firing temperatures of the archaeological glazes are presumably between 800 and 1000ºC which is required for certain reactions to occur. The presence of tridymite (forming between 870-1100ºC) and/or cristobalite (forming above 1470ºC) crystals, polymorphs of silicon oxide, help to refine the firing temperature of archaeological faience glazes. Their presence can first be detected using SEM-BSE and identified using RAMAN. Although Cardiff University School of History, Archaeology and Religion do have a RAMAN, it was not setup until after the initial submission of this thesis and, therefore, was not accessible for use.

The archaeological faience sherds are almost undoubtable glazed through application. This project provided an opportunity to look at compositional profiles to see if they confirm expectations for the type of glazing. Compositional profiles were examined using SEM-EDS (wt%) to determine if they confirm application glazing for the sherds (see Chapter 7). This could have been conducted using NPA but use of wt% facilitated

the individual element results positioning on a single graph while also providing a scale (i.e. 1-100%). NPA does not lend itself as easily where counts may be in the order of 1k for sodium, 600k for calcium and 2.5M for copper.

MVS of HH-XRF NPA results will provide clusters that may represent workshops or raw material selection. All elements associated with faience are detectable with HH-XRF in ideal circumstances (e.g. no weathering or surface deposits). Sodium and magnesium may be difficult to detect in non-ideal circumstances due to limitations of HH-XRF and possible weathering having depleted the sodium content. Decisions on their use in MVS was conducted in Chapters 9 and 10.

In conclusion, this chapter covered the production of archaeological faience and contemporary faience reproductions. There was a brief overview of the history of analysis on faience glazes revealing some of the questions that can be answered regarding intentional clay inclusions, copper and cobalt colourant sources, natron and potash alkali sources, indication for type of glazing and potential use for workshop and raw material sourcing. The following chapter is a continuation of background for the project and examines the use of HH-XRF, its benefits and limitations and provides case studies of glass and glaze analytical studies.

Chapter 3: Background: Hand Held X-Ray Fluorescence

The previous chapter covered Egyptian faience and the materials and technology used in its construction. The following chapter provides a basic introduction to HH-XRF and the principles of how it works, benefits and limitations of its general use and its use with vitreous materials. Published analyses are investigated to determine methodology and how HH-XRF limitations were addressed. A Bruker Tracer III-SD co-owned by the National Museum of Wales and Cardiff University is used for this study.

3.1 Hand Held X-Ray Fluorescence: The Growing Phenomena

The Department of Earth and Planetary Sciences and Anthropology at the University of California, Berkeley, spearheaded the application of XRF in archaeology with the 1960 analysis of Roman coins (Hall 1960, cited in Shackley 2011:11) and were the leaders in XRF archaeological research throughout most of the rest of the century (ibid.). Advances in computers and other technologies (e.g. X-ray tubes) led to miniaturization of components (e.g. detectors) and to the development of small compact portable XRF systems for quick tests in mining and metal recycling (Shugar 2013:173; Speakman et al. 2011:3483). Field geologists and archaeologists adopted the technology for in situ analysis and by 2005 there were 200 units estimated to be supporting archaeologists, curators and conservators worldwide (Homqvist 2016:363; Speakman et al. 2011:3483).

Development of X-ray tubes and miniaturization of detectors probably contributed most to the HH-XRF analyser evolution. X-ray tubes provided a source of X-rays that can be turned off when required unlike sealed radioactive sources which requires registering as a “mobile radioactive apparatus” and of which transportation is more controlled through legislation (Radioactive Substances Act 1993; Ionizing Radiation Regulations 1999; Potts et al. 2008:6). Lithium drifted silicon (Si(Li)) detectors were commonly used for XRF analysis and were good for energies between 1 and 50 kV but could only process 40,000 counts/second (cps) and required liquid nitrogen to reduce temperatures below 250 kelvin which was not conducive for portable hand held instruments (Hall 2016:348; Janssen 2013:95). Si-PIN (silicon-p-type semiconductors) detectors were smaller and could be cooled using thermoelectric coolers (i.e. Peltier-

cooled), instead of liquid nitrogen, facilitating HH-XRF innovation and portability. The detectors could process up to 40,000 cps in laboratory-based XRF units but less in the portable units (e.g. the Bruker Tracer III-V can process ~10,000-15,000 cps (Kaiser and Wright 2008:8, 45)). Si-PIN detectors were being adopted by the early 2000's and many instruments with them are still being used at the time of this writing (e.g. Bruker Tracer III-V HH-XRF) (Hall 2016:348).The silicon drift detector (SSD) was the next great innovation in HH-XRF technology allowing processing of in excess of 100,000 cps with lower electronic noise (ibid.). The Bruker Tracer III-SD used in this project contains a SDD.

3.2 Principles of X-Ray Fluorescence

Taking measurements with HH-XRF is possible with little training but an understanding of the principles of X-ray spectrometry are required to select appropriate settings and interpret the data. XRF works on the principle that X-rays displace inner shell (K, L, M) electrons in the surface atoms of a sample forcing higher shell elections to fill the vacancy to maintain atom stability (Fig. 3-1) (Kaiser and Wright 2008:4; Pollard et al. 2007:101; Shackley 2011:16). Outer shell electrons have higher potential energy and are less bound to the nucleus. When transitioning to inner shells they de-excite by releasing low energy emission X-rays (i.e. characteristic energy) which are equal to the difference in energy required to hold them in the two shells. Some of the released energy escapes the sample and is detected by the analyser detection unit. The characteristic emission energies (fluorescing energies) for all elements are known, fixed and unique allowing identification of elements that are fluoresced within a sample. An atom will only fluoresce if the primary energy (incident radiation from the

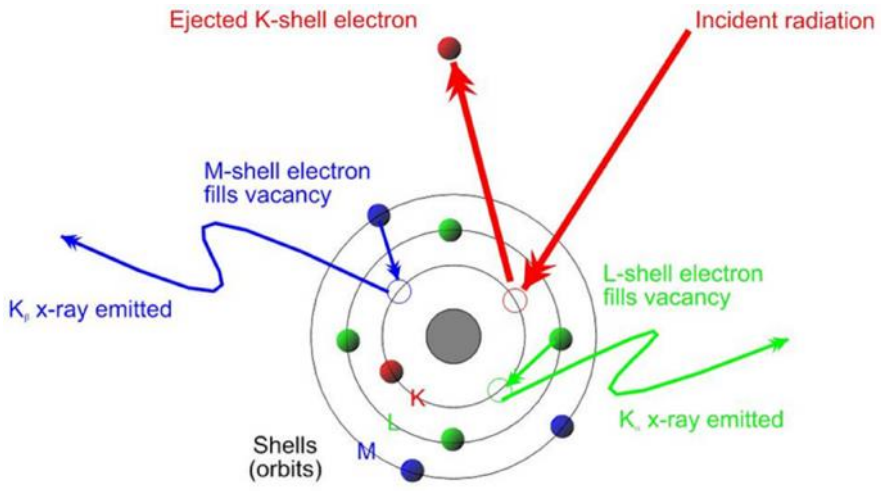

Fig. 3-1: Fluorescence of an atom (after Bruker 2016). Green emission line is for Kα X-rays (L shell to K shell); blue is for Kβ X-rays (M shell to K shell).

unit or characteristic energy from another element) exceeds the binding energy of the electrons.

3.2.1 X-Ray Fluorescence Parameter Settings

Parameter settings allow the analytical optimization of the HH-XRF unit for selected regions or elements of interest. Voltage (incident beam energy) effectively determines the elements that will appear in the spectrum, and the peak energy of the X-rays. Voltage is set through the X-Ray Ops program with Bruker systems. An individual X-ray's energy can be between 0 and the highest voltage selected for the measurement. The most abundant energy of all the X-rays combined is at half of the voltage selected as a result. Therefore, voltage should be 1.5-2x the absorption edge of the element of interest, or the highest energy element of a series in the acquisition, for optimal detection (Shackley 2011:28-29). Fifteen kV is optimal for elements lighter than iron whereas 40 kV will reveal all the elements the unit is capable of detecting, depending on beam filtering and target (target used in this project is rhodium but other elements can be used including copper, silver or tungsten). A single setup condition can be used for an element of interest by choosing a voltage that is slightly higher than the absorption edge energy for the element. Two or three conditions are required to characterize low, medium and high Z elements in an unknown sample. For example, two conditions have been selected for most analyses, 1) voltage of 40 kV good for all elements but is required for detection of the heavier elements (Z27-94; cobalt to plutonium) and 2) voltage of 15 kV which is optimal to reveal the lower Z elements (Z12-26; magnesium to iron) (Kaiser and Wright 2008:45-48).

The Bruker Tracer III-SD contains a 4 watt bulb. It is recommended that settings never exceed 1.5 w or the lifetime of the X-ray tube will be significantly shortened (Pers. Comm. Lee Drake and Rebecca Scott). Wattage determines the upper limits of the voltage/current combination and is calculated by the following equation:

$$W = 0.001(c * v) \qquad (3\text{-}1)$$

Current (µA) selection affects the number of fluoresced X-ray photons (counts) that reach the detector. Current is set through the X-Ray Ops program. The Tracer III-SD is capable of detecting 200,000 cps. The ideal count rate for processing is 100,000 cps for optimal dead time (50%) (Drake 2015), or the time the detector is unable to detect after interaction with a photon (Fitton 2014:102-103; Shackley 2011:29). A range between 1000 and 100,000 cps is sufficient for quantitative analysis. Valid counts outside of this range are not optimal and may misrepresent the sample composition.

Filters are commonly used in HH-XRF analysis and are placed between the X-ray tube and the sample to absorb X-rays immediately above the filter absorption edge although transmitting those below. The effect is a low background area 2 FWHM (full width - half maximum of peak) widths above the absorption edge of the filter (Shackley 2011:28; Wobrauschek 2010:7). Characteristic peaks in this area have an increased signal-to-noise ratio (SNR) and limit of detection (LOD). Filters can consist of metal foils, plastic and neutral absorbers such as aluminium and cellulose (Shackley 2011:28). The Bruker Tracer III-SD HH-XRF unit comes supplied with four filters composed of copper, aluminium and titanium at differing ratios (Table 3-1).

Acquisition time controls the quantity of photons hitting the detector throughout the measurement duration (not to be confused with cps rate which is controlled by current). Acquisition time is set through the S1PXRF software. Greater acquisition time provides greater resolution of the spectra. Acquisition time is generally determined by type of analysis (i.e. qualitative vs quantitative), precision and convenience (Shackley 2011:31). Quantitative analysis will always require a longer acquisition time than qualitative analysis because of the benefits of increased precision and SNR.

The use of the supplied vacuum to remove the air column in the HH-XRF unit is important for low Z elements (e.g. sodium, magnesium, etc.) whose signal might otherwise be attenuated. Vacuum use for higher Z elements is not suggested because the lower Z elements will cause a dead-time bottle-neck at the detector and resulting in

Table 3-1: Filters and filter designations provided with the Bruker Tracer III-SD HH-XRF unit. The table contains the filter designation, colour designation, filter components and thicknesses, the keV optimized transmission range (keV Trans.), the elements optimization and the recommended use for the filters.

Bruker Tracer Filter Designations							
Filters	Colour	Al	Ti	Cu	KeV Trans.	Optimized for…	Recommended Use
Filter 1	Yellow	12 mil	1 mil		12-40	Ti-Ag K lines W-Bi L lines; Little Sensitivity Below Ca	Metals
Filter 2	Absence of Filter				1-40	Shows all elements but is optimized for none	All Materials Mg-Pu (40 kV); Mg-Si and P-Cu (15 kV)
Filter 3	Green	12 mil	1 mil	6 mil	17-40	Fe-Mo; Specifically Rb, Sr, Y, Zr and Nb	Higher Z Elements of Ceramics and Obsidian
Filter 4	Blue		1 mil		3-12 (15 kV)	Mg-Fe except Ti and Sc; Filters Rh and Pd L lines	Cl and S Detection
Filter 5	Red	12 mil	1 mil	1 mil	14-40	Hg, Pb, Br and As	Poisons and Heavy Metals

an under-estimation of higher Z elements. Restricting the use of a vacuum for these measurements allows the air column to act as a filter for lower Z elements therefore reducing deadtime and allowing greater sensitivity for higher Z elements (Shackley 2011:30). The system can be modified to accept helium flushing to remove heavier elements in the air that may attenuate the signal of lower Z elements.

3.2.2 Spectral Interpretation

Several phenomena may occur simultaneously within the detector and the sample during a live HH-XRF measurement. Most of these manifest on the spectra and can be misinterpreted as characteristic emission lines of the sample. An understanding of these phenomena are required to reduce confusion, misidentification and erroneous results.

Photoelectric absorption is the excitement and ionization of an atom due to incident radiation. Two outcomes can occur when an electron is emitted from the sample material (i.e. ionization): X-ray emission and the auger process (Pollard 2007:96). X-ray emission is the result of an electron being emitted from the inner shell of a sample atom and being replaced by an outer-shell electron as discussed in section 3.2 (Fig. 3-2, see Fig. 3-1). The target is bombarded with electrons to produce X-rays which, in turn, bombard the sample producing characteristic energy lines and other phenomena. Many of the electrons excite but do not ionize the target atoms. These atoms immediately de-excite releasing a photon of the same energy which form the continuum and can vary from the infrared to the X-ray region of the electromagnetic spectrum depending on which electrons are excited within the atom (Pollard et al. 2007:99). Bremsstrahlung, German for “braking radiation” (because of transition of decelerated kinetic energy to X-ray energy), is the portion of the continuum upon which the target characteristic emission lines are found (also known as background radiation).

The same change to the electronic structure occurs with the Auger process but instead of a release of energy, an upper-shell electron of the same energy is released and stability of the atom is maintained with no characteristic energy released (Fig. 3-3). Auger electrons are primarily produced during K shell ionization of light elements ($Z \leq 20$) (Janssens 2013:82). Heavier elements have a propensity to release characteristic emission energy rather than auger electrons (ibid.).

Rayleigh scattering is the result of target (anode) X-rays that have been deflected without loss of energy, some of which enter the detector to produce characteristic

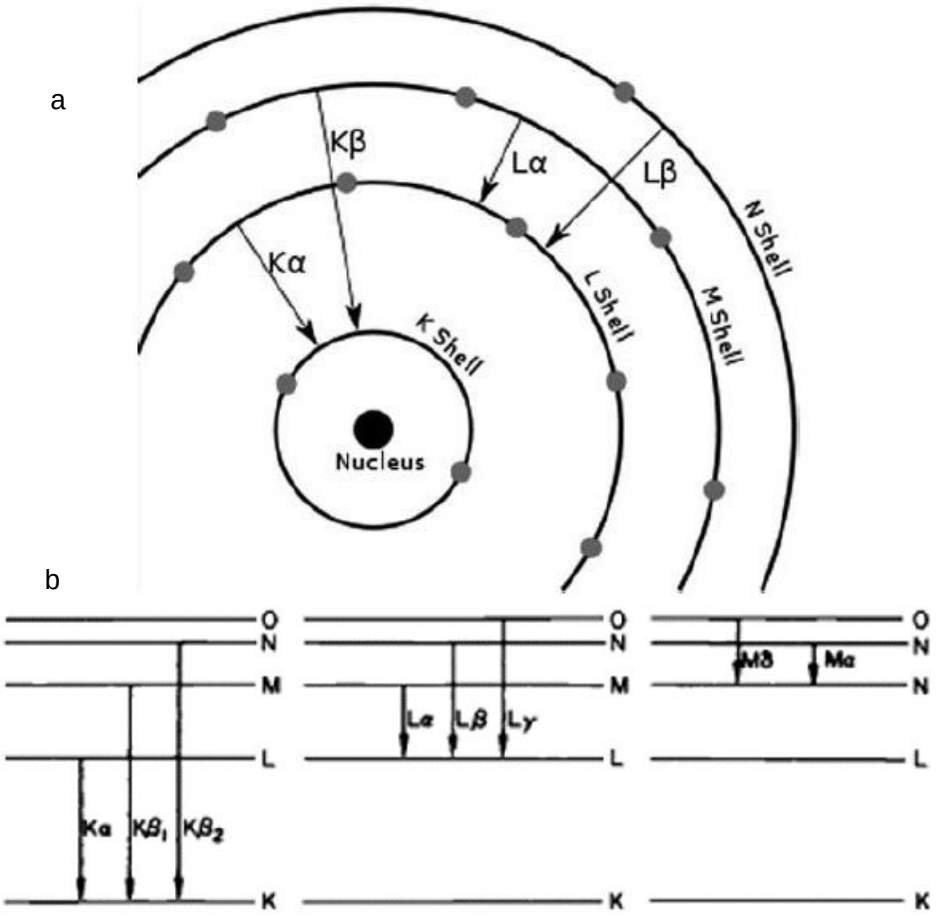

Fig. 3-3: Orbital transmissions and emission lines in schematic view (A; from Shackley 2011:17) and Siegbahn notation (B; from Jenkins 1999:55).

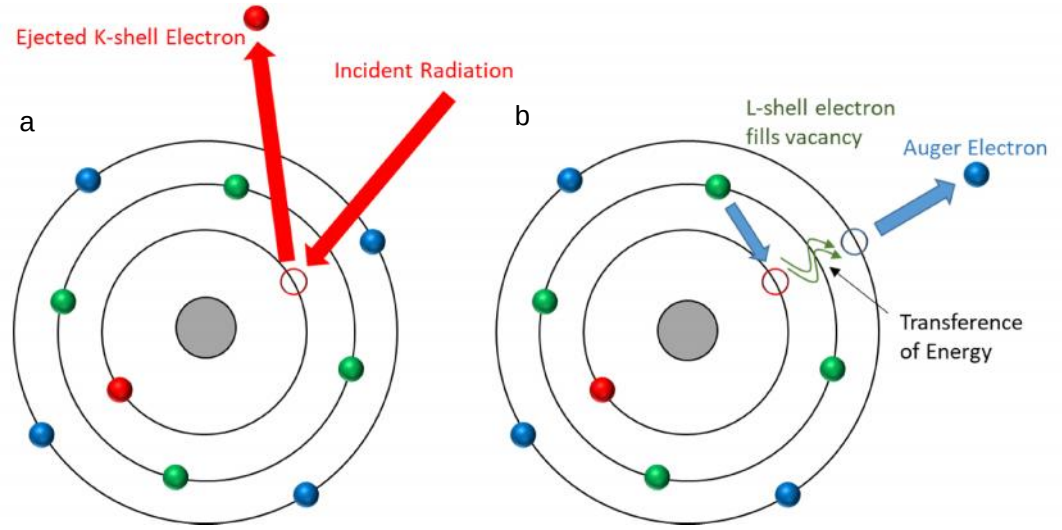

Fig. 3-2: Ejection of a k-shell electron (a) resulting in the release of an auger electron (b).

peaks of all target lines within the spectrum (Pollard et al. 2007:101). Compton scattering is directly related to Rayleigh scattering and is produced when the target (anode) X-rays are partially absorbed (not enough to cause fluorescence), lose energy and are deflected back into the detector (ibid.). The amount of energy lost is not fixed resulting in the broad peaks just below the emission lines of the target material in the spectrum. Compton peaks can provide qualitative comparative information on object density; greater density is represented by lower Compton peaks and vice versa (Shackley 2011:23).

Bragg scattering is the diffraction and interference of two incidental X-ray photons resulting in narrow peaks that will migrate on the kilo-electron volt (kV) axis of the spectrum as the object orientation (i.e. crystal face) is changed. It is encountered when analysing crystalline materials such as metals, minerals, gemstones and pigments (Shugar and Mass 2012:32-33) and is not expected with the analysis of faience glazes.

Sum peaks and escape peaks are phenomena that occur in the detector (Kaiser and Wright 2008:11-12; Shugar and Mass 2012:32-33) and are represented on the spectra. Sum peaks result when two emission X-rays strike the detector at the same time. The detector records this as a single pulse the value of which is equal to the sum of the two emission energies. The accumulation of these will result in a peak on the spectrum. Sum peaks can be a combination of any characteristic energies (Kaiser and Wright 2008:11) but are usually visible when derived from elements in high concentrations. Escape peaks occur when characteristic X-rays from the sample strike the silicon detector causing it to fluoresce. The remaining characteristic energy, minus the energy used to fluoresce the silicon detector, is recorded and a peak will be present in the spectrum 1.74 kV (Si-K absorption edge) below the fluoresced element. There are also usually visible when derived from elements in high concentrations.

Artificial enhancement and reduction of emission intensity will occur because of mass absorption effects (Pollard et al. 2007:107-108; Shackley 2011:19). Emission X-rays may be absorbed by coexisting elements reducing intensity, or secondary and tertiary fluorescence (or even greater depending on emission energy and elements involved) may occur producing artificially reduced intensities for higher Z elements, and higher intensities for lower Z elements (Shackley 2011:19; Shugar and Sirios 2012:324). For example, the manganese absorption edge is slightly lower (6.53 kV) than the characteristic energy of Fe ($K\beta_1$ line = 7.06 kV), therefore manganese will be excited by the iron emission X-rays that encounter it (not just the incident X-rays).

Some elemental characteristic lines in a complex material can overlap making distinction between the lines more challenging. One common overlap is arsenic ($K\alpha_1$ = 10.54 kV) and lead ($L\alpha_1$ = 10.55 kV). The lead $L\beta_1$ line (12.61 kV) is approximately 70% intensity compared to the lead $K\alpha_1$ line and can be used for detection and quantification in the presence of arsenic (Pollard et al. 2007:96, 108). Arsenic is more challenging to determine; the only way to determine presence of arsenic in a matrix with lead is the detection of the $K\beta_1$ line (11.73 kV). The $K\beta_1$ line is approximately 10% intensity of the $K\alpha_1$ line, thusly, arsenic is less sensitive during quantification in the presence of lead (ibid.). A review of the X-ray emission lines may indicate additional overlaps and provide solutions as in the case of lead and arsenic.

3.2.3 Sample Characteristics

Samples will have characteristics that affect HH-XRF. The ideal sample characteristics are addressed in section 3.4. The homogenous glassy matrix of obsidian is ideal for HH-XRF analysis assuming the thickness is appropriate. Pottery glazes are not ideal because the origin (i.e. glaze or clay body) of the fluoresced photons is unknown. The glaze layer may contain unreacted components and weathered surfaces. Faience glazes may prove more difficult because the body and glaze are generally composed of the same materials but differing in ratios (e.g. less alkali in applied glaze bodies than in the applied glaze itself).

Depth of measurement is important when working with layered samples. The secondary X-ray signal is attenuated as it passes through matter. Attenuation is greater for lower energy emission X-rays from light elements (e.g. sodium, magnesium) resulting in shallow depth of analysis (a few microns). Higher emission X-rays from heavier elements will be less attenuated and can be detected at greater depths in a sample (a few hundred microns). The consequence of this characteristic is that elements are detected from different depths within a sample (Table 3-2). The depth of measurement for each element is defined by the thickness of the sample, its density and its absorption coefficient:

$$I = I_0 e^{((-\mu/\rho)x)} \qquad (3\text{-}2)$$

where I is beam intensity, I_0 is beam intensity without attenuation, ρ is density of material, μ/ρ is mass attenuation coefficient for a given material and X-ray energy, and x is mass thickness (Kaiser and Shugar 2012:456; Shugar and Mass 2012:26). Determination of the depth of detection for specific elements in a matrix is based on the following equation:

$$t = -L \ (I/I_0)/((\mu/\rho)\rho) \qquad (3\text{-}3)$$

where t= thickness (cm), I is beam intensity, I_0 is beam intensity without attenuation, ρ is density of material and μ/ρ is mass attenuation coefficient for a given material and X-ray energy. The natural log of .01 is 4.61. The term 4.61 can be used in place of $-LN(I/I_0)$ which assumes that all but 1.0% of X-rays have been fully attenuated before reaching the detector when determining detection depth (Kaiser and Shugar 2012:456). The critical penetration depth (d_{crit}(measured in cm)) is the depth in which 99% of the signal from an element is attenuated by the surrounding sample matrix and 1% of the signal is available for detection (Markowicz 2008:18):

$$d_c = \frac{m_{thi}}{\rho} = 4.61/(\rho \; t \;) \qquad (3\text{-}4)$$

where ρ is density of material and 4.61 results from a sample thickness/signal attenuation ratio that assumes that all but 1.0% of X-rays have been fully attenuated. μ_{tot} is sum of mass attenuation coefficients of the primary and characteristic radiations multiplied by the cosecant of the incident and take-off angles:

$$\mu_{t} = \mu(E_0)c \; \varphi_1 + \mu(E_i)c \; \varphi_2 \qquad (3\text{-}5)$$

where $\mu(E_0)$ is the mass attenuation of the primary radiation, φ_1 is the incident angle of the beam, $\mu(E_i)$ is the mass attenuation of the characteristic radiation and φ_2 is the take-off angle of the beam. Mass attenuations can be found at the NIST website (NIST 2016).

The data from Table 3-2 reveal that the detection of lighter elements (Na-Co) is restricted to a depth of 60 µm because of attenuation of the secondary signal in the matrix. Heavier elements will be detected at greater depths (e.g. barium and bismuth detected to 500 µm). This presents a problem for thin or layered samples where characteristic peaks will be detected but the origin cannot be confidently sourced to a particular layer (e.g. glaze, body and interaction zone).

Surface conditions such as dealkalization and surface deposits will affect measurement accuracy. Table 3-2 reveals the shallow depths to which light elements can be measured in a typical glass. These emission signals are easily attenuated and surface deposits could completely mask the presence of these elements. Dealkalization changes the chemistry of the glaze replacing sodium and potassium with hydrogen in leached areas (Davison 2003:175). The leaching can extend to a depth of 500 µm in glass (Koob 2006:14) and will result in lower detection of alkali, enhancement of silicon, and reduction in the accuracy of HH-XRF results (Shugar and Mass 2012:29). Any affect to surface chemistry including crizzling, dealkalization, dirt, or other deposits will affect the analytical results unless the surface is removed to

Table 3-2: Depth of analysis (based on Eq. 3.3) for specific elements found in Corning Glass B and commonly found in blue faience glazes. Mass attenuations are found on the NIST website (Berger et al. 2010). The numbers on the right indicate the depths from which that percent of the photons have emerged. Results are individually based on the minimum primary energy (keV) required to excite each specific element (Absorption Edge). The numbers have been calculated with the incident angle as 52° and the take-off angle as 63°.

Critical Penetration Depths (μm)							
		Absorption		Actual Critical Penetration Depths			
Element	Line	Edge	cm2 g-1	99%	90%	80%	50%
Na	Kα1	1.072	495.6	2.3	1.1	0.8	0.3
Mg	Kα1	1.305	401.4	3.5	1.8	1.2	0.5
Al	Kα1	1.560	329.0	5.6	2.8	2.0	0.8
Si	Kα1	1.839	281.3	7.4	3.7	2.6	1.1
K	Kα1	3.607	125.2	7.5	3.7	2.6	1.1
Ca	Kα1	4.038	110.2	10.4	5.2	3.6	1.6
Ti	Kα1	4.966	77.0	17.2	8.6	6.0	2.6
Mn	Kα1	6.539	54.1	32.8	16.4	11.5	4.9
Fe	Kα1	7.112	50.1	38.2	19.1	13.4	5.8
Co	Kα1	7.709	44.9	51.6	25.8	18.0	7.8
Ni	Kα1	8.333	42.8	59.4	29.7	20.7	8.9
Cu	Kα1	8.979	37.5	72.6	36.3	25.4	10.9
Zn	Kα1	9.659	33.9	81.1	40.6	28.3	12.2
Rb	Kα1	15.200	17.1	241.0	120.5	84.2	36.3
Sr	Kα1	16.105	16.2	277.7	138.9	97.1	41.8
Zr	Kα1	17.997	14.3	308.1	154.0	107.7	46.4
Sn	Kα1	29.200	7.6	254.0	127.0	88.8	38.2
Sn	Lα1	4.465	946.6	9.6	4.8	3.3	1.4
Sb	Kα1	30.491	7.1	391.5	195.7	136.8	58.9
Sb	Lα1	4.698	870.8	11.2	5.6	3.9	1.7
Ba	Kα1	37.441	5.3	483.5	241.7	169.0	72.8
Ba	Lα1	5.989	593.6	18.7	9.3	6.5	2.8
Pb	Lα1	15.861	132.7	273.5	136.7	95.6	41.2
Pb	Mα1	3.851	1319.9	6.2	3.1	2.2	0.9
Bi	Lα1	16.388	126.6	446.4	223.2	156.0	67.2
Bi	Mα1	3.999	1208.8	6.9	3.5	2.4	1.0

reveal a chemically unaltered area below (Kaiser and Shugar 2012:458) negating the non-destructive benefit of HH-XRF.

Net peak analysis is affected by the presence of surface deposits. Dealkalization (i.e. loss of sodium and potassium) of the surface will have less of an affect if the elements of interest exclude those that have been leached. Sodium and potassium have emission lines that are not near the absorption lines of other elements and will not directly affect the characteristic line intensity of other elements. The replacement of sodium and potassium with hydrogen may decrease attenuation of the secondary X-rays of the remaining elements resulting in an artificial intensity increase. Therefore, in the presence of dealkalization, the ratios of any two detected elements (excluding sodium and potassium) should be nearly the same as ratios from a pristine glaze.

Samples should be homogenous and uniform so that a few measurements will accurately represent the whole. Uniform particle size ensures that particle size effects resulting in misrepresentation of abundance does not occur (Shugar and Mass 2012:28). Homogeneity requires that the sample be composed of one element or that the components are evenly dispersed throughout the matrix so that an analysis in one area is equivalent to another on the same sample. Heterogeneous samples will require several measurements so that differences can be averaged out. The presence of object layers, another form of heterogeneity, has been addressed in section 3.4. Results of quantitative analysis without sample uniformity must be wrong (Kaiser and Shugar 2012:451). Traditionally, destructive sampling (i.e. powdering) in XRF negated this problem by ensuring sample uniformity.

Light elements ($Z \leq 20$ (calcium)) are more difficult to detect than heavier elements but are important for bulk characterization of glass and glaze (Kaiser and Shugar 2012:455). X-ray emissions are exponentially lower for low Z elements (sodium-calcium) than for heavier elements (e.g. lead and bismuth) and are easily attenuated and scattered by air and overlying matter before reaching the detector (Kaiser and Shugar 2012:454; Shugar and Mass 2012:27; Potts 2008:8). They have a propensity to produce auger electrons over characteristic emission lines. For instance, the peaks for lighter elements will be lower in a sample that contains equal portions of light and heavy elements because of attenuation of the low Z signal. To the untrained observer, it might appear that there is less of the low Z and more of the high Z elements. The secondary X-ray signal from light elements are restricted to the first few microns of the sample surface making analysis more challenging when there are surface deposits or alkali depletion because of attenuation.

3.2.4 Compositional Data, Net Peak Area or Net Peak Height

Data has to be collected in specific ways; analysts interested in conducting compositional analysis have to decide the units of measurement (e.g. wt%, ppm) before any work occurs. From a statistical point of reference, compositional data is just one of many outputs of compositional analysis. Compositional data sums to a constant (e.g. 100%) (Atchison 1986) and is what many have come to expect from compositional analysis. It is very useful for providing an immediate understanding of relative elemental abundance in HH-XRF analysis. They can be compared across different instruments and to results from literature (i.e. across temporal spans) assuming they have been collected and calibrated correctly. That, therein, lies a potential problem for an analyst and/or institution. Compositional data (e.g. wt%, ppm) of glass and glazes requires several glass reference standards (18 to 20 have been suggested (Scott pers. Com.)) to cover the potential ranges of all the variables in the sample. These references are generally fairly expensive and cost prohibitive for many users of HH-XRF. Johnson (2014:584) has shown that quantification using S1CalProcess (Bruker macros) with limited reference standards produced inaccurate results. The work load for calibrations can be hefty requiring linear regression analysis to determine individual results to include and omit. The process with the Bruker system S1CalProcess macros for Microsoft® Excel amplifies the complexity for beginners because of a lack of visual graphs for confirmation although Bruker will be remedying this in the near future with a new version of the Spectra software which includes visual graphs and a direct live link to acquire Tracer HH-XRF analyses (Lee Drake, Pers. Con.).

Net peak height of an element is proportional to concentration of that given element but does not take mass absorption effects into consideration when comparing different element concentrations and ratios. X-ray emissions of lower Z elements are exponentially lower than higher Z elements resulting in lower characteristic peaks in the spectra (Kaiser and Shugar 2012:455). Artificial enhancement and reduction of emission intensity will occur because of mass absorption effects (Pollard et al. 2007:107-108; Shackley 2011:19). Therefore, using net peak height to determine concentration of an element can be misleading.

Essentially, wt% is a translation of Net peak area (NPA) into a 1-100% range based on standard reference materials and linear regression. In this sense, NPA is proportional to concentration and provides lower statistical uncertainty than net peak height for small peaks (Janssens 2013:104). Semi-quantitative net peak intensity analysis is used in obsidian sourcing (De Francesco et al. 2008; 2011; Shackley 1988). Ternary

graphs (Shackley 1988) and biplots (De Francesco et al. 2008; 2011) were used to plot net intensity counts to characterize various obsidian sources and debitage. There are two potential problems with this method: inconsistency in net intensity versus quantitative results, and overlapping plotted graphs of distinct materials (Hughes 1984:2, 13; Shackley 1988:763; Shackley 2010:19-20). Inconsistencies between net intensity and quantitative analysis may be a moot issue. Shackley (1988:763) states that the inconsistency was mostly a result of having to manually strip the overlapping kβ peaks from the kα peaks, a deconvolution process that is currently handled by software. The remaining margin of error could be from inter-instrument comparison. Net peak values are dependent on the sample and the instrument, and should not be compared to other data unless the same instrument and parameters were used. Quantitative results (wt% and ppm) allow for inter-instrument comparisons but are not used because of cost and the number of reference samples required.

Overlapping plotted results is an issue of similar chemical make-up between various obsidian sources. Multiple examples of overlapped plotted sources have been demonstrated (Hughes 1984: Fig. 3; Shackley 2010:19-20; Shackley 2011:19). Shackley (1988:763) suggests adding additional incompatible elements to the plots to further differentiate between sources. Faience material sourcing consists of sand origin, alkali source (natron and/or pot ash) and whether calcium was intentionally added or is an inclusion associated with other components. Faience workshop sourcing can be a combination of material sourcing, working parameters (e.g. firing temperature), colourants and workmanship. The chances of plot overlapping incorporating all of these variables, even if isolated to material sourcing, is less of a concern because of the greater number of variables involved with faience.

3.3 Benefits of HH-XRF

HH-XRF has provided archaeologists and conservators with greater flexibility and accessibility when working with objects through benefits that include portability, minimal sample preparation, non-destructive analysis, quick results and relative low-cost (Kaiser and Shugar 2012:450; Shackley 2011:8-9; Shugar and Mass 2012:17, 20). Portability of the HH-XRF reduces the potential of damage, theft or loss to objects subject to analysis which can happen when loaned to a laboratory. The unit can be battery operated allowing in situ chemical analysis of objects, soil matrices, sculptures and structures where mains or power outlets are not accessible (Shugar and Mass 2012:17). The units use miniature tube technology (versus a radiological source) allowing easier transportation across national boundaries (Potts et al. 2008:6; Nazaroff

et al. 2010:887) which is beneficial for international researchers of Egyptian materials in particular. Egypt forbids the export of antiquities (Law 117) forcing analysis of excavated materials to be conducted within the country.

Analysis can be conducted directly onto the object or a fractured edge of an object allowing non-destructive analysis as sampling is not required. Object preparation is minimal (e.g. requiring light cleaning) if weathering, corrosion, or other surface deposits are absent (Kaiser and Shugar 2012:454). Non-destructive analysis is beneficial for sensitive materials prohibited from methods requiring sampling (e.g. NAA, ICP-MS). Analysis can consist of several measurements across a specimen, an aspect not afforded by destructive sampling of sensitive materials (Shugar and Mass 2012:20). Qualitative results are almost immediate. Quantitative results are possible if suitable standards required for calibration are available but the process is more challenging and time consuming (Kaiser and Shugar 2012:454). Semi-quantitative results (NPA) fall somewhere in between. HH-XRF is relatively more affordable when compared to the expense of other forms of analyses such as NAA or SEM-EDS (Nazaroff et al. 2010:887). These benefits have led to greater collections-based material research in cultural institutions lacking scientific staff and it is estimated that 1500 HH-XRF units were being used by 2012 in the cultural heritage sector (Shugar and Mass 2012:17).

3.4 Limitations of HH-XRF

Major industrial applications including geology, environmental remediation and recycling have driven the production and progression of HH-XRF (Shugar 2013:174; Shugar and Mass 2012:24). Archaeologists, conservators and other members of the cultural heritage sector are atypical users of HH-XRF from the manufacturer's perspective and require greater demands from the HH-XRF analysis; for example, non-destructive analysis of non-ideal objects (e.g. thin or layered materials) is often the goal. The non-destructive quality is the source of critical suspicion of the technique. In traditional laboratory-based XRF, samples are pulverized and pressed into pellets to homogenize them before being analysed under a vacuum. HH-XRF lacks proper vacuum facilities and, when used in a non-destructive capacity, the range of elements detectable and quantifiable are reduced. For this reason, low Z detection and quantification is problematic but HH-XRF has been shown to work well with a range of high Z elements. Although having proven to discern identical compositional groups as NAA, WD-XRF, ED-XRF and ICP-MS, the individual element quantifications were different (Craig et al. 2007; Goodale et al. 2012; Nazaroff et al. 2009, 2010; Scott et al.

2012b). Johnson (2014:564) states that based on these outcomes, HH-XRF “produces inaccurate elemental concentrations which pattern in accurate ways”. Francesco et al. (2011) has demonstrated that photon intensities (NPA) could distinguish between groupings in the same way as quantitative analysis (ppm and wt%). NPA were used in the current project because they dispense with the complications of calibration required for wt% concentrations along with potential erroneous results although retaining a similar capacity for categorization.

Like with all methods, it is important to know HH-XRF limitations (covered in more detail in other sections): measurement depth, unsuitable surface conditions, sample non-uniformity and light elements. Individual elements will be detected at different depths within the object making it imperative to know the elements of interest beforehand and the theoretical depth from which they will contribute to the spectra. For this reason, analysis of glazed ceramics is considered bulk analysis which includes glaze and body. For the current project, theoretical detection depths for individual elements are determined and used to produce a suitable variable set facilitating analysis restricted mostly to the glaze.

For successful data collection, the glaze should be infinitely thick with regards to HH-XRF measurement (i.e. critical thickness is 99% of depth of measurement (see section 3.2.3)). Surface conditions such as weathering/corrosion or deposition of dirt will contribute to the analyses. Corrosion and dirt should be removed through cleaning if accurate analysis is required. Weathered surfaces can be removed but this negates the non-destructive quality of HH-XRF.

Homogenous samples are ideal; heterogeneous characteristics (e.g. non-uniformity; different particle sizes or particle compositions) will affect the analysis by exhibiting greater quantities for larger particles within the area of measurement. These differences can be reduced by increasing the number of measurements across the surface of an object. Light elements such as sodium and magnesium are difficult to detect and to accurately quantify. They will only be detected within the first few µm of the object depth and surface coatings and air columns between object and detector easily attenuate their signals.

3.5 HH-XRF Considerations and Issues with Faience Glazes

Faience is a less than ideal material for HH-XRF analysis but given the importance of faience and the need for field analysis, it is worth investigating if and how the technique can be applied. Faience is a layered structure consisting of a soda-lime-silica glaze on a ground quartz or sand body. The major components of the glaze and

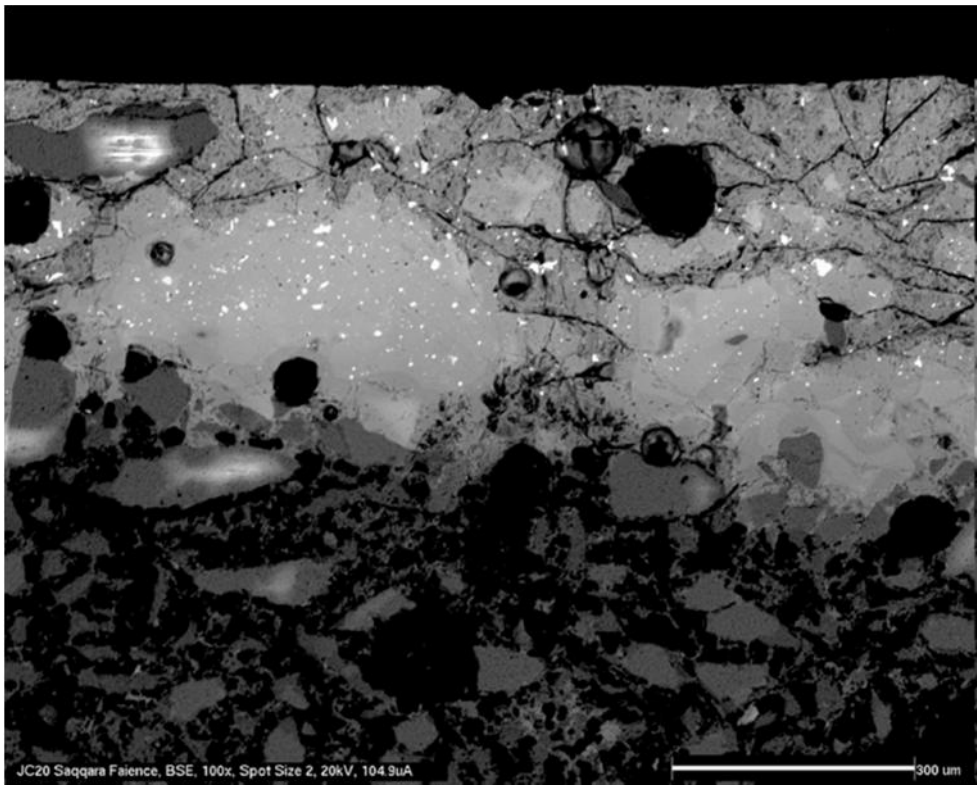

Fig. 3-4: SEM photomicrograph of green-glazed faience. The glaze layer is weathered with cracks and alkali depletion (revealed by changes in contrast along the cracks; Darker areas representing depletion). Bright specks in the glaze are lead antimonate (confirmed through SEM-EDS) used as a colourant. Dark grey solid structures are ground quartz. The interaction layer (IAL) between glaze and body is negligible to non-existent.

body are light elements (sodium, silica, potassium and calcium). The glaze is neither homogenous in composition nor particle size and is commonly found to have weathered surfaces (Fig. 3-4). Archaeological glasses and glazes have been subjected to chemical changes during deposition resulting in porous and/or layered microstructures. These materials are unsuitable for non-destructive compositional (wt%) analysis (Shugar and Mass 2012:18). Without surface preparation quantitative analysis will be wrong but the level of accuracy depends on the specific characteristics for each sampling site and each sample. Cluster analysis remains a possibility but care must be taken in which variables to include in the analysis; alkalis, being particularly susceptible to weathering, could produce erroneous NPA results.

3.6 HH-XRF Evaluations and Related Case Studies

Selected case studies reveal HH-XRF evaluations and use of HH-XRF with related material types to assist in determining a suitable methodology for the current project. Of interest are the areas of concern and how the authors dealt with them. HH-XRF and its use with obsidian provenancing is seen as a success (e.g. Drake et al. 2009; Frahm

2013; Frahm et al. 2014a and 2014b; Forster et al. 2011, 2012; Gooddale et al. 2012; Milic 2014; Millhauser et al. 2011; Nazaroff et al. 2010; Nazaroff and Shackly 2009; and Phillips and Speakman 2009). Its use with other vitreous materials is less well documented in the archaeological literature. The case-study materials are divided into two categories: layered vitreous materials and homogenous vitreous materials. Layered vitreous category more closely resembles the characteristics of the faience material in the current study where substrate may add to the glaze spectra. The homogenous vitreous category includes glass, both manufactured and natural (i.e. obsidian). These disperse with the substrate issue and show capacity of HH-XRF for cluster analysis.

3.6.1 Layered Vitreous Material

Layered vitreous materials consist of ceramic and faience glazes (Table 3-3). Depth of measurement, weathered surfaces, light elements and heterogeneity are a concern with these materials. Because they are so few, a detailed description of the faience analyses is provided first.

A total of four articles (Abe et al. 2012; De Viguerie et al. 2009; Giumlia-Mair and Soles 2013; Toffolo et al 2013) and one honours thesis were identified involving the analysis of Egyptian or similar faience with pXRF. Whisenant (2012) wrote an honours thesis on the HH-XRF analysis on faience tiles. It is included in Table 3-3 specfically because of the sample material, the provision of HH-XRF parameters which were borrowed from Speakman et al (2011) analysis of ceramic fabrics and the paucity of articles relating HH-XRF and faience material.

An Ourstex 100FA-IV portable XRF (weighing 15 kg) was used on cobalt coloured glass and faience glazes to determine the compositional characteristics of the cobalt colourant (Abe et al. 2012). Calibration of the analytical results for 19 elements required 32 standard glass samples. Corning glass A was used for verification of the calibrations. Their “preliminary” findings indicate a new distinct cobalt source was used between the New Kingdom and Late Period but indicate that surface weathering affected the results through alkali and calcium depletion, and aluminium enrichment.

A small rounded yellow faience pendant was analysed by de Viguerie (et al. 2009) using two custom built component pXRF systems constructed in the C2RMF laboratory located at the Louvre. They used thin film and thick element samples to calibrate the X-ray tube and fundamental parameters to produce compositional results. They failed to address the layered structure of faience, depth of analysis, potential

Table 3-3: HH-XRF parameters from the literature for the analysis of layered vitreous materials. C-pXRF are component systems built to custom specifications. They are portable but are too large to be considered handheld. Missing information was not reported.

HH-XRF Selected Articles for Layered Vitreous Materials										
Authors	Analyzer	Material	Target (Anode)	kV	µA	Notes	Live Time (seconds)	Atmosphere	Filter	Assays
Pappalardo et al. 2004	C-pXRF	Glaze	Cd	22.1						
Gianoncelli et al. 2006	C-pXRF	Glaze	Ag	40	90		900	Air and Helium		
Sendova et al. 2009	Bruker Tracer III-V	Glaze	Rh	15	11	Low Z				
				40	1.1	High Z			F5	
				15	20		60	Vacuum	F4	
De Viguerie et al. 2009	C-pXRF	Faience	Ag	35	95		180	Helium		3
Abe et al. 2012	C-pXRF	Glass and Faience	Pd	40	250 and 1000		200	Vacuum		
Domony 2012	X-Met5100	Porcelain	Rh	see text			see text	Air	see text	10
Whisenant 2012	Bruker Tracer III-SD	Faience	Rh	40	15			Vacuum		5
				15	55			Vacuum		5
				15	55			Vacuum	F4	5
				40	15				F3	5
Forster and Grave 2013	Bruker Tracer III-V	Glaze	Rh	40	13		300s		F3	3
Giumlia-Mair and Soles	C-pXRF	Faience					600-900			
Toffolo et al. 2013	Bruker Tracer III-V	Faience		40	22		60		F1	1
				15	30.5		60			1
Fischer and Hsieh 2017	Niton XL3t	Porcelain	Ag	50	200		120 and 90s	Air		2

surface deposits and dealkalized glaze layers, but did, however, recognize that the geometry of the pendant had a detrimental effect on their analytical results.

Giumlia-Mair and Soles (2013) analysed suspected Egyptian glassy faience beads from a necklace recovered from a Mycenaean tomb in the Limenaria cemetery at Mochlos, Crete. They do not describe the pXRF instrument other than it was transportable and used software specifically designed for the analysis of metal. Instrument parameters were not indicated. The lack of quantitative tables and spectra, and their expressed interest in identifying elements in the glaze and specifically the colourants used, suggests that qualitative analysis was conducted.

A Bruker Tracer III-V was used in conjunction with Fourier transform infrared spectroscopy (FTIR) and SEM-EDS for the analysis of faience beads from Ashkelon, Israel, to characterize the mineralogical composition of the glazes (Toffolo et al. 2013). They found that filtered HH-XRF measurements provided better results for z>18 (argon) and unfiltered measurements for z>12 (magnesium). The HH-XRF analysis was qualitative and based on element presence/absence.

Toffolo et al (2013) and Giumlia and Soles (2013) conducted qualitative analysis on glassy faience beads and had no concern about depth of analysis because of the material type (glassy faience has no layers). Abe et al. (2012) and De Viguirie (2009) were investigating faience systems that would have contained a distinct glaze and body. Although not specifically stated, these analyses were conducted on the bulk composition based on the voltage used which would result in elements being detected below the glaze layer. They recognized issues with weathering (Abe et al. 2009) and sample geometry (De Viguirie 2009) but failed to take measures to compensate.

Pappalardo et al. (2004), Gianoncelli et al. (2006) and Sendova et al. (2009) used pXRF and HH-XRF systems on 16th century Della Robbia glazed terracotta to confirm attribution of the works based on the glaze chemical characteristics. Pappalardo et al. (2004) used pure element standards (n=4) to calibrate their custom system to produce compositional (wt%, ppm) results for mid and high Z elements. Light elements were not measured. They recognized that glazes tend to be heterogeneous because of unreacted components. The heterogeneity was addressed by using a spot size of 1 cm^2 to average out discrepancies in the results.

Gianoncelli et al. (2006) used a similar system and fundamental parameters to produce compositional results for light and heavy elements. Light element detection was increased with the use of a helium flush to remove the air column that would

otherwise attenuate the signal. They recognized that these glazes were typically 100-200 µm thick but failed to further address the depth of detection.

Sendova et al. (2009) used HH-XRF qualitative analysis and compared the spectra with a spectrum of reference lazurite. The conditions affecting the depth of measurement (i.e. voltage, element of interest) are mentioned but the discussion does not proceed any further. The analysis most likely includes elements from the body and glaze based on the voltage used although lighter elements may only have been detected from the glaze.

Domoney (2012) conducted thorough evaluations of HH-XRF before analysing 18th century to modern Meissen and Vincennes-Sèvres porcelain. A description of the parameters used is too verbose to be restricted to Table 3-3. The analyser unit consisted of the Oxford Instrument X-Met 5100 HH-XRF using two fundamental parameter programs for soil: 1) soil FP – 45 kV, 15 µA, 25 µm Fe filter, and 2) soil LE – alternating conditions 15/45 kV, 45/15 µA, 500 µm Al / 25 µm Fe filter. The experiments were used to test acquisition time (15, 30, 60 120 and 240 seconds) precision, accuracy, sample geometry (0°, 22.5° and 45° to the window), window coverage (25, 50 75 and 100%) and source-to-sample distance (1-5 and 10 mm). Reference materials consisted of Corning C and D and soil standard 3a2. Domoney (ibid., p.99) determined that acquisition times between 30 and 120 seconds were analytically consistent with 240 seconds. Thirty seconds was chosen for live-time counts for the remainder of the experiments. The relative standard deviation (%RSD – precision) was 7 to 18% for Corning C and 3 to 18% for 3a2 excluding single outliers. Corning D %RSD was between 2 and 15% with no excluded outliers. The relative accuracy errors (RAE%) of the FP programs were high (3a2 – 48%; Corning C – 3466%, Corning D – 743%), and this was decisive in determining that the FP programs were not going to be used for the analysis of the greater study on porcelain (ibid., p.104). Tests of the sample geometries indicate that ratios of potassium and higher Z elements could be determined for samples with irregular geometrical surfaces, however, concentrations (wt%) could not be determined because of the analyser unit and the parameters chosen for the study (ibid., p.109). Ratios and concentrations for lower Z elements could not be determined. HH-XRF window coverage of 50% or greater was consistent with data quantification only if the area was in the direction of the beam path (the beam exits the device at ~45° angle) (ibid., p.114). The source-to-sample distance experiment demonstrated that consistent ratios and concentrations were obtained at 3 mm or less although flat, intimate contact against the window is optimal (ibid., p.115). Depth of analysis was acknowledged but not addressed.

Fischer and Hsieh (2017) conducted compositional analysis on 16th -17th century export Chinese porcelain to determine in which of two folk-kiln workshops they were produced. They conducted analyses of the body and the glaze but admit the glaze measurements included body components in the spectra. They used the Niton system which has internal software that allows the user to select from predetermined settings. 'Mining' and 'soil' modes were used with acquisition times of 120 and 90 seconds, respectively.

3.6.2 Homogenous Vitreous Material

Table 3-4 exhibits the HH-XRF parameters for articles involving the analysis of man-made and volcanic glass. The list of articles is too extensive to provide a description of each so only those of addressing the issues in section 3.4 are included.

Scott et al. (2012a) conducted an evaluation of HH-XRF on experimental Roman glass to determine appropriate HH-XRF parameter settings (i.e. current and acquisition time) using the Bruker Tracer III-SD analyser at 40 kV with a vacuum to maximize element detection. The current varied between 5 and 50 µA at 5 µA increments. The signal/background ratio for each element at each current was plotted against time (10 to 180 seconds live-time count at various intervals and 300 and 900). Thirteen elements (aluminium, silicon, potassium, calcium, titanium, chromium, manganese, iron, nickel, copper, rubidium, strontium and zirconium) were the focus of the investigation. The signal/background ratio stabilized with greater acquisition times but Scott admitted that the experimental setup could have masked fluctuations at specific live-time counts. Scott demonstrated that individual elements are affected independently by HH-XRF parameter settings (Fig. 3-5) emphasizing the need to know elements of interest before analysis which are dictated by the questions being asked and the detection characteristics of those elements (e.g. precision, limit of detection).

Tantrakarn et al. (2009) used an Ourstex 100FA-IV C-pXRF system to analyse 109 Roman soda-lime-silica glass objects from Croatia. A total of 11 glass standards were used to calibrate the results. Sodium and magnesium analysis was facilitated by being measured within a vacuum chamber. Measurements were taken in areas that exhibited reduced or no corrosion layer on the glass surface.

Kato et al. (2010) used a similar C-pXRF system to analyse 231 9th to 11th century Islamic soda-lime-silica glass objects from Sinai. They used 21 glass reference standards and synthetic glasses (measured with inductively coupled plasma atomic

Table 3-4: HH-XRF parameters from the literature for the analysis of layered vitreous materials. C-pXRF are component systems built to custom specifications and are portable but are too large to be considered handheld. Missing information was not reported. Trinomial sets under Live Time represent internal software parameter changes during live analysis; the length of analysis is the sum of the figures.

HH-XRF Selected Articles for Homogenous Vitreous Materials										
Authors	Analyzer	Material	Target (Anode)	kV	µA	Notes	Live Time (seconds)	Atmosphere	Filter	Assays
Craig et al. 2007	C-pXRF	Obsidian	Ag	30	20		200	Air		
Kato et al. 2009	C-pXRF	Glass	Pd	40	250 and 1000		300	Vacuum		
Phillips and Speakman 2009	Bruker Tracer III-V	Obsidian	Rh	40	15		200		76 µm Cu; 30 µm Al	
Tantrakarn et al. 2009	C-pXRF	Glass	Pd	40	250 and 1000		300	Vacuum		
Jia et al. 2010	Bruker Tracer III-V	Obsidian	Rh	40	15		180		F3	1
Kato et al. 2010	C-pXRF	Glass	Pd	6	1500	Low Z	300	Vacuum		
				40	250 and 1000	High Z	300	Vacuum		
Nazaroff et al. 2010	Bruker Tracer III-V	Obsidian	Rh	40	9		300		F3	
Millhauser et al. 2011	Innov-X Alpha Series	Obsidian	Tg	40	20		60 (120)			1+
Forster and Grave 2012	Bruker Tracer III-V	Obsidian	Rh	40	13		300		F3	10
Liu et al. 2012	C-pXRF	Glass	Pd	15	500 - 1000	Na to Zn	100	Vacuum		12
				40	500 - 1000	Ag to Ba	100	Vacuum		12
				40	500 - 1000	for other elements	100	Vacuum		12

Table 3-4 continued: HH-XRF parameters from the literature for the analysis of layered vitreous materials. C-pXRF are component systems built to custom specifications and are portable but are too large to be considered handheld. Missing information was not reported. Trinomial sets under Live Time represent internal software parameter changes during live analysis; the length of analysis is the sum of the figures.

HH-XRF Selected Articles for Homogenous Vitreous Materials										
Authors	Analyzer	Material	Target (Anode)	kV	µA	Notes	Live Time (seconds)	Atmosphere	Filter	Assays
Scott et al. 2012a	Bruker Tracer III-SD	glass	Rh	40	5-50 @ 5 µA		see text	Vacuum		
Scott et al. 2012b	Oxford Instruments X-Met5100	Glass		15			30s, 15s			
				45			15s			
	Bruker Tracer III-SD	Glass		40			200s	Vacuum		+1
Susak Pitzer 2012	Bruker Tracer III-V	Glass	Rh	40	25		180 and 300			3
Kaiser and Shugar 2013	Bruker Tracer III-SD	Glass	Rh	15	24.7		300	Helium		
Kennedy 2013	Niton XL3t	Glass					15-15-20	Helium		
Liu et al. 2013	C-pXRF	Glass	Pd	15	500 - 1000	Na to Zn	100	Vacuum		
				40	500 - 1000	Ag to Ba	100	Vacuum		
Milic 2014	Olympus Innov-X Delta	Obsidian	Rh	40			10-10-10			
Zhao et al. 2014	C-pXRF	Glass	Pd	15 or 40	500 - 1000		300			
Adlington and Freestone 2017	Olympus Innov-X Delta	Glass		40	89		20		Cu	
				40	52		20		2mm Al	
				15	68		20		0.1mm Al	

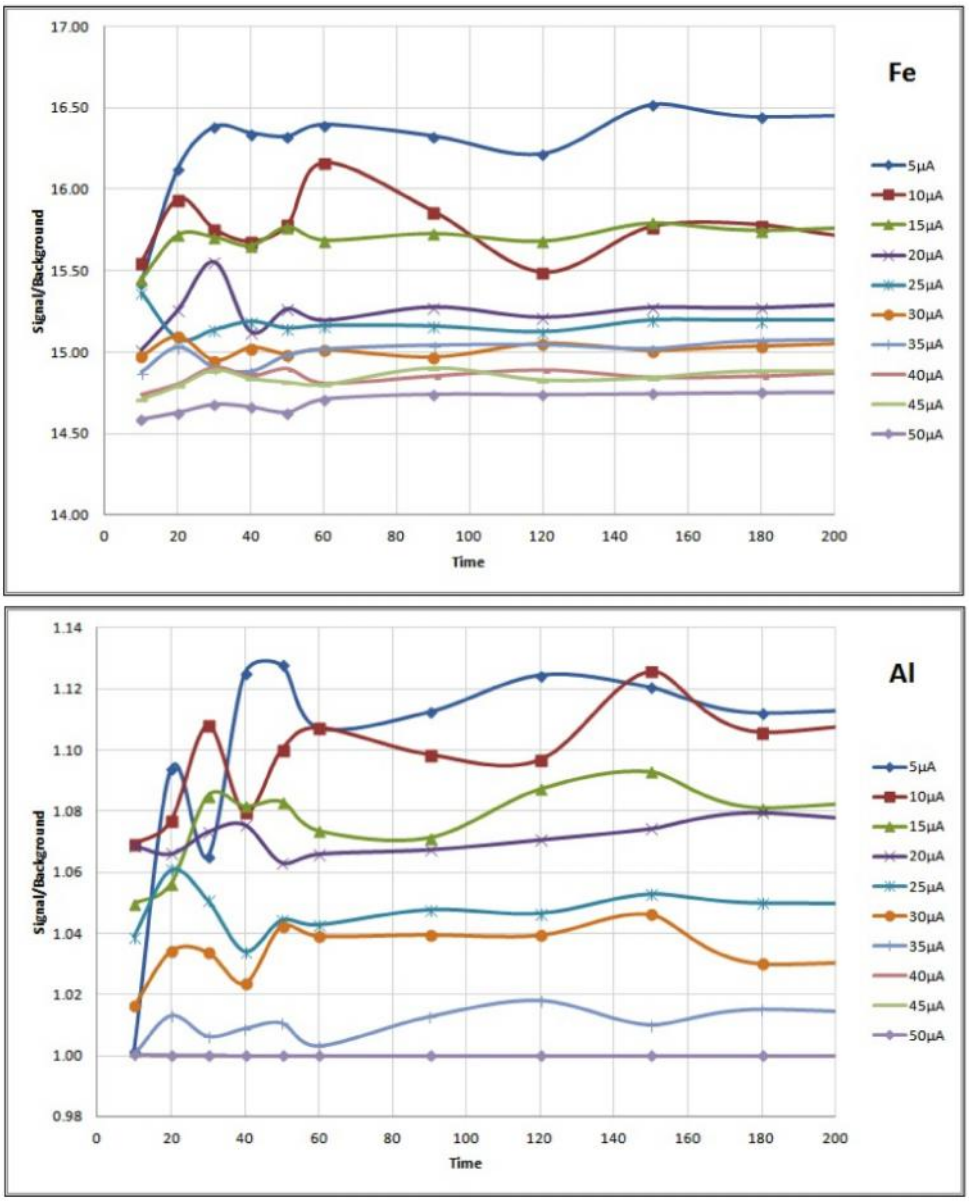

Fig. 3-5: (a) Iron signal/background ratio and (b) aluminium signal/background ratio measured against acquisition time and current. (Scott et al. 2012, Figs 6 and 3). These figures reveal that optimal HH-XRF parameters will vary depending on element.

emission spectroscopy (ICP-AES)) to produce calibrations. They recognized that the margin of error was be greater for sodium but still found it useful in the analysis.

Adlington and Freestone (2017) conducted HH-XRF and electron probe micro-analysis (EPMA) analysis of 30 medieval glass shards from the Great East Window of York Minister. Results exhibited similar clustering capacity between HH-XRF and EMPA but HH-XRF failed to reproduce the EPMA glass compositions within each cluster. This is similar to the results for Scott (2012b) with Roman glass. This was especially true for the lower Z elements which exhibited poor precision. Corroded glass surfaces were

determined to be the cause and the results were improved when using higher Z elements which are detected below the corrosion layers.

Millhauser et al. (2011) conducted HH-XRF analysis on 103 obsidian objects from Mexico to determine raw material provenance and compared the results to instrumental nuclear activation analysis (INAA) and laboratory-based XRF. They were able to source 100 of the 103 objects using HH-XRF results and published measurements of the obsidian outcrops. The HH-XRF results were a 97% correspondence with XRF and INAA; two objects remained unattributed with HH-XRF but could be attributed with the higher dimensional laboratory based methods. An increase in acquisition time to 120 seconds permitted the consistent measuring of four additional elements (barium, calcium, chromium and lead).They determined that sample measurements were accurate with 33% of the detector window covered by the sample. Concave sample surfaces introduced an air column that attenuated the lower Z X-ray signal (ibid., pp.3141, 3149).

Many of the articles indicate an HH-XRF analytical consistency with XRF, EPMA, NAA, ICP-MS and ICP-OES in identifying groupings and outliers based on geochemical sources using smaller dimensional datasets for glazes (Forster and Grave 2013;), glass (Adlington and Freestone 2017; Scott 2012b) and obsidian (Craig et al. 2007; Forster and Grave 2012; Millhauser et al. 2011; Nazaroff et al. 2010; Phillips and Speakman 2009); many of these same articles indicate that compositional results are not comparable despite similar clustering with the higher dimensional techniques.

HH-XRF elemental detection is improved assuming proper protocols are followed; the surface of the object should be flat or convex and placed directly on the detector window oriented to minimize the introduction of an air column between sample and detector. Avoid conducting analyses on concave surfaces for the same reasons just given. The analytical surface should, at the very least, be cleaned although surface removal of weathering/corrosion effects will provide greater accuracy. The detector windows do not require full coverage to produce accurate results although it is still desirable. The effects of sample heterogeneity can be minimized by multiple analyses. Highest available HH-XRF current is not recommended because it increases the background along with the characteristic peaks and does not produce the greatest peak/background ratio. Finally, elements of interest are individually affected by the HH-XRF parameters. This last point might require testing of individual HH-XRF analysers as there are intra-instrument differences even among the same models (Brand and Brand 2014:135).

3.7 Research Objectives

The potential of HH-XRF analysis with faience glazes were highlighted in the previous sections. The objectives outlined here serve to form and test a protocol for extracting useful information with the HH-XRF. The objectives are as follows:

1) An assessment of portable X-ray fluorescence analytical parameters (e.g. acquisition time, voltage and current). Analytical parameters will be assessed using Corning Glass B to determine a suitable setup for HH-XRF with glass and glazes (see Chapter 6). Net peak areas will be used in place of wt% and ppm.

2) The production of a suitable replicate material that resembles blue faience glazes of the Late through Roman Periods. A review of literature concerning faience composition and replication was used to determine potential faience body and glaze recipes. The production of faience based on these recipes was conducted and glazes most resembling the blue faience glazes from antiquity were selected for continued tests (see Chapter 5).

3) An assessment of the effect of replicate faience glaze characteristics (e.g. composition and glaze thickness) on HH-XRF analysis. The faience replications were analysed using HH-XRF to determine if the glaze batches could be discerned and how this relates to the composition. Other glaze characteristics such as glaze thickness and porosity may have affected the analysis (see Chapter 9).

4) A comparison of scanning electron microscopy and portable X-ray fluorescence analysis of applied faience glaze replicates and archaeological material. Multivariate analysis of the archaeological and replicate glazes SEM-EDS and HH-XRF results will be conducted to determine if both techniques discern the same clusters (see Chapter 9).

5) Minor and trace element analysis using portable X-ray fluorescence will be conducted on archaeological material to determine if groupings can be discerned. Multivariate analysis of the HH-XRF results will be conducted as a case study to see if group clusters can be formed. If so, this may represent differences in raw material sources or workshop-specific processing (see Chapter 10).

Chapter 4: Methodology

4.1 Introduction

The purpose of this research project is to conduct an evaluation of HH-XRF use on blue application-glazed faience from the Late Period to Roman Period and to provide a protocol for glaze analysis to archaeologists and other users in the field or laboratory space. Methods and materials that are accessible to archaeologists (e.g. use of accessible blanks, open source software for statistics) are investigated to facilitate the development of the protocol. As discussed in Chapter 2, Egyptian faience is a soda-lime-silica glaze on a ground sand and/or quartz body formed into various shapes and glazed through various methods. The period of interest has been selected because relatively little research has been conducted; most research is concerned with pharaonic period faience. Investigating the elemental composition of faience glazes will exhibit clustering of samples which may be indicative of individual faience workshops and/or raw material sources, locations of which are beyond the purview of this study.

HH-XRF is a relatively new and cheap alternative to other traditional means of elemental analysis (e.g. SEM-EDS, NAA, Benchtop XRF) whose use has grown dramatically in the last 15 years (Shugar and Mass 2012:17; Speakman et al. 2011:3483) and has possibly outpaced the dissemination of knowledge required for a complete understanding of its use. HH-XRF qualitative analysis is excellent for revealing colourants used in the glaze. The current analysis is looking beyond the glaze colourants to determine if other relationships can be discerned based on minor and trace elements. The study assemblage is restricted to blue replicated glazes and a case study composed mostly of blue archaeological glazes to reduce the added convolution of looking at several different colourants. Semi-quantitative analysis will provide measurable units (cps) that can be used to determine glaze clusters that are potentially based on source materials or workshops However, faience is not an ideal analyte because of its layered structure (glaze/body), inclusion of light elements, heterogeneous nature and a glaze surface possibly affected by deposits and/or corrosion. HH-XRF parameters (e.g. voltage, current, acquisition time) need to be tested to find optimal settings that balance a high signal-to-noise ratio coupled with high precision to tease out the details in data that is potentially restricted to the glaze

layer. Replicated faience glazes provide a known material for analysis after optimal parameters are determined. SEM provides a ground test/comparison method to HH-XRF and provides compositional data (EDS) as well as visualized microstructural details (BSE). HH-XRF analysis of archaeological faience from Saqqara will provide a case study on the capabilities of HH-XRF on archaeological glazed materials.

4.2 Experiments

The thesis aims to offer a systematic evaluation of the use of HH-XRF on Late through Roman Period blue faience through the analysis of replicated faience and a case study on faience material from Saqqara (Fig. 4-1). The evaluation consists of several experiments and tests to establish optimal HH-XRF parameter settings (Chapter 6) for the analysis of glass and glazes. The Bruker Tracer III-SD analyser allows the end-user to manipulate the parameters (e.g. current, voltage, filters) forming a multitude of combinations whereas in some other units this is controlled or restricted. This provides

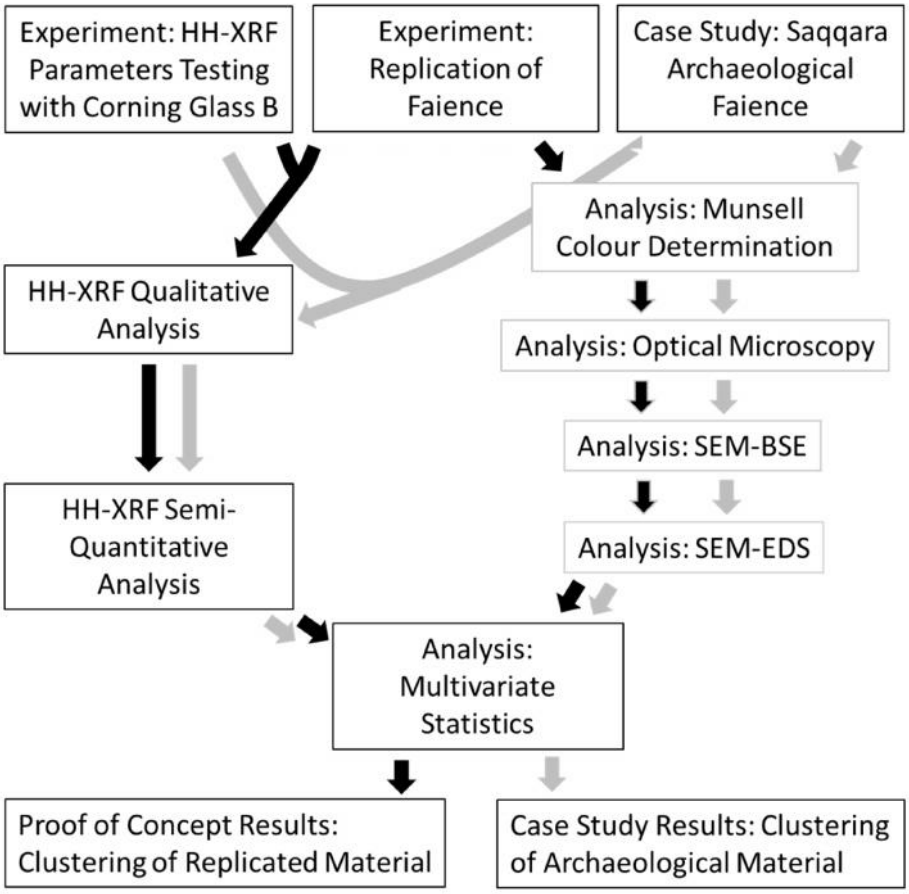

Fig. 4-1: Methodological diagram of the research project scope. HH-XRF parameter testing will determine parameters for use with analysis of replicated and archaeological material, hence the 'y' connections.

a large range of variables that can be manipulated to produce optimal settings for element signal-to-noise ratio, precision and detection. The methodology for each individual parameter experimentation is covered in detail in each relevant section of Chapter 5.

The faience analogues and archaeological faience sherds were examined visually and optically to determine the condition of the glaze, presence of surface deposits and the paste substrates. The colours were recorded and both sets of faience glazes were analysed with HH-XRF and SEM-EDS (analogue faience – Chapter 9, archaeological faience – Chapter 10) with the SEM results used as a comparative control. These methods are covered in greater detail in section 4.4.

Replicate faience bodies and glazes were produced to provide a known layered/coated material to test the capabilities of HH-XRF. The characteristics of the faience analogues were determined as a result of production and many batches were produced to obtain a material that was similar to archaeological faience. Methodology is covered in detail in Chapter 5.

Multivariate analysis is used to reveal relationships in high dimensional data. There is some conjecture about the proper way to prepare data before the use of multivariate analysis. Chapter 8 presents a background for multivariate analysis and tests three common transformation methods in data preparation to determine the most suitable procedure for glass and glazes.

4.3 Experimental Sample Set

There are three types of sample sets in use for this research: glass reference standards, replicated faience glazes and archaeological faience sherds. Corning Glass B standard is used for evaluation of HH-XRF parameter setup and for SEM-EDS beam optimization. The replicated faience glazes provide a known material with similar characteristics to archaeological sherds that were used for continued evaluation of the HH-XRF. The archaeological sherds were used as a case study to validate the effective use of HH-XRF and to examine HH-XRF potential for minor and trace element analysis.

4.3.1 Corning Glass

Corning Glass A and B were produced to emulate Egyptian glass (Brill 1971:93) (Table 4-1). Corning Glass B will be used to determine accuracy and precision of SEM-EDS and will be used for HH-XRF parameters setup evaluations. The glass is used with the parameter setup evaluations because it contains all the elements expected in Egyptian

Table 4-1: Corning Glass Reference Compositions. Wagner (2012) provides updated figures for some elements using LA-ICP-MS.

	Corning Glass A			Corning Glass B		
Elements	Reference Composition (Oxides wt%)	Theoretical Composition (Oxides wt%)	Wagner 2012 (Oxides wt%)	Reference Composition (Oxides wt%)	Theoretical Composition (Oxides wt%)	Wagner 2012 (Oxides wt%)
Li	--	0.010		--	0.001	
B	--	0.200		--	0.020	0.004
Na	14.300	14.540		17.000	18.510	
Mg	2.660	3.010		1.030	0.800	
Al	1.000	0.800		4.360	4.000	
Si	66.560	65.830		61.550	62.030	
P	0.130	0.100	0.085	0.820	0.600	
S		0.100		--	0.500	
Cl		0.100		1.000	0.200	
K	2.870	3.010		1.000	0.300	
Ca	5.030	5.010		8.560	8.000	
Ti	0.790	0.800		0.089	0.080	
V	--	0.006		0.036	0.030	
Cr	--	0.001	0.003	--	0.005	0.010
Mn	1.000	1.220		0.250	0.250	
Fe	1.090	1.100		0.340	0.300	
Co	0.170	0.200		0.046	0.050	
Ni	--	0.020		0.099	0.100	
Cu	1.170	1.200		2.660	3.000	
Zn	0.044	0.040		0.190	0.200	
As	--			--	--	
Rb	--	0.010		--	0.001	
Sr	0.100	0.100		0.019	0.010	
Zr	--	0.005		--	0.025	
Ag	--	0.002		--	0.010	
Sn	0.190	0.200		0.040	0.020	0.024
Sb	1.750	1.810		0.460	0.400	
Ba	0.560	0.500	0.460	0.120	0.050	0.077
Pb	0.120	0.050	0.073	0.610	0.500	
Bi	--	0.001		--	0.005	0.004
Total	99.534	99.975		100.279	99.971	

Notes: Theoretical Composition is from the batch components (Brill 1999). Reference composition is the recommended reference figures. Wagner (2012) has suggested adjustments but these have yet to be tested.

faience whereas an individual faience glaze may not necessarily contain the full range of elements. The upper and lower limits of elements typically found in blue faience are interspersed between the two Corning Glass standards based on analysis of blue faience glazes (Abe et al. 2012, Griffin 2002, Hatcher et al. (forthcoming as cited in Tite and Shortland 2003), Kaczmarczyk and Hedges 1983, Kaczmarczyk and Vandiver 2008, Manti 2013, McGovern 1993, Shortland 2000, Shortland and Tite 2005, Tite et al. 1983 and 2007, Vandiver 1983, and Vandiver and Kingery 1987). Corning Glass B has lower wt% for several trace elements found in Egyptian faience (e.g. rubidium, strontium, and barium) and the difficulty in detecting these may reflect the same difficulty in archaeological faience which has been subjected to deposition and weathering. Corning Glass A was not subject to the same treatment as Corning Glass B but is checked against the suggested parameters to determine capability of detecting the lower wt% constituent elements found in Corning Glass A (i.e. vanadium, chromium, nickel, zinc and zirconium). These elements are generally reported less in faience from the Late through Roman Periods.

4.3.2 Replicated Faience Glazes

Faience analogues were produced (see Appendix A) to have standard structures to evaluate the usefulness of HH-XRF for the non-destructive analysis of faience and its ability to produce minor and trace element groupings of faience glazes. Application glazed faience replications were produced from recipes based on a literature review of archaeological faience sherd compositions and replication experiments (see Chapter 5). The aim of the faience replication study is to determine a suitable recipe, glaze application process and firing methodology to replicate faience body and blue application glaze that matches the chemical, microstructural and aesthetic characteristics of copper and cobalt-coloured blue archaeological material from similar faience of the Late, Ptolemaic and Roman Periods. Faience analogues provide a heterogeneous material (e.g. glass, partially melted silica grains, inclusions introduced from sand) and a layered structure that closely resembles faience from the archaeological record. Replication glazes lack surface deposits and weathering commonly found on the archaeological material which can affect the analysis. The replicate glazes facilitate multiple samplings not usually granted for archaeological materials if required for SEM or other analyses.

4.3.3 Archaeological Faience Sherds

A total of 24 archaeological faience sherds were selected for HH-XRF analysis as part of a case study validating the effectiveness of HH-XRF on real archaeological material

which are characterized by authentic faience microstructures, weathered layers and surface deposits (Fig. 4-2; see Appendix B). The sherds were recovered from disturbed zones and on the surface in the south and west dumps of sector 7 at Saqqara (Dayton 1981:135). Dayton describes the sherds as belonging to the 30th dynasty (Late Period) or to the early Ptolemaic Period, c. 355 BC. The sherds are now a part of the Egyptian Exploration Society collection held at Cardiff University and have been kindly provided by Dr Paul Nicholson. Several of these sherds have been previously analysed (Dayton 1981); Dayton conducted qualitative X-ray emission spectrometry on an unknown number of sherds representing various colours from the collection (Table 4-2) and Manti (unpublished) conducted energy dispersive spectroscopy on four of the sherds. The small size of the archaeological sample set was deemed acceptable as it was not used for evaluating HH-XRF parameter settings, batch discernment nor depth of analysis. Instead it was an opportunity to use selected HH-XRF parameters with real-world materials which could be expanded with future projects.

Twenty of the 24 sherds were a hue of blue. These were selected based on presence of a covering glaze and absence of soil or other surface deposits as detected with the stereomicroscope. The other four sherds, representing purple, green, apple green and yellowish-green, were included to provide analytical contrast to the blue glazes.

4.4 Selection of Investigation Methods

The main scope of the research is the evaluation of the HH-XRF technique on blue faience material, the provision of parameters suitable for the material and a suggested workflow for application of the parameters on the faience material. To this end visual examination and optical microscopy were combined with scanning electron microscopy (SEM) and HH-XRF.

4.4.1 Visual Examination (Macroscopy)

Archaeological sherds and replicate faience bodies were empirically examined macroscopically to determine friability and durability. Body colours help to indicate the presence of silica filtering/quartz usage and instances when glaze was added providing strength to the body. Glazes were examined to assess colour, texture, opacity, presence of pinholes and general coverage of the body (e.g. presence of glaze creep) (see Appendices A and B). The presence of drips, finger and brush marks can indicate the glazing technique as application (Nicholson 2009:5; Vandiver 2008:49). These qualities reflect technology such as firing conditions and colourants. Visual examination detected other indicators of firing processes such as kiln setters

Table 4-2: Partial compositions by colour of faience recovered from Saqqara as reported by Dayton (1981:136) in text.

Qualitative X-Ray Emission Spectroscopy of Faience from the Animal Necropolis at Saqqara									
Faience Glaze Colour	Ca	Mn	Fe	Co	Ni	Cu	Zn	Sb	Pb
Reddish-Purple		3.00%	XX			Tr			Tr
Bright Apple-Green			XX			3.00%			2-3.00%
Yellow						Tr		1%	2.00%
Dark Green			XX	Tr	Tr	XXX	Tr		0.20%
Turquoise Blue	XXX					2.00%	Tr		0.07%
Dark Blue			XXX	0.50%		XXX			

Notes: According to Dayton (1981: 136) calcium was 3 times greater in the turquoise blue than in the other samples.
Tin was not found with any sample.
The percentages and traces (Tr) are Dayton's. The relative amounts provided by the X's are the authors and indicate strong (XXX) or a modification (XX) of a colour as stated by Dayton.

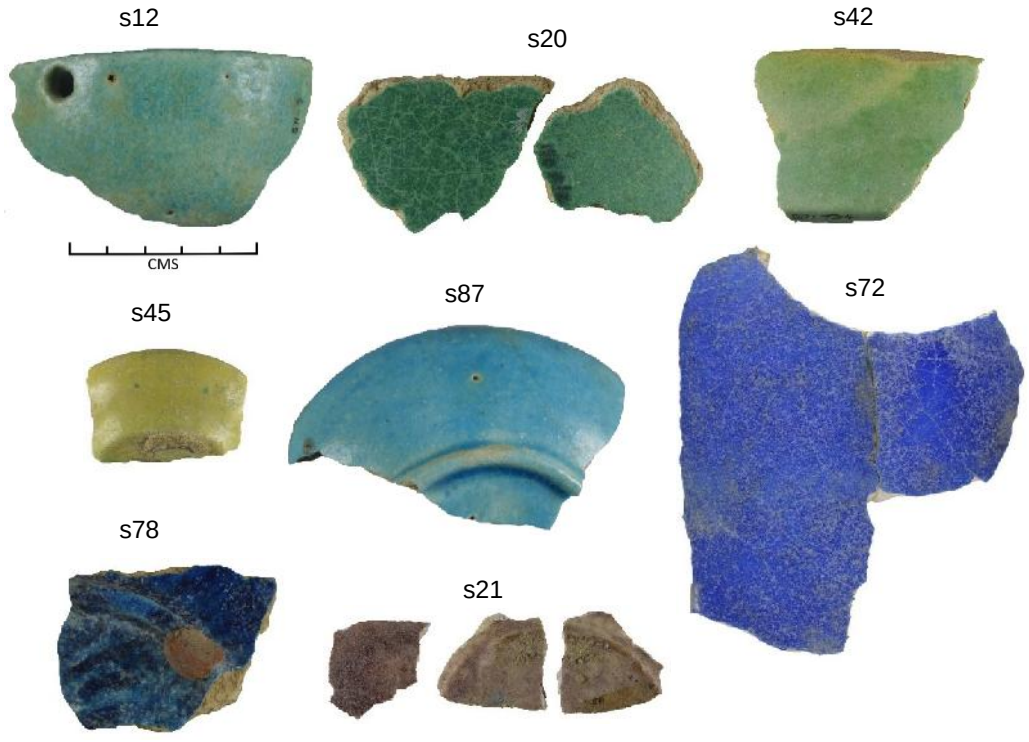

Fig. 4-2: A selection of archaeological sherds representing all colours used in the study (s12 pale turquoise; s20 green; s21 purple; s42 apple green; s45 yellowish green; s72 and s78 ultramarine blue; s87 blue) Note the kiln setter on the foot ring of s78.

and setter remnants on the interior of vessels indicating they were stacked during firing.

4.4.2 Optical Microscopy

Glazes were examined under a Nikon SMZ1000 research microscope (magnification x4, x10, x20 and x40) using GX imaging software to determine glaze quality, presence of bubbles and erupting bubbles undetected during visual examination(see Appendices A and B). It can be used to identify tool marks, seams, gaps and misalignments related to forming and porosity in the body (Griffin 2002). The software was calibrated using a stage micrometer before analysis.

4.4.3 Munsell Systematic Colour Determination

The Munsell colour determination system defines colours by degree of hue, value and chroma to form a trinomial designation (Nickerson 1976:121). Hue is a colour in its relation to red, yellow, blue, green and purple (Munsell Color 1994: 1) and is indicated by the initial letters of the perceived colour (e.g. R for red, Y-R for yellow-red) (Fig. 4-3)

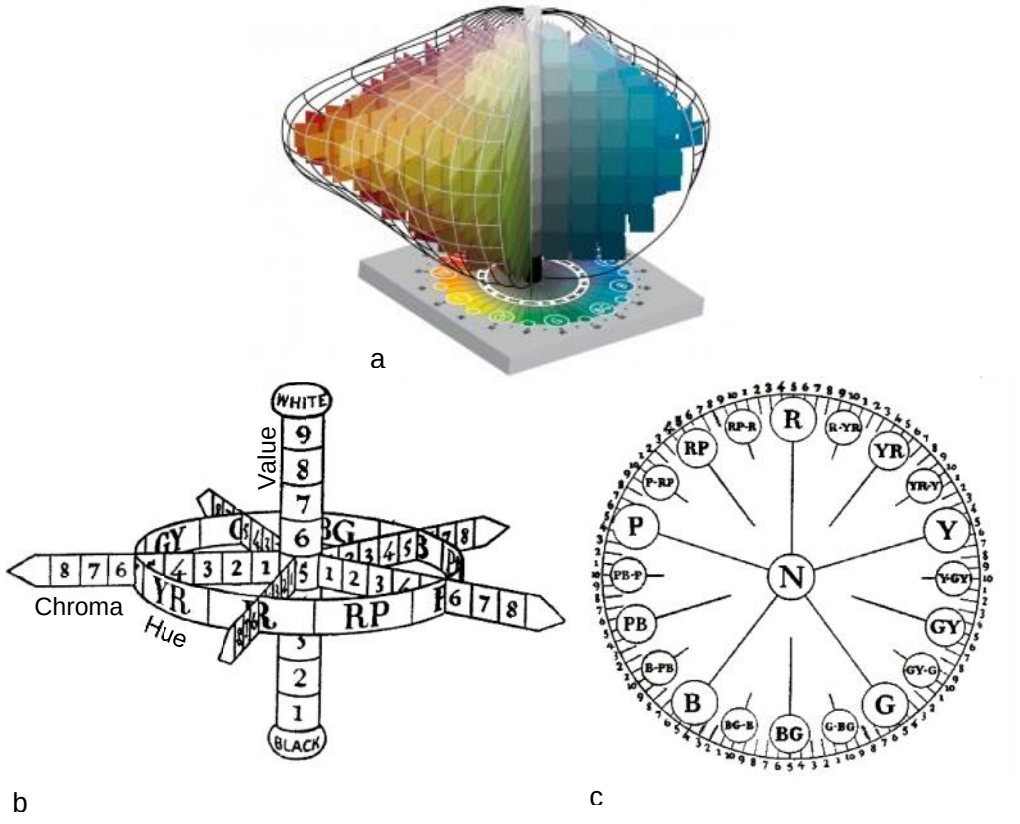

Fig. 4-3: a) The Munsell colour space (Munsell Color 2017), b) the relationship of hue, value and chroma (Cooper 1929: 14, fig. 2 (modified))and c) the relationship between hue and intermediate hue notations (the 100 hue circuit) (ibid., p. 20, fig. 26 (modified)).

(Cooper 1929:9). Value[1] is the strength of light between pure white (value of 10) and pure black (value of 0), light colours being nearer to white and dark colours to black (ibid., p. 10). Halfway between these two values is neutral grey designated by N (ibid.). All chroma designations that fall directly on the value axis are designated as neutrals (N). Chroma is the designation for colour strength or "its departure from a neutral of the same lightness" (Munsell Color 1994:1). As a final step, each hue can have up to 10 intermediate hue numbers, '5' representing the principle hue (Cooper 1929:19-21). Combining all the criteria provides the quad-nominal colour designation where hue intermediate designation is presented first followed by hue and value over chroma. For example, a red colour with a value halfway between white and black and three steps out in chroma will be designated as 5R 5/3.

The Munsell Book of Color, Matte Edition, (2010) was used to collect Munsell designations for the archaeological sherds and the faience replicate glazes to provide an international standard to convey the colour information. The book contains 1600 coloured chips corresponding to various colour designations organized by hue notations. The book and the glazes were placed ~30 cm under a 60 W 240 V daylight bulb producing ~700 lumen. Hue was judged first. The value and chroma were determined by comparing the glazes to the chips, first going beyond the possible colour range then narrowing the selection until only one chip remained. This resulted in a colour designation for each glaze.

4.4.4 Scanning Electron Microscopy

SEM-EDS is used to determine glaze composition profiles and are compared to HH-XRF surface analysis. Replicate and archaeological samples were examined using a CamScan 2040 Scanning Electron Microscope with the Oxford Link Pentafet 5518 Energy Dispersive X-ray spectrometer operating at 20 kV for compositional analysis. The spectrometer's window (ATW2) allows X-ray detection of light elements down to boron (Z>4). The SEM is maintained at the Department of Archaeology and Conservation, Cardiff University.

The SEM consists of a gun that produces electrons from a tungsten filament within 0.1 – 30 kV. The electrons are sent through the microscope column in a vacuum where they are filtered and focused through the use of collimators to produce a fine beam spot (<10 nm) that interacts with the sample surface to a depth of ~1 µm (Fig. 4-4)

[1] Cooper (1929:12) states that black (value = 0) and white (value =10) can never be designated as colours. The human eye perceives black and white as values in the colour space of 1 and 9 respectively.

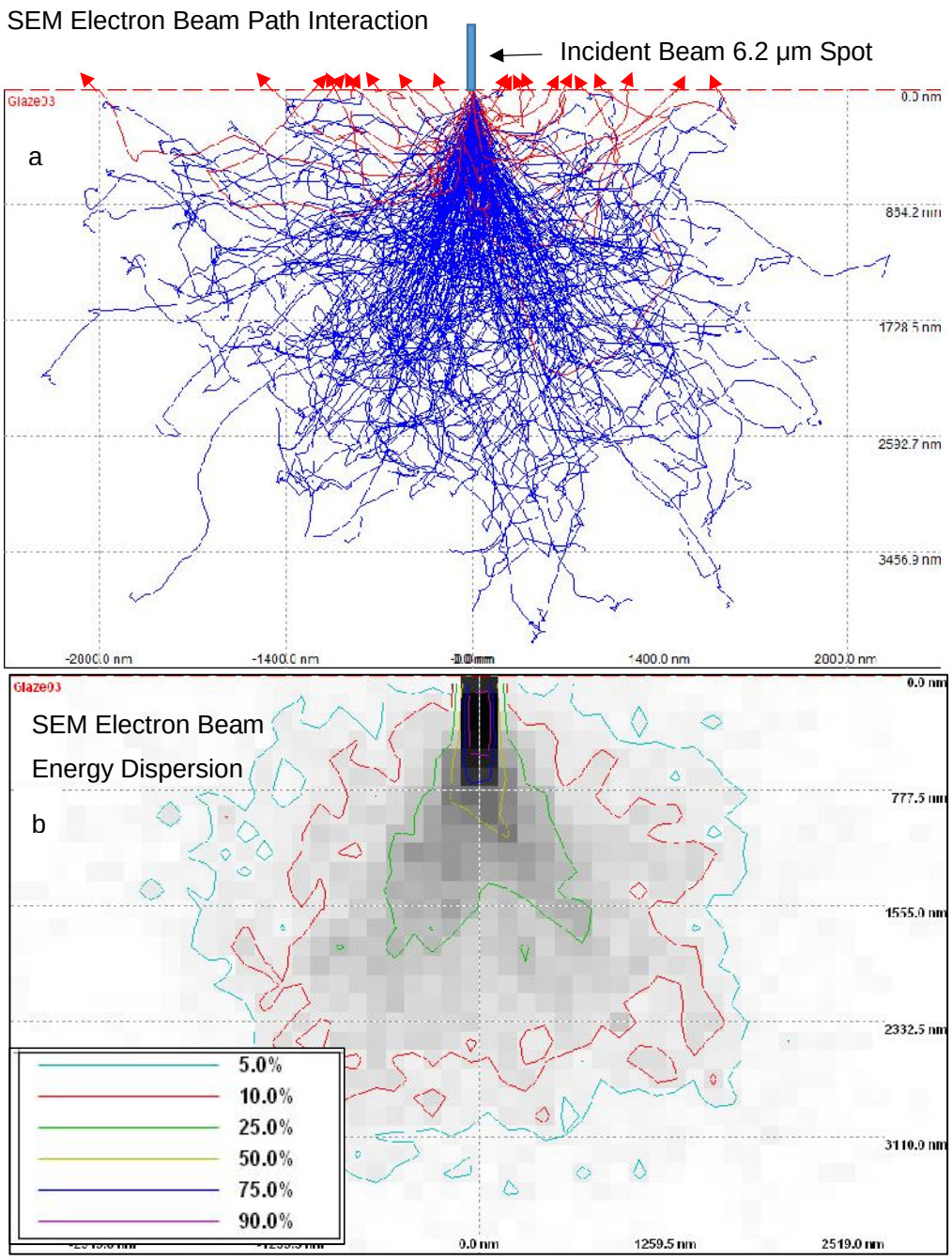

Fig. 4-4: SEM electron beam / sample matrix interaction simulation based on 1000 electrons at 20 keV incident beam energy with a 6.2 beam spot size. The sample matrix is similar to faience replicate copper colourant glaze 03. The sample density is set for 2.24 g/cm^3. Red paths (a) indicate electrons (a total of 21) that escaped the sample and were available for detection. An increase in the angle of interception will increase the escape volume of electrons. Note that 50% of the energy is dispersed at ~1 µm (1000 nm) depth (b). HH-XRF photon sample interaction is similar to this except the spot size is measured in millimetres and the depths from 60 to 4000 µm. The image was produced using Casino (ver. 2.48) software (Demers et al. 2011).

(Goldstein et al. 2003:22). The electron beam is focused to a particular plane and glides across the analytical surface as a raster through the use of scan coils producing secondary electrons (SE), backscattered electrons (BSE), characteristic X-rays and a variety of lessor signals (Goldstein 2003:1; Henderson 2000:18). The resultant electrons and photons strike detectors surrounding the sample stage producing SE images, BSE images and energy dispersive X-ray spectra depending on the detector being used. The process occurs within a vacuum to reduce electron scatter and photon attenuation that would otherwise occur in an air column. BSE are electrons that have entered into the sample matrix as part of the incident radiation and exited through elastic scattering to become available for detection. Elastic scattering is a limited interaction with sample matrix atoms that cause a change in trajectory (Goodhew 2001:30). The angle of the trajectory change is dependent on the atomic number of the atoms encountered. The detected electrons can be used to create a BSE image revealing compositional contrast based on atomic weight of the elements encountered, higher Z showing brighter in the image. In essence, BSE are electrons that enter and escape a sample matrix carrying information regarding the sample subsurface to the detector (Goldstein 2003:86).

BSE imaging was used on archaeological and replicated faience to reveal the glaze, interaction layer between glaze and body, silica grains in the body, interparticle glass between the silica grains, and inclusions in the various layers. The images were analysed using Fiji (Schindelin et al. 2012), an open source image analysis program, to determine thicknesses of the glaze, the interaction layer between glaze and body, and particle size.

A variety of signals (e.g. BSE, SE) are released upon interaction between electron beam and sample. A portion of the signals is composed of X-rays produced when a primary electron dislodges an inner electron from a sample matrix atom. The ejected electron leaves the atom unstable and to equilibrate, an upper electron drops down to the inner shell to replace the ejected electron. The result is a release of X-ray energy equal to the loss of energy of the replacement electron when changing shells (Goodhew et al. 2001:171). This release of energy is called fluorescence. The energy released (measured as frequency) is specific to each shell of each element and can be identified. The released X-ray photons can be absorbed back into the matrix or escape it to become available for detection. The detection and identification of shell and element origin is called energy dispersive spectroscopy (EDS). Figure 4-4 reveals beam penetration depth of ~4 µm but most of the photons available for detection are from within 0.5 µm (500 nm) of the impacted surface.

The EDS limit of detection is in the range of 0.1-0.3 wt% (1000-3000 ppm) depending on element and current (Goldstein et al. 2003:20). It is typically used to determine major and minor elements (ibid., p.12). EDS and XRF are very similar except for the equipment and the exciting energy used in the analysis. The detection of photons in both analyses can cause several of the same phenomena to occur. These are covered in detail under section 3.2.2.

Only a few of the electrons impinging on the sample will cause the interactions that are useful for SEM analysis. The remainder of the electrons collect on the surface of the sample causing it to have a negative electrical charge which will eventually have a repelling effect on the incident beam causing an obscured image on the SEM monitor (Goodhew 2001:164). A solution is to coat the sample surface with an electrically conducting material (i.e. gold or carbon) that, in effect, grounds it. Alternatively, the instrument can be setup as an environmental SEM when the column contains a vacuum (~10^{-6} torr) and the sample chamber contains a reduced-pressure atmosphere (1-10 torr) which is useful when an object can potentially be damaged within a vacuum or cannot be coated for grounding purposes (Goodhew et al. 2001:166).

Samples for the project were removed from archaeological and replicated faience and mounted on cross-section in Struers Epofix™ epoxy resin. Four to six samples were placed in each mount to reduce the exchange period and keep chamber door opening to a minimum. A segment of cobalt wire was included in the resin for optimization measurements. The resulting resin blocks were ground and polished using Struers Labopol-5™ polishing machine with progressively finer grit silicon carbide papers (180, 320, 1200, 1600, 2500, and 4000) and lapping oil as a lubricant. The polishing produces a smooth sample surface that will reduce electron scatter and facilitate expedient analysis by reducing changes in sample depths of field. Use of oil as a lubricant in the place of water reduces potential alkali depletion during polishing of the replicate and archaeological samples. The resin blocks were carbon coated using the Emitech K450™ Carbon Coater before analysis in the SEM.

The SEM was provided with a 30 minute warm-up and stabilization period before any measurements. Corning glass reference standard B was used to determine precision and verify accuracy for each SEM session. Analytical totals between 98% and 102% were considered adequate for the analysis of the samples as suggested by Goldstein et al. (2003:421). The standard was measured at the start and end of each session and every time the SEM chamber door was opened (see Appendix C). Cobalt wire optimization measurements were conducted at the beginning of each session and every three analytical sample measurements thereafter. Generally optimization

measurements were within 0.5% of the previous measurement. If optimization measurements revealed >2% difference, the beam was recalibrated and the Corning glass reference was measured again for precision and accuracy.

SEM has to be calibrated to provide accurate wt% calculations. Pure elements and mineral standards (No. 4629, Micro-Analysis Consultants Ltd) were used for calibration of the SEM. EDS analysis of the glaze was conducted at 20 kV and a live time of 100 seconds. Spot beam size was x1000 magnification and the detection limit is 2 sigma unless otherwise stated. Nine measurements were conducted on a cross-section of the sample with three measurements near the glaze surface, three in the centre of the glaze layer and three near the interaction zone between body and glaze. Results of the glaze analysis are presented as normalized compound wt% with raw (not normalized) wt% analytical totals. Measurements near the surface may reflect weathering whereas measurements near the glaze middle should reveal nominal compositions. All the measurements were used to reveal the compositional profile and may exhibit element migration within and even through the glaze (e.g. sodium and copper).

Fiji (ImageJ vers. 1.51n; Schindelin et al. 2012), an open source image analysis program, allows calibration with scaled images and was used to determine thicknesses of the faience glazes, the interaction layer between glaze and body, and particle sizes (Chapter 7). Ten equidistant measurements were taken across each glaze BSE image to record the glaze surface to the upper interaction-layer (IAL (glaze layer between glassy glaze and body)) plane (glaze) and the upper IAL plane to the lower IAL plane (IAL). The upper IAL plane is demarcated by a level of unreacted silica. The lower IAL plane exhibits an extension of the unreacted silica into the body and the cessation of heavy interparticle glass/glaze. The distance between each measurement was dependant on the length of the sample within the BSE image.

Selection of body silica particles for measurement were determined by placing a point grid (plug-in developed by Wayne Rasband at NIH.Gov) across the surface of a back scattered image of the body cross section (Fig. 4-5). The point distribution was set to 16k μm^2 resulting in 72 points each being separated by 126.5 µm. The longest axis of each silica particle on which a grid point fell was measured and entered into the database. Subsequent points that fell on a particle already measured were ignored as were points that fell into interparticle space.

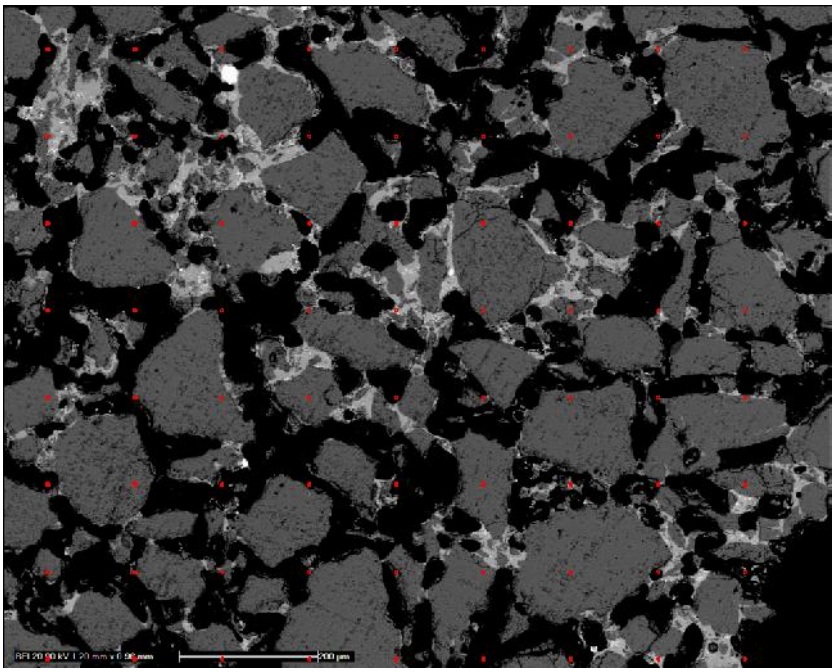

Fig. 4-5: SEM-BSE image of replicated faience sample R429 body silica particles. Red grid points overlying the image determine which particles were included in the particle size determination for each sample.

4.4.5 Hand Held X-Ray Fluorescence

The HH-XRF is being evaluated to determine the type of useful information it can provide in the non-destructive analysis of faience glazes in the field or in museum environments. The parameters required for setup include voltage, current, use of filter, use of vacuum and acquisition time. Experiments are required to fine tune these parameters for optimal detection capability with glass and glaze. Some object geometries may form a signal attenuating air column between sample and detector. Experimentation will reveal the amount of distance that is available before the analysis is detrimentally affected. Section 3.2 provides greater detail into these issues.

A Bruker Tracer III-SD HH-XRF analyser was used for each parameter evaluation experiment (Chapter 6) and for the analysis of faience replicates and archaeological sherds as part of the main study. The system uses a rhodium tube and silicon drift detector. It has a resolution of 150V, 150 HWFM, and a beam spot size of 3 x 4 mm. The sample was placed directly on the unit window for all analyses unless indicated. Ten areas across the sample were measured for each setting unless otherwise stated. X-ray Ops 2.2.31 was used to optimize X-ray voltage and current. Data acquisition was obtained using S1PXRF v3.8.30. Artax Spectra 7.4 is used for processing including peak deconvolution and net peak area (NPA) calculations.

All measurements were taken within a benchtop X-ray cabinet for safety and dosimeters were used to identify presence of radiation exposure (see Appendices D (risk assessment) and E (local rules regarding HH-XRF use)). Ungridded Prolene end windows (Window B) were used for all tests unless specifically stated. Variables are addressed specifically for each experiment (Fig. 4-6; Table 4-3). All references to elements on the HH-XRF spectra are associated with the Kα line unless otherwise stated. Settings A and B (see Table 4-3) are based on recommendations by Kaiser and Wright (2008:45-48) and all other test settings are based on these two but with different variables.

4.5 Data Exploration: Basic Statistics

This section covers basic statistics used in the project. The aim of using basic statistical analysis in this study is to determine if HH-XRF is suitable for the analysis of faience glazes. Basic statistics are the foundation of the project and are required for the initial evaluation of HH-XRF setup procedures. The various basic statistics and how they were implemented are defined and explained in this section. The instrumental analysis of faience glazes produces a large quantity of numerical data. Some of the data may share relationships that indicate a greater data structure, thereby generating potentially useful archaeological information. Basic statistics can provide a quick summary of the data. Multivariate methods are required to provide a deeper interpretation of the data by reducing the number of dimensions, facilitating the grouping of faience data sets, and modelling the relationships that may exist between variables associated with the samples (Cordella 2012:1; Josse and Husson 2016:1-2). Multivariate methods will be covered in Chapter 8.

Basic descriptive statistics are commonly used in the archeaometric literature to gain insight into data sets. Basic statistics used for this project include mean (μ), median (M), standard deviation of a population (σ), coefficient of variance (C_v), signal-to-noise ratio (SNR), and limit of determination of a method (LDM). These are measures of central tendency, dispersion, precision and detection. ‘Standard deviation of a population’ is used instead of ‘standard deviation of a sample’, which uses predictive measures, because the sample size is relatively small and easily handled.

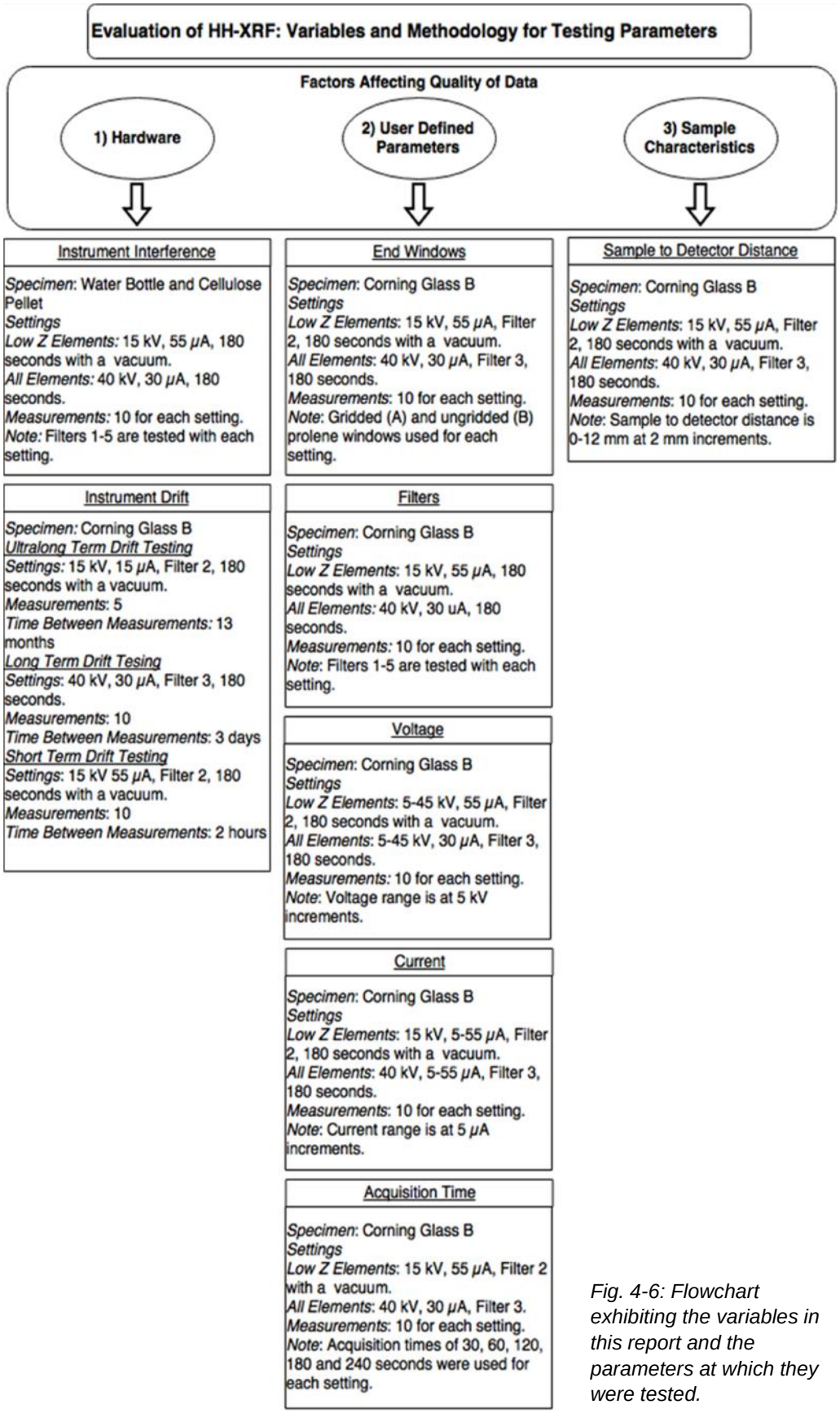

Fig. 4-6: Flowchart exhibiting the variables in this report and the parameters at which they were tested.

Table 4-3: Parameter settings used during the evaluation of the HH-XRF.

HH-XRF Evaluation Parameter Settings					
Setting	Voltage (kV)	Current (μA)	Filter	Acquisition (Seconds)	Vacuum
A	15	55	2	180	Yes
B	40	30	3	180	No
C	40	30	2	180	No
D	15	55	Variable	180	Yes
E	40	30	Variable	180	No
F	Variable	55	2	180	Yes
G	Variable	30	3	180	No
H	15	Variable	2	180	Yes
I	40	Variable	3	180	Yes
J	15	55	2	Variable	Yes
K	40	30	3	Variable	No

4.5.1 Basic Statistics Data Handling Software

Computing the statistical investigation on the quantity of data generated by the instrumental analyses requires appropriate software. Microsoft ® Excel 2013 (ver. 15.0.4903.1002) is an electronic spreadsheet software with limited statistical capabilities. Excel was used to determine basic descriptive statistics including mean (μ), median (M), standard deviation (σ), coefficient of variance (C_v), signal-to-noise ratio (SNR), and limit of determination of a method (LDM). The INCA (SEM) and Artax Spectra (HH-XRF) software export analytical results directly into Excel allowing the generation of quick basic statistics. All generated instrument analytical data is stored in the excel format (.xls) for this reason but can be easily exported in various formats for use with other software. The software used for multivariate analysis is covered in section 8.3.3.

4.5.2 Basic Statistics Used in Project

Basic statistics were used to provide a general description of individual specimens or datasets. This data can be useful when examining analytical results of individual sherds to determine the spread of the mean, precision, detection limits and bivariate correlations. Accuracy (quantitative) was not measured because of the required use of ~18 material reference standards with glass/glazes and HH-XRF analysis.

A few basic statistics were used as part of the HH-XRF evaluation. Standard deviation (σ) is the quantified dispersion of a dataset (Eq. 4-1). Coefficient of variance (C_V), also known as relative standard deviation (RSD%), is a measure of precision (Eq. 4-2). C_V is adopted in this study because it is becoming more prevalent than RSD% in the literature.

$$\sigma = \sqrt{\frac{\Sigma(x-\mu)^2}{N}} \qquad (4\text{-}1)$$

$$C_V = 100\ X\ \frac{\sigma}{\mu} \qquad (4\text{-}2)$$

C_v provides a precision of measurement for each method. Lower results for σ and C_v indicate greater precision of the respective measured data. The relative absolute percent error (RAE%) is a measure of accuracy (Eq.4-3)

$$RAE\% = 100\ X \left(\frac{\frac{1}{n}\sum_{i=1}^{n} a_i - y}{y} \right) \qquad (4\text{-}3)$$

where y is the known value and the first part of the numerator is the average, multiplying the result of which provides the percent.

Limit of determination of a method (LDM) (Eq. 4-4) is the level of uncertainly attributed to a set of measurements with a 95.4% confidence level (Rousseau 2001:41).

$$LDM = 2\sqrt{\frac{\sum_{m=1}^{n}(C_m - \bar{C})^2}{n-1}} \qquad (4\text{-}4)$$

LDM is the uncertainty number (±) provided aside an analytical result and indicates that 95.4% of the measurement results of a given setting will be contained within the range. Quantitatively, LDM is ~2σ of a set of results (n=10) of the same representative sample. The equation for %difference (Eq. 4-5) is applied with the analysis of instrument drift (section 6.3.3). Negative signs of the results are dropped to provide absolute %difference between two measurements taken at separate times.

$$\%difference = 100\ X\ \frac{(m_{1} - m_{2})}{\left\{\frac{m_{1} + m_{2}}{2}\right\}} \qquad (4\text{-}5)$$

Net peak analysis was conducted partly by determining the signal-to-noise ratio (SNR) using deconvoluted data provided by the Artax Spectra software. The ratio represents the height of the peak above the associated background noise. The standard process

of determining SNR in many scientific analyses is by dividing the peak intensity by the standard deviation (σ) of the background under the peak (ACS 1980:2246-2247; Ernst et al. 2014:20) (Eq. 4-6).

$$S = N P I_1 / \sigma_B \quad (4\text{-}6)$$

The SNR of energy dispersive XRF is different because of sample geometry, density, thickness and consistency which directly affect the background (Ernst et al. 2014:20). The relationship between the specimen and the background require a more vigorous method of calculating noise (N) that takes the sample matrix into account. The accepted expression for N in this relationship is the square root of the background under the peak of interest (Commission 1976:103) (Eq. 4-7), and this provides an appropriate equation for XRF SNR (Eq. 4-8).

$$N = \sqrt{B I_1} \quad (4\text{-}7)$$

$$S = N P I_1 / N \quad (4\text{-}8)$$

This data is useful for determining the LOD and the limit of quantification (LOQ) (Ernst et al. 2014: 14; Pers. Comm. Rebecca Scott). The LOD (SNR ≥3) determines if a peak is significantly greater than the background and can be confidently identified (Keith et al. 1983:2217). The LOQ (SNR ≥10) indicates the element can be confidently quantified and that semi-quantitative ratio comparisons will be accurate (Ernst et al. 2014: 17). Uncertainty increases for a SNR closer to three although its use may be justified. Counts-based LOD (Eq. 4-9) and LOQ (Eq. 4-10) can be calculated by the following equations (Ernst et al. 2014: 20):

$$L_{(C)} = 3N \quad (4\text{-}9)$$

$$L_{(C)} = 10N \quad (4\text{-}10)$$

The concentration-based result for LOD (Eq.4-11) and LOQ (Eq.4-12) is calculated using samples with known concentrations (c) by the following equations:

$$L_{(C)} = 3c/S \quad (4\text{-}11)$$

$$L_{(C)} = 10c/S \quad (4\text{-}12)$$

Pearson's r correlation coefficient (r) represents the strength of the correlation between two or more variables. Squaring Pearson's r provides the coefficient of determination (r^2) which represents the percentage of data points that fall on the regression line. It is a measure of fit to the trend. The p-value (p) indicates level of confidence that the dataset has meaning or is a product of random chance.

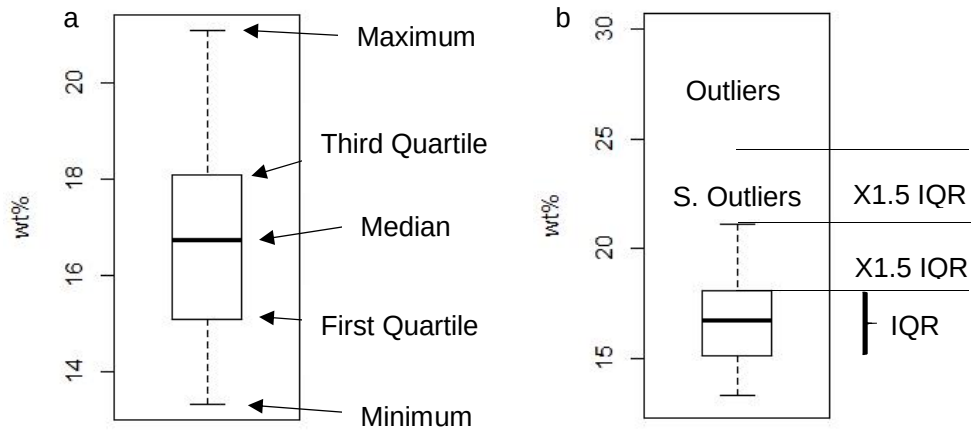

Fig. 4-7: Box-Plot diagram. Figure a exhibits the general components of the box plot where most of the data points will be distributed. Figure b exhibits how the box plot is useful for identifying outliers. The Interquartile Range (IQR) represents 50% of the data. Outliers are 3x the IQR and suspected outliers (S. Outliers) are x1.5 the IQR, either above or below the IQR.

The Shapiro-Wilk test (Shapiro and Wilk 1965) is an indicator of data normality where the null hypothesis supports normally distributed data. It will be used to determine the effectiveness of the data transformations before multivariate analysis. The test produces two figures, w and p-value. Normality of data is indicated by w which ranges from 0 to 1 where 1 is normality. A p-value of >0.05% is a non-rejection of the null hypothesis and a p-value of <0.05 is a rejection of the null hypothesis. The Shapiro-Wilk test can be represented graphically for verification as a histogram and a normal probability plot.

The Hopkins Statistic is a spatial randomness test or a measure of clustering tendency of the data (Lawson and Jurs 1990). It is the nature of cluster analysis to force clusters whether they exist or not. The Hopkins Statistic provides a general level of confidence for cluster analysis; it produces a result in the range of 0-0.5 where 0 indicates a tendency to cluster and results closer to 0.5 indicate increasing randomness.

The box-plot, as it is used here, is a graphical measure of distribution of points for a single variable (Fig. 4-7). It is composed of a box representing 50% of the data, a black line in the box representing the median of the data and the minimum and maximum lines. The min/max lines extend up to x1.5 the interquartile range (IQR) or to the most extreme point if no points go beyond this limit, thereby demarcating the data range (Baxter and Cool 2016:64-65). Points outside of the minimum or maximum are considered potential outliers. Box plots are better suited for unimodal data (Baxter 2015:35). Multimodal data is more difficult to interpret because points indicated to be outliers could be part of a tail of a mode situated on that side of the IQR.

Chapter 5: Replication of Faience

5.1 Introduction

Replications of application-glazed faience have been produced to imitate the chemical, microstructural and aesthetical characteristics of copper and cobalt-coloured blue archaeological material from the Late through the Ptolemaic and Roman Periods of Egypt. This project is evaluating the use of HH-XRF on faience vessels. Application glazing is replicated because it is the prominent glazing technique used on vessels during the Ptolemaic and Roman Periods. Replications will be used as a known material to produce analytical results as part of the HH-XRF evaluation. Replication experiments enabled the testing of compositions, application methods (i.e. dipping and painting) and firing parameters. Corning glass standards are sufficient for most of the HH-XRF evaluations (e.g. voltage, current) (see Chapter 6) having the full complement of elements expected in blue glazed faience but replicated faience samples provide a known glaze on a known substrate and help to indicate the effects of a layered structure on the analytical results.

The replication process was conducted in a laboratory setting at Cardiff University over the course of a year. Most of the work was conducted during the spring and summer months to avoid the higher humidity levels typically associated with winter months in Wales, and to facilitate the evaporation of the water component of the applied glaze.

5.2 Materials and Replication Setup

The batches for body and glaze (Tables 5-1 and 5-2) were derived from published analytical and replication data (see Table 2-8). The raw materials selected for replication were obtained from ceramic and chemical supply companies (Appendix F). Two silica sources consisting of filtered sand and quartz powder were selected for testing. Both sources had to be ground with a mortar and pestle for use but the crushed quartz offered a less intensive process. All components were mixed and ground together. The selection of chemicals was based on requirements and economics; carbonates produce carbon dioxide during firing but are generally financially cheaper than oxides (tens versus hundreds of pounds). Copper oxide was selected over copper carbonate (only slightly less expensive) to reduce the amount of

Table 5-1: Composition of faience replication batches. Silica source is quartz powder (QP) or ground sand (GS).

Replicate Faience Batch Composition by Weight % (Normalized to 100%)															
Batch	**Silica Source**	**SiO_2**	**Na_2CO_3**	**K_2CO_3**	**$CaCO_3$**	**CuO**	**$Al(OH)_3$**	**$MgCO_3$**	**FeO**	**MnO**	**SnO**	**CoO**	**PbO**	**Sb_2O_3**	**Clay**
B01	QP	97.66		0.63	1.70										
B02	QP	91.81		0.60	1.60										5.99
B03	QP	88.80		0.59	4.83										5.78
B04	QP	92.34			1.64										6.02
B05	GS	97.66		0.63	1.70										
B06	GS	67.52	1.76	0.43	29.70				0.24	0.02	0.12		0.05	0.15	
B07	GS	96.21	1.74	0.43	1.05				0.24	0.02	0.12		0.05	0.15	
B08	GS	54.09	2.43	0.51	42.50				0.19	0.02	0.10		0.04	0.12	
B09	GS	94.07	2.91	0.62	1.83				0.23	0.02	0.12		0.05	0.15	
GLZ01	QP	73.98	19.39		5.10		1.54								
GLZ02	GS	71.42	18.72		4.93	3.45	1.48								
GLZ03	GS	59.17	25.84	2.46	7.49	2.52	2.52								
GLZ04	GS	20.62	52.57	7.22	7.22	6.19									6.19
GLZ05	GS	68.68	13.13	4.04	5.05	2.02	2.02	1.58	1.21	0.10	0.73	0.30	0.55	0.61	
GLZ06	QP	67.60	12.92	2.70	7.16	1.99	2.60	1.57	1.19	0.10	0.71	0.30	0.55	0.60	
GLZ07	GS	72.98	13.06	1.58	4.12	2.28	1.67	1.14	1.24	0.13	0.38	0.17	0.95	0.29	
GLZ08	GS	85.54	3.06	1.14	3.06	1.64			1.14	0.16	0.20	0.28	3.26	0.52	
GLZ09	GS	73.98	19.39		5.10		1.54								

Table 5-2: Composition of faience replication batches based on oxide conversion. Silica source is quartz powder (QP) or ground sand (GS).

Replicate Faience Oxide Composition (Converted) by wt% (Normalized to 100%)														
Batch	**Silica Source**	**SiO_2**	**Na_2O**	**K_2O**	**CaO**	**CuO**	**Al_2O_3**	**MgO**	**FeO**	**MnO**	**SnO**	**CoO**	**PbO**	**Sb_2O_3**	**Clay**
B01	QP	98.60		0.44	0.96										
B02	QP	92.64		0.41	0.91										6.04
B03	QP	90.90		0.41	2.77										5.92
B04	QP	93.01			0.92										6.06
B05	GS	98.60		0.44	0.96										
B06	GS	78.45	1.20	0.34	19.33				0.28		0.14		0.06	0.18	
B07	GS	97.50	1.03	0.30	0.60				0.24		0.12		0.05	0.15	
B08	GS	67.50	1.77	0.43	29.72				0.24		0.12		0.05	0.15	
B09	GS	96.20	1.74	0.43	1.05				0.24		0.12		0.07	0.15	
GLZ01	QP	82.95	12.71		3.20		1.13								
GLZ02	GS	79.76	12.22		3.09	3.85	1.08								
GLZ03	GS	70.18	17.92	1.99	4.97	2.99	1.95								
GLZ04	GS	28.36	42.29	6.77	5.56	8.51									8.51
GLZ05	GS	76.72	8.57	3.07	3.16	2.26	1.47	0.84	1.35	0.11	0.81	0.34	0.61	0.68	
GLZ06	QP	76.02	8.50	2.08	4.52	2.24	1.92	0.85	1.34	0.11	0.80	0.34	0.62	0.67	
GLZ07	GS	80.12	8.38	1.18	2.53	2.51	1.20	0.60	1.36	0.15	0.42	0.19	1.04	0.32	
GLZ08	GS	88.16	1.85	0.80	1.77	1.69			1.18	0.16	0.21	0.29	3.36	0.53	
GLZ09	GS	82.95	12.71		3.20		1.13								

carbonates in the faience replication mixtures and off-gassing (e.g. carbon dioxide) during firing.

5.2.1 Replicated Body and Glaze Overview

The composition ranges provided by Vandiver (1982) and analysis by Griffin (2002) and Shortland and Tite (2005) influenced the body recipes (B01-09). Ground sand and quartz powder are compared in bodies B01 and B05 which are identical in every other aspect. B02-04 all have ~6 wt% clay added as a binder based on replications by Griffin (2002:335) who found that 1-12 wt% clay facilitates forming, moulding and throwing. B02 and B03 differ in the amount of calcium and B04 was experimental to see the effects of no alkali in a fired body. Bodies B06 and B08 were experimental with increased calcium content. Bodies B07 and B09 represent the typical concentrations of Roman material as determined through analysis (Griffin 2002; Shortland and Tite 2005). They offered a substrate with markers (i.e. iron, tin, lead and antimony) that could potentially be detected by HH-XRF.

Glazes GLZ01-03 and 09 were influenced by replications of application glazes (Tite and Bimson 1986). Three of these four glazes are similar with portion variability restricted to one component or the replacement of ground sand with quartz powder. Glaze 03 has the most variability resulting from replacement of some silica with alkali which has affected the concentrations of the remaining oxides upon normalization. The introduction of ~8 wt% clay to GLZ04 is based on Binn's (1932:272) applied glaze which contained clay to reduce fluidity. Glazes 05 (ground sand) and 06 (quartz powder) are average concentrations found in blue glazes from Ptolemaic/Roman Memphis (Berman 1999; Griffin 2002; and Manti 2013). A typical cobalt-coloured Ptolemaic/Roman Period glaze, represented by GLZ07, is based on analysis by Abe et al. (2012), Manti (2013), Shortland and Tite (2005) and Vandiver (1983). Glaze 08 is based on low-alkali Ptolemaic Period glazes analysed by Mao (2000).

5.2.2 Batch Component Conversion

Batches consisted of oxides, carbonates and hydroxides (see Appendix F; see Table 5-1). Faience components are reported as oxides in most published analysis requiring some of the batch material to be converted from oxides to carbonates and hydroxide (aluminium) to determine the amount of material to include in each batch mixture. The conversion factor is determined by dividing the atomic weight of the elements in the given formula by the atomic weight of the elements in the desired formula. Multiplying the given weight% by the conversion factor enables oxides to be converted to carbonates and vice versa. For example, the conversion factor to convert 5 wt% CaO

to $CaCO_3$ is determined by dividing 100.086 (40.078 (Ca) + 12.011 (C) + (3 * 15.999 (O)) by 56.077 (40.078 (Ca) + 15.999 (O)) resulting in 1.7848. The conversion factor (1.7848) is multiplied by the given oxide (5 wt%) to convert it to carbonate (8.924 wt%). Therefore, it can be determined that 8.924 wt% $CaCO_3$ will produce 5 wt% CaO after the loss of CO_2 on ignition assuming there is complete conversion.

The aluminium hydroxide conversion is conducted in a similar fashion using molar mass and stoichiometry (Eq. 5-1 and Table 5-3; see Eq. 2-2). The key to determining the conversion factors of aluminium hydroxide is knowing its molar mass (78.0 g/mol), then converting it to grams:

$$2A\,(O\ \ )_3 = (2\,m\ \ )\left(78.0036\ \frac{g}{m}\right) = 156.01\ g \qquad (5\text{-}1)$$

Table 5-3: Factor determination for aluminium hydroxide using stoichiometry.

Factor Determination for Aluminium Hydroxide Conversions							
	$2Al(OH)_3$	→	Al_2O_3	+	$3(H_2O)$		
Molar Mass (g)	156.01	=	101.96	+	54.05	=	156.01
	Factor		Factor		Factor		
Al(OH)3	1		0.65		0.35		
Al2O3	1.53		1		0.53		
3(H2O)	2.89		1.89		1		

5.2.3 Material Grinding and Mixing

A large reserve of pre-grounded sand was maintained for use with all batches (glaze and body). Sand was ground using an agate mortar and pestle until it was <180 µm in diameter as measured through nesting sieves (180 µm representing the smallest screen mesh). The use of quartz powder for some experiments reduced the time and effort in grinding.

Ground sand and other materials required by the batches were measured to the nearest centigram using a scientific scale. Batch components were placed together into the nesting sieves (of various sizes down to 180 µm) and ground using the agate mortar and pestle when required to reach the next smallest sieve until all particles were <180 µm in diameter. The sieving and grinding of components helped to mix them. The batches were mixed through agitation within a sealed bag for 5 minutes. Batches were stored ready for use in labelled polythene bags.

5.2.4 Sample Preparation

Sample bodies and solid glaze pellets were prepared by measuring 4 grams of batch material in a weigh boat on a scientific scale. The powder was mixed to a good working consistency with deionized water using a dropper and 18 to 24 drops per sample which equates to 0.9 to 1.2 ml of water (each drop is ~0.05 ml). The wet paste was placed into a stainless steel 2 cm diameter circle cutter (used in craft and baking) with a small spatula and tamped down. The circle cutter was immediately removed and the paste, being thixotropic in nature, retained its shape unless agitated. The samples were air dried in a fume hood for at least 24 hours before handling. The dried samples were weighed after drying but before firing, and again after firing to provide an indication of fractionation. Prefired and unfired bodies were required for experimentation. A minority of the sample pastes were either placed in crucibles (with and without a calcium bed) or hand-formed.

Many of the experiments required the use of a prefired body and/or prefritted glaze powder. These bodies and glazes were kiln fired after drying at 850 °C for 1 hour to drive off bound water and carbon dioxide. Prefired bodies were ready for glazing upon removal from the kiln. Fritted glaze pellets had to be ground with an agate mortar and pestle to a particle size of <180 µm diameter before application as a glaze powder or slurry.

Raw glazes were applied to raw and prefired bodies through slurry immersion, slurry painting and as a dry powder to a wetted body. Slurries were produced by adding deionized water to a workable consistency. Dry powder was applied to bodies by moistening the body surface with deionized water and burying the body in glaze powder before being removed and fired. Dry powder application is an experimental method and is not based on archaeological evidence. Prefritted glazes were added as a painted slurry after determining that other application methods were inferior.

5.2.5 Firing Process

Samples were fired in a CU4 electric kiln with Bentrup T405 Thermo-computer controller (Fig. 5-1) using various settings depending on the experiment (a and b). The computer allows for a heating ramp up to a dwell, a second heating ramp to the soak and a cooling ramp. Temperature increase/decrease rate of the ramps can be restricted (°C/hour). Most of the composition testing occurred early in the project before a common firing parameter was established resulting in greater parameter variability evident in Table 5-4a and b. Faience replications used for the HH-XRF

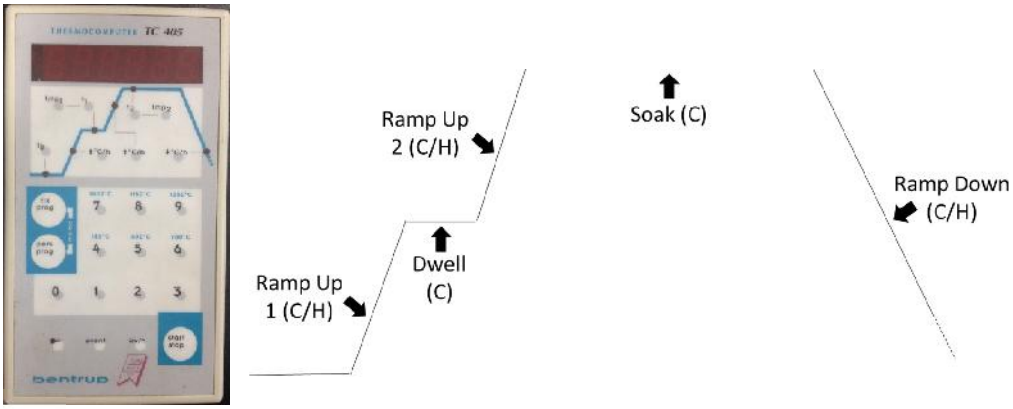

Fig. 5-1: a) Thermo-computer control for inputting kiln firing parameters. b) The diagram illustrates the ramp ups, dwell, soak and ramp down cycles.

evaluation were produced with a systematic firing regimen where minor changes only occur when testing a specific variable.

5.3 Experimentation

Several experimentations were conducted to produce a faience analogue that was similar to archaeological faience from the periods of interest. Two of the tests involved composition and glaze application of the faience replicates. Two experiments tested firing parameters on use with faience replications and accuracy/precision of the kiln computer so that the actual temperatures attained were known.

5.3.1 Variable Batch Composition

All compositions in Tables 5-1 and 5-2 were fired to determine colour of the resultant glazes and friability/durability of the bodies. The friability and durability of the bodies were assumed to be a product of the amount of alkalis (see section 5.4.2). The colours were expected to be influenced by the amount and types of colourants and alkalis. Compositional changes incorporated body condition (i.e. unfired and prefired), glaze slurry thickness (i.e. thick and thin) and glaze powder condition (prefritted vs raw). Ultimately the goal was to produce a faience replicate that would serve as an analogue to archaeological faience without the surface deposits and weathering.

Table 5-4a: Replication experiments and firing parameters. Prefired bodies are designated with PrF.

Replication Firing Experiments									
Body Batch	Glaze Batch	Subject	Ramp Up 1 (°C/H)	Dwell (°C)	Dwell Period (min)	Ramp Up 2 (°C/H)	Soak Temp (°C)	Soak Period (min)	Ramp Down (°C/H)
Common Setting			200	400	0	100	850	60	200
Composition Testing									
B01			400	400	0	200	850	60	200
B02			400	400	0	200	850	60	200
B03			400	400	0	200	850	60	200
B04			400	400	0	200	850	60	200
B05			400	400	0	200	850	60	200
B06			100	100	0	200	850	60	200
B07			100	100	0	200	850	60	200
B08			200	400	0	100	850	60	200
B09			200	400	0	100	850	60	200
	GLZ01		999	800	0	999	800	180	999
	GLZ02		999	800	0	999	800	180	999
	GLZ03		200	400	0	100	850	60	200
	GLZ04		999	800	0	999	850	180	999
	GLZ04		999	800	0	999	800	180	999
	GLZ05		200	400	0	100	850	60	200
	GLZ06		200	400	0	100	850	60	200
	GLZ07		200	400	0	100	850	60	200
	GLZ08		200	400	0	100	850	60	200
Application Testing									
B06	GLZ02	Immersion	200	400	0	100	850	60	100
B06	GLZ02	Painted Slurry	200	400	0	100	850	60	100
B06	GLZ02	Dry Powder	200	400	0	100	850	60	100
B06 PrF	GLZ02	Immersion	200	400	0	100	850	60	100
B06 PrF	GLZ02	Painted Slurry	200	400	0	100	850	60	100
B06 PrF	GLZ02	Dry Powder	200	400	0	100	850	60	100
B07	GLZ02	Immersion	200	400	0	100	850	60	100
B07	GLZ02	Painted Slurry	200	400	0	100	850	60	100
B07	GLZ02	Dry Powder	200	400	0	100	850	60	100
B07 PrF	GLZ02	Immersion	200	400	0	100	850	60	100
B07 PrF	GLZ02	Painted Slurry	200	400	0	100	850	60	100
B07 PrF	GLZ02	Dry Powder	200	400	0	100	850	60	100
B08	GLZ03	Immersion	200	400	0	100	850	60	100
B08	GLZ03	Painted Slurry	200	400	0	100	850	60	100
B08	GLZ03	Dry Powder	200	400	0	100	850	60	100
B08 PrF	GLZ03	Immersion	200	400	0	100	850	60	100
B08 PrF	GLZ03	Painted Slurry	200	400	0	100	850	60	100
B08 PrF	GLZ03	Dry Powder	200	400	0	100	850	60	100
B09	GLZ03	Immersion	200	400	0	100	850	60	100
B09	GLZ03	Painted Slurry	200	400	0	100	850	60	100
B09	GLZ03	Dry Powder	200	400	0	100	850	60	100
B09 PrF	GLZ03	Immersion	200	400	0	100	850	60	100
B09 PrF	GLZ03	Painted Slurry	200	400	0	100	850	60	100
B09 PrF	GLZ03	Dry Powder	200	400	0	100	850	60	100

Table 5-4b: Replication experiments and firing parameters. Prefired bodies are designated with PrF. Prefritted glazes are designated with PF. Firing parameter variables are in bold and encased.

Replication Firing Experiments (continued)

Body Batch	Glaze Batch	Subject	Ramp Up 1 (°C/H)	Dwell (°C)	Dwell Period (min)	Ramp Up 2 (°C/H)	Soak Temp (°C)	Soak Period (min)	Ramp Down (°C/H)
Common Setting			200	400	0	100	850	60	200
Firing Parameter Testing									
B09	GLZ03 PF	Soak Period	200	400	0	100	850	**360**	200
B09 PrF	GLZ03 PF	Soak Period	200	400	0	100	850	**360**	200
B09	GLZ03	Soak Period	200	400	0	100	850	**360**	200
B09 PrF	GLZ03	Soak Period	200	400	0	100	850	**360**	200
B09	GLZ03 PF	Soak Period	200	400	0	100	850	**180**	200
B09 PrF	GLZ03 PF	Soak Period	200	400	0	100	850	**180**	200
B09	GLZ03	Soak Period	200	400	0	100	850	**180**	200
B09 PrF	GLZ03	Soak Period	200	400	0	100	850	**180**	200
B09	GLZ03	Soak Period	200	400	0	100	850	**60**	200
B09 PrF	GLZ03	Soak Period	200	400	0	100	850	**60**	200
B09	GLZ03 PF	Soak Period	200	400	0	100	850	**60**	200
B09 PrF	GLZ03 PF	Soak Period	200	400	0	100	850	**60**	200
B09	GLZ03 PF	Peak Temp	200	400	0	100	**970**	60	200
B09 PrF	GLZ03 PF	Peak Temp	200	400	0	100	**970**	60	200
B09	GLZ03	Peak Temp	200	400	0	100	**970**	60	200
B09 PrF	GLZ03	Peak Temp	200	400	0	100	**970**	60	200
B09	GLZ03 PF	Peak Temp	200	400	0	100	**900**	60	200
B09 PrF	GLZ03 PF	Peak Temp	200	400	0	100	**900**	60	200
B09	GLZ03 PF	Peak Temp	200	400	0	100	**800**	60	200
B09 PrF	GLZ03 PF	Peak Temp	200	400	0	100	**800**	60	200
B09	GLZ03	Peak Temp	200	400	0	100	**850**	60	200
B09 PrF	GLZ03	Peak Temp	200	400	0	100	**850**	60	200
B09	GLZ03 PF	Peak Temp	200	400	0	100	**850**	60	200
B09 PrF	GLZ03 PF	Peak Temp	200	400	0	100	**850**	60	200
B09	GLZ03 PF	Temp Rate	200	400	0	**999**	850	60	200
B09 PrF	GLZ03 PF	Temp Rate	200	400	0	**999**	850	60	200
B09	GLZ03 PF	Temp Rate	200	400	0	**200**	850	60	200
B09 PrF	GLZ03 PF	Temp Rate	200	400	0	**200**	850	60	200
B09	GLZ03 PF	Temp Rate	200	400	0	**100**	850	60	200
B09 PrF	GLZ03 PF	Temp Rate	200	400	0	**100**	850	60	200
B09	GLZ03 PF	Temp Rate	200	400	0	**50**	850	60	200
B09 PrF	GLZ03 PF	Temp Rate	200	400	0	**50**	850	60	200
B09	GLZ05 PF	Peak Temp	200	400	0	100	**850**	60	200
B09 PrF	GLZ05 PF	Peak Temp	200	400	0	100	**850**	60	200
B09	GLZ05 PF	Peak Temp	200	400	0	100	**900**	60	200
B09 PrF	GLZ05 PF	Peak Temp	200	400	0	100	**900**	60	200
B09	GLZ05 PF	Peak Temp	200	400	0	100	**970**	60	200
B09 PrF	GLZ05 PF	Peak Temp	200	400	0	100	**970**	60	200
B09	GLZ07 PF	Peak Temp	200	400	0	100	**850**	60	200
B09 PrF	GLZ07 PF	Peak Temp	200	400	0	100	**850**	60	200
B09	GLZ07 PF	Peak Temp	200	400	0	100	**900**	60	200
B09 PrF	GLZ07 PF	Peak Temp	200	400	0	100	**900**	60	200
B09	GLZ07 PF	Peak Temp	200	400	0	100	**970**	60	200
B09 PrF	GLZ07 PF	Peak Temp	200	400	0	100	**970**	60	200

5.3.2 Variable Glaze Application Methods

Four bodies (B06-09) and two glazes (GLZ02 and GLZ03) were chosen from the variable batch composition experimentation to test methods of application glazing (i.e. object immersion, slurry painting and dry powder application) (see section 5.4.4). The bodies were chosen because they had compositions similar to the faience bodies of the period of interest, looked similar to archaeological faience bodies and had greater strength upon firing than the other bodies. The glazes were chosen because they look similar to copper blue glazes found on the Saqqara materials housed at Cardiff University. Object immersion and slurry painting are glazing techniques shown to have been used during the periods of interest (Griffin 2002:328; Vandiver 1983:A27). Dry powder application is a method not mentioned in the literature but used here to determine effectiveness as a potential application method.

5.3.3 Variable Firing Parameters

A comparison was conducted on the temperature reading of the Bentrup T405 computer attached to the kiln and a HH-612 Type K hand held dual input Thermosense© thermocouple to know the full extent of the firing temperature range with the faience replicates (see section 5.4.1). The 3 foot wire probe thermocouple sensor was pressed through high temperature insulation wool plugging the upper bung-hole of the kiln and positioned 5 cm below and 1cm in front of the kiln sensor in the approximate location of where the firing samples were located. Temperature readings were recorded every 5 minutes starting at the zero minute mark and ending after the kiln and the thermocouple temperature readings corresponded at ±2 °C for a total of four or more consecutive measurements during the cooling cycle. Peaks and troughs as displayed on the thermocomputer were recorded over a 5 minute period at peak soak to determine fluctuations and to have a better understanding of real temperatures attained for this specific kiln.

The faience replicate body B09 was selected because of its characteristics (see section 5.4.2) to act as a substrate for the testing of kiln variables on glazes GLZ03 (copper blue), GLZ05 and GLZ07 (cobalt blues). The glazes were selected because they looked the most similar to the Saqqara copper and cobalt blue archaeological sherd glazes. The tested kiln variables included temperature increase rate, soak temperature, and soak time.

5.4 Results and Discussion

Nine bodies and nine glaze pellets (see Tables 5-1 and 5-2) were fired separately to determine the general friability of the bodies and resultant colours of the glaze pellets.

Glazes were fired in a raw and prefritted state. See Chapter 7 for a comparison of the replicated faience with archaeological material.

5.4.1 Kiln Temperature Disparity

The kiln computer temperature readings were compared with a thermocouple to determine differences and actual temperatures reached during a firing cycle. Graphing the firing profile of the kiln revealed that the kiln computer is slow to respond to temperature changes during the ramp-up and ramp-down cycles (Fig. 5-2 and Tables 5-5 and 5-6). The heating coils of the kiln are activated/deactivated during the ramp up of the temperature unless there is no temperature increase rate restriction entered into the computer. The setting 1 firing profile (see Fig. 5-2a) exhibited a difference up to 77 °C during the ramp up cycle but it was generally between 25 °C and 35 °C. The Settings 2 firing profile (see Fig. 5-2b) exhibited an 85 °C difference early in the ramp up cycle but the difference was more typically 30°C. The ramp down (cooling) cycle exhibited ~2 °C difference with no cooling restrictions entered into the computer.

The temperatures of the kiln computer and thermocouple were recorded and compared over a 5 minute soaking period at temperatures of 800, 850, 900 and 970 °C (Fig. 5-3 and see Table 5-6). Figure 5-3 reveals a pattern in the activation/deactivation cycle of the heating coils which repeats every 120 seconds regardless of the peak temperature during the soak. The lines representing the kiln computer and the thermocouple converge (increasing the accuracy and precision) as the temperature increases. Table 5-6 exhibits a decrease in the recorded average temperature difference and median temperatures with an increase in the soaking temperature.

A comparison of the display readings of the kiln computer and the thermocouple revealed a disparity and a slow response to temperature changes by the kiln computer (see Table 5-6). The temperature difference is greatest at lower soak temperatures and decreases as the temperature of the soak is increased. Comparing these differences highlighted the 120 second cycle the kiln follows in the heating and cooling of coils to maintain a given temperature. Therefore, the temperature in the kiln is not stable but is constantly rising and falling in a range of which the median and target temperature differential is dependent on the target temperature. For example, the actual temperature range when firing at 800 °C is 801-827 °C. This range is slightly

Table 5-5 Kiln firing parameters for comparisons between the thermocouple and the kiln computer.

Kiln Testing Parameter Settings							
Parameters	Ramp Up 1 (°C/H)	Dwell (°C)	Dwell Period (min)	Ramp Up 2 (°C/H)	Soak Temp (°C)	Soak Period (min)	Ramp Down (°C/H)
Setting 1	800	800	-	-	800	30	999
Setting 2	999	800	-	-	800	30	999
Setting 3	999	850	-	-	850	10	999
Setting 4	999	900	-	-	900	10	999
Setting 5	999	970	-	-	970	10	999

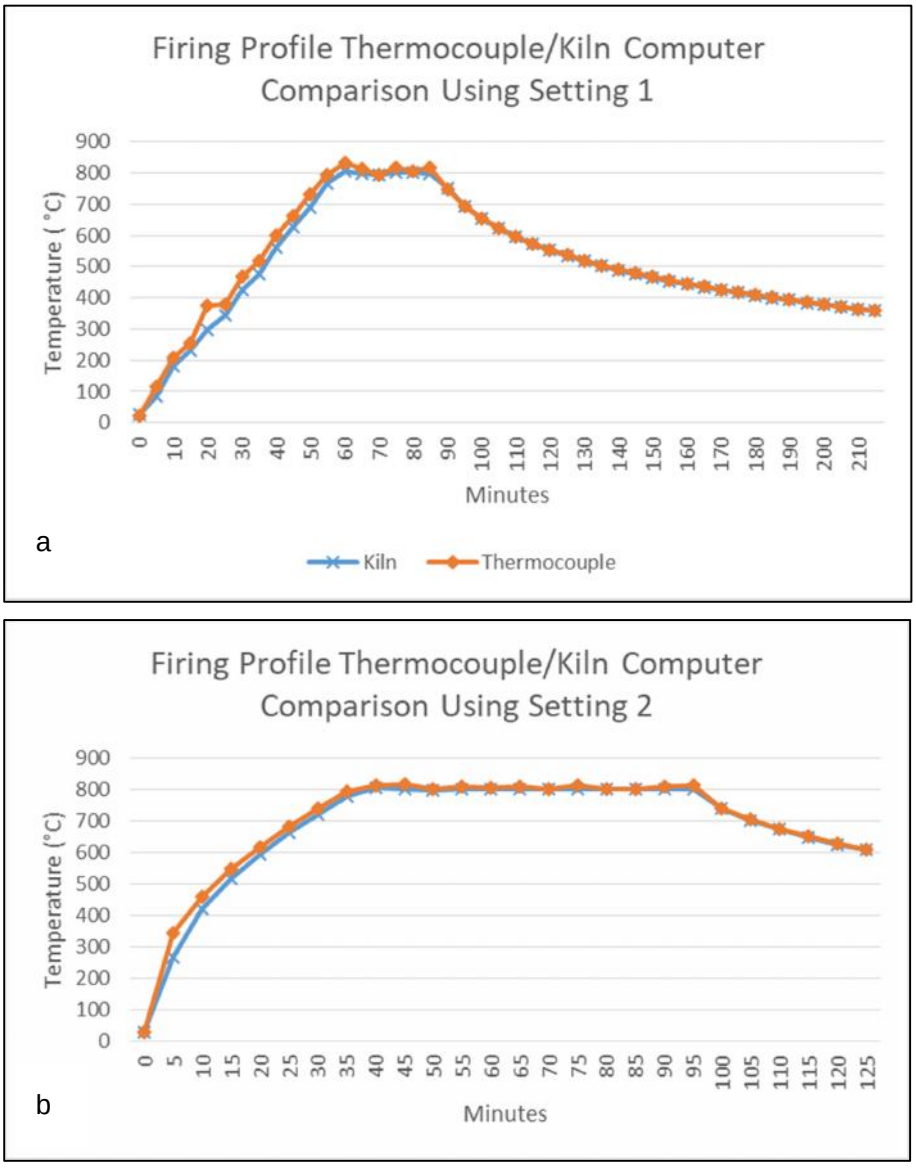

Fig. 5-2: Kiln firing profiles with an 800°C/60 min ramp-up restriction (a) and with no restrictions (b).

Table 5-6 Comparison of the recorded readings of four different soak temperatures over a 5 minute soak period using thermocouple and kiln computer.

5 Minute Soak Period Thermocouple/Kiln Computer Comparison												
	Setting 2 (800 °C)			Setting 3 (850 °C)			Setting 4 (900°C)			Setting 5 (970 °C)		
Reading No.	Thermo-couple	Kiln	Difference	Thermo-couple	Kiln	Difference	Thermo-couple	Kiln	Diference	Thermo-couple	Kiln	Difference
1	809	799	10	827	832	-5	901	898	3	985	970	15
2	823	801	22	865	837	28	907	896	11	967	972	-5
3	817	801	16	847	843	4	890	895	-5	984	971	13
4	826	805	21	853	841	12	920	900	20	968	972	-4
5	812	804	8	835	840	-5	902	903	-1	978	969	9
6	819	804	15	872	846	26	920	901	19	964	969	-5
7	801	799	2	849	850	-1	903	904	-1	988	972	16
8	816	798	18	857	846	11	909	900	9	969	974	-5
9	806	797	9	839	845	-6	891	899	-8	976	971	5
10	823	800	23	876	850	26	924	902	22	960	969	-9
11	818	801	17	855	854	1	903	905	-2	989	970	19
12	827	805	22	860	851	9	911	902	9	968	976	-8
13	812	805	7	842	848	-6	893	900	-7	976	971	5
14	819	804	15	876	851	25	924	904	20	957	967	-10
Mean	816.3	801.6	14.6	853.8	845.3	8.5	907.0	900.6	6.4	973.5	970.9	2.6
Median	817.5	801.0	15.5	854.0	846.0	6.5	905.0	900.5	6.0	972.5	971.0	0.5
Minimum	801	797	2	827	832	-6	890	895	-8	957	967	-10
Maximum	827	805	23	876	854	28	924	905	22	989	976	19

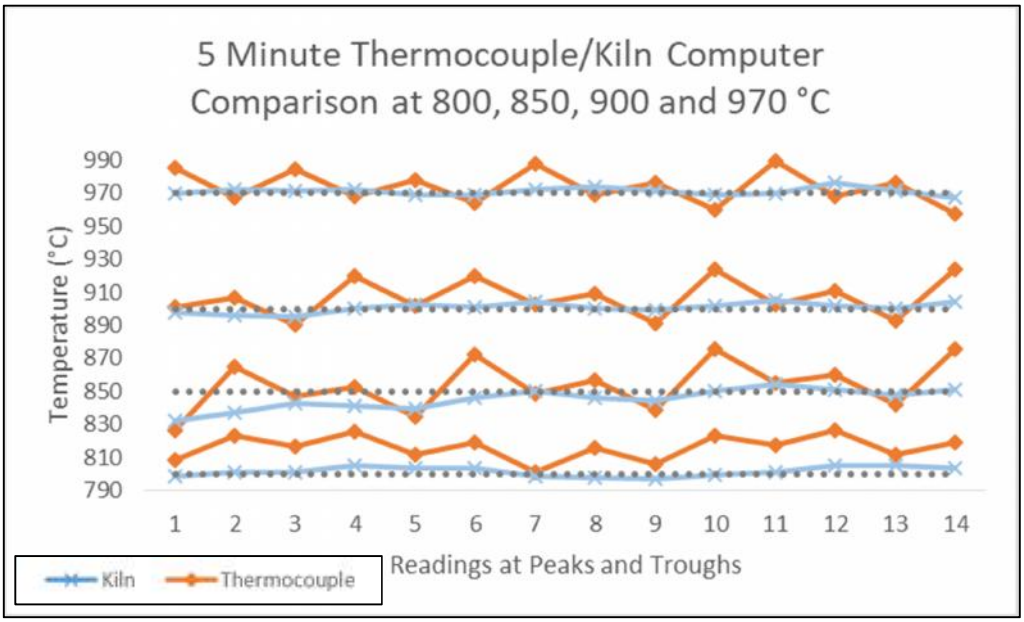

Fig. 5-3: Comparison of the thermocouple (orange) and kiln computer (blue) readings over a 5 minute soak period at the four targeted temperatures. The dotted line represents the target temperature for each of the settings.

above the target temperature of 800 °C with a mean temperature differential of 14.6 °C. Raising the target temperature to 850 °C produces a mean differential of 8.5 °C. A target temperature of 970 °C produces a mean differential of 2.5 °C.

The temperature range at a specific soak setting have negligible effects on the production of faience glazes if the mean temperature is maintained at the soak temperature target. The soak temperature range of furnaces used in antiquity could be much greater and still produce glazes on frit bodies. Nicholson and Jackson (1998:115) replicated a large furnace similar to one found at Amarna and conducted firing experiments to determine if these were used for glass. They noted a temperature decrease in excess of 50 °C when stoking the furnace fire several times over the 9 hour firing but were able to produce a coloured frit and melted cullet.

5.4.2 Faience Bodies

All the fired body mixtures produced intact forms of various colours (Fig. 5-4a-c). Most of the bodies were friable and a few were low in durability. Body sample B01 is composed of quartz powder and has a slight pink colour. Samples B02-04 have a reddish hue due to the iron in the clay that compose part of the body. These samples more closely resembled clay pottery than faience fabrics. All four of these bodies were friable and left a powdery residue when handled because of low alkali and quartz powder. Sample B04 easily fragmented during handling because of the lack of an alkali. Sample B05 was much coarser in texture and left a gritty residue when handled

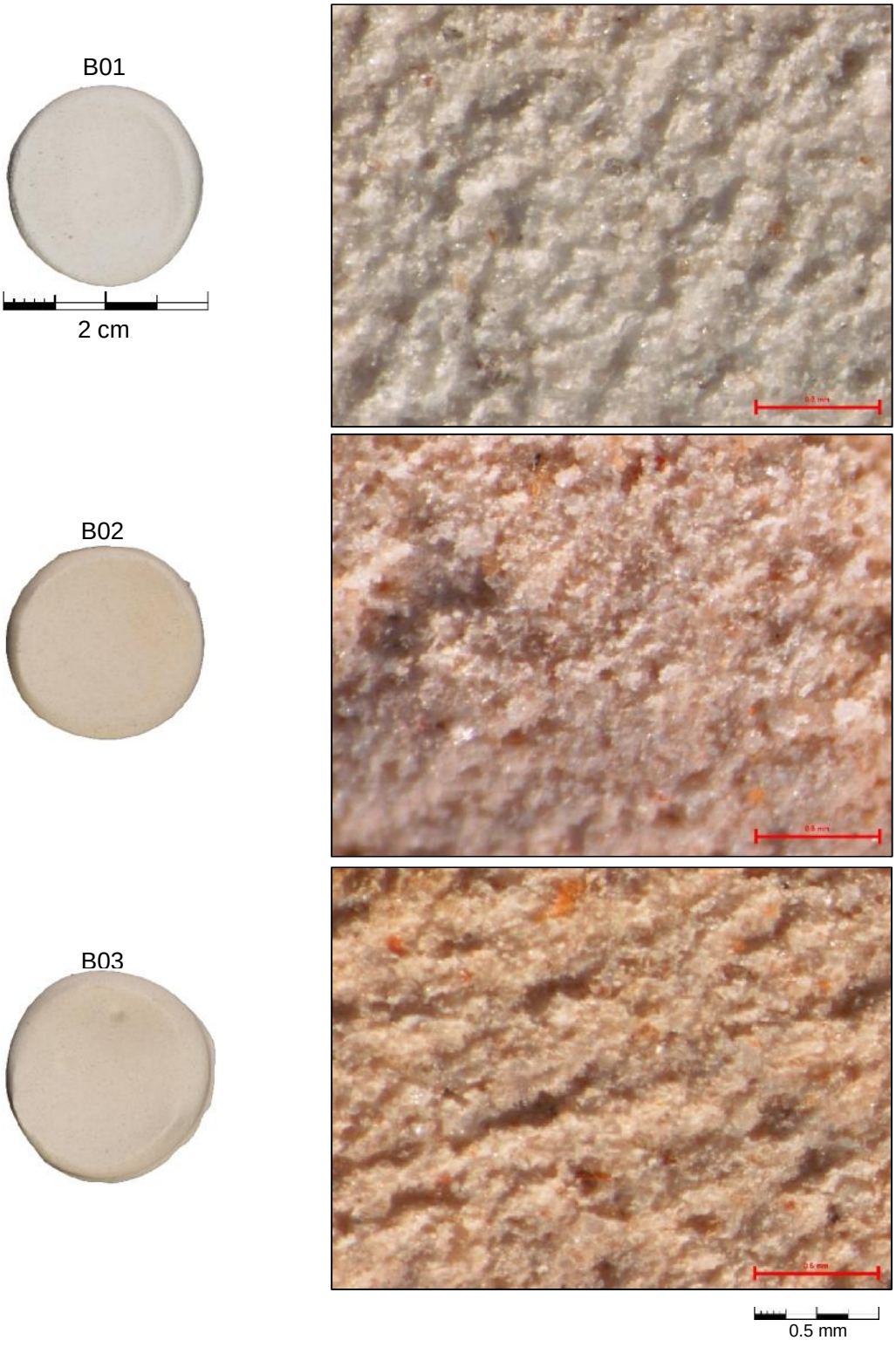

Fig. 5-4a: Bodies (B01-B03) and associated micrographs (x40 magnification; red scales read 0.5 mm).

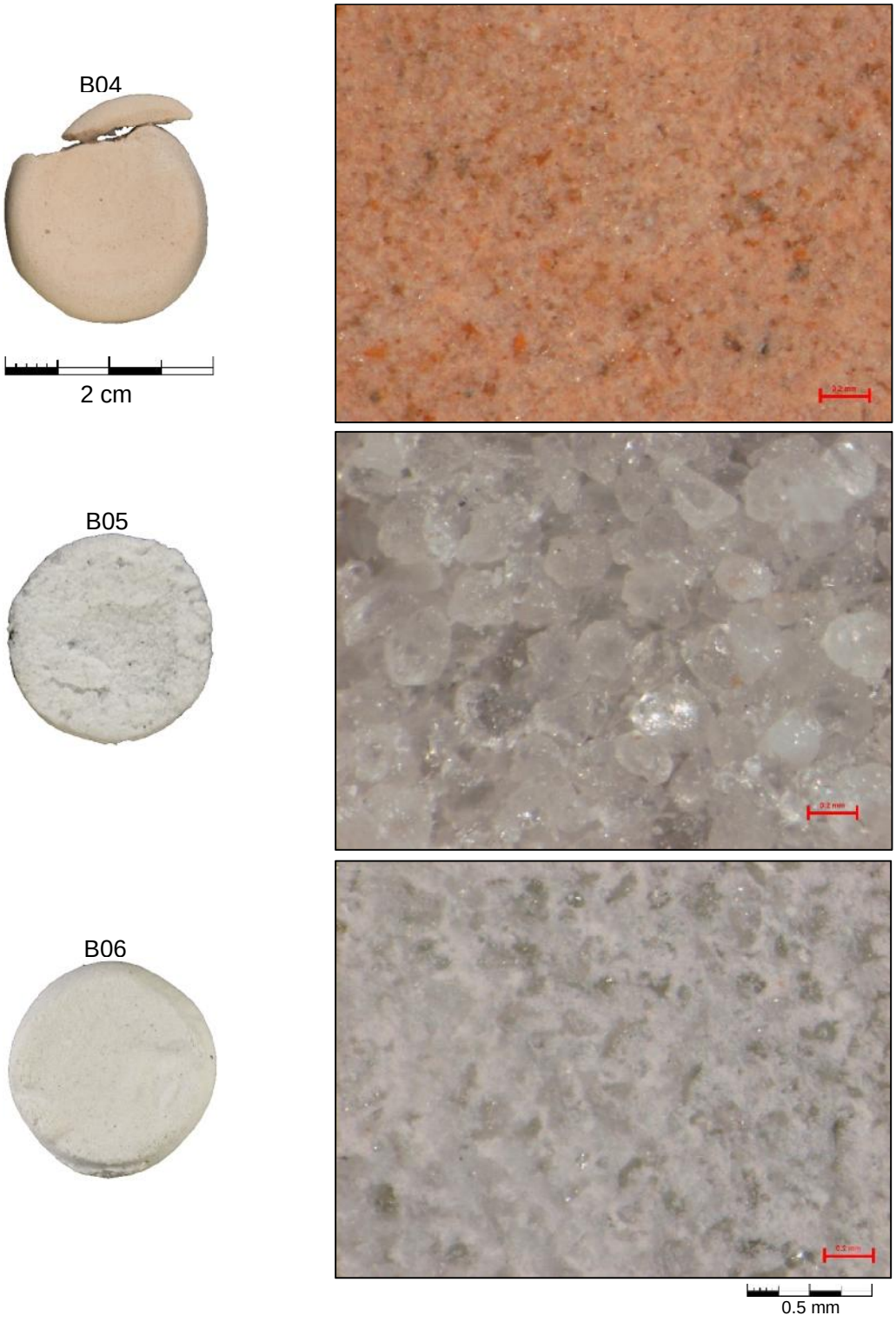

Fig. 5-4b: Bodies (B04-B06) and associated micrographs (x40 magnification; red scales read 0.2 mm).

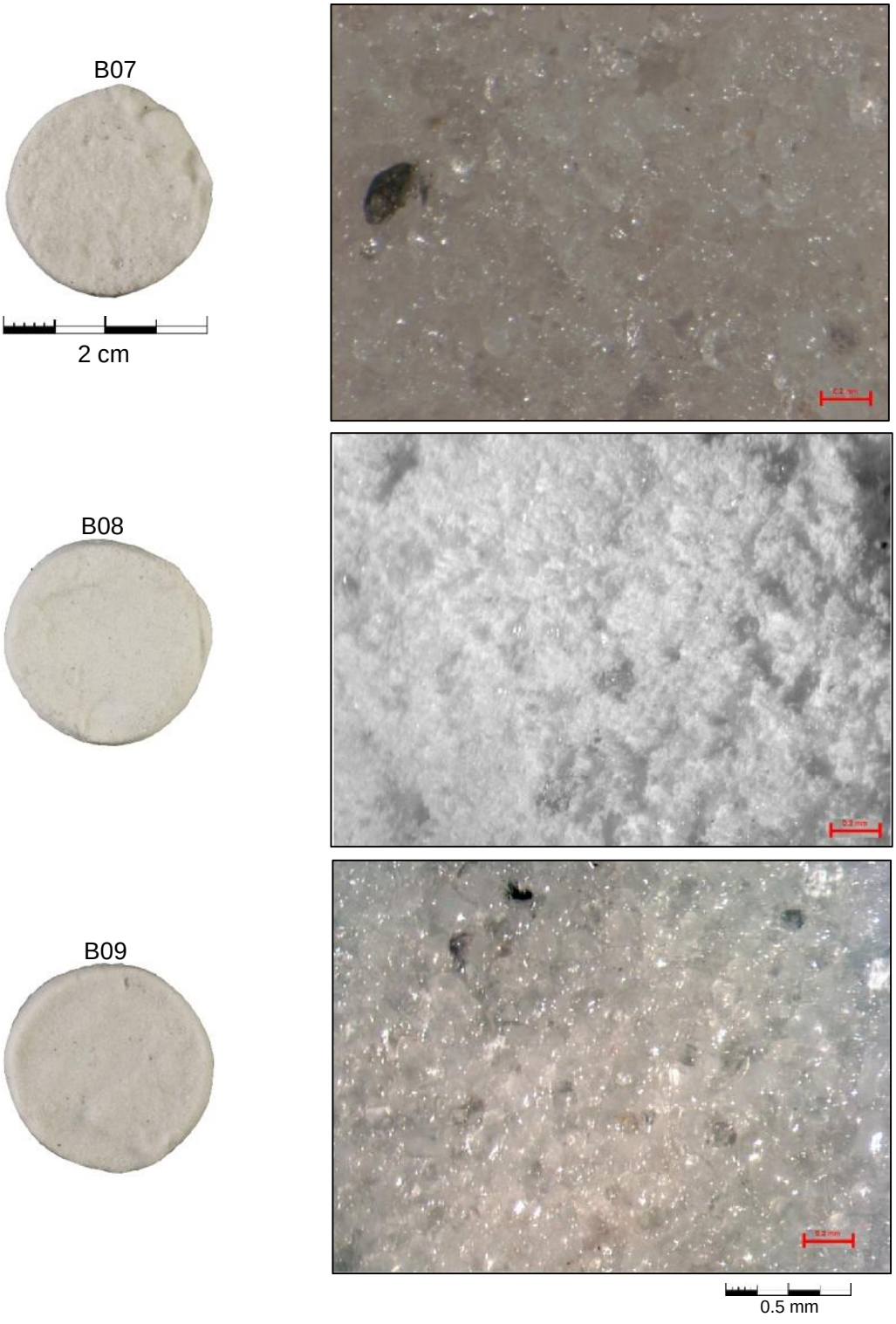

Fig. 5-4c: Bodies (B07-B09) and associated micrographs (x40 magnification; red scales read 0.2 mm).

because of the low alkali and ground sand components. The weight of the quartz powder samples (3.1-3.4 g) were lighter than similar samples composed of ground sand (3.7-3.9 g). Body samples B05-09 are clearly silica-rich frit and are similar in appearance to the archaeological material. Samples B06 and B07 are generally the same but have vastly different amounts of calcium in place of silica. These bodies were white and friable leaving a gritty residue when handled. Samples B08 and B09 have more alkali and are generally the same but calcium content differs between them as well. Body B08 left a gritty residue when handled and B09 left no residue. The bodies were stored in polyvinyl sealable bags. All the bodies except B09 exhibited some sign of mechanical decomposition after a few weeks in storage. All of the B08 samples and some of the B06 and B07 samples had disintegrated to powder. Micrographs of the body surfaces (see Fig 5-4a-c) taken after firing exhibit differences because of addition of clay or various amounts of calcium and sodium. B01 is a quartz powder-based body and exhibits an off-white colour with particle flecks possibly consisting of iron. These bodies have a pinkish hue when compared to ground sand bodies. Samples B02-04 are composed of quartz powder and clay. Individual silica particles in a matrix of clay and inclusions are barely perceptible. Body B05 is a ground sand composed body and the individual angular quartz particles are lightly fused together because of minor sintering of the silica grains. The angular quartz particles in B06 are partially obscured by calcium. Sample B07 exhibits sintered rounded quartz particles fused together. The quartz particles in sample B08 are obscured by calcium similar to B06. Partially melted and fused quartz particles are exhibited in the micrograph of B09. This is similar to B07 but the quartz has melted to a greater degree resulting in a more cohesive body.

The experimentation produced one body (B09) that was durable and had limited or no friability after firing. The appearance of the body had a greater influence as a qualifying factor than originally expected. Archaeological faience bodies can vary in colour and friability but the silica-rich frit composition is clearly identifiable. Experimental bodies containing a clay component looked more similar to a clay ceramic than frit. The clay component was ~6 wt% of the total body mass. This is well within the 5 – 25% calcareous clay suggested by Vandiver (1998:123) or the 1-12 wt% suggested by Griffin (2002:35). The remaining experimental bodies contained no clay but many suffered from a lack of alkali or an overabundance of calcium oxide which interfered with fusing of the sintered quartz grains. These bodies usually failed while in storage and many were reduced to a powdery mass.

5.4.3 Faience Glazes

The raw and prefritted glazes have varying texture and amounts of glassiness after firing (Fig. 5-5). Generally the prefritted glazes are smoother textured but some exhibited large erupting bubbles. Glazes GLZ01 and 09 are identical except for the network former when introduced to the mixture (quartz powder and ground sand, respectively). Neither had a colourant introduced to the batch and both produced an off-white to light grey colour. Of the two, GLZ01 has a smoother glassy texture with the prefritted and raw fired batch material because of smaller particle size of the quartz powder. All the glaze samples with copper and cobalt colourants produced various shades of blue. Glaze GLZ02 samples produced a glassy glaze in prefritted and raw fired forms. The raw fired forms exhibited erupted bubbles on the surfaces. Glazes GLZ03, 05 and 07 produced a coarse textured raw fired pellet. The prefritted pellet was glassy but more voluminous than the raw fired samples and exhibited erupting bubbles on the surfaces. Sample GLZ04 produced a dark blue clay-like material as a raw fired glaze. It was not fired in a prefritted form. Samples GLZ05 (quartz powder) and 06 (ground sand) formed a glassy glaze and are identical except the form of silica when introduced into mixture. Glaze GLZ08 in raw and prefritted forms failed to produce a glassy glaze material. The texture is coarse and the resultant form resembled a coloured body more than a glaze. All glazes stored well with the exception of GLZ04 which continued to effloresce salts, even when sampled and prepared in a polished resin block for SEM analysis.

The glazes pellets with colourant (copper and copper/cobalt) produced similar to the archaeological material based on the same colourants. One exception was GLZ04 which contained 8 wt% clay and produced a Prussian blue gritty clay. There are no parallels in the archaeological faience record. The soaking temperature, soaking time, temperature ramp up and whether it was on a fired or unfired body affected the colour of a glaze. Longer soaking periods and quicker temperature ramp ups produced a greenish hue to the blue glazes which was not perceivable without a microscope (see section 5.4.5). Vandiver (2008:44) states that an increase in potassium in the glaze melt will result in a greener copper blue. This explanation might work for the longer soaking periods as the glaze is increasingly absorbed into the body allowing potassium from the body to enter into the glaze melt and take effect. This does not explain why faster temperature increase rates or low soak temperatures produce a green hue. Unfired bodies produce a barely perceptible deeper shade of blue. The potassium in

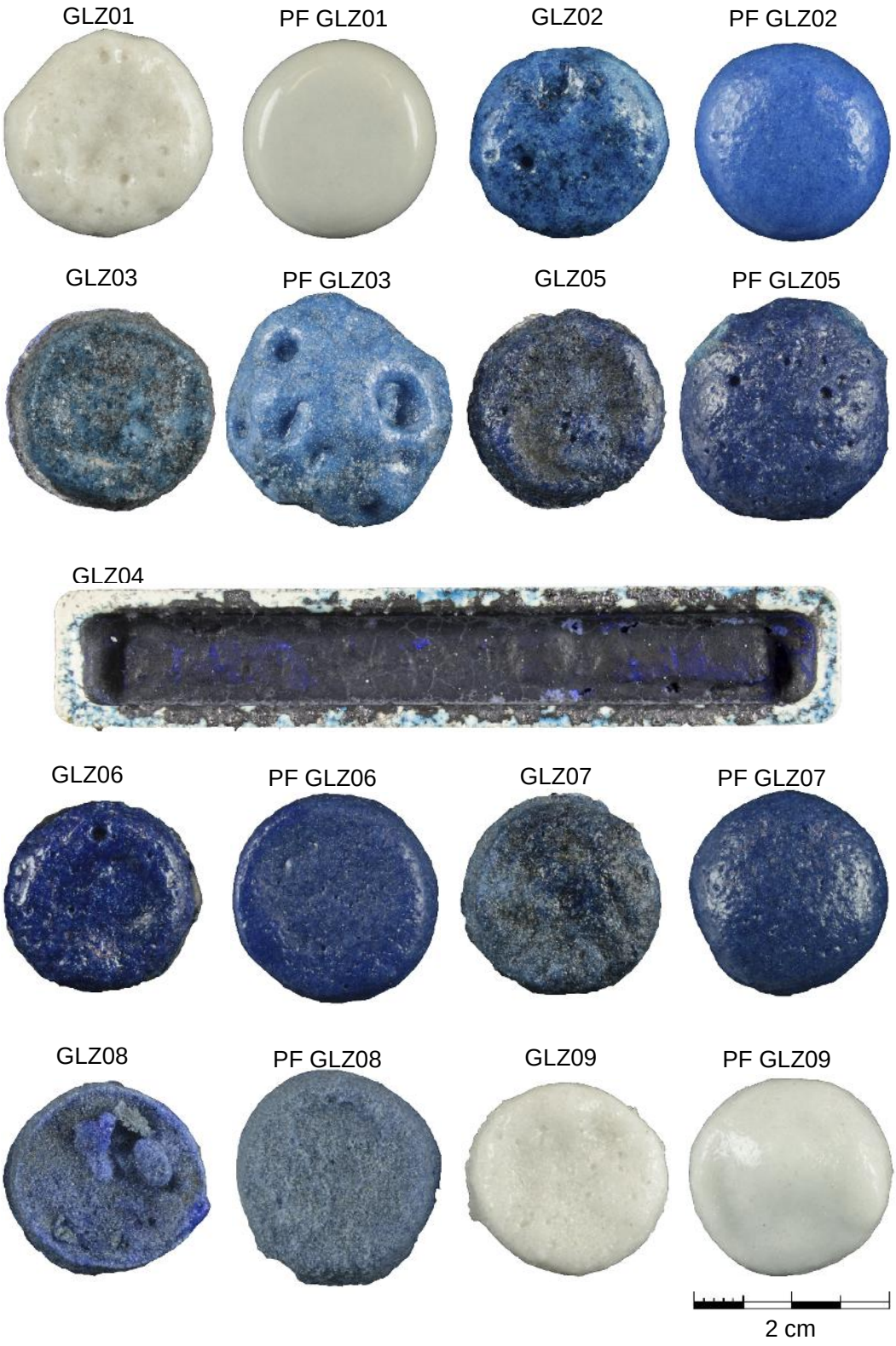

Fig. 5-5: Fired glaze pellets (GLZ01-03, GLZ05-09) and glaze fired in crucible (GLZ04). PF designation indicates prefritting prior to final firing. The blue tint of PF GLZ09 may be from copper ions in kiln atmosphere due to blue glaze in same firing.

the unfired bodies (as opposed to fired bodies when they have already entered into reaction) would be freer to enter into the glaze melt producing a greenish hue, not a deeper blue.

The texture of the glazes varied with the kiln parameters and the form of the glaze mixture (i.e. raw or prefritted). None of the batches used in the raw form produced a smooth glaze surface. Three glazes pellets (GLZ01, 02 and 06) produced from raw batch material resulted in a rough surfaced glassy glaze and two (GLZ03 and 05) resulted in a rough surfaced semi-glassy glaze (see Fig. 5-5). When applied to a body (B09), the raw batch powder failed to produce a glassy glaze (Fig. 5-6). This parallels with the results of Tite and Bimson (1986) who failed to produce a glassy glaze. Most of the prefritted glaze pellets produced smooth glassy glaze. Three (GLZ03, 05 and 07) produced a more voluminous pellet with erupting bubbles on the surface. These same three exhibited possible scorched sodium on the surface of the fired raw glaze. The sodium was probably incorporated into the glaze melt in the prefritted glaze causing more carbon dioxide to be released when the temperature reach 750 °C. Prefritted glazes 03, 05 and 07 were applied to B09 bodies and produced a glassy smooth surfaced glaze.

The ability of a glaze to completely cover a body was a product of the body. All of the glazes (raw and prefritted) placed on a B09 body formed a cohesive coating with the exception of a few pinholes and two minor cases of glaze creep. Glazes placed on B06-08 bodies exhibited major glaze creep (see Fig. 5-6). A combination of increased calcium and decreased alkali in these bodies compared to B09 is a factor. Decreased alkali results in less sintering of the silica grains in the body and a decreased melt overall. The glaze material exhibited greater attraction to itself than to the body and pulled away leaving a portion of the body surface exposed. B08 had adequate alkali for a melt but too much calcium (a non-wetting agent) which interfered with the fusing of the body particles and absorption of the glaze into the body. This is a potential concern if using calcium as a binder during body formation.

5.4.4 Glaze Application

Slurry immersion, slurry painting and dry powder application methods were tested on samples B06-09 in prefired and raw states using GLZ03 (see Fig. 5-6). Slurry immersion techniques resulted in various degrees of glaze coverage. Some of the samples were fully encapsulated in a blue glaze whereas others had localized areas of

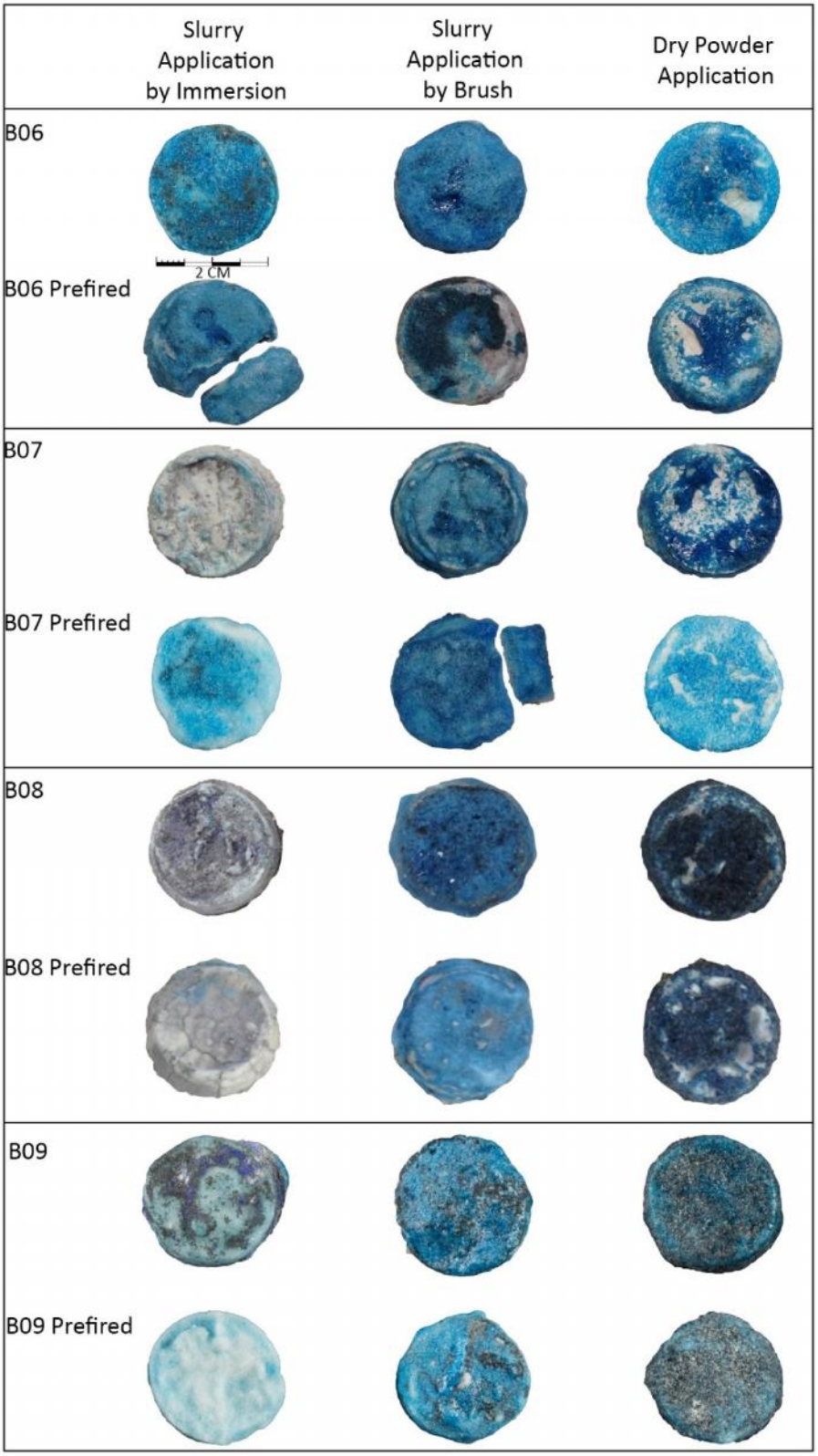

Fig. 5-6: Results of application experiments using various body recipes with GLZ03. Prefired B06 sample fragmentation is a result of body preparation and not glaze application. Fragmented prefired B07 sample is a result of glaze application.

coverage or almost none. Immersion of the raw body samples resulted in an exothermic reaction as sodium in the body reacted with water in the slurry. Raw bodies immersed into the slurry maintained shape if handled with care but were still susceptible to dimensional changes. There was no dimensional affect to prefired bodies.

Painting of slurry onto the bodies resulted in full coverage to applied areas. Upon firing, glaze creep and pin holes were identified in two separate samples. The unfired bodies were more susceptible to dimensional changes during application than those subjected to immersion. These changes consisted mostly of a slight squeezing of the body but one sample did exhibit slumping and complete separation of a portion of the body (see Fig. 5-6).

Dry powder glaze application resulted in complete coverage in applied areas but exhibited severe creeping upon firing. Body B09, raw and fired, was an exception and creeping did not affect glaze coverage but the glaze did appear scorched possibly because of sodium burn-off.

Application of a glaze slurry by painting produced a fully covered body regardless if the glaze was glassy. Application as a dry powder provided full coverage for the B09 bodies but the other bodies exhibited major glaze creep. Application by immersion resulted in the greatest variation of coverage. The coatings were generally thin or patchy. Too much water in the slurry and/or particles that were too large to be held in suspension are probable causes. As explained in section 5.4.1, the average size quartz particle in the replicated faience body was much larger than those of the archaeological material. The same is probably true for the glazes. Sieves with openings <180 μm would have required continued grinding of the batch material and resulted in smaller particles that would have been better held in suspension.

Thinly applied glazes exhibited fewer imperfections than thicker applications. Bubbles formed during the generation of carbon dioxide required less time to escape leaving more time for the viscous melt to fill in the cavity. Thin glazes were more susceptible to near complete absorption into the body.

5.4.5 Firing Parameters

Kiln soaking period (Fig. 5-7), temperature increase rate (Fig. 5-8), and peak temperatures (Fig. 5-9 and 5-10) were tested using body B09 coated with glazes GLZ03, 05 and 07. Testing of the soaking period was composed of a peak temperature firing using the common kiln setting with times of 60, 180 and 360

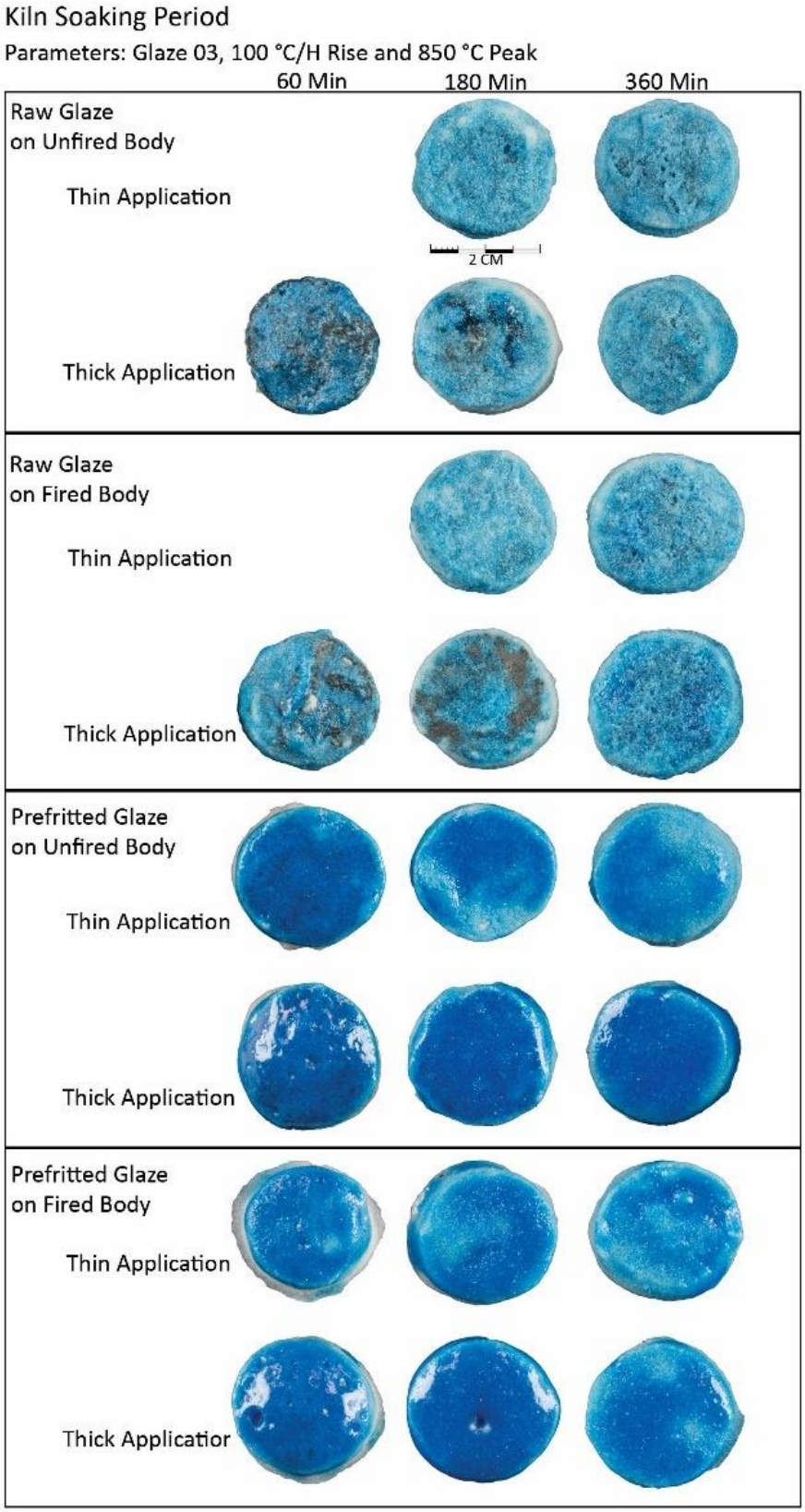

Fig. 5-7: Kiln soaking periods of 60, 180 and 360 minutes were tested on copper colourant glaze 03 (raw and prefritted) coated on body 09 (raw and prefired).

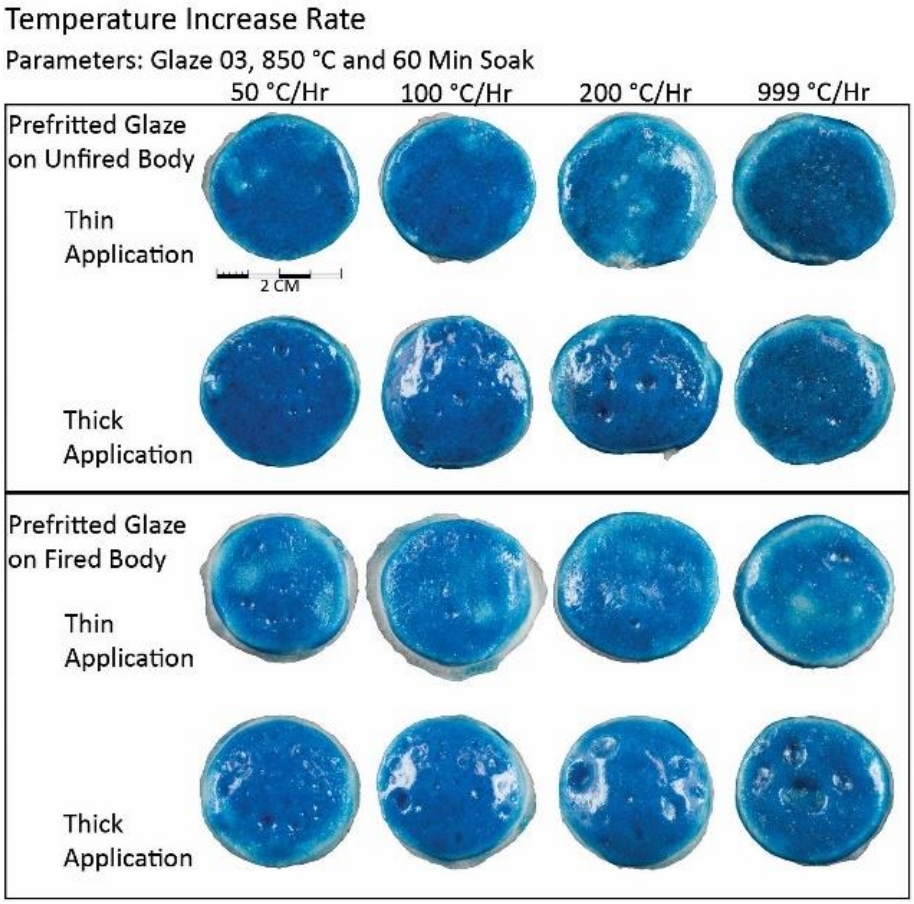

Fig. 5-8: Temperature ramp up rates of 50, 100, 200 and 999 °C/Hr testing on prefritted copper colourant glaze 03 on raw and prefired body B09.

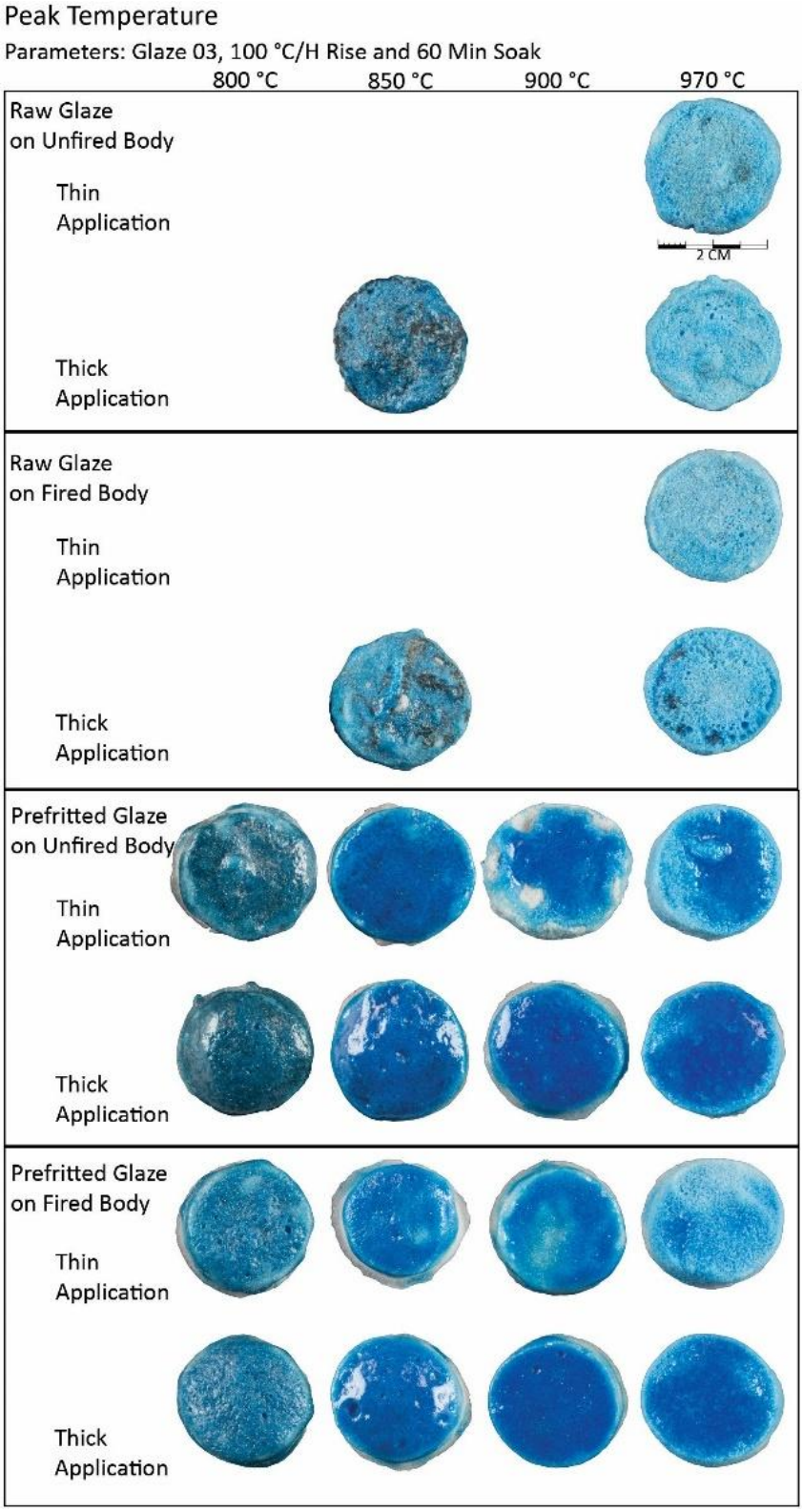

Fig. 5-9: Prefritted glazes 03 applied on raw and prefired body B09 were subjected to kiln firings of 800, 850, 900 and 970 °C peak temperatures for 60 minutes. Blank areas represent a failure to produce a glassy glaze.

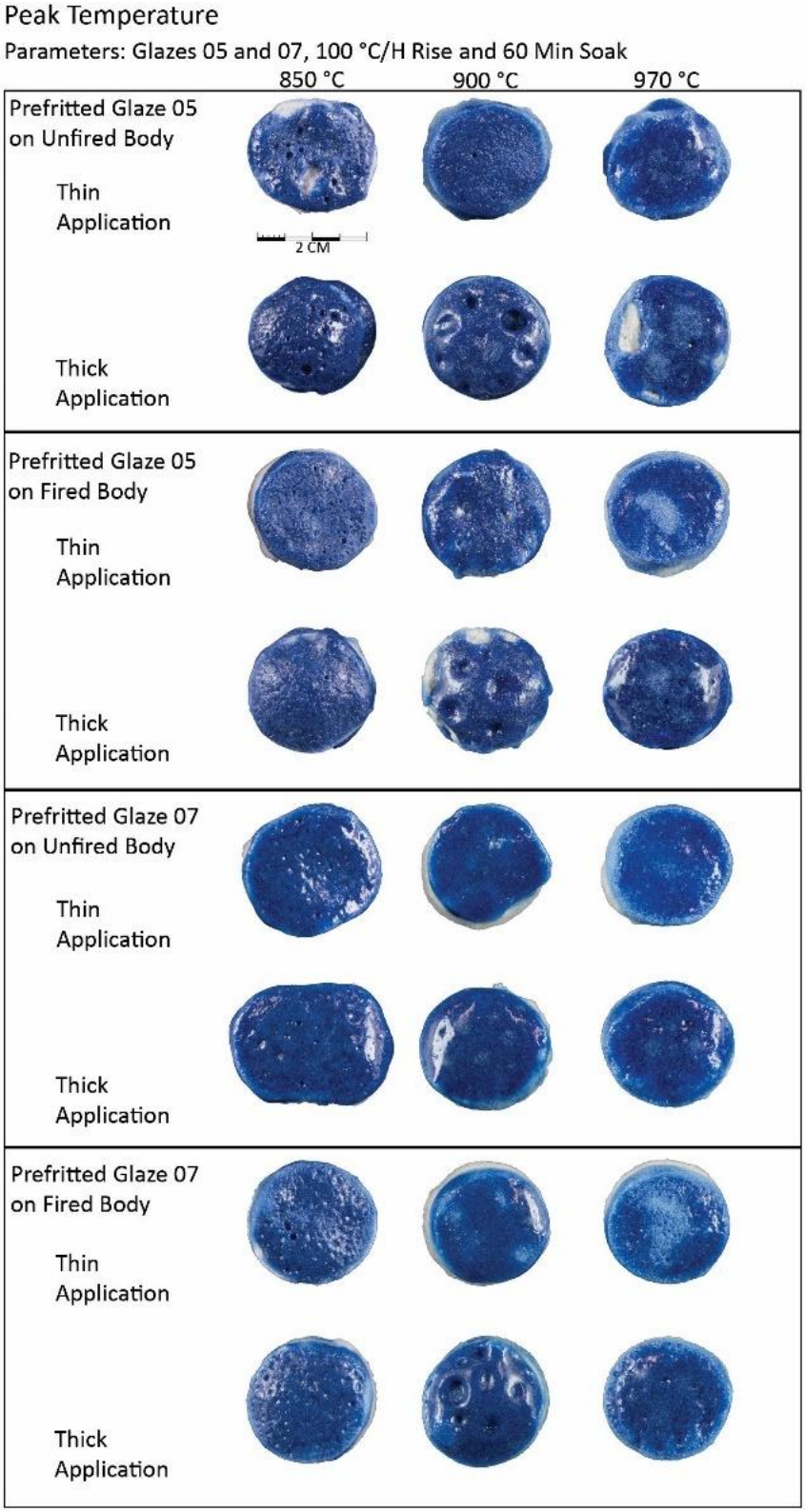

Fig. 5-10: Prefritted glazes 05 and 07 applied on raw and prefired body B09 were subjected to kiln firings of 800, 850, 900 and 970 °C peak temperatures for 60 minutes.

minutes (see Fig. 5-7). Thickly applied raw glazes exhibited a greater amount of sodium burning at lower soak times whereas thin glazes reveal almost no scorching with all firings. The raw glazes failed to produce a full coverage glassy glaze although localized glassy areas existed. Prefritted glazes do not exhibit sodium burning. Absorption of these glazes into the body is increased with longer firing times resulting in localized thin glazes where the body is perceptible underneath and the glaze surface is more textured. Large erupting bubbles are more prevalent with thickly applied prefritted glazes and lower soaking periods. Increase of the soaking period results in a thicker interaction zone (Fig. 5-11) and a more greenish hue to the glaze (Fig. 5-12) An increase in the soaking time and quicker kiln ramp-ups to target temperature affect the colour (Figs. 5-13 and 5-14). Smaller bubbles in the glaze are associated with the shorter 60 minute soaking period but there is no change in the density of bubbles across all the soaking periods (see Fig. 5-12).

Common kiln settings were used to test the effects of 800, 850, 900 and 970 °C peak temperatures on the samples (see Figs. 5-9 and 5-10). Samples coated in raw glaze 03 were fired at 970 °C peak temperature but failed to produce a glassy glaze and were dropped from the remainder of the kiln parameter testing. Darker blue glaze 03, present at 800 °C on raw bodies, is replaced by the typical copper blue at greater temperatures. Glazes on fired and unfired bodies at 800 °C are opaque. Glazes fired at greater temperatures exhibited greater opacity. Glaze creep was noted on one thinned glazed raw bodied sample fired to 900 °C. Thin glazes exhibit less erupting bubbles than the thicker samples but are prone to higher absorption resulting in a bodied textured surface with extremely thin to no glaze. The glazes on unfired bodies produce darker colours than glazes on fired bodies. Glazes 05 and 07 produced the same results as glaze 03 but changes in colour were harder to perceive because of the darker blue associated with cobalt coloured glazes. Glaze creep was noted on two of the glaze 05 raw bodied samples.

Glaze 03 samples subjected to the kiln peak temperature experimentation were examined with SEM-BSE and OM. An increase in temperature resulted in thicker interaction zones and less bubbles in the glaze (Figs. 5-15 and 5-16). The colour changes from a greenish-blue at 800 °C to a brilliant blue at 850 °C, to a muted blue at greater temperatures (see Fig. 5-12). Glazes 05 and 07 exhibit a similar microstructural result to the effects of increasing kiln peak temperature (Figs. 5-17 through 5-20); there is an increase in the thickness of the interaction layer. There are fewer and smaller bubbles at greater temperatures. Colour changes are not perceptible and may be overpowered by the strong colouring characteristic of cobalt.

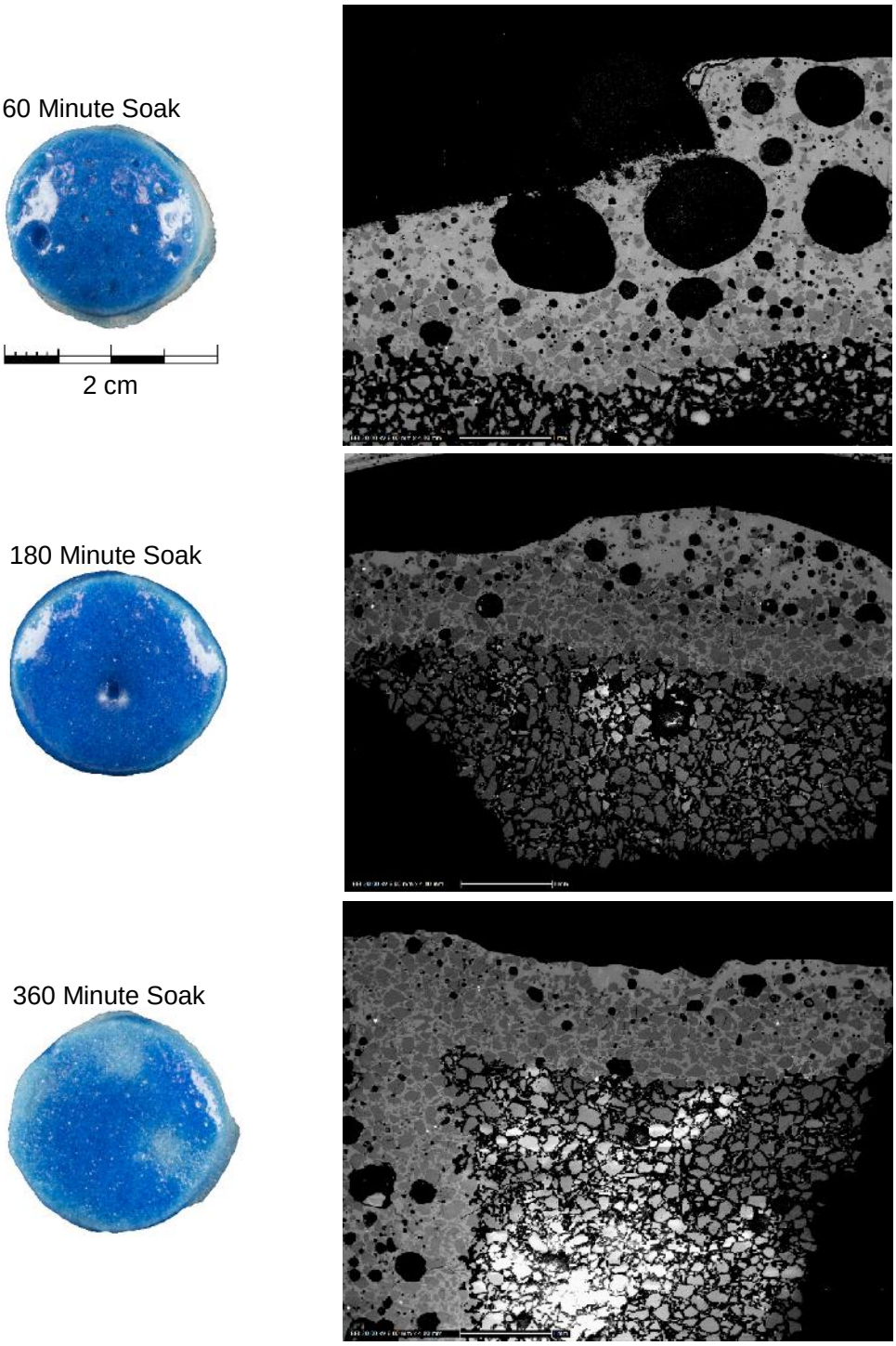

Fig. 5-11: A comparison of the microstructure of prefritted copper colourant glaze 03 on prefired B09 at 60, 180 and 360 minute soak period at 850 °C peak restricted to 100 °C /Hr temperature increase. The BSE image magnification is x20 and the scale reads 1 mm. Interaction zone thickness of glaze 03 is 903 µm (60 min), 943 µm (180 min) and 1442 µm (360 min). Electron charging on the polished surface is caused by lapping oil seeping from the porous body under the high vacuum.

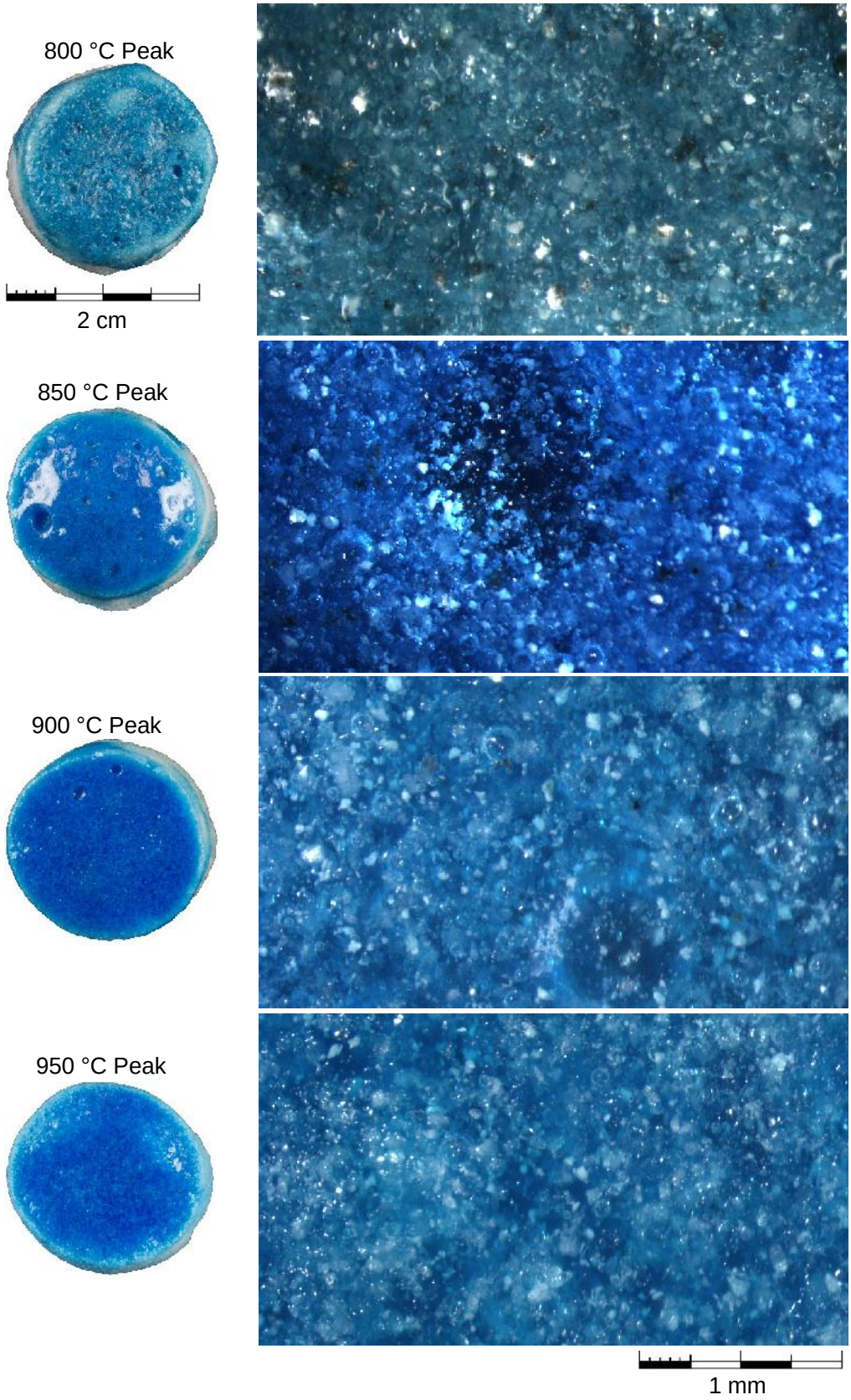

Fig. 5-12: Peak temperature and effects on copper colourant glaze 03 on B09 bodies fired using 100 °C/Hr rise restriction and 60 minute soak.

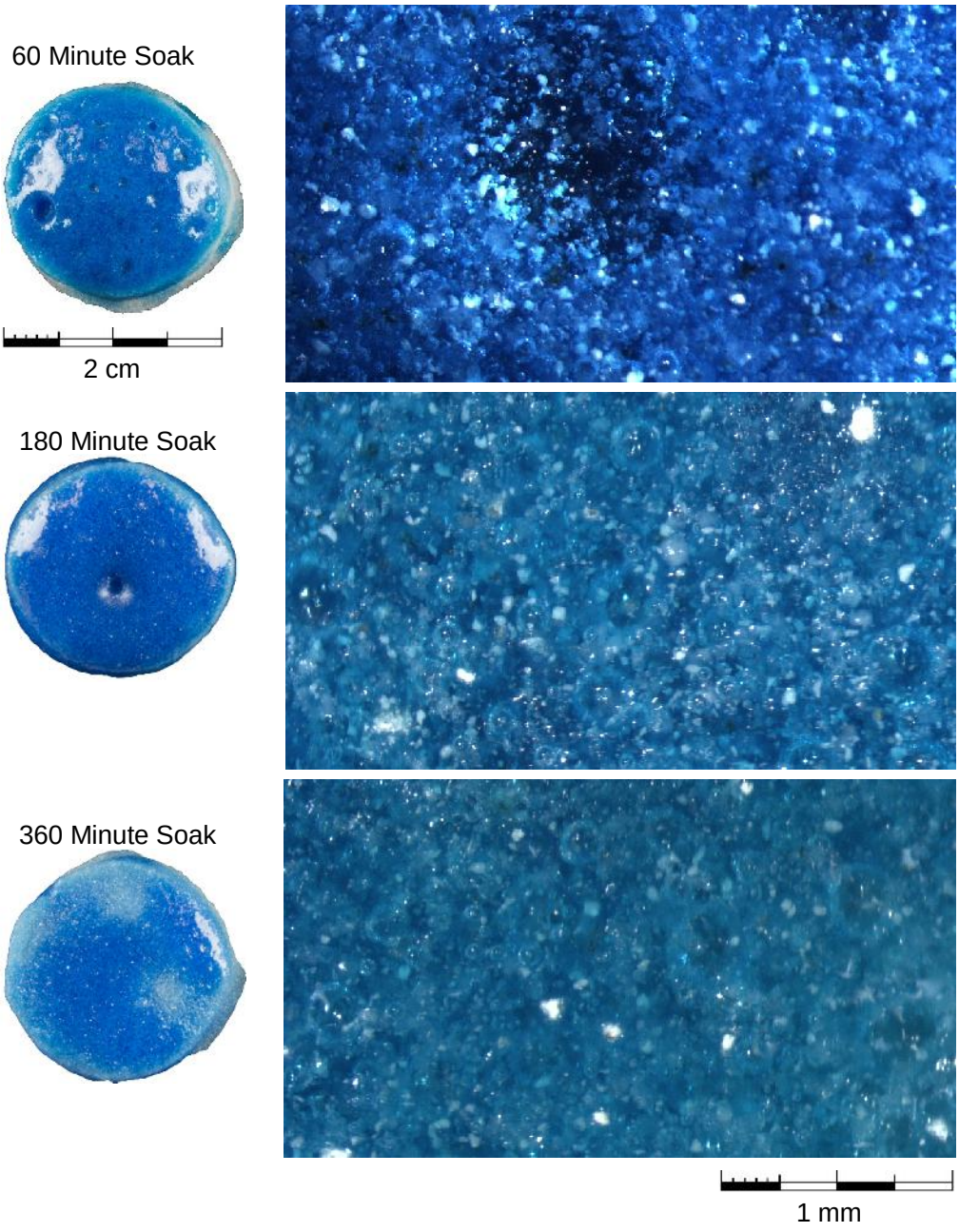

Fig. 5-13: Kiln soaking period and the effects on copper colourant glaze 03 on B09 bodies fried using 850 °C peak and 100 °C/Hr rise restriction.

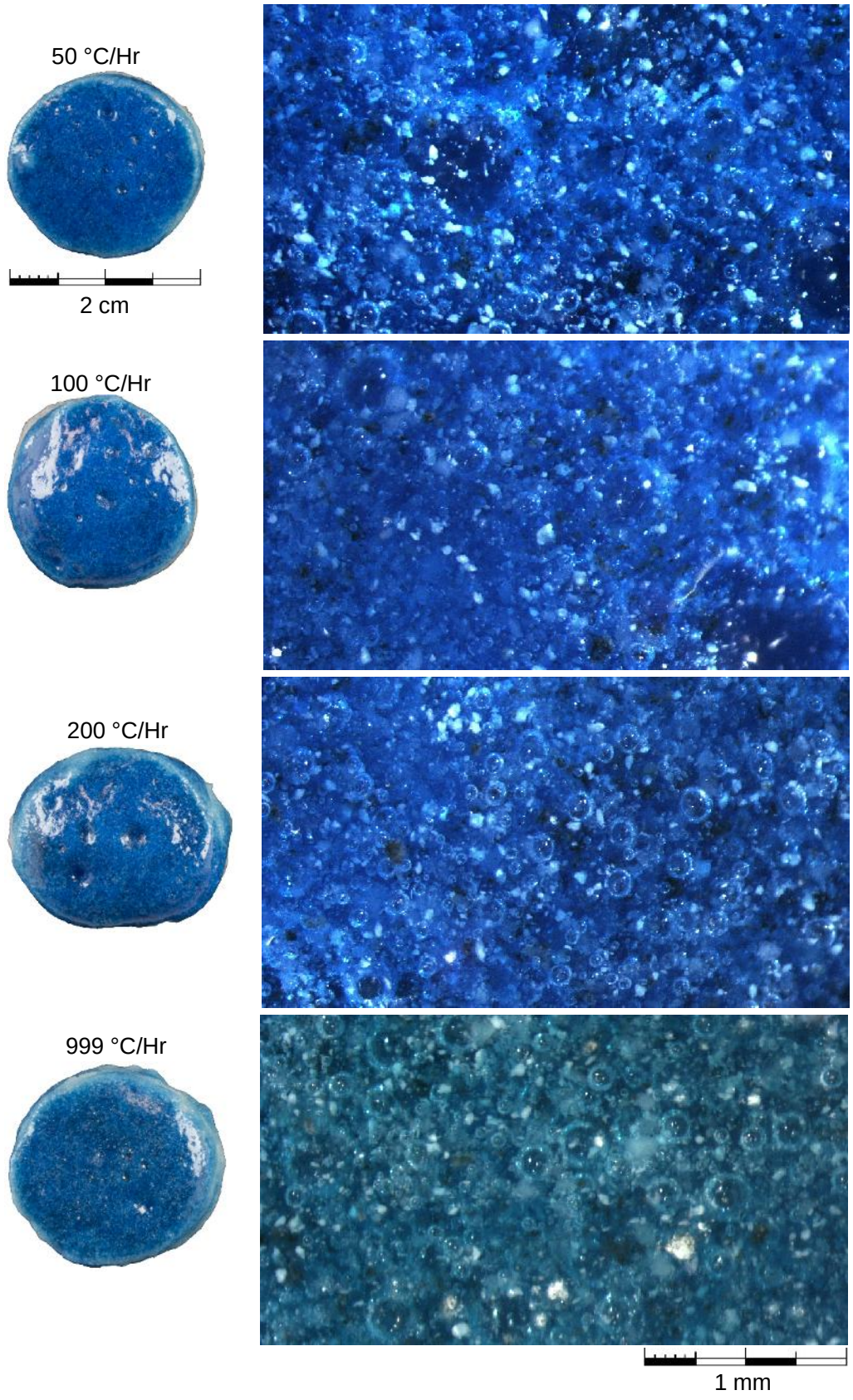

Fig. 5-14: Temperature increase rate and the effects on copper colourant glaze 03 on body 09 fired using 850 °C peak and 60 minute soak period.

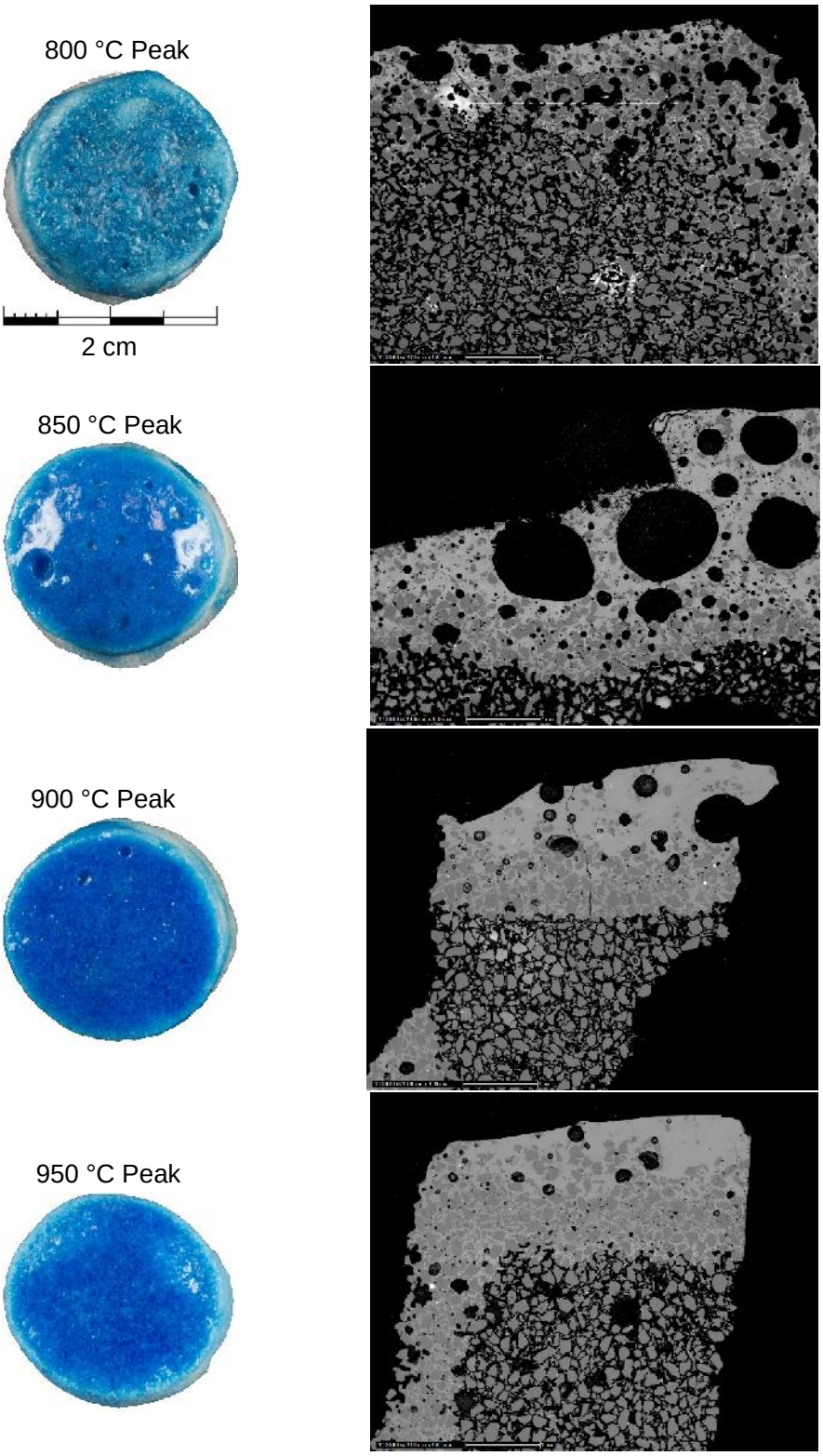

Fig. 5-15: Kiln peak temperatures and effects on microstructure. Copper colourant glaze 03 on fired bodies with a 100 °C/Hr temperature rise restriction and 60 minute soak. The BSE image magnification is x20 and the scale reads 1 mm. Interaction zone thicknesses are 555 µm (800 °C), 850 µm (850 °C), 1100 µm (900 °C) and 1200 µm (970 °C).

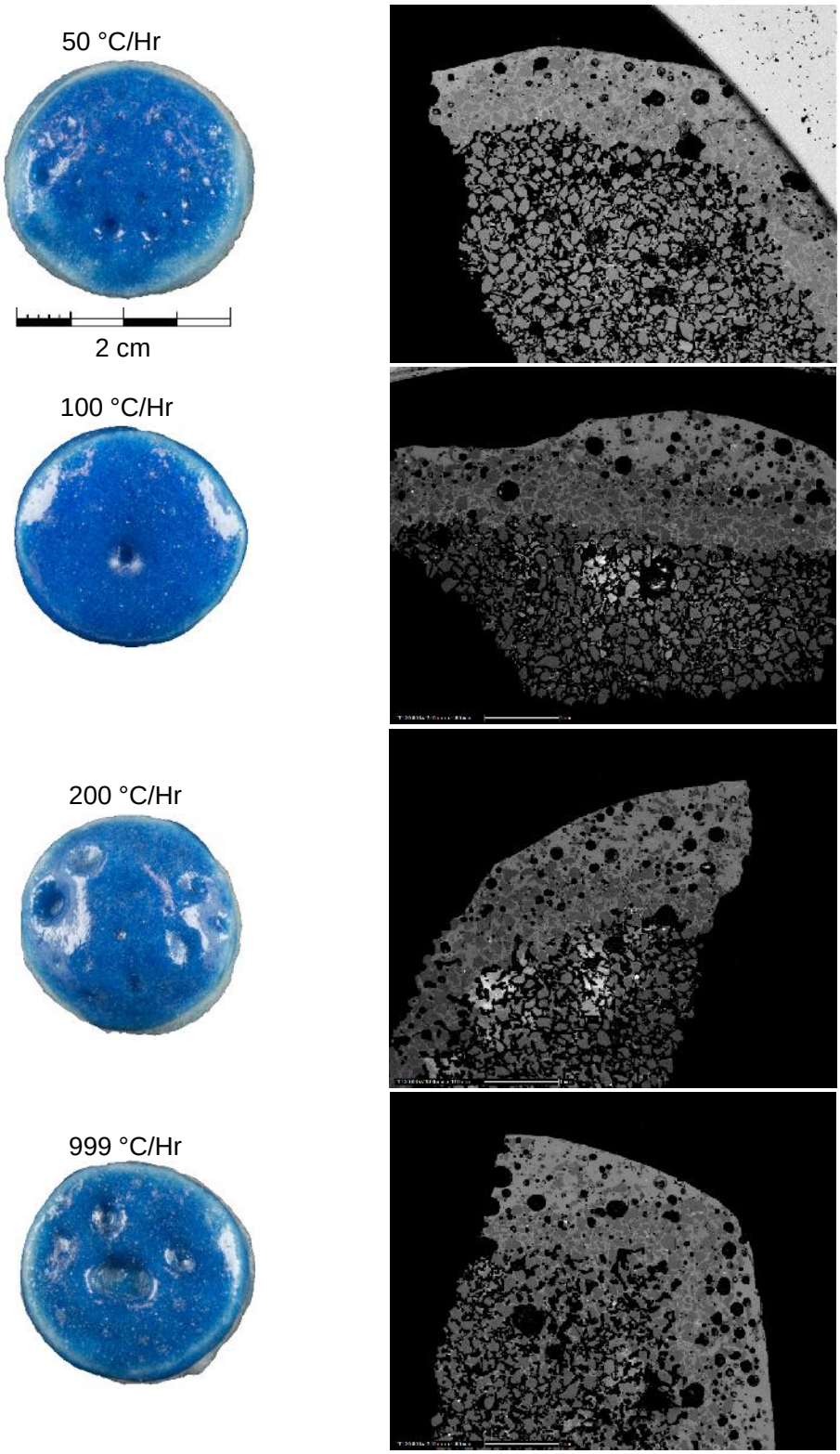

Fig. 5-16: Temperature ramp up rate and the effects on glaze microstructure. Copper colourant glaze 03 on fired bodies with a 100 °C/Hr temperature rise restriction and 60 minute soak. The BSE image magnification is x20 and the scale reads 1 mm. Interaction zone thickness are 1000 µm (50 °C/Hr), 971 µm (100 °C/Hr), 758 µm (200 °C/Hr) and 671 µm (850 °C/Hr).

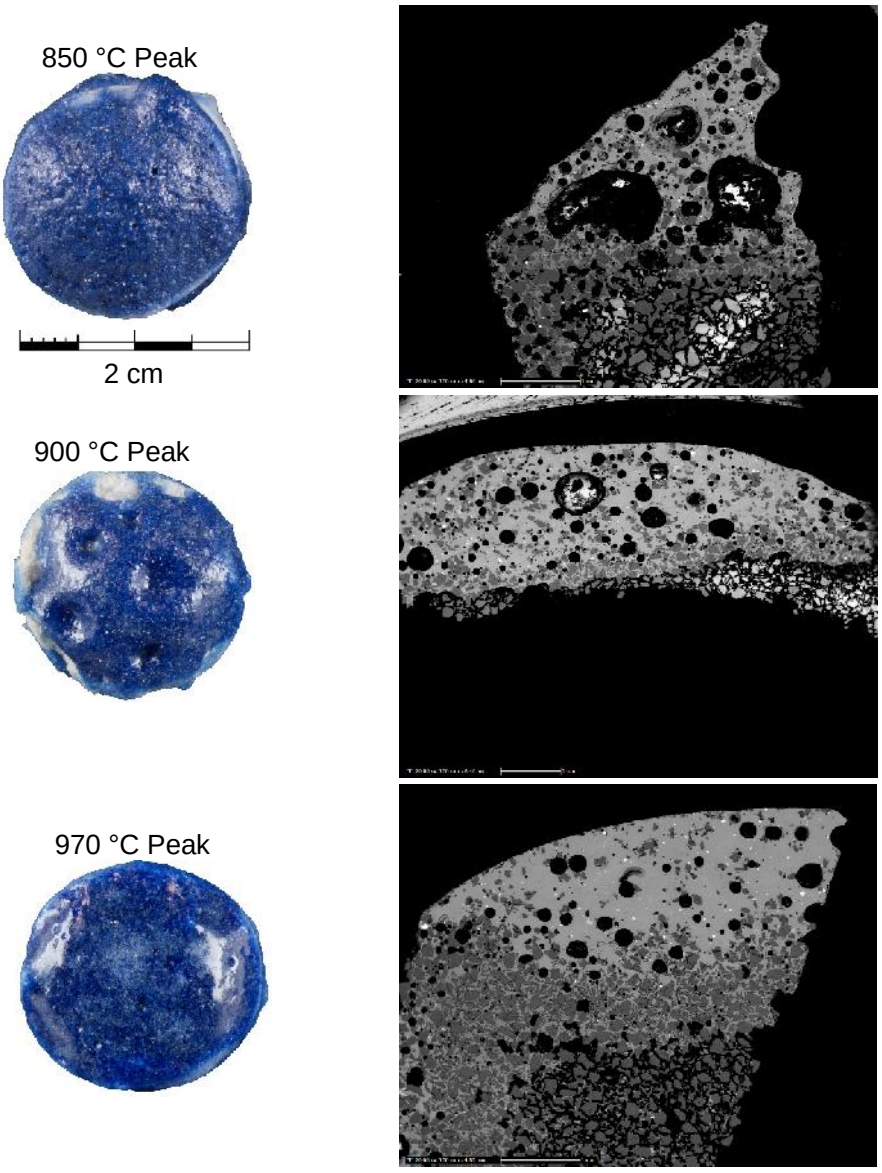

Fig. 5-17: Kiln peak temperature effects on microstructure of cobalt colourant glaze 05 on fired bodies. Temperature rise was restricted to 100 °C/Hr and soak period was 60 minutes. Interaction zone thicknesses are 547 µm (850 °C), 566 µm (900 °C) and 1020 µm (970 °C). The BSE image magnification is x20 and the scale reads 1 mm.

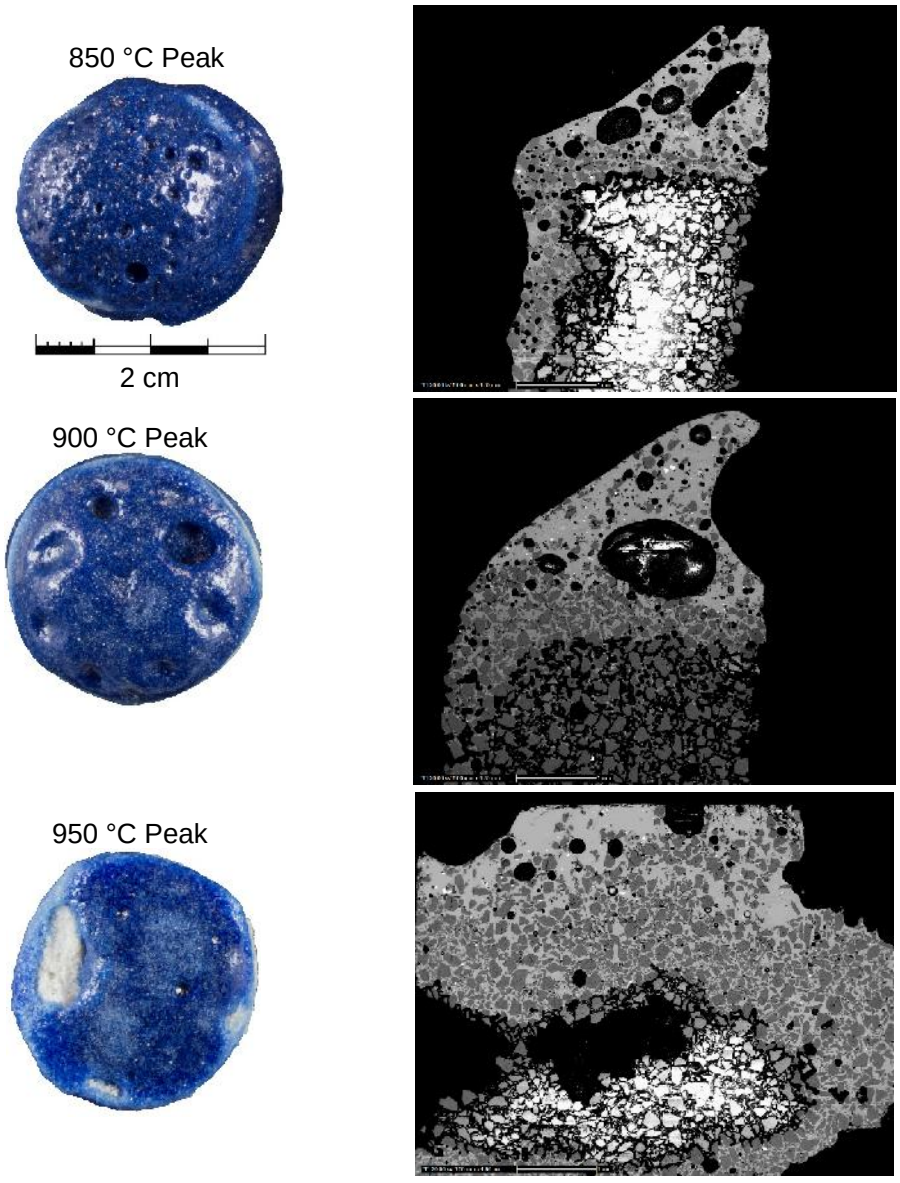

Fig. 5-18: Kiln peak temperature effects on microstructure of cobalt colourant glaze 05 on unfired bodies. Temperature rise was restricted to 100 °C/Hr and soak period was 60 minutes. Interaction zone thicknesses are 377 µm (850 °C), 754 µm (900 °C), and 1717 µm (970 °C). The BSE image magnification is x20 and the scale reads 1 mm. Charging on the surface is caused by lapping oil seeping from the porous body under the high vacuum.

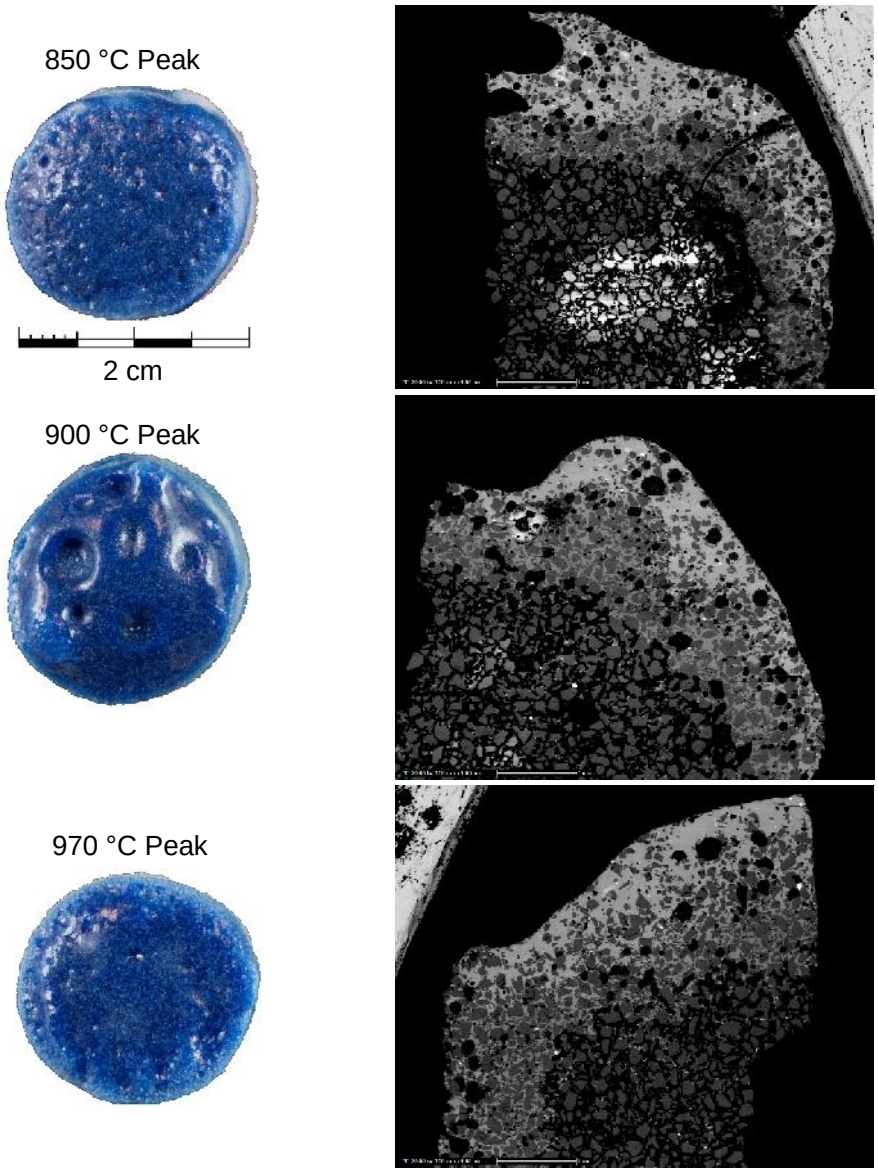

Fig. 5-19: Kiln peak temperature effects on microstructure of cobalt colourant glaze 07 on fired bodies. Temperature rise was restricted to 100 °C/Hr and soak period was 60 minutes. Interaction zone thicknesses are 547 µm (850 °C), 1188 µm (900 °C), and 1189 µm (970 °C). The BSE image magnification is x20 and the scale reads 1 mm. Electron charging on the polished surface is caused by lapping oil seeping from the porous body under the high vacuum.

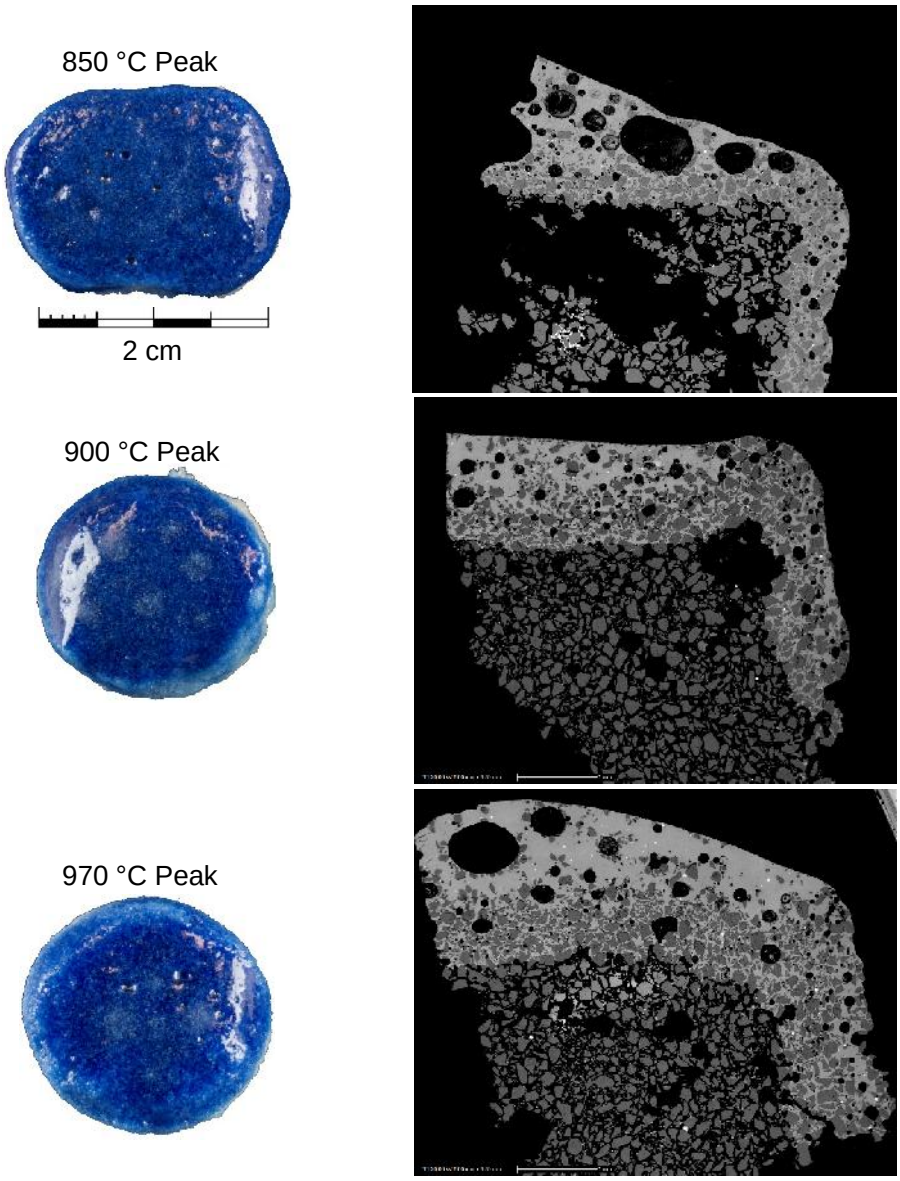

Fig. 5-20: Kiln peak temperature effects on microstructure of cobalt colourant glaze 07 on unfired bodies. Temperature rise was restricted to 100 °C/Hr and soak period was 60 minutes. Interaction zone thicknesses are 415 µm (850 °C), 622 µm (900 °C) and 886 µm (970 °C). The BSE image magnification is x20 and the scale reads 1 mm.

Prefritted glaze 03 samples were fired at increasingly higher kiln ramp up rates (see Fig. 5-8). Higher rates result in a greater chance of erupting bubbles but the amount of bubbles were dependent on glaze thickness. The interaction zone thickness decreases with an increase in temperature rates (see Fig. 5-16). Bubbles within the glaze increase in size and density as the temperature rate increases and the glaze colour changes from blue to greenish blue (see Fig. 5-14).

Firing prefritted glazes to 900 °C (for 60 minutes) produced a transparent glassy glaze with few erupting bubbles. Increasing the temperature increased the absorption of the glaze into the body and results in extremely thin glazes covering individual quartz particles leaving a lighter coloured glaze surface with the texture of the body beneath. Decreasing the temperature increased the amount of bubbles in the glaze. At 800 °C, the glaze was opaque, voluminous and cratered with erupting bubbles on the surface because of the evolution of gases in a viscous liquid melt. Higher temperatures required more time and lowered the viscosity of the melt allowing the bubbles to reach the surface and the melt to fill the cavity. Increasing soak period at the same temperature and/or slowing the temperature ramp up had the same effect.

5.4.6 Potential Improvements for Future Research

In hindsight it is clear that several changes to the methods could have led to improved results and including them here allows future researchers to avoid similar mistakes. Glaze 02 as a pellet appears to be a very good glaze (see Fig. 5-4). It produced a semi-glassy raw fired glaze and a compact prefritted fired glassy smooth-textured glaze. At the time it was determined that the alkali content was too low and that an increase would produce better results. Glaze 03 represents the alkali increase but it is more voluminous in its prefritted fired state with erupting bubbles than in the raw fired state indicating an increased off-gassing of carbon dioxide. Prefritted glaze 03 sufficed as a glaze layer on prepared bodies and did not exhibit the same degree of imperfection as did the glaze pellet begging the question of the potential quality of a prefritted glaze 02 on prepared bodies. One such firing did occur and the results of the glaze 02 firing were marginally better exhibiting less of a propensity for erupting bubbles.

The perfect amount of alkali in a glaze is a fine line. Although glaze 03 could have fared better if the alkali content was slightly reduced, glazes 05 and 07 could have used more. The 850 °C soak temperature firing resulted in glazes 05 and 07 looking similar to glaze 03 at the 800 °C temperature. It was for this reason that an 800 °C soak temperature firing did not occur for glazes 05 and 07.

The use of filtered sand provided greater control over the elemental components entering the body and glaze. It may have inadvertently affected the results. Smaller quartz particles and possibly other inclusions such as crushed flint or feldspar could have improved the similarity between the replicate body and the archaeological material. Smaller particles and less homogeny may have decrease the absorption of the glaze melt into the body resulting in a thinner interaction zone.

Drying of the samples before firing occurred in an active fume hood. The kiln and other ovens were in intermittent use during the production phase restricting their use in the drying process. Use of the fume hood is a compromise between practicalities and the systematic production of faience samples where all production methods are restricted to very little variation. In future projects, especially those taking part in wet countries like Wales, oven use for drying should be scheduled in conjunction with kiln use.

Prefritting of glazes has been shown to be very effective in producing a glassy glaze in the experimentation. However, the amount of off-gassing has been shown to be less than a third of the potential off-gassing (see Chapter 7). Additional prefritting episodes using the same parameters are suggested for future research. If smartly introduced, these additional firing will only add a day/firing assuming that there are several batches or batch firings in the production cycle. As a one-off, several days will have to be scheduled to include kiln firings (a one hour peak time will still require 24 hours for the complete kiln cycle), grinding of glaze pellet combined with reformation using water and associated 24+ hour drying period before the next firing (an additional 24 hours). Use of a drying oven will greatly reduce the drying periods.

5.4.7 Chosen Batches for HH-XRF Testing

The batches chosen for continued HH-XRF evaluation consist of body 09 and glazes 03, 05 and 07 (see Tables 5-1 and 5-2). Body 09 offers a reliable substrate composed of oxides at quantities equating to those measured for bodies of the periods of interest. This body is the least friable of all the bodies tested has exhibited the most resistance to fracturing during long term storage. The chosen glazes produce colours that are similar to the archaeological material and produce an aesthetic glaze covering over the faience body. Within these qualifications, samples were selected that represented different kiln firing parameters and glaze thicknesses.

5.5 Conclusion

Application of the glaze to the body is best conducted by painting the slurry with a brush. Slurry immersion techniques can be improved by reducing the particle size and possibly by adding a suspension agent to the slurry which would burn away during the

firing. A slow temperature increase rate coupled with a long soak period at 900 °C results in a transparent blue glaze with fewer bubbles trapped in the glaze and erupting on the surface.

The substrate selected for the glazes (body 09) is robust and similar in aesthetics and composition to faience from the archaeological record. The selected copper and cobalt blue glazes provide good coverage of the body, have a potential to produce a glassy glaze (depending on firing conditions), are durable and are similar in colour to archaeological faience.

The replication of faience occurred in a Cardiff University laboratory in Wales using laboratory grade materials and a self-learning basis over the course of a year. This is very different from faience produced in the arid/semi-arid conditions in Egypt where a craftsman would probably have worked for years as an apprentice before becoming a master. Vandiver (1998: 124) has addressed similar issues regarding previous efflorescence replication experiments. The point is that testing of replicates produces results for replicates based on the production conditions in hope that it somewhat represents the archaeological material which has most likely been produce in somewhat different conditions. This is not so much a limitation as it is a note of caution.

Chapter 6: Choosing HH-XRF Parameter Setup

6.1 Introduction

The HH-XRF parameters were tested as a part of this project to determine the optimum settings for detecting elements in faience glazes and to understand the potential usefulness of HH-XRF with archaeological faience in the field or in collections. Corning Glass reference standards A and B mirror Egyptian glass of the pharaonic periods (Brill 1971:93). Glass reference samples NIST610 and 612 contain 61 trace elements each at a set consistency (~500 and ~50 ppm, respectively) (Hinton 1999:197). The Corning Glass and NIST standards are compared in Appendix C using HH-XRF settings A, B and C (see Table 4-3). Corning Glass compositions are provided in Table 4-1 and the compositions for all four standards are also included in Appendix C. Corning Glass B contains all the elements expected in a faience glaze and is the analyte for the parameter evaluations. This single glass standard was chosen for the HH-XRF experimental evaluations to reduce the number of analyses which currently number 3000+ for Corning Glass A, B and NIST610 and 612 without including three of the standards (Corning Glass A, NIST610 and NIST612) in the HH-XRF evaluation experimentations. Corning Glass B has lower concentrations than Corning Glass A in several elements commonly found in faience and may provide the same difficulty in detecting those elements as in the archaeological material where the glaze is weathered (see Table 4-1). The HH-XRF experimental evaluations using Corning Glass B were divided into hardware factors, user defined parameters and sample characteristics (Table 6-1). Hardware factors are contributions of the analyser unit (e.g. unit signature and drift). User defined parameters are those that can be manipulated by the user (e.g. voltage, acquisition time) and sample characteristics are attributes of the object that affect measurements (e.g. sample geometry).

6.2 Experimental Setup

The experimental setup follows that outlined in section 4.4.5 using a variety of measurement parameters (see Table 4-3) that are specific for each test. Figure 4-6 provides a flowchart with associated parameters for clarification and each section describes the setup parameters in detail.

Table 6-1: X-ray physics factors determining fluorescence of samples (expanded on Kaiser and Shugar 2012:450). Some factors are not explored further but their inclusion helps to reveal the complicated nature of HH-XRF.

X-Ray Physics: Factors Affecting HH-XRF	
Factor	Factor Means
▪Inverse Square - Distance from Sample to Detector	Sample Characteristic
▪Matrix Density	Sample Characteristic
▪Elemental X-Ray Emission	Sample Characteristic
▪Element Location in Matrix	Sample Characteristic
▪Incident Beam Energry	User Defined
▪Incident Beam Filtering	User Defined
▪Incident Beam Distribution	Hardware/User Defined
▪Incident Beam Angle	Hardware

The HH-XRF parameter settings for the analysis of faience analogues and archaeological sherds were determined through a series of tests using Corning Glass B as the known analyte. Experimentation was implemented to determine presence of analyser drift and elements of instrument interference. Results will determine if instrument interference affects the detection of minor and trace elements. Optimal peak resolution and maximum peak to background signal ratio for elements of interest (see Shugar and Sirois 2012:319) (Fig. 6-1) were determined using voltage, current, acquisition time and filtering as variables. Two types of end windows are available and were tested to determine the effect on the detection of light elements. Source to sample distance experimentation was conducted to determine the potential effect of signal attenuation on the measurement of non-ideal specimen surface geometries.

The aim of the experimentation is to determine a high and low kV setting that will detect the most elements of interest (see Chapter 2) and provide the greatest SNR and precision for those elements. Eight parameters were tested (see Fig. 4-6) as a part of the HH-XRF evaluation: instrument signature, filter use, instrument drift, end window type, voltage, current, acquisition time and sample to detector distance. The variables for each of the testing parameters are described in sections to follow. A high ratio of net peak counts to background is a desired result of analysis (Shugar and Sirois 2012:319). The quality of detection is affected by parameter choices; for instance, the voltage determines elements that can potentially be detected and use of

Fig. 6-1: Elements most commonly found in faience categorized by structural elements, colourants and inclusions. Elements not detectable with the Bruker Tracer series are indicated. The structure elements, colourants and inclusions are the elements of interest for the analytical evaluation of HH-XRF with the exceptions of chlorine and sulfur; the HH-XRF filter selections do not optimize this region of the spectra.

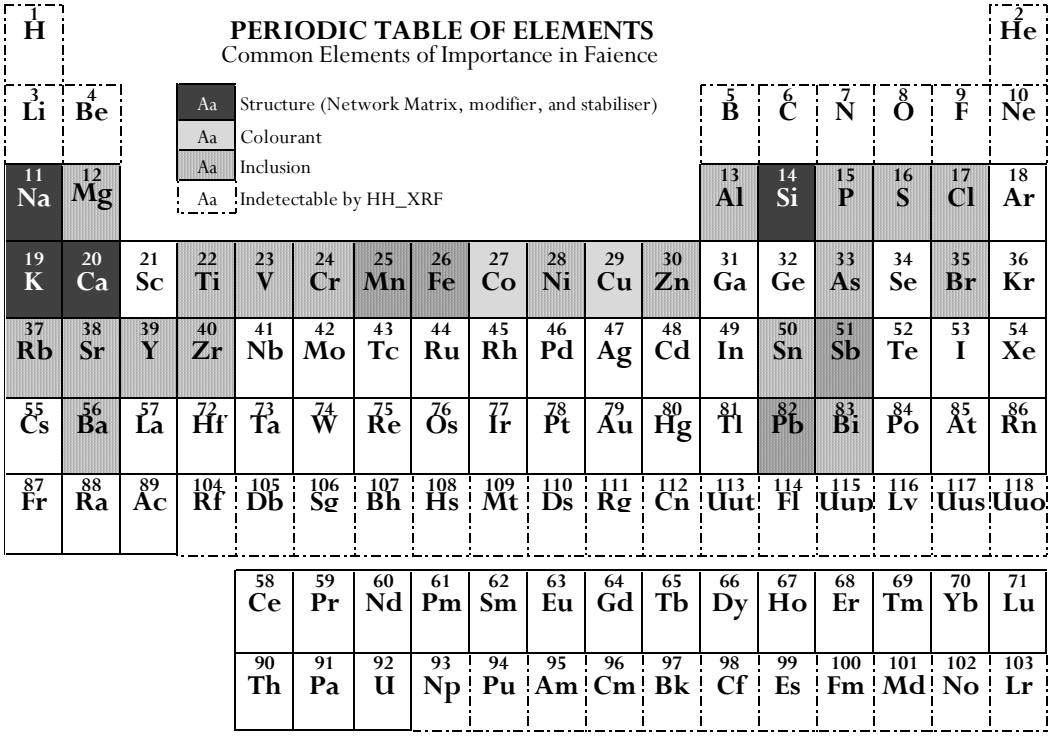

filters enhance detection of elements in specific regions, sometimes to the detriment of others. Other parameters and some analyser unit structural factors will have various effects on the data.

6.3 Experimental Results: HH-XRF Hardware Factors

Hardware factors represent inherent structural issues of the specific analytical unit and how they affect the data. Instrument signature, and the effect of filters thereon, are investigated. A discussion on filters, as a user defined factor, are explored further through the analysis of Corning Glass B and is included with the instrument signature section. The use of blanks, required to determine instrument signature, is addressed and two materials are measured: deionized water-filled bottle and pelletized cellulose. Instrument drift, a product of unit stability, is tested using three time intervals: 2 hours, 2 days and 5 months. Incident beam distribution and angle were not investigated but requiring mentioning because of the effect on data. The incident beam forms a cone as it departs from the source but can be tightened through the use of collimators. The beam spot size at the unit window has been described as 3 x 4 mm (Kaiser and Wright 2008:6) but expands as the distance from the X-ray tube increases. The unit window

size is 8 x 10 mm to avoid backscatter from the interaction of the beam with the window edges. The incident beam angle of the Bruker Tracer series is fixed at 53 degrees from the window to provide the greatest concentration of X-rays (Bruker 2010:7). The beam angle has a direct relationship with penetration depth of X-rays. The take-off angle is 62 degrees.

6.3.1 Instrument Signature and Filters

X-rays traveling from the source (the rhodium target) to the sample may fluoresce internal components of the HH-XRF unit resulting in trace peaks on the spectra (Kaiser and Wright 2008: 17-18). These contributions, as a group, are the *instrument signature* and are unique to each analyser unit. They can be reduced or eliminated with the use of filters. Kaiser and Wright (2008:9-10, 17-18) identify some of the Tracer III-SD unit signature peaks that appear on spectra but indicate others may be present as well:

- Rhodium (Rayleigh Scattering: X-ray Tube Target K and L lines)
- Iron, Cobalt and Nickel (Detector Can)
- Calcium (Window)
- Aluminium, Copper, Palladium, and Zinc (Tube, Collimator, Unit Structure)

Quantification of the instrument signature is termed *instrument interference*. Instrument interference can be subtracted from subsequent analyses to provide results free of instrument contribution. Matching the density of the calibration blank to the sample matrix is the main difficulty of this technique. Any discrepancy in the match will over- or underestimate the level of interference (Pers. Comm. Rebecca Scott) providing erroneous results. Silicon wafers of appropriate thickness (i.e. 2 cm) will provide a close approximation of a silicon-based glaze but can be cost prohibitive. Producing them in a non-specialized laboratory can be difficult mainly because of inclusions in the raw material and the high melting point of silica (~1700 ºC) which exceeds the limitations of many smaller kilns.

Any contribution of the instrument signature to the analysis of major elements will be small and have a negligible effect (Kaiser and Wright 2008:9-10; Pers. Comm. Rebecca Scott). They will have greater effect on elements at minor and trace levels. It is important to identify the instrument signature as this may determine which elements can be used for characterizing the sample and which should possibly be avoided.

Filters contribute their own characteristic energy to the bremsstrahlung region of the spectrum and will affect the instrument signature. For this reason, a discussion on

filters, although considered a user-defined parameter, is included within the instrument signature section.

Blanks are required to determine the instrument signature. A deionized water filled water bottle (Pers. Comm. Lee Drake) and cellulose pellet (see Appendix G for inclusion of Perspex) were analysed to determine their suitability as blanks and ultimately the instrument signature. Most water bottles are composed of polyethylene terephthalate (PET) and H_2O. PET is a polymer resin consisting of carbon, hydrogen and oxygen. The low Z element emission signals are easily attenuated and undetectable by the HH-XRF. The PET bottle was emptied of its contents, rinsed and filled with deionized water in preparation for analysis. Removal of water from the bottle also removed the possibility that some elements detected may have originated from minerals in the bottled water. Refilling with deionized water worked to the same effect by mostly removing the possibility that elements detected were introduced with the new water.

A cellulose pellet was produced, analysed and the results were compared with those of the water bottle using the same parameters to determine if either contribute additional peaks to the spectra. Cellulose is an organic compound consisting of carbon, hydrogen and oxygen, all which are undetectable using the HH-XRF. Cellulose is commonly used as a binder in pelletized powdered samples in X-ray spectroscopy (Jenkins 1999:146). The pellet was formed by compressing 1.2 grams of cellulose powder under 1 ton for 30 seconds followed by 11 tons for 60 seconds. This produced a pellet ~12 mm in diameter and ~5 mm thick. The pellet completely covered the unit window and provided infinite analytical thickness as ideally required for HH-XRF analysis.

Ten measurements for each filter were conducted on the water-filled bottle using settings A and B (Figs. 6-2 and 6-3). Ten measurements were conducted on the cellulose tablet using settings A, B and C. The water bottle and cellulose pellet results were compared (Fig. 6-4). All samples were placed directly on the window and measurements were made on clean surfaces. The data was examined to determine the instrument signature.

6.3.2 Instrument Signature Results and Discussion

The baseline (filter 2: data collected without a filter) reveals all the elements of the instrument signature without contribution or attenuation associated with filter use (Table 6-2). The rhodium Lα, Lβ (Setting A) and Kα (Setting B) line peaks exhibited with all blanks using parameter settings A, B (see Figs. 6-2 through 6-4) are notably

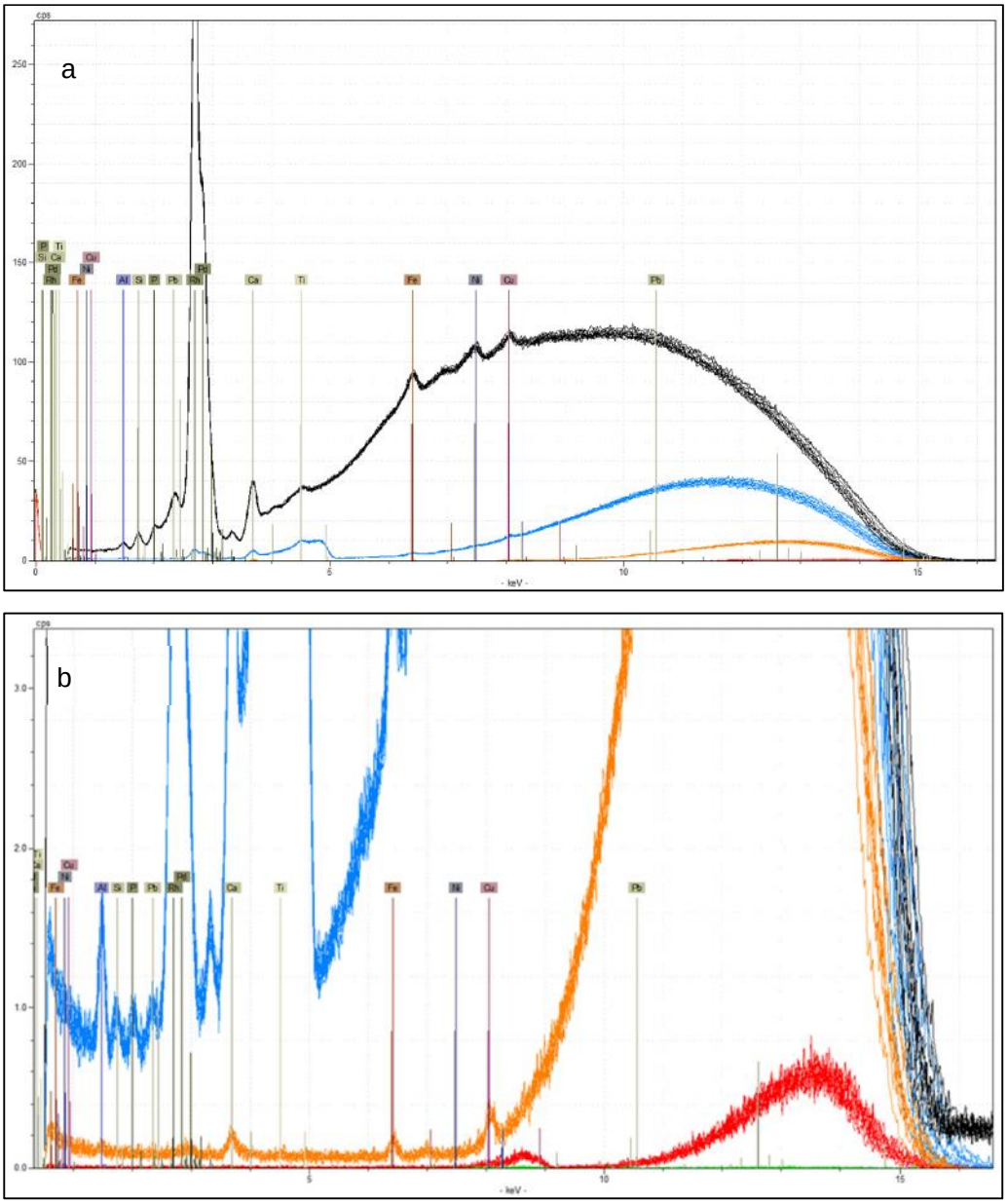

Fig. 6-2: Instrument interference spectra using filters 1-5 and water-filled PET bottle as a blank. The parameters are 15 kV, 55 µA with a vacuum for 180 seconds. Fig. 6-2b has been vertically expanded to exhibit additional information from filters with lower background. The filters are designated as follows: Filter 1 – orange; filter 2 – black; filter 3 – green (Fig. b at baseline below filter 5); filter 4 – blue; and filter 5 - red.

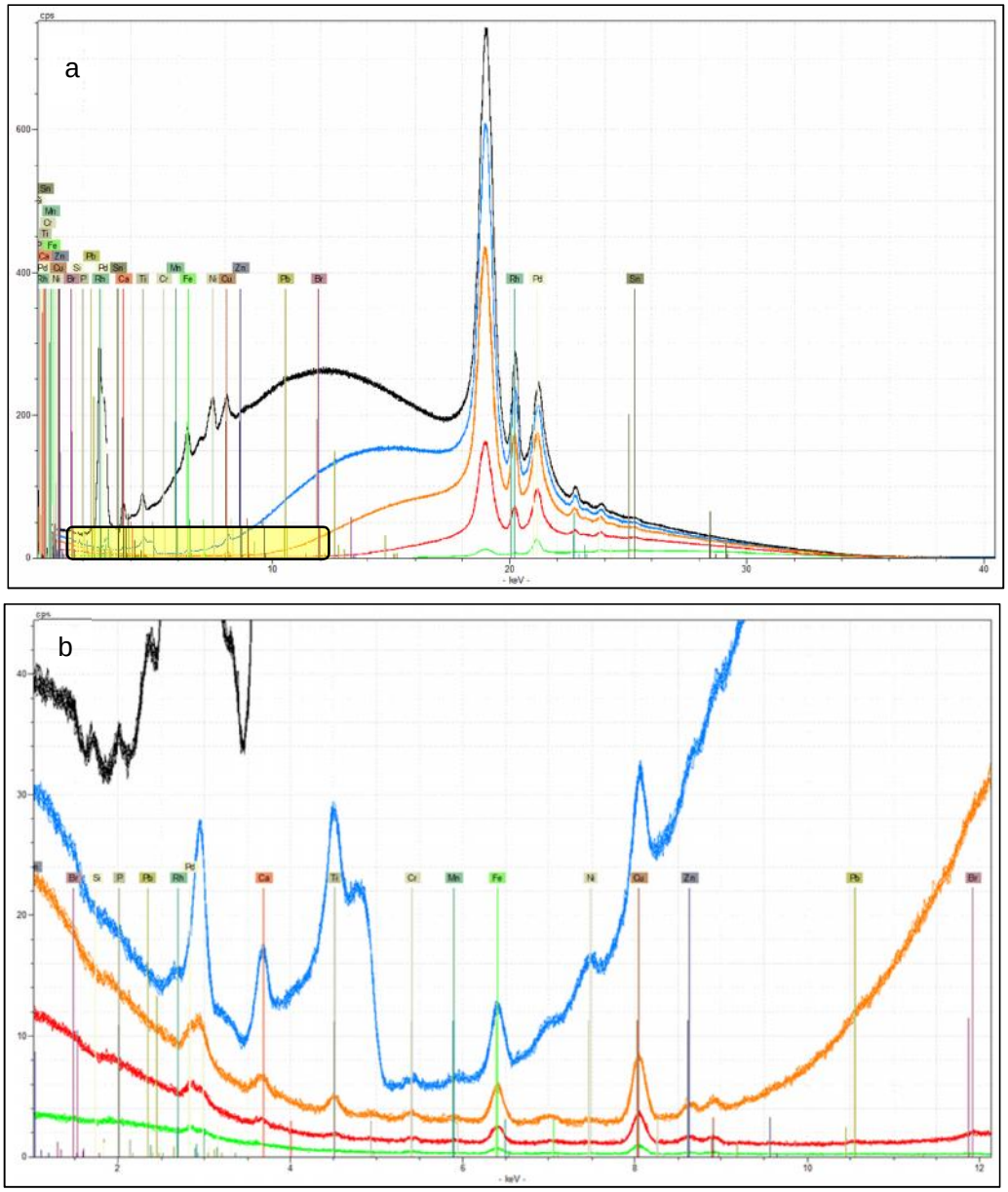

Fig. 6-3: Instrument interference spectra using filters 1-5 and water-filled PET bottle as a blank. The parameters are 40 kV, 30 µA with a vacuum for 180 seconds. Fig. b (shown in Fig. a as the yellow box) has been vertically expanded to reveal additional information from filters with lower background. Filter 1 – orange; filter 2 – black; filter 3 – green; filter 4 – blue; and filter 5 - red. Filter 3 (green) is barely perceptible along the x axis.

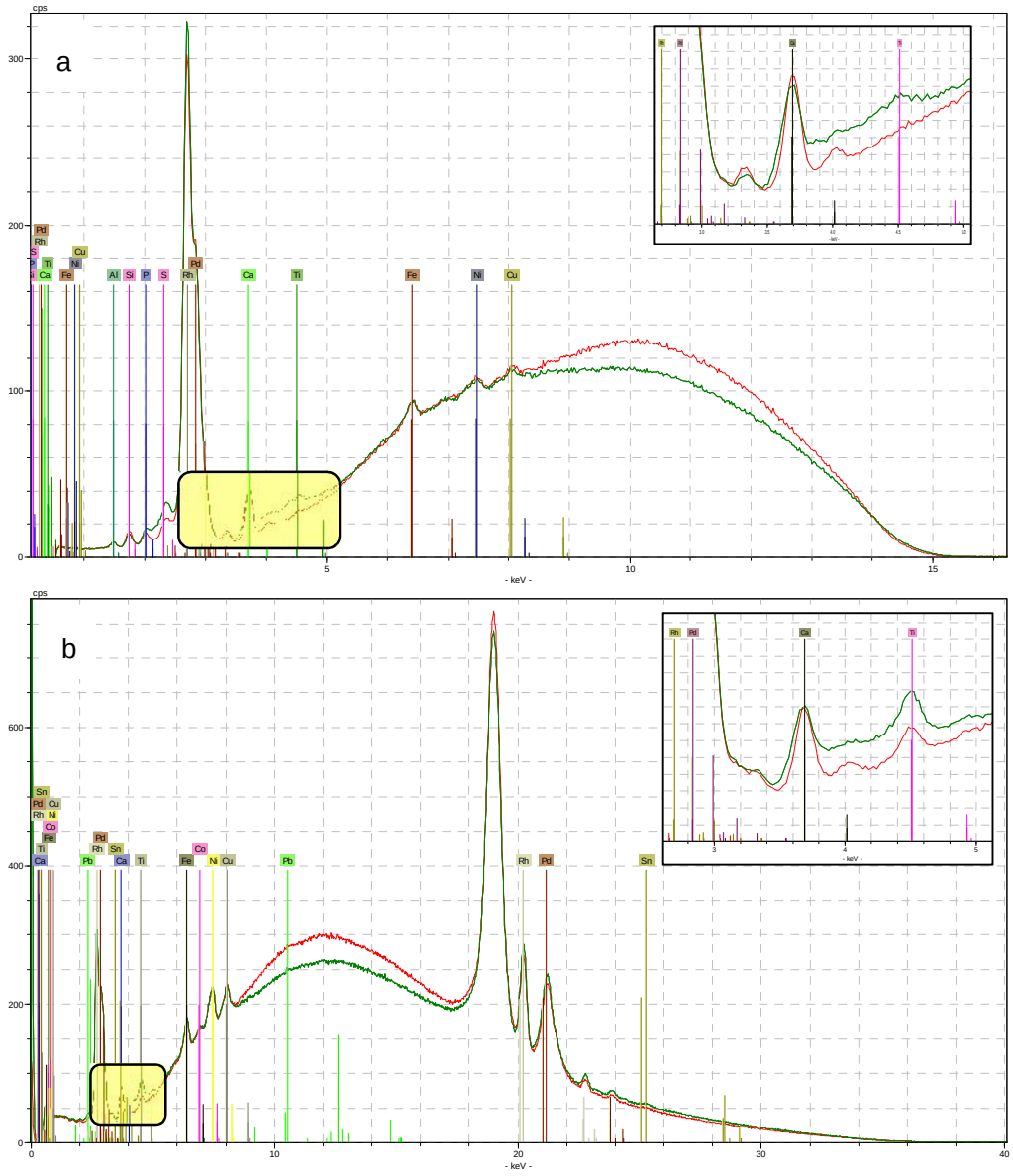

Fig. 6-4: Comparison between cellulose (red) and water filled PET bottle (green) blanks. Fig. a was analysed using 15 kV and 55 µA for 180 seconds with a vacuum and no filter. Fig. b was analysed using 40 kV and 30 µA for 180 seconds with no vacuum or filter. The insets for each spectra cover the region between 2.6 and 5 keV and exhibit the calcium and titanium peaks in relation to the rhodium (target) peak.

Table 6-2: Instrument signature elements for the HH-XRF used in the study as determined through measurements of a PET water bottle (DI water) blank and confirmed with cellulose pellet and Perspex plate blanks (see appendix G). Settings represent the analytical setup used to identify the instrument signature. Lines represents the characteristic peak line locations on the spectrum for the K and L lines indicated. Associations represent the most probable source of the element.

Instrument Signature Elements for Unit Used in Project

Settings A: 15 kV, 55 µA, vacuum, no filter, 180 second acuisition
Settings B: 40 kV, 30 µA, vacuum, no filter, 180 second acquisition

		Lines (keV)			
Element	Settings	Kα1	Lα1	Lα2	Associations
Aluminium	A and B	1.487	-	-	Tube, Collimator, Unit Structure
Silicon	A and B	1.740	-	-	Detector
Phosphorus	A and B	2.014	-	-	Unexplained - SDD dopent?
Sulphur	A	2.308	-	-	Unexplained - possibly the Ll (LIIIMI; 2.387 keV)) line of rhodium
Calcium	A and B	3.692	-	-	Interior Window
Titanium	A and B	4.511	-	-	Filters; unexplained for measurements without filter (HH-PXRF Component?).
Chromium	B	5.415	-	-	Unexplained - possibly sum peak of Lα1 and Lα2 lines (keV 5.39) of rhodium.
Iron	A and B	6.404	-	-	Detector Can
Cobalt	B	6.93	-	-	Detector Can
Nickel	A and B	7.478	-	-	Detector Can
Copper	A and B	8.048	-	-	Tube, Collimator, Unit Structure
Zinc	B	8.639	1.012	-	Tube, Collimator, Unit Structure
Bromine	B	11.924	1.408	-	Unexplained, only with filters 3 and 5 (Water Bottle Contribution?)
Rhodium	A and B	20.216	2.698	2.692	Target
Palladium	A and B	21.178	2.838	2.833	Tube, Collimator, Unit Structure
Tin	B	25.272	3.442	3.433	Unexplained - Solder (Drake Pers Comm 2015)?
Lead	B	-	10.555	10.453	Unexplained - solder?

higher than the other elements indicating that contribution of the signature elements to the spectra will not greatly affect the results of major and minor elements in unknown samples (Fig. 6-5) (Pers. Comm. Rebecca Scott). This is demonstrated with NPA where the highest non-target signature element using 15 kV (iron) represents only 13% NPA of the target (rhodium) (Table 6-3) and the highest non-target signature element using 40 kV (nickel[1]) is 28% NPA of the target (Table 6-4). The rhodium peak is a medium peak using setting A and generally one of the smaller peaks using setting B in faience and Corning Glass B measurements (see appendix C).

The setting A results are exhibited in Figs. 6-2, 6-5 and Table 6-3. Filters 1 and 4 generally have lower NPA and SNR due to attenuation of the signal and they exhibit lower precision (higher C_v) than baseline for all elements with the exception of lead (L lines). Elements lower than calcium (Z<20) have little to no sensitivity with filter 1 (Kaiser and Wright 2008:47). Lead results for filter 1 are below detection. Aluminium results are compromised by filter 1 construction which contains aluminium (see Table 3-1). Filter 3 attenuates most of the continuum and characteristic peaks cannot be discerned from the remaining noise making NPA and SNR assessments impossible. Filter 4 data reveal elevated titanium due to filter composition. Copper is above the optimization zone (3-12 kV) for filter 4 and the results represent a combination of characteristic energy and elevated background noise from the filter potentially affecting precision. The L lines for lead (~10.5 kV) are within the optimization range (3-12 kV) and are enhanced. Filter 5 data do not confidently reveal any characteristic peaks. There is a decrease of the continuum between 9 and 12 kV which is the optimal region for elements associated with pesticides (lead, bromine, arsenic and mercury) giving this filter the moniker of “poisons filter.” A residual of the continuum lies to the left of this region (7.5 to 9 kV; see fig. 6-2) which could be mistaken for a broad zinc characteristic peak.

The setting B results are exhibited in Figs. 6-3, 6-5 and Table 6-4. Generally, filters 1 and 3-5 exhibit lower NPA and SNR, and higher C_v than baseline. Filter 4 has higher SNR and NPA and lower C_v for titanium due to filter construction (see Table 3-1), and a reduction of SNR for most other elements within the optimization zone when compared to baseline. Nickel, copper, zinc and tin are above the optimization zone and are a combination of characteristic energy and elevated background noise from the filter. Chromium reveals higher NPA with filters 1 and 4. Chromium reveals higher

[1] This ignores palladium which constitutes the collimator and is directly in the X-ray beam path. As a result it usually displays the highest NPA (even higher than the rhodium target) of the signature.

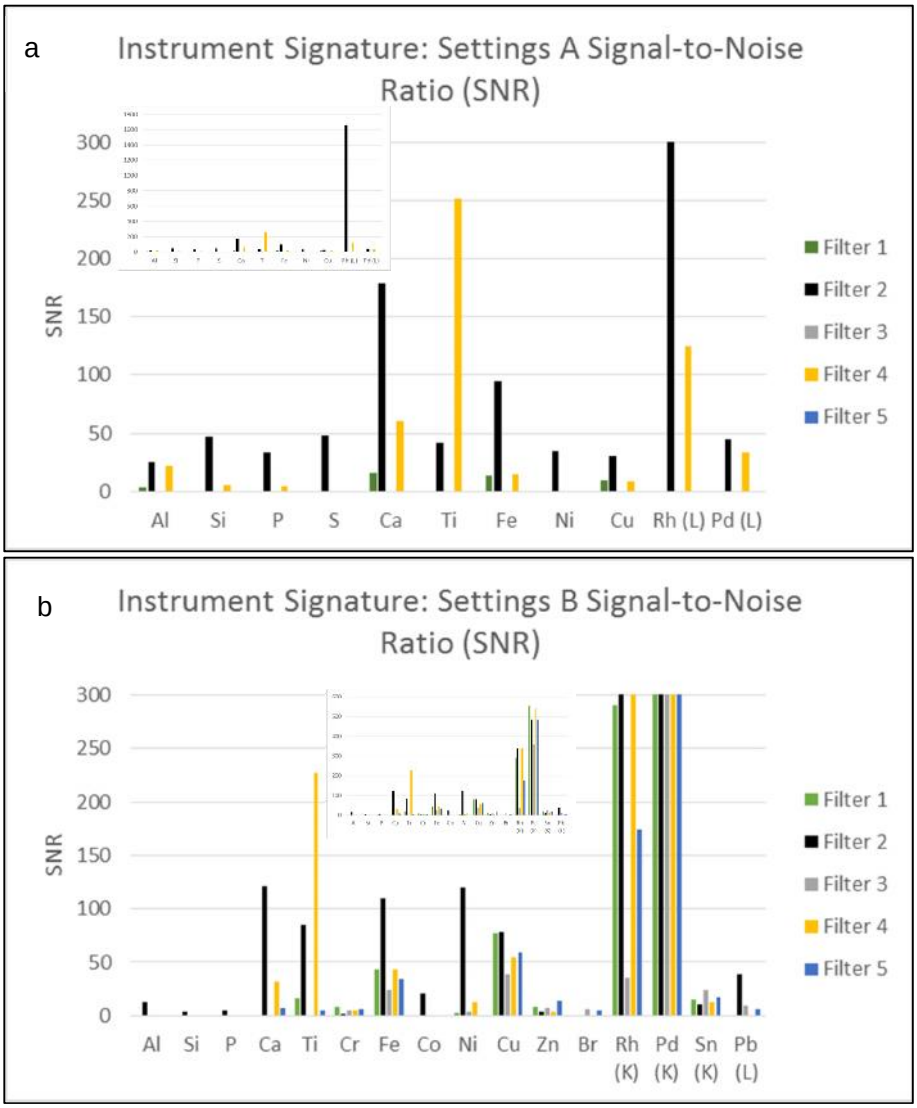

Fig. 6-5: Signal to noise ratio for detected elements by filter. The rhodium L line for the settings A measurements (a) extends beyond the chart limits to 1680 cps. The settings B (b) rhodium K line with filter 2 is 338 cps and filter 3 is 337 cps. All palladium lines for this setting extend beyond 300 cps (see Table 6-4). Note that rhodium (X-ray target) has a substantially higher SNR than all other elements of the instrument signature. Rhodium was below detection with filter 1. Filters 3 and 5 attenuated most of the element signals using settings A. Filter 4 is composed of titanium resulting in the high SNR for titanium. Specific SNR results can be seen in Table 6-4 and Table 6-5. The instrument signature will have negligible effect on major and minor elements of samples. The insets exhibit each chart without truncation of the rhodium and palladium lines.

Table 6-3: Statistics for Measurements at 15 kV (settings A) including net peak area (NPA), coefficient of variation (C_v) (precision of measurements), limit of detection of a method (±) (range for 94.5% of measurements) and signal to noise ratio (SNR). The limit of detection is SNR >3 and the limit of quantification is SNR>10. Filter 3 has no SNR due to low counts and lack of background because of filter attenuation. Filter 5 has no results due to lack of characteristic peaks. BD is below detection. Blank spaces indicate peak not observed.

Instrument Interference: Low Volage Statistics Parameters: 15 kV, 55 µA, Vacuum, 180 seconds, 10 Measurements											
		Al	Si	P	Ca	Ti	Fe	Ni	Cu	Rh (L)	Pd (L)
Filter 1	NPA	51.20			218.30		190.50		237.00	23.00	36.40
	C_v	22.49			12.83		23.30		20.28	60.66	26.67
	±	23.03			56.02		88.76		96.11	27.90	19.42
	SNR	3.55			15.40		13.35		9.93	BD	BD
Filter 2	NPA	2741.90	5846.20	5372.10	34401.60	11778.00	44489.00	18882.20	17325.70	347063.40	8625.40
	C_v	7.55	4.11	3.83	0.93	4.37	1.91	4.64	4.39	1.26	32.88
	±	414.17	480.08	411.21	637.85	1028.95	1698.56	1752.14	1521.04	8762.69	5672.89
	SNR	25.13	46.74	33.93	178.85	41.38	95.06	34.98	30.61	1663.77	42.78
Filter 3	NPA	1.20	0.40	0.90	0.80	0.50	1.10	0.90	5.20	0.40	0.20
	C_v	35.14	394.41	35.14	79.06	105.41	67.08	142.96	42.33	129.10	210.82
	±	0.84	3.16	0.63	1.26	1.05	1.48	2.57	4.40	1.03	0.84
	SNR										
Filter 4	NPA	869.50	226.10	201.40	4394.10	23453.10	1374.00	329.20	1687.70	5985.90	1614.60
	C_v	9.29	15.51	28.43	2.63	1.73	16.53	43.38	15.17	3.58	8.89
	±	161.50	70.15	114.50	231.13	812.36	454.13	285.64	512.16	428.81	287.03
	SNR	21.52	5.44	4.81	60.94	251.18	14.47	BD	8.67	125.06	33.28

Table 6-4: Statistics for Measurements at 40 kV (settings B) including net peak area (NPA), coefficient of variation (C_v)(precision of measurements), limit of detection of a method (±)(range for 94.5% of measurements) and signal to noise ratio (SNR). The limit of detection is SNR >3 and the limit of quantification is SNR>10. BD is below detection. Blank spaces indicate peak not observed.

Instrument Interference: High Voltage Statistics

Parameters: 40 kV, 30 µA, 180 seconds, 10 Measurements

		Al	Si	P	Ca	Ti	Cr
Filter 1	NPA					1498.90	681.80
	Cv					8.66	13.24
	±					259.58	180.50
	SNR					16.30	7.83
Filter 2	NPA	2685.50	749.50	1068.40	30145.40	26058.90	543.70
	Cv	13.68	19.61	23.97	1.43	2.10	86.35
	±	734.63	293.91	512.22	862.70	1092.55	938.97
	SNR	13.24	3.81	5.22	121.15	85.17	1.45
Filter 3	NPA					85.30	163.90
	Cv					36.19	26.62
	±					61.75	87.25
	SNR					BD	5.31
Filter 4	NPA				4612.30	34265.40	565.20
	Cv				4.00	0.86	18.87
	±				368.70	591.56	213.34
	SNR				31.92	227.02	4.98
Filter 5	NPA				542.60	322.20	364.60
	Cv				22.40	27.94	26.90
	±				243.04	180.05	196.14
	SNR				6.95	5.02	6.17
		Fe	Co	Ni	Cu	Zn	Br
Filter 1	NPA	3760.20		266.60	7161.70	859.50	
	Cv	4.15		43.24	3.58	11.79	
	±	311.93		230.57	513.40	202.75	
	SNR	43.66		3.03	77.35	8.53	
Filter 2	NPA	53779.40	10735.70	66521.20	46627.70	2551.90	
	Cv	1.61	7.97	1.79	1.67	32.52	
	±	1727.53	1712.07	2380.39	1561.93	1659.81	
	SNR	109.76	20.39	119.63	78.43	4.15	
Filter 3	NPA	708.30		93.30	1120.50	214.50	184.90
	Cv	8.21		46.06	7.89	22.37	22.91
	±	116.28		85.96	176.72	95.97	84.72
	SNR	23.88		3.36	39.04	7.54	6.43
Filter 4	NPA	5559.20		2323.90	12213.90	1158.30	
	Cv	5.20		12.20	2.50	25.49	
	±	578.14		567.15	610.70	590.55	
	SNR	43.67		12.70	54.42	4.09	
Filter 5	NPA	1958.30		114.60	3616.60	886.70	350.80
	Cv	4.54		50.22	2.73	9.91	42.34
	±	177.89		115.09	197.45	175.66	297.05
	SNR	33.61		BD	59.33	14.41	4.32

Table 6-4 continued: Statistics for Measurements at 40 kV (settings B) including net peak area (NPA), coefficient of variation (C_v)(precision of measurements), limit of detection of a method (±)(range for 94.5% of measurements) and signal to noise ratio (SNR). The limit of detection is SNR >3 and the limit of quantification is SNR>10. BD is below detection. Blank spaces indicate peak not observed.

Instrument Interference: High Voltage Statistics Parameters: 40 kV, 30 µA, 180 seconds, 10 Measurements						
		Rh	Rh (L)	Pd	Sn	Pb (L)
Filter 1	NPA	194011.80	77.10	355123.60	7305.60	
	Cv	1.42	181.13	0.79	14.12	
	±	5506.16	117.46	5592.32	2063.66	
	SNR	289.83	BD	554.99	15.01	
Filter 2	NPA	235720.10	193918.80	309825.60	4624.00	25751.50
	Cv	1.05	0.73	0.94	5.98	3.66
	±	4951.92	2830.88	5834.19	552.70	1885.34
	SNR	338.13	808.60	482.19	10.09	38.14
Filter 3	NPA	6085.40	1.50	70057.00	6251.00	251.90
	Cv	5.18	154.76	1.03	4.24	19.21
	±	631.00	4.64	1443.62	530.01	96.76
	SNR	35.52	BD	357.49	24.55	9.53
Filter 4	NPA	246549.60	1404.30	365981.30	6229.00	
	Cv	0.68	11.61	0.61	14.33	
	±	3336.66	326.00	4434.95	1784.77	
	SNR	337.22	9.34	539.69	12.64	
Filter 5	NPA	82177.00	0.10	228752.60	7330.80	336.80
	Cv	1.41	316.23	0.55	8.77	62.51
	±	2324.23	0.63	2496.81	1285.72	421.07
	SNR	174.05	BD	483.21	17.51	5.59

SNR with all filters but C_v is lower than baseline. This may indicate that chromium is a component of the unit enhanced with filter use, or a contribution of the filters (it is below detection without filters), or both. Chromium data with filter 3 is below the optimization zone (17-40 kV) reducing precision of the results. Zinc data displays lower C_v and higher SNR with filters compared to baseline. Bromine is detected using filters 3 and 5. The NPA and precision are greater with filter 5 but SNR (4.32) indicates bromine is just above the LOD. Bromine SNR with filter 3 is slightly higher (6.43). Tin is detected with setting B but is outside of the optimization zone with all filters.

Kaiser and Wright (2008:9-10, 17-18) note many of the elements that will be detected as part of the instrument signature (e.g. rhodium, palladium, calcium, etc.) but detection of phosphorus, sulphur, chromium, titanium, bromine, tin and lead were not indicated nor expected. Bayesian deconvolution within the Artax Spectra software suggests the presence of these elements but the presence can only be partly explained. HH-XRF window contamination can be ruled out as the window was cleaned with each change of sample and was replaced when punctured resulting in no difference in the spectra. The cellulose pellet and water bottle blanks were measured on one occasion with no window present (therefore without a vacuum) to explicitly test window contamination and contribution but resulted in no change in detected elements. Internal contamination is highly unlikely as a window is always present on the unit unless the window is being changed. It is more likely that these elements represent a minor component of the HH-XRF unit.

Bayesian deconvolution indicates the presence of phosphorus (Fig. 6-6). Phosphorus is used as a dopant on n-type semiconductors and is associated with line at 2.387 kV which is definitely present. The sulphur peak is pulled toward the significantly larger rhodium Lα1 line (2.698 kV) and this drift is nearly matched by the Bayesian deconvolution line. The presence of titanium can usually be explained as a filter component (see Table 3-1). Its presence with unfiltered measurements may indicate the source as a minor component of the HH-XRF unit. A small chromium peak is present in the spectra (5.415 kV) and could represent a minor component of the HH-XRF unit or could be a sum peak (5.39 kV) of the Lα1 and Lα2 lines of rhodium. PET is not detectable with HH-XRF but antimony oxide, used as a catalyst in the production of PET (NAPCOR n.d.: 11) and bromine, as a disinfectant, could contribute to the spectra if the quantities are sufficient. A small bromine peak occurs in conjunction with filters 3 and 5 but is barely above LOD (see Table 6-4). Bromate has been identified in bottled water as a residual of the disinfectant process (Sharif 2014:19). Bromine was present

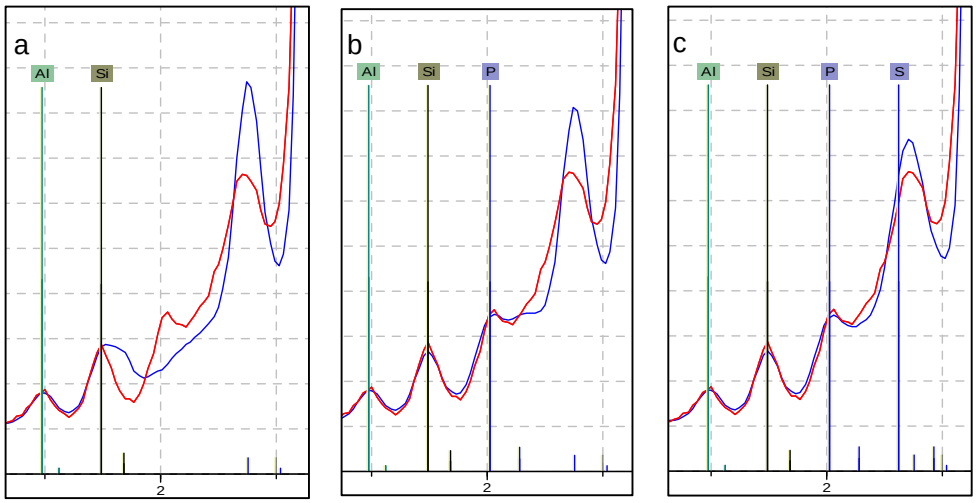

Fig. 6-6: The series of images exhibits the spectrum (red line), Bayesian deconvolution line (blue line) and elemental characteristic lines between 1.3 and 2.6 keV. Fig. a exhibits a matched aluminium peak and Bayesian line indicating presence of the element. In the subsequent images (Fig. b and c) the Bayesian line forms a better match with the spectrum as more elements (silicon, phosphorus and sulphur) are included. The identification of sulphur, although not perfectly matched, exhibits greater correspondence between the spectrum line and the Bayesian line than when not selected as an element.

with store bought water and tap water and may originate from the bottle itself. Tin is detected with all the filters but has greater precision at baseline and filter 3. Tin is above the optimization zone for filter 3 and the results are expected to contain characteristic energy and noise from the filter but it has greater precision than baseline. The source of tin in the HH-XRF unit may be solder (Pers. Comm. Lee Drake). This may also identify the source of lead in the spectra. The water bottle is sufficient to identify the instrument signature but is not a true blank as there is a potential for the addition of bromine at trace levels in the spectra.

The measuring of blanks using various filters exhibit a decrease in SNR and the NPA from the baseline (no filter) (see Tables 6-3 and 6-4; Figs. 6-2 and 6-3) measurements even though they are designed to enhance the SNR for some of the elements at these settings. Placing a filter between the target and the sample will attenuate the signal blocking many of the photons from the instrument signature elements before they reach the blank. The result is a reduction of SNR and NPA for most elements. A greater SNR result is expected when measuring samples containing elements located within the optimization zones the filters were designed to enhance.

Comparison of the cellulose tablet and the water bottle (Table 6-5) generally reveal that all but a few elements correspond. Silicon NPA and SNR is significantly higher in the cellulose pellet whereas titanium is much lower with settings A and B. Palladium is

Table 6-5: Statistics for instrument signature measurements with cellulose tablets and water bottle using settings A and B (with and without filter 3). Statistics include net peak area (NPA) and signal to noise ratio (SNR). The limit of detection is SNR >3 and the limit of quantification is SNR>10.

Low Voltage (15 kV) Net Peak Area and Signal to Noise Ratio

Parameters: 15 kV, 55 µA, Filter 2, 180 seconds

		Al	Si	P	S	Ca	Ti	Fe	Ni	Cu	Rh (L)	Pd (L)
Cellulose	NPA	2642.20	8197.10	4375.60	2237.20	33599.40	1470.40	42800.70	17417.20	13765.00	322939.60	27710.80
	SNR	24.17	65.50	31.00	13.01	192.29	5.68	91.71	32.17	24.16	1673.00	146.06
Waterbottle	NPA	2741.90	5846.10	5312.20	9533.70	34399.20	11778.00	44489.00	18882.20	17325.70	346460.50	9049.00
	SNR	25.13	46.74	33.55	48.32	178.84	41.38	95.06	34.98	30.61	1660.88	44.89

High Voltage (40 kV) Net Peak Area and Signal to Noise Ratio

Parameters: 40 kV, 30 µA, Filter 3, 180 seconds

		Ti	Cr	Fe	Ni	Cu	Zn	Br	Rh	Sn	Sb	Pb (L)
Cellulose	NPA	130.10	154.50	645.60	81.20	1075.20	184.80	153.60	5715.70	5679.80	2222.80	323.50
	SNR	3.72	5.21	24.13	3.07	40.64	6.65	5.65	33.81	23.99	9.13	12.70
Waterbottle	NPA	71.10	163.40	708.30	93.20	1120.50	214.60	185.00	6239.10	6015.50	3631.60	251.90
	SNR	1.98	5.29	23.88	3.36	39.04	7.54	6.43	36.42	23.62	13.81	9.53

High Voltage (40 kV) Net Peak Area and Signal to Noise Ratio

Parameters: 40 kV, 30 µA, Filter 2, 180 seconds

		Al	Si	P	Ca	Ti	Cr	Fe	Co	Ni	Cu	Zn	Rh	Sn	Pb
Cellulose	NPA	2669.30	1328.40	1403.60	33935.00	13406.60	1568.80	52580.40	9265.50	61487.50	43760.60	2495.30	208333.70	4206.00	38390.80
	SNR	13.56	6.96	7.23	150.55	48.53	4.31	108.99	17.81	111.57	73.84	4.03	301.38	9.74	54.05
Waterbottle	NPA	2685.50	749.50	1068.40	30145.40	26058.90	543.70	53779.40	10735.50	66521.10	46626.70	2515.50	235720.10	4624.00	25751.50
	SNR	13.24	3.81	5.22	121.15	85.17	1.45	109.76	20.39	119.63	78.43	4.09	338.13	10.09	38.14

much higher in the cellulose tablet with setting A but is similar to the water bottle with setting B. The discrepancy of the palladium L line may be due to deconvolution and peak overlap. The palladium L line is in an area of the spectrum that is convoluted with characteristic lines of rhodium, potassium and chlorine. Chromium with setting B exhibits higher NPA and SNR in the cellulose tablet whereas tin is much higher in the water bottle measurements. The cellulose blank matches each peak exhibited with the water bottle spectra at the parameters tested (see Fig. 6-4 and Table 6-5). Figure 6-4 reveals a very similar but slightly higher Compton peak for the cellulose pellet indicating that it has lower density than the water-filled PET bottle. The Compton peak is a direct reflection of the mass of the sample (Longoni and Finori 2006:204; Shackley 2011:23; Shugar 2013:179). Dense materials will exhibit smaller Compton peaks because of restricted signal penetration (Shugar and Mass 2012:32) and a less dense sample will exhibit larger Compton peaks because of greater depth of measurement. Data (see Table 6-5) indicate that the cellulose blank and the water bottle blank are comparable but not exact. The data acquired at 15 kV reveals titanium SNR and NPA 10 times greater with the water bottle blank. The data acquired at 40 kV reveals the SNR and NPA to be twice the amount with the water bottle blank. Tin has the same relationship. These results indicate that either the cellulose is absorbing the titanium and tin signals, the water bottle has a greater capacity for reflecting the signals, or the water and/or bottle are contaminated. Alternatively the end window could be contaminated with titanium and tin but this is unlikely as the window is cleaned for each measurement and has been changed when punctured without any change to the spectra. Silicon in the cellulose pellet is nearly twice that found with the water bottle. This disparity is most likely the result of silicon uptake within the plant material used to produce the cellulose (Jones and Handreck 1967; see also Table 2 in Tite et al. (2006:1287)). Chromium is nearly four times greater in the cellulose which could represent modern pollutants in the plant material used to produce the cellulose (Singh et al. 2013:230).

Spectra of Corning Glass B using the various filters exhibit a lower continuum in the areas of optimization for each filter (see Table 3-1, Figs. 6-7 and 6-8). The baseline (filter 2) for the Corning Glass B measurement using settings D reveal the highest NPA and SNR (Table 6-6). Exceptions to this are chromium which reveals highest SNR with filter 1, and chlorine, barium and lead which exhibit highest SNR with filter 4. Baseline exhibits lowest C_v with the exceptions of barium and lead (filter 4). There is complete signal attenuation with filter 3 and no spectrum has been produced. Filter 5 has partial

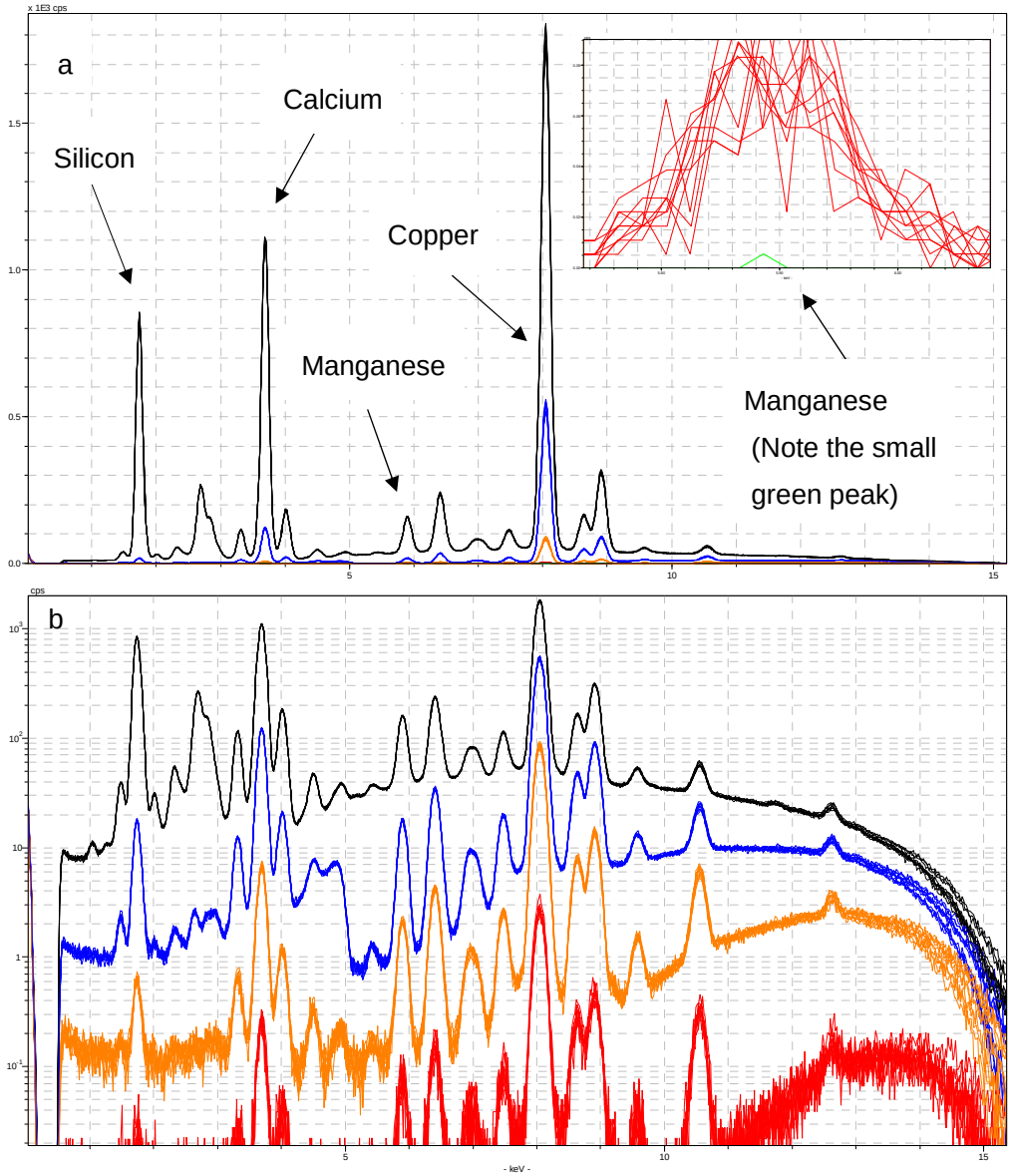

Fig. 6-7: Comparison of filters using parameters D and Corning Glass B as the sample. Filter 1 is orange, filter 2 (no filter) is black, filter 3 is green (inset), filter 4 is blue and filter 5 is red. Fig. b is the same spectrum on a logarithmic scale enabling the viewing of more details of spectral lines associated with filters not visible in Fig. a. The inset spectrum exhibits filter 3 in relation to the manganese characteristic peak (5.9 keV) with filter 5. Most peak labels are removed for clarity.

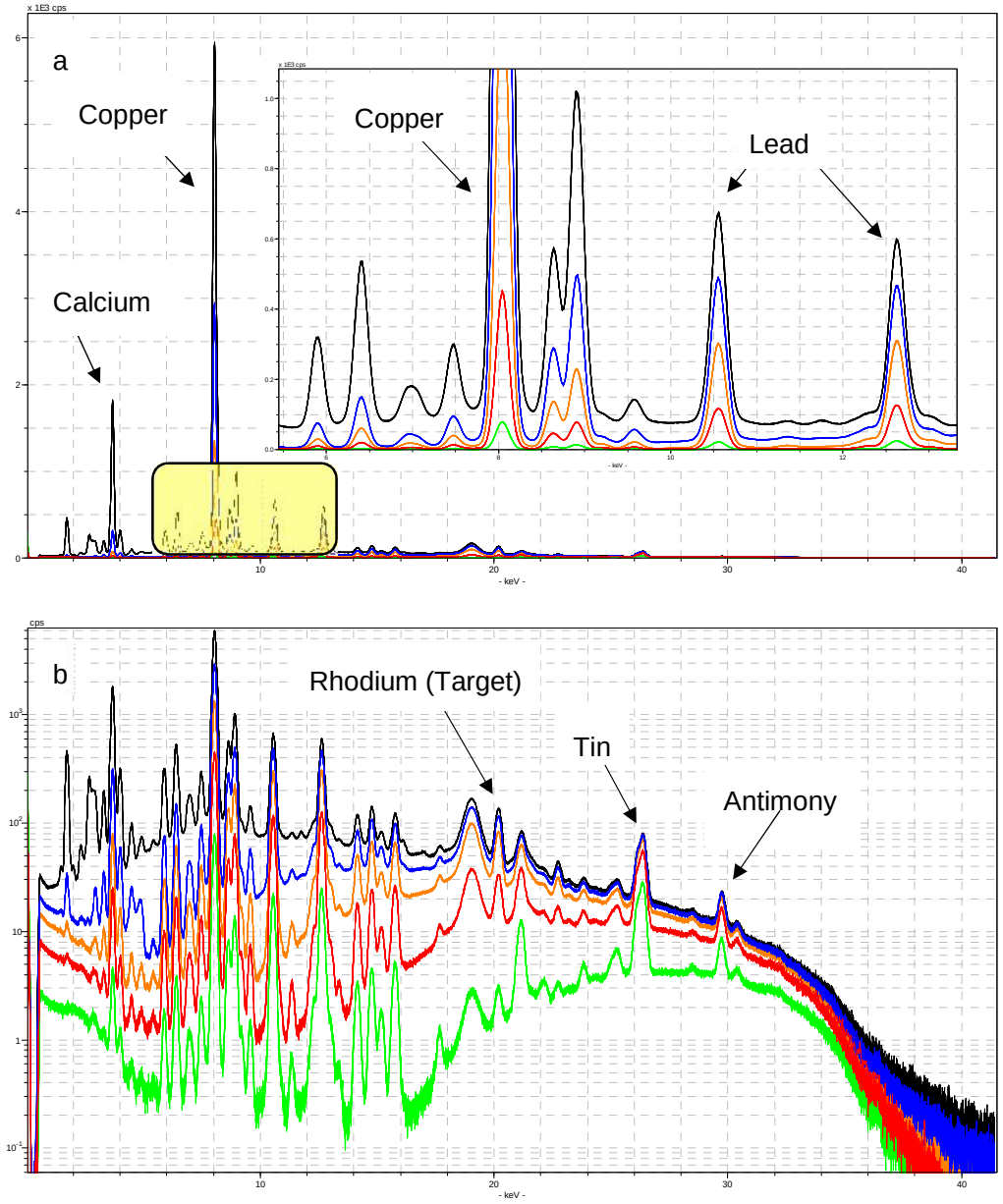

Fig. 6-8: Comparison of filters using parameters E and Corning Glass B as the sample. Filter 1 is orange, filter 2 (no filter) is black, filter 3 is green, filter 4 is blue and filter 5 is red. Fig. a clearly exhibits the lowered continuum in the optimization zones for the various filters when compared to the continuum without a filter (filter 2, orange). Fig. b is the same spectrum on a logarithmic scale enabling the viewing of more details of spectral lines associated with filters not visible in the upper image, specifically filter 3 (purple). The inset exhibits more detail for the 5.75-12.75 keV range.

Table 6-6: Statistical results of Corning Glass B with various filters (F1-F5) including net peak area (NPA), coefficient of variation (C_v), limit of detection of a method (±) and signal to noise ratio (SNR). The limit of detection is SNR >3 and the limit of quantification is SNR>10. Red highlighted results indicate greatest precision (lowest C_v) and highest SNR for each element. Blank spaces indicate peak not observed.

Testing of Filters; Corning Glass B as Sample; Sodium through Titanium

Parameters: 15 kV, 55 µA, Vacuum, 180 Seconds, 10 measurements

		Sodium	Magnesium	Aluminium	Silicon	Phosphorus	Sulfur	Chlorine	Potassium	Calcium	Titanium
F1	NPA µ			71.90	577.70				607.50	8629.80	350.40
	σ			28.63	27.06				57.91	458.99	30.22
	Cv			39.82	4.68				9.53	5.32	8.62
	±			60.36	57.04				122.08	967.65	63.70
	SNR			4.66	23.51				23.18	220.03	18.16
F2	NPA µ	1465.50	332.10	26127.10	794741.10	12230.30	26808.80		82886.70	1229654.90	23821.20
	σ	146.08	73.10	298.04	4185.92	292.01	248.08		705.01	7791.63	453.04
	Cv	9.97	22.01	1.14	0.53	2.39	0.93		0.85	0.63	1.90
	±	307.96	154.10	628.32	8824.70	615.61	523.00		1486.29	16426.20	955.09
	SNR	11.40	2.42	168.39	4551.43	68.01	135.64		385.05	5534.70	108.75
F3	NPA µ										
	σ										
	Cv										
	±										
	SNR										
F4	NPA µ			1382.50	17951.40	261.10	696.20	1081.10	12164.70	150282.70	5497.80
	σ			54.33	238.56	55.88	66.79	90.28	191.05	1914.96	127.77
	Cv			3.93	1.33	21.40	9.59	8.35	1.57	1.27	2.32
	±			114.53	502.92	117.80	140.81	190.33	402.76	4037.09	269.37
	SNR			29.89	367.64	5.38	13.74	18.79	167.52	1805.68	68.75
F5	NPA µ			13.90	27.00	7.70				326.50	
	σ			3.81	7.13	3.47	* Insufficient continuum data			30.56	
	Cv			27.39	26.40	45.01	for SNR determination.			9.36	
	±			8.02	15.03	7.31				64.42	
	SNR			8.39	*	*				117.95	

Table 6-6: Continued: Statistical results of Corning Glass B with various filters (F1-F5) including net peak area (NPA), coefficient of variation (C_v), limit of detection of a method (±) and signal to noise ratio (SNR). The limit of detection is SNR >3 and the limit of quantification is SNR>10. Red highlighted results indicate greatest precision (lowest C_v) and highest SNR for each element. Blank spaces indicate peak not observed.

Testing of Filters; Corning Glass B as Sample; Chromium through Bismuth											
Parameters: 15 kV, 55 µA, Vacuum, 180 Seconds, 10 measurements											
		Chromium	Manganese	Iron	Cobalt	Nickel	Copper	Zinc	Barium	Lead	Bismuth
F1	NPA µ	56.90	2890.40	5869.20	1204.60	3392.90	136512.00	12035.20		9519.00	
	σ	26.39	139.80	291.90	98.20	175.25	7519.98	600.95		985.15	
	Cv	46.38	4.84	4.97	8.15	5.17	5.51	4.99		10.35	
	±	55.64	294.73	615.39	207.02	369.46	15853.50	1266.92		2076.88	
	SNR	23.21	76.74	136.99	32.46	59.64	1680.07	148.09		94.77	
F2	NPA µ	4830.80	155189.00	249051.50	39689.80	88029.60	2460319.10	169633.50	10330.50	16612.50	2201.50
	σ	462.55	1544.39	2740.83	501.59	1431.60	35067.68	2557.51	398.08	1342.66	480.69
	Cv	9.58	1.00	1.10	1.26	1.63	1.43	1.51	3.85	8.08	21.83
	±	975.14	3255.86	5778.17	1057.44	3018.07	73929.16	5391.71	839.22	2830.58	1013.38
	SNR	17.13	494.20	749.43	111.43	239.45	6466.18	452.08	47.78	53.22	7.25
F3	NPA µ										
	σ										
	Cv										
	±										
	SNR										
F4	NPA µ	47.20	23305.50	46012.90	8752.40	23381.40	827554.20	65030.90	5799.80	30409.80	
	σ	37.69	562.03	971.35	163.03	594.00	21208.87	1858.38	124.85	2037.55	
	Cv	79.85	2.41	2.11	1.86	2.54	2.56	2.86	2.15	6.70	
	±	79.45	1184.87	2047.78	343.69	1252.26	44712.23	3917.81	263.22	4295.53	
	SNR	0.99	427.84	698.46	103.16	208.52	5952.88	421.63	71.46	171.00	
F5	NPA µ		113.60	212.50	46.10	113.00	4317.90	433.40	15.30	611.30	
	σ		13.18	25.87	11.18	18.07	488.47	58.93	3.00	84.49	
	Cv		11.60	12.18	24.24	15.99	11.31	13.60	19.62	13.82	
	±		27.78	54.55	23.56	38.10	1029.78	124.24	6.33	178.13	
	SNR		51.17	65.62	11.59	17.74	492.34	47.73	*	104.72	

attenuation of the continuum resulting in the inability to determine SNR and NPA for the characteristic peaks in those areas (see Fig. 6-7b). Lower Z element signals are attenuated with filter 1 and the remaining signal produces lower NPA and SNR, and higher C_v with the exception of chromium. Filter 4 allows the measurement of chlorine and sulphur without peak overlap and interference of the rhodium lines (Rayleigh scatter) but offers no advantage beyond this. The spectra (see Fig. 6-7) exhibit a low continuum for all filters when compared to the higher voltage spectra, the highest when no filters were used.

The results of setting E with Corning Glass B generally reveal highest NPA with filter 2 (baseline) (Table 6-7). Precision is scattered between the filters and is element based. Highest SNR breaks down into three categories: potassium through manganese with filter 2, iron through zinc with filter 4, and strontium through antimony with filter 5. Rubidium and lead are outliers and reveal highest SNR with filter 1. Filter 3 allows detection of the largest amount of elements. The spectra (see Fig. 6-8) exhibit lowest continuum in the area of optimization for each filter (see Table 3-1) and a high continuum when measurements were taken with no filter.

Measurement statistics of Corning Glass B using settings D indicate filter 2 (baseline) as having the best precision and SNR. The 15 kV used in the analysis is better for the fluorescing of lower Z elements whose signal is attenuated by use of a filter. Using a vacuum in conjunction with the lower voltage further enhances sensitivity to the lower Z elements. The measurement of elements at higher voltage (40 kV) is more complicated and break down into three filter groupings based on Z (see Table 6-6). Use of a vacuum will reduce sensitivity to higher Z elements as lower Z element photons reaching the detector are enhanced and increase deadtime. Attenuation of the lower Z photons by the air column in the unit is preferred allowing processing time for higher Z elements for these measurements. Filter 4 exhibits better SNR and C_v than the other filters but is mainly used to removed rhodium and palladium L line peaks so that sulphur and chlorine can be more accurately measured. The SNR and C_v for filter 3 are slightly lower than filter 4 but the filter allows for the identification of more elements. It is used to optimize the 17-40 kV region which contains typical glass provenance markers consisting of rubidium, strontium, zirconium and niobium.

In conclusion, a total of 17 elements have been identified in the instrument signature for the HH-XRF unit used in the experiments. The characteristic peaks for the signature elements are significantly smaller than the rhodium Lα1 and Lα2 lines and the Compton peak indicating that there will be negligible effect on major and minor

Table 6-7: Statistical results of Corning Glass B with various filters (F1-F5) including net peak area (NPA), coefficient of variation (C_v), limit of detection of a method (±) and signal to noise ratio (SNR). The limit of detection is SNR >3 and the limit of quantification is SNR>10. Red highlighted results indicate greatest precision (lowest C_v) and highest SNR for each element.

Testing of Filters; Corning Glass B as Sample; Potassium through Zinc											
Parameters: 40 kV, 30 µA, 180 Seconds, 10 measurements											
		Potassium	Calcium	Titanium	Chromium	Manganese	Iron	Cobalt	Nickel	Copper	Zinc
F1	NPA µ	4354.50	84493.60	3457.90	761.30	35887.50	77045.90	15960.00	46664.30	1995560.20	187802.50
	σ	118.06	703.35	149.10	71.47	137.78	367.13	138.64	329.90	5857.12	879.35
	C_v	2.71	0.83	4.31	9.39	0.38	0.48	0.87	0.71	0.29	0.47
	±	248.89	1482.79	314.33	150.67	290.46	773.97	292.29	695.48	12347.89	1853.84
	SNR	39.03	807.16	39.66	8.56	376.02	740.65	140.19	334.38	12247.43	1106.94
F2	NPA µ	72757.00	1349386.10	45662.60	5179.30	234619.70	424816.60	68758.50	189277.60	5962284.80	471188.50
	SD	568.84	5831.74	462.72	475.96	813.37	1275.35	519.57	781.26	13602.04	1171.00
	C_v	0.78	0.43	1.01	9.19	0.35	0.30	0.76	0.41	0.23	0.25
	±	1199.21	12294.39	975.51	1003.41	1714.74	2688.66	1095.36	1647.05	28675.61	2468.68
	SNR	246.78	4600.56	170.94	16.19	678.74	1128.11	166.36	424.91	12560.55	985.09
F3	NPA µ	6.50	4793.10	189.70	129.80	2165.20	4933.40	991.40	2961.60	129394.50	12445.80
	σ	16.50	119.66	59.03	45.81	72.46	94.77	93.10	82.96	742.84	149.83
	C_v	253.85	2.50	31.12	35.29	3.35	1.92	9.39	2.80	0.57	1.20
	±	34.79	252.28	124.45	96.58	152.76	199.79	196.27	174.89	1566.05	315.86
	SNR	BD	107.41	5.81	4.37	70.47	152.66	29.39	75.80	2865.38	268.16
F4	NPA µ	18565.30	302662.40	22176.80	321.10	82769.00	169746.50	34230.00	96616.70	3897555.50	345987.00
	σ	159.27	1055.92	250.66	170.77	521.48	687.23	183.79	502.83	6484.31	664.24
	C_v	0.86	0.35	1.13	53.18	0.63	0.40	0.54	0.52	0.17	0.19
	±	335.77	2226.08	528.45	360.02	1099.38	1448.81	387.46	1060.06	13670.14	1400.34
	SNR	117.79	1893.23	154.97	BD	657.00	1164.12	204.44	452.49	15426.90	1234.06
F5	NPA µ	1123.70	28073.30	1263.40	402.60	12324.40	27242.10	5533.90	16441.40	715656.90	68645.60
	σ	149.68	164.52	75.66	101.58	168.51	177.28	141.73	134.88	1924.90	320.01
	C_v	13.32	0.59	5.99	25.23	1.37	0.65	2.56	0.82	0.27	0.47
	±	315.55	346.85	159.51	214.15	355.25	373.75	298.80	284.36	4058.06	674.63
	SNR	10.57	375.46	21.14	6.83	197.13	419.61	76.39	188.70	7050.33	662.66

Table 6-7: Continued: Statistical results of Corning Glass B with various filters (F1-F5) including net peak area (NPA), coefficient of variation (C_v), limit of detection of a method (±) and signal to noise ratio (SNR). The limit of detection is SNR >3 and the limit of quantification is SNR>10. Red highlighted results indicate greatest precision (lowest C_v) and highest SNR for each element. Blank spaces indicate peak not observed.

Testing of Filters; Corning Glass B as Sample; Rubidium through Bismuth									
Parameters: 40 kV, 30 µA, 180 Seconds, 10 measurements									
		Rubidium	Strontium	Zirconium	Tin	Antimony	Barium	Lead	Bismuth
F1	NPA µ	7727.30	65736.70	80838.90	19658.50	181717.70		522761.30	
	σ	283.31	570.99	504.61	730.57	2843.02		1312.83	
	Cv	3.67	0.87	0.62	3.72	1.56		0.25	
	±	597.27	1203.75	1063.82	1540.17	5993.61		2767.69	
	SNR	32.56	258.10	271.23	59.45	561.10		4107.56	
F2	NPA µ	8288.60	75052.30	79261.60	14633.30	134703.80		689701.40	
	SD	550.10	846.83	713.14	541.58	2275.15		2223.62	
	Cv	6.64	1.13	0.90	3.70	1.69		0.32	
	±	1159.72	1785.27	1503.43	1023.89	3578.05		4687.81	
	SNR	19.88	179.12	195.43	BD	343.30		1710.99	
F3	NPA µ	318.20	6515.90	9698.50	10035.10	89015.00	2196.30	41362.30	1564.40
	σ	44.49	68.50	148.18	293.18	1434.82	301.46	290.18	75.45
	Cv	13.98	1.05	1.53	2.92	1.61	13.73	0.70	4.82
	±	93.78	144.41	312.40	618.08	3024.86	635.53	611.76	159.07
	SNR	8.33	194.16	254.94	60.90	510.01	14.52	1377.28	51.88
F4	NPA µ	10315.70	81932.70	93945.00	18720.20	176101.20		730728.60	
	σ	445.48	547.95	406.65	407.93	2631.80		1460.47	
	Cv	4.32	0.67	0.43	2.18	1.49		0.20	
	±	939.16	1155.18	857.29	860.00	5548.33		3078.94	
	SNR	28.09	223.19	244.36	55.28	541.99		2794.82	
F5	NPA µ	1452.90	31185.20	42218.70	17496.30	157065.60		215438.80	7499.80
	σ	96.64	371.17	325.73	514.63	2873.61		677.37	167.70
	Cv	6.65	1.19	0.77	2.94	1.83		0.31	2.24
	±	203.74	782.50	686.70	1084.94	6058.11		1428.02	353.55
	SNR	14.79	299.87	290.80	62.49	568.72		3409.19	117.66

elements found in samples. Trace element analysis could potentially be affected. However, it has been demonstrated that NPA results cannot be reliably compared to results from other sources and that all results are internally consistent when analysed with the same HH-XRF unit (Nazaroff 2010:892 and 894). This means that a titanium result measured with a blank will be consistent with another measurement of the same blank if using the same HH-XRF unit and parameters. Statistical analysis will still discern between groupings in the same way as if there was no internal fluorescence of the analytical unit because the instrument signature is relatively static within multiple measurements of samples with similar densities using the same parameters. This research takes the direction that HH-XRF, at least when using NPA, is merely a field assistance technique to separate various faience sherds. If using wt%, the addition of the instrument signature counts become a greater issue, and it then becomes the task of the user to find or develop a sample matrix-matched blank in addition to several reference standards so that signature totals (instrument interference) can be subtracted from the final analysis.

The individual filters do not contribute additional elements with setting A although the existing elements are affected by attenuation and contribution by filter construction, specifically titanium and lead. The filter which is partly constructed of titanium causes the titanium discrepancy with filter 4. The result is a higher NPA and lower C_v. Filter 4 enhances the lead characteristic peaks and SNR as the L lines for lead fall within the region of optimization. The titanium NPA and SNR are elevated over the results of having no filter because of the filter construction. Chromium and zinc exhibit elevated SNR and NPA with filter use possibly indicating filter contribution and/or optimization of the element contributed as part of the unit structure.

The water bottle and cellulose pellets are not true blanks. They add their signature in the form of enhanced counts for specific elements. Cellulose seems the better blank although silicon and chromium results are enhanced. Chromium is very abundant in the Earth's crust but is only detected in trace amounts (i.e. 0.05 and 0.02 wt%) in two of the hundreds of faience objects analysed by Kaczmarczyk and Hedges (1983) using XRF. Chromium is currently used as a colourant but appears to not have been exploited during the Pharaonic, Ptolemaic and Roman Periods in Egypt. Silicon effect is less of a concern as silicon is a non-diagnostic element in faience and is usually not included in post-measurement analysis. Alternatively, silicon wafers could be used as a blank (Pers. Comm. Rebecca Scott).The ideal blank is invisible to HH-XRF ($Z<11$ (Sodium)) to provide an instrument interference signature without contributing characteristic peaks. The counts of the blank can be subtracted from a sample

measurement to form unit consistent results but the analysis is semi-quantitative at best because enhancements from elements in the sample (matrix effects) are not taken into account with the blank. The 'internally consistent' results can provide good data but cannot be reproduced without using the original unit. Comparisons of semi-quantitative results cannot be compared to publish results unless the same instrument was used (see Frahm 2013 and Speakman et al. 2013 for an ongoing discussion).

The evaluation of the filters indicate that filter 2 (i.e. no filter) used with a vacuum is optimal for the detection of the lower Z elements and some mid Z elements (sodium-zinc) using 15 kV voltage (setting A). Use of filters will attenuate the signal of the low energy photons reducing or possibly eliminating detection of some low Z elements. Use of the vacuum will decrease attenuation of the signal because of air trapped inside of the analyser unit housing. Higher Z elements (strontium through bismuth) including those associated with glass provenance (e.g. strontium and zirconium) are better detected using filter 3 with no vacuum and 40 kV voltage (setting B). Filter 3 allows detection of elements that could not be discerned from the continuum with other filters or lack of filter (i.e. barium and bismuth). Removing the vacuum allows lower Z element photons to be attenuated by the air column in the unit housing thereby reducing dead-time and enhancing higher Z element detection.

6.3.3 Instrument Drift

Drift is a variation in photon output from a source and cannot be prevented (Jenkins 1999:93; Johnson 2014:567). It is a factor of hardware and a potential source of error. Four types of drift and their sources are identified (Table 6-8) (ibid., pp.93-94). Ultrashort term drift is an electrical component issue resulting in the inability of the unit to respond to micro-changes in the power supplied. Short term drift is associated with source (e.g. anode) instability and provides the main limiting factor in analysis. Long term drift is due to aging of the components and focal spot migration in the X-ray tube. Ultra-long term drift is caused by filament deposition on the inner surfaces of the X-ray tube. Tungsten filaments are used to provide an electron beam directed at the target (rhodium). Tungsten residue is deposited on the interior of the X-ray tube (Jenkins

Table 6-8: Forms of Drift in X-ray Tube Sources (Jenkins 1999:93). The

Forms of Drift in X-Ray Tube Sources			
Form of Drift	Time Duration	Magnitude	Source
Ultralong	Months	1-20%	Aging of X-ray Tube
Long Term	Days	0.2-0.5%	Thermal Changes
Short Term	30-120 Minutes	<0.1%	Stabilization Circuits
Ultrashort	50-500 Millisecs	0.2-10%	Transients

1999:93-4) which absorbs X-rays and results in lower beam intensity (Bertin 1975:467).

Jenkins drift terminology is used in the project, however, Johnson (2014:567-571) subsequently published an article identifying three drift patterns while evaluating a Bruker Tracer III-V: Micro-drift (µ-drift), long term drift (l-drift) and short term (s-drift). µ-Drift occurs within measurements and manifests as different results for consecutive measurements on the same sample using identical parameters. This is seen as differences between individual measurements in the current study and is a partial reason why 10 measurements per sample were collected (the main issue being that of heterogeneity). The effects of this drift on analysis is reduced with multiple measurements (essentially they are averaged out). Johnson (ibid.) recognizes s-drift as occurring in time periods longer than a typical measurement but within a typical HH-XRF session. The effects are long lasting (measured in hours) compared to µ-drift (measured in seconds or minutes) and manifest as a slow change of intensity on consecutive measurements on the same sample using identical parameters. Johnson's (ibid.) l-drift corresponds to Jenkins' (1999: 93) ultra-long term drift.

The use of the X-ray Ops software with the Bruker system allows the user to optimize the beam with each setup before measuring to mitigate the drift effects. In the absence of programs like X-ray Ops, long term and ultra-long term drift can be corrected by periodically measuring a standard containing mid-levels of all elements anticipated (instrument reference) from the unknown samples (Jenkins 1999: 93-94). This correction is conducted by taking ratios of count rates of the elements in the unknown sample to counts of the instrument reference.

Measurements of Corning Glass B reference material were compared after 2 hours (short term), 2 days (long term) and 5 months (ultra-long term) to determine instrument drift (see Table 4; Jenkins 1999:93-94) of the Bruker Tracer III-SD HH-XRF. HH-XRF settings A and B were used for all drift assessments. Ten measurements were taken at each setting for each drift term. A second set of 40 kV measurements (setting C) were conducted without the use of a filter using the same time intervals.

The results of the experimentation reveal a total of 22 elements of the sample having been detected during the drift assessments (Tables 6-9 through 6-14). Rhodium (HH-XRF target) is included in the tables for comparison. Disparity between the measurement sets can usually be attributed to a few factors. Some of the lower Z element signals are easily attenuated and more difficult to detect. Slight variations between the measurements such as how the sample is positioned on the stage can

Table 6-9: Short term drift testing of the Bruker Tracer III-SD using Corning Glass B with 10 measurements on setting A. Average net peak signal (NPA), standard deviation of NPA (σ), coefficient of variance (C_v), Signal to Noise Ratio (SNR) and %Difference (%Diff) are provided.

Short Term (2 Hours) Unit Measurement Drift Using Corning Glass B with Setting A (n=10)											
		Sodium	Magnesium	Aluminium	Silicon	Phosphorus	Potassium	Calcium	Titanium	Chromium	Manganese
NPA		1465.50	332.10	26127.60	794523.50	12285.00	82863.60	1229660.70	23783.10	4830.50	155188.20
σ		153.98	77.05	314.22	4412.45	310.48	765.05	8209.69	442.60	487.43	1628.60
(±)		307.96	154.10	628.44	8824.90	620.96	1530.09	16419.38	885.19	974.86	3257.20
C_v		10.51	23.20	1.20	0.56	2.53	0.92	0.67	1.86	10.09	1.05
SNR		11.40	2.42	168.39	4550.18	68.32	384.94	5534.73	108.58	17.13	494.20
NPA		1444.30	379.20	26342.80	799507.20	12445.50	83074.30	1231880.10	24131.60	4731.10	154473.60
σ		90.78	105.64	392.83	6336.37	424.93	1178.70	11387.12	645.84	239.29	1816.81
(±)		181.56	211.28	785.65	12672.74	849.86	2357.41	22774.24	1291.67	478.59	3633.62
C_v		6.29	27.86	1.49	0.79	3.41	1.42	0.92	2.68	5.06	1.18
SNR		11.19	2.86	169.55	4577.25	69.27	385.96	5548.65	110.05	16.77	506.57
%Diff	NPA	1.46	13.24	0.82	0.63	1.30	0.25	0.18	1.45	2.08	0.46
	SNR	1.79	16.79	0.68	0.59	1.38	0.26	0.25	1.35	2.14	2.47
		Iron	Cobalt	Nickel	Copper	Zinc	Rhodium (L)	Barium (L)	Lead (L)	Bismuth (L)	Bismuth (M)
NPA		249051.60	39689.80	88029.60	2460319.10	169633.50	268223.90	10368.30	16616.20	2201.50	5190.10
σ		2889.08	528.72	1509.04	36964.58	2695.86	1598.51	449.89	1416.45	506.69	79.94
(±)		5778.15	1057.44	3018.07	73929.16	5391.71	3197.02	899.77	2832.90	1013.38	159.89
C_v		1.16	1.33	1.71	1.50	1.59	0.60	4.34	8.52	23.02	1.54
SNR		749.43	111.43	239.45	6466.18	452.08	1237.13	47.96	53.23	7.25	25.03
NPA		248298.60	39573.60	87979.20	2451741.10	168842.40	268653.20	9718.70	17208.80	2320.70	5201.10
σ		3704.56	688.23	1702.63	53796.62	4637.33	2126.04	848.84	2573.08	420.20	310.90
(±)		7409.12	1376.46	3405.25	107593.23	9274.65	4252.08	1697.69	5146.16	840.40	621.80
C_v		1.49	1.74	1.94	2.19	2.75	0.79	8.73	14.95	18.11	5.98
SNR		747.89	111.25	239.61	6450.07	450.52	1194.28	44.91	55.17	7.65	25.09
%Diff	NPA	0.30	0.29	0.06	0.35	0.47	0.16	6.47	3.50	5.27	0.21
	SNR	0.21	0.16	0.07	0.25	0.34	3.53	6.58	3.58	5.36	0.27

Table 6-10: Short term drift testing of the Bruker Tracer III-SD using Corning Glass B with 10 measurements on setting B. Average net peak signal (NPA), standard deviation of NPA (σ), coefficient of variance (C_v), Signal to Noise Ratio (SNR) and %Difference (%Diff) are provided.

Short Term (2 Hours) Unit Measurement Drift Using Corning Glass B with Setting B (n=10)										
		Calcium	Titanium	Chromium	Manganese	Iron	Cobalt	Nickel	Copper	Zinc
NPA		4911.40	202.60	125.50	2156.30	5026.70	1002.80	2957.90	129769.30	12760.90
σ		126.82	81.17	54.18	94.88	104.68	57.39	89.36	899.58	179.75
(±)		253.64	162.34	108.36	189.77	209.36	114.79	178.72	1799.17	359.49
C_v		2.58	40.07	43.17	4.40	2.08	5.72	3.02	0.69	1.41
SNR		109.28	6.17	4.19	71.48	155.41	29.55	74.76	2947.38	269.98
NPA		4149.50	196.80	117.80	2009.30	4725.80	869.90	2678.70	122736.30	11867.30
σ		212.16	66.71	37.72	59.99	164.10	89.06	116.24	1122.06	165.50
(±)		424.31	133.41	75.44	119.98	328.19	178.12	232.49	2244.12	331.01
C_v		5.11	33.90	32.02	2.99	3.47	10.24	4.34	0.91	1.39
SNR		93.67	6.08	4.02	65.50	151.05	25.70	66.91	2630.82	246.77
%Diff	NPA	16.82	2.90	6.33	7.06	6.17	14.19	9.91	5.57	7.26
	SNR	15.38	1.46	4.18	8.72	2.85	13.94	11.08	11.35	8.98
		Rubidium	Strontium	Zirconium	Rhodium	Tin	Antimony	Barium	Lead (L)	Bismuth (L)
NPA		301.20	6683.40	9726.00	4215.20	10360.00	91796.50	2209.50	42011.80	1540.80
σ		48.93	85.35	160.99	216.49	182.86	1644.06	316.55	482.48	72.14
(±)		90.63	214.08	292.20	430.27	510.50	3792.82	619.92	550.19	198.27
C_v		16.24	1.28	1.66	5.14	1.77	1.79	14.33	1.15	4.68
SNR		7.64	199.74	254.11	45.49	62.56	528.61	14.46	1399.31	51.48
NPA		269.90	6093.70	9033.00	3516.10	9471.10	84392.40	1958.60	39387.80	1572.40
σ		45.32	107.04	146.10	215.14	255.25	1896.41	309.96	275.10	99.13
(±)		97.85	170.69	321.99	432.98	365.71	3288.11	633.11	964.97	144.28
C_v		16.79	1.76	1.62	6.12	2.70	2.25	15.83	0.70	6.30
SNR		7.11	175.34	231.79	38.22	58.96	502.03	13.31	1297.02	52.04
%Diff	NPA	10.96	9.23	7.39	18.08	8.96	8.40	12.04	6.45	2.03
	SNR	7.19	13.01	9.19	17.37	5.92	5.16	8.27	7.59	1.08

Table 6-11: Long term drift testing of the Bruker Tracer III-SD using Corning Glass B with 10 measurements on setting A. Average net peak signal (NPA), standard deviation of NPA (σ), coefficient of variance (C_v), Signal to Noise Ratio (SNR) and %Difference (%Diff) are provided.

Long Term (2 Days) Unit Measurement Drift Using Corning Glass B with Setting A (n=10)											
		Sodium	Magnesium	Aluminium	Silicon	Phosphorus	Potassium	Calcium	Titanium	Chromium	Manganese
NPA		1144.80	315.70	24683.10	750152.80	11887.00	86325.80	1224165.00	24153.70	4727.70	154616.90
σ		178.04	102.74	357.05	4790.71	239.29	702.79	9995.97	726.76	469.12	1727.20
(±)		356.09	205.48	714.10	9581.42	478.57	1405.58	19991.95	1453.51	938.24	3454.40
C_v		15.55	32.54	1.45	0.64	2.01	0.81	0.82	3.01	9.92	1.12
SNR		8.94	2.40	160.11	4317.09	66.25	396.22	5427.89	110.05	16.71	505.36
NPA		1442.10	250.20	24336.50	751540.80	11333.60	79727.20	1211846.70	23189.00	4512.00	153149.80
σ		140.95	84.73	314.68	4742.43	349.35	596.86	9374.13	626.17	248.52	1977.77
(±)		281.90	169.46	629.36	9484.85	698.70	1193.71	18748.25	1252.34	497.04	3955.54
C_v		9.77	33.87	1.29	0.63	3.08	0.75	0.77	2.70	5.51	1.29
SNR		11.15	1.89	156.00	4274.15	65.17	366.41	5380.16	105.81	16.02	503.27
%Diff	NPA	22.99	23.15	1.41	0.18	4.77	7.95	1.01	4.08	4.67	0.95
	SNR	21.99	23.95	2.60	1.00	1.64	7.82	0.88	3.93	4.21	0.42
		Iron	Cobalt	Nickel	Copper	Zinc	Rhodium (L)	Barium (L)	Lead (L)	Bismuth (L)	Bismuth (M)
NPA		251499.00	39612.70	88710.60	2513302.50	170358.60	267938.30	10181.10	17968.70	2184.40	4075.00
σ		3325.89	839.01	1666.95	48407.75	4406.04	2103.61	489.41	1938.49	413.99	428.93
(±)		6651.78	1678.01	3333.91	96815.50	8812.07	4207.22	978.82	3876.99	827.98	857.86
C_v		1.32	2.12	1.88	1.93	2.59	0.79	4.81	10.79	18.95	10.53
SNR		754.50	110.87	240.45	6580.43	452.59	1187.93	47.01	57.37	7.17	19.62
NPA		245058.70	38399.60	85746.00	2410123.70	166968.90	261494.80	10823.90	16437.40	2120.20	5206.90
σ		2916.82	715.84	1862.31	43934.03	3564.08	1934.45	416.61	1869.76	468.14	120.73
(±)		5833.63	1431.68	3724.62	87868.06	7128.16	3868.90	833.21	3739.51	936.29	241.45
C_v		1.19	1.86	2.17	1.82	2.13	0.74	3.85	11.38	22.08	2.32
SNR		717.90	108.01	233.41	6510.71	445.56	1157.95	50.04	54.35	7.05	25.02
%Diff	NPA	2.59	3.11	3.40	4.19	2.01	2.43	6.12	8.90	2.98	24.39
	SNR	4.97	2.62	2.97	1.07	1.57	2.56	6.26	5.41	1.67	24.21

Table 6-12: Long term drift testing of the Bruker Tracer III-SD using Corning Glass B with 10 measurements on setting B. Average net peak signal (NPA), standard deviation of NPA (σ), coefficient of variance (C_v), Signal to Noise Ratio (SNR) and %Difference (%Diff) are provided.

Long Term (2 Days) Unit Measurement Drift Using Corning Glass B with Setting B (n=10)										
		Calcium	Titanium	Chromium	Manganese	Iron	Cobalt	Nickel	Copper	Zinc
NPA		4982.00	171.60	146.10	2169.10	5106.20	990.30	3042.00	132619.40	12810.50
σ		129.41	46.08	27.52	87.38	110.66	74.82	90.86	1390.39	172.30
(±)		258.83	92.17	55.04	174.77	221.33	149.65	181.71	2780.78	344.60
C_v		2.60	26.85	18.84	4.03	2.17	7.56	2.99	1.05	1.35
SNR		109.31	5.13	4.86	72.29	158.01	29.01	76.85	2966.38	271.53
NPA		4911.40	202.60	125.50	2156.30	5026.70	1002.80	2957.90	129769.30	12760.90
σ		126.82	81.17	54.18	94.88	104.68	57.39	89.36	899.58	179.75
(±)		253.64	162.34	108.36	189.77	209.36	114.79	178.72	1799.17	359.49
C_v		2.58	40.07	43.17	4.40	2.08	5.72	3.02	0.69	1.41
SNR		109.28	6.17	4.19	71.48	155.41	29.55	74.76	2947.38	269.98
%Diff	NPA	1.43	16.57	15.17	0.59	1.57	1.25	2.80	2.17	0.39
	SNR	0.03	18.35	14.85	1.13	1.66	1.84	2.75	0.64	0.57
		Rubidium	Strontium	Zirconium	Rhodium	Tin	Antimony	Barium	Lead (L)	Bismuth (L)
NPA		321.10	6673.30	9881.00	4014.20	10383.70	91266.80	2052.50	42110.70	1534.10
σ		53.16	115.94	133.43	199.91	334.10	2203.21	248.11	572.23	95.49
(±)		106.32	231.88	266.87	399.81	668.20	4406.42	496.22	1144.47	190.98
C_v		16.56	1.74	1.35	4.98	3.22	2.41	12.09	1.36	6.22
SNR		8.16	197.63	254.84	42.96	62.78	526.97	13.41	1363.08	51.41
NPA		301.20	6683.40	9726.00	4215.20	10360.00	91796.50	2209.50	42011.80	1540.80
σ		48.93	85.35	160.99	216.49	182.86	1644.06	316.55	482.48	72.14
(±)		97.85	170.69	321.99	432.98	365.71	3288.11	633.11	964.97	144.28
C_v		16.24	1.28	1.66	5.14	1.77	1.79	14.33	1.15	4.68
SNR		7.64	199.74	254.11	45.49	62.56	528.61	14.46	1399.31	51.48
%Diff	NPA	6.40	0.15	1.58	4.88	0.23	0.58	7.37	0.24	0.44
	SNR	6.52	1.06	0.29	5.70	0.35	0.31	7.51	2.62	0.13

Table 6-13: Ultra-Long term drift testing of the Bruker Tracer III-SD using Corning Glass B with 10 measurements on setting A. Average net peak signal (NPA), standard deviation of NPA (σ), coefficient of variance (C_v), Signal to Noise Ratio (SNR) and %Difference (%Diff) are provided.

Ultra-Long Term (5 Months) Unit Measurement Drift Using Corning Glass B with Setting A (n=10)											
		Sodium	Magnesium	Aluminium	Silicon	Phosphorus	Potassium	Calcium	Titanium	Chromium	Manganese
NPA		1144.80	315.70	24683.10	750152.80	11887.00	86325.80	1224165.00	24153.70	4727.70	154616.90
σ		178.04	102.74	357.05	4790.71	239.29	702.79	9995.97	726.76	469.12	1727.20
(±)		356.09	205.48	714.10	9581.42	478.57	1405.58	19991.95	1453.51	938.24	3454.40
C_v		15.55	32.54	1.45	0.64	2.01	0.81	0.82	3.01	9.92	1.12
SNR		8.94	2.40	160.11	4317.09	66.25	396.22	5427.89	110.05	16.71	505.36
NPA		1549.00	299.30	24978.60	764866.70	12291.70	81494.70	1215178.30	23513.30	4698.30	153168.70
σ		157.76	82.57	444.13	8995.52	342.58	670.61	15494.24	513.52	290.60	2646.59
(±)		315.52	165.14	888.25	17991.04	685.15	1341.23	30988.48	1027.03	581.21	5293.19
C_v		10.18	27.59	1.78	1.18	2.79	0.82	1.28	2.18	6.19	1.73
SNR		12.02	2.16	161.56	4406.25	71.62	380.81	5497.79	107.88	16.74	489.32
%Diff	NPA	30.01	5.33	1.19	1.94	3.35	5.76	0.74	2.69	0.62	0.94
	SNR	29.40	10.86	0.91	2.04	7.79	3.97	1.28	1.99	0.19	3.23
		Iron	Cobalt	Nickel	Copper	Zinc	Rhodium (L)	Barium (L)	Lead (L)	Bismuth (L)	Bismuth (M)
NPA		251499.00	39612.70	88710.60	2513302.50	170358.60	267938.30	10181.10	17968.70	2184.40	4075.00
σ		3325.89	839.01	1666.95	48407.75	4406.04	2103.61	489.41	1938.49	413.99	428.93
(±)		6651.78	1678.01	3333.91	96815.50	8812.07	4207.22	978.82	3876.99	827.98	857.86
C_v		1.32	2.12	1.88	1.93	2.59	0.79	4.81	10.79	18.95	10.53
SNR		754.50	110.87	240.45	6580.43	452.59	1187.93	47.01	57.37	7.17	19.62
NPA		245214.80	39071.40	86843.20	2412486.70	165815.20	268030.50	10212.20	16875.30	2144.90	5557.70
σ		4684.55	927.18	2010.18	64806.77	4650.26	2602.04	787.68	2751.78	411.32	247.46
(±)		9369.10	1854.35	4020.35	129613.54	9300.53	5204.09	1575.37	5503.56	822.63	494.92
C_v		1.91	2.37	2.31	2.69	2.80	0.97	7.71	16.31	19.18	4.45
SNR		736.84	110.40	237.75	6378.19	456.10	1196.50	47.49	55.75	7.11	26.95
%Diff	NPA	2.53	1.38	2.13	4.09	2.70	0.03	0.31	6.28	1.82	30.78
	SNR	2.37	0.43	1.13	3.12	0.77	0.72	1.03	2.86	0.82	31.51

Table 6-14: Ultra-Long term drift testing of the Bruker Tracer III-SD using Corning Glass B with 10 measurements on setting A. Average net peak signal (NPA), standard deviation of NPA (σ), coefficient of variance (C_v), Signal to Noise Ratio (SNR) and %Difference (%Diff) are provided.

Ultra-Long Term (5 Months) Unit Measurement Drift Using Corning Glass B with Setting B (n=10)										
		Calcium	Titanium	Chromium	Manganese	Iron	Cobalt	Nickel	Copper	Zinc
NPA		4982.00	171.60	146.10	2169.10	5106.20	990.30	3042.00	132619.40	12810.50
σ		129.41	46.08	27.52	87.38	110.66	74.82	90.86	1390.39	172.30
(±)		258.83	92.17	55.04	174.77	221.33	149.65	181.71	2780.78	344.60
C_v		2.60	26.85	18.84	4.03	2.17	7.56	2.99	1.05	1.35
SNR		109.31	5.13	4.86	72.29	158.01	29.01	76.85	2966.38	271.53
NPA		4855.10	192.20	145.10	2187.30	4968.00	950.90	2934.00	128366.50	12440.90
σ		116.22	41.74	37.30	88.47	119.68	51.53	84.65	809.52	126.17
(±)		232.44	83.47	74.59	176.94	239.36	103.06	169.29	1619.04	252.35
C_v		2.39	21.72	25.70	4.04	2.41	5.42	2.89	0.63	1.01
SNR		110.84	5.93	4.98	74.57	156.32	28.14	74.89	2925.40	265.13
%Diff	NPA	2.58	11.32	0.69	0.84	2.74	4.06	3.61	3.26	2.93
	SNR	1.39	14.33	2.33	3.11	1.08	3.06	2.58	1.39	2.38
		Rubidium	Strontium	Zirconium	Rhodium	Tin	Antimony	Barium	Lead (L)	Bismuth (L)
NPA		321.10	6673.30	9881.00	4014.20	10383.70	91266.80	2052.50	42110.70	1534.10
σ		53.16	115.94	133.43	199.91	334.10	2203.21	248.11	572.23	95.49
(±)		106.32	231.88	266.87	399.81	668.20	4406.42	496.22	1144.47	190.98
C_v		16.56	1.74	1.35	4.98	3.22	2.41	12.09	1.36	6.22
SNR		8.16	197.63	254.84	42.96	62.78	526.97	13.41	1363.08	51.41
NPA		295.20	6505.80	9602.50	3944.00	9974.10	87927.00	2063.90	41182.90	1509.40
σ		44.60	72.67	200.62	197.35	369.03	1832.10	246.86	343.99	74.42
(±)		89.19	145.34	401.24	394.71	738.07	3664.21	493.72	687.97	148.83
C_v		15.11	1.12	2.09	5.00	3.70	2.08	11.96	0.84	4.93
SNR		7.63	193.82	248.90	42.48	61.14	510.29	13.82	1362.78	49.47
%Diff	NPA	8.40	2.54	2.86	1.76	4.02	3.73	0.55	2.23	1.62
	SNR	6.62	1.95	2.36	1.12	2.65	3.22	3.01	0.02	3.85

affect the outcome of which sodium and magnesium are easily affected. Several element characteristic lines exhibit peak overlap with stronger signals and precision is affected across several measurements. Bismuth and rubidium exhibit peak overlap with lead and the barium L line is affected by peak overlap with titanium.

The choice of voltage and filter will affect the area of optimization for the measurements. Barium is a difficult element for the Bruker Tracer III-SD due to a K line absorption edge of 37.44 kV. The optimal voltage (1.5-2x the absorption edge) for its detection is 56 to 74.88 kV, voltages beyond the limits of most HH-XRF units. Shugar (2011:17) states that the limits of HH-XRF with barium are still sufficient for obsidian source assignments but the level of instrument precision is uncertain. The lead L lines are detected using 15 kV but are considered on or beyond the edge of optimization. The L-I line absorption edge for lead is 15.86 kV and optimization would require an incident voltage of 23-32 kV. Some elements were detected but lay outside the optimization region for specific filters. Filter 3, used in the higher voltage measurements of this evaluation, is optimized for elements between iron and molybdenum but allows for the detection of calcium, titanium and chromium albeit with higher background. Variations in the background will present small discrepancies between the drift measurements. Larger %differences are exhibited with changes in characteristic peaks containing low counts/second. Titanium and chromium results for the various measurements typically exhibit this characteristic. Short term measurement comparisons taken 2 hours apart using setting A reveal that NPA and SNR differences between most of the elements are ~2% or less (see Table 6-9) and are barely perceptible in the spectra (Fig. 6-9). Greater differences for NPA and SNR were recorded for elements on the edge of the optimization zone including magnesium and lead (L line), or those that experience peak interference with other elements including barium (L line) with titanium and bismuth (La and M lines) with lead (L and M lines). These sources of disparity are consistent with all setting A results. The short term %difference figures of setting B are much larger (see Table 6-10) and difficult to explain. The same parameters including filter type were used for each set of measurements. The measurements were conducted after the HH-XRF analyser had been used for several hours. As a result, all measurements were conducted on a warmed HH-XRF unit; No comparisons were made between cold unit and warm unit results. The same filter was in use before the drift measurements so a temperature differential for the filter itself is not a consideration. Target instability is the probable cause for the differences.

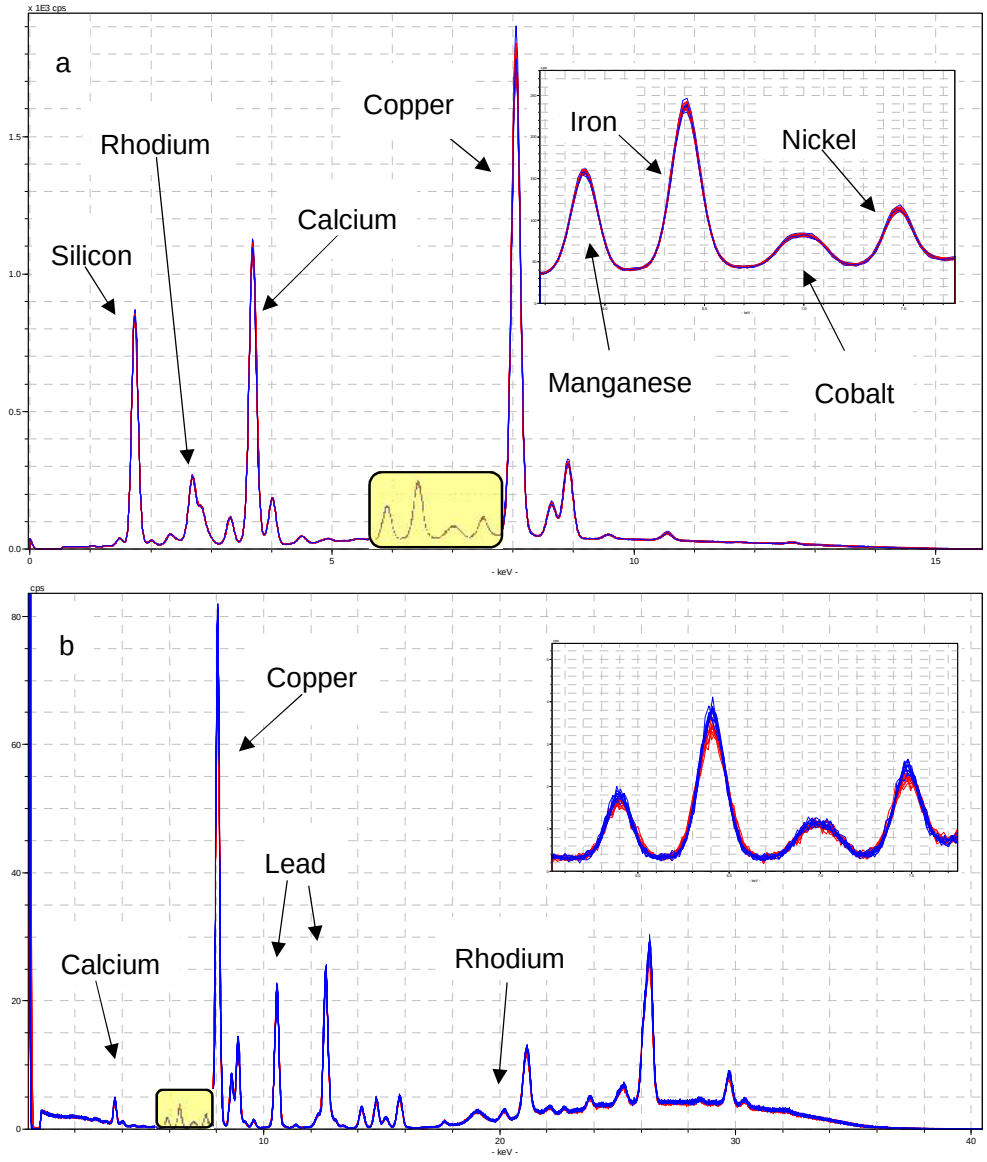

Fig. 6-9: Each spectra (Fig. a setting A, Fig. b setting B) exhibits short term drift measurements taken 2 hours apart (red followed by blue). The inset figures are of the region between 5.6-7.7 keV and reveal the peaks for manganese, iron, cobalt and nickel. The thickness of the spectral lines is a good indicator of the relative drift magnitude.

Long term measurement comparisons taken 2 days apart using settings A and B exhibited differences for NPA and SNR at <4% for most elements (see Tables 6-11 and 6-12; Fig. 6-10). Differences >4% for most elements are due to peak interference (barium with titanium, bismuth with lead), easily attenuated signals (sodium and magnesium) or being on the margin of the optimization zone (lead). Potassium revealed a %difference of ~7. This is not repeated with other elements indicating that deposits on the sample surface are not an issue. Homogeneity of the sample is not considered an issue as the Corning Glass B reference material is homogeneous.

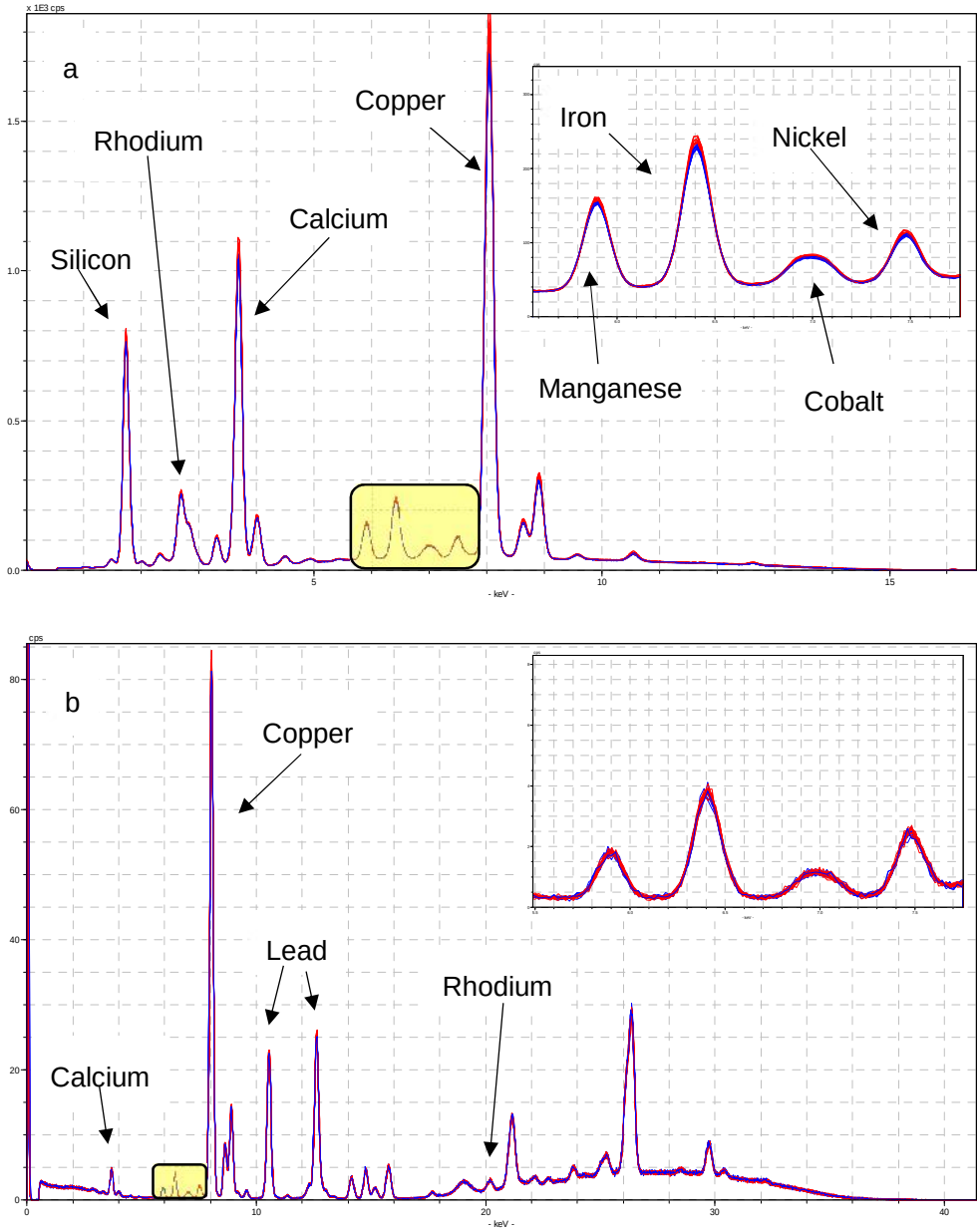

Fig. 6-10: Each spectra (Fig. a setting A, Fig. b setting B) exhibits long term drift measurements taken 2 days apart (red followed by blue). The inset figures are of the region between 5.6-7.7 keV and reveal the peaks for manganese, iron, cobalt and nickel. The thickness of the spectral lines is a good indicator of the relative drift magnitude.

Elements with >4%difference for setting B can be sourced to low counts/second (titanium and chromium), peak interference (rubidium and bismuth with lead) or laying on the edge of optimization (barium).

Ultra-long term measurements taken 5 months apart for settings A and B revealed <4% difference of NPA and SNR for most elements (see Tables 6-13 and 6-14; Fig. 6-11). The SNR %difference of potassium and the NPA %difference of phosphorus are >4%. The source of the larger %difference remains unknown. Low count rates for

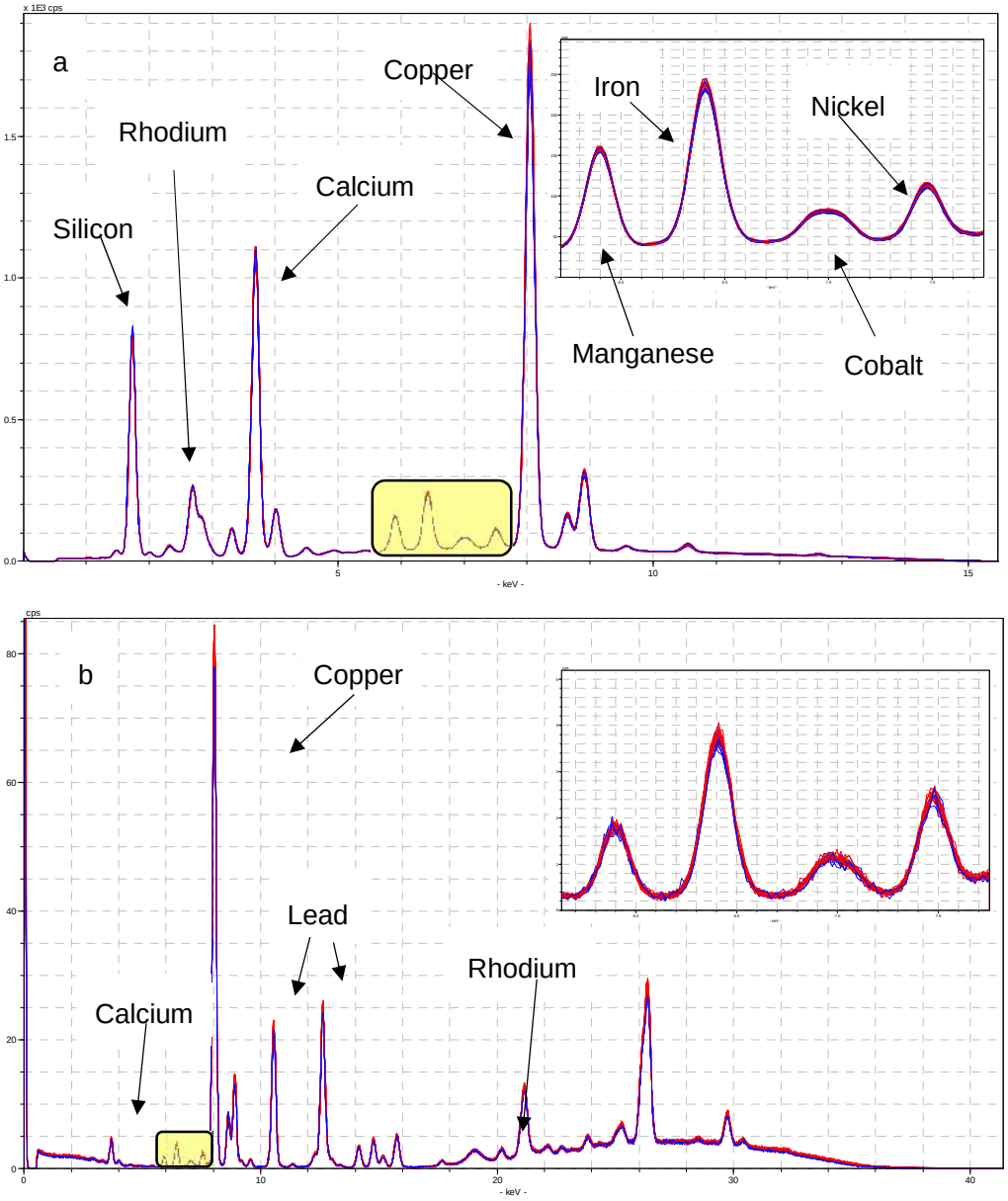

Fig. 6-11: Each spectra (Fig. a setting A, Fig. b setting B) exhibits ultra-long term drift measurements taken 5 months apart (red followed by blue). The inset figures are of the region between 5.6-7.7 keV and reveal the peaks for manganese, iron, cobalt and nickel. The thickness of the spectral lines is a good indicator of the relative drift magnitude.

titanium and peak interference for rubidium (with lead) explain disparities for the setting B interval comparison results.

A second set of measurements using setting C were conducted for comparison. The short term %difference for most elements were ~2% or less (Table 6-15). The discrepancy of barium can be attributed to being on the margin whereas that of rubidium can be attributed to peak interference with lead. Calcium, chromium and tin discrepancies are possibly due to target instability. The long term and ultra-long term

Table 6-15: Short term drift testing using Corning Glass B (40 kV, 30 uA, Filter 2, 180 seconds, n=10). Average net peak signal (NPA), standard deviation of NPA (σ), coefficient of variance (C_v), Signal to Noise Ratio (SNR) and %Difference (%Diff) are provided.

Short Term (2 Hours) Unit Measurement Drift: Corning Glass B (40 kV, 30 uA, 180s, Filter 2, n=10)										
		Calcium	Titanium	Chromium	Manganese	Iron	Cobalt	Nickel	Copper	Zinc
NPA		1356936.20	36627.40	5680.70	234604.80	427466.20	69314.50	191958.70	6015336.70	475367.90
σ		7755.01	671.51	478.89	797.50	1211.68	612.18	739.56	17226.09	1723.01
(±)		15510.03	1343.03	957.79	1595.00	2423.36	1224.35	1479.13	34452.18	3446.02
C_v		0.57	1.83	8.43	0.34	0.28	0.88	0.39	0.29	0.36
SNR		4457.32	133.17	17.25	660.60	1133.53	167.95	428.29	12688.12	1020.66
NPA		1368453.50	36461.30	5806.90	235293.80	434284.10	69325.60	190440.70	5926026.70	473339.70
σ		3581.80	417.22	391.02	921.89	1047.75	799.49	995.58	8448.03	1309.49
(±)		7163.60	834.45	782.03	1843.79	2095.50	1598.98	1991.17	16896.06	2618.97
C_v		0.26	1.14	6.73	0.39	0.24	1.15	0.52	0.14	0.28
SNR		4615.32	132.67	18.12	662.60	1152.50	171.36	416.58	12490.12	1014.36
%Diff	NPA	0.85	0.45	2.20	0.29	1.58	0.02	0.79	1.50	0.43
	SNR	3.48	0.38	4.91	0.30	1.66	2.01	2.77	1.57	0.62
		Rubidium	Strontium	Zirconium	Rhodium	Tin	Antimony	Barium	Lead (L)	Bismuth (L)
NPA		3135.10	77264.40	82386.50	170717.40	15630.40	144841.90	2388.70	682506.40	18327.70
σ		501.37	803.40	547.95	1585.35	524.30	2054.81	359.09	3011.79	1017.58
(±)		1002.74	1606.80	1095.90	3170.70	1048.60	4109.62	718.19	6023.58	2035.17
C_v		15.99	1.04	0.67	0.93	3.35	1.42	15.03	0.44	5.55
SNR		7.42	187.33	202.32	412.81	49.93	480.45	12.29	1731.90	46.68
NPA		3047.40	76363.10	81435.20	165207.10	15027.60	141708.90	1847.80	680496.00	18776.30
σ		314.41	909.51	666.13	756.51	438.39	1398.28	440.29	2520.40	521.97
(±)		628.81	1819.02	1332.26	1513.02	876.77	2796.56	880.57	5040.79	1043.93
C_v		10.32	1.19	0.82	0.46	2.92	0.99	23.83	0.37	2.78
SNR		7.14	184.97	199.85	399.88	48.04	473.09	9.51	1725.69	46.74
%Diff	NPA	2.84	1.17	1.16	3.28	3.93	2.19	25.54	0.29	2.42
	SNR	3.86	1.26	1.23	3.18	3.86	1.54	25.55	0.36	0.13

results (Tables 6-16 and 6-17) were similar to the short term setting B results (see Table 6-10) and are not easily explained but could be the result of target instability as well. The difference is not uniform across the elements and is probably not due to aging of the unit components nor deposition of tungsten on the X-ray tube. Spectra of these figures have not been provided because they would be indiscernible from Figs. 6-9 through 6-11.

The data from the %difference tables have been averaged for a simple comparison (Table 6-18). Assuming the short term setting B measurements and the long term and ultra-long term 40 kV baseline measurements are considered anomalous, the data generally breaks down to what would be expected: short term drift has less affect than long term and ultra-long term drift. Target instability, if it is the cause, cannot be discounted and remains a concern for NPA analysis. Converting the NPA results to wt% will affect the %difference figures.

Quick tabulations (without calibration) exhibit a general reduction of the %difference except for elements with low counts which exhibit a %difference increase. The wt% results were compared and are very similar with difference no greater than 1%, and usually much less. Tables for these are not included because they provide normalized but uncalibrated data and were produced merely to check the difference on wt% and %difference figures.

In conclusion, the Bruker Tracer III-SD was tested for machine drift by comparing NPA and SNR of measurements taken 2 hours, 2 days and 5 months apart. The data exhibits that %difference for most elements is below 4% for ultra-long and long term durations. Short term duration data reveals a %difference for most elements below 2%. Elements closer to LOD have larger %differences. The inconsistent results reported in the various tables is disconcerting but needs to be put into perspective. Converting the NPA to wt% and recalculating the %difference for SNR and NPA will have an effect on the figures, in most cases a reduction. The tables reveal that there is some instability in the measurements but the spectra do not exhibit much of a qualitative difference. The machine drift of NPA and SNR is acceptable for the low voltage generation of the Tracer series.

Table 6-16: Long term drift testing using Corning Glass B (40 kV, 30 uA, Filter 2, 180 seconds, n=10). Average net peak signal (NPA), standard deviation of NPA (σ), coefficient of variance (C_v), Signal to Noise Ratio (SNR) and %Difference (%Diff) are provided.

Long Term (2 Days) Unit Measurement Drift: Corning Glass B (40 kV, 30 uA, 180s, Filter 2, n=10)										
		Calcium	Titanium	Chromium	Manganese	Iron	Cobalt	Nickel	Copper	Zinc
NPA		1368453.50	36461.30	5806.90	235293.80	434284.10	69325.60	190440.70	5926026.70	473339.70
σ		3581.80	417.22	391.02	921.89	1047.75	799.49	995.58	8448.03	1309.49
(±)		7163.60	834.45	782.03	1843.79	2095.50	1598.98	1991.17	16896.06	2618.97
C_v		0.26	1.14	6.73	0.39	0.24	1.15	0.52	0.14	0.28
SNR		4615.32	132.67	18.12	662.60	1152.50	171.36	416.58	12490.12	1014.36
NPA		1199909.20	31705.50	4497.80	225156.40	402504.60	63069.10	173413.00	5675253.40	454167.60
σ		5407.59	624.62	329.69	1496.23	1939.47	761.25	1186.88	20907.43	2276.55
(±)		10815.18	1249.24	659.39	2992.46	3878.94	1522.49	2373.76	41814.86	4553.09
C_v		0.45	1.97	7.33	0.66	0.48	1.21	0.68	0.37	0.50
SNR		3880.01	119.17	14.21	656.32	1041.07	152.85	387.61	12044.56	941.93
%Diff	NPA	13.12	13.95	25.41	4.40	7.60	9.45	9.36	4.32	4.13
	SNR	17.31	10.72	24.21	0.95	10.16	11.42	7.21	3.63	7.41
		Rubidium	Strontium	Zirconium	Rhodium	Tin	Antimony	Barium	Lead (L)	Bismuth (L)
NPA		3047.40	76363.10	81435.20	165207.10	15027.60	141708.90	1847.80	680496.00	18776.30
σ		314.41	909.51	666.13	756.51	438.39	1398.28	440.29	2520.40	521.97
(±)		628.81	1819.02	1332.26	1513.02	876.77	2796.56	880.57	5040.79	1043.93
C_v		10.32	1.19	0.82	0.46	2.92	0.99	23.83	0.37	2.78
SNR		7.14	184.97	199.85	399.88	48.04	473.09	9.51	1725.69	46.74
NPA		2547.20	72174.60	76544.30	153310.90	13721.70	129689.80	1378.80	649353.40	20725.60
σ		616.35	919.27	657.66	798.14	654.37	1687.30	317.64	3301.85	780.46
(±)		1232.69	1838.54	1315.31	1596.28	1308.74	3374.60	635.27	6603.71	1560.91
C_v		24.20	1.27	0.86	0.52	4.77	1.30	23.04	0.51	3.77
SNR		6.08	177.90	191.23	379.90	45.27	447.19	7.54	1637.30	53.86
%Diff	NPA	17.88	5.64	6.19	7.47	9.08	8.86	29.07	4.68	9.87
	SNR	15.96	3.90	4.41	5.13	5.95	5.63	23.01	5.26	14.15

Table 6-17: Ultra-long term drift testing using Corning Glass B (40 kV, 30 uA, Filter 2, 180 seconds, n=10). Average net peak signal (NPA), standard deviation of NPA (σ), coefficient of variance (C_v), Signal to Noise Ratio (SNR) and %Difference (%Diff) are provided.

Ultra-Long Term (5 Months) Unit Measurement Drift: Corning Glass B (40 kV, 30 uA, Filter 2, n=10)										
		Calcium	Titanium	Chromium	Manganese	Iron	Cobalt	Nickel	Copper	Zinc
NPA		1351314.90	36762.70	5399.50	234336.60	424849.90	68757.00	189277.70	5962285.60	471141.90
σ		6021.14	833.26	411.67	867.46	1342.31	547.91	823.50	14338.21	1234.93
(±)		12042.28	1666.52	823.34	1734.93	2684.62	1095.82	1647.00	28676.42	2469.86
C_v		0.45	2.27	7.62	0.37	0.32	0.80	0.44	0.24	0.26
SNR		4607.13	137.62	16.87	677.92	1128.20	166.36	424.91	12560.55	985.00
NPA		1199909.20	31705.50	4497.80	225156.40	402504.60	63069.10	173413.00	5675253.40	454167.60
σ		5407.59	624.62	329.69	1496.23	1939.47	761.25	1186.88	20907.43	2276.55
(±)		10815.18	1249.24	659.39	2992.46	3878.94	1522.49	2373.76	41814.86	4553.09
C_v		0.45	1.97	7.33	0.66	0.48	1.21	0.68	0.37	0.50
SNR		3880.01	119.17	14.21	656.32	1041.07	152.85	387.61	12044.56	941.93
%Diff	NPA	11.87	14.77	18.22	4.00	5.40	8.63	8.75	4.93	3.67
	SNR	17.13	14.37	17.17	3.24	8.03	8.46	9.18	4.19	4.47
		Rubidium	Strontium	Zirconium	Rhodium	Tin	Antimony	Barium	Lead (L)	Bismuth (L)
NPA		2679.20	75040.10	80192.50	162001.40	14633.10	134752.10	1550.40	673968.90	18527.30
σ		402.93	886.88	743.10	1587.23	569.93	2405.43	288.73	2496.27	652.78
(±)		805.86	1773.75	1486.20	3174.46	1139.87	4810.86	577.46	4992.53	1305.55
C_v		15.04	1.18	0.93	0.98	3.89	1.79	18.62	0.37	3.52
SNR		6.42	179.09	197.73	394.73	47.52	451.53	8.32	1671.96	46.28
NPA		2547.20	72174.60	76544.30	153310.90	13721.70	129689.80	1378.80	649353.40	20725.60
σ		616.35	919.27	657.66	798.14	654.37	1687.30	317.64	3301.85	780.46
(±)		1232.69	1838.54	1315.31	1596.28	1308.74	3374.60	635.27	6603.71	1560.91
C_v		24.20	1.27	0.86	0.52	4.77	1.30	23.04	0.51	3.77
SNR		6.08	177.90	191.23	379.90	45.27	447.19	7.54	1637.30	53.86
%Diff	NPA	5.05	3.89	4.66	5.51	6.43	3.83	11.72	3.72	11.20
	SNR	5.47	0.67	3.34	3.83	4.87	0.97	9.77	2.09	15.15

Table 6-18: Comparison of the average NPA and SNR %difference figures with associated standard deviation (SD) for the drift measurements based on interval. The shaded figures were produced using setting C and are provided as a comparison.

Unit Measurement Drift: Average NPA and SNR of Corning Glass B Measurements					
		Setting A		Setting B	
Interval		Average	SD	Average	SD
Short Term	NPA	1.95	3.19	8.88	4.29
2 Hours	SNR	2.40	3.86	8.48	4.65
Long Term	NPA	6.56	7.63	3.54	4.97
2 Days	SNR	6.09	7.71	3.69	5.25
Ultra-Long	NPA	5.23	8.79	3.32	2.66
5 Months	SNR	5.32	8.99	3.14	3.12
Measurements For Comparison: 40 kV with no filter					
Short Term	NPA			2.83	5.78
2 Hours	SNR			3.26	5.74
Long Term	NPA			10.58	7.10
2 Days	SNR			9.80	6.71
Ultra-Long	NPA			7.57	4.33
5 Months	SNR			7.36	5.42

6.4 Experimental Results: HH-XRF User Defined Parameters

User defined parameters are essential in setting the optimal conditions for HH-XRF analysis: high intensity and low background (Shackley 2011:25). These two conditions work against each other; the conditions that result in high intensity will produce high background and vice versa. The optimal ratio is a compromise between these two fundamentals. Parameters used in optimal settings include choices in filters, voltage, current and acquisition time. The optimal ratio is dependent on the elements of interest, detection of which is affected through choice of user defined parameters.

6.4.1 End Window Selection

End windows have been added to this section because they are a variable that will have an effect on lower Z elements. End windows on the HH-XRF are necessary for two reasons, they protect the detector and other components of the HH-XRF unit from being damaged by material entering the unit housing, and they are needed to facilitate a vacuum in the unit housing when analysing lower Z elements or elements at trace levels. Bruker sells two end windows for the Tracer III-SD HH-XRF unit (Fig. 6-12). The larger of the two contains a semi-rigid grid (Window A - #485079-200) that is used when there is no grid present in the HH-XRF unit. The grid is enveloped between two 4 µm prolene sheets. The window sheet is slightly over-sized and partly covers the IR

Fig. 6-12: Windows available for the Bruker Tracer Series. The window to the left is the gridded (window A) and slightly larger than the window to the right containing no grid (window B).

safety window affecting safe operation of the unit and potentially (depending on coverage) allowing the unit to continue producing X-rays after an object has been removed from the window. The smaller of the two windows (Window B - #485079-000) is composed of a single 4 um prolene sheet and is used when a built-in grid is present in the analyser unit housing (Pers. Comm. Lee Drake). Additional material between the sample and the detector, as found in window A, will increase attenuation of the signal which will affect the detection of lower Z elements. The analyser unit used in the evaluation contains a built-in grid and requires window B.

An arbitrary replacement of a punctured window provided an opportunity to compare the two types of available windows for the unit. Measurements taken with window A were replicated using window B and the spectra were compared to determine the effect to the detection of elements (Fig. 6-13). Corning glass B was used for all measurements. The only differences between the measurement setups for each set of parameters is the choice of window and the date of measurement.

The results of the experimentation exhibit the background slightly lower for the gridded window in both sets of spectra (setting A and B) because of the extra thickness of the window. Most elements with a Z ≤25 (manganese) and measured using setting A have greater differences because of window type. Setting B results reveal less of a general effect.

Attenuation of lower Z photons while using Setting A with window A have resulted in a noticeable difference for silicon, potassium, and calcium (see Fig. 6-13). A comparison of the NPA and SNR (Table 6-19) reveals the following:

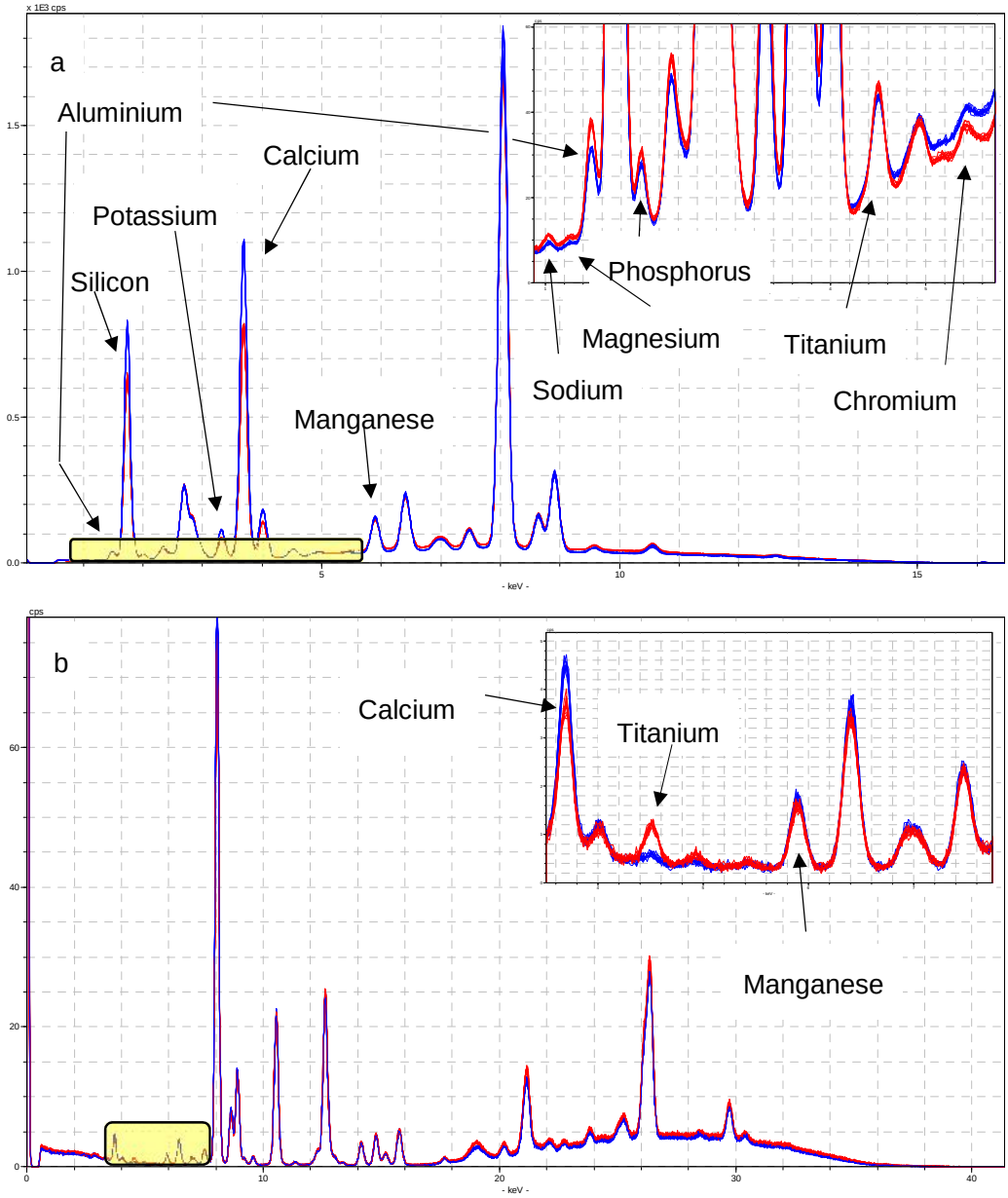

Fig. 6-13: Corning Glass B sample measured at 15 kV and 55 µA with a vacuum for 180 seconds (a) and 40 kV and 30 µA using filter 3 (Al-12 mil; Ti-1 mil; Cu-6 mil) for 180 seconds (b). The ungridded window is represented by the red spectrum and the gridded window by the blue. The effects of attenuation can be seen in the peak height and continuum differences between the two spectra. Time period between measurements is 7 months. The elements with NPA %differences greater than 10% are labelled.

Table 6-19: Comparison of end windows (gridded and non-gridded) using Corning Glass B (15 kV, 55 uA, Filter 2, 180 seconds, n=10). Average net peak signal (NPA), standard deviation of NPA (σ), coefficient of variance (C_v), Signal to Noise Ratio (SNR) and %Difference (%Diff) are provided.

End Window Comparison: Corning Glass B using Setting A											
		Sodium	Magnesium	Aluminium	Silicon	Phosphorus	Potassium	Calcium	Titanium	Chromium	Manganese
NPA	Grid	1002.60	253.50	20225.10	608496.60	10740.10	57814.80	913438.00	20858.30	3802.10	136241.00
σ	Grid	122.30	95.42	254.53	4370.14	337.29	646.10	7238.01	583.45	293.44	1710.14
(±)	Grid	244.60	190.84	509.05	8740.27	674.57	1292.19	14476.03	1166.89	586.87	3420.27
C_v	Grid	12.20	37.64	1.26	0.72	3.14	1.12	0.79	2.80	7.72	1.26
SNR	Grid	8.26	2.04	138.04	3660.50	64.47	281.12	4258.66	91.06	12.55	396.50
NPA	No Grid	1549.00	299.30	24978.00	765063.60	12238.80	81710.30	1215148.10	23470.20	4698.00	153167.40
σ	No Grid	157.76	82.57	443.88	8996.27	337.59	776.07	15483.61	510.05	290.88	2646.63
(±)	No Grid	315.52	165.14	887.77	17992.55	675.19	1552.14	30967.23	1020.11	581.76	5293.27
C_v	No Grid	10.18	27.59	1.78	1.18	2.76	0.95	1.27	2.17	6.19	1.73
SNR	No Grid	12.02	2.16	161.56	4407.38	71.31	381.82	5497.66	107.69	16.74	489.32
%Diff	NPA	42.83	16.57	21.03	22.80	13.04	34.25	28.35	11.78	21.08	11.70
%Diff	SNR	37.07	5.55	15.70	18.52	10.07	30.38	25.40	16.73	28.59	20.96
		Iron	Cobalt	Nickel	Copper	Zinc	Rhodium (L)	Barium (L)	Lead (L)	Bismuth (L)	Bismuth (M)
NPA	Grid	227307.30	37196.00	81772.60	2317745.50	161544.00	280241.00	6855.60	17891.20	2286.80	5337.30
σ	Grid	2519.54	980.38	1852.22	37618.99	2768.07	2002.75	573.23	1934.50	450.85	114.80
(±)	Grid	5039.08	1960.76	3704.44	75237.98	5536.15	4005.50	1146.46	3868.99	901.71	229.60
C_v	Grid	1.11	2.64	2.27	1.62	1.71	0.71	8.36	10.81	19.72	2.15
SNR	Grid	602.92	94.50	202.32	5576.28	403.22	1276.72	30.37	53.16	6.83	26.39
NPA	No Grid	245214.90	39071.30	86843.20	2412486.70	165815.20	271623.60	10255.10	16858.80	2144.90	6463.60
σ	No Grid	4684.74	927.37	2010.18	64806.77	4650.26	2659.68	773.42	2768.44	411.33	209.50
(±)	No Grid	9369.47	1854.75	4020.35	129613.54	9300.53	5319.37	1546.83	5536.88	822.65	418.99
C_v	No Grid	1.91	2.37	2.31	2.69	2.80	0.98	7.54	16.42	19.18	3.24
SNR	No Grid	736.84	110.40	237.75	6378.19	456.10	1212.54	47.69	55.70	7.11	31.35
%Diff	NPA	7.58	4.92	6.01	4.01	2.61	3.12	39.74	5.94	6.40	19.09
%Diff	SNR	19.99	15.52	16.10	13.42	12.31	5.16	44.40	4.66	4.11	17.17

- Lead and bismuth (L lines) have higher NPA with the gridded window because of attenuation of lower Z photons allowing more processing time for higher Z photons.
- Precision (C_v) for most elements has not been affected with the window change. Magnesium and chromium exhibit a greater C_v difference and greater precision with window B. Zinc and lead exhibit a greater C_v difference but have greater precision with window A due to the window attenuating some lower Z photons resulting in less detector deadtime.
- The standard deviation of NPA results is generally lower with window A. This is because of a reduction in incident beam scatter which is attenuated.
- The SNR is higher for window B due to reduced attenuation of the photons.

Setting A is designed for the detection of low Z elements. Window B has exhibited greater precision for some low Z elements with no significant change for others. It exhibits higher SNR for all elements. The effects of the two window types on higher Z elements (e.g. lead and bismuth) is less of a concern as the measurement results for these will be calculated using setting B.

The setting B comparisons of the two window types reveal less of an effect on all elements with the exception of titanium. The Compton peak is slightly lower (see Fig. 6-13) with the gridded window indicating greater density of window A. A comparison (Table 6-20) of NPA and SNR reveals the following.

- NPA are higher with window B for elements with $Z \leq 37$ due to less photon attenuation with the exception of titanium. Elements with $Z > 37$ exhibit higher NPA with window A except for bismuth. This is because of attenuation of the lower Z photons allowing more processing time for higher Z elements. Titanium, and calcium to a much lesser extent, reveal significant differences between the windows.
- The standard deviation of NPA results is generally lower with window A. This is because of a reduction in incident beam scatter which is attenuated by the window. Only higher Z elements exhibit lower standard deviation with window B but the differences are not significant.
- Precision (C_v) is generally greater with the window A measurements. Titanium exhibits the only significant difference with a preference for window B.

Table 6-20: Comparison of end windows (gridded and non-gridded) using Corning Glass B (40kV, 30 uA, Filter 3, 180 seconds, n=10). Average net peak signal (NPA), standard deviation of NPA (σ), coefficient of variance (C_v), Signal to Noise Ratio (SNR) and %Difference (%Diff) are provided.

End Window Comparison: Corning Glass B with Setting B										
		Calcium	Titanium	Chromium	Manganese	Iron	Cobalt	Nickel	Copper	Zinc
NPA	Grid	3622.50	977.50	123.30	1904.30	4642.50	904.30	2772.50	124557.50	12185.40
σ	Grid	113.78	58.38	38.24	47.15	97.07	62.21	66.35	711.55	120.04
(±)	Grid	227.57	116.77	76.49	94.30	194.13	124.42	132.70	1423.11	240.07
C_v	Grid	3.14	5.97	31.02	2.48	2.09	6.88	2.39	0.57	0.99
SNR	Grid	79.22	28.26	4.06	61.56	147.13	26.33	69.71	2751.42	263.53
NPA	No Grid	4793.10	189.70	129.80	2165.20	4933.40	991.40	2961.60	129394.50	12445.80
σ	No Grid	126.14	62.23	48.29	76.38	99.89	98.14	87.44	783.03	157.93
(±)	No Grid	252.28	124.45	96.58	152.76	199.79	196.27	174.89	1566.05	315.86
C_v	No Grid	2.63	32.80	37.20	3.53	2.02	9.90	2.95	0.61	1.27
SNR	No Grid	107.41	5.81	4.37	70.47	152.66	29.39	75.80	2865.38	268.16
%Diff	NPA	27.82	134.99	5.14	12.82	6.08	9.19	6.60	3.81	2.11
%Diff	SNR	30.22	131.84	7.45	13.49	3.69	11.01	8.36	4.06	1.74
		Rubidium	Strontium	Zirconium	Rhodium	Tin	Antimony	Barium	Lead (L)	Bismuth (L)
NPA	Grid	312.40	6613.50	9904.80	4388.50	10636.80	92732.40	2254.30	41505.70	1526.40
σ	Grid	26.97	129.57	122.22	191.38	268.81	1625.10	359.10	345.59	69.02
(±)	Grid	53.93	259.15	244.45	382.77	537.62	3250.19	718.20	691.18	138.04
C_v	Grid	8.63	1.96	1.23	4.36	2.53	1.75	15.93	0.83	4.52
SNR	Grid	7.86	182.72	240.13	43.14	61.54	514.38	14.24	1310.51	48.59
NPA	No Grid	318.20	6515.90	9698.50	4023.30	10035.10	89015.00	2196.30	41362.30	1564.40
σ	No Grid	46.89	72.21	156.20	246.31	309.04	1512.43	317.76	305.88	79.54
(±)	No Grid	93.78	144.41	312.40	492.62	618.08	3024.86	635.53	611.76	159.07
C_v	No Grid	14.74	1.11	1.61	6.12	3.08	1.70	14.47	0.74	5.08
SNR	No Grid	8.33	194.16	254.94	43.37	60.90	510.01	14.52	1377.28	51.88
%Diff	NPA	1.84	1.49	2.10	8.68	5.82	4.09	2.61	0.35	2.46
%Diff	SNR	5.86	6.07	5.98	0.53	1.04	0.85	1.95	4.97	6.54

- SNR is generally higher with window B. Titanium exhibits the only significant difference with a preference for window A.

The setting B results have been affected little by the window change with the exception of calcium and titanium. Calcium exhibits a significant change in NPA and SNR. It is the lowest Z element identified using setting B and the photons are relatively easily attenuated by the thicker window (A) when compared to the other elements detected with this setting. Titanium exhibits a preference for the thicker window (A) exhibiting higher NPA, precision and SNR. This is the strongest evidence for the majority of the titanium signal originating from within the unit. Attenuation of the signal, resulting in lower NPA and SNR, would be expected if the signal originated from within the sample. The reverse is true indicating an unobstructed signal detection. Titanium is at trace levels in the Corning Glass B sample and the HH-XRF results appear to be greatly affected by the titanium signal originating from the unit. Great care needs to be implemented when using this instrument for the detection of titanium at trace levels from within a sample.

In conclusion, the effect of window attenuation is low but is greater for gridded windows. Window attenuation is not a concern when measuring metal samples or higher Z elements but the difference can readily be seen when measuring Lower Z elements such as those typically associated with glass and glazes (e.g. potassium, calcium and silicon). A quick survey of common users of this specific HH-XRF unit indicate that most are unaware of the existence of differences between the windows occasionally resulting in an indiscriminate window exchange. This will produce inaccurate quantitative results when measuring or comparing the lower Z and/or trace elements. The end window type is usually not reported in published HH-XRF methodologies but should be considered when attempting to reproduce the analytical conditions for comparisons.

6.4.2 Voltage (kV) Experiment

The aim and objective of the experiment is to assess various voltages on the Corning Glass B reference material to determine two suitable voltages (low-mid Z and mid-high Z element settings (hereafter called low and high Z, respectively)) that will adequately fluoresce the elements. Most of the elements of the Corning Glass B reference material are expected to be found within the faience glazes and density of the reference material should be close to that of the faience glaze. Highest SNR and lowest Cv. determine adequacy of settings.

Corning Glass standard B was analysed using two currents, 55 µA (setting F) and 30 µA (Setting G) combined with voltages applied as a range of 5-45 at 5 kV increments for each current. A vacuum with no filter is applied for 55 µA measurements and filter 3 with no vacuum for 30 µA measurements. Each setting was measured 10 times for 180 seconds each. The reference standard was positioned directly on the window of the unit for each measurement.

A comparison of the settings by element was originally conducted by adding the figures for SNR, C_v and LDM, and dividing by SNR which results in a trivariate quotient. Lowest number determines best C_v and LDM whereas highest number determines SNR proficiency. Dividing by SNR provided a combined trivariate quotient whose best quality (as determined by highest C_v and LDM, and lowest SNR) was determined by the lowest result for each particular element. However, the LDM figures were skewing the results because of a strong relationship between the NPA and LDM high/low values. The LDM figures were dropped from the combination resulting in a bivariate quotient based on empirical results and differing only slightly from the original trivariate quotient (Tables 6-21 and 6-22). The LDM results are provided for comparison. The proposed analytical methodology that results from the evaluation will be restricted to two HH-XRF parameter setups to facilitate a relatively quick reliable method to capture all elements.

The elements were divided into two groups: low z (sodium to iron) and high z (cobalt to bismuth). The groupings are based on the results of the experimentations and area on the periodic table at which mid-Z elements were better measured with low kV. The results of the experimentation reveal all the elements in the Corning Glass B sample are detectable at 40 kV and higher (see Tables 6-21 and 6-22; Fig. 6-14 through 6-16). Choice of voltage below 40 kV is insufficient to excite all the elements in the sample. Conversely, elements with a Z<20 (calcium) are more difficult to detect at higher kV.

The smallest range for LDM using setting F is achieved at 5 kV (the lowest setting used). This is likely because of low cps and short spectral range (e.g. net peak heights and kV). This is not to suggest that a LDM range increase coincides with an increase in voltage used. For most of the elements the highest LDM is associated with a kV anywhere in the range of the kV used (5-45 kV). Only zirconium, silver and barium (Kα line) reveal highest LDM at 45 kV.

Most of the elements using setting G exhibited lowest LDM between 25 and 30 kV with a few exceptions. Copper, zinc, strontium and zirconium revealed lowest LDM at 20 kV, which coincides with the lowest voltage that exhibited a characteristic peak and

Table 6-21: The bivariate quotient (Bi-Q), precision (C_v), limit of determination of a method (LDM, ±) and signal-to-noise ratio (SNR) voltage testing results of the analysis of Corning Glass B. The C_v, ±, and SNR figures are a ratio of the results for the particular element at the specific kV setting divided by the highest result for the element at all kV settings. The red numbers indicate the optimum results for each statistic. The 5 kV LDM (±) stats have been ignored and the next optimum result has been highlighted. Blanks represent insufficient kV to produce peaks.

Voltage Testing; Sodium - Nickel

Corning Glass B

Parameters: 5-45 kV, 55 µA, Filter 2, Vacuum, 180 Seconds, 10 measurements

		Na	Mg	Al	Si	P	K	Ca	Ti	Cr	Mn	Fe	Co	Ni
kV 5	Bi-Q	3.04	3.21	5.17	4.99	5.84	11.99	17.49						
	Cv	0.64	0.88	1.00	1.00	1.00	1.00	1.00						
	±	0.13	0.16	0.10	0.08	0.17	0.06	0.03						
	SNR	0.31	0.40	0.24	0.25	0.21	0.09	0.06						
kV 10	Bi-Q	1.63	1.59	1.97	2.44	1.43	1.60	2.02	3.61	4.35	4.15	5.23	5.28	8.27
	Cv	0.47	0.48	0.57	0.91	0.29	0.40	0.56	1.00	1.00	1.00	1.00	1.00	1.00
	±	0.67	0.53	0.38	0.44	0.38	0.57	0.53	0.27	0.27	0.47	0.44	0.41	0.38
	SNR	0.74	0.82	0.59	0.63	0.67	0.66	0.55	0.38	0.30	0.32	0.24	0.23	0.14
kV15	Bi-Q	1.23	1.25	1.52	2.02	1.25	1.27	1.52	1.69	2.13	1.96	1.94	1.99	1.69
	Cv	0.23	0.23	0.45	0.92	0.24	0.24	0.44	0.52	0.57	0.66	0.59	0.61	0.39
	±	0.75	0.50	0.69	1.00	0.67	0.70	1.00	0.40	0.38	1.00	1.00	1.00	1.00
	SNR	1.00	0.92	0.86	0.90	0.95	0.89	0.85	0.75	0.51	0.68	0.63	0.61	0.56
kV20	Bi-Q	1.16	1.36	1.36	1.30	1.20	1.13	1.13	1.31	1.51	1.19	1.19	1.40	1.14
	Cv	0.13	0.36	0.34	0.29	0.19	0.13	0.12	0.29	0.35	0.17	0.16	0.34	0.12
	±	0.43	1.00	0.68	0.40	0.70	0.53	0.39	0.33	0.36	0.40	0.46	0.93	0.55
	SNR	0.85	1.00	0.93	0.95	0.98	0.99	0.97	0.92	0.67	0.90	0.86	0.85	0.84
kV25	Bi-Q	1.26	1.34	1.32	1.15	1.17	1.15	1.08	1.40	1.77	1.10	1.08	1.16	1.11
	Cv	0.23	0.32	0.32	0.15	0.17	0.15	0.08	0.39	0.67	0.10	0.08	0.15	0.11
	±	0.87	0.95	0.78	0.25	0.73	0.70	0.31	0.53	1.00	0.28	0.27	0.51	0.67
	SNR	0.87	0.94	1.00	1.00	1.00	1.00	1.00	0.97	0.88	0.99	0.97	0.98	0.98
kV 30	Bi-Q	1.45	1.58	1.25	1.38	1.21	1.14	1.14	1.69	1.33	1.15	1.15	1.29	1.09
	Cv	0.28	0.35	0.25	0.36	0.19	0.13	0.14	0.69	0.33	0.15	0.15	0.29	0.09
	±	0.78	0.70	0.64	0.60	0.77	0.62	0.52	1.00	0.55	0.45	0.53	0.99	0.57
	SNR	0.62	0.61	0.99	0.95	0.92	0.92	0.95	1.00	0.98	1.00	1.00	1.00	1.00
kV 35	Bi-Q	1.73	1.92	1.43	1.54	1.25	1.33	1.32	1.70	1.47	1.27	1.13	1.15	1.11
	Cv	0.31	0.39	0.40	0.47	0.20	0.25	0.25	0.62	0.47	0.26	0.13	0.14	0.11
	±	0.62	0.55	1.00	0.72	0.72	0.97	0.80	0.83	0.79	0.72	0.43	0.47	0.70
	SNR	0.43	0.42	0.94	0.86	0.79	0.76	0.79	0.89	1.00	0.97	0.99	0.97	0.99
kV40	Bi-Q	3.32	3.14	1.25	1.48	1.49	1.44	1.31	1.60	1.25	1.17	1.14	1.22	1.08
	Cv	0.70	0.60	0.22	0.37	0.33	0.29	0.21	0.51	0.23	0.16	0.13	0.20	0.08
	±	1.00	0.59	0.53	0.51	1.00	1.00	0.61	0.64	0.36	0.40	0.42	0.62	0.46
	SNR	0.30	0.28	0.90	0.77	0.67	0.66	0.68	0.85	0.93	0.94	0.97	0.91	1.00
kV45	Bi-Q	7.03	5.48	1.37	1.40	1.43	1.32	1.20	1.71	1.33	1.20	1.13	1.29	1.13
	Cv	1.00	1.00	0.34	0.31	0.27	0.20	0.13	0.58	0.33	0.18	0.12	0.25	0.12
	±	0.80	0.79	0.89	0.43	0.78	0.66	0.35	0.68	0.52	0.43	0.37	0.73	0.70
	SNR	0.17	0.22	0.94	0.77	0.63	0.63	0.64	0.82	1.00	0.90	0.95	0.89	0.98

Table 6-21 continued: The bivariate quotient (Bi-Q), precision (Cv), limit of determination of a method (LDM, ±) and signal-to-noise ratio (SNR) voltage testing results of the analysis of Corning Glass B. The Cv, ±, and SNR figures are a ratio of the results for the particular element at the specific kV setting divided by the highest result for the element at all kV settings. The red numbers indicate the optimum results for each statistic. The 5 kV LDM (±) stats have been ignored and the next optimum result has been highlighted. Blanks represent insufficient kV to produce peaks.

Voltage Testing; Copper - Bismuth

Corning Glass B

Parameters: 5-45 kV, 55 µA, Filter 2, Vacuum, 180 Seconds, 10 measurements

		Cu	Zn	As	Rb	Sr	Zr	Ag	Sn	Sb	Ba (kα1)	Ba (Lα1)	Pb	Bi
kV 5	Bi-Q													
	Cv													
	±													
	SNR													
kV 10	Bi-Q	14.92	36.15									1.90		
	Cv	1.00	1.00									0.47		
	±	0.29	0.22									0.20		
	SNR	0.07	0.03									0.52		
kV15	Bi-Q	1.54	1.33	2.57								1.97	31.52	11.25
	Cv	0.27	0.15	1.00								0.73	1.00	1.00
	±	1.00	1.00	0.76								0.63	0.41	0.40
	SNR	0.51	0.46	0.64								0.75	0.03	0.10
kV20	Bi-Q	1.09	1.06	2.20		6.48	19.41					1.46	1.55	2.59
	Cv	0.07	0.04	0.88		1.00	1.00					0.39	0.18	0.38
	±	0.51	0.59	1.00		0.46	0.64					0.48	1.00	0.48
	SNR	0.80	0.75	0.73		0.18	0.05					0.85	0.33	0.24
kV25	Bi-Q	1.01	1.01	1.54	3.93	1.44	1.46					1.37	1.07	1.76
	Cv	0.01	0.01	0.47	1.00	0.18	0.13					0.36	0.04	0.31
	±	0.13	0.22	0.70	0.63	0.23	0.53					0.54	0.37	0.77
	SNR	0.94	0.92	0.87	0.34	0.42	0.28					0.95	0.56	0.41
kV 30	Bi-Q	1.04	1.02	1.27	2.95	1.74	1.20					1.60	1.03	1.31
	Cv	0.04	0.02	0.26	0.98	0.47	0.11					0.60	0.02	0.18
	±	0.38	0.45	0.45	0.95	0.93	0.94					1.00	0.32	0.64
	SNR	1.00	0.99	0.99	0.50	0.64	0.54					1.00	0.76	0.59
kV 35	Bi-Q	1.05	1.03	1.26	1.98	1.37	1.07			4.77		2.19	1.02	1.29
	Cv	0.05	0.03	0.26	0.71	0.30	0.05			1.00		0.81	0.01	0.22
	±	0.48	0.54	0.45	1.00	0.75	0.63			1.00		0.90	0.23	1.00
	SNR	1.00	1.00	1.00	0.72	0.81	0.75			0.27		0.68	0.89	0.77
kV40	Bi-Q	1.03	1.02	1.57	1.50	1.39	1.05	2.25	2.49	1.49	4.67	1.71	1.02	1.13
	Cv	0.03	0.02	0.55	0.49	0.36	0.05	1.00	1.00	0.33	1.00	0.45	0.02	0.12
	±	0.29	0.47	0.89	0.89	1.00	0.74	0.89	1.00	0.95	0.75	0.47	0.40	0.62
	SNR	0.98	0.99	0.97	0.98	0.92	0.93	0.80	0.67	0.67	0.27	0.64	0.97	0.93
kV45	Bi-Q	1.04	1.03	1.48	1.36	1.24	1.06	1.90	1.41	1.12	1.31	2.68	1.02	1.12
	Cv	0.04	0.03	0.47	0.36	0.24	0.06	0.90	0.41	0.12	0.31	1.00	0.02	0.12
	±	0.35	0.52	0.72	0.65	0.69	1.00	1.00	0.63	0.52	1.00	0.94	0.31	0.65
	SNR	0.98	0.94	0.97	1.00	1.00	1.00	1.00	1.00	1.00	1.00	0.60	1.00	1.00

Table 6-22: The bivariate quotient (Bi-Q), precision (C_v), limit of determination of a method (LDM, ±) and signal-to-noise ratio (SNR) voltage testing results of the analysis of Corning Glass B at a range of kV (in 5 kV increments). The red numbers indicate the optimum results for each statistic. The 5 kV LDM stats have been ignored and the next optimum result has been highlighted. Blanks represent insufficient kV for fluorescence.

Voltage Testing: Calcium - Zinc Corning Glass B Parameters: 5-55 kV, 30 µA, Filter 3, 180 Seconds, 10 measurements										
		Ca	Ti	Cr	Mn	Fe	Co	Ni	Cu	Zn
kV20	Bi-Q								1.50	2.50
	Cv								1.00	1.00
	±								0.05	0.06
	SNR								0.10	0.09
kV25	Bi-Q	2.48	1.81		3.65	4.50	3.76	4.96	2.95	2.87
	Cv	0.81	0.55		1.00	1.00	0.77	1.00	0.49	0.44
	±	0.12	0.05		0.17	0.38	0.21	0.40	0.36	0.38
	SNR	0.55	0.68		0.38	0.29	0.28	0.25	0.25	0.24
kV 30	Bi-Q	2.81	1.69	2.09	2.65	2.17	4.62	2.73	2.22	2.42
	Cv	1.00	0.69	1.00	0.68	0.35	1.00	0.42	0.29	0.34
	±	0.14	0.09	0.12	0.11	0.13	0.28	0.16	0.20	0.28
	SNR	0.55	1.00	0.92	0.41	0.30	0.28	0.24	0.24	0.24
kV 35	Bi-Q	1.57	1.97	1.93	1.39	1.22	1.56	1.17	1.20	1.17
	Cv	0.57	0.67	0.70	0.33	0.16	0.41	0.12	0.15	0.12
	±	0.71	0.30	0.31	0.47	0.59	1.00	0.45	1.00	1.00
	SNR	1.00	0.69	0.75	0.85	0.75	0.73	0.73	0.74	0.72
kV40	Bi-Q	1.42	1.56	1.63	1.32	1.18	1.24	1.17	1.06	1.06
	Cv	0.40	0.42	0.63	0.32	0.16	0.22	0.16	0.05	0.06
	±	0.80	0.32	0.54	0.73	1.00	0.89	1.00	0.58	0.75
	SNR	0.94	0.75	1.00	1.00	0.92	0.89	0.92	0.93	0.89
kV45	Bi-Q	1.46	2.56	2.06	1.34	1.12	1.17	1.11	1.03	1.05
	Cv	0.38	1.00	0.95	0.33	0.12	0.17	0.11	0.03	0.05
	±	1.00	1.00	1.00	1.00	0.96	0.93	0.96	0.40	0.89
	SNR	0.84	0.64	0.90	0.97	1.00	1.00	1.00	1.00	1.00

background for the elements. Rubidium, tin and barium revealed lowest LDM at 35 kV but were first detected at this voltage; these elements were not detected at lower voltages. Potassium, silver and antimony reveal lowest LDM at 45 kV (the highest voltage measured). Generally, the highest LDM is found between 35 and 45 kV for all elements.

The lowest LDM results rarely coincided with the highest SNR, precision (C_v) and bivariate quotient results. For example, the measurements taken at 40-45 kV, 30 µA with filter 3 reveal greater SNR and precision for most of the elements while the smallest LDM ranges are associated with 30 kV. Corroboration of results occurs when

Table 6-22 continued: The bivariate quotient (Bi-Q), precision (C_v), limit of determination of a method (LDM, ±) and signal-to-noise ratio (SNR) voltage testing results of the analysis of Corning Glass B at a range of kV (in 5 kV increments). The red numbers indicate the optimum results for each statistic. The 5 kV LDM stats have been ignored and the next optimum result has been highlighted. Blanks represent insufficient kV for fluorescence.

Voltage Testing: Rubidium - Bismuth										
Corning Glass B										
Parameters: 5-55 kV, 30 µA, Filter 3, 180 Seconds, 10 measurements										
		Rb	Sr	Zr	Ag	Sn	Sb	Ba	Pb	Bi
kV20	Bi-Q		4.54	7.48						
	Cv		1.00	1.00						
	±		0.04	0.05						
	SNR		0.06	0.02						
kV25	Bi-Q		2.60	2.87					4.74	6.01
	Cv		0.36	0.25					1.00	1.00
	±		0.20	0.15					0.36	0.23
	SNR		0.23	0.13					0.27	0.20
kV 30	Bi-Q		2.56	2.72					3.36	3.97
	Cv		0.33	0.22					0.64	0.61
	±		0.17	0.13					0.22	0.14
	SNR		0.21	0.13					0.27	0.20
kV 35	Bi-Q	2.58	1.13	1.13	3.45	5.38	5.84	113.30	1.38	1.27
	Cv	1.00	0.09	0.09	1.00	1.00	1.00	1.00	0.28	0.20
	±	0.45	0.51	0.59	0.95	0.62	0.89	0.07	1.00	0.57
	SNR	0.63	0.72	0.65	0.41	0.23	0.21	0.01	0.75	0.71
kV40	Bi-Q	2.19	1.04	1.10	1.73	1.86	1.52	1.21	1.14	1.23
	Cv	0.99	0.04	0.08	0.52	0.51	0.31	0.07	0.13	0.20
	±	0.79	0.38	1.00	1.00	1.00	1.00	0.53	0.75	1.00
	SNR	0.82	0.90	0.86	0.72	0.60	0.60	0.32	0.92	0.86
kV45	Bi-Q	1.87	1.08	1.03	1.21	1.25	1.13	1.03	1.08	1.12
	Cv	0.87	0.08	0.03	0.21	0.25	0.13	0.03	0.08	0.12
	±	1.00	1.00	0.57	0.59	0.91	0.76	1.00	0.61	0.81
	SNR	1.00	1.00	1.00	1.00	1.00	1.00	1.00	1.00	1.00

the LDM is part of the quotient calculation (trivariate) and in most cases the bi- and trivariate quotient results agreed.

The SNR results of setting F (see Table 6-21) were clustered into three major groupings with some single elements interspersed in-between. Aluminium through calcium exhibited highest SNR at 25 kV, titanium, barium (Lα1 Line) and manganese through copper at 30 kV, and rubidium through bismuth at 45 kV. There is a minor grouping of copper (same SNR as 30 kV), zinc and arsenic at 35 kV. Individual elements consist of sodium (15 kV), magnesium (20 kV) and nickel (peak SNR share

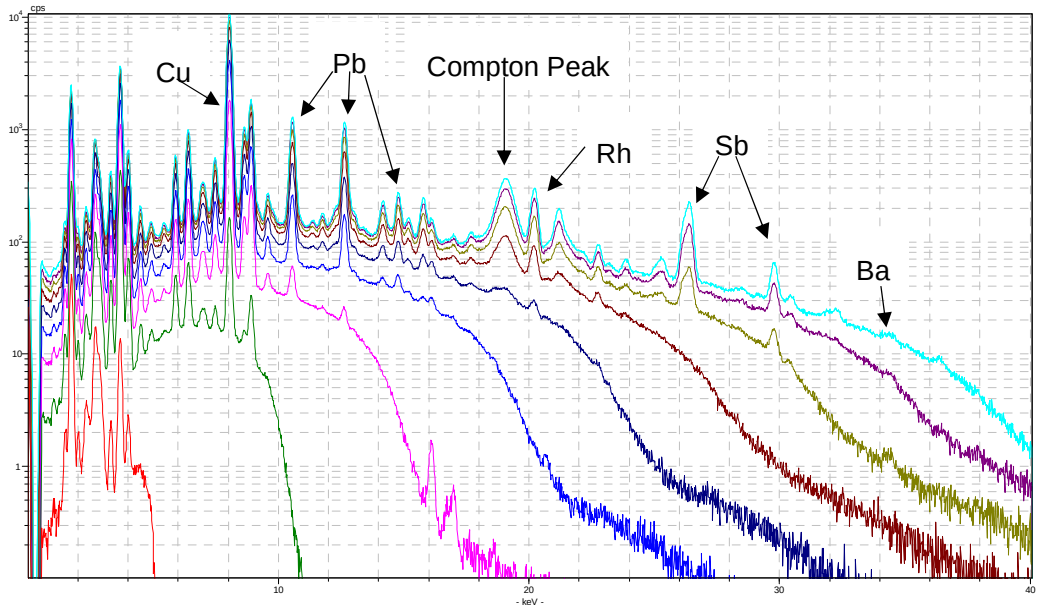

Fig. 6-14: Spectra of various voltages using 55 µA with a vacuum and no filter. The display is logarithmic to clearly exhibit a division amongst the various kV used. Most element labels have been removed to facilitate clear spectra. The voltages are designated as follows: red is 5 kV, green is 10 kV, magenta is 15 kV, blue is 20 kV, dark blue is 25 kV, brown is 30 kV, mustard is 35 kV, purple is 40 kV and teal is 45 kV.

with 30 and 40 kV). The lowest SNR results are associated with the lowest kV in which the element was first detected with the exception of sodium and magnesium at 45 kV.

The setting G results (see Table 6-22) exhibited SNR peak at a voltage of 45 kV for most of the elements (iron through bismuth). Elements outside this group consisted of chromium and manganese (40 kV peak), calcium (35 kV peak) and titanium 30 kV (peak). The lowest SNR results for copper and manganese through bismuth are generally at the lowest kV of detection or 5 kV higher. Titanium exhibits lowest SNR at 45 kV, and chromium at 35 kV.

The lowest C_v (highest precision) results generally follow the same pattern as SNR. Most of them fall in line with or are 5 kV off the highest SNR results for both settings (F and G (see Tables 6-21 and 6-22, respectively)) with a few exceptions. For setting F the exceptions are aluminium, titanium, zinc, strontium and lead. For setting G it is calcium and titanium. The highest C_v (lowest precision) generally occurs at the lowest kV in which the element was detected. The exceptions for settings F are sodium and magnesium which occur at 45 kV, and the Lα1 line of barium at 30 kV. The exceptions for settings G are calcium (30 kV), titanium (45 kV) and cobalt (25 kV).

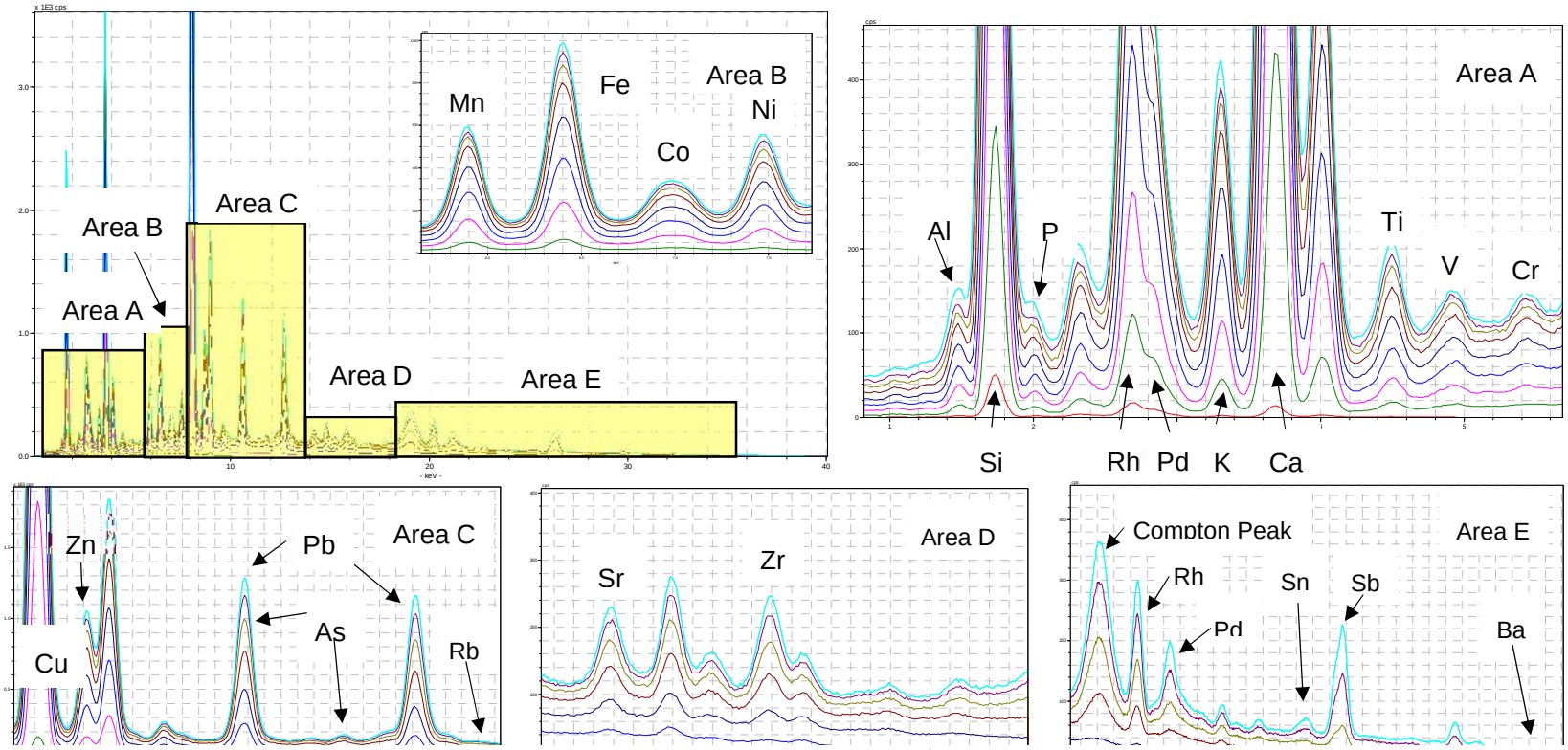

Fig. 6-15: The top-right spectra are the same spectra as shown in Fig. 6-14: Spectra of various voltages using 55 µA with a vacuum and no filter. The display is logarithmic to clearly exhibit a division amongst the various kV used. Most element labels have been removed to facilitate clear spectra. The voltages are designated as follows: red is 5 kV, green is 10 kV, magenta is 15 kV, blue is 20 kV, dark blue is 25 kV, brown is 30 kV, mustard is 35 kV, purple is 40 kV and teal is 45 kV. . It has been divided into five sections, labelled A-D, to reveal details at various magnification along the spectrum. The voltages are designated as follows: red is 5 kV, green is 10 kV, magenta is 15 kV, blue is 20 kV, dark blue is 25 kV, brown is 30 kV, mustard is 35 kV, purple is 40 kV and teal is 45 kV. Unlabelled peaks represent kβ, L and/or M lines of elements that have been labelled.

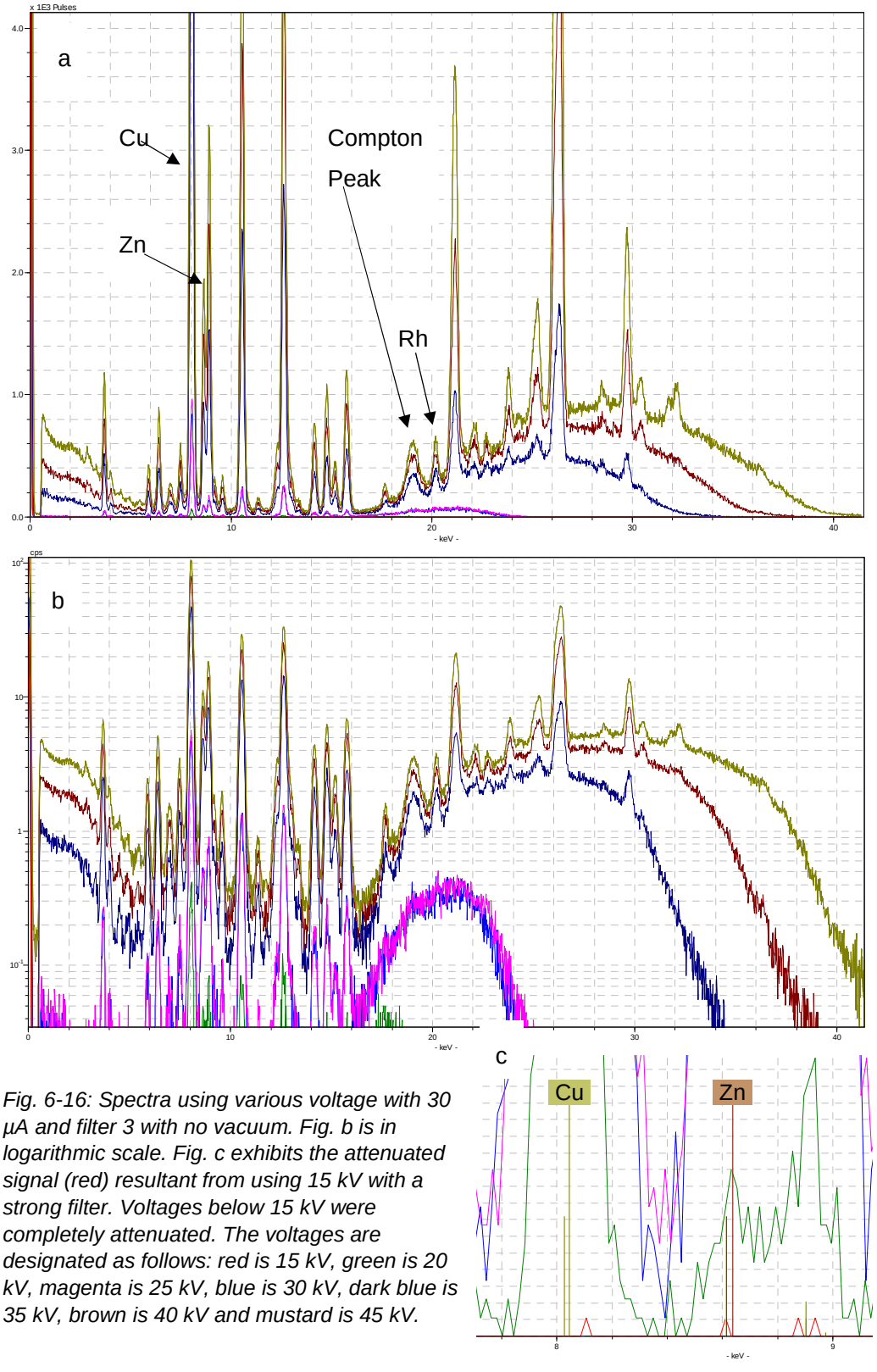

Fig. 6-16: Spectra using various voltage with 30 µA and filter 3 with no vacuum. Fig. b is in logarithmic scale. Fig. c exhibits the attenuated signal (red) resultant from using 15 kV with a strong filter. Voltages below 15 kV were completely attenuated. The voltages are designated as follows: red is 15 kV, green is 20 kV, magenta is 25 kV, blue is 30 kV, dark blue is 35 kV, brown is 40 kV and mustard is 45 kV.

The low Z group (sodium to iron) is best analysed with a voltage of 25 kV based on highest SNR and precision combination while using 55 µA with a vacuum. However, this reduces the detection of the lightest potentially detectable elements (sodium and magnesium) and goes against recommendations of using 15 kV for the lower Z elements (Kaiser and Wright 2008:47). A voltage of 15 kV is sensible based on an applied voltage 1.5 to 2 times the absorption edge of the highest Z element of the group (Shackley 2011:28) (e.g. iron 10.668 – 14.224 kV (absorption edge 7.112)). A voltage of 15 kV is optimized for magnesium using the bivariate quotient and sodium based on the SNR statistic. In lieu of the bivariate results indicating 25 kV, a return to the 15 kV convention for lighter Z elements seems appropriate for the optimum detection of sodium and magnesium. Most of the other low Z elements are still within 85% of the optimum value for voltage selection.

Based on the same current and vacuum settings, the high Z group (cobalt to bismuth) is best analysed with 40 kV with the exception of copper, zinc and the Lα1 line of barium. A voltage of 45 kV actually produces higher SNR and precision, but a kV of 40 provides a longer life for the HH-XRF filament without much detriment to the detection capabilities. Barium (Kα1 line) is the most affected with an SNR difference of 3.35 in the bivariate quotient between 40 and 45 kV (the SNR differences for other elements between 40 and 45 kV is 1 or usually much less). This is due to poor energy optimization for the detection of the barium Kα1 line. The line is located at 32 kV and requires an applied energy of 56 to 75 kV for optimum excitation, well above the HH-XRF limits. Exceptions to 40 kV optimization are copper, zinc and barium (Lα1 line) (25 kV) and cobalt and arsenic (35 kV). Lead is optimized between 35 and 45 kV with best precision (lowest C_v) at 35 kV and highest SNR at 45 kV. A voltage of 40 kV is a compromise between high SNR and high precision but all three voltages (35, 40 and 45 kV) have the same bivariate quotient rating.

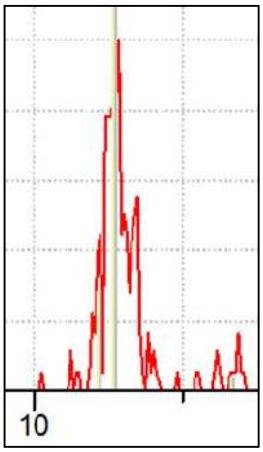

Fig. 6-17: Spectrum of the Lα1 peak for lead in Corning Glass B measured at 20 kV, 30 µA with filter 3 for 180 seconds. Note that the continuum falls below the x-axis of the spectrum.

Application of filter 3 effectively attenuated the X-ray radiation of the lower Z elements (sodium to potassium) for all voltages tested (see Table 6-22 and Fig. 6-16). A voltage of 20 kV enables 12 elements to be detected by the presence of associated characteristic peaks but lacks the background for most elements precluding the calculation of standard deviation which is required to compute SNR and the limit of detection (SNR>3) (Fig. 6-17). The SNR of copper, zinc, strontium and

zirconium can be calculated at this voltage because of the presence of a detectable continuum. Voltages below 20 kV reveal no characteristic peaks because of near complete attenuation of the X-ray radiation.

A voltage of 40 kV is optimal for use with filter 3 and a current of 30 µA. Most of the elements (i.e. iron to rubidium and zirconium to bismuth) have a higher bivariate quotient at 45 kV but 40 kV has been selected as a compromise between good results and the life of the filament. Several elements are optimized at 40 kV (i.e. calcium to manganese and strontium).

In conclusion, voltage was tested at 5 kV increments (5-45 kV) with 55 µA and a vacuum, and 30 µA with filter 3. Lower Z elements (sodium to iron) are best measured with 15 kV in conjunction with 55 µA and a vacuum to enable detection of sodium and magnesium. The higher Z elements of this group are optimized at 25 kV but this is to the detriment of sodium and magnesium. The high Z elements (cobalt to bismuth) are best measured using 40 kV in conjunction with 30 µA and filter 3; the higher kV is required to fluoresce heavier elements, the kV and µA settings protect the life of the HH-XRF filament and the use of filter 3 optimizes the detection of trace elements introduced in sand. Optimum current selection will be covered in the next section.

6.4.3 Current (µA) Experiment

The aim and objective of this experiment is to determine the optimum current with settings H and I for the detection of elements of interest using Corning Glass B as the analyte. Current is applied between 5 and 55 µA in 5 µA increments. The current is applied to settings H and I parameters through 10 measurements at 180 seconds each. The reference standard is positioned directly on the window of the unit for each measurement.

The experimental results reveal the current has a direct effect on the quantity of counts per second (cps) and all measurements have valid counts between 1k and 61k cps (Table 6-23). NPA, sum of the counts under the peak, would be expected to rise as the current is increased. This is generally the case but elements at the edge of detection with HH-XRF (i.e. Na, Mg and Ba) trace level (i.e. Bi) or whose source is suspected of being mostly from the instrument signature (i.e. Ti and Cr) exhibit a drop with 10 µA measurements in combination with 15 kV and a vacuum. This is not exhibited with higher voltage.

The low and high LDM results generally correspond with the level of current applied to the analysis indicating a strong relationship with NPA counts. The lowest LDM is associated with 5-15 µA and the highest with 55 µA measurements for low and high

Table 6-23: The average valid count per second as determined by the current and voltage. The 15 kV parameters include vacuum use. The 40 kV parameters include use of filter 3. Corning Glass B is the sample.

Average Counts Per Second by Current		
	Setting A (15 kV)	Setting B (40 kV)
µA	CPS	CPS
5	10894	1017
10	10908	1679
15	16606	2522
20	22119	3933
25	28073	5542
30	33066	6918
35	38051	7411
40	43913	8165
45	48800	8966
50	54518	9893
55	60174	10776

voltage settings (Tables 6-24 and 6-25). Approximately a third of the lowest C_v results associated with 15 kV are found at 5-10 µA but beyond this they generally do not have a pattern and are element specific (see Table 6-24). Most of the lowest C_v results associated with 40 kV are found between 35 and 50 µA. Greatest SNR for both settings occur at the highest current (Figs. 6-18 and 6-19).

The low Z group (sodium to iron) is best analysed using a current of 50 µA, in conjunction with 15 kV and a vacuum, based on the bivariate quotient which takes into account the highest SNR and precision (see Table 6-24). The results of SNR indicate the optimal current at 55 µA. This follows general recommendations by Kaiser and Wright (2008:47) for the analysis of low to mid Z elements. However, for this experiment the interest is a compromise between the greatest SNR and precision (C_v). For the voltage experiments the C_v corresponded with the greatest SNR. The C_v results for the current experiment did not have a pattern and each element exhibited highest precision within small groups or individually at the lower or higher end of the current spectrum used for the experiment. Scott (2012:270-272) had similar element-specific results for experiments based on acquisition time and current. Specifically for iron, Scott found that the highest and most stable peak/noise ratio was at 5 µA. This research indicates 10 µA is optimal (5 µA second best) based on a precision/SNR ratio. The bivariate quotient is lowest for the greatest number of elements at 50 µA. One group of outliers consist of calcium, copper, silicon, iron and lead. Bi-variant quotients indicate currents as low as 5 µA as optimum. These elements are typically in

Table 6-24: The bivariate quotient (Bi-Q), precision (C_v), limit of determination of a method (LDM, ±) and signal-to-noise ratio (SNR) current testing results of the analysis of Corning Glass B using 15 kV at a range of µA (in 5 µA increments). The red numbers indicate the optimum results for each statistic.

Current Testing; Corning Glass B as Sample										
Parameters: 15 kV, 5-55 µA, Filter 2, Vacuum, 180 Seconds, 10 measurements										
		Na	Al	Si	P	S	K	Ca	Ti	Cr
5 µA	Bi-Q	3.62	3.18	1.71	3.29	3.00	2.82	1.31	3.09	3.53
	Cv	0.96	1.00	0.33	0.99	0.90	0.83	0.14	1.00	1.00
	±	0.38	0.40	0.07	0.28	0.33	0.24	0.03	0.57	0.49
	SNR	0.37	0.46	0.46	0.43	0.45	0.46	0.46	0.48	0.40
10 µA	Bi-Q	3.84	2.18	1.68	2.70	3.13	3.19	1.40	2.71	2.75
	Cv	1.00	0.54	0.31	0.78	1.00	1.00	0.18	0.81	0.63
	±	0.38	0.22	0.07	0.23	0.38	0.28	0.04	0.46	0.29
	SNR	0.35	0.46	0.46	0.46	0.47	0.46	0.46	0.47	0.36
15 µA	Bi-Q	2.64	2.09	1.90	2.36	2.30	2.53	1.90	2.08	2.33
	Cv	0.67	0.61	0.51	0.70	0.73	0.85	0.50	0.60	0.61
	±	0.36	0.37	0.16	0.30	0.41	0.36	0.15	0.49	0.43
	SNR	0.41	0.56	0.57	0.52	0.57	0.55	0.56	0.56	0.46
20 µA	Bi-Q	2.04	1.32	1.72	1.95	1.72	2.02	1.63	1.72	2.44
	Cv	0.61	0.21	0.47	0.57	0.47	0.65	0.40	0.46	0.77
	±	0.53	0.17	0.19	0.32	0.35	0.36	0.16	0.50	0.73
	SNR	0.58	0.65	0.65	0.59	0.65	0.63	0.64	0.64	0.54
25 µA	Bi-Q	2.31	1.80	1.85	2.50	1.64	2.29	1.93	1.65	2.26
	Cv	0.75	0.57	0.61	1.00	0.47	0.91	0.65	0.47	0.74
	±	0.73	0.56	0.31	0.70	0.43	0.63	0.33	0.63	0.86
	SNR	0.57	0.72	0.72	0.67	0.73	0.71	0.71	0.72	0.59
30 µA	Bi-Q	1.81	1.58	1.80	2.20	1.80	1.85	1.68	1.60	1.81
	Cv	0.62	0.44	0.61	0.91	0.61	0.63	0.53	0.47	0.51
	±	0.86	0.49	0.36	0.75	0.64	0.51	0.31	0.75	0.69
	SNR	0.77	0.76	0.76	0.76	0.76	0.74	0.77	0.79	0.63
35 µA	Bi-Q	1.81	1.38	1.77	1.78	1.42	2.04	1.82	1.52	1.61
	Cv	0.64	0.31	0.63	0.64	0.34	0.82	0.68	0.43	0.45
	±	0.96	0.39	0.42	0.60	0.40	0.76	0.46	0.77	0.75
	SNR	0.79	0.81	0.82	0.81	0.81	0.79	0.83	0.82	0.74
40 µA	Bi-Q	1.55	1.54	1.80	1.77	1.63	1.94	1.89	1.48	1.38
	Cv	0.49	0.47	0.69	0.66	0.54	0.82	0.78	0.42	0.30
	±	0.89	0.68	0.53	0.70	0.72	0.86	0.60	0.85	0.57
	SNR	0.89	0.86	0.87	0.86	0.86	0.88	0.88	0.87	0.79
45 µA	Bi-Q	1.46	1.48	1.75	1.82	1.74	1.56	1.77	1.48	1.31
	Cv	0.43	0.44	0.69	0.74	0.67	0.51	0.71	0.45	0.28
	±	0.86	0.70	0.58	0.87	1.00	0.59	0.60	1.00	0.64
	SNR	0.94	0.91	0.91	0.91	0.91	0.91	0.92	0.92	0.90
50 µA	Bi-Q	1.46	1.27	1.55	1.70	1.32	1.75	1.54	1.32	1.42
	Cv	0.45	0.25	0.52	0.67	0.30	0.72	0.52	0.31	0.40
	±	1.00	0.45	0.48	0.87	0.49	0.91	0.48	0.75	1.00
	SNR	0.99	0.96	0.96	0.96	0.95	0.96	0.96	0.96	0.95
55 µA	Bi-Q	1.39	1.52	2.00	1.71	1.55	1.73	2.00	1.34	1.30
	Cv	0.39	0.52	1.00	0.71	0.55	0.73	1.00	0.34	0.30
	±	0.91	1.00	1.00	1.00	0.99	1.00	1.00	0.90	0.82
	SNR	1.00	1.00	1.00	1.00	1.00	1.00	1.00	1.00	1.00

Table 6-24 continued: The bivariate quotient (Bi-Q), precision (C_v), limit of determination of a method (LDM, ±) and signal-to-noise ratio (SNR) current testing results of the analysis of Corning Glass B using 15 kV at a range of µA (in 5 µA increments). The red numbers indicate the optimum results for each statistic.

Current Testing; Corning Glass B as Sample										
Parameters: 15 kV, 5-55 µA, Vacuum, 180 Seconds								Ba	Pb	Bi
		Mn	Fe	Co	Ni	Cu	Zn	(La1)	(La1)	(La1)
5 µA	Bi-Q	2.04	1.57	2.56	2.09	1.29	1.80	3.48	1.54	2.67
	Cv	0.48	0.25	0.69	0.48	0.13	0.35	1.00	0.25	0.93
	±	0.10	0.05	0.17	0.10	0.03	0.07	0.41	0.12	0.34
	SNR	0.46	0.44	0.44	0.44	0.45	0.43	0.40	0.46	0.56
10 µA	Bi-Q	2.17	1.49	3.21	3.06	1.33	1.84	3.16	1.31	2.39
	Cv	0.54	0.22	0.99	0.92	0.15	0.36	0.85	0.14	0.73
	±	0.11	0.04	0.24	0.20	0.03	0.08	0.34	0.07	0.25
	SNR	0.46	0.44	0.45	0.45	0.45	0.43	0.39	0.46	0.53
15 µA	Bi-Q	2.22	1.92	2.51	2.08	1.78	1.88	1.92	1.52	2.29
	Cv	0.70	0.51	0.83	0.59	0.43	0.47	0.49	0.31	0.73
	±	0.21	0.16	0.30	0.19	0.13	0.15	0.32	0.23	0.34
	SNR	0.57	0.56	0.55	0.55	0.55	0.54	0.53	0.60	0.57
20 µA	Bi-Q	1.58	2.09	2.39	2.17	1.73	1.70	2.21	1.36	2.32
	Cv	0.38	0.70	0.87	0.73	0.46	0.43	0.72	0.24	0.95
	±	0.15	0.28	0.42	0.31	0.19	0.18	0.61	0.24	0.65
	SNR	0.65	0.64	0.62	0.62	0.63	0.62	0.60	0.68	0.72
25 µA	Bi-Q	1.96	1.86	2.04	1.78	1.85	2.01	1.89	1.41	1.66
	Cv	0.69	0.61	0.73	0.55	0.61	0.70	0.60	0.33	0.55
	±	0.35	0.31	0.43	0.30	0.31	0.37	0.63	0.44	0.48
	SNR	0.72	0.71	0.70	0.71	0.71	0.70	0.67	0.81	0.83
30 µA	Bi-Q	1.76	1.73	2.30	1.99	1.79	2.01	1.71	1.53	2.00
	Cv	0.59	0.57	1.00	0.76	0.61	0.78	0.51	0.45	0.76
	±	0.35	0.33	0.71	0.47	0.36	0.47	0.62	0.68	0.66
	SNR	0.77	0.77	0.77	0.76	0.77	0.77	0.72	0.85	0.76
35 µA	Bi-Q	1.95	1.77	1.87	2.10	1.87	2.18	1.26	1.53	1.63
	Cv	0.78	0.63	0.71	0.90	0.71	0.96	0.21	0.46	0.48
	±	0.52	0.42	0.56	0.64	0.47	0.66	0.31	0.75	0.46
	SNR	0.82	0.82	0.81	0.81	0.81	0.81	0.81	0.87	0.77
40 µA	Bi-Q	1.86	1.84	2.13	1.68	1.87	1.93	1.36	1.48	2.31
	Cv	0.75	0.73	0.98	0.59	0.76	0.81	0.31	0.48	1.00
	±	0.57	0.56	0.89	0.47	0.58	0.64	0.54	0.92	1.00
	SNR	0.87	0.88	0.87	0.86	0.87	0.87	0.88	0.99	0.76
45 µA	Bi-Q	1.95	1.83	2.09	2.10	1.88	2.10	1.31	1.47	1.49
	Cv	0.87	0.76	0.99	1.00	0.80	1.00	0.29	0.47	0.44
	±	0.73	0.64	0.99	0.89	0.67	0.87	0.54	0.96	0.55
	SNR	0.92	0.92	0.91	0.91	0.91	0.91	0.92	1.00	0.91
50 µA	Bi-Q	1.69	1.64	1.61	1.65	1.66	1.77	1.51	2.30	1.55
	Cv	0.66	0.62	0.57	0.62	0.63	0.74	0.49	0.53	0.54
	±	0.61	0.57	0.63	0.60	0.58	0.70	1.00	0.46	0.78
	SNR	0.96	0.96	0.95	0.95	0.96	0.96	0.95	0.41	0.99
55 µA	Bi-Q	2.00	2.00	1.83	1.94	2.00	1.96	1.43	3.25	1.48
	Cv	1.00	1.00	0.83	0.94	1.00	0.96	0.43	1.00	0.48
	±	1.00	1.00	1.00	1.00	1.00	1.00	0.97	1.00	0.73
	SNR	1.00	1.00	1.00	1.00	1.00	1.00	1.00	0.44	1.00

Table 6-25: The bivariate quotient (Bi-Q), precision (C_v), limit of determination of a method (LDM, ±) and signal-to-noise ratio (SNR) current testing results of the analysis of Corning Glass B using 40 kV at a range of µA (in 5 µA increments). The red numbers indicate the optimum results for each statistic.

Current Testing; Corning Glass B as Sample										
Parameters: 40 kV, 5-55 µA, Filter 3, 180 Seconds, 10 measurements										
		Ca	Ti	Cr	Mn	Fe	Co	Ni	Cu	Zn
5 µA	Bi-Q	3.53	5.85	2.81	3.63	4.25	4.41	4.06	3.79	4.41
	Cv	0.75	1.00	0.82	0.89	0.99	1.00	0.90	0.85	0.97
	±	0.20	0.19	0.16	0.25	0.26	0.40	0.24	0.22	0.25
	SNR	0.30	0.21	0.45	0.34	0.31	0.29	0.29	0.30	0.28
10 µA	Bi-Q	1.92	2.48	2.38	2.16	1.95	2.56	2.35	1.21	1.53
	Cv	0.34	0.59	0.58	0.47	0.36	0.59	0.51	0.08	0.19
	±	0.15	0.29	0.14	0.21	0.16	0.40	0.22	0.04	0.09
	SNR	0.37	0.40	0.42	0.40	0.38	0.38	0.38	0.39	0.37
15 µA	Bi-Q	1.53	2.30	2.89	1.94	1.69	1.73	1.78	1.11	1.31
	Cv	0.24	0.54	1.00	0.47	0.32	0.32	0.36	0.05	0.14
	±	0.16	0.34	0.38	0.32	0.21	0.32	0.23	0.04	0.09
	SNR	0.45	0.41	0.53	0.50	0.46	0.44	0.46	0.48	0.46
20 µA	Bi-Q	2.77	1.72	2.03	2.68	2.73	1.85	2.77	2.69	2.73
	Cv	1.00	0.44	0.71	1.00	1.00	0.46	1.00	1.00	1.00
	±	1.00	0.51	0.43	1.00	1.00	0.69	1.00	1.00	1.00
	SNR	0.57	0.61	0.69	0.59	0.58	0.55	0.57	0.59	0.58
25 µA	Bi-Q	1.38	1.60	2.03	1.44	1.30	1.30	1.50	1.08	1.20
	Cv	0.25	0.43	0.66	0.31	0.20	0.19	0.34	0.05	0.14
	±	0.33	0.67	0.43	0.42	0.26	0.40	0.46	0.07	0.18
	SNR	0.66	0.71	0.64	0.70	0.66	0.66	0.68	0.68	0.68
30 µA	Bi-Q	1.31	1.44	2.02	1.52	1.29	1.54	1.34	1.08	1.17
	Cv	0.22	0.33	0.77	0.39	0.21	0.40	0.26	0.06	0.12
	±	0.36	0.60	0.65	0.62	0.33	1.00	0.42	0.10	0.20
	SNR	0.72	0.76	0.75	0.75	0.72	0.75	0.75	0.75	0.74
35 µA	Bi-Q	1.17	1.34	1.39	1.30	1.24	1.24	1.41	1.07	1.15
	Cv	0.13	0.29	0.32	0.24	0.19	0.19	0.31	0.06	0.12
	±	0.24	0.63	0.31	0.46	0.35	0.56	0.58	0.11	0.22
	SNR	0.78	0.84	0.81	0.82	0.80	0.80	0.77	0.79	0.78
40 µA	Bi-Q	1.24	1.33	1.47	1.35	1.21	1.11	1.23	1.06	1.18
	Cv	0.20	0.29	0.44	0.30	0.18	0.09	0.20	0.05	0.15
	±	0.42	0.69	0.53	0.63	0.38	0.28	0.41	0.12	0.32
	SNR	0.83	0.88	0.94	0.86	0.85	0.83	0.84	0.85	0.85
45 µA	Bi-Q	1.15	1.31	1.45	1.56	1.17	1.25	1.21	1.07	1.16
	Cv	0.13	0.30	0.42	0.68	0.15	0.22	0.19	0.06	0.15
	±	0.32	0.83	0.53	0.25	0.35	0.82	0.46	0.15	0.34
	SNR	0.89	0.96	0.92	1.21	0.90	0.90	0.91	0.90	0.89
50 µA	Bi-Q	1.16	1.17	1.65	1.20	1.16	1.16	1.18	1.06	1.13
	Cv	0.15	0.16	0.56	0.18	0.15	0.15	0.18	0.06	0.12
	±	0.40	0.46	0.71	0.47	0.38	0.60	0.47	0.15	0.32
	SNR	0.94	0.92	0.87	0.93	0.95	0.93	0.96	0.95	0.95
55 µA	Bi-Q	1.15	1.31	1.67	1.28	1.14	1.17	1.14	1.07	1.10
	Cv	0.15	0.31	0.67	0.28	0.14	0.17	0.14	0.07	0.10
	±	0.45	1.00	1.00	0.79	0.40	0.76	0.40	0.21	0.30
	SNR	1.00	1.00	1.00	1.00	1.00	1.00	1.00	1.00	1.00

Table 6-25 continued: The bivariate quotient (Bi-Q), precision (C_v), limit of determination of a method (LDM, ±) and signal-to-noise ratio (SNR) current testing results of the analysis of Corning Glass B using 40 kV at a range of µA (in 5 µA increments). The red numbers indicate the optimum results for each statistic.

Current Testing; Corning Glass B as Sample										
Parameters: 40 kV, 5-55 µA, Filter 3, 180 Seconds									Pb	
		Rb	Sr	Zr	Ag	Sn	Sb	Ba	(La1)	Bi
5 µA	Bi-Q	4.03	3.72	3.93	4.61	4.10	3.94	2.94	3.99	4.29
	Cv	0.73	0.80	0.87	1.00	0.93	0.89	0.81	0.92	1.00
	±	0.19	0.21	0.23	0.29	0.24	0.23	0.21	0.24	0.26
	SNR	0.24	0.29	0.30	0.28	0.30	0.30	0.42	0.31	0.30
10 µA	Bi-Q	4.20	1.77	2.08	2.69	1.51	1.36	3.19	1.26	3.14
	Cv	1.00	0.30	0.42	0.63	0.20	0.14	1.00	0.10	0.80
	±	0.45	0.14	0.18	0.32	0.08	0.06	0.36	0.04	0.34
	SNR	0.31	0.39	0.38	0.37	0.38	0.40	0.46	0.39	0.37
15 µA	Bi-Q	2.75	1.53	1.42	2.01	1.79	1.31	1.94	1.17	2.65
	Cv	0.68	0.25	0.19	0.46	0.38	0.15	0.58	0.08	0.78
	±	0.45	0.17	0.13	0.34	0.25	0.10	0.34	0.05	0.52
	SNR	0.39	0.47	0.46	0.45	0.48	0.48	0.61	0.48	0.47
20 µA	Bi-Q	2.69	2.75	2.72	2.06	2.66	2.67	1.78	2.69	2.41
	Cv	0.79	1.00	1.00	0.58	1.00	1.00	0.54	1.00	0.82
	±	0.78	1.00	1.00	0.65	1.00	1.00	0.45	1.00	0.83
	SNR	0.47	0.57	0.58	0.55	0.60	0.60	0.69	0.59	0.59
25 µA	Bi-Q	1.33	1.11	1.22	1.48	1.42	1.22	1.39	1.12	1.79
	Cv	0.23	0.08	0.15	0.33	0.29	0.15	0.31	0.08	0.52
	±	0.38	0.11	0.20	0.53	0.39	0.21	0.35	0.11	0.68
	SNR	0.70	0.68	0.68	0.69	0.70	0.69	0.80	0.69	0.66
30 µA	Bi-Q	1.48	1.14	1.20	1.47	1.30	1.20	1.49	1.10	1.50
	Cv	0.35	0.11	0.15	0.35	0.23	0.15	0.45	0.07	0.37
	±	0.65	0.17	0.25	0.65	0.36	0.24	0.61	0.12	0.59
	SNR	0.72	0.75	0.76	0.74	0.76	0.75	0.91	0.75	0.74
35 µA	Bi-Q	1.45	1.21	1.15	1.50	1.31	1.21	1.37	1.07	1.30
	Cv	0.35	0.17	0.12	0.39	0.26	0.17	0.34	0.06	0.24
	±	0.76	0.31	0.22	0.85	0.48	0.32	0.51	0.11	0.44
	SNR	0.77	0.80	0.80	0.79	0.82	0.81	0.92	0.81	0.79
40 µA	Bi-Q	1.51	1.15	1.17	1.37	1.11	1.14	1.56	1.05	1.62
	Cv	0.37	0.13	0.15	0.31	0.09	0.12	0.50	0.04	0.50
	±	0.82	0.27	0.31	0.75	0.19	0.24	0.75	0.08	1.00
	SNR	0.73	0.86	0.87	0.83	0.87	0.86	0.88	0.86	0.81
45 µA	Bi-Q	1.34	1.15	1.10	1.36	1.15	1.16	1.41	1.08	1.21
	Cv	0.33	0.13	0.09	0.34	0.14	0.15	0.37	0.07	0.19
	±	1.00	0.32	0.21	0.97	0.33	0.35	0.61	0.18	0.45
	SNR	0.97	0.91	0.91	0.94	0.92	0.92	0.90	0.91	0.91
50 µA	Bi-Q	1.16	1.14	1.16	1.27	1.16	1.15	1.34	1.09	1.33
	Cv	0.16	0.13	0.15	0.25	0.16	0.15	0.33	0.09	0.30
	±	0.51	0.35	0.39	0.77	0.40	0.37	0.61	0.24	0.76
	SNR	1.00	0.96	0.95	0.94	0.95	0.95	0.98	0.96	0.91
55 µA	Bi-Q	1.26	1.14	1.14	1.30	1.20	1.15	1.50	1.07	1.17
	Cv	0.25	0.14	0.14	0.30	0.20	0.15	0.50	0.07	0.17
	±	0.86	0.42	0.40	1.00	0.57	0.41	1.00	0.20	0.49
	SNR	0.98	1.00	1.00	1.00	1.00	1.00	1.00	1.00	1.00

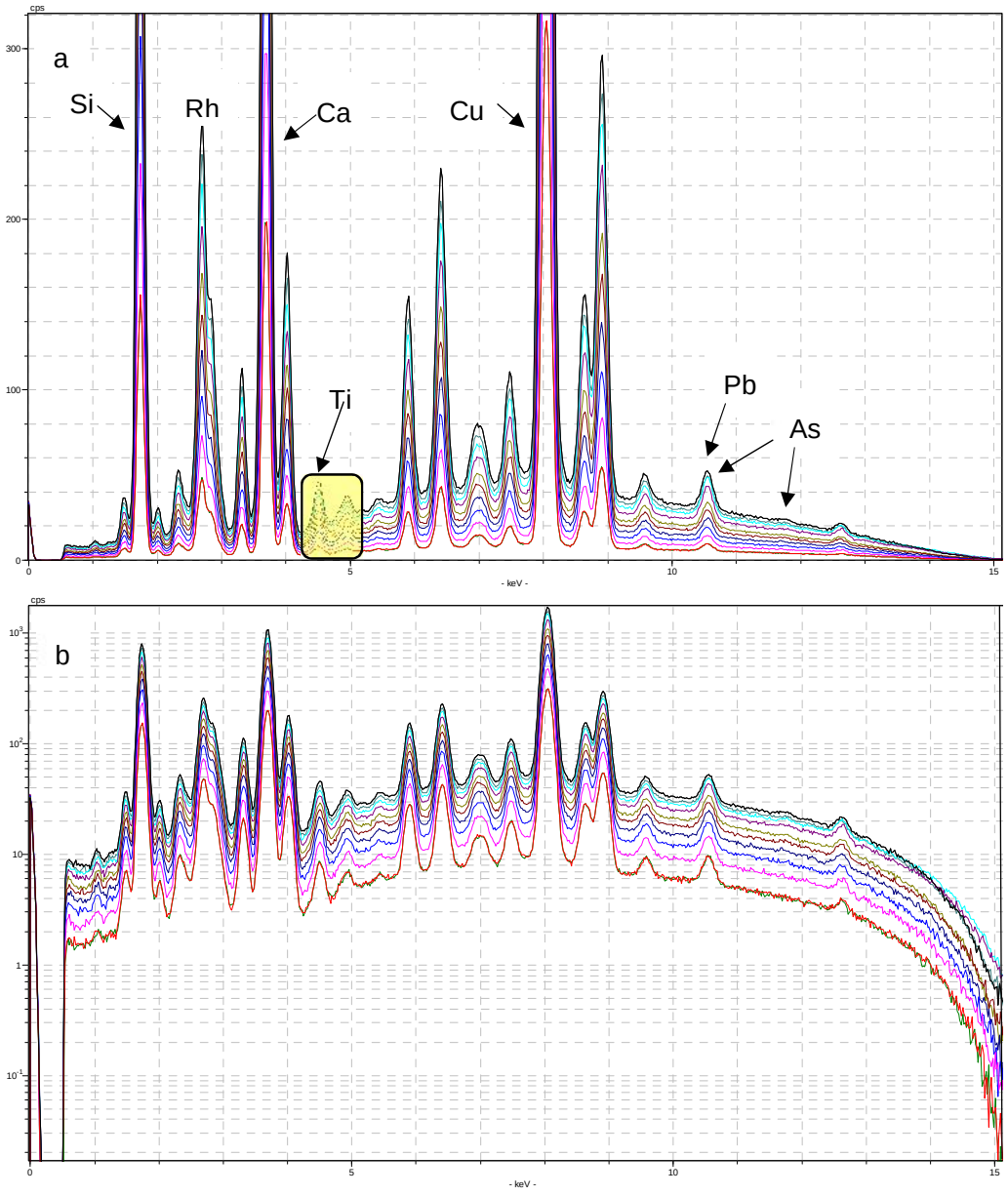

Fig. 6-18: Spectra of Corning Glass B using variable µA (5-55 at 5 µA increments) and 15 kV with a vacuum for 180s. Peaks heights are extended as the current increases. Most peaks remain unlabelled to present clear spectra. Fig. b is the spectra in logarithmic scale. Fig. c is a detail of the Kα and Kβ peaks for titanium. The 5 and 10 µA measurements (two lowest spectra; red and mustard) are qualitatively the same.

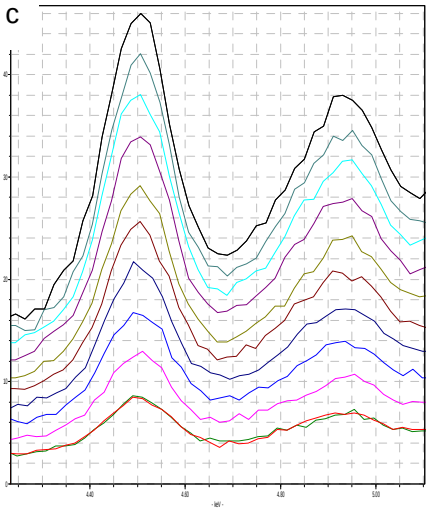

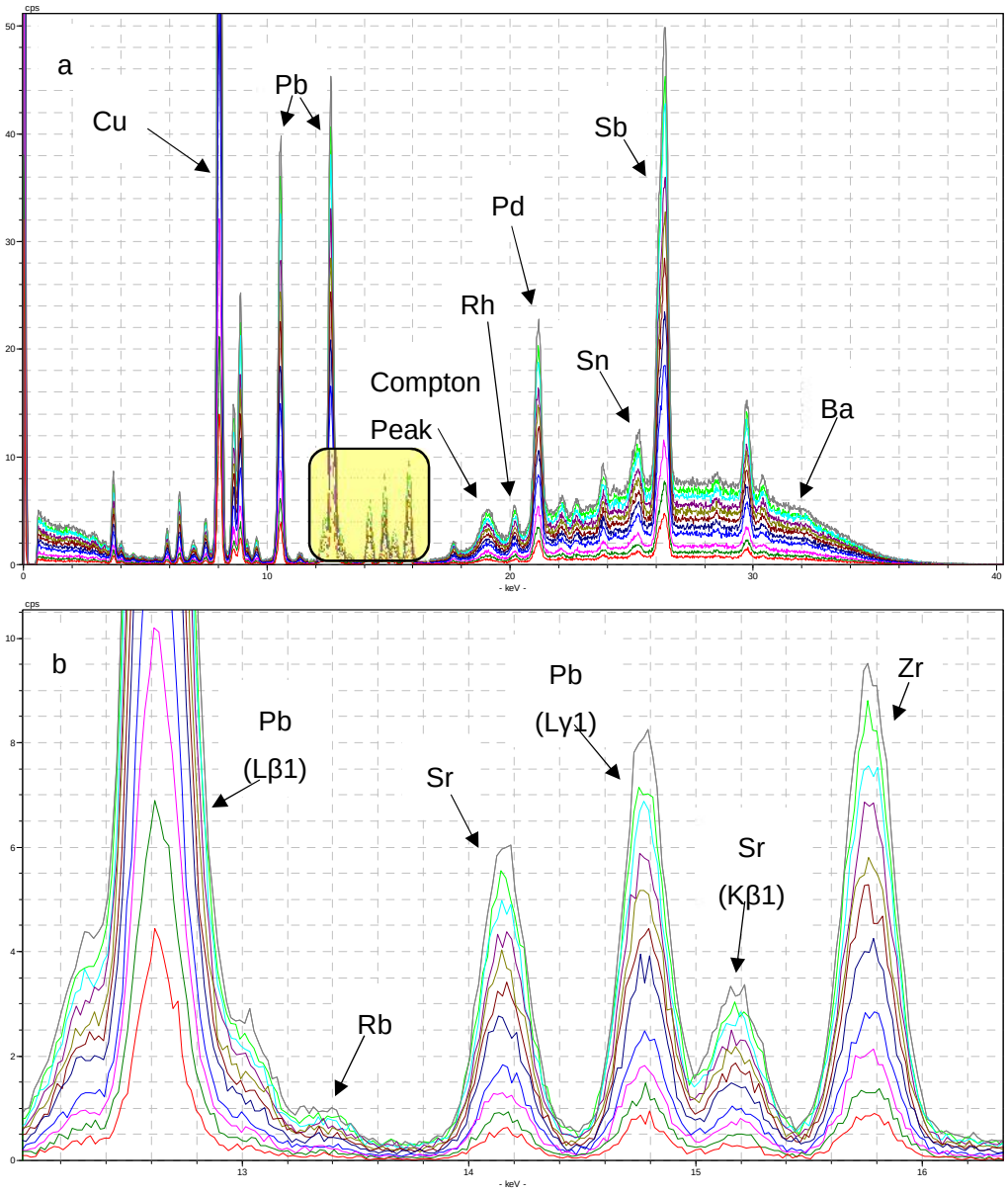

Fig. 6-19: Spectra of Corning Glass B using variable µA (5-55 at 5 µA increments) and 40 kV with filter 3 for 180s. Peaks heights are extended as the current increases (red is 5 µA and lowest height). Most peaks remain unlabelled to present clear spectra. Fig. b is a detail of the region between 12 and 16.2 keV exhibiting peaks for lead, rubidium, strontium and zirconium.

minor to major amounts within a faience glaze and do not need to be 'teased-out' by fine tuning the HH-XRF settings. Copper and lead are typical colourants and their presence in the glaze can be somewhat accurately guessed simply by the colour of the glaze.

Iron can be used as a colourant but is more typically an inclusion at trace levels in the sand used to make up most bodies and glazes. Iron is an element of interest and a current of 50 µA is half as precise as 10 µA but the SNR is 96% of its optimum at 55

µA. The data can be misleading and when put into perspective one can see that the difference between C_v at its lowest (0.42% at 10 µA) and at its highest (1.91% at 55 µA) for iron is 1.49%. The low differences in percentage are true for all the outliers with the exception of lead (difference ~12%) but this would typically be measured at a higher voltage.

The high Z group (cobalt to bismuth) is best analysed using a current of 30 µA in conjunction with 40 kV and filter 3 (see Table 6-25). All the elements in this group are optimized above this current except for strontium and barium (25 µA). The decision to use 30 µA is based on a wattage of less than 1.5 resulting in an extension of the HH-XRF filament life. The SNR for most of the elements at 30 µA are at 75% or higher of the optimum SNR current (µA). The precision (C_v) is relatively high except for titanium and chromium which would typically be measured at a lower voltage. LDM is lowest at lower currents.

In conclusion, a range of current (5-55 µA) was tested in 5 µA increments using 15 kV with a vacuum and 40 kV with filter 3. Acquisition time for both settings was 180 seconds and 10 measurements were made for each current increment. The data indicate that optimal current for the analysis of lower Z elements (sodium to iron) as a group is 50 µA. Optimal current for the analysis of higher Z elements (cobalt to bismuth) as a group is 30 µA.

6.4.4 Acquisition Time Experiment

Five acquisition times (30, 60, 120, 180 and 240 seconds) have been tested using the Corning Glass B standard with settings J and K. Ten measurements were taken with each parameter setting and acquisition time. The reference standard was placed directly on the window and moved between each individual measurement.

The results for both parameter settings (Tables 6-26 and 6-27) reveal that LDM is lowest with a shorter acquisition time and photon count accumulation, and SNR is greatest with the longest acquisition time (Figs. 6-20 and 6-21). These were expected and optimization of acquisition time was to be determined through C_v and time convenience. The lowest bi-variate quotient for the acquisition times is between 180 and 240 seconds and generally corresponds with the C_v.

Precision (C_v) results of setting J are generally lowest with 240 second acquisition time (Fig. 6-22). Exceptions to this (i.e. potassium, titanium, chromium, iron and zinc) exhibited optimal precision at 180 seconds. The precision difference between 180 and 240 seconds for most of the elements is small ($C_v \leq 0.16$). Elements with a greater difference include Corning Glass B trace elements (see Table 4-1) cobalt, nickel and

Table 6-26: Experimental testing of acquisition time using setting J with Corning Glass B as the sample. Statistics include bi-variate quotient (Bi-Q), coefficient of variance (C_v), limit of determination of a method (±) and signal to noise ratio (SNR) and are based on the NPA for each element. Numbers in red indicate optimum value of the statistic for the specific element.

Acquisition Time: Determining Optimization of Low Voltage Analysis Using Corning Glass B as Sample																		
Parameters: 15 kV, 55 µA, Vacuum, Filter 2, 180 seconds, 10 Measurements																Ba	Pb	Bi
Seconds		Na	Al	Si	P	K	Ca	Ti	Cr	Mn	Fe	Co	Ni	Cu	Zn	(Lα1)	(Lα1)	(Lα1)
30	Bi-Q	4.47	4.04	3.93	3.78	3.84	3.83	3.80	3.78	3.84	3.85	3.91	3.71	3.57	3.83	3.89	3.51	2.74
	Cv	1.00	1.00	0.99	1.00	1.00	1.00	1.00	1.00	1.00	1.00	1.00	0.95	0.90	1.00	1.00	0.85	0.86
	±	0.34	0.42	0.16	0.48	0.16	0.18	0.23	0.27	0.19	0.16	0.25	0.18	0.15	0.17	0.22	0.15	0.37
	SNR	0.29	0.33	0.34	0.36	0.35	0.35	0.36	0.36	0.35	0.35	0.34	0.35	0.35	0.35	0.35	0.34	0.49
60	Bi-Q	2.98	2.32	2.86	1.95	2.71	2.89	2.03	2.42	2.99	2.93	2.52	3.01	2.73	2.72	2.26	2.46	3.15
	Cv	0.96	0.64	0.89	0.48	0.84	0.94	0.52	0.67	0.98	0.95	0.75	1.00	0.85	0.85	0.58	0.72	1.00
	±	0.77	0.55	0.28	0.45	0.27	0.33	0.24	0.33	0.38	0.31	0.38	0.38	0.28	0.29	0.24	0.26	0.57
	SNR	0.49	0.48	0.48	0.50	0.49	0.50	0.51	0.47	0.49	0.50	0.49	0.50	0.49	0.49	0.46	0.50	0.47
120	Bi-Q	1.81	1.85	2.48	1.44	2.16	2.25	1.80	1.90	2.28	2.33	1.65	1.97	2.43	2.15	1.90	2.42	1.74
	Cv	0.59	0.58	1.00	0.32	0.81	0.88	0.57	0.63	0.90	0.94	0.46	0.68	1.00	0.82	0.58	1.00	0.51
	±	1.00	0.99	0.63	0.60	0.53	0.62	0.51	0.66	0.69	0.61	0.47	0.52	0.65	0.56	0.48	0.72	0.60
	SNR	0.73	0.68	0.68	0.71	0.70	0.70	0.71	0.70	0.70	0.70	0.71	0.71	0.70	0.71	0.65	0.70	0.68
180	Bi-Q	1.38	1.36	2.01	1.40	1.79	1.95	1.47	1.36	1.87	1.87	1.74	2.00	1.91	1.76	1.37	1.93	1.58
	Cv	0.34	0.31	0.88	0.35	0.69	0.83	0.41	0.33	0.75	0.76	0.64	0.87	0.79	0.66	0.31	0.82	0.52
	±	0.88	0.86	0.88	1.00	0.69	0.89	0.56	0.54	0.87	0.74	1.00	1.00	0.78	0.69	0.42	0.90	1.00
	SNR	0.89	0.87	0.87	0.87	0.87	0.87	0.88	0.91	0.87	0.87	0.87	0.87	0.87	0.87	0.84	0.88	0.90
240	Bi-Q	1.25	1.27	1.75	1.19	1.75	1.70	1.55	1.47	1.65	1.77	1.35	1.52	1.76	1.72	1.55	1.69	1.40
	Cv	0.25	0.27	0.75	0.19	0.75	0.70	0.55	0.47	0.65	0.77	0.35	0.52	0.76	0.72	0.55	0.69	0.40
	±	0.85	1.00	1.00	0.72	1.00	1.00	1.00	1.00	1.00	1.00	0.72	0.78	1.00	1.00	1.00	1.00	0.99
	SNR	1.00	1.00	1.00	1.00	1.00	1.00	1.00	1.00	1.00	1.00	1.00	1.00	1.00	1.00	1.00	1.00	1.00

Table 6-27: Experimental testing of acquisition time using setting K with Corning Glass B as the sample. Statistics include bi-variate quotient (Bi-Q), coefficient of variance (C_v), limit of determination of a method (±) and signal to noise ratio (SNR) and are based on the NPA for each element. Numbers in red indicate optimum value of the statistic for the specific element.

Acquisition Time: Determining Optimization of High Voltage Analysis Using Corning Glass B as Sample																		
Parameters: 40 kV, 30 µA, Filter 3, 180 seconds, 10 Measurements																	Pb	Bi
Seconds		Ca	Ti	Cr	Mn	Fe	Co	Ni	Cu	Zn	Ru	Sr	Zr	Sn	Sb	Ba	(Lα1)	(Lα1)
30	Bi-Q	3.72	4.22	2.94	3.61	3.76	3.72	3.19	3.90	3.78	4.13	3.84	3.93	3.98	3.53	4.46	3.95	3.89
	Cv	1.00	1.00	1.00	1.00	1.00	0.95	0.72	1.00	0.96	1.00	1.00	1.00	1.00	0.83	1.00	1.00	1.00
	±	0.27	0.30	0.24	0.34	0.44	0.28	0.22	0.14	0.23	0.23	0.31	0.17	0.23	0.11	0.20	0.19	0.19
	SNR	0.37	0.31	0.51	0.38	0.36	0.35	0.33	0.34	0.34	0.32	0.35	0.34	0.34	0.33	0.29	0.34	0.35
60	Bi-Q	2.59	2.74	2.42	2.36	1.80	2.97	3.18	2.58	3.03	2.51	2.67	3.03	2.17	3.05	2.08	2.83	3.04
	Cv	0.82	0.90	0.73	0.69	0.41	1.00	1.00	0.77	1.00	0.61	0.81	1.00	0.58	1.00	0.57	0.87	0.96
	±	0.44	0.64	0.26	0.45	0.36	0.60	0.60	0.21	0.50	0.26	0.50	0.35	0.28	0.29	0.30	0.34	0.36
	SNR	0.51	0.52	0.51	0.50	0.51	0.51	0.46	0.49	0.49	0.41	0.48	0.49	0.49	0.49	0.53	0.48	0.47
120	Bi-Q	2.06	1.88	2.22	1.90	1.28	1.58	2.07	2.17	1.67	2.04	1.85	1.98	2.23	2.34	1.87	1.67	1.87
	Cv	0.77	0.67	0.83	0.65	0.20	0.39	0.72	0.82	0.48	0.67	0.58	0.68	0.86	0.91	0.54	0.45	0.59
	±	0.84	1.00	0.56	0.84	0.36	0.46	0.88	0.45	0.48	0.62	0.72	0.48	0.82	0.52	0.46	0.36	0.46
	SNR	0.72	0.76	0.68	0.72	0.73	0.68	0.67	0.70	0.71	0.65	0.69	0.70	0.70	0.68	0.62	0.68	0.69
180	Bi-Q	1.59	1.41	1.72	1.38	1.42	1.66	1.62	1.61	1.39	1.33	1.58	1.54	1.53	1.85	1.72	1.67	1.59
	Cv	0.52	0.37	0.59	0.32	0.37	0.56	0.53	0.53	0.34	0.27	0.48	0.46	0.45	0.71	0.55	0.57	0.49
	±	0.85	0.84	0.58	0.63	1.00	1.00	0.99	0.44	0.51	0.39	0.89	0.49	0.65	0.61	0.71	0.67	0.56
	SNR	0.88	0.92	0.81	0.86	0.87	0.85	0.85	0.87	0.87	0.82	0.84	0.86	0.85	0.84	0.76	0.84	0.83
240	Bi-Q	1.46	1.20	1.71	1.38	1.17	1.56	1.39	1.89	1.50	1.50	1.40	1.70	1.52	1.85	1.50	1.63	1.63
	Cv	0.46	0.20	0.71	0.38	0.17	0.56	0.39	0.89	0.50	0.50	0.40	0.70	0.52	0.85	0.50	0.63	0.63
	±	1.00	0.58	1.00	1.00	0.62	1.36	1.00	1.00	1.00	1.00	1.00	1.00	1.00	1.00	1.00	1.00	1.00
	SNR	1.00	1.00	1.00	1.00	1.00	1.00	1.00	1.00	1.00	1.00	1.00	1.00	1.00	1.00	1.00	1.00	1.00

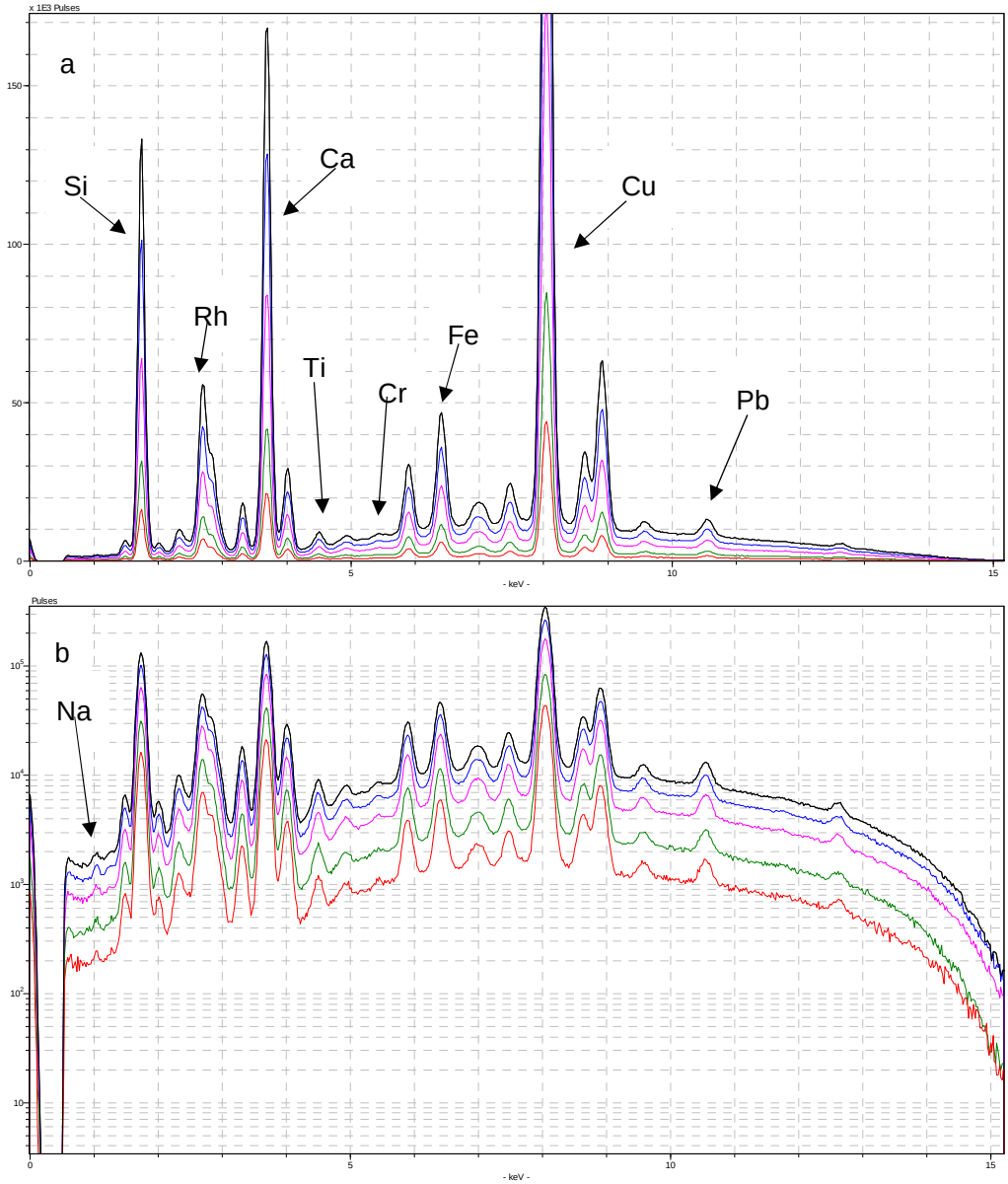

Fig. 6-20: Fig. a is a standard spectra of Corning Glass B using setting J with various acquisition times: red is 30 seconds, green is 60 seconds, purple is 120 seconds, blue is 180 seconds and black is 240 seconds. Fig. b is the same spectra using logrithmic scaling to reveal further detail not seen in the standard spectra. Some peaks remain unlabelled to present a set of clear spectra.

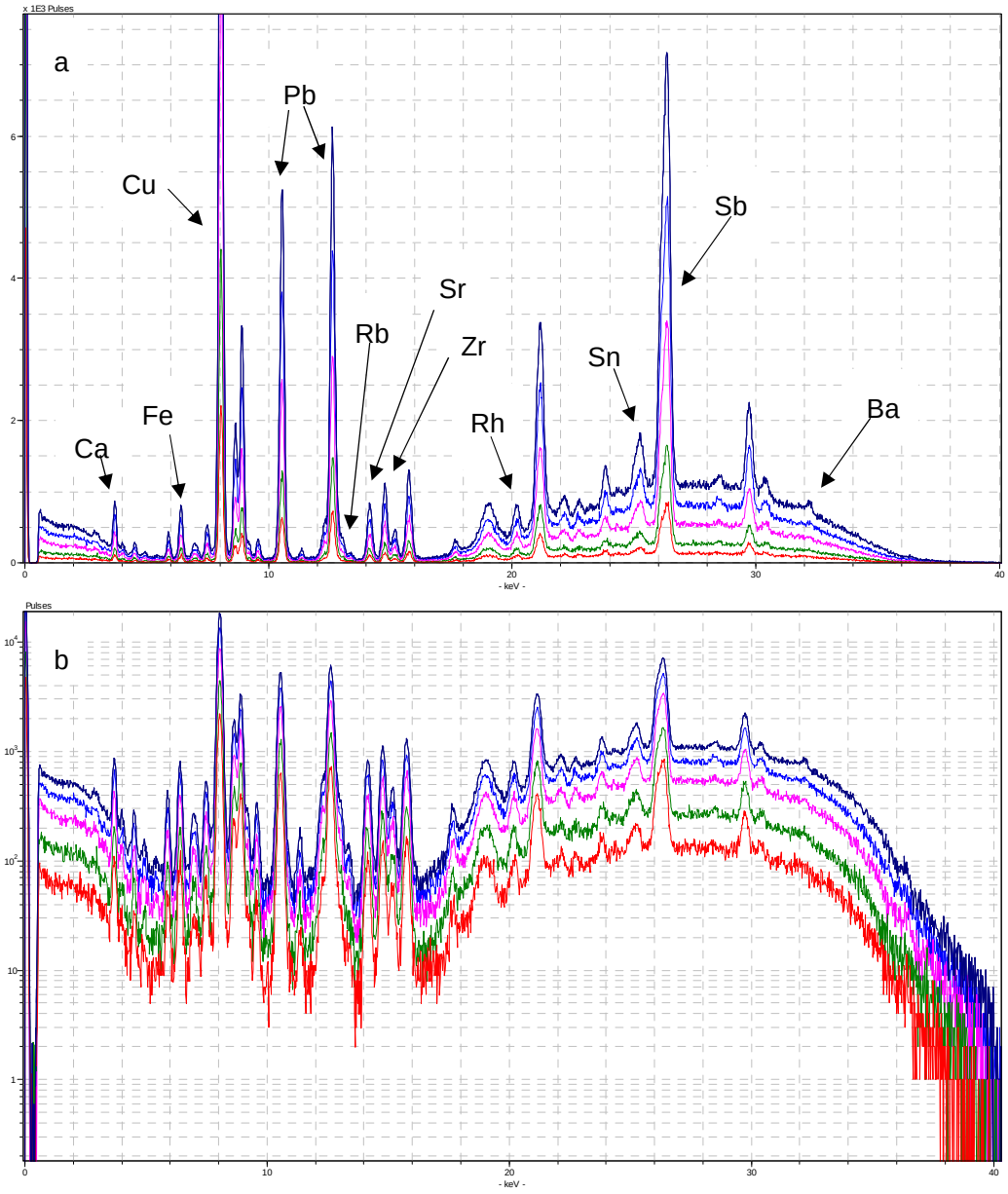

Fig. 6-21: Fig. a is a standard spectra of Corning Glass B using setting K with various acquisition times: red is 30 seconds, green is 60 seconds, purple is 120 seconds, blue is 180 seconds and dark blue is 240 seconds. Fig. b is the same spectra using logrithmic scaling to reveal further detail not seen in the standard spectra. Some peaks remain unlabelled to present a set of clear spectra.

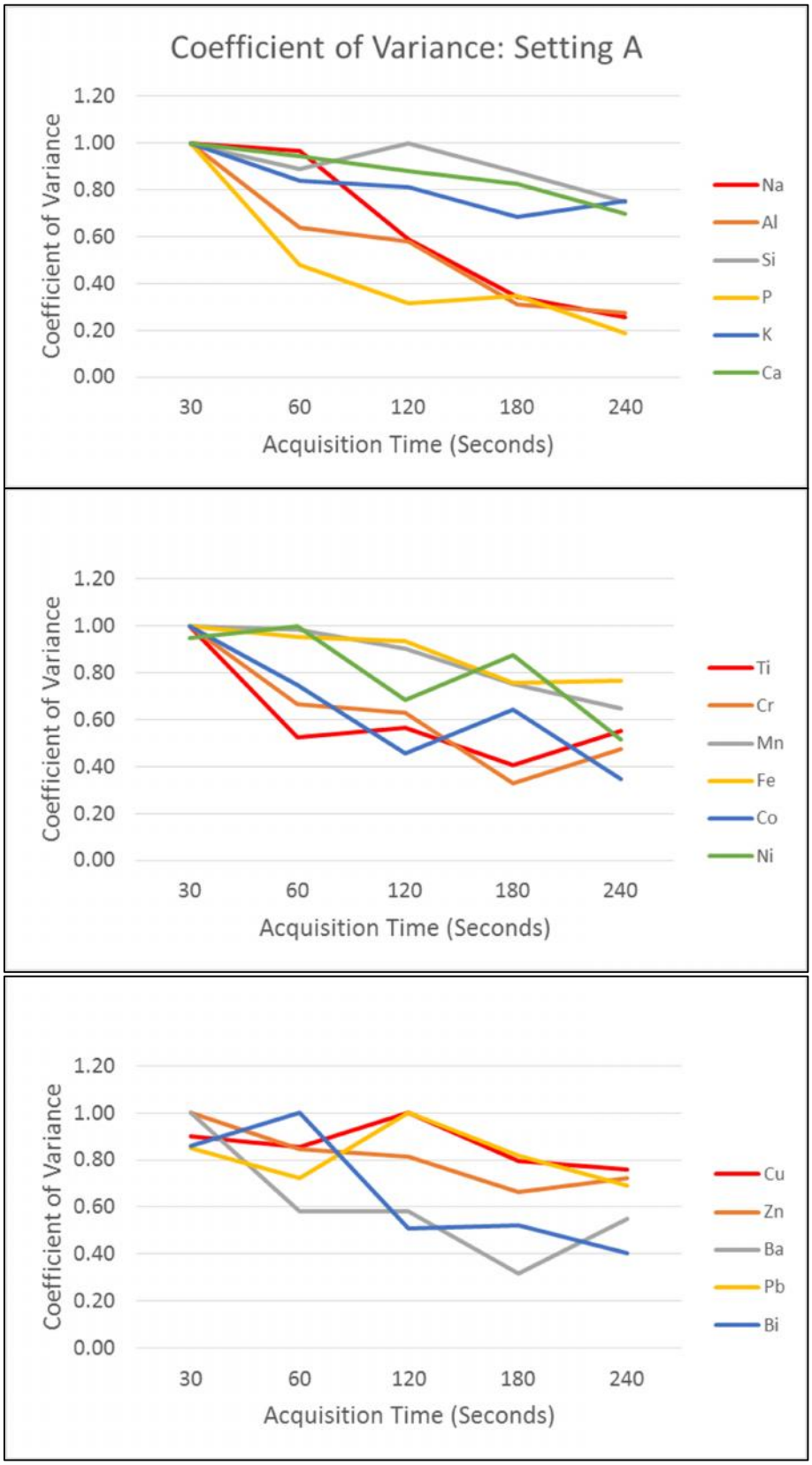

Fig. 6-22: Line graphs exhibiting the effects of acquisition time on coefficient of variance by element. Lowest C_v corresponds to highest precision for a set of measurements. Parameters are setting J using Corning Glass B as sample.

barium (Lα1). Precision results of setting K (Fig. 6-23) are reversed to those of setting J; Most of the elements are optimized at 180 seconds with a majority of the exceptions at 240 seconds. Precision of cobalt and lead is optimized at 120 seconds.

In conclusion, the optimum acquisition time is a balance between precision and convenience. An acquisition time of 180 seconds with both settings provides sufficient precision for elements of the Corning Glass B standard. An increase in the acquisition time would result in greater precision and SNR for most of the elements but the difference would be so small as to become time inefficient.

6.5 Experimental Results: HH-XRF Sample Characteristics

Ideal samples for HH-XRF, whether liquid, solid or gas, require preparation. This often includes the powdering and pelletizing of solid samples which provides a homogenous analyte with flat surface large enough to completely cover the analytical window. Non-destructive analysis requires that the sample is unmodified save a general surface cleaning to remove dust and burial matrix deposits. Some samples may not provide complete coverage of the window because of sample geometry. In this section, sample-to-detector distance is tested to mimic sample geometry and to determine effect on analysis with increased distance. Effects of other sample characteristics including matrix density, elemental X-ray emission and element location within the matrix were discussed in section 3.2.3 but have not been tested.

Samples must be placed flat against the detector window to avoid attenuation of the signal by air. A flat placement will facilitate reproduction of the analytical condition. Bench top systems normally require samples to be ground and pressed into discs avoiding this problem (Bruker 2010:31). Many cultural heritage objects are prohibited from sampling but have surfaces that do not facilitate optimal positioning thereby affecting data quality (Kaiser and Shugar 2012:450). An air gap between the X-ray source and the sample decreases intensity of the primary beam, increases attenuation of the emission signal and results in a misrepresentation of elemental consistencies. The primary X-ray beam is divergent and source-to-sample distance inversely affects the intensity (inverse square law) (Beckoff et al. 2006:94). Air molecules can absorb the emission energy from lower Z elements reducing or blocking their detection.

Corning Glass standard B is measured using settings A and B at 0 - 12 mm from the window at 2 mm increments. Wooden hobby match sticks, 2 mm thick, were chosen as a support because they do not contribute to characteristic peaks on the spectra. The sticks were placed outside of the HH-XRF analytical window to support the reference standard for the measurement sets at 2-12 mm distance. The glass specimen was

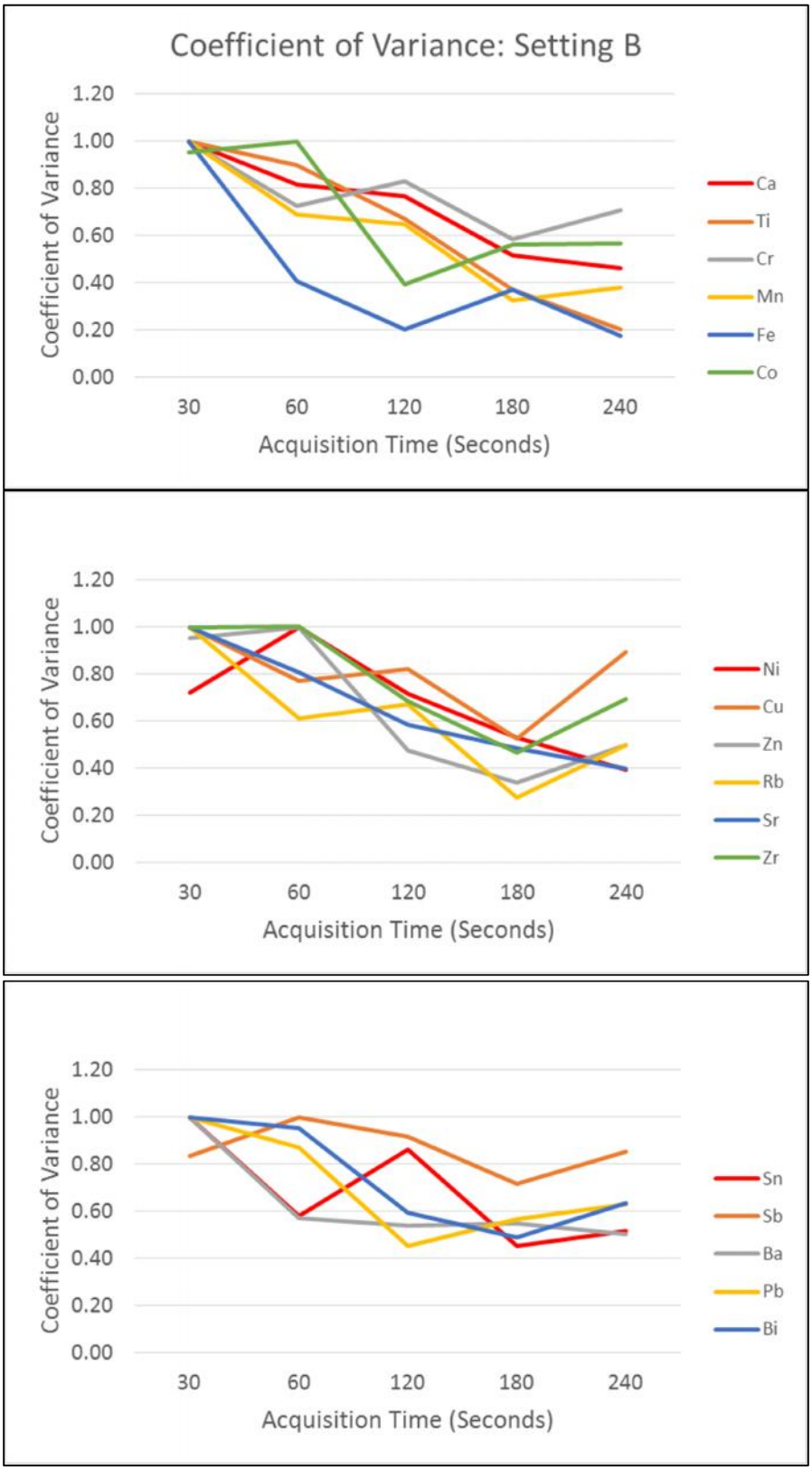

Fig. 6-23: Line graphs exhibiting the effects of acquisition time on coefficient of variance by element. Lowest C_v corresponds to highest precision for a set of measurements. Parameters are setting K using Corning Glass B as sample.

placed at each elevation and measured 10 times across the standard. The objective is to determine the effects of attenuation on the spectral data and to determine optimal source-to-sample distance for the sample.

The results for both settings (Tables 6-28 and 6-29) reveal the LDM is lowest with greatest distance and highest when the sample is directly on the window. The LDM is directly dependant on the photon counts hitting the detector. The SNR is generally greatest with direct placement of the sample as well (Figs. 6-24 and 6-25). The C_v (inversely related to precision) is generally lowest for the lower Z elements (sodium to potassium) with direct placement of the sample. The C_v of higher Z elements (greater than potassium) is scattered across various distances but reveal no patterning. Interpretation of the bi-variate quotients, taking into account the SNR and C_v for each element, indicate direct placement of the sample on the window for nearly all the elements. The exceptions to this are titanium (2 mm), chromium (12 mm) and manganese (2 mm) using setting B. These elements would not typically be analysed using setting B (higher voltage) and setting A results reveal best placement at 0 mm.

In conclusion, interpretation of the data indicate that the optimal distance for the individual elements in the sample is 0 mm. This distance produces minimal attenuation because of air.

6.6 Evaluation Discussion and Conclusions

HH-XRF is an emerging portable technology that allows non-destructive analysis of objects in-house (e.g. museum or lab) or in the field. There are potential limitations to its use in the form of chemical knowledge of the user as well as technology and physics (see Chapter 3). HH-XRF requires further material-specific explorations (see for example Domoney 2012; Mitchell et al. 2012; Morgenstein and Redmount 2005; Nazaroff 2010). Using various measuring parameters the technique was investigated to find the limits of its capabilities for the analysis of faience glazes using Corning Glass B as a surrogate because of its known post-production composition (see Table 4-1). The relatively low and high voltages of settings A and B were used with variations specific to each experiment.

Each individual HH-XRF unit will have a unique instrument signature that can be determined through the use of an analytical blank. These are elements associated with the unit construction which are fluoresced and can add to a resulting spectrum. These additions are typically small and insignificant when measuring major and minor elements. They can be an issue when measuring trace elements as the resulting

Table 6-28: Experimental testing of source-to-sample distance using setting A with Corning Glass B as the sample. Statistics include bi-variate quotient (Bi-Q), coefficient of variance (C_v), limit of determination of a method (±) and signal to noise ratio (SNR) and are based on the NPA for each element. Numbers in red indicate optimum value of the statistic for the specific element.

Source-to-Sample Distance: Low Voltage Attenuation of Signal Using Corning Glass B as Sample										
Parameters: 15 kV, 55 µA, Filter 2, Vacuum, 180 Seconds, 10 Measurements										
Source to Sample Distance		Na	Al	Si	P	K	Ca	Ti	Cr	Mn
0 mm	Bi-Q	1.05	1.26	1.22	1.42	1.08	1.63	1.36	1.23	1.31
	(±)	1.00	1.00	1.00	1.00	1.00	1.00	1.00	0.88	1.00
	C_v	0.05	0.26	0.22	0.42	0.08	0.63	0.36	0.23	0.31
	SNR	1.00	1.00	1.00	1.00	1.00	1.00	1.00	1.00	1.00
2 mm	Bi-Q	1.57	2.07	1.66	1.78	1.16	2.05	1.41	1.72	1.42
	(±)	0.58	0.74	0.54	0.81	0.78	0.83	0.62	1.00	0.81
	C_v	0.15	0.50	0.30	0.56	0.10	0.79	0.31	0.45	0.33
	SNR	0.26	0.47	0.46	0.72	0.64	0.75	0.76	0.63	0.80
4 mm	Bi-Q	15.58	3.82	2.38	2.14	1.35	2.18	1.61	1.74	1.43
	(±)	0.28	0.40	0.18	0.72	0.40	0.35	0.40	0.33	0.36
	C_v	0.55	0.64	0.27	0.68	0.12	0.59	0.31	0.27	0.23
	SNR	0.04	0.23	0.20	0.59	0.33	0.49	0.51	0.37	0.55
6 mm	Bi-Q	71.87	7.45	6.51	2.54	2.74	2.56	2.99	3.01	1.81
	(±)	0.17	0.38	0.06	0.85	0.31	0.15	0.54	0.45	0.26
	C_v	1.00	1.00	0.34	0.89	0.24	0.47	0.68	0.54	0.29
	SNR	0.01	0.16	0.06	0.58	0.14	0.30	0.34	0.27	0.35
8 mm	Bi-Q	26.57	6.58	25.57	2.03	21.20	5.80	3.42	3.34	3.13
	(±)	0.21	0.32	0.05	0.63	0.43	0.21	0.33	0.36	0.35
	C_v	0.70	0.89	0.65	0.64	1.00	1.00	0.59	0.53	0.54
	SNR	0.03	0.16	0.03	0.62	0.05	0.21	0.24	0.23	0.26
10 mm	Bi-Q	13.05	6.52	63.52	2.57		8.00	7.35	7.81	7.20
	(±)	0.28	0.32	0.04	1.00		0.09	0.35	0.42	0.31
	C_v	0.58	0.91	0.96	1.00		0.84	1.00	1.00	0.90
	SNR	0.05	0.16	0.02	0.64		0.12	0.16	0.15	0.15
12 mm	Bi-Q	15.21	4.66	64.91	2.01		10.06	7.57	7.07	11.08
	(±)	0.24	0.25	0.04	0.65		0.07	0.25	0.26	0.23
	C_v	0.59	0.67	1.00	0.66		0.82	0.87	0.75	1.00
	SNR	0.04	0.18	0.02	0.65		0.09	0.13	0.12	0.10

Table 6-28 Continued: Experimental testing of source-to-sample distance using setting A with Corning Glass B as the sample. Statistics include bi-variate quotient (Bi-Q), coefficient of variance (C_v), limit of determination of a method (±) and signal to noise ratio (SNR) and are based on the NPA for each element. Numbers in red indicate optimum value of the statistic for the specific element.

Source-to-Sample Distance: Low Voltage Attenuation of Signal Using Corning Glass B as Sample Parameters: 15 kV, 55 µA, Filter 2, Vacuum, 180 Seconds, 10 Measurements										
Source to Sample Distance		Fe	Co	Ni	Cu	Zn	Rh	Ba (Lα1)	Pb (Lα1)	Bi (Lα1)
0 mm	Bi-Q	1.57	1.48	1.70	1.76	1.71	1.78	1.32	1.26	1.32
	(±)	1.00	1.00	1.00	1.00	1.00	0.89	0.57	1.00	1.00
	C_v	0.57	0.48	0.70	0.76	0.71	0.67	0.32	0.26	0.32
	SNR	1.00	1.00	1.00	1.00	1.00	0.86	1.00	1.00	1.00
2 mm	Bi-Q	1.81	1.48	1.87	2.08	1.90	1.96	1.90	1.30	1.61
	(±)	0.83	0.62	0.75	0.84	0.79	1.00	1.00	0.74	0.68
	C_v	0.63	0.39	0.70	0.87	0.73	0.83	0.73	0.25	0.38
	SNR	0.78	0.81	0.80	0.80	0.81	0.86	0.81	0.84	0.63
4 mm	Bi-Q	1.83	2.07	1.90	1.97	1.79	1.58	2.07	1.35	1.98
	(±)	0.39	0.66	0.36	0.35	0.32	0.62	0.54	0.45	0.64
	C_v	0.46	0.63	0.51	0.56	0.46	0.52	0.60	0.23	0.50
	SNR	0.55	0.59	0.57	0.58	0.59	0.90	0.56	0.65	0.51
6 mm	Bi-Q	1.56	2.09	2.58	2.40	2.35	1.54	3.73	1.37	1.56
	(±)	0.12	0.31	0.27	0.21	0.23	0.59	0.55	0.20	0.51
	C_v	0.21	0.45	0.62	0.55	0.54	0.50	1.00	0.17	0.36
	SNR	0.38	0.41	0.39	0.39	0.40	0.94	0.37	0.45	0.64
8 mm	Bi-Q	3.41	3.96	4.17	4.44	4.37	2.04	3.89	2.14	1.91
	(±)	0.27	0.53	0.31	0.27	0.30	1.19	0.44	0.30	0.46
	C_v	0.69	1.00	0.96	1.00	1.00	1.00	0.93	0.37	0.45
	SNR	0.29	0.34	0.30	0.29	0.30	0.96	0.32	0.33	0.49
10 mm	Bi-Q	6.08	4.05	5.84	6.27	4.41	1.85	3.86	5.39	2.87
	(±)	0.25	0.27	0.20	0.12	0.12	1.00	0.49	0.54	0.48
	C_v	1.00	0.75	1.00	0.87	0.66	0.84	1.00	1.00	0.69
	SNR	0.20	0.24	0.21	0.17	0.19	0.98	0.35	0.23	0.37
12 mm	Bi-Q	5.42	4.35	6.42	8.58	4.44	1.66	3.62	8.86	3.62
	(±)	0.12	0.24	0.14	0.08	0.06	0.80	0.36	0.23	0.69
	C_v	0.66	0.75	0.91	0.84	0.47	0.66	0.82	0.89	1.00
	SNR	0.15	0.22	0.17	0.11	0.14	1.00	0.32	0.11	0.38

Table 6-29: Experimental testing of source-to-sample distance using setting B with Corning Glass B as the sample. Statistics include bi-variate quotient (Bi-Q), coefficient of variance (C_v), limit of determination of a method (±) and signal to noise ratio (SNR) and are based on the NPA for each element. Numbers in red indicate optimum value of the statistic for the specific element.

Source-to-Sample Distance: High Voltage Attenuation of Signal Using Corning Glass B as Sample

Parameters: 40 kV, 30 µA, Filter 3, 180 Seconds, 10 Measurements

Source to Sample Distance		Ca	Ti	Cr	Mn	Fe	Co	Ni	Cu	Zn
0 mm	Bi-Q	1.22	1.96	2.37	1.35	1.33	1.18	1.22	1.51	1.23
	(±)	1.00	1.00	1.00	1.00	1.00	0.92	1.00	1.00	1.00
	Cv	0.22	0.96	1.00	0.35	0.33	0.18	0.22	0.51	0.23
	SNR	1.00	1.00	0.73	1.00	1.00	1.00	1.00	1.00	1.00
2 mm	Bi-Q	1.31	1.62	2.08	1.29	1.36	1.35	1.27	1.64	1.35
	(±)	0.72	0.41	0.82	0.53	0.71	1.00	0.76	0.77	0.97
	Cv	0.24	0.52	0.87	0.25	0.32	0.28	0.23	0.54	0.30
	SNR	0.78	0.85	0.80	0.87	0.87	0.81	0.85	0.85	0.86
4 mm	Bi-Q	1.45	1.91	1.64	1.52	1.66	1.53	1.22	1.97	1.45
	(±)	0.48	0.52	0.31	0.45	0.69	0.75	0.33	0.60	0.65
	Cv	0.26	0.78	0.45	0.33	0.46	0.33	0.15	0.65	0.30
	SNR	0.58	0.87	0.69	0.65	0.69	0.62	0.68	0.67	0.68
6 mm	Bi-Q	2.25	2.45	1.72	2.29	2.00	1.89	1.68	2.12	1.84
	(±)	0.43	0.40	0.48	0.54	0.52	0.48	0.42	0.31	0.57
	Cv	0.46	0.96	0.65	0.64	0.54	0.38	0.33	0.56	0.44
	SNR	0.37	0.66	0.90	0.50	0.54	0.43	0.49	0.50	0.52
8 mm	Bi-Q	1.97	2.20	1.48	3.00	2.14	2.37	2.34	2.94	1.97
	(±)	0.14	0.37	0.29	0.39	0.35	0.43	0.45	0.28	0.36
	Cv	0.25	0.92	0.45	0.72	0.51	0.48	0.52	0.75	0.40
	SNR	0.26	0.76	0.92	0.36	0.45	0.35	0.39	0.39	0.42
10 mm	Bi-Q	7.24	2.42	1.74	4.25	3.47	4.69	3.45	4.59	2.68
	(±)	0.31	0.34	0.29	0.24	0.41	0.45	0.35	0.23	0.29
	Cv	1.00	1.00	0.58	0.76	0.87	0.86	0.67	1.00	0.52
	SNR	0.16	0.70	0.78	0.24	0.35	0.23	0.27	0.28	0.31
12 mm	Bi-Q	9.06	2.44	1.41	6.19	4.08	6.33	5.85	4.31	5.05
	(±)	0.20	0.26	0.22	0.22	0.37	0.36	0.33	0.10	0.38
	Cv	1.00	0.97	0.41	1.00	1.00	1.00	1.00	0.70	1.00
	SNR	0.12	0.68	1.00	0.19	0.32	0.19	0.21	0.21	0.25

Table 6-29 Continued: Experimental testing of source-to-sample distance using setting B with Corning Glass B as the sample. Statistics include bi-variate quotient (Bi-Q), coefficient of variance (C_v), limit of determination of a method (±) and signal to noise ratio (SNR) and are based on the NPA for each element. Numbers in red indicate optimum value of the statistic for the specific element.

Source-to-Sample Distance: High Voltage Attenuation of Signal Using Corning Glass B as Sample Parameters: 40 kV, 30 µA, Filter 3, 60 Seconds, 10 Measurements										
Source to Sample Distance		Rb	Sr	Zr	Rh	Sn	Sb	Ba	Pb (Lα1)	Bi (Lα1)
0 mm	Bi-Q	1.21	1.14	1.44	1.37	1.21	1.73	1.31	1.46	1.27
	(±)	1.00	0.63	1.00	0.98	0.81	1.00	1.00	1.00	0.80
	Cv	0.21	0.14	0.44	0.37	0.21	0.73	0.31	0.46	0.27
	SNR	1.00	1.00	1.00	1.00	1.00	1.00	1.00	1.00	1.00
2 mm	Bi-Q	1.26	1.38	1.74	1.81	1.38	2.19	1.43	1.56	1.59
	(±)	0.84	1.00	0.97	1.00	0.89	0.91	0.84	0.72	1.00
	Cv	0.23	0.31	0.60	0.58	0.31	0.94	0.35	0.46	0.48
	SNR	0.87	0.83	0.81	0.71	0.81	0.79	0.82	0.82	0.82
4 mm	Bi-Q	1.32	1.42	1.71	1.91	1.82	2.39	1.67	1.54	1.76
	(±)	0.57	0.55	0.49	0.74	1.00	0.52	0.68	0.37	0.67
	Cv	0.23	0.27	0.45	0.56	0.52	0.83	0.44	0.36	0.49
	SNR	0.73	0.63	0.64	0.62	0.63	0.60	0.65	0.66	0.65
6 mm	Bi-Q	1.87	1.73	3.10	2.49	2.46	3.26	2.16	2.19	2.36
	(±)	0.64	0.45	0.67	0.60	0.82	0.39	0.46	0.36	0.58
	Cv	0.46	0.35	1.00	0.70	0.69	1.00	0.52	0.58	0.67
	SNR	0.52	0.48	0.48	0.47	0.47	0.44	0.45	0.48	0.49
8 mm	Bi-Q	1.90	1.75	2.56	3.47	3.46	3.19	2.00	1.69	3.20
	(±)	0.43	0.25	0.27	0.60	0.79	0.20	0.37	0.11	0.49
	Cv	0.41	0.29	0.59	0.97	0.94	0.76	0.47	0.26	0.85
	SNR	0.46	0.39	0.38	0.39	0.38	0.35	0.47	0.38	0.39
10 mm	Bi-Q	5.31	2.91	3.12	4.10	4.17	4.17	2.33	4.71	4.04
	(±)	0.35	0.28	0.17	0.39	0.59	0.16	0.27	0.26	0.37
	Cv	0.88	0.52	0.59	0.93	1.00	0.89	0.49	1.00	0.92
	SNR	0.20	0.27	0.28	0.30	0.32	0.28	0.37	0.27	0.30
12 mm	Bi-Q	7.71	5.82	5.37	5.03	3.50	4.18	4.50	4.38	5.31
	(±)	0.24	0.35	0.18	0.31	0.24	0.08	0.36	0.12	0.25
	Cv	1.00	1.00	0.92	1.00	0.60	0.67	1.00	0.70	1.00
	SNR	0.15	0.21	0.21	0.25	0.24	0.21	0.29	0.21	0.23

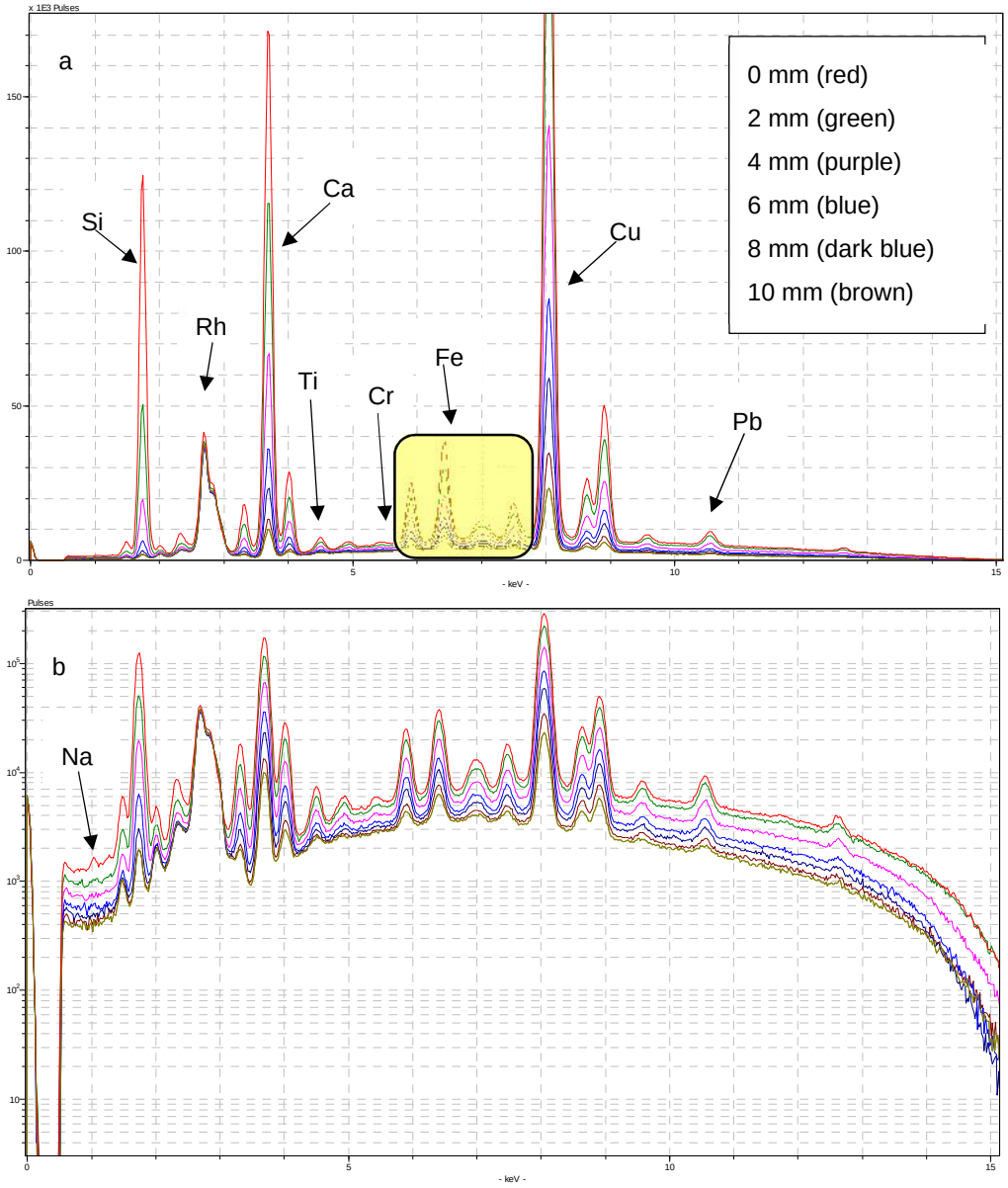

Fig. 6-24: Fig. a is a standard spectra of Corning Glass B using setting A with various distances between the sample and the detector: Fig. b is the same spectra using logrithmic scaling to reveal further detail not seen in the standard spectra. Some peaks remain unlabelled to present a set of clear spectra. Fig. c is the region between 5.6 and 7.7 keV revealing the peaks for manganese, iron, cobalt and nickel.

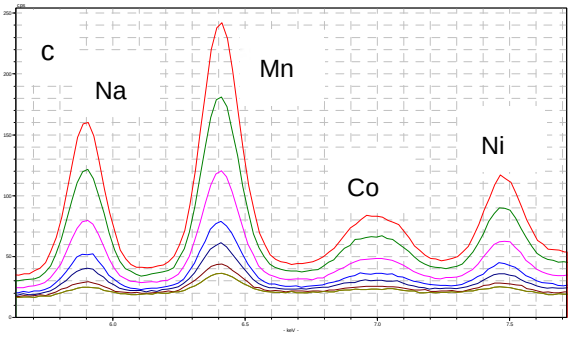

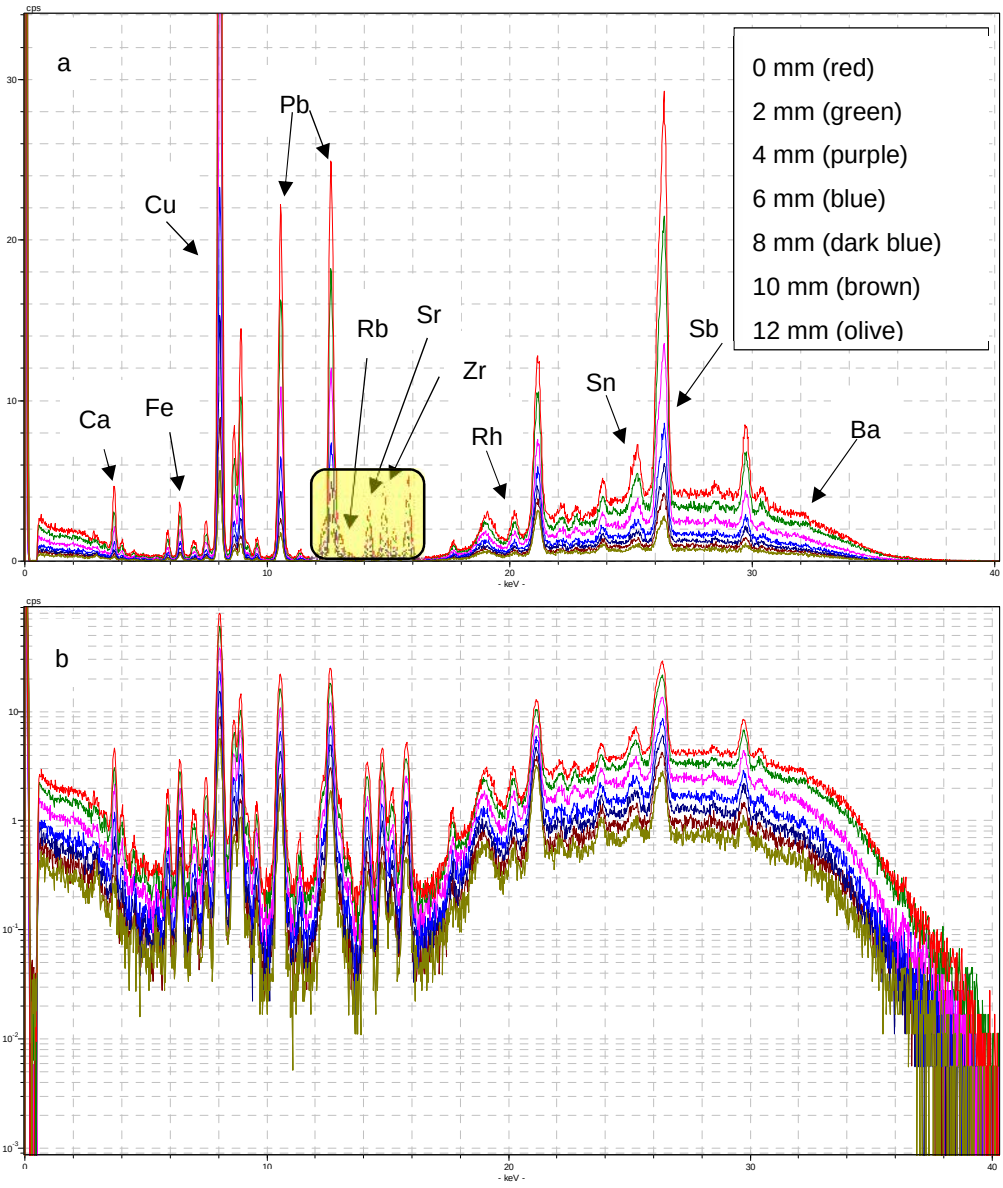

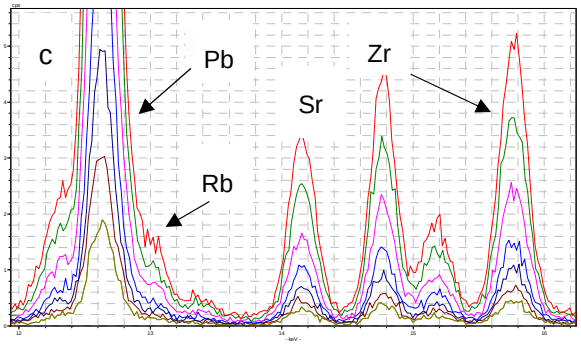

Fig. 6-25: Fig. a is a standard spectra of Corning Glass B using setting B with various distances between the sample and the detector: Fig. b is the same spectra using a logrithmic scale. Some peaks remain unlabelled to present a set of clear spectra. Fig. c is the region between 12 and 16.2 keV revealing the peaks for lead, rubidium, strontium and zirconium.

sample consistencies will be inaccurate. A total of 17 elements (see Table 6-2) have been identified in the instrument signature of the particular HH-XRF unit used for the evaluation. The characteristic peaks for all the signature elements are significantly smaller than the rhodium lines and the Compton peak indicating negligible effect on major and minor elements found in samples. The signature does not have to be removed from the analysis if using some form of cluster analysis with NPA and the same instrument and settings. They will remain constant throughout the measurements and retention/removal of them should not affect the cluster analysis. However, if the intent is to use calibration to produce wt% or ppm results, these signature contributions have to be dealt with and can be removed by using a blank to determine impact based on cps, then subtracting those cps counts from the final analytical counts prior to calibration of results.

Blanks were measured as a part of the instrument signature experiments. A filled water bottle (PET) was suggested (Pers. Comm. Lee Drake) for use in this capacity. The contents were emptied and the bottle was filled with deionized water. A cellulose pellet was produced to compare against the water bottle results to see if either contributed to the instrument signature (see Table 6-5). The cellulose pellet contributed silicon and chromium to the instrument signature, probably as a remnant of the cellulose while alive in plant form. The water bottle contributed antimony and barium, both a part of the processing of PET water bottles. All contributions are far below the rhodium (target) results indicating negligible effects during analysis.

Filters (see Table 3-1) were tested as part of the instrument signature determination to see if they contributed to the spectra. Filters are designed to attenuate some signals so that others can be enhanced. Using setting A (see Table 6-3), titanium in filter 4 appears to be the only instrument signature element that was enhanced because of titanium in the filter construction. Beyond this, filters failed to noticeably contribute to the spectra using setting A. The aluminium, titanium and copper found in the filters most likely did contribute but attenuation coupled with low voltage resulted in no instrument signature element containing higher cps than measurements without a filter beyond that of titanium in filter 4. In other words, all results were lower with filters than without using setting A with the exception of titanium in filter 4. Filter 4 increased the titanium cps by 50%, but when measured against Corning Glass B (titanium = .089 wt%) there is a 23% drop in the cps. This reveals that titanium, as a part of the instrument signature, has had little effect (~11.5%) on the detection of it in trace levels in the Corning Glass B standard. To put it into perspective, this is the equivalent of .01

wt% contribution of the titanium instrument signature. Testing of filters with setting B (see Table 6-4) reveal an increase in titanium and chromium with filter 4 use.

Evaluating the filters with setting A using Corning Glass B as a surrogate for faience (see Table 6-6) exhibits greatest quantity of element detection with no filter. The use of a filter attenuates the signal and make detection of some elements impossible using the chosen parameters. The enhancement of titanium seen with filter 4 in the instrument signature experiments is not repeated with a sample on the stage. Undoubtable there has been some contribution of the filter but the attenuation had a greater effect resulting in 23% lower cps for titanium with filter 4. Titanium levels in Corning Glass B is 0.089 wt% and at trace levels. Measurements with setting A are optimally conducted without use of a filter (filter 2) because it facilitates the detection of the greatest number of elements in the glass sample and provides the greatest SNR for most of those elements; Chlorine (filter 4), chromium (filter 1), barium (filter 4) and lead (filter 4) being the exceptions.

Most of the elements with setting B can be separated into three filter groups based on highest SNR: potassium – manganese (filter 2); iron through rubidium (filter 4) and strontium through bismuth (filter 5). However for a single setting, filter 3 is optimal because it detects the greatest number of elements which will be useful in categorizing the samples based on elements and NPA.

The HH-XRF unit was tested for machine drift by comparing NPA and SNR of measurements taken 2 hours, 2 days and 5 months apart. The %difference for most of the elements is below 4% for the 2 day and 5 month term durations. The same differences were below 2% for the 2 hour duration. Conversion of the NPA to wt% will reduce the %difference further for most elements. These small differences are acceptable for the relatively low voltage generation of the HH-XRF.

End windows cover the HH-XRF X-ray beam aperture and provides protection to the detector and X-ray tube. It is required for the formation of a vacuum within the unit to remove the column of air (source of attenuation) from between the end window and the detector. Two types of windows (gridded and ungridded) are available for the Bruker Tracer III-SD depending on whether the unit comes with a built-in grid. The gridded window is approximately twice as thick as the ungridded window and will attenuate more of the X-ray signal. Window attenuation is not a concern when using higher voltage to measure metal samples or higher Z elements but the difference can readily be seen when using lower voltage to measure lower Z elements such as those typically associated with glass and glazes (e.g. potassium, calcium and silicon). The

HH-XRF unit in the study comes with a grid and does not require the gridded window. Window type will not affect the results of the analyses used for comparative studies as long as the window type is consistently used throughout the process. The end window type is usually not reported in published HH-XRF methodologies but should be considered because it will have an effect when attempting to recreate the analytical condition for comparative studies.

Voltage and current settings were tested in 5 unit increments. The parameter constants correspond to settings A and B with only voltage and current as separate variables. Interpretation of the results suggest the low Z elements (sodium to iron) are optimally measured with 15 kV, 50 µA and a vacuum to enable detection of the element group. A voltage of 25 kV resulted in greater SNR and lower C_v for elements between aluminium and iron but eliminated the detection of sodium and magnesium. A current of 55 µA produced higher SNR, though not significantly. The bi-variate quotient, taking into account optimum SNR and C_v, indicated 50 µA as a better compromise. Precision was the driving force in this calculation and was much worse at 55 µA. Conversely, Scott's research (2012)[7] suggests that 50 µA produced the lowest signal/background ratio, although it was most stable at this current. The reduction of the ratio was due to an increase in the peak heights and the background. Scott did conclude that current should be based on settings that produce the greatest stability.

The high Z elements (cobalt to bismuth) are optimally measured using 40 kV in conjunction with 30 µA and filter 3. The elements of this group exhibited higher SNR and lower C_v at higher voltages and currents. However, increases in voltage and current will result in a significantly reduced lifespan of the filament within the X-ray tube. The use of filter 3 for higher voltage measurements is discussed in section 6.3.2.

The optimum acquisition time is a balance between precision and convenience. An acquisition time of 180 seconds with both settings provides sufficient precision for elements of the Corning Glass B standard. An increase in the acquisition time would result in greater precision and SNR for most of the elements but the difference would be so small as to become time inefficient. Scott (2012:270-272) found that the signal/background ratio was dependant on the acquisition time; The optimal current for

[7] Scott was using a direct peak height to background level ratio for the calculations. Scott later informed me that using SNR was a better predictor and offered a detection capability as well (i.e. SNR>3 = detection, SNR>10 = quantifiable data). Scott used the Tracer III-SD with Rh target and 40 kV with a vacuum for all measurements. Current and acquisition time were variables.

aluminium, for example, is 5 µA at 20 second acquisition time, and 10 µA at 40 second acquisition time.

Interpretation of the data indicate that the optimal distance for the individual elements in the sample is 0 mm. This distance produces minimal attenuation because of air. The best SNR for bulk analysis is produced when the attenuation is reduced as much as possible and the analyte is positioned directly on the end window. This was expected. What was not expected is that lead produced a greater ratio at 2 mm. This is probably because of attenuation of the lower Z photons and over-representation of the lead. Titanium producing greatest ratio at 10 mm was not expected but can be explained as instrument interference directly interacting with the detector while other photons from the sample are attenuated. Domoney (2012:115)[8] determined that the optimum distance for the analysis of porcelain glazes was between 0-3 mm, 0 mm being ideal.

It has been noted that titanium is a bit of an outlier with some of the testing in this report. It has appeared as an unexplained peak with the end window testing, it has exhibited higher than expected differences with changes in acquisition time, it has a greater magnitude of error with long and utlralong term drift testing, and is an anomaly with the attenuation testing exhibiting greatest disparity between characteristic peak and background at 10 mm distance from the end window. Some of this could be because of it being a component in the analyser unit but one would expect this to reduce or cushion the affect in other experiments where it is revealed as an extreme. The effects of titanium in this evaluation have yet to be explained but the analyst should be aware of these properties before conducting analysis. It is apparent that the instrument signature for titanium does not affect the detection of titanium at 44 ppm (0.0044 wt%) and should not affect future analyses based on a comparison of four glass reference materials (Corning Glass A and B, and NIST Glass 610 and 612) using setting A normalized at 4.22 kV (Fig. 6-26).

The following parameters provide the greatest SNR and precision as well as the highest number of elements detected when measuring Corning Glass B, and by extension, blue faience glazes.

- For low Z elements (sodium to iron):

[8] Domoney (2012) used an X-MET 5100 analyzer which provides the user with six parameter settings and 13 methods from which to choose. Soil FP (45kV, 15µA, 25µm Fe filter) and Soil LE (15/45kV, 45/15µA, 500µmAl/25µm Fe filter (alternating conditions) programs were used during the evaluation of the unit.

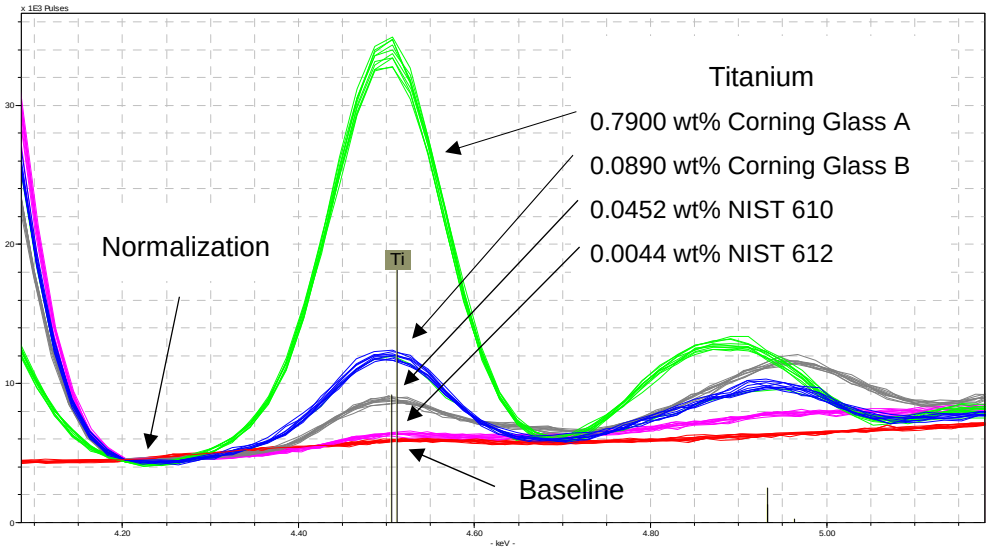

Fig. 6-26: Spectra of Corning Glass A (green) and B (blue), NIST 610 (grey) and 612 (purple) and the PET blank (red). The spectra are normalized in an area devoid of characteristic peaks but in close proximity of the titanium kα peaks (4.22 keV).

- Voltage: 15 kV
- Current: 50 µA
- Filter: None
- Air Purge: Vacuum or helium
- Acquisition Time: 180 seconds.

- For general bulk analysis and detection of higher Z elements (cobalt and higher Z elements):
  - Voltage: 40 kV
  - Current: 30 µA
  - Filter: 3 (12 mil aluminium, 1 mil titanium, 6 mil copper)
  - Air Purge: None
  - Acquisition Time: 180 seconds.

Analysis of individual elements of interest may require different parameters based on the findings of this report.

For safety reasons, local rules for Cardiff University (XRF Risk Assessment based on OSHEU Guidance Documents RP0, RP1, RP3, RP6 and RP7) or the institution where the analyser unit is being used need to be reviewed and possibly signed prior to use. All measurements should be taken in a bench top stand or on the detachable stage

with the X-ray shield in place. Only the user should handle the unit and all bystanders should be beyond a 3 m radius. After setup the following workflow should be implemented:

1. Use XRayOps (version 1.2.15 or later) to optimize the beam according to the parameters chosen (e.g. kV, µA, filter, etc. A pulse length of 200 ±2 should be maintained by manipulating the beam properties (i.e. high voltage and current filament settings).
2. Use S1PXRF (version 3.8.30 or later) to collect data on the reference materials to check drift and monitor stability. Data will be saved as .pdz files.
3. Use S1PXRF to collect data on objects. Run several measurements per object: three, five or 10 per object. A greater number of measurements per object will increase the averaging power when anomalies are encountered. Use same number of measurements for all objects. Data will be saved as .pdz files.
4. Check window for contamination between measurements. Check pump readings to monitor punctures to the end window when using a vacuum.
5. Reference standards are measured at the beginning and end of each session to facilitate monitoring of drift and generally stability of the HH-XRF unit.
6. Spectra characteristic peaks can be identified while in S1PXRF but will have to be re-identified if importing in Artax Spectra. Note: Use of the Tracer III-SD negates the requirement of converting .pdf files into .txt (Artax) files (Pers. Comm. Bruce Kaiser).
7. Once imported into Artax Spectra (vers. 7.4 or later) the characteristic peaks will have to be identified again. Bayesian deconvolution can be used to determine presence of elements.
8. Spectra are analysed using a selected method within Artax to produce NPA which can be exported to excel for further data mining.

The HH-XRF is not an instrument that can be used straight out of the box. It requires some forethought and understanding about the instrument and the analyte. The evaluation of the HH-XRF has revealed that even the results in this report require some interpretation and consideration.

Chapter 7: Replicated and Archaeological Faience Glaze Analysis

7.1 Introduction

Faience glaze and body replications were produced to provide a known analyte for the evaluation of HH-XRF. After experimentation with several glaze mixtures, three glaze batches (one copper coloured, two cobalt coloured and consisting of 30 total replicated glazes) matching the colour of some of the blue faience sherds from Saqqara (Fig. 7-1; Tables 7-1 and 7-2) were selected for further analysis. The 30 replicated faience glazes were compared to an assemblage of 24 selected archaeological faience sherds from Saqqara representing mostly blue (but also green, purple and yellow) colours. Both sample sets were examined to determine glaze structures and compositional profiles using visual examination, optical microscopy, HH-XRF, SEM-BSE and EDS. Glaze structures and compositional profiles have been used in the literature to help determine glazing technique (Kaczmarczyk and Vandiver 2008; Tite et al. 2007:1572;

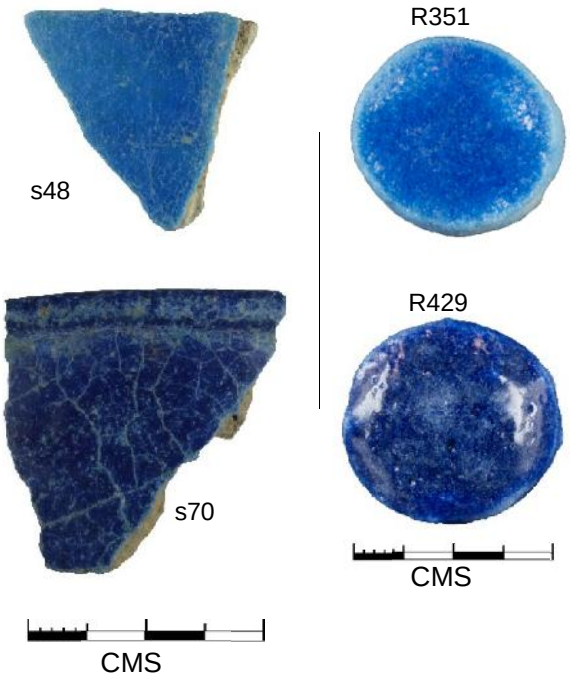

Fig. 7-1: A comparison of glaze colours between archaeological faience (s48 and s70) and replicated samples (R351 (copper coloured) and R429 (cobalt coloured)).

Table 7-1: Munsell colour designations for replicated faience glazes.

Munsell Colour Designations Replicated Faience Glazes				
Sample	Glaze Batch	Colourant	Munsell Colour Name	Munsell Colour Designation
R327	Glaze 03	Copper	Blue	2.5PB 4/10
R328	Glaze 03	Copper	Blue	10B 5/10
R340	Glaze 03	Copper	Blue	10B 5/12
R342	Glaze 03	Copper	Blue	10B 5/10
R349	Glaze 03	Copper	Blue	2.5PB 4/10
R351	Glaze 03	Copper	Blue	2.5PB 4/10
R356	Glaze 03	Copper	Blue	10B 4/8
R359	Glaze 03	Copper	Blue	2.5PB 4/10
R360	Glaze 03	Copper	Blue	10B 5/6
R363	Glaze 03	Copper	Blue	10B 5/6
R364	Glaze 03	Copper	Blue	10B 4/8
R367	Glaze 03	Copper	Blue	10B 4/8
R383	Glaze 03	Copper	Blue	10B 4/8
R384	Glaze 03	Copper	Blue	10B 5/10
R386	Glaze 03	Copper	Blue	10B 4/8
R388	Glaze 03	Copper	Blue	10B 5/10
R390	Glaze 03	Copper	Blue	10B 4/8
R392	Glaze 03	Copper	Blue	10B 5/10
R406	Glaze 07	Cobalt	Dark Blue	5PB 3/8
R408	Glaze 07	Cobalt	Dark Blue	5PB 3/8
R411	Glaze 07	Cobalt	Dark Blue	5PB 3/8
R412	Glaze 07	Cobalt	Dark Blue	5PB 3/8
R415	Glaze 07	Cobalt	Dark Blue	5PB 3/8
R416	Glaze 07	Cobalt	Dark Blue	5PB 3/8
R418	Glaze 05	Cobalt	Dark Blue	5PB 3/8
R421	Glaze 05	Cobalt	Dark Blue	5PB 3/8
R423	Glaze 05	Cobalt	Dark Blue	5PB 3/8
R424	Glaze 05	Cobalt	Dark Blue	5PB 3/8
R426	Glaze 05	Cobalt	Dark Blue	5PB 3/8
R429	Glaze 05	Cobalt	Dark Blue	5PB 3/8

Vandiver 1998, 2008). In this project, compositional profiles are measured to determine if there is a difference between what a surface analysis (i.e. HH-XRF) may detect versus a cross-sectional analysis (i.e. SEM-EDS with sampling) and to describe elemental migration in the glaze melt during firing. SEM-EDS (wt%) is used to recreate replicate batch recipes and to determine if analytical results of archaeological materials can be back-engineered to reproduce an approximate recipe used during the initial

Table 7-2: Munsell colour designations for archaeological faience glazes from Saqqara.

Munsell Colour Designations Saqqara Faience Glazes				
Sherd	Munsell Colour Name	Main Colourant(s)	Munsell Colour Designation	Empirical Colour Designation
s12	Bluish Green	Copper/Lead Antimonate	5BG 8/4	Bluish Green
s17	Blue	Copper	7.5B 6/8	Blue
s20	Green	Copper/Lead Antimonate	7.5G 6/6	Green
s21	Reddish Purple	Manganese	7.5RP 4/4	Purple
s22	Bluish Green	Copper	7.5BG 7/4	Turquoise
s31	Blue	Copper	2.5B 7/6	Turquoise
s42	Green	Copper/Lead Antimonate	2.5G 8/4	Green
s45	Yellow	Lead Antimonate	7.5Y 8.5/4	Yellowish Green
s48	Blue	Copper/Cobalt	7.5B 5/10	Dark Blue
s53	Bluish Green	Copper	10BG 8/4	Turquoise
s70	Purplish Blue	Cobalt	5PB 3/8	Ultra-Marine Blue
s72	Purplish Blue	Cobalt	5PB 4/10	Purplish Blue
s74	Purplish Blue	Cobalt	5PB 3/8	Purplish Blue
s78	Purplish Blue/Blue	Cobalt	10B 4/8 and 2.5PB 2.5/4	Ultra-Marine Blue
s80	Bluish Green	Copper	7.5BG 9/2	Turquoise
s81	Bluish Green	Copper	5BG 9/2	Bluish Green
s82	Blue	Copper	5B 6/8	Blue
s83	Blue	Copper	2.5B 7/6	Turquoise
s84	Blue	Copper	7.5B 6/10	Blue
s85	Blue	Copper	7.5B 6/10	Dark Blue
s87	Blue	Copper	2.5B 7/6	Blue
s89	Blue	Copper	2.5B 7/6	Blue
s90	Blue	Copper	7.5B 5/10	Blue
s91	Bluish Green	Copper	10BG 7/6	Turquoise

production. Fractionation of the glaze components during firing is explored as a means to this end.

7.2 Replicated and Archaeological Glaze Colours

The first recognized aspect of any glaze is its colour. Faience glaze colours have been described, for example, as dark blue and ultra-marine blue or green and apple green but it is often difficult to define the line between the colours without a system. Munsell colour determinations offers a systematic method that can be used with glaze colour comparisons. The colour of the faience glazes in this study were determined by using Munsell colour designations obtained by the process described in section 4.4.3. It became readily evident that the Munsell designation are a good means for comparing colours but the Munsell designation colour names (one name can be attributed to many designations) cannot account for the ability of the human eye to discern multitudes of hues.

Munsell designations for the replicated materials are found in Table 7-1. The replicated glaze hues for glaze samples R327 – R360 corresponded with the thickness of the glaze. The thickness of the glaze did not correspond with the colour designation beyond these first nine glazes. The state of the body before glost firing (bisque fired or raw) and the various kiln parameters (e.g. peak temperature, soaking time) were not factors.

Munsell designations for the archaeological glazes from Saqqara are in Table 7-2. The Munsell colour designations reflected subtle hue changes recognized by the human eye. The Munsell colour names, on the other hand, are defined by groups of Munsell colour designations. For example, the colour name of ‘blue’ is given to a variety of hues, chroma and values. The Munsell colour designations are sufficient for identifying colours for comparison with other studies but the Munsell colour names are inadequate for this study and empirical colour designations were used instead.

7.3 Macrostructures

Appendices A and B contain tables exhibiting structural data for the replicated faience glazes and archaeological faience sherds used in the study. The replicated samples are ground sand discs (~ 2 cm diameter and 1 cm thick) covered in a glaze on the top and sides except where manufacturing processes resulted in pin holes or creeping glaze (Fig. 7-2). All the replicated glazes exhibit either a smooth surface or a rough textured surface resembling an orange peel. Most of the glazes with a rough surface were thinly applied with a surface texture contoured by the underlying ground sand body. The rough surface of thickly applied glazes were mostly a result of erupting bubbles. Four sample glazes have pin holes that reveal the body substrate (R340, R418, R424 and R426) and two of these exhibit a rough surface (R418 and R424). Only two samples exhibit glaze crawling and are associated with thinly applied glazes (R356 and R418).

Some of the archaeological sherds exhibit full profiles and represent vessel forms identified by Nenna (2013 and 2014) but most are unidentified body, rim and basal sherds. The morphology of the basal sherds include either flat bases or foot rings. Most of these basal sherds contain firing evidence on the exterior consisting of either rough surfaces where kiln setters were attached or with intact setters (Fig. 7-3). Sherd s78 contains an attached clay setter. Sherd s91, representing a bowl, has setter marks on the exterior and interior. Most of the foot ring sherds exhibit glaze pooling; an indicator of application glazing. Prefired carving of some sherds is evident; sherd s12 has suspension holes and sherd s81 exhibits drilling through the lid handle (Fig. 7-4).

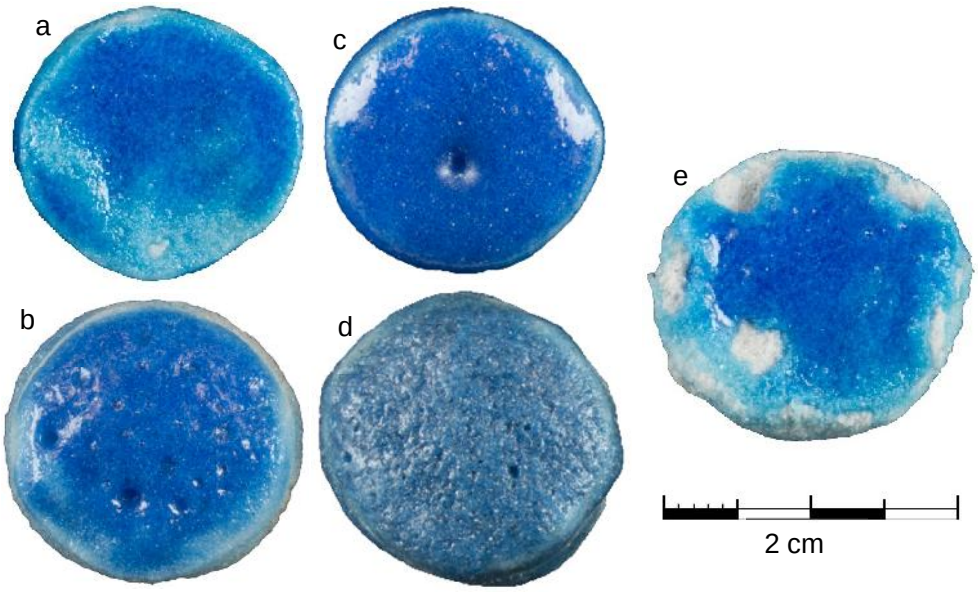

Fig. 7-2: Representative glaze defects of the replicated faience glazes. Sample R340 (a) exhibits a relatively smooth glaze surface with a pin hole. Sample R393 (b) exhibits a relatively rough orange peel surface because of erupting bubbles. Sample R343 (c) exhibits a smooth surface with a single erupting bubble. Sample R363 (d) exhibits a rough orange peel like surface revealing body substrate topography because of thinness of the glaze. The surface of replicated glazes were generally smooth or exhibited an orange peel-like surface texture. Sample R356 (e) exhibits a relatively smooth surface with some glaze crawling around the edges.

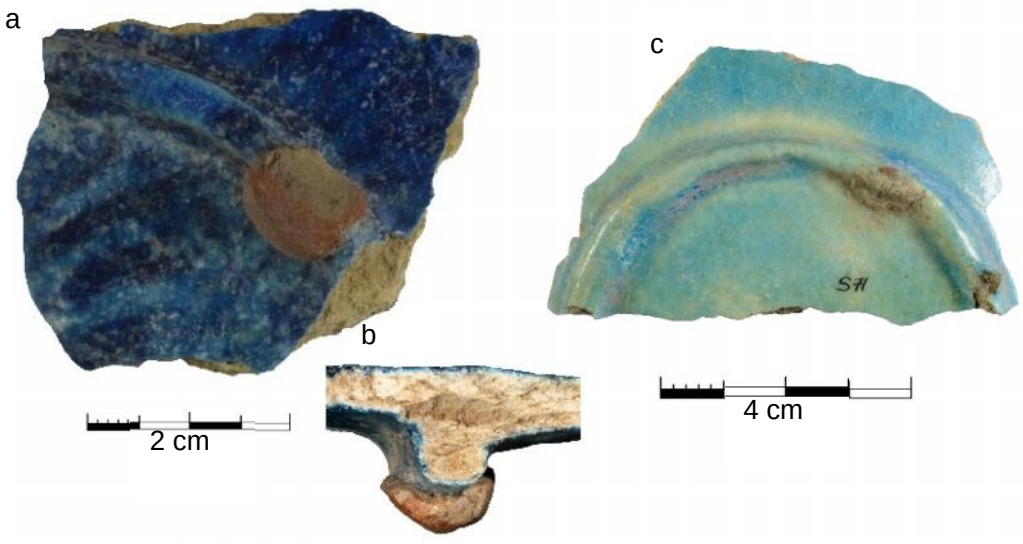

Fig. 7-3: Setters on archaeological faience. Sherd s78 (a and b) exhibits a complete setter on the foot ring. Sherd s90 exhibits the remnant of a foot ring setter where it had been removed. Setters provide an indication of how the vessels were fired.

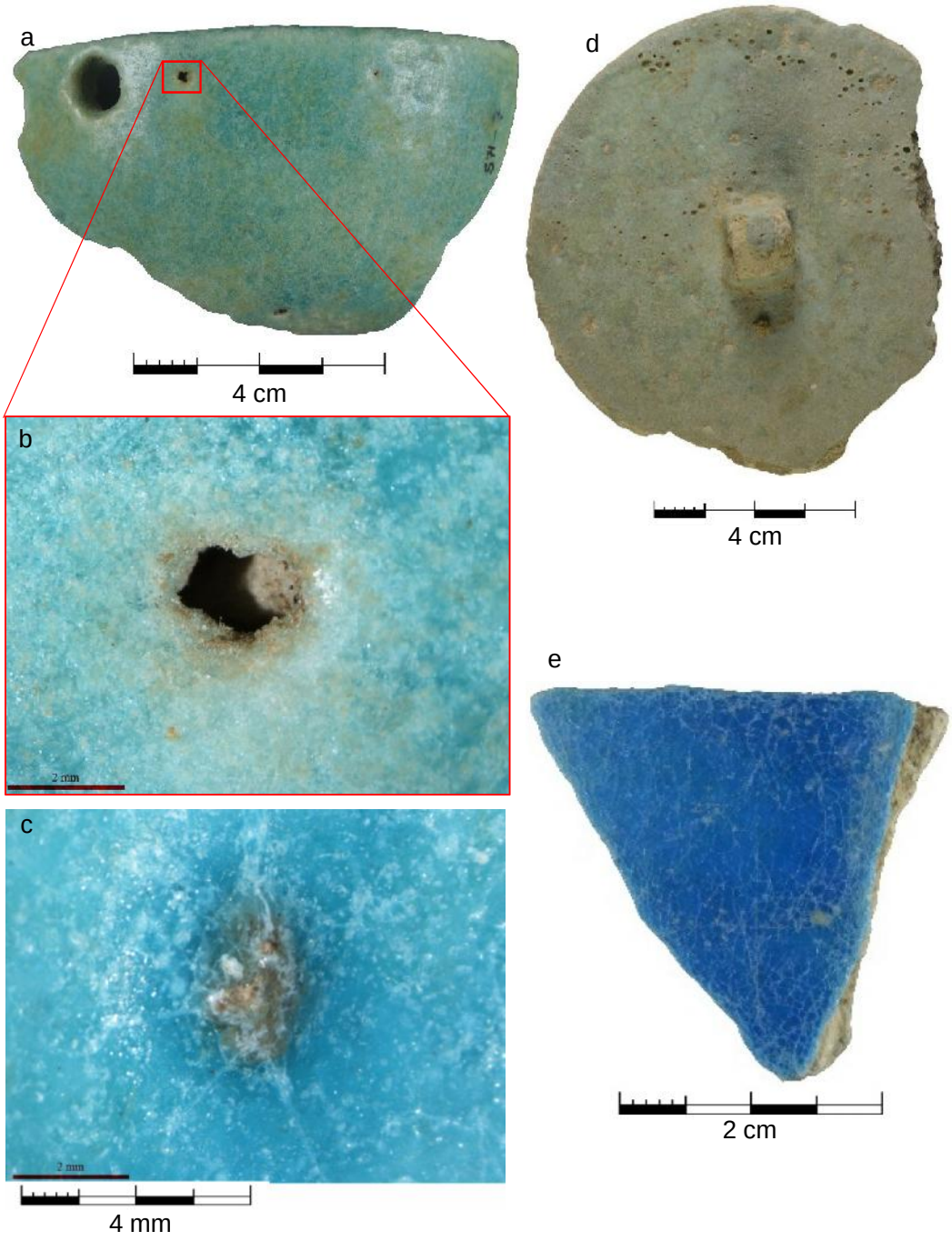

Fig. 7-4: Representative glaze defects in the Saqqara Faience assemblage. Sherd s12 (a) exhibits crizzling, pin holes (a and b) and embedded materials (c). Sherd s81 (d) exhibits erupting bubbles on the surface and sherd s48 (e) exhibits crizzling.

The glazes on the sherds exhibit complete coverage with no intentional ending lines or breaks. Approximately half of the glazes exhibit pinholes, or small voids in glaze coverage exposing the body material beneath (see Fig. 7-4). Over half of the glazes exhibit crazing and one (s17) exhibits crawling where the glaze melt pulled away from the body (an exaggerated pinhole). Three sherds exhibit a hard thin white deposit on the glaze surface.

7.4 Microstructures

Microscopic examination of the replicate and archaeological glazes reveal all to be transparent, many with erupting bubbles on the surface (Fig. 7-5). Unreacted quartz particles are visible below the glaze surface on some specimens. A third of the archaeological glazes exhibit embedded materials within the glaze. All the ultra-marine blue (cobalt coloured) glazes exhibit faint iridescence indicative of alkali depletion and gel layer formation during deposition. The purple (s21) and one green sherd (s42) exhibit the same phenomena.

Figure 7-5 exhibits a comparison between a replicated glaze and an archaeological glaze. The surface of the archaeological glaze has been exposed to use and burial abrasion reducing the transparency. The archaeological surface exhibits crizzling which appears as cracks at x40 optical magnification. Bubbles are apparent in both images and unreacted quartz particles are easy to discern in the replicated glaze. The whitish areas under the glaze in the archaeological material may represent unreacted quartz but it is difficult to determine because of the reduced transparency.

The same replicated body type (B09) was used as a substrate for all replicated glazes. Examining replicated body sections with SEM-BSE reveals a disparity between the analogue and material from Saqqara. The Saqqara material reveals sub-angular quartz particles of various shapes and sizes between the sherds and within each sherd. Quartz particles in sherd s17 (Fig. 7-6) are angular and mostly <65 µm but a few are >200 µm whereas those in s48 are angular to linear and reveal a gentle gradient from <65 µm to >400 µm. Quartz particles in B09 (Fig. 7-7) are sub-angular to sub-rounded with an average diameter of 105 µm and appear relatively homogenous in the backscatter image. The particles are well within the range encountered with archaeological material but lack heterogeneity exhibited by most of the archaeological glazes (Figs. 7-8 and 7-9).

Silica in the replicated faience body substrate exhibit relatively homogenous particles when compared to the archaeological sherds (Table 7-3; see Figs. 7-6 and 7-7). The average long axis size for all the replicated samples is 105 µm. The lowest average

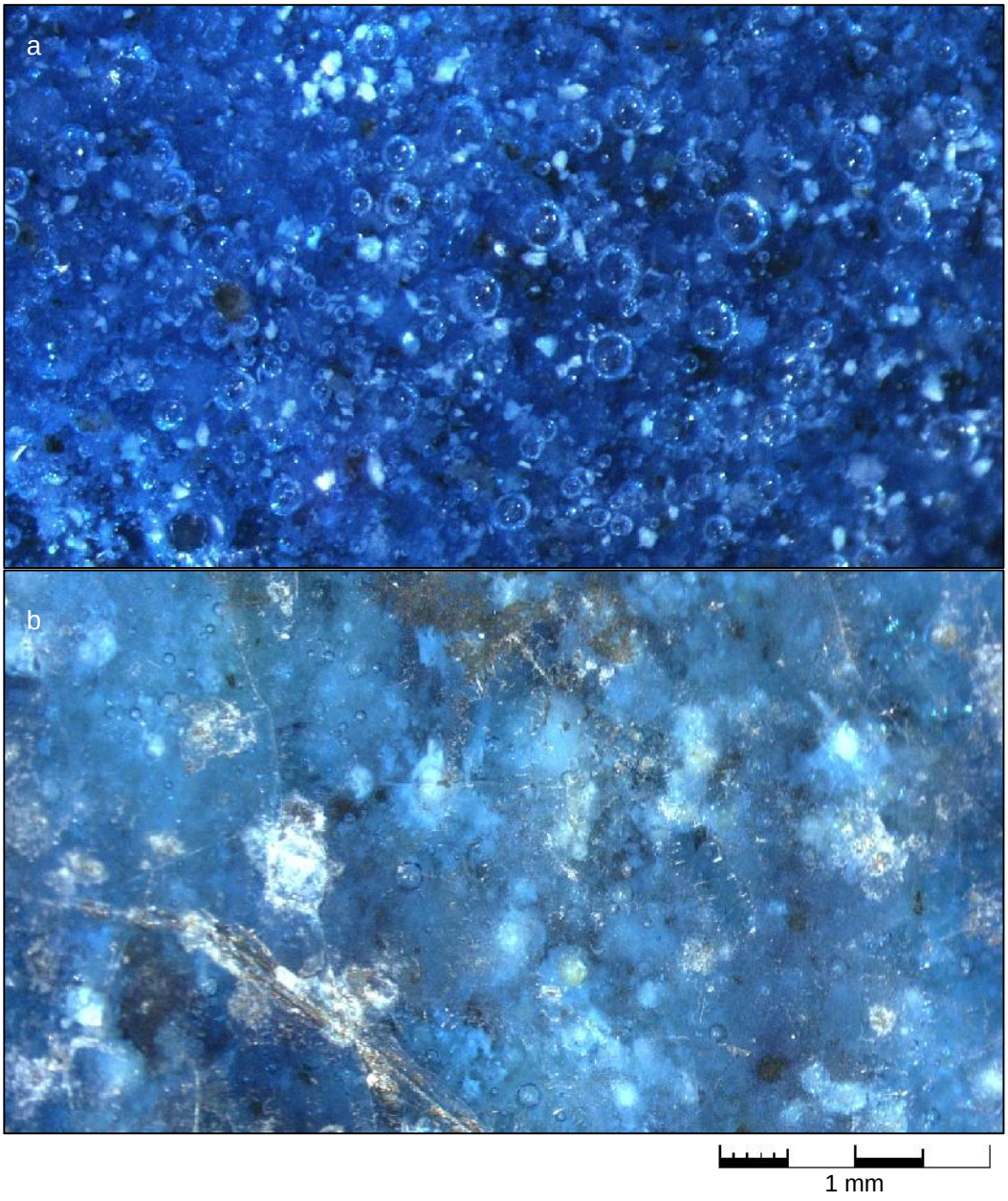

Fig. 7-5: Comparison of replicated glaze (a - R383) and archaeological glaze (b - s78) with optical microscopy at x40 magnification. The surface of b has been abraded possibly through use and deposition thereby reducing the transparency.

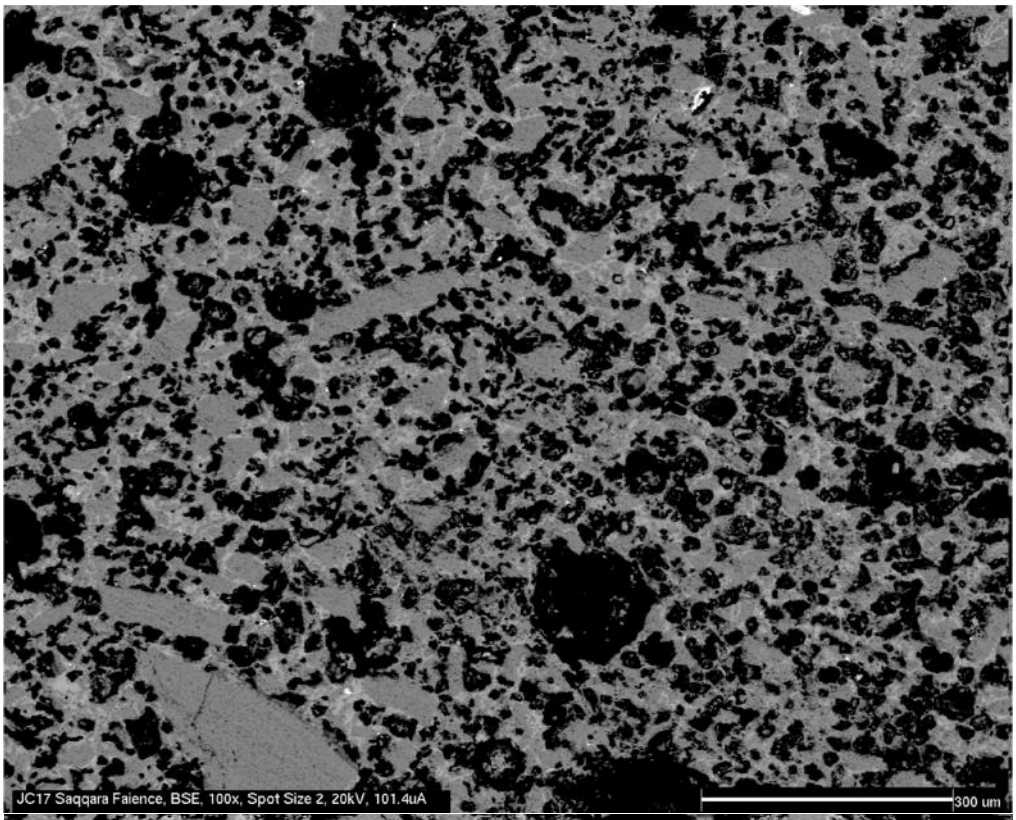

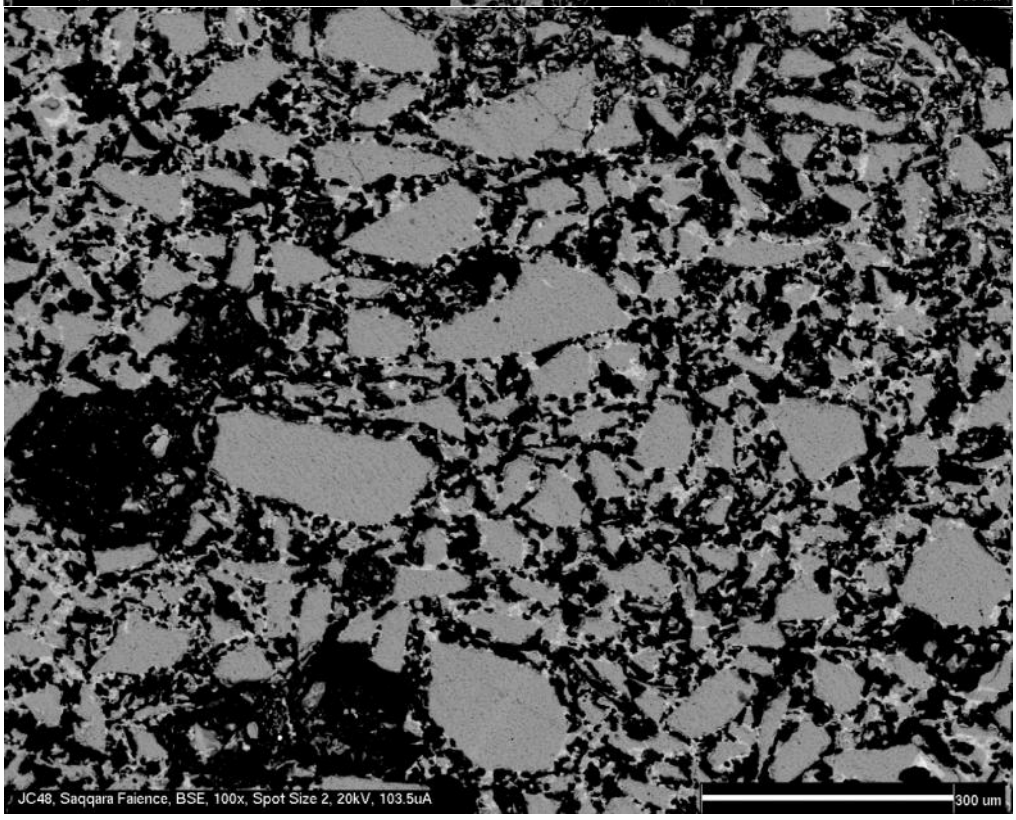

Fig. 7-6: SEM-BSE images of the silica body particles for sherds s17 (a) and s48 (b) at a magnification of x100. The scale bars read 300 µm.

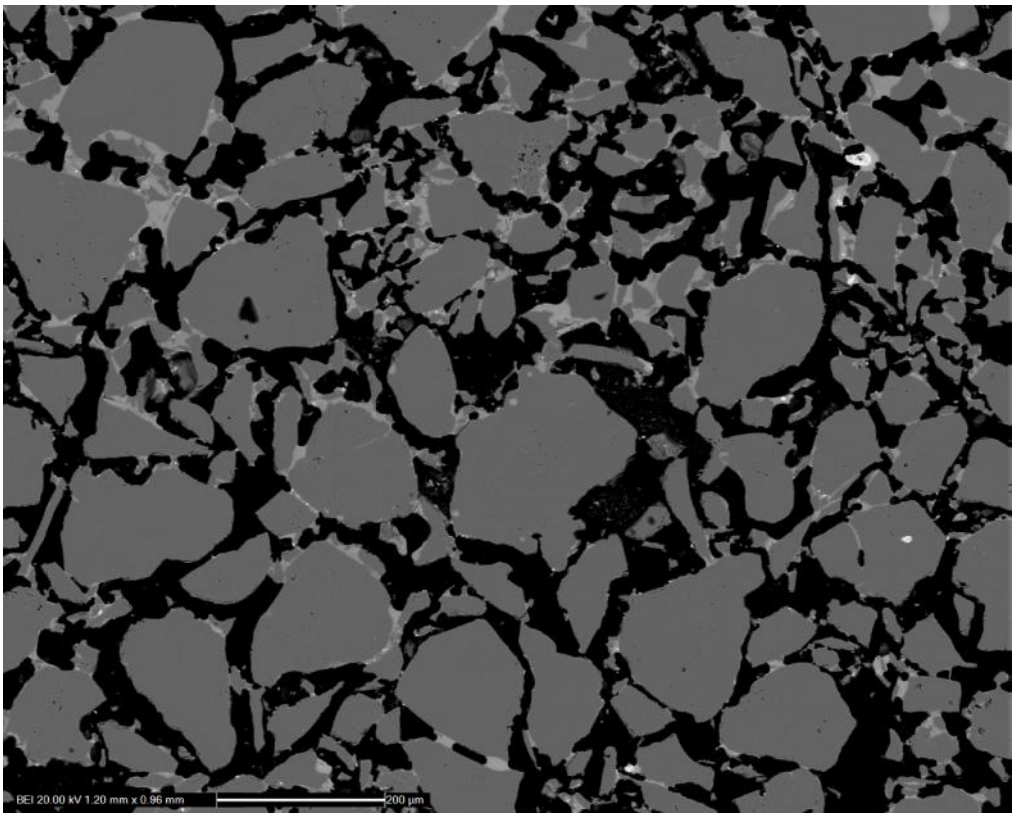

Fig. 7-7: SEM-BSE image of the body matrix (mag. 100x; scale reads 200 µm) for replicate faience sample R328. The particle sizes are more uniform at an average of ~ 99 µm along the long axis. Interparticle glass abundance is lower moderate based on the subjective archaeological sherd IPG scale. All bodies for the replicated material are batch B09 and are therefore the same.

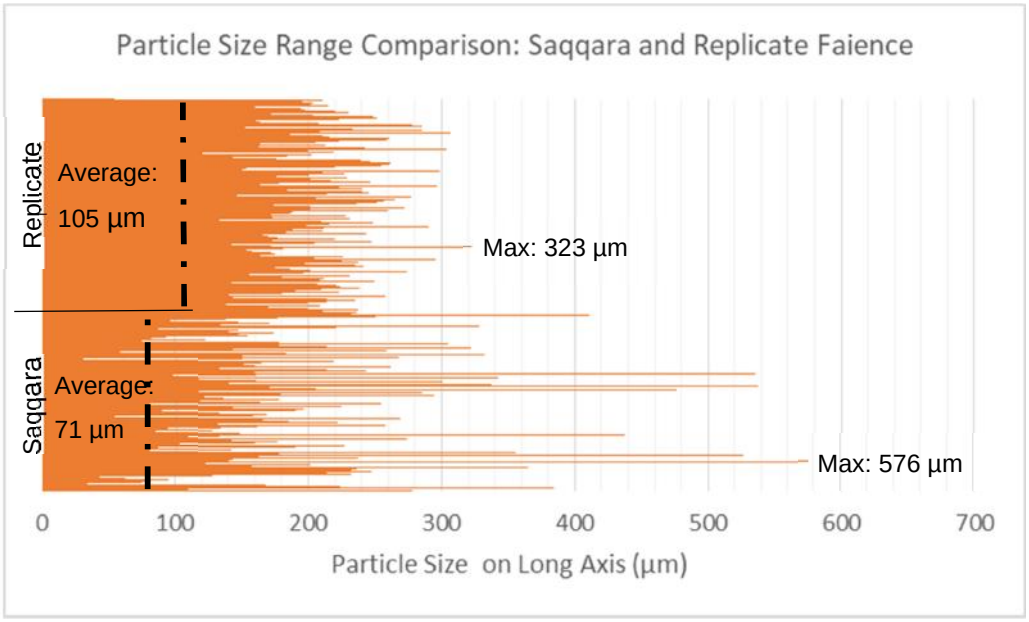

Fig. 7-8: Body particle size range comparison between Saqqara and replicated faience. The graph exhibits the average size and maximum particle size recorded for each data assemblage. A total of 2343 particles were measured.

Table 7-3: Body silica particle size for each archaeological sherd. Interparticle glass (binding the silica particles) is subjectively determined and divided into three categories: sparse (x), light (xx), and moderate (xxx). Particle size average, minimum size, maximum size (along the longest dimension) and standard deviations are shown. Particles counted is based on a maximum of 80.

Saqqara Faience Body Microstructures							
			Particle Size (um)				Particles
Sample	Glaze	IPG	Average	Min.	Max.	SD	Counted
R327	GLZ03	xx	101	6	237	71.63	44
R328	GLZ03	xx	99	9	235	62.25	55
R340	GLZ03	xx	111	7	257	65.33	44
R342	GLZ03	xx	112	14	238	57.07	47
R349	GLZ03	xx	104	11	250	71.59	48
R351	GLZ03	xx	97	6	274	76.19	47
R356	GLZ03	xx	117	12	295	68.53	41
R359	GLZ03	xx	104	5	226	64.55	49
R360	GLZ03	xx	96	7	323	70.99	40
R363	GLZ03	xxx	99	10	248	58.49	40
R364	GLZ03	xx	99	13	244	62.83	41
R367	GLZ03	xx	103	8	290	67.57	41
R383	GLZ03	xx	110	8	248	62.29	39
R384	GLZ03	xx	95	9	228	64.41	40
R386	GLZ03	xx	105	13	272	68.24	36
R388	GLZ03	xx	126	11	265	78.20	39
R390	GLZ03	xx	98	6	277	69.38	48
R392	GLZ03	xx	99	8	296	71.72	47
R406	GLZ07	xx	125	17	246	62.62	31
R408	GLZ07	xx	101	6	298	73.44	48
R411	GLZ07	x	114	14	260	69.94	36
R412	GLZ07	xx	104	11	262	65.13	43
R415	GLZ07	xx	102	6	304	71.07	46
R416	GLZ07	xx	107	10	243	63.96	43
R418	GLZ05	x	101	7	261	75.89	43
R421	GLZ05	xx	92	9	306	81.77	40
R423	GLZ05	xx	104	13	285	85.26	40
R424	GLZ05	x	100	9	252	74.28	43
R426	GLZ05	x	124	9	230	52.26	43
R429	GLZ05	xx	105	7	215	71.87	40

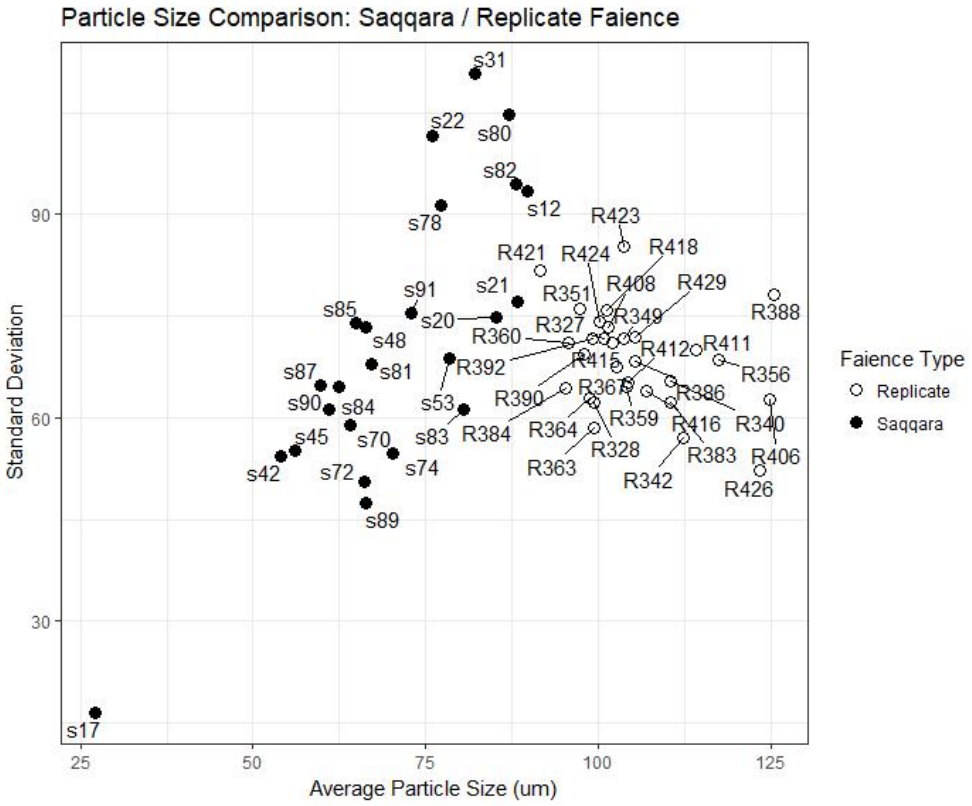

Fig. 7-9: Structural comparison between archaeological sherds from Saqqara and replicated faience samples. Replicated body particles, although larger, are more homogenous than the particles from the archaeological material.

size for the samples is 92 µm and the highest is 126 µm. The smallest particle size is 5 µm and the largest is 323 µm.

The archaeological sherd profiles exhibit silica particles of various sizes within each sherd and across all the sherds (Table 7-4; Figs. 7-10 through 7-12). The average particle long axis size for all the archaeological sherds is 71 µm, the lowest average size for an individual sherd is 27 µm (s17 (Fig. 7-13)) and the highest average size for an individual sherd is 90 µm (s12). Sherd s91 has an average long axis particle size of 73 µm (Fig. 7-14) and represents a good moderate sherd in this respect. The smallest particle size (5 µm) was encountered with sherd s17 (see Fig. 7-13) and the largest 576 µm with sherd s22 (see Fig. 7-14). This particle is 3.2x larger than the finest mesh (180 µm) used to process replicate body particles (see Fig. 7-7).

Particle sizes in the archaeological materials are more heterogeneous than the particles associated with the replicated material. The heterogeneity is true for archaeological material as a group and is true for individual sherds which exhibit more variability than any individual replicated sample.

Table 7-4: Body silica particle size for each archaeological sherd. Interparticle glass (binding the silica particles) is subjectively determined and divided into four categories: sparse (x), light (xx), moderate (xxx) and heavy (xxxx). Particle size average, minimum size, maximum size (along the longest dimension) and standard deviations are shown. Particles counted is based on a maximum of 80.

Saqqara Faience Body Microstructures (10 Assays)							
			Particle Size (um)				Particles
Sample	Glaze Colour	IPG	Average	Min.	Max.	SD	Counted
s12	Bluish Green	x	90	6	384	93.54	38
s17	Blue	xxxx	29	5	95	19.09	48
s20	Green	xx	85	6	247	74.76	41
s21	Purple	xx	88	9	365	77.19	36
s22	Turquoise	xx	76	6	576	101.66	40
s31	Turquoise	xxx	82	6	527	110.80	40
s42	Green	xx	54	8	227	54.36	52
s45	Yellowish Green	xx	56	8	274	55.19	37
s48	Dark Blue	xxx	66	8	438	73.36	43
s53	Turquoise	x	79	11	257	68.80	41
s70	Ultra-Marine Blue	xxx	64	6	268	58.91	52
s72	Purplish Blue	xxx	66	10	225	50.64	48
s74	Purplish Blue	xx	70	13	254	54.65	46
s78	Ultra-Marine Blue	xx	77	9	476	91.29	44
s80	Turquoise	x	87	8	537	104.82	44
s81	Bluish Green	xxx	67	7	342	67.97	47
s82	Blue	xxx	88	10	536	94.56	40
s83	Turquoise	xxx	81	11	262	61.19	43
s84	Blue	xxx	62	8	333	64.65	44
s85	Dark Blue	xxx	65	7	322	74.00	51
s87	Blue	xxx	60	11	304	64.81	40
s89	Blue	xxx	66	6	174	47.49	51
s90	Blue	xx	61	9	328	61.21	50
s91	Turquoise	xxx	73	11	411	75.47	45

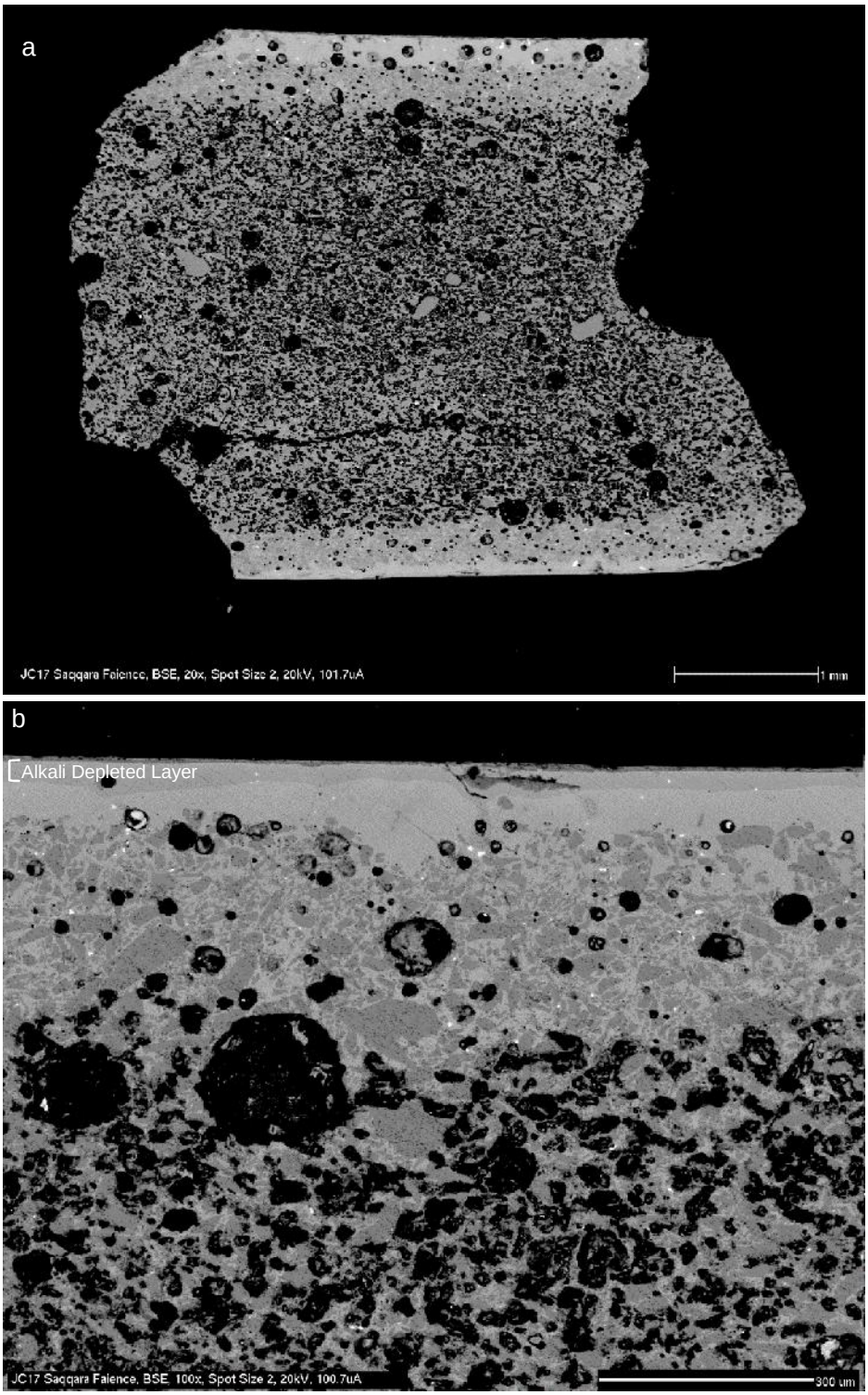

Fig. 7-10: SEM-BSE images of the exterior glaze of s17. This glaze represents the thinnest (~100 µm) of the archaeological samples. The interaction layer is approximately 260 µm thick on average. Magnifications are (a) x20 and (b) x100.

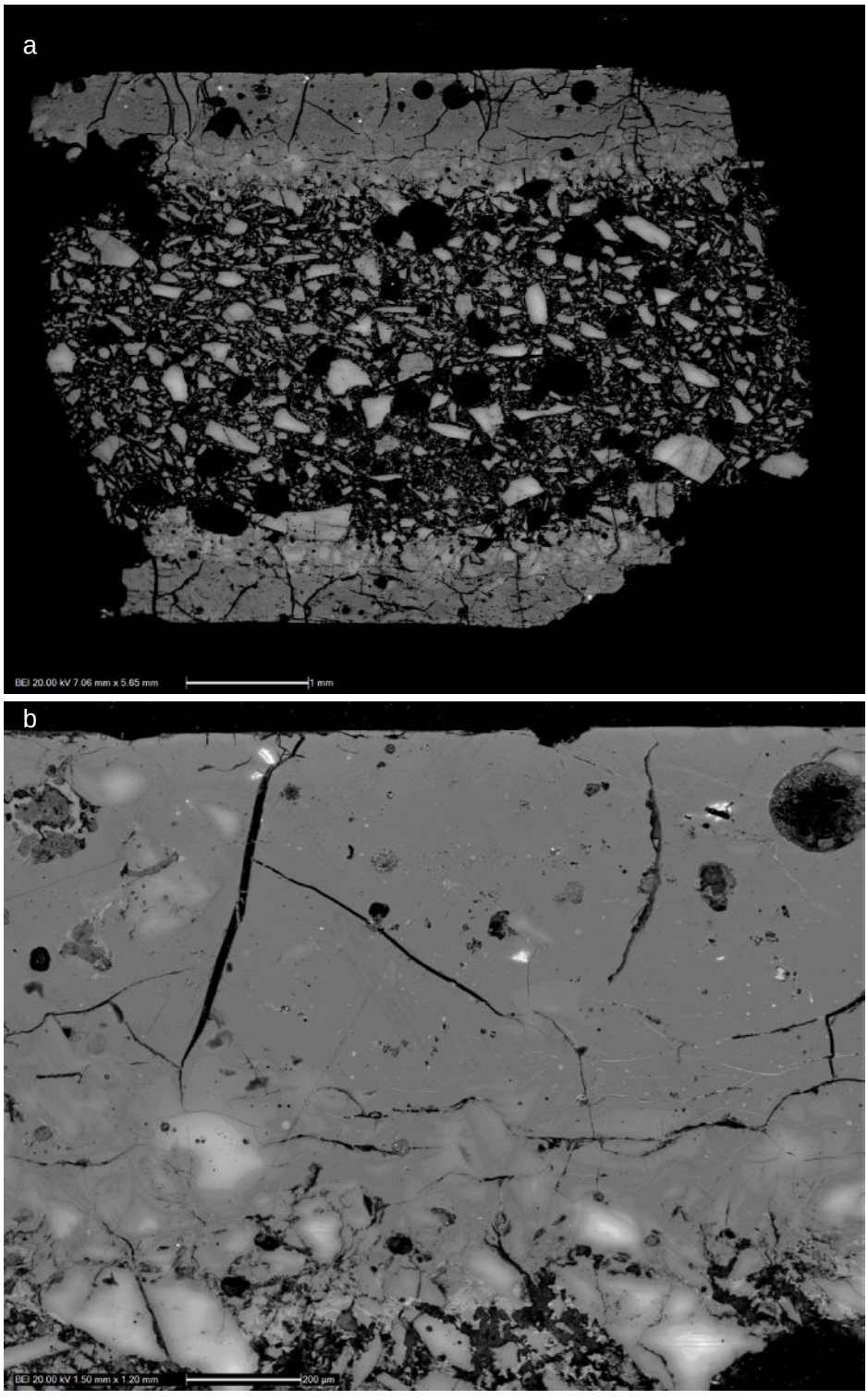

Fig. 7-11: SEM-BSE image of the exterior glaze of sherd s53. This glaze layer represents the thickest of the samples (~916 µm). The interaction zone is negligible. The body substrate is visible near the bottom edge of the image. The magnifications are (a) x17 and (b) x80.

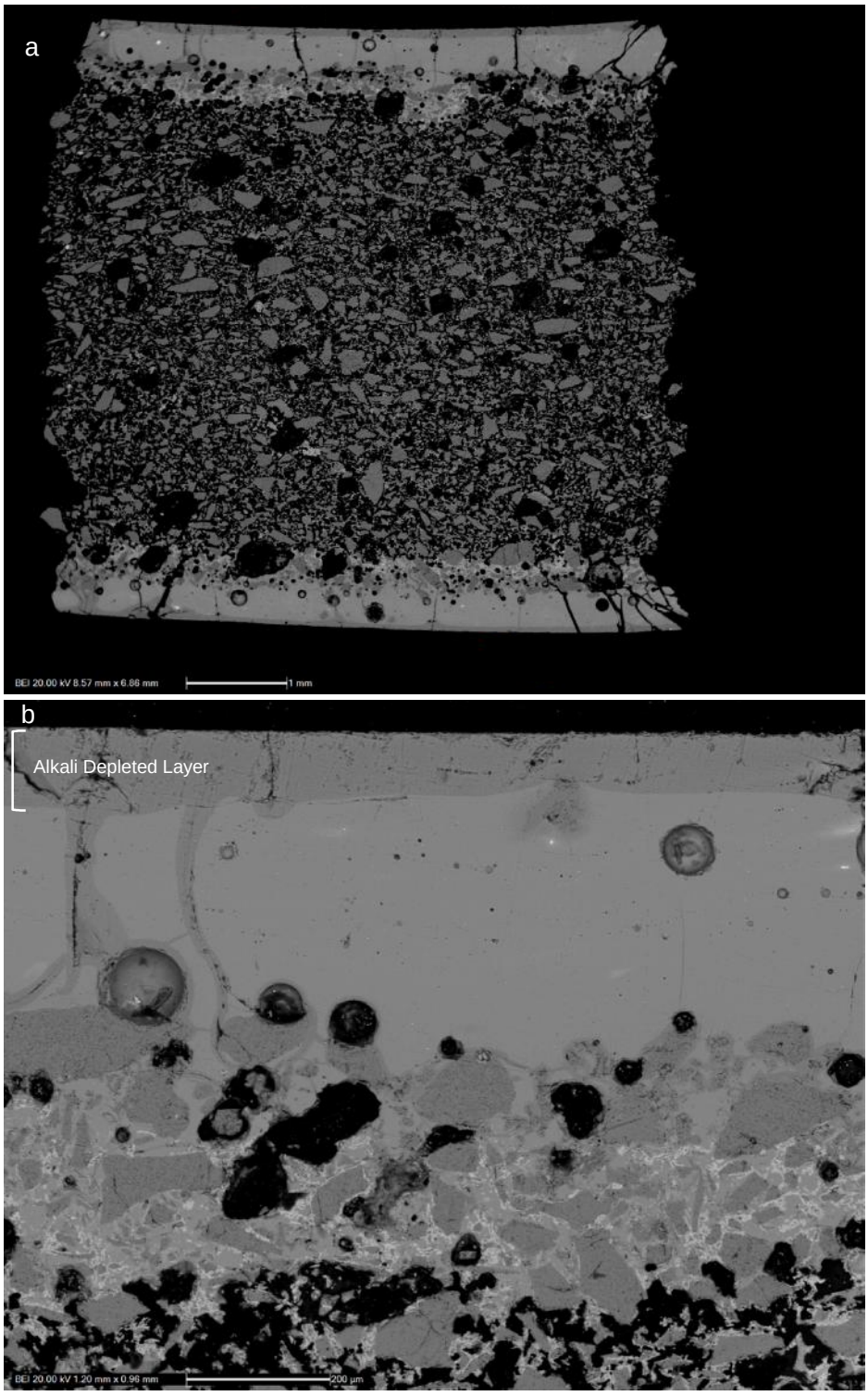

Fig. 7-12: SEM-BSE images of s83 (a) sherd profile and (b) exterior glaze profile. The glaze depth (~456 µm) is closest to the average depth for all the sample glazes (~444 µm). The interaction layer is approximately 128 µm thick on average. Magnification is (a) x14 and (b) x100.

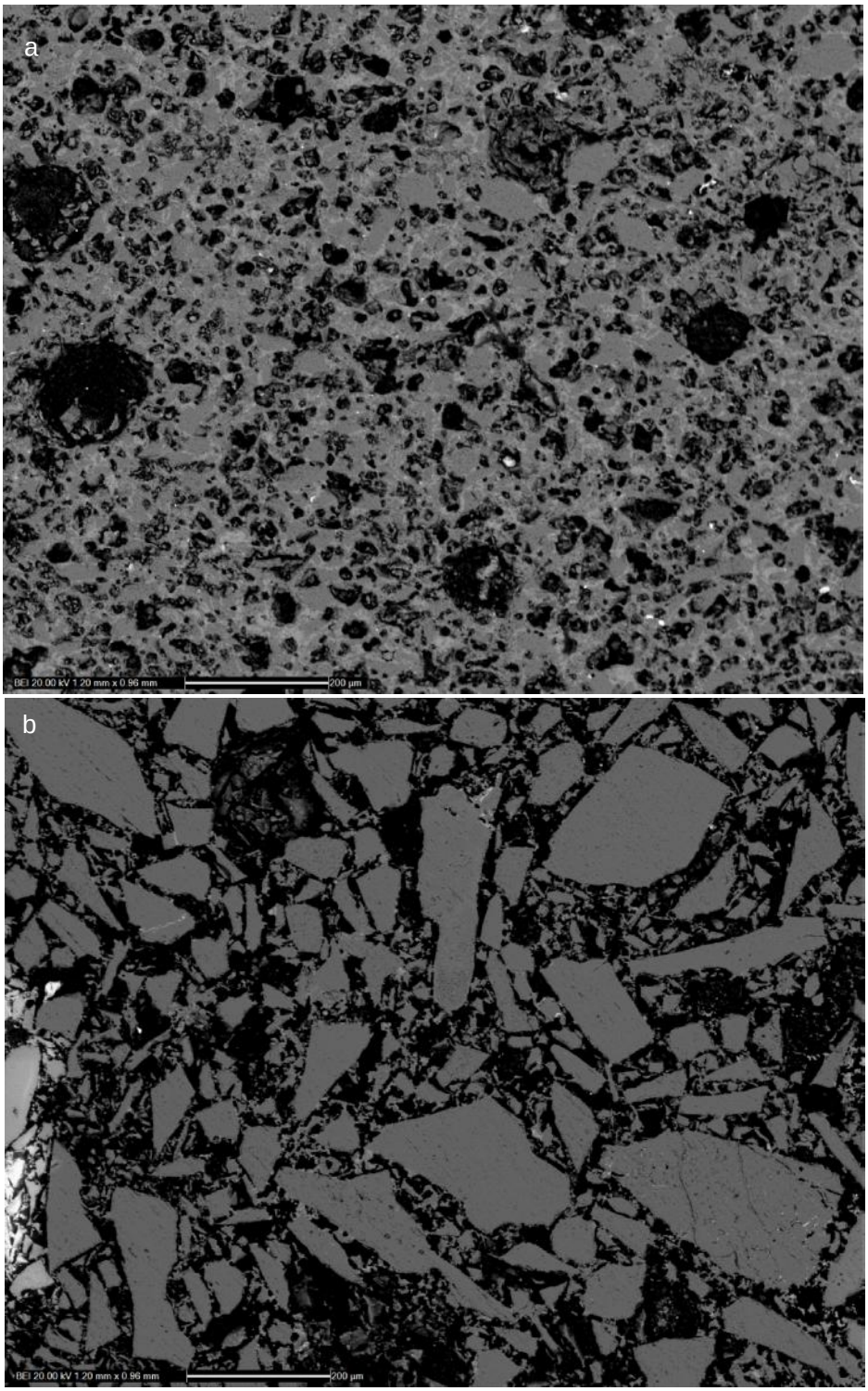

Fig. 7-13: SEM-BSE image of the body matrix (mag. 100x; scales read 200 µm) for sherds s17 and s12. Sherd s17 (a) exhibits the smallest average particle size and the most abundant interparticle glass of all the archaeological sherds in the study. The individual angular silica particles are slightly darker surrounded by lighter interparticle glass that binds the grains together. Sherd s12 (b) exhibits the largest particle size and the least abundant interparticle glass of the assemblage.

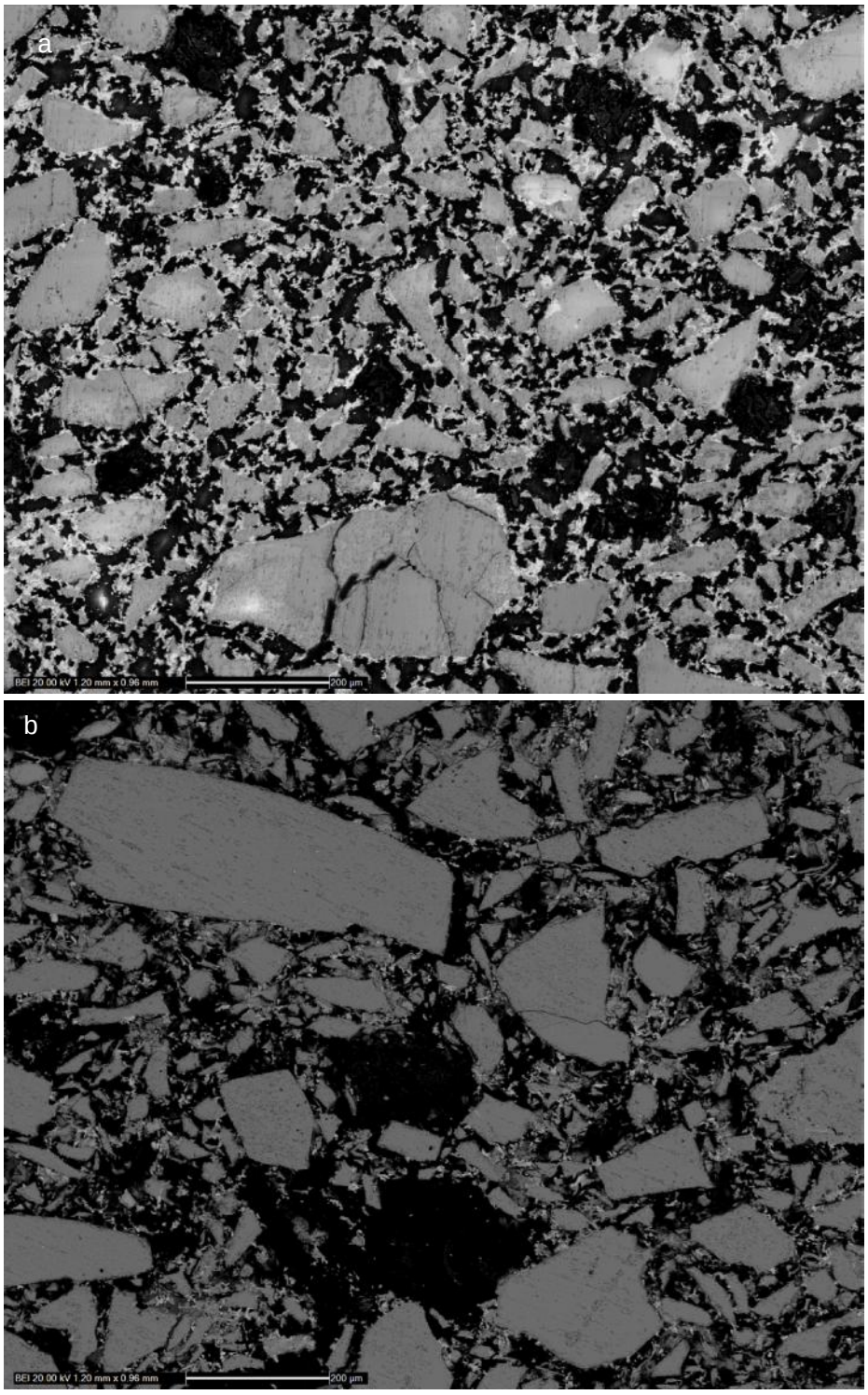

Fig. 7-14: SEM-BSE image of the body matrix (mag. 100x; scales read 200 µm) for sherds s91 and s22. Sherd s91 (a) exhibits the higher moderate interparticle glass (IPG) and average silica particle sizes. The individual angular silica particles are slightly darker surrounded by lighter interparticle glass that binds the grains together. Sherd s22 (b) exhibits lower moderate IPG and average silica grain size. It exhibits the largest measured grain at 576 µm along the long axis.

There is considerable range in glaze and interaction layer depths with the replicated faience samples (Table 7-5). The large standard deviations indicate considerable range of depth within each set of 10 measurements for each glaze. This is due to the morphology of the glaze surface and the upper IAL plane. The IAL plane is the result of the original body morphology and glaze melt interaction. Figure 7-15 exhibits the range of replication glaze thicknesses; thin (R328-183 µm), average (R351-818 µm) and thick (R423-2093 µm). The interaction layers for these same three samples represent one of the thickest, average and one of the thinnest respectively. Figure 7-15b reveals unreacted silica particles lifted from the upper IAL plane by the generation of large CO_2 bubbles. The image is analogous to an explosion captured on still during the moment debris is expelled from the crater. The range in the glaze and interaction layer depths for the archaeological faience is large (Table 7-6) but considerably less than the replicated faience glazes (Fig. 7-16). The average standard deviation for the glaze measurements (10 measurements / profile layer (glaze and interaction)) is approximately 52 (compared to 219 for the replicate faience). This indicates that the layers are relatively smooth and flat especially when compared to the replicated material. Smaller body particle size is partly responsible for this characteristic. Hammerle (2012:184-5) and Griffin (2002:332) have demonstrated the improved workability of fine versus coarse body particle size. The thinnest glaze is ~100 µm (s17 (see Fig. 7-10)) and the thickest is ~916 m (s53 (see Fig. 7-11)) with an average of ~444 µm (sherd s83 (see Fig. 7-12)).

Table 7-5: Faience replication glaze and interaction layer depths. Glazes were applied as thin and thick layers prior to firing.

Faience Replication Glaze Depths (10 Measurements / Sample)							
Sample	Glaze	Colourant	Glaze Application	Mean Depth (µm)	SD	Interaction Layer Mean Depth (µm)	SD
R327	GLZ03	Copper	Thick	709.99	81.95	587.55	89.04
R328	GLZ03	Copper	Thin	183.21	162.87	1095.85	123.99
R340	GLZ03	Copper	Thin	356.92	101.16	571.99	98.83
R342	GLZ03	Copper	Thin	360.98	146.08	803.73	155.77
R349	GLZ03	Copper	Thick	632.86	91.48	911.73	114.80
R351	GLZ03	Copper	Thick	818.05	204.25	894.43	152.45
R356	GLZ03	Copper	Thin	395.96	540.55	1230.62	657.38
R359	GLZ03	Copper	Thick	825.00	347.13	874.34	125.83
R360	GLZ03	Copper	Thin	785.30	243.48	235.79	58.46
R363	GLZ03	Copper	Thick	1412.50	390.64	523.97	177.03
R364	GLZ03	Copper	Thin	605.26	84.94	306.48	68.87
R367	GLZ03	Copper	Thick	849.33	220.60	616.90	124.43
R383	GLZ03	Copper	Thick	704.23	217.47	452.39	92.05
R384	GLZ03	Copper	Thin	616.29	97.76	599.41	121.52
R386	GLZ03	Copper	Thin	631.37	146.35	550.07	137.95
R388	GLZ03	Copper	Thin	713.69	89.98	626.10	94.38
R390	GLZ03	Copper	Thin	523.41	232.92	444.79	78.52
R392	GLZ03	Copper	Thin	611.48	146.76	737.56	177.52
R406	GLZ07	Cobalt	Thin	991.92	244.88	538.85	194.04
R408	GLZ07	Cobalt	Thin	1545.80	231.73	418.26	111.69
R410	GLZ07	Cobalt	Thin	425.36	196.13	585.02	141.03
R411	GLZ07	Cobalt	Thick	687.47	135.67	657.32	134.63
R412	GLZ07	Cobalt	Thin	437.93	137.39	662.07	146.45
R414	GLZ07	Cobalt	Thin	364.08	188.93	928.39	214.27
R415	GLZ07	Cobalt	Thick	1022.53	236.24	861.27	148.23
R416	GLZ07	Cobalt	Thin	620.45	105.70	964.46	153.54
R418	GLZ05	Cobalt	Thin	1123.61	326.50	351.64	125.62
R421	GLZ05	Cobalt	Thick	1717.20	664.23	432.63	189.28
R423	GLZ05	Cobalt	Thick	2093.11	397.38	535.71	109.71
R424	GLZ05	Cobalt	Thin	755.55	287.24	404.71	116.12
R426	GLZ05	Cobalt	Thin	623.30	151.28	715.78	150.81
R429	GLZ05	Cobalt	Thick	1628.77	182.21	1003.81	274.88
Means from All Glazes (n=32)				805.40	219.75	660.11	151.85
Thin Copper Glaze Means (n=11)				525.81	181.17	654.76	161.20
Thick Copper Glaze Means (n=7)				850.28	221.93	694.47	125.09
Thin Cobalt Glaze Means (n=9)				765.33	207.75	618.80	150.40
Thick Cobalt Glaze Means (n=5)				1429.82	323.15	698.15	171.35

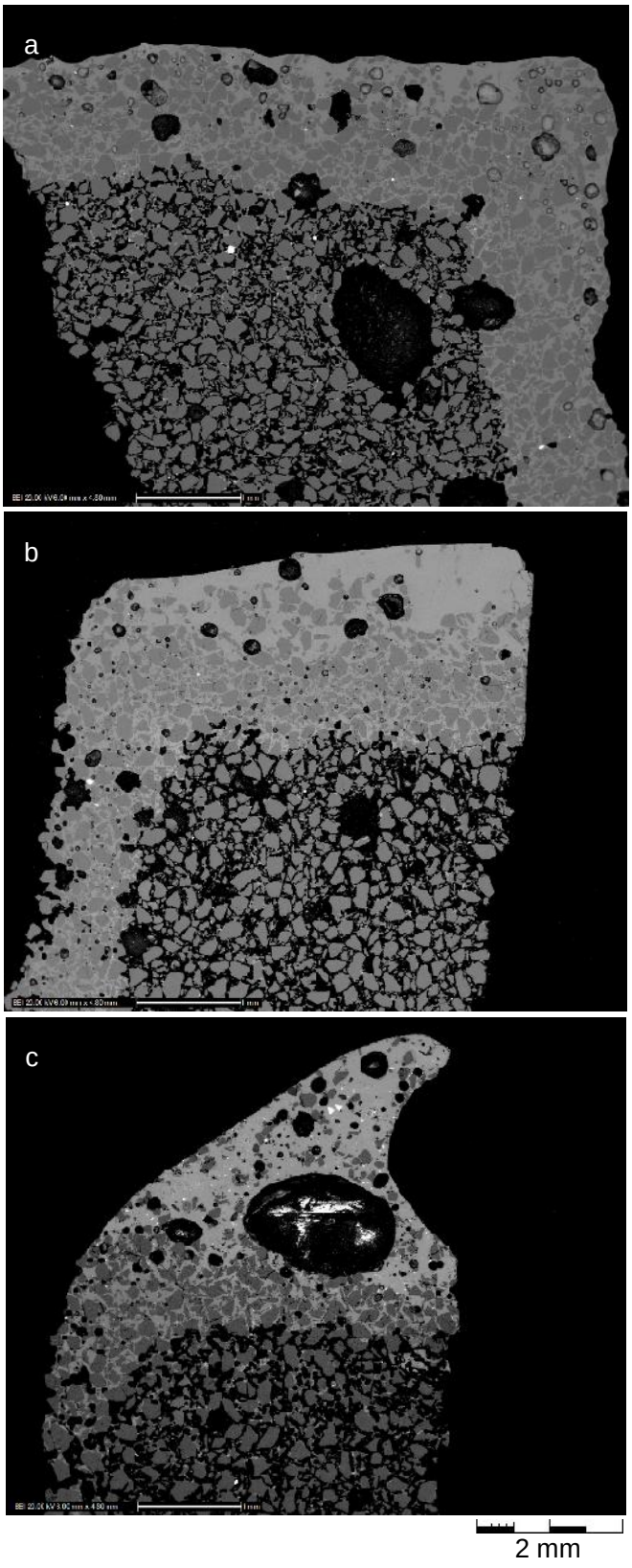

Fig. 7-15: Three glaze microstructures that provide the full range of replicate glaze thickness. Scale bar reads 1 mm.

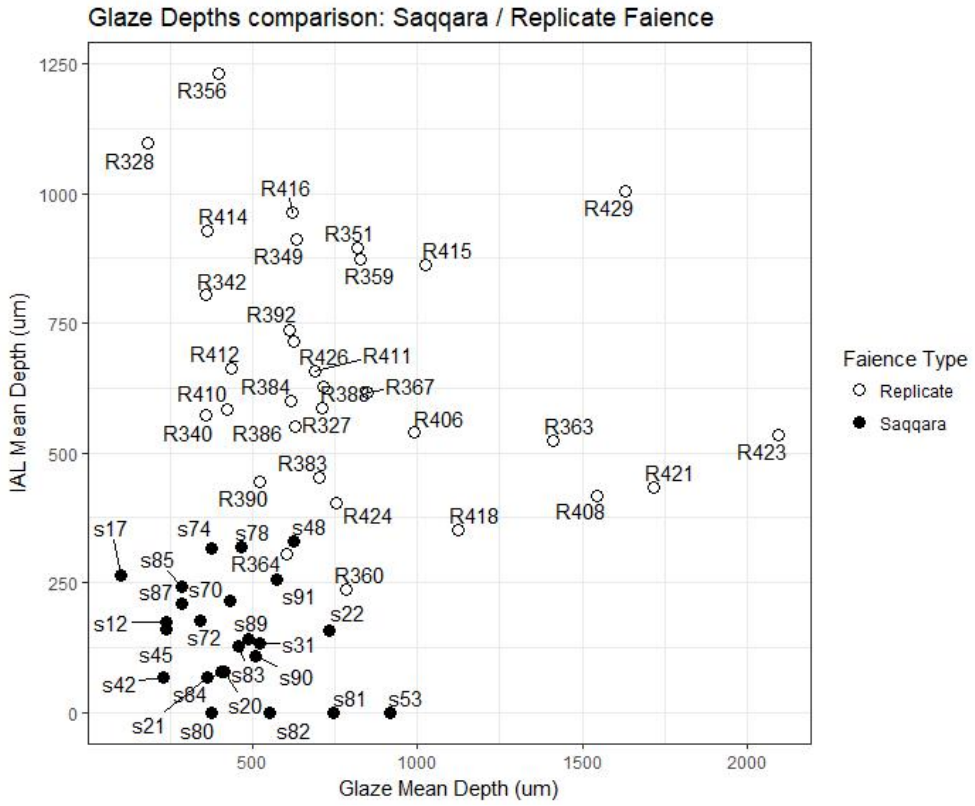

Fig. 7-16: Glaze depth comparison of the Saqqara and replicated faience samples.

Table 7-6: Saqqara archaeological faience glaze and interaction layer depths with associated standard deviations (SD). Blanks associated with the interaction layer indicates the layer is negligible.

Saqqara Faience Glaze Depths (10 Measurements / Profile Layer)						
Sample	Colour	Main Colourant(s)	Mean Depth (µm)	SD	Interaction Layer Mean Depth (µm)	SD
s12	Bluish Green	Copper/Lead Antimonate	239.565	70.02	175.085	64.728
s17	Blue	Copper	100.669	27.237	264.148	34.224
s20	Green	Copper/Lead Antimonate	415.119	48.408	78.588	28.63
s21	Purple	Manganese	361.266	63.568	67.786	49.161
s22	Turquoise	Copper	730.527	63.448	157.96	47.161
s31	Turquoise	Copper	522.019	45.511	132.701	36.429
s42	Green	Copper/Lead Antimonate	228.704	70.713	68.021	34.015
s45	Yellowish Green	Lead Antimonate	239.085	31.5	161.344	56.002
s48	Dark Blue	Copper/Cobalt	623.508	41.78	330.784	70.438
s53	Turquoise	Copper	916.348	90.638		
s70	Ultra-Marine Blue	Cobalt	430.918	110.844	216.023	45.773
s72	Purplish Blue	Cobalt	342.214	14.664	178.117	41.77
s74	Purplish Blue	Cobalt	374.839	40.859	316.94	49.81
s78	Ultra-Marine Blue	Cobalt	468.255	43.783	317.814	88.374
s80	Turquoise	Copper	375.082	42.271		
s81	Bluish Green	Copper	746.957	93.237		
s82	Blue	Copper	551.867	29.553		
s83	Turquoise	Copper	456.281	59.999	128.019	45.133
s84	Blue	Copper	406.306	44.051	78	32.016
s85	Dark Blue	Copper	286.655	33.893	241.665	54.831
s87	Blue	Copper	286.049	55.982	210.72	67.423
s89	Blue	Copper	487.439	39.021	142.228	41.624
s90	Blue	Copper	508.557	48.19	108.009	14.014
s91	Turquoise	Copper	572.948	42.262	256.903	100.995
Means from All Glazes (n=24)			444.63	52.14	181.54	50.13
Copper Colourant Glaze Means (n=15)			479.15	52.35	172.31	48.96
Cobalt Colourant Glaze Means (n=5)			447.95	50.39	271.94	59.23

7.5 HH-XRF and SEM-EDS Analytical Results

The HH-XRF parameters used for the analysis of the glaze replicates and the archaeological faience were determined through testing of the various settings (Chapter 6). The low voltage HH-XRF parameters chosen for the analysis of elements Z11-Z26 (sodium through iron) are 15 kV, 50 µA, with no filter, under a vacuum for 180 seconds; higher voltage HH-XRF analysis for heavier elements (Z26+) are 40 kV, 30 µA with filter 3 (aluminium - 12 mil, titanium – 1 mil, copper – 6 mil) and no vacuum for 180 seconds. Additional HH-XRF analytical setup for HH-XRF and SEM-EDS is discussed in sections 4.4.4 and 4.4.5.

7.5.1 HH-XRF Qualitative Analysis: Replicated Material

HH-XRF qualitative analysis was conducted to determine if the three replicate glazes (copper colourant glaze 03 and cobalt blue glazes 05 and 07) could be distinguished based on peak heights, and to determine if preparation before glost firing exhibited any differences. These differences include the body being fired or unfired, the glaze being applied thickly or thinly and final glaze depths.

Qualitative analysis was conducted on all the glazes (4 samples each) to determine differences based on peak height representing presence and abundance of glaze batch components. Presence of lead, cobalt, manganese, elevated iron and lower copper peaks distinguish the cobalt blue glazes from the copper blue glazes in the 15 kV spectra (Fig. 7-17). Differences between the two cobalt blue glazes are evident in the peak heights of cobalt and lead. The spectra representing the 40 kV measurements exhibit differences between the two cobalt glazes in the tin, antimony and lead peak heights (Figs. 7-18 and 19). These distinguishing characteristics of the replicated glazes correspond with the glaze batch recipes.

The spectra were examined to determine if replicated faience body condition (unfired or fired) before glost firing exhibited a difference in alkali content. Some of the sodium and potassium in unfired bodies could potentially be incorporated into the glaze melt but 15 kV spectra of samples comparing fired and unfired bodies before glazing exhibited no differences. The amount of migrated elements may be small and go unnoticed in the spectra. Qualitative spectral analysis of thin and thick copper blue glazes (glaze 03) were compared to determine if the HH-XRF could detect elements isolated to the body (i.e. iron, tin, antimony and lead). The 15 kV spectra exhibited no difference for the presence of iron indicating that iron in the body was not detected at this voltage. The 40 kV spectra peak heights for lead (Peak Pb Lβ1 Fig. 7-20), tin and

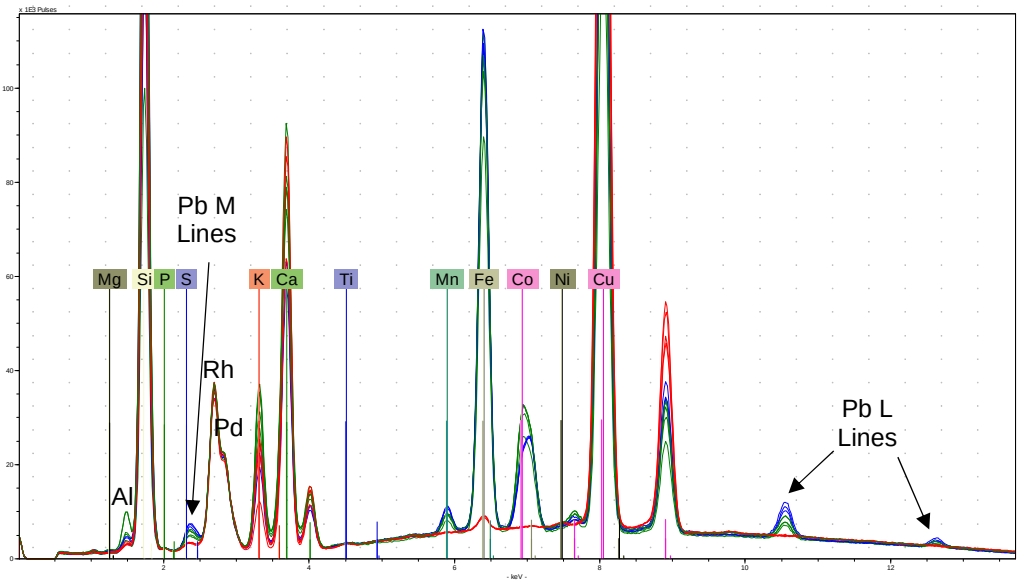

Fig. 7-17: HH-XRF 15 kV spectrum of glazes 03 (red), 05 (green) and 07 (blue). Presence of lead, cobalt, manganese and elevated iron distinguish the cobalt glazes (glazes 05 and 07). Elevated copper distinguishes the copper glazes. These findings correspond with the replicated glaze batch recipes.

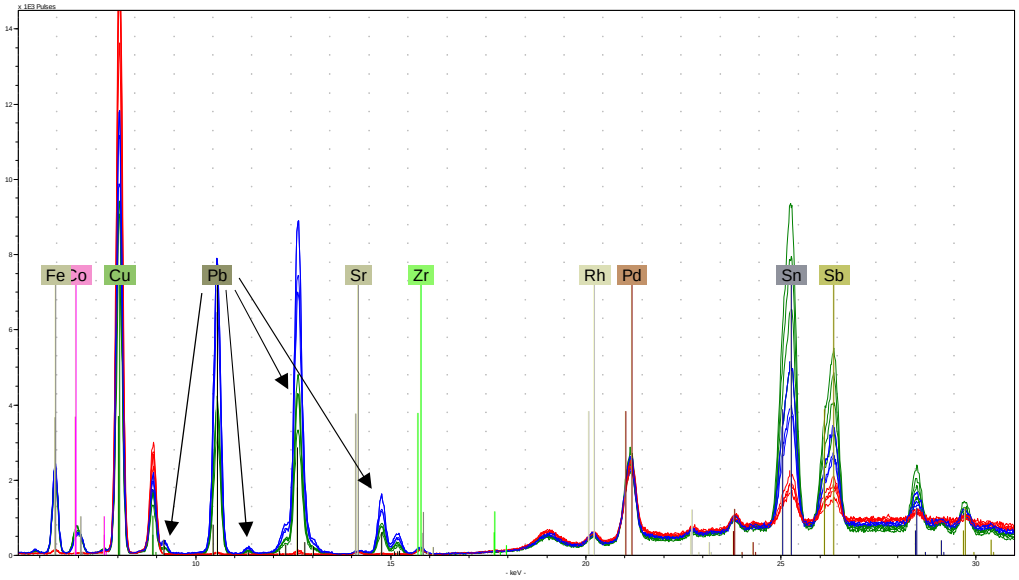

Fig. 7-18: HH-XRF 40 kV spectrum of glazes 03 (red), 05 (green) and 07 (blue). Elevated iron, lead, tin and antimony distinguish the cobalt glaze (glazes 05 and 07). Copper blue glazes are distinguished by higher copper lines.

antimony (Fig. 7-21) were inversely related to thickness of the glaze. This indicates that these elements are being detected in the body with all glazes. Iron has been detected in all glazes using 40 kV exciting voltage. This indicates that 15 kV measurements does not have enough energy to return iron photons from the body to the detector whereas the 40 kV measurements do have adequate energy to accomplish this in the replicated glazes.

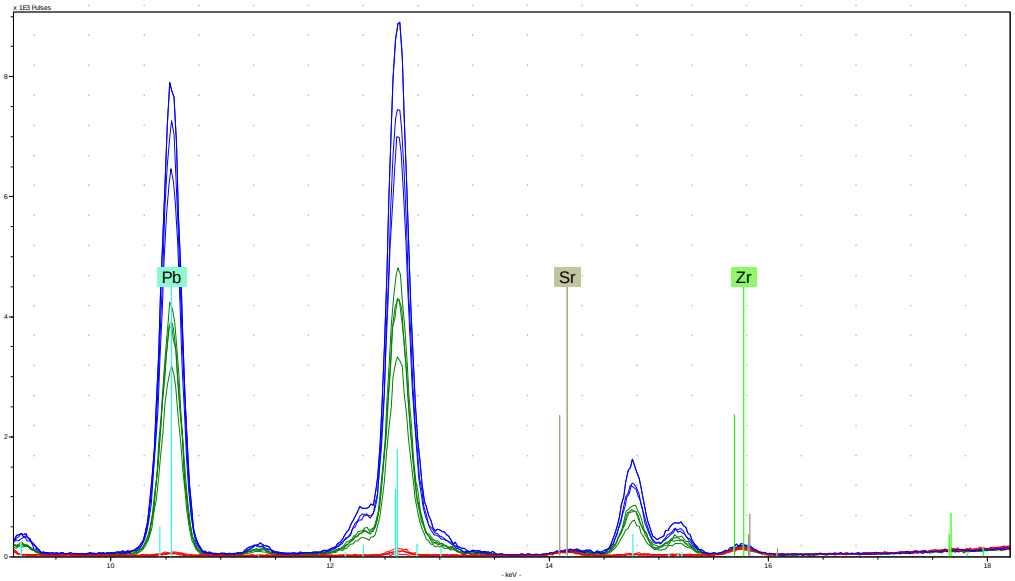

Fig. 7-20: A portion of the HH-XRF 40 kV spectrum (9 – 18 keV) for replicated glazes exhibiting highest lead glaze peaks for cobalt colourant glaze 07 (blue) and lowest for copper colourant glaze 03 (red). These findings correspond to the glaze batch recipes.

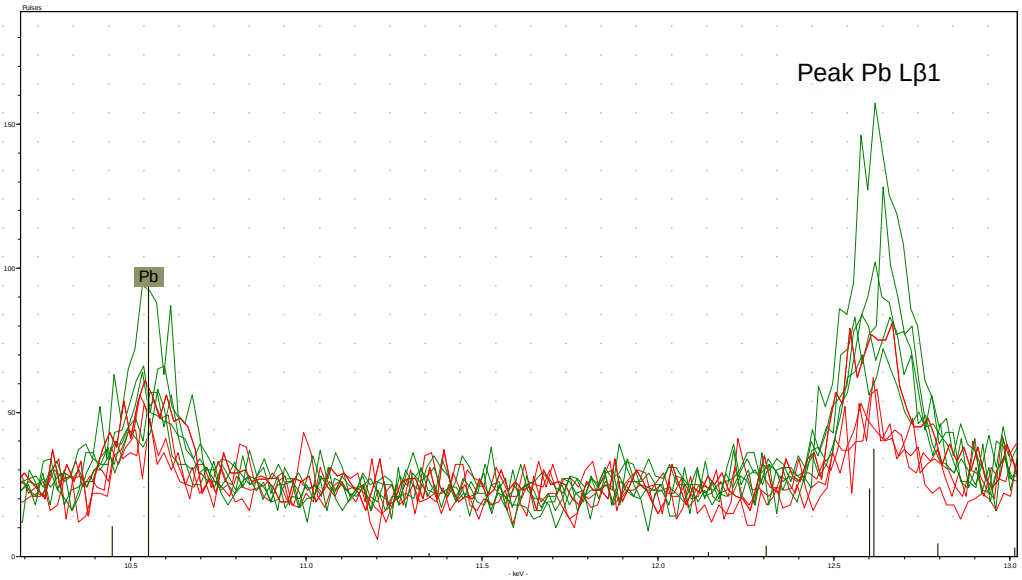

Fig. 7-19: A portion of the HH-XRF 40 kV spectrum (10.25 – 13 keV) for replicated glazes exhibiting higher lead peaks with thinner replicated glazes (green). The samples consist of thick (red) and thin (green) copper blue prefritted glazes on prefired bodies with the only difference being how thick the glaze was applied.

7.5.2 HH-XRF Qualitative Analysis: Saqqara Faience Glazes

Qualitative analysis was conducted on all the Saqqara faience glazes (n=30) representing the colours blue (20), dark blue (5), green (4) and purple (1) to determine differences based on peak height. The HH-XRF 15 kV spectra of the glazes (Fig. 7-22) exhibits immediate distinction for the green, dark blue and purple glazes. The green

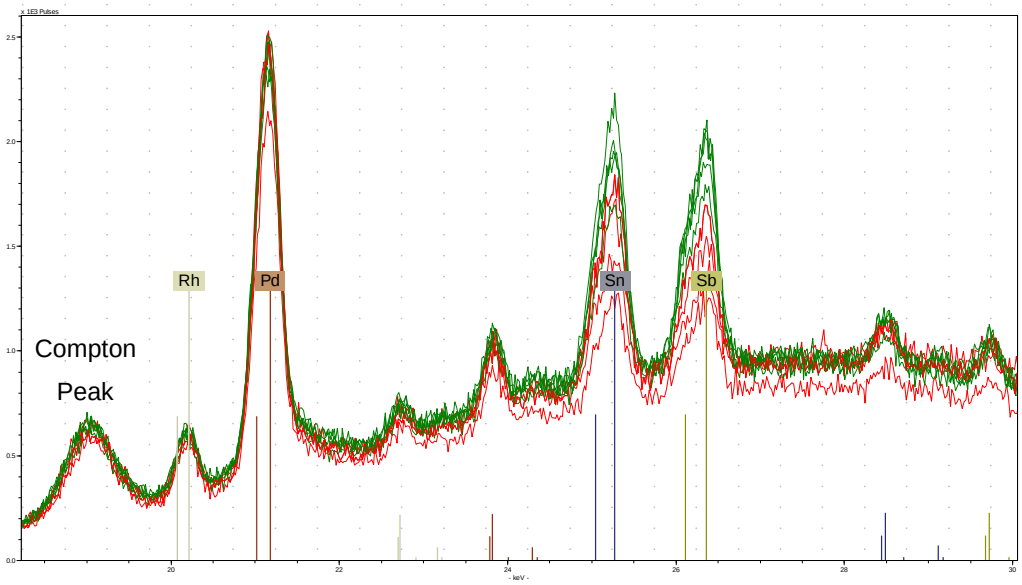

Fig. 7-22: A portion of the HH-XRF 40 kV spectrum (19 – 30 keV) for replicated glazes exhibiting higher tin and antimony peaks for thinner glazes. The samples consist of thick (red) and thin (green) copper blue prefritted glazes on prefired bodies with the only difference being how thick the glazing powder was applied.

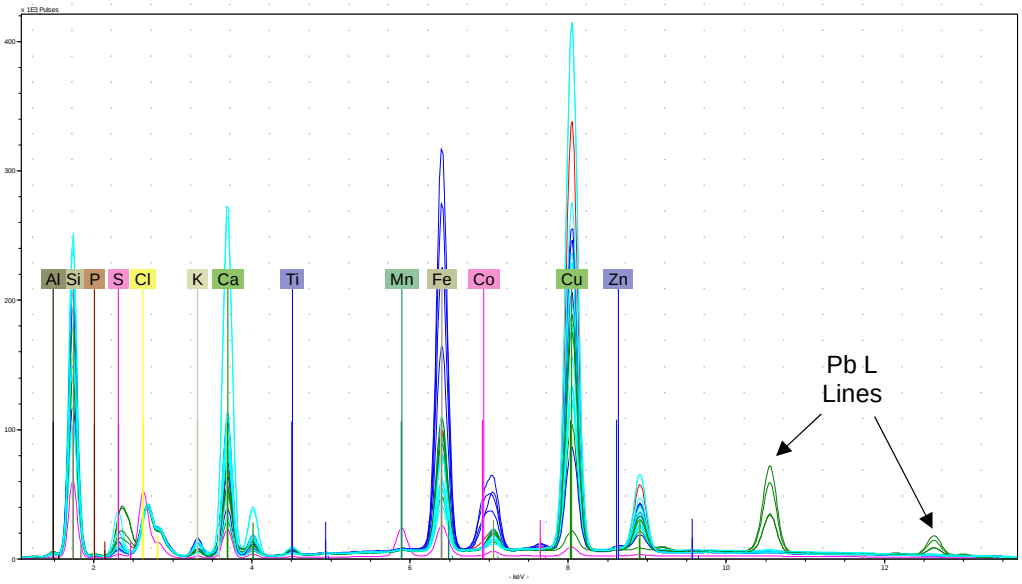

Fig. 7-21: HH-XRF 15 kV spectra of all the Saqqara faience glazes. The glaze colours consist of blue (20 (teal)), dark blue (5 (dark blue and red)), green (4(green)) and purple (1 (purple)). The green glazes are coloured by the addition of lead antimonate and are distinguished by the lead Lα and Lβ lines. The purple glaze is coloured by manganese. The dark blue glazes are coloured by cobalt. The blue glazes are hard to see because of the colour of the spectra. These are examined in Fig. 7-25.

glazes are coloured by the addition of lead antimonate and are distinguished by the lead Lα and Lβ lines. The purple glaze has the largest peak for manganese (manganese is the colourant). The dark blue glazes are coloured by cobalt and are distinguished by cobalt and iron. The HH-XRF 40 kV spectra of the Saqqara faience

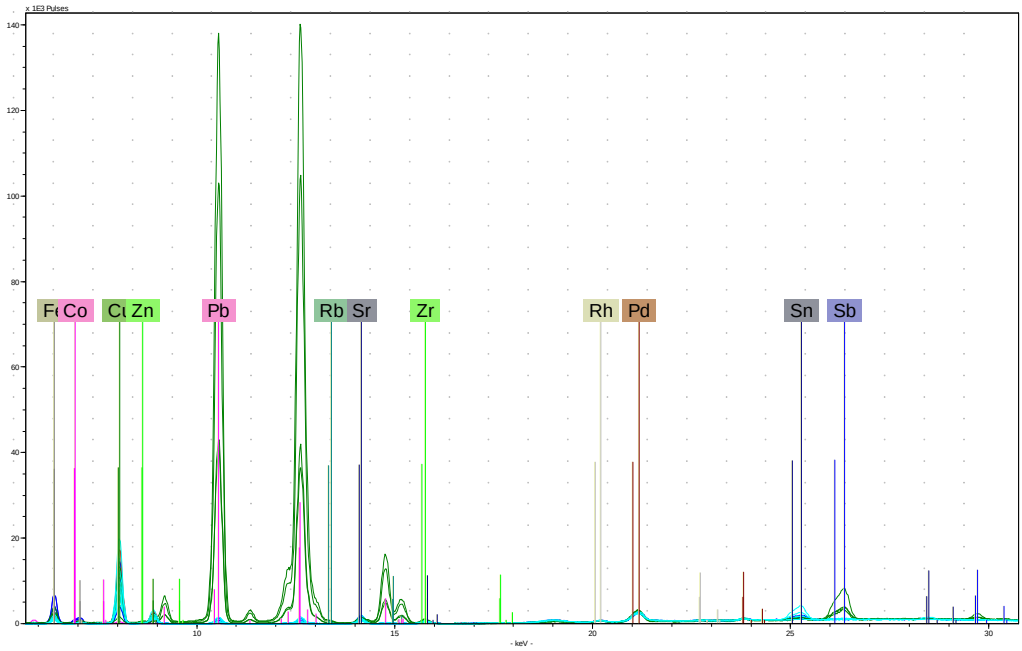

Fig. 7-23: HH-XRF 40 kV spectra of all the Saqqara faience glazes. The green glazes are coloured by the addition of lead antimonate. The lead lines and antimony lines (to a lesser extent) distinguish the green coloured glazes from the others. The cobalt glazes are distinguished by the iron and cobalt lines but these are more readily visible in the 15 kV spectra.

assemblage (Fig. 7-23) exhibits high lead and antimony lines for the green glazes as expected. It exhibits high iron and cobalt lines for the cobalt coloured glazes but these are more readily visible in the 15 kV spectra (see Fig. 7-22). The green glazes exhibit higher zirconium peaks whereas all the other colours exhibit higher strontium (Fig. 7-24).

The blue glaze spectra have been qualitatively examined separate from the other colours. Saqqara sherd s48 is included with these spectra. This glaze is anomalous to the other blue glazes because of the inclusion of cobalt and high copper representing a hybrid copper/cobalt colourant (Figs. 7-25 and 7-26). It is the only glaze in the assemblage to exhibit this characteristic and has been designated with a red spectrum to make it stand out in the figures. Saqqara sherd s81 is anomalous due to the high calcium peak. Saqqara glaze s17 has a turquoise hue and exhibits the highest copper and tin peaks, but beyond this the turquoise glazes are qualitatively indistinguishable from the other blue glazes.

The cobalt blue glazes (s70, s72, s74 and s78) have been qualitatively examined along with the copper/cobalt coloured glaze s48. MVS analysis (Chapter 10) has revealed relationship pairings between s70/s78 and s72/s74. Glaze pairing s70/s78 exhibiting higher iron and copper than glaze pairing s72/s74 in the HH-XRF 15 and 40

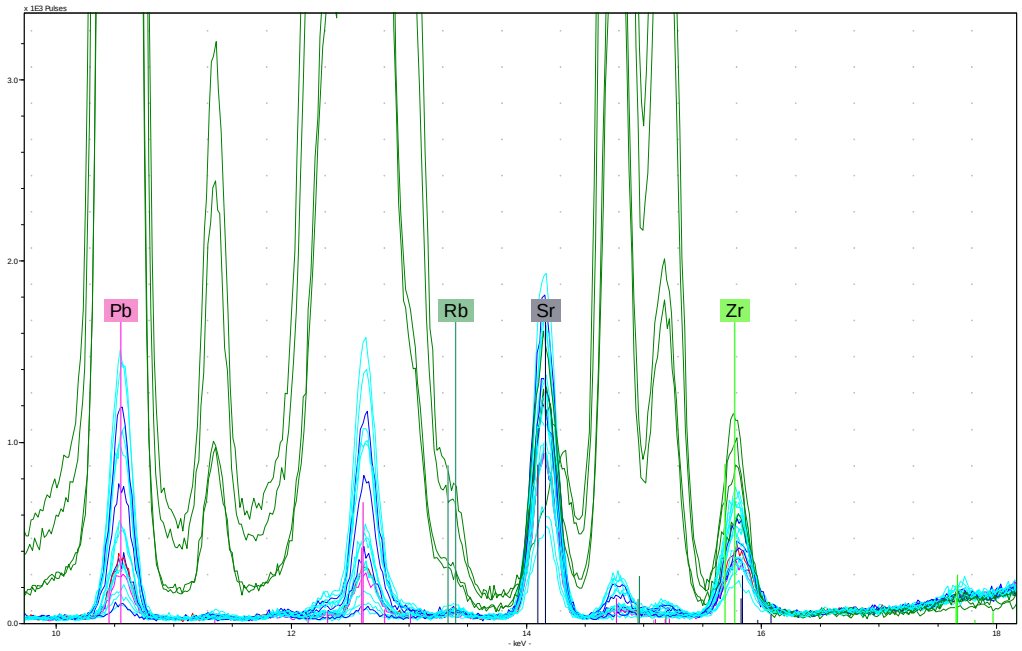

Fig. 7-25: A segment of the HH-XRF 40 kV spectra (10 – 18 keV) of the Saqqara glazes exhibiting elevated zirconium associated with the green glazes whereas elevated strontium is associated with all the other glazes. The large green peaks that extend off the top of the figure are for lead.

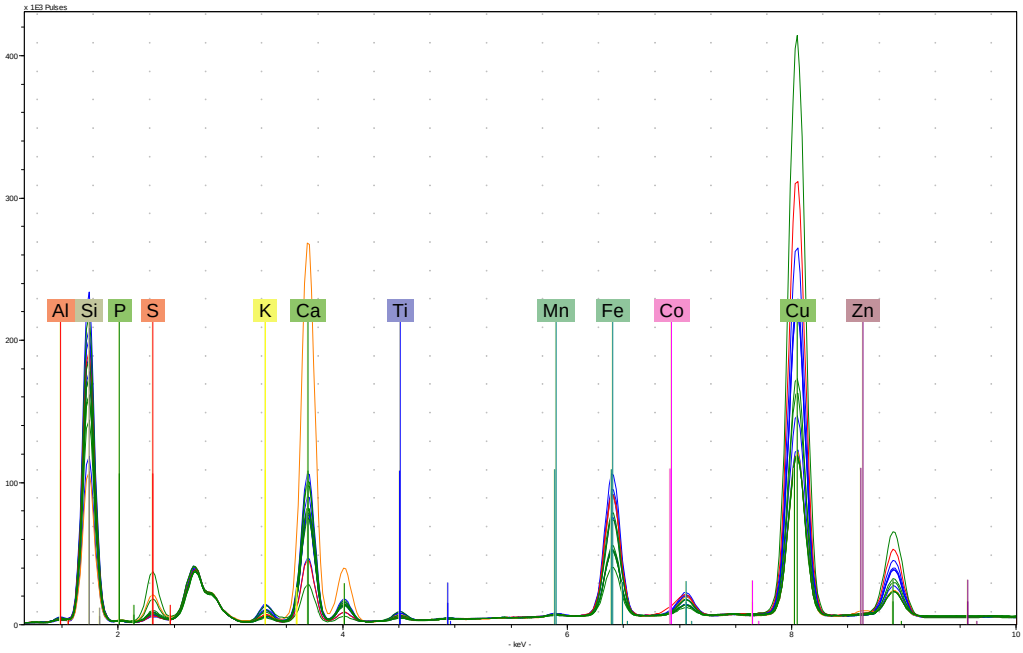

Fig. 7-24: HH-XRF 15 kV spectra of all the Saqqara blue glazes consisting of the hues of turquoise (green) and medium blue (blue). Glaze s48 (red) is coloured by cobalt and copper. The cobalt in this sample is distinguished by the small red shoulder to the left of the iron Kβ lines. This sample has the second highest copper peak (s17 has the highest). Glaze s81 (orange) has the highest calcium peak distinguishing it from all the other glazes.

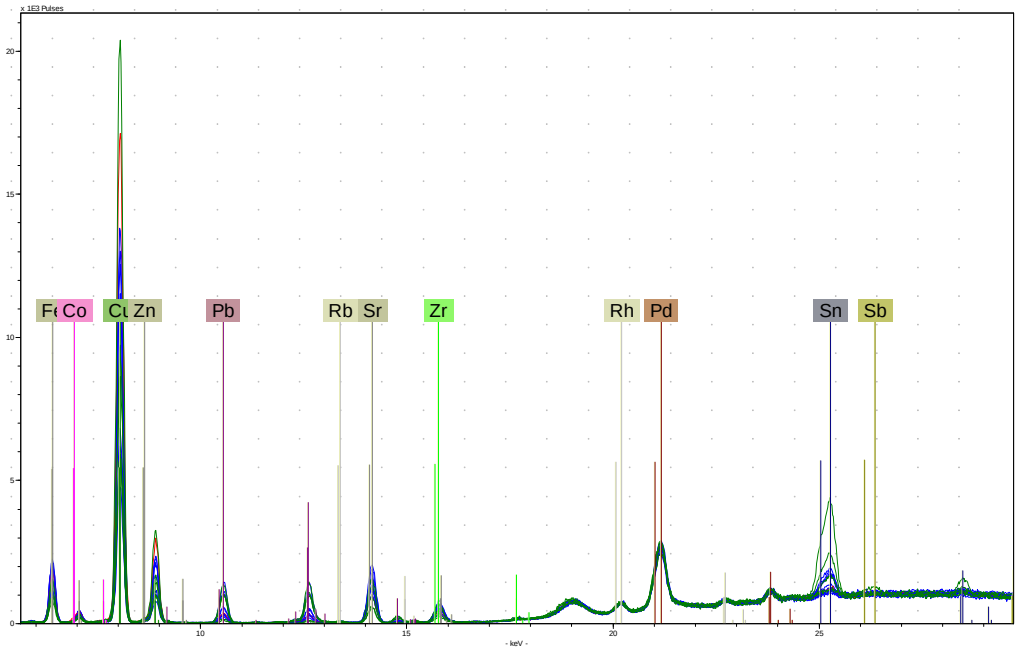

Fig. 7-26: HH-XRF 40 kV spectra of the Saqqara glaze assemblage. Turquoise glaze (green) s17 exhibits the highest copper and tin peaks but as a group turquoise glazes are qualitatively indistinguishable from the other glazes.

kV spectra (Figs. 7-27 and 28). Glaze s48 exhibits the lowest cobalt and highest copper peaks. Glaze pairing s72/s74 exhibits a higher zirconium peak (Fig. 7-29). The cobalt glazes are indistinguishable from each other beyond these associations.

7.5.3 HH-XRF and SEM-EDS Elemental Analysis Results

The analytical results for the HH-XRF analysis of the replicated materials are found in Tables 7-7 and 7-8 (low voltage (15 kV)) and Tables 7-9 and 7-10 (high voltage (40 kV)). The HH-XRF results for the Saqqara archaeological materials are in Table 7-11 (15 kV) and Table 7-12 (40 kV). Table 7-13 and Table 7-14 provide the SEM-EDS results for the replicated glazes, and Table 7-15 provide the SEM-EDS results for the archaeological glazes. These results inform section 7.6 and MVS analyses of Chapters 8, 9 and 10.

The elemental analyses for HH-XRF were conducted using net peak area (NPA) counts per second. The SEM-EDS analysis was conducted using compound wt% normalized to 100%. The average standard deviation (σ) and coefficient of variance (C_v) (see section 4.5 for more detail) are included with the HH-XRF and SEM-EDS results to provide an idea of the measurement range and precision of measurements, respectively. Signal-to-noise ratio (SNR) is provided for the HH-XRF results. The SEM-

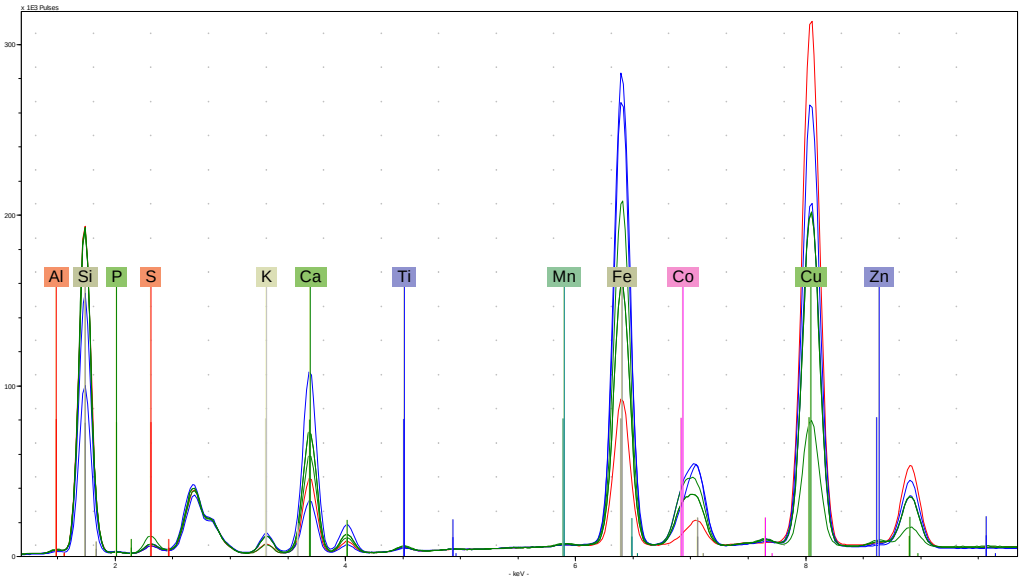

Fig. 7-28: HH-XRF 15 kV spectra of the Saqqara cobalt coloured glazes (s48 (red), s70, s72, s74, and s78). MVS analysis (Chapter 10) has revealed relationship pairings between s70/s78 and s72/s74, and the spectra have been coloured blue and green respectively. Glazes s70/s78 exhibit higher iron and copper than s72/s74. Glaze s48 exhibits the lowest cobalt and highest copper peaks.

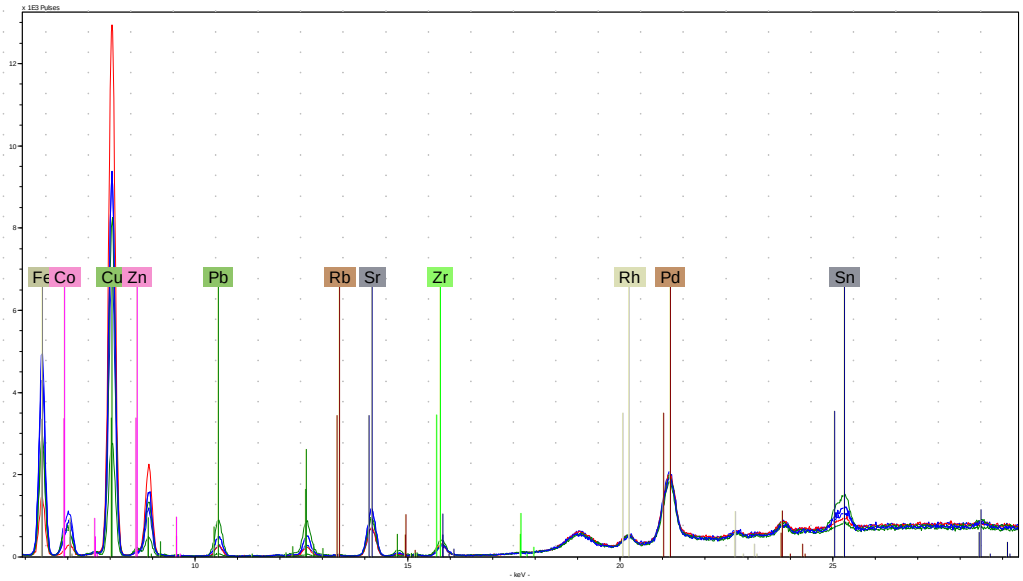

Fig. 7-27: HH-XRF 40 kV spectra of the Saqqara cobalt coloured glazes (s48 (red), s70, s72, s74, and s78). There are no distinguishing glaze spectral characteristics other than higher iron and copper peaks associated with pairing s70/s78, and s48 exhibiting highest copper and lowest cobalt peaks.

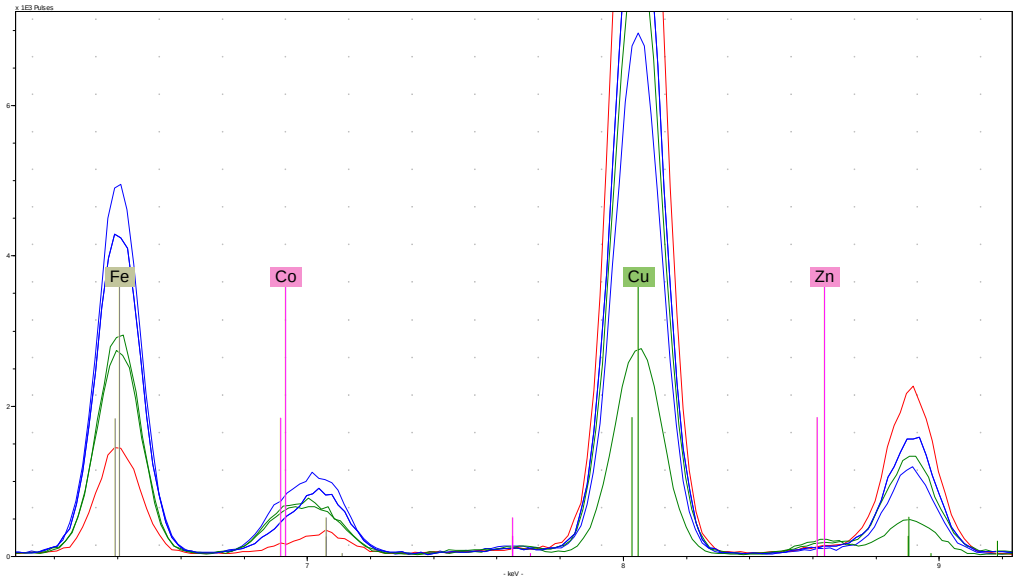

Fig. 7-29: A segment (6 - 9.25 keV) of HH-XRF 40 kV spectra of the Saqqara cobalt coloured glazes (s48 (red), s70, s72, s74, and s78). Glazes s70/s78 exhibit higher iron and copper than s72/s74. Glaze s48 exhibits the lowest cobalt and highest copper peaks. Glaze pairing s72/s74 has higher zinc peaks than the other glazes.

EDS tables include raw analytical totals to provide information pertaining to quality of analysis and/or glaze. The SEM-EDS archaeological material results (Table 7-15) are divided by measurements taken near the surface, in the glaze middle and near the interaction zone; measurements taken to determine glaze composition is restricted to the three middle glaze analyses unless noted. This area may best represent the original glaze composition of the archaeological materials before weathering.

Table 7-7: HH-XRF (15 kV) analytical results for faience copper colourant glaze 03 replicated material. The table includes average NPA (NPA μ), average standard deviation (σ_μ) coefficient of variance (C_v) and signal-to noise ratio (SNR).

HH-XRF 15 kV Faience Replicate Copper Blue Samples R327-R351																
Parameters: 15 kV, 50 uA, vacuum, 180 seconds aquisition time, 10 Measurements per sample; Glaze 03 (R327-R392)																
Sample	Stat.	Na Kα	Al Kα	Si Kα	P Kα	S Kα	K Kα	Ca Kα	Ti Kα	Cr Kα	Fe Kα	Ni Kα	Cu Kα	Zn Kα	Rh Lα	Pd Lα
R327	NPA μ	10892	18889	1108357	2756	5167	151000	618988	5329	8234	37038	19024	2788349	20424	259737	10295
	σ_μ	189	281	8328	121	218	1456	5521	249	406	822	626	56439	1040	2097	577
	C_v	1.73	1.49	0.75	4.39	4.22	0.96	0.89	4.68	4.93	2.22	3.29	2.02	5.09	0.81	5.60
	SNR	103	145	7772	19	33	815	3349	26	31	118	56	7966	60	1532	60
R328	NPA μ	8189	15156	910906	2823	5697	129038	587794	5844	7963	36545	17333	2304683	17100	246118	14188
	σ_μ	360	222	7115	132	198	3750	14397	479	662	578	879	81491	612	869	570
	C_v	4.39	1.46	0.78	4.68	3.48	2.91	2.45	8.20	8.31	1.58	5.07	3.54	3.58	0.35	4.02
	SNR	82	122	6595	20	37	711	3174	28	30	117	50	6576	50	1480	84
R340	NPA μ	8105	13424	829303	2970	5173	143905	535285	4533	6948	35222	17767	2581829	18633	247493	14301
	σ_μ	171	176	7755	180	184	1456	6008	299	325	694	574	59981	644	2424	516
	C_v	2.12	1.31	0.94	6.05	3.56	1.01	1.12	6.59	4.68	1.97	3.23	2.32	3.46	0.98	3.61
	SNR	83	109	6084	21	34	790	2942	22	26	114	51	7449	55	1489	84
R342	NPA μ	7783	14851	807166	2954	5414	113766	626044	4615	6722	37015	17602	2589220	18994	243063	14510
	σ_μ	606	842	88494	147	155	2019	20619	384	1285	668	490	65565	597	1984	694
	C_v	7.79	5.67	10.96	4.98	2.85	1.78	3.29	8.32	19.12	1.81	2.78	2.53	3.14	0.82	4.78
	SNR	79	121	5916	21	35	630	3388	23	25	120	51	7513	57	1470	86
R349	NPA μ	10968	21019	1264327	2697	5096	140140	531218	4317	8919	34303	18063	2653820	19648	254454	11188
	σ_μ	189	193	8097	190	230	1086	4060	248	423	312	674	46509	609	1363	655
	C_v	1.72	0.92	0.64	7.04	4.51	0.77	0.76	5.75	4.75	0.91	3.73	1.75	3.10	0.54	5.85
	SNR	103	161	8849	18	33	769	2909	21	33	108	52	7483	57	1522	66
R351	NPA μ	946	12813	1170133	1719	2856	63874	442164	4183	6936	27336	9673	2409313	13842	233631	8980
	σ_μ	152	223	11377	130	276	517	4605	288	370	460	570	57508	599	1777	392
	C_v	16.02	1.74	0.97	7.56	9.67	0.81	1.04	6.89	5.33	1.68	5.89	2.39	4.33	0.76	4.37
	SNR	8	93	7783	12	18	369	2480	21	26	85	27	6632	39	1306	51

Table 7-7 continued: HH-XRF (15 kV) analytical results for faience copper colourant glaze 03 replicated material. The table includes average NPA (NPA μ), average standard deviation (σ_μ) coefficient of variance (C_v) and signal-to noise ratio (SNR).

HH-XRF 15 kV Faience Replicate Copper Blue Samples R356-R367																
Parameters: 15 kV, 50 uA, vacuum, 180 seconds aquisition time, 10 Measurements per sample; Glaze 03 (R327-R392)																
Sample	Stat.	Na Kα	Al Kα	Si Kα	P Kα	S Kα	K Kα	Ca Kα	Ti Kα	Cr Kα	Fe Kα	Ni Kα	Cu Kα	Zn Kα	Rh Lα	Pd Lα
R356	NPA μ	7610	13458	851805	2966	5157	98798	552188	4451	9575	37923	17116	2473529	18218	246975	14055
	σ_μ	173	182	7796	166	221	1238	5710	477	416	831	494	57585	565	2468	459
	C_v	2.28	1.35	0.92	5.60	4.29	1.25	1.03	10.72	4.34	2.19	2.88	2.33	3.10	1.00	3.27
	SNR	78	110	6268	21	34	558	3108	22	36	122	50	7079	54	1513	83
R359	NPA μ	8511	15926	1028719	2736	5309	88173	520101	4188	9640	32886	17084	2475650	17843	248479	12649
	σ_μ	175	221	6665	89	129	879	3600	377	311	600	546	39599	356	1601	338
	C_v	2.05	1.39	0.65	3.24	2.43	1.00	0.69	8.99	3.22	1.83	3.20	1.60	2.00	0.64	2.67
	SNR	84	127	7430	19	35	503	2939	21	36	105	50	7080	52	1527	77
R360	NPA μ	9491	14633	772135	2953	5558	165208	677108	5121	6087	34546	18598	2710252	19316	262681	12550
	σ_μ	244	329	5347	238	308	1317	4964	494	170	659	387	44653	470	1793	589
	C_v	2.57	2.25	0.69	8.06	5.53	0.80	0.73	9.64	2.79	1.91	2.08	1.65	2.43	0.68	4.69
	SNR	95	117	5544	20	35	884	3652	26	23	113	55	7889	58	1541	72
R363	NPA μ	12104	23326	1113011	2762	5583	124301	772410	4146	7882	37659	19593	2898423	21520	263140	9973
	σμ	288	229	7317	159	254	1222	5659	532	341	259	407	44044	564	1369	569
	Cv	2.38	0.98	0.66	5.76	4.55	0.98	0.73	12.84	4.33	0.69	2.08	1.52	2.62	0.52	5.70
	SNR	113	177	7685	18	35	667	4162	20	30	121	58	8345	64	1539	57
R364	NPA μ	9390	16543	909528	2922	5349	164482	648112	4665	6779	38915	18497	2748819	19329	256309	12500
	σμ	178	326	9402	186	270	1911	7629	183	213	597	591	72318	704	2395	719
	Cv	1.89	1.97	1.03	6.36	5.04	1.16	1.18	3.92	3.15	1.53	3.20	2.63	3.64	0.93	5.75
	SNR	92	130	6481	20	34	883	3492	23	26	125	53	7879	57	1509	72
R367	NPA μ	10358	21072	1057035	2827	5596	124682	628293	4944	7919	34414	18123	2667449	18329	255330	10200
	σμ	184	304	11209	224	260	1595	7160	478	457	911	734	72562	816	2633	574
	Cv	1.77	1.44	1.06	7.94	4.65	1.28	1.14	9.67	5.77	2.65	4.05	2.72	4.45	1.03	5.62
	SNR	100	164	7506	19	36	686	3467	25	31	113	53	7845	56	1531	60

Table 7-7 continued: HH-XRF (15 kV) analytical results for faience copper colourant glaze 03 replicated material. The table includes average NPA (NPA μ), average standard deviation (σ_μ) coefficient of variance (C_v) and signal-to noise ratio (SNR).

HH-XRF 15 kV Faience Replicate Copper Blue Samples R383-R392																
Parameters: 15 kV, 50 uA, vacuum, 180 seconds aquisition time, 10 Measurements per sample; Glaze 03 (R327-R392)																
Sample	Stat.	Na Kα	Al Kα	Si Kα	P Kα	S Kα	K Kα	Ca Kα	Ti Kα	Cr Kα	Fe Kα	Ni Kα	Cu Kα	Zn Kα	Rh Lα	Pd Lα
R383	NPA μ	12888	19620	1215642	2754	5660	156147	541481	4516	7563	36652	18630	2642006	18567	265103	8366
	σμ	291	294	11153	196	244	1388	5376	244	475	592	342	59438	423	2261	752
	Cv	2.26	1.50	0.92	7.12	4.31	0.89	0.99	5.41	6.28	1.62	1.84	2.25	2.28	0.85	8.98
	SNR	120	150	8490	19	36	854	2964	22	29	118	55	7636	55	1580	48
R384	NPA μ	2562	16511	1085117	1807	2973	101129	633502	4308	5861	33637	10287	2769866	14304	250359	5204
	σμ	137	284	8277	131	276	763	4739	300	327	750	466	53757	732	1705	606
	Cv	5.36	1.72	0.76	7.27	9.28	0.75	0.75	6.97	5.58	2.23	4.53	1.94	5.12	0.68	11.65
	SNR	21	117	7075	12	18	549	3365	21	22	107	30	7804	42	1354	28
R386	NPA μ	9152	16330	922638	2852	5377	142782	501564	5129	8185	34053	17908	2551931	18311	254074	12150
	σμ	161	225	6494	238	196	1098	3749	485	320	369	538	45235	607	1874	378
	Cv	1.76	1.38	0.70	8.33	3.64	0.77	0.75	9.45	3.91	1.08	3.01	1.77	3.32	0.74	3.11
	SNR	92	132	6721	20	35	788	2768	25	31	109	51	7329	54	1535	72
R388	NPA μ	2228	17743	1147291	1678	2913	114329	629898	4556	5437	29961	9585	2610469	13859	252206	5742
	σμ	218	277	7890	111	150	1109	4475	221	492	691	472	45242	370	2024	679
	Cv	9.78	1.56	0.69	6.62	5.15	0.97	0.71	4.84	9.04	2.31	4.92	1.73	2.67	0.80	11.83
	SNR	18	124	7384	11	17	611	3298	22	20	94	27	7196	40	1350	31
R390	NPA μ	7655	12858	774272	2984	5662	146059	442475	4950	6740	32715	17136	2473312	18332	246928	14738
	σμ	423	1007	49881	295	408	2576	3774	456	343	689	642	49884	531	4032	599
	Cv	5.53	7.83	6.44	9.89	7.20	1.76	0.85	9.21	5.10	2.10	3.75	2.02	2.90	1.63	4.07
	SNR	79	106	5756	21	37	810	2395	24	25	106	49	7128	54	1500	88
R392	NPA μ	9949	18707	1079592	2740	5166	98861	569611	4926	7871	36668	18737	2698836	20249	248174	12606
	σμ	263	362	8167	164	144	1006	4954	352	407	571	733	55328	675	1781	569
	Cv	2.65	1.93	0.76	5.99	2.79	1.02	0.87	7.14	5.17	1.56	3.91	2.05	3.33	0.72	4.51
	SNR	96	147	7701	19	34	555	3180	24	30	117	53	7681	59	1510	76

Table 7-8: HH-XRF (15 kV) analytical results for cobalt colourant faience glazes 05 and 07 replicated material. The table includes average NPA (NPA μ), average standard deviation (σ_μ), coefficient of variance (C_v) and signal-to-noise ratio (SNR).

HH-XRF 15 kV Faience Replicate Glaze Cobalt Blue Samples R406-R416																						
Parameters: 15 kV, 50 uA, vacuum, 10 Measurements per sample; Glaze 07 (R406-R416)																						
Sample	Stat.	Na Kα	Mg Kα	Al Kα	Si Kα	P Kα	S Kα	K Kα	Ca Kα	Ti Kα	Cr Kα	Mn Kα	Fe Kα	Co Kα	Ni Kα	Cu Kα	Zn Kα	Rh Lα	Pd Lα	Sn Lα	Sb Lα	Pb Lα
R406	NPA μ	6561	1847	13410	760965	2687	16105	140766	382302	4724	5480	49795	876438	120668	7661	1686166	10231	246227	6132	2350	13303	79142
	σ_μ	189	69	252	5879	114	371	1104	3491	521	508	486	10151	1661	463	27465	572	1844	857	266	1030	4883
	C_v	2.87	3.71	1.88	0.77	4.25	2.30	0.78	0.91	11.03	9.26	0.98	1.16	1.38	6.05	1.63	5.59	0.75	13.97	11.30	7.74	6.17
	SNR	65	16	106	5407	18	101	756	2043	23	20	167	2793	373	22	4926	31	1439	35	13	69	273
R408	NPA μ	7530	2725	22590	1007687	2409	19837	107636	424353	4674	7082	52320	902066	124768	7937	1636607	9723	245813	503	3163	13801	72783
	σ_μ	124	73	325	8611	262	391	1137	3704	335	365	653	11768	1743	451	32499	585	2144	283	221	602	5231
	C_v	1.65	2.66	1.44	0.85	10.87	1.97	1.06	0.87	7.18	5.15	1.25	1.30	1.40	5.69	1.99	6.02	0.87	56.17	6.98	4.36	7.19
	SNR	71	23	172	6976	16	125	592	2308	23	27	177	2905	380	24	4859	30	1452	3	17	73	249
R411	NPA μ	9054	3567	24790	1308095	2224	18565	128463	406463	3984	7290	50272	855980	123863	8551	1805050	10713	246667	36	4019	16209	84005
	σ_μ	232	119	332	4837	155	327	849	2593	170	433	453	5342	1196	417	19375	273	790	19	376	876	2940
	C_v	2.57	3.35	1.34	0.37	6.95	1.76	0.66	0.64	4.27	5.94	0.90	0.62	0.97	4.87	1.07	2.55	0.32	52.80	9.34	5.40	3.50
	SNR	81	28	181	8757	15	115	694	2169	19	27	165	2665	375	24	5161	31	1436	0	22	84	276
R412	NPA μ	7985	3247	23409	1152225	2291	18796	107024	450661	4467	6221	56483	957802	136373	8535	1830759	11153	244307	663	3422	15787	81710
	σ_μ	215	122	213	8172	161	334	952	3090	485	525	633	10532	1600	372	32039	486	1702	426	272	815	4950
	C_v	2.69	3.75	0.91	0.71	7.02	1.78	0.89	0.69	10.86	8.43	1.12	1.10	1.17	4.36	1.75	4.36	0.70	64.20	7.94	5.16	6.06
	SNR	73	26	174	7801	15	117	578	2404	21	23	185	2984	413	25	5250	33	1422	4	18	81	268
R415	NPA μ	7790	3133	18313	1286795	2472	14842	105409	347435	5166	8159	46524	764261	111671	9342	1664365	10543	239022	5414	2135	14305	85473
	σ_μ	181	144	329	9840	169	392	1018	2823	200	410	465	8927	1647	481	30313	466	1779	794	846	805	5587
	C_v	2.32	4.59	1.79	0.76	6.86	2.64	0.97	0.81	3.88	5.03	1.00	1.17	1.47	5.14	1.82	4.42	0.74	14.66	39.65	5.63	6.54
	SNR	72	26	138	8889	17	95	588	1902	25	30	152	2368	335	26	4711	31	1438	32	12	76	282
R416	NPA μ	6929	2701	18302	1098137	2573	14062	79003	344502	4202	7239	43620	714410	99475	8436	1374585	8083	236371	3881	3206	10643	67774
	σ_μ	170	60	325	11559	217	309	1010	3890	360	639	579	11824	1684	409	33066	510	2569	633	333	595	5397
	C_v	2.45	2.22	1.78	1.05	8.42	2.20	1.28	1.13	8.57	8.83	1.33	1.66	1.69	4.85	2.41	6.31	1.09	16.32	10.38	5.59	7.96
	SNR	66	23	143	7801	18	92	452	1931	21	27	147	2276	298	25	3981	24	1451	23	18	58	219

Table 7-8 continued: HH-XRF (15 kV) analytical results for cobalt colourant faience glazes 05 and 07 replicated material. The table includes average NPA (NPA μ), average standard deviation (σ_μ), coefficient of variance (C_v) and signal-to-noise ratio (SNR).

HH-XRF 15 kV Faience Replicate Glaze Cobalt Blue Samples R418-R429

Parameters: 15 kV, 50 uA, vacuum, 10 Measurements per sample; Glaze 05 (R418-R429)

Sample	Stat.	Na Kα	Mg Kα	Al Kα	Si Kα	P Kα	S Kα	K Kα	Ca Kα	Ti Kα	Cr Kα	Mn Kα	Fe Kα	Co Kα	Ni Kα	Cu Kα	Zn Kα	Rh Lα	Pd Lα	Sn Lα	Sb Lα	Pb Lα
R418	NPA μ	5019	1438	18317	603831	3000	9535	166350	492452	4264	4171	30662	706236	155521	6990	1138029	5667	242291	7274	9088	26145	36027
	σμ	141	97	137	3821	222	342	1001	2739	267	411	361	6948	1894	308	16474	375	1387	464	349	733	1861
	Cv	2.80	6.76	0.75	0.63	7.41	3.58	0.60	0.56	6.26	9.86	1.18	0.98	1.22	4.41	1.45	6.61	0.57	6.37	3.85	2.80	5.17
	SNR	52	13	151	4467	21	62	891	2629	21	16	108	2374	508	22	3512	18	1441	42	48	134	126
R421	NPA μ	8872	3624	28919	1084764	2662	14459	229109	616452	3983	5378	41081	909401	208828	8160	1588646	8856	256631	174	14597	34175	50698
	σμ	117	124	465	12901	120	485	3096	8335	341	418	444	17993	4278	385	48898	384	2507	163	471	791	5431
	Cv	1.32	3.43	1.61	1.19	4.49	3.35	1.35	1.35	8.56	7.78	1.08	1.98	2.05	4.72	3.08	4.34	0.98	93.95	3.23	2.32	10.71
	SNR	79	29	211	7253	17	88	1144	3080	19	20	139	2934	656	24	4744	27	1425	1	72	164	178
R423	NPA μ	8528	3963	57004	1263937	2479	12564	214729	518136	3793	7822	39317	852943	202006	9304	1577612	9345	251116	2091	12726	36852	54751
	σμ	225	106	502	10693	176	336	1967	4953	429	446	396	12018	3259	340	35470	378	1871	684	446	1078	3599
	Cv	2.64	2.68	0.88	0.85	7.09	2.68	0.92	0.96	11.31	5.71	1.01	1.41	1.61	3.65	2.25	4.04	0.75	32.69	3.50	2.93	6.57
	SNR	74	31	408	8345	16	77	1078	2557	17	29	130	2673	616	27	4557	28	1405	11	63	178	185
R424	NPA μ	5776	2043	27078	773115	2760	9639	187242	541937	3852	5313	38042	825730	191039	8163	1438498	8576	243486	9223	9868	32098	44743
	σμ	255	84	265	5128	191	480	1627	4671	426	361	466	9773	2270	302	25315	331	1668	581	1931	4726	3145
	Cv	4.42	4.13	0.98	0.66	6.90	4.98	0.87	0.86	11.07	6.79	1.22	1.18	1.19	3.69	1.76	3.86	0.69	6.30	19.57	14.72	7.03
	SNR	56	18	212	5461	19	60	962	2770	19	20	129	2659	598	24	4256	26	1397	52	50	158	155
R426	NPA μ	6091	2403	26032	974100	2617	9051	175701	435804	4439	8822	34706	745871	174563	7965	1365812	8561	242779	8461	8990	25890	46432
	σμ	297	114	142	6867	199	386	1252	3864	318	385	400	8266	2393	280	24255	506	1948	884	265	847	2765
	Cv	4.88	4.74	0.55	0.70	7.59	4.26	0.71	0.89	7.16	4.36	1.15	1.11	1.37	3.52	1.78	5.91	0.80	10.44	2.95	3.27	5.96
	SNR	58	20	202	6870	18	58	926	2273	21	33	116	2375	524	24	3989	26	1422	48	47	130	154
R429	NPA μ	8311	3962	43746	1348491	2309	10929	191985	460704	4279	9072	36406	768274	183821	8211	1420602	8444	251510	474	10379	29162	49187
	σμ	244	101	344	7076	207	345	1052	2574	318	678	584	6368	1813	416	17329	406	1013	280	300	811	2220
	Cv	2.94	2.55	0.79	0.52	8.96	3.16	0.55	0.56	7.43	7.48	1.60	0.83	0.99	5.07	1.22	4.81	0.40	59.02	2.89	2.78	4.51
	SNR	73	31	317	9000	15	68	996	2371	20	34	121	2425	564	24	4118	25	1441	3	53	145	162

Table 7-9: HH-XRF (40 kV) analytical results for faience copper colourant glaze 03 replicated material. The table includes average NPA (NPA μ), average standard deviation (σ_μ), coefficient of variance (C_v) and signal-to-noise ratio (SNR).

HH-XRF 40 kV Faience Replicate Copper Blue Samples R327-R351																
Parameters: 40 kV, 30 uA, Filter 3, 180 seconds aquisition time, 10 Measurements per sample; Glaze 03 (R327-R392)																
Sample	Stat.	K Kα	Ca Kα	Ti Kα	Cr Kα	Fe Kα	Ni Kα	Cu Kα	Zn Kα	Sr Kα	Zr Kα	Rh Kα	Pd Kα	Sn Kα	Sb Kα	Pb Lα
R327	NPA μ	271	2393	96	129	857	430	153626	963	903	1054	3899	36664	20648	21983	452
	σ_μ	61	80	38	27	78	84	918	65	31	51	185	423	305	269	67
	C_v	22.46	3.34	39.24	21.31	9.12	19.53	0.60	6.76	3.47	4.87	4.74	1.15	1.48	1.22	14.93
	SNR	5	55	3	5	30	13	4648	30	37	35	38	304	116	117	22
R328	NPA μ	231	2373	112	129	860	372	124655	832	683	1267	3971	38165	27435	25771	746
	σ_μ	87	125	45	28	51	42	1152	68	62	40	219	702	537	629	90
	C_v	37.62	5.27	40.79	21.81	5.97	11.19	0.92	8.16	9.05	3.18	5.51	1.84	1.96	2.44	12.03
	SNR	5	55	4	5	30	12	3900	27	27	40	37	308	150	135	35
R340	NPA μ	319	2121	112	132	817	419	139595	911	748	1068	3714	35969	23079	20938	527
	σ_μ	64	74	58	43	61	59	859	28	60	54	144	597	515	424	37
	C_v	19.98	3.50	52.03	32.70	7.43	14.20	0.62	3.10	8.00	5.10	3.87	1.66	2.23	2.03	7.09
	SNR	7	51	4	5	30	13	4275	29	32	35	36	304	130	112	25
R342	NPA μ	254	2606	102	124	908	451	152779	953	848	1251	3841	36864	24420	24720	481
	σ_μ	66	77	37	35	57	63	573	27	46	58	252	319	474	383	58
	C_v	25.79	2.95	36.10	28.02	6.30	13.86	0.38	2.88	5.47	4.64	6.57	0.86	1.94	1.55	11.99
	SNR	5	61	3	5	31	14	4491	30	35	41	36	308	136	130	23
R349	NPA μ	269	1831	88	148	777	359	135930	905	871	1047	4084	37800	16869	15830	329
	σ_μ	36	92	43	54	74	53	1282	69	72	65	163	484	345	427	58
	C_v	13.28	5.01	49.00	36.83	9.52	14.67	0.94	7.63	8.24	6.21	3.98	1.28	2.04	2.70	17.78
	SNR	5	42	3	5	28	11	4118	29	36	35	40	319	94	84	16
R351	NPA μ	119	1851	107	157	841	419	143195	992	961	1317	4063	39197	17743	13373	336
	σ_μ	44	89	48	59	72	33	1423	26	82	48	223	915	370	329	40
	C_v	36.67	4.83	44.93	37.76	8.58	7.98	0.99	2.58	8.56	3.63	5.49	2.33	2.08	2.46	11.99
	SNR	2	41	3	6	30	13	4265	32	39	42	39	321	98	69	16

Table 7-9 continued: HH-XRF (40 kV) analytical results for faience copper colourant glaze 03 replicated material. The table includes average NPA (NPA μ), average standard deviation (σ_μ), coefficient of variance (C_v) and signal-to-noise ratio (SNR).

HH-XRF 40 kV Faience Replicate Copper Blue Samples R356-R367																
Parameters: 40 kV, 30 uA, Filter 3, 180 seconds aquisition time, 10 Measurements per sample; Glaze 03 (R327-R392)																
Sample	Stat.	K Kα	Ca Kα	Ti Kα	Cr Kα	Fe Kα	Ni Kα	Cu Kα	Zn Kα	Sr Kα	Zr Kα	Rh Kα	Pd Kα	Sn Kα	Sb Kα	Pb Lα
R356	NPA μ	221	2246	79	140	851	409	144436	899	787	1071	3981	35269	21498	17369	489
	σ_μ	51	90	37	40	65	41	667	40	42	40	280	629	460	408	57
	C_v	22.96	4.02	47.34	28.27	7.59	10.01	0.46	4.50	5.28	3.75	7.02	1.78	2.14	2.35	11.58
	SNR	5	54	3	5	31	13	4404	29	33	36	39	299	123	94	24
R359	NPA μ	188	2108	106	139	809	412	145808	962	923	1278	4336	36435	12909	11672	275
	σ_μ	56	69	44	46	55	45	1187	36	58	78	218	783	394	374	57
	C_v	29.72	3.27	41.91	32.96	6.79	10.86	0.81	3.76	6.29	6.14	5.03	2.15	3.05	3.21	20.84
	SNR	4	49	3	5	29	13	4368	30	37	41	42	306	73	62	13
R360	NPA μ	421	3061	112	138	928	473	157586	980	817	1221	4108	34800	18325	20581	708
	σ_μ	76	96	42	41	84	50	595	45	56	44	184	371	496	403	27
	C_v	17.97	3.13	37.09	29.53	9.01	10.66	0.38	4.60	6.83	3.64	4.48	1.07	2.71	1.96	3.88
	SNR	9	72	4	5	33	15	4649	31	33	38	38	286	103	110	34
R363	NPA μ	231	3090	84	137	856	439	159149	975	898	1137	3747	32362	11874	11188	302
	σμ	48	72	46	58	51	39	961	38	55	55	278	526	258	245	74
	Cv	20.88	2.33	54.80	42.22	5.96	8.88	0.60	3.85	6.14	4.82	7.43	1.63	2.17	2.19	24.52
	SNR	5	76	3	5	30	14	4879	31	39	40	38	282	71	64	16
R364	NPA μ	388	2666	69	131	954	458	156287	996	888	1155	3950	36491	16726	16618	639
	σμ	49	66	28	62	69	54	1019	60	61	63	132	866	335	396	63
	Cv	12.57	2.48	41.15	47.41	7.25	11.75	0.65	6.01	6.90	5.43	3.34	2.37	2.00	2.39	9.78
	SNR	8	62	2	5	34	14	4599	31	37	39	38	307	94	89	30
R367	NPA μ	314	2601	130	152	982	464	151696	976	865	1028	3859	36212	20016	17504	423
	σμ	61	103	62	49	91	65	746	61	64	34	233	573	438	337	55
	Cv	19.51	3.95	48.23	32.17	9.23	14.03	0.49	6.21	7.34	3.31	6.03	1.58	2.19	1.92	13.02
	SNR	6	61	4	6	35	14	4501	31	36	34	38	310	115	94	20

Table 7-9 continued: HH-XRF (40 kV) analytical results for faience copper colourant glaze 03 replicated material. The table includes average NPA (NPA μ), average standard deviation (σ_μ), coefficient of variance (C_v) and signal-to-noise ratio (SNR).

HH-XRF 40 kV Faience Replicate Copper Blue Samples R383-R392																
Parameters: 40 kV, 30 uA, Filter 3, 180 seconds aquisition time, 10 Measurements per sample; Glaze 03 (R327-R392)																
Sample	Stat.	K Kα	Ca Kα	Ti Kα	Cr Kα	Fe Kα	Ni Kα	Cu Kα	Zn Kα	Sr Kα	Zr Kα	Rh Kα	Pd Kα	Sn Kα	Sb Kα	Pb Lα
R383	NPA μ	348	2032	107	150	817	413	145829	891	699	1035	3540	32223	14275	13077	383
	σμ	34	103	35	39	77	53	1030	33	55	58	302	647	301	485	45
	Cv	9.77	5.05	32.57	25.78	9.43	12.81	0.71	3.71	7.86	5.62	8.52	2.01	2.11	3.71	11.64
	SNR	8	51	4	6	29	13	4558	29	31	37	36	283	85	74	19
R384	NPA μ	196	2416	115	132	823	460	147660	908	728	1092	3767	35398	18409	20271	403
	σμ	52	67	34	37	46	67	1003	57	58	55	255	577	342	464	46
	Cv	26.64	2.79	29.45	28.27	5.63	14.47	0.68	6.25	7.94	5.04	6.77	1.63	1.86	2.29	11.45
	SNR	4	58	4	5	28	14	4519	29	32	37	37	297	104	109	19
R386	NPA μ	325	2038	110	156	819	436	155253	950	763	1256	4006	38769	21631	20311	634
	σμ	51	79	51	52	42	32	686	54	52	53	289	536	381	425	79
	Cv	15.68	3.87	45.79	33.19	5.18	7.33	0.44	5.66	6.75	4.20	7.21	1.38	1.76	2.09	12.50
	SNR	6	46	3	6	28	13	4519	30	31	40	38	316	119	106	29
R388	NPA μ	155	2345	98	144	887	435	146260	910	686	1604	4119	38559	22986	23462	433
	σμ	60	85	42	41	43	41	834	65	80	98	216	720	616	524	59
	Cv	38.59	3.61	42.61	28.43	4.88	9.44	0.57	7.19	11.68	6.08	5.24	1.87	2.68	2.23	13.57
	SNR	3	54	3	5	30	13	4398	28	28	51	39	310	125	122	21
R390	NPA μ	335	1985	94	141	822	394	140099	878	638	1098	4022	35746	25363	26087	1213
	σμ	52	95	34	45	49	47	1518	40	67	46	234	897	918	865	92
	Cv	15.50	4.80	36.58	31.73	5.94	12.05	1.08	4.60	10.56	4.16	5.81	2.51	3.62	3.32	7.57
	SNR	7	48	3	5	29	12	4222	28	27	36	38	300	143	141	58
R392	NPA μ	187	2306	109	159	854	432	154239	996	741	1239	4213	38516	22982	25050	363
	σμ	65	101	27	42	70	43	1105	67	74	46	275	636	287	453	47
	Cv	34.90	4.37	24.96	26.67	8.18	9.94	0.72	6.70	9.94	3.74	6.52	1.65	1.25	1.81	12.94
	SNR	4	53	3	6	29	13	4503	31	30	40	39	316	125	129	17

Table 7-10: HH-XRF (40 kV) analytical results for cobalt blue faience glazes 05 and 07 replicated material. The table includes average NPA (NPA μ), average standard deviation (σ_μ), coefficient of variance (C_v) and signal-to-noise ratio (SNR).

HH-XRF 40 kV Faience Replicate Glaze Cobalt Blue Samples R406-R416																				
Parameters: 40 kV, 30 uA, filter 3, 180 second aquisition time, 10 Measurements per sample; Glaze 07 (R406-R416)																				
Sample	Stat.	K Kα	Ca Kα	Ti Kα	Cr Kα	Mn Kα	Fe Kα	Co Kα	Ni Kα	Cu Kα	Zn Kα	Rb Kα	Sr Kα	Zr Kα	Rh Kα	Pd Kα	Sn Kα	Sb Kα	Pb Lα	Bi Lα
R406	NPA μ	56	1839	133	138	747	20458	3718	87	101567	622	386	912	1605	3647	34541	60366	38912	76546	1904
	σ_μ	47	117	48	73	45	149	95	45	785	62	49	61	63	199	779	1343	999	791	63
	C_v	83.68	6.38	36.05	53.11	6.04	0.73	2.57	51.04	0.77	9.91	12.59	6.72	3.91	5.45	2.26	2.22	2.57	1.03	3.30
	SNR	1	42	4	5	25	620	111	3	2943	17	11	29	46	37	303	359	223	2420	60
R408	NPA μ	1	1717	95	130	700	18817	3429	94	91184	609	360	845	1531	3699	35763	66842	40448	68622	1724
	σ_μ	0	67	65	49	44	145	56	47	442	59	47	52	63	164	421	914	537	528	61
	C_v	0.00	3.88	67.93	37.99	6.27	0.77	1.64	50.12	0.48	9.64	12.96	6.11	4.12	4.43	1.18	1.37	1.33	0.77	3.54
	SNR	0	39	3	4	23	578	104	3	2662	18	11	28	47	39	324	392	226	2226	55
R411	NPA μ	1	1753	95	146	736	19397	3760	107	107971	669	488	1119	1701	4432	39778	88574	53300	84430	2177
	σ_μ	0	86	34	56	58	217	91	50	1043	54	69	37	78	191	686	1578	1222	805	75
	C_v	0.00	4.93	35.47	38.49	7.86	1.12	2.43	46.89	0.97	8.01	14.11	3.35	4.58	4.31	1.72	1.78	2.29	0.95	3.46
	SNR	0	38	3	5	23	560	107	3	2958	18	13	33	46	45	349	508	293	2470	65
R412	NPA μ	1	1953	117	143	813	21351	4006	100	108587	668	427	1009	1626	4356	40197	73549	46987	81786	2042
	σ_μ	0	150	41	51	70	283	79	48	833	45	46	70	65	176	731	1472	899	778	44
	C_v	28.75	7.68	34.75	35.29	8.59	1.32	1.97	47.93	0.77	6.68	10.83	6.92	4.01	4.05	1.82	2.00	1.91	0.95	2.13
	SNR	0	41	3	5	25	611	114	3	2970	18	12	30	45	43	339	410	251	2406	61
R415	NPA μ	1	1481	115	120	608	16889	3298	84	95983	617	462	1075	1577	4030	39166	89158	51985	78376	2001
	σ_μ	0	85	33	36	61	217	49	44	1007	66	33	46	95	184	1092	2321	1480	926	116
	C_v	0.00	5.72	28.83	29.69	10.08	1.29	1.50	51.71	1.05	10.67	7.15	4.30	6.03	4.56	2.79	2.60	2.85	1.18	5.81
	SNR	0	32	3	4	19	513	97	2	2670	17	13	33	46	41	356	519	287	2336	60
R416	NPA μ	1	1740	93	121	696	17755	3332	116	90925	588	363	865	1734	4157	39617	70049	44273	70044	1723
	σ_μ	0	77	33	50	67	192	76	46	513	80	45	91	60	177	756	902	587	416	77
	C_v	0.00	4.43	35.78	40.84	9.67	1.08	2.27	40.18	0.56	13.63	12.47	10.51	3.44	4.26	1.91	1.29	1.33	0.59	4.49
	SNR	0	38	3	4	22	535	100	3	2599	17	11	27	50	41	340	390	233	2207	53

Table 7-10 continued: HH-XRF (40 kV) analytical results for cobalt blue faience glazes 05 and 07 replicated material. The table includes average NPA (NPA μ), average standard deviation (σ_μ), coefficient of variance (C_v) and signal-to-noise ratio (SNR).

HH-XRF 40 kV Faience Replicate Glaze Cobalt Blue Samples R418-R429																				
Parameters: 40 kV, 30 uA, filter 3, 180 second aquisition time, 10 Measurements per sample; Glaze 05 (R418-R429)																				
Sample	Stat.	K Kα	Ca Kα	Ti Kα	Cr Kα	Mn Kα	Fe Kα	Co Kα	Ni Kα	Cu Kα	Zn Kα	Rb Kα	Sr Kα	Zr Kα	Rh Kα	Pd Kα	Sn Kα	Sb Kα	Pb Lα	Bi Lα
R418	NPA μ	54	2539	110	140	472	16405	4872	83	69652	483	166	695	1064	3212	35344	91588	54643	33606	833
	σμ	64	110	47	57	52	179	102	55	489	51	38	32	76	258	508	1059	843	190	61
	Cv	119.74	4.35	42.43	40.53	10.96	1.09	2.09	65.43	0.70	10.51	23.14	4.59	7.18	8.03	1.44	1.16	1.54	0.57	7.27
	SNR	1	59	4	5	17	542	161	3	2287	16	6	25	34	34	317	549	317	1281	32
R421	NPA μ	24	2505	95	143	531	18461	5643	115	82125	551	242	888	1128	3531	37807	151023	87671	40752	1043
	σμ	40	103	37	45	38	153	61	35	495	29	54	61	48	194	416	1997	1263	290	81
	Cv	165.62	4.12	39.19	31.35	7.13	0.83	1.09	30.37	0.60	5.22	22.19	6.85	4.24	5.51	1.10	1.32	1.44	0.71	7.76
	SNR	0	57	3	5	18	574	175	4	2527	17	8	30	34	39	364	950	531	1456	36
R423	NPA μ	1	2081	108	177	525	17803	5753	119	86452	607	274	1013	1316	4036	42748	176656	100394	43990	1152
	σμ	0	86	32	38	58	88	103	47	421	53	37	84	75	238	682	2116	1256	332	92
	Cv	0.00	4.12	29.81	21.41	11.14	0.50	1.80	39.60	0.49	8.69	13.45	8.28	5.69	5.90	1.60	1.20	1.25	0.75	7.97
	SNR	0	45	3	6	17	548	172	4	2486	17	8	33	38	43	402	1065	585	1442	38
R424	NPA μ	27	2403	95	111	536	18239	5654	88	82819	537	210	907	1318	3719	38562	115003	68312	40880	999
	σμ	38	80	34	39	61	202	114	45	467	45	46	53	55	201	356	1447	875	298	57
	Cv	142.15	3.34	35.96	35.41	11.44	1.11	2.02	50.97	0.56	8.35	21.70	5.80	4.15	5.41	0.92	1.26	1.28	0.73	5.67
	SNR	1	53	3	4	18	567	175	3	2506	16	7	31	40	39	345	676	385	1453	35
R426	NPA μ	6	1926	104	130	488	17196	5499	129	82627	555	292	1006	1507	3920	41857	152008	84057	43835	1133
	σμ	12	126	59	52	46	132	53	42	596	49	73	81	62	196	616	1548	1201	243	57
	Cv	203.97	6.55	56.77	40.36	9.47	0.77	0.97	32.50	0.72	8.84	24.82	8.03	4.09	4.99	1.47	1.02	1.43	0.55	5.02
	SNR	0	41	3	4	16	530	167	4	2411	16	9	33	44	40	373	881	473	1461	39
R429	NPA μ	1	1927	118	161	493	17650	5709	95	86036	588	298	1077	1546	4341	45683	180906	103007	46035	1141
	σμ	0	57	35	63	40	198	101	38	670	61	39	88	67	148	829	3596	2304	576	75
	Cv	0.00	2.94	29.76	39.00	8.03	1.12	1.77	40.50	0.78	10.35	13.00	8.14	4.31	3.42	1.82	1.99	2.24	1.25	6.61
	SNR	0	40	3	5	16	518	166	3	2459	16	9	33	42	44	398	1031	569	1491	36

Table 7-11: HH-XRF (15 kV) analytical results for Saqqara archaeological sherds. The table includes average NPA (NPA μ), average standard deviation (σ_μ), coefficient of variance (C_v) and signal-to-noise ratio (SNR). Blank spaces indicate peak not observed. BD is below detection.

HH-XRF 15 kV Archaeological Faience from Saqqara s12-s31

Parameters: 15 kV, 50 uA, vacuum, 180 seconds aquisition time, Average of 10 Measurements

Sample	Stat.	Na Kα	Mg Kα	Al Kα	Si Kα	P Kα	S Kα	K Kα	Ca Kα	Ti Kα	Cr Kα	Mn Kα	Fe Kα	Co Kα	Ni Kα	Cu Kα	Zn Kα	Rh Lα	Pb Lα	Pb Mα	Bi Lα	Bi Mα
s12	NPA μ	2974	2063	27014	1025895	5959		28424	217156	21633	4139	15653	379957	13772	11714	925680	16239	236936	704375	200812	10545	28622
	σ_μ	296	164	268	5879	230		422	1542	525	542	383	3881	358	404	14536	547	1271	50690	1138	669	722
	C_v	9.96	7.95	0.99	0.57	3.86		1.48	0.71	2.43	13.09	2.44	1.02	2.60	3.45	1.57	3.37	0.54	7.20	0.57	6.34	2.52
	SNR	24	14	167	5580	30		67	1253	100	15	50	1140	39	32	2466	43	1176	2074	979	32	139
s17	NPA μ	5876	2811	23759	981125	5114	44021	78925	574024	47673	4558	20171	617514		18849	3708415	22914	323485	20706	2477		
	σ_μ	147	130	381	8981	334	359	746	5450	549	293	398	8919		760	83164	437	2686	953	120		
	C_v	2.50	4.62	1.60	0.92	6.54	0.82	0.94	0.95	1.15	6.42	1.97	1.44		4.03	2.24	1.91	0.83	4.60	4.86		
	SNR	51	22	166	6203	31	256	429	3050	225	17	69	1932		55	10582	67	1756	71	14		
s20	NPA μ	4099	2081	28353	929541	4268		19104	436947	38253	3946	21351	742734		13403	1695728	11156	290086	364258	97762		
	σ_μ	136	355	2596	17646	508		5527	22556	4136	441	546	46114		297	160342	1309	2781	43694	17065		
	C_v	3.31	17.04	9.16	1.90	11.90		28.93	5.16	10.81	11.17	2.56	6.21		2.21	9.46	11.74	0.96	12.00	17.46		
	SNR	35	16	193	5643	25		104	2336	177	14	72	2296		38	4731	31	1493	1159	528		
s21	NPA μ	7495	2364	13836	979984	3207		11341	425110	18569		486045	507727	8953	7886	165845	7221	893682	21494	35759		
	σ_μ	154	125	312	6261	235		277	2990	420		4742	6287	296	415	2223	311	5337	669	412		
	C_v	2.05	5.30	2.25	0.64	7.34		2.44	0.70	2.26		0.98	1.24	3.30	5.26	1.34	4.30	0.60	3.11	1.15		
	SNR	62	18	90	5648	17		70	2502	89		1650	1597	27	23	476	20	4694	65	189		
s22	NPA μ	5827	2287	15647	1152660	2525	102247	53514	186858	14683	7293	15950	303015	10993	9968	1545178	16356	282711	24811			
	σ_μ	265	152	255	11933	158	1289	607	2066	605	545	329	4461	335	314	34279	693	3033	1289			
	C_v	4.54	6.64	1.63	1.04	6.28	1.26	1.13	1.11	4.12	7.48	2.06	1.47	3.05	3.15	2.22	4.24	1.07	5.20			
	SNR	54	19	115	7635	16	623	329	1107	72	27	55	955	32	29	4354	46	1656	77			
s31	NPA μ	4361	4063	16457	998154	3149	33036	23434	531149	30286	6818	25058	588475	13758	9543	1452398	10701	298876				
	σ_μ	130	170	265	6160	174	379	284	3743	540	387	354	6867	451	310	25290	423	2294				
	C_v	2.98	4.18	1.61	0.62	5.53	1.15	1.21	0.70	1.78	5.68	1.41	1.17	3.28	3.25	1.74	3.96	0.77				
	SNR	41	34	125	6897	21	209	141	3097	148	25	84	1864	42	28	4165	31	1831				

Table 7-11 continued: HH-XRF (15 kV) analytical results for Saqqara archaeological sherds. The table includes average NPA (NPA μ), average standard deviation (σ_μ), coefficient of variance (C_v) and signal-to-noise ratio (SNR). Blank spaces indicate peak not observed. BD is below detection.

HH-XRF 15 kV Archaeological Faience from Saqqara s42-s72

Parameters: 15 kV, 50 uA, vacuum, 180 seconds aquisition time, Average of 10 Measurements

Sample	Stat.	Na Kα	Mg Kα	Al Kα	Si Kα	P Kα	S Kα	K Kα	Ca Kα	Ti Kα	Cr Kα	Mn Kα	Fe Kα	Co Kα	Ni Kα	Cu Kα	Zn Kα	Rh Lα	Pb Lα	Pb Mα	Bi Lα	Bi Mα
s42	NPA μ	3917	1685	28027	904789	9533	79034	34536	559221	36455	3918	21892	823330	20584	9142	1611693	10235	298829	341883		6460	34983
	σ_μ	118	126	414	4338	234	696	422	3068	535	293	496	5732	432	341	17710	474	1611	15839		383	289
	C_v	3.00	7.46	1.48	0.48	2.46	0.88	1.22	0.55	1.47	7.48	2.27	0.70	2.10	3.73	1.10	4.63	0.54	4.63		5.93	0.82
	SNR	34	13	189	5441	54	428	189	2885	167	14	74	2549	60	26	4526	29	1527	1087		21	187
s45	NPA μ	3830	4623	15829	1158507	3668		36165	434751	37505	3433	19187	918344	21115	8940	147555	8912	235343	615257	191367	9391	32136
	σ_μ	162	230	207	6197	181		452	2669	314	392	536	9759	522	516	2642	533	1648	40768	1188	678	420
	C_v	4.23	4.98	1.31	0.53	4.93		1.25	0.61	0.84	11.41	2.79	1.06	2.47	5.78	1.79	5.98	0.70	6.63	0.62	7.22	1.31
	SNR	30	33	98	6380	19		174	2229	170	12	64	2815	61	26	410	24	1115	1859	939	30	157
s48	NPA μ	6420	3030	16908	1186755	3632	22068	30207	311281	19037	4999	18030	732039	47280	10986	2794572	21958	298334	15400	1677		
	σ_μ	242	147	262	13461	187	305	388	3959	838	367	367	13116	1188	417	72854	945	3485	657	101		
	C_v	3.78	4.84	1.55	1.13	5.14	1.38	1.29	1.27	4.40	7.33	2.04	1.79	2.51	3.79	2.61	4.30	1.17	4.26	6.05		
	SNR	59	25	126	8040	24	139	182	1807	91	18	59	2262	137	31	7860	64	1832	51	11		
s53	NPA μ	4719	2671	10135	638564	5406	71274	20221	1651737	13383	5325	16283	289008	10202	13003	1589092	16179	307332	19927	9		
	σ_μ	312	227	389	14397	635	1015	2587	344224	469	388	770	4069	786	532	74093	703	2321	772	23		
	C_v	6.61	8.49	3.84	2.25	11.75	1.42	12.79	20.84	3.51	7.28	4.73	1.41	7.70	4.09	4.66	4.35	0.76	3.87	262.41		
	SNR	43	22	72	4016	32	395	104	8662	68	20	58	936	31	38	4558	46	1568	63	0		
s70	NPA μ	4813	1387	11564	610929	4202	21923	71885	216098	15793	4954	18501	2203961	270674	7592	1828039	11955	269314	8703	1318		
	σ_μ	186	47	189	5236	175	355	702	1949	470	502	436	28192	3822	541	32693	602	2438	647	99		
	C_v	3.86	3.42	1.63	0.86	4.16	1.62	0.98	0.90	2.98	10.14	2.35	1.28	1.41	7.12	1.79	5.03	0.91	7.43	7.51		
	SNR	48	12	92	4327	28	139	421	1245	76	18	61	6914	812	23	5462	37	1637	30	8		
s72	NPA μ	5283	2673	19844	1169014	3155	61532	28337	403182	26645	5890	24846	1696671	262610	11021	658186	34594	298762				
	σ_μ	187	112	312	8489	144	907	359	2834	510	572	466	19051	3880	599	11446	987	2013				
	C_v	3.54	4.18	1.57	0.73	4.55	1.47	1.27	0.70	1.91	9.71	1.88	1.12	1.48	5.44	1.74	2.85	0.67				
	SNR	48	22	146	7769	21	378	171	2341	128	21	83	5118	778	33	1924	100	1739				

Table 7-11 continued: HH-XRF (15 kV) analytical results for Saqqara archaeological sherds. The table includes average NPA (NPA μ), average standard deviation (σ_μ), coefficient of variance (C_v) and signal-to-noise ratio (SNR). Blank spaces indicate peak not observed. BD is below detection.

HH-XRF 15 kV Archaeological Faience from Saqqara s74-s83

Parameters: 15 kV, 50 uA, vacuum, 180 seconds aquisition time, Average of 10 Measurements

Sample	Stat.	Na Kα	Mg Kα	Al Kα	Si Kα	P Kα	S Kα	K Kα	Ca Kα	Ti Kα	Cr Kα	Mn Kα	Fe Kα	Co Kα	Ni Kα	Cu Kα	Zn Kα	Rh Lα	Pb Lα	Pb Mα	Bi Lα	Bi Mα
s74	NPA μ	6111	3085	18114	1173289	2951	27804	60416	507426	22723	4652	21002	1317397	196686	11189	1783910	26342	312732	19989	2692		
	σ_μ	201	117	233	8874	180	219	622	4093	566	431	570	15018	2690	406	27899	598	2253	898	107		
	C_v	3.29	3.79	1.29	0.76	6.10	0.79	1.03	0.81	2.49	9.27	2.72	1.14	1.37	3.63	1.56	2.27	0.72	4.49	3.97		
	SNR	55	25	132	7769	19	170	345	2839	109	17	71	4091	578	33	5144	76	1776	66	16		
s78	NPA μ	6927	2380	15477	941410	4471	24690	58249	760064	17038	4848	16696	2316921	168112	7330	2320400	18902	330689	17229	3252		
	σ_μ	192	70	260	3971	286	491	492	3592	744	378	449	20899	2231	437	32136	640	1173	1002	199		
	C_v	2.77	2.95	1.68	0.42	6.39	1.99	0.84	0.47	4.37	7.80	2.69	0.90	1.33	5.96	1.38	3.39	0.35	5.82	6.10		
	SNR	61	18	109	5978	27	143	312	4038	80	17	54	7183	511	22	6830	58	1838	60	19		
s80	NPA μ	4058	1586	12639	866035	4002	218442	14603	706484	14332	8771	17752	398828	15641	8753	1012815	10026	315827				
	σ_μ	215	138	239	6958	220	1662	343	4778	493	500	342	4270	352	352	15452	345	2091				
	C_v	5.29	8.71	1.89	0.80	5.50	0.76	2.35	0.68	3.44	5.70	1.93	1.07	2.25	4.02	1.53	3.45	0.66				
	SNR	36	12	86	5167	22	1181	86	4101	71	33	60	1267	47	26	2867	28	1735				
s81	NPA μ	4468	3183	11487	650578	4411	117632	26342	1959044	34629	5766	26161	737015	15711	10936	1060826	38968	316660				
	σ_μ	78	105	217	5650	207	1374	298	19469	543	493	561	11025	324	493	23068	943	2723				
	C_v	1.75	3.30	1.89	0.87	4.70	1.17	1.13	0.99	1.57	8.55	2.14	1.50	2.06	4.51	2.17	2.42	0.86				
	SNR	38	24	77	3861	24	617	131	10107	175	22	90	2405	48	33	3113	113	1602				
s82	NPA μ	6395	2701	16757	1107525	3466	23049	56735	324947	17071	5746	16567	411025	13738	12489	2461044	19890	316266	26545	2889		
	σ_μ	277	85	212	11116	176	397	730	3900	394	443	490	7374	400	388	61707	642	3335	1749	61		
	C_v	4.33	3.16	1.27	1.00	5.07	1.72	1.29	1.20	2.31	7.71	2.96	1.79	2.91	3.11	2.51	3.23	1.05	6.59	2.12		
	SNR	59	22	126	7551	23	145	333	1848	82	21	54	1274	40	36	6867	57	1915	85	18		
s83	NPA μ	5144	3540	20332	1340659	3906	39556	43395	699362	23330	8397	20351	427188	13374	10011	1032560	8090	288657	23807	538		
	σ_μ	174	120	211	7692	334	405	462	4280	417	271	368	3820	386	403	14598	312	1289	671	96		
	C_v	3.38	3.40	1.04	0.57	8.54	1.02	1.06	0.61	1.79	3.22	1.81	0.89	2.89	4.03	1.41	3.86	0.45	2.82	17.92		
	SNR	46	29	148	8875	25	243	249	3931	115	31	70	1359	40	29	2961	23	1652	75	3		

Table 7-11 continued: HH-XRF (15 kV) analytical results for Saqqara archaeological sherds. The table includes average NPA (NPA μ), average standard deviation (σ_μ), coefficient of variance (C_v) and signal-to-noise ratio (SNR). Blank spaces indicate peak not observed. BD is below detection.

HH-XRF 15 kV Archaeological Faience from Saqqara s84-s91

Parameters: 15 kV, 50 uA, vacuum, 180 seconds aquisition time, Average of 10 Measurements

Sample	Stat.	Na Kα	Mg Kα	Al Kα	Si Kα	P Kα	S Kα	K Kα	Ca Kα	Ti Kα	Cr Kα	Mn Kα	Fe Kα	Co Kα	Ni Kα	Cu Kα	Zn Kα	Rh Lα	Pb Lα	Pb Mα	Bi Lα	Bi Mα
s84	NPA μ	4341	1651	12422	718064	3160	19443	17669	549746	39170	5383	24885	721445	19862	9432	1908370	13069	295375	10034	1555		
	σ_μ	157	96	228	6790	245	516	328	5523	725	431	519	11199	486	240	45751	539	2622	720	108		
	C_v	3.62	5.81	1.84	0.95	7.75	2.66	1.86	1.00	1.85	8.00	2.08	1.55	2.45	2.54	2.40	4.12	0.89	7.17	6.97		
	SNR	43	15	99	5128	21	124	105	3206	192	20	84	2318	60	28	5576	38	1811	34	10		
s85	NPA μ	5648	3661	23854	1270620	3962	37590	47422	636725	44541	5579	27011	811714	22698	9557	1851004	13085	306870	14360	1303		
	σ_μ	182	175	239	12305	195	986	1980	14203	2548	318	734	20776	712	347	43520	451	1964	714	93		
	C_v	3.22	4.78	1.00	0.97	4.91	2.62	4.17	2.23	5.72	5.69	2.72	2.56	3.14	3.63	2.35	3.44	0.64	4.97	7.18		
	SNR	50	28	170	8292	25	228	271	3572	215	21	89	2553	67	28	5324	38	1805	47	8		
s87	NPA μ	5693	3100	22262	1238384	3224	38549	78690	749413	41160	6033	23115	730315	19282	8480	1282621	8934	302729	16178	1317		
	σ_μ	168	89	169	6440	230	358	515	4028	436	361	419	5630	451	308	12726	532	1605	669	54		
	C_v	2.96	2.88	0.76	0.52	7.12	0.93	0.66	0.54	1.06	5.98	1.81	0.77	2.34	3.63	0.99	5.95	0.53	4.13	4.12		
	SNR	51	25	161	8128	20	233	435	4114	201	23	80	2339	58	25	3758	26	1685	53	8		
s89	NPA μ	5908	3576	23270	1443953	3321	25350	74496	535436	31626	6285	23827	605167	16084	9070	1087366	8932	303502	18024	2011		
	σ_μ	178	127	253	13695	157	364	944	5757	434	274	453	9341	554	443	22983	483	2735	617	93		
	C_v	3.02	3.54	1.09	0.95	4.73	1.44	1.27	1.08	1.37	4.37	1.90	1.54	3.44	4.89	2.11	5.41	0.90	3.42	4.61		
	SNR	53	29	170	9649	22	158	428	3009	154	23	80	1921	48	27	3140	26	1820	57	12		
s90	NPA μ	5448	3349	27509	1172867	3108	26886	26637	553427	40262	5829	28267	777077	21809	10137	2096534	14887	331356	14299	2519		
	σ_μ	156	136	318	8734	257	351	421	4506	744	375	499	9935	263	523	39802	580	2531	700	89		
	C_v	2.86	4.07	1.16	0.74	8.27	1.31	1.58	0.81	1.85	6.43	1.76	1.28	1.21	5.16	1.90	3.89	0.76	4.89	3.55		
	SNR	49	27	199	7744	20	165	157	3167	194	21	93	2439	64	30	6015	43	1977	47	15		
s91	NPA μ	4261	2770	16054	1089216	4175	39427	24671	583393	23437	6774	20785	401565	13032	9848	1016842	7922	292765	22034	633		
	σ_μ	113	158	171	10366	156	528	512	5380	350	234	526	4338	454	500	13405	429	2921	720	133		
	C_v	2.65	5.69	1.06	0.95	3.73	1.34	2.07	0.92	1.50	3.45	2.53	1.08	3.49	5.08	1.32	5.42	1.00	3.27	21.05		
	SNR	40	24	121	7435	27	247	147	3361	115	25	72	1282	39	29	2914	22	1743	69	4		

Table 7-12: HH-XRF (40 kV) analytical results for Saqqara archaeological sherds. The table includes average NPA (NPA μ), average standard deviation (σ_μ), coefficient of variance (C_v) and signal-to-noise ratio (SNR). Blank spaces indicate peak not observed.

HH-XRF 40 kV Archaeological Faience from Saqqara s12-s31																					
Parameters: 40 kV, 30 uA, filter 3, 180 second aquisition time, Average of 10 Measurements																					
Sample	Stat.	Ca Kα	Ti Kα	Cr Kα	Mn Kα	Fe Kα	Co Kα	Ni Kα	Cu Kα	Zn Kα	Br Kα	Rb Kα	Sr Kα	Zr Kα	Rh Kα	Pd Kα	Sn Kα	Sb Kα	Pb Lα	Bi Lα
s12	NPA μ	814	253			8230			55067	1188			5440	3814	3817	22284	3016	26739	796398	19815
	σ_μ	89	57			134			575	48			163	115	134	452	168	690	6589	209
	C_v	10.91	22.44			1.63			1.04	4.06			3.00	3.02	3.50	2.03	5.58	2.58	0.83	1.05
	SNR	16	6			176			1047	19			103	88	58	288	24	196	10575	256
s17	NPA μ	1674	668	100	178	9778	363	198	162409	816	259	588	7692	5189	3701	35452	56157	6493	7676	172
	σ_μ	203	51	55	53	915	54	46	19187	89	45	54	636	448	304	2014	4350	591	481	45
	C_v	12.11	7.60	54.70	29.56	9.35	14.89	23.02	11.81	10.92	17.39	9.18	8.26	8.63	8.21	5.68	7.75	9.09	6.26	25.94
	SNR	40	22	4	6	317	11	6	4615	25	10	21	276	155	36	305	328	36	344	8
s20	NPA μ	1138	693	118	211	12996		203	80862	556		1175	11146	3845	3459	28938	5300	44685	321309	7875
	σ_μ	216	87	75	58	2065		68	9450	71		160	2365	559	479	2965	605	4938	32820	958
	C_v	18.97	12.58	63.41	27.72	15.89		33.62	11.69	12.75		13.58	21.22	14.54	13.85	10.25	11.41	11.05	10.21	12.16
	SNR	26	19	4	6	368		5	1950	13		23	259	94	40	294	35	284	6396	152
s21	NPA μ	1059	490	106	5367	8488		78	5524	382	107	238	10126		3767	34034	5116	2906	95	
	σ_μ	581	65	43	962	808		37	3452	35	29	176	1194		233	2216	324	565	35	
	C_v	54.81	13.20	40.84	17.93	9.52		47.59	62.49	9.13	27.47	74.13	11.79		6.19	6.51	6.33	19.44	37.10	
	SNR	27	18	4	222	348		4	253	17	5	9	393		35	277	30	144	5	
s22	NPA μ	692	152	126	128	6020		240	83950	1478	290	215	6058	2499	4153	39970	30342	2739	14194	338
	σ_μ	85	42	51	36	89		32	475	38	55	42	82	60	247	679	357	255	130	48
	C_v	12.35	27.51	40.45	28.52	1.48		13.20	0.57	2.56	18.81	19.56	1.35	2.39	5.94	1.70	1.18	9.31	0.92	14.34
	SNR	16	5	5	5	216		8	2659	48	10	7	208	73	38	315	165	14	572	14
s31	NPA μ	2034	259	118	247	11548	216	117	70046	560	426	439	13579	2954	4503	35475	4943		875	
	σ_μ	69	56	59	52	97	39	34	486	42	36	47	145	59	298	714	298		30	
	C_v	3.40	21.63	49.77	21.26	0.84	17.88	28.94	0.69	7.46	8.56	10.76	1.07	2.00	6.61	2.01	6.02		3.45	
	SNR	50	9	5	9	433	8	4	2426	21	18	16	488	86	41	280	28		41	

Table 7-12 continued: HH-XRF (40 kV) analytical results for Saqqara archaeological sherds. The table includes average NPA (NPA μ), average standard deviation (σ_μ), coefficient of variance (C_v) and signal-to-noise ratio (SNR). Blank spaces indicate peak not observed.

HH-XRF 40 kV Archaeological Faience from Saqqara s42-s72																					
Parameters: 40 kV, 30 uA, filter 3, 180 second aquisition time, Average of 10 Measurements																					
Sample	Stat.	Ca Kα	Ti Kα	Cr Kα	Mn Kα	Fe Kα	Co Kα	Ni Kα	Cu Kα	Zn Kα	Br Kα	Rb Kα	Sr Kα	Zr Kα	Rh Kα	Pd Kα	Sn Kα	Sb Kα	Pb Lα	Bi Lα	
s42	NPA μ	1668	615	130	293	16986			70194	564		1121	10862	2790	4077	35626	5914	42493	329517	7654	
	σ_μ	142	54	48	56	1178			11502	65		113	437	343	330	1400	215	3255	26518	653	
	C_v	8.54	8.72	36.48	19.06	6.94			16.39	11.56		10.07	4.03	12.30	8.08	3.93	3.64	7.66	8.05	8.53	
	SNR	34	16	4	8	462			1691	13		22	253	68	43	325	35	241	6457	146	
s45	NPA μ	1389	626		20005	382			8153	632			9673	5207	3729	30209	4032	84778	623780	15621	
	σ_μ	243	106		1155	78			1942	183			660	191	179	1462	321	11106	76343	1923	
	C_v	17.50	16.95		5.77	20.50			23.82	28.88			6.82	3.67	4.79	4.84	7.96	13.10	12.24	12.31	
	SNR	28	15		480	9			177	12			185	115	47	326	27	548	8960	223	
s48	NPA μ	942	518	109	142	13082	1079		129019	1037	302	257	9303	2427	4065	34281	6522		2903		
	σ_μ	70	40	55	37	1234	114		9805	117	45	78	541	229	520	2807	762		306		
	C_v	7.39	7.74	50.24	25.98	9.43	10.55		7.60	11.30	14.86	30.21	5.81	9.44	12.80	8.19	11.68		10.54		
	SNR	23	17	4	5	446	35		4051	33	13	10	361	76	39	281	38		140		
s53	NPA μ	3586	168	135	154	6421		257	88871	857	254		12067	1675	4916	38985	22090		5996	167	
	σ_μ	131	47	53	39	84		56	759	42	50		159	75	294	640	437		98	32	
	C_v	3.65	28.13	38.86	25.08	1.30		21.83	0.85	4.92	19.79		1.32	4.46	5.97	1.64	1.98		1.64	19.37	
	SNR	82	5	5	6	231		8	2824	28	9		401	46	43	298	118		255	7	
s70	NPA μ	920	475	123	171	42080	6355	129	74138	637	180	140	7802	1899	3570	30341	8094		3360		
	σ_μ	222	46	49	32	3996	678	38	12321	95	58	34	658	209	350	1989	508		582		
	C_v	24.16	9.77	39.97	18.72	9.49	10.66	29.88	16.62	14.89	32.33	24.00	8.43	10.98	9.81	6.56	6.27		17.32		
	SNR	24	16	5	6	1433	218	5	2667	23	8	6	311	63	36	267	50		169		
s72	NPA μ	1691	232	107	247	34023	6880	249	35000	2481	292	440	15334	4278	4991	37813	7073		910		
	σ_μ	85	56	55	46	236	116	39	314	50	64	49	101	104	317	675	192		78		
	C_v	5.01	24.34	51.05	18.56	0.69	1.69	15.78	0.90	2.01	21.91	11.23	0.66	2.44	6.36	1.78	2.71		8.60		
	SNR	40	7	4	9	1160	240	9	1200	89	12	16	546	121	45	299	39		41		

Table 7-12 continued: HH-XRF (40 kV) analytical results for Saqqara archaeological sherds. The table includes average NPA (NPA μ), average standard deviation (σ_μ), coefficient of variance (C_v) and signal-to-noise ratio (SNR). Blank spaces indicate peak not observed.

HH-XRF 40 kV Archaeological Faience from Saqqara s74-s83																				
Parameters: 40 kV, 30 uA, filter 3, 180 second aquisition time, Average of 10 Measurements																				
Sample	Stat.	Ca Kα	Ti Kα	Cr Kα	Mn Kα	Fe Kα	Co Kα	Ni Kα	Cu Kα	Zn Kα	Br Kα	Rb Kα	Sr Kα	Zr Kα	Rh Kα	Pd Kα	Sn Kα	Sb Kα	Pb Lα	Bi Lα
s74	NPA μ	2231	222	116	264	29389	5682	253	94894	1842	298	287	13402	2309	4720	38101	22061		11702	274
	σ_μ	89	67	64	35	306	104	37	610	82	38	68	141	96	116	599	503		171	42
	C_v	3.98	30.00	54.94	13.39	1.04	1.82	14.43	0.64	4.47	12.69	23.78	1.05	4.17	2.46	1.57	2.28		1.46	15.16
	SNR	52	7	4	9	941	178	8	2823	57	10	9	428	65	43	305	122		475	11
s78	NPA μ	2053	463	110	166	36996	3596	114	83679	902	244	107	13186	1438	3421	28690	11774		5082	118
	σ_μ	205	32	38	29	2358	237	24	4744	69	42	55	1133	214	318	1418	1246		261	27
	C_v	9.98	6.96	34.26	17.64	6.37	6.58	21.03	5.67	7.68	17.32	50.86	8.60	14.86	9.30	4.94	10.58		5.14	23.27
	SNR	54	16	4	6	1285	125	4	2983	32	10	4	505	48	36	260	75		254	6
s80	NPA μ	1280	433	100	109	6610	230	70	37470	504	148	98	6577	1195	4115	38144	5170		888	
	σ_μ	577	57	43	37	1051	35	23	10880	79	34	52	1451	121	424	3286	435		364	
	C_v	45.08	13.19	43.26	33.69	15.90	15.21	32.29	29.04	15.74	23.09	53.23	22.07	10.13	10.31	8.62	8.42		40.96	
	SNR	31	15	4	4	259	9	3	1473	20	7	4	257	37	38	300	29		44	
s81	NPA μ	3700	567	109	202	11884		115	38249	1421	251	171	16745	1575	3938	36078	5075		2036	
	σ_μ	1077	100	28	77	4474		45	5678	1138	38	50	2161	413	419	2455	400		366	
	C_v	29.10	17.66	25.84	37.94	37.65		39.44	14.84	80.09	15.29	29.22	12.91	26.21	10.64	6.80	7.88		17.99	
	SNR	89	19	4	8	454		4	1467	53	10	6	623	48	37	293	29		96	
s82	NPA μ	1320	449	119	115	7388		281	97810	636	199	310	9734	2199	4090	39302	14325		12401	308
	σ_μ	198	74	34	42	571		49	6918	62	76	65	676	166	370	1445	1179		883	65
	C_v	15.01	16.55	28.20	36.67	7.73		17.33	7.07	9.74	38.21	20.84	6.94	7.54	9.05	3.68	8.23		7.12	21.23
	SNR	30	14	4	4	256		9	3111	20	7	10	336	64	38	313	79		513	13
s83	NPA μ	2487	177	130	177	8688		182	56732	446	336	370	17438	3057	4630	38183	18965	4555	10647	222
	σ_μ	84	39	44	29	111		49	521	59	71	75	219	121	253	905	536	293	144	28
	C_v	3.39	22.05	34.01	16.32	1.27		26.90	0.92	13.27	21.03	20.37	1.26	3.94	5.46	2.37	2.83	6.43	1.35	12.83
	SNR	57	6	5	7	321		6	1942	16	12	12	567	88	43	313	106	24	449	9

Table 7-12 continued: HH-XRF (40 kV) analytical results for Saqqara archaeological sherds. The table includes average NPA (NPA μ), average standard deviation (σ_μ), coefficient of variance (C_v) and signal-to-noise ratio (SNR). Blank spaces indicate peak not observed.

HH-XRF 40 kV Archaeological Faience from Saqqara s84-s91																				
Parameters: 40 kV, 30 uA, filter 3, 180 second aquisition time, Average of 10 Measurements																				
Sample	Stat.	Ca Kα	Ti Kα	Cr Kα	Mn Kα	Fe Kα	Co Kα	Ni Kα	Cu Kα	Zn Kα	Br Kα	Rb Kα	Sr Kα	Zr Kα	Rh Kα	Pd Kα	Sn Kα	Sb Kα	Pb Lα	Bi Lα
s84	NPA μ	2445	317	114	306	15389	469	176	103290	656	250		11462	4589	3724	31034	4374		2332	84
	σ_μ	74	62	63	69	149	67	31	890	61	23		161	33	156	590	186		53	25
	C_v	3.02	19.71	54.79	22.72	0.97	14.38	17.64	0.86	9.37	9.31		1.41	0.73	4.18	1.90	4.25		2.26	29.49
	SNR	63	11	5	12	565	17	6	3415	23	11		441	145	37	269	26		114	4
s85	NPA μ	1866	634	130	279	15477	421	166	96384	667	245	363	12364	4889	4234	37374	4838	3360	2978	
	σ_μ	153	62	41	26	435	63	44	4261	63	38	52	481	650	189	774	311	197	106	
	C_v	8.22	9.82	31.96	9.17	2.81	14.88	26.68	4.42	9.50	15.53	14.39	3.89	13.29	4.47	2.07	6.43	5.88	3.56	
	SNR	43	20	5	10	530	14	5	3145	22	10	13	443	144	39	302	27	18	134	
s87	NPA μ	2718	258	123	295	15001	394	113	75928	544	171		14153	5419	4368	35481	7952		5018	138
	σ_μ	83	34	27	52	207	60	45	890	47	60		175	150	263	877	389		141	32
	C_v	3.04	13.32	21.70	17.70	1.38	15.15	39.59	1.17	8.55	35.24		1.24	2.76	6.02	2.47	4.89		2.81	23.42
	SNR	64	8	5	11	543	14	4	2559	19	7		503	161	41	299	45		228	6
s89	NPA μ	2227	255	131	258	12821	241	83	58279	504	286	338	24238	3663	4905	39656	20150		5648	139
	σ_μ	72	55	44	47	128	23	29	453	53	58	50	273	131	327	540	458		95	36
	C_v	3.21	21.70	33.68	18.38	0.99	9.61	34.78	0.78	10.58	20.30	14.80	1.13	3.59	6.67	1.36	2.27		1.68	25.75
	SNR	50	8	5	9	460	9	3	1951	18	10	10	752	97	43	311	109		240	6
s90	NPA μ	2609	376	108	316	17852	547	184	114406	799	295	366	14331	5544	4956	39533	5274	3493	3229	99
	σ_μ	89	41	46	66	232	53	36	1010	72	65	38	162	98	281	764	364	238	54	57
	C_v	3.41	10.90	42.25	20.77	1.30	9.75	19.35	0.88	9.08	22.22	10.50	1.13	1.78	5.67	1.93	6.91	6.81	1.67	57.62
	SNR	59	12	4	11	590	18	6	3460	26	11	12	469	150	45	316	29	18	142	4
s91	NPA μ	2400	189	108	178	8594	214	76	53375	440	342	343	18279	3091	4706	37573	17993	4328	10638	247
	σ_μ	97	46	47	46	120	51	40	372	25	42	68	161	155	109	551	540	231	107	31
	C_v	4	24	44	26	1	24	53	1	6	12	20	1	5	2	1	3	5	1	12
	SNR	56	6	4	7	324	8	3	1826	15	12	11	576	84	43	299	99	23	440	10

Table 7-13: SEM-EDS analytical results for faience copper colourant glaze 03 replicated material. The table includes average wt% (wt% μ), average standard deviation (σ_μ) and coefficient of variance (C_v). Totals are analytical totals, not normalized totals. Blank spaces indicate peak not observed.

SEM-EDS Faience Replicate Glaze 03 Copper Blue Samples (Normalized wt%)																							
Parameters 20 kV, 9 Measurements per Sample; Glaze 03 (R327-R392)																							Analytical
Sample	Stats	Na_2O	MgO	Al_2O_3	SiO_2	P_2O_5	SO_3	K_2O	CaO	TiO_2	Cr_2O_3	FeO	CoO	NiO	CuO	ZnO	As_2O_3	Rb_2O	SrO	Ag_2O	SnO_2	BaO	PbO	Total
R327	wt% μ	17.98		1.08	69.01	0.33		2.10	5.61				0.09	0.19	3.62									100.08
	σμ	0.53		0.13	1.09	0.06		0.13	0.43				0.00	0.00	0.26									
	Cv	2.93		11.91	1.56	18.18		6.04	7.65				0.00	0.00	7.15									
R328	wt% μ	12.99		1.52	64.06	0.46		2.28	5.19					0.17	3.68		1.38	4.96	2.59		0.72			96.44
	σμ	3.82		0.83	2.71	0.19		0.17	0.47					0.00	0.52		0.18	2.76	1.01		0.00			
	Cv	27.16		50.60	3.92	38.00		6.85	8.34					0.00	13.01		11.81	51.33	35.89		0.00			
R340	wt% μ	18.32	0.18	0.85	68.98	0.32		2.38	5.35						3.62									95.49
	σμ	0.57	0.00	0.15	0.86	0.02		0.11	0.32						0.20									
	Cv	3.05	0.00	17.03	1.22	6.29		4.39	5.94						5.48									
R342	wt% μ	16.34	0.19	1.01	68.92	0.24		1.62	7.00						4.68									98.13
	σμ	0.66	0.00	0.25	0.94	0.00		0.10	1.25						0.30									
	Cv	3.94	0.00	24.24	1.34	0.00		5.89	17.45						6.39									
R349	wt% μ	15.42		1.38	72.48			1.97	4.98						3.54								0.24	96.21
	σμ	0.74		0.58	1.44			0.08	0.58						0.46								0.00	
	Cv	4.72		41.46	1.96			3.86	11.45						12.71								0.00	
R351	wt% μ	16.52		1.40	70.50			1.40	5.92			0.13			4.13									101.50
	σμ	0.66		0.27	1.18			0.08	0.51			0.00			0.44									
	Cv	3.96		19.27	1.65			5.82	8.57			0.00			10.46									
R356	wt% μ	18.09		1.14	69.67	0.27		1.56	5.59						3.69									97.00
	σμ	0.88		0.20	1.54	0.00		0.08	0.60						0.29									
	Cv	4.78		17.50	2.17	0.00		4.76	10.50						7.79									
R359	wt% μ	16.85		1.01	70.09	0.00		1.41	5.89						4.35				0.40					100.37
	σμ	0.39		0.18	0.49			0.07	0.29						0.23				0.00					
	Cv	2.29		17.48	0.68			4.56	4.77						5.26				0.00					
R360	wt% μ	18.66		1.44	67.83	0.14		2.39	5.74		0.18				3.41					0.21				97.67
	σμ	3.45		0.92	5.37	0.00		0.22	1.63		0.00				0.72					0.00				
	Cv	18.20		62.96	7.81	0.00		9.01	27.94		0.00				20.75					0.00				

Table 7-13 continued: SEM-EDS analytical results for faience copper colourant glaze 03 replicated material. The table includes average wt% (wt% μ), average standard deviation (σ_μ) and coefficient of variance (C_v). Totals are analytical totals, not normalized totals. Blank spaces indicate peak not observed.

SEM-EDS Faience Replicate Glaze 03 Copper Blue Samples (Normalized wt%)																							
Parameters 20 kV, 9 Measurements per Sample; Glaze 03 (R327-R392)																							Analytical
Sample	Stats	Na_2O	MgO	Al_2O_3	SiO_2	P_2O_5	SO_3	K_2O	CaO	TiO_2	Cr_2O_3	FeO	CoO	NiO	CuO	ZnO	As_2O_3	Rb_2O	SrO	Ag_2O	SnO_2	BaO	PbO	Total
R363	wt% μ	17.17		1.07	67.88			3.28	6.04						4.37							0.19		94.87
	σμ	1.37		0.45	1.34			1.41	0.98						0.32							0.00		
	Cv	7.91		41.48	1.96			42.54	16.03						7.24							0.00		
R364	wt% μ	20.86		1.03	67.16			2.22	5.29						3.44									102.47
	σμ	1.18		0.39	0.97			0.10	0.80						0.25									
	Cv	5.61		37.50	1.42			4.30	14.96						7.14									
R367	wt% μ	16.73		1.15	68.39	0.25		3.35	5.93						4.20									100.41
	σμ	0.87		0.53	1.31	0.00		1.05	0.52						0.39									
	Cv	5.17		45.73	1.90	0.00		31.12	8.64						9.32									
R383	wt% μ	21.11		1.15	67.37			2.36	4.59						3.42									99.43
	σμ	1.41		0.35	1.18			0.14	0.36						0.38									
	Cv	6.63		30.29	1.74			6.08	7.79						10.88									
R384	wt% μ	17.19	0.21	1.19	68.16	0.25	0.18	1.44	6.16	0.17					4.62				0.43					99.86
	σμ	0.66	0.00	0.37	1.34	0.02	0.00	0.08	0.67	0.00					0.22				0.00					
	Cv	3.77	0.00	30.44	1.92	5.88	0.00	5.15	10.53	0.00					4.62				0.00					
R386	wt% μ	20.10		0.82	68.80			2.28	4.39						3.34	0.27								97.43
	σμ	1.05		0.21	0.79			0.11	0.52						0.33	0.00								
	Cv	5.17		25.15	1.13			4.85	11.77						9.74	0.00								
R388	wt% μ	16.87		1.03	69.71			1.48	5.92						4.51		0.17				0.31			99.96
	σμ	0.33		0.19	1.63			0.16	1.42						0.27		0.00				0.00			
	Cv	1.91		18.18	2.30			10.86	23.63						5.97		0.00				0.00			
R390	wt% μ	19.64		1.19	68.07		0.11	2.02	5.15						3.81						0.00			100.01
	σμ	2.15		0.88	1.86		0.00	0.08	0.62						0.23									
	Cv	10.82		72.74	2.69		0.00	3.77	11.87						5.85									
R392	wt% μ	16.36		0.89	67.00		0.32	1.57	5.81	0.20					4.48		0.27	1.61	1.48					97.52
	σμ	0.45		0.27	1.77		0.00	0.08	0.81	0.00					0.22		0.00	0.62	0.36					
	Cv	2.65		30.04	2.56		0.00	4.69	13.61	0.00					4.82		0.00	37.79	23.28					

Table 7-14: SEM-EDS analytical results for faience cobalt colourant glaze 07 replicated material. The table includes average wt% (wt% μ), average standard deviation (σ_μ) and coefficient of variance (C_v). Totals are analytical totals, not normalized totals. Blank spaces indicate peak not observed.

SEM-EDS Faience Replicate Glaze 07 Cobalt Blue Samples (Normalized wt%)																				
Parameters 20 kV, 9 Measurements per Sample; Glaze 07 (R406-R416)																				Analytical
Sample	Stat	Na_2O	MgO	Al_2O_3	SiO_2	P_2O_5	SO_3	K_2O	CaO	Cr_2O_3	MnO	FeO	CoO	CuO	Rb_2O	Ag_2O	SnO_2	Sb_2O_5	BaO	PbO	Total
R406	wt% μ	16.59	1.24	0.86	67.15			2.46	4.51		0.19	1.72	0.29	3.44			0.16	0.28		1.11	98.03
	σμ	1.75	0.22	0.17	2.32			0.09	0.38		0.04	0.30	0.05	0.36			0.00	0.00		0.15	
	Cv	10.38	17.25	19.61	3.39			3.62	8.19		20.67	17.15	16.85	10.38			0.00	0.00		13.37	
R408	wt% μ	13.98	1.27	1.02	67.33	0.30		1.70	5.54		0.17	2.04	0.24	3.84			0.53	0.81		1.23	99.11
	σμ	0.70	0.14	0.34	1.91	0.00		0.11	1.16		0.00	0.32	0.03	0.25			0.02	0.05		0.16	
	Cv	4.90	11.05	32.51	2.78	0.00		6.37	20.44		0.00	15.54	11.66	6.34			2.75	6.02		12.41	
R411	wt% μ	15.70	1.14	1.13	67.53	0.29		2.17	4.67			1.77	0.24	3.23			0.51	0.55		1.06	98.69
	σμ	1.12	0.11	0.35	1.34	0.00		0.16	0.31			0.25	0.02	0.25			0.34	0.00		0.10	
	Cv	7.02	9.79	30.41	1.95	0.00		7.03	6.55			13.73	9.77	7.73			63.81	0.00		8.77	
R412	wt% μ	13.33	1.19	1.34	69.66			1.83	4.82		0.18	1.86	0.23	3.68			0.00	0.57	0.17	1.14	99.80
	σμ	0.79	0.17	1.26	2.00			0.12	0.39		0.01	0.15	0.01	0.24				0.01	0.00	0.19	
	Cv	5.81	13.81	92.93	2.82			6.33	7.97		6.80	8.07	5.59	6.42				1.72	0.00	16.14	
R415	wt% μ	14.45	1.06	1.23	70.31	0.28		2.04	4.12		0.15	1.61	0.27	3.04			0.00	0.51		0.93	99.12
	σμ	0.94	0.10	0.58	0.86	0.00		0.10	0.27		0.00	0.16	0.06	0.26				0.06		0.18	
	Cv	6.39	9.24	46.28	1.20	0.00		5.03	6.40		0.00	9.88	20.33	8.56				10.68		19.18	
R416	wt% μ	12.67	1.14	1.24	68.77			1.65	4.59		0.19	3.99	0.31	3.13			0.51	0.80		1.01	99.65
	σμ	0.49	0.06	0.49	1.33			0.07	0.21		0.02	4.77	0.02	0.21			0.07	0.00		0.20	
	Cv	3.67	4.67	37.86	1.84			3.77	4.39		10.00	119.41	5.10	6.27			12.15	0.00		18.78	

Table 7-14 continued: SEM-EDS analytical results for faience cobalt colourant glaze 05 replicated material. The table includes average wt% (wt% μ), average standard deviation (σ_μ) and coefficient of variance (C_v). Totals are analytical totals, not normalized totals. Blank spaces indicate peak not observed.

SEM-EDS Faience Replicate Glaze 05 Cobalt Blue Samples (Normalized wt%)																				
Parameters 20 kV, 9 Measurements per Sample; Glaze 05 (R418-R429)																				Analytical
Sample	Stat	Na_2O	MgO	Al_2O_3	SiO_2	P_2O_5	SO_3	K_2O	CaO	Cr_2O_3	MnO	FeO	CoO	CuO	Rb_2O	Ag_2O	SnO_2	Sb_2O_5	BaO	PbO	Total
R418	wt% μ	15.65	1.80	1.05	64.60			3.17	6.09		0.26	1.96	0.34	2.93			0.60	0.90		0.65	100.57
	σμ	0.96	0.27	0.99	1.56			0.18	1.02		0.01	0.20	0.07	0.29			0.04	0.24		0.14	
	Cv	6.02	14.55	92.04	2.38			5.60	16.51		3.85	10.24	19.27	9.69			5.79	26.05		21.73	
R421	wt% μ	14.23	1.78	0.86	64.93			2.95	6.51		0.17	1.88	0.37	3.36			1.49	0.90	-0.13	0.69	98.16
	σμ	0.43	0.16	0.19	0.91			0.21	0.85		0.00	0.19	0.06	0.28			0.00	0.29	0.00	0.14	
	Cv	2.93	8.49	21.02	1.37			6.82	12.67		0.00	9.66	14.39	7.98			0.00	31.38	0.00	19.47	
R423	wt% μ	14.05	1.69	1.21	66.12			2.86	6.36	0.15		1.82	0.38	3.03			0.78	0.87		0.67	99.15
	σμ	0.73	0.14	0.38	1.96			0.14	0.87	0.00		0.12	0.08	0.21			0.00	0.12		0.14	
	Cv	5.11	8.37	30.39	2.90			4.83	13.46	0.00		6.72	20.04	6.95			0.00	13.57		21.00	
R424	wt% μ	14.30	1.52	1.21	67.43			2.89	6.02		0.17	1.84	0.35	2.77		0.22	0.00	0.67		0.63	96.83
	σμ	0.27	0.10	0.32	1.05			0.10	0.37		0.00	0.15	0.08	0.20		0.00		0.06		0.10	
	Cv	1.87	6.65	26.06	1.52			3.42	5.97		0.00	8.25	23.35	7.09		0.00		9.09		15.81	
R426	wt% μ	12.66	1.51	1.13	68.60		0.30	2.69	5.84			1.69	0.35	2.52	0.43		0.81	0.86		0.61	101.44
	σμ	0.26	0.14	0.38	1.02		0.00	0.11	0.22			0.16	0.09	0.20	0.00		0.00	0.11		0.12	
	Cv	2.03	9.12	33.13	1.45		0.00	4.04	3.71			9.09	24.62	7.86	0.00		0.00	12.77		18.33	
R429	wt% μ	12.60	1.48	1.17	69.29			2.70	5.91			1.76	0.35	2.79			0.58	0.87		0.51	100.08
	σμ	0.28	0.09	0.33	0.61			0.07	0.32			0.16	0.08	0.09			0.00	0.16		0.06	
	Cv	2.17	6.26	27.75	0.87			2.50	5.38			8.74	23.88	3.31			0.00	18.08		11.42	

Table 7-15: SEM-EDS analytical results for Saqqara archaeological faience glazes. The table includes average wt% (wt% μ), average standard deviation (σ_μ) and coefficient of variance (C_v).

SEM-EDS Analytical Results for Saqqara Faience (Normalized wt%)																								Analytical
Sherd	Stat.	Location	Na_2O	MgO	Al_2O_3	SiO_2	P_2O_5	SO_3	Cl	K_2O	CaO	TiO_2	V_2O_5	Cr_2O_3	MnO	FeO	CoO	NiO	CuO	ZnO	As_2O_3	SrO	Ag_2O	SnO_2	Sb_2O_5	PbO	Total
s12	wt% μ	Surface	8.55	0.42	0.64	67.59		0.45	1.48	0.91	2.23	0.27				0.59			1.54	0.07				0.30	0.62	14.36	94.01
	σ_μ		5.99	0.04	0.04	7.89		0.00	0.22	0.35	0.04	0.00				0.04			0.29	0.00				0.00	0.14	1.63	
	C_v		69.04	8.84	6.23	11.50		0.00	14.98	38.04	1.57	0.00				6.17			18.75	0.00				0.00	21.60	11.15	
	wt% μ	Middle	10.00	0.46	0.55	66.33			1.41	1.01	2.20	0.32				0.59			1.29						0.65	15.17	94.71
	σ_μ		3.24	0.03	0.10	3.34			0.15	0.14	0.16	0.06				0.16			0.12						0.09	1.27	
	C_v		31.53	5.51	18.29	4.90			10.12	13.76	6.89	18.18				25.43			9.28						14.29	8.13	
	wt% μ	Interior	8.00	0.43	0.60	68.35		0.70	1.45	0.91	2.47	0.24				0.61			1.44						0.58	14.21	93.44
	σ_μ		5.83	0.08	0.17	3.23		0.00	0.18	0.34	0.26	0.00				0.11			0.13						0.08	1.41	
	C_v		70.88	16.98	27.29	4.59		0.00	12.41	36.20	10.27	0.00				16.85			8.76						13.33	9.66	
	wt% μ	Total	8.85	0.44	0.60	67.42		0.58	1.45	0.95	2.30	0.28				0.60			1.42	0.07				0.30	0.62	14.58	
	σ_μ		5.25	0.06	0.12	5.37		0.13	0.19	0.30	0.22	0.06				0.11			0.22					0.00		1.52	
	C_v		57.96	12.26	19.73	7.77		22.03	12.78	30.86	9.33	18.80				18.20			15.29					0.00		10.16	
s17	wt% μ	Surface	14.16	0.90	2.23	68.11		0.40	1.70	0.60	3.36	0.42		0.15		1.06			6.33					0.58			93.52
	σ_μ		1.11	0.17	0.07	1.76		0.00	0.08	0.18	0.35	0.00		0.00		0.30			0.81					0.00			
	C_v		7.71	19.10	3.26	2.54		0.00	4.53	29.65	10.16	0.00		0.00		27.87			12.65					0.00			
	wt% μ	Middle	15.53	1.13	1.86	67.45			1.73	0.57	3.77	0.55				0.88			6.21					0.31			97.96
	σ_μ		1.55	0.20	0.51	1.59			0.14	0.17	0.24	0.32				0.07			0.66					0.00			
	C_v		10.00	17.39	27.32	2.36			7.86	29.20	6.29	57.80				8.39			10.70					0.00			
	wt% μ	Interior	15.32	0.86	1.96	68.46		0.50	1.58	0.56	3.50	0.27				0.72			5.73					0.54			97.80
	σ_μ		0.99	0.23	0.46	2.52		0.00	0.11	0.22	0.20	0.08				0.08			1.34					0.02			
	C_v		6.44	26.28	23.61	3.67		0.00	6.85	38.71	5.59	30.22				10.68			23.32					3.70			
	wt% μ	Total	15.00	0.96	2.01	68.01		0.45	1.67	0.58	3.54	0.41		0.15		0.89			6.09					0.48			
	σ_μ		1.34	0.23	0.43	2.13		0.05	0.13	0.19	0.31	0.23		0.00		0.23			1.02					0.11			
	C_v		8.90	23.93	21.40	3.11		9.89	7.62	32.79	8.62	58.23		0.00		26.03			16.69					22.15			
s20	wt% μ	Surface	11.69	0.62	1.17	66.23	0.48		2.27	0.29	3.51	0.33				1.14			3.86						1.00	7.43	90.88
	σ_μ		0.00	0.12	0.33	5.79	0.15		0.15	0.00	0.51	0.13				0.15			0.29						0.04	0.86	
	C_v		0.00	18.17	25.92	7.92	27.62		6.11	0.00	13.23	36.11				11.73			6.82						3.40	10.44	
	wt% μ	Middle	12.81	0.64	1.52	64.04			2.28	0.31	4.15	0.72				1.29			3.75						1.44	7.05	98.66
	σ_μ		1.40	0.10	0.33	1.89			0.14	0.06	0.19	0.50				0.34			0.02						0.36	0.74	
	C_v		10.68	15.55	21.40	2.89			6.08	19.26	4.45	67.35				25.69			0.44						24.49	10.25	
	wt% μ	Interior	10.11	0.73	1.37	67.68	0.36	0.36	2.12	0.32	5.29	0.30				1.09			3.35						1.13	5.80	96.81
	σ_μ		3.35	0.11	0.06	4.51	0.00	0.00	0.03	0.05	0.34	0.07				0.21			0.32						0.00	0.31	
	C_v		32.34	14.15	4.40	6.49	0.00	0.00	1.30	14.36	6.25	21.31				19.13			9.26						0.00	5.25	
	wt% μ	Total	11.54	0.66	1.35	65.98	0.42	0.36	2.22	0.31	4.32	0.45				1.17			3.65						1.19	6.76	
	σ_μ		2.73	0.12	0.30	5.36	0.14	0.00	0.18	0.05	0.76	0.35				0.26			0.42						0.27	1.15	
	C_v		22.91	16.94	20.86	7.72	29.39	0.00	7.86	15.73	16.76	75.83				21.26			10.85						21.81	16.08	

Table 7-15 continued: SEM-EDS analytical results for Saqqara archaeological faience glazes. The table includes average wt% (wt% μ), average standard deviation (σ_μ) and coefficient of variance (C_v).

SEM-EDS Analytical Results for Saqqara Faience (Normalized wt%)																									Analytical
Sherd	Stat.	Location	Na_2O	MgO	Al_2O_3	SiO_2	P_2O_5	SO_3	Cl	K_2O	CaO	TiO_2	V_2O_5	Cr_2O_3	MnO	FeO	CoO	NiO	CuO	ZnO	As_2O_3	SrO	Ag_2O	SnO_2	Sb_2O_5	PbO	Total
s21	wt% μ	Surface	10.80	0.43	1.82	78.20			1.59	1.15	2.54				1.33	1.20			0.30							0.65	84.92
	σ_μ		5.63	0.06	0.63	5.12			0.82	0.37	0.82				0.09	0.51			0.00							0.03	
	C_v		48.97	12.93	32.36	6.16			48.29	30.43	30.48				6.68	40.28			0.00							4.35	
	wt% μ	Middle	13.77	0.38	1.00	73.92			1.81	0.98	5.08				0.52	0.59			0.24			0.98				0.73	86.69
	σ_μ		6.22	0.02	0.19	6.02			0.03	0.23	0.11				0.15	0.09			0.00			0.05				0.21	
	C_v		41.54	3.98	17.94	7.49			1.66	21.94	2.05				27.05	13.69			0.00			4.67				27.08	
	wt% μ	Interior	13.15	0.47	1.41	75.38			1.41	1.18	4.11				0.84	0.85			0.27							0.94	90.59
	σ_μ		4.76	0.05	0.37	5.15			0.80	0.14	0.58				0.23	0.30			0.00							0.21	
	C_v		33.37	9.16	24.07	6.30			52.43	10.90	13.02				25.27	32.80			0.00							20.41	
	wt% μ	Total	12.57	0.42	1.41	75.83			1.60	1.10	3.91				0.90	0.88			0.27			0.98				0.77	
	σ_μ		5.77	0.06	0.56	5.56			0.69	0.28	1.31				0.40	0.43			0.02			0.05				0.23	
	C_v		42.49	12.98	36.68	6.81			39.63	23.69	30.89				41.27	45.87			8.45			4.67				26.90	
s22	wt% μ	Surface	7.55	0.63	0.81	83.86	0.60	0.93	0.47	0.69	1.13					0.37			2.48							0.48	87.28
	σ_μ		0.19	0.06	0.09	0.99	0.00	0.05	0.32	0.06	0.04					0.08			0.20							0.00	
	C_v		2.42	8.96	10.84	1.14	0.00	4.71	65.95	8.55	3.87					20.72			8.00							0.00	
	wt% μ	Middle	8.12	0.71	0.83	82.81		0.89	0.56	0.90	1.61					0.48			2.49							0.59	87.83
	σ_μ		0.26	0.08	0.08	0.53		0.17	0.19	0.15	0.38					0.19			0.16							0.00	
	C_v		3.20	10.82	9.27	0.63		18.61	33.65	16.23	23.57					39.16			6.27							0.00	
	wt% μ	Interior	10.93	0.59	0.81	79.07		0.66	1.44	0.82	2.65				0.19	0.41			1.96					0.47			92.14
	σ_μ		3.58	0.09	0.09	3.77		0.05	0.26	0.35	0.81				0.00	0.03			0.36					0.00			
	C_v		32.26	14.40	11.09	4.70		7.97	17.80	42.15	30.10				0.00	6.94			18.25					0.00			
	wt% μ	Total	8.87	0.64	0.82	81.91	0.60	0.83	0.83	0.81	1.80				0.19	0.42			2.31					0.47	0.54		
	σ_μ		2.55	0.09	0.09	3.44	0.00	0.17	0.51	0.24	0.82				0.00	0.13			0.36					0.00	0.05		
	C_v		28.20	13.70	10.47	4.12	0.00	20.19	61.38	28.85	45.11				0.00	29.85			15.51					0.00	8.26		
s31	wt% μ	Surface	12.37	1.14	2.94	74.08		0.61	1.56	0.87	3.69					0.81			1.92								96.08
	σ_μ		8.01	0.15	2.04	8.82		0.23	0.15	0.36	0.49					0.05			0.22								
	C_v		64.07	13.26	68.80	11.79		37.68	9.62	41.25	13.11					6.22			11.41								
	wt% μ	Middle	18.21	0.81	1.42	69.58		0.61	1.65	1.10	4.08	0.24				0.70			1.61								100.02
	σ_μ		0.57	0.07	0.05	0.80		0.07	0.03	0.05	0.08	0.00				0.06			0.13								
	C_v		3.14	8.54	3.51	1.15		11.16	2.06	4.52	1.97	0.00				8.81			8.33								
	wt% μ	Interior	16.08	0.86	1.34	72.60			1.48	1.08	4.42					0.73			1.41								98.23
	σ_μ		1.69	0.19	0.13	1.13			0.07	0.05	0.14					0.10			0.18								
	C_v		10.53	21.90	9.44	1.55			4.58	5.02	3.14					13.87			12.82								
	wt% μ	Total	15.55	0.94	1.90	72.09		0.61	1.56	1.02	4.06	0.24				0.75			1.65								
	σ_μ		5.30	0.21	1.40	5.54		0.17	0.12	0.24	0.41	0.00				0.09			0.28								
	C_v		33.94	22.08	73.13	7.65		27.79	7.65	23.14	10.10	0.00				12.07			17.15								

Table 7-15 continued: SEM-EDS analytical results for Saqqara archaeological faience glazes. The table includes average wt% (wt% μ), average standard deviation (σ_μ) and coefficient of variance (C_v).

SEM-EDS Analytical Results for Saqqara Faience (Normalized wt%)																								Analytical
Sherd	Stat.	Location	Na_2O	MgO	Al_2O_3	SiO_2	P_2O_5	SO_3	Cl	K_2O	CaO	TiO_2	V_2O_5	Cr_2O_3	MnO	FeO	CoO	NiO	CuO	ZnO	As_2O_3	SrO	Ag_2O	SnO_2	Sb_2O_5	PbO	Total
s42	wt% μ	Surface	0.35	0.76	1.20	72.22			2.58		3.72					1.81			3.23						2.17	11.96	88.69
	σ_μ		0.26	0.24	0.28	0.65			0.15		0.52					0.20			0.48						0.58	0.92	
	C_v		72.04	30.42	23.00	0.89			5.91		13.83					11.09			14.77						26.50	7.59	
	wt% μ	Middle		0.87	1.19	73.42			2.50	0.19	4.78				0.17	1.44			2.85						1.27	11.32	89.36
	σ_μ			0.12	0.17	1.38			0.20	0.00	0.15				0.00	0.16			0.13						0.34	1.08	
	C_v			13.61	14.16	1.81			7.86	0.00	2.96				0.00	10.50			4.29						25.88	9.22	
	wt% μ	Interior		0.84	1.18	73.80	0.35		2.43		5.16	0.26				1.41	0.22		2.90						1.11	10.34	92.14
	σ_μ			0.18	0.14	1.92	0.00		0.17		0.10	0.00				0.27	0.00		0.19						0.33	1.34	
	C_v			20.48	11.53	2.53	0.00		6.86		1.92	0.00				18.52	0.00		6.42						29.31	12.58	
	wt% μ	Total	0.35	0.82	1.19	73.15	0.35		2.50	0.19	4.55	0.26			0.17	1.55	0.22		2.99						1.52	11.21	
	σ_μ		0.26	0.19	0.21	1.92	0.00		0.19	0.00	0.73	0.00			0.00	0.28	0.00		0.34						0.64	1.30	
	C_v		72.04	22.63	16.97	2.55	0.00		7.20	0.00	15.57	0.00			0.00	17.42	0.00		11.17						41.02	11.27	
s45	wt% μ	Surface	13.58	0.65	1.08	62.57			1.73	0.97	3.89	0.24				2.10									2.20	10.98	94.60
	σ_μ		0.73	0.03	0.51	1.02			0.22	0.02	0.16	0.09				0.28									0.22	0.53	
	C_v		5.29	4.97	47.01	1.60			12.39	2.08	3.99	38.08				13.01									9.87	4.72	
	wt% μ	Middle	14.62	0.57	0.72	62.43			1.72	0.92	4.04	0.35				1.82									1.84	10.98	94.60
	σ_μ		0.11	0.15	0.16	1.81			0.10	0.02	0.07	0.14				0.23									0.43	0.94	
	C_v		0.76	25.30	21.90	2.83			5.90	2.61	1.80	39.37				12.31									22.72	8.35	
	wt% μ	Interior	14.30	0.52	0.73	63.40			1.74	0.96	4.39	0.36				1.48									1.71	10.42	94.37
	σ_μ		1.45	0.07	0.18	2.66			0.13	0.06	0.03	0.06				0.24									0.35	0.73	
	C_v		9.90	13.69	24.77	4.10			7.50	6.16	0.63	15.07				16.10									19.80	6.84	
	wt% μ	Total	14.17	0.58	0.84	62.80			1.73	0.95	4.10	0.32				1.80									1.92	10.79	
	σ_μ		1.05	0.11	0.37	2.01			0.16	0.04	0.24	0.12				0.36									0.40	0.79	
	C_v		7.28	18.80	42.96	3.13			9.05	4.56	5.75	37.74				19.38									20.49	7.21	
s48	wt% μ	Surface	10.02	0.64	1.14	77.79		0.58	1.61	0.61	2.76					1.08			3.76								91.61
	σ_μ		1.68	0.08	0.17	2.20		0.08	0.15	0.08	0.11					0.04			0.07								
	C_v		16.55	12.37	14.98	2.79		13.35	9.46	13.69	4.10					4.11			1.91								
	wt% μ	Middle	16.86	0.57	0.73	71.06	0.37	0.48	2.00	0.65	3.06					0.75			3.47								96.17
	σ_μ		0.13	0.07	0.06	0.91	0.00	0.10	0.06	0.20	0.07					0.06			0.11								
	C_v		0.74	11.79	7.54	1.26	0.00	19.59	2.75	30.21	2.25					7.66			3.08								
	wt% μ	Interior	9.26	0.49	0.68	80.85	0.42	0.48	1.14	0.55	3.17					0.56			2.40								93.07
	σ_μ		5.54	0.10	0.09	7.09	0.00	0.09	0.54	0.21	0.28					0.21			0.48								
	C_v		59.29	19.47	12.52	8.69	0.00	17.53	46.48	37.91	8.76					37.65			19.85								
	wt% μ	Total	12.05	0.57	0.85	76.57	0.40	0.51	1.58	0.60	2.99					0.80			3.21								
	σ_μ		4.82	0.10	0.24	5.89	0.02	0.10	0.48	0.18	0.25					0.25			0.66								
	C_v		39.57	18.04	27.86	7.60	5.00	18.87	30.00	29.48	8.21					31.37			20.41								

Table 7-15 continued: SEM-EDS analytical results for Saqqara archaeological faience glazes. The table includes average wt% (wt% μ), average standard deviation (σ_μ) and coefficient of variance (C_v).

SEM-EDS Analytical Results for Saqqara Faience (Normalized wt%)																									Analytical
Sherd	Stat.	Location	Na_2O	MgO	Al_2O_3	SiO_2	P_2O_5	SO_3	Cl	K_2O	CaO	TiO_2	V_2O_5	Cr_2O_3	MnO	FeO	CoO	NiO	CuO	ZnO	As_2O_3	SrO	Ag_2O	SnO_2	Sb_2O_5	PbO	Total
s53	wt% μ	Surface	8.42	0.24	0.81	82.59	0.41	0.48	0.95	0.44	0.81					0.42			4.43								88.31
	σ_μ		0.61	0.04	0.08	0.60	0.00	0.04	0.79	0.10	0.36					0.16			1.03								
	C_v		7.17	16.55	10.01	0.72	0.00	8.16	82.57	23.25	43.85					38.64			23.10								
	wt% μ	Middle	8.38	0.33	0.59	85.40	0.38	0.61	1.03	0.32	1.14					0.31			1.50								89.39
	σ_μ		1.00	0.08	0.08	0.85	0.00	0.09	0.36	0.03	0.26					0.06			0.22								
	C_v		11.71	22.91	12.98	0.98	0.00	14.49	34.42	8.57	22.11					17.86			14.45								
	wt% μ	Interior	8.05	0.32	0.71	84.70		0.69	0.93	0.47	2.87					0.32			0.96								86.99
	σ_μ		0.97	0.09	0.09	1.75		0.07	0.25	0.05	0.21					0.04			0.06								
	C_v		11.92	29.43	13.20	2.05		9.81	26.39	10.21	7.42					13.50			6.57								
	wt% μ	Total	8.28	0.30	0.70	84.23	0.39	0.59	0.97	0.41	1.61					0.35			2.30								
	σ_μ		0.90	0.09	0.12	1.90	0.01	0.11	0.52	0.09	0.95					0.11			1.66								
	C_v		10.70	28.29	17.27	2.23	2.50	17.34	53.48	22.23	58.53					32.17			71.21								
s70	wt% μ	Surface	12.59	0.38	0.92	72.96		0.46	1.78	1.10	2.78					3.93	0.34		2.75								95.71
	σ_μ		1.31	0.04	0.08	0.82		0.04	0.20	0.29	0.88					0.31	0.09		0.16								
	C_v		10.35	10.69	8.37	1.12		8.70	10.99	26.73	31.46					7.79	27.56		5.67								
	wt% μ	Middle	17.87	0.30	0.77	68.42			2.05	0.75	3.33		0.17			3.77	0.25		2.33								98.23
	σ_μ		0.52	0.04	0.08	1.56			0.23	0.16	0.49		0.00			1.04	0.01		0.11								
	C_v		2.91	13.61	10.63	2.27			11.17	21.52	14.64		0.00			27.36	4.92		4.88								
	wt% μ	Interior	16.44	0.34	0.74	70.38		0.41	1.74	0.79	4.13					2.51	0.20	0.22	1.85			0.26					98.26
	σ_μ		1.44	0.10	0.08	1.37		0.00	0.10	0.22	0.18					0.56	0.09	0.00	0.10			0.00					
	C_v		8.62	29.14	10.81	1.92		0.00	5.61	27.41	4.24					22.04	44.91	0.00	5.54			0.00					
	wt% μ	Total	15.63	0.34	0.81	70.59		0.44	1.86	0.88	3.41		0.17			3.40	0.26	0.22	2.31			0.26					
	σ_μ		2.57	0.07	0.11	2.19		0.04	0.23	0.28	0.83		0.00			0.94	0.10	0.00	0.38			0.00					
	C_v		16.32	21.81	13.51	3.07		8.44	12.19	31.51	24.04		0.00			27.35	36.17	0.00	16.38			0.00					
s72	wt% μ	Surface	16.53	0.49	1.13	71.41		0.55	1.57	0.83	3.57	0.26				1.92	0.27		1.46								99.03
	σ_μ		1.25	0.05	0.07	2.22		0.02	0.12	0.08	0.49	0.00				0.24	0.10		0.03								
	C_v		7.41	9.49	5.75	3.05		3.02	7.55	9.79	13.34	0.00				12.32	34.58		2.28								
	wt% μ	Middle	16.92	0.49	1.20	69.43	0.33	0.56	1.86	0.76	4.73					1.71	0.19		1.83								95.83
	σ_μ		0.47	0.06	0.07	0.32	0.00	0.05	0.09	0.03	0.21					0.36	0.00		0.39								
	C_v		2.74	11.66	5.83	0.45	0.00	8.95	4.97	4.40	4.44					20.61	0.00		20.81								
	wt% μ	Interior	13.97	0.63	1.00	72.57	0.31	0.43	1.60	0.71	5.51	0.34				1.13	0.20		1.60								95.61
	σ_μ		1.07	0.01	0.22	1.27	0.00	0.07	0.02	0.04	0.48	0.00				0.56	0.02		0.30								
	C_v		7.53	2.21	21.34	1.72	0.00	16.70	1.53	5.20	8.50	0.00				48.60	10.80		18.41								
	wt% μ	Total	15.80	0.53	1.11	71.14	0.32	0.51	1.68	0.76	4.60	0.30				1.59	0.22		1.63								
	σ_μ		1.67	0.08	0.16	1.98	0.01	0.08	0.16	0.08	0.91	0.04				0.53	0.08		0.32								
	C_v		10.34	14.80	14.28	2.72	3.03	15.18	9.36	9.67	19.40	12.90				32.96	32.54		19.48								

Table 7-15 continued: SEM-EDS analytical results for Saqqara archaeological faience glazes. The table includes average wt% (wt% μ), average standard deviation (σ_μ) and coefficient of variance (C_v).

SEM-EDS Analytical Results for Saqqara Faience (Normalized wt%)																									Analytical
Sherd	Stat.	Location	Na_2O	MgO	Al_2O_3	SiO_2	P_2O_5	SO_3	Cl	K_2O	CaO	TiO_2	V_2O_5	Cr_2O_3	MnO	FeO	CoO	NiO	CuO	ZnO	As_2O_3	SrO	Ag_2O	SnO_2	Sb_2O_5	PbO	Total
s74	wt% μ	Surface	16.10	0.56	1.18	67.34	0.58	0.43	1.78	0.35	4.31	0.58				2.08			3.50			1.19					97.07
	σ_μ		0.24	0.08	0.07	0.65	0.00	0.00	0.03	0.03	0.22	0.00				0.29			0.07			0.00					
	C_v		1.46	13.61	5.42	0.94	0.00	0.00	1.56	9.08	4.88	0.00				13.34			1.93			0.00					
	wt% μ	Middle	16.52	0.52	1.18	67.96	0.54		1.85	0.38	4.63	0.23			0.22	2.23	0.29		3.43								96.10
	σ_μ		0.16	0.06	0.12	0.66	0.00		0.08	0.07	0.26	0.00			0.00	0.32	0.00		0.05								
	C_v		0.97	12.03	9.92	0.95	0.00		4.48	17.89	5.51	0.00			0.00	13.89	0.00		1.49								
	wt% μ	Interior	14.81	0.62	0.95	68.97	0.60	0.91	1.87	0.38	5.45					1.26	0.29		3.00					0.88			95.53
	σ_μ		0.44	0.04	0.16	1.28	0.00	0.00	0.17	0.02	0.17					0.13	0.00		0.12					0.00			
	C_v		2.93	5.65	16.66	1.82	0.00	0.00	8.86	6.28	3.09					9.96	0.00		3.84					0.00			
	wt% μ	Total	15.81	0.57	1.10	68.09	0.57	0.67	1.84	0.37	4.80	0.41			0.22	1.86	0.29		3.31			1.19		0.88			
	σ_μ		0.86	0.07	0.17	0.98	0.03	0.25	0.11	0.05	0.51	0.18			0.00	0.51	0.00		0.25			0.00		0.00			
	C_v		5.31	12.81	15.04	1.40	4.47	35.77	6.08	12.70	10.46	42.86			0.00	26.99	0.00		7.48			0.00		0.00			
s78	wt% μ	Surface	17.58	0.38	0.58	64.68	0.42		1.22	0.40	6.11					3.57	0.22		3.39			1.44					97.35
	σ_μ		0.22	0.11	0.04	0.65	0.00		0.12	0.15	0.37					0.73	0.00		0.17			0.21					
	C_v		1.17	26.86	5.83	0.96	0.00		9.27	36.42	5.71					19.51	0.00		4.84			14.19					
	wt% μ	Middle	18.26	0.38	0.81	65.14	0.42	0.62	1.34	0.44	5.82					4.22	0.29		2.27								98.95
	σ_μ		0.65	0.01	0.12	1.49	0.00	0.00	0.05	0.18	0.24					0.89	0.00		0.17								
	C_v		3.52	2.63	14.50	2.26	0.00	0.00	3.68	39.51	4.09					20.92	0.00		7.47								
	wt% μ	Interior	16.39	0.40	0.54	70.26		0.34	1.00	0.44	5.44					3.09	0.28		1.81								101.86
	σ_μ		0.85	0.00	0.15	3.45		0.00	0.12	0.11	0.38					1.61	0.08		0.17								
	C_v		5.19	0.00	28.33	4.89		0.00	12.39	25.14	7.02					51.75	26.32		9.27								
	wt% μ	Total	17.41	0.38	0.64	66.69	0.42	0.48	1.19	0.43	5.79					3.63	0.26		2.49			1.44					
	σ_μ		1.13	0.08	0.16	2.93	0.01	0.15	0.18	0.15	0.51					1.24	0.06		0.75			0.21					
	C_v		6.37	19.41	24.92	4.31	2.33	29.90	15.05	34.30	8.66					33.36	21.46		29.39			14.19					
s80	wt% μ	Surface	0.66	0.15	0.32	95.68		0.56	0.76	0.04	0.89	-0.10				0.20			0.60	0.24							92.86
	σ_μ		0.21	0.02	0.03	1.07		0.00	0.27	0.01	0.30	0.00				0.02			0.16	0.00							
	C_v		30.21	13.33	8.92	1.10		0.00	34.65	11.11	33.22	0.00				10.11			25.82	0.00							
	wt% μ	Middle	1.06	0.28	0.48	93.55	0.26		1.25	0.14	1.67	0.16				0.35			0.80								93.47
	σ_μ		0.16	0.06	0.03	1.39	0.01		0.27	0.00	0.24	0.00				0.07			0.19								
	C_v		14.62	20.89	6.84	1.44	1.89		20.54	0.00	14.01	0.00				20.39			22.92								
	wt% μ	Interior	0.88	0.29	0.53	92.61	0.27	0.31	1.14		2.70					0.35	0.15		0.76								93.42
	σ_μ		0.13	0.06	0.15	0.72	0.00	0.00	0.16		0.06					0.09	0.00		0.06								
	C_v		13.97	18.95	26.73	0.76	0.00	0.00	13.94		2.26					25.22	0.00		7.90								
	wt% μ	Total	0.87	0.24	0.45	93.95	0.27	0.44	1.05	0.09	1.75	0.03				0.30	0.15		0.72	0.24							
	σ_μ		0.24	0.08	0.13	1.76	0.01	0.13	0.32	0.04	0.79	0.14				0.10	0.00		0.17	0.00							
	C_v		26.56	31.35	27.78	1.82	3.02	28.09	30.00	58.66	43.94	385.71				32.70	0.00		23.43	0.00							

Table 7-15 continued: SEM-EDS analytical results for Saqqara archaeological faience glazes. The table includes average wt% (wt% μ), average standard deviation (σ_μ) and coefficient of variance (C_v).

SEM-EDS Analytical Results for Saqqara Faience (Normalized wt%)																									Analytical
Sherd	Stat.	Location	Na_2O	MgO	Al_2O_3	SiO_2	P_2O_5	SO_3	Cl	K_2O	CaO	TiO_2	V_2O_5	Cr_2O_3	MnO	FeO	CoO	NiO	CuO	ZnO	As_2O_3	SrO	Ag_2O	SnO_2	Sb_2O_5	PbO	Total
s81	wt% μ	Surface	1.67	0.72	1.66	89.07		0.41	1.58	0.33	2.20				0.14	0.49			1.56							0.18	89.78
	σμ		0.72	0.25	1.04	2.45		0.08	0.27	0.21	0.10				0.01	0.13			0.21							0.00	
	C_v		41.83	33.51	61.20	2.68		19.05	16.46	61.66	4.26				7.14	26.50			12.82							0.00	
	wt% μ	Middle	0.99	0.69	0.91	88.36	0.27	0.46	2.05	0.16	3.26					0.51		0.17	1.70					0.47			89.02
	σμ		0.20	0.04	0.11	1.86	0.00	0.03	0.20	0.01	1.16					0.07		0.00	0.04					0.00			
	C_v		19.43	5.49	12.07	2.06	0.00	6.26	9.46	5.66	34.72					12.85		0.00	2.31					0.00			
	wt% μ	Interior	0.50	0.74	0.88	87.46		0.42	2.10	0.18	5.58	0.31				0.60		0.00	1.24								88.29
	σμ		0.08	0.08	0.08	0.38		0.08	0.24	0.02	0.88	0.00				0.09			0.26								
	C_v		14.97	10.39	8.75	0.42		20.00	11.27	9.07	15.56	0.00				14.48			20.51								
	wt% μ	Total	1.05	0.71	1.15	88.30	0.27	0.43	1.91	0.22	3.68	0.31			0.14	0.53		0.08	1.50					0.47		0.18	
	σμ		0.66	0.15	0.71	2.05	0.00	0.07	0.33	0.14	1.66	0.00			0.01	0.11		0.00	0.28					0.00		0.00	
	C_v		60.84	20.88	60.44	2.27	0.00	15.68	17.07	62.77	44.10	0.00			7.14	20.25		0.00	18.05					0.00		0.00	
s82	wt% μ	Surface	10.01	0.33	0.76	80.07	0.30	0.39	1.57	0.84	2.75		0.20			0.55			2.24								90.31
	σμ		3.64	0.02	0.05	3.39	0.00	0.07	0.19	0.26	0.49		0.00			0.07			0.18								
	C_v		35.72	5.10	6.84	4.16	0.00	17.65	11.85	29.80	17.65		0.00			12.50			7.91								
	wt% μ	Middle	13.45	0.31	0.69	76.98		0.47	1.93	0.86	3.03					0.44			1.85								88.85
	σμ		2.30	0.05	0.04	2.32		0.09	0.06	0.20	0.16					0.07			0.13								
	C_v		16.92	14.66	6.49	2.98		19.00	3.16	22.64	5.24					15.85			6.72								
	wt% μ	Interior	8.32	0.34	0.59	82.85		0.38	1.46	0.81	3.49					0.33			1.44								88.82
	σμ		1.16	0.02	0.03	2.18		0.03	0.19	0.13	0.52					0.04			0.18								
	C_v		13.79	6.80	5.44	2.59		7.69	12.82	15.91	14.66					10.78			12.49								
	wt% μ	Total	10.59	0.33	0.68	79.97	0.30	0.41	1.65	0.84	3.09		0.20			0.44			1.84								
	σμ		3.35	0.03	0.08	3.70	0.00	0.08	0.26	0.20	0.52		0.00			0.11			0.37								
	C_v		31.20	10.50	12.28	4.56	0.00	19.26	15.29	23.76	16.66		0.00			25.44			20.01								
s83	wt% μ	Surface	19.19	0.66	1.37	68.49		0.88	1.39	0.48	4.31	0.32				0.66			1.78					0.47			99.67
	σμ		0.74	0.09	0.08	1.10		0.25	0.10	0.06	0.10	0.11				0.05			0.04					0.00			
	C_v		3.83	12.98	6.00	1.59		27.88	7.10	12.37	2.40	32.31				6.89			2.51					0.00			
	wt% μ	Middle	19.88	0.80	1.21	67.67		0.80	1.58	0.47	4.74					0.63			1.68					0.54			99.06
	σμ		0.61	0.14	0.08	0.21		0.19	0.04	0.06	0.19					0.11			0.06					0.00			
	C_v		3.04	17.17	6.85	0.31		23.79	2.60	12.53	3.97					16.85			3.57					0.00			
	wt% μ	Interior	18.11	0.45	1.16	70.28	0.33	0.48	1.41	0.45	5.11					0.51			1.37	0.33				0.00			98.06
	σμ		0.20	0.08	0.13	0.62	0.00	0.16	0.15	0.02	0.30					0.10			0.17	0.01							
	C_v		1.11	17.55	11.33	0.86	0.00	32.44	10.20	3.67	5.67					18.28			12.18	2.94							
	wt% μ	Total	19.06	0.64	1.25	68.81	0.33	0.72	1.46	0.47	4.72	0.32				0.60			1.61	0.33				0.33			
	σμ		0.83	0.18	0.13	1.73	0.00	0.27	0.13	0.05	0.41	0.11				0.10			0.20	0.01				0.04			
	C_v		4.33	27.42	10.69	2.49	0.00	36.46	8.92	10.68	8.62	32.31				17.30			12.33	2.94				6.93			

Table 7-15 continued: SEM-EDS analytical results for Saqqara archaeological faience glazes. The table includes average wt% (wt% μ), average standard deviation (σμ) and coefficient of variance (Cv).

SEM-EDS Analytical Results for Saqqara Faience (Normalized wt%)																									Analytical
Sherd	Stat.	Location	Na_2O	MgO	Al_2O_3	SiO_2	P_2O_5	SO_3	Cl	K_2O	CaO	TiO_2	V_2O_5	Cr_2O_3	MnO	FeO	CoO	NiO	CuO	ZnO	As_2O_3	SrO	Ag_2O	SnO_2	Sb_2O_5	PbO	Total
s84	wt% μ	Surface	17.48	0.94	2.29	68.50		0.46	1.58	0.57	4.77	0.25				1.05			2.10								100.69
	σμ		0.23	0.05	0.30	1.39		0.00	0.10	0.06	0.47	0.01				0.08			0.05								
	Cv		1.32	5.37	12.90	2.01		0.00	6.37	10.99	9.81	4.00				7.74			2.31								
	wt% μ	Middle	19.34	0.75	2.96	65.34		0.56	1.63	0.54	5.18	0.36				1.07			2.27								101.57
	σμ		0.49	0.04	0.98	0.47		0.07	0.06	0.06	0.38	0.00				0.06			0.10								
	Cv		2.50	5.49	32.77	0.71		12.28	3.71	10.39	7.25	0.00				5.29			4.30								
	wt% μ	Interior	17.80	0.55	1.16	69.89		0.47	1.34	0.51	6.01	0.19				0.43			1.66								101.56
	σμ		0.26	0.04	0.45	0.27		0.08	0.01	0.00	0.38	0.01				0.22			0.02								
	Cv		1.44	8.08	38.69	0.39		18.05	0.93	0.92	6.20	5.26				51.69			1.50								
	wt% μ	Total	18.20	0.75	2.14	67.91		0.50	1.52	0.54	5.32	0.27				0.85			2.01								
	σμ		0.93	0.17	0.99	1.93		0.09	0.15	0.06	0.65	0.07				0.34			0.27								
	Cv		5.05	22.09	45.98	2.82		17.15	9.92	10.32	12.14	26.53				38.97			13.52								
s85	wt% μ	Surface	16.39	0.85	2.27	68.65		0.43	1.55	0.88	5.70	0.30				1.12			1.86								95.69
	σμ		0.85	0.05	0.28	1.58		0.06	0.15	0.03	0.52	0.02				0.08			0.15								
	Cv		5.09	6.23	12.03	2.27		14.52	9.43	2.96	9.00	7.77				7.20			7.88								
	wt% μ	Middle	17.73	0.71	3.01	66.83		0.43	1.71	0.85	5.52	0.24				1.16			1.79								97.21
	σμ		0.39	0.01	1.87	1.84		0.04	0.11	0.06	0.53	0.07				0.32			0.24								
	Cv		2.18	1.13	61.44	2.71		9.82	6.15	6.64	9.47	26.96				26.78			13.14								
	wt% μ	Interior	7.46	0.47	0.61	80.83		0.44	1.33	0.58	6.51	0.17				0.38			1.22								93.30
	σμ		3.42	0.08	0.33	4.51		0.08	0.16	0.14	0.14	0.00				0.17			0.19								
	Cv		45.32	17.16	53.82	5.52		17.50	11.98	24.48	2.09	0.00				43.67			15.59								
	wt% μ	Total	13.86	0.68	1.96	72.10		0.43	1.53	0.77	5.91	0.24				0.89			1.62								
	σμ		5.05	0.17	1.51	6.90		0.06	0.21	0.16	0.61	0.06				0.42			0.35								
	Cv		36.02	24.53	75.78	9.45		14.33	13.67	20.84	10.22	24.84				46.91			21.36								
s87	wt% μ	Surface	17.01	0.74	1.63	69.41		0.74	1.48	0.44	5.13	0.29				1.00			2.15								101.26
	σμ		0.70	0.15	0.20	0.68		0.06	0.14	0.05	0.22	0.06				0.05			0.10								
	Cv		4.04	20.17	11.86	0.96		8.00	9.63	11.75	4.30	21.26				4.92			4.49								
	wt% μ	Middle	17.17	0.75	1.79	68.61	0.33	0.59	1.51	0.46	5.23	0.27				1.06			2.21								99.30
	σμ		1.01	0.02	0.24	1.31	0.00	0.20	0.06	0.06	0.19	0.08				0.15			0.07								
	Cv		5.75	2.46	13.15	1.87	0.00	33.33	3.96	13.06	3.60	28.57				13.63			2.89								
	wt% μ	Interior	15.81	0.72	1.65	69.58	0.27	0.58	1.58	0.48	5.69	0.22				1.12	0.18		2.12								98.69
	σμ		1.55	0.10	0.04	1.50	0.00	0.17	0.07	0.02	0.14	0.01				0.09	0.00		0.12								
	Cv		9.61	13.28	2.29	2.12	0.00	27.73	4.23	5.13	2.35	5.50				7.83	0.00		5.78								
	wt% μ	Total	16.66	0.74	1.69	69.20	0.30	0.64	1.52	0.46	5.35	0.26				1.06	0.18		2.16								
	σμ		1.30	0.11	0.20	1.25	0.03	0.17	0.11	0.05	0.31	0.06				0.12	0.00		0.11								
	Cv		7.66	14.03	11.40	1.78	11.48	26.17	6.96	11.03	5.72	23.75				10.79	0.00		4.91								

Table 7-15 continued: SEM-EDS analytical results for Saqqara archaeological faience glazes. The table includes average wt% (wt% μ), average standard deviation (σ_μ) and coefficient of variance (C_v).

SEM-EDS Analytical Results for Saqqara Faience (Normalized wt%)																									Analytical
Sherd	Stat.	Location	Na_2O	MgO	Al_2O_3	SiO_2	P_2O_5	SO_3	Cl	K_2O	CaO	TiO_2	V_2O_5	Cr_2O_3	MnO	FeO	CoO	NiO	CuO	ZnO	As_2O_3	SrO	Ag_2O	SnO_2	Sb_2O_5	PbO	Total
s89	wt% μ	Surface	17.60	0.89	1.46	70.29		0.38	1.75	0.48	4.24	0.27				0.94			1.70								101.32
	σ_μ		1.44	0.08	0.13	1.79		0.05	0.29	0.13	0.32	0.00				0.37			0.13								
	C_v		8.11	8.65	8.73	2.52		11.69	16.28	25.97	7.52	0.00				38.58			7.54								
	wt% μ	Middle	18.43	0.64	1.42	69.15		0.30	1.81	0.49	4.98	0.20				0.98			1.60								103.17
	σ_μ		0.22	0.02	0.36	0.35		0.01	0.09	0.05	0.69	0.00				0.27			0.15								
	C_v		1.18	2.51	24.71	0.50		3.33	5.12	9.80	13.60	0.00				26.80			9.35								
	wt% μ	Interior	16.90	0.45	1.00	71.56		0.37	1.41	0.44	6.14					0.49			1.24								101.11
	σ_μ		0.61	0.05	0.39	1.08		0.00	0.22	0.09	0.57					0.13			0.07								
	C_v		3.58	11.90	38.56	1.50		0.00	15.82	20.91	9.31					26.50			5.25								
	wt% μ	Total	17.64	0.66	1.29	70.33		0.35	1.66	0.47	5.12	0.23				0.80			1.51								
	σ_μ		1.15	0.19	0.38	1.43		0.05	0.28	0.10	0.95	0.04				0.35			0.24								
	C_v		6.44	28.38	28.88	2.02		14.12	16.97	20.56	18.40	14.89				43.57			15.52								
s90	wt% μ	Surface	19.13	0.79	1.86	67.11		0.49	1.70	0.32	4.66	0.23				1.23			2.48								100.21
	σ_μ		0.52	0.06	0.31	0.76		0.00	0.07	0.03	0.15	0.00				0.23			0.08								
	C_v		2.68	7.20	16.29	1.13		0.00	3.96	10.21	3.18	0.00				18.58			3.35								
	wt% μ	Middle	19.99	0.81	2.34	65.60		0.44	1.69	0.36	4.98	0.23				1.07			2.49								100.42
	σ_μ		0.29	0.11	0.34	0.95		0.00	0.08	0.06	0.23	0.03				0.11			0.12								
	C_v		1.44	13.10	14.37	1.45		0.00	4.85	16.87	4.61	13.04				10.01			4.96								
	wt% μ	Interior	18.09	0.41	1.08	70.13		0.40	1.37	0.30	5.79	0.00				0.55			1.88								100.17
	σ_μ		1.30	0.12	0.36	2.32		0.00	0.23	0.00	0.25					0.22			0.19								
	C_v		7.07	28.04	32.57	3.27		0.00	16.60	1.54	4.19					39.47			9.90								
	wt% μ	Total	19.07	0.67	1.76	67.61		0.44	1.59	0.33	5.14	0.15				0.95			2.28								
	σ_μ		1.07	0.21	0.62	2.67		0.04	0.21	0.05	0.54	0.02				0.35			0.31								
	C_v		5.59	30.39	34.79	3.92		8.30	13.08	14.13	10.35	10.65				36.34			13.61								
s91	wt% μ	Surface	20.98	0.74	1.36	66.28	0.30	0.90	1.67	0.56	4.36	0.22				0.65			1.99								100.22
	σ_μ		0.28	0.08	0.24	0.87	0.00	0.16	0.10	0.05	0.38	0.01				0.07			0.07								
	C_v		1.31	10.50	17.46	1.30	0.00	17.12	6.14	8.24	8.63	2.22				11.34			3.44								
	wt% μ	Middle	20.69	0.69	1.17	66.63	0.31	0.79	1.72	0.50	4.40	0.22				0.54			1.83				0.51				99.75
	σ_μ		0.15	0.03	0.09	0.81	0.00	0.34	0.17	0.05	0.33	0.03				0.08			0.03				0.00				
	C_v		0.70	4.83	7.32	1.19	0.00	42.40	9.90	8.91	7.24	13.64				15.07			1.81				0.00				
	wt% μ	Interior	18.62	0.62	1.22	69.56	0.08	0.61	1.52	0.51	4.94	0.26				0.62			1.44								99.76
	σ_μ		0.88	0.04	0.06	1.55	0.00	0.09	0.04	0.05	0.09	0.00				0.04			0.13								
	C_v		4.62	5.94	4.75	2.19	0.00	14.03	2.41	8.74	1.78	0.00				6.33			8.91								
	wt% μ	Total	20.10	0.68	1.25	67.49	0.23	0.76	1.64	0.52	4.57	0.23				0.60			1.75				0.51				
	σ_μ		1.18	0.07	0.17	1.94	0.11	0.25	0.15	0.05	0.40	0.03				0.08			0.25				0.00				
	C_v		5.78	10.54	13.35	2.82	46.60	32.61	8.91	9.66	8.65	11.69				13.53			13.94				0.00				

7.6 Analytical Interpretations

7.6.1 HH-XRF Depth of Analysis Interpretation

The depth of analysis and knowing whether elements are being detected in the glaze or body is the main consideration in the elemental analysis of glazes using HH-XRF. The depth of analysis is dependent on the voltage (15/40 kV), density of matrix (copper blue replicate glazes = 2.85 g cm^{-3}; cobalt blue 3.0 g cm^{-3}), angles of incidence (52) and take-off (63) and the element of interest. The general equations are covered in more detail in section 3.2.3. Table 7-16 provides the theoretical depths of measurement based on the parameters used in the analysis.

Figure 7-30 provides a visual representation of the depths of measurement based on a thin (~100 µm) and medium thickness (~456 µm) glaze from the Saqqara case study. Knowing the depth of the glaze is useful in determining the optimum parameters for the analysis. However, this knowledge is not always available to the analyst. Table 7-17 and Fig. 7-30 reveal that most of the elemental information is originating from the glaze for 15 and 40 kV measurements in the medium thickness (~456 µm) glaze. It reveals that most of the 15 kV detection occurs in the corroded layer with this specific glaze. This will result in underrepresented alkalis and copper colourant.

7.6.2 Replicate Faience: Recipe Back-Engineering

The three measurements from the centre of the glazes were used to determine if SEM-EDS could produce an approximation of the glaze recipe used during replication, and if wt% results for archaeological materials can be back-engineered to recreate the possible glaze batch recipe used during the initial production. The glaze centre measurements were used because they would provide compositional information least affected by body chemistry (e.g. ion migration between body and glaze) and by glaze surface chemistry (e.g. sodium vaporization during kiln firing).

The SEM-EDS oxide results were converted to represent the form (e.g. carbonates, hydroxides) in which they entered into the glaze mixture and the results were normalized to produce a recipe estimation for each glaze batch. Tables 7-17 and 7-18 reveal the estimated results for each of the three glazes. The SEM exhibits greatest accuracy (RAE%) and precision (C_V) with sodium carbonate and silica for glaze 03 (copper colourant) (Table 7-17). Most of the elements are underestimated with the exception of calcium carbonate and copper oxide which are greatly overestimated (~67 and 66 RAE% respectively). The SEM-EDS is good at quantifying major elements (i.e. sodium and silica) but loses accuracy relatively rapidly as the quantities decrease. Precision is similarly affected but the loss is less pronounced.

Table 7-16: Theoretical critical penetration depths for 15 and 40 kV HH-XRF measurements. Mass attenuation coefficient is denoted by the column heading 'cm² g-1'. The percentages represent how much of the signal is attenuated from each depth.

Critical Penetration Depths (μm) for 15 kV and 40 kV Primary Energies with a Rhodium Target											
Element	Line	Absorbtion Edge	cm^2 g-1	15 kV				40 kV			
				99%	90%	80%	50%	99%	90%	80%	50%
Na	Kα1	1.072	522.46	25.6	12.8	9.0	3.9	26.7	13.3	9.3	4.0
Mg	Kα1	1.305	481.90	27.6	13.8	9.6	4.2	28.8	14.4	10.1	4.3
Al	Kα1	1.560	371.36	35.0	17.5	12.2	5.3	37.0	18.5	12.9	5.6
Si	Kα1	1.839	343.85	37.5	18.8	13.1	5.7	39.9	19.9	13.9	6.0
K	Kα1	3.607	157.95	72.8	36.4	25.5	11.0	82.1	41.1	28.7	12.4
Ca	Kα1	4.038	131.10	84.3	42.1	29.5	12.7	96.9	48.5	33.9	14.6
Ti	Kα1	4.966	92.98	108.5	54.2	37.9	16.3	130.4	65.2	45.6	19.6
Mn	Kα1	6.539	66.33	135.7	67.9	47.4	20.4	171.9	85.9	60.1	25.9
Fe	Kα1	7.112	64.29	138.4	69.2	48.4	20.8	176.2	88.1	61.6	26.5
Co	Kα1	7.709	59.68	144.8	72.4	50.6	21.8	186.7	93.4	65.3	28.1
Ni	Kα1	8.333	58.49	146.6	73.3	51.2	22.1	189.6	94.8	66.3	28.5
Cu	Kα1	8.979	43.92	172.1	86.0	60.1	25.9	234.7	117.3	82.0	35.3
Zn	Kα1	9.659	49.06	162.1	81.1	56.7	24.4	216.5	108.3	75.7	32.6
Rb	Kα1	15.200	23.75	226.7	113.3	79.2	34.1	349.5	174.7	122.1	52.6
Sr	Kα1	16.105	21.90	233.5	116.7	81.6	35.1	365.9	182.9	127.9	55.1
Zr	Kα1	17.997	21.79	233.9	117.0	81.8	35.2	367.0	183.5	128.2	55.2
Sn	Kα1	29.200	12.07	277.8	138.9	97.1	41.8	487.8	243.9	170.5	73.4
Sn	Lα1	4.465	450.80	29.4	14.7	10.3	4.4	30.8	15.4	10.7	4.6
Sb	Kα1	30.491	10.69	285.4	142.7	99.7	43.0	511.7	255.8	178.8	77.0
Sb	Lα1	4.698	401.73	32.6	16.3	11.4	4.9	34.4	17.2	12.0	5.2
Ba	Kα1	37.441	7.98	301.6	150.8	105.4	45.4	566.2	283.1	197.9	85.2
Ba	Lα1	5.989	327.45	39.2	19.6	13.7	5.9	41.8	20.9	14.6	6.3
Pb	Lα1	15.861	16.66	255.2	127.6	89.2	38.4	422.1	211.1	147.5	63.5
Pb	Mα1	3.851	849.10	16.2	8.1	5.7	2.4	16.6	8.3	5.8	2.5
Bi	Lα1	16.388	2.31	342.2	171.1	119.6	51.5	728.6	364.3	254.6	109.7
Bi	Mα1	3.999	829.87	16.6	8.3	5.8	2.5	17.0	8.5	5.9	2.6

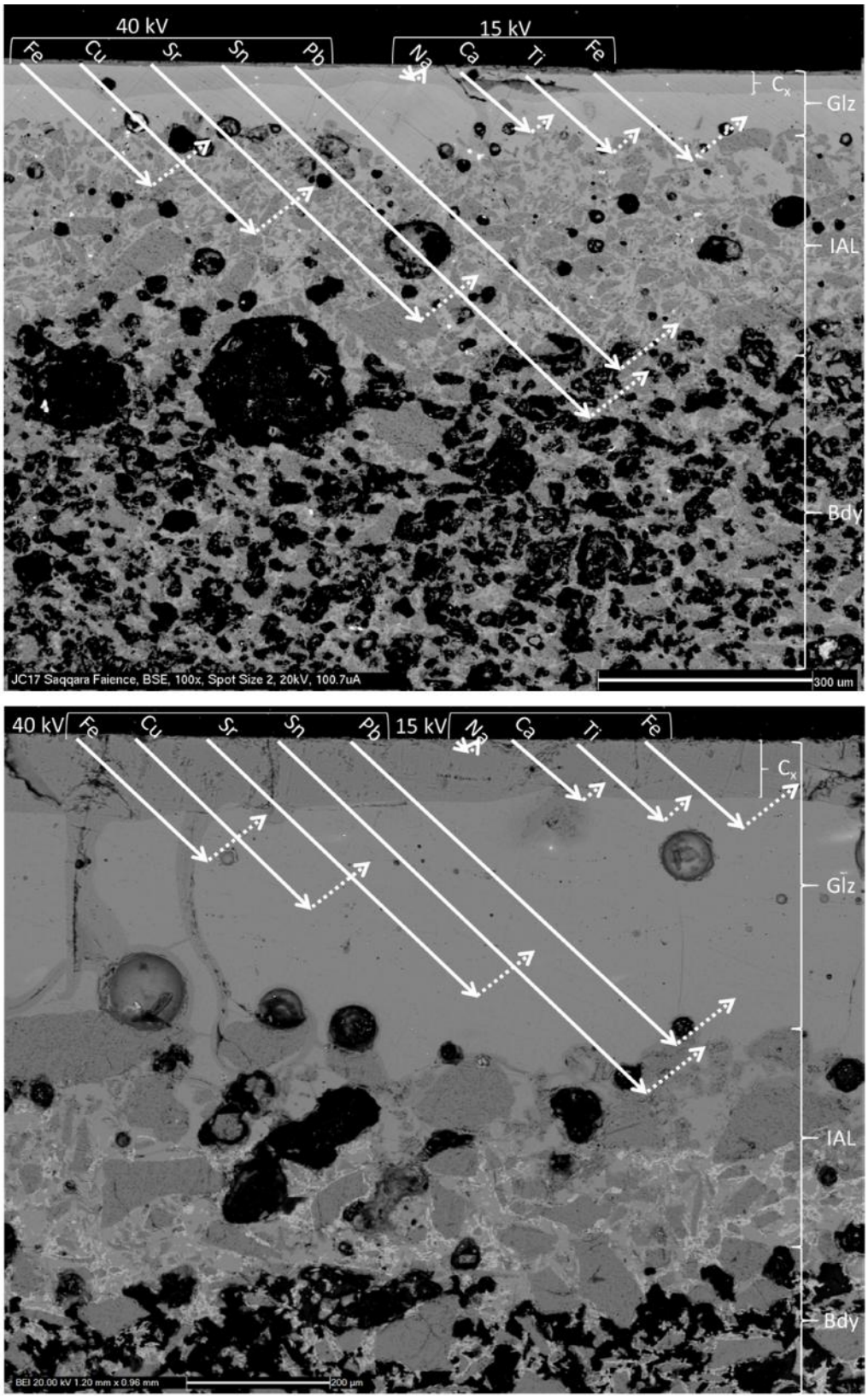

Fig. 7-30: Depths of measurement for selected elements in a thin (s17 - ~100 µm) and average glaze thickness (s83 - ~456 µm) (of case study samples) based on 2.83 g cm^{-3} density. The glaze (Glz), interaction layer (IAL), body (Bdy) and corrosion layer (C_x) are indicated.

Table 7-17: Recipe determination for copper colourant glaze 03 using SEM-EDS (normalized). The batch represents the original recipe based on material quantities that produced the glaze mixture.

Replicate Faience Glaze 03 Recipe Based on SEM-EDS						
Glaze 03	Na_2CO_3	$Al(OH)_3$	SiO_2	K_2CO_3	$CaCO_3$	CuO
Batch	25.84	2.02	68.68	4.04	5.05	2.02
R327	26.39	1.41	57.21	2.46	9.27	3.25
R328	19.57	3.27	65.70	3.86	10.22	3.91
R340	26.86	1.28	57.70	2.85	8.13	3.18
R342	23.49	1.24	58.32	1.94	11.03	3.99
R349	21.75	2.24	62.31	2.53	8.02	3.15
R351	24.20	1.71	59.46	1.73	9.28	3.63
R356	26.04	1.31	58.51	1.90	9.13	3.11
R359	24.20	1.41	59.86	1.75	9.06	3.71
R360	25.98	1.63	60.24	3.18	6.41	2.56
R363	23.32	1.28	57.82	4.46	9.63	3.49
R364	30.06	0.95	56.05	2.69	7.34	2.91
R367	24.40	1.02	58.85	3.91	8.37	3.45
R383	29.87	1.10	56.65	2.78	6.90	2.70
R384	25.08	1.13	59.11	1.90	8.98	3.80
R386	29.47	1.01	57.58	2.80	6.38	2.76
R388	24.50	1.38	60.63	1.96	7.83	3.70
R390	26.23	2.23	58.33	2.58	7.48	3.14
R392	24.97	1.38	58.77	2.08	8.65	4.15
Average	25.35	1.50	59.06	2.63	8.45	3.37
σ	2.62	0.56	2.17	0.77	1.23	0.45
RAE%	-1.88	-25.82	-14.00	-34.84	67.34	66.60
C_V	10.31	37.17	3.67	29.43	14.59	13.44

Precision concerning glazes 05 and 07 (cobalt colourant) (see Table 7-18) are greater than with glaze 03 (copper colourant). Again, accuracy is affected by the quantity of the analyte with major elements represented best with the exception of lead. Lead in these glazes is at trace levels (<1 wt%) but exhibits high accuracy and moderate precision.

Table 7-18: Recipe determination for glazes 05 and 07 using SEM-EDS (normalized). The batch represents the original recipe based on the material quantities that produced the glaze mixture. Blank spaces indicate the oxide was not identified in the spectra.

Replicate Faience Glaze 05 and 07 Recipes Based on SEM-EDS												
Glaze 05	Na_2CO_3	$MgCO_3$	$Al(OH)_3$	SiO_2	K_2CO_3	$CaCO_3$	MnO	FeO	CoO	CuO	Sb_2O_3	PbO
Batch	13.13	1.58	2.02	68.68	4.04	5.05	0.1	1.21	0.3	2.02	0.61	0.55
R418	22.95	3.14	0.98	55.18	4.00	9.08		1.52	0.27	2.69	0.83	
R421	20.64	3.12	1.05	55.56	3.69	10.60		1.68	0.30	2.93		0.65
R423	20.12	2.96	1.11	57.38	3.65	9.59		1.61	0.32	2.61	0.82	0.61
R424	20.51	2.58	1.35	58.43	3.68	8.93		1.52	0.35	2.28		0.56
R426	18.71	2.84	1.39	59.36	3.43	9.35		1.52	0.38	2.23	0.83	0.68
R429	18.40	2.84	1.62	59.86	3.48	8.94		1.62	0.30	2.46	0.86	
Average	20.22	2.91	1.25	57.63	3.65	9.41		1.58	0.32	2.54	0.84	0.62
σ	1.49	0.19	0.22	1.78	0.18	0.58		0.06	0.03	0.24	0.01	0.05
RAE%	54.02	84.20	-38.17	-16.09	-9.56	86.43		30.34	6.23	25.53	36.91	13.49
C_V	7.37	6.56	17.87	3.08	5.00	6.16		3.92	10.85	9.53	1.73	7.36
Glaze 07	Na_2CO_3	$MgCO_3$	$Al(OH)_3$	SiO_2	K_2CO_3	$CaCO_3$	MnO	FeO	CoO	CuO	Sb_2O_3	PbO
Batch	13.06	1.14	1.67	72.98	1.58	4.12	0.13	1.24	0.17	2.28	0.29	0.95
R406	23.82	2.41	1.29	56.30	3.07	7.10	0.22	1.63	0.30	3.14		1.06
R408	20.07	2.22	1.51	60.22	2.21	7.82		1.51		3.32		1.11
R411	23.06	2.24	1.51	57.58	2.73	7.48		1.70		2.76		0.95
R412	20.25	2.21	1.28	60.10	2.42	7.55		1.71		3.31		1.17
R415	20.94	1.95	1.19	61.88	2.61	6.36		1.47		2.79		0.80
R416	19.74	2.07	1.45	61.29	2.25	7.68		1.75		2.89		0.89
Average	21.31	2.19	1.37	59.56	2.55	7.33	0.22	1.63	0.30	3.04		1.00
σ	1.56	0.14	0.12	1.99	0.30	0.49	0.00	0.10	0.00	0.23		0.13
RAE%	63.20	91.69	-17.81	-18.39	61.21	77.94	69.50	31.27	75.04	33.16		4.93
C_V	7.32	6.55	9.01	3.33	11.63	6.66	0.00	6.30	0.00	7.69		12.82

Table 7-19: Fractionation (decomposition) of recipe ingredients in the glaze melt based on pre/post firing weight difference. Glaze weight represent prefired weight.

Replicate Faience Glaze Weight Differences (Fractionation)							
Replication Sample Number	Glaze	Temp Ramp Up (°C/Hr)	Peak Temp (°C)	Peak Time (min)	Glaze Weight (g)	Wieght Difference (g)	wt% Difference
R328	GLZ03	100	850	360	0.486	0.028	5.82
R329	GLZ03	100	850	360	0.671	0.048	7.15
R332	GLZ03	100	850	360	4.581	0.317	6.91
R333	GLZ03	100	850	360	4.583	0.298	6.50
R342	GLZ03	100	850	180	0.725	0.029	3.93
R343	GLZ03	100	850	180	1.107	0.045	4.03
R346	GLZ03	100	850	180	4.232	0.070	1.66
R347	GLZ03	100	850	180	4.196	0.107	2.56
R351	GLZ03	100	970	60	0.891	0.037	4.10
R355	GLZ03	100	970	60	5.569	0.712	12.79
R358	GLZ03	100	900	60	0.331	0.014	4.11
R359	GLZ03	100	900	60	1.034	0.042	4.08
R362	GLZ03	100	800	60	0.445	0.020	4.50
R363	GLZ03	100	800	60	0.903	0.037	4.10
R366	GLZ03	999	850	60	0.372	0.015	4.08
R367	GLZ03	999	850	60	0.749	0.029	3.81
R384	GLZ03	200	850	60	0.632	0.033	5.22
R385	GLZ03	200	850	60	1.018	0.045	4.41
R388	GLZ03	100	850	60	0.538	0.029	5.32
R389	GLZ03	100	850	60	1.008	0.037	3.67
R392	GLZ03	50	850	60	0.492	0.027	5.51
R393	GLZ03	50	850	60	0.683	0.032	4.65
R408	GLZ07	100	850	60	0.581	0.015	2.55
R412	GLZ07	100	900	60	0.538	0.021	3.81
R416	GLZ07	100	970	60	0.527	0.017	3.29
R421	GLZ05	100	850	60	1.179	0.038	3.22
R424	GLZ05	100	900	60	0.550	0.059	10.71
R429	GLZ05	100	970	60	1.212	0.032	2.66

7.6.3 Replicate Faience: Fractionation

The generation and escape of carbon dioxide and water from carbonates and hydroxides, respectively, during firing of the faience replicates will result in a decrease in weight (see section 2.4.1). The presence of bubbles resultant of off-gassing in the glaze are evidence that fractionation is occurring. The hypothetical weights and actual weights of the bodies and glazes are compared pre- and post-firing to provide an estimate of the amount of fractionation occurring during the firing process.

Samples were weighed immediately before and after being fired to determine the weight difference as an indicator of fractionation. Only samples with prefired bodies are included in Table 7-19. These bodies introduce less carbon dioxide into the glaze melt and will contribute less to the weight difference than unfired bodies. The other variables included in the table were compared to the weight difference values to determine relationship using a scatter plot in MS Excel (2013). No obvious relationships exist between these variables and the weight difference.

The amount of fractionation has been determined to be a factor of temperature with peak temperature soak time playing a minor role. Temperature and fractionation are discussed under section 2.6. The carbonates and hydroxides used to produce the glaze mixtures decompose at different temperatures dependent on the oxide with which they are combined. There is probably an initial release of carbon dioxide gas when the temperature reaches a critical point that relatively quickly decreases until the atmospheric carbon dioxide pressure is greater than the equilibrium pressure resulting in a cessation of carbon dioxide generation. Taking into consideration the carbonates and hydroxides used for the copper colourant glaze 03 mixture, the complete carbon dioxide and water decomposition would reduce the weight of the sample by approximately 15.68% (see Table 7-19). Most of the samples have been reduced in weight by 4.5% indicating that only 25-30% of the potential off-gassing has occurred (Table 7-20). This figure can be further affected by incomplete water evaporation in the glaze before firing.

Table 7-20: Potential weight difference with complete off-gassing of carbon dioxide and water with copper colourant glaze 03.

Glaze 03	Na_2CO_3	K_2CO_3	$CaCO_3$	$Al(OH)_3$	Total off-gassing
wt% of batch ingredient	25.84	2.46	7.49	2.52	
Oxide wt% of batch ingredient	15.11	1.68	4.20	1.65	
CO2 wt% of batch ingredient	10.73	0.78	3.29		14.81
H2O wt% of batch ingredient				0.87	0.87
			CO2 and H2O wt%		15.68

7.6.4 Compositional Profiles

Compositional profiles are measured to determine if there is a difference between what a surface analysis (i.e. HH-XRF) may detect versus an interior glaze analysis (i.e. SEM-EDS with sampling) but have been used in other studies to help determine glazing technique (Kaczmarczyk and Vandiver 2008; Tite et al. 2007:1572; Vandiver

1998, 2008). The samples were subjected to EDS analysis to determine glaze compositional profiles. Nine measurements were taken through the glaze column at regular intervals (dependent on glaze thickness) representing the glaze near the surface, in the middle and near the interaction layer to provide a compositional profile (see Tables 7-13 and 7-14). Sodium and copper will migrate through efflorescent and cementation glazes during drying and/or firing (see section 2.4.1). Application glazes operate differently by not requiring salt efflorescence on the surface nor an interaction with a powdered matrix during firing. A static glaze element migration pattern is expected but slight movement of sodium because of evaporation of water during the drying period is possible.

The glaze compositional profiles exhibit little variation throughout the glaze in the replicated materials. This is expected from an application glaze that has not experienced weathering. The variation that does exist is not uniform across all glazes indicating heterogeneity in individual samples that are not a function nor result of the manufacturing processes. Figure 7-31 exhibits one of the most dynamic profiles (R328) and an average profile (R351) for copper colourant glaze 03 samples. Figure 7-32 exhibits an average profile (R423) and the most dynamic (R429) for cobalt colourant glaze 05. The cobalt levels in four of the six glazes measured tended to be lowest in the glaze middles. But the remaining glazes exhibit cobalt levels at their highest in the glaze middles indicating the initial four were probably just a coincidence and not a function of systematic element migration within the glaze melt. Cobalt colourant glaze 07 revealed compositional profiles consistent in their variability (Fig. 7-33). The least consistent variable is the detection of cobalt. Only one glaze revealed cobalt above detection levels throughout the glaze profile (R406). Two profiles only reveal cobalt at the interior and the remaining three profiles exhibited no cobalt at all. Cobalt levels in glaze 07 are approximately half that of glaze 05. Any indications contrary to that in these figures is a result of low precision in quantifying the element with SEM-EDS.

The glaze compositional profiles for the Saqqara archaeological material generally reveal lower quantities of the highly soluble alkali elements sodium and potassium near the surface and in the interior (Fig. 7-34 and Fig. 7-35). Low quantities near the surface are because of weathering of the glaze and leaching of the alkali components. A break in the glaze coating will allow water to enter into the porous body providing an opportunity to leach the alkali from the glaze interiors resulting in the lower quantities seen in the data. Alkali leached areas of the glaze can be delineated using SEM-BSE where a slight change in the molecular weight of the glaze (because of leaching) is

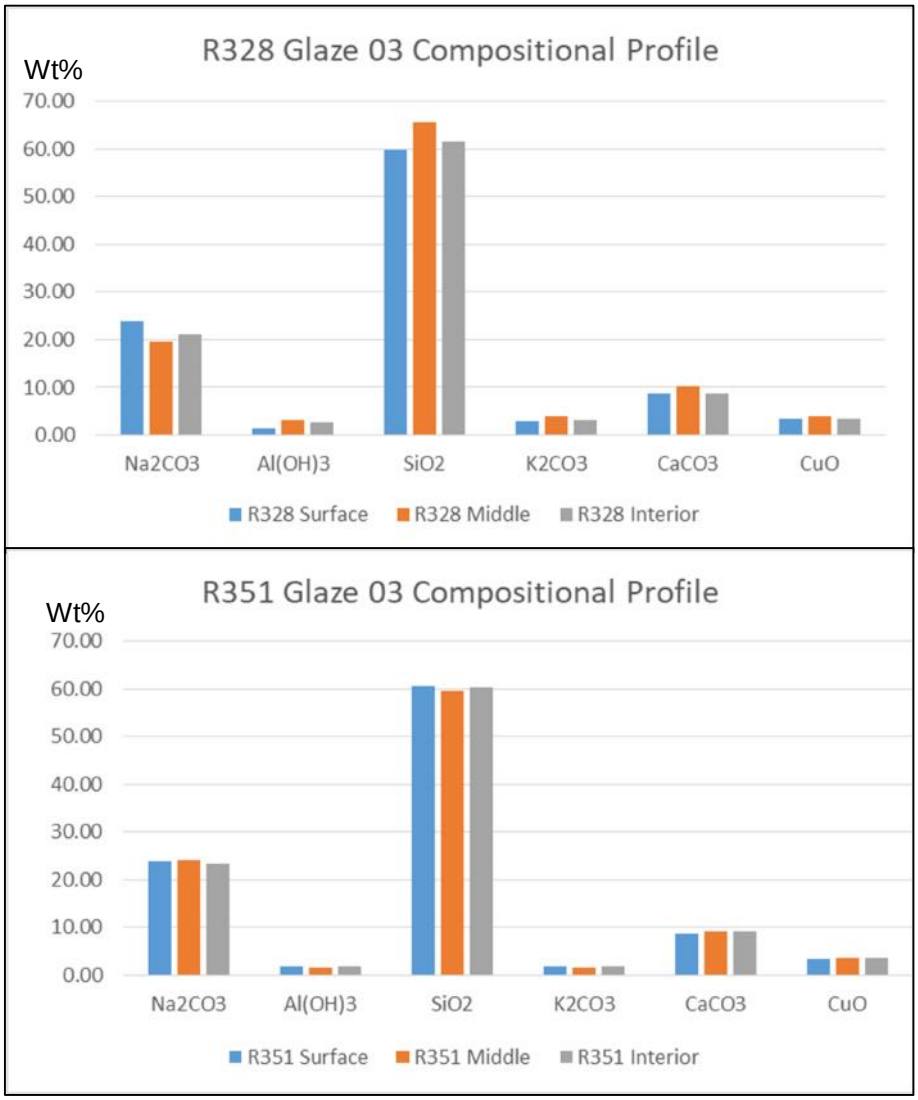

Fig. 7-31: Selected glaze composition profiles for copper colourant glaze 03.

exhibited as a slightly darker area in the image. Figure 7-12b is a good example of this where the leached areas near the surface are quite visible. Cracks in the glaze allowed water to enter deeper into the glaze leaching alkali from glaze areas near the crack.

Copper and silicon exhibit greater quantities near the surface. These results may be due to an artificial enhancement of the elements as alkalis were leached from the glaze. Silicon also exhibits elevated levels in the interior where alkalis may be been leached as well. Copper does not exhibit this characteristic. Instead, it tends to be highest near the surface and lowest in the interior.

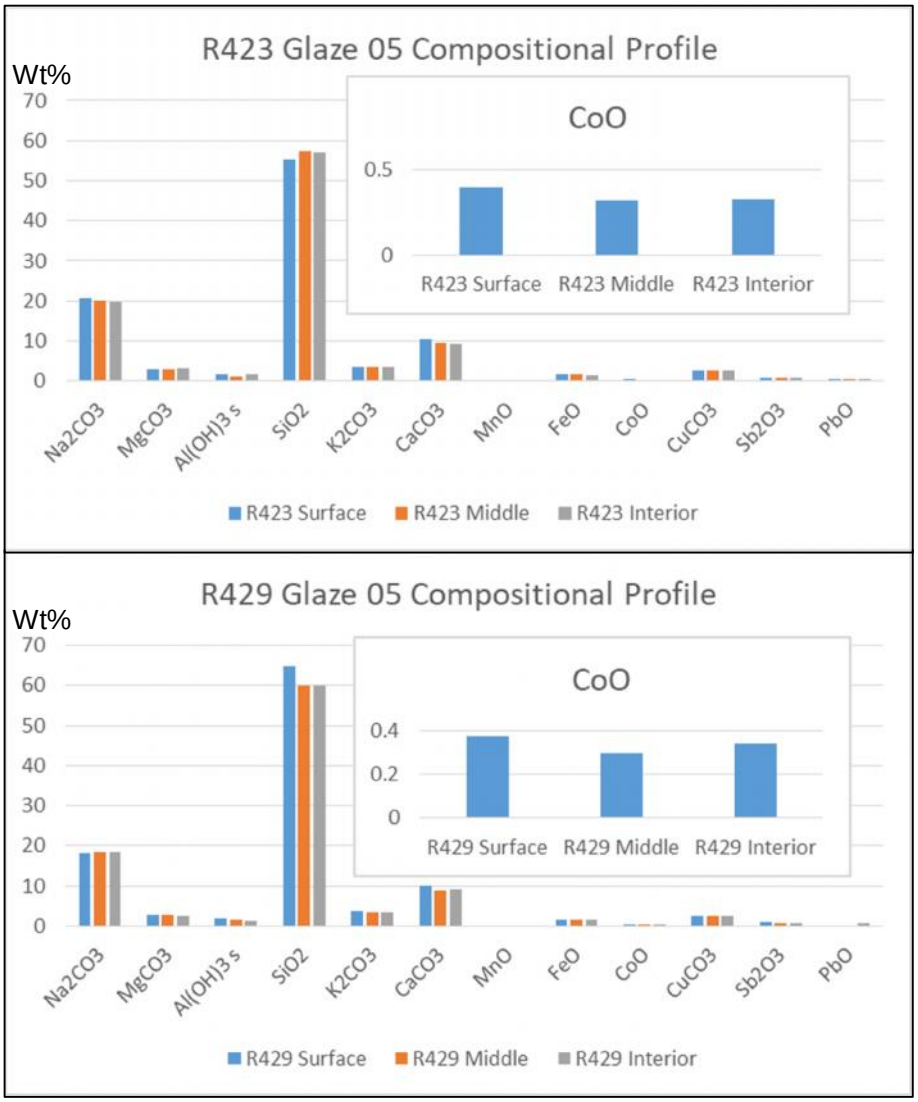

Fig. 7-32: Selected glaze composition profiles for cobalt colourant glaze 05.

The five cobalt blue glazes (s48, s70, s72, s74, s78) exhibit cobalt in various degrees (see Table 7-15). The cobalt results for s48 are below detection. Sherds s70 and s72 exhibit cobalt at highest quantities near the surface and lowest near the interior. Cobalt in s74 is below detection near the surface but the middle and interior measurements are nearly equal. Sherd s78 exhibits lowest cobalt quantities near the surface with nearly equal results for the glaze middle and interior.

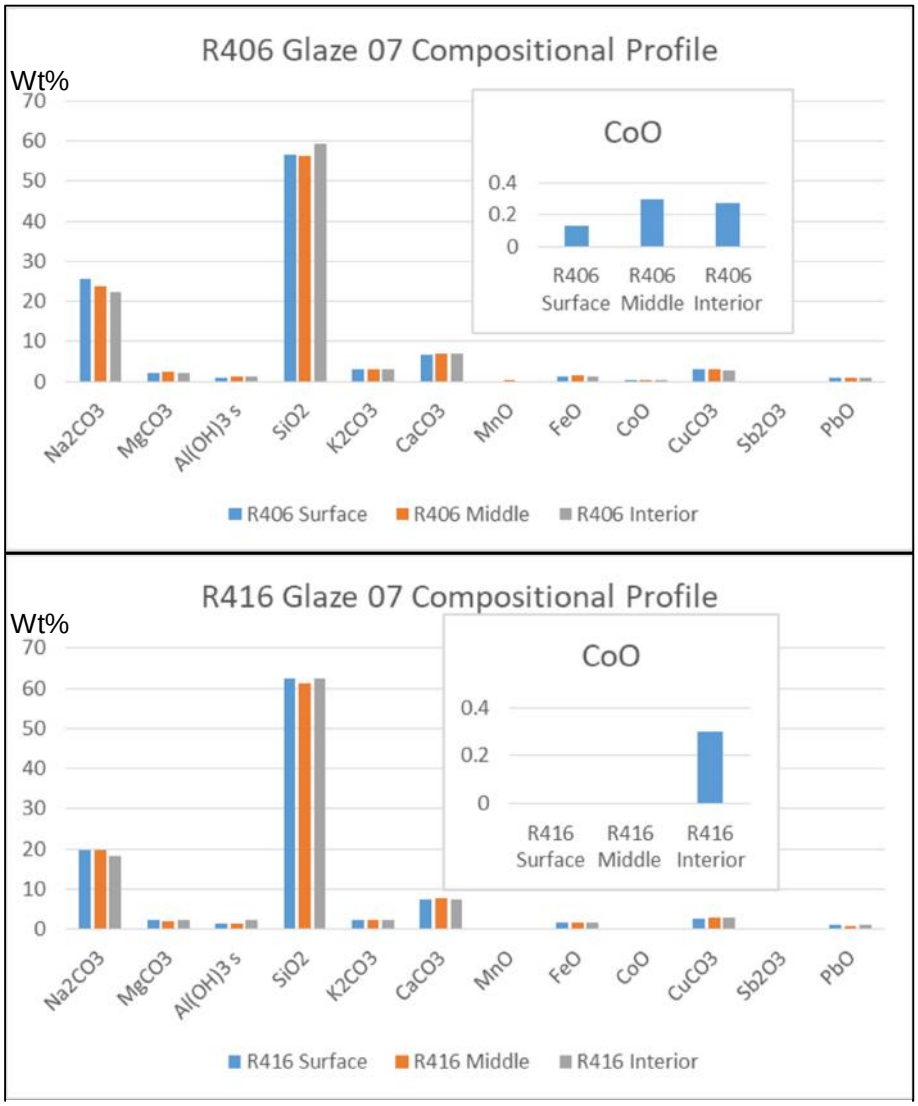

Fig. 7-33: Selected glaze composition profiles for cobalt colourant glaze 07.

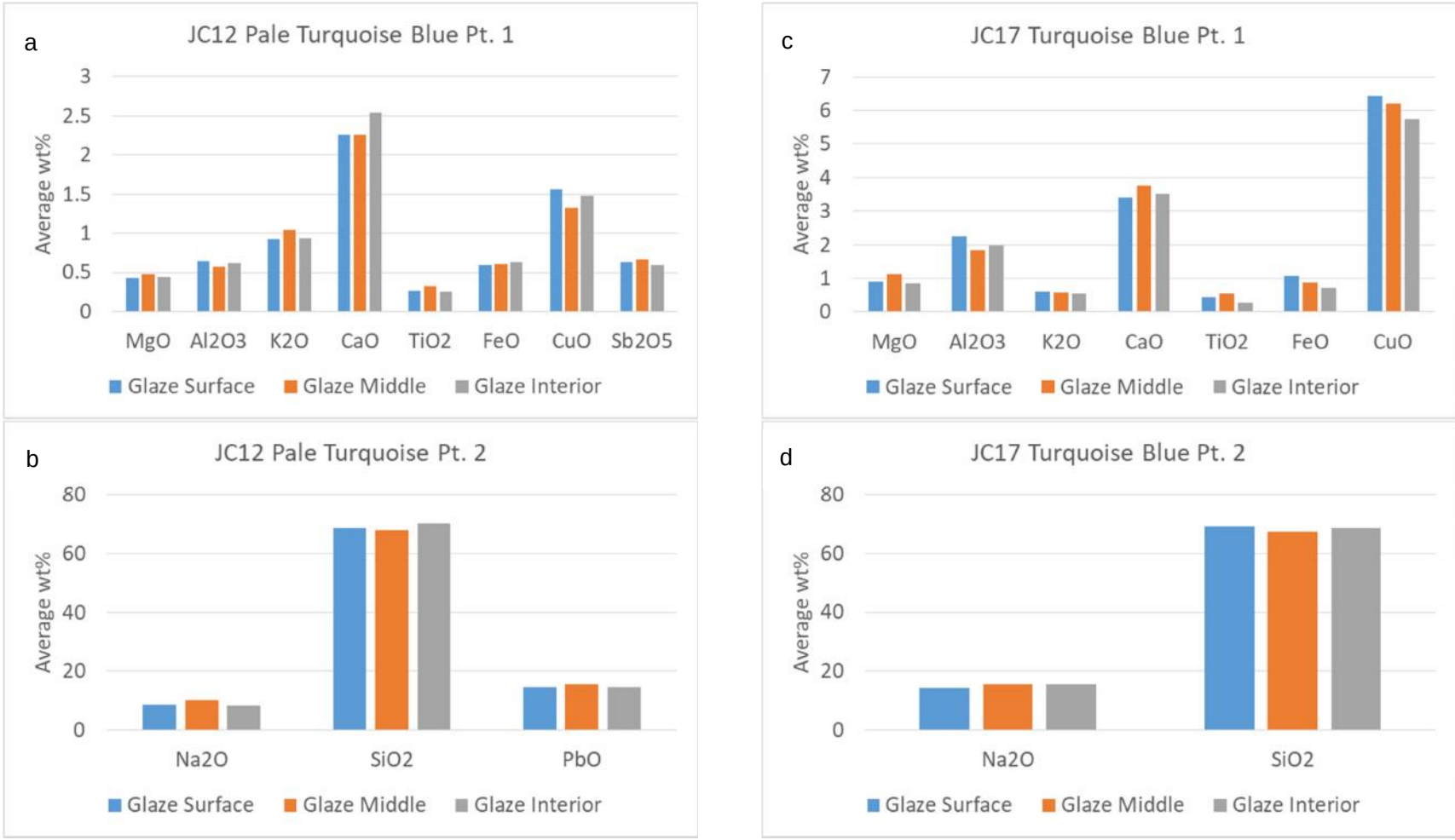

Fig. 7-34: Compositional profiles for two copper blue glazes (s12 (a and b) and s17 (c and d)).

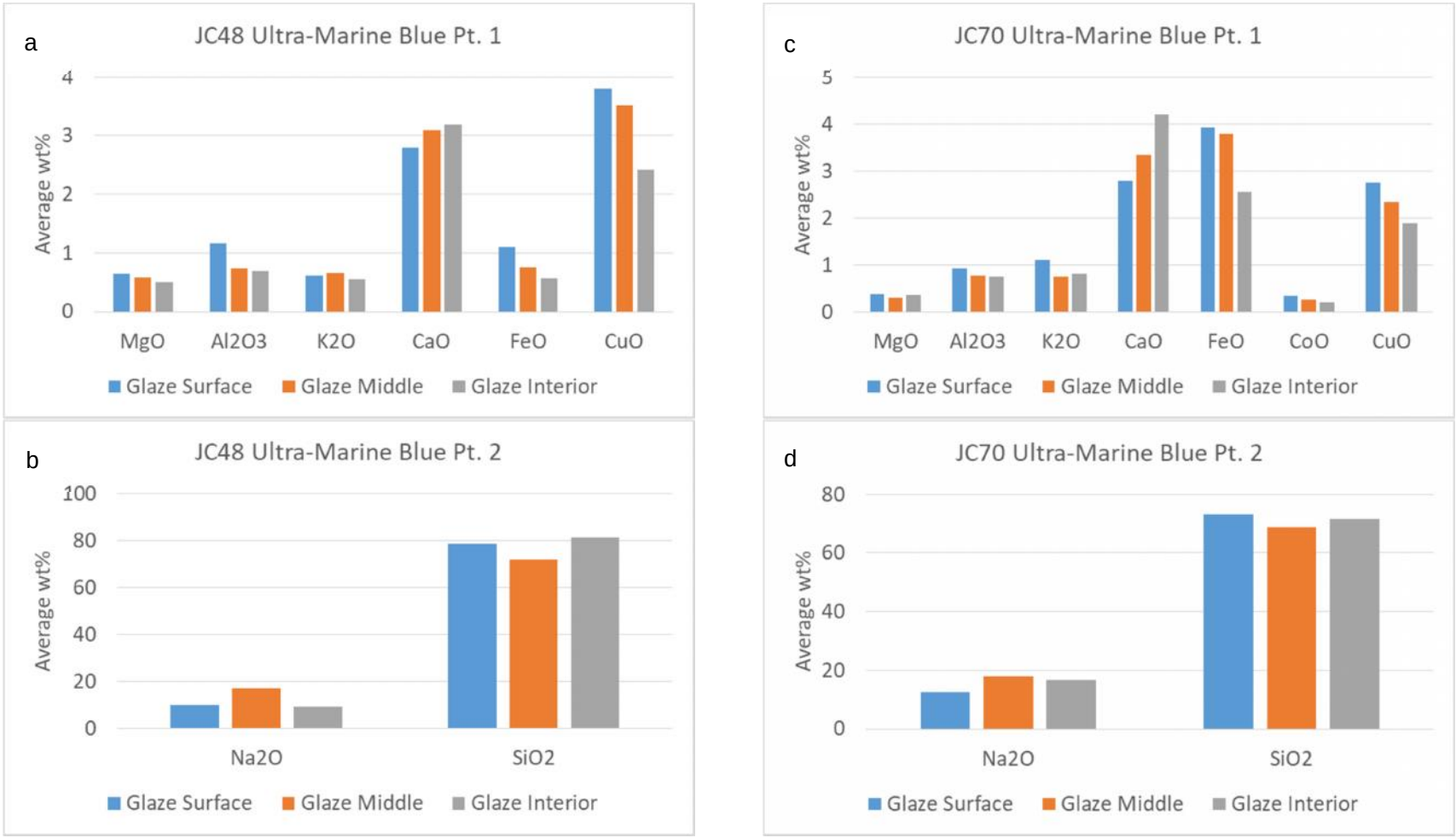

Fig. 7-35: Compositional profiles for two cobalt blue samples (s48 (a and b) and s70 (c and d)).

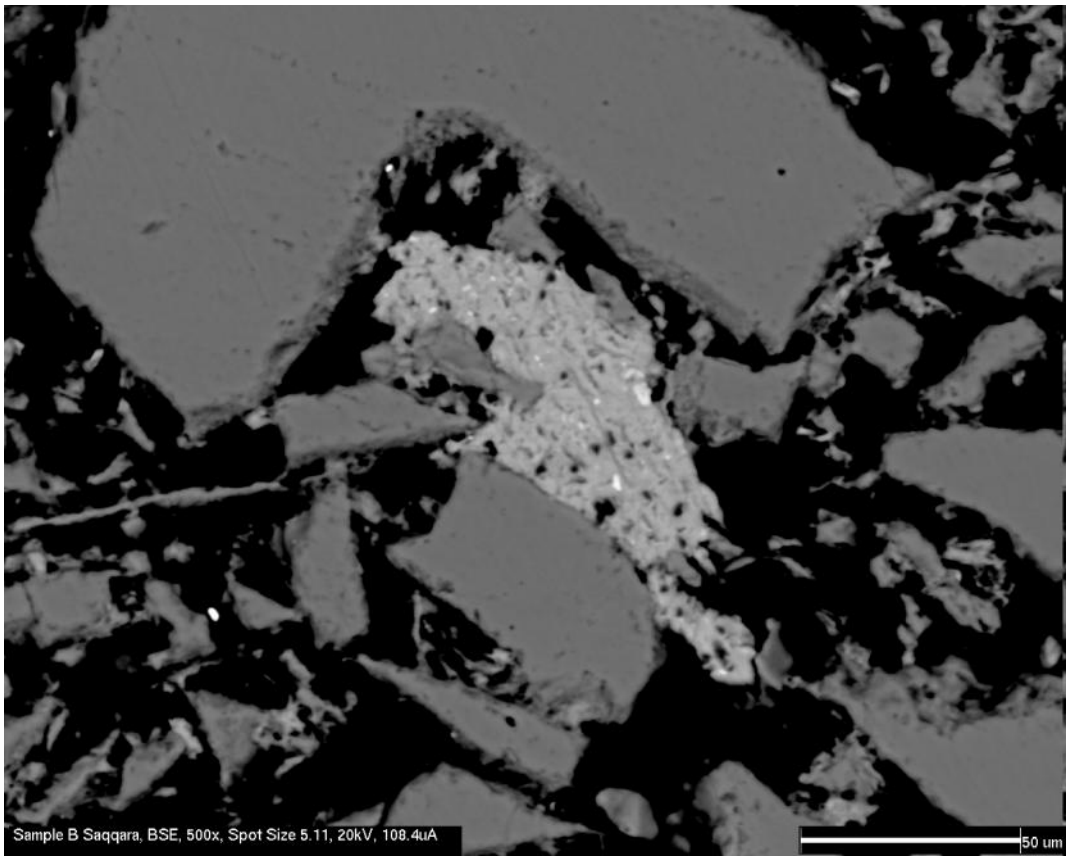

Fig. 7-36: Saqqara sherd s81 showing a potential clay particle wedged between several silica particles. This fleck of material produced high SEM-EDS peaks for aluminium and magnesium.

7.6.5 Archaeological Faience Case Study: Presence of Clay

Some authors (Griffin 2002:335; Kiefer and Allibert 1971:110-1; Mao 2001:20; Nicholson 2013:135; Tite et al. 1998:112; Vandiver 1983:A124) have suggested that clay could have been introduced to the faience body to facilitate formation. The addition of clay would have made throwing on the wheel an option, otherwise the ground sand bodies would collapse due to their thixotropic nature.

The bodies of the archaeological glazes were not generally examined directly using HH-XRF and SEM-EDS. They were, however, examined using SEM-BSE. There was no evidence of clay particles within the faience bodies except for one sherd, blue glazed s81 (Fig. 7-36). Qualitative SEM-EDS analysis indicated high levels of aluminium and magnesium within this fleck. This particle is approximately 50 x 100 µm in size. Other aluminium particles were identified in the sherd s81 body but they were much smaller in size (~1-5 µm in diameter). The amount of clay in this sherd is not enough to state, without a doubt, that clay was intentionally introduced, and it was not identified in other faience bodies. It is much more probable that it was unintentionally

introduced as a fleck in the workshop during production. The lack of clay in most of the bodies does not discount the use of resin as a binder. However, there is no evidence indicating its use either.

7.6.6 Archaeological Faience Case Study: Cobalt Ore

Section 2.5.2 discussed three potential cobalt ores used during the New Kingdom, Third Intermediate Period and the Late Period and after. The New Kingdom cobalt ores were associated with high alumina and magnesia. The Third Intermediate Period cobalt ores were associated with high manganese (~70%) and moderate iron (~0.85%) contents, and the Late Period and after cobalt ores were associated with high iron (~1.9-7.0%) and low manganese (<0.05%) (Kaczmarczyk and Vandiver 2008:75).

Saqqara sherds s70, s72, s74 and s78 manifest the characteristics of a cobalt blue glaze; they are dark purple to ultra-marine and cobalt is identified in the EDS analysis. A review of table 7-16 reveals a relatively high iron content (1.71 - 4.22 wt%) that is similar to the range provided by Kaczmarczyk and Vandiver (2008:75) for cobalt ore used during the Late Period and after. Manganese is below the limit of detection and magnesium and aluminium are between 0.34 and 0.57 wt%, and 0.64 and 1.11 wt%, respectively. These characteristics are not consistent with the cobalt ores used during the New Kingdom and Third Intermediate Periods.

The HH-XRF analysis of Saqqara sherd s48 revealed relatively high levels of cobalt and copper possibly indicating that both were intentionally used as the colourant (Tables 7-12 and 7-13). The cobalt content was below the limit of detection with EDS (0.1 wt%) and the iron content is 0.75 wt% (Table 7-15). Alumina and magnesia are 0.89 and 0.57 wt%, respectively, and manganese is below the detection limit with EDS. HH-XRF is capable of detecting these elements. These characteristics are not associated with any cobalt ore known as a colourant source. A new cobalt colourant source is not being suggested but perhaps the cobalt revealed by HH-XRF represents an inclusion of some sort; whether it was intentional or accidental, or even evidence of a workshop accident is up for question.

7.6.7 Archaeological Faience Case Study: Alkali Source - Natron or Potash

Section 2.5.3 describes the sodium/potassium ratio that may indicate the alkali (natron or potash) that was used in the manufacturing of the glazes. A ratio of ~2-6 indicates plant ash and a ratio >10 indicates natron (Kaczmarczyk and Vandiver 2008:66-67). The ratios produced as a result of the EDS analysis are dependent on the weathering impaction on the glaze. All ratios used to determine alkali source from the EDS of the Saqqara sherds were taken from the three middle glaze measurements to reduce

impaction from weathering, although some glazes may be highly weathered therefore exhibiting greatly reduced sodium and potassium levels, and will produce erroneous results.

Nearly all Saqqara sherds exhibit sodium/potassium ratios >10 (Table 7-15) which, by this method, would indicate that natron was used during the glaze manufacture. Saqqara sherds s12, s21, s22, s80 and s81 exhibit a sodium/potassium ratio <10 with only one (s81) being in the 2-6 ratio range that would indicate potash as the alkali source. However, the BSE images of the glazes reveal a fractured glaze with cracks leading from the surface deep into the interior of the glazes. All these glazes reveal low to very low levels of sodium indicating that weathering resulted in dealkalization of these glazes. Saqqara sherd s42 exhibited levels of sodium and potassium below the level of detection and therefore did not produce a sodium/potassium ratio.

7.6.8 Archaeological Faience Case Study: Copper-Tin-Lead ratio

The copper, tin and lead ratio may indicate the use of contemporary Egyptian bronze filings or dust as a colourant. The copper/tin ratio in contemporary bronze after the New Kingdom Period equates to 4% to 10% tin in bronze (Kaczmarczyk and Hedges 1983: 83; Kaczmarczyk and Vandiver 2008: 74). A slightly elevated ratio over 10 could be due to copper depletion from weathering. A ratio over 15 suggests that tin was introduced to the glaze in another form separate from contemporary bronze.

A review of table 7-15 exhibits six blue and one green glaze in which tin was above the 2-sigma limit of detection. The copper/tin ratio for most of these glazes is 0.03 to 0.04 (3-4%) (s22, s74, s81, s83 and s91). The single green glaze (s12) has a ratio of 0.05 (5%) whereas glaze s17 exhibits a ratio of 0.14 (14%). These results indicate that contemporary Egyptian bronze may have been used as the colourant.

7.6.9 Replicate and Archaeological Faience Case Study: Lead-Antimony Colourant

Lead/antimony ratio may suggest use of lead antimonate ($Pb_2Sb_2O_7$) as a colorant for yellow, or green when mixed with copper (Kaczmarczyk and Hedges 1983: 101) (see sections 2.5.4). The stoichiometric ratio of lead/antimony in lead antimonate is 1.38 but often excess lead is added to initiate the reaction resulting in recorded ratios of 5 to 15 often found in yellow Egyptian glass (Molina et al. 2014: 172).

The EDS ratio of lead/antimony in the yellowish-green (s45) and two of the green glazes (s20 and s42) are 5.98, 4.91 and 8.93, respectively (Table 7-15). These ratios strongly suggest the intentional use of lead antimonate as part of the colourant

process. Saqqara sherd s12 which has a slight bluish hue has a lead/antimony ratio of 23.44. It has similar levels of lead as the other green glazes but much less antimony.

The HH-XRF NPA lead/antimony ratios in the green glazes s20 and s42 and the yellow glaze s45 are 7.2, 7.8 and 7.4, respectively. Saqqara sherd s12 exhibits a ratio of 29.8 revealing an excess of lead in the glaze. These findings generally correspond with the EDS results although the ratio number is different. This difference is based on depth of detection and the number of cps returned to the detector for lead and antimony with NPA. The depths of detection are similar although lead is detected to greater depths which will increase the lead cps and the lead/antimony ratio to provide an inaccurate result. The NPA lead/antimony ratio in the field may provide an idea of the actual relationship but the NPA results need to be converted to wt% or another technique used for greater accuracy.

7.7 Discussion and Conclusions

The archaeological sherd glazes exhibit more refinement and greater variability in structure and composition. The archaeological glazes are generally much thinner on average than the replicated material. The mean glaze depths do overlap but the mean interaction layer depths are greater in the replicates with very little overlap (see Fig. 7-16). This is because of a nearly uniform large silica particle size within the replicated bodies (see Fig. 7-8 and 7-9) which has allowed the glaze to penetrate much deeper in the replicates. The replicate material is sufficient for the evaluation of the HH-XRF because it still represents a known material and is within the glaze depth and silica particle size range that is found in the archaeological material.

SEM-EDS analysis of the replicate and archaeological sample glaze columns resulted in a compositional profile. The compositional profile of the replicated faience glazes exhibited very little variation through the glaze. This is expected in a glaze that has not been affected by weathering.

The compositional profiles of the archaeological material exhibited more variation with depleted alkalis near the surface and in the glaze interior near the interaction zone between the glaze and body. Water can easily deplete the alkali components at the surface of a glaze. It can affect the glaze zone near the body if there is a break in the glaze coating allowing water to enter the porous body. Copper and silicon exhibited greater quantities near the surface of the archaeological glazes. The higher quantities of copper and silicon may be the result of artificial enhancement in the alkali depleted glazes. Kaczmarczyk and Hedges (1983:56, 61-62) noticed this effect and determined it was caused by cementation and efflorescence glazing techniques although they

suggest copper could migrate from an underglaze to an over-glaze. The results obtained in this study reveal the tendency of copper to migrate towards the surface. The glaze profile of the archaeological glazes does not exhibit the same copper dispersion in the replicated faience glaze profiles which generally exhibit a balanced composition for copper through the glaze column. This may indicate that the copper migration in applied glazes is a product of weathering and not processing. Conversely, calcium generally exhibits higher quantities in the glaze interior and lower quantities at the surface, however this is not always the case. The same trend can be seen in the replicated materials indicating that this is a product of glaze manufacture and not weathering.

The EDS analytical results were used to recreate the known glaze recipes of the fired batches. The results of the major elements were relatively accurate but the accuracy fell dramatically with the minor and trace elements. This is an indication that the analytical results from the SEM-EDS cannot provide accurate recipes for the archaeological faience in the case study. This is compounded when the materials have been affected by weathering. Fractionation of the component oxides will compound the problem of recreating recipes from analyses.

The EDS analysis of the archaeological materials revealed that the cobalt ore used in the production of the dark blue glazes is consistent with other cobalt blue glaze of the Late Period and after based on lower quantities of aluminium and manganese, and higher quantities of iron. The sherds were assumed to be from the Late or Ptolemaic Periods (Dayton 1981:135) and these findings are consistent with this notion.

The ratio of sodium to potassium indicates that the Saqqara sherd glazes were produced using natron in preference to potash. However, potassium is more soluble than sodium and weathered glaze can easily affect the results. All archaeological glazes in the study have some form of weathering. These results can be used as a possible indicator but should not be relied upon. The analysis of a pristine glaze that has somehow been protected from the weathering process would provide more reliable results. HH-XRF NPA cannot be used to determine this ratio. Sodium and potassium have a great disparity in the depth of detection. Any ratio produced will be inaccurate and impractical for use in determining alkali source.

HH-XRF and SEM-EDS analytical results indicate that lead antimonate was intentionally used as the colourant for the green and yellow glazes. This was a little side experiment facilitated by the analysis of two green, one yellow and one green that was initially identified as blue. The results are not a surprise as lead antimonate was

used to produce green glazes during later periods. This may be useful in the future when determining if a green hued glaze was deliberately produced from a green colourant or is a result of a copper depleted blue glaze that has turned greenish as a response to weathering. The HH-XRF NPA results produced similar ratios to those of the wt% produced by SEM-EDS. This is because lead and antimony have similar depths of detection. Lead is detected at a slightly greater depth resulting in NPA lead/antimony ratios slightly higher than the wt% counterparts. HH-XRF NPA can be used to provide an idea of the lead/antimony relationship but accurate results will require conversion to wt% or use of another technique.

SED-EDS analysis of six blue glazed sherds and one bluish-green glazed sherd revealed a copper/tin ratio of 0.03-0.14 (3-14%) indicating that the copper colourant is most likely due to a contemporaneous leaded bronze. Tin in most of the glazes was not above the 2 sigma limit of detection.

Qualitative analysis of the replicated faience glazes indicates that 15 kV measurements of low Z elements (sodium - iron) do not return fluoresced photons from the body to the HH-XRF detector. The 15 kV measurements appear to be restricted to the glaze layer of the replicated material. The 40 kV measurements do fluoresce elements in the body which are detected by the instrument. However, most of the signal will originate from the glaze layer.

Chapter 8: Methodology: Multivariate Statistics and Data Preparation

"Statistics can be made to prove anything – even the truth."

"Facts are stubborn things, but statistics are more pliable."

"There are three kinds of lies: Lies, Damn Lies, and Statistics."

-Anonymous[1]

8.1 Introduction

This chapter discusses data preparation methods for multivariate statistical analysis (MVS) using a faience replicate dataset analysed by HH-XRF and SEM-EDS. The goal of conducting MVS during this project is to form compositional clusters that may indicate separate workshops or raw material sources. Elemental analysis of faience glazes produces a great quantity of information. The HH-XRF analysis generates multidimensional data composed of variables and measurements (i.e. net peak areas) that can be in the order of several hundred to hundreds of thousands. It is difficult and time consuming to interpret relevant relationships without the use of MVS. Basic statistics can be calculated but the data is too large to easily extract useful comparative information concerning all the relevant variables. MVS has been devised to handle such large quantities of information.

Data generated from instrumental analysis has to be prepared before MVS can be performed. The raw data requires transformation, outliers have to be identified and zeros have to be dealt with. According to Aitchison (1986) closed data (data that adds to a predefined number (i.e. 100%) and resides in the simplex (see section 8.2)) has to be opened before statistical analysis can be performed. Opened data (data in absolute values that resides in Euclidean space (see section 8.2)) may be skewed and require transformation to make the results more clear. Logratio transformation has been specified by Aitchison (1986) but more recent work indicates that transformation may

[1]These quotes have been inconclusively attributed to several authors of which Mark Twain is invariably one. See https://www.york.ac.uk/depts/maths/histstat/lies.htm for an interesting discussion on the topic.

simply be based on which method presents clear data and makes archaeological sense (Baxter 2016:55; Drennan 2009:310).

Data preparation evaluations are conducted on types of transformation, determination of outliers and methods of dealing with zeros. The evaluations are based on the analysis of three different replicate faience glaze batches (one copper; two cobalt) which represent known materials. Section 8.2 is a discussion involving the processes of determining variables to include in the statistical analysis, dealing with zeros and censored data (data below limit of detection) and identifying outliers. An evaluation of censored data replacement methods and data transformation methods are included as a part of the section. The instrumental results undergo statistical analysis consisting of principal component analysis (PCA), hierarchical cluster analysis (HCA) and K-means clustering analysis (k-means). The preference was to have these discussed along with the actual MVS of the faience replicates but all three techniques have limited use as part of data preparation and, therefore, are discussed here as a precursor. The evaluations are performed to determine which methods are suitable for the MVS of glazes and glass. The findings of the evaluations will be used on subsequent statistical data analyses in the chapters after this one which will include MVS performed in greater detail to that provided here.

The objectives of this chapter are:

- To provide a background to the MVS used in the study;
- To determine statistical procedures for replacing censored data and transforming data before MVS of glazes and glass;
- To determine if analysis will discern known groups within the dataset
- To provide detailed information on data preparation that will subsequently be handled by one or two paragraphs in the next two chapters.

The quotes opening this chapter serve more than as a campy introduction; they are a warning. Statistical analysis will always provide results. Whether the results approximate the truth depends on how the data was collected and handled thereafter. A sequence for statistics and MVS is included in Appendix H.

8.2 Multivariate Analysis Background

There is no standard methodology for statistical analysis in cultural heritage. As a result the methodology for statistical analysis for this project is based on the methods provided by previous studies of HH-XRF with glass, obsidian, stone and ceramics. Published discussions on MVS are consulted where case studies are lacking. Table 8-1 is a list of selected articles that pertain to HH-XRF and MVS. Most of the authors do not include a methodology for data preparation/statistical analysis suggesting that the raw data was directly entered into the statistical software and the results reported. A few minor exceptions are presented in this section.

Table 8-1: Select samples of published literature involving evaluations of HH-XRF and the types of MVS used.

Select Published Literature Involving HH-XRF and Multivariate Statistical Analysis							
Author	**Year**	**PCA**	**HCA**	**K-Means**	**Data Form**	**Material**	**Aim**
Morgenstein and Redmount	2005		✓		wt%, ppm	Earthenware	Assessment HH-XRF for fieldwork
Craig (et al.)	2007	✓			wt%, ppm	Obsidian	Comparison with XRF
Kato (et al.)	2009		✓		wt%, ppm	Glass	Egyptain Glass Analysis
Nazaroff (et al.)	2010			✓	wt%, ppm	Obsidian	Comparison with XRF and NAA
Jia (et al.)	2010	✓			wt%, ppm	Obsidian	Obsidian Analysis
Kato (et al.)	2010	✓	✓		wt%, ppm	Glass	Islamic Glass Analysis
Barone (et al.)	2011	✓	✓		wt%, ppm	Earthenware	Comparison with XRF
Forster (et al.)	2011	✓			NPA	Earthenware	Comparison with NAA
Millhauser (et al.)	2011	✓	✓		NPA	Obsidian	Comparison with XRF and NAA
Speakman (et al.)	2011	✓			wt%, ppm	Earthenware	Comparison with NAA
Forster and Grave	2012	✓			wt%, ppm	Obsidian	Comparison with PIXE and ICP-MS
Grave (et al.)	2012	✓			NPA	Stone	Comparison with ICP-OE, MS and NAA
Mitchell (et al.)	2012	✓	✓		NPA	Glazed Stoneware	Comparison with ICP-OES and NAA
Forster and Grave	2013	✓			NPA, ppm	Glazed Earthenware	Sourcing / Categorizing Clay Fabric
Tanasi (et al.)	2017	✓			ppm	Earthenware	Comparison with XRF
Emmitt (et al.)	2017	✓			wt%, ppm	Earthenware	Categorizing Clay Fabric

A review of Table 8-1 reveals that PCA is the preferred method for categorization in the selected cases. The PCA has been presented as 2D component biplots, three-dimensional component plots and a combination of both although the PCA loadings and eigenvalues have not consistently been reported.

Four of the 14 articles listed in Table 8-1 provide some form of data preparation. Kato (et al. 2009) conducted portable XRF analysis on 110 9th to 13th century Islamic glass objects recovered from sites on the Sinai Peninsula, Egypt, to see if a difference based on temporal association and production locale exists. The data was standardized (z-transformed) and the Ward's method algorithm was used with hierarchical cluster analysis to indicate four compositional types based on diagnostic elements limited to aluminium, potassium, calcium, titanium, iron and strontium. The analysis revealed that earlier glass deposits were associated with Syria-Palestine and later assemblages with Egypt. The differences between the two assemblages was based on the amount of iron and titanium found within the glass. A year later Kato (et al. 2010) conducted portable XRF analysis on 231 9th to 11th century Islamic glass objects recovered from the same areas on the Sinai Peninsula. Ward's method algorithm was used for hierarchical cluster analysis of the standardized data (limited to magnesium, aluminium, potassium, calcium, titanium, manganese, iron copper, strontium and lead). This combined with PCA (component biplots limited to aluminium, calcium, titanium, iron and lead) indicated four major clusters and five minor clusters within the data which related to Egyptian, Syrian-Palestinian and Mesopotamian glass production centers. These cases reveal that HH-XRF analysis of glass objects can produce production locale categories based on a limited number of variables.

Barone (et al. 2011) conducted HH-XRF analysis and MVS on 27 Corinthian B transport amphora to compare results with benchtop XRF and to determine production centers. The resulting data was in ppm and was transformed using centered logratios to convert from the simplex to Euclidean space so that parametric analysis could be conducted. The use of MVS including PCA (biplots) and hierarchical cluster analysis clearly distinguished the pottery produced in Greece from that produced in Magnae Grecia (Southern Italy) matching the results of the benchtop XRF analysis.

Milhauser (et al. 2011) conducted HH-XRF analysis on 103 obsidian flakes from Xaltocan, Mexico, which were previously analyzed using benchtop XRF and INAA. The goal was to evaluate and compare HH-XRF to the other methods used while determining raw material sources for the obsidian tools. PCA and HCA were conducted on data that was $\log_{10}$ transformed. The PCA and HCA results indicated

three clusters and six outliers. A total of 98% of the samples could be attributed to various known sources.

Mitchell et al. (2012) conducted non-destructive analysis on 27 12th-13th century AD glazed stoneware sherds from two sites in far eastern Russia to compare HH-XRF (of seven elements: titanium, iron, rubidium, strontium yttrium, zirconium, niobium), NAA (23 elements) and ICP-OES (19 elements). PCA and HCA (Wards Method) were used with standardized (z-transformed) data to determine sherd clusters in the MVA data. HH-XRF was demonstrated to be analytically consistent with NAA and ICP-OES in discerning geochemical source groupings. They determined that the higher dimensionality of ICP-OES and NAA failed to offer increased discernment of clusters.

Tanasi (et al. 2017) conducted HH-XRF analysis on 52 Early to Middle Bronze Age ceramic pottery samples from Ognina islet near Syracuse, Sicily, to determine if they were imported from Malta. Additionally, 19 clay samples from Malta and four from Sicily were analyzed and compared to the results of ceramic sherd analysis. Ten of the ceramic samples were analyzed using HH-XRF and XRF to compare results in an evaluation of the HH-XRF method. The trace element values (for thorium, rubidium, strontium, zirconium and niobium) were transformed using base $\log_{10}$. PCA was used to categorize the various samples using the number of components indicated by Eigenvalues >1. All the trace elements loaded with component 1 with the exception of strontium which was primarily loading on the second component with all the samples. The HH-XRF and XRF results were compatible. The conclusion of the analysis indicated that raw clay material and finished ceramic products were imported from Malta into Sicily. Objects stylistically Maltese were shown to be produced from Maltese and Sicilian clay.

Emmitt (et al. 2017) used HH-XRF analysis of 1626 ceramic artefacts to interpret mobility and settlement patterns from four middle Holocene contexts (The Fayum, Hemamieh, Maadi, and Merimda) in Egypt. Using their defined criteria resulted in the use of four elements (iron, rubidium, strontium and zirconium) for MVA analysis. PCA was used to categorize the samples based on clay composition and materials used during manufacture. PCA analysis was conducted as an inclusive dataset using all the collected samples, and as data-subsets with samples divided by site origin. PCA was conducted on all elements omitted from the initial PCA analysis which were higher than Fe (excluding gallium and zinc). This PCA produced similar though less pronounced results. Their conclusions supported the use of HH-XRF for ceramic categorizations based on clay components consisting of the four elements previously mentioned. They determined that raw clay or finished ceramic products were being

transferred between different regions to a greater degree than previously thought based on geochemical signatures.

Three of the case studies stand out in that they used logratio transformations instead of standardizations. All the cases revealed the ability of MVS to attribute individual samples to various raw material sources, production centers and/or geochemical categories. It is clear that even when some data preparation methods are present, they are not always consistent. An evaluation of the methods for data preparation need to be performed on the raw data specific to this project to determine optimal procedures for elucidating compositional clusters.

In the realm of statistics, the term ‘compositional data’ is data that sums up to a constant (i.e. wt% when the whole equals 100%) or represents part of that whole (Aitchison 1986) although the term is more loosely used in other disciplines to indicate data pertaining to the composition of the subject. Compositional data in the statistical sense is constrained or closed and some statisticians suggest that it requires transformation to ‘open’ for parametric tests and MVS. This is because compositional data is situated in the ‘closed’ or constricted simplex space (Aitchison 1986) and requires transformation to ‘open’ it for interpretation in Euclidean space. Otero et al. (2005:1405) states that compositional data fundamentally informs on the relative abundance of the parts of the whole. This encompasses wt%, ppm, proportions and molarity; and places emphasis on ratios (i.e. closed data) over absolute values (i.e. open data). The Euclidian coefficient is ideal for true measurement variables (i.e. absolute values) (Drennan 2009:280) but is inappropriate for compositional data without some preparation.

A description of Euclidean space and the simplex is provided to help demonstrate the perceived problems of closed data in the simplex. Aitchison (1982:139) suggests that a lack of variable independence creates a statistical problem for analysis of data in the simplex. The coefficients for measuring similarity are conducted in Euclidean space. Euclidean space is a two or three dimensional space that uses Euclidean geometry such as the Pythagorean Theorem on which Euclidean distance is based (Fig. 8-1). This is the space that uses x, y and z coordinates. A change in one variable will not cause a shift in the other variables nor in the space they occupy. A description of the simplex is more convoluted. For the purposes of this project, the simplex can be considered a bound geometrical shape composed of as many vertices as there are variables in the data. The position of a single sample within the simplex has to consider all vertices (or variables). A change in that position results in a recalculation of all the variables just as any change in normalized compositional (i.e. wt%) data

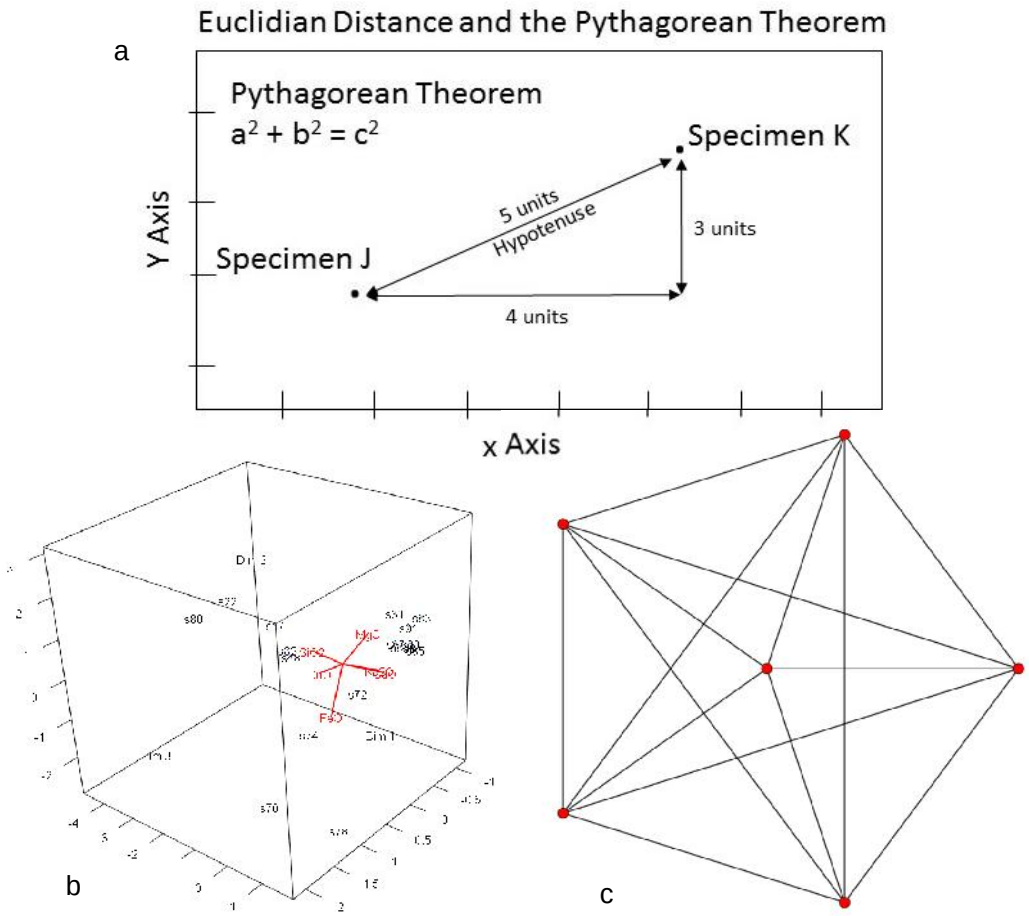

Fig. 8-1: Representation of the measure of distance (the hypotenuse) in 2-D Euclidean space (a), a representation of 3-D Euclidian space with several points and six variables in red (b) and a representation of the simplex with six variables in red (c).

requires re-normalization to retain the relationships between the variables and maintain the 100% sum of the data. The x, y, z coordinates are not sufficient to determine where a point exists within a multiple sided geometric shape (i.e. the simplex) thus requiring the data to be transformed into Euclidean space. A change in one variable (a single vertex) within the simplex causes a shift in the values and in the geometric space they occupied. If one could determine the coordinates a single point occupies, those coordinates will have changed with a shift in the vertices. This is generally not the case in Euclidean space; a coordinate can change along one axis (x) without affecting the other two (y, z).

8.2.1 Variables, Zeros and Outliers

There is a widely held view that the number of variables for MVS should be as inclusive as possible. But high variable count may not be beneficial for statistical analysis; a variable may not be informative and the inclusion of too many can obscure

real patterns (Baxter and Jackson 2001:254). A reduction of variables can result in data that is easier to interpret and present (Jackson and Baxter 1999:159). Variables essential to glass forming should be included at least with the initial data mining (Jackson and Baxter 1999: 160). Afterwards, major contributors (e.g. sodium, calcium and potassium with glass) to the analysis can be removed to see underlying relationships previously masked by the more dominate elements (Jackson and Baxter 1999:161). Ideally the analyst would remove all insignificant variables leaving a subset of highly correlated variables that reflect the whole dataset. The choice in variables may be case specific but needs to make archaeological sense. For instance, a subset of variables can be related to a process or form a part of the same branch on a cluster tree (Templ et al. 2008:2204). The full analysis may consist of several subsets of data individually interpreted (Jackson and Baxter 1999:162).

Elements chosen for participation in the analysis require values greater than the limit of detection and, in the case of compositional measurements (i.e. wt%), have values within the calibration range (Hall 2016:254). A limit of C_V <10% (a measure of precision) is commonly used on materials such as glasses and metals (Forster and Grave 2012:730; Mitchell et al. 2012:2923). A C_V larger than this makes it difficult to discern material source from analytical source data dispersion (Hancock and Carter 2010:243). There is no standard C_V cutoff for MVS; the analyst can decide on a cutoff based on the variables they wish to include with the understanding that C_V is the measure of precision and a higher C_V inclusion will result in greater randomness to the data under analysis. The C_V of a variable can be decreased by increasing the instrument time of acquisition but this will result in diminished returns and a decision on limiting acquisition time will still have to be made. Drennan (2009:307, 317) suggests that the number of variables in MVS should be restricted to no more than half of the number of cases to avoid spurious patterns.

Natural zeros and censored data can potentially skew statistical analysis. These results have to be replaced with a figure that will reduce the skewness while retaining important relationships between variables. Censored data is data below the limit of detection (LOD) or outside of the calibration range; essential zeros are natural zero values (Aitchison 1982:173). These values can be handled several different ways; they can be substituted with values at 50-75% the detection limit for the given element (Sandford et al. 1993; Palarea-Albaladejo et al. 2014:72; Templ et al. 2008:2201) or by the mean of the qualified data (Sandford et al. 1993). A form of multiple imputation to calculate missing values can be devised (Neff 2002) or the element can be dropped from the statistical analysis (Sandford et al. 1993; Palarea-Albaladejo et al. 2007).

Datasets with a significant portion of identical data (because of data substitution (e.g. half the LOD)), will influence MVS results. These elements can be dropped from the analysis. Alternatively, Templ (et al. 2008) recognized that many of the elements with missing values were important to the analysis. They omitted elements with more than 5% of all values below detection (ibid., 2201). Martin-Fernandez (et al. 2003) found that a substitution rate of ~65%LOD minimize the skewing of the relative relationship data structure when proportion of zeros in the data is <10%. Any replacement of the censored or essential values will affect the MVS results. Many statistical programs and packages (e.g. R FactoMineR (Husson et al. 2017) and Factoextra (Kassambara and Mundt 2017)) use the mean of the data as a default replacement strategy for missing or censored data with PCA, HCA and k-means clustering.

The R package missMDA (Josse and Husson 2016) replaces censored data using a 'leave-one-out' cross validation method. This method encompasses the individual removal and prediction of each observed value in the data matrix for a determined number of dimensions using the PCA model. The operation repeats for each predicted value. The number that minimizes the mean square error of prediction is retained (Josse and Husson 2016:8). Essentially, the number replacing the missing value is calculated, then recalculated until it obtains best fit with valid values along a PCA regression line. There is no adjustment of other values resulting in a slight variable ratio shift.

Multiplicative lognormal replacement is one of many possible replacement strategies required for data in the simplex. These methods retain ratios important for compositional data. Multiplicative lognormal replacement takes into account the imputed detection limit values to estimate geometric means of the values (Palarea-Albaladejo et al. 2014:73). This strategy replaces the censored/zero data with estimated values which will more than likely be different to one another while retaining the compositional ratios by adjusting the known values. This method avoids repetitive replacement values sometimes encountered by other methods (e.g. multiplicative simple replacement).

An outlier in MVS is a case or observable variable of a case that lacks similarity with other cases or groups in the data (Baxter 1999:323). They can disrupt the data resulting in skewed results. Outliers can be omitted if they do not represent an important aspect (Drennan 2009:21). Conversely, they should be included in some instances when they represent unexpected behaviour in a data environment or region of interest (Templ et al. 2008:2201). In cases when outliers fall into single clusters or disrupt homogenous clusters, solutions would be either to delete the specific case or

increase the number of clusters (ibid., p.2201). The course to take with outliers is a subjective matter when prior knowledge of the data and dataset will advise the analyst.

Finding outliers can be difficult. Many statistical packages allow the use of draftsman plots, a series of biplots that will reveal outliers, but identifying the specific specimen is difficult. Another solution is using Mahalanobis distances but this requires a large sample to variable ratio of 3 to 5 (Baxter and Jackson 2001:254) which the current dataset is lacking. Viewing the PCA plots of the first few components can indicate outliers because of extremity of a single variable (Baxter 1999:326). Examining the biplots of the last few components may exhibit outliers because of other factors. The use of single and average linkage hierarchical cluster analysis are helpful in identifying outliers (Baxter 1999:326). Box-plots are useful for identifying potential outliers but are not well suited to multimodal data (Baxter 2015:35). The potential outliers resulting from box-plots should be interpreted but not immediately accepted if they can be explained as representing a slight tail to the data.

8.2.2 Transformations

Elemental analysis can produce highly skewed (i.e. asymmetrical) results. Transformation of data changes the values to reflect a standard single-peaked symmetrical shape (Drennan 2009:53). Baxter (2015:25) suggests that normality of the data is not the prime concern with transformations, but that symmetry facilitates an easier interpretation of the data during statistical analysis. Normality of archaeometric data is a low priority because of the inclusion of variables that are inherently multimodal (ibid., pp.25-26). Archaeometricians are divided on how to transform compositional data. There are various methods of transformation not restricted to Box-Cox transformation, additive logratio, centred logratio, isometric logratio and z-transformations. Logratio transformation of compositional data became the dominant form starting in the 1980s (Aitchison 1986; Aitchison 1982). Centered logratio (CLR) transformation is the re-expression of the observations using a log-base 10 or natural log mathematically expressed as:

$$C \quad (x) = \left(l\epsilon \quad \left(\frac{x1}{g(x)}\right), \ldots, l\epsilon \quad \left(\frac{x}{g(x)}\right)\right) \qquad (8\text{-}1)$$

where x is the composition vector, g(x) is the geometric mean of composition x, and xD is the Euclidean distances between individual variables. Its use is based on compositional data providing component data as relative values characterized by ratios (Aitchison et al. 2002:296). The use of logratios, logarithms of the original ratios, results in no loss of information during transformation.

MVS is optimally handled with variables that have been stripped of their units but still exhibit a measure of 'unusualness' within a dataset. This is called standardization and it is a common statistical transformation used in MVS (Drennan 2009:275-276). Concerning the current project, the faience glaze measurements are produced in counts/second. After standardization the units of measurement (i.e. counts/second) will have been transformed into units based on standard deviations above and below the counts/second mean for each variable. This is the universal method of standardization and is called z-transformation (Templ et al. 2008:2201). This process is displayed as:

$$Z = \frac{x-\mu}{\sigma} \qquad (8\text{-}2)$$

where x is the variable, μ is the mean, σ is the standard deviation and z is the standardized variable. An alternative to this uses the median and the median absolute deviation in place of the mean and mean standard deviation (Templ et al. 2008:2201).

There is a debate within the archaeometrician community about the usefulness of logratio transformations with compositional data. Early proponents for using logratios were heavily influenced by Aitchison (1982, 1986). Aitchison et al. (2002) state that MVS of standardized raw data is meaningless and requires the logratio transformation for relevancy. The compositional sample space is simplex represented by a polytope (a geometric shape of any number of dimensions with flat sides (see Fig. 8-1) whereas unconstrained data exists in Euclidean space (two or three dimensions) (ibid., p.295). Pro-logratio arguments contend that long-tailed distributions become more symmetrical after transformation and a similar order of magnitude is applied to variables (Baxter and Freestone 2006). Sometimes logratios resulted in greater differentiation for clustering than raw data (Wilson 1978:228). Aitchison et al. (2002:296) suggest that logratios are easier to implement and interpret. Compositional data, it is argued, should be transformed to 'open' it for MVS. Without transformation MVS on 'closed' compositional data may produce biased results (Templ et al. 2008:2199).

Universal use of logratio transformations within the archaeological community began to decline with practical application. Tangri and Wright (1993) found that PCA on standardized data produced better results than the logratios championed by Aitchison. Baxter and Freestone (2006) found that logratio transformations tend to lose data structure relationships because of inclusion of elements not associated with the interpretable archaeological data structure. Standardized data tended to be more beneficial for MVS of compositional data than the logratio transformations. Relative differences are emphasized in logratio transformations whereas standardized data will

identify relationships with absolute differences important for reflecting recipes and source materials. Baxter (1992; 2016:31) writes that data transformation rarely is better than typical standardization methods (e.g. z-scores) and that it can produce poor results when structurally uninformative elements of low yield command the elemental analysis. This is collaborated by Pearce et al. (2008:1363) who found PCA of centered logratio data placed emphasis on less precisely determined elements. Baxter (2016:98-88) cites the manufacture of glass of the same type (including impurities introduced by material sourcing and production) in which the major components may carry the archaeological information of interest but are reduced in importance by transformation. Transformation of data concerning minor and trace elements that are not correlated with major oxides may produce misleading information (ibid.). Beardah et al. (2003) found that logratio transformation obscured glass compositional relationships because it emphasized variables with high relative variation to produce unsatisfactory results. They found that PCA of standardized data did interpret a known data structure that unstandardized logratios failed to detect (Ibid.). Standardized data and standardized logratio data produced similar results. It has been stated by some of the same authors that neither is typically better than the other and that both methods (standardization and logratio transformations) should be conducted to see if either provides relevant information (Baxter 2016:55; Drennan 2009:310) therefore requiring an evaluation of the techniques with the current project data.

8.2.3 Multivariate Statistical Analysis Options

MVS is a common technique to gain insight into datasets in the archaeometric literature and has been used in the evaluation of HH-XRF on different materials (see Table 8-1). MVS used in this project include PCA, HCA and k-means clustering analysis as these have been demonstrated in the literature to be acceptable means for answering archaeological questions regarding compositional clustering. PCA exhibits the relationships between variables, will reveal outliers and has clustering capabilities. HCA will reveal relationships between samples (i.e. clustering) and variables (i.e. variable clustering) but can indicate outliers. It is complementary to PCA. K-means is an alternative discriminatory clustering method.

PCA is typically the first step into data mining. The process is a way of reducing the number of variables of a dataset while retaining the patterns (Drennan 2009:300). It does this by determining correlations of variables. A set of variables that exhibit strong correlation are assumed to be manipulated by the same underlying mechanism and are, therefore, reduced to a single variable that exhibits the same relationship. The

Table 8-2: Example dataset exhibiting tabulations for PCA Eigenvalues and loadings. Dimensions (e.g. Dim.1) are the PCA components. The variance for the Eigenvalues is the amount of data represented by each component. The cumulative variance of a PCA biplot of components 1 (75.40%) and 2 (15.81%) for the HH-XRF data represents 91.21% of all the data. PCA loadings indicate the influence of each variable on each component. Component 1 of the HH-XRF data is mostly influenced by a positive correlation of potassium (0.84) and negative correlation of silicon (-0.48) in each sample. Copper has the least influence (-0.03). The varimax rotation results are the PCA loadings having been turned at right angles to each other to produce loadings which clearly indicate the major influence factor on the loadings. Any discrepancies between the loadings and varimax rotated results can be considered noise.

PCA Eigenvalues and Variance Tabulation Example

HH-XRF 15 kV CLR Dataset				SEM-EDS Z-Transfromed Dataset		
	Eigenvalue	Variance %	Cumulative Variance %	Eigenvalue	Variance %	Cumulative Variance %
Dim.1	0.04	75.40	75.40	1.86	55.23	55.23
Dim.2	0.01	15.81	91.21	0.93	27.70	82.94
Dim.3	0.00	5.75	96.97	0.39	11.73	94.67
Dim.4	0.00	3.03	100.00	0.18	5.33	100.00
Dim.5	0.00	0.00	100.00	0.00	0.00	100.00

PCA Loadings and Varimax Rotation Tabulations Example

PCA Loadings

HH-XRF 15 kV CLR Dataset						SEM-EDS Z-Transfromed Dataset					
	Dim.1	Dim.2	Dim.3	Dim.4	Dim.5		Dim.1	Dim.2	Dim.3	Dim.4	Dim.5
Na	-0.21	0.06	0.70	-0.51		Na_2O	-0.59	0.02	0.44	0.03	0.67
Si	-0.48	-0.50	0.02	0.56		SiO_2	0.27	-0.34	-0.62	0.00	0.66
K	0.84	-0.16	0.14	0.21		K_2O	0.11	0.94	-0.24	0.08	0.22
Ca	-0.12	0.82	-0.19	0.28		CaO	0.49	0.06	0.40	-0.74	0.20
Cu	-0.03	-0.22	-0.67	-0.55		CuO	0.56	-0.05	0.46	0.66	0.17

PCA Varimax Rotation

	Dim.1	Dim.2	Dim.3	Dim.4	Dim.5		Dim.1	Dim.2	Dim.3	Dim.4	Dim.5
Na	-0.14	-0.14	0.86	-0.14		Na_2O					1.00
Si	-0.14	-0.14	-0.14	0.86		SiO_2			-1.00		
K	0.86	-0.14	-0.14	-0.14		K_2O		1.00			
Ca	-0.14	0.86	-0.14	-0.14		CaO				-1.00	
Cu	-0.45	-0.45	-0.45	-0.45		CuO	1.00				

new variable is called a unique principal component. The component is a combination of a scores matrix and loadings matrix (Cordella 2012:3). The scores are the values recalculated to a reduced dimensionality. Loadings are correlations and denote contributions of the original variables (Cordella 2012:7; Drennan 2009: 303). Eigenvalues are the sums of loadings that have been squared and divided by the number of original variables to reveal the proportion of the variation explained by each component. The first component will exhibit the largest eigenvalue and represent the majority of information and variation followed by the other components in decreasing order (Drennan 2009:313; Cordella 2012:5). The loadings and eigenvalues can be represented in tabulation to assist in the interpretation of PCA analysis (Table 8-2). The scores (recalculated x, y and z coordinates in a matrix) are already represented by the component biplots.

There are various ways to determine how many components should be expressed as part of an analysis. Guttman-Kaiser Criterion (Guttman 1954; Kaiser 1960) indicates components with Eigenvalues greater than one should be used for PCA. This is a common method adopted from factor analysis in determining the number of components to examine in PCA (Bandalos and Boehm-Kaufman 2008; Jackson 2005:47). It has been criticized as too inflexible and to potentially over-extract components. Scree plots place the components on the X axis and the corresponding eigenvalues on the y-axis. Scree is the detriment that lies at the bottom of a steep slope and the suggested cut-off of components is where the scree plot exhibits an ‘elbow’, in effect, where the scree on a slope would be located. This method can be subjective and perhaps the ‘loose’ counter-part to the Guttman-Kaiser criterion. Baxter (2015:118; 2016:57) suggests looking at pairs plots of the various principle component scores and further examining those that produce useful information. For instance, pairs plots of principle components 2 and 4 may reveal information that principle component 3 does not. In this case it makes sense to scrutinize a biplot of components 2 and 4 for more information.

PCA loadings can undergo orthogonal (e.g. Varimax) rotation in which the coordinate axes are rotated as a set at right angles to each other (Drennan 2009:306). Orthogonal rotation ensures there is no redundancy among the components (Cordella 2012:5). The orthogonal rotation can produce some discrepancies with lessor patterning elements and is, therefore, not universally used (Drennan 2009:306). Drennan (ibid.) suggests that any comparative differences between the rotated and non-rotated results can be accepted as background noise.

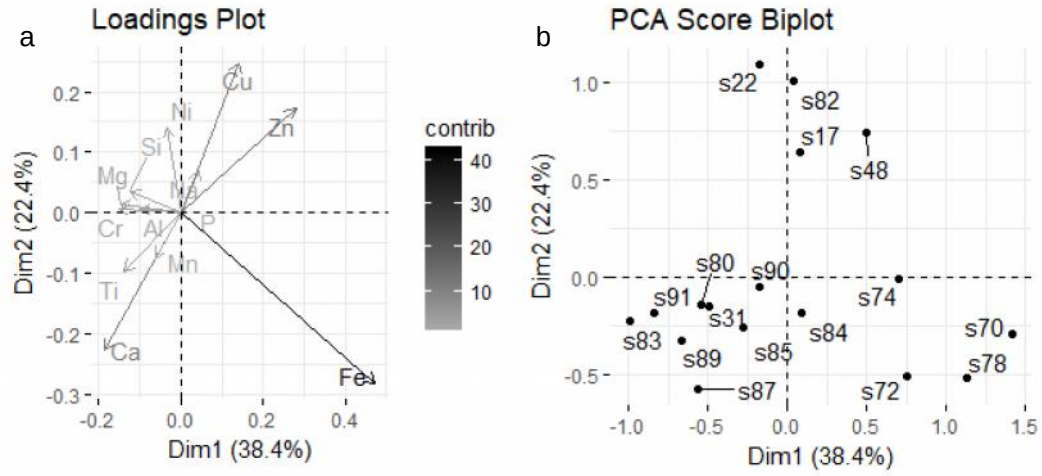

Fig. 8-2: PCA loadings plot (a) exhibiting relationships between the variables and PCA scores plot (b) exhibiting samples plotted on same graph (although scale may be different). The loadings and score plots have been combined into a single plot for this project so that the relationship between samples and variables can be directly seen.

Component loadings (tabular representations (see Table 8-2)) are examined to determine relationships amongst the variables. The signs of loadings indicate type of relationship. Strong loadings sharing signs have strong positive or negative relationships (depending on sign) whereas loadings near 0 have almost no relationships (Drennan 2009:304).

Correlation circles/loading plots (Fig. 8-2a) present the relationship between the variables (Cordella 2012:7). Angles between variables indicate correlation between those variables: an angle close to 0 indicates a positive correlation, angle close to 180 indicates a negative correlation, and angles at 90 indicate no relationship. Correlation circles/loading plots should be jointly interpreted along with score-plots.

Score-plots (Fig. 8-2b) present the specimens on a two dimensional plane identified by the axes which represent any two components (Cordella 2012:7). The specimens are grouped by similarity based on the variables that are represented by the components. Score plots and loadings have been combined into single figures for this project so that relationships can be easily detected.

Discriminatory cluster analysis determines structure based on relationships of variables by grouping similar cases more closely than less similar cases. After comparing all the variables, cases may be organized into various groupings with strength indicated by cohesiveness. The goal of cluster analysis is to “partition multivariate observations into many meaningful homogenous groups” based on the centroids (i.e. group centers and summaries) (Templ et al. 2008:2198). The ideal scenario is where cluster observations are very similar and cluster differences are very

large. A measure of similarity between observations defined by distances within the data space (different from PCA which uses a correlation matrix) is the method that most clustering techniques use (Templ et al. 2008:2198). Clustering analysis can be used on specimen observations for grouping related cases, and variables for revealing variable relationships.

HCA is usually agglomerative and works by combining individual specimen into larger and larger groupings based on similarity (Drennan 2009:309-310). The result is a dendrogram, or a graph where the individual cases are on one axis and the height, similarity as a measure of distance, on the other. Two common HCA variations used in the project include Ward's D^2 and single linkage. Ward's method merges clusters based on sums of squares and is good for elemental cluster analysis (Templ et al. 2008:2209). Single linkage clustering combines variables based on the strength of single similarity scores between the variables. The first grouping is based on the strongest similarity score, followed by the second and continues until all scores are accounted for. Single linkage clustering works fine for identifying outliers but not for compositional clustering (Drennan 2009:311-12).

K-means (partitioning) cluster analysis partitions observations into clusters based on the nearest centroid (centre of a grouping) by minimizing the average squared distance between the observations and their cluster centroid (Templ et al. 2008:2203). The methods starts with an assigned number of clusters (K) as determined pragmatically by the analyst or through another statistical method. The algorithm assigns each case to the nearest centroid, then recalculates distances and reallocates the cases on the newly produced centroids (Baxter 2015:2; Templ et al. 2008:2203). K-means usually uses Euclidean distances whereas the alternative method of k-mediods uses Manhattan distances. K-means clustering exhibits relationships based on the centroids of the number of clusters specified for the dataset. K-means cluster analysis is used as a part of a partitioning method to determine the number of sherd glaze clusters present based on composition.

The initial K value can be determined through a scree plot, some other algorithm[1] or pragmatically by the analyst. A bad K selection will be misleading with respect to the clusters it produces. A solution is to apply several different k values and determine the best fit using prior knowledge or by what seems to make sense (Drennan 2009: 310).

[1] See Charrad et al. (2014) for a description of 19 algorithms used to determine 'K' in K-means analysis.

Silhouettes are a graphical validation method for clustering analysis when k >1 (Rousseeuw 1987; Kaufman and Rousseeuw 1990:83-88). It compares the 'cluster-within' dissimilarity of a sample with the 'cluster-between' dissimilarity. A result close to 1 indicates the sample is well-clustered (Rousseeuw 1987:56). A result around 0 indicates the cluster centroids are nearly equidistant from the sample and the cluster assignment being questionable. A result closer to -1 indicates the sample has been misassigned to a cluster.

8.3 Multivariate Dataset Preparation

8.3.1 Data Collection

A dataset composed of HH-XRF and SEM-EDS analysis of faience replicate glazes (Tables 8-3 8-4 and 8-5) will be used to exhibit data preparation and to conduct evaluations on censored data replacement strategies and data transformations. The data was collected as outlined in sections 4.4.4 (SEM-EDS) and 4.4.5 (HH-XRF) using HH-XRF setup A for lower Z elements (15 kV, 50 uA with a vacuum for 180 seconds) and B for all elements (40 kV, 30 uA for 180 seconds without vacuum) (see Table 4-3). The HH-XRF parameter setup was determined through the parameter testing of the HH-XRF (see Chapter 6). Ten HH-XRF measurements were conducted across the surface for each glaze. Nine measurements were conducted with SEM-EDS for glaze profiles where they were equally divided between near surface, middle, and near interaction zone to produce compositional profiles (see Chapter 9). The middle three measurements were used to avoid alkali depleted areas near the glaze surface and the glaze/body interaction area. The centre glaze measurements are more likely to represent the condition of the glaze during its use life. The statistical analysis evaluation of HH-XRF at 15 kV will be conducted as part of a direct comparison with SEM-EDS data where the variables are shared. The 40 kV HH-XRF measurements are considered standalone because there is no overlap with EDS after the variable sorting criteria discussed in section 8.2.1 have been applied. A dataset consisting of all variables that meet the criteria and a second dataset containing all non-major, non-alkali and non-colourant variables (i.e. sodium, potassium, silicon, calcium, cobalt and copper) that meet the criteria have been evaluated for each method. SEM-EDS and HH-XRF analysis should discern the three glaze batches based on elemental make-up. The various analyses will be compared and should discern the same groupings through MVS, thereby confirming each method's results.

Table 8-3: HH-XRF 15 kV Average Net Peak Areas for Dataset 1.1 (Faience Replicates)

HH-XRF 15 kV (NPA) Faience Replicates Dataset 1.1												
Parameters 15 kV, 50 uA with a vacuum for 180 seconds (no filter)												
Average of 10 Measurements												
Sample	Glaze	Na	Al	Si	P	K	Ca	Ti	Cr	Fe	Cu	Zn
R327	G3	10892	18889	1108357	2756	151000	618988	5329	8234	37038	2788349	20424
R328	G3	8189	15156	910906	2823	129038	587794	5844	7963	36545	2304683	17100
R340	G3	8105	13424	829303	2970	143905	535285	4533	6948	35222	2581829	18633
R342	G3	7783	14851	807166	2954	113766	626044	4615	6722	37015	2589220	18994
R349	G3	10968	21019	1264327	2697	140140	531218	4317	8919	34303	2653820	19648
R351	G3	946	12813	1170133	1719	63874	442164	4183	6936	27336	2409313	13842
R356	G3	7610	13458	851805	2966	98798	552188	4451	9575	37923	2473529	18218
R359	G3	8511	15926	1028719	2736	88173	520101	4188	9640	32886	2475650	17843
R360	G3	9491	14633	772135	2953	165208	677108	5121	6087	34546	2710252	19316
R363	G3	12104	23326	1113011	2762	124301	772410	4146	7882	37659	2898423	21520
R364	G3	9390	16543	909528	2922	164482	648112	4665	6779	38915	2748819	19329
R367	G3	10358	21072	1057035	2827	124682	628293	4944	7919	34414	2667449	18329
R383	G3	12888	19620	1215642	2754	156147	541481	4516	7563	36652	2642006	18567
R384	G3	2562	16511	1085117	1807	101129	633502	4308	5861	33637	2769866	14304
R386	G3	9152	16330	922638	2852	142782	501564	5129	8185	34053	2551931	18311
R388	G3	2228	17743	1147291	1678	114329	629898	4556	5437	29961	2610469	13859
R390	G3	7655	12858	774272	2984	146059	442475	4950	6740	32715	2473312	18332
R392	G3	9949	18707	1079592	2740	98861	569611	4926	7871	36668	2698836	20249
R406	G7	6561	13410	760965	2687	140766	382302	4724	5480	876438	1686166	10231
R408	G7	7530	22590	1007687	2409	107636	424353	4674	7082	902066	1636607	9723
R411	G7	9054	24790	1308095	2224	128463	406463	3984	7290	855980	1805050	10713
R412	G7	7985	23409	1152225	2291	107024	450661	4467	6221	957802	1830759	11153
R415	G7	7790	18313	1286795	2472	105409	347435	5166	8159	764261	1664365	10543
R416	G7	6929	18302	1098137	2573	79003	344502	4202	7239	714410	1374585	8083
R418	G5	5019	18317	603831	3000	166350	492452	4264	4171	706236	1138029	5667
R421	G5	8872	28919	1084764	2662	229109	616452	3983	5378	909401	1588646	8856
R423	G5	8528	57004	1263937	2479	214729	518136	3793	7822	852943	1577612	9345
R424	G5	5776	27078	773115	2760	187242	541937	3852	5313	825730	1438498	8576
R426	G5	6091	26032	974100	2617	175701	435804	4439	8822	745871	1365812	8561
R429	G5	8311	43746	1348491	2309	191985	460704	4279	9072	768274	1420602	8444

Table 8-4: SEM-EDS (wt%) for Dataset 1 (Faience Replicates)

SEM-EDS (wt%) Faience Replicates Dataset 1.2						
Parameters 20 kV, Average of 3 Measurements						
Sample	Glaze	Na_2O	SiO_2	K_2O	CaO	CuO
R327	G3	18.28	70.19	2.14	5.71	3.68
R328	G3	14.73	72.64	2.59	5.88	4.17
R340	G3	18.57	69.93	2.42	5.42	3.67
R342	G3	16.58	69.92	1.65	7.11	4.75
R349	G3	15.68	73.67	2.00	5.06	3.59
R351	G3	16.77	71.60	1.42	6.01	4.20
R356	G3	18.35	70.66	1.58	5.67	3.74
R359	G3	17.09	71.09	1.43	5.97	4.41
R360	G3	19.04	69.17	2.44	5.86	3.49
R363	G3	17.39	68.75	3.32	6.12	4.43
R364	G3	21.07	67.86	2.25	5.34	3.48
R367	G3	16.97	69.36	3.40	6.02	4.26
R383	G3	22.49	64.81	3.00	5.09	4.61
R384	G3	17.62	69.86	1.48	6.31	4.73
R386	G3	20.32	69.56	2.31	4.44	3.37
R388	G3	17.13	70.78	1.51	6.00	4.58
R390	G3	19.91	68.96	2.05	5.22	3.86
R392	G3	17.18	70.35	1.65	6.10	4.71
R406	G7	17.62	71.31	2.61	4.79	3.66
R408	G7	15.13	72.87	1.84	6.01	4.15
R411	G7	16.82	72.38	2.33	5.01	3.46
R412	G7	14.29	74.64	1.97	5.17	3.94
R415	G7	15.38	74.83	2.17	4.39	3.23
R416	G7	16.17	67.90	3.32	6.35	6.26
R418	G5	16.93	69.90	3.43	6.58	3.17
R421	G5	15.47	70.59	3.21	7.07	3.66
R423	G5	15.20	71.53	3.10	6.88	3.28
R424	G5	15.31	72.18	3.10	6.44	2.97
R426	G5	13.72	74.31	2.91	6.33	2.73
R429	G5	13.50	74.28	2.90	6.33	2.99

Table 8-5: HH-XRF 40 kV Net Peak Areas for Dataset 1 (Faience Replicates)

HH-XRF 40 kV (NPA) Faience Replicates Dataset 1.3									
Parameters 40 kV, 30 uA and filter 3 for 180 seconds, Average of 10 Measurements									
Sample	Glaze	Fe	Cu	Zn	Sr	Zr	Sn	Sb	Pb
R327	G3	857	153626	963	903	1054	20648	21983	452
R328	G3	860	124655	832	683	1267	27435	25771	746
R340	G3	817	139595	911	748	1068	23079	20938	527
R342	G3	908	152779	953	848	1251	24420	24720	481
R349	G3	777	135930	905	871	1047	16869	15830	329
R351	G3	841	143195	992	961	1317	17743	13373	336
R356	G3	851	144436	899	787	1071	21498	17369	489
R359	G3	809	145808	962	923	1278	12909	11672	275
R360	G3	928	157586	980	817	1221	18325	20581	708
R363	G3	856	159149	975	898	1137	11874	11188	302
R364	G3	954	156287	996	888	1155	16726	16618	639
R367	G3	982	151696	976	865	1028	20016	17504	423
R383	G3	817	145829	891	699	1035	14275	13077	383
R384	G3	823	147660	908	728	1092	18409	20271	403
R386	G3	819	155253	950	763	1256	21631	20311	634
R388	G3	887	146260	910	686	1604	22986	23462	433
R390	G3	822	140099	878	638	1098	25363	26087	1213
R392	G3	854	154239	996	741	1239	22982	25050	363
R406	G7	20458	101567	622	912	1605	60366	38912	76546
R408	G7	18817	91184	609	845	1531	66842	40448	68622
R411	G7	19397	107971	669	1119	1701	88574	53300	84430
R412	G7	21351	108587	668	1009	1626	73549	46987	81786
R415	G7	16889	95983	617	1075	1577	89158	51985	78376
R416	G7	17755	90925	588	865	1734	70049	44273	70044
R418	G5	16405	69652	483	695	1064	91588	54643	33606
R421	G5	18461	82125	551	888	1128	151023	87671	40752
R423	G5	17803	86452	607	1013	1316	176656	100394	43990
R424	G5	18239	82819	537	907	1318	115003	68312	40880
R426	G5	17196	82627	555	1006	1507	152008	84057	43835
R429	G5	17650	86036	588	1077	1546	180906	103007	46035

The SEM-EDS and 15 kV HH-XRF measurements are considered glaze analysis. EDS was conducted on glaze profiles and all penetration of the electron beam was restricted to the glaze. The HH-XRF 15 kV voltage theoretically does not allow detection of elements beyond ~195 µm (copper) at 99% critical depth, or the depth where 99% of the signal is absorbed leaving 1% of the signal available for detection (see Table 7-17). A reduction to a critical depth of 90% means that 10% of the signal is available for detection and most of the signal was fluoresced from a depth of 97 µm or less. Average glaze depths for the replicates is ~850 µm. The thinnest of the measured replicate glazes is ~183 µm thick. The 40 kV measurements are considered bulk analysis even though the depth of many of the replicate glazes will not facilitate measurements of elements in the body. A 99% critical depth for these measurements is 578 µm (antimony) and is reduced by half to 289 µm when using 90% critical depth. The high voltage of the measurements theoretically will penetrate deeper into the faience than the depth of the faience glaze therefore detecting elements within the body of the faience as well.

8.3.2 Faience Replicate Samples

The faience replicates used in the analysis include one copper blue and two smaller cobalt blue batches (Table 8-6 and see Appendix A).These samples were selected to evaluate the use of HH-XRF on compositionally known faience material. The sample glazes were applied as non-descript thin and thick layers (depth later determined in cross-section) and fired using various kiln parameters (e.g. peak temperature and length of firing (see section 5.4)) within each batch to determine if differences could be detected. The faience replications were analysed in three groupings: all glazes (dataset 1), copper-blue coloured glazes (dataset 2) and cobalt-blue coloured glazes (dataset 3). Dataset 1 is used to demonstrate the data preparation methods and

Table 8-6: Replicate faience Samples Used in Multivariate Statistical Analysis. The samples represent three replicate faience glazes on a prepared body.

Replicate Faience Sample Colourants				
	Copper		Cobalt	Cobalt
	GLZ03		GLZ05	GLZ07
R327	R356	R383	R418	R406
R328	R359	R384	R421	R408
R340	R360	R386	R423	R411
R342	R363	R388	R424	R412
R349	R364	R390	R426	R415
R351	R367	R392	R429	R416

evaluations covered in this chapter. Full MVS of all three groups are covered in the next chapter.

8.3.3 Software and Software Packages Used in Multivariate Analysis

R (ver. 3.3.1) (R Core Team 2016) is a language and code-based platform that has statistical capabilities limited by the availability of user-submitted packages (currently over 10k based on search within R). RStudio (ver. 1.0.136) (R Studio Team 2016) is an integrated development environment (IDE) for the R platform providing tools for R workspace management. The R developer team retain end-user and data confidence by requiring the package developers to submit materials to the Comprehensive R Archive Network (CRAN). CRAN has several policies in place for submittal that protect the end-user, statistical integrity and the copy-right holders of the submitted packages. The R software was used for computational statistics including data preparation, PCA, determining number of clusters (K), K-means cluster analysis HCA. Data transformation and censored/zero data replacement was conducted through R (see Appendix I for coding).

8.4 Dataset 1 Preparation Evaluation

Dataset 1 is used to demonstrate data preparation methods including the selection of variables for analysis and determining outliers. Dataset 1 consists of five subsets (see Table 8-7). An evaluation of replacement strategies was conducted for censored data using the 'leave-one-out' method (LOO) and multiplicative replacement (MR). Centered logratio (CLR), standardization (also known as z-scores, z-transformation and z-trans) and standardized centered logratios (combination of the two methods) were evaluated as transformation methods for MVS.

8.4.1 Determining Variables

The elements (HH-XRF) and oxides (SEM-EDS) used in the testing of dataset 1 were limited by occurrence. In other words, more than 1 censored/zero of the three (EDS) or

Table 8-7: Dataset 1 breakdown including analytical technique and elements/oxides of interest.

Dataset 1: Faience Replication Samples				
Data Supersets	Data Subset	Technique	Data sub-subsets	Elements/Oxides of Interest
1	1.1	HH-XRF 15 kV	1.1.1 Comparative	Na, Si, K, Ca, Cu
			1.1.2 Standalone	Na, Al, Si, P, K, Ca, Ti, Cr, Fe, Cu, Zn
	1.2	SEM-EDS	1.2.1 Comparative	Na_2O, SiO_2, K_2O, CaO, CuO
			1.2.2 Standalone	Na_2O, SiO_2, K_2O, CaO, CuO
	1.3	HH-XRF 40 kV	1.3.1 Standalone	Fe, Cu, Zn, Sr, Zr, Sn, Sb, Pb

ten (HH-XRF) measurements for each sample resulted in the variable being omitted. One exception has been allowed (R426) for a 40 kV HH-XRF result exhibiting three lead readings below detection but determined to be of importance for the analysis. The 15 kV HH-XRF analysis detected more elements but for direct comparison (dataset 1.1.1) the variables for HH-XRF and SEM-EDS (dataset 1.2.1) have been restricted to the same elements. A second 15 kV standalone (dataset 1.1.2) comparison with SEM-EDS (dataset 1.2.2) has been performed taking full advantage of the HH-XRF 15 kV detection capabilities. SEM-EDS data was normalized after selection.

The SEM-EDS analysis of the three replicate glaze batches (dataset 1) detected several oxides most of which had to be omitted (e.g. TiO_2, MnO_2, SnO_2) because censored results are more than 10% of the data. This has resulted because dataset 1 is the analysis of all three glazes combined. The copper colourant glaze 03 batch contains far fewer oxide components than the two cobalt colourant batches so that when combined, several oxide components in glazes 05 and 07 have to be omitted. Many of these omitted variables will be available for statistical analysis when analysis is restricted to glazes 05 and 07 (the cobalt blue glazes) (i.e. MgO, FeO, PbO).

The HH-XRF 15 kV analysis of the glaze batches detected several elements (see Tables 7-7 and 7-8), some of which had to be omitted because the censored data represents more than 10% of the total data for each element (i.e. magnesium, manganese, cobalt, tin antimony, lead). These omitted elements are included for the cobalt blue glaze analysis (glazes 05 and 07). It is common knowledge within the HH-XRF community that sodium is difficult to detect and initial analysis with HH-XRF software Artax (vers. 7.2) exhibited sodium values below detection. The re-analysis using Artax (vers. 7.4) exhibited sodium well above detection limits with a relatively low C_V and standard deviation. Algorithms in the more recent software enables a greater detection of the element. Sodium has been retained for statistical analysis.

A C_V limit of 10% is commonly applied to variable selection but can be adjusted as deemed necessary. The SEM-EDS data exhibit a C_V average >12% for calcium. This is because of a few instances when the result for a single measurement is significantly higher than the others for a sample set, probably as a result of encountering unreacted particles in or possibly on the glaze. The samples were fired on a bed of calcium and every effort was made to clean the samples before analysis. The 40 kV HH-XRF measurements (dataset 1.3.1) shared one element (copper) in common with the SEM-EDS measurements. The 40 kV measurements were not directly comparable with the SEM-EDS and selection of variables were based on detection limits and C_v. This provided these measurements with a greater number of variables with a C_v<10%

including iron, copper, strontium, zirconium, antimony and lead (see Tables 7-13 and 7-14). Zinc, C_v<15%, was included in the analysis. Nickel and bismuth were omitted because the censored data represents more than 10% of the total data for each of the elements.

The HH-XRF data subsets were explored having removed major elements (i.e. silicon and sodium) and copper (colourant) to see additional relationships of the samples that might be otherwise obscured. Sodium was removed because the occurrence of the element in the archaeological material will be unreliable because of alkali depletion. Potassium, a minor component, was removed for the same reason. The results were mixed with the lower and higher dimensional datasets revealing greater cluster tendency at different times. For this MVS evaluation, only the higher dimensional datasets were used. Higher and lower dimensional datasets are retained for the final MVS analysis on the replicated and archaeological glazes.

8.4.2 Zeros, Censored Data and HH-XRF Detection Limits

Two strategies were evaluated to deal with zeros and censored values: leave-one-out (LOO) method and multiplicative lognormal replacement (MR). The results were nearly identical with a few minor differences consisting of the rearrangement of three samples within a branch and the reassignment of a fourth (Fig. 8-3). MR is required for compositional data (i.e. data in the simplex; SEM-EDS data (wt%)) to retain element ratios while transforming into Euclidean space. MR is only applied to the SEM-EDS data. HH-XRF data only requires replacement when 3 times the standard deviation of the background is used to determine limit of detection. The quantity of replaced values is small and both methods (LOO and MR) were evaluated and exhibited no difference.

The detection limits of HH-XRF can be calculated using two methods: SNR (see section 4.5.2) and 3 times the standard deviation of the background. SNR is the square root of the background under the peak of interest and provides a readily interpretable result (i.e. SNR>3 is detectable data, SNR>10 is quantifiable data). Both methods produce nearly identical results (Fig. 8-4) although SNR does have slightly lower detection limits. The standard deviation method provides greater detection limits and is onerous in the sense that the results must be compared to individual element NPA counts and a second calculation is required to determine quantification limits. SNR will be applied to all subsequent analysis because of its readily interpretable results, lower detection limits and similarity of measurements with the commonly used

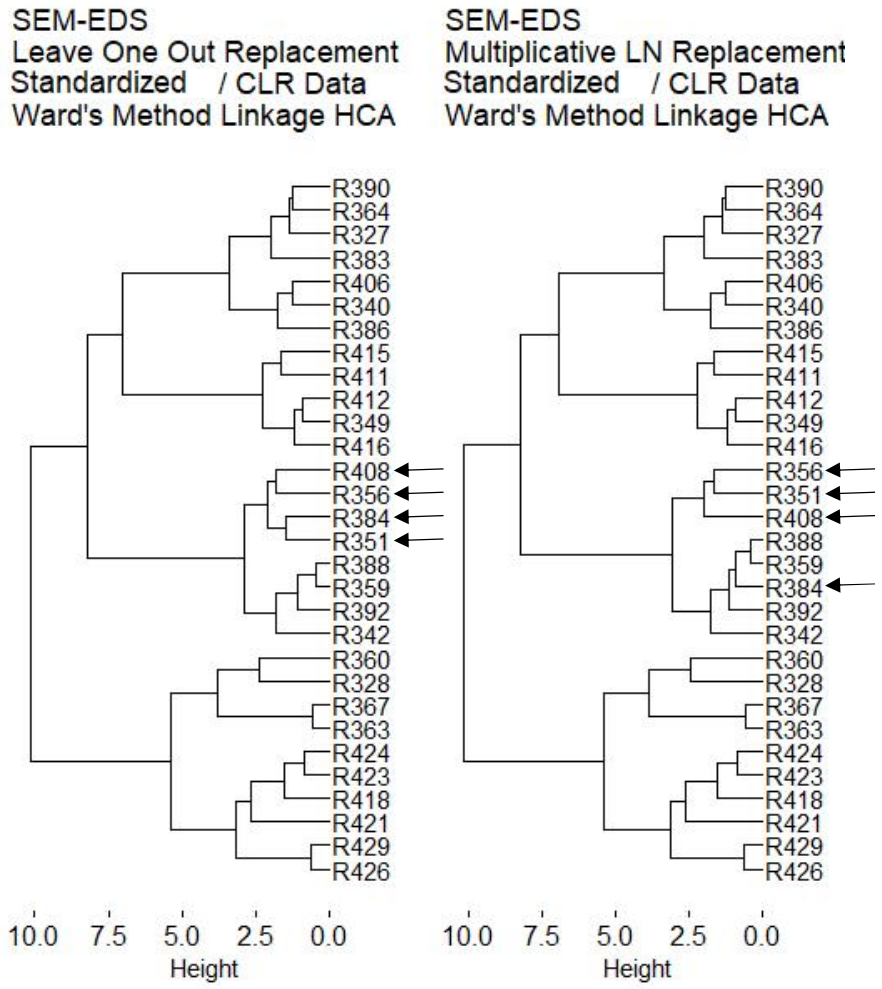

Fig. 8-3: Censored and zero values replacement methods of 'leave-one-out' and multiplicative lognormal used on SEM-EDS data. The results are similar but with a few differences as indicated by the arrows.

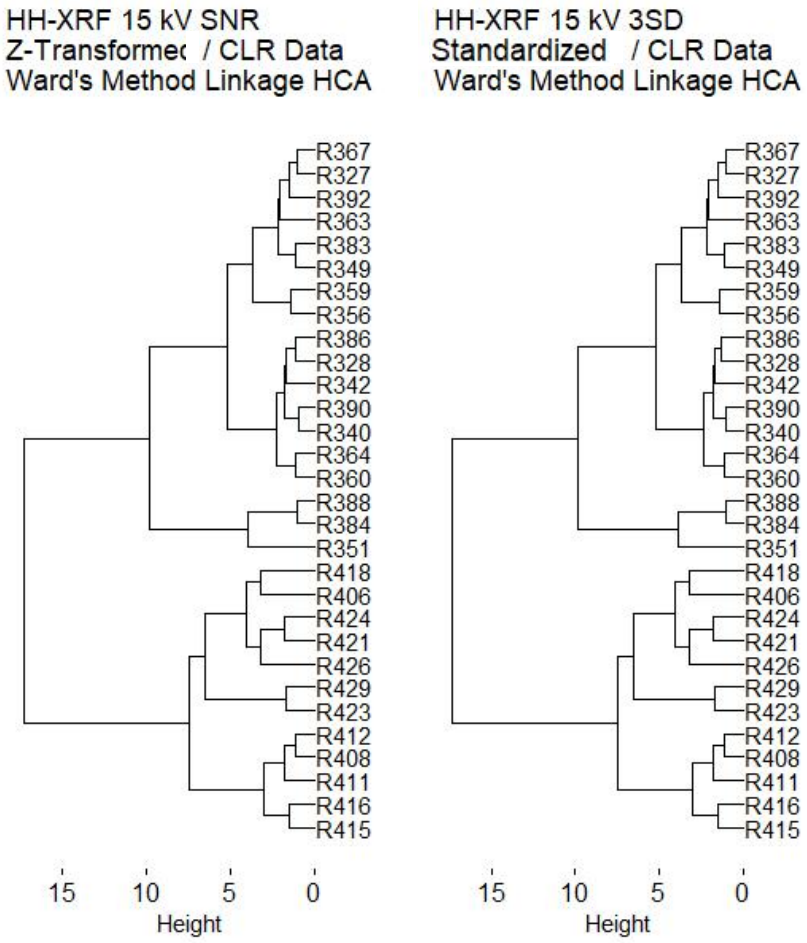

Fig. 8-4: Comparison of 15 kV HH-XRF results for SNR and '3 x the standard deviation of the background' (3SD) using HCA (Ward's method) and standardized / CLR data. The dendrograms are identical.

3 times the standard deviation of the background. A replacement strategy for natural or censored zeros was not required as none occurred.

8.4.3 Determining Outliers

HCA using single linkage process isolated three outliers (R351, R384 and R388) for the 15 kV HH-XRF measurements using the CLR and a combination of the CLR and standardized data (Fig. 8-5). The analysis involving only standardized data isolated the same three samples and two additional samples (R423 and 429). Dendrograms for the HH-XRF 40 kV measurements identified a potential outlier (R418) with the standardized data only (Fig. 8-6). Dendrograms for SEM-EDS revealed two potential outliers (R383 and 416) with the standardized data (Fig. 8-7).

Box-plots of the three transformation methods of the 15 kV data (Figs. 8-8 through 8-11) are identical and correspond with the dendrograms in identifying the same potential five outliers: three associated with sodium and two with aluminium.

PCA biplots of the three transformation methods with the HH-XRF 15 kV data confirmed the presence of the three consistently identified outliers but failed to conclusively reveal R423 and R429 as outliers on the 2D PCA biplot (Fig. 8-12). The PCA biplots of the SEM-EDS data confirmed all three of the outliers identified by HCA. The outliers R351, R384, and R388 will be removed from further analysis with this dataset. Samples R423 and R429 will be retained. HCA and the box-plots indicated that R423 and R429 were potential outliers but they failed to influence the PCA biplots other than resulting in a slightly more disperse cluster for cobalt colourant glaze 05, and they were not identified with the SEM-EDS measurements. The removed outliers will be re-included in subsequent analyses (e.g. cobalt and copper blue batch analysis) unless identified as outliers again.

The identification of three outliers (R351, R384 and R388) with HH-XRF are manifested by an increase in silicon detection and a decrease in sodium detection. The sodium in these three samples is the lowest of all the replicate samples analysed. The preference in silicon detection is due to an attribute of the samples that reduce the detectability of the sodium. This could be because of a localized reduction in the amount of sodium in the area of analysis although this is highly doubtful. More likely is the presence of pores in the glaze or the creation of an air column between the sample and the HH-XRF window because of surface geometry which has the effect of filtering low z photons. An inspection of the BSE profile images and of the sample surfaces was inconclusive. Sample geometry was not an issue as the samples were relatively smooth with no erupting bubbles.

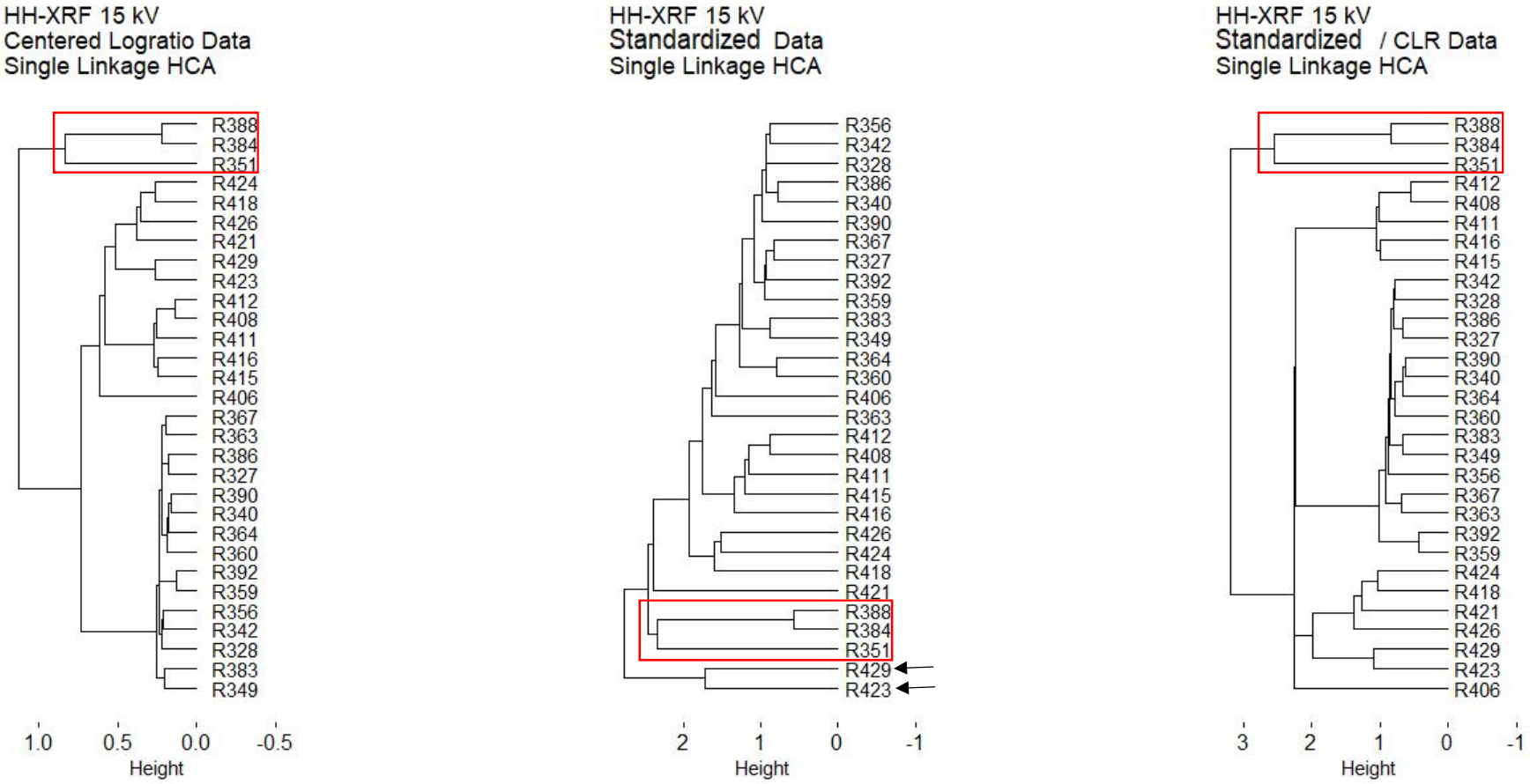

Fig. 8-5: Determination of outliers using single linkage HCA. All three transformation methods identified the same three outliers outlined by the box. Standardization identified two additional outliers (arrows) that the other methods did not. HCA of HH-XRF 40 kV data (not shown) failed to identify outliers.

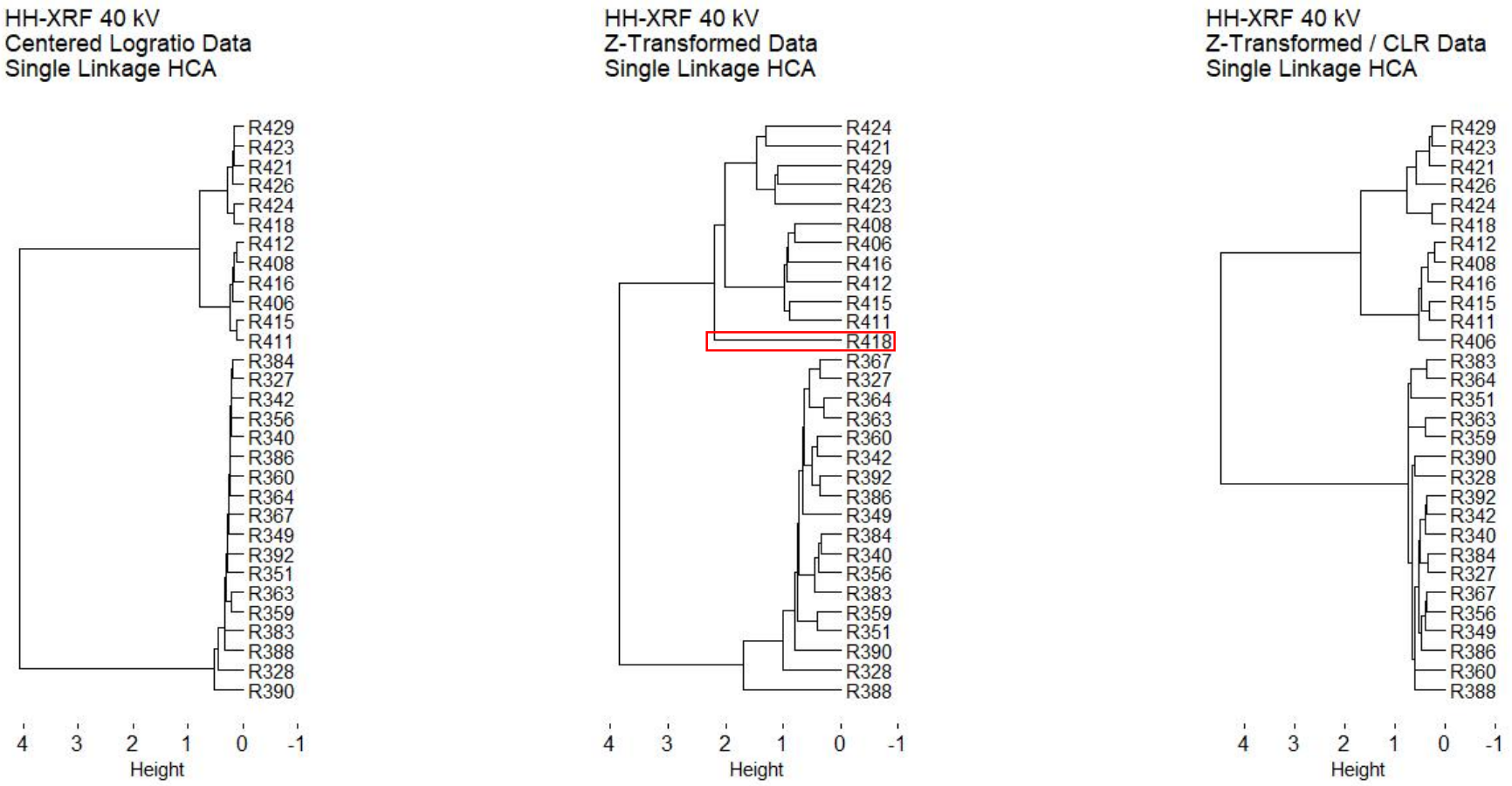

Fig. 8-6: Determination of outliers for HH-XRF 40 kV measurements using single linkage HCA. Only the standardized data indicated a possible outlier (R418).

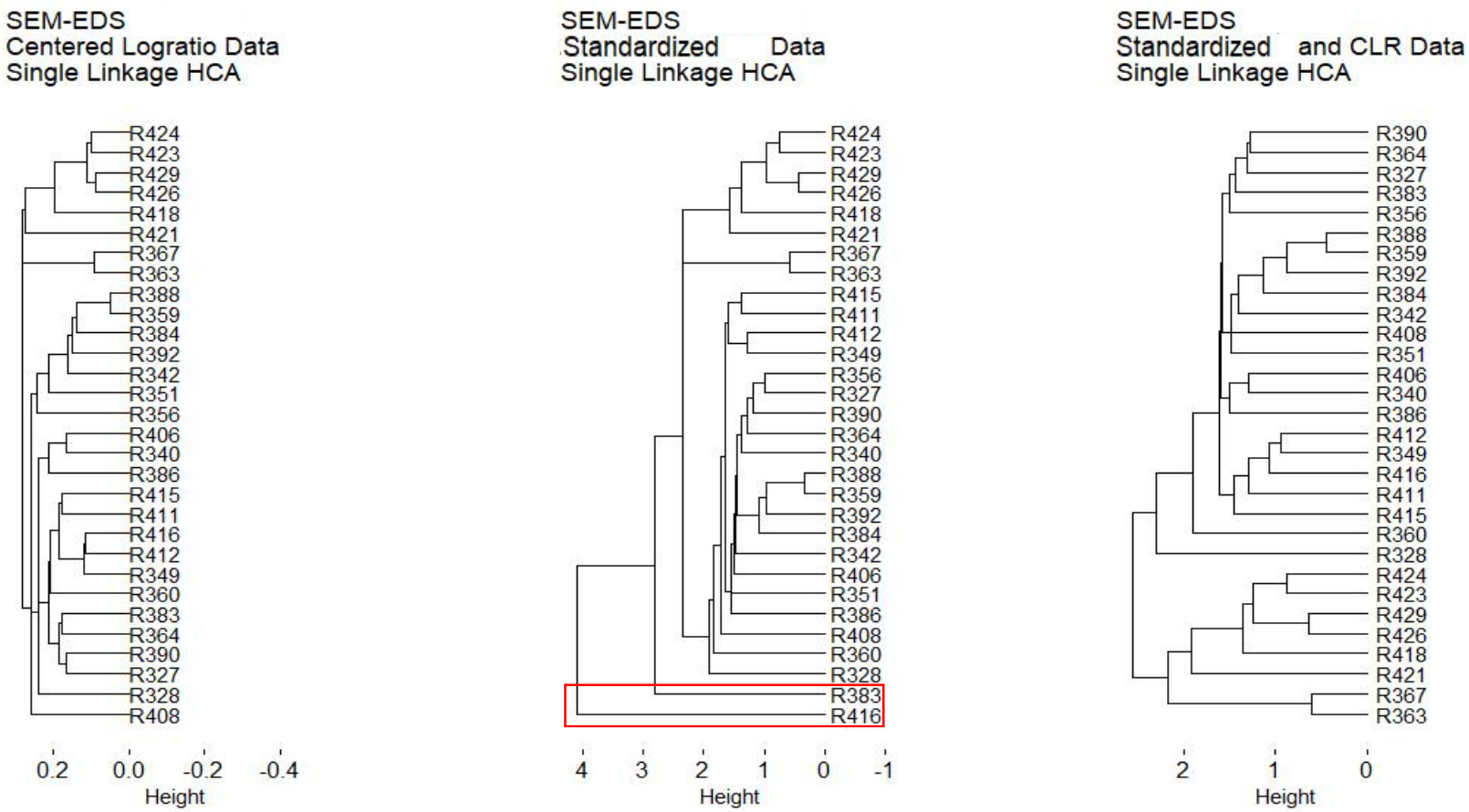

Fig. 8-7: Determination of outliers for SEM-EDS measurements using single linkage HCA. Only the standardized data indicated a potential outliers (R383 and R416).

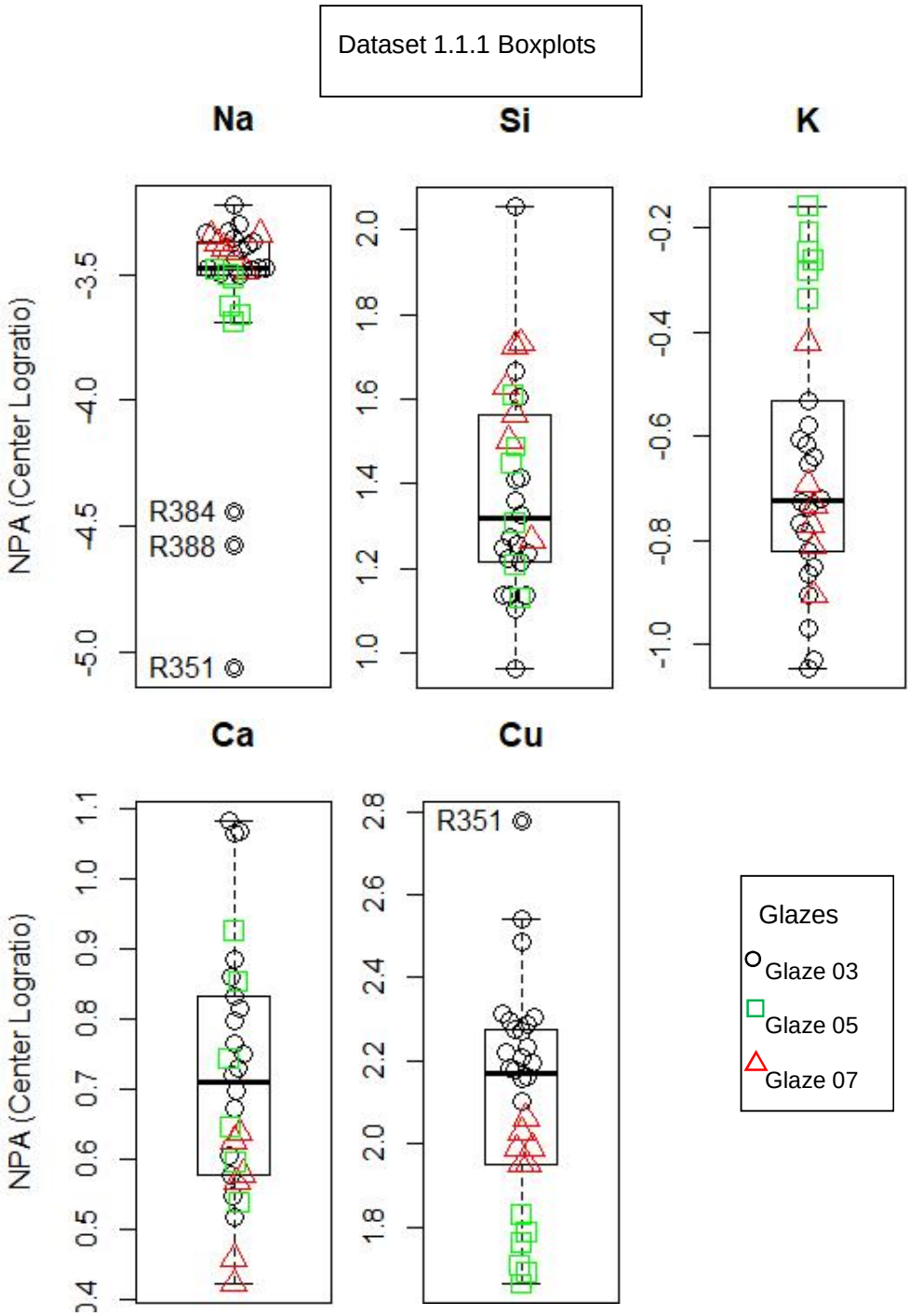

Fig. 8-8: Box-plots of centered logratio transformed HH-XRF 15 kV data (dataset 1.1.1). Standardized, standardized/centered logratio and untransformed box-plots of the data exhibited the same results. Outliers are labelled and are represented by smaller circles within each glaze outlier symbol which resides outside of the brackets.

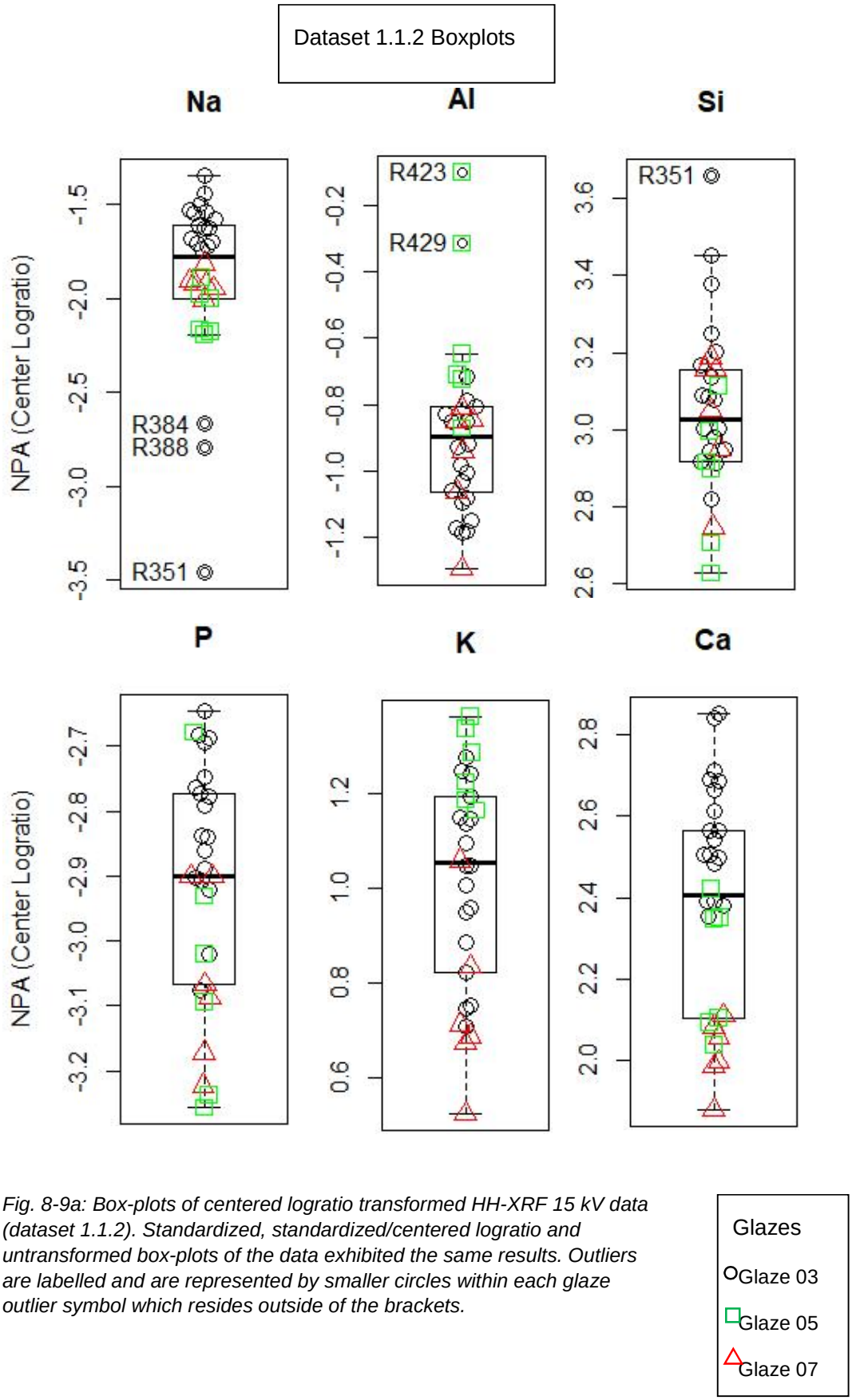

Fig. 8-9a: Box-plots of centered logratio transformed HH-XRF 15 kV data (dataset 1.1.2). Standardized, standardized/centered logratio and untransformed box-plots of the data exhibited the same results. Outliers are labelled and are represented by smaller circles within each glaze outlier symbol which resides outside of the brackets.

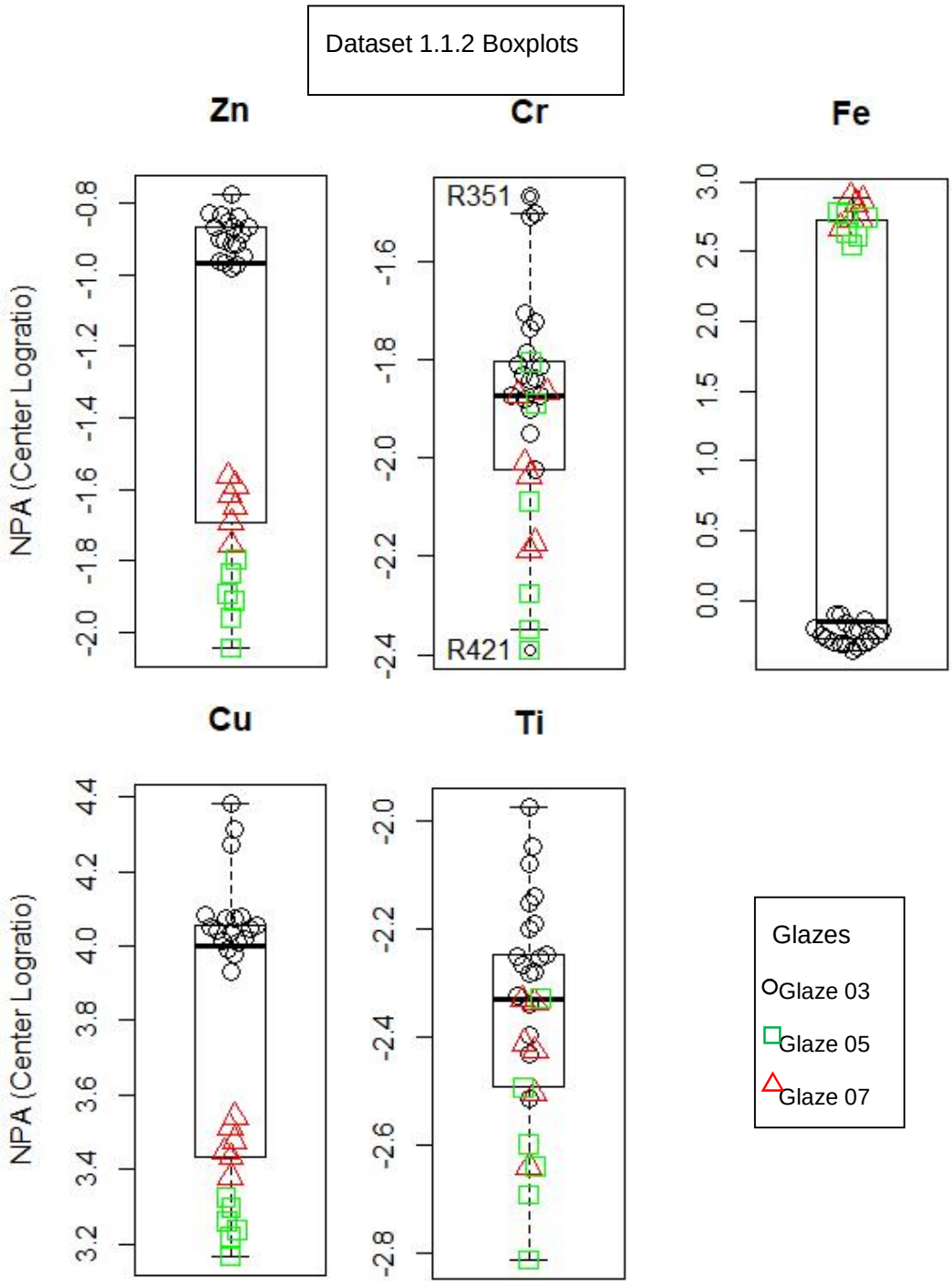

Fig. 8-9a: Box-plots of centered logratio transformed HH-XRF 15 kV data (dataset 1.1.2). Standardized, standardized/centered logratio and untransformed box-plots of the data exhibited the same results. Outliers are labelled and are represented by smaller circles within each glaze outlier symbol which resides outside of the brackets. Sample R421 revealed as an outliers with chromium is considered a tail of the data and not an outlier.

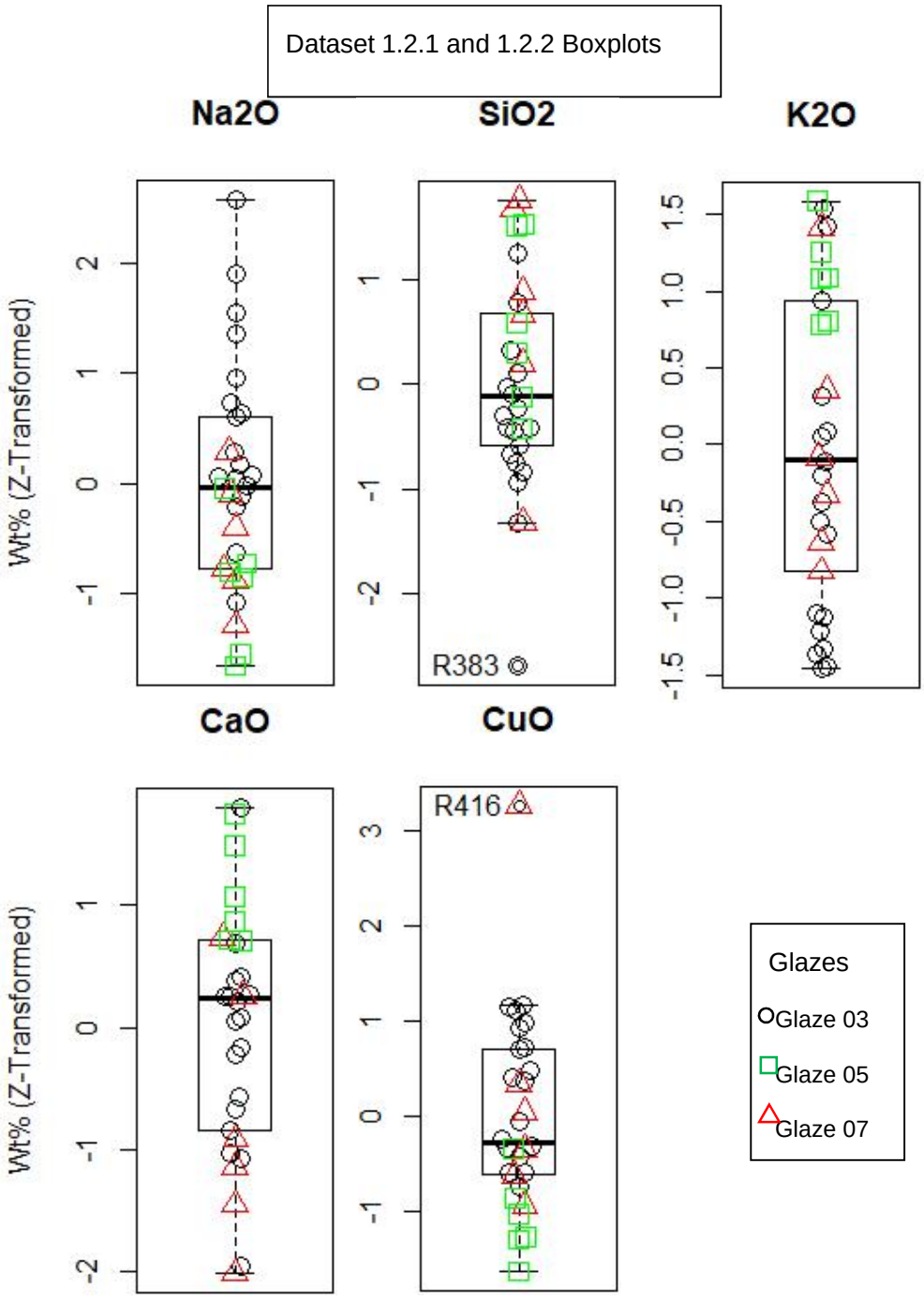

Fig. 8-10: Box-plots of centered logratio transformed HH-XRF 15 kV data (dataset 1.2.1 and 1.2.2). Standardized, standardized/centered logratio and untransformed box-plots of the data exhibited the same results. Outliers are labelled and are represented by smaller circles within each glaze outlier symbol which resides outside of the brackets.

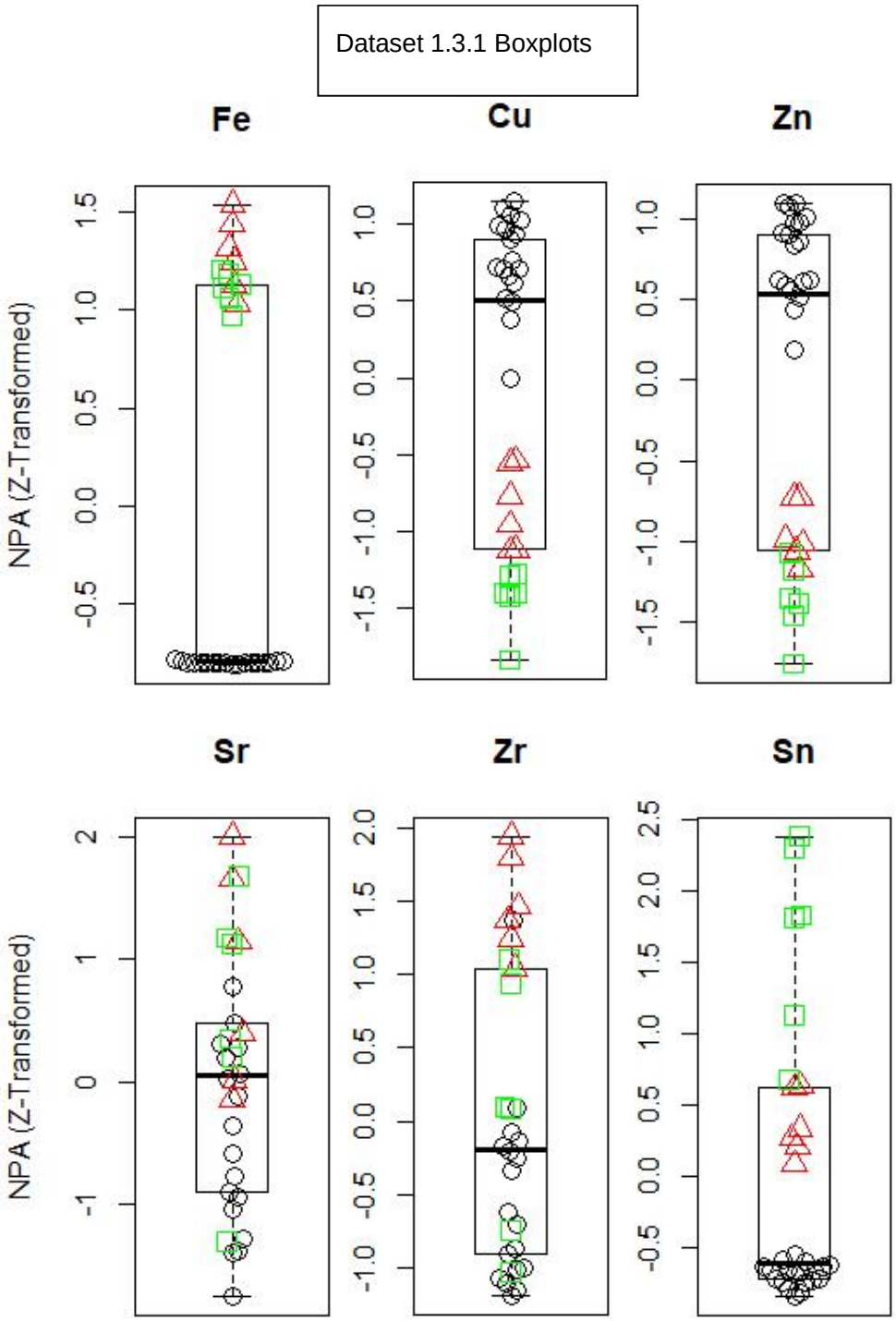

Fig. 8-11a: Box-plots of centered logratio transformed HH-XRF 15 kV data (dataset 1.3.1). Standardized, standardized/centered logratio and untransformed box-plots of the data exhibited the same results. Outliers are labelled and are represented by smaller circles within each glaze outlier symbol which resides outside of the brackets.

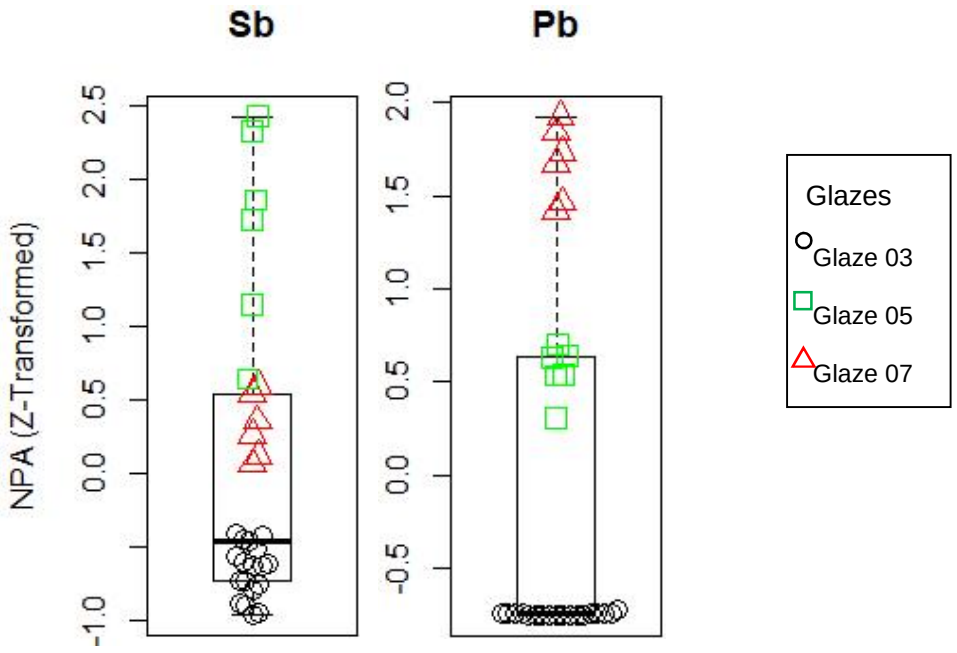

Fig. 8-11a: Box-plots of centered logratio transformed HH-XRF 15 kV data (dataset 1.3.1). Standardized, standardized/centered logratio and untransformed box-plots of the data exhibited the same results. Outliers are labelled and are represented by smaller circles within each glaze outlier symbol which resides outside of the brackets.

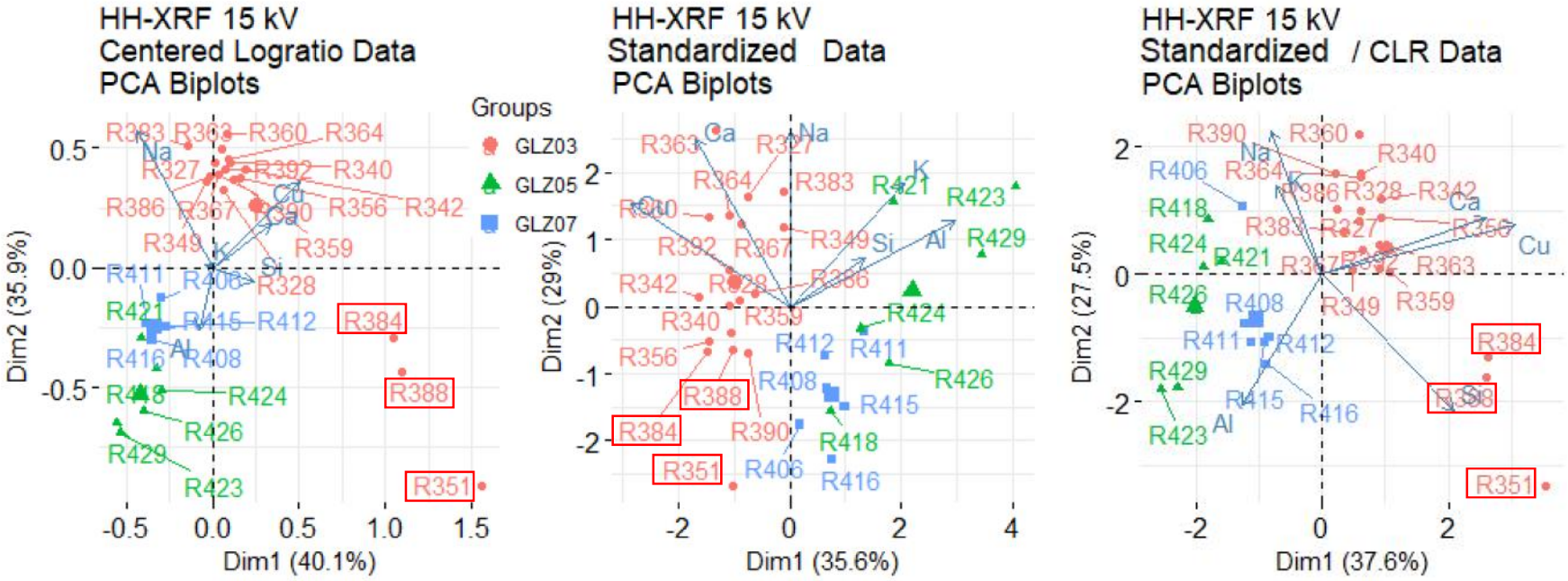

Fig. 8-12: Determination of outliers using PCA biplots of the three transformation methods. HCA analysis (Fig. 6-6) identified the outliers consistently (R351, R384 and R388). They are the only samples located in Q4 of the CLR and standardized / CLR data. R351 is readily identifiable as an outlier in Q3 of the standardized data but R384 and R388 are not. Sample R423 and R429 are not readily identified as outliers in Q1 of the standardized data and seem to fit within the cluster for cobalt colourant glaze 05. R351, R384 and R388 will be removed from the continued evaluation of the statistical data preparation methods. R423 and R429 will be retained. These figures are for the identification and HCA confirmation of outliers. The inclusion of sample numbers has made the biplots too convoluted for most other analyses.

8.5 Data Transformations

An evaluation was conducted on standardization, centered logratio and a combination of the two to determine which was optimal to reveal the known relationships of the glazes. An evaluation of the transformation methods was made using HH-XRF 15 kV and the SEM-EDS data. The HH-XRF data was restricted to the elements matching the oxides of SEM-EDS analysis. The restricting of the variables for the 15 kV HH-XRF measurements suffice for the evaluation of the MVS techniques but was not optimized for the actual analytical results. The direct comparison of HH-XRF 15 kV and SEM-EDS measurements where all variables are shared is restricted to this chapter. HH-XRF 40 kV data was included for evaluation purposes but there is little overlap between the elements detected with this voltage and the oxides above the limit of detection with SEM-EDS. The matrices charts exhibiting the bivariate plots of the elements for each analytical procedure do not exhibit high correlations for dataset 1 or the individual batches (although individual glaze batches exhibited higher correlation) for the 15 kV HH-XRF and the SEM-EDS measurements. PCA is not the ideal option for determining the clusters of these measurements using the two analytical procedures because of the low correlations. However, the PCA of these measurements is still included for interest and comparison with the 40 kV HH-XRF measurements. The 40 kV HH-XRF measurements exhibited higher correlations for dataset 1 and PCA is suitable for its analysis. PCA biplots were examined to determine cluster compactness and segregation from other clusters. The PCA biplots only exhibit the first two dimensions for this evaluation which make up the maximum variance of the data. Individual samples in the resulting biplots are coded based on known batches. Samples in k-means analysis are coded based on statistical clustering but the biplots were inspected similarly to the PCA biplots. The k value was set to ‘3’ representing the three known glaze batches. A k-means output exhibiting sample groupings within clusters was examined for inclusion and miss-calculations of clustering based on known glaze batches. HCA dendrograms are examined in a similar fashion to the k-means output.

8.5.1 Data Transformation: Pairwise Matrices and Bivariate Plots

Pairwise matrices charts were produced to see if bivariate plots were influenced by the transformation method. The CLR and the combination of CLR with standardization for each analytical method consistently exhibited the same chart. Therefore, only the CLR charts will be included for comparison with the standardization charts. The charts exhibit correlation factors on the left side (all variables followed by each glaze batch

beneath (glaze “3”, “5” and “7”)) and variable scatter biplots on the right (Figs. 8-13, 8-15, 8-17 and 8-18). This enables quick examination of several pieces of information at once. Copper, sodium, potassium and aluminium exhibit the greatest cluster discerning power according to the batch recipes (see Table 5-1and 5-2).

A comparison of the CLR and standardized data matrices for the HH-XRF 15 kV measurements exhibit vaguely similar results (Fig. 8-13). The scatterplots containing copper exhibit well separated batch clusters for both transformation methods but an examination of the copper/calcium CLR bivariate plot reveals that cobalt colourant glaze 05 could be interpreted as two separate clusters whereas the standardized data reveals it as a single dispersed cluster (Fig. 8-14). The CLR data has been coerced through transformation to present maximum variation and compact clusters. In this case it has visually split a known cluster in the process. The bivariate plots for sodium/aluminium, and sodium/potassium reflect the correct relationships for the three elements according to the recipes used. All three transformation methods reveal generally correct relationships between the elements. The CLR data increase variance between the samples/clusters sometimes visually clustering samples incorrectly (which will be tested again using k-means). The standardized data is slightly harder to interpret because the clusters are more likely to overlap but the cluster results represent the known recipes. Correlation factors are relatively low indicating these measurements as a poor candidate for PCA.

The SEM-EDS data for the same elements reveals similar results to the HH-XRF 15 kV measurements; the CLR reveals more variance and tighter clusters, and the standardized data exhibits greater cluster dispersion (Fig. 8-15). The scatterplots (Fig. 8-16) reveal the same trend. The SEM-EDS scatter plots, although generally correct concerning the batch recipes, are more muddled and not as easily interpreted as the HH-XRF 15 kV plots (see Fig. 8-14). Neither transformation method is particularly better than the other is. The correlation factors are lower than the HH-XRF 15 kV measurements indicating this data is a poor candidate for PCA.

The HH-XRF 40 kV data exhibits the optimum clustering of the three analytical methods (Fig. 8-17 and Fig. 8-18). However, this data was not constrained to the same six elements as the 15 kV and the SEM-EDS measurement and cannot be directly compared. Both transformation methods were good at clustering the three glaze batches into their perspective clusters. The CLR transformation method clearly demarcated the individual clusters by exaggerating the variance between them. This is

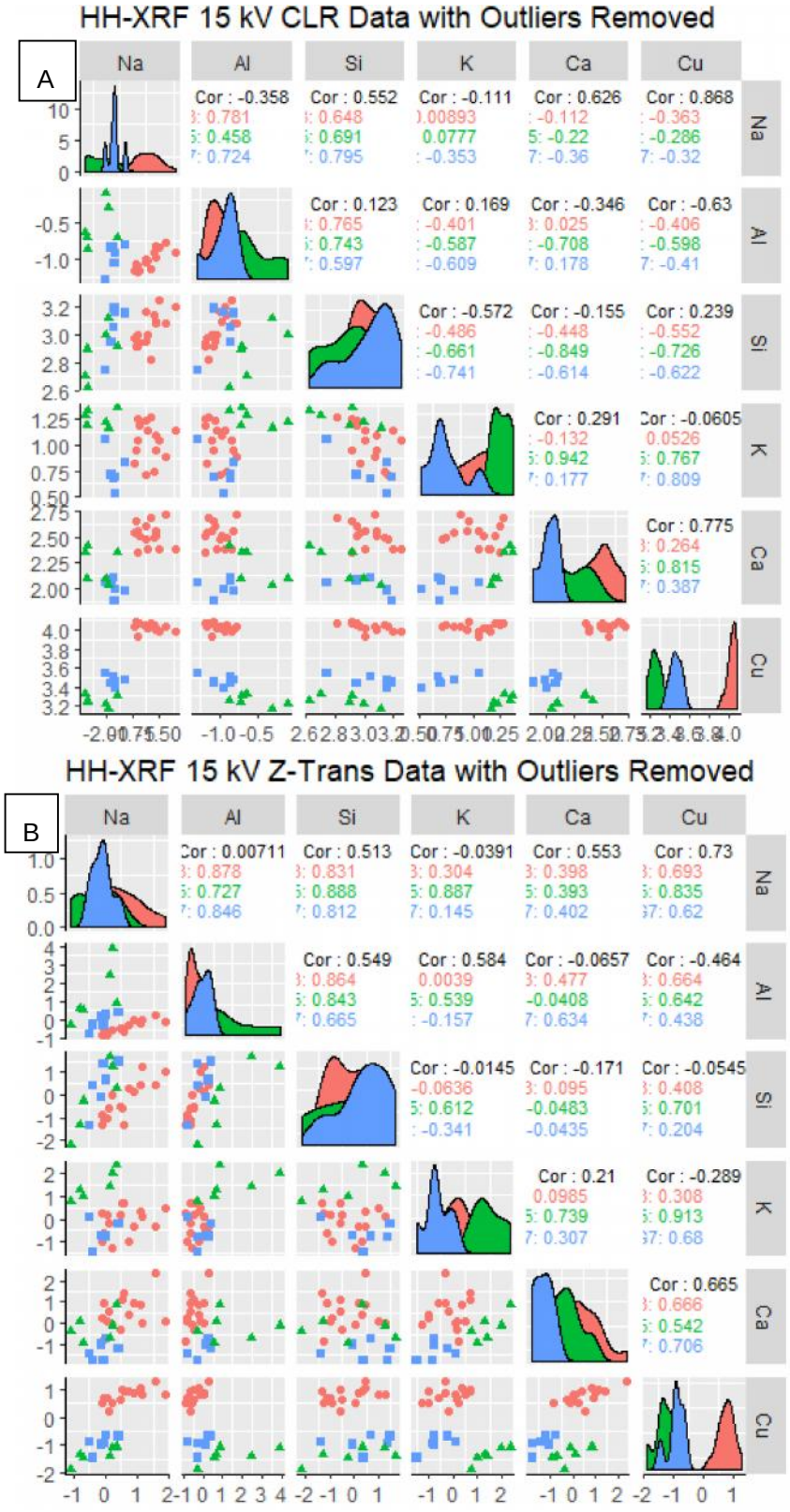

Fig. 8-13: Pairwise charts for 15 kV HH-XRF CLR (A) and standardized (z-trans)(B) data with outliers removed. The top right corner exhibits the correlation factor for all batches and the factors for each individual batch (glaze 03, 05 and 07) beneath.

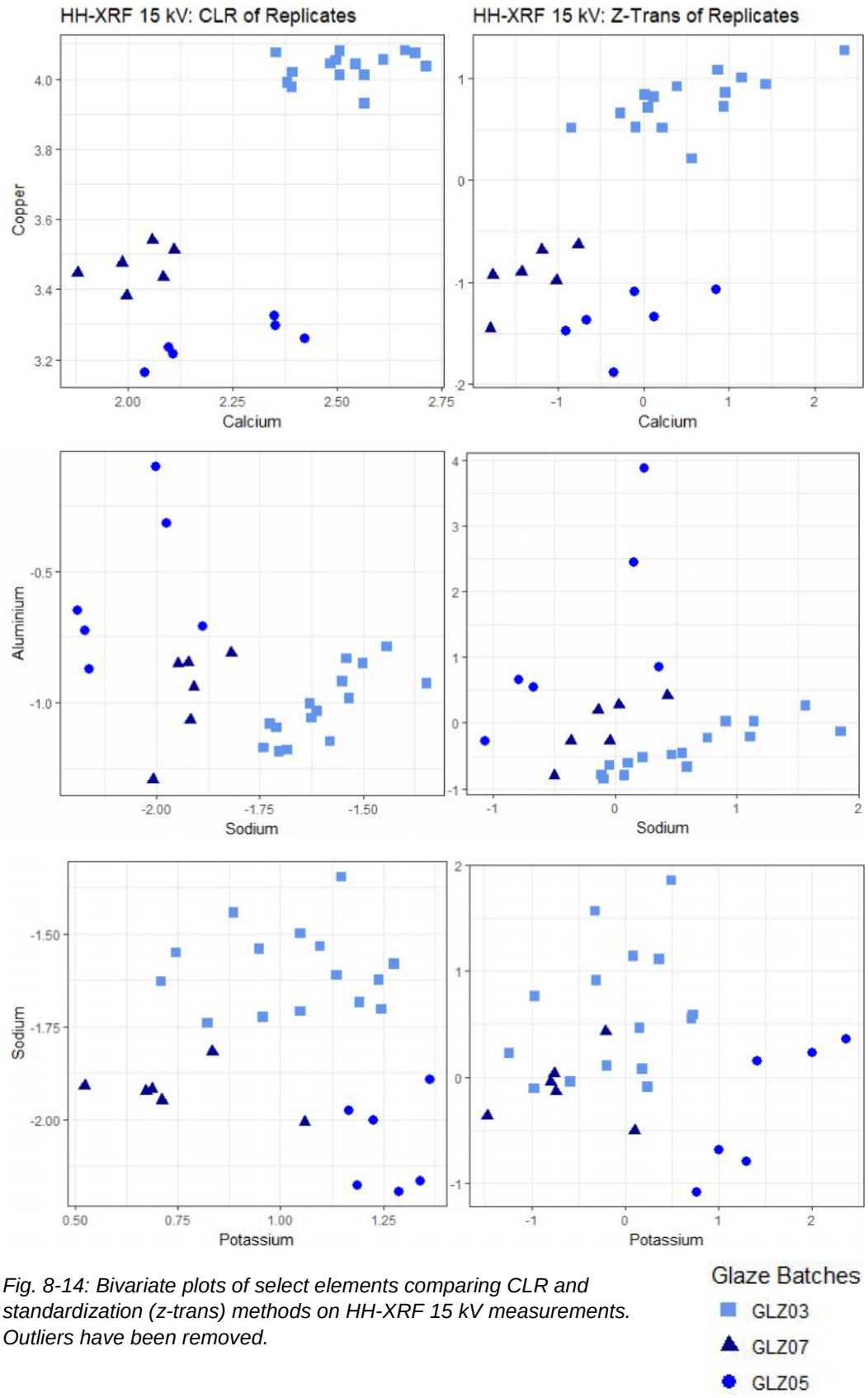

Fig. 8-14: Bivariate plots of select elements comparing CLR and standardization (z-trans) methods on HH-XRF 15 kV measurements. Outliers have been removed.

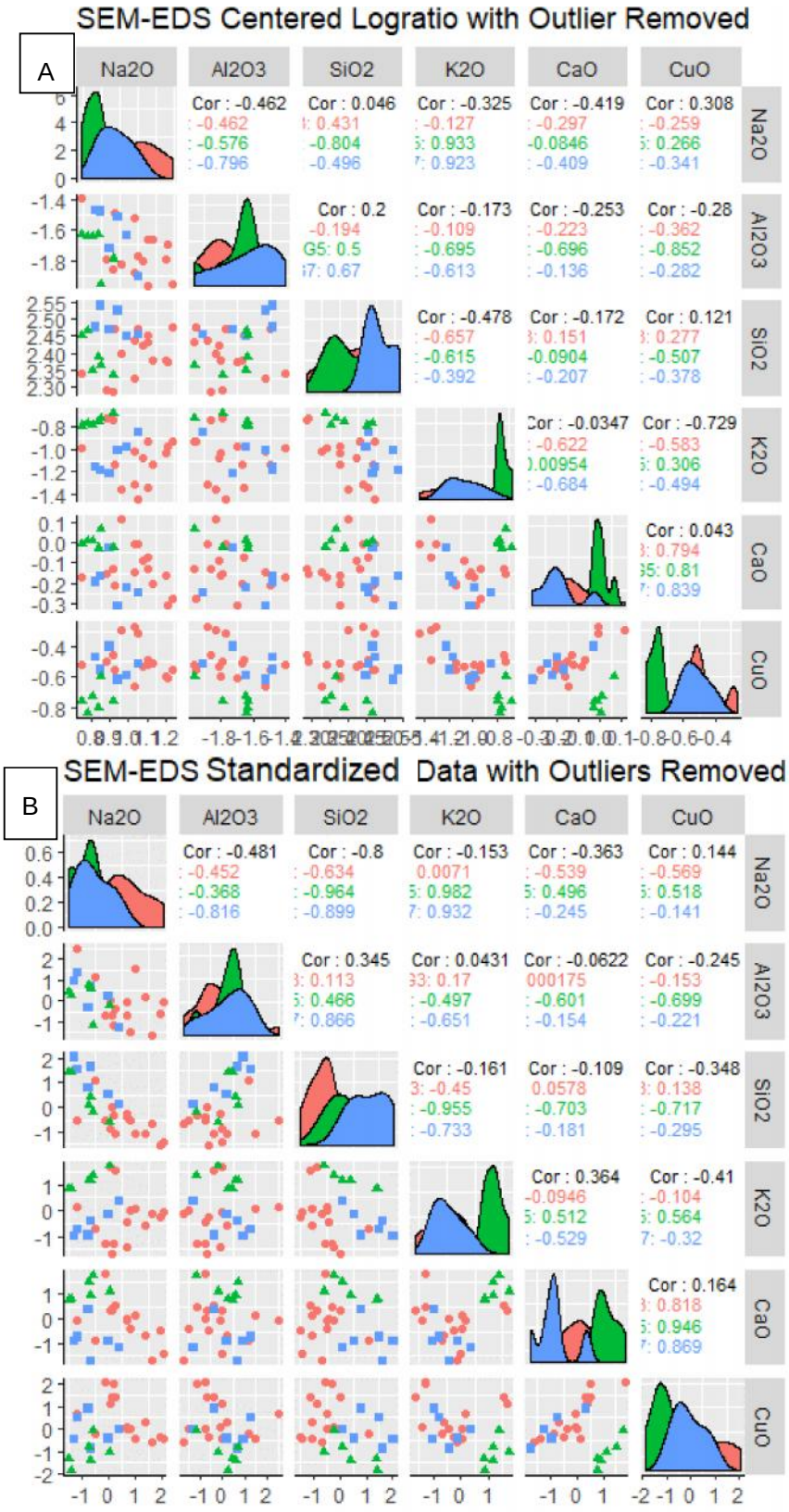

Fig. 8-15: Pairwise charts for SEM-EDS CLR (A) and standardized (B) data with outliers removed. The top right corner exhibits the correlation factor for all batches and the factors for each individual batch (glaze 03, 05 and 07) beneath.

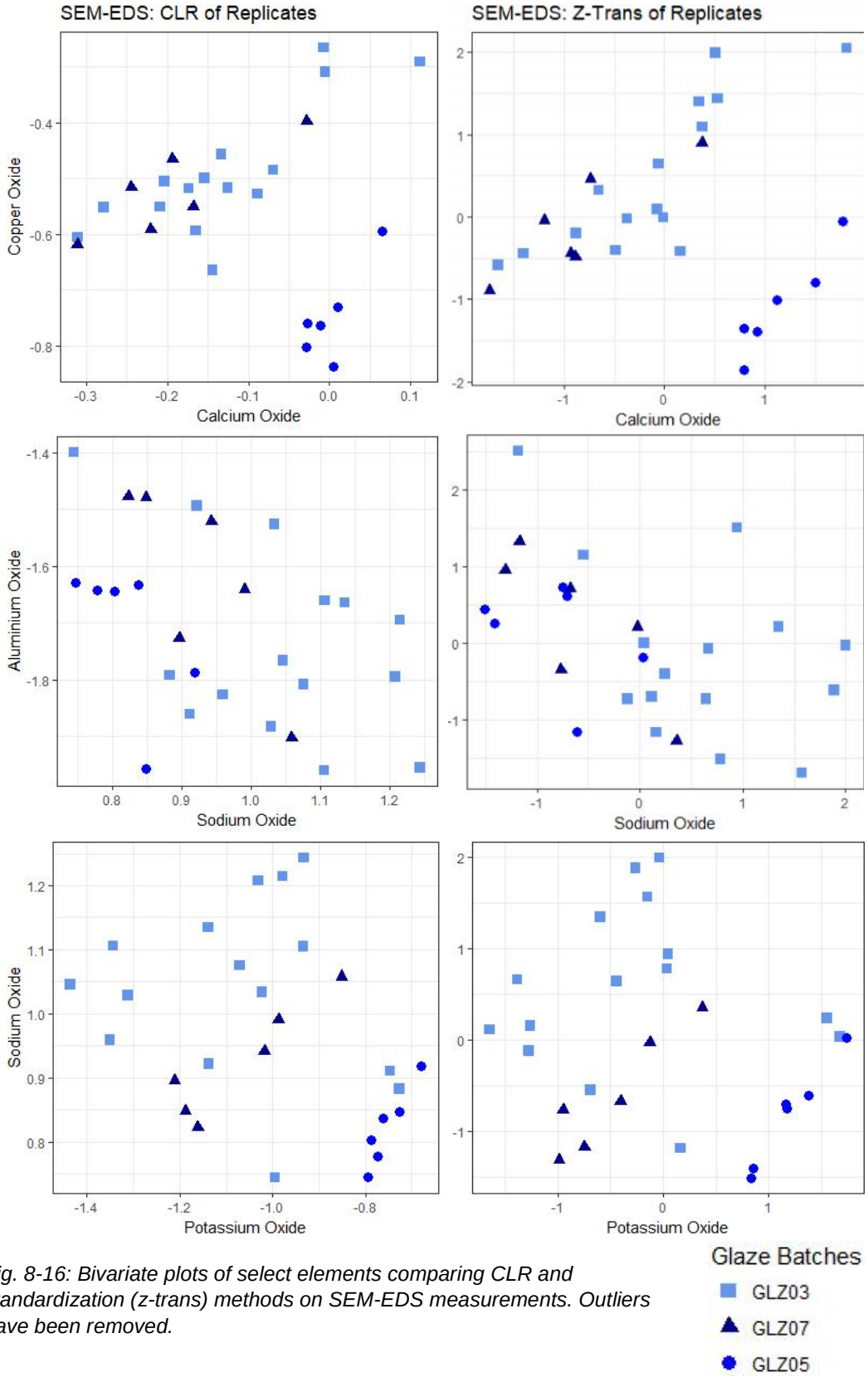

Fig. 8-16: Bivariate plots of select elements comparing CLR and standardization (z-trans) methods on SEM-EDS measurements. Outliers have been removed.

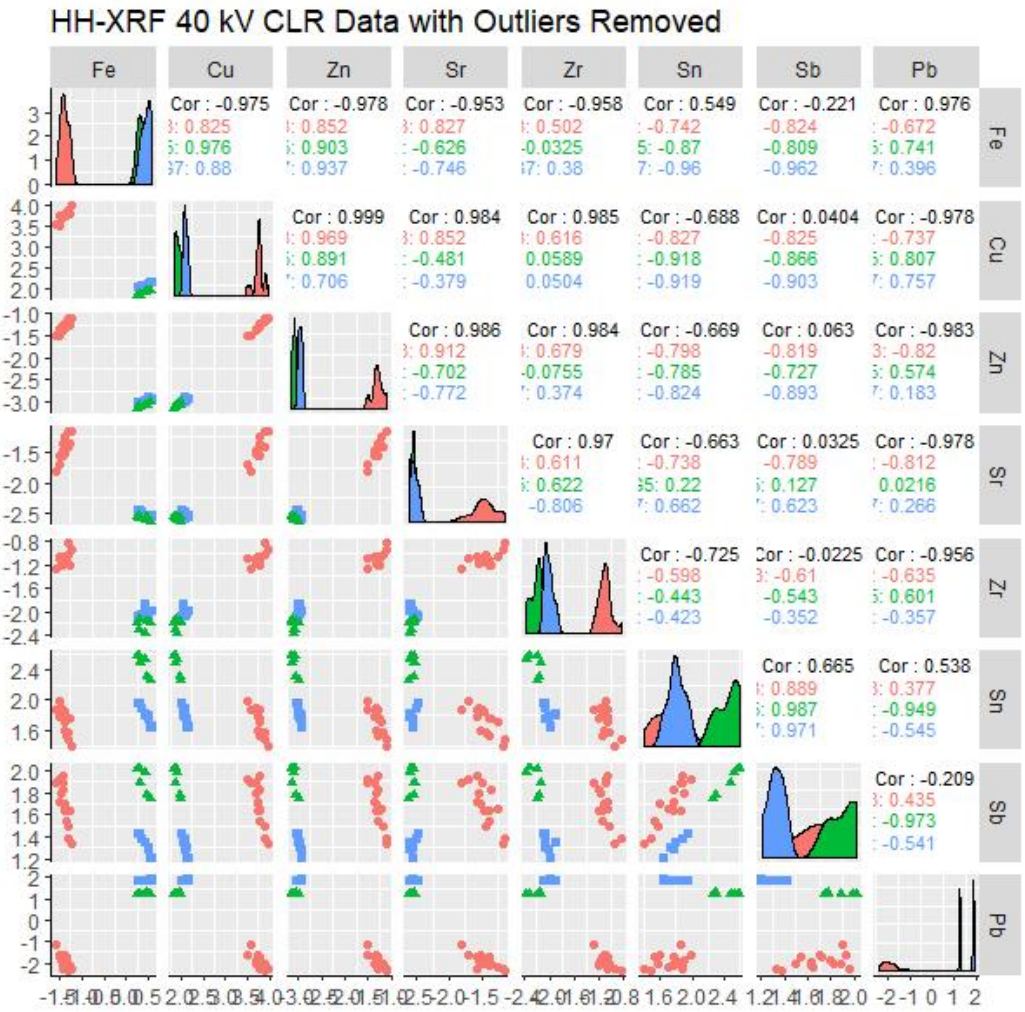

Fig. 8-17: Pairwise charts for HH-XRF 40 kV CLR data with outliers removed. The top right corner exhibits the correlation factor for all batches and the factors for each individual batch (glaze 03, 05 and 07) beneath.

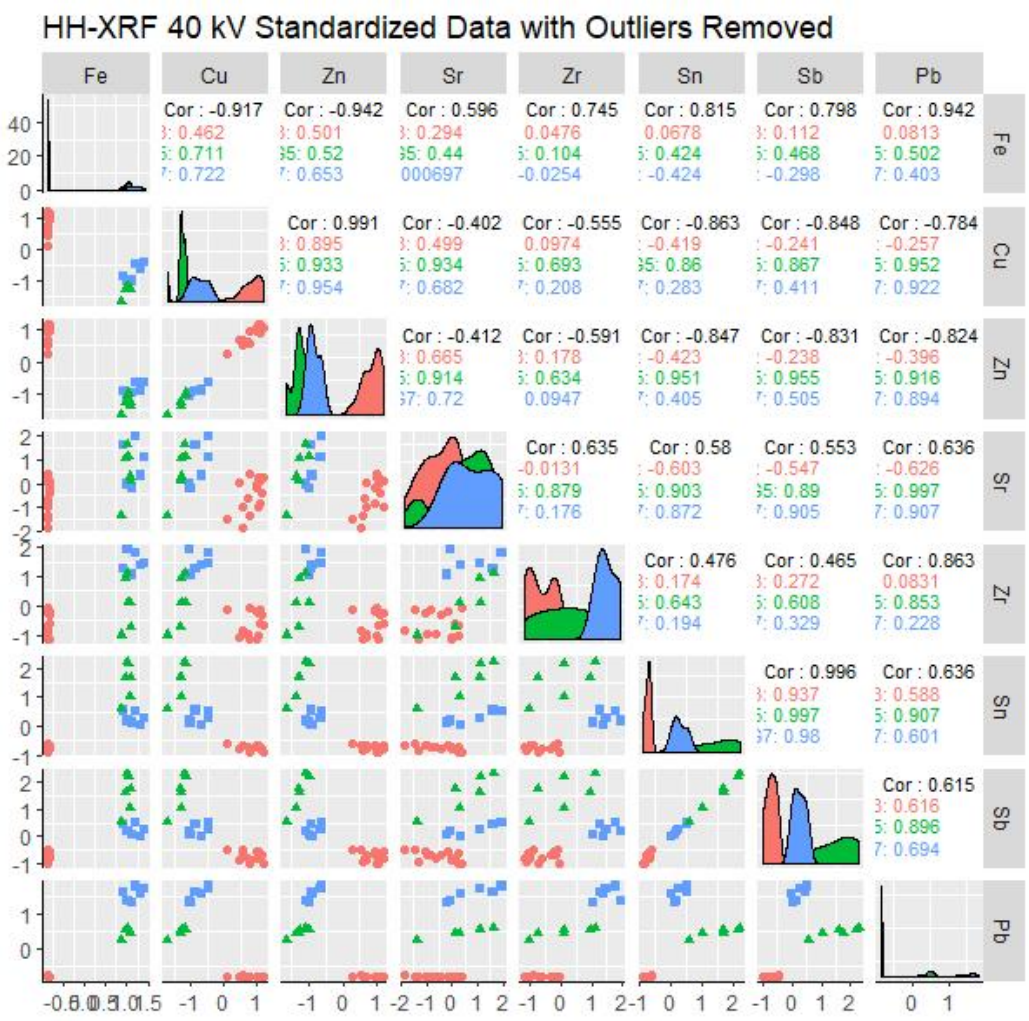

Fig. 8-18: Pairwise charts for HH-XRF 40 kV standardized data with outliers removed. The top right corner exhibits the correlation factor for all batches and the factors for each individual batch (glaze 03, 05 and 07) beneath.

excellent for clearly seeing the clusters if using unknown samples. Standardization clearly exhibits the known clusters but more accurately portrays the known recipes. The correlation factors are high indicating these measurements are a good candidate for PCA. The matrices and the bivariate plots reveal that neither transformation method is particularly better but that both have particular aspects that may be useful in certain situations. The CLR method can better differentiate between clusters by increasing variance and has the potential of splitting known clusters into separate groups. Standardization portrays the known recipes more accurately through clustering but is harder to interpret as clusters are more dispersed and can overlap.

8.5.2 Data Transformation: PCA Biplots

PCA biplots were used to examine the clustering of the three replicate glaze batches after transformation using CLR, standardization and a combination of the two. The previous statistical methods indicated that the HH-XRF 15 kV and SEM-EDS measurements were not good candidates for this analysis because of low correlation figures. They were, however, included for comparison of the data transformation methods to see if they provide unforeseen information. HH-XRF 40 kV measurements are included to see how a different and more plentiful set of variables would affect the analysis.

The PCA biplots of the three transformation methods on HH-XRF 15 kV data (Fig. 8-19) generally exhibit similar results. The CLR data biplot components 1 and 2 represent ~80% of the total variance and exhibits similar compactness of clusters to the other transformation methods and the greatest cluster segregation. The standardized data biplot components 1 and 2 represent ~71% of the total variance. The cluster separation is the worst of the three transformation methods with some overlap between the glaze 5 and 7 clusters. The CLR/standardized data biplot components 1 and 2 represents ~77% of the variation and is similar to the CLR data biplot but the cluster segregation is slightly less exaggerated. The best representation of the three glaze batches using HH-XRF at 15 kV is rendered by the CLR biplot. The standardized data provides the worst glaze batch discernment because of overlapping clusters.

The PCA biplots of the SEM-EDS data (Fig. 8-20) exhibit very little compactness and minor overlapping of glazes 03 and 07. The CLR biplot (comprising ~76% of the data variation) and CLR/standardized biplot (~61% variation) exhibit major overlapping between the batches. The standardized data (~ 57% variation) exhibits the greatest

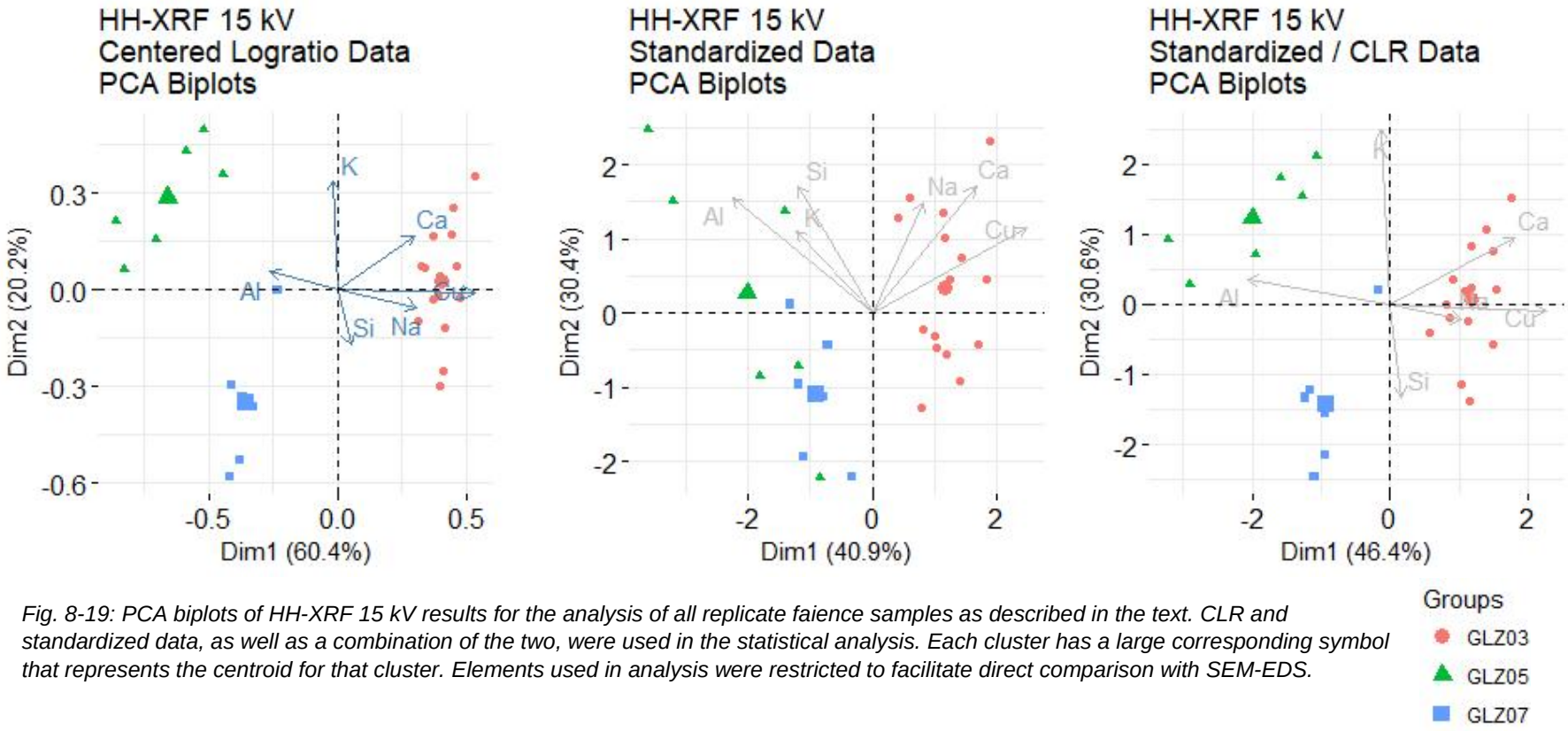

Fig. 8-19: PCA biplots of HH-XRF 15 kV results for the analysis of all replicate faience samples as described in the text. CLR and standardized data, as well as a combination of the two, were used in the statistical analysis. Each cluster has a large corresponding symbol that represents the centroid for that cluster. Elements used in analysis were restricted to facilitate direct comparison with SEM-EDS.

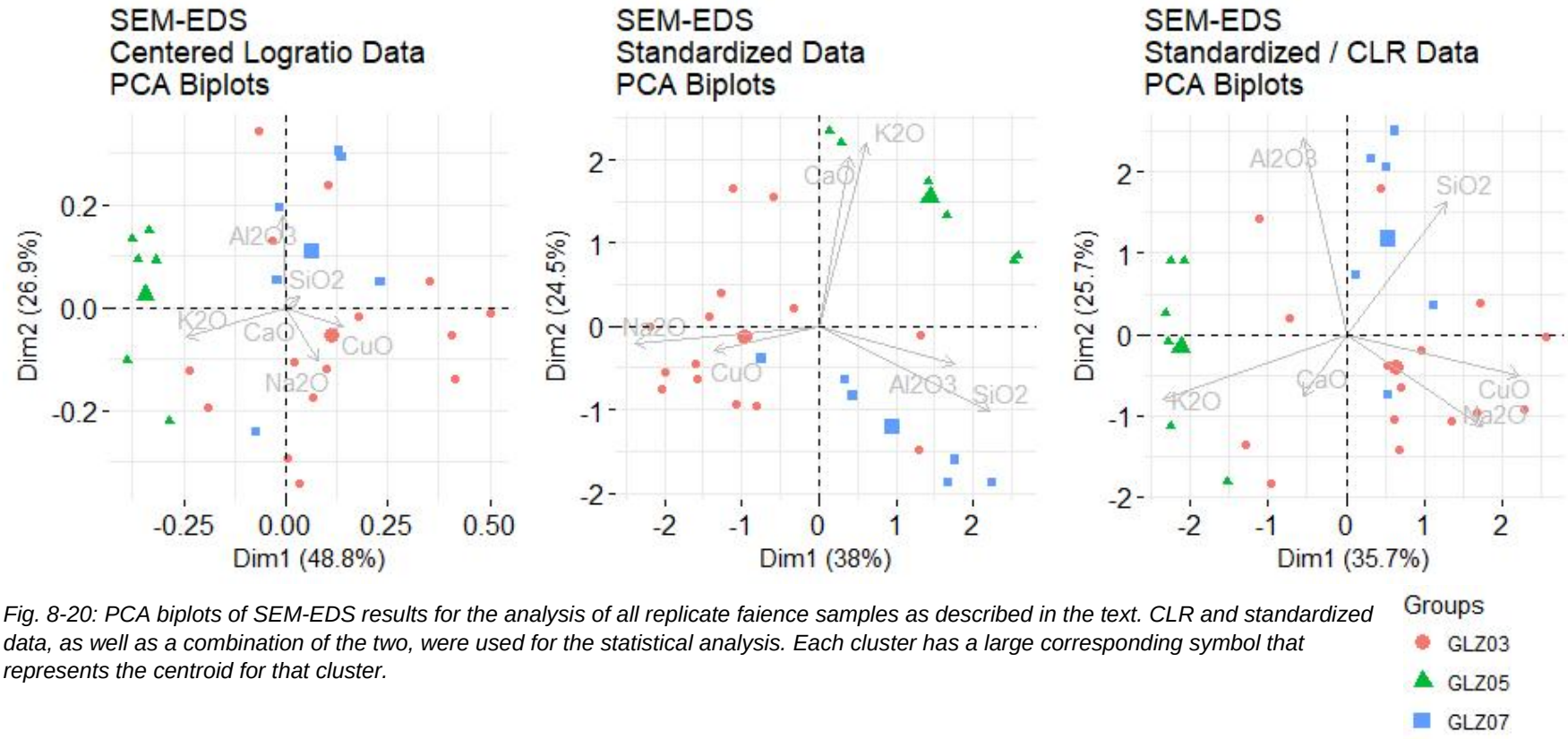

Fig. 8-20: PCA biplots of SEM-EDS results for the analysis of all replicate faience samples as described in the text. CLR and standardized data, as well as a combination of the two, were used for the statistical analysis. Each cluster has a large corresponding symbol that represents the centroid for that cluster.

cluster separation with little overlapping of the methods although the separation is minimal. The SEM-EDS glaze results are best represented by the standardized data.

The PCA biplots of the HH-XRF 40 kV data (Fig. 8-21) exhibit good cluster separation and compactness due to the higher correlation figures compared to the two other analytical methods and the selection of variables which include major, minor and trace elements. The CLR (comprising ~ 98% of the data variation), standardized (~89% variation) and a combination of the two methods (~99% variation) all exhibit cluster compactness and segregation. The CLR and the combination method are better for clustering cobalt colourant glaze 05 and 07 batches but the clusters have been coerced into a linear shape. Standardization exhibits better compactness for the copper colourant glaze 03 batch and all clusters are globular in shape. All three transformation methods provide adequate discernment of the three glaze batches.

Table 8-8 exhibits the evaluation of the three transformation methods on the three analytical methods. Transformation methods had more of an effect on separation of the clusters than on their compactness. CLR exhibited greatest cluster separation with HH-XRF at 15 kV. Standardization provided greater separation with SEM-EDS results. The transformation methods had equal effect on the quality of the HH-XRF 40 kV cluster characteristics which exhibited good cluster compactness and segregation. The correlation figures have a direct effect on the reduction of dimensionality in PCA. The total variance of the HH-XRF 40 kV biplots were 89-99% depending on the transformation process. These were expected because of the high correlation values (see Figs. 8-13, 8-15, 8-17, and 8-18). As expected the total variance of the HH-XRF 15 kV and SEM-EDS measurements were lower (71-80% for 15 kV HH-XRF, 57-76% for SEM-EDS) because of lower correlation figures and less dimensionality reduction. A higher variance has the effect of requiring a lower number of principle components when describing the PCA results in detail. The PCA biplot analysis is insufficient by itself to determine the optimal transformation method to use in the MVS.

8.5.3 Transformation: K-means Biplots

K-means biplots of the HH-XRF 15 kV data exhibit similar patterns with the CLR (Fig. 8-22) and the combination CLR/standardized method. Standardization has clustered the glazes slightly differently resulting in two formed clusters (clusters 2 and 3) and one centroid (cluster 1) without sufficient points to demarcate a confidence ellipse. Examining the k-means cluster assignment (Table 8-9) reveals that CLR and CLR/standardized data are identical with the same sample cluster assignments. All the cobalt blue glazes (glaze 05 and 07) were grouped into the same clusters (cluster 1

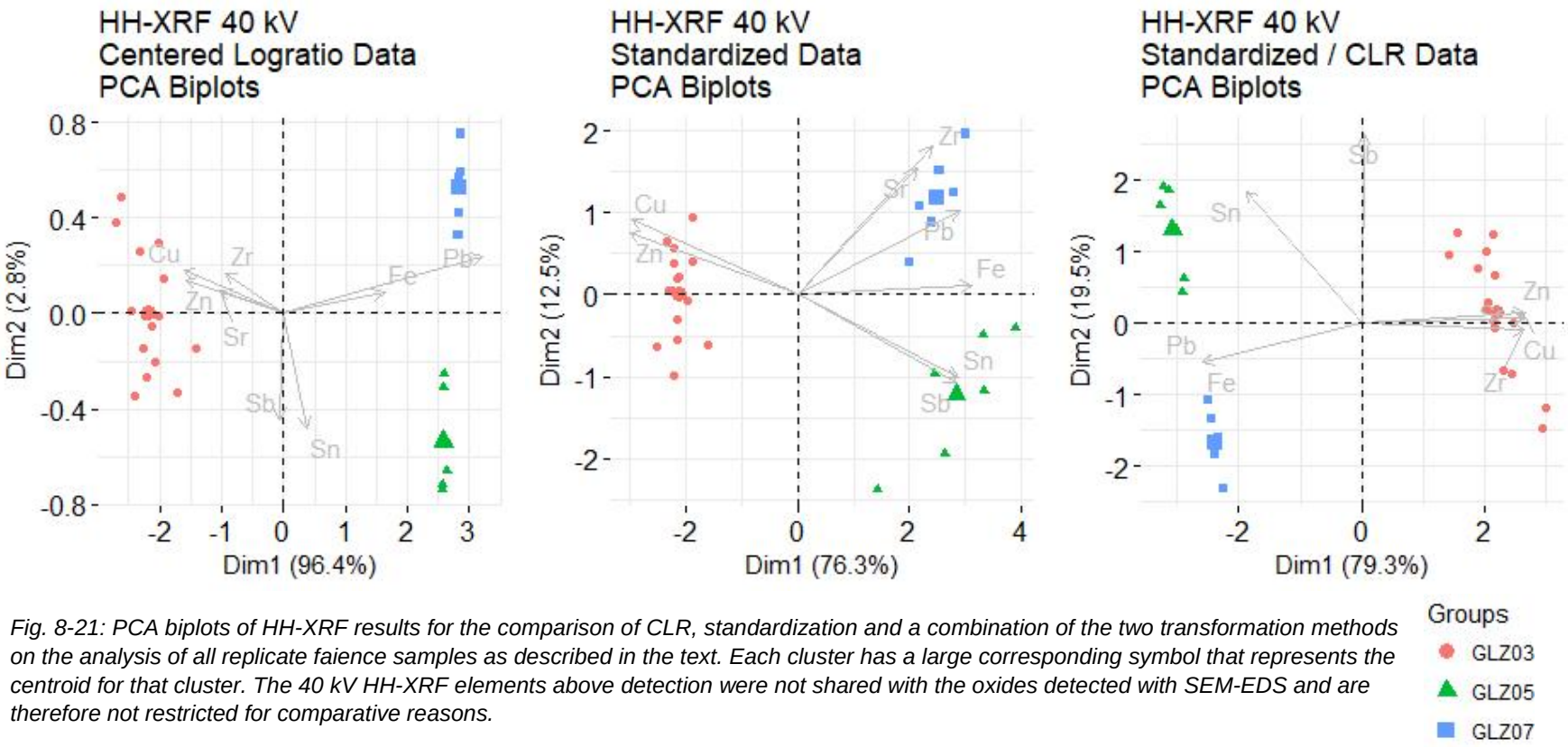

Fig. 8-21: PCA biplots of HH-XRF results for the comparison of CLR, standardization and a combination of the two transformation methods on the analysis of all replicate faience samples as described in the text. Each cluster has a large corresponding symbol that represents the centroid for that cluster. The 40 kV HH-XRF elements above detection were not shared with the oxides detected with SEM-EDS and are therefore not restricted for comparative reasons.

Table 8-8: Comparisons of the three data transformation methods with three analytical methods for the preparation of data prior to MVS. The results have been judged good (XXX), adequate (XX) and poor (X) based on an empirical evaluation of clustering (tightly clustered is good, dispersed is bad). The three transformation methods (centered logratio (CLR), standardization and a combination of the two) for each type of instrumental analysis are presented in the second column. The compactness variable indicates tightness of the cluster groupings. Separation is how well the clusters are separated from each other. The k-means and HCA GLZ05 and GLZ07 indicate how well the individual specimen were grouped into the corresponding clusters for glazes 05 and 07. The miss-clusters indicate how many specimen were erroneously grouped based on the known recipes of the replicate glazes. The draftsman/corr charts indicate how well the glaze groups were separated in bivariate scatter-plots. The evaluation tally is a score applied to each transformation method based on the variables provided with XXX representing the best of the three and X the worst. The generally poor/adequate results for the SEM-EDS data should not be seen as an evaluation of the method for the analysis of the replicate material.

Comparison of Transformation Methods on HH-XRF and SEM-EDS Data

HH-XRF 15 kV and SEM-EDS are restricted to shared elements/oxides. HH-XRF 40 kV includes all detected elements. Outliers removed.

		PCA Cluster		K-means Cluster		K-means		K-means	HCA Inclusion		HCA Miss-	Draftsman /	Evaluation
		Compactness	Separation	Compactness	Separation	GLZ05	GLZ07	Miss-Calc	GLZ05	GLZ07	Calc	Corr Charts	Tally
HH-XRF 15 kV	CLR	XX	XXX	XX	XXX	XXX	XXX	0	XXX	XXX	0	XX	XXX
	Standardized	XX	X	XXX	XXX	X	XX	3	XX	XX	3	XXX	X
	Combination	XX	XX	XX	XXX	XXX	XXX	0	XXX	XX	1	X	XX
SEM-EDS	CLR	XX	X	XX	X	XXX	XX	12	XX	XX	11	X	X
	Standardized	XX	XX	XX	X	XXX	XX	3	XX	XX	6	XX	XXX
	Combination	XX	X	XX	XX	XXX	XX	12	XX	XX	11	X	XX
HH-XRF 40 kV	CLR	XXX	XXX	XXX	XXX	XXX	XXX	0	XXX	XXX	0	XXX	XXX
	Standardized	XXX	XXX	XXX	XXX	XXX	XXX	0	XXX	XXX	0	XXX	XXX
	Combination	XXX	XXX	XXX	XXX	XXX	XXX	0	XXX	XXX	0	XXX	XXX

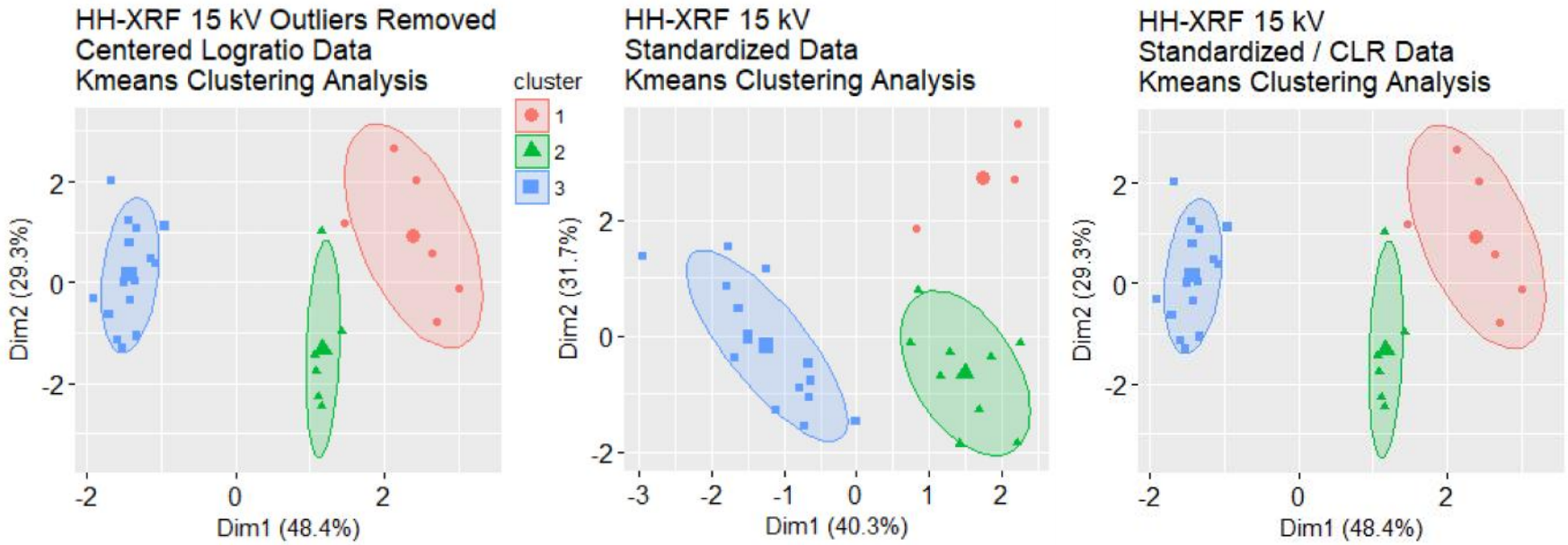

Fig. 8-22: K-means biplots of HH-XRF 15 kV results for the analysis of dataset 1 containing all replicate faience samples as described in the text. The CLR and CLR/standardization methods are identical. The standardization method failed to produce enough data points to demarcate a cluster 1 because of sample miss-calculations (Table 8-9).

Table 8-9: K-means cluster assignment for each transformation method with outliers removed. Glaze batches are divided by grey-scale gradient: White = copper colourant glaze 03, light grey = cobalt colourant glaze 07 and dark grey = cobalt colourant glaze 05. Red boxes indicate miss-calculations.

K-means Cluster Assignment: Outliers Removed

	HH-XRF 15 kV			SEM-EDS			HH-XRF 40 kV		
	CLR	Stand	CLR / Stand	CLR	Stand	CLR / Stand	CLR	Stand	CLR / Stand
R327	3	3	3	3	2	3	3	3	3
R328	3	3	3	3	3	2	3	3	3
R340	3	3	3	3	2	3	3	3	3
R342	3	3	3	1	2	1	3	3	3
R349	3	3	3	3	3	3	3	3	3
R356	3	3	3	1	2	1	3	3	3
R359	3	3	3	1	2	1	3	3	3
R360	3	3	3	3	2	2	3	3	3
R363	3	3	3	2	2	2	3	3	3
R364	3	3	3	3	2	3	3	3	3
R367	3	3	3	2	2	2	3	3	3
R383	3	3	3	3	2	3	3	3	3
R386	3	3	3	3	2	3	3	3	3
R390	3	3	3	3	2	3	3	3	3
R392	3	3	3	1	2	1	3	3	3
R406	2	2	2	3	2	3	2	2	2
R408	2	2	2	1	3	1	2	2	2
R411	2	2	2	3	3	3	2	2	2
R412	2	2	2	3	3	3	2	2	2
R415	2	2	2	3	3	3	2	2	2
R416	2	2	2	3	3	3	2	2	2
R418	1	2	1	2	1	2	1	1	1
R421	1	1	1	2	1	2	1	1	1
R423	1	1	1	2	1	2	1	1	1
R424	1	2	1	2	1	2	1	1	1
R426	1	2	1	2	1	2	1	1	1
R429	1	1	1	2	1	2	1	1	1

and 2, respectively) and all the copper blue glazes (glaze 03) were grouped into a single cluster (cluster 3). These groupings represent the known recipes and the results reveal that CLR and CLR/standardized transformations work well with this data. Standardized data has discerned the glaze 03 (cluster 3) and glaze 07 (cluster 2) data but has misassigned three of the glaze 05 samples to glaze 07. The data reveals that the CLR and the combination methods are optimal for discerning the glaze batches. The k-means results of the SEM-EDS data exhibit similar results as the HH-XRF 15 kV

k-means analysis. The CLR and combination methods (Fig. 8-23) revealed three clusters although the confidence ellipses slightly overlap between the glaze 03 and glaze 05. These two biplots are nearly identical with the exception of two samples (R328 and R360) which were assigned to cluster 3 with the CLR and reassigned to cluster 1 with the combination data. The standardized biplot has correctly assigned most of the samples to their respective glaze cluster. The CLR and combination method (Table 8-9) exhibits that glazes 05 and 07 were discerned reasonable well but with one glaze 07 sample (R408) being miscalculated to glaze 03 with both methods. The glaze 03 samples contained 11 misassignments attributed to glaze 05 and glaze 07. The standardization method correctly assigned most glaze 05 and all glaze 07 samples. One glaze 07 sample was miscalculated to glaze 03. Most of the glaze 03 samples were correctly assigned with only two misassignments. Standardization without CLR provided the best glaze assignments and biplots for representing the replicate glazes with SEM-EDS.

The HH-XRF 40 kV k-means biplots of the three transformation methods are identical (Fig. 8-24). Clusters are compact and spaced apart with no sample misassignments accurately displaying the three glaze batches. Any of the three transformation methods will adequately reflect the three glaze batches within k-means analysis.

The transformation methods have had a minor effect on the compactness of the clusters as evinced in Table 8-8 and the biplots. The standardized data for HH-XRF 15 kV measurements and all the transformed data of the 40 kV measurements exhibit good compactness. The remaining methods for the 15 kV and the SEM-EDS measurements have all been classified as adequate. The differences are revealed in the separation of clusters and the sample glaze assignments for cobalt colourant glaze 05 and 07. The HH-XRF measurements for both voltages exhibit good results for cluster separation with segregated clusters. The SEM-EDS combined CLR/standardization method produced cluster overlap for clusters 1 and 3. The sample assignments for glazes 05 and 07 are good for all HH-XRF measurements with the exception of the standardized data at 15 kV. Table 8-9 exhibits poor glaze 05 sample assignment where three of the batch samples have been miscalculated to glaze 07. All glaze batch samples for glazes 03 (copper colourant) and 07 (cobalt colourant) have been correctly assigned to their respective categories. The SEM-EDS CLR and CLR combination data exhibits adequate glaze 05 and 07 assignments and poor glaze 03 assignments resulting in a total of 12 misassignments out of 27 samples (3 outliers removed). Standardization results exhibited only three misassignments across all three glazes. The transformations capacity to

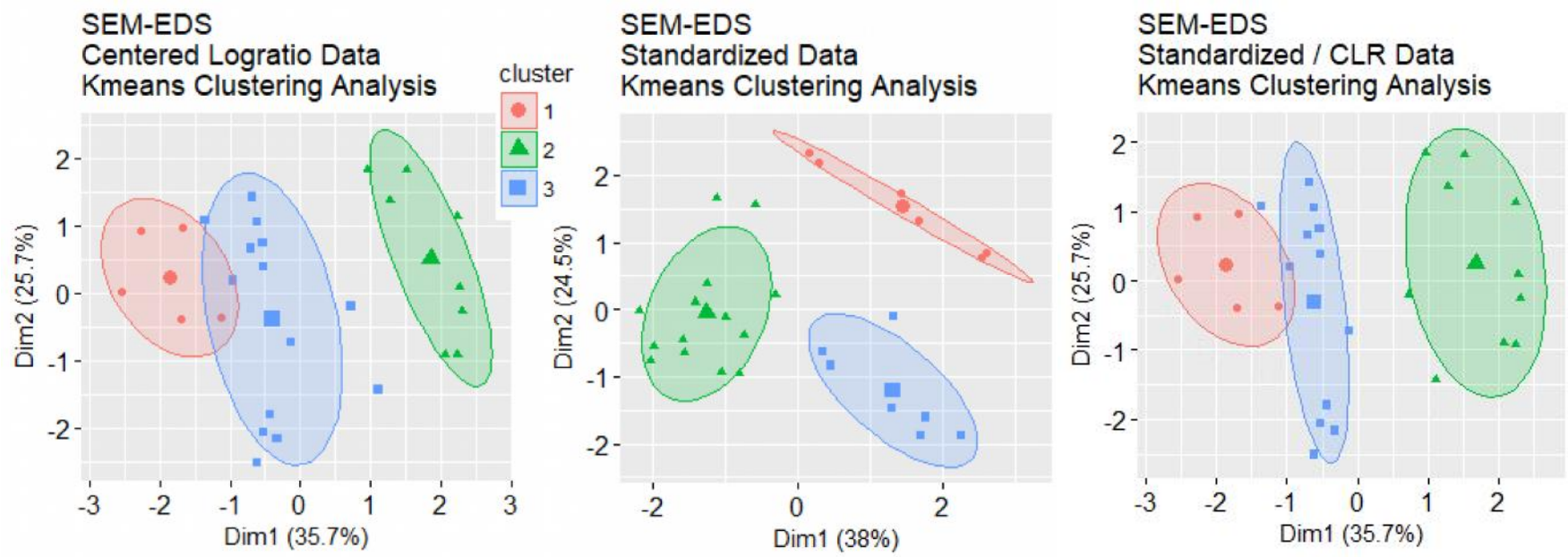

Fig. 8-23: K-means biplots of SEM-EDS results for the analysis of dataset 1 containing all replicate faience samples as described in the text. The CLR and CLR/standardization methods are nearly identical except for the reassignment of two samples from cluster 3 (CLR) to cluster 2 (CLR/standardization). Overlapping between clusters 1 and 3 are evident in both methods. The standardization method produced three clusters with good separation.

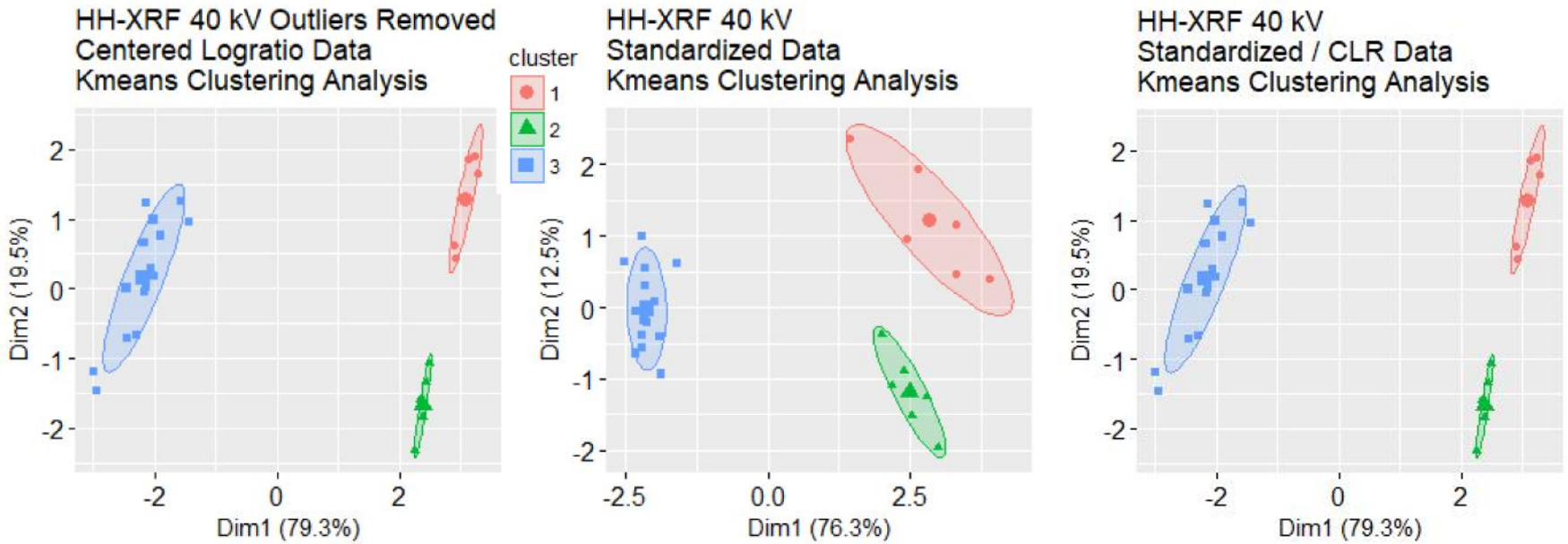

Fig. 8-24: K-means biplots of HH-XRF 40 kV results for the analysis of dataset 1 containing all replicate faience samples as described in the text. All transformation methods produced three clusters with good separation and no miss-calculations of samples (see Table 6-4).

cluster was adequate to good but standardization proved to be the optimal method because of low misassignments.

8.5.4 Transformation: HCA and Dendrograms

HCA (Ward's Method) was used to determine the optimum data transformation methods based on the clustering of the known glazes on a dendrogram. The CLR method of the HH-XRF 15kV measurements clustered each glaze batch onto its own dendrogram branch (Fig. 8-25). The combination CLR/standardization method was nearly perfect as well but miscalculated one cobalt colourant glaze 07 sample (R406) to the copper colourant glaze 03 branch. Standardization on its own assigned the cobalt blue samples (glaze 05 and 07) to the same major branch but miscalculated glaze 05 samples among the glaze 07 samples. The CLR method was optimal at clustering known samples because of no sample misassignments and the correct segregation of each cobalt blue batch onto its own branch separate from the glaze 03 branch. The standardization and CLR/standardization methods were fairly good but suffered from a few sample misassignments.

The SEM-EDS HCA CLR and CLR/standardization dendrograms appear very similar to each other (Fig. 8-26). Several samples from each group had been miscalculated between the three glaze clusters and the cobalt colourant glaze 07 batch had been incorporated into a separate branch within the copper colourant glaze 03 cluster. The cobalt colourant glaze 05 cluster in both methods is correctly situated on its own separate branch. Standardization has the least number of sample misassignments and has clustered glaze 05 and 07 separately on the same branch, but on a separate branch from glaze 03 reflecting the known recipes. Standardization was the most capable of assigning the samples to their respective glaze clusters and was the best at separating the glaze colours respective of known recipes. The HH-XRF 40 kV measurements were very well clustered into the respective glaze groupings with no misassignments (Fig. 8-27).

The HCA evaluation of the transformation methods reveals CLR and the CLR/standardization methods as slightly worse overall at assigning samples within known glaze groups. The CLR method exhibited best results with HH-XRF and cobalt colourant glazes 05 and 07 were perfectly segregated from copper colourant glaze 03. Standardization and a combination of the CLR and standardization methods were only slightly less capable. The transformations of the SEM-EDS data were adequate at discerning the three glaze batches but only standardized data separated the two cobalt blue batches from the copper blue batch resulting in fewer misassignments. All the

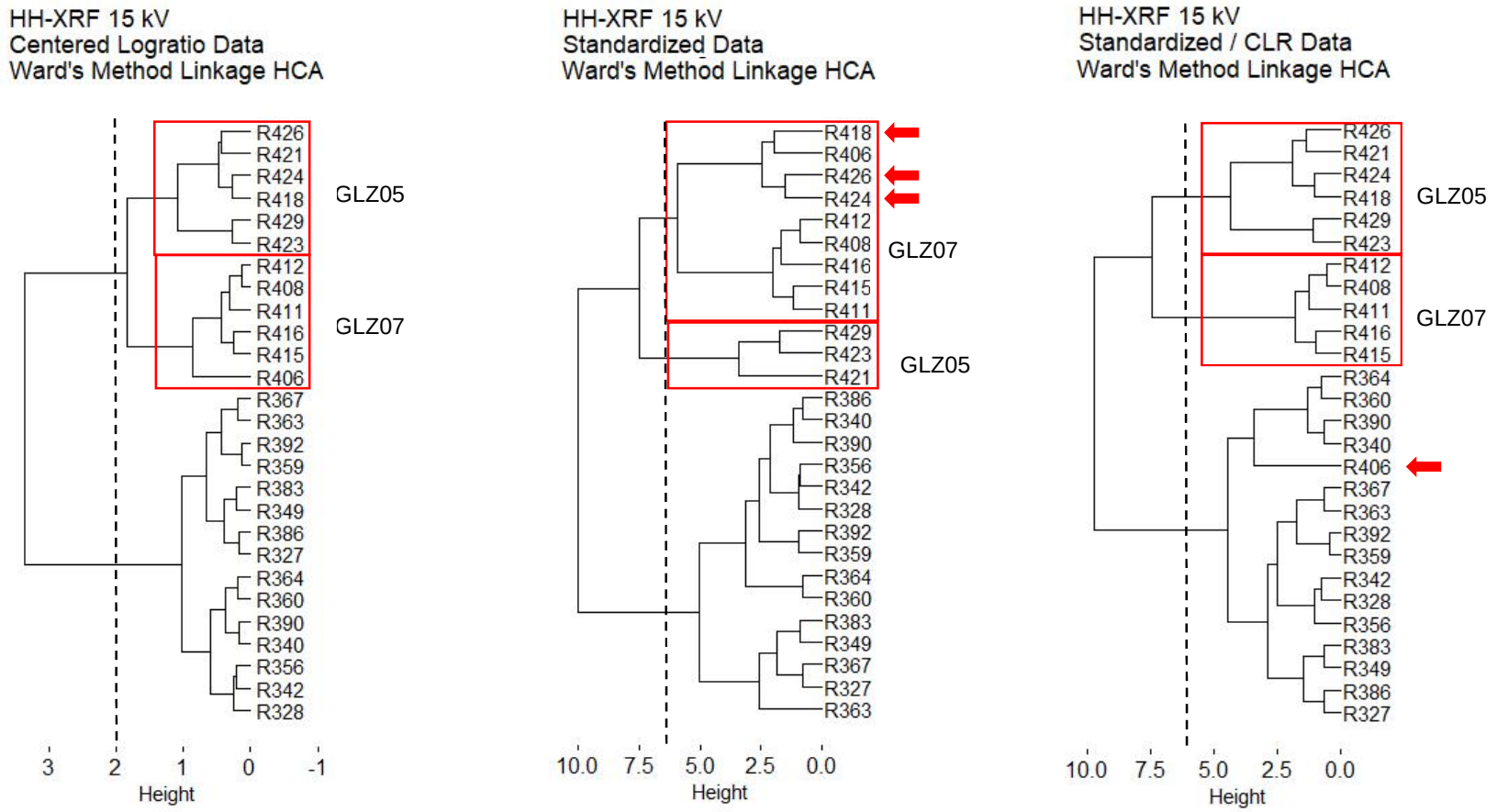

Fig. 8-25: HH-XRF 15 kV HCA dendrograms exhibiting good cluster segregation for the three transformation methods according to the known recipes. The CLR method was perfect. The standardization exhibited a few miss-calculations within the cobalt blue samples. The CLR/standardization method exhibits one miss-assignment resulting in a cobalt blue sample being clustered with copper blue samples.

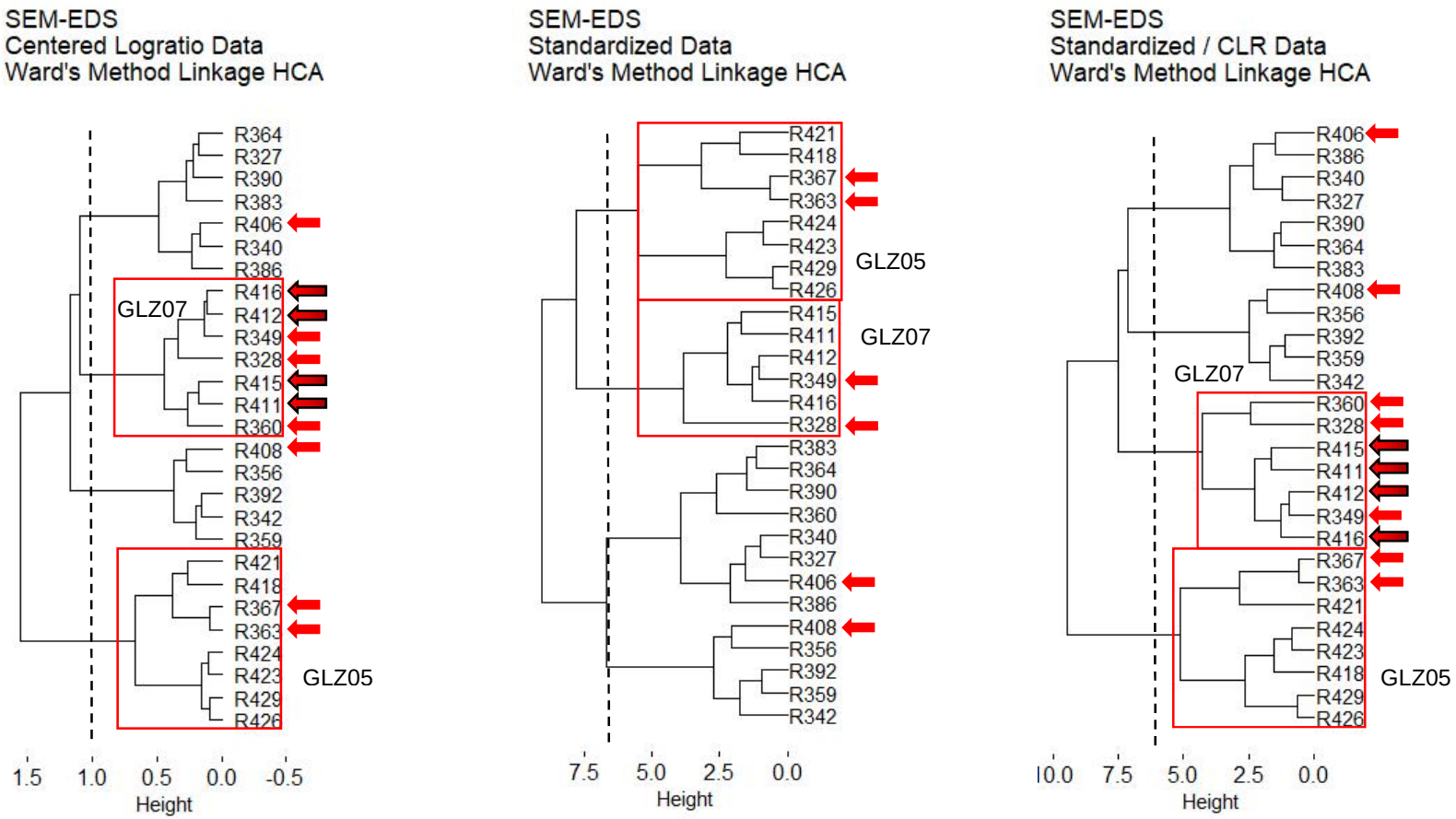

Fig. 8-26: SEM-EDS HCA dendrograms exhibiting adequate cluster segregation for the standardization method. The cobalt glazes (glazes 05 and 07) have been segregated from the copper blue glazes (glaze 03) but there are a few miss-calculations (arrows). The CLR and combination methods correctly segregated glaze 05 but placed glaze 07 within the glaze 03 cluster. Larger arrows indicate glaze 07 samples correctly assigned to glaze 07 cluster but that are still considered miss-calculations. Miss-calculations were much higher for these transformation methods.

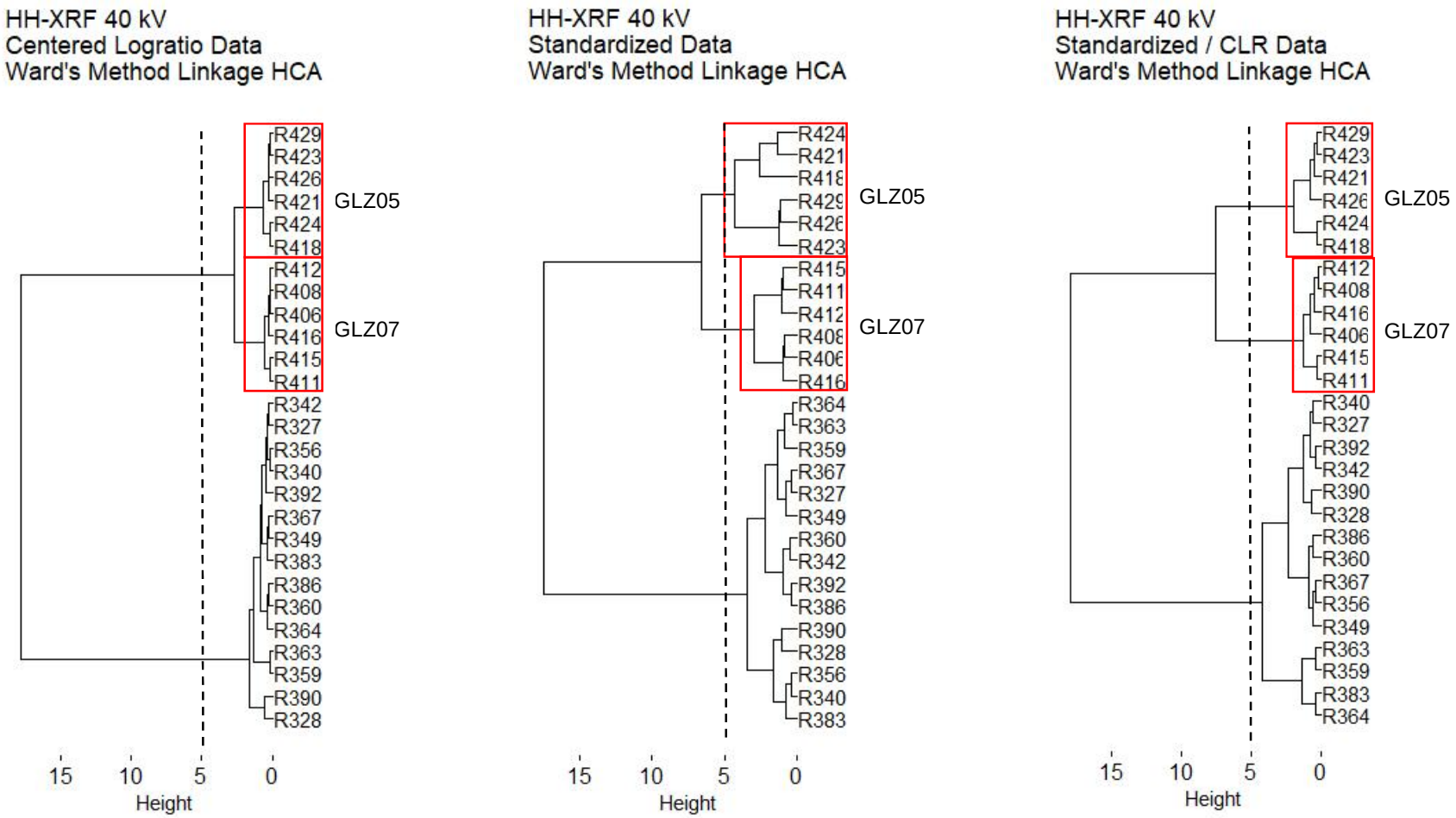

Fig. 8-27: HH-XRF 40 kV HCA dendrograms exhibiting perfect segregation of all three glaze clusters. The transformation methods do reveal differences within the glaze clusters the meaning of which may be determined in the next chapter.

transformations on the 40 kV HH-XRF measurements were correctly assigned to each glaze cluster with the cobalt blue clusters separated from the copper blue cluster. The HCA evaluation of the transformation methods is inconclusive. This method produced far less miscalculated samples and correctly placed the cobalt blue glazes on the same branch separated from the copper blue glazes.

8.6 Discussion

This chapter discussed the MVS data preparation for a single dataset using direct comparison (shared variables: HH-XRF 15 kV and SEM-EDS) and stand-alone analysis (HH-XRF 40 kV) where the variables were not restricted to those shared between the techniques.

Variables were selected based on C_V, detection limit and percent of missing data. The percent of missing data was heavily influenced by the inclusion of the three batches; one copper and two cobalt blue glazes. The recipe components were laboratory grade and heavily filtered. The copper blue batch contained the basic components required to make a blue glaze and the cobalt blue batches had minor and trace components intentionally added. These glazes only share the major elements resulting in a large percentage of missing data resulting in a lower variable pool for statistical analysis. It is presumed that the archaeological material will not be filtered to such a degree regardless of its colourants and that many more elements/oxides will be available because of inclusions in source materials and production techniques (see Chapter 2 and Chapter 10). The resulting dataset for SEM-EDS contained six oxides. The HH-XRF 15 kV variables were restricted to the same corresponding elements for comparison during this MVS evaluation. The direct comparison using only shared variables was not optimal for the low voltage HH-XRF technique and will not be used beyond this evaluation.

Censored data and zeros were handled using LOO and MR. The two methods produced similar results with the dataset. MR was chosen for subsequent SEM-EDS analysis because it maintains ratios between the variables by changing the known values when a substitution is made. This is required when using logratio transformations which are based on ratios and not absolute values. HH-XRF data required no value replacements when using SNR to determine LOD. Some replacement was necessary when using 3 times the standard deviation above the background to determine LOD. LOO was used for this although there was very little difference between the two replacement strategies.

Outliers were identified using HCA and PCA biplots. Bivariate scatterplots were utilized but were less useful with this dataset for determinations of outliers. Boxplots were useful but this method identified outliers that in some cases represented tails of the data instead. Three outliers were found consistently between the statistical techniques indicating required removal to reduce skewed results. Standardized HCA identified two additional potential outliers not substantiated with the other transformation methods nor with the PCA biplots for all transformation methods. These two samples were retained. This highlights the importance of using various statistical techniques when determining and confirming the presence of outliers. This is one of the few steps in a statistical analysis procedure when potential data transcription errors are highlighted by the occurrence of outliers.

Evaluation of the transformation methods revealed the maximum data variation was greater for methods involving CLR. This was expected because of logratios having the tendency to exaggerate variation to promote one or more variables as the driving mechanic in the process. This generally works well with metal alloys where one element is expected to be dominate in the mixture. It is questionable in the analysis of glass and glazes where there may be several elements of low presence and variability that contain the archaeological information of interest (see Baxter and Freestone 2006; Beardah et al. 2003). Standardization not involving logratios generally exhibits relationships between variables that are reflective of the original glaze recipes. Baxter and Freestone (2006) came to the same conclusion. They found standardization and CLR/standardization methods to have the same results. This statistical evaluation found that CLR and CLR/standardization had the same results, thus differing from Baxter and Freestone's results. A test with the R statistical software revealed that CLR figures could be standardized but CLR of standardized figures returned non-results.

The use of standardization with the HH-XRF data may reveal results that reflect the glass and glaze recipes. These results make more sense when using wt% totals. This project is concerned with clustering the various samples based on element ratios using NPA and not wt%. In this sense, the recipe of the glaze is less important than the ability to discern clusters based on the element ratios. Standardization and CLR will produce the same clustering but CLR will slightly exaggerate the divisions making the clusters more clear on biplots and three-dimensional PCA scores plots. CLR produced better clustering results using the replicated faience samples and HH-XRF.

The transformation evaluation revealed differences in the selection of analytical technique. The most difficult analyses to interpret were those involving SEM-EDS due to dispersed and overlapping clusters in the PCA biplots and bivariate scatterplots.

Correlation factors did indicate that the SEM-EDS results were not ideal for PCA. However standardized HCA data revealed good clustering on par with the HH-XRF 15 and 40 kV measurements. The SEM-EDS CLR transformation methods were generally ineffectual in segregating the known glaze batches which demonstrates Baxter and Freestone (2006) findings that logratio transformation can obscure variable relationships when working with compositional glass data. Standardization exhibited greater clustering tendency for SEM-EDS data.

The 40 kV HH-XRF statistical analysis illustrated that the transformation method does not really matter provided the information carrying variables are confirming Baxter's general transformation summation (2016:55). The difficulty is knowing which variables are important in unknown samples. Standardization outperformed logratios with SEM-EDS replicated sample data. HH-XRF 15 kV exhibited greater clustering using CLR data on known materials. All three methods were nearly equal with CLR exhibiting slightly greater clustering tendency for HH-XRF 40 kV measurements. For optimized results, CLR will be used with the HH-XRF data, and standardization with the SEM-EDS data when preparing analytical data for MVS.

The data preparation has revealed that it is possible to discern the three known glaze batches even before in-depth MVS occurs. Based on the findings of the evaluations, the following data preparation procedures are proposed for subsequent statistical analysis:

1. Determine pool of available variables based on:
    a. Detection limit
    b. CV<10% unless a larger percent can be justified
    c. Percent of missing/censored values is <10% of all values for each element/oxide
2. Use MR to maintain variable ratios on censored/missing data representing <10% of all values for each element of the SEM-EDS data. LOO is better for absolute values (e.g. NPA) when replacement is required although there was very little difference between the two replacement strategies.
3. Use standardization for SEM-EDS and CLR for HH-XRF to transform data before MVS.
4. Determine outliers of standardized data and remove or retain based on questions being asked.

Chapter 9: Faience Replicates: Multivariate Statistical Analysis

9.1 Introduction

This chapter uses the techniques and outcomes of the previous chapter's MVS evaluations to conduct rigorous MVS analysis on the HH-XRF and SEM-EDS compositional results of the three faience glaze replication groups (glazes 03, 05 and 07). This chapter demonstrates that the HH-XRF is capable of detecting subtle faience glaze nuisances that may indicate production techniques, workshops and raw materials used by the craftsmen of the archaeological sherds. The previous chapter covered data preparation required before conducting MVS analysis. Techniques for data transformation (e.g. z-transformation, logratios) and replacement of censored values for data preparation (e.g. leave-one-out method, multiplicative replacement) were evaluated for use on glass/glazes. The objectives of the current testing are:

- To determine if analysis will discern known groups based on NPA;
- To determine if SEM-EDS and HH-XRF produce similar results;
- To compare results of analysis using datasets with all variables meeting criteria (Chapter 7) and those using reduced variable datasets (reduced dimensional datasets) having removed silicon (major element) and copper (colourant) that will have a major influence on MVS analysis and alkali components (sodium and potassium) which are susceptible to dissolution.

The faience replicates used in the elemental analysis include one copper blue (R300 series) and two smaller cobalt blue batches (R400 series) (Table 8-6). The datasets represent copper and cobalt coloured glazes (dataset 1), copper-blue coloured glazes (dataset 2) and cobalt-blue coloured glazes (dataset 3). The datasets are subdivided based on analytical technique: x.1 for 15 kV HH-XRF, x.2 for SEM-EDS and x.3 for 40 kV HH-XRF (Table 9-1). The elemental data was collected as discussed in section 4.4.4 (SEM-EDS) and 4.4.5 (HH-XRF; see Fig. 4-6).

Table 9-1: Faience Replication Multivariate Dataset Summary.

Datasets for Faience Replication Samples				
Datasets	Sample	Data Subset (Datasetx.x)	Technique	Elements/Oxides of Interest
1	All Samples	1.1	HH-XRF 15 kV	Na, Al, Si, P, K, Ca, Ti, Cr, Fe, Cu, Zn
		1.2	SEM-EDS	Na_2O, SiO_2, K_2O, CaO, CuO
		1.3	HH-XRF 40 kV	Fe, Cu, Zn, Sr, Zr, Sn, Sb, Pb
2	Copper Colourant	2.1	HH-XRF 15 kV	Na, Al, Si, P, K, Ca, Ti, Cr, Fe, Cu, Zn
		2.2	SEM-EDS	Na_2O, SiO_2, K_2O, CaO, CuO
		2.3	HH-XRF 40 kV	Fe, Cu, Zn, Sr, Zr, Sn, Sb, Pb
3	Cobalt Colourant	3.1	HH-XRF 15 kV	Na, Mg, Al, Si, P, K, Ca, Cr, Mn, Fe, Co, Cu, Zn, Pb
		3.2	SEM-EDS	Na_2O, SiO_2, K_2O, CaO, FeO, CuO, PbO
		3.3	HH-XRF 40 kV	Fe, Co, Cu, Zn, Rb, Sr, Zr, Sn, Sb, Pb, Bi
Reduced Dimensionality Datasets (HH-XRF Only)				
1	All Samples	1.1R	HH-XRF 15 kV	Al, P, Ti, Cr, Fe
		1.3R	HH-XRF 40 kV	Fe, Sr, Zr, Sn, Sb, Pb
2	Copper Samples	2.1R	HH-XRF 15 kV	Al, P, Ti, Cr, Fe
		2.3R	HH-XRF 40 kV	Fe, Sr, Zr, Sn, Sb, Pb
3	Cobalt Samples	3.1R	HH-XRF 15 kV	Mg, Al, P, Ti, Cr, Mn, Fe, Pb
		3.3R	HH-XRF 40 kV	Fe, Sr, Zr, Sn, Sb, Pb

All three datasets were prepared having selected variables, removed outliers and replaced censored data as outlined in the previous chapter (see Tables 7-7 through 7-10 (HH-XRF) and Tables 7-13 through 7-14 (SEM-EDS)). Variables with censored data representing more than 10% of the cases were removed from MVS analysis. In the previous chapter aluminium was retained for analysis despite the high C_V value but has been removed from the current analysis where its C_V is >10%. Multiplicative lognormal replacement strategies were used to replace SEM-EDS censored data. Outliers were determined through a consensus of PCA biplots, HCA dendrograms and box plots.

Jackson and Baxter (1999:160) write that the initial MVS analysis should include components essential to glass formation before reducing the dimensionality of the datasets. Therefore, the HH-XRF data have been divided into two data subsets: the first including all variables that meet the selection criteria, and the second excluding major elements (i.e. silicon), alkali components (i.e. sodium and potassium) and elements that are affected by matrix effects in the form of peak interference (i.e. zinc with copper in the replicated glazes). The lower dimensional data subsets are reported

in this chapter. Higher dimensional datasets will be reported if additional information is revealed.

Silicon was removed from these low dimensionality analyses due its reduced discrimination capacity. Silicon is a major element consistently found in a general range within a faience glaze (60-80%) and much higher within the body (90+%). Minor and trace element inclusions (e.g. titanium, iron, chromium, rubidium, zinc) found within silica sand offer much greater discrimination capacity for glaze clusters based on glaze composition.

Alkali components (sodium and potassium) were removed from the low dimensional HH-XRF analyses because of their susceptibility to alkali dissolution from the outer surface of the glaze during deposition. HH-XRF is generally non-destructively used to analyse the surfaces of objects and the alkali components affected by dissolution do not represent the original composition of the glaze.

During initial data exploration, zinc and copper were found to have very high correlation coefficients ($R^2 = 0.99$) for the 15 kV and 40 kV measurements (Fig. 9-1). Zinc is not a glaze batch recipe component and its strong relationship with the copper component in the glazes indicates that it has possibly been introduced with the CaO used for the batch mixtures. However, a more plausible origin for the zinc/copper relationship is a function of peak deconvolution in the HH-XRF Spectra software. Bayesian deconvolution indicates that a small zinc Kα peak is present but its spectral relationship with the copper Kβ peak may leave it susceptible to interference from the copper (Fig. 9-2) resulting in a false correlation. The zinc peak is small and represented as a shoulder on the copper Kβ peak. The zinc probably originates from the HH-XRF analyser unit as instrument interference (see Table 6-2). A similar relationship exist with lead (Lα1 at 10.55 kV) and bismuth (Lα1 at 10.83 kV) ($R^2 = 0.99$) with the HH-XRF 40 kV measurements. Zinc and bismuth were removed from the low dimensional datasets.

Hunt and Speakman (2015:2) indicate that low levels of phosphorus (2.02 kV) in HH-XRF analysis are either the calcium escape peak (1.95 kV) or are heavily influenced by the escape peak interference when calcium is present in the sample. Low phosphorus levels reported from HH-XRF analyses should be suspect. A high correlation between phosphorus and calcium is an indicator of the interference. Initial data exploration exhibited low phosphorus NPA totals and a low phosphorus Kα peak in the spectra. However the calcium/phosphorus correlation is generally moderate to low. Phosphorus has been retained in the analysis.

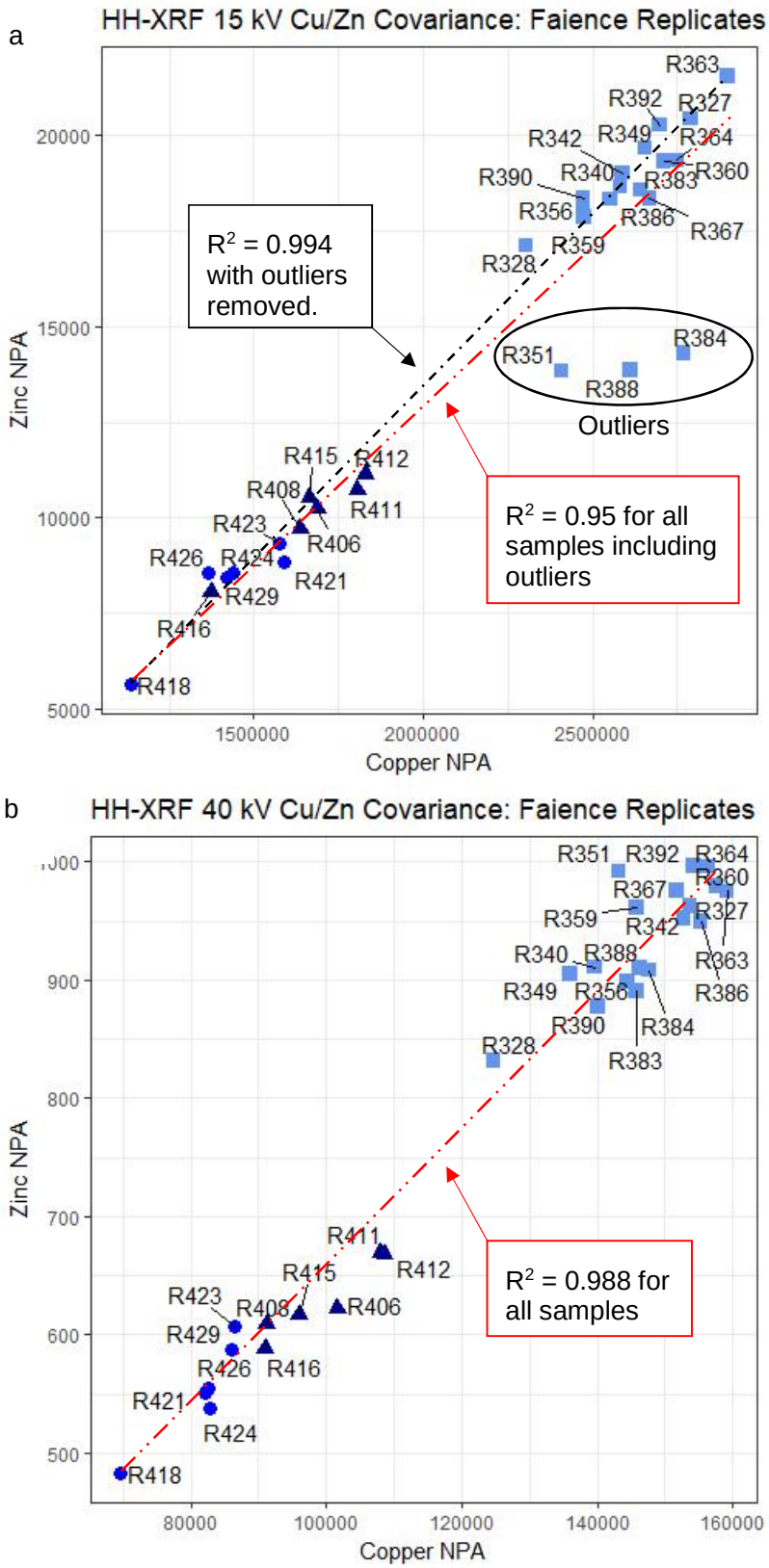

Fig. 9-1: Coefficient of determination (R^2) for Raw HH-XRF 15 kV (a) and 40 kV (b) data. R^2 for 15 kV glaze groups are 0.905 (glaze 03), 0.971 (glaze 07) and 0.924 (glaze 05). For 40 kV glaze groups they are 0.803 (glaze 03), 0.954 (glaze 07) and 0.933 (glaze 05).

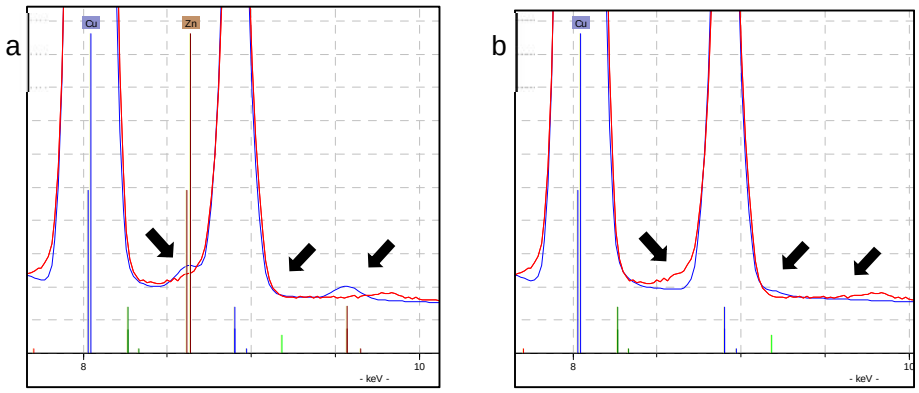

Fig. 9-2: The high copper / zinc correlation may be a result of deconvolution. Figures a and b are the same spectrum with and without zinc listed as an element. The red line is the spectrum. The blue line is the Bayesian deconvolution line used during peak identification, the goal of which is to match the two lines based on elements selected. A comparison of both spectra indicate that zinc might be present in low quantities based on greater correlation of the two lines, although the difference between the two spectra is minor. Arrows indicate differences between the spectra.

The following sections provide MVS analysis and a discussion for each dataset. MVS consisted of HCA, PCA, and K-means. Draftsmen plots exhibit correlation factors, histograms and bivariate plots of the variables. Data preparation resulted in several tables and figures to support decisions for removal of outliers and retention of variables. Only pertinent tables and figures are presented in this chapter, however, all data generated with MVS was treated to outlier determination (not included in the text for brevity). The coding used with the R statistical program is in appendix I.

9.2 Dataset 1 Multivariate Analysis (Copper and Cobalt Coloured Samples)

The tables containing datasets 1.1 (15 kV HH-XRF), 1.2 (SEM-EDS) and 1.3 (40 kV HH-XRF) are in chapter 8 (see Tables 8-3, 8-4 and 8-5). The reduced dimensional variable dataset 1.1R is exhibited in Table 9-2.

9.2.1 Datasets 1.1R and 1.1: HH-XRF 15 kV

The pairwise plots of dataset 1.1R reveal that all the selected variables contribute to defining two clusters which correspond to the replicated glaze groups (based on colourant) despite copper and cobalt being absent. MVS analysis reveals the two clusters are most influenced by iron and aluminium contents.

The initial exploratory PCA biplot for dataset 1.1R (Fig. 9-3; Table 9-3) reveals two cobalt coloured glaze samples (R423 and R429) that could potentially be identified as

Table 9-2: Dataset 1.1R with reduced variable set for all replicated samples.

HH-XRF 15 kV (NPA) Faience Replicates Dataset 1.1R						
Parameters 15 kV, 50 uA with a vacuum for 180 seconds (no filter)						
10 Measurements per Sample						
Sample	Glaze	Al	P	Ti	Cr	Fe
R327	G3	18889	2756	5329	8234	37038
R328	G3	15156	2823	5844	7963	36545
R340	G3	13424	2970	4533	6948	35222
R342	G3	14851	2954	4615	6722	37015
R349	G3	21019	2697	4317	8919	34303
R351	G3	12813	1719	4183	6936	27336
R356	G3	13458	2966	4451	9575	37923
R359	G3	15926	2736	4188	9640	32886
R360	G3	14633	2953	5121	6087	34546
R363	G3	23326	2762	4146	7882	37659
R364	G3	16543	2922	4665	6779	38915
R367	G3	21072	2827	4944	7919	34414
R383	G3	19620	2754	4516	7563	36652
R384	G3	16511	1807	4308	5861	33637
R386	G3	16330	2852	5129	8185	34053
R388	G3	17743	1678	4556	5437	29961
R390	G3	12858	2984	4950	6740	32715
R392	G3	18707	2740	4926	7871	36668
R406	G7	13410	2687	4724	5480	876438
R408	G7	22590	2409	4674	7082	902066
R411	G7	24790	2224	3984	7290	855980
R412	G7	23409	2291	4467	6221	957802
R415	G7	18313	2472	5166	8159	764261
R416	G7	18302	2573	4202	7239	714410
R418	G5	18317	3000	4264	4171	706236
R421	G5	28919	2662	3983	5378	909401
R423	G5	57004	2479	3793	7822	852943
R424	G5	27078	2760	3852	5313	825730
R426	G5	26032	2617	4439	8822	745871
R429	G5	43746	2309	4279	9072	768274

outliers but boxplot and HCA (single linkage) analysis failed to identify them as such. They are retained for further analysis of this dataset.

The pairwise plots (Fig. 9-4) reveals relatively high negative correlations with aluminium/phosphorus, aluminium/titanium, and iron/chromium relationships and relatively high correlation with titanium/phosphorus in cobalt colourant glazes 05 and 07. Aluminium/phosphorus exhibit a relatively high negative correlation for copper colourant glaze 03.

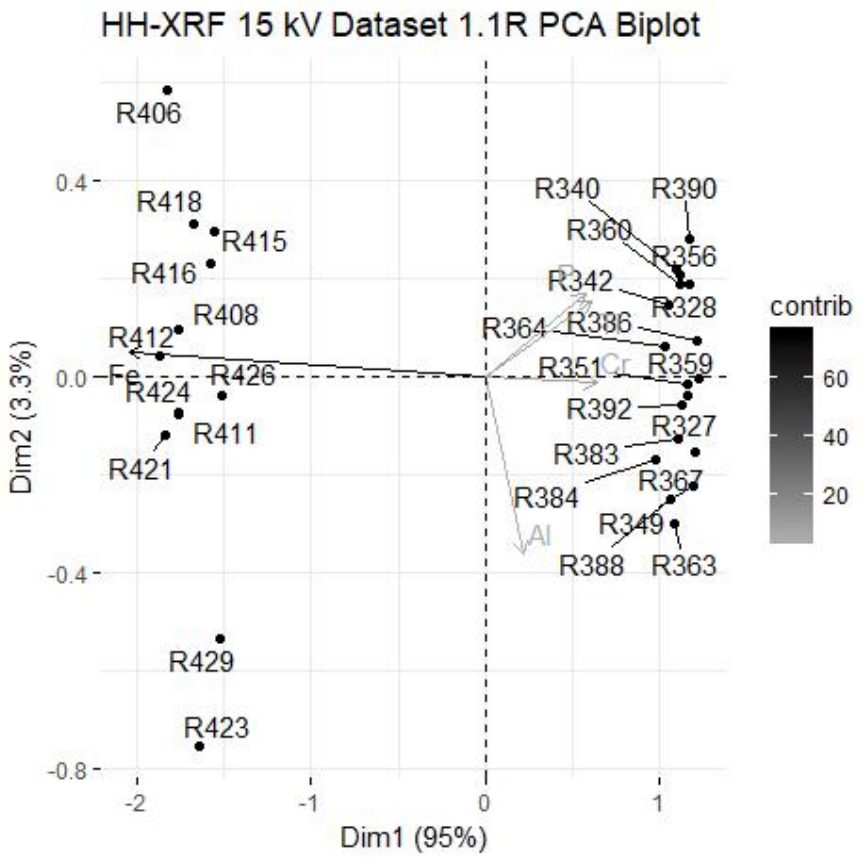

Fig. 9-3: Dataset 1.1R PCA biplot of components 1 and 2 exhibiting the cobalt and copper coloured samples separated mainly by the iron variable. Samples R423 and R429 were not identified as outliers by HCA and boxplots and have been retained for further analysis.

Table 9-3: Loadings, Eigenvalues and Variance for dataset 1.1R. Components 1 and 2 exhibit most variance with iron and aluminium, respectively.

Dataset 1.1R HH-XRF 15 kV PCA Loadings

	Non-Rotated Results					Varimax Rotated Results					
	Dim.1	Dim.2	Dim.3	Dim.4	Dim.5		Dim.1	Dim.2	Dim.3	Dim.4	Dim.5
Al	0.09	-0.84	0.29	0.06	0.45	Al		-1.00			
P	0.25	0.39	0.49	-0.59	0.45	P					-1.00
Ti	0.27	0.36	0.10	0.77	0.45	Ti				1.00	
Cr	0.28	-0.03	-0.82	-0.24	0.45	Cr			-1.00		
Fe	-0.88	0.12	-0.06	0.00	0.45	Fe	-1.00				

Dataset 1.1R Eigenvalues and Variance

	Eigenvalue	Variance %	Cumulative Variance %
Dim.1	1.92	95.00	95.00
Dim.2	0.07	3.33	98.33
Dim.3	0.02	1.10	99.43
Dim.4	0.01	0.57	100.00
Dim.5	0.00	0.00	100.00

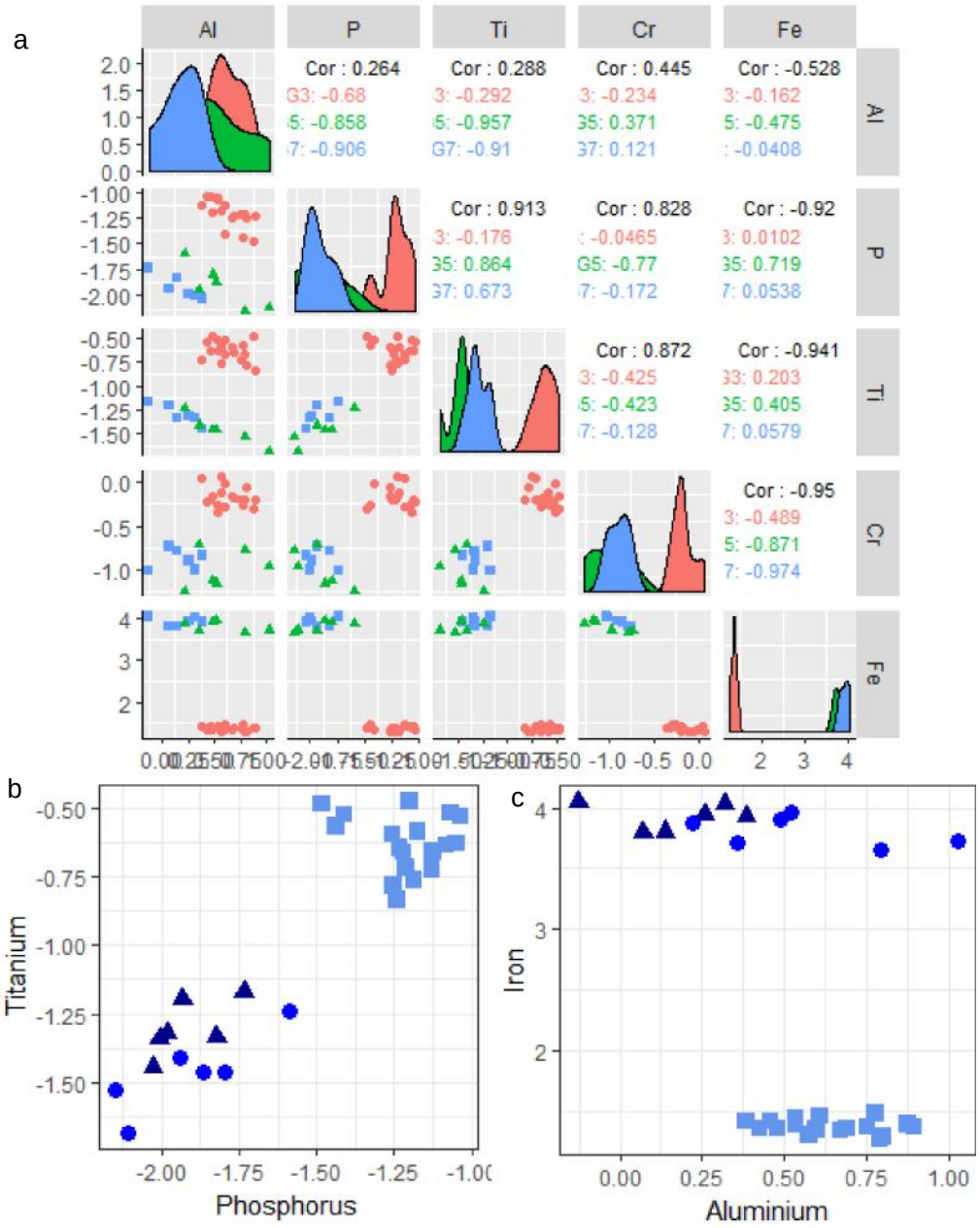

Fig. 9-4: Pairwise graph of centred logratio dataset 1.1R exhibiting bivariate plots, histogram and correlations of the variables (a). The highest correlation is for phosphorus and titanium of cobalt colourant glaze 05 and 07 (a and b). Aluminium and iron define the clusters for this dataset and a bivariate plot (c) exhibits similar results to PCA.

Phosphorus, titanium and chromium were not added as components to the replicated glaze and are assumed to be inclusions in some other component (e.g. sand).

The PCA Eigenvalues for dataset 1.1R indicate that the first two components exhibit 98.3% of the data variance (see Table 9-3). The PCA biplot of components 1 and 2 (see Fig. 9-3) exhibits the cobalt and copper blue coloured glazes distinctly separated because of iron which has the highest contribution. Samples R423 and R429 are separated from both clusters but are clearly more related to the cobalt blue cluster. The loadings exhibit component 1 mostly influenced by iron and component 2 by aluminium. These results indicate that iron and aluminium are the best indicators of variance for the replicate datasets using low-kV HH-XRF.

HCA (Ward's Method) (Fig. 9-5) exhibits distinct cobalt and copper coloured groupings. The cobalt cluster is intermixed with glaze 05 and 07 except for samples R423 and R429 (glaze 05) which have been separated into a sub-cluster of the cobalt glazes. The two major clusters exhibit a silhouette width of 0.85 indicating the samples have been allocated into the two clusters with 85% confidence that they have been correctly assigned. K-means biplot exhibits similar results to the PCA biplot and the exact same results with HCA therefore sharing the same silhouette graph with HCA.

Dataset 1.1 results using the full variable set are included because they exhibit a clustering of the individual cobalt coloured glazes where dataset 1.1R did not. Exploratory analysis of dataset 1.1 using HCA (single linkage) and PCA biplot (first two components) indicated three outliers (R351, R384 and R388) and their presence was confirmed by boxplots for sodium and phosphorus. The boxplot for aluminium indicated samples R423 and R429 as additional outliers. All outliers were removed from further analysis of this dataset.

Draftsman plots (Fig. 9-6) and boxplots reveal that most of the elements have clustering contributions. The elements with the least contributions are silicon and aluminium. Silicon is present in all samples as the network former and the amount of silicon added to each batch is relatively similar. The lack of cluster contribution for silicon is not surprising. Aluminium exhibited cluster contribution with dataset 1.1R indicating that its clustering contribution with dataset 1.1 is masked by the occurrence of other elements.

The PCA biplots (Fig. 9-7) of the first two components exhibit the samples clustering in correspondence with the glaze colour; the presence of iron and potassium, respectively, exhibiting greatest variance (Table 9-4). HCA (Ward's method) and k-means analysis (Fig. 9-8) exhibit the samples clustered in a way that corresponds to

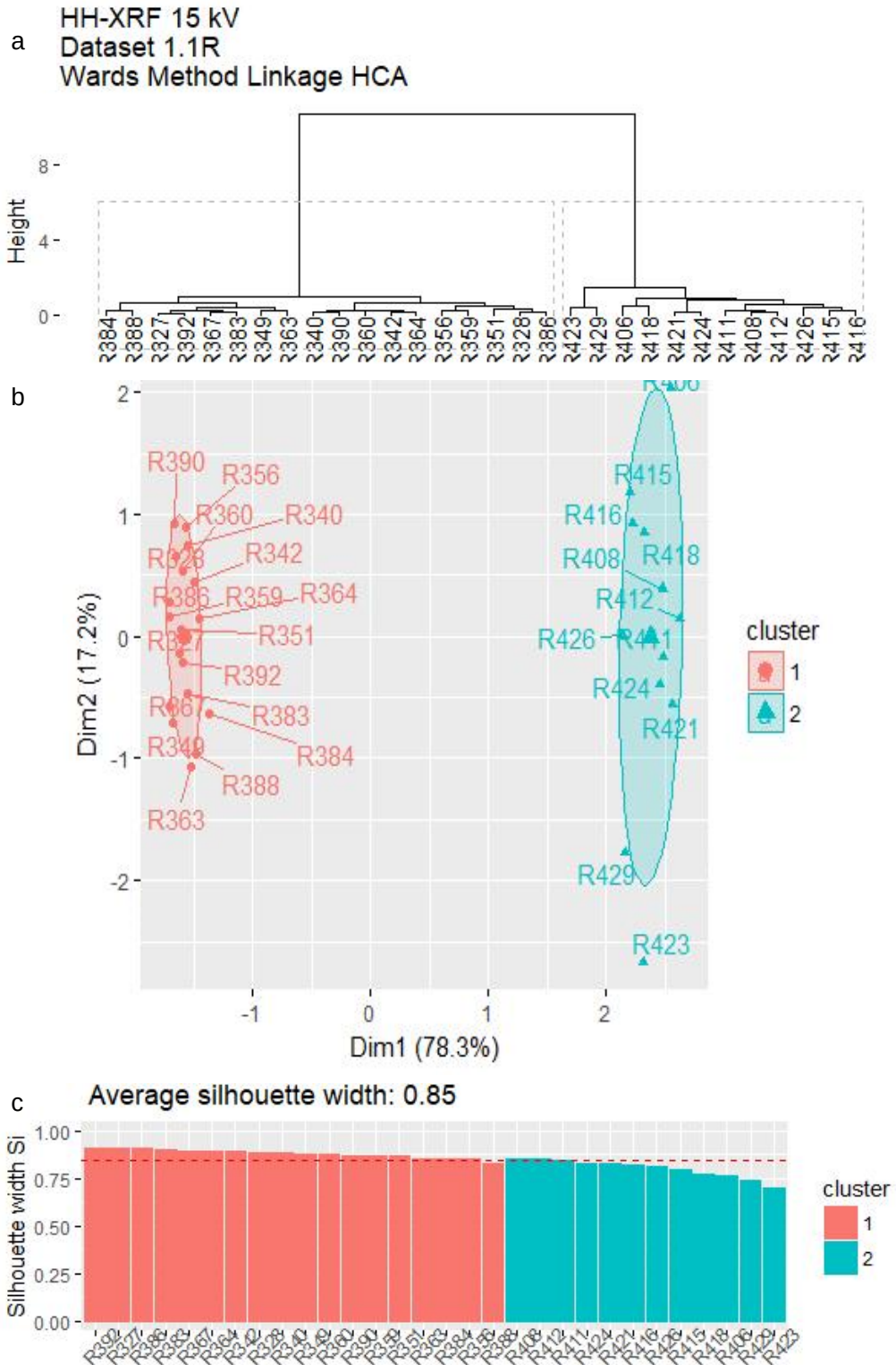

Fig. 9-5: a) HCA (Ward's Method), b) k-means analysis and c) the associated silhouette graph for dataset 1.1R.

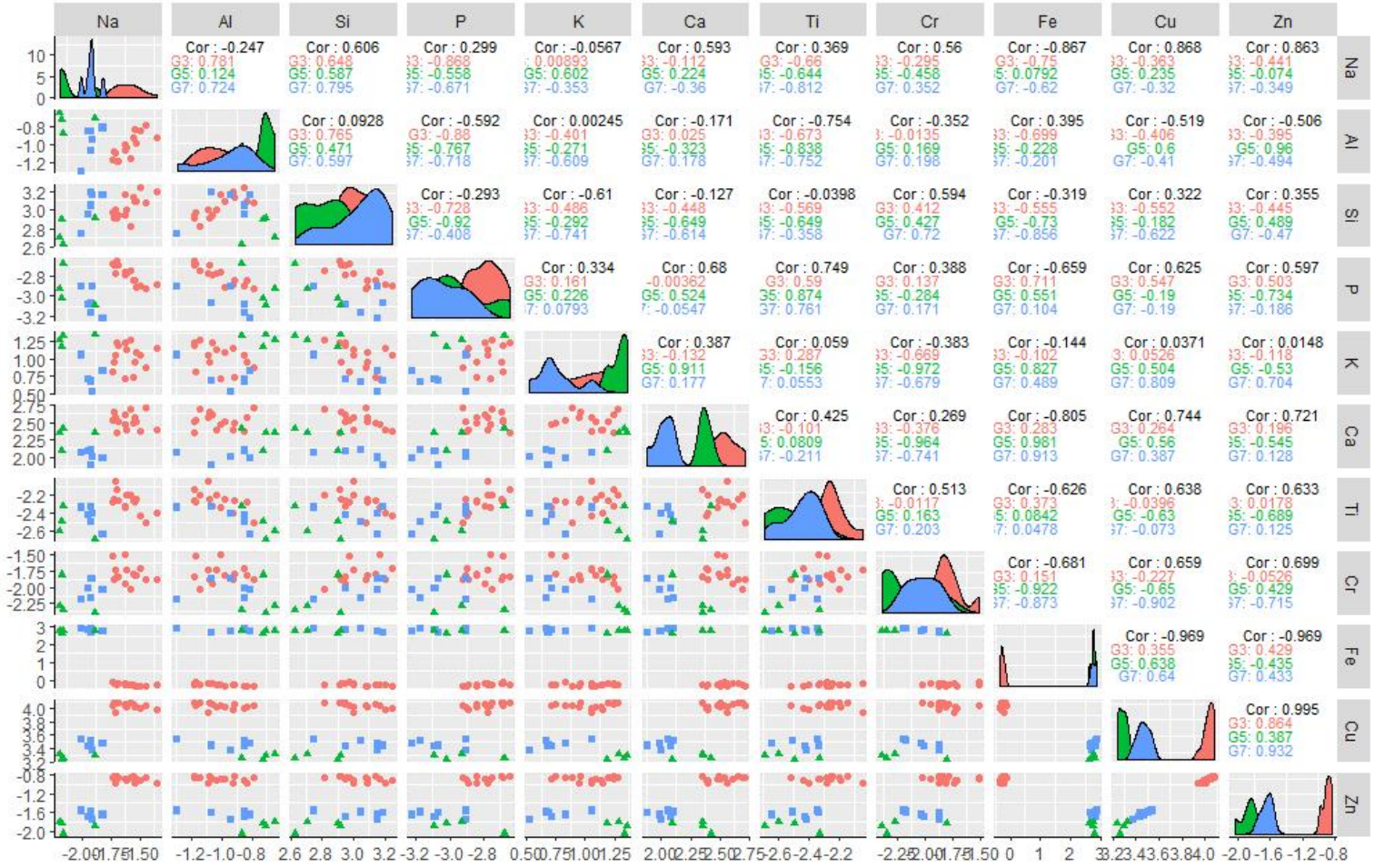

Fig. 9-6: Draftsman plots of dataset 1.1 with outliers removed. Bivariate plots are lower left, correlation figures are upper right and variable histograms are diagonal. Glazes are demarcated by colour (copper colourant glaze 03 = red, cobalt colourant glaze 05 = green and cobalt colourant glaze 07 = blue).

a

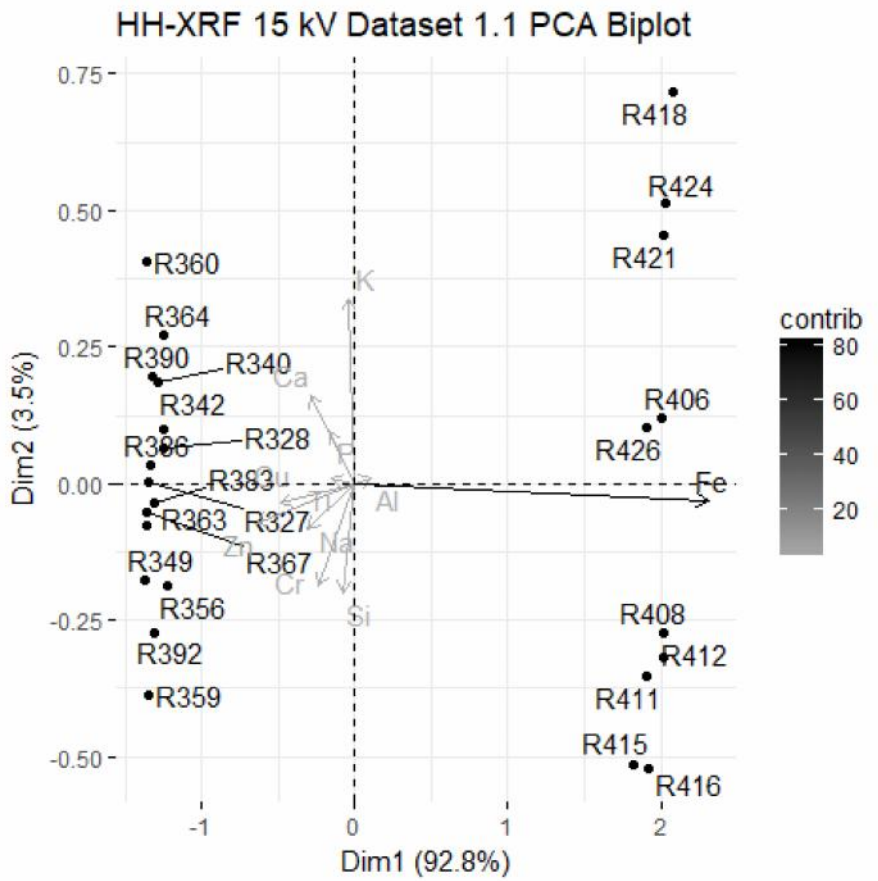

b

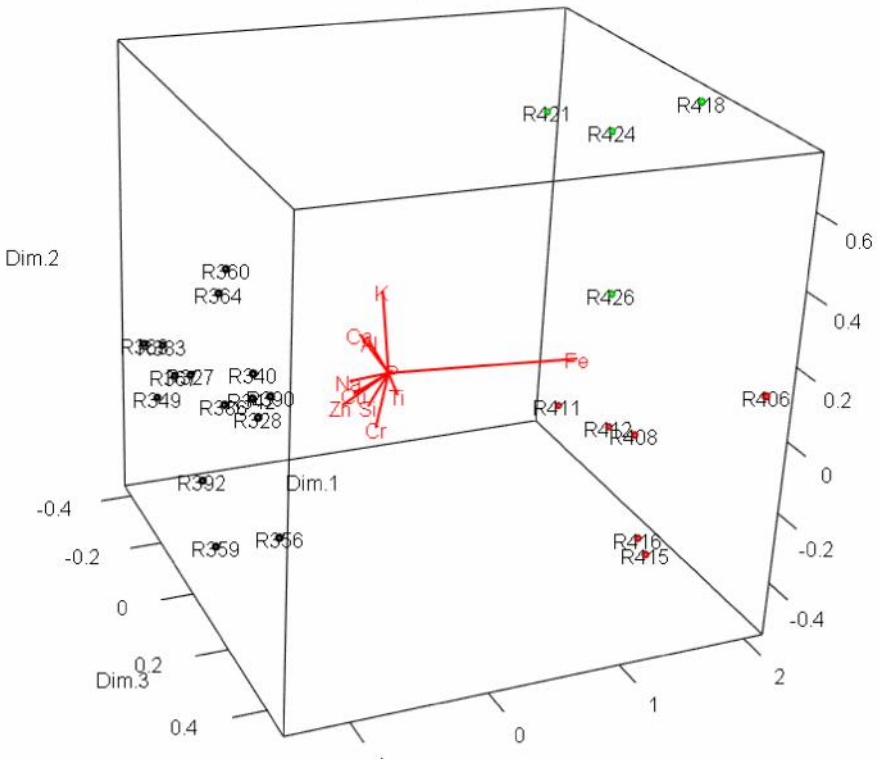

Fig. 9-7: Dataset 1.1 PCA biplots. The biplots exhibit a primary cluster division based on Fe, and a secondary division of the cobalt samples based on K.

Table 9-4: Loadings, Eigenvalues and Variance for dataset 1.1. Components 1 and 2 represent 96.28% of the data variation and reveal most variance with iron and potassium, respectively.

Dataset 1.1 HH-XRF 15 kV PCA Loadings

	Non-Rotated Results					Varimax Rotated Results				
	Dim.1	Dim.2	Dim.3	Dim.4	Dim.5	Dim.1	Dim.2	Dim.3	Dim.4	Dim.5
Na	-0.12	-0.17	-0.29	-0.40	-0.12			-0.48	-0.26	
Al	0.04	0.02	-0.62	0.35	0.16	-0.16	-0.13	-0.35	0.56	0.24
Si	-0.03	-0.41	-0.27	-0.01	-0.25		-0.15	-0.38		-0.35
P	-0.06	0.20	0.36	0.24	0.15			0.49		0.11
K	-0.02	0.69	-0.10	-0.03	-0.61		0.91		0.17	
Ca	-0.12	0.33	-0.13	0.08	0.66	-0.11	-0.15	0.10		0.73
Ti	-0.06	0.02	0.46	0.06	-0.07			0.41	-0.16	-0.16
Cr	-0.09	-0.38	0.19	0.59	-0.20	-0.25	-0.32	0.28	0.33	-0.49
Fe	0.92	-0.06	0.11	-0.16	0.07	0.93			0.13	
Cu	-0.19	-0.08	0.13	-0.35	0.13				-0.44	
Zn	-0.26	-0.15	0.16	-0.38	0.08				-0.50	

Dataset 1.1 Eigenvalues and Variance

	Eigenvalue	Variance %	Cumulative Variance %
Dim.1	2.60	92.76	92.76
Dim.2	0.10	3.53	96.28
Dim.3	0.05	1.71	97.99
Dim.4	0.02	0.80	98.80
Dim.5	0.02	0.65	99.44
Dim.6	0.01	0.28	99.72
Dim.7	0.00	0.14	99.87
Dim.8	0.00	0.09	99.95
Dim.9	0.00	0.04	99.99
Dim.10	0.00	0.01	100.00
Dim.11	0.00	0.00	100.00

glaze colour. HCA and k-means produced the same results and share a silhouette graph (Fig. 9-8c) that exhibits the copper coloured glazes distinctly separated from the cobalt coloured glazes. Cluster division of the cobalt coloured glazes was less clear which is represented by the lower sil widths of the individual samples for these two groups. The silhouette graph indicates a confidence of 66% that the samples for dataset 1.1 have been clustered correctly.

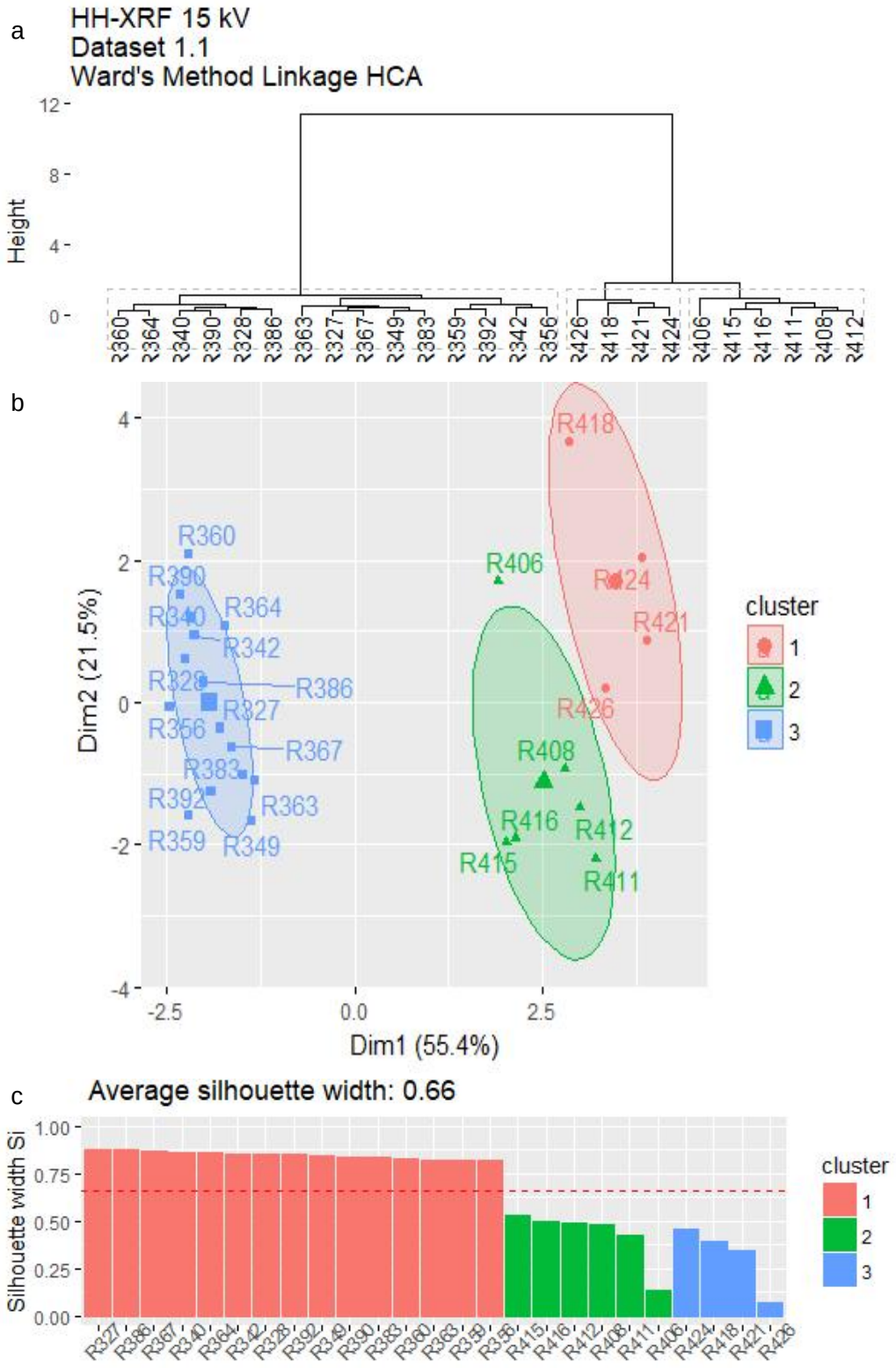

Fig. 9-8: a) HCA (Ward's Method), b) k-means analysis and c) the associated silhouette graph for dataset 1.1.

9.2.2 Dataset 1.2: SEM-EDS

The MVS results for dataset 1.2 (see Table 8-4) were convoluted and failed to clearly define clusters due to a criterion-restricted variable set (see section 8.4.1). HCA (single linkage), pairwise plots and boxplots indicated two outliers (R383 and R416) which are removed before further analysis of dataset 1.2.

The pairwise plots of dataset 1.2 (Fig. 9-9) reveal that calcium and copper contribute to defining two clusters: a glaze 05 (cobalt) cluster and a cluster including glazes 03 (copper) and 07 (cobalt). PCA (Figs. 9-10 and 9-11 and Table 9-5) and K-means (Fig. 9-12)

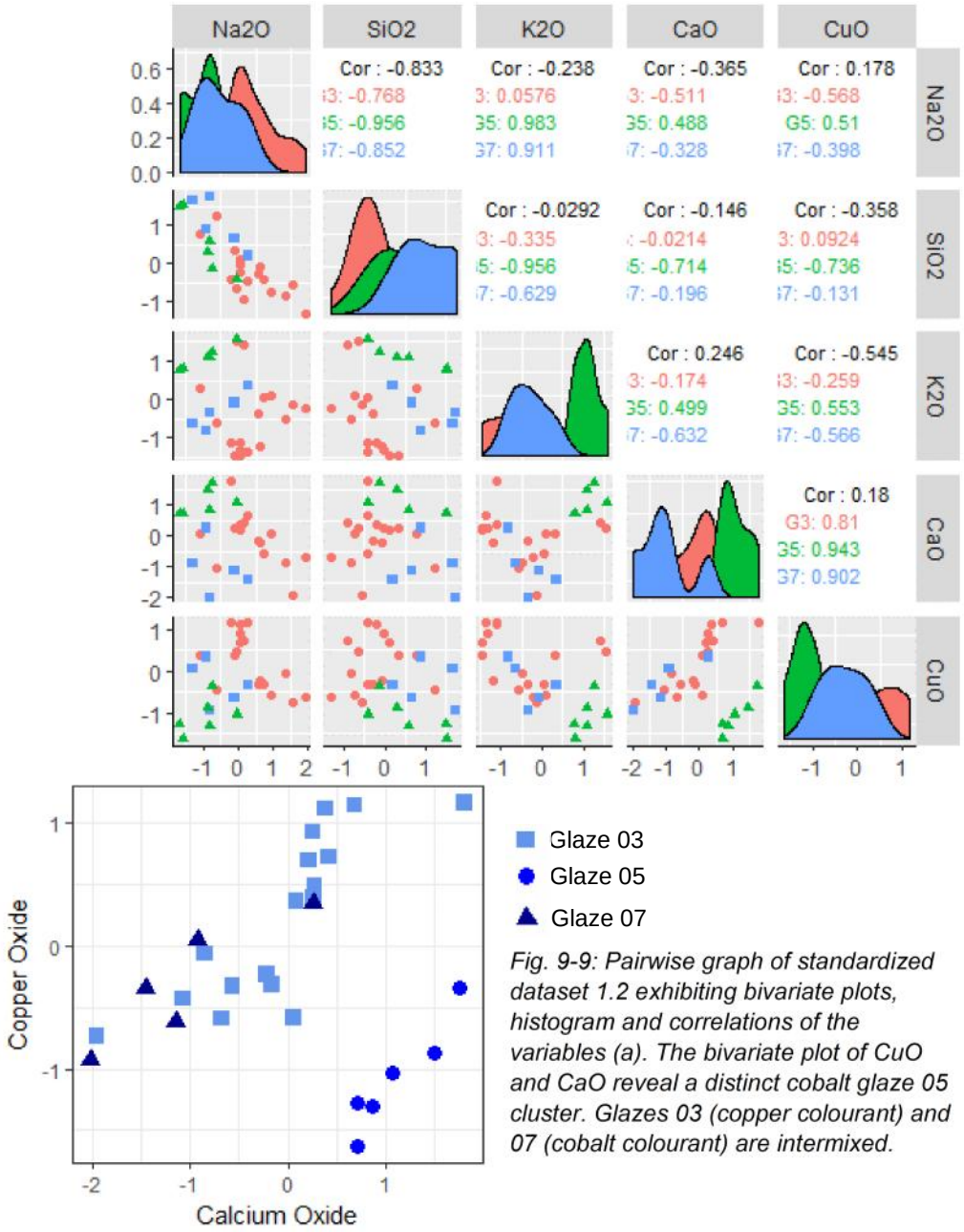

Fig. 9-9: Pairwise graph of standardized dataset 1.2 exhibiting bivariate plots, histogram and correlations of the variables (a). The bivariate plot of CuO and CaO reveal a distinct cobalt glaze 05 cluster. Glazes 03 (copper colourant) and 07 (cobalt colourant) are intermixed.

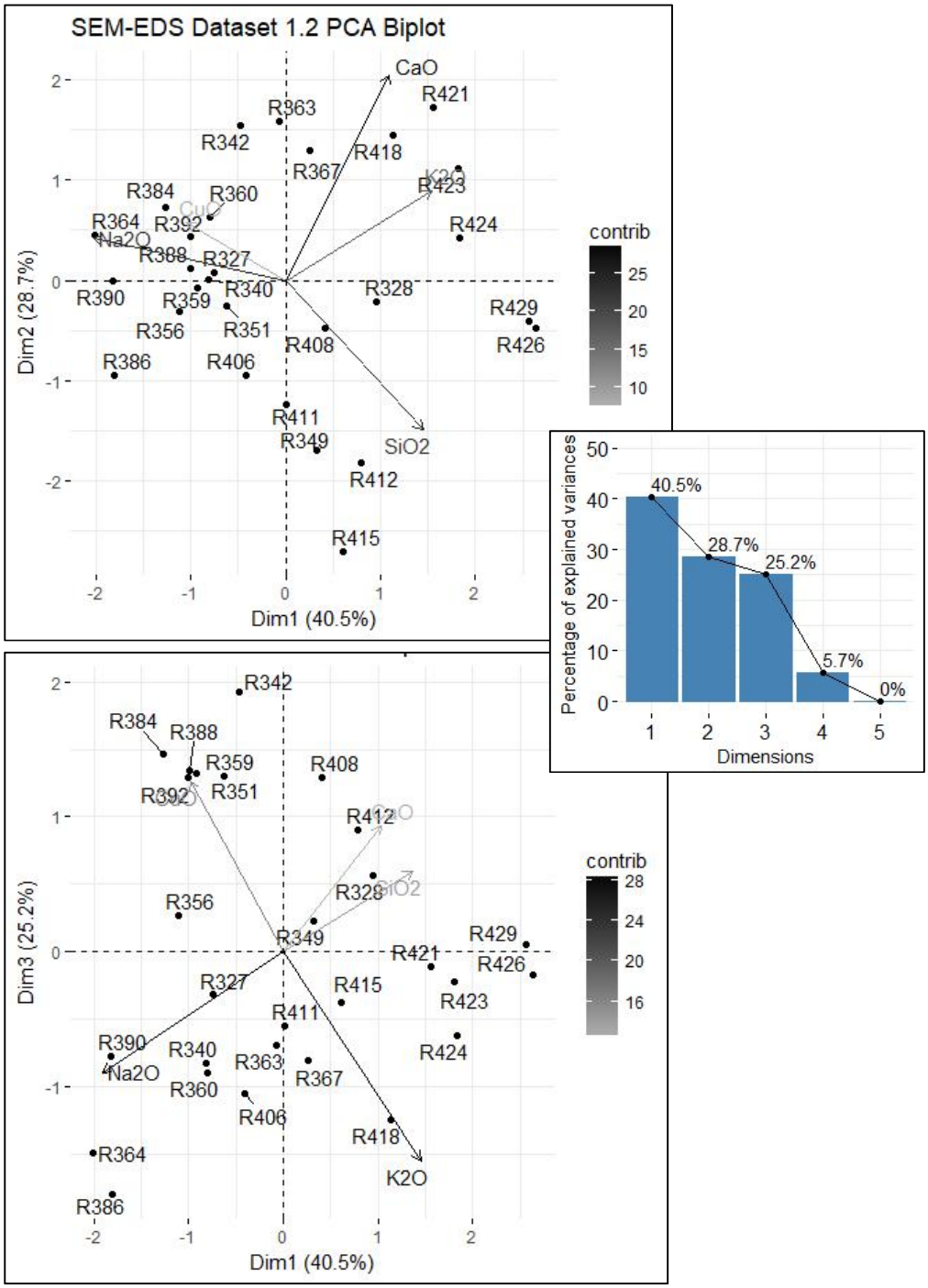

Fig. 9-10: Dataset 1.2 PCA biplots of components (a) 1 and 2, and (b) 1 and 3. A scree plot (c) is presented to exhibit that at least three components are required to reveal significant variance in the data. The biplots exhibit a cobalt colourant glaze 05 cluster and a disperse cluster composed of glazes 03 (copper colourant) and 07 (cobalt colourant).

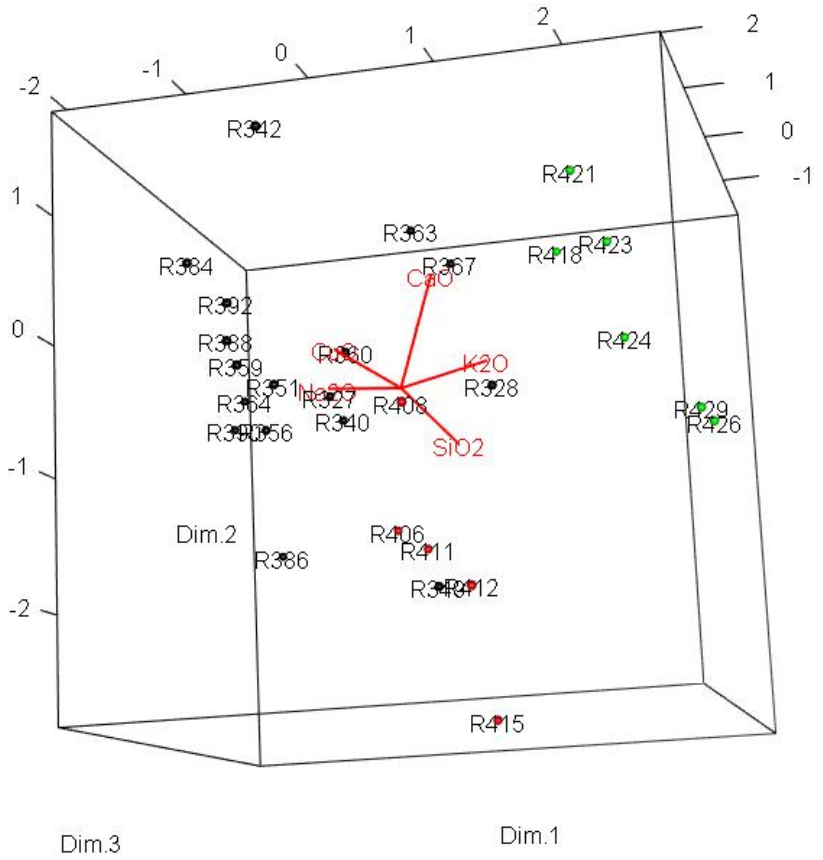

Fig. 9-11: A 3-dimensional representation of the first three components of the PCA results reveal more clarity than two biplots shown in the previous figure. This plot exhibits a cobalt colourant glaze 05 cluster (green) and a disperse cluster composed of glazes 03 (copper colourant, black) and 07 (cobalt colourant, red).

Table 9-5: Loadings, Eigenvalues and Variance for dataset 1.2. Components 1 through 3 represent 94.34% of the data variation and reveal most variance with NaO_2, CaO and K_2O, respectively.

Dataset 1.2 SEM-EDS PCA Loadings

Non-Rotated Results						Varimax Rotated Results					
	Dim.1	Dim.2	Dim.3	Dim.4	Dim.5		Dim.1	Dim.2	Dim.3	Dim.4	Dim.5
Na_2O	-0.62	0.15	-0.36	-0.24	0.64	Na_2O	-1				
SiO_2	0.44	-0.54	0.24	-0.03	0.68	SiO_2					1
K_2O	0.47	0.32	-0.63	0.49	0.20	K_2O			-1		
CaO	0.33	0.74	0.38	-0.39	0.21	CaO		1			
CuO	-0.32	0.21	0.51	0.74	0.22	CuO				1	

Dataset 1.2 Eigenvalues and Variance

	Eigenvalue	Variance %	Cumulative Variance %
Dim.1	1.61	40.47	40.47
Dim.2	1.14	28.66	69.13
Dim.3	1.01	25.22	94.34
Dim.4	0.23	5.66	100.00
Dim.5	0.00	0.00	100.00

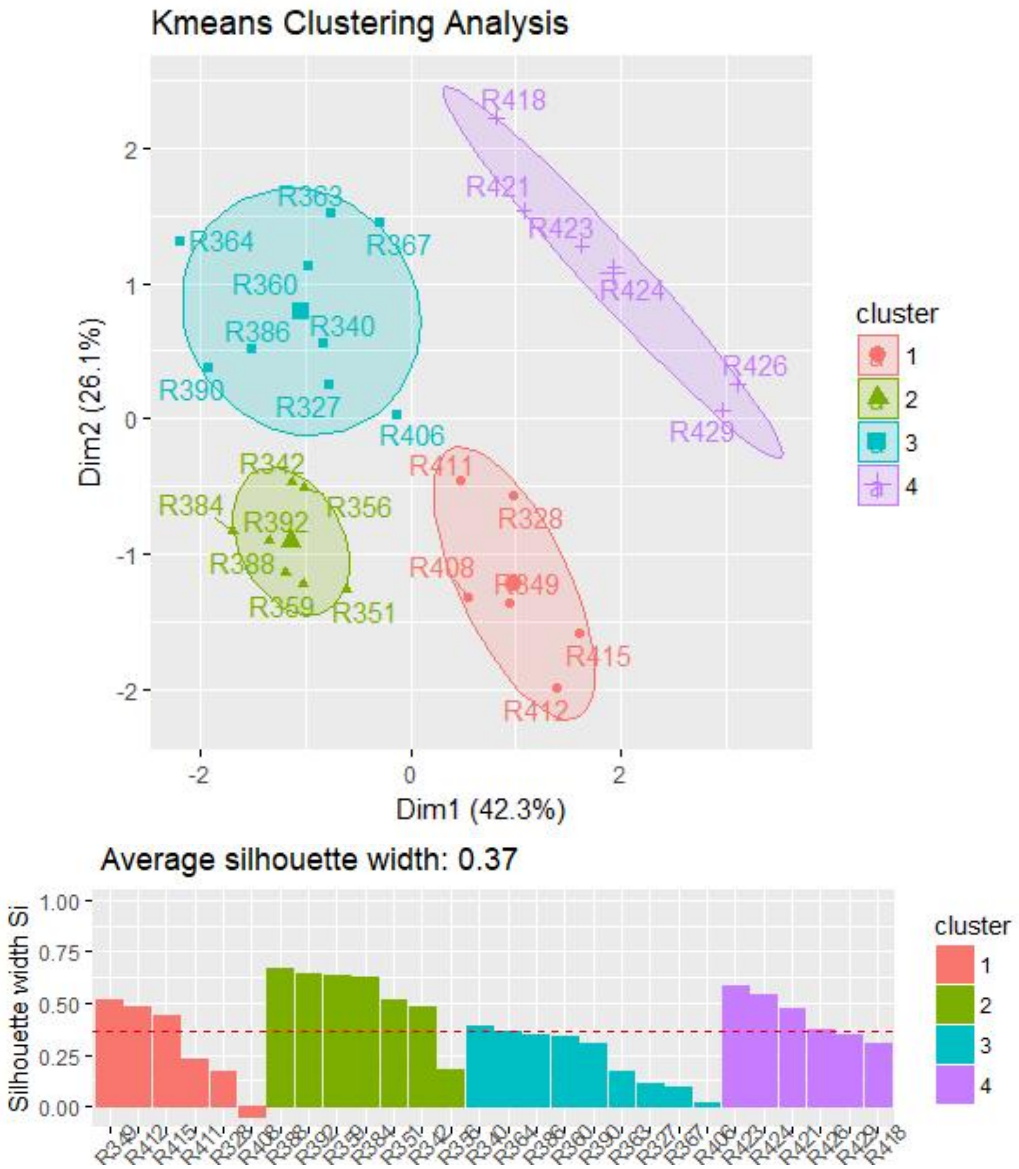

Fig. 9-12: K-means analysis and silhouette validation for dataset 1.2. K-means required an imputation of k=4 to accurately cluster cobalt colourant glaze 05. The other three clusters represent copper colourant glaze 03 (2 clusters) and cobalt colourant glaze 07. Glazes 03 and 07 are slightly intermixed in two of the three latter mentioned clusters.

exhibit the same cluster groupings. PCA tabulations reveal the Eigenvalues >1 for the first three components. These components exhibit significant variance (94.34%) for the dataset. The variables exhibiting greatest variance for each of the three components are Na_2O, CaO and K_2O, respectively.

The K-means analysis required the imputation of k=4 to accurately separate cobalt colourant glaze 05 from the other clusters. This is coercing the data into four groups of glazes when there are only three replicated glazes. It failed to accurately cluster cobalt colourant glaze 07 which includes some copper colourant glaze 03 samples. Most of the glaze 03 samples are divided into two clusters,

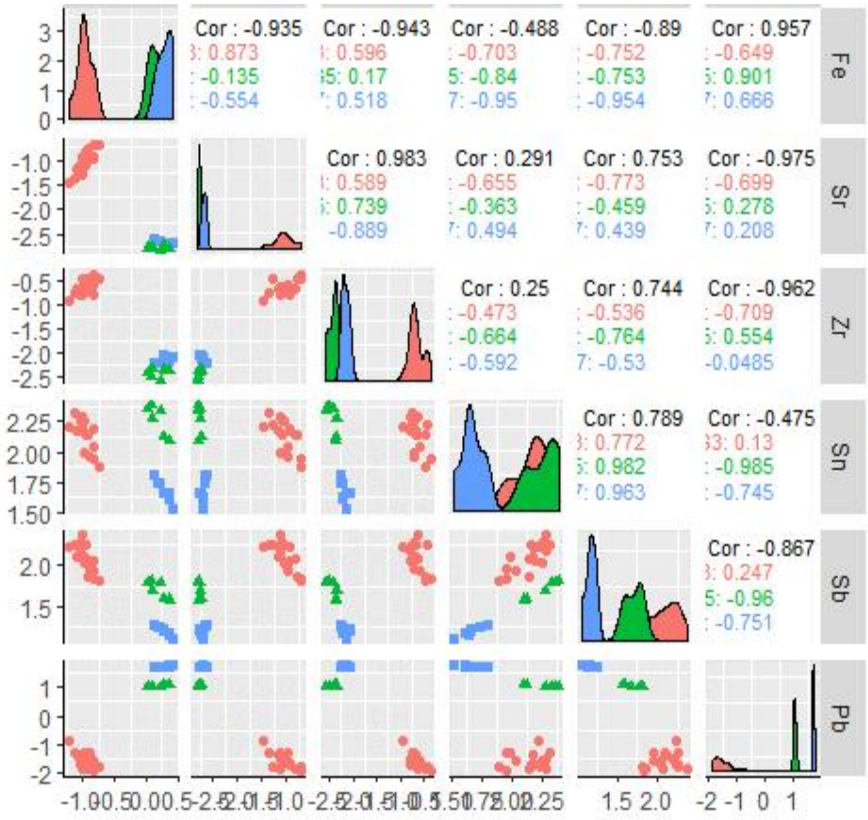

Fig. 9-13: Pairwise graph of centred logratio dataset 1.3R exhibiting bivariate plots, histogram and correlations of the variables.

one of which contains a glaze 07 sample. The bodies of most of the samples in cluster 03 were unfired (samples R363 and R367 were fired) before glazing whereas most of the sample bodies of cluster 02 underwent a bisque firing first (sample R356 did not). It is difficult to determine if these cluster assignments are based on this parameter or if it is a coincidence because of the presence of a few samples that did not fit the characteristics of most of the samples in each cluster.

9.2.3 Dataset 1.3R: HH-XRF 40 kV

The HH-XRF 40 kV MVS and pairwise results for dataset 1.3R (Table 9-6) exhibit the three replicated glazes clustered separately with no outliers. The pairwise plots reveal that all the selected variables contribute to defining clusters which correspond to the replicated glaze groups despite the copper and cobalt being absent. MVS analysis reveals the two clusters are most influenced by iron and aluminium contents. MVS analysis of dataset 1.1 (includes variable that meet criteria) failed to add information regarding clusters. The pairwise plots (Fig. 9-13) exhibit a medium to strong correlation with strontium and zirconium (Fig. 9-14), two elements that were not intentionally added to the replicate glaze suggesting that they are inclusions in the sand and/or

Table 9-6: Dataset 1.3R with reduced variable set for all replicated samples.

HH-XRF 40 kV (NPA) Faience Replicates Dataset 1.3R							
Parameters 40 kV, 30 uA and filter 3 for 180 seconds without vacuum							
10 Measurements per Sample							
Sample	Glaze	Fe	Sr	Zr	Sn	Sb	Pb
R327	G3	857	903	1054	20648	21983	452
R328	G3	860	683	1267	27435	25771	746
R340	G3	817	748	1068	23079	20938	527
R342	G3	908	848	1251	24420	24720	481
R349	G3	777	871	1047	16869	15830	329
R351	G3	841	961	1317	17743	13373	336
R356	G3	851	787	1071	21498	17369	489
R359	G3	809	923	1278	12909	11672	275
R360	G3	928	817	1221	18325	20581	708
R363	G3	856	898	1137	11874	11188	302
R364	G3	954	888	1155	16726	16618	639
R367	G3	982	865	1028	20016	17504	423
R383	G3	817	699	1035	14275	13077	383
R384	G3	823	728	1092	18409	20271	403
R386	G3	819	763	1256	21631	20311	634
R388	G3	887	686	1604	22986	23462	433
R390	G3	822	638	1098	25363	26087	1213
R392	G3	854	741	1239	22982	25050	363
R406	G7	20458	912	1605	60366	38912	76546
R408	G7	18817	845	1531	66842	40448	68622
R411	G7	19397	1119	1701	88574	53300	84430
R412	G7	21351	1009	1626	73549	46987	81786
R415	G7	16889	1075	1577	89158	51985	78376
R416	G7	17755	865	1734	70049	44273	70044
R418	G5	16405	695	1064	91588	54643	33606
R421	G5	18461	888	1128	151023	87671	40752
R423	G5	17803	1013	1316	176656	100394	43990
R424	G5	18239	907	1318	115003	68312	40880
R426	G5	17196	1006	1507	152008	84057	43835
R429	G5	17650	1077	1546	180906	103007	46035

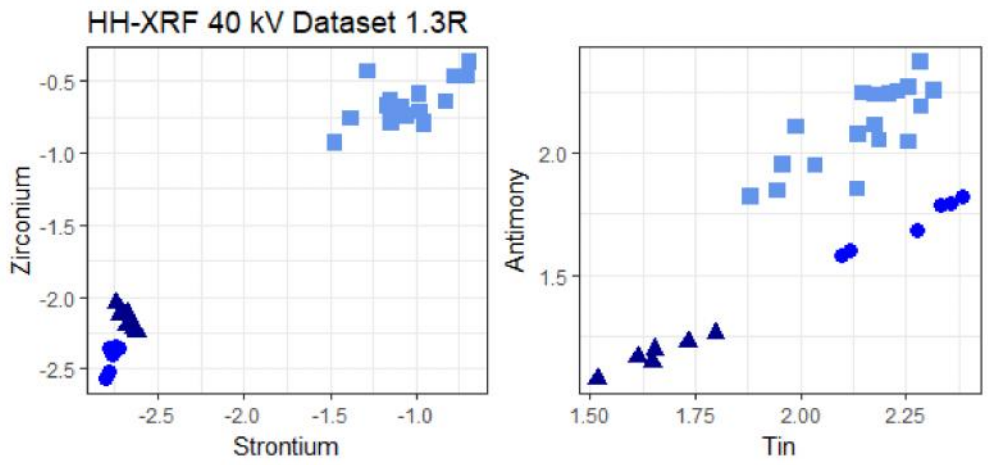

Fig. 9-14: Bivariate plots of strontium/zirconium and tin/antimony. Strontium and zirconium were not intentionally added to the glaze but are inclusions with another glaze component. Tin and antimony were intentionally added to the glaze. This would suggest use of scrap bronze as a colourant with archaeological faience glazes.

calcium glaze components. Tin and antimony (see Fig. 9-14) exhibit strong correlation. The tin/antimony relationship could indicate use of scrap leaded bronze with archaeological faience glazes. It only reveals a positive additive relationship with the replicated glazes which used CuO as colourant.

The PCA biplot (Fig. 9-15) exhibits the three glaze groups separated into distinct clusters. The loadings (Table 9-7) indicate the main cluster variance (component 1) is defined by the presence of lead and the absence of tin. This component separates the copper coloured glazes from the cobalt coloured glazes. Component 2 is defined by the absence of zirconium and the presence of tin. This component separates cobalt colourant glaze 05 from copper colourant glaze 03 and cobalt colourant glaze 07. The presence or absence of tin is important to the five components exhibited in Table 9-7. The HCA (Ward's Method) and K-means analysis (Fig. 9-16) each exhibit the three replicated glaze groups accurately assigned to clusters with an 80% confidence they are correctly assigned.

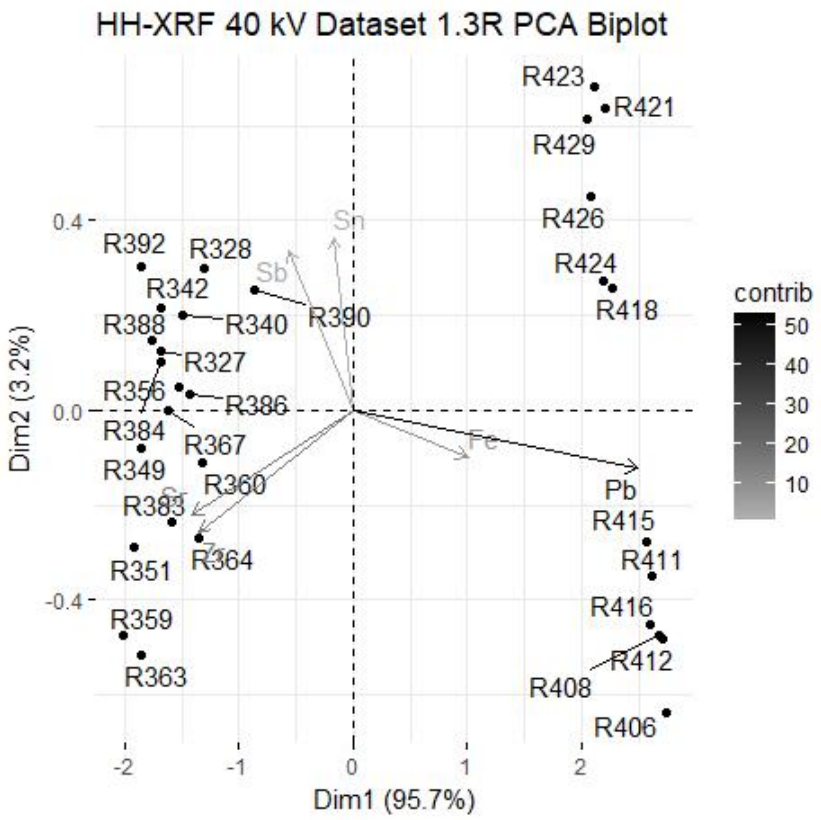

Fig. 9-15: Dataset 1.3 PCA biplots of components 1 and 2 representing 98.9% of the variance of the data. The biplots exhibit the three known glazes groups properly clustered.

Table 9-7: Loadings, Eigenvalues and variance for dataset 1.3R. Two components are required to exhibit 98.92% of the data variance. Using the varimax rotated results, component 1 variance is defined by the presence of lead and the absence of tin. Component 2 variance is defined by the absence of zirconium and the presence of tin.

Dataset 1.3R HH-XRF 40 kV PCA Loadings

Non-Rotated Results	Dim.1	Dim.2	Dim.3	Dim.4	Dim.5
Fe	0.30	-0.16	-0.77	-0.32	-0.15
Sr	-0.42	-0.36	-0.15	0.71	-0.10
Zr	-0.40	-0.41	0.35	-0.58	0.22
Sn	-0.05	0.59	-0.10	0.10	0.68
Sb	-0.17	0.54	0.22	-0.11	-0.67
Pb	0.74	-0.20	0.46	0.20	0.02

Varimax Rotated Results	Dim.1	Dim.2	Dim.3	Dim.4	Dim.5
Fe	-0.12	0.12	-0.88	-0.12	0.12
Sr	-0.12	0.12	0.12	0.88	0.12
Zr	-0.12	-0.88	0.12	-0.12	0.12
Sn	-0.41	0.41	0.41	-0.41	0.41
Sb	-0.12	0.12	0.12	-0.12	-0.88
Pb	0.88	0.12	0.12	-0.12	0.12

Dataset 1.3R Eigenvalues and Variance

	Eigenvalue	Variance %	Cumulative Variance %
Dim.1	3.91	95.69	95.69
Dim.2	0.13	3.23	98.92
Dim.3	0.03	0.78	99.70
Dim.4	0.01	0.22	99.92
Dim.5	0.00	0.08	100.00
Dim.6	0.00	0.00	100.00

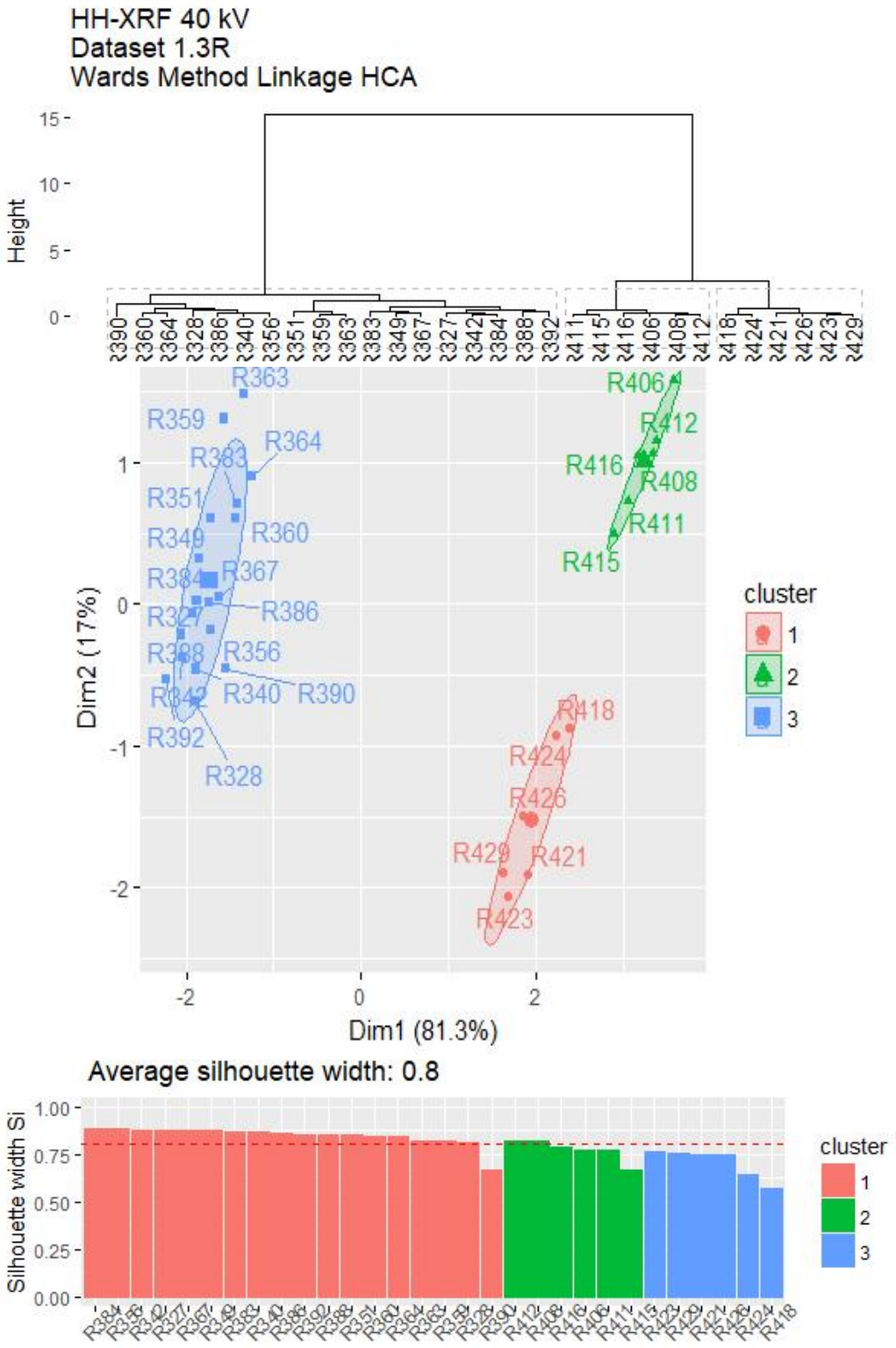

Fig. 9-16: HCA (Ward's Method) and K-means analysis has accurately defined three clusters representing the three replicated glaze groups. The shared silhouette plot exhibits the groups clustered with 80% confidence that they are correctly assigned.

9.3 Dataset 2 Multivariate Analysis (Copper Coloured Samples)

Dataset 2 consists of analytical results for copper coloured replicate glazes. It shares the same variable set as dataset 1 (see Table 9-1; Table 9-8).

9.3.1 Dataset 2.1R: HH-XRF 15 kV

No outliers were identified for dataset 2.1R. HCA (Single Linkage) identified four potential outliers (R356, R359, R384 and R388) but these were not substantiated with the PCA biplot, pairwise plot nor the variable boxplots. Sample R388 was identified as a potential outlier with the phosphorus boxplot but is more likely the tail of the data. No distinct clusters exist within the data and the data points are almost evenly spread across the various plots. Dataset 2.1 with the full variable set was examined through MVS but failed to provide additional information regarding clusters.

The pairwise plot (Fig. 9-17) exhibits very little clustering with the data points. The highest correlation is a negative relationship between aluminium and phosphorus (R^2 = -0.68). Small cluster seeds are evident with phosphorus/chromium, phosphorus/iron and chromium/iron relationships (Fig. 9-18) but whether this has greater implications or is a product of coincidence is hard to determine. Body condition before glazing (bisque fired, unfired) was not responsible as the samples were mixed.

The PCA biplot (Fig. 9-19) for dataset 2.1R exhibits data points spread across the plot field with no clusters. The majority of the samples are on a gradient from low to high titanium/phosphorus components and high to low chromium/aluminium components. The four samples identified by HCA (single linkage) are outside of this general gradient: R359 with high chromium and low titanium, R356 with high chromium/phosphorus and low aluminium/titanium, and R384 and R388 with high aluminium/titanium and low chromium/phosphorus. The first two components represent 77.72% of the data variance and are influenced most by aluminium and chromium, respectively (Table 9-9).

The HCA dendrogram (Ward's Method) (Fig. 9-20) exhibits two large copper colourant glaze 03 clusters but this is mainly due to the bootstrapping algorithm not having identified a distinct k, and k being set to 2 as a consequence. The failure of bootstrapping to identify clusters is further evidence that there are no clusters within the data. The low sil width is a result of a lack of clusters in the data.

The K-means analysis (Fig. 9-21) produced similar results to HCA. A review of the firing parameters for the two clusters revealed with the K-means biplot reveal that

Table 9-8: Dataset 2.1R with the reduced variable set for copper coloured replicated samples.

HH-XRF 15 kV (NPA) Faience Replicates Dataset 2.1R						
Parameters 15 kV, 50 uA with a vacuum for 180 seconds (no filter)						
10 Measurements per Sample						
Sample	Glaze	Al	P	Ti	Cr	Fe
R327	G3	18889	2756	5329	8234	37038
R328	G3	15156	2823	5844	7963	36545
R340	G3	13424	2970	4533	6948	35222
R342	G3	14851	2954	4615	6722	37015
R349	G3	21019	2697	4317	8919	34303
R351	G3	12813	1719	4183	6936	27336
R356	G3	13458	2966	4451	9575	37923
R359	G3	15926	2736	4188	9640	32886
R360	G3	14633	2953	5121	6087	34546
R363	G3	23326	2762	4146	7882	37659
R364	G3	16543	2922	4665	6779	38915
R367	G3	21072	2827	4944	7919	34414
R383	G3	19620	2754	4516	7563	36652
R384	G3	16511	1807	4308	5861	33637
R386	G3	16330	2852	5129	8185	34053
R388	G3	17743	1678	4556	5437	29961
R390	G3	12858	2984	4950	6740	32715
R392	G3	18707	2740	4926	7871	36668

cluster 1 is mostly composed of bisque fired body samples and cluster 2 is of mostly unfired bodies before glazing. Both clusters contained three samples that did not fit this relationship. It is difficult to determine if these firing parameters had an effect on cluster assignments or if it is coincidence.

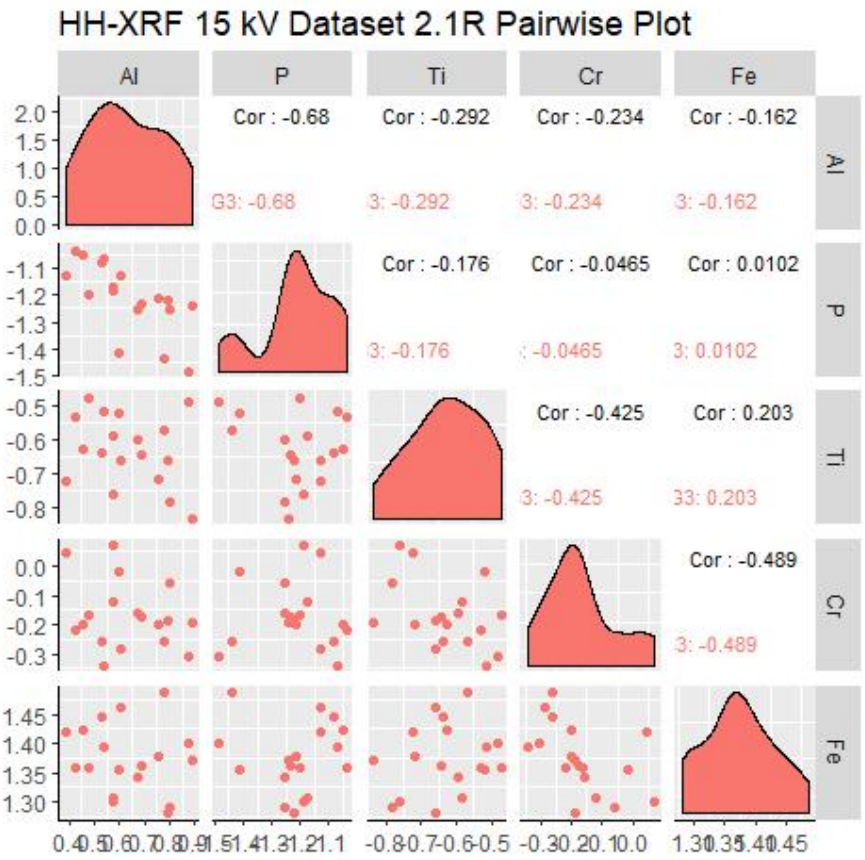

Fig. 9-17: Pairwise graph of centred logratio dataset 2.1R exhibiting bivariate plots, histogram and correlations of the variables.

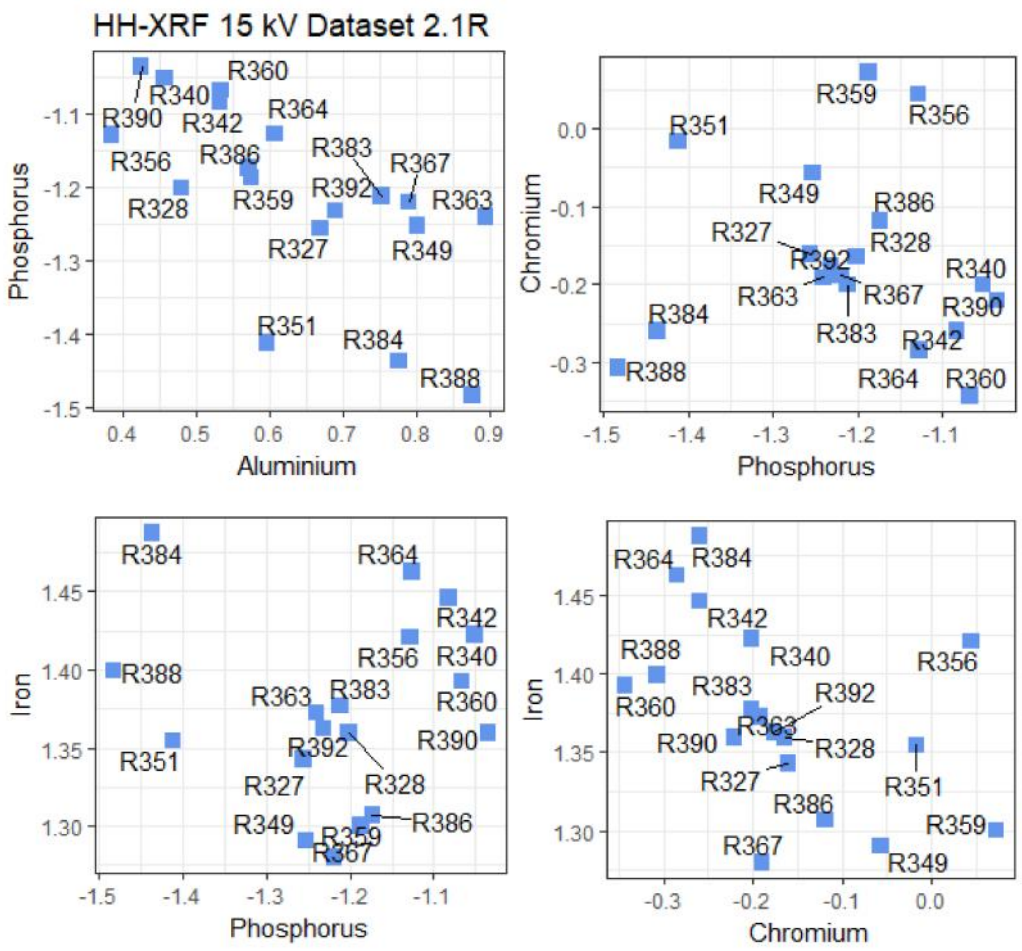

Fig. 9-18: Bivariate plots of select element pairings. Aluminium and phosphorous exhibit a negative correlation (R^2 = -0.68) although the removal of R351, R384 and R388 (outliers for this pairing) increase the correlation (R^2 = -0.761). The three other biplots (chromium/phosphorus, iron/phosphorus and chromium/iron) exhibit seedlings of clusters are probably a result of coincidence.

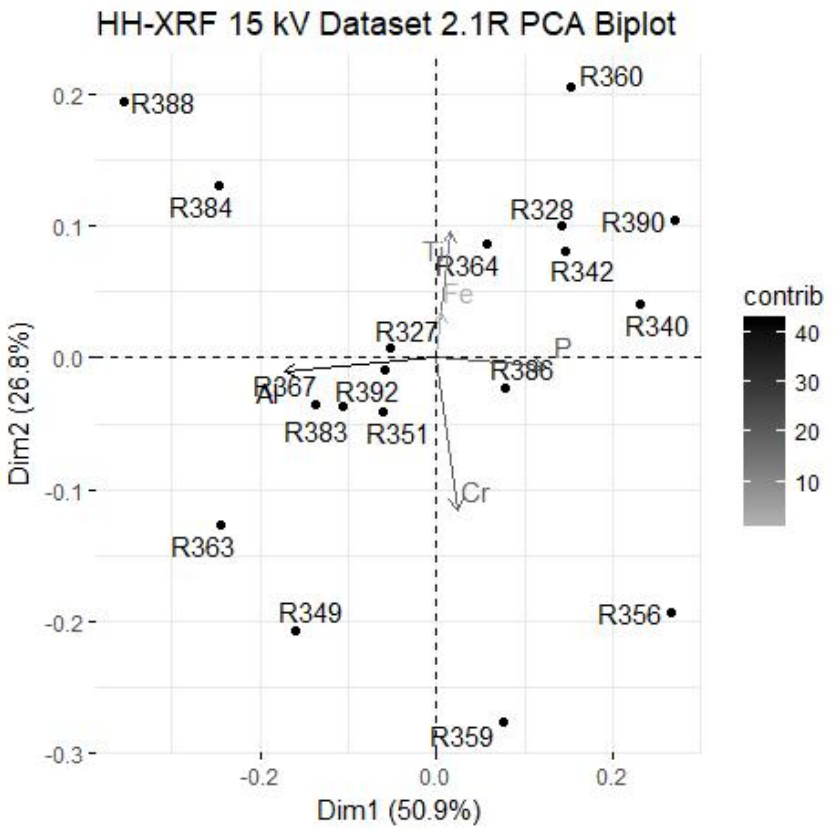

Fig. 9-19: Dataset 2.1R PCA biplot of components 1 and 2. There is a lack of distinct clustering which is reflective of the sample set consisting of the same glaze.

Table 9-9: Loadings, Eigenvalues and Variance for dataset 2.1R. Aluminium and chromium explain most of the variance in components 1 and 2, respectively. Titanium has moderate variance through all the components.

Dataset 2.1R HH-XRF 15 kV PCA Loadings

Non-Rotated Results	Dim.1	Dim.2	Dim.3	Dim.4	Dim.5
Al	-0.80	-0.06	0.33	0.21	
P	0.58	-0.04	0.62	0.29	
Ti	0.08	0.62	-0.53	0.36	
Cr	0.11	-0.75	-0.48	0.01	
Fe	0.03	0.23	0.06	-0.86	

Varimax Rotated Results	Dim.1	Dim.2	Dim.3	Dim.4	Dim.5
Al	-0.86	0.14	-0.14	0.14	
P	0.14	0.14	0.86	0.14	
Ti	0.45	0.45	-0.45	0.45	
Cr	0.14	-0.86	-0.14	0.14	
Fe	0.14	0.14	-0.14	-0.86	

Dataset 2.1R Eigenvalues and Variance

	Eigenvalue	Variance %	Cumulative Variance %
Dim.1	0.03	50.92	50.92
Dim.2	0.02	26.81	77.72
Dim.3	0.01	17.42	95.15
Dim.4	0.00	4.85	100.00
Dim.5	0.00	0.00	100.00

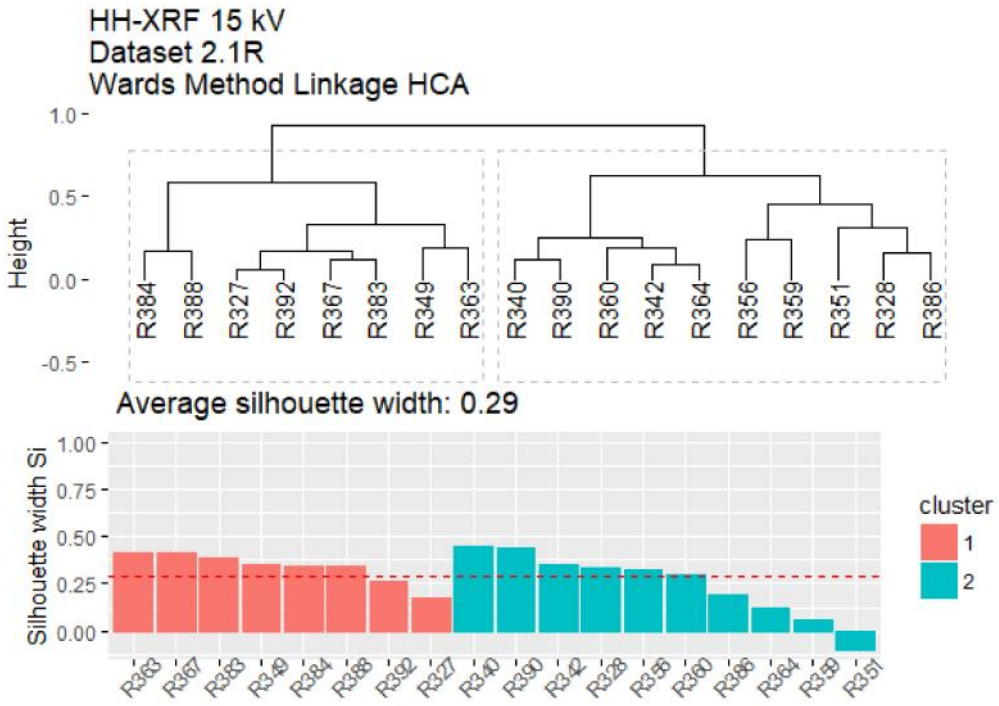

Fig. 9-20: HCA (Ward's Method) of dataset 2.1R. The copper colourant glaze 03 samples have been coerced into 2 insignificant subclusters. The low sil width indicates the samples have been assigned to the clusters with low confidence they are correctly assigned. Sample R351 exhibits ~10% confidence that the sample has been incorrectly assigned.

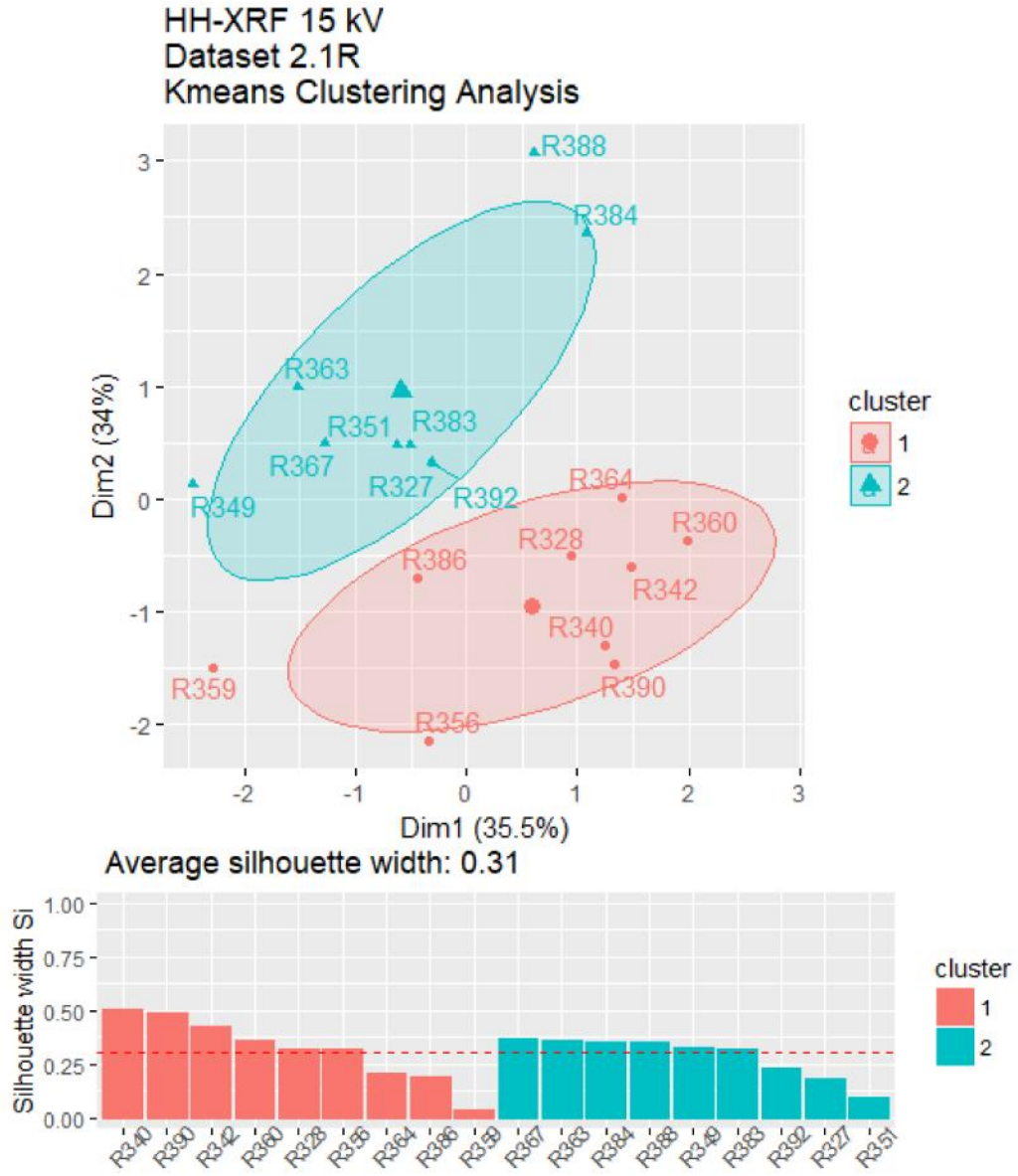

Fig. 9-21: The K-means of dataset 2.1R have clustered the samples differently than the HCA. The sil width is still low with 31% confidence that the samples are correctly assigned. The clusters are most likely insignificant and the data may represent a single cluster.

9.3.2 Dataset 2.2: SEM-EDS

MVS and pairwise plots of Dataset 2.2 (Table 9-10) exhibit two possible clusters within the copper colourant glaze 03 group. HCA (single linkage) reveals three potential outliers (R363, R367 and R383). The PCA biplot reveals samples R328 and R342 as potential outliers. Boxplots reveal outliers for Na_2O (R383), SiO_2 (R349 and R383) and CaO (R342). A review of all the data indicates that R328, R363 and R367 are tails of the data and will be retained for further analysis of this dataset. Samples R342, R349 and R383 are outliers and will be removed from further analysis of this dataset.

Table 9-10: Dataset 2.2 with the full variable set for copper coloured replicated samples.

SEM-EDS (wt%) Faience Replicates Dataset 2.2						
Normalized Data; Parameters 20 kV, 3 Measurements per Sample						
Sample	Glaze	Na_2O	SiO_2	K_2O	CaO	CuO
R327	G3	18.28	70.19	2.14	5.71	3.68
R328	G3	14.73	72.64	2.59	5.88	4.17
R340	G3	18.57	69.93	2.42	5.42	3.67
R342	G3	16.58	69.92	1.65	7.11	4.75
R349	G3	15.68	73.67	2.00	5.06	3.59
R351	G3	16.77	71.60	1.42	6.01	4.20
R356	G3	18.35	70.66	1.58	5.67	3.74
R359	G3	17.09	71.09	1.43	5.97	4.41
R360	G3	19.04	69.17	2.44	5.86	3.49
R363	G3	17.39	68.75	3.32	6.12	4.43
R364	G3	21.07	67.86	2.25	5.34	3.48
R367	G3	16.97	69.36	3.40	6.02	4.26
R383	G3	22.49	64.81	3.00	5.09	4.61
R384	G3	17.62	69.86	1.48	6.31	4.73
R386	G3	20.32	69.56	2.31	4.44	3.37
R388	G3	17.13	70.78	1.51	6.00	4.58
R390	G3	19.91	68.96	2.05	5.22	3.86
R392	G3	17.18	70.35	1.65	6.10	4.71

The pairwise plot for dataset 2.2 (Fig. 9-22) exhibits the highest correlations for SiO_2/Na_2O (R^2 = -0.784), CaO/Na_2O (R^2 = -0.712), CuO/Na_2O (R^2 = -0.697) and CuO/CaO (R^2 = 0.776). Disperse clusters are exhibited for variable relationships including all CuO associations, Na_2O/K_2O and SiO_2/K_2O. Bivariate plots of these relationships (Fig. 9-23) exhibits two disperse clusters that are defined by the firing condition of the body. These clusters reveal that alkalis (sodium and potassium) could be entering the glaze from non-bisque bodies during glost firing. The alkalis are mostly locked into the partially melted grains of bodies that underwent a bisque firing and cannot migrate into the glaze during glost firing of the samples. The bivariate plots exhibit the three potential outliers (R328, R363 and R367) retained for the MVS analysis.

The PCA biplot (Fig. 9-24) exhibits two clusters, one distinct and one disperse, and three outliers (R328, R363 and R367). The three-dimensional PCA plot reveals that the disperse cluster is actually composed of two sub-clusters: one defined by high Na_2O and the other by high alkali combination (Na_2O and K_2O). The three-dimensional plot exhibits sample R386 which could be either part of one sub-cluster or an outlier to all the clusters. The loadings (Table 9-11) indicate that the two components are

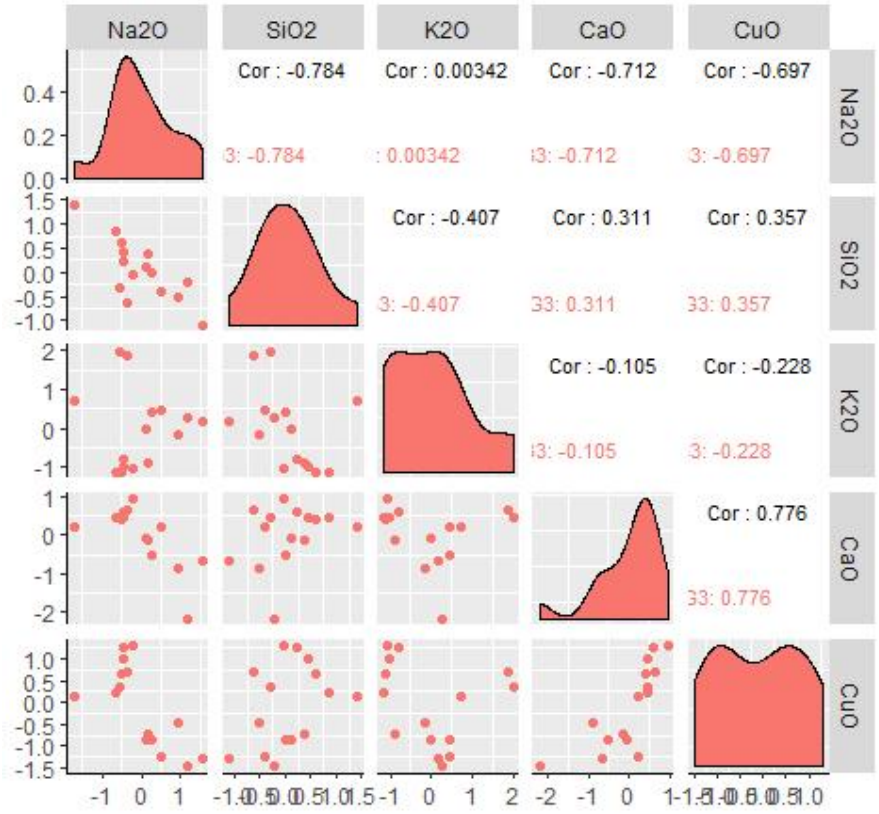

Fig. 9-22: Pairwise plot of standardized dataset 2.2 exhibiting two disperse clusters for all CuO pairings, Na_2O/K_2O and SiO_2/K_2O

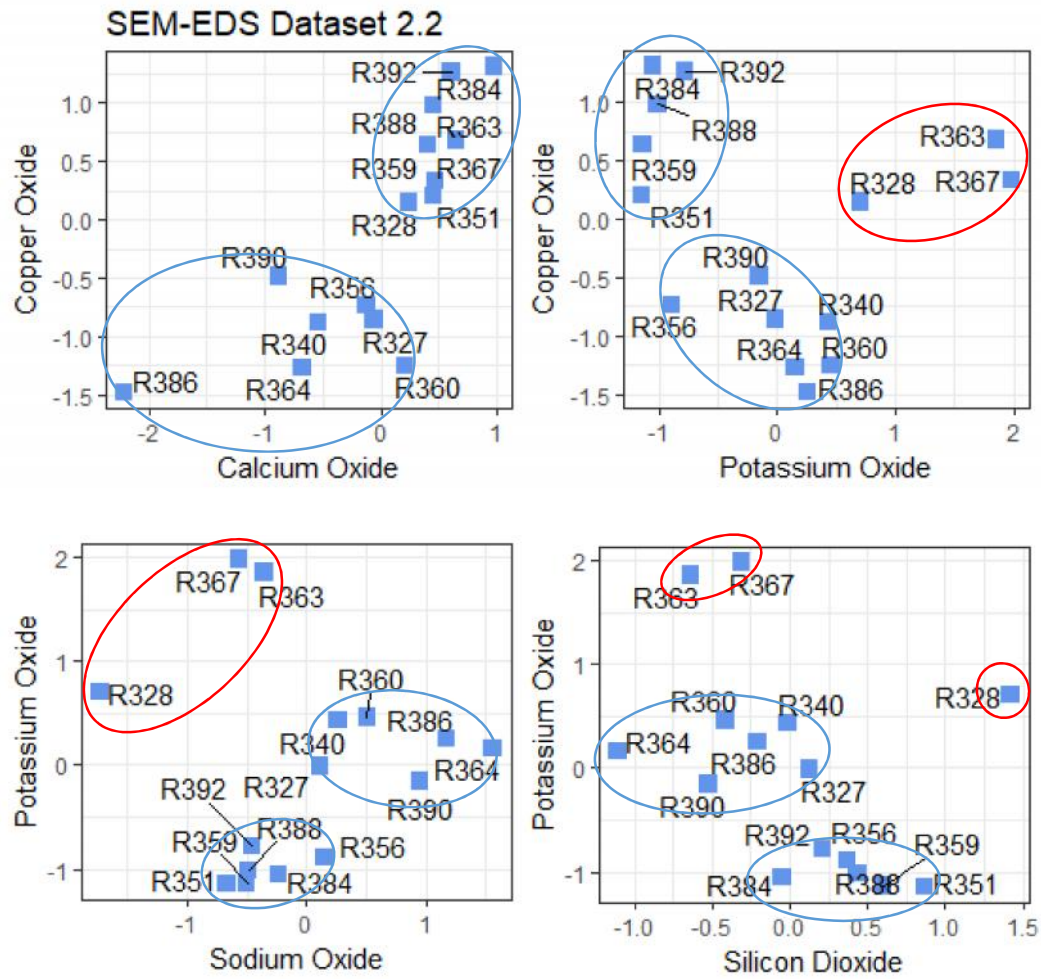

Fig. 9-23: Bivariate plots for CaO/CuO, K_2O/CuO, Na_2O/K_2O and SiO_2/K_2O exhibiting two disperse clusters (blue circles) and three outliers (circled in red) to those clusters (R328, R363 and R367).

influenced most by CuO and K_2O variables, respectively. The two PCA components represent 83.42% of the total data variance.

The HCA (Ward's Method) reveals three clusters and three outliers (R328, R363 and R367). The three clusters are the same identified with the three-dimensional PCA analysis. However, this exhibits sample R386 as a part of a cluster with samples R364 and R390. This highlights the problem of incorrectly perceiving patterns in the PCA data which is not designed to reveal clusters. The K-means analysis biplot exhibits the same clusters as HCA. HCA and the K-means analysis share the same sample assignments and therefore, share the same silhouette graph. The silhouette graph exhibits a 46% confidence that the samples have been correctly assigned to clusters. The clusters revealed in the HCA and K-means analysis are defined by the firing parameter. Clusters 1 and 2 are composed of samples that were unfired before glazing. Clusters 3, 4 and 5 contain samples that were bisque fired before glazing.

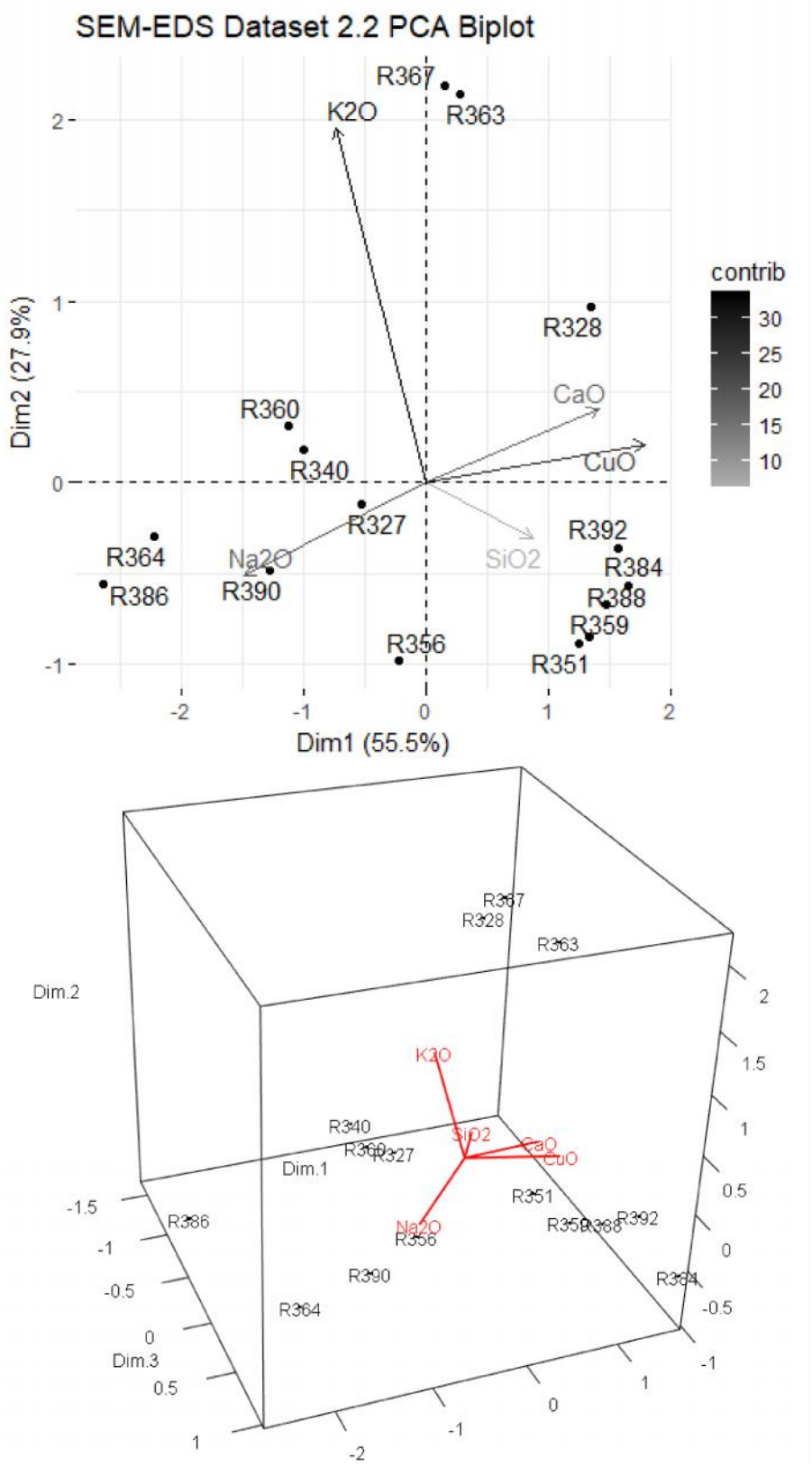

Fig. 9-24: PCA analysis of dataset 2.2. The PCA biplot exhibits two clusters: one distinct and one disperse. The 3D PCA plot exhibits that the disperse cluster is actually two subclusters.

Table 9-11: Loadings, Eigenvalues and Variance for dataset 2.2. CaO and K_2O explain most of the variance in components 1 and 2, respectively. The two components explain 83.42% of the variance in the data.

Dataset 2.2 SEM-EDS PCA Loadings

Non-Rotated Results	Dim.1	Dim.2	Dim.3	Dim.4	Dim.5
Na_2O	-0.50	-0.25	0.48	0.00	0.67
SiO_2	0.29	-0.15	-0.68	-0.05	0.66
K_2O	-0.25	0.93	-0.09	-0.10	0.22
CaO	0.48	0.19	0.31	0.77	0.20
CuO	0.61	0.10	0.45	-0.62	0.17

Varimax Rotated Results	Dim.1	Dim.2	Dim.3	Dim.4	Dim.5
Na_2O					1
SiO_2			-1		
K_2O		1			
CaO				1	
CuO	1				

Dataset 2.2 Eigenvalues and Variance

	Eigenvalue	Variance %	Cumulative Variance %
Dim.1	1.92	55.48	55.48
Dim.2	0.96	27.94	83.42
Dim.3	0.42	12.17	95.59
Dim.4	0.15	4.41	100.00
Dim.5	0.00	0.00	100.00

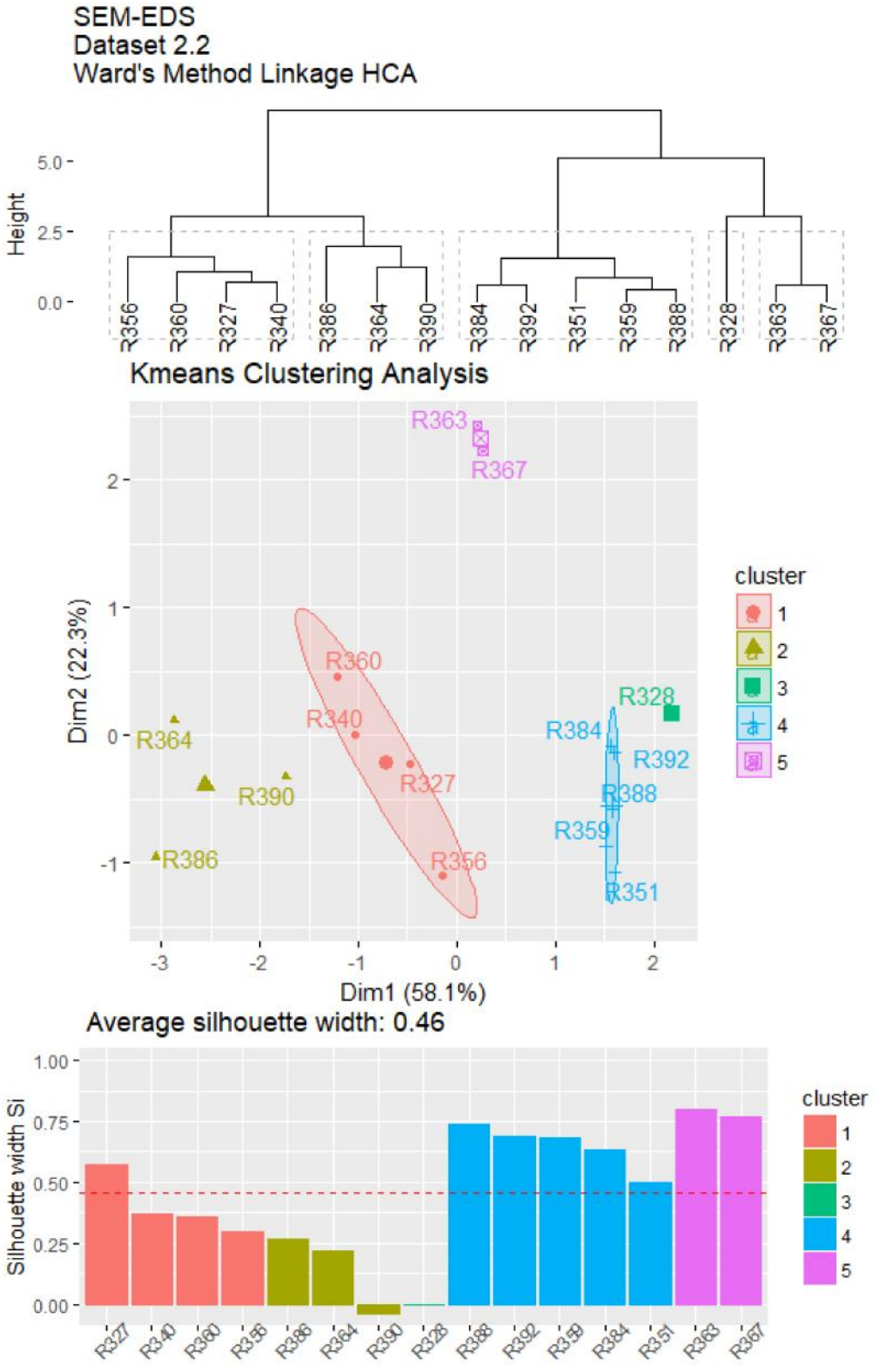

Fig. 9-25: HCA (Ward's Method), K-means analysis and the associated silhouette graph for both methods. The silhouette graph indicates a 46% confidence that the samples have been correctly assigned to clusters.

9.3.3 Dataset 2.3R: HH-XRF 40 kV

The HCA (single linkage), PCA biplot and the strontium boxplot identified sample R390 as an outlier for dataset 2.3R (Table 9-12). A review of the pairwise plot reveals R390 as a possible outlier with lead but not strontium. However, the boxplot for lead reveals R390 as a tail of the data. MVS was applied to the dataset with and without R390 but both set of results indicate that there are no clusters within this dataset. Sample R390 was retained for further analysis with this dataset. Dataset 2.3 with the full variable compliment was examined but failed to add any additional information.

The pairwise plot (Fig. 9-26) for dataset 2.3R exhibits several moderate and high correlations for element pairings. These relationships are readily visible with each of the bivariate plots (see Fig. 9-26; Fig. 9-27) but no clusters are apparent. The PCA analysis and three-dimensional PCA plot (see Fig. 9-27) failed to reveal clustering. The PCA loadings (Table 9-13) for components 1 and 2 indicate lead and antimony as the main influence on those components, respectively. The first two PCA components explain 90.46% of the total data variance.

Table 9-12: Dataset 2.3R with the reduced variable set for copper coloured replicated samples.

HH-XRF 40 kV (NPA) Faience Replicates Dataset 2.3R							
Parameters 40 kV, 30 uA and filter 3 for 180 seconds without vacuum							
10 Measurements per Sample							
Sample	Glaze	Fe	Sr	Zr	Sn	Sb	Pb
R327	G3	857	903	1054	20648	21983	452
R328	G3	860	683	1267	27435	25771	746
R340	G3	817	748	1068	23079	20938	527
R342	G3	908	848	1251	24420	24720	481
R349	G3	777	871	1047	16869	15830	329
R351	G3	841	961	1317	17743	13373	336
R356	G3	851	787	1071	21498	17369	489
R359	G3	809	923	1278	12909	11672	275
R360	G3	928	817	1221	18325	20581	708
R363	G3	856	898	1137	11874	11188	302
R364	G3	954	888	1155	16726	16618	639
R367	G3	982	865	1028	20016	17504	423
R383	G3	817	699	1035	14275	13077	383
R384	G3	823	728	1092	18409	20271	403
R386	G3	819	763	1256	21631	20311	634
R388	G3	887	686	1604	22986	23462	433
R390	G3	822	638	1098	25363	26087	1213
R392	G3	854	741	1239	22982	25050	363

HCA (Ward's Method) bootstrapping failed to reveal any clusters. A k of 3 was entered into the algorithm to indicate three clusters as observed by the analyst (Fig. 9-28). The clusters are not defined by body condition before firing; sample bodies were mixed bisque and unfired before glazing. The silhouette graph indicates a 28% confidence that the samples are correctly assigned to clusters. Some of the samples exhibit a probability for being incorrectly assigned. For instance, sample R356 exhibits a ~25% confidence that the sample is incorrectly assigned.

The K-means analysis (Fig. 9-29) used three clusters (k=3) as determined through HCA. The silhouette graph exhibits a 31% confidence that the samples are correctly assigned to clusters. The clusters do not appear to be defined by firing parameter as the sample bodies were mixed bisque and unfired before glazing. The HCA and K-means analysis failed to share the same cluster sample composition. This disparity may indicate that no clusters exist in this dataset.

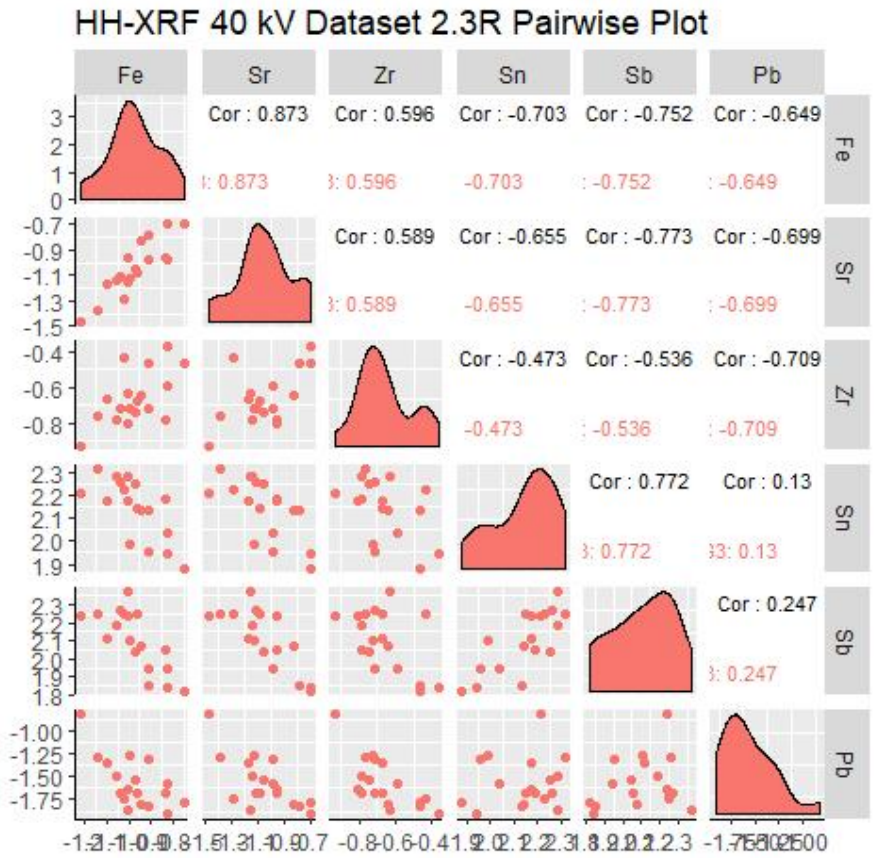

Fig. 9-26: Pairwise graph of centred logratio dataset 2.3R exhibiting bivariate plots, histogram and correlations of the variables.

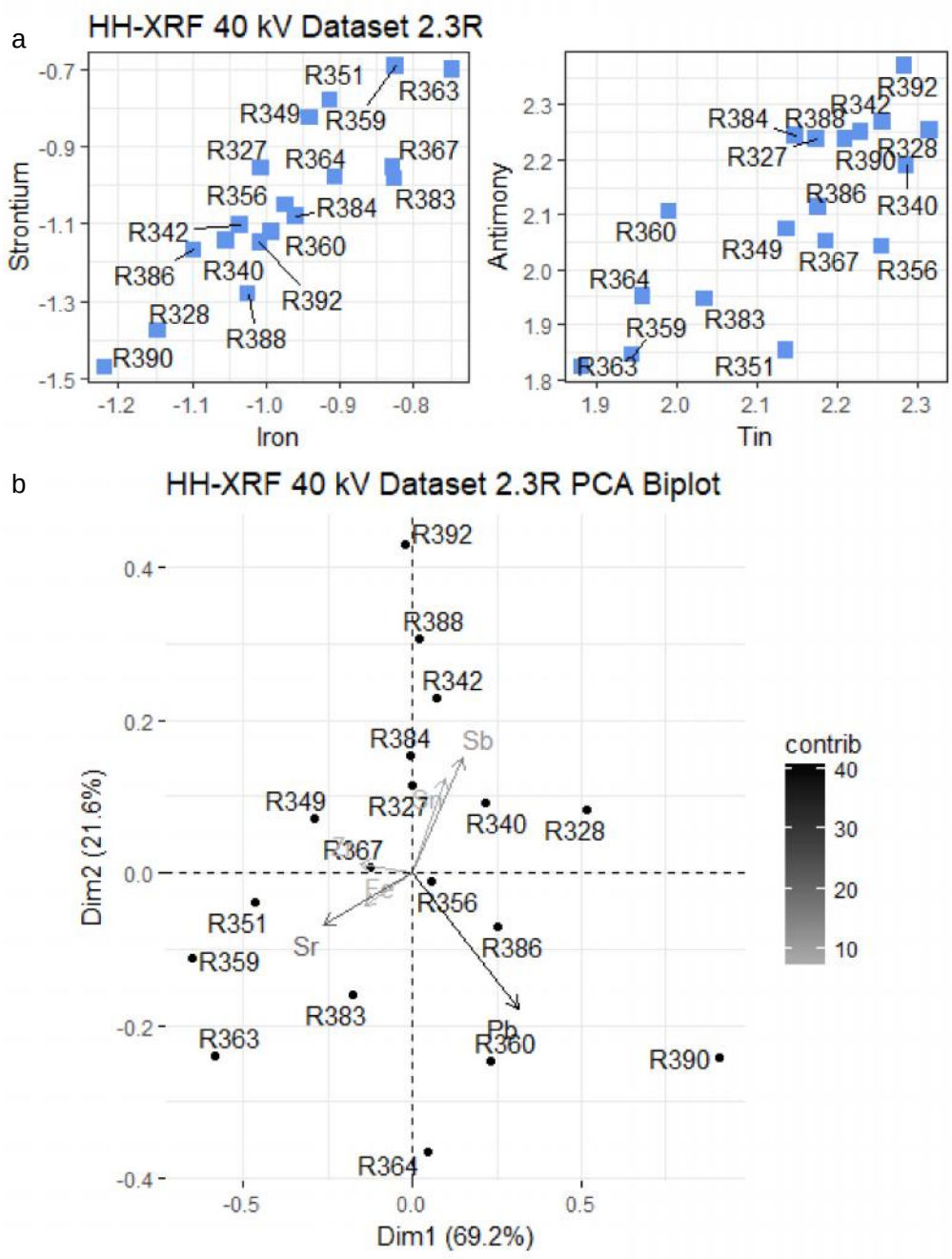

Fig. 9-27: Bivariate plots (a) of iron/strontium (R2=0.873) and tin/antimony (R2=0.772). No cluster is visible but there is a relationship between the variables. The PCA biplot (b) exhibits no clustering.

Table 9-13: Loadings, Eigenvalues and Variance for dataset 2.3R. Lead and antimony explain most of the variance in components 1 and 2, respectively. The two components explain 90.46% of the variance in the data.

Dataset 2.3 H-XRF 40 kV PCA Loadings

	Non-Rotated Results					Varimax Rotated Results					
	Dim.1	Dim.2	Dim.3	Dim.4	Dim.5		Dim.1	Dim.2	Dim.3	Dim.4	Dim.5
Fe	-0.18	-0.09	0.08	-0.09	0.51	Fe	-0.16	-0.37	0.20	-0.13	0.31
Cu	-0.25	-0.11	0.10	-0.45	0.25	Cu	-0.16		0.17	-0.47	0.25
Zn	-0.26	-0.08	0.10	-0.13	0.08	Zn	-0.15	-0.13		-0.25	
Sr	-0.41	-0.16	0.38	0.40	-0.58	Sr					-0.90
Zr	-0.19	0.12	-0.88	0.11	-0.16	Zr			-0.93		
Sn	0.28	0.46	0.14	0.60	0.38	Sn	-0.20	-0.14	0.19	0.83	0.14
Sb	0.37	0.53	0.15	-0.48	-0.40	Sb		0.90	0.11		0.11
Pb	0.65	-0.66	-0.07	0.06	-0.08	Pb	0.93				

Dataset 2.3 Eigenvalues and Variance

	Eigenvalue	Variance %	Cumulative Variance %
Dim.1	0.16	71.34	71.34
Dim.2	0.04	19.12	90.46
Dim.3	0.01	4.86	95.32
Dim.4	0.01	2.72	98.04
Dim.5	0.00	1.17	99.21
Dim.6	0.00	0.68	99.89
Dim.7	0.00	0.11	100.00
Dim.8	0.00	0.00	100.00

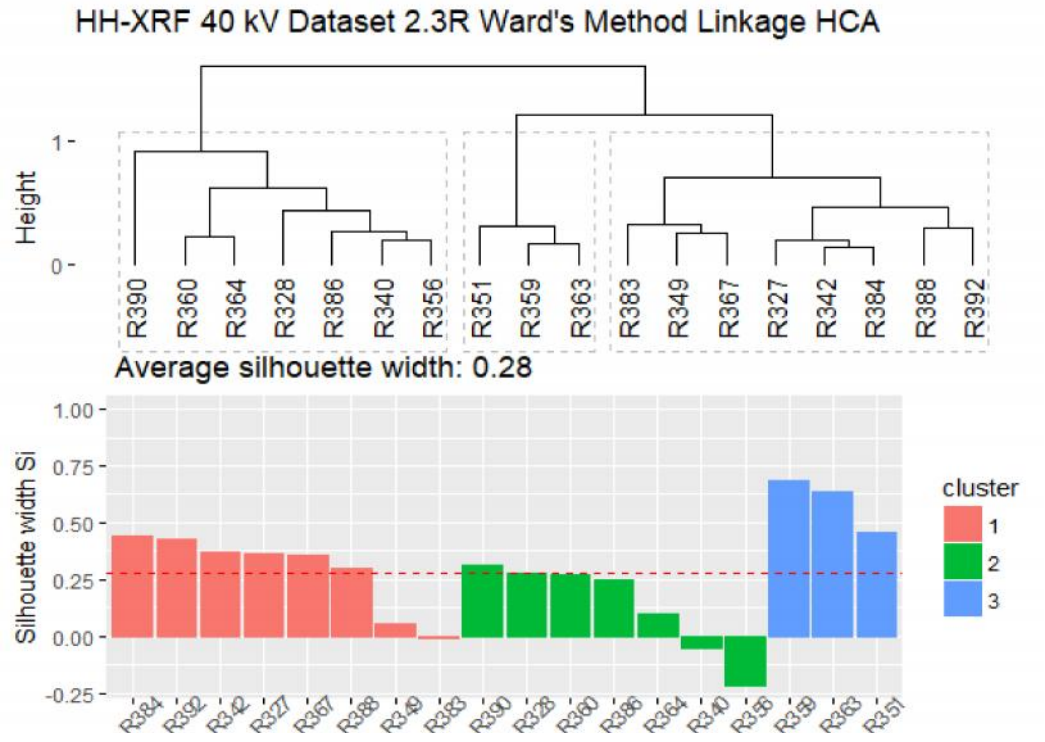

Fig. 9-28: HCA (Ward's Method) and the associated silhouette graph exhibit 28% confidence in cluster assignments for dataset 2.3R.

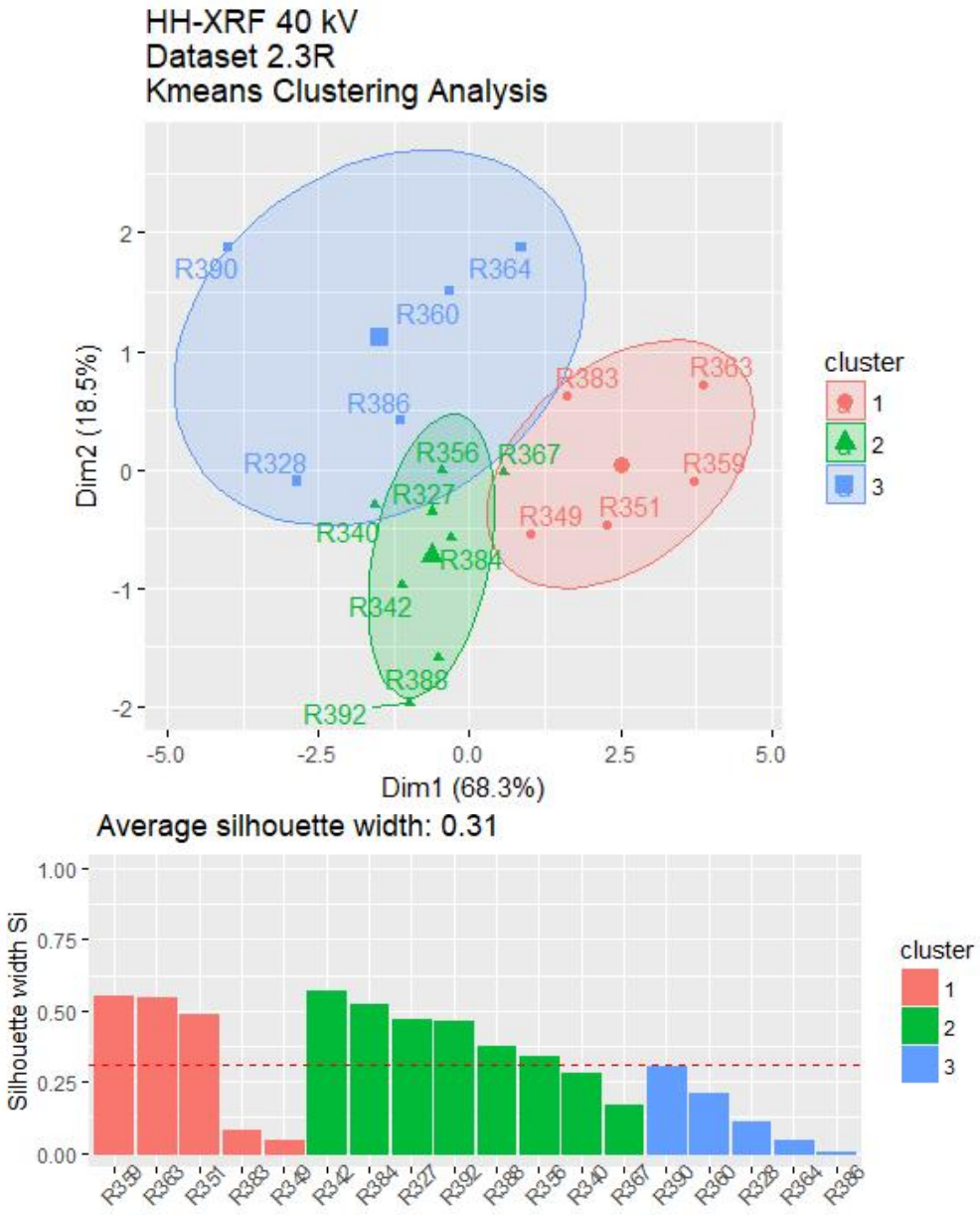

Fig. 9-29: K-means analysis and the associated silhouette graph for dataset 2.3R exhibiting a 31% confidence that the samples are assigned correctly.

9.4 Dataset 3 Multivariate Analysis (Cobalt Coloured Samples)

Cobalt blue replicate glazes contain a greater number of elements than the copper blue glazes. The variable set, as a consequence, is lower for dataset 3. Tables 9-14, 9-16 and 9-18 contain the data for datasets 3.1 (HH-XRF 15 kV), 3.2 (SEM-EDS) and 3.3 (HH-XRF 40 kV).

9.4.1 Dataset 3.1R: HH-XRF 15 kV

HCA (single linkage) identified two samples as outliers (R423 and R429) (Table 9-14). PCA biplot, pairwise plots and boxplots failed to identify any outliers. These two samples are considered tails of the data and will be retained for further analysis.

The pairwise plots (Fig. 9-30) exhibit several element pairings with moderate to high correlations. Clustering is evident with all lead element pairings. The manganese pairings exhibit clustering with the replicated glazes but this relationship might go unnoticed with previously unknown analytical composition such as archaeological faience sherds.

The PCA biplot (Fig. 9-31) exhibits two nearly linear clusters that correspond with the known glaze groups. The loadings (Table 9-15) indicate aluminium and phosphorus as the main influence on the first two components, respectively. The two components represent 85.75% of the total data variance.

The clustering techniques of HCA (Ward's method) and K-means correctly assigned the two known glaze groups into clusters. The silhouette graph is shared for both

Table 9-14: HH-XRF 15 kV Net Peak Areas for Dataset 3.1R.

HH-XRF 15 kV (NPA) Faience Replicates Dataset 3.1R

Parameters 15 kV, 50 uA with a vacuum for 180 seconds (no filter)

10 Measurements per Sample

Sample	Glaze	Mg	Al	P	Ti	Cr	Mn	Fe	Pb
R406	G7	1847	13410	2687	4724	5480	49795	876438	79142
R408	G7	2725	22590	2409	4674	7082	52320	902066	72783
R411	G7	3567	24790	2224	3984	7290	50272	855980	84005
R412	G7	3247	23409	2291	4467	6221	56483	957802	81710
R415	G7	3133	18313	2472	5166	8159	46524	764261	85473
R416	G7	2701	18302	2573	4202	7239	43620	714410	67774
R418	G5	1438	18317	3000	4264	4171	30662	706236	36027
R421	G5	3624	28919	2662	3983	5378	41081	909401	50698
R423	G5	3963	57004	2479	3782	7822	39317	852943	54751
R424	G5	2043	27078	2760	3852	5313	38042	825730	44743
R426	G5	2403	26032	2617	4439	8822	34706	745871	46432
R429	G5	3962	43746	2309	4279	9072	36406	768274	49187

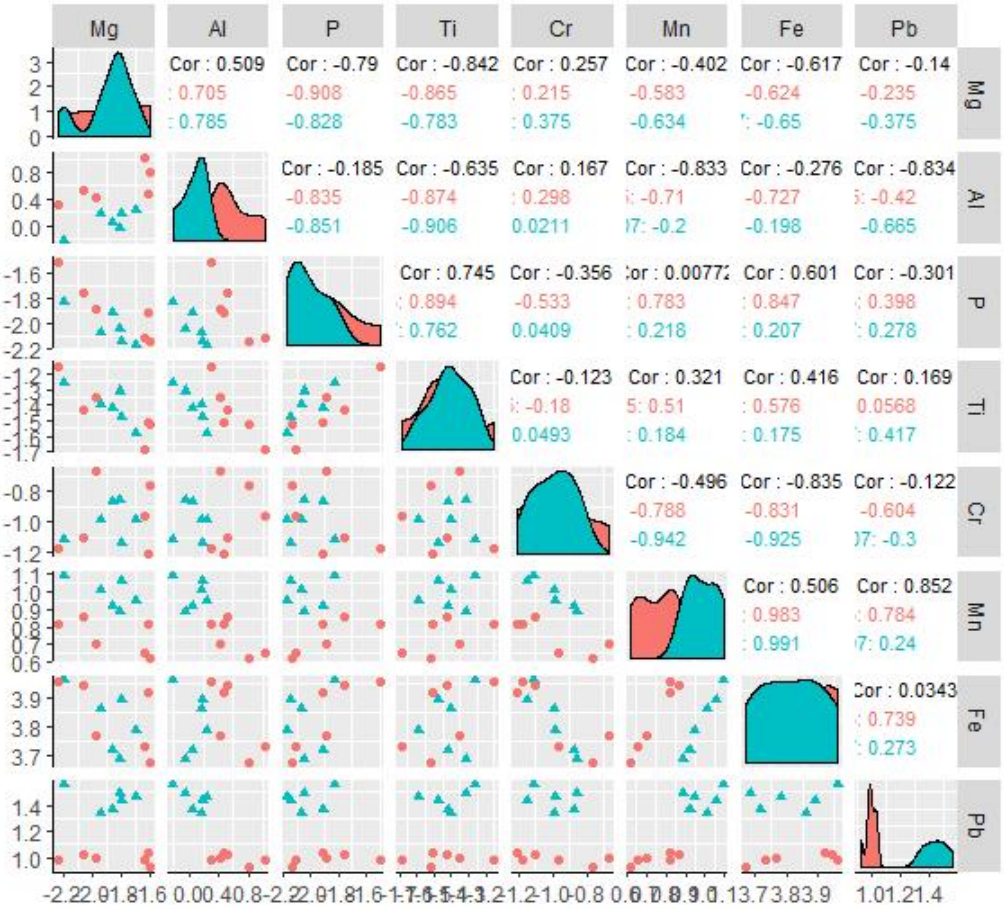

Fig. 9-30: Pairwise plot for dataset 3.1R.

methods and indicates a 34% confidence that the samples have been assigned correctly.

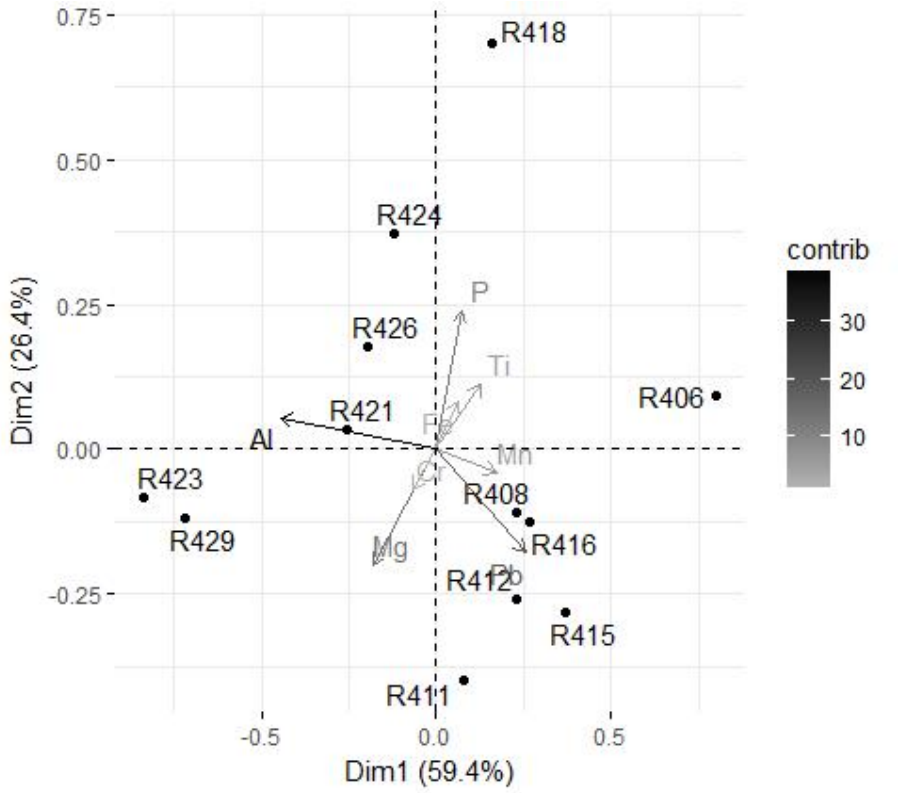

Fig. 9-31: PCA biplot of components 1 and 2 for dataset 3.1R.

Table 9-15: Loadings, Eigenvalues and Variance for dataset 3.1R. Aluminium and phosphorus explain most of the variance in components 1 and 2, respectively. The two components explain 85.75% of the variance in the data.

Dataset 3.1R HH-XRF 15 kV PCA Loadings

Non-Rotated Results	Dim.1	Dim.2	Dim.3	Dim.4	Dim.5
Mg	-0.30	-0.50	0.15	-0.71	-0.04
Al	-0.75	0.14	0.20	0.41	0.17
P	0.12	0.60	-0.04	-0.31	0.54
Ti	0.21	0.28	-0.25	-0.20	-0.31
Cr	-0.11	-0.17	-0.80	0.21	-0.15
Mn	0.29	-0.10	0.30	0.24	-0.27
Fe	0.10	0.21	0.36	0.09	-0.46
Pb	0.43	-0.45	0.09	0.28	0.53

Varimax Rotated Results	Dim.1	Dim.2	Dim.3	Dim.4	Dim.5
Mg				-0.93	
Al	-0.89				-0.12
P	0.12	0.81	0.24	0.18	
Ti	0.41			0.12	-0.37
Cr			-0.85	0.11	
Mn	0.12	-0.45	0.25	0.18	
Fe		-0.36	0.37	0.17	-0.33
Pb					0.85

Dataset 3.1R Eigenvalues and Variance

	Eigenvalue	Variance %	Cumulative Variance %
Dim.1	0.19	59.38	59.38
Dim.2	0.09	26.36	85.75
Dim.3	0.03	10.10	95.85
Dim.4	0.01	2.61	98.46
Dim.5	0.00	0.82	99.28
Dim.6	0.00	0.58	99.86
Dim.7	0.00	0.14	100.00
Dim.8	0.00	0.00	100.00

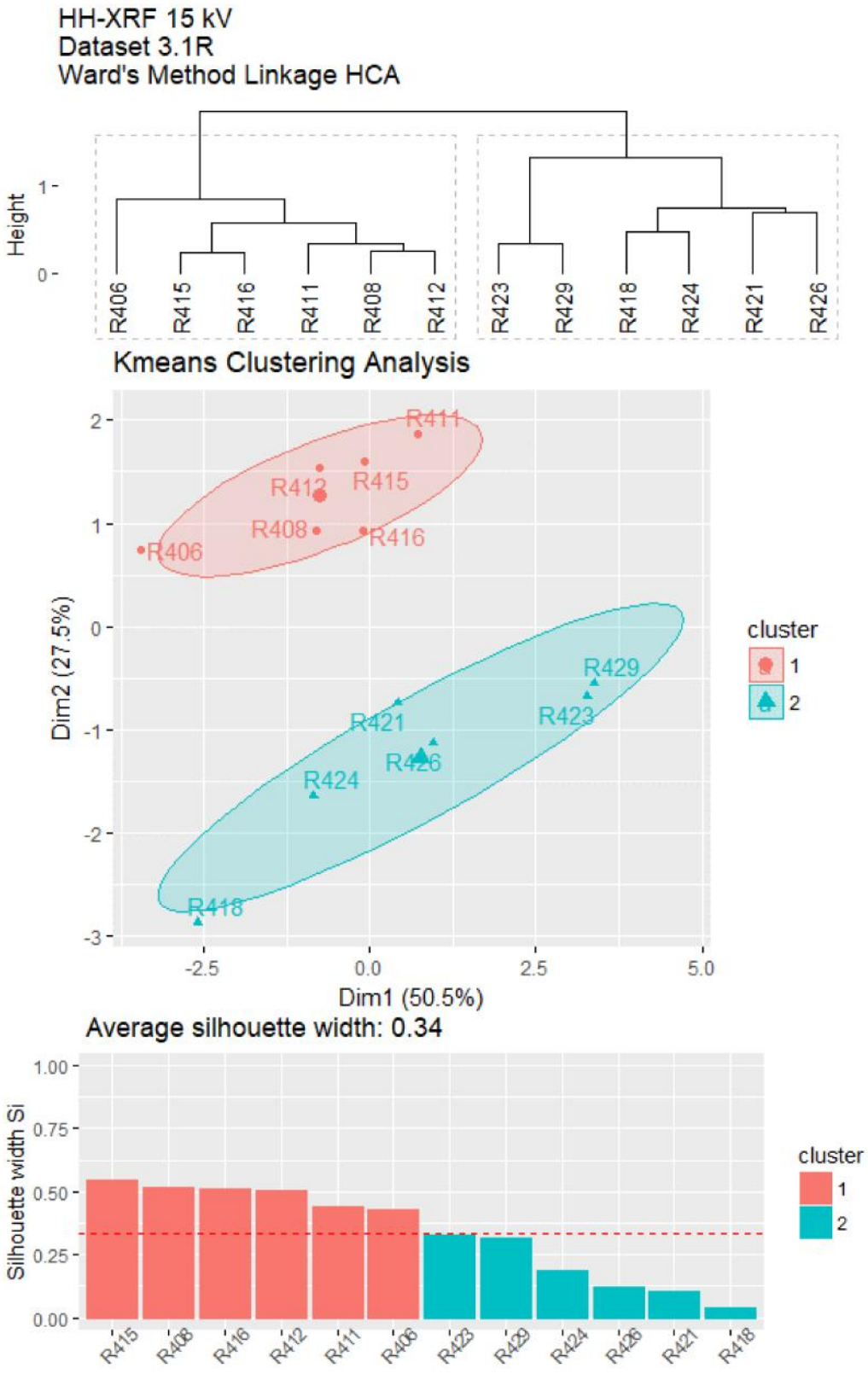

Fig. 9-32: HCA and K-means analysis of dataset 3.1R. The two known glaze groups have been assigned to two corresponding clusters. The silhouette graph indicates a 34% confidence that the samples are assigned correctly.

9.4.2 Dataset 3.2: SEM-EDS

Sample R416 of dataset 3.2 (Table 9-16) was distinctly identified as an outlier by HCA (single linkage), PCA biplot and bivariate plots. Boxplots identified it as an outlier for iron, copper and lead. This sample was removed from further analysis of the dataset.

The pairwise plots (Fig. 9-33) reveal that most element pairings with copper, lead and potassium exhibit clustering of the two known cobalt glaze groups. Several of the element pairings exhibit moderate to high correlations. The PCA biplot of the first two components and the PCA three-dimensional plot (Fig. 9-34) exhibit the two glaze batches separated by potassium content. The PCA loadings (Table 9-17) indicate that the alkalis, potassium for component 1 and sodium for component 2, exhibit greatest variance between the two groups. The two components represent 85.20% of the total data variance.

HCA (Ward's Method) and K-means clustering analysis correctly assigned the two known cobalt glaze groups into clusters. The silhouette graph indicates a confidence of 40% that the samples are correctly assigned.

Table 9-16: SEM-EDS (wt%) for Dataset 1 (Faience Replicates).

SEM-EDS (wt%) Faience Replicates Dataset 3.2								
Parameters 20 kV, 3 Measurements per Sample								
Sample	Glaze	Na_2O	SiO_2	K_2O	CaO	FeO	CuO	PbO
R406	G7	17.11	69.24	2.54	4.65	1.77	3.55	1.14
R408	G7	14.62	70.38	1.78	5.80	2.14	4.01	1.29
R411	G7	16.33	70.24	2.26	4.86	1.84	3.36	1.11
R412	G7	13.84	72.32	1.90	5.01	1.93	3.82	1.18
R415	G7	14.97	72.86	2.11	4.27	1.67	3.15	0.96
R416	G7	14.53	64.16	2.78	5.62	3.21	5.24	4.46
R418	G5	16.47	67.97	3.33	6.40	2.06	3.08	0.69
R421	G5	15.05	68.67	3.12	6.88	1.99	3.56	0.73
R423	G5	14.81	69.66	3.02	6.70	1.92	3.19	0.70
R424	G5	14.91	70.33	3.02	6.28	1.92	2.89	0.65
R426	G5	13.38	72.50	2.84	6.18	1.79	2.66	0.65
R429	G5	13.18	72.51	2.83	6.18	1.84	2.92	0.54

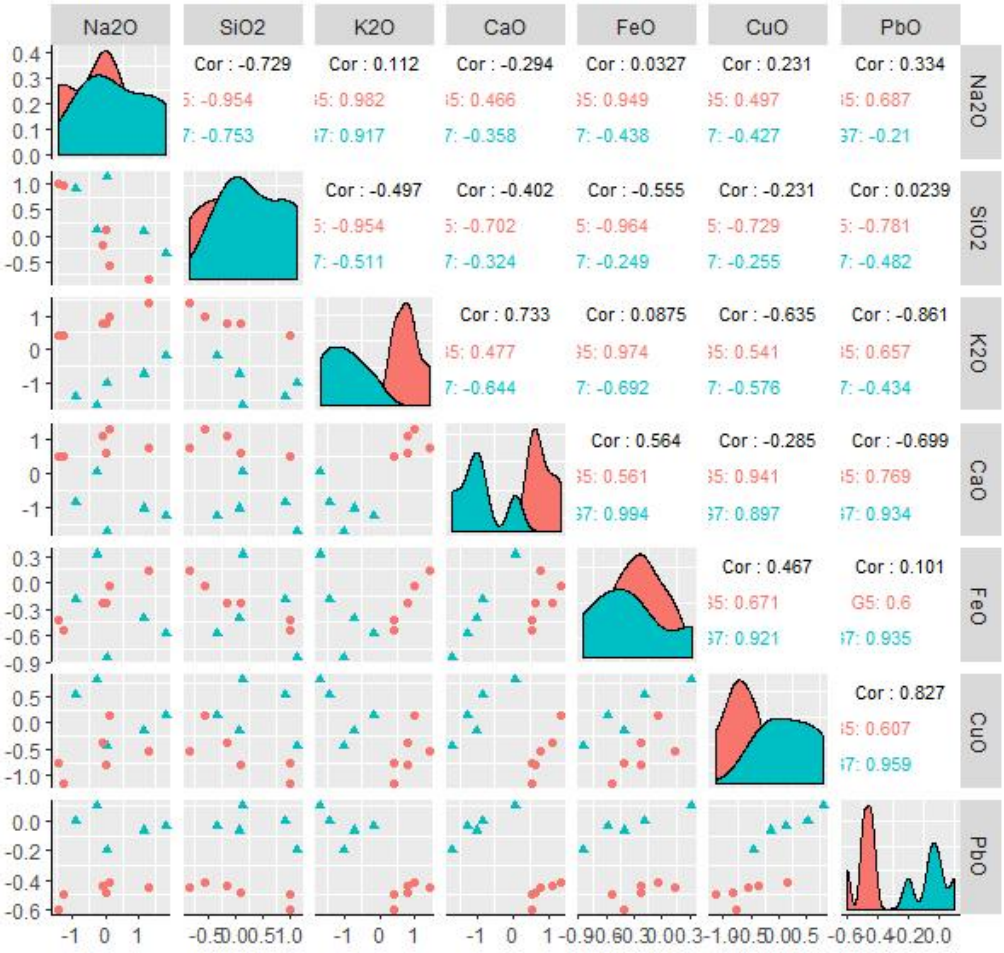

Fig. 9-33: Pairwise plot for dataset 3.2.

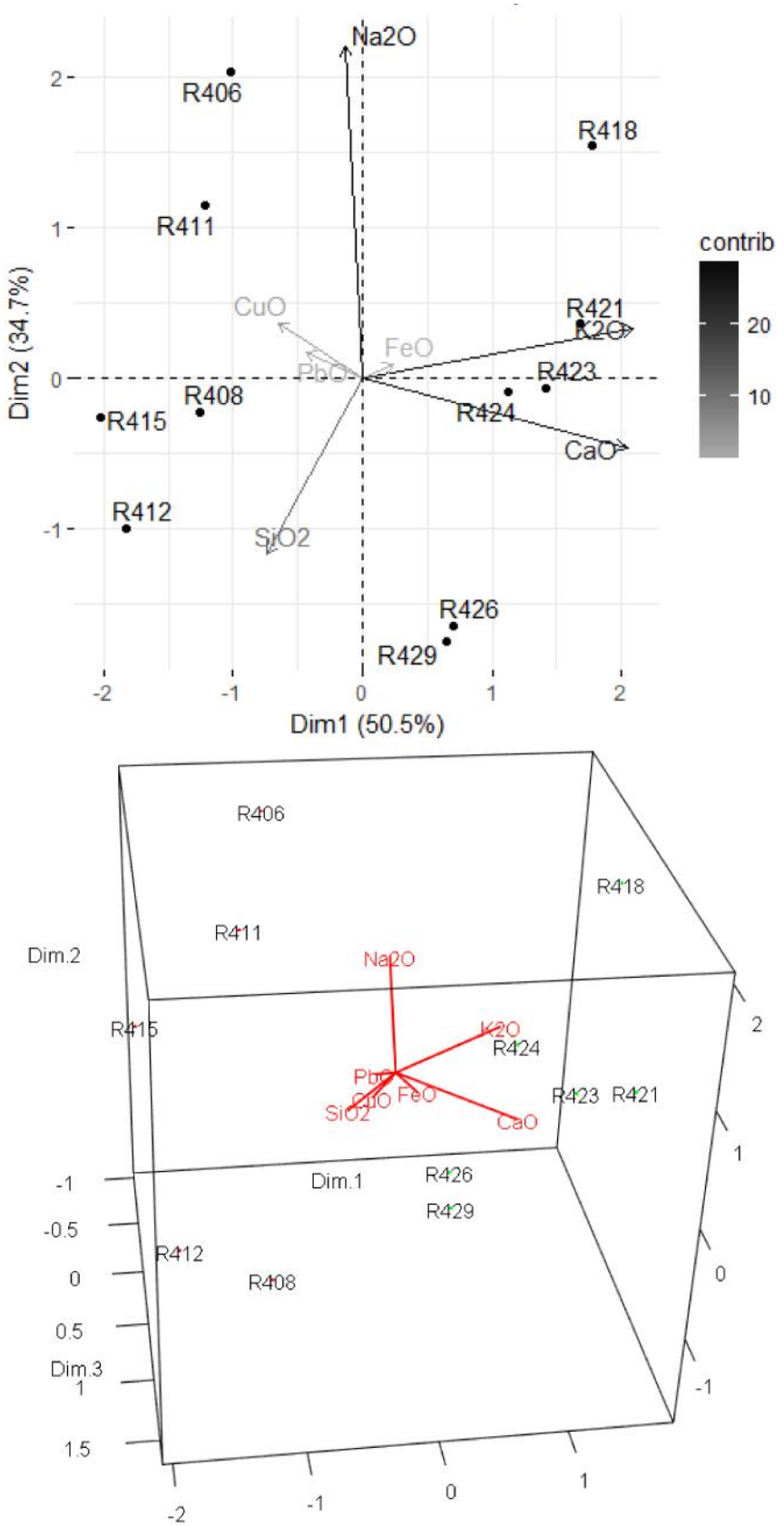

Fig. 9-34: PCA biplot and 3D plot of dataset 3.2 exhibiting the two glaze batches in two linear clusters.

Table 9-17: Loadings, Eigenvalues and Variance for dataset 3.1R. Aluminium and chromium explain most of the variance in components 1 and 2, respectively. The two components explain 93.03% of the variance in the data.

Dataset 3.2 SEM-EDS PCA Loadings

Non-Rotated Results						Varimax Rotated Results					
	Dim.1	Dim.2	Dim.3	Dim.4	Dim.5		Dim.1	Dim.2	Dim.3	Dim.4	Dim.5
Na_2O	-0.04	0.85	-0.13	-0.23	-0.15	Na_2O	-0.11	0.87	-0.14	-0.14	
SiO_2	-0.23	-0.45	-0.30	-0.01	0.05	SiO_2		-0.48	-0.25	-0.23	-0.11
K_2O	0.67	0.13	-0.39	0.48	0.33	K_2O	0.97				
CaO	0.65	-0.18	0.46	-0.25	-0.43	CaO			0.96		
FeO	0.08	0.04	0.38	-0.40	0.82	FeO					0.99
CuO	-0.21	0.14	0.61	0.70	0.03	CuO				0.96	
PbO	-0.14	0.07	0.13	-0.04	-0.08	PbO	-0.20				

Dataset 3.2 Eigenvalues and Variance

	Eigenvalue	Variance %	Cumulative Variance %
Dim.1	1.97	50.54	50.54
Dim.2	1.35	34.66	85.20
Dim.3	0.52	13.46	98.66
Dim.4	0.04	0.97	99.64
Dim.5	0.01	0.32	99.96
Dim.6	0.00	0.04	100.00
Dim.7	0.00	0.00	100.00

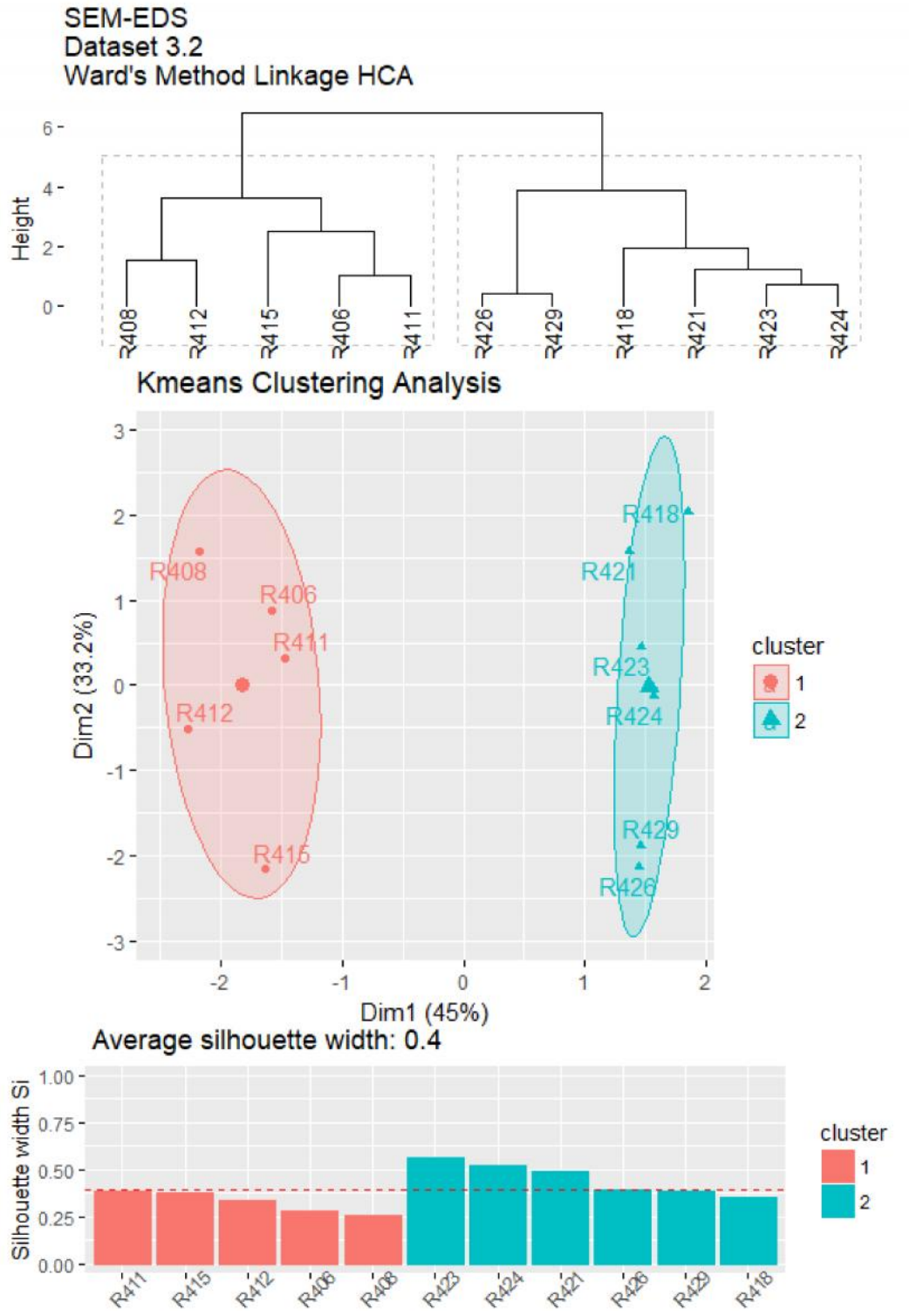

Fig. 9-35: HCA and K-means analysis of dataset 3.2. Clustering analysis exhibits the two cobalt glaze groups in separate assigned clusters. The silhouette graph indicates a 40% confidence that the samples have been correctly assigned.

9.4.3 Dataset 3.3R: HH-XRF 40 kV

No outliers were identified for dataset 3.3R (Table 9-18). The MVS analysis exhibits the two cobalt glaze groups correctly assigned to two clusters.

Pairwise graph (Fig. 9-36) reveal that most of the elements have a clustering contribution. Those with tin, antimony and lead exhibit the greatest variance in the bivariate plots (Fig. 9-37). Many of the element parings have moderate to high correlations.

PCA biplots (Fig. 9-38) exhibit the two batches clustered separately based on lead and tin batch components. The loadings (Table 9-19) reveal that lead and iron have greatest variance in the first two PCA components. Tin exhibits a strong influence with the first component as well but exhibits moderate influence with all components in the rotated results. The first two PCA components represent 98.20% of the total data variance.

HCA (Ward's Method) and K-means analysis (Fig. 9-39) assigned the two cobalt glaze batches to separate clusters. The two methods share the same silhouette graph which exhibits a 74% confidence that the samples are correctly assigned.

Table 9-18: HH-XRF 40 kV Net Peak Areas for Dataset 1 (Faience Replicates).

HH-XRF 40 kV (NPA) Faience Replicates Dataset 3.3R							
Parameters 40 kV, 30 uA and filter 3 for 180 seconds without vacuum							
10 Measurements per Sample							
Sample	Glaze	Fe	Sr	Zr	Sn	Sb	Pb
R406	G7	20458	912	1605	60366	38912	76546
R408	G7	18817	845	1531	66842	40448	68622
R411	G7	19397	1119	1701	88574	53300	84430
R412	G7	21351	1009	1626	73549	46987	81786
R415	G7	16889	1075	1577	89158	51985	78376
R416	G7	17755	865	1734	70049	44273	70044
R418	G5	16405	695	1064	91588	54643	33606
R421	G5	18461	888	1128	151023	87671	40752
R423	G5	17803	1013	1316	176656	100394	43990
R424	G5	18239	907	1318	115003	68312	40880
R426	G5	17196	1006	1507	152008	84057	43835
R429	G5	17650	1077	1546	180906	103007	46035

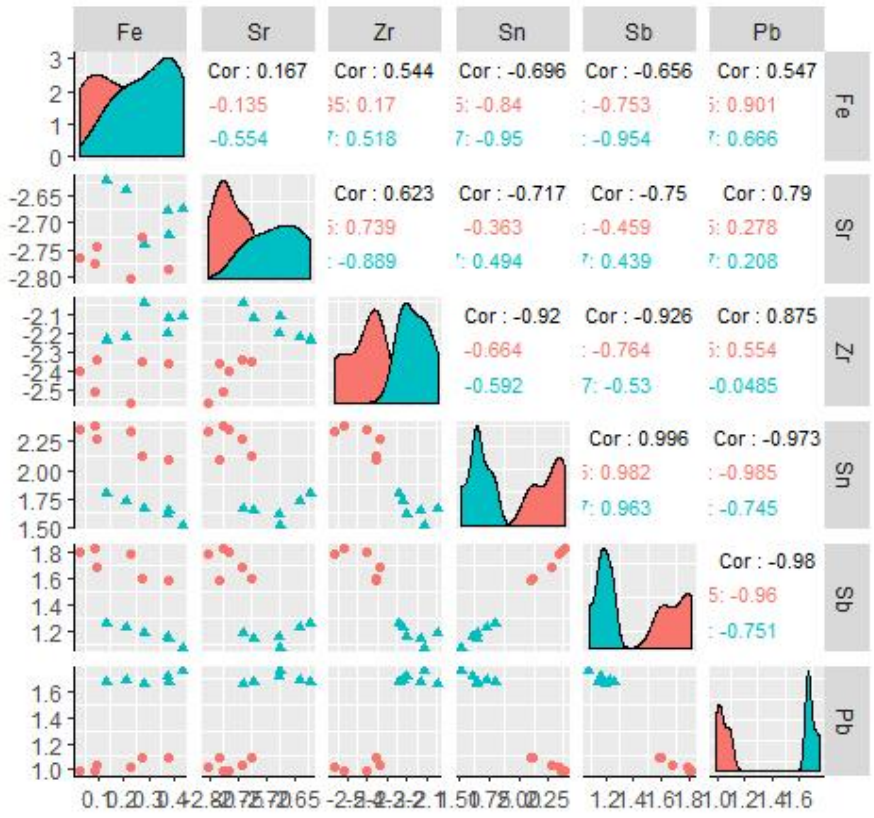

Fig. 9-36: Pairwise graph of dataset 3.3R. Most of the elements have clustering contributions.

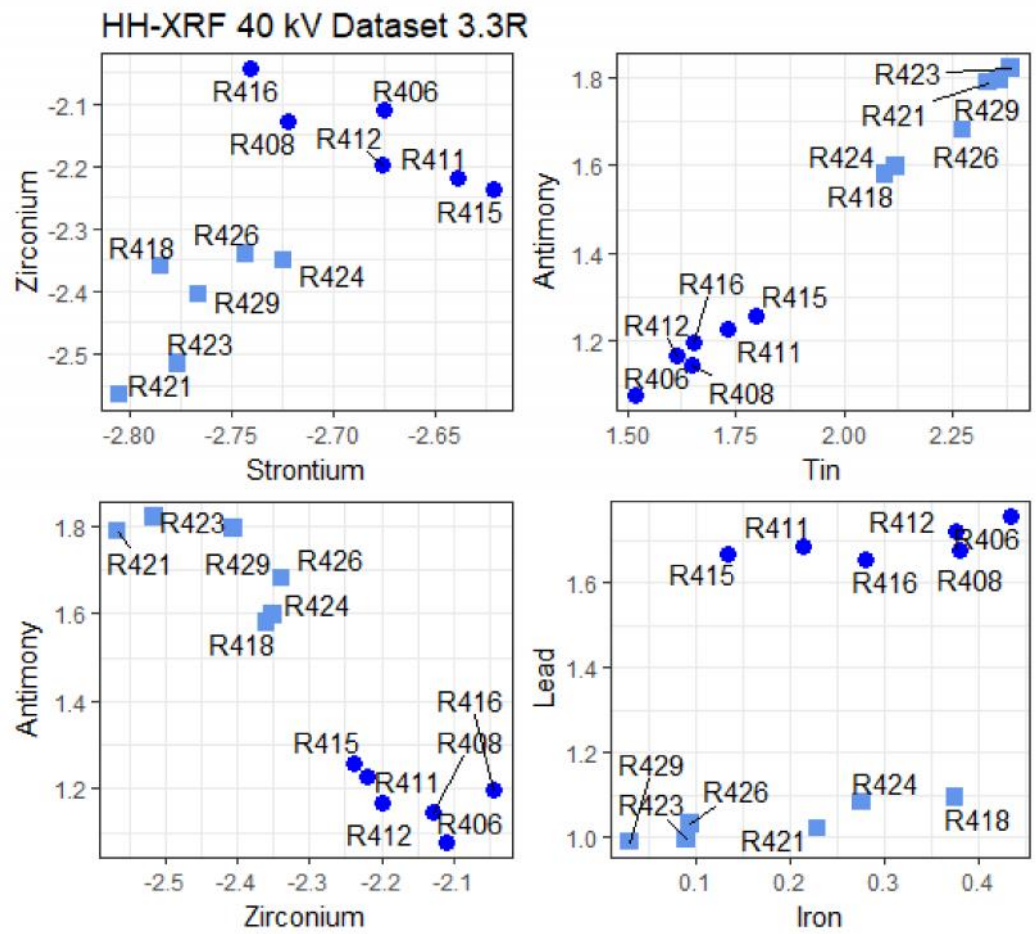

Fig. 9-37: Select bivariate plots for dataset 3.3R exhibiting the two cobalt glaze batches correctly assigned to clusters.

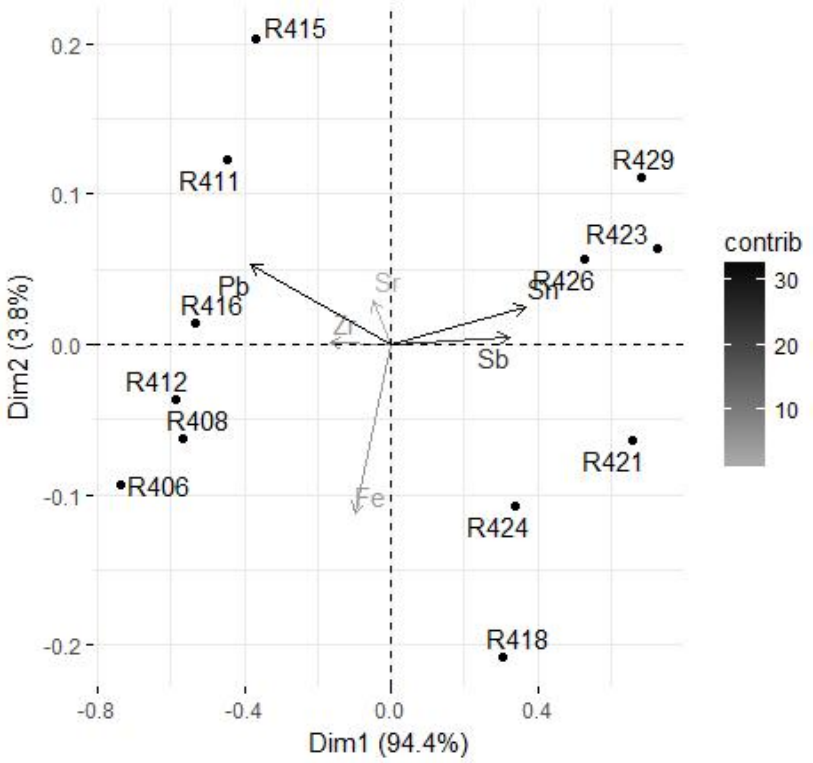

Fig. 9-38: PCA biplot of components 1 and 2 of dataset 3.3R. The biplot exhibits 98.20% of the data variation. The two known cobalt groups have been correctly clustered.

Table 9-19: Loadings, Eigenvalues and Variance for dataset 3.3R. Lead and iron explain most of the variance in components 1 and 2, respectively. The two components explain 98.20% of the variance in the data.

Dataset 3.3R HH-XRF 40 kV PCA Loadings

	Non-Rotated Results					Varimax Rotated Results					
	Dim.1	Dim.2	Dim.3	Dim.4	Dim.5		Dim.1	Dim.2	Dim.3	Dim.4	Dim.5
Fe	-0.15	-0.86	0.23	0.01	0.11	Fe	0.12	-0.88	0.12	-0.12	0.12
Sr	-0.08	0.22	0.11	0.86	-0.14	Sr	0.12	0.12	0.12	0.88	0.12
Zr	-0.25	0.01	-0.87	-0.10	0.00	Zr	0.12	0.12	-0.88	-0.12	0.12
Sn	0.57	0.19	0.04	-0.09	0.68	Sn	0.41	0.41	0.41	-0.41	0.41
Sb	0.50	0.03	0.08	-0.28	-0.71	Sb	0.12	0.12	0.12	-0.12	-0.88
Pb	-0.58	0.40	0.41	-0.40	0.05	Pb	-0.88	0.12	0.12	-0.12	0.12

Dataset 3.3R Eigenvalues and Variance

	Eigenvalue	Variance %	Cumulative Variance %
Dim.1	0.31	94.44	94.44
Dim.2	0.01	3.77	98.20
Dim.3	0.00	1.46	99.66
Dim.4	0.00	0.29	99.95
Dim.5	0.00	0.05	100.00
Dim.6	0.00	0.00	100.00

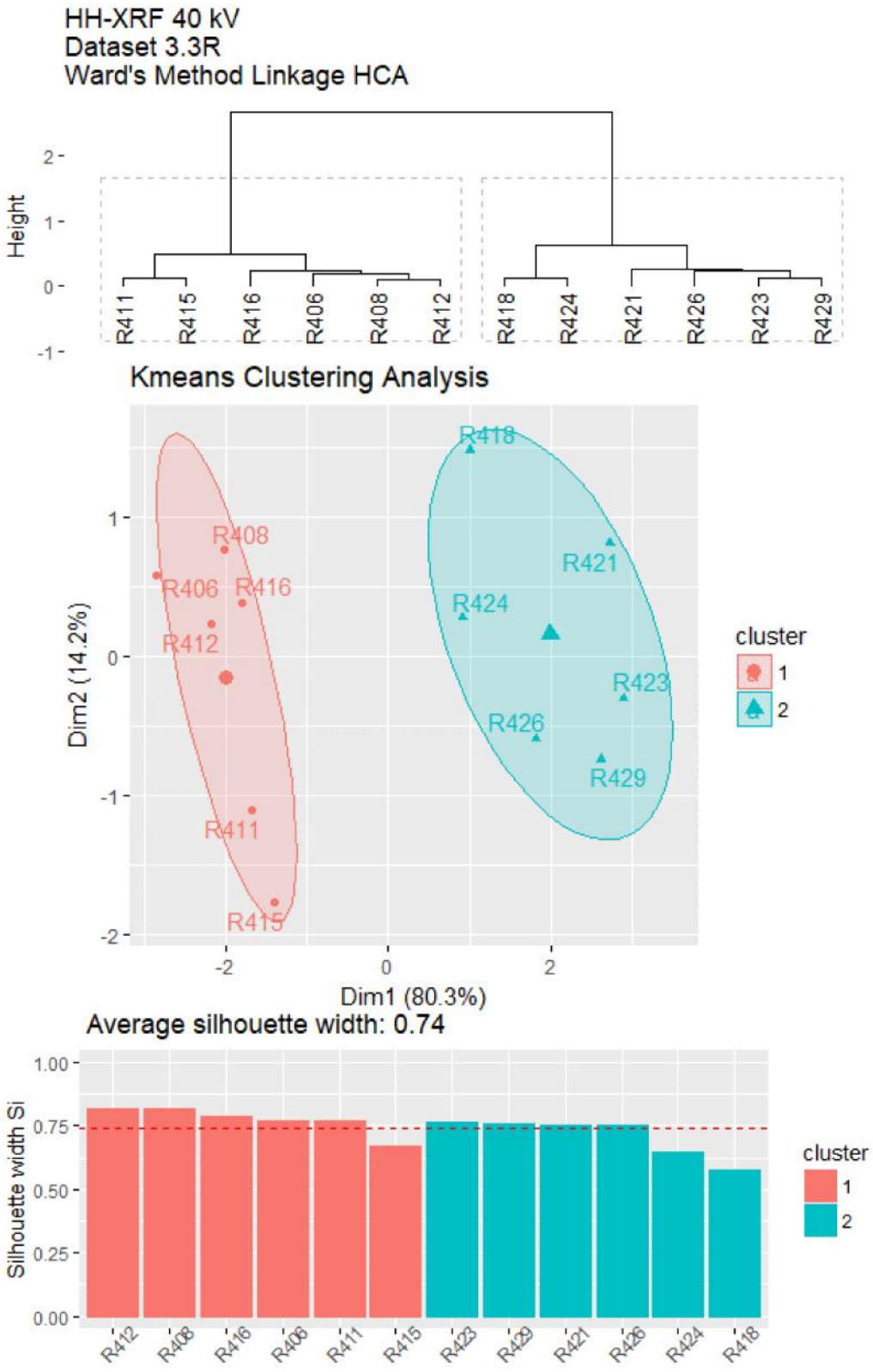

Fig. 9-39: HCA (Ward's Method) and K-means clustering analysis exhibiting the two known cobalt groups correctly clustered. The silhouette graph exhibits 74% confidence that the samples are correctly assigned.

9.5 Discussion

The purpose of this analysis is to determine if HH-XRF can discern the three known glaze groups based on a select number of variables representing minor and trace levels in the glazes, and by a number of variables determined through the criteria discussed in the previous chapter.

9.5.1 Dataset 1

HH-XRF at 40 kV (dataset 1.3R) distinctly discerned the three glaze groups. Analysis at this kV is considered a bulk analysis due to possible detection of elements occurring below the average glaze depth for archaeological faience of the Late through Roman Periods. HH-XRF at 15 kV (dataset 1.1R) is considered a glaze analysis due to the detection of elements within a typical glaze depth from the same period. Dataset 1.1R analysis distinguished the copper from the cobalt coloured glazes but the inclusion of the potassium variable with dataset 1.1 resulted in the separate clustering of all three groups. The SEM-EDS data (dataset 1.2) assigned cobalt colourant glaze 05 to a single cluster but combined glazes 03 (copper colourant) and 07 (cobalt colourant) into a single cluster.

MVS using dataset 1.1R resulted in two distinct clusters that correspond to the glaze colours but are dependent on the variables included which are represented by intentional additives (i.e. aluminium, iron) and unintentional inclusions (i.e. titanium, chromium, phosphorus) in the replicate batches. Analysis of the variable set failed to distinguish the two known cobalt coloured groups. MVS of dataset 1.1 using the full variable set did distinguish the two cobalt coloured groups and the copper coloured group with iron and K influencing most of the data variance. This is fine for relatively freshly produced glazes but using K would not accurately reflect glaze recipes that have been affected by alkali depletion.

The cobalt colourant glaze 05 group was assigned to its own cluster using SEM-EDS dataset 1.2. Glazes 03 (copper colourant) and 07 (cobalt colourant) were intermixed and assigned to a single cluster which failed to reflect the two distinct glaze material components. This is the result of using a restricted set of variables because of the LOD (2σ) selection criteria discussed in the previous chapter.

The PCA biplots for dataset 1.2 were convoluted but the use of three-dimensional PCA plotting reveals a clear distinction of the cobalt colourant glaze 05 group from the other two glaze groups. NaO_2, CaO and K_2O exhibited the greatest variance for PCA components 1, 2 and 3, respectively. Two of these three oxides are alkalis. The inclusion of the alkalis with the SEM-EDS datasets is not of concern. The

measurement were taken from the glaze interior halfway between the surface and the glaze/body interaction zone. This area is expected to exhibit the least, if any, alkali depletion in the archaeological material.

Limit of detection of the SEM-EDS present MVS a problem for analysis with this data. Typically this is set at 3σ above the background but has been reduced to 2σ to allow for a greater number of variables for this analysis. A further reduction to 1σ provides CoO, MgO, and Al_2O_3 for analysis with specific sample sets: Al_2O_3 with archaeological cobalt blue glazes, MgO and CoO with replicated cobalt blue glazes. The addition of Al_2O_3 with the archaeological cobalt blues glazes does not add any further distinction for the glazes which are already distinct from the other glazes.

The MVS analysis of the HH-XRF 40 kV measurements distinctly assigned the three replicated glaze groups to separate clusters using dataset 1.3R. The MVS analysis of dataset 1.3 failed to provide any more distinction of the groups. The variance of this dataset is defined by the occurrence lead and zirconium in the clusters.

A review of Table 3-2 reveals that tin and antimony have the deepest theoretical detection depths of all the expected elements in the glaze replicates and archaeological sherds. This highlights a limitation with the HH-XRF analysis. Analysis of tin and antimony should be associated with bulk analysis of the faience sherd because of the probability that part of the signal will originate in the body. Tin and antimony have a strong relationship with similar statistical results to the raw copper and zinc HH-XRF data discussed at the beginning of this chapter; the zinc NPA cps being strongly influenced by the proximity of the copper peaks (Kα1 8.04 kV and Kβ1 8.90 kV) to the zinc peak (Kα1 8.63 kV). Tin and antimony were added as separate components to cobalt colourant glazes 05 and 07, and to the substrate chosen for all the glazes (body 09). Copper colourant glaze 03 results were revealing very small amounts of tin and antimony when none were added to that glaze mixture. The strongest probability for the origin of the tin and antimony signal with glaze 03 is the body substrate. The origin of most of the tin and antimony signal for glazes 05 and 07 is from the glazes themselves. It is not known if a signal from the substrate has enough energy to reach the detector for these latter glazes.

The K-means analysis for dataset 1.2 using three defined clusters gave spurious results. Changing the number of clusters to four resulted in accurate clustering of cobalt colourant glaze 05 and less accurate clustering of cobalt colourant glaze 07. Copper colourant glaze 03 was divided into two sub-clusters; one that was influenced by the NaO_2 content and the other by the CaO content. Reviewing the firing

parameters revealed that all but one of the CaO influenced glaze 03 samples were glazes on bisque-fired bodies. All but two of the Na_2O influenced glaze 03 samples were on unfired bodies. This may indicate that sodium from the unfired body was migrating through the glaze melt and compositional profile during glost firing and was detected by SEM-EDS. The materials in the bisque-fired bodies reacted with the sodium leaving it unavailable for migration into the glaze melt. This analysis was conducted on known samples but similar processes may go unnoticed with, or might not be as easy to detect on previously unknown sample composition such as the archaeological sherds from Saqqara covered in the next chapter.

9.5.2 Dataset 2

MVS analysis of datasets 2.1R (15 kV HH-XRF) and 3.1R (40 kV HH-XRF) failed to reveal clusters. This was expected as all the copper colourant glaze 03 samples were prepared in the same way with the exception that some glazes were applied to bisque-fired bodies and some not.

MVS analysis of dataset 2.2 (SEM-EDS) analytical results was capable of differentiating between the bisque fired bodies and the unfired glazed bodies without direct measurement by examining the glaze centers in profile. The bivariate plot of CaO and CuO for dataset 2.2 (Fig. 9-22) exhibits two clusters corresponding to the amounts of CaO and CuO in the glaze and to the state of the body (i.e. bisque fired and unfired) before glost firing. The state of the body before glost firing corresponds to the clusters defined by PCA and K-means biplots and their associated silhouette graphs. The ability of SEM-EDS to detect such a discrepancy was revealed with dataset 1.2. Unknown archaeological glazes exhibiting the same calcium, sodium and copper relationships may indicate the same processes but will be difficult to confirm.

The higher dimensional datasets were examined to see if they added to the information provided by the lower dimensional dataset. Strontium and zirconium were not intentionally added to the glaze batches and their presence is a result of inclusions

Table 9-20: Cross-voltage HH-XRF correlations of select element pairings.

Cross-Voltage HH-XRF Correlations		
15 kV	40 kV	Correlation Coefficient
Zinc	Zinc	0.94
Calcium	Strontium	-0.36
Silicon	Zinc	-0.03
Silicon	Strontium	0.53
Silicon	Zirconium	0.31

entering the mixture with known glaze components: strontium with the calcium carbonate and zirconium with the sand. Dataset 2.3 exhibits the highest correlation for strontium (0.56) and zirconium (0.59) with zinc. A correlation across HH-XRF voltages (i.e. 15 and 40 kV) was conducted to see if these pairings could be confirmed. Zinc is detected with both voltages and was used to test the cross-voltage correlations (Table 9-20). The results indicate that strontium was not introduced with the calcium carbonate but was probably introduced with the sand. The same is true for zirconium. Zinc can be an inclusion in sand but there appears to be little relationship between zinc and silicon with the replicated faience.

MVS results seemingly exhibiting a random pattern of data points provides a stopping point when looking deeper into glaze assemblages and their relationships. The dataset 1 analyses were examining all the glazes and generally exhibited clustering corresponding to the known glaze batches. Dataset 2 was examining the copper colourant glaze 03 batch for further information. HH-XRF failed to produce additional clustering that has archaeological meaning. This provides a stopping point for further analysis of the glaze 03 batch using HH-XRF results and associated MVS analysis.

9.5.3 Dataset 3

The MVS analysis of datasets 3.1R (15 kV HH-XRF) 3.2 (SEM-EDS) and 3.3R (40 kV HH-XRF) accurately assigned the two known cobalt blue glaze groups into two separate clusters. SEM-EDS and the 15 kV HH-XRF MVS results for HCA (Ward's Method) and K-means exhibit similar confidence (~35%) that the samples have been correctly assigned. The 40 kV HH-XRF results for the same MVS techniques exhibited a much higher positive confidence at 74%. The 40 kV HH-XRF analyses reveal the ability of MVS to accurately cluster samples into known groups.

In conclusion, the HH-XRF and SEM-EDS results mostly match. Both techniques were capable of discerning the three glaze batches of dataset 1 and the two batches of dataset 3. There are some discrepancies when the results are examined in detail. HH-XRF results exhibited less intermixing of samples from different batches in the analyses. When intermixing did occur with HH-XRF, it was between the two cobalt glaze batches. SEM-EDS intermixing was generally between the copper and cobalt glaze batches.

SEM-EDS revealed greater cluster centroid dispersal. Low variable dimension HH-XRF analysis, especially at 15 kV, exhibited less dispersal of the centroids that resulted in samples from different clusters situated near each other. This is not a

problem when the analysis is of known materials. The clusters will be harder to discern when this situation occurs with archaeological or other unknown materials.

The lower dimensional data for HH-XRF exhibited the same clustering tendency as the higher dimensional data with the exception of the dataset 1.1R and 1.1 comparison. Dataset 1.1R did differentiate the copper and cobalt glazes but failed to differentiate between the two known cobalt glazes. With the addition of more variables provided by dataset 1.1, all three known glaze batches were accurately assigned to their own MVS clusters. The division of the cobalt blue glaze samples would have been revealed anyways as the MVS analysis further examined the two resulting clusters of dataset 1.1R. This does not present a concern for the use of lower dimensions with the HH-XRF analysis assuming that the selection of variables makes archaeological sense.

Two element pairings consistently exhibited high correlation: copper and zinc, and tin and antimony. The copper and zinc relationship is probably based on deconvolution within the Artax Spectra software. Bayesian deconvolution may indicate that a small zinc Kα peak is present but its spectral relationship with the copper Kβ peak may leave it susceptible to interference from the copper net peak counts (see Fig. 9-2) resulting in a false correlation. Zinc was not intentionally added to the replicated glazes and does not typically exhibit high correlation with any element except copper. Zinc peaks in the HH-XRF spectra are small with the replicated glazes and probably originates from the HH-XRF analyser unit as instrument interference (see Table 6-2).

Tin and antimony were added to cobalt colourant glazes 05 and 07 and to the bodies as a substrate for all the glazes. Copper colourant glaze 03 results exhibited very small amounts of tin and antimony when none were added to that glaze mixture. The strongest probability for the origin of the tin and antimony signal with glaze 03 is the body substrate. The origin of most of the tin and antimony signal for glazes 05 and 07 is from the glazes themselves. It is not known if a signal from the substrate has enough energy to reach the detector for these glazes due to their thickness. A review of Table 3-2 reveals that tin and antimony have the deepest theoretical detection depths of all the expected elements in the glaze replicates and archaeological sherds. Using the L lines of tin (Lα1 at 3.44) and antimony (Lα1 at 3.60) were not attempted due to their proximity to the K lines of calcium (Kα1 at 3.69) and potassium (Kα1 at 3.31). Tin and antimony will be removed from the archaeological case study analyses and its removal from future faience glaze analysis is suggested unless the glaze is uncommonly thick.

Some sub-clusters of copper colourant glaze 03 of dataset 2 were caused by differing values for copper and NaO_2 or CuO and CaO values with the SEM-EDS analysis. This corresponded with the nature of the body (bisque fired vs unfired state) before the glost firing. The theoretical detection depths for calcium (12 µm) and sodium (2 µm) are too shallow for the signal to be originating in the body and copper was not a body component. Bodies unfired before the glost firing contributed some sodium and calcium to the glaze melt during the firing. This resulted in greater values for these two elements/oxides in the glaze which was subsequently detected with EDS. Unknown samples exhibiting the same calcium, sodium and copper relationships may indicate the same processes but it will be difficult to confirm.

MVS analysis of the HH-XRF (15 and 40 kV) dataset 2 measurements revealed no clustering. This was expected because dataset 2 is composed of only copper colourant glaze 03 samples which were similarly produced with the exception of the fired state of the body prior to glazing. HH-XRF failed to differentiate the glaze 03 samples in the same way that SEM-EDS did. This resulted in a seemingly random pattern of data points which signify a stopping point for further HH-XRF analysis of the glaze 03 samples.

The results of this testing reveal that HH-XRF is capable of accurately clustering the known glaze batches using the reduced dimensional variables for 15 and 40 kV measurements. Higher dimensional datasets only provided additional information regarding clustering with dataset 1.1. However, this information would have been gained with the subsequent examinations of the individual replicated glaze batches. The lower dimensional datasets (1.1R, 1.2R and 1.3R) were sufficient for clustering the known glaze batches in most instances. SEM-EDS clusters match the results of HH-XRF and has the potential of differentiating between bisque fired and unfired bodies before glazing when all other parameters are known. Therefore the results will probably go unnoticed with unknown materials such as the archaeological glazes from Saqqara covered in the next chapter.

Chapter 10: Saqqara Faience: Multivariate Statistical Analysis

10.1 Introduction

An assemblage of 24 faience sherds from Saqqara were used as a case study to determine if HH-XRF can categorize the glazes based on composition which may reflect technical aspects as well as material and workshop associations. These sherds are introduced in section 4.3.3 and are described further in Appendix B. The glazes cover a range of colours including yellowish-green, purple, and green but are primarily blue to reduce the influence of colourants in MVS analysis. MVS analysis is used to produce glaze groupings based on HH-XRF and SEM-EDS elemental results.

The objectives of the current testing are:

- To determine if archaeological glaze groups exist based on MVS of compositional analysis;
- To determine if SEM-EDS and HH-XRF analytical results produce similar glaze groupings;
- To compare results of analysis using datasets with all variables meeting criteria (Chapter 8) and those using reduced variable datasets (reduced dimensional datasets) having removed silicon (major element) and copper (colourant) that will have a major influence on MVS analysis, and alkali components (sodium and potassium) which are susceptible to dissolution.

The datasets are composed of a range of elements/oxides that meet the variable criteria discussed in chapter 8. The HH-XRF datasets have a reduce dimensionality data sub-set having removed major structural variables, alkalis and colourants. The datasets represent all glaze colours (dataset 1), all copper and cobalt blue coloured glazes (dataset 2) and copper blue coloured glazes (dataset 3). These are subdivided based on analytical technique: x.1 for 15 kV HH-XRF, x.2 for SEM-EDS and x.3 for 40 kV HH-XRF (Table 10-1). Each HH-XRF dataset has a reduced dimensional data-subset designated with the suffix ‘R’ (i.e. x.xR). All HH-XRF datasets are examined but

Table 10-1: Saqqara Archaeological Faience Multivariate Dataset Summary.

Datasets for Saqqara Archaeological Faience Glazes				
Data Supersets	Sample	Data Subset (Archx.x)	Technique	Elements/Oxides of Interest
1	All Samples	1.1	HH-XRF 15 kV	Na, Mg, Al, Si, P, Ca, Ti, Mn, Fe, Ni, Cu, Zn
		1.2	SEM-EDS	Mg, Al, Si, Ca, Fe
		1.3	HH-XRF 40 kV	Fe, Cu, Zn, Sr, Sn, Pb
2	All Blue Coloured Samples	2.1	HH-XRF 15 kV	Na, Mg, Al, Si, P, Ca, Ti, Cr, Mn, Fe, Ni, Cu, Zn
		2.2	SEM-EDS	Na, Mg, Si, Ca, Fe, Cu
		2.3	HH-XRF 40 kV	Fe, Cu, Zn, Sr, Zr, Sn, Pb
3	Copper Coloured Samples	3.1	HH-XRF 15 kV	Na, Mg, Al, Si, P, Ca, Ti, Cr, Mn, Fe, Ni, Cu, Zn
		3.2	SEM-EDS	Na, Mg, Al, Si, Ca, Fe, Cu
		3.3	HH-XRF 40 kV	Fe, Cu, Zn, Sr, Zr, Sn, Pb
1	All Samples	1.1R	HH-XRF 15 kV	Mg, Al, P, Ti, Mn, Fe, Ni, Zn
		1.3R	HH-XRF 40 kV	Fe, Zn, Sr, Sn, Pb
2	All Blue Samples	2.1R	HH-XRF 15 kV	Mg, Al, P, Ti, Cr, Mn, Fe, Ni, Zn
		2.3R	HH-XRF 40 kV	Fe, Zn, Sr, Zr, Sn, Pb
3	Copper Samples	3.1R	HH-XRF 15 kV	Mg, Al, P, Ti, Cr, Mn, Fe, Ni, Zn
		3.3R	HH-XRF 40 kV	Fe, Zn, Sr, Zr, Sn, Pb

only reduced dimensionality datasets are reported unless the corresponding higher dimensional dataset adds information regarding compositional clusters. All dataset were treated to outlier determination (not included in report for brevity).

The SEM-EDS data was collected as discussed in section 4.4.4 (see Table 7-15). Nine measurements were conducted through the glaze profile in cross-section. The middle three measurements were used to avoid alkali depleted areas near the glaze surface and the glaze/body interaction area. The centre glaze measurements are more likely to represent the condition of the glaze during its use life. The HH-XRF data was collected as discussed in section 4.4.5 (see Fig. 4-6 and Tables 7-11 through 7-12). All measurements occurred inside the HH-XRF cabinet for health and safety concerns. Parameters for low Z elements (Z≤26 (iron)) are 15 kV, 50 µA for 180 seconds using a vacuum. Parameters for high Z elements (Z>26) are 40 kV, 30 µA for 180 seconds with filter 3 (12 mil aluminium, 1 mil titanium, and 6 mil copper) and no vacuum. Ten measurements were conducted across each of the glaze surfaces.

Copper and zinc NPA exhibited a high correlation for the replicate material (see section 9.1). The archaeological data was examined for the same relationship but the

correlations are very low. Therefore, zinc will be included in the analysis when the variable meets all the criteria discussed in chapter 8.

Correlation factors are partly dependant on the number of samples being investigated. Within this faience sherd assemblage are fifteen copper blue glazes, four cobalt blue glazes, four lead antimonate green glazes (one yellowish-green) and one manganese purple glaze. A review of the data reveals that the green glazes consistently have high correlation factors for variable pairings. The cobalt blue glazes exhibit a similar although slightly less consistent pattern of high correlations. These may be a true representation of the relationships between the variables but it may result in a misinterpretation of data that has statistically resulted in a relationship based on random fluctuation in the batch components or instrument detection. This effect is less prominent with larger sample sizes. The copper blue glazes exhibit similar high correlations but with much less frequency than the green and cobalt blue glazes. Confidence in these results are higher because of the larger number of copper coloured glaze samples.

10.2 Dataset Arch 1 Multivariate Analysis (All Sherds)

Dataset 1 contains all samples consisting of blue, dark blue, yellow, green and purple glazed faience sherds. Dataset 1.1 (Table 10-2) is the result of HH-XRF at 15 kV, dataset 1.2 (Table 10-3) is SEM-EDS and dataset 1.3 (Table 10-4) is HH-XRF at 40 kV. The tables represent the full variable dimensionality. The HH-XRF reduced dimensional data subsets (see Table 10-1) are designated with an ‘R’ (e.g. Dataset Arch 1.3R). The sample variable values are extracted from the full dimensional datasets with no change (e.g. Arch 1.3).

10.2.1 Datasets Arch 1.1R and 1.1

The HCA dendrogram (single linkage method) and PCA biplot for dataset Arch 1.1R reveals a single outlier (s21). The pairwise plot and bivariate scatter plots (Fig. 10-1) associated with manganese reveal the same outlier. Sample s21 is on or near the scatter peripheries for all element associations exhibited on the pairwise plot. The boxplots reveal s21 as an outlier for manganese. The iron boxplots reveal samples s70 and s78 as outliers and s42 as an outlier for phosphorus. These are evident with the pairwise plot for each specific element. The latter three samples are considered tail ends of the data and have been retained for the analysis.

Table 10-2: HH-XRF 15 kV Net Peak Areas for Dataset Arch 1.1.

HH-XRF 15 kV (NPA) Saqqara Faience Dataset Arch 1.1

All Coloured Glazes

Parameters 15 kV, 50 uA with a vacuum for 180 seconds (no filter)

Average of 10 Measurements

Sample	Glaze	Na	Mg	Al	Si	P	Ca	Ti	Mn	Fe	Ni	Cu	Zn
s12	Bluish Green	2974	2063	27014	1025895	5959	217156	21633	15653	379957	11714	925680	16239
s17	Blue	5876	2811	23759	981125	5114	574024	47673	20171	617514	18849	3708415	22914
s20	Green	4099	2081	28353	929541	4268	436947	38253	21351	742734	13403	1695728	11156
s21	Purple	7495	2364	13836	979984	3207	425110	18569	486045	507727	7886	165845	7221
s22	Turquoise	5827	2287	15647	1152660	2525	186858	14683	15950	303015	9968	1545178	16356
s31	Turquoise	4361	4063	16457	998154	3149	531149	30286	25058	588475	9543	1452398	10701
s42	Green	3917	1685	28027	904789	9533	559221	36455	21892	823330	9142	1611693	10235
s45	Yellowish Green	3830	4623	15829	1158507	3668	434751	37505	19187	918344	8940	147555	8912
s48	Dark Blue	6420	3030	16908	1186755	3632	311281	19037	18030	732039	10986	2794572	21958
s53	Turquoise	4719	2671	10135	638564	5406	1651737	13383	16283	289008	13003	1589092	16179
s70	Ultra-Marine Blue	4813	1387	11564	610929	4202	216098	15793	18501	2203961	7592	1828039	11955
s72	Purplish Blue	5283	2673	19844	1169014	3155	403182	26645	24846	1696671	11021	658186	34594
s74	Purplish Blue	6111	3085	18114	1173289	2951	507426	22723	21002	1317397	11189	1783910	26342
s78	Ultra-Marine Blue	6927	2380	15477	941410	4471	760064	17038	16696	2316921	7330	2320400	18902
s80	Turquoise	4058	1586	12639	866035	4002	706484	14332	17752	398828	8753	1012815	10026
s81	Bluish Green	4468	3183	11487	650578	4411	1959044	34629	26161	737015	10936	1060826	38968
s82	Blue	6395	2701	16757	1107525	3466	324947	17071	16567	411025	12489	2461044	19890
s83	Turquoise	5144	3540	20332	1340659	3906	699362	23330	20351	427188	10011	1032560	8090
s84	Blue	4341	1651	12422	718064	3160	549746	39170	24885	721445	9432	1908370	13069
s85	Dark Blue	5648	3661	23854	1270620	3962	636725	44541	27011	811714	9557	1851004	13085
s87	Blue	5693	3100	22262	1238384	3224	749413	41160	23115	730315	8480	1282621	8934
s89	Blue	5908	3576	23270	1443953	3321	535436	31626	23827	605167	9070	1087366	8932
s90	Blue	5448	3349	27509	1172867	3108	553427	40262	28267	777077	10137	2096534	14887
s91	Turquoise	4261	2770	16054	1089216	4175	583393	23437	20785	401565	9848	1016842	7922

Table 10-3: SEM-EDS (wt%) for Dataset Arch 1.2 (Saqqara Faience).

SEM-EDS (wt%) Saqqara Faience Dataset Arch 1.2 All Coloured Glazes Parameters 20 kV, Average of 3 Measurements						
Sample	Glaze	MgO	Al2O3	SiO2	CaO	FeO
s12	Bluish Green	0.66	0.79	94.56	3.14	0.85
s17	Blue	1.51	2.47	89.82	5.03	1.18
s20	Green	0.90	2.12	89.38	5.80	1.80
s21	Purple	0.47	1.23	91.29	6.28	0.73
s22	Turquoise	0.83	0.96	95.79	1.86	0.56
s31	Turquoise	1.06	1.85	90.85	5.32	0.91
s42	Green	1.06	1.45	89.87	5.86	1.76
s45	Yellowish Green	0.82	1.04	89.72	5.80	2.61
s48	Dark Blue	0.75	0.95	93.30	4.02	0.98
s53	Turquoise	0.38	0.67	97.29	1.30	0.36
s70	Ultra-Marine Blue	0.39	1.01	89.34	4.34	4.92
s72	Purplish Blue	0.63	1.54	89.53	6.09	2.21
s74	Purplish Blue	0.68	1.55	88.81	6.05	2.92
s78	Ultra-Marine Blue	0.43	1.06	85.36	7.63	5.52
s80	Turquoise	0.29	0.50	97.11	1.73	0.37
s81	Bluish Green	0.73	0.97	94.28	3.48	0.54
s82	Blue	0.38	0.84	94.53	3.72	0.53
s83	Turquoise	1.06	1.62	90.17	6.32	0.84
s84	Blue	1.00	3.93	86.78	6.88	1.42
s85	Dark Blue	0.92	3.90	86.52	7.15	1.51
s87	Blue	0.97	2.31	88.59	6.76	1.37
s89	Blue	0.83	1.84	89.60	6.45	1.27
s90	Blue	1.08	3.13	87.70	6.66	1.43
s91	Turquoise	0.94	1.59	90.75	5.99	0.73

Table 10-4: HH-XRF 40 kV Net Peak Areas for Dataset Arch 1.3

HH-XRF 40 kV (NPA) Saqqara Faience Dataset Arch 1.3

All Coloured Glazes

Parameters 40 kV, 30 uA and filter 3 for 180 seconds without vacuum

Average of 10 Measurements

Sample	Glaze	Fe	Cu	Zn	Sr	Sn	Pb
s12	Bluish Green	8230	55067	1188	5440	3016	796398
s17	Blue	9778	162409	816	7692	56157	7676
s20	Green	12996	80862	556	11146	5300	321309
s21	Purple	8488	5524	382	10126	5116	2906
s22	Turquoise	6020	83950	1478	6058	30342	14194
s31	Turquoise	11548	70046	560	13579	4943	875
s42	Green	16986	70194	564	10862	5914	329517
s45	Yellowish Green	20005	8153	632	9673	4032	623780
s48	Dark Blue	13082	129019	1037	9303	6522	2903
s53	Turquoise	6421	88871	857	12067	22090	5996
s70	Ultra-Marine Blue	42080	74138	637	7802	8094	3360
s72	Purplish Blue	34023	35000	2481	15334	7073	910
s74	Purplish Blue	29389	94894	1842	13402	22061	11702
s78	Ultra-Marine Blue	36996	83679	902	13186	11774	5082
s80	Turquoise	6610	37470	504	6577	5170	888
s81	Bluish Green	11884	38249	1421	16745	5075	2036
s82	Blue	7388	97810	636	9734	14325	12401
s83	Turquoise	8688	56732	446	17438	18965	10647
s84	Blue	15389	103290	656	11462	4374	2332
s85	Dark Blue	15477	96384	667	12364	4838	2978
s87	Blue	15001	75928	544	14153	7952	5018
s89	Blue	12821	58279	504	24238	20150	5648
s90	Blue	17852	114406	799	14331	5274	3229
s91	Turquoise	8594	53375	440	18279	17993	10638

The pairwise plot and associated bivariate plots without s21 exhibits a high correlation for aluminium and magnesium for green and cobalt blue glazes (Figs. 10-2 and 10-3). Iron levels are higher in the cobalt blue glazes. Nickel and iron have a large negative correlation for all samples. Zinc and iron exhibit a large negative correlation for green and cobalt blue glazes.

The PCA biplots for components 1 and 2 represent ~66% of the total data variance. Component 3 was added to the analysis to represent a cumulative ~82% of the total data variance (Fig. 10-4, Table 10-5). These figures reveal cobalt blues as two distinct pairs groupings (s70/s78 and s72/s74) based on iron and zinc. Samples s48 and s81, distinctive by the zinc variable, may represent an additional pair separate from the main group of samples. The green and yellow glazes (s12, s20, s42 and s45) are intermixed with the main group of samples and do not represent a distinct group.

The data in the pairwise plots and in the PCA biplots failed to reveal distinct clustering except for the s70/s78 and s72/s74 sample pairs. Gap statistics, average silhouette

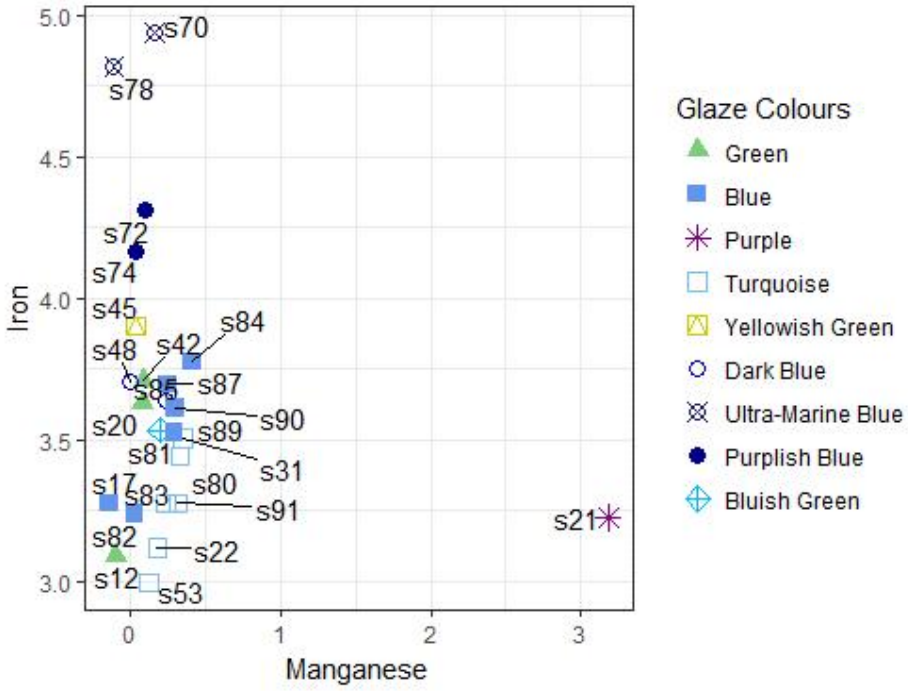

Fig. 10-1: Bivariate plot of manganese and iron revealing sample s21 as an outlier for manganese. Samples s70 and s78 are shown as potential outliers for iron but are considered data tails and have been retained for further analysis.

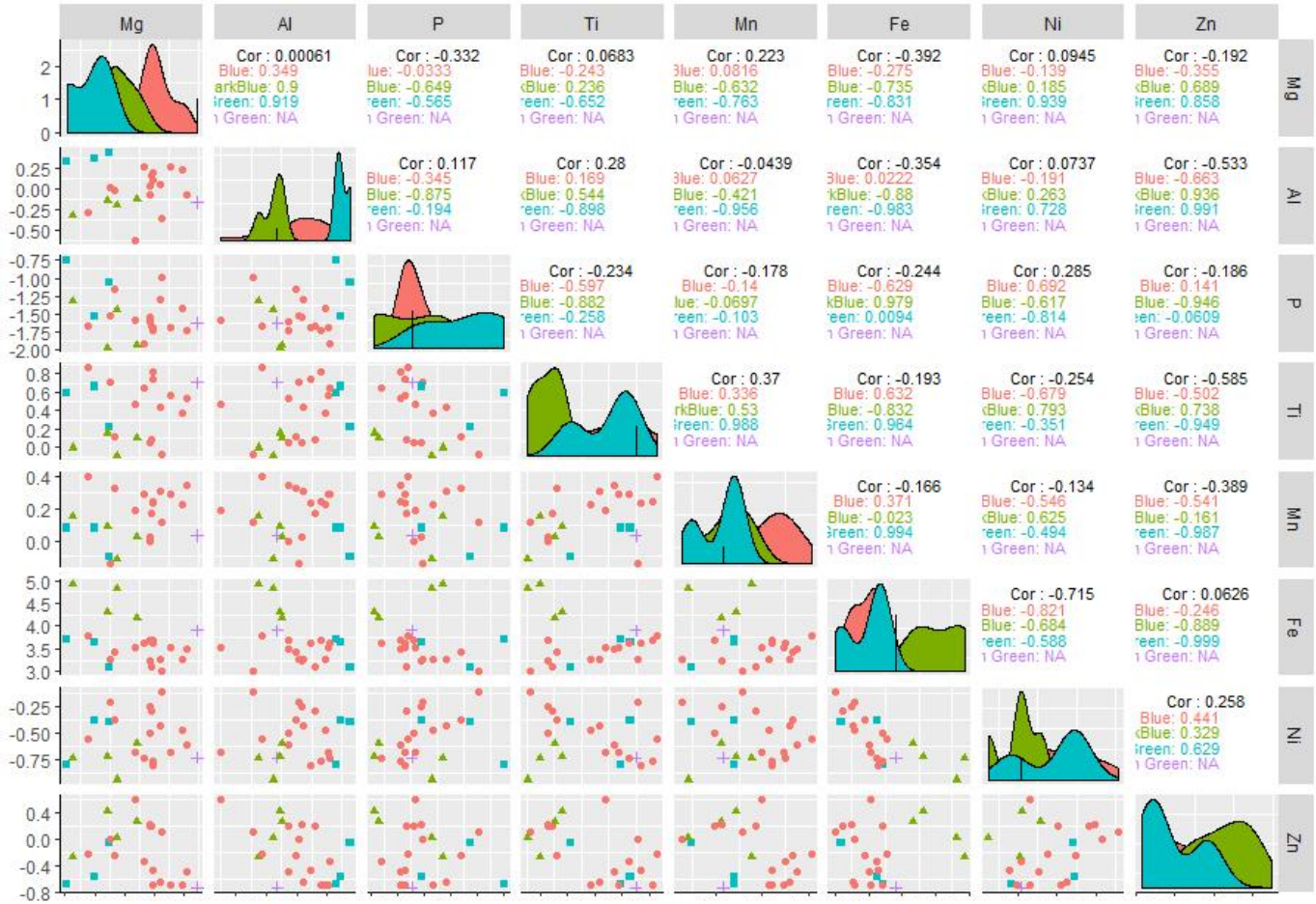

Fig. 10-2: Pairwise plot of dataset Arch 1.1R with outliers removed exhibiting bivariate plots, histogram and correlations of the variables. The first correlation represents all samples. The other correlations represent Cu blues, dark blues, greens and bluish greens.

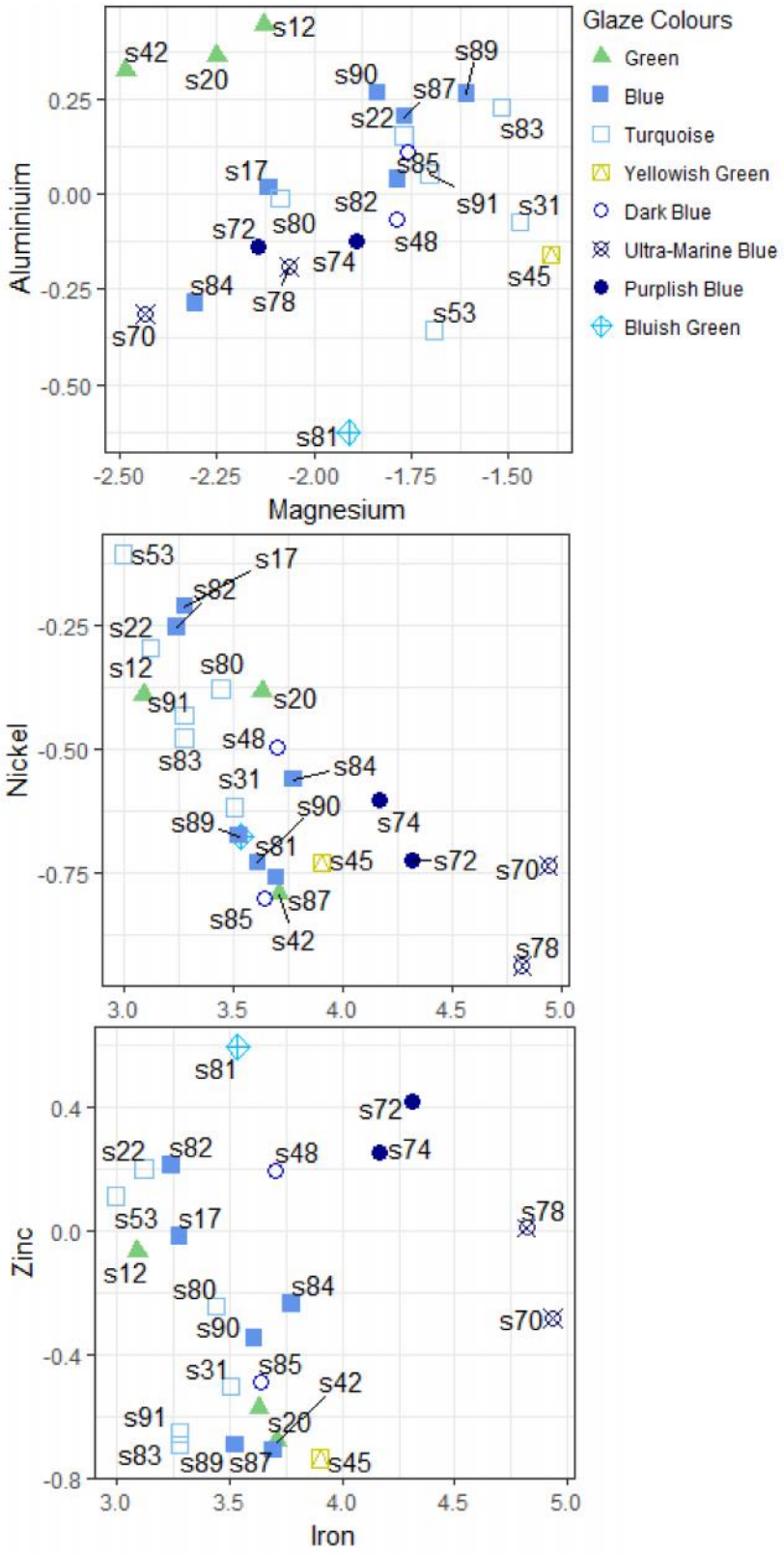

Fig. 10-3: Bivariate plots of dataset Arch 1.1R for magnesium/aluminium, iron/nickel, and iron/zinc. Aluminium/magnesium exhibiting positive correlation for greens and cobalt blues. All samples exhibit a negative correlation for iron/nickel and iron/zinc. Aluminium is a good identifier for green glazes and iron is for cobalt blue (s70, s72, s74 and s78).

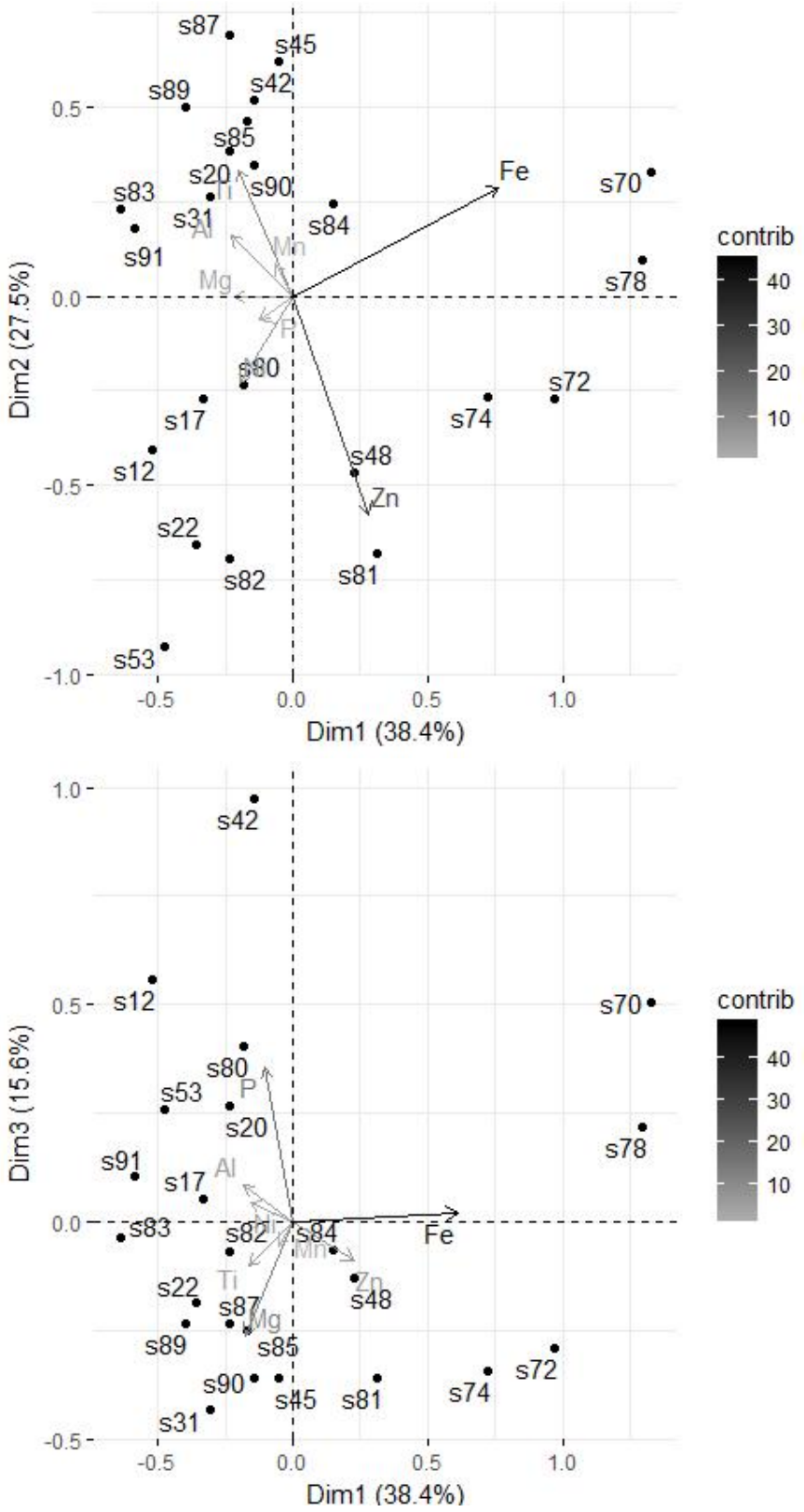

Fig. 10-4: PCA biplots of components 1 through 3 for dataset Arch 1.1R. Cobalt blue glazes are represented by two distinct pair groupings (s70/s78 and s72/s74). Dark blue (s48) and bluish green (s81) glazed samples may represent an additional grouping separate from the other samples.

Table 10-5: Loadings, Eigenvalues and Variance for dataset Arch 1.1R. Iron, zinc and phosphorus explain most of the variance in components 1 through 3. The three components explain 81.56% of the variance in the data.

Dataset Arch1.1R HH-XRF 15 kV PCA Loadings

	Non-Rotated Results						Varimax Rotated Results				
	Dim.1	Dim.2	Dim.3	Dim.4	Dim.5		Dim.1	Dim.2	Dim.3	Dim.4	Dim.5
Mg	-0.23	0.00	-0.55	-0.65	0.03	Mg		0.16	-0.18	-0.84	0.17
Al	-0.25	0.20	0.18	0.10	-0.83	Al	-0.13	0.30	-0.21		-0.82
P	-0.14	-0.08	0.75	-0.25	0.35	P	-0.13	0.16	0.84	0.13	
Ti	-0.22	0.43	-0.21	0.61	0.33	Ti	-0.10	0.32	-0.43	0.52	0.43
Mn	-0.07	0.11	-0.12	0.00	0.27	Mn		0.11			0.30
Fe	0.82	0.37	0.05	-0.15	-0.06	Fe	0.91				
Ni	-0.21	-0.29	0.09	0.02	-0.03	Ni	-0.33	-0.14	0.11		
Zn	0.30	-0.73	-0.19	0.32	-0.05	Zn	-0.13	-0.85	-0.14		

Dataset Arch1.1R Eigenvalues and Variance

	Eigenvalue	Variance %	Cumulative Variance %
Dim.1	0.31	38.38	38.38
Dim.2	0.22	27.53	65.91
Dim.3	0.13	15.65	81.56
Dim.4	0.07	8.36	89.91
Dim.5	0.05	5.92	95.84
Dim.6	0.02	2.33	98.16
Dim.7	0.01	1.84	100.00
Dim.8	0.00	0.00	100.00

width and a scree plot (Fig. 10-5) were used to determine the number of clusters (k) required for input for HCA and K-means analysis. The gap statistics indicate a single cluster but could easily indicate between three and seven clusters with five exhibiting the greatest possibility. Average silhouette graph indicates three clusters with five being a close second possibility. The scree plot exhibits three clusters. This discordance in the number of clusters predicted is an indicator that the data is not distinctly clustered. The analyses were conducted using three to five clusters with three exhibiting optimum results for HCA (Ward's method) and five for K-means based on glaze colours.

The HCA (Ward's Method) reveals three clusters (Fig. 10-6). The cobalt coloured samples (s70, s72, s74 and s78) and a blueish green sample (s81) are assigned to a single cluster. The cobalt samples exhibit between 25% and 40% confidence in being correctly assigned to a cluster. Sample s81 exhibits a~16% confidence of being incorrectly assigned to the same cluster. The green glazes sherds have been intermixed between the other two clusters. Sample s17 is the only other sample that shows a confidence in being incorrectly assigned to a cluster (~16%).

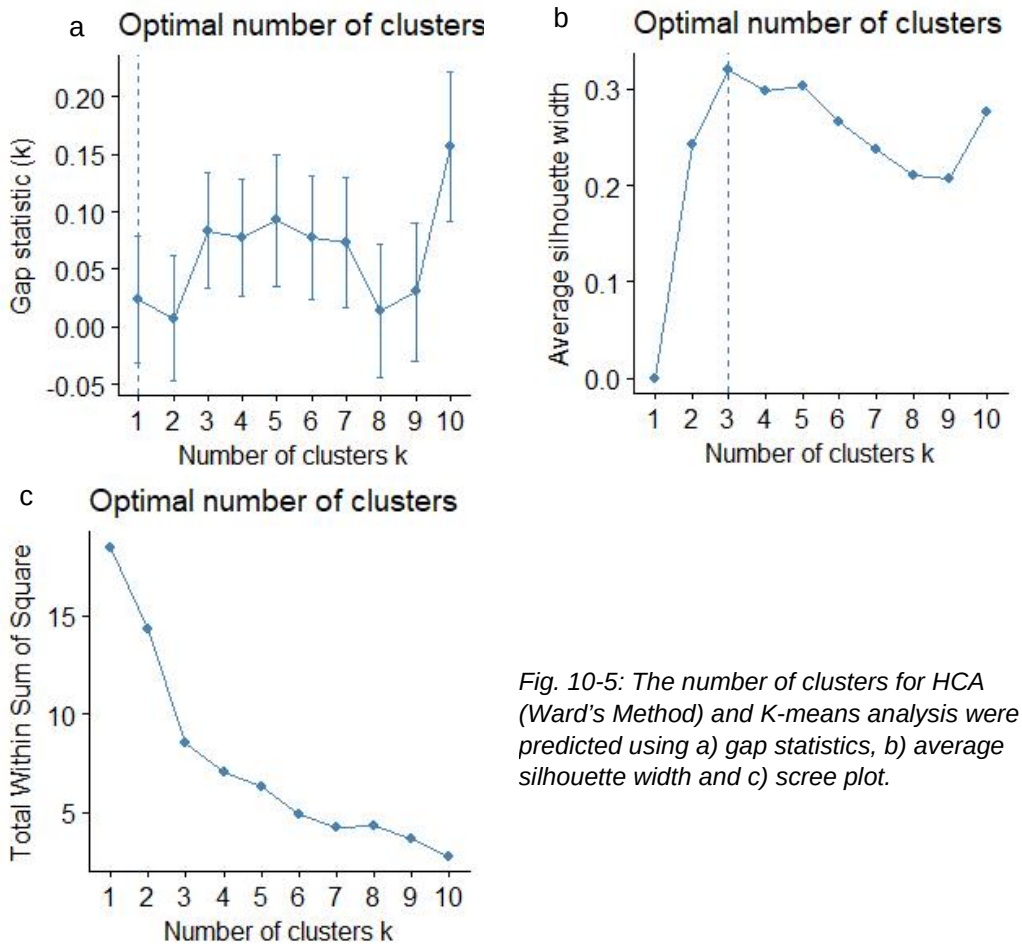

Fig. 10-5: The number of clusters for HCA (Ward's Method) and K-means analysis were predicted using a) gap statistics, b) average silhouette width and c) scree plot.

The K-means analysis reveals five clusters (Fig. 10-7). Clusters 1 and 3 make up the bulk of the copper blue coloured glazes with the green glazes intermixed. Cluster 2 is composed of two cobalt samples (s70 and s78) which represent one of the cobalt coloured pairs identified in the iron associated bivariate plots. Cluster 4 represents the other cobalt blue pair (s72 and s74) along with samples s48 and s81 which were identified as a separate pair cluster with the PCA biplots. Cluster 5 is composed of two green sherds (s20 and s42) and a blue sherd (s84). Samples s20 and s84 exhibit ~5% confidence that they have been incorrectly assigned to cluster 4.

Hierarchical K-means analysis was conducted on the dataset as a validation tool and revealed that HCA and K-means failed to correspond with the same cluster sample assignments. This possibly indicates that the data is not distinctly clustered and that outliers influenced HCA and K-means.

Dataset Arch 1.1 using the full variable set is included because it exhibits greater clustering capability than Arch 1.1R. The clustering is influenced by the colourants.

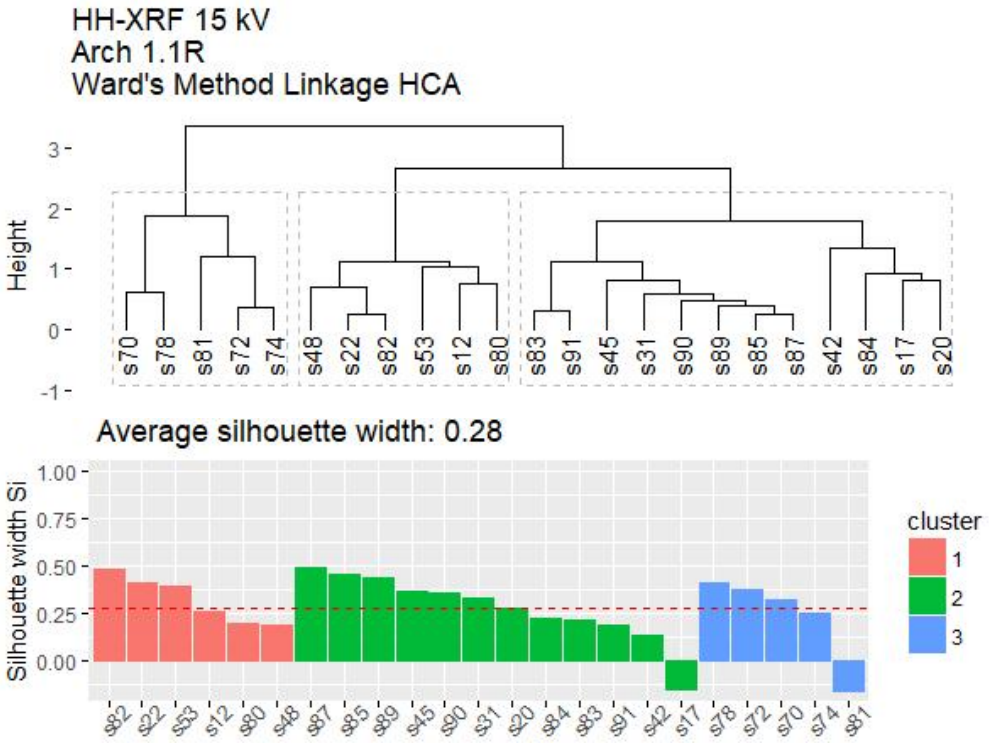

Fig. 10-6: HCA (Ward's Method) of dataset Arch 1.1R. The silhouette graph indicates a 28% confidence that the samples are assigned correctly. Two samples (s17 and s81) have ~16% confidence that they have been incorrectly assigned to a cluster. These represent samples that lie in-between clusters and may belong to either one. The cobalt samples (s70, s72, s74 and s78) have been clustered together.

The PCA biplot and boxplot identify samples s53 and s81 as outliers based on calcium. The surface of these glazes have a white encrustation in areas of the glaze. Although measurements were conducted from these areas, it is possible that the entire surface has a thin coating that is not always visible to the naked eye. These two samples have been removed from further analysis. The HCA (single linkage), PCA biplots, boxplots and pairwise plot identified sample s21 as an outlier based on manganese. Sample s21 is the only purple specimen with manganese as the colourant. Sample variance for this dataset is expected to be influenced most by the colourants used in the glaze. Samples s21 and s45 are identified as outliers with the copper boxplot. This is reasonable because the colour of these two sherd glazes (purple and yellowish-green, respectively) are not determined by the copper content. The phosphorus boxplot identified sample s42 as an outlier. Samples s70 and s78 were identified by the iron boxplot as outliers. These three samples are considered as tails of the data. Samples s21, s42, s45, s70 and s78 were retained for further analysis.

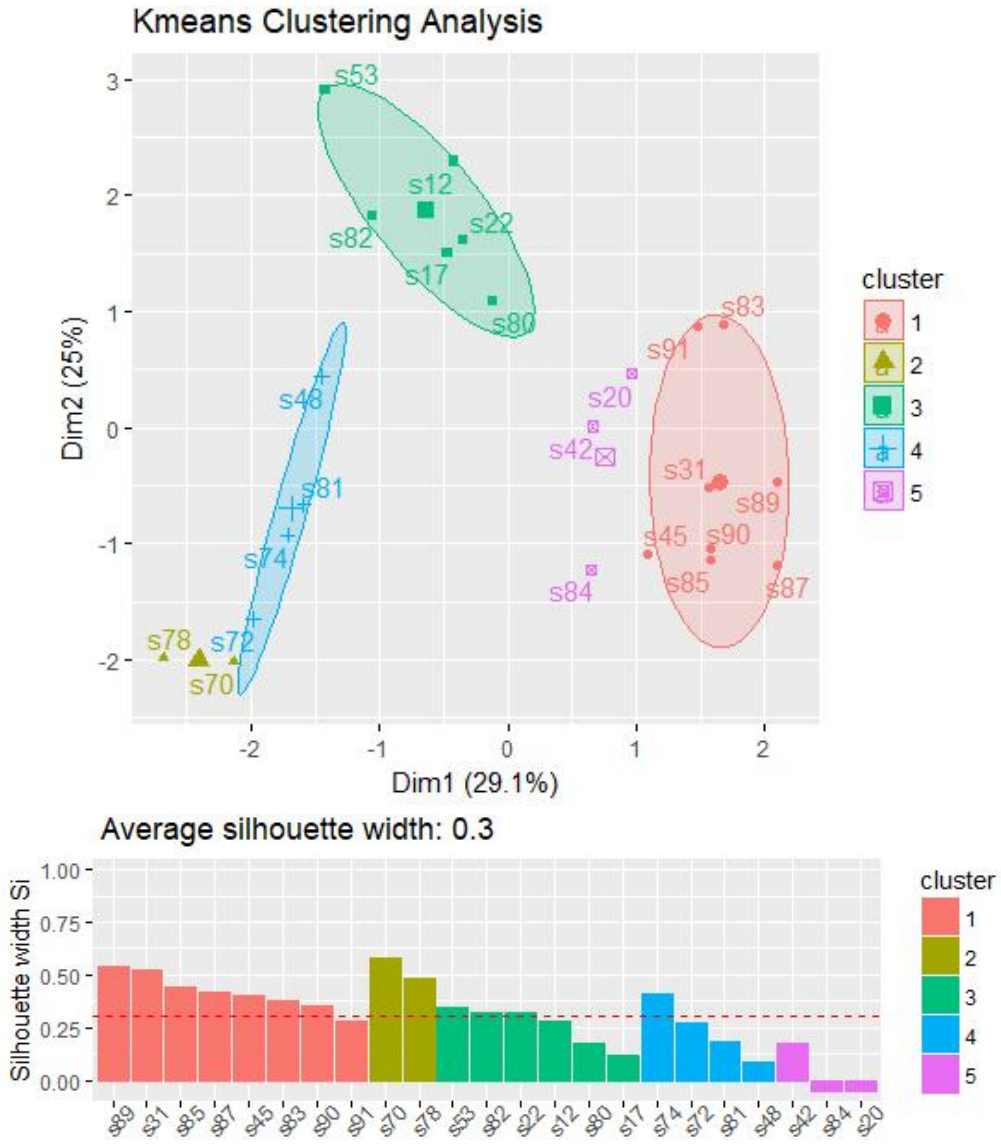

Fig. 10-7: K-means analysis of dataset Arch 1.1R exhibiting five clusters. Clusters 2 and 4 represent dark blue glazes with the exception of sample s81 which is bluish green. Cluster 5 is composed to two green glazes and a blue glaze although one green and the blue exhibit ~5% confidence in being incorrectly assigned to the cluster. Clusters 1 and 3 are composed of the bulk of the copper blue coloured sherds.

The pairwise plot for dataset Arch 1.1 reveals some high correlations between variables (Table 10-6). Many of these high correlations are associated with green glazes but this may be a result of only three green glazes existing in the set. This number of green glazes is not enough to confidently identify true high correlations. Bivariate plots (Fig. 10-8) reveal that aluminium is a good marker variable for separating the green glazes from the assemblage whereas iron is a good marker

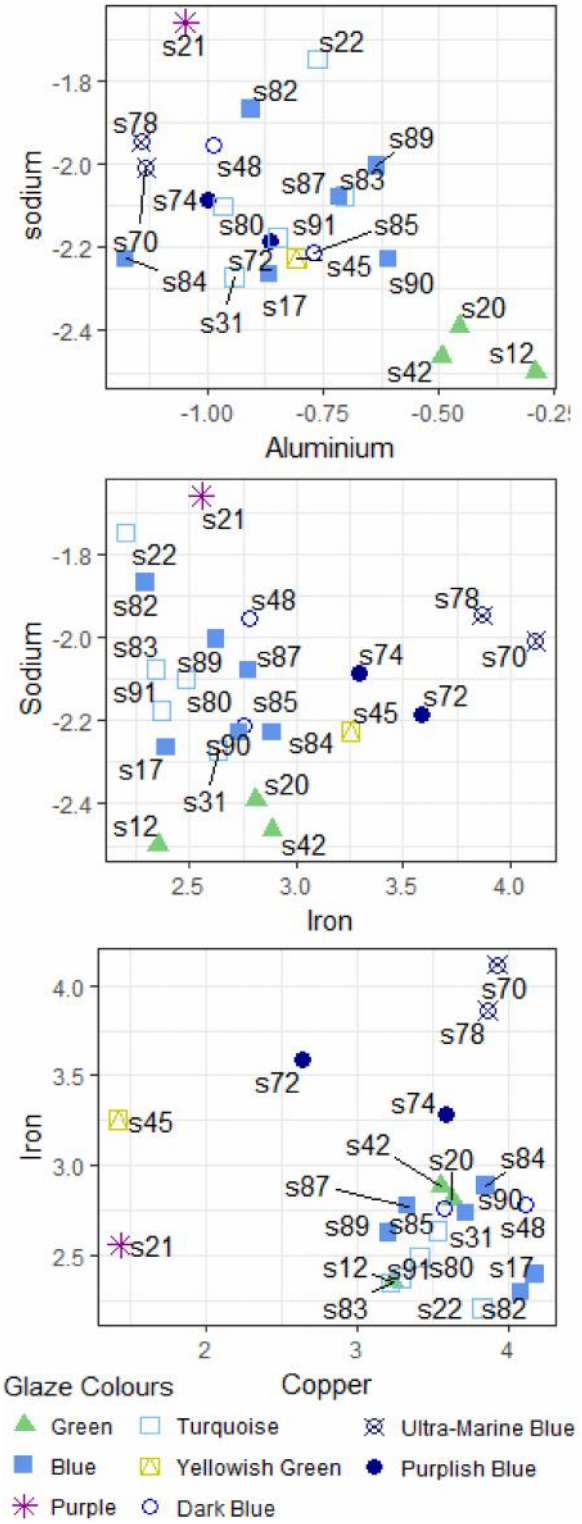

Fig. 10-8: Bivariate plots for sodium/aluminium, sodium/iron and iron/copper for dataset Arch 1.1. Aluminium is an identifier for green glazes whereas iron is for cobalt blue and the single yellow glazes. The copper/iron combination separates the cobalt blues, yellow and purple glazes from the greens and copper blues glazes.

Table 10-6: Arch 1.1 Correlations > R^2 ±0.8

Correlations for Arch 1.1 > R^2= ±0.8			
Variables	Cu Blue	Co Blue	Green
Al/Na	0.4	-0.98	-0.63
Si/Na	0.72	-0.8	-0.66
P/Na	-0.06	0.69	-0.81
Ti/Na	-0.57	-0.97	0.87
Ni/Na	0.31	-0.83	0.04
Cu/Na	0.33	0.92	0.86
Zn/Na	0.02	-0.91	-0.65
Al/Mg	0.35	0.69	0.93
Si/Mg	0.81	0.88	0.99
P/Mg	-0.18	-0.99	-0.33
Ca/Mg	-0.06	0.45	-0.97
Mn/Mg	0.12	-0.16	-0.84
Fe/Mg	-0.15	-0.97	-0.91
Ni/Mg	-0.27	0.31	0.95
Zn/Mg	-0.37	0.8	0.91
Si/Al	0.81	0.89	0.99
Ca/Al	-0.62	-0.16	-0.99
Ti/Al	0.27	0.9	-0.93
Mn/Al	0.12	0.53	-0.98
Fe/Al	0.12	-0.66	-0.99
Cu/Al	0.01	-0.96	-0.94
Zn/Al	-0.66	0.98	1
P/Si	-0.22	-0.97	0.96
Ca/Si	-0.59	0.23	-0.99
Ti/Si	-0.16	0.64	-0.95
Mn/Si	0.13	0.13	-0.99
Fe/Si	-0.09	-0.91	-1
Cu/Si	-0.09	-0.79	-0.95
Zn/Si	-0.56	0.96	1
Fe/P	-0.65	0.98	-0.1
Zn/P	0.08	-0.86	0.08
Ti/Ca	-0.03	-0.58	0.87
Mn/Ca	0.19	-0.91	0.95
Fe/Ca	-0.14	-0.31	0.98
Ni/Ca	-0.06	-0.71	-0.83
Cu/Ca	-0.61	0.12	0.88
Zn/Ca	0.02	0.07	-0.99
Mn/Ti	0.49	0.85	0.98
Fe/Ti	0.7	-0.42	0.95
Ni/Ti	-0.63	0.91	-0.46
Cu/Ti	-0.2	-0.84	1
Zn/Ti	-0.4	0.78	-0.94
Fe/Mn	0.5	0.07	0.99
Ni/Mn	-0.66	0.85	-0.62
Cu/Mn	-0.61	-0.51	0.99
Zn/Mn	-0.48	0.33	-0.99
Ni/Fe	-0.81	-0.44	-0.72
Cu/Fe	-0.2	0.47	0.95
Zn/Fe	-0.17	-0.75	-1
Zn/Cu	0.4	-0.94	-0.94

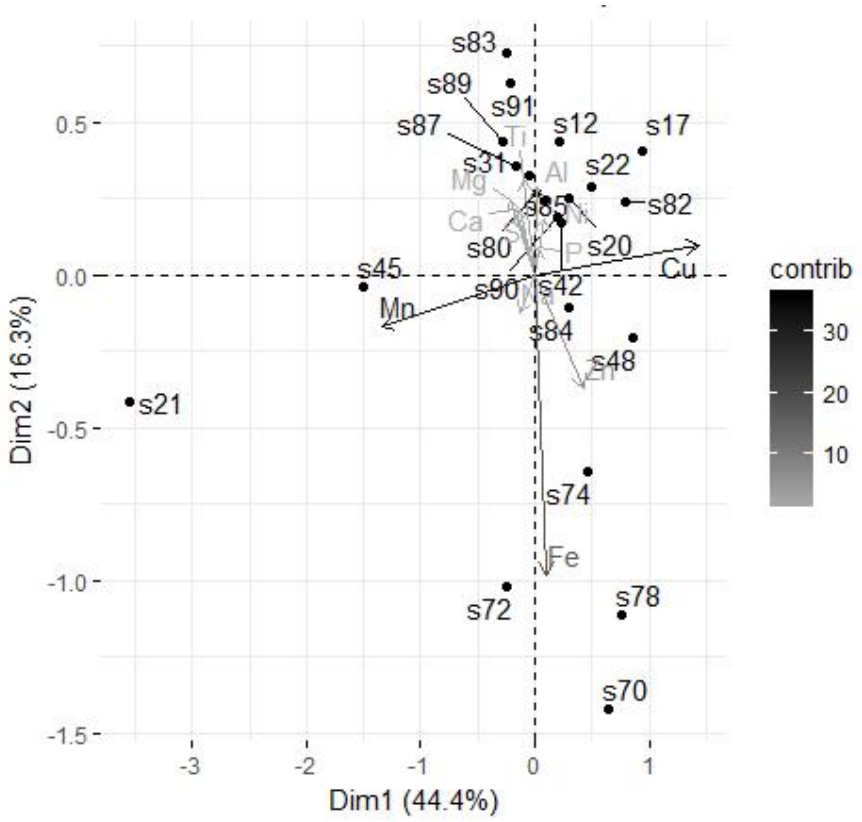

Fig. 10-9: PCA biplots of components 1 and 2 for dataset Arch 1.1. Cobalt blue glazes (s70, s72, s74 and s78) are represented by a cluster with iron separating them from the main assemblage. The manganese variable has isolated the yellow (s45) and purple (s21) glazes.

for the cobalt blue glazes. The lack of a copper variable is a good marker for isolating yellow and purple.

The PCA biplot for components 1 and 2 (Fig. 10-9) represent ~61% of the total data variance. The third PCA component and the three-dimensional PCA plot were examined but failed to reveal additional information. A cluster represents cobalt blue glazes (s70, s72, s74 and s78) with iron and zinc components segregating them from the main glaze assemblage. The manganese component segregates the yellow (s45) and purple (s21) glazes from the other glazes. Sample s48 is on the edge of the copper blue and green glazes (s12, s20 and s42) glaze cluster. The PCA non-rotated loadings (Table 10-7) indicate manganese as the main influencer of the first PCA component. The presence of copper and the absence of magnesium has the most influence on PCA component 1 with the varimax rotated results. Both result reveal iron as a major influence for the second component.

Table 10-7: Loadings, Eigenvalues and Variance for dataset Arch 1.1. Iron, manganese, copper and magnesium explain most of the variance of the two components. The two components explain 60.66% of the variance in the data.

Dataset Arch1.1 HH-XRF 15 kV PCA Loadings

	Non-Rotated Results						Varimax Rotated Results				
	Dim.1	Dim.2	Dim.3	Dim.4	Dim.5		Dim.1	Dim.2	Dim.3	Dim.4	Dim.5
Na	-0.06	-0.10	0.22	0.06	-0.30	Na					-0.38
Mg	-0.11	0.20	-0.20	0.32	-0.42	Mg	-0.56		-0.14		-0.16
Al	0.01	0.23	-0.11	0.10	0.30	Al		0.15			0.37
Si	-0.07	0.17	-0.04	0.27	-0.17	Si	-0.34	0.14			
P	0.01	0.07	-0.10	-0.11	0.62	P	0.28				0.57
Ca	-0.08	0.17	-0.28	-0.48	-0.38	Ca				-0.68	
Ti	-0.05	0.25	-0.34	-0.16	0.15	Ti				-0.28	0.38
Mn	-0.66	-0.14	0.56	-0.24	0.08	Mn	0.18		0.86		-0.22
Fe	0.05	-0.79	-0.40	-0.15	0.00	Fe	0.16	-0.88			
Ni	0.04	0.15	0.09	0.23	0.19	Ni		0.20		0.24	0.16
Cu	0.70	0.08	0.43	-0.37	-0.11	Cu	0.64	0.35	-0.43		-0.34
Zn	0.21	-0.30	0.16	0.52	0.03	Zn			-0.14	0.61	-0.17

Dataset Arch1.1 Eigenvalues and Variance

	Eigenvalue	Variance %	Cumulative Variance %
Dim.1	0.87	44.35	44.35
Dim.2	0.32	16.31	60.66
Dim.3	0.26	13.07	73.73
Dim.4	0.20	10.04	83.77
Dim.5	0.14	6.98	90.74
Dim.6	0.08	4.29	95.03
Dim.7	0.05	2.64	97.67
Dim.8	0.02	1.20	98.87
Dim.9	0.01	0.58	99.45
Dim.10	0.01	0.43	99.88
Dim.11	0.00	0.12	100.00
Dim.12	0.00	0.00	100.00

A scree plot indicates six clusters as optimal for use with HCA and K-means analysis. The HCA (Ward's Method) dendrogram (Fig. 10-10) exhibits the samples generally divided by glaze colour. This is especially true for yellow, purple and cobalt blue glazes which are assigned to their own clusters. The green glazes have been assigned to a single cluster along with two copper blue samples (s17 and s84). The two copper glazes have the highest negative confidence (-5-10%), although low, indicating that they may be misassigned to a cluster. The remainder of the copper blue glazes have been assigned to a single cluster.

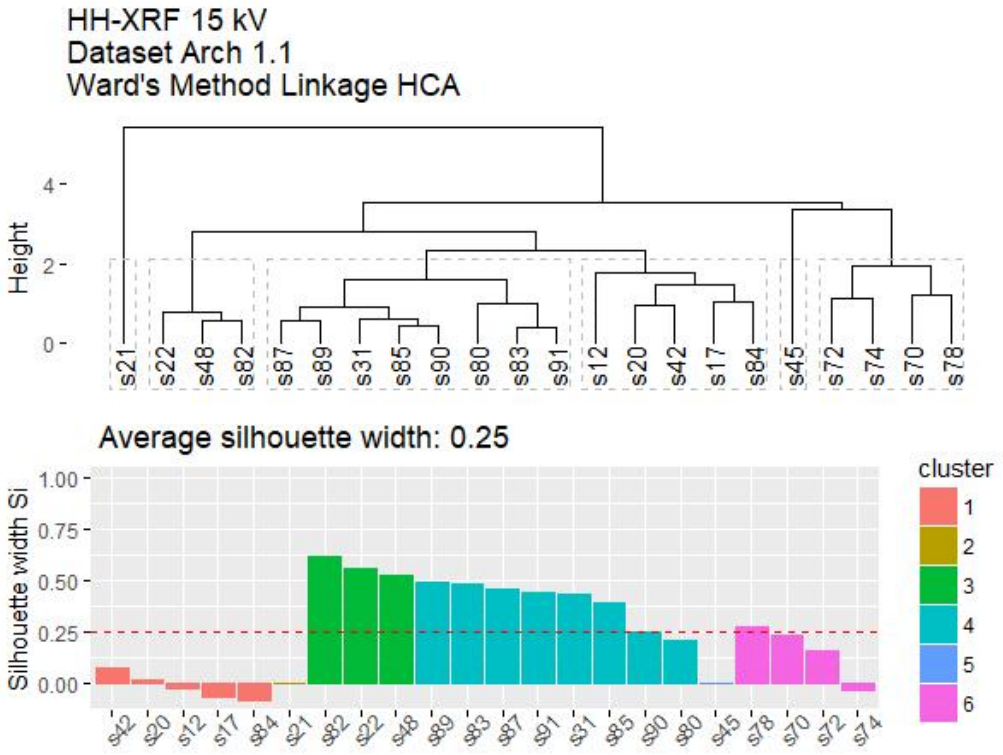

Fig. 10-10: HCA (Wards Method) of dataset Arch 1.1 assigned samples to clusters mostly corresponding to glaze colours. This is especially true for yellow (s45), purple (s21) and cobalt blue (s70, s72, s74 and s78). Greens (s12, s20 and s42) and two copper blue samples (s17 and s84) were intermixed into cluster 1 although the two copper samples exhibit the highest negative confidence (~8-10%) in their being assigned correctly. Clusters 3 and 4 are composed of all copper blue samples.

The K-means analysis (Fig. 10-11) has assigned samples to clusters which correspond to glaze colours. The copper coloured glazes have been subdivided into two clusters. A review of the bivariate plot (see Fig. 10-8) and the PCA biplot (see Fig. 10-9) indicates that the smaller of the two copper coloured glaze clusters contains greater amounts of copper than the remaining copper coloured glazes.

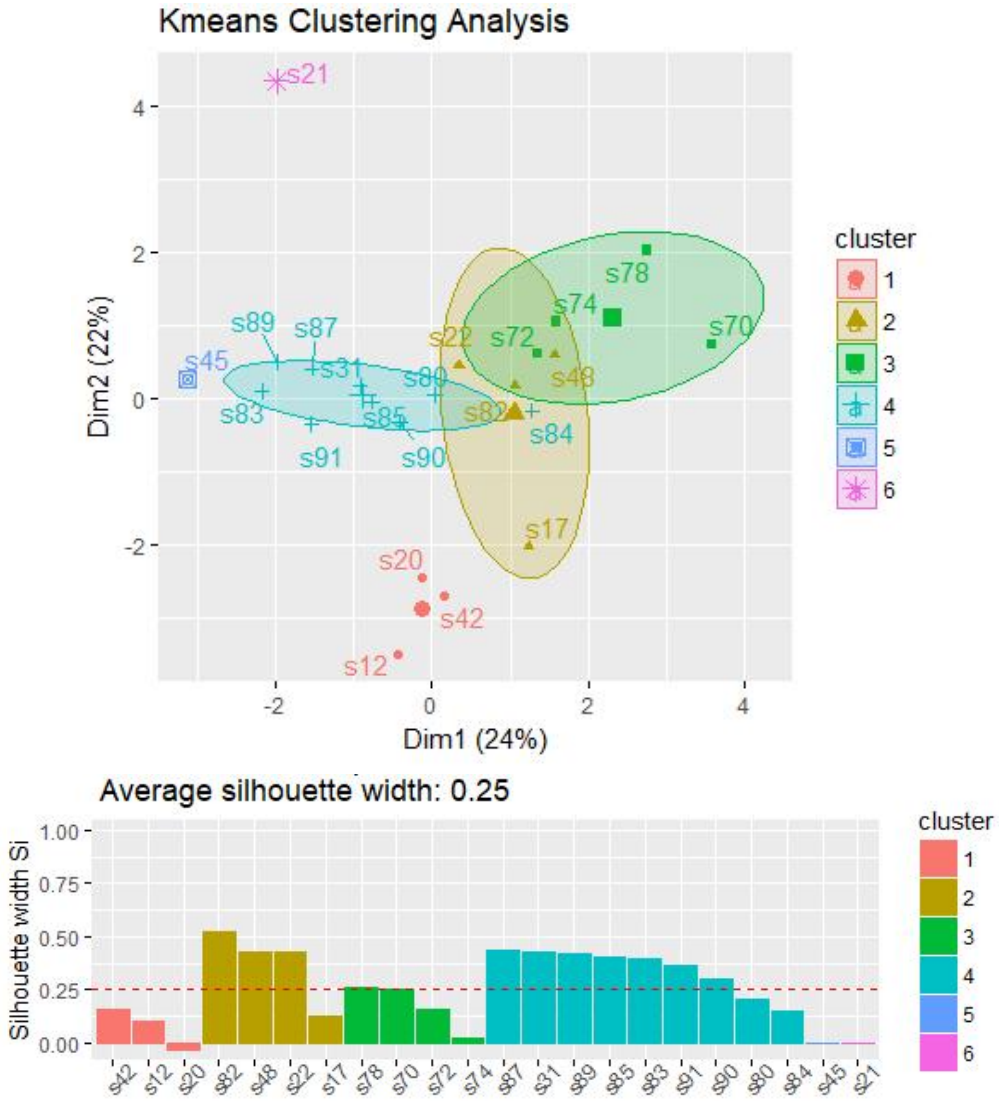

Fig. 10-11: K-means analysis of dataset Arch 1.1. The samples have been assigned to clusters which correspond to glaze colour. The copper blue glazes have been divided amongst clusters 2 and 4.

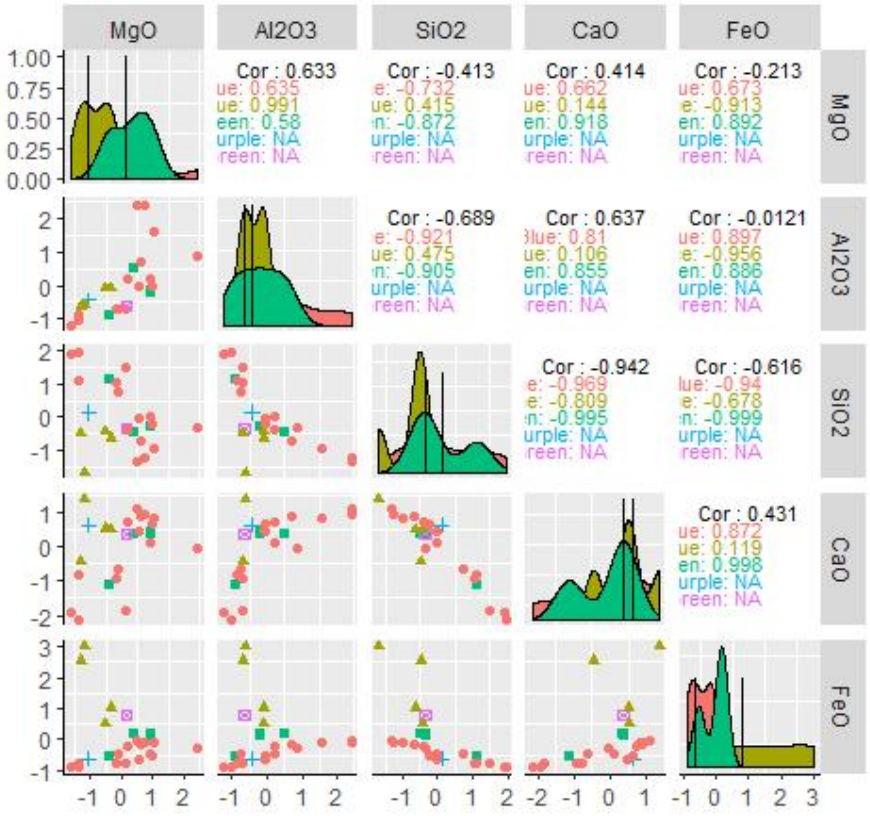

Fig. 10-12: Pairwise plot of dataset Arch 1.2 exhibiting bivariate plots, histogram and correlations of the variables. The first correlation represents all samples. There is a strong correlation with SiO_2 and CaO.

10.2.2 Dataset Arch 1.2

The HCA (single linkage) dendrogram and the PCA biplot revealed samples s70 and s78 as potential outliers. Boxplots associated the potential outliers with iron. Boxplots also exhibited samples s84 and s85 as potential outliers associated with aluminium. A review of the data reveals them as either tails of the data (s84 and s85) or as a separate cluster (s70 and s78). All four samples are retained for analysis.

The pairwise graph (Fig. 10-12) exhibits high correlation with silicon dioxide and calcium oxide for all three glazes (copper blue R^2 =-0.97, cobalt blue R^2 = -0.81 and green R^2 = -1). High correlations exist for the copper blue glazes with many of the variable pairings. The same is true for the cobalt blue and green glazes but are less significant because of the low number of samples (four and three, respectively). Bivariate plots for magnesium and aluminium oxides (Fig. 10-13) exhibit close associations for variable the pairings

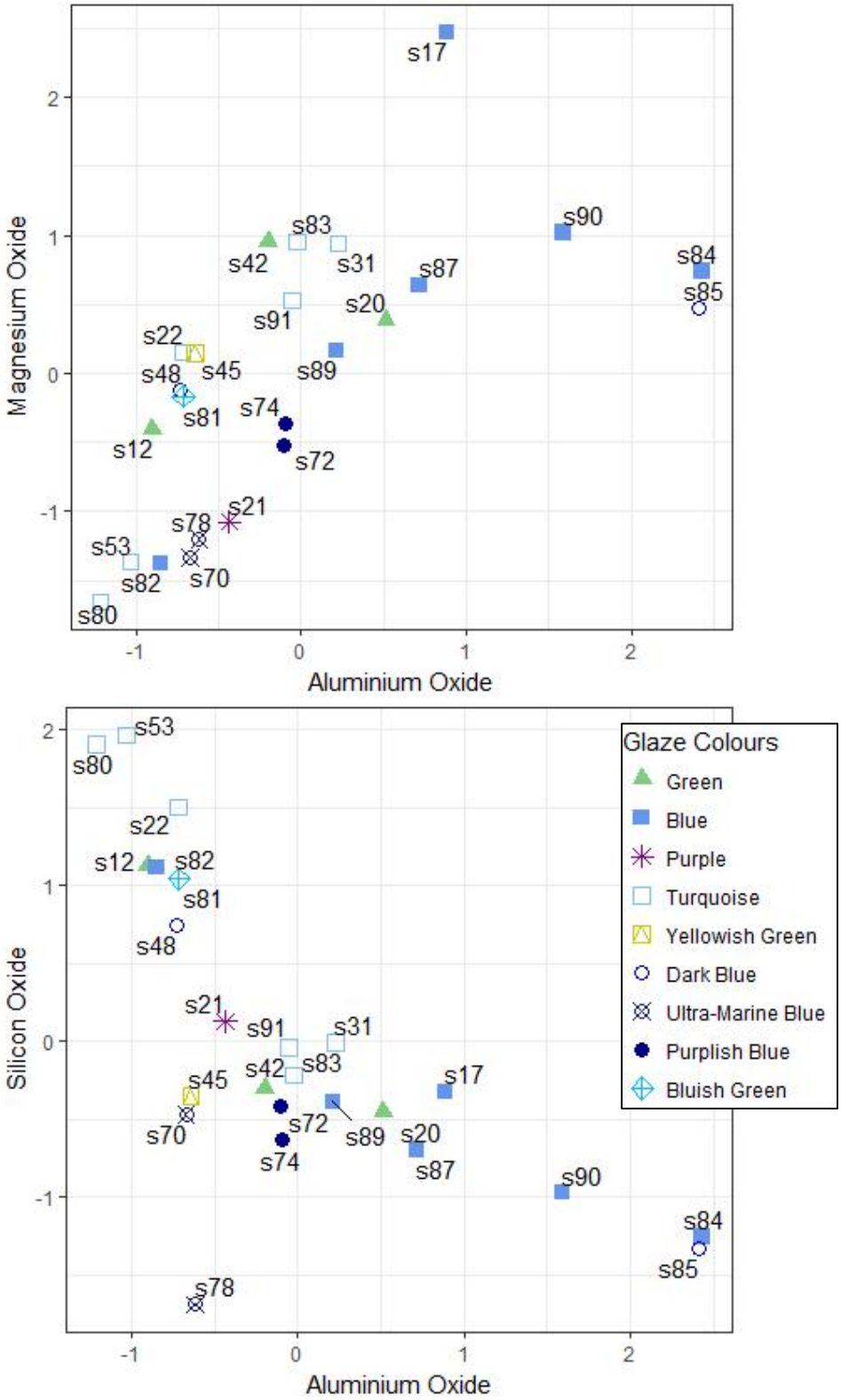

Fig. 10-13: Bivariate plots for magnesium/aluminium oxides and silicon/aluminium oxides for dataset Arch 1.2. See text for further descriptions.

consisting of cobalt blue (s70/s78 and s72/s74) and copper blue samples s48 and s81 which was noted with the HH-XRF 15 kV MVS. The bivariate plot for aluminium and silicon oxides potentially exhibit two copper blue glaze clusters. The same clusters are recognizable in the silicon and calcium oxide bivariate plots (Fig. 10-14). The aluminium/iron plot exhibits distinct separation of the yellow and cobalt blue glazes from the remainder of the assemblage.

The PCA biplot (Fig. 10-15) exhibits the same associations as the bivariate plots but in a single figure. The two cobalt blue pairings (s70/s78 and s72/s74) are recognizable although the single yellow glaze (s45) disrupts the patterning slightly. Samples s48 and s81 are in close proximity to each other. The copper blue glazes are divided into two potential clusters based on the SiO_2 variable. PCA component 1 is influenced by all the variables in the non-rotated results (Table 10-8). Most of the variables influence the component by their presence, however, SiO_2 exhibits a slightly greater influence by its absence. The rotated results indicate aluminium as the main influence for the first component. Both results indicate iron as the influencing variable for the second component. The two components represent 88.6% of the total data.

The optimal number of clusters based in gap statistics, average silhouette width and a scree plot is 4 to 6. The HCA (Ward's method) and K-means analysis were conducted using a k of 4 to 6 with 5 optimally representing the known colour characteristics. A k of 4 assigned two of the cobalt glazes with the copper coloured glazes. A k of 6 subdivided one of the copper clusters by splitting off two samples (s80 and s53) to form their own cluster. Neither of these were determined to sufficiently explain the assemblage as did the analysis with k=5.

The HCA (Ward's Method) dendrogram (Fig. 10-16) and the K-means analysis biplot reveal the same five clusters and therefore share the same silhouette graph. Cluster 1 is composed of three copper blue glazes separated from the other copper blue glazes by a higher amount of aluminium as indicated by the aluminium boxplot and the aluminium/magnesium bivariate plot (see Fig. 10-13). Cluster 2 is composed of two cobalt blue glazes separated by the amount of iron in the glaze. Cluster 3 is a copper blue and green glaze cluster with a higher amount of silicon dioxide as exhibited in the PCA biplot (see Fig. 10-15) and the silicon dioxide and calcium bivariate plot (see Fig. 10-14). Cluster 4 is an intermix of the other two cobalt blue glazes with the purple and yellow glazes separated from the other clusters by their iron content which is exhibited in the PCA biplot (see Fig. 10-15). Cluster 5 is composed of the remaining green and copper blue glazes. Sample s17 of this cluster has the most magnesium forcing it

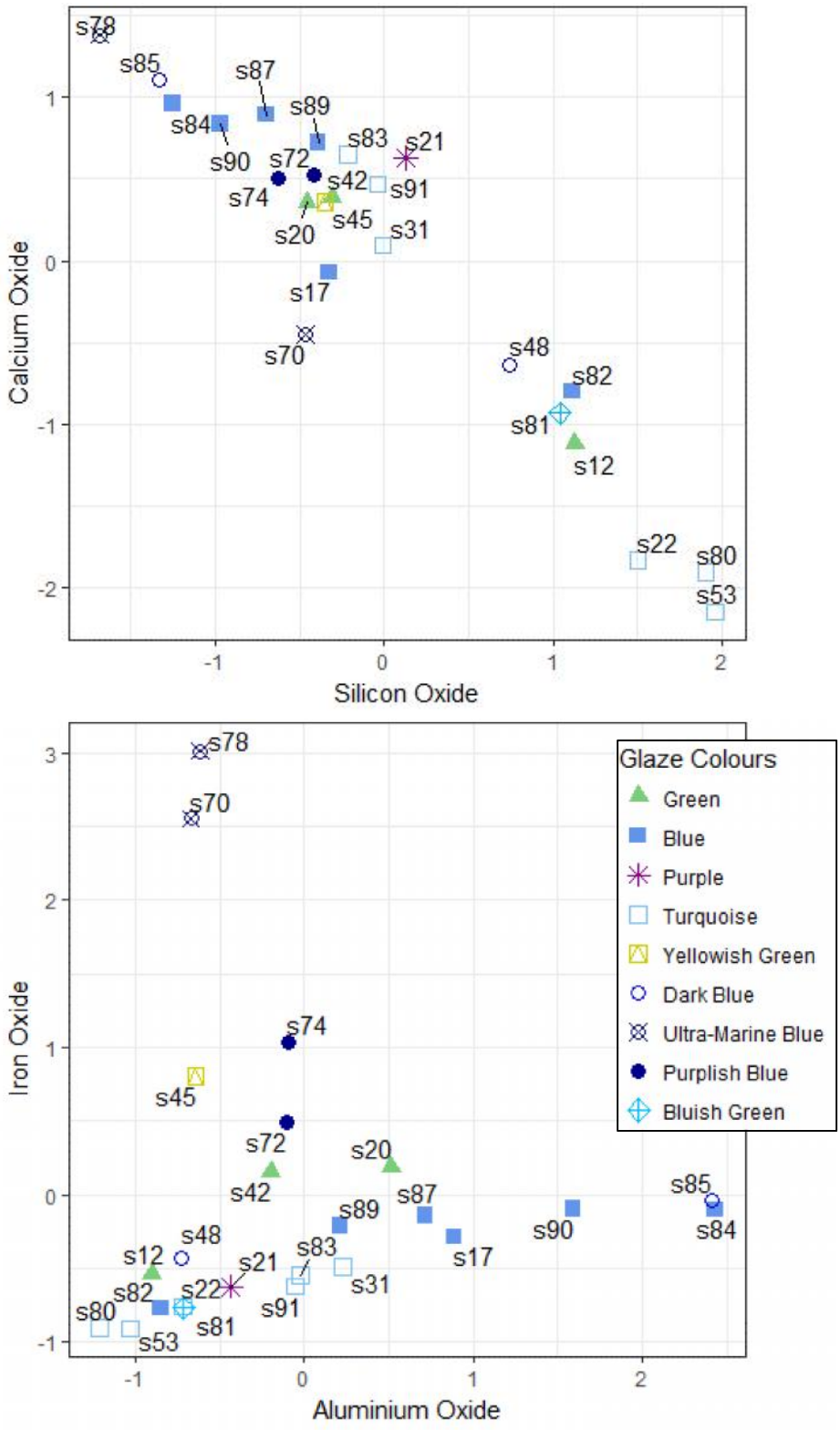

Fig. 10-14: Bivariate plots for silicon/calcium oxides and aluminium/iron oxides with dataset Arch 1.2. The silicon/calcium bivariate plot exhibits a strong negative correlation. It potentially exhibits two copper blue glaze clusters. See text for further description.

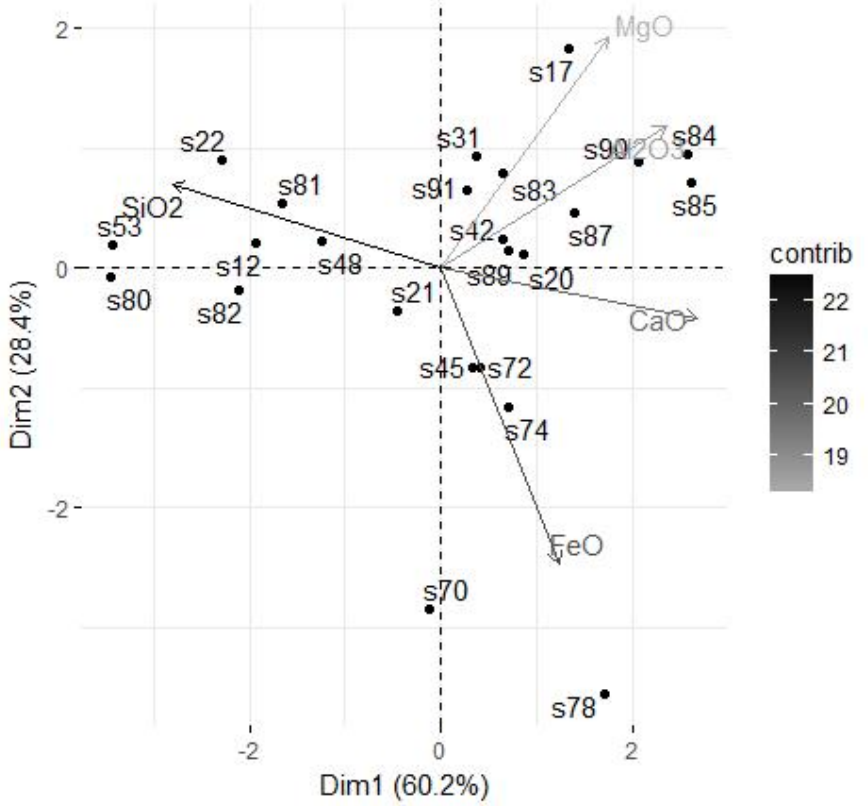

Fig. 10-15: PCA biplot of components 1 and 2 for dataset Arch 1.2. The yellow and cobalt blue samples (s45, s70, s72, s74 and s78) are separated from the copper blue samples. The copper blue samples are divided into two potential clusters.

Table 10-8: Loadings, Eigenvalues and Variance for dataset Arch 1.2. Iron and aluminium explain most of the variance in the first two components. The two components explain 88.6% of the variance in the data.

Dataset Arch1.2 SEM-EDS PCA Loadings

Non-Rotated Results	Dim.1	Dim.2	Dim.3	Dim.4	Dim.5
MgO	0.35	0.56	0.75	0.03	0.07
Al_2O_3	0.47	0.34	-0.52	0.58	0.23
SiO_2	-0.56	0.20	0.03	0.04	0.80
CaO	0.54	-0.12	-0.17	-0.69	0.44
FeO	0.25	-0.72	0.37	0.43	0.32

Varimax Rotated Results	Dim.1	Dim.2	Dim.3	Dim.4	Dim.5
MgO			1		
Al_2O_3	1				
SiO_2					1
CaO				-1	
FeO		-1			

Dataset Arch1.2 Eigenvalues and Variance

	Eigenvalue	Variance %	Cumulative Variance %
Dim.1	2.88	60.18	60.18
Dim.2	1.36	28.43	88.60
Dim.3	0.33	6.88	95.48
Dim.4	0.22	4.52	100.00
Dim.5	0.00	0.00	100.00

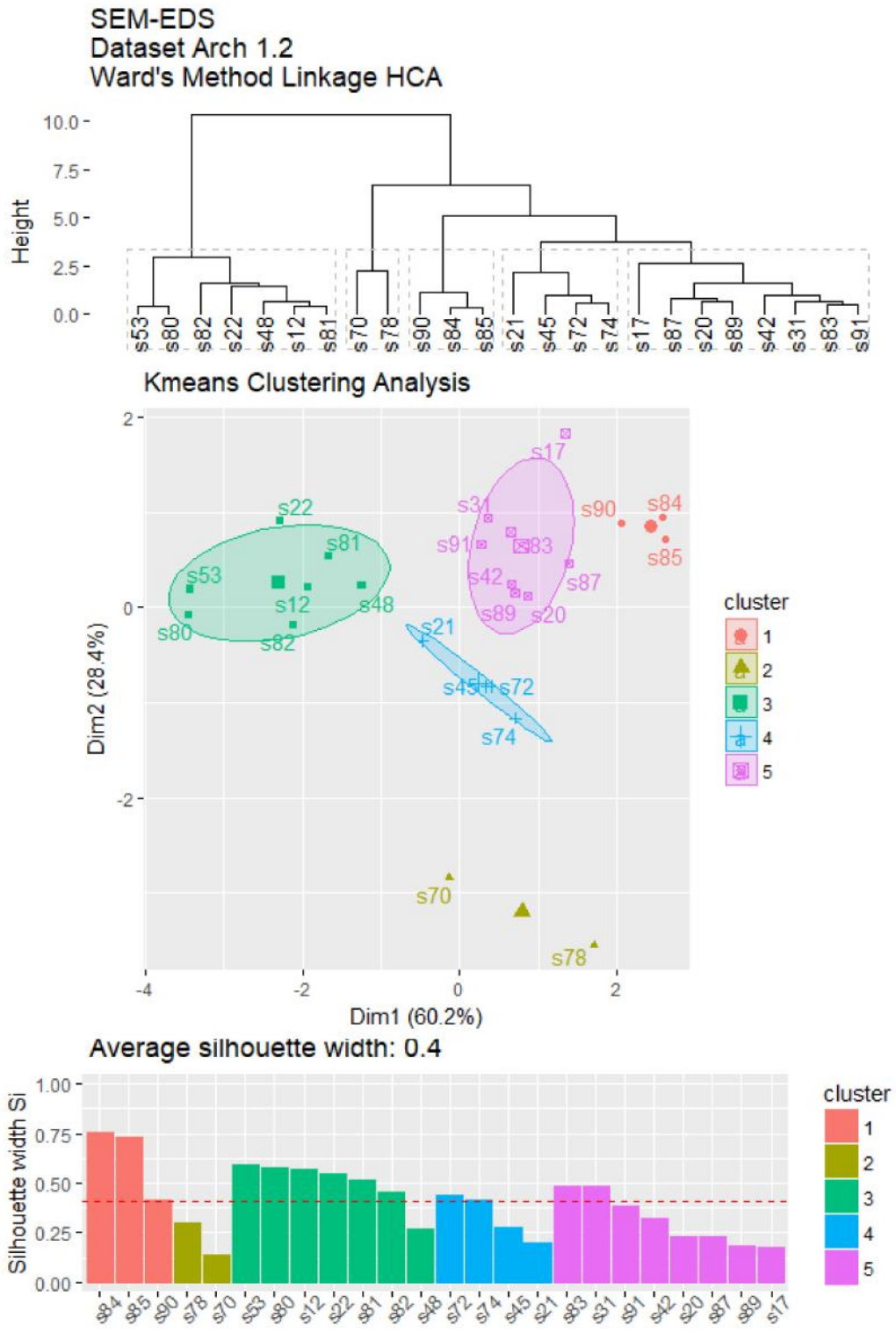

Fig. 10-16: HCA (Ward's Method) and K-means analysis of dataset Arch 1.2. The results reveal three copper blue clusters (clusters 1, 3 and 5), a cobalt blue pairing cluster (cluster 2) and an intermixed cobalt blue, yellow and purple glaze cluster (cluster 4). The green glaze samples (s12, s20 and s42) are intermixed between copper blue clusters 3 and 5.

outside of the confidence bubble in the K-means biplot. This division is evident in the HCA dendrogram.

10.2.3 Dataset Arch 1.3R

No outliers were identified with dataset Arch 1.3R. Sherds s12, s20, s42 and s45 were identified by HCA (single linkage), PCA biplot and the lead boxplot as potential outliers. These sherds are all green or yellow glazed and represent a distinct cluster.

The pairwise plot (Fig. 10-17) exhibits a moderately strong negative correlation for tin/iron (R^2 = -0.85), and lead/iron (R^2 = -0.8) element pairings with the copper coloured blue glazes. The remainder of the correlations are moderate to low. The green and cobalt blue glazes exhibit higher correlations which have been explained away in the introduction to this chapter. Tin and lead exhibit the greatest clustering tendency for the samples (see Fig. 10-17; Fig. 10-18). The yellow and green coloured glazes form a distinct cluster in most of the bivariate plots. The bivariate plots associated with iron reveal a single bi-lobed cluster or two separate copper coloured glaze clusters. These clusters do not correspond with the clusters revealed with SEM-EDS.

The PCA biplot (Fig. 10-19) exhibits the same clustering as the bivariate plots; yellow and green glazes form a distinct cluster and the copper blue glazes are subdivided into two clusters based on the iron and tin content. The loadings (Table 10-9) indicate lead and tin as the main influence on the first two components, respectively.

The optimum number of clusters (k) based in gap statistics, average silhouette width and a scree plot is 3. The HCA (Ward's Method) and K-means analysis were conducted using a k of 3. HCA (Ward's Method) dendrogram (Fig. 10-20) exhibits cluster 1 composed of the yellow and green coloured glazes. Cluster 2 is composed of all copper blue glazes. Copper and cobalt blue glazes are intermixed in Cluster 3. The dendrogram does exhibit three cobalt blue glazes on a single branch and the fourth cobalt blue glaze alone on its own branch.

The K-means analysis (Fig. 10-21) exhibits the yellow and green glazes assigned to a distinct cluster. The copper and cobalt blue glazes are intermixed and have been assigned to two clusters. The cluster sample assignments do not fully correspond with the HCA results.

Dataset Arch 1.3 containing all elements that meet the criteria (see Chapter 8) only introduced the element copper among the variable set. A review of the MVS of this

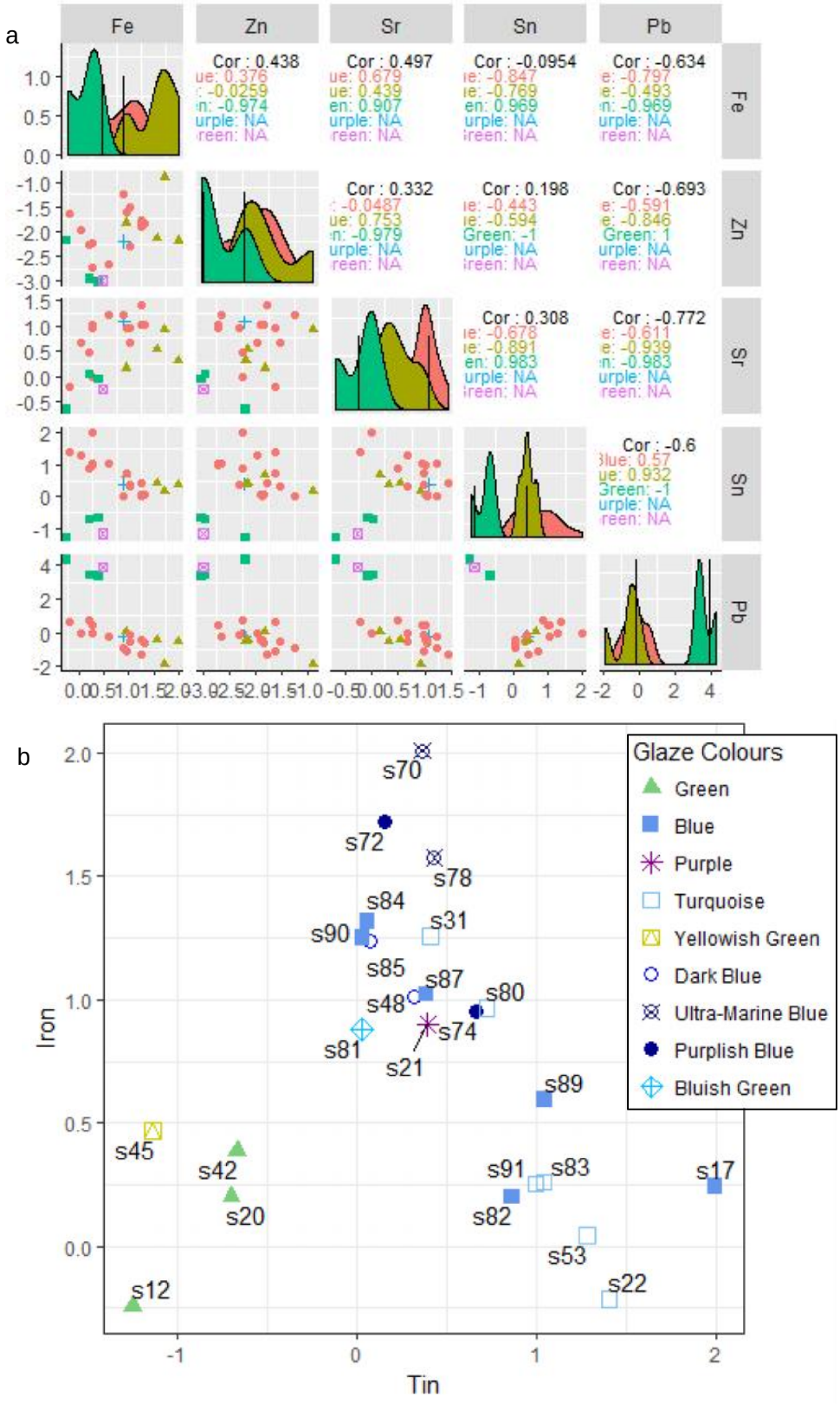

Fig. 10-17: a) Pairwise plot of dataset Arch 1.3R revealing bivariate plots, histogram and correlations of the variables. b) Bivariate plot of tin and iron for dataset Arch 1.3R. The yellow and green coloured sherds form a distinct cluster.

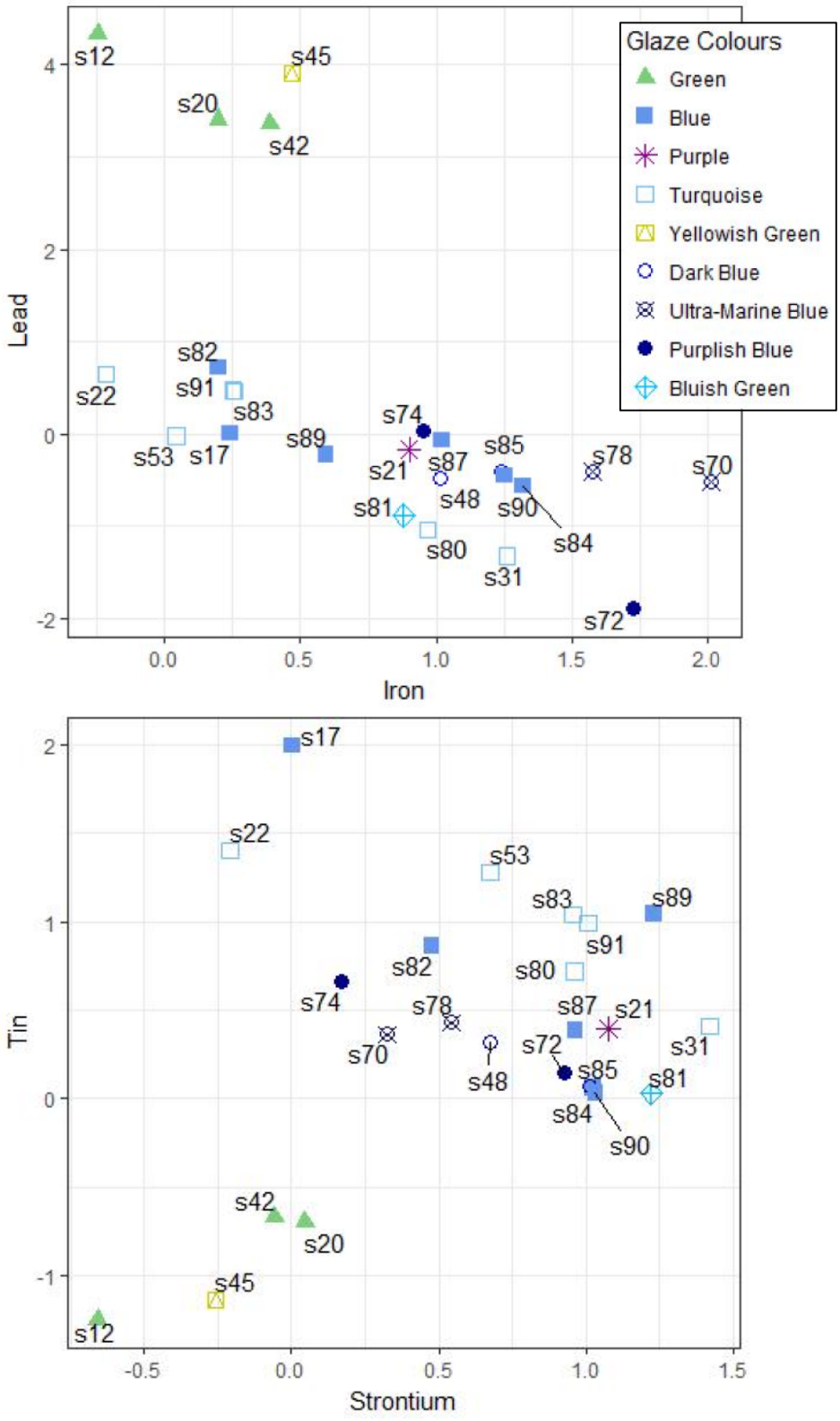

Fig. 10-18: Bivariate plots of iron/lead and strontium/tin for dataset Arch 1.3R. The yellow and green glazed sherds for a distinct cluster.

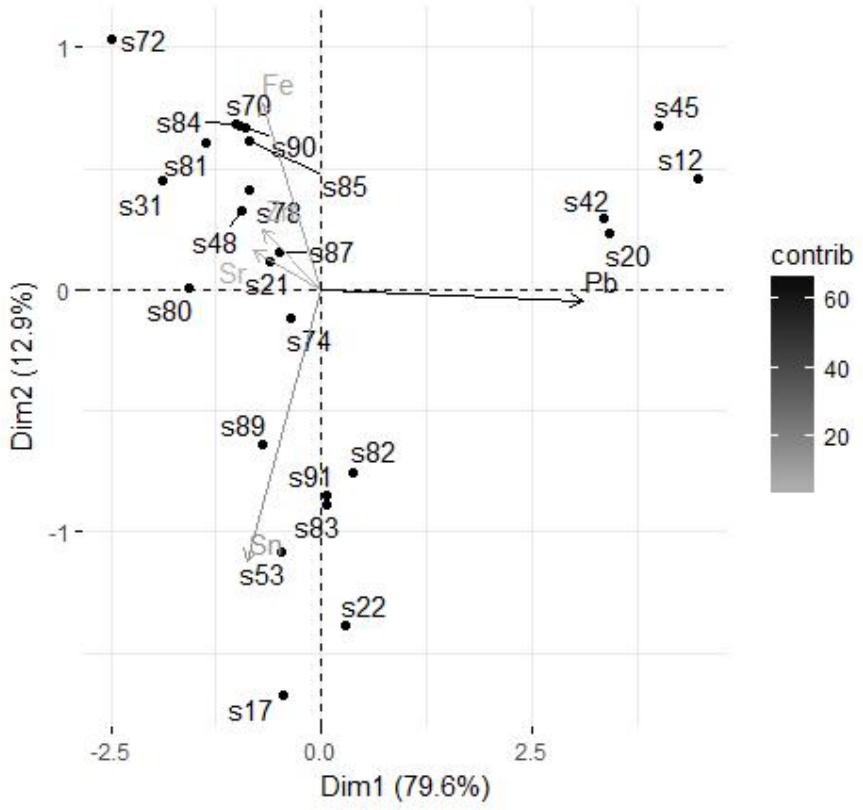

Fig. 10-19: PCA biplot of components 1 and 2 for dataset Arch 1.3R revealing 92.47% of the data variance. The yellow (s45) and green (s12, s20 and s42) glazes form a distinct cluster. The copper coloured samples are subdivided by the iron and tin content.

Table 10-9: Loadings, Eigenvalues and Variance for dataset Arch 1.3R. Lead and tin explain most of the variance in the first two components.

Dataset Arch1.3R HH-XRF 40 kV PCA Loadings

	Non-Rotated Results						Varimax Rotated Results				
	Dim.1	Dim.2	Dim.3	Dim.4	Dim.5		Dim.1	Dim.2	Dim.3	Dim.4	Dim.5
Fe	-0.20	0.55	0.15	0.66	0.45	Fe				1.00	
Zn	-0.20	0.18	-0.79	-0.33	0.45	Zn			-1.00		
Sr	-0.23	0.12	0.60	-0.61	0.45	Sr					-1.00
Sn	-0.25	-0.81	0.02	0.29	0.45	Sn		-1.00			
Pb	0.89	-0.03	0.02	0.00	0.45	Pb	1.00				

Dataset Arch1.3R Eigenvalues and Variance

	Eigenvalue	Variance %	Cumulative Variance %
Dim.1	3.32	79.59	79.59
Dim.2	0.54	12.88	92.47
Dim.3	0.20	4.73	97.20
Dim.4	0.12	2.80	100.00
Dim.5	0.00	0.00	100.00

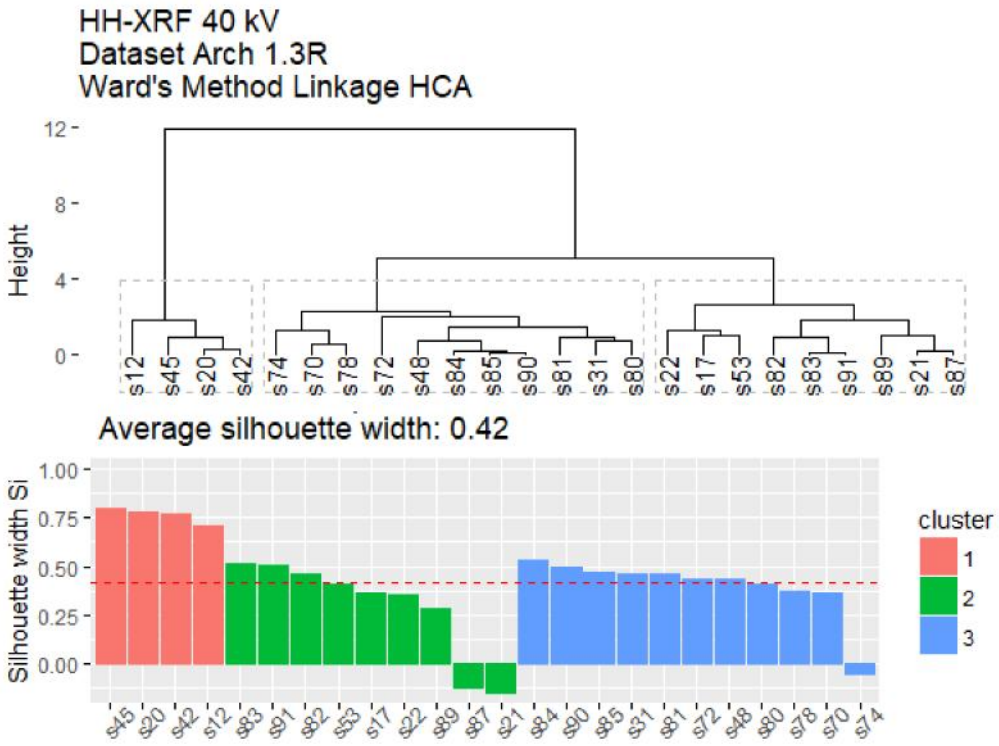

Fig. 10-20: HCA (Ward's Method) of dataset Arch 1.3R. The yellow (s45) and green glazes (s12, s20 and s42) form a distinct branch on the dendrogram. The copper blue glazes are divided into two branches. The cobalt blue glazes (s70, s72, s74, and s78) are intermixed with one of the copper blue glaze clusters although they are on their own branches. The silhouette graph exhibits a confidence that all the samples are correctly assigned to clusters at 42%, although three of the samples (s74, s21 and s87) in the two copper glaze clusters reveal a 5-15% confidence that they have been incorrectly assigned to their respective clusters.

dataset failed to reveal any new information. A noted difference between the two datasets is that sample s45 (yellow) was further afield of the other green glazes but was still assigned to the same clusters with them as assigned by HCA (Ward's Method) and K-means analysis.

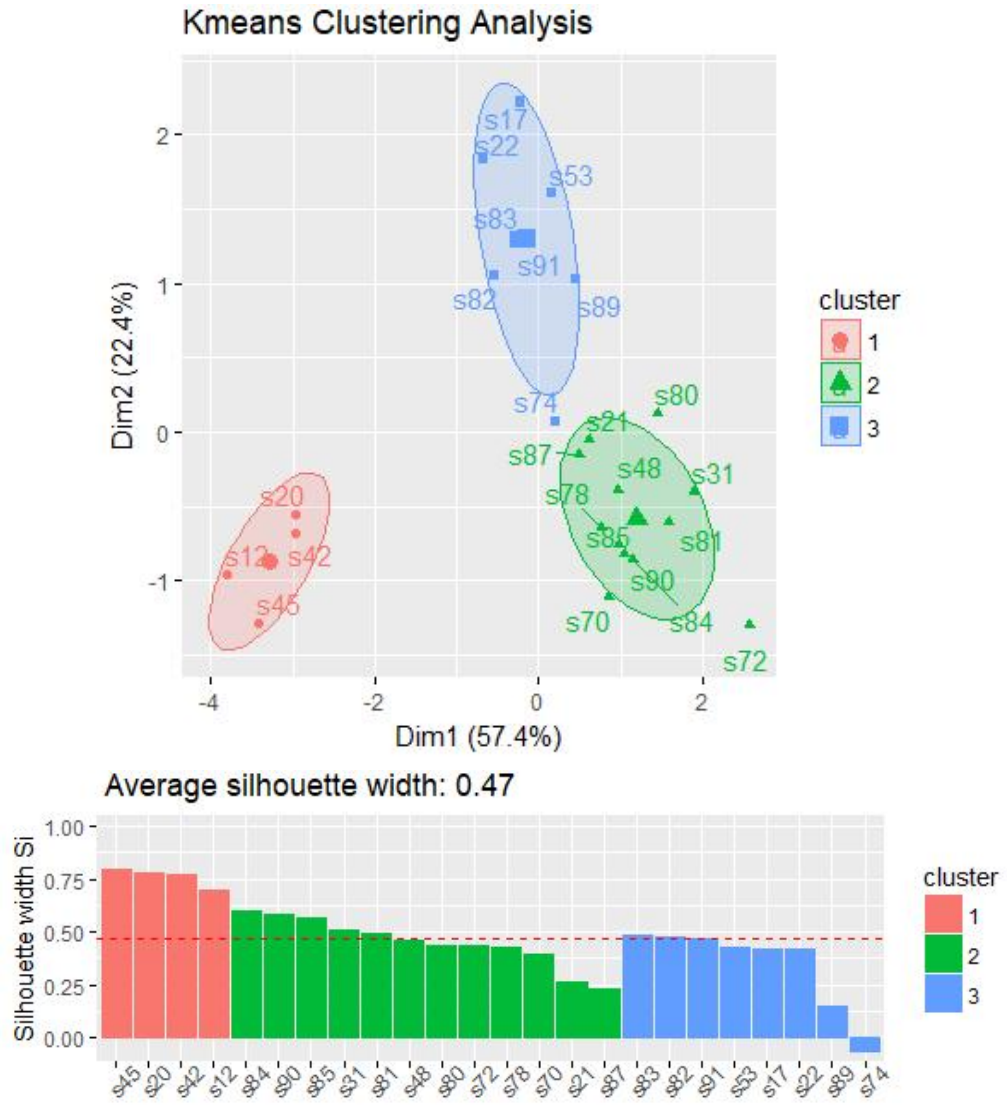

Fig. 10-21: K-means analysis of dataset Arch 1.3R. The yellow (s45) and green glazes (s12, s20 and s42) form a distinct cluster. The copper blue glazes are divided into two branches with the cobalt blue glazes (s70, s72, s74, and s78) intermixed. The silhouette graph exhibits a confidence that all the samples are correctly assigned to clusters at 47%, although one sample (s74) in cluster 3 exhibits a 10% confidence that it has been incorrectly assigned to its respective cluster. The biplot exhibits it situated between the two copper blue clusters.

10.3 Dataset Arch 2 Multivariate Analysis (All Blue Sherds)

Restricting the statistical analysis to only copper and cobalt blue glazes allows the inclusion of chromium to HH-XRF (15 kV) dataset Arch 2.1 (Table 10-10) and zirconium to HH-XRF (40 kV) dataset Arch 2.3 (Table 10-11) based on the variable criteria discussed in chapter 8. The SEM-EDS dataset Arch 2.2 (Table 10-12) loses aluminum hydroxide from the variable set but allows the inclusion of sodium and copper oxide based on the same criteria.

10.3.1 Dataset Arch 2.1R

The HCA (single linkage) dendrogram identified samples s70, s78 and s17 as possible outliers. The boxplots indicated samples s80 (chromium), s81 (aluminium), s70 and s78 (iron) as potential outliers. A review of the data indicates that the identified samples are tails of the data or represent a distinct cluster (s70 and s78). The samples have been retained for further analysis.

The pairwise plot (Fig. 10-22) exhibits a moderately high nickel/iron (R^2 = -0.74) and Ni/Mn (R^2 = -0.73) correlations with the copper blue glazed sherds. Other correlations are moderate at best. The bivariate plot for titanium and zinc (Fig. 10-23) is useful to exhibit the Group 4a and b division. The bivariate plot for titanium and iron is useful to exhibit the Group 4 split and the Group 2 cobalt blue glazes. The bivariate plot for nickel and zinc (Fig. 10-25) reveals that sample s17 is not a part of either copper blue subgroup but may represent a group upon itself.

The PCA biplot (Fig. 10-24) exhibits cobalt blue glaze group 2a as a distinct pairing separated from the other samples by iron and zinc. Cobalt glaze group 2b is separated from the other samples by the iron content whereas sample s48 and s81 are separated by the zinc content although these two do not represent a cluster. The two copper blue glaze groups are separated by the amount of nickel and zinc (Group 4a) and by titanium and aluminium (Group 4b) in the glaze. The PCA loadings (Table 10-13) for the first two PCA components indicate iron and zinc as providing the greatest variance.

The optimum number of clusters (k) based in gap statistics, average silhouette width and a scree plot is 2 to 3. HCA (Ward's Method) and K-means analysis were conducted with a k of 2 and 3. Two clusters combined the samples whereas three clusters divided the samples in a meaningful way.

The HCA (Ward's Method) dendrogram (Fig. 10-26) exhibits the cobalt blue glazes on a separate branch from the copper blue glaze samples. Samples s48 and s81

Table 10-10: HH-XRF 15 kV Net Peak Areas for Dataset Arch 2.1 (Saqqara Faience).

HH-XRF 15 kV (NPA) Saqqara Faience Dataset Arch 2.1

All Blue Glazes

Parameters 15 kV, 50 uA with a vacuum for 180 seconds (no filter)

Average of 10 Measurements

Sample	Glaze	Na	Mg	Al	Si	P	Ca	Ti
s17	Blue	5876	2811	23759	981125	5114	574024	47673
s22	Turquoise	5827	2287	15647	1152660	2525	186858	14683
s31	Turquoise	4361	4063	16457	998154	3149	531149	30286
s48	Dark Blue	6420	3030	16908	1186755	3632	311281	19037
s53	Turquoise	4719	2671	10135	638564	5406	1651737	13383
s70	Ultra-Marine Blue	4813	1387	11564	610929	4202	216098	15793
s72	Purplish Blue	5283	2673	19844	1169014	3155	403182	26645
s74	Purplish Blue	6111	3085	18114	1173289	2951	507426	22723
s78	Ultra-Marine Blue	6927	2380	15477	941410	4471	760064	17038
s80	Turquoise	4058	1586	12639	866035	4002	706484	14332
s81	Bluish Green	4468	3183	11487	650578	4411	1959044	34629
s82	Blue	6395	2701	16757	1107525	3466	324947	17071
s83	Turquoise	5144	3540	20332	1340659	3906	699362	23330
s84	Blue	4341	1651	12422	718064	3160	549746	39170
s85	Dark Blue	5648	3661	23854	1270620	3962	636725	44541
s87	Blue	5693	3100	22262	1238384	3224	749413	41160
s89	Blue	5908	3576	23270	1443953	3321	535436	31626
s90	Blue	5448	3349	27509	1172867	3108	553427	40262
s91	Turquoise	4261	2770	16054	1089216	4175	583393	23437

Sample	Glaze	Cr	Mn	Fe	Ni	Cu	Zn
s17	Blue	4558	20171	617514	18849	3708415	22914
s22	Turquoise	7293	15950	303015	9968	1545178	16356
s31	Turquoise	6818	25058	588475	9543	1452398	10701
s48	Dark Blue	4999	18030	732039	10986	2794572	21958
s53	Turquoise	5325	16283	289008	13003	1589092	16179
s70	Ultra-Marine Blue	4954	18501	2203961	7592	1828039	11955
s72	Purplish Blue	5890	24846	1696671	11021	658186	34594
s74	Purplish Blue	4652	21002	1317397	11189	1783910	26342
s78	Ultra-Marine Blue	4848	16696	2316921	7330	2320400	18902
s80	Turquoise	8771	17752	398828	8753	1012815	10026
s81	Bluish Green	5766	26161	737015	10936	1060826	38968
s82	Blue	5746	16567	411025	12489	2461044	19890
s83	Turquoise	8397	20351	427188	10011	1032560	8090
s84	Blue	5383	24885	721445	9432	1908370	13069
s85	Dark Blue	5579	27011	811714	9557	1851004	13085
s87	Blue	6033	23115	730315	8480	1282621	8934
s89	Blue	6285	23827	605167	9070	1087366	8932
s90	Blue	5829	28267	777077	10137	2096534	14887
s91	Turquoise	6774	20785	401565	9848	1016842	7922

Table 10-11: HH-XRF 40 kV Net Peak Areas for Dataset Arch 2.3 (Saqqara Faience).

HH-XRF 40 kV (NPA) Saqqara Faience Dataset Arch 2.3								
All Blue Glazes								
Parameters 40 kV, 30 uA and filter 3 for 180 seconds without vacuum								
Average of 10 Measurements								
Sample	Glaze	Fe	Cu	Zn	Sr	Zr	Sn	Pb
s17	Blue	9778	162409	816	7692	5189	56157	7676
s22	Turquoise	6020	83950	1478	6058	2499	30342	14194
s31	Turquoise	11548	70046	560	13579	2954	4943	875
s48	Dark Blue	13082	129019	1037	9303	2427	6522	2903
s53	Turquoise	6421	88871	857	12067	1675	22090	5996
s70	Ultra-Marine Blue	42080	74138	637	7802	1899	8094	3360
s72	Purplish Blue	34023	35000	2481	15334	4278	7073	910
s74	Purplish Blue	29389	94894	1842	13402	2309	22061	11702
s78	Ultra-Marine Blue	36996	83679	902	13186	1438	11774	5082
s80	Turquoise	6610	37470	504	6577	1195	5170	888
s81	Bluish Green	11884	38249	1421	16745	1575	5075	2036
s82	Blue	7388	97810	636	9734	2199	14325	12401
s83	Turquoise	8688	56732	446	17438	3057	18965	10647
s84	Blue	15389	103290	656	11462	4589	4374	2332
s85	Dark Blue	15477	96384	667	12364	4889	4838	2978
s87	Blue	15001	75928	544	14153	5419	7952	5018
s89	Blue	12821	58279	504	24238	3663	20150	5648
s90	Blue	17852	114406	799	14331	5544	5274	3229
s91	Turquoise	8594	53375	440	18279	3091	17993	10638

have been assigned to the cobalt blue cluster based on the zinc component in the glaze.

The copper blue glazes have been divided into two groups which mostly correspond with the description of Group 4a and b. The difference being that samples s91 and s83 have been included with the samples from Group 4a and sample s17 with Group 4b.

The K-means analysis biplot (Fig. 10-27) exhibits the Group 2 cobalt blue glazes in the same cluster. The copper blue glazes are divided into Groups 4a and b. Samples s48 and s81 have been included with Group 4a.

A review of the MVS results for dataset Arch 2.1 is similar to the Arch 2.1R results with the exception that s17 is further segregated from the other copper blue glazes because of the magnesium content. This supports s17 as being a distinct glaze.

Table 10-12: SEM-EDS (wt%) for Dataset Arch 2.2 (Saqqara Faience).

SEM-EDS (wt%) Saqqara Faience Dataset Arch 2.2 All Blue Glazes Parameters 20 kV, Average of 3 Measurements							
Sample	Glaze	Na_2O	MgO	SiO_2	CaO	FeO	CuO
s17	Blue	16.35	1.19	71.01	3.97	0.93	6.54
s22	Turquoise	8.44	0.74	86.06	1.67	0.50	2.58
s31	Turquoise	19.17	0.85	73.25	4.29	0.73	1.70
s48	Dark Blue	17.61	0.59	74.20	3.19	0.78	3.62
s53	Turquoise	8.64	0.34	87.98	1.17	0.32	1.54
s70	Ultra-Marine Blue	18.61	0.31	71.26	3.46	3.92	2.43
s72	Purplish Blue	17.79	0.51	73.00	4.97	1.80	1.93
s74	Purplish Blue	17.34	0.54	71.32	4.86	2.34	3.60
s78	Ultra-Marine Blue	19.02	0.34	67.83	6.07	4.39	2.36
s80	Turquoise	1.08	0.29	95.75	1.71	0.36	0.82
s81	Bluish Green	1.04	0.72	92.52	3.41	0.53	1.78
s82	Blue	14.00	0.32	80.15	3.15	0.45	1.93
s83	Turquoise	20.84	0.84	70.93	4.97	0.66	1.76
s84	Blue	20.59	0.80	69.55	5.51	1.14	2.41
s85	Dark Blue	18.91	0.76	71.29	5.89	1.24	1.91
s87	Blue	18.07	0.79	72.19	5.51	1.11	2.33
s89	Blue	19.24	0.67	72.19	5.20	1.03	1.67
s90	Blue	21.05	0.85	69.10	5.24	1.13	2.62
s91	Turquoise	21.83	0.73	70.30	4.64	0.57	1.93

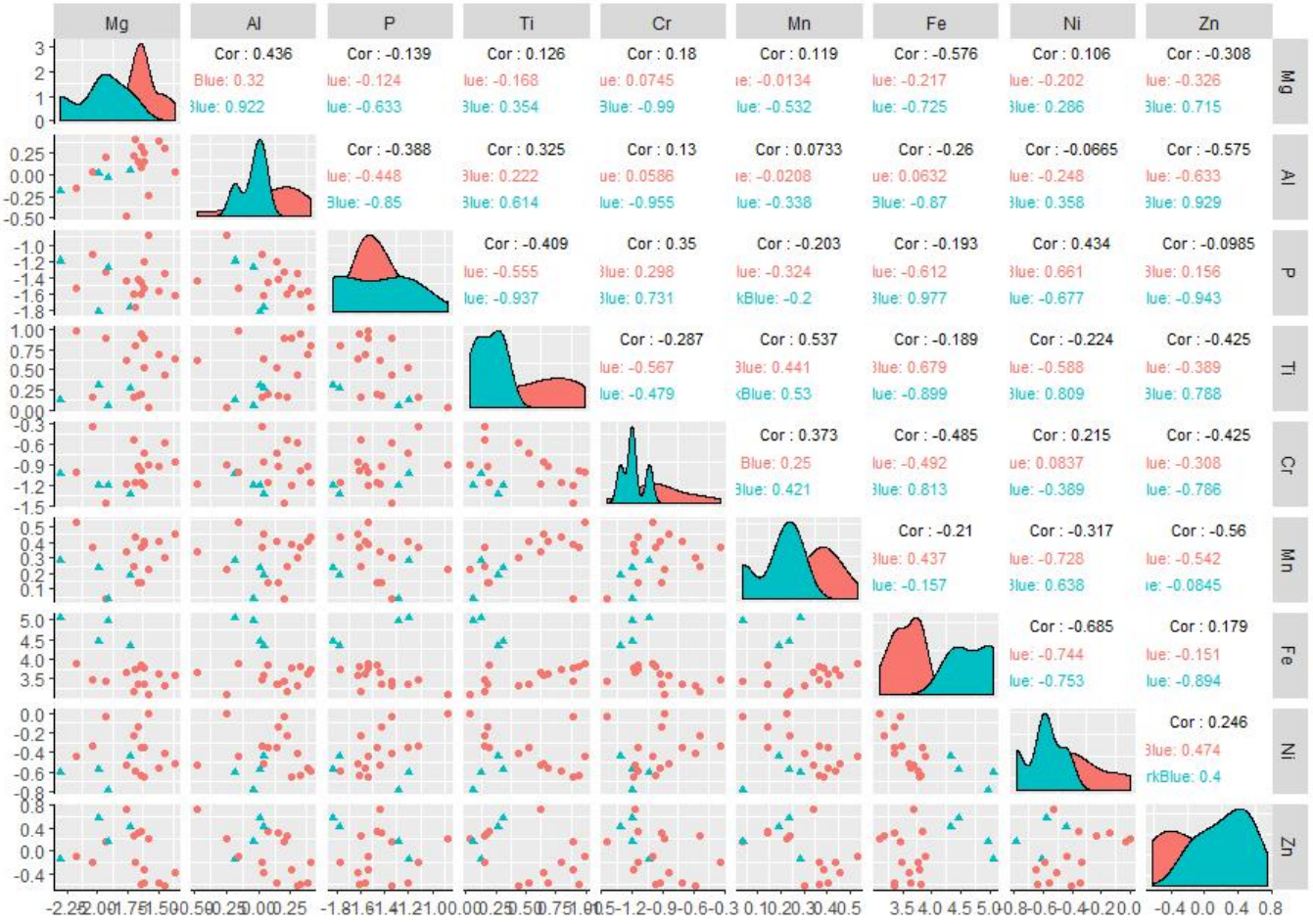

Fig. 10-22: Pairwise plot of dataset Arch 2.1R revealing bivariate plots, histogram and correlations of the variables.

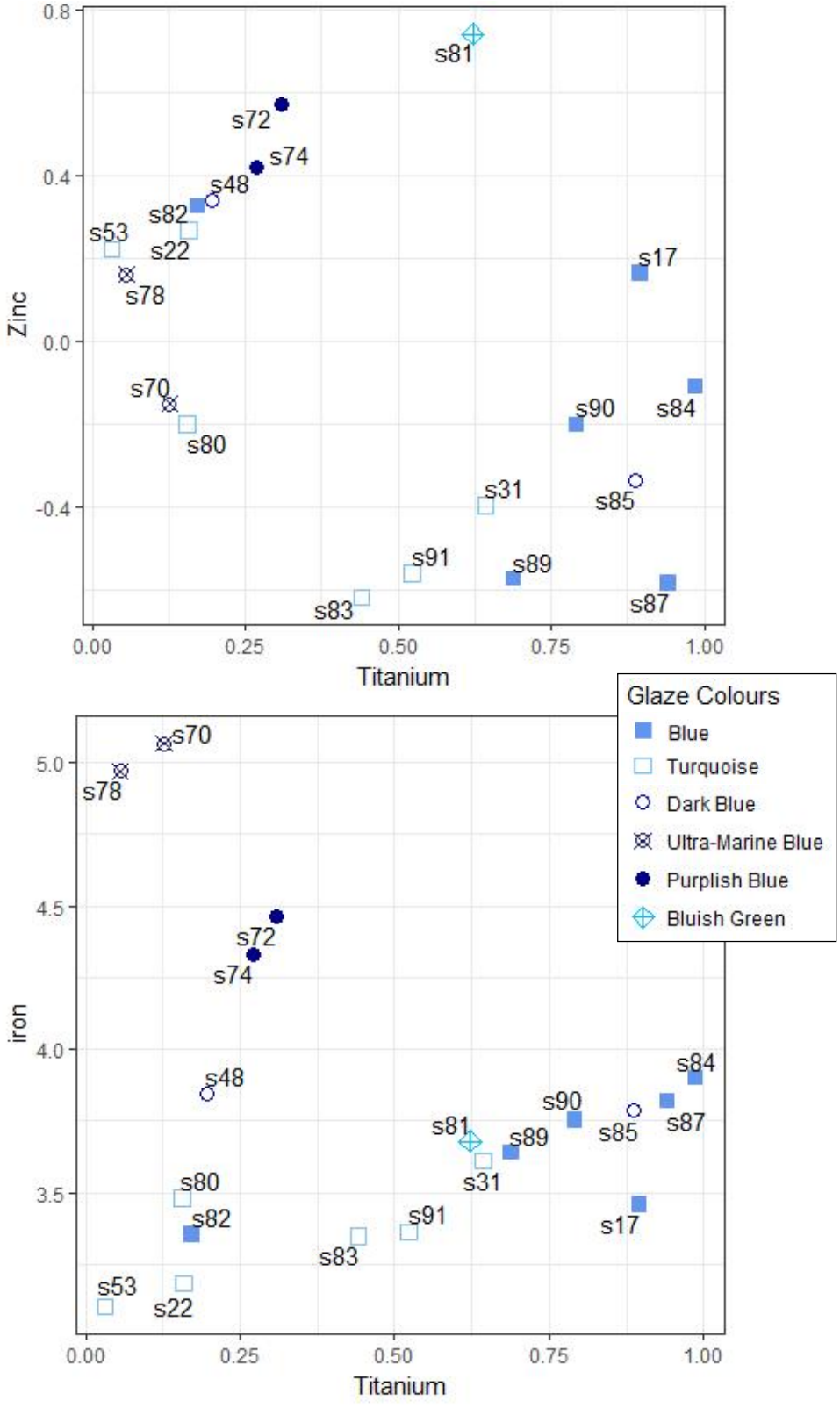

Fig. 10-23: The bivariate plots for titanium and zinc, and titanium and iron reveal the Group 4a and b copper blue glaze division as well as the Group 2 a and b cobalt blue division.

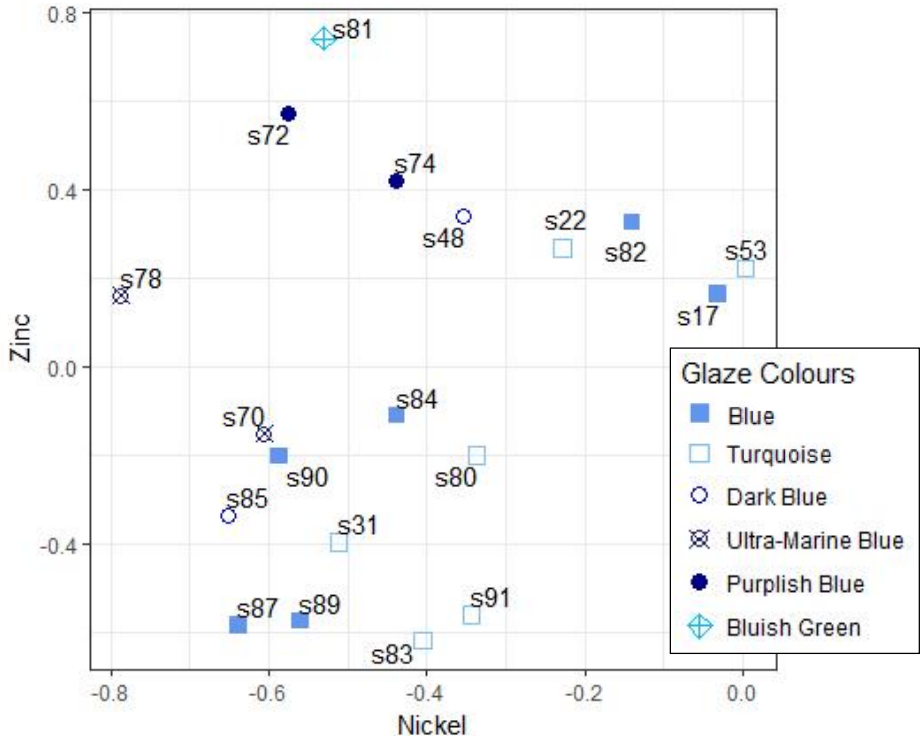

Fig. 10-24: The bivariate plot for nickel and zinc for dataset Arch 2.1R. A comparison of the bivariate plots for different element pairings reveal sample s17 as not truly a part of either copper blue subgroup.

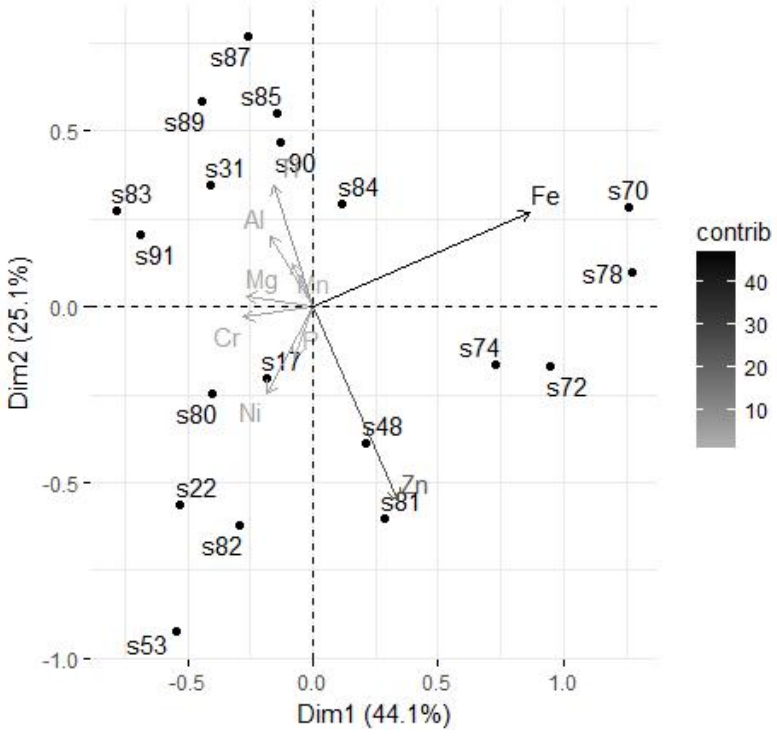

Fig. 10-25: PCA biplot for dataset Arch 1.1R. Group 2a (s72 and s74) and 2b are shown as distinct pairings based on iron/zinc and iron, respectably. Samples s48 and s81 are closely associated based on the zinc content in the glaze. The two copper blue glaze clusters are visible with s17 in between them. The first two PCA components explain 69.23% of the variance of the data.

Table 10-13: Loadings, Eigenvalues and Variance for dataset Arch 1.3R. Lead and zinc explain the bulk of the variance in the first two components.

Dataset Arch2.1R HH-XRF 15 kV PCA Loadings											
Non-Rotated Results						Varimax Rotated Results					
	Dim.1	Dim.2	Dim.3	Dim.4	Dim.5		Dim.1	Dim.2	Dim.3	Dim.4	Dim.5
Mg	-0.25	0.04	-0.11	0.54	0.25	Mg	-0.12			0.63	
Al	-0.16	0.25	-0.07	0.47	0.20	Al		0.12		0.58	
P	-0.07	-0.18	0.43	-0.45	0.50	P	-0.13	0.41	0.17	-0.37	0.57
Ti	-0.15	0.43	-0.56	-0.48	-0.07	Ti		0.10	-0.83	-0.13	-0.15
Cr	-0.26	-0.04	0.52	0.07	-0.60	Cr	-0.20	0.19	0.50	-0.18	-0.59
Mn	-0.08	0.16	0.01	-0.15	-0.39	Mn				-0.18	-0.40
Fe	0.82	0.34	0.21	0.07	0.06	Fe	0.91			-0.10	
Ni	-0.17	-0.31	-0.02	-0.15	0.27	Ni	-0.29				0.36
Zn	0.32	-0.69	-0.41	0.08	-0.23	Zn		-0.88		-0.17	

Dataset Arch2.1R Eigenvalues and Variance			
	Eigenvalue	Variance %	Cumulative Variance %
Dim.1	0.38	44.13	44.13
Dim.2	0.22	25.11	69.23
Dim.3	0.13	14.67	83.90
Dim.4	0.06	7.10	91.01
Dim.5	0.04	4.50	95.51
Dim.6	0.03	3.45	98.96
Dim.7	0.01	0.73	99.69
Dim.8	0.00	0.31	100.00
Dim.9	0.00	0.00	100.00

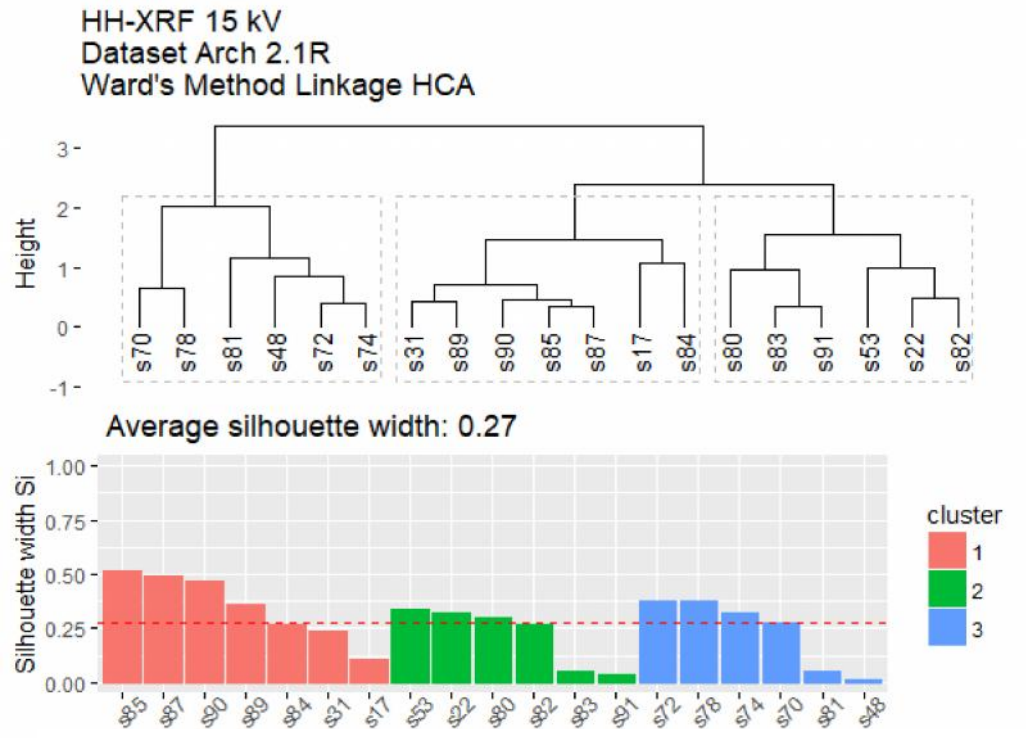

Fig. 10-26: HCA (Ward's Method) dendrogram exhibiting one cobalt blue glaze cluster, which includes samples s48 and s81, and two copper blue glaze clusters.

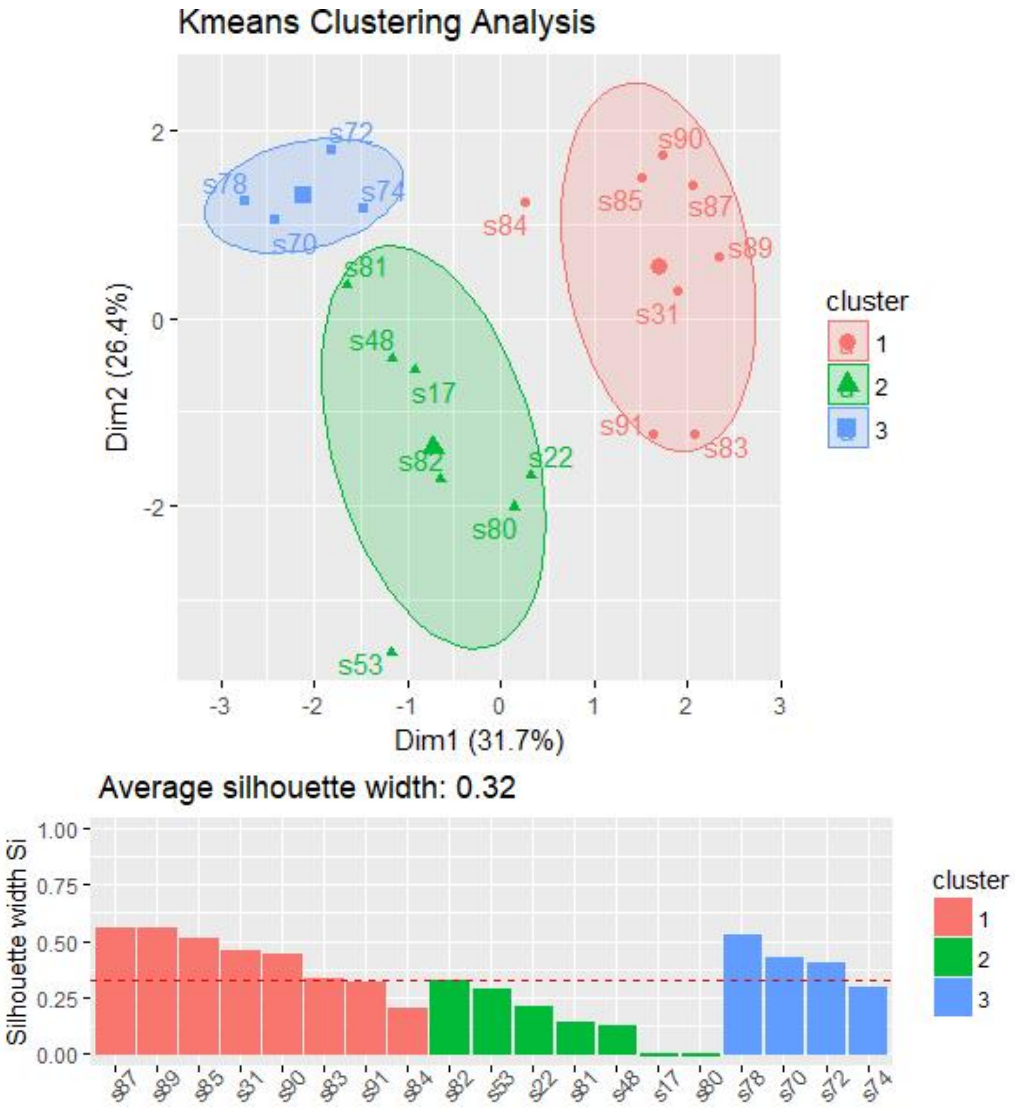

Fig. 10-27: K-means analysis of dataset Arch 2.1R. The Group 2 cobalt blue glazes are clustered together. The copper blue glazes are subdivided as described for Group 4. Samples s48 and s81 have been included with Group 4a.

10.3.2 Dataset Arch 2.2

The HCA (single linkage) dendrogram and PCA biplot have identified samples s17, s70 and s78 as potential outliers. Boxplots identified potential outliers associated with Na_2O (s22, s53, s80 and s81), SiO_2 (s53, s80 and s81), FeO (s70, s74 and s78) and CuO (s17 and s48). Samples s17, s70, s74 and s78 represent known clusters from previous analysis in this chapter and have been retained for further analysis. Samples s22, s53, s80 and s81 are considered tails of the data and have been retained.

The pairwise plot (Fig. 10-28) exhibits higher correlations for SiO_2 and Na_2O (R^2 = -0.97), CaO and SiO_2 (R^2 = -0.82) and CaO and Na_2O (R^2 = 0.75). Dealkalized glazes may exhibit lower sodium and higher silicon (Fig. 10-29). The FeO/CuO bivariate plot isolates Group 2b and sample s17 which may represent its own cluster. The FeO/CaO bivariate plot (Fig. 10-30) isolates the Group 2 samples. The copper coloured glaze Group 4a is partly isolated. Sample s82 and samples s48 and 81 which are

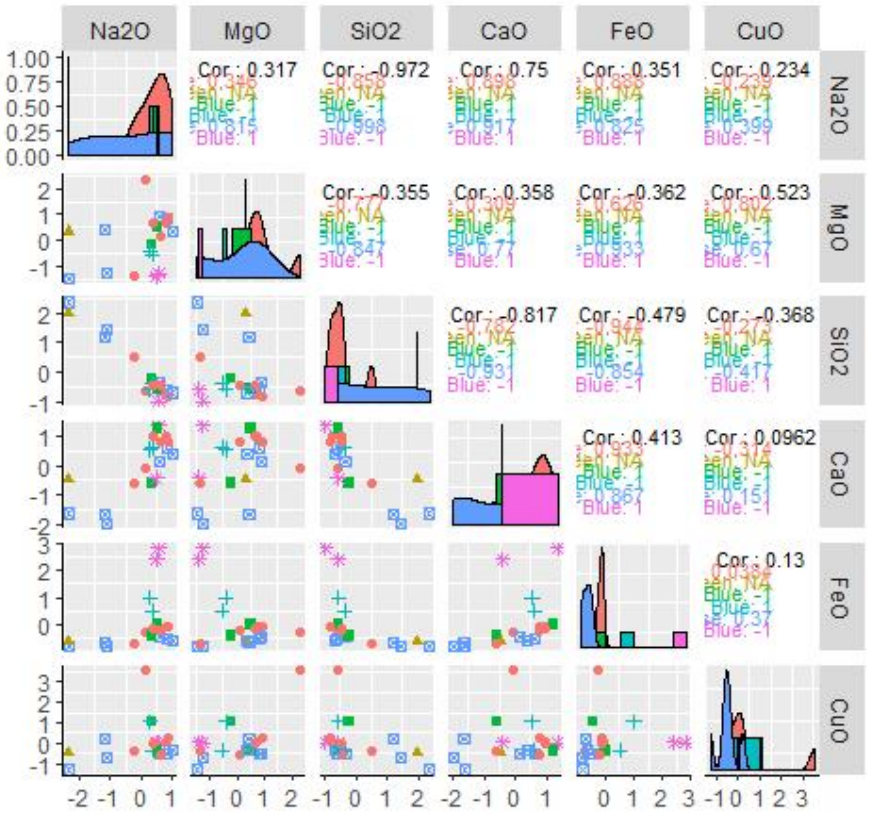

Fig. 10-28: Pairwise plot of dataset Arch 2.2 exhibiting bivariate plots, histogram and correlations of the variables.

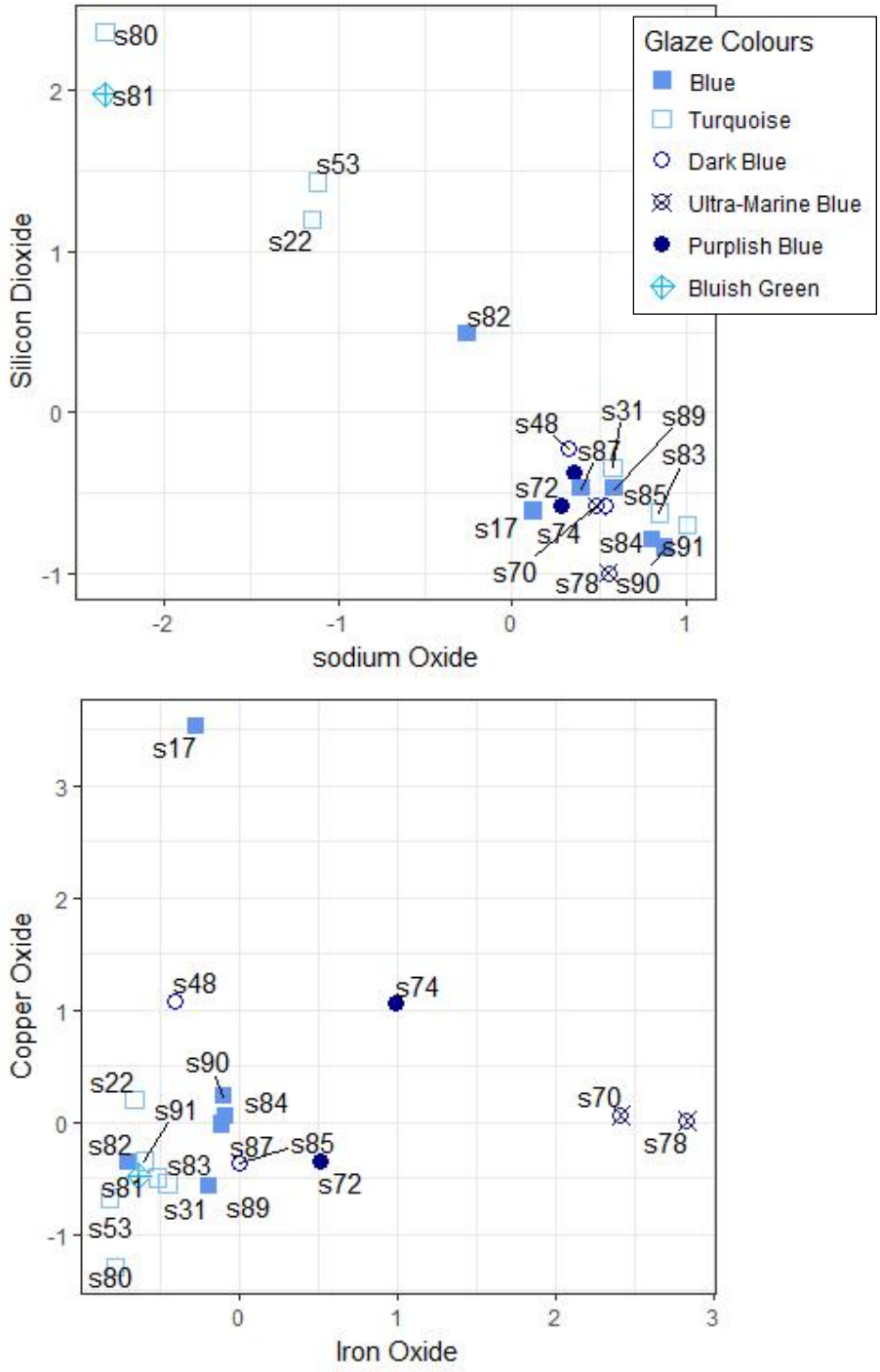

Fig. 10-29: The silicon/sodium oxide bivariate plot might reveal the dealkalization of glazes by exhibiting lower sodium and higher silicon. The iron/copper oxide bivariate plot isolates Group 2a and sample s17 which may represent its own group. Group 2b and sample s48 is on the edge of the copper glaze cluster.

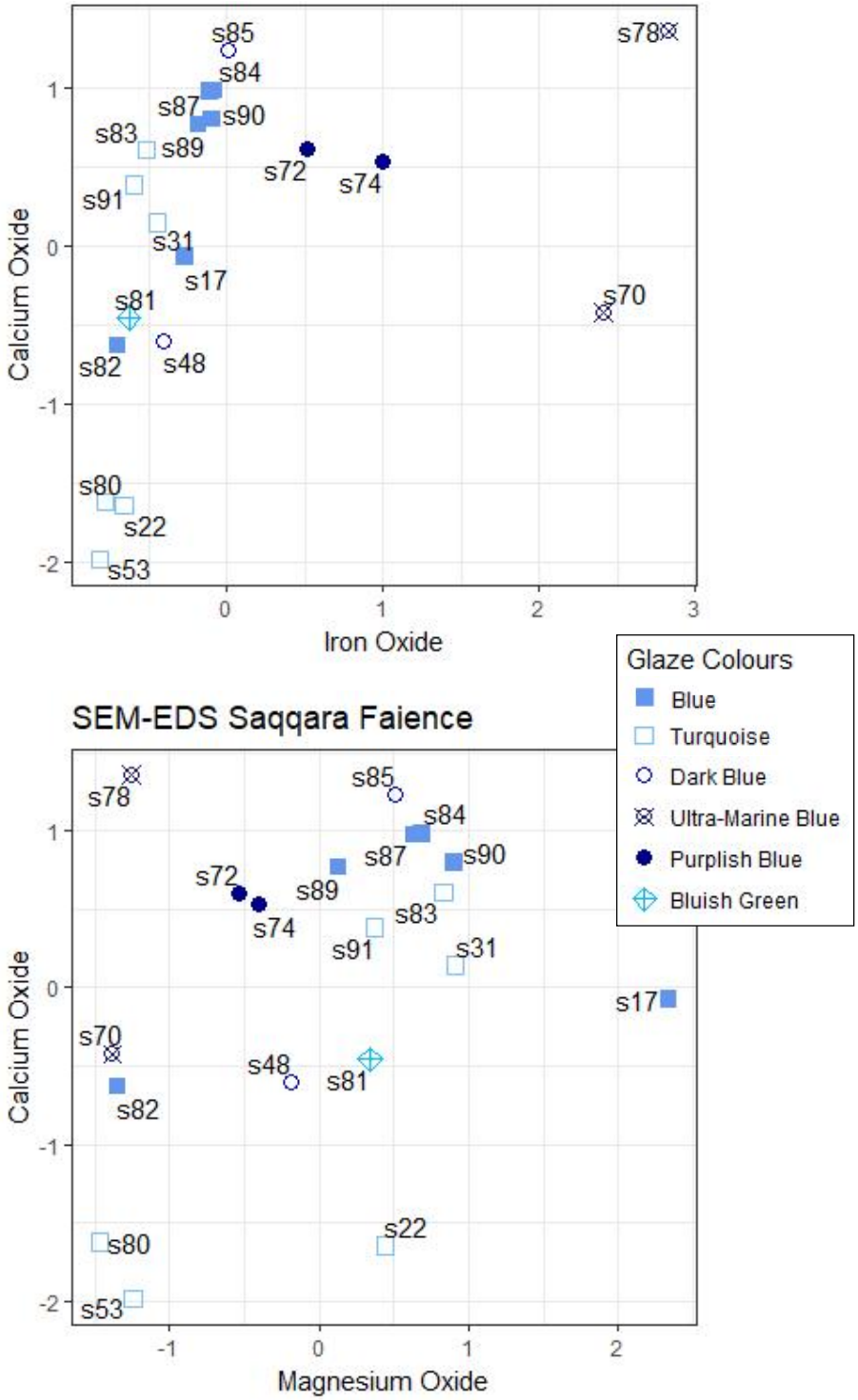

Fig. 10-30: The iron/calcium oxide bivariate plot isolates the Group 2 samples. The copper coloured glaze Group 4a is partly isolated. Sample s82 and samples s48 and 81 which are sometime associated with Group 4a are less distinct than the other samples of the group (s22, s53 and s80). The magnesium/calcium oxides bivariate plot exhibits s17 as distinct, Group 2a (s72 and s74) Copper blue glaze group 4b is distinct but 4a is disperse and appears to be associated with s70 and possibly s48 and s81.

sometimes associated with Group 4a are less distinct than the other samples of the group (s22, s53 and s80). A plot consisting of MgO and CaO exhibits s17 and Group 2a (s72 and s74) as two distinct groups. Copper blue glaze group 4a is disperse and appears associated with cobalt blue s70. Sample s48 and s81 could be identified as part of this group.

The PCA biplot and three-dimensional plot (Fig. 10-31) reveal s17 as an isolated sample based on MgO component of the glaze. Cobalt blue glaze group 2a and 2b are separated from the copper blue glazes based on the iron content. The three-dimensional plot reveals that the Group 2b samples (s72 and s74) are more separated from the copper blue glazes than the biplot reveals. Both plots exhibit the copper blue glaze groups, one as distinct (Group 4b) and the other as disperse (Group 4a). Sample s81 is associated with Group 4a. Sample s48 is in close proximity to Group 4b but not necessarily associated with it.

The PCA loadings (Table 10-14, Fig. 10-31) indicate that SiO2, CaO and Na2O mostly define the first PCA component variance. MgO and FeO define component 2 variance. The varimax rotated results exhibit the first component defined by silicon and sodium oxides. MgO defines the second component variance.

The optimum number of clusters (k) based in gap statistics, average silhouette width and a scree plot is 2 to 4. A k of 2 to 5 was used for HCA and K-means analysis to determine optimum cluster prediction number. A k of 4 was determined to be optimal for both MVS methods.

The HCA (Ward's method) dendrogram (Fig. 10-32) reveals s17 as a distinct glaze. Cobalt glaze group 2b is isolated as a cluster. Group 2a is a part of the HCA cluster 3 composed mostly of copper blue glaze group 4b.Group 2a cobalt blue glazes are on a separate branch from the copper blue Group 4b glazes. The cobalt blue glazes are relatively closely linked to s48 (copper and cobalt coloured glaze) and s82 (copper blue glaze associated with Group 4a). The silhouette graph exhibits a 5-10% confidence that it has been incorrectly assigned to the cluster. Copper blue glaze group 4a has been assigned to a cluster with sample s81.

The K-means biplot and silhouette graph (Fig. 10-33) exhibits s17 as a distinct glaze. Cobalt blue glaze group 2b has been assigned to a cluster with the Group 2a sample s74. Sample s72 is associated with the copper blue glaze group 4b.

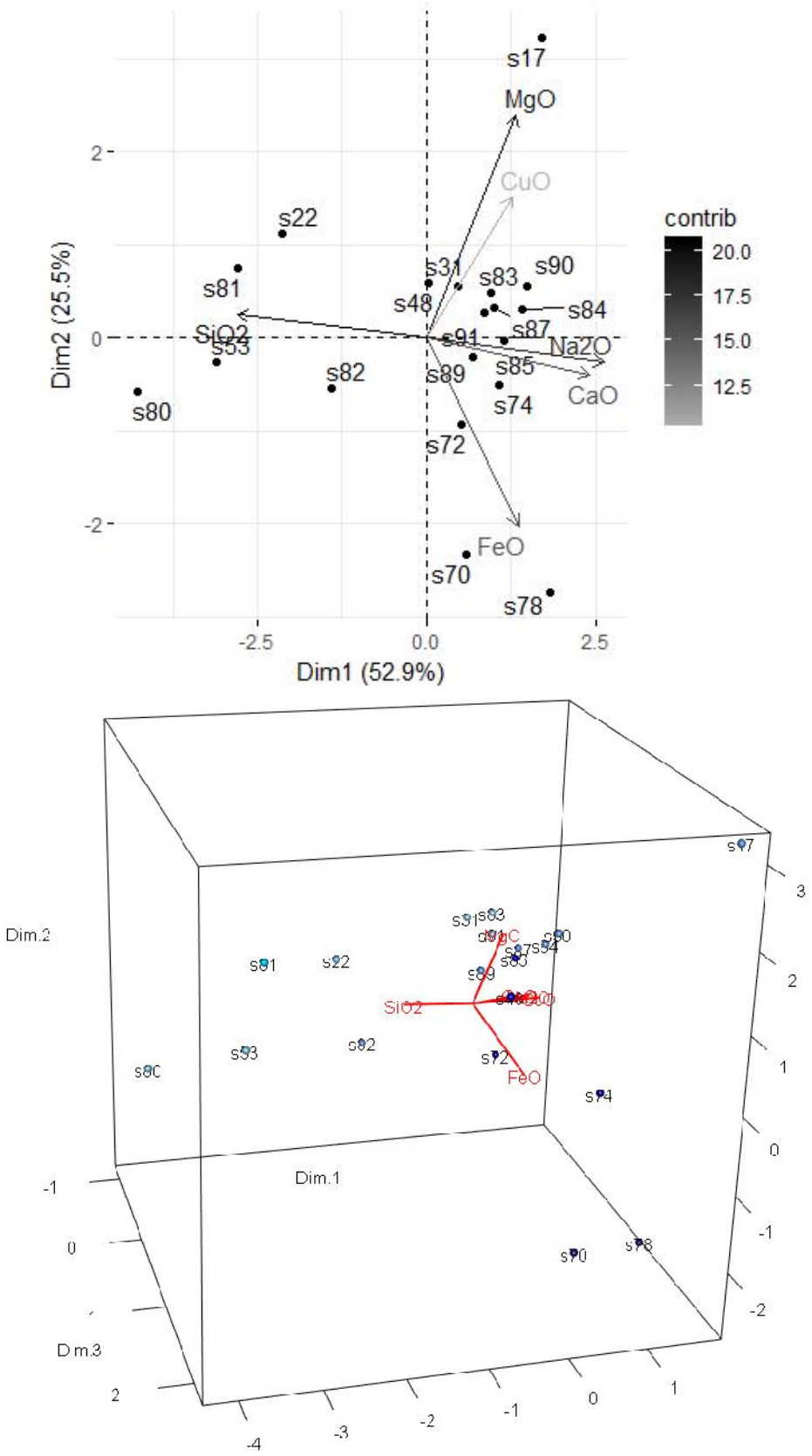

Fig. 10-31: The PCA biplot and 3D plot for dataset Arch 2.2.

Table 10-14: Loadings, Eigenvalues and Variance for dataset Arch 2.2. The non-rotated loadings results exhibit PCA component 1 variance defined by sodium, silicon and calcium oxides. Component 2 variance is explained by magnesium and iron. The Varimax rotated results exhibit the first component explained by sodium and silicon oxide, and component 2 by magnesium oxide. The first two components explain 78.47% of the variance in the data.

Dataset Arch2.2 SEM-EDS PCA Loadings

Non-Rotated Results						Varimax Rotated Results					
	Dim.1	Dim.2	Dim.3	Dim.4	Dim.5		Dim.1	Dim.2	Dim.3	Dim.4	Dim.5
Na_2O	0.52	-0.07	-0.21	-0.57	0.14	Na_2O	0.80				
MgO	0.26	0.68	-0.14	0.37	0.56	MgO		1.00			
SiO_2	-0.55	0.07	0.04	0.28	-0.03	SiO_2	-0.60				
CaO	0.48	-0.11	-0.32	0.58	-0.55	CaO				0.99	
FeO	0.27	-0.58	0.50	0.36	0.46	FeO					0.99
CuO	0.25	0.43	0.76	-0.09	-0.39	CuO			0.99		

Dataset Arch2.2 Eigenvalues and Variance

	Eigenvalue	Variance %	Cumulative Variance %
Dim.1	3.11	52.94	52.94
Dim.2	1.50	25.52	78.47
Dim.3	0.84	14.35	92.82
Dim.4	0.32	5.47	98.29
Dim.5	0.10	1.71	100.00
Dim.6	0.00	0.00	100.00

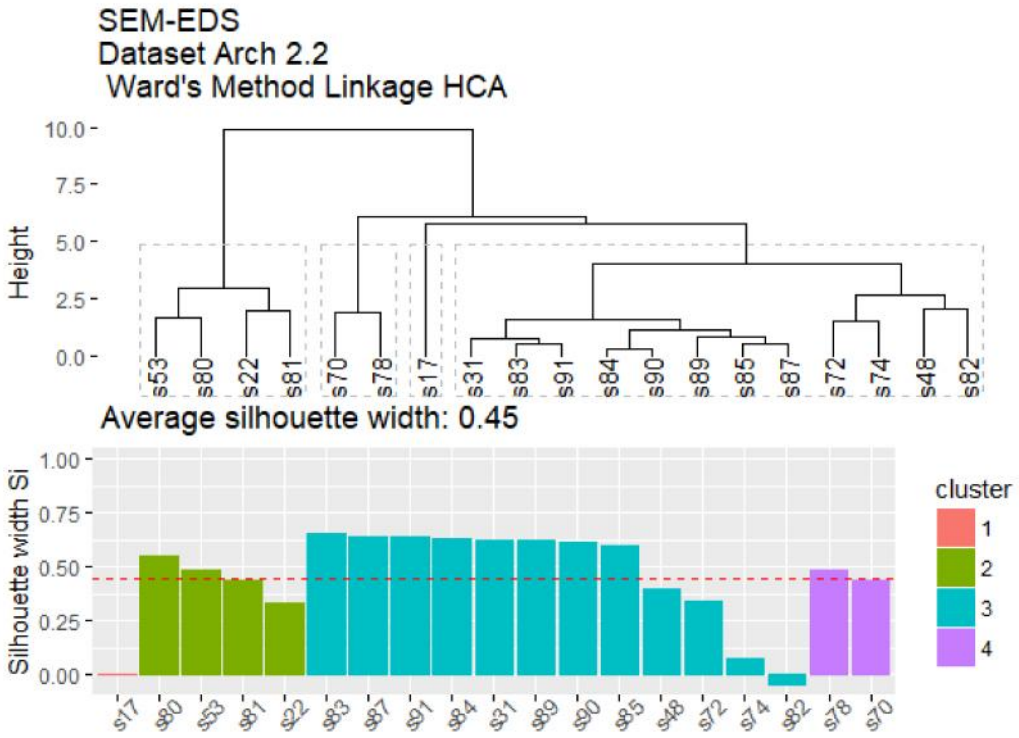

Fig. 10-32: HCA (Ward's Method) dendrogram and silhouette graph for dataset Arch 2.2.

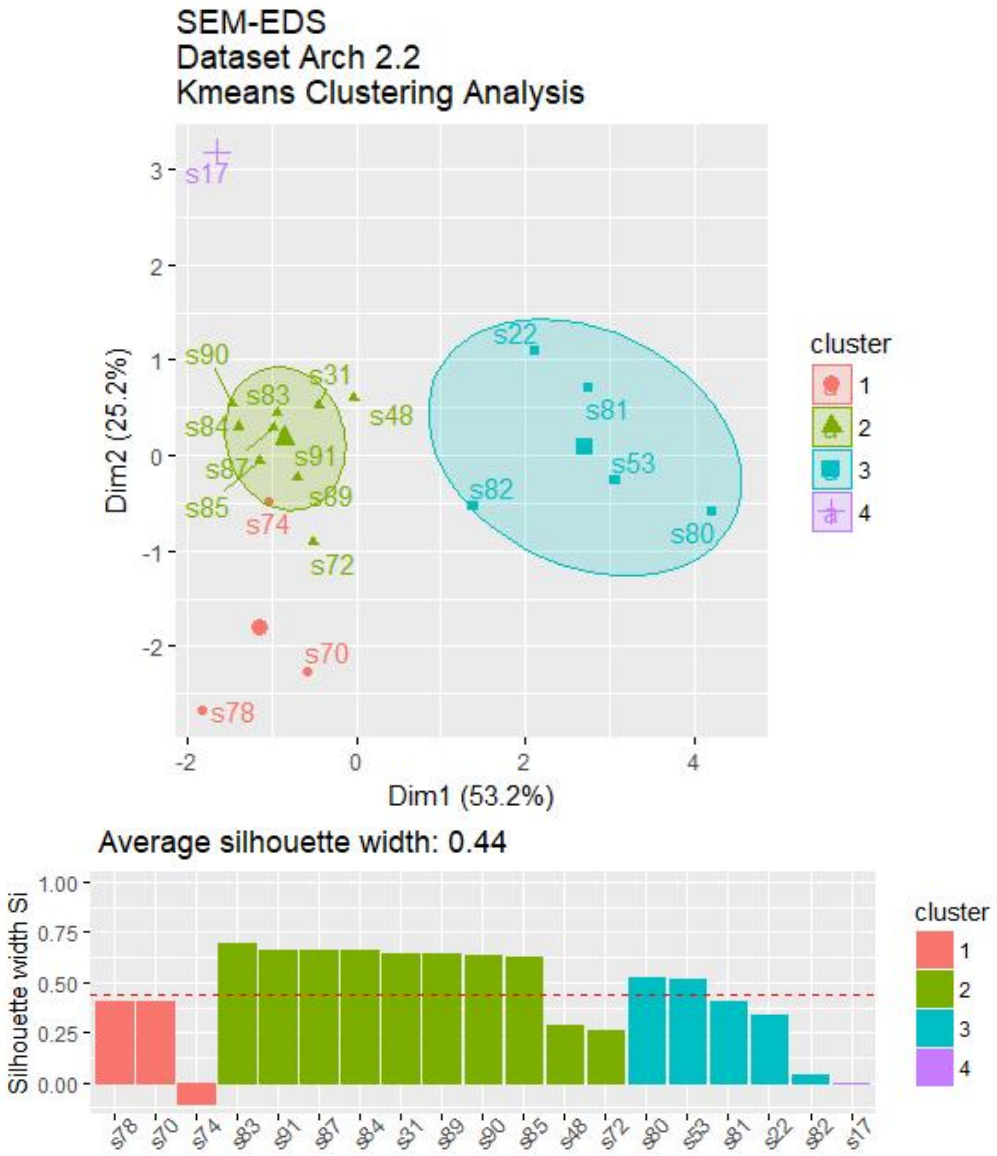

Fig. 10-33: K-means analysis results for dataset Arch 2.2.

K-means cluster 3 is composed of copper blue glaze group 4a and sample s81. K-means cluster 2 is composed of copper blue glaze group 4b and samples s48 (cobalt and copper glaze) and s72 (Group 2a).

K-means analysis was run with k = 4. Cobalt blue glaze group 2b was isolated when k=3. However, cobalt glaze group 2a was incorporated into the copper blue glaze group 4b. Increasing the k to 5 resulted in all the cobalt blue glazes assigned to a single cluster which included s82 of the copper blue group 4a.

10.3.3 Dataset Arch 2.3R

HCA (single linkage) identified sample s17 as an outlier. The boxplots identified samples s17 and s22 (strontium), and s72 (lead) as outliers. A review of the data indicated that s22 and s72 are tails of the data. Sample s17 is statistically an outlier but is distinct and represents a separate group.

The pairwise plot (Fig. 10-34) exhibits low to moderate correlations. The highest correlations are for tin/iron (R^2 = -0.72), lead/iron (R^2 = -0.68) and lead/tin (R^2 = 0.63) (Fig. 10-35). Distinct clusters are not readily observed in the bivariate plots. The bivariate plot for iron and strontium exhibited greatest isolation for the cobalt blue glazes (Fig. 10-36). The zirconium/tin bivariate plot isolated sample s17.

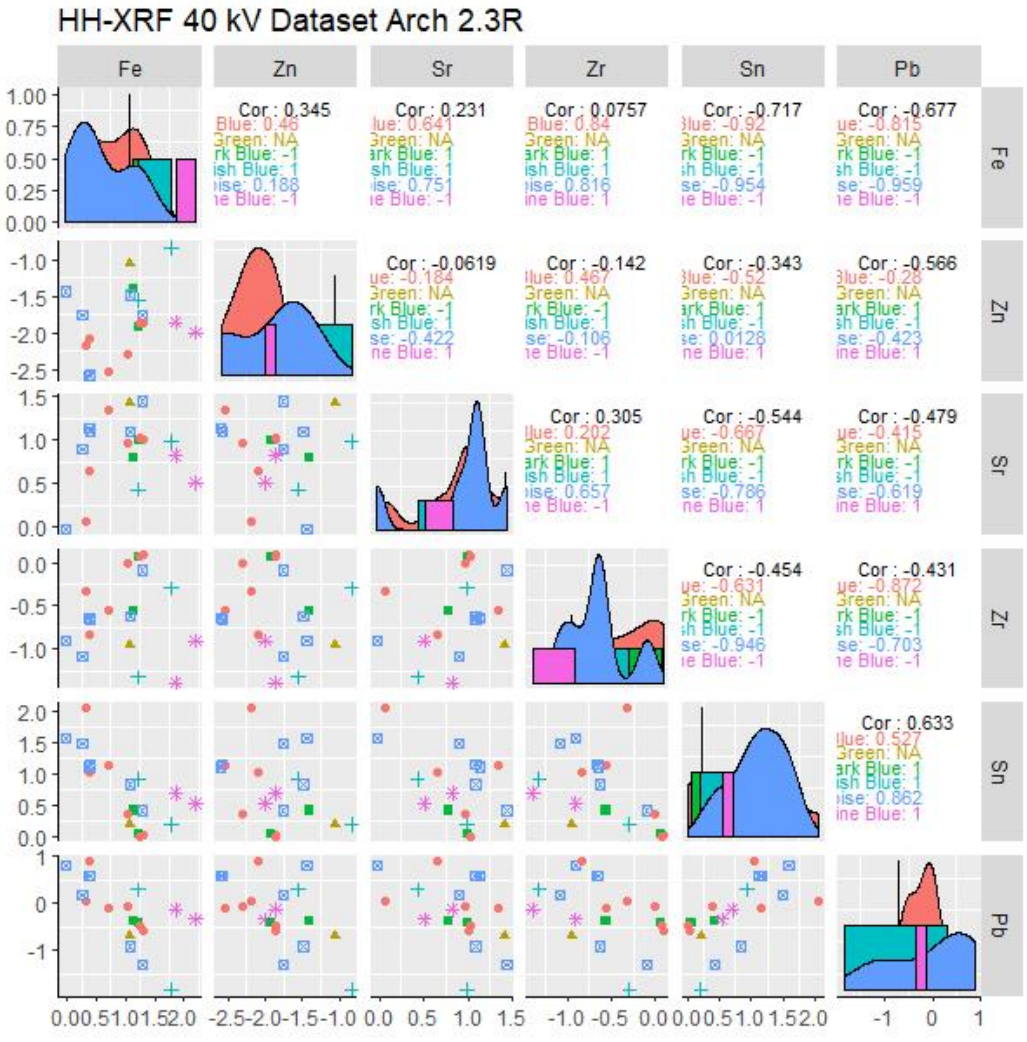

Fig. 10-34: Pairwise plot of dataset Arch 2.3R exhibiting bivariate plots, histogram and correlations of the variables.

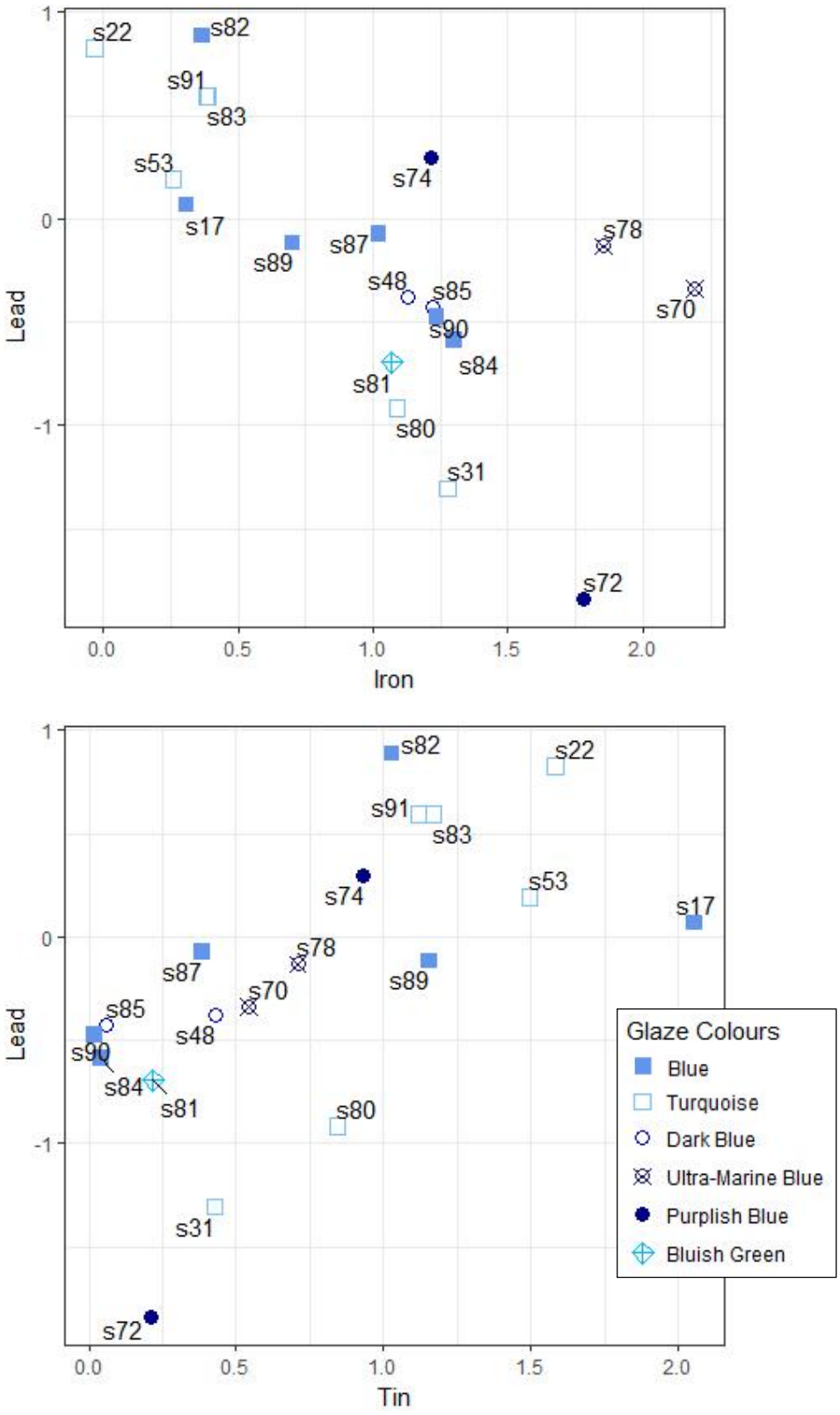

Fig. 10-35: The bivariate plots for iron/lead and tin/lead exhibit moderate correlations (R^2 = -0.68 and -0.63, respectively). There are no distinct clusters.

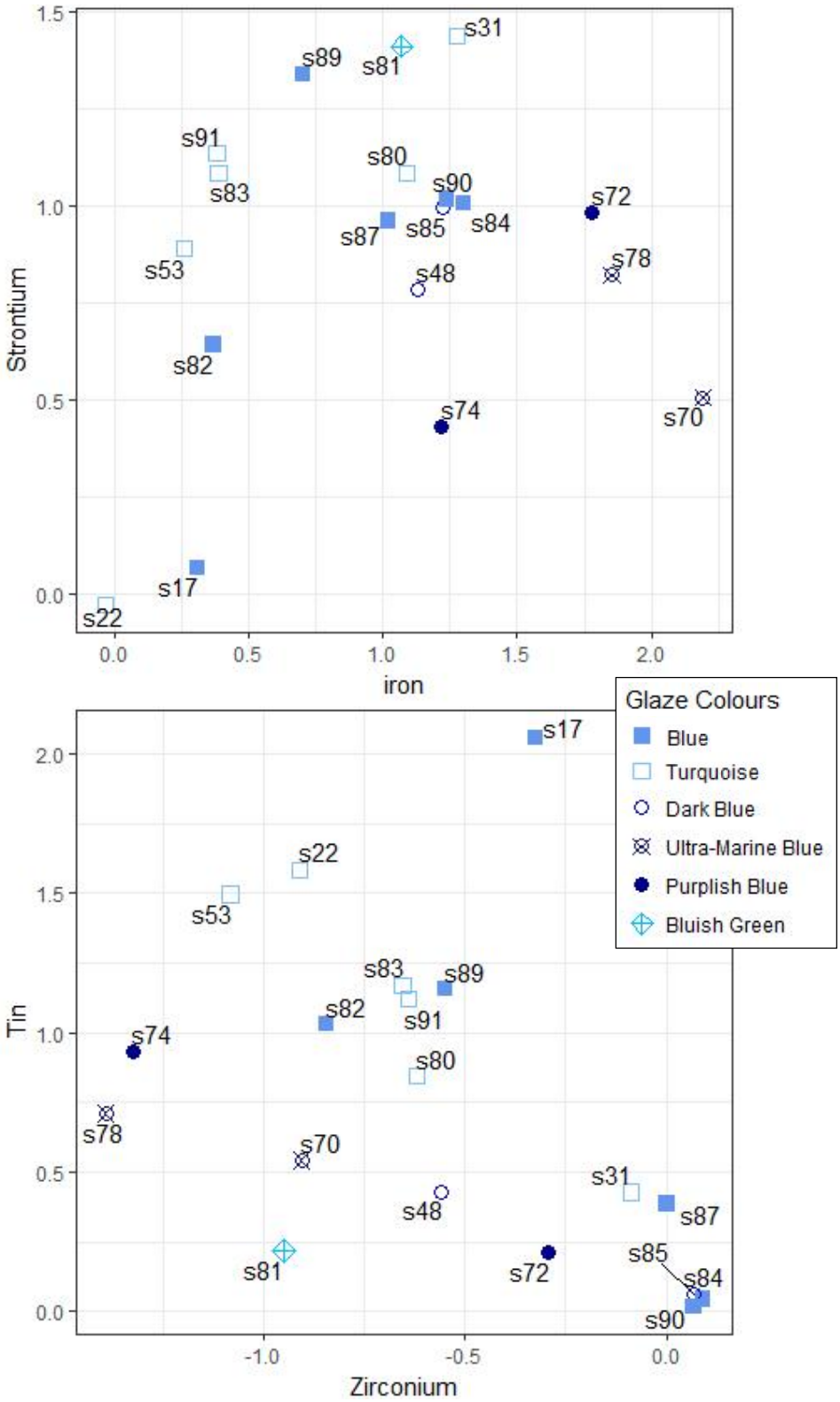

Fig. 10-36: The bivariate plots for iron/strontium and zirconium/tin exhibit moderate correlations (R2 = 0.23 and -0.45, respectively). The iron/strontium does reveal a cobalt blue cluster (s70, s72, s74 and s78). Zirconium/tin is best for isolating sample s17 from the sherd glaze assemblage.

The PCA biplot and three-dimensional plot (Fig. 10-37) exhibit the cobalt blue glazes in a disperse cluster defined by iron and zinc. Samples s48 and s81 are associated with the cobalt blue glazes. The biplot reveals sample s80 associated with the cobalt blue glazes as well but the three-dimensional plot reveals that this is not the case. The copper blue glaze groups 4a and 4b are correctly clustered. Group 4a is disperse and defined by the tin content of the glaze. Group 4b is linear and more compact. It is defined by zirconium in the glaze. Sample s17 appears associated with Group 4a but the three-dimensional plot reveals that it is isolated from the other samples.

The PCA loadings (Table 10-15) exhibit the variance of PCA component 1 defined by iron, tin and lead. Component 2 is defined by zirconium and zinc. The Varimax rotated results define component 1 by lead and zinc, and component 2 by zirconium. The two PCA components represent 76.04% of the total data variance.

The optimum number of clusters (k) based in gap statistics, average silhouette width and a scree plot is 2 to 4. A k of 2 to 6 was used for HCA and K-means analysis to determine optimum cluster prediction number. A k of 3 was determined to be the optimal for both MVS methods.

The HCA (Ward's Method) and K-means analysis (Fig. 10-38) reveal the same results. Three of the cobalt blue glazes (s70, s74 and s78) were assigned to cluster 1 and the copper blue samples were divided into clusters 2 and 3. The copper clusters do not correspond with the copper blue glaze groups identified with previous analysis in this chapter. Samples s17, s48 and s81 are intermixed with the copper blue glaze clusters. The cobalt blue glaze sample s72 is associated with the copper blue glaze cluster 3.

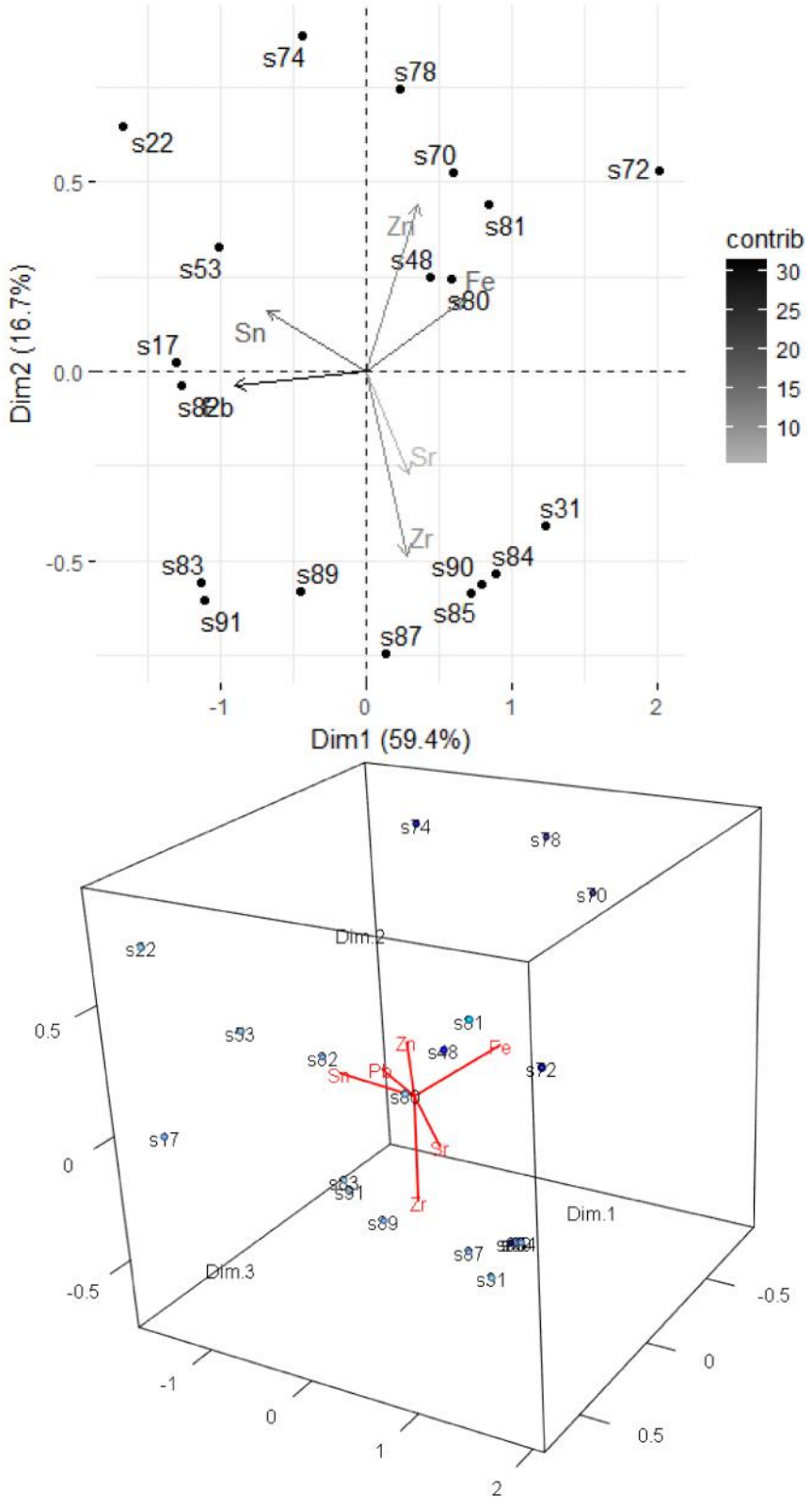

Fig. 10-37: The PCA biplot and 3D plot for dataset Arch 2.3R. The copper blue glaze groups are clustered; Group 4a is disperse and defined by tin. Group 4b is linear and defined by zirconium. The cobalt blue glazes are defined by iron and zinc.

Table 10-15: Loadings, Eigenvalues and Variance for dataset Arch 2.3R.

Dataset Arch2.3R H-XRF 40 kV PCA Loadings											
Non-Rotated Results						Varimax Rotated Results					
	Dim.1	Dim.2	Dim.3	Dim.4	Dim.5		Dim.1	Dim.2	Dim.3	Dim.4	Dim.5
Fe	0.48	0.26	-0.61	0.25	0.33	Fe	0.12	0.12	-0.88	0.12	-0.12
Zn	0.25	0.58	0.44	-0.03	-0.49	Zn	0.41	0.41	0.41	0.41	-0.41
Sr	0.20	-0.36	-0.03	-0.81	0.03	Sr	0.12	0.12	0.12	-0.88	-0.12
Zr	0.19	-0.64	0.32	0.52	-0.08	Zr	0.12	-0.88	0.12	0.12	-0.12
Sn	-0.48	0.21	0.35	0.00	0.66	Sn	0.12	0.12	0.12	0.12	0.88
Pb	-0.63	-0.05	-0.46	0.07	-0.46	Pb	-0.88	0.12	0.12	0.12	-0.12

Dataset Arch2.3R Eigenvalues and Variance			
	Eigenvalue	Variance %	Cumulative Variance %
Dim.1	1.02	59.38	59.38
Dim.2	0.29	16.67	76.04
Dim.3	0.19	11.16	87.20
Dim.4	0.11	6.66	93.86
Dim.5	0.11	6.14	100.00
Dim.6	0.00	0.00	100.00

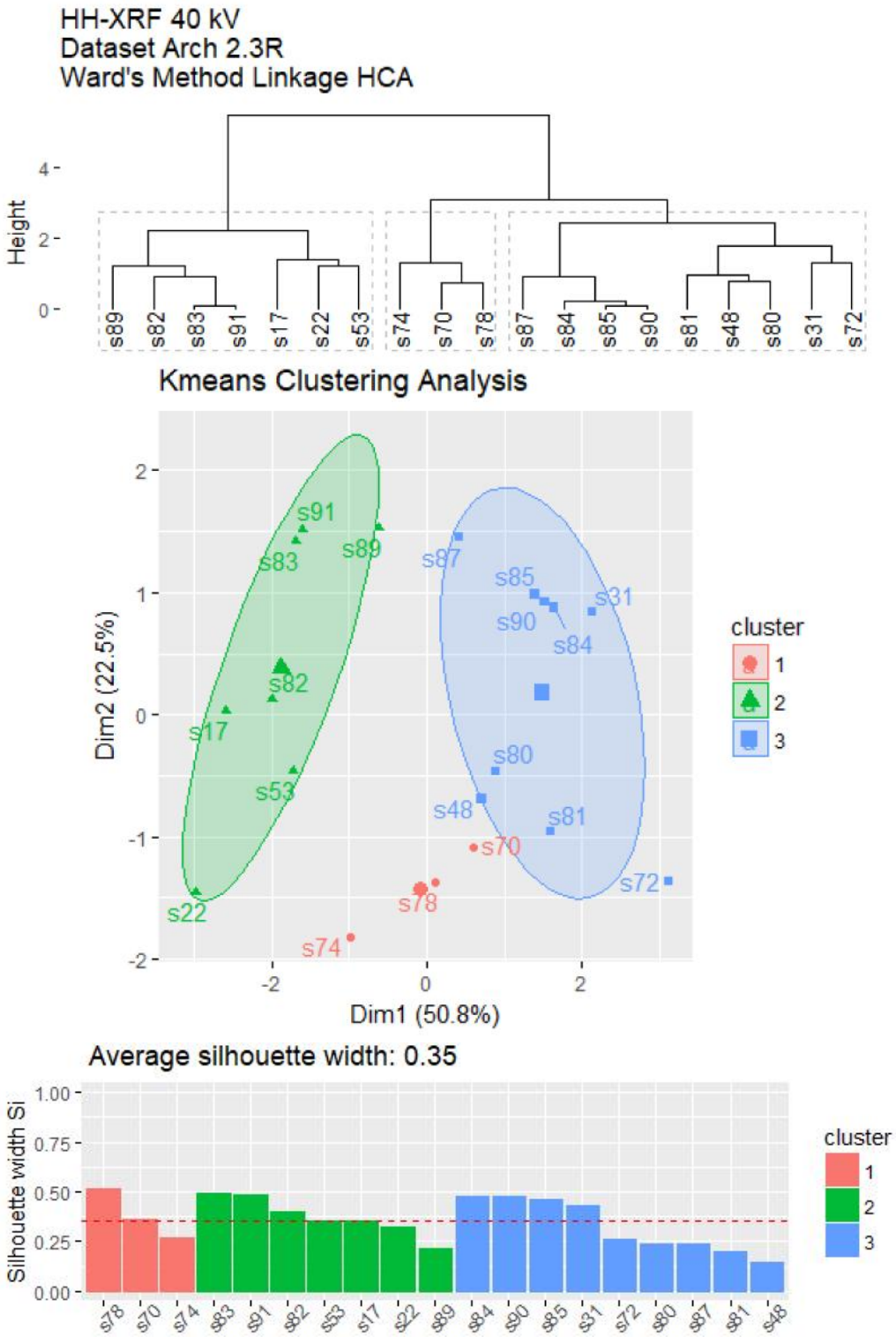

Fig. 10-38: HCA (Ward's Method) and K-means analysis for dataset Arch 2.3R.

10.4 Dataset Arch 2 Multivariate Analysis (Copper Coloured Sherds)

The dataset is composed of 14 copper blue glazed sherds. The samples have been subdivided into hues consisting of blues, bluish-green, dark blues and turquoise. The blue and turquoise blue represent to two largest groups in this dataset. The bluish-green and dark blue categories consist of one sample each.

The analysis of the dataset using SEM-EDS and HH-XRF (15 kV) has resulted in three copper blue glaze groups and two distinct glazes (s17 and s81) after the removal of the green, yellow, purple and cobalt blue glazes. These three categories do not correspond to the glaze hue but to the batch components used in the glaze. For example, sample s17 is a copper blue glaze categorized as a blue hue but has been revealed to be a distinct glaze separate from all other glazes.

The variables for datasets Arch 3.1 (Table 10-16) and 3.3 (Table 10-17) have not changed although the samples have. The variables for dataset Arch 3.2 (Table 10-18) includes aluminium hydroxide based on the variable selection criteria (see chapter 8).

Table 10-16: HH-XRF 15 kV Net Peak Areas for Dataset Arch 3.1 - Sodium through Titanium (Saqqara Faience).

HH-XRF 15 kV (NPA) Saqqara Faience Dataset Arch 3.1

Copper Blue Glazes

Parameters 15 kV, 50 uA with a vacuum for 180 seconds (no filter)

Average of 10 Measurements

Sample	Glaze	Na	Mg	Al	Si	P	Ca	Ti	Cr	Mn	Fe	Ni	Cu	Zn
s17	Blue	5876	2811	23759	981125	5114	574024	47673	4558	20171	617514	18849	3708415	22914
s22	Turquoise	5827	2287	15647	1152660	2525	186858	14683	7293	15950	303015	9968	1545178	16356
s31	Turquoise	4361	4063	16457	998154	3149	531149	30286	6818	25058	588475	9543	1452398	10701
s53	Turquoise	4719	2671	10135	638564	5406	1651737	13383	5325	16283	289008	13003	1589092	16179
s80	Turquoise	4058	1586	12639	866035	4002	706484	14332	8771	17752	398828	8753	1012815	10026
s81	Bluish Green	4468	3183	11487	650578	4411	1959044	34629	5766	26161	737015	10936	1060826	38968
s82	Blue	6395	2701	16757	1107525	3466	324947	17071	5746	16567	411025	12489	2461044	19890
s83	Turquoise	5144	3540	20332	1340659	3906	699362	23330	8397	20351	427188	10011	1032560	8090
s84	Blue	4341	1651	12422	718064	3160	549746	39170	5383	24885	721445	9432	1908370	13069
s85	Dark Blue	5648	3661	23854	1270620	3962	636725	44541	5579	27011	811714	9557	1851004	13085
s87	Blue	5693	3100	22262	1238384	3224	749413	41160	6033	23115	730315	8480	1282621	8934
s89	Blue	5908	3576	23270	1443953	3321	535436	31626	6285	23827	605167	9070	1087366	8932
s90	Blue	5448	3349	27509	1172867	3108	553427	40262	5829	28267	777077	10137	2096534	14887
s91	Turquoise	4261	2770	16054	1089216	4175	583393	23437	6774	20785	401565	9848	1016842	7922

Table 10-18: HH-XRF 40 kV Net Peak Areas for Dataset Arch 3.3 (Saqqara Faience).

HH-XRF 40 kV (NPA) Saqqara Faience Dataset Arch 3.3 Copper Blue Glazes Parameters 40 kV, 30 uA and filter 3 for 180 seconds without vacuum Average of 10 Measurements								
Sample	Glaze	Fe	Cu	Zn	Sr	Zr	Sn	Pb
s17	Blue	9778	162409	816	7692	5189	56157	7676
s22	Turquoise	6020	83950	1478	6058	2499	30342	14194
s31	Turquoise	11548	70046	560	13579	2954	4943	875
s53	Turquoise	6421	88871	857	12067	1675	22090	5996
s80	Turquoise	6610	37470	504	6577	1195	5170	888
s81	Bluish Green	11884	38249	1421	16745	1575	5075	2036
s82	Blue	7388	97810	636	9734	2199	14325	12401
s83	Turquoise	8688	56732	446	17438	3057	18965	10647
s84	Blue	15389	103290	656	11462	4589	4374	2332
s85	Dark Blue	15477	96384	667	12364	4889	4838	2978
s87	Blue	15001	75928	544	14153	5419	7952	5018
s89	Blue	12821	58279	504	24238	3663	20150	5648
s90	Blue	17852	114406	799	14331	5544	5274	3229
s91	Turquoise	8594	53375	440	18279	3091	17993	10638

Table 10-17: SEM-EDS (wt%) for Dataset Arch 3.2 (Saqqara Faience).

SEM-EDS (wt%) Saqqara Faience Dataset Arch 3.2 Copper Blue Glazes Parameters 20 kV, Average of 3 Measurements								
Sample	Glaze	Na_2O	MgO	Al_2O_3	SiO_2	CaO	FeO	CuO
s17	Blue	16.04	1.17	1.92	69.65	3.90	0.91	6.41
s22	Turquoise	8.37	0.74	0.86	85.32	1.66	0.49	2.56
s31	Turquoise	18.88	0.84	1.47	72.18	4.23	0.72	1.68
s53	Turquoise	8.58	0.34	0.60	87.45	1.17	0.32	1.54
s80	Turquoise	1.08	0.29	0.49	95.28	1.70	0.36	0.81
s81	Bluish Green	1.03	0.71	0.94	91.65	3.38	0.53	1.76
s82	Blue	13.90	0.32	0.71	79.58	3.13	0.45	1.91
s83	Turquoise	20.58	0.83	1.26	70.04	4.91	0.65	1.74
s84	Blue	19.96	0.78	3.05	67.43	5.34	1.10	2.34
s85	Dark Blue	18.33	0.74	3.11	69.07	5.71	1.20	1.85
s87	Blue	17.74	0.78	1.85	70.86	5.40	1.09	2.29
s89	Blue	18.96	0.66	1.46	71.14	5.12	1.01	1.65
s90	Blue	20.55	0.83	2.41	67.43	5.12	1.10	2.56
s91	Turquoise	21.56	0.72	1.22	69.45	4.59	0.56	1.91

10.4.1 Dataset Arch 3.1R

The HCA (single linkage) dendrogram identified samples s17 and s81 as outliers. The PCA biplot exhibits s81 as on the edge of the range of the other samples based on the amount of zinc in the glaze. The boxplots identified samples s80 and s84 (magnesium), s81 (aluminium) and s53 (phosphorus) as outliers. A review of the data indicates that these samples represent tails of the data and have been retained for further analysis. Sample s81 is the most distinct of these samples and could be considered an outlier or a distinct copper blue glaze as the previous analyses in this chapter have indicated. This sample has been retained for further analysis

The pairwise plot (Fig. 10-39) exhibits several moderately strong correlations. These are exhibited as bivariate plots. The iron/titanium bivariate plot (Fig. 10-40) has a joint correlation factor for blue and turquoise blue glazes of 0.85. Most of the blue, dark blue and bluish green glazes with the exception of s82 (blue) and s17 (blue) exhibit more iron and titanium than the turquoise blue glazes. Sample s17 exhibits higher titanium but moderate amounts of iron in the glaze. Sample s82 exhibits lower titanium and iron and is more closely associated with most of the turquoise glazes. Sample s31 is a turquoise glaze that exhibits moderately high iron and turquoise and is more closely associated with the blue hue glazes.

The manganese/iron bivariate plot (Fig. 10-40; blue sample $R^2 = 0.89$; turquoise samples $R^2 = 0.93$)) exhibits a similar plotting of glazes; blue hue glazes exhibit more manganese and iron than turquoise blue glazes with the exceptions of s17 and s82. Sample s82 exhibits moderately low manganese and iron. Sample s17 exhibits moderately low iron and low manganese. Sample s31 (turquoise blue) is more closely associated with the blue glazes.

The bivariate plot for nickel and iron (Fig. 10-41; $R^2 = -0.8$) reveals the blue glazes having lower nickel and higher manganese. The turquoise glazes generally have moderate nickel and manganese. Sample s31 is more closely associated with the blue hue glazes. Samples s82 and s17 are more closely associated with the turquoise glazes. Both samples have more nickel than the other turquoise samples with the exception of sample s53, and have less manages than all the samples of the dataset.

The nickel/iron ($R^2 = 0.8$) and zinc/iron ($R^2 = \sim0.66$ for both groups separately) bivariate plots (Fig. 10-42) exhibit a similar relationship between the samples with sample s31 closely associated with the blue hue glazes, sample s82 closely associated to the turquoise glazes and s17, which as a distinct glaze being associated with turquoise and blue hue glazes depending on the variables being assessed.

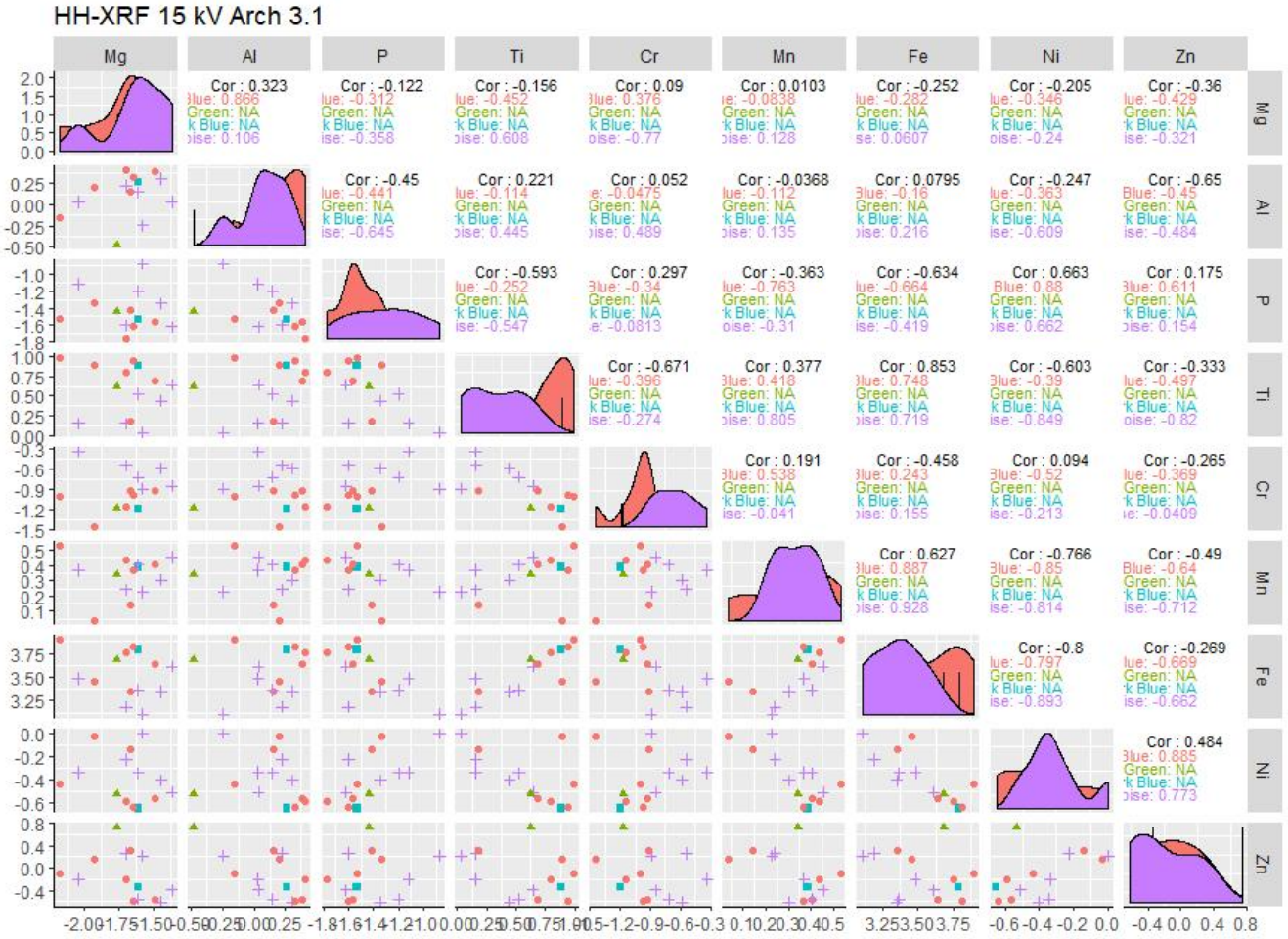

Fig. 10-39: Pairwise plot of dataset Arch 3.1R exhibiting bivariate plots, histogram and correlations of the variables.

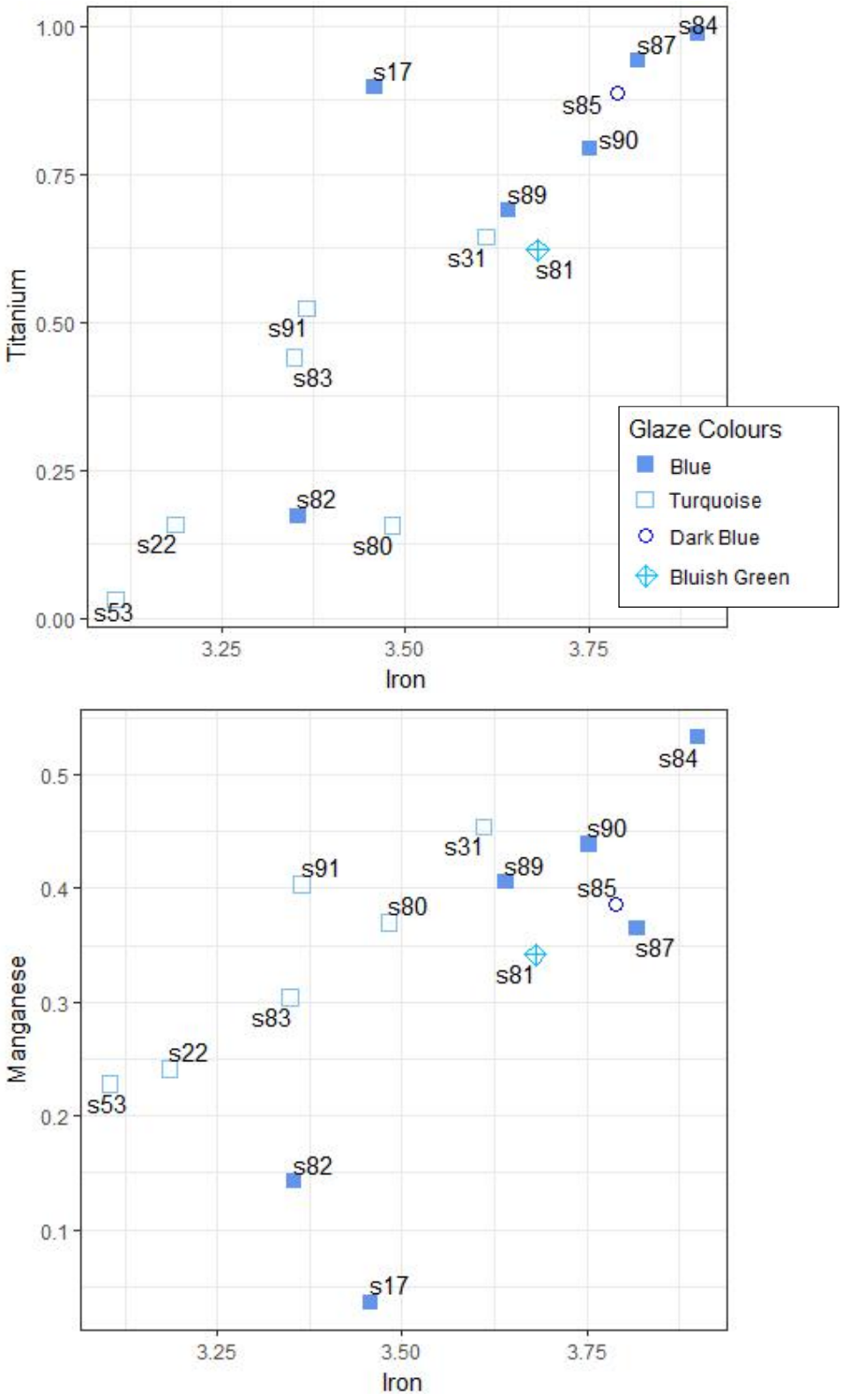

Fig. 10-40: The bivariate plots for iron/titanium and iron/manganese for dataset Arch 3.1R. The samples are divided by hue with the turquoise glaze s31 more closely associated with the blue hue glazes, and blue glaze s82 more closely associated with the turquoise blue glazes. Sample s17 is distinct.

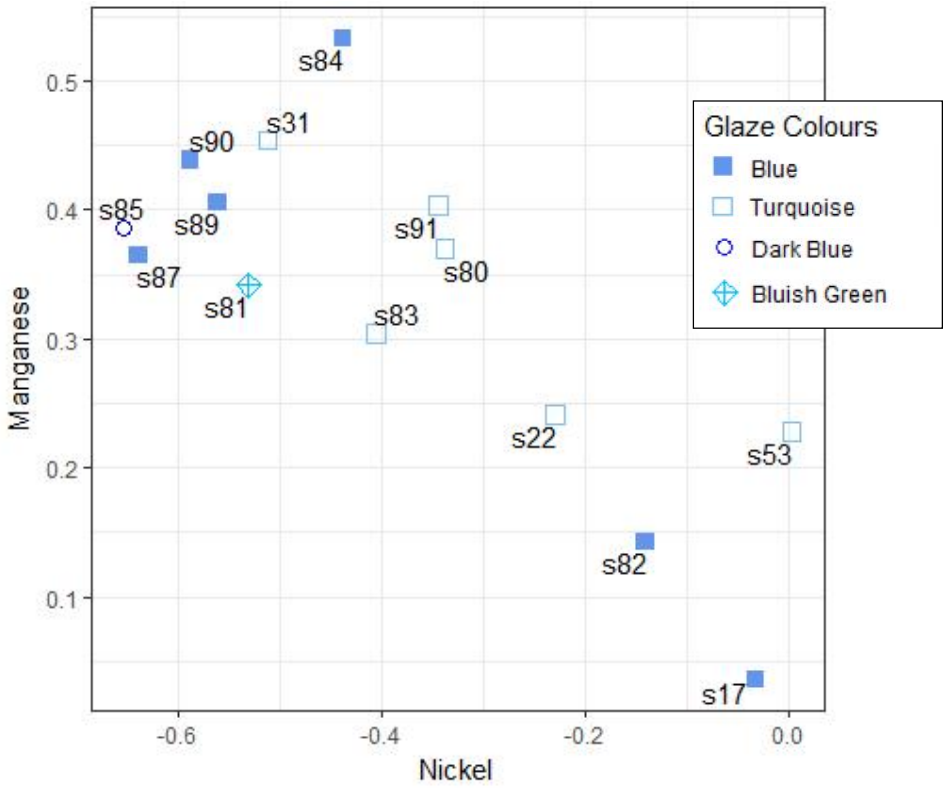

Fig. 10-41: The bivariate plot for nickel/manganese for dataset Arch 3.1R. The samples are divided by hue with the turquoise glaze s31 more closely associated with the blue hue glazes, and blue glaze s82 more closely associated with the turquoise blue glazes. Sample s17 has been shown to be distinct.

The PCA biplot and three-dimensional plot (Fig. 10-43) exhibits division in the copper blue glazes. A small group consisting of samples s22, s53, s80 and s82 are divided from the other samples by the amount of nickel in the glaze. Samples s84, s85, s87 and s90 are defined by titanium. Samples s31, s83, s89 and s91 are defined by aluminium. Distinct samples s17 and s81 are defined by the amount of zinc in the glazes. These groupings become clearer when compared to HCA (Ward's Method) and K-means analysis of the dataset. The distinctness of samples s17 and s81 are recognized by previous analysis in this chapter.

The PCA loadings (Table 10-19) indicate that zinc and titanium define the variance of the first PCA component whereas zinc, titanium and chromium define the second component. The Varimax rotated results indicate zinc for the first component and titanium and chromium for the second component. The two components represent 74.24% of the total data variance.

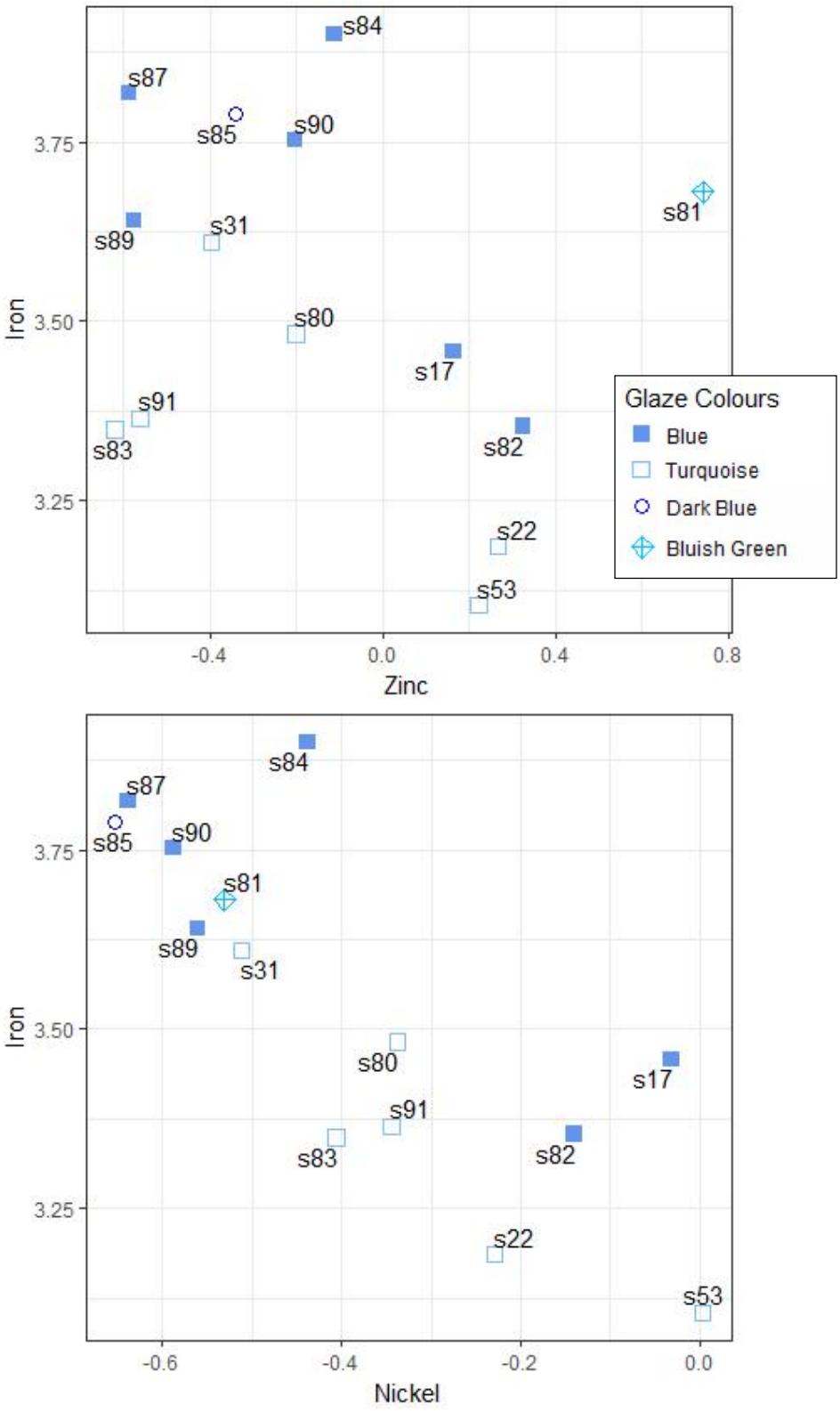

Fig. 10-42: The bivariate plots for zinc/iron and nickel/iron for dataset Arch 3.1R. The samples are divided by hue with the turquoise glaze s31 more closely associated with the blue hue glazes, and blue glaze s82 more closely associated with the turquoise blue glazes. Sample s17 has been shown to be distinct.

The optimum number of clusters (k) based in gap statistics, average silhouette width and a scree plot is 2 to 4. A k of 2 to 6 was used for HCA and K-means analysis to determine optimal cluster prediction number to include for the algorithm.

A k of 4 was determined to be optimal for HCA (Ward's Method) (Fig. 10-44). Cluster 2 is composed of samples s22, s53 and s82. Cluster 3 is composed of samples s31, s85 s87, s89 and s90. These sample groups keep recurring after having been identified dataset Arch 1.1R MVS results. Cluster 4 is composed of samples s80, s83 and s91. Samples s83 and s91 have previously been associated with the samples of cluster 3. Sample s80 was previously associated with cluster 2 samples but appears disassociated in the many of the bivariate plots and in the three-dimensional PCA plot. Cluster 1 is composed of samples that did not fit the other clusters. Samples s17 and s81 have been recognized as distinct by previous analysis. Previous PCA analysis has demonstrated that their relationship is based on zinc but that they are not closely associated. Sample s84 has been associated with the cluster 3 samples in previous analysis. This sample exhibits ~-15% confidence that it has been assigned incorrectly. This indicates that the sample may belong to another group such as cluster 3. This is the only sample of the dataset that exhibits a negative confidence on the HCA silhouette graph.

The K-means analysis (Fig. 10-45) used a k of 4 in predicting the number of clusters. Cluster 1 corresponds to the HCA cluster 2. K-means cluster 2 corresponds with the HCA cluster 3. Both clusters are composed of samples that have been associated in previous analysis starting with dataset 1.1R. The K-means cluster 3 is composed of samples that have been statistically forced together based on the low silhouette width results. This cluster corresponds with the HCA cluster 1.

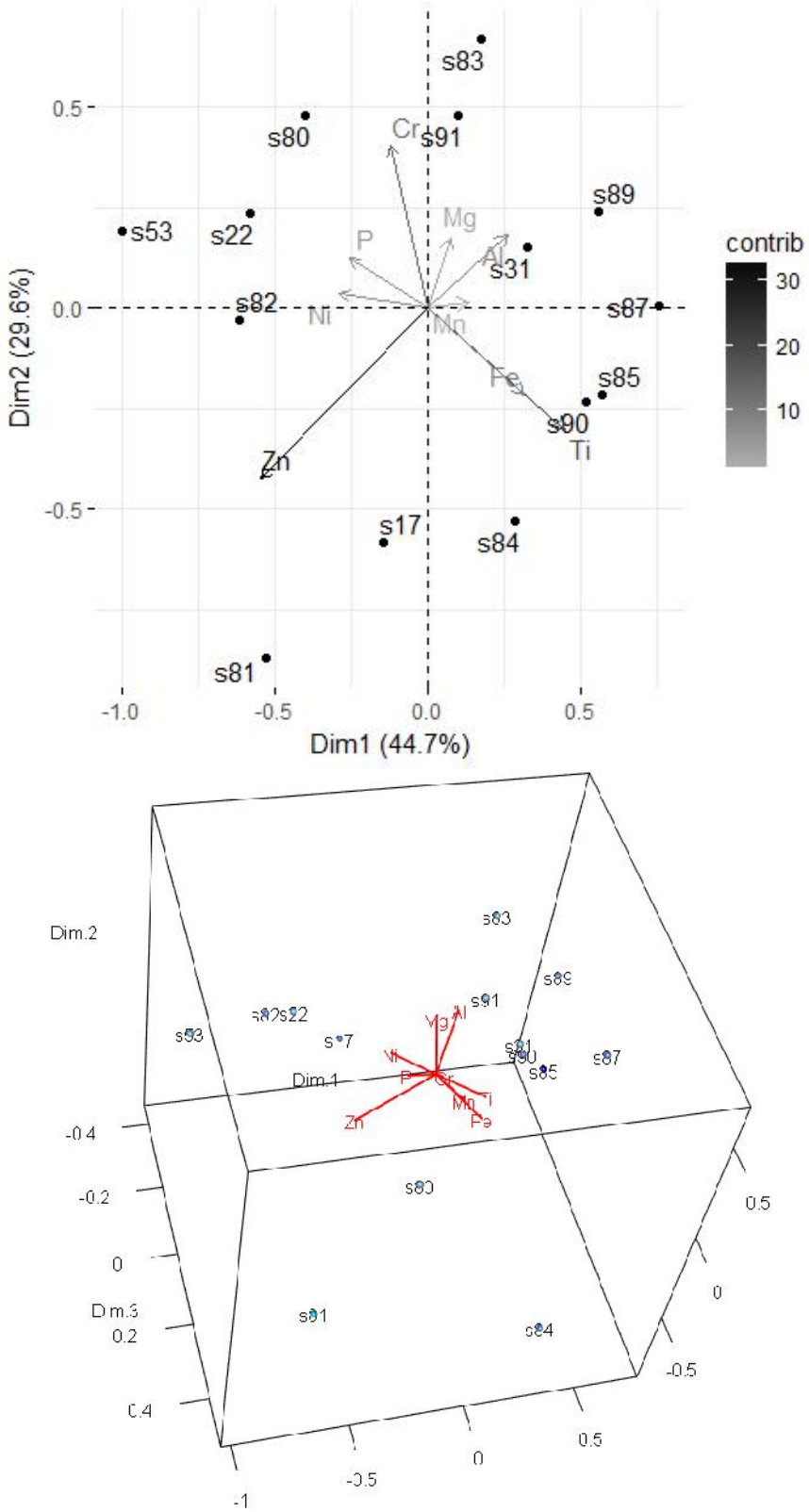

Fig. 10-43: The PCA biplot and 3D plot for dataset Arch 3.1R. The three copper blue glaze groups are defined by nickel, titanium and aluminium. Distinct samples s17 and s81 are defined by zinc.

Table 10-19: Loadings, Eigenvalues and Variance for dataset Arch 3.1R.

Dataset Arch3.1R HH-XRF 15 kV PCA Loadings

	Non-Rotated Results					Varimax Rotated Results				
	Dim.1	Dim.2	Dim.3	Dim.4	Dim.5	Dim.1	Dim.2	Dim.3	Dim.4	Dim.5
Mg	0.08	0.23	-0.43	-0.38	0.68					0.92
Al	0.28	0.24	-0.51	-0.08	-0.55	0.24		-0.36	-0.72	
P	-0.28	0.17	0.12	0.63	0.31	0.25		-0.30	0.67	
Ti	0.48	-0.40	-0.01	0.27	0.01	0.16	-0.62	0.18		-0.18
Cr	-0.13	0.54	0.50	-0.26	-0.25	0.15	0.75	0.23		-0.20
Mn	0.14	0.02	0.34	-0.12	0.14			0.39	0.10	
Fe	0.34	-0.29	0.33	-0.07	-0.02		-0.22	0.47		-0.20
Ni	-0.32	0.05	-0.27	0.39	-0.20			-0.57	0.10	-0.17
Zn	-0.59	-0.56	-0.06	-0.38	-0.12	-0.91				

Dataset Arch3.1R Eigenvalues and Variance

	Eigenvalue	Variance %	Cumulative Variance %
Dim.1	0.28	44.66	44.66
Dim.2	0.18	29.58	74.24
Dim.3	0.06	10.04	84.28
Dim.4	0.05	7.73	92.01
Dim.5	0.04	5.96	97.97
Dim.6	0.01	1.19	99.16
Dim.7	0.00	0.53	99.70
Dim.8	0.00	0.30	100.00
Dim.9	0.00	0.00	100.00

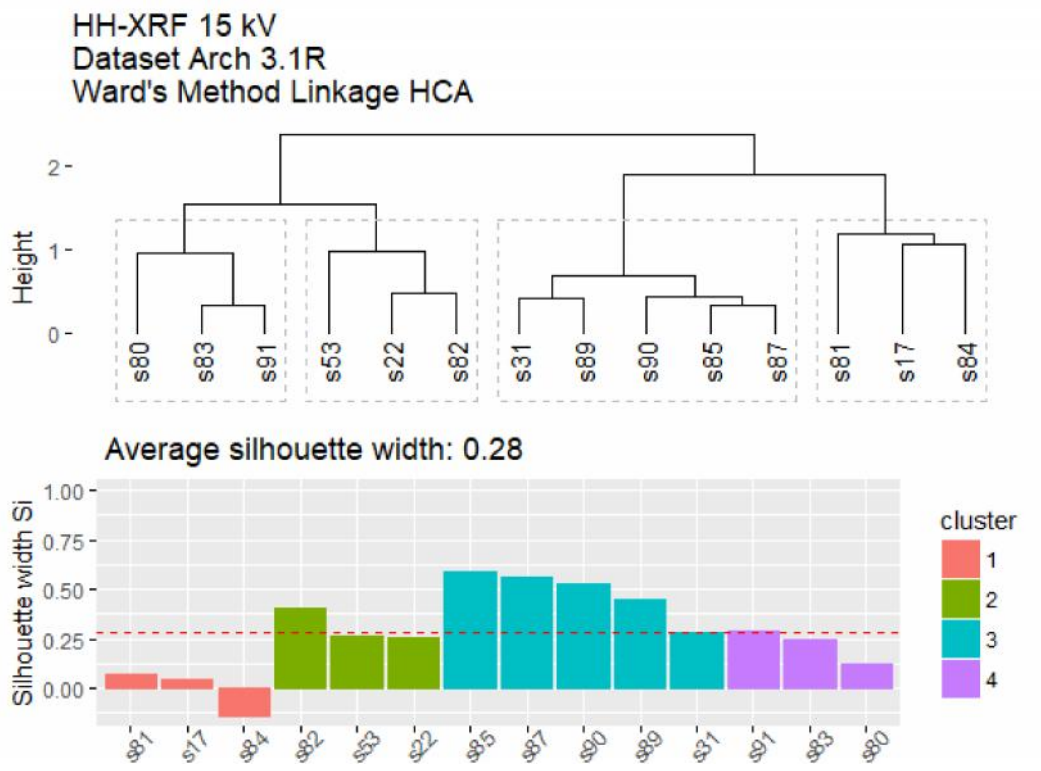

Fig. 10-44: HCA (Ward's Method) dendrogram for dataset Arch 3.1R exhibiting the copper blue glazes assigned to three clusters with moderate confidence in their cluster assignments, and cluster 4 with low confidence which probably represents a forced statistical grouping.

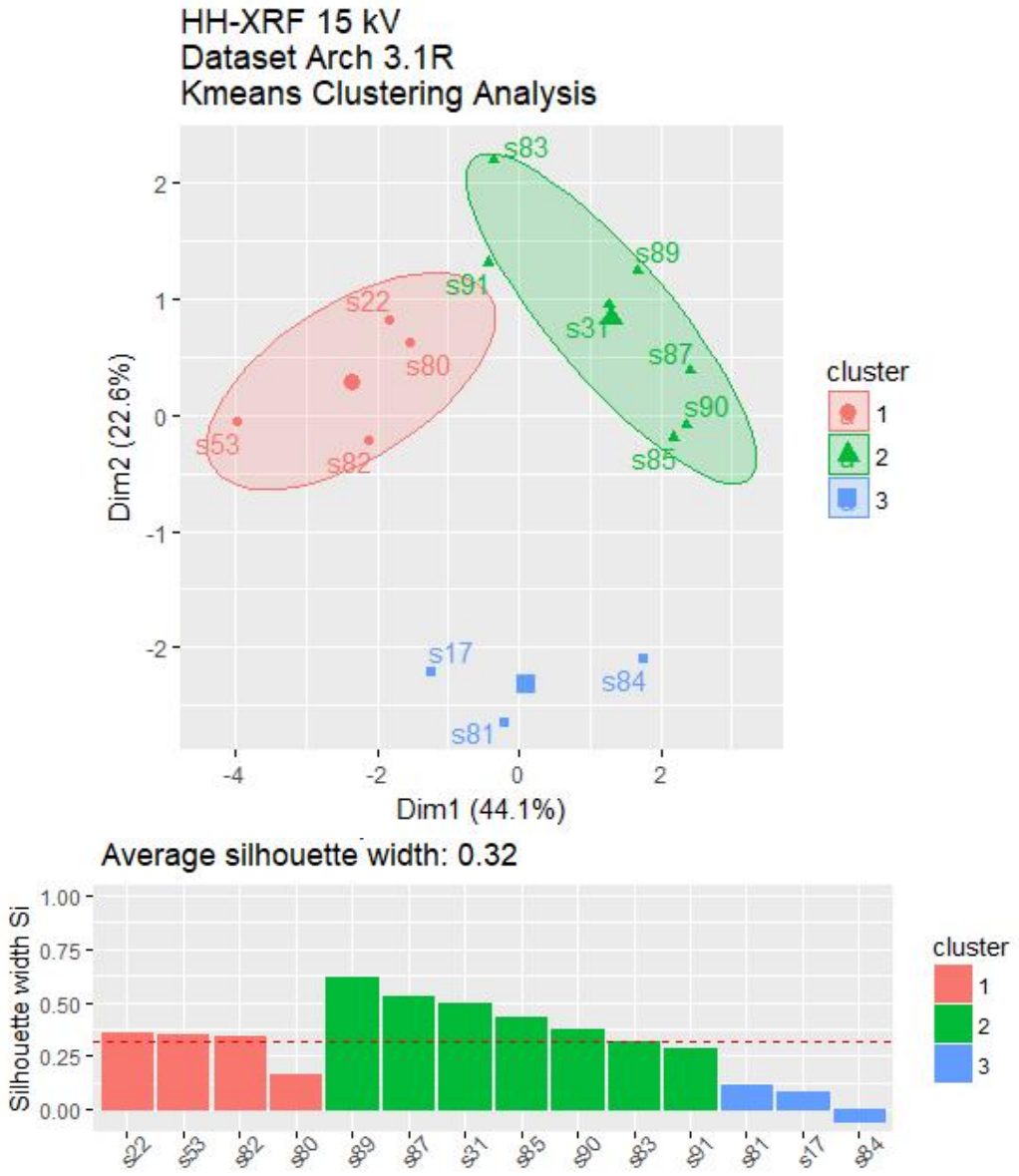

Fig. 10-45: K-means analysis for dataset Arch 3.1R exhibiting the copper blue glazes assigned to two clusters with moderate confidence in their cluster assignments, and cluster 3 with low confidence which probably represents a forced statistical grouping.

10.4.2 Dataset Arch 3.2

The HCA (single linkage) dendrogram and PCA biplot identified sample s17 as an outlier. The bivariate plots on the pairwise plot are skewed due to the presence of sample s17. The boxplots identified samples s17, s22, s53 and s80 (MgO), and s17 (CuO) as outliers. Samples s22, s53 and s80 are considered tails of the data and have been retained. Sample s17 is a statistical outlier but has already been identified as a distinct glaze from the other copper glazes. It has been removed from further analysis to help interpretation of the results.

The pairwise plot (Fig. 10-46) reveals that most of the variable relationships have a high correlation. The bivariate plot for Al_2O_3 and FeO (Fig. 10-47) exhibits a high correlation ($R^2 = 0.92$). The turquoise blue glazes are lower in iron and aluminium than the sky blue glazes with the exception of sample s82 (sky blue) which is more closely associated with the turquoise glazes. Sample s81 (bluish green) is more closely associated with the turquoise glazes.

The MgO/FeO bivariate plot (see Fig. 10-47) exhibits a similar relationship between the glazes; the sky blue glazes exhibit more iron and magnesium with the exception of sample s82 which exhibits low iron and magnesium. The turquoise glazes exhibit low to moderate iron and exhibit three groupings based on the magnesium content. The correlations for the turquoise and sky blue glazes are 0.93 and 0.98, respectively, but are 0.64 collectively.

The PCA biplot and three-dimensional plot (Fig. 10-48) failed to reveal clustering. The general associations of samples identified with previous analysis are present but the clustering is disperse and nonpattern-forming. The loadings (Table 10-20) indicate that all the variables with the exception of CuO define the variance of the first component. The second component is defined by Na_2O, FeO and Al_2O_3. The Varimax rotated results indicate Al_2O_3 as defining the first component with Na_2O and SiO_2 defining the second. The first two PCA components represent 89.17% of the total data variance.

The optimum number of clusters (k) based in gap statistics, average silhouette width and a scree plot is 2 to 3. A k of 2 to 6 was used for HCA and K-means analysis to determine optimal cluster prediction number. A k of 3 was determined optimal for HCA (Ward's Method) and K-means analysis.

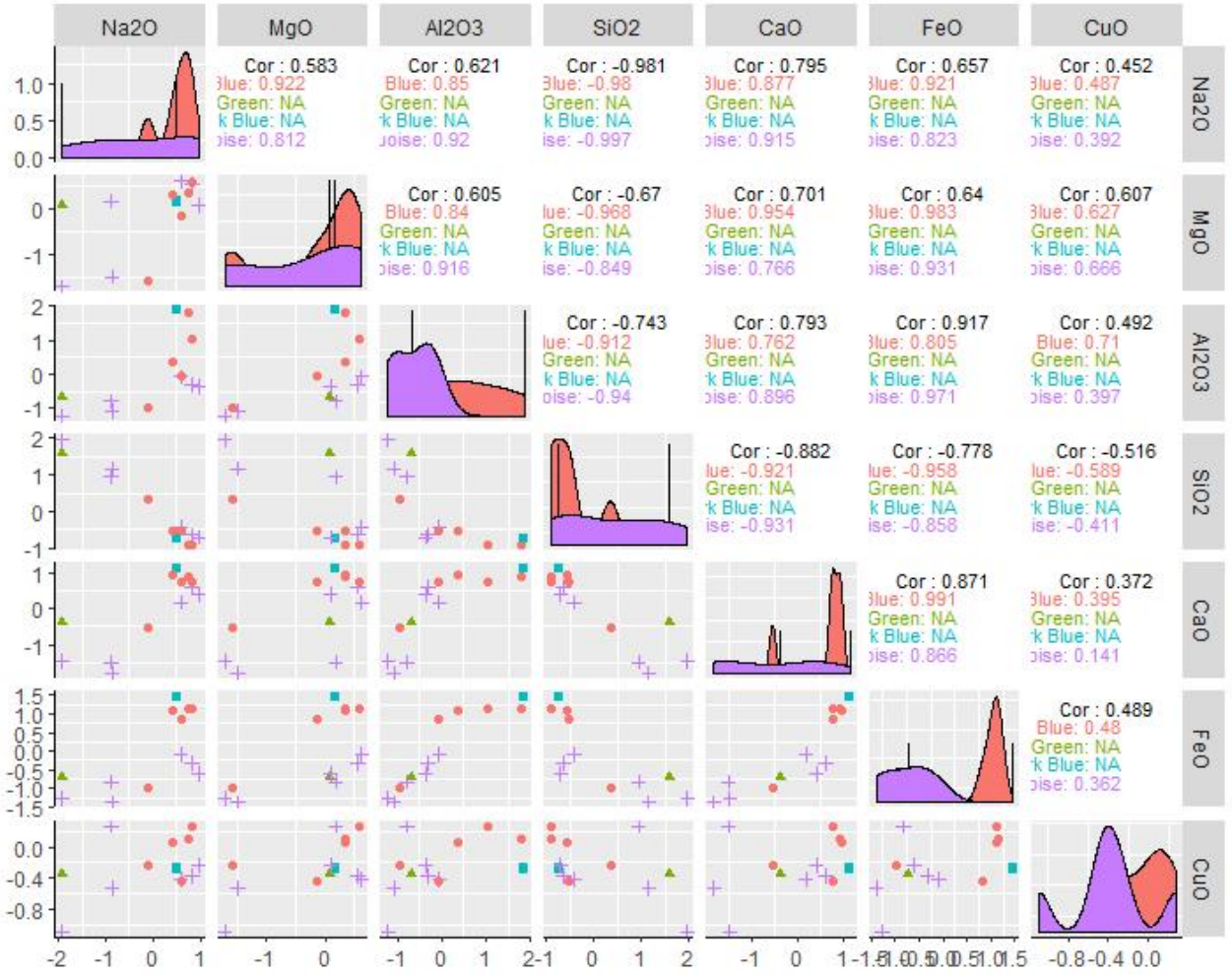

Fig. 10-46: Pairwise plot of dataset Arch 3.2 exhibiting bivariate plots, histogram and correlations of the variables.

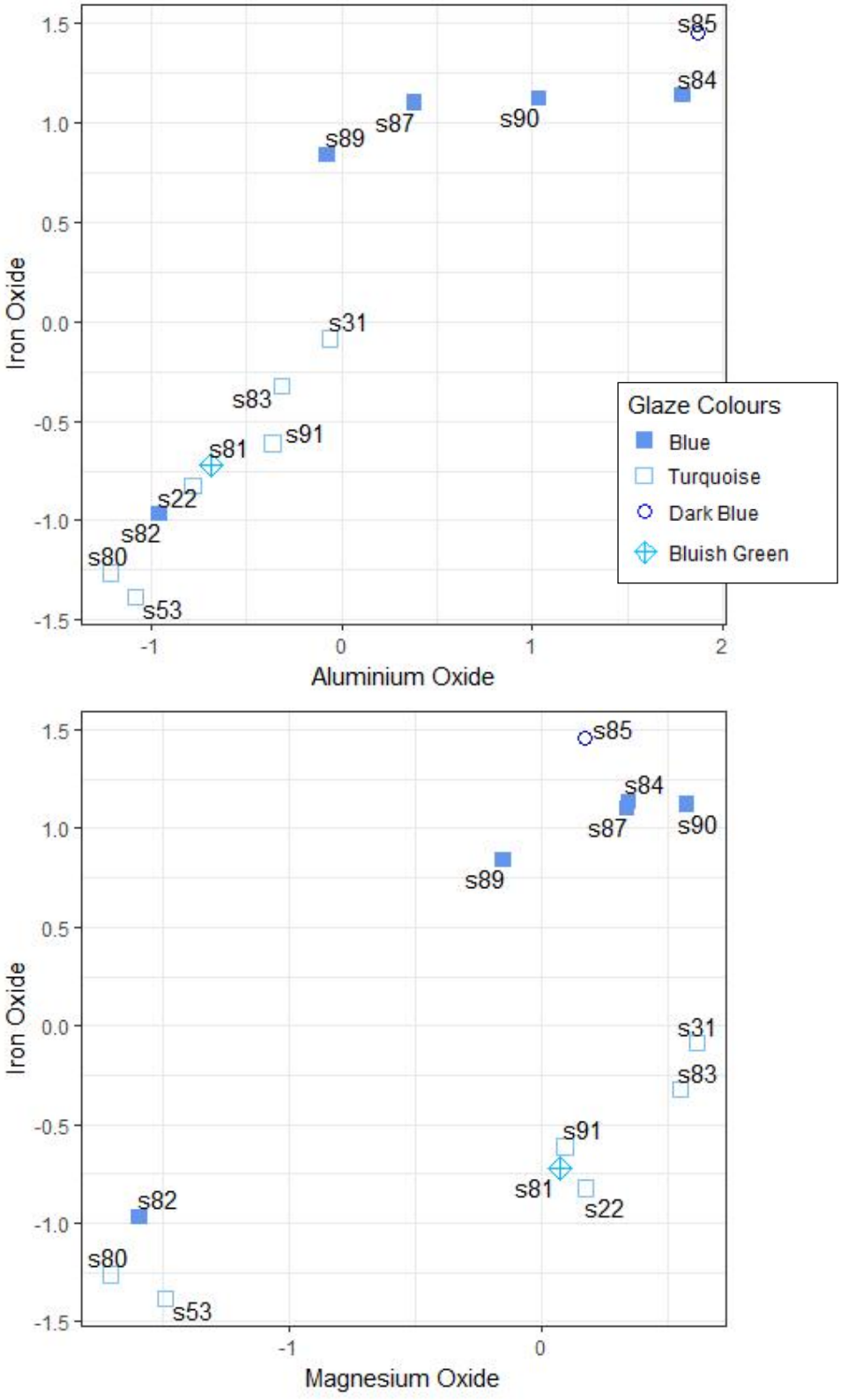

Fig. 10-47: Bivariate plots of aluminium/iron and magnesium/iron oxides revealing a division between the turquoise and sky blue copper based glazes. The turquoise glazes are further divided when analysing magnesium oxide.

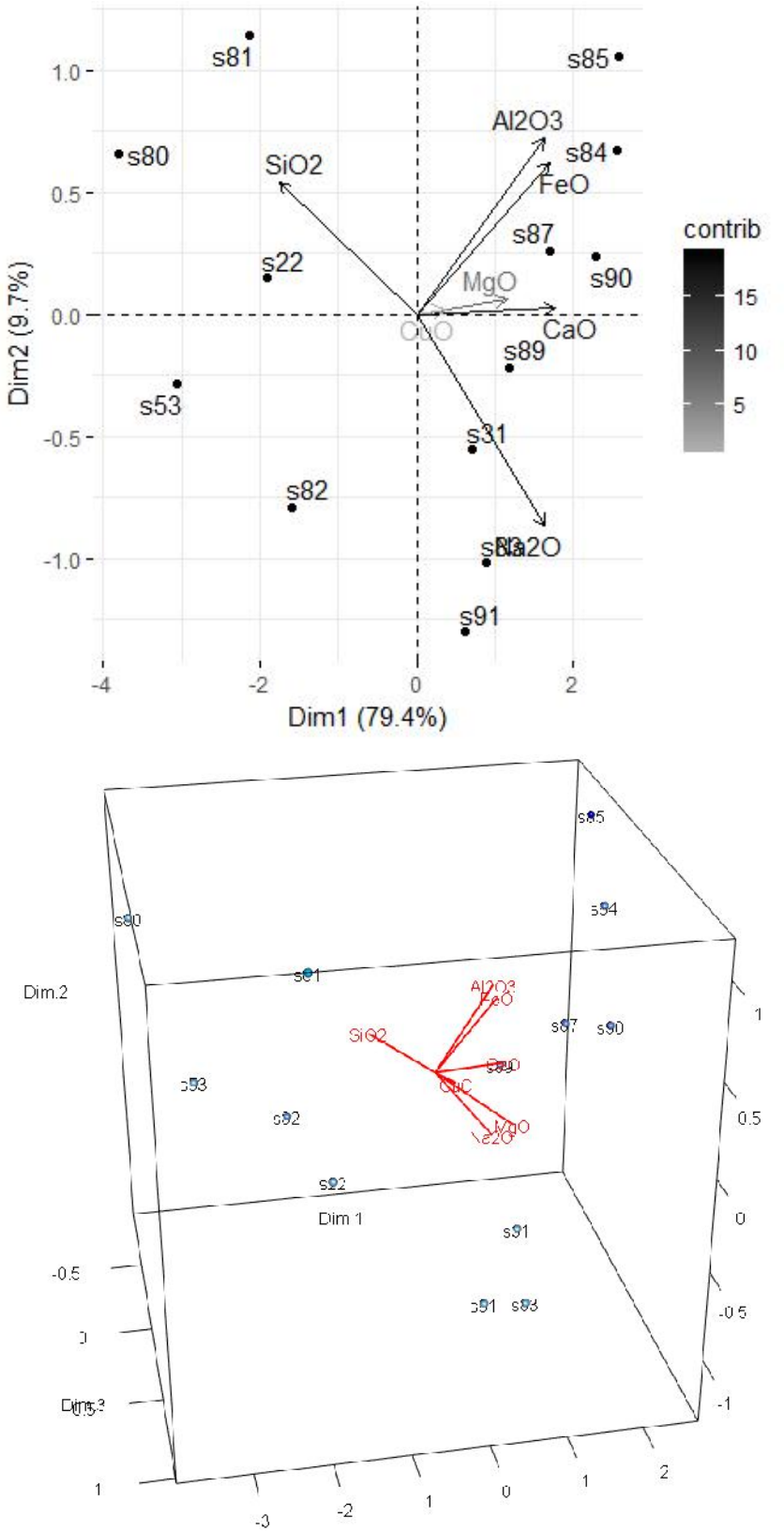

Fig. 10-48: The PCA biplot and 3D plot for dataset Arch 3.2. The samples do not exhibit clustering but relationships can be determined based on the variables.

Table 10-20: Loadings, Eigenvalues and Variance for dataset Arch 3.2.

Dataset Arch3.2 SEM-EDS PCA Loadings											
Non-Rotated Results						Varimax Rotated Results					
	Dim.1	Dim.2	Dim.3	Dim.4	Dim.5		Dim.1	Dim.2	Dim.3	Dim.4	Dim.5
Na_2O	0.41	-0.62	-0.17	0.21	-0.02	Na_2O		-0.78			
MgO	0.29	0.04	0.92	0.01	-0.14	MgO			0.97		
Al_2O_3	0.41	0.52	-0.22	0.43	-0.56	Al_2O_3	0.99				
SiO_2	-0.44	0.39	0.10	-0.13	-0.01	SiO_2		0.60			
CaO	0.44	0.02	-0.02	-0.74	-0.09	CaO			0.11	-0.83	0.19
FeO	0.43	0.45	-0.16	-0.08	0.63	FeO					0.90
CuO	0.09	0.02	0.22	0.45	0.50	CuO	-0.11	-0.12	0.19	0.55	0.39

Dataset Arch3.2 Eigenvalues and Variance			
	Eigenvalue	Variance %	Cumulative Variance %
Dim.1	4.54	79.44	79.44
Dim.2	0.56	9.74	89.17
Dim.3	0.34	5.89	95.06
Dim.4	0.17	3.01	98.07
Dim.5	0.07	1.25	99.32
Dim.6	0.04	0.68	100.00
Dim.7	0.00	0.00	100.00

The HCA (Ward's Method) dendrogram (Fig. 10-49) exhibits three clusters. Cluster 1 and a combination of clusters 2 and 3 have been recognized since the initial analysis of dataset Arch 1.1R. The sample relationships in clusters 2 and 3 were recognized with the analysis of dataset Arch 3.1R.

The K-means analysis (Fig. 10-50) reveal three clusters. The sample relationships in cluster 1 have been recognized since the initial analysis of dataset Arch 1.1R. Cluster 2 is compact and distinct whereas cluster 3 is slightly more disperse. The sample relationships in these two clusters have been noted with the analysis of dataset Arch 3.1R.

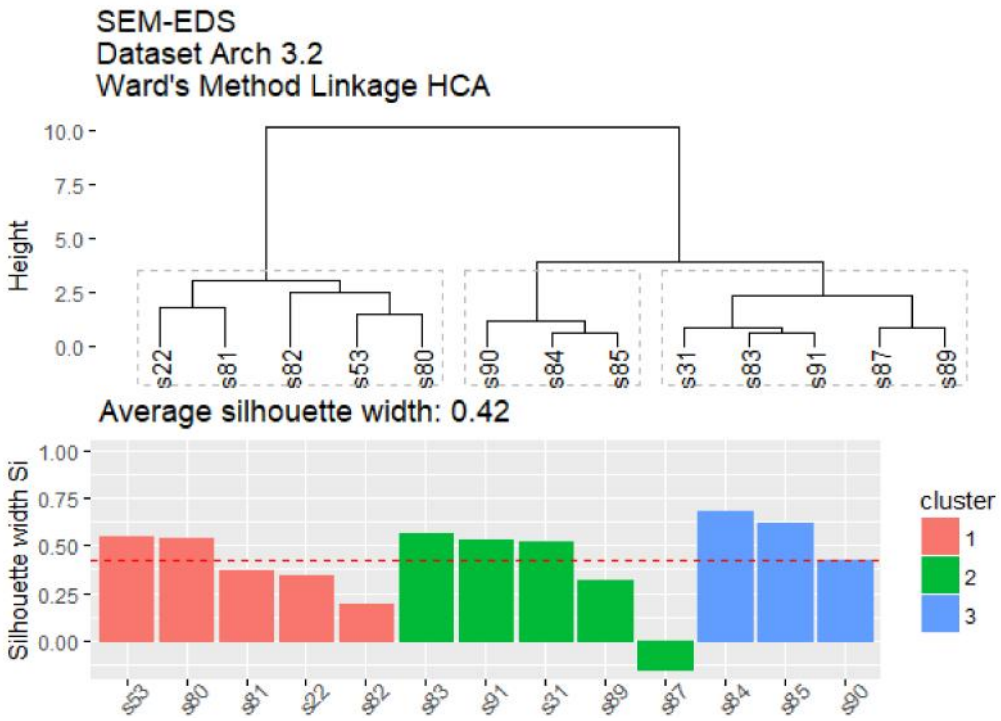

Fig. 10-49: HCA (Ward's Method) dendrogram for dataset Arch 3.1R exhibiting the copper blue glazes divided into three clusters.

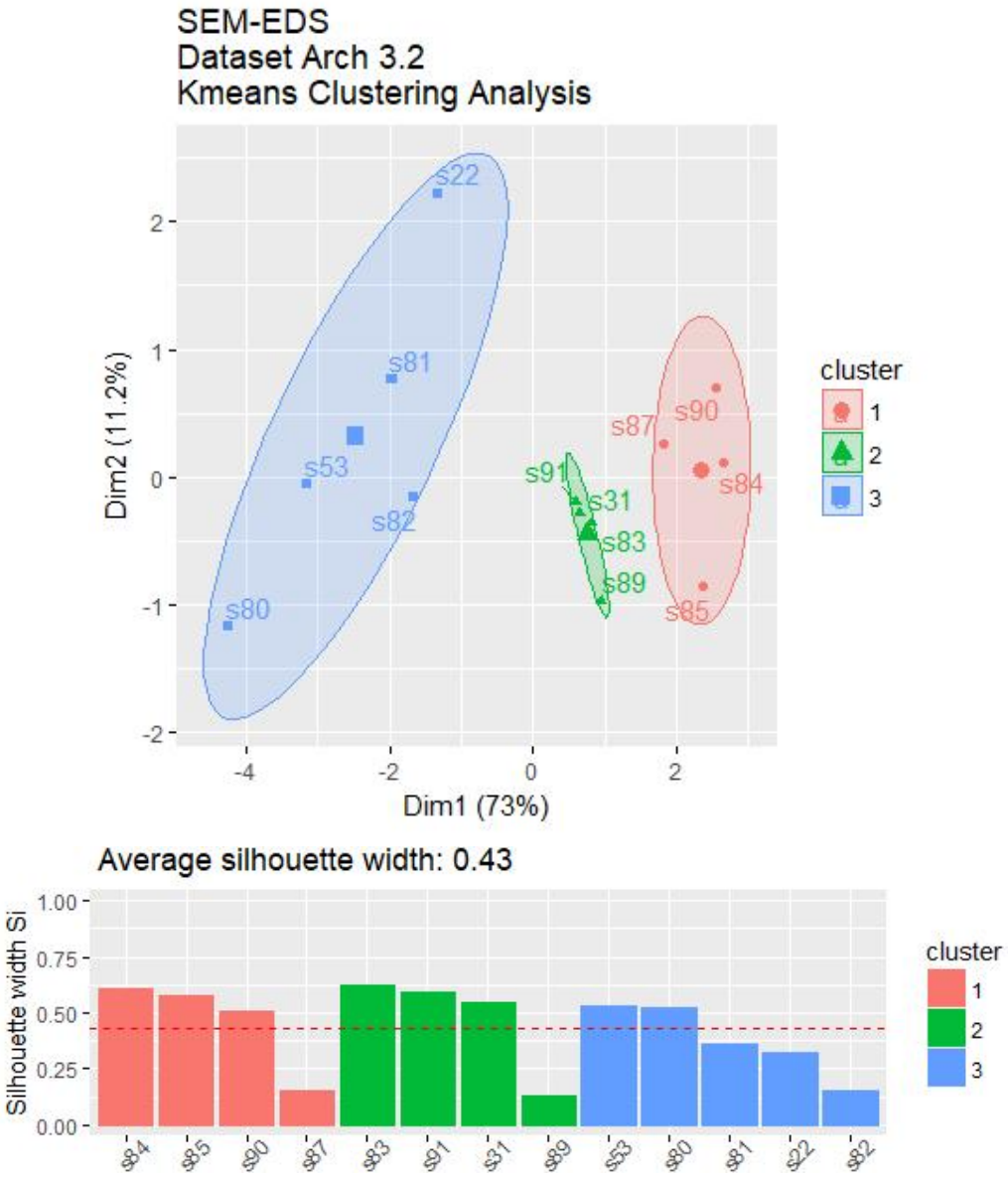

Fig. 10-50: The K-means analysis of dataset Arch 3.2 exhibiting the copper blue glazes divided into two distinct and one disperse cluster.

10.4.3 Dataset Arch 3.3R

The HCA (single linkage) dendrogram identified sample s17 as an outlier. The boxplots indicate samples s17 and s22 as outliers for strontium. The PCA biplot and the bivariate plots reveal these samples as tails of the data. They have been retained for further analysis.

The pairwise plot (Fig. 10-51) exhibits a few high correlations between variables for all samples, most notably for iron/tin (R2 = -0.89) and iron/lead (R2 = -0.87) (Fig. 10-52). No distinct clusters are present. Samples s84, s85 and s90 do consistently occur in close proximity throughout the MVS analysis.

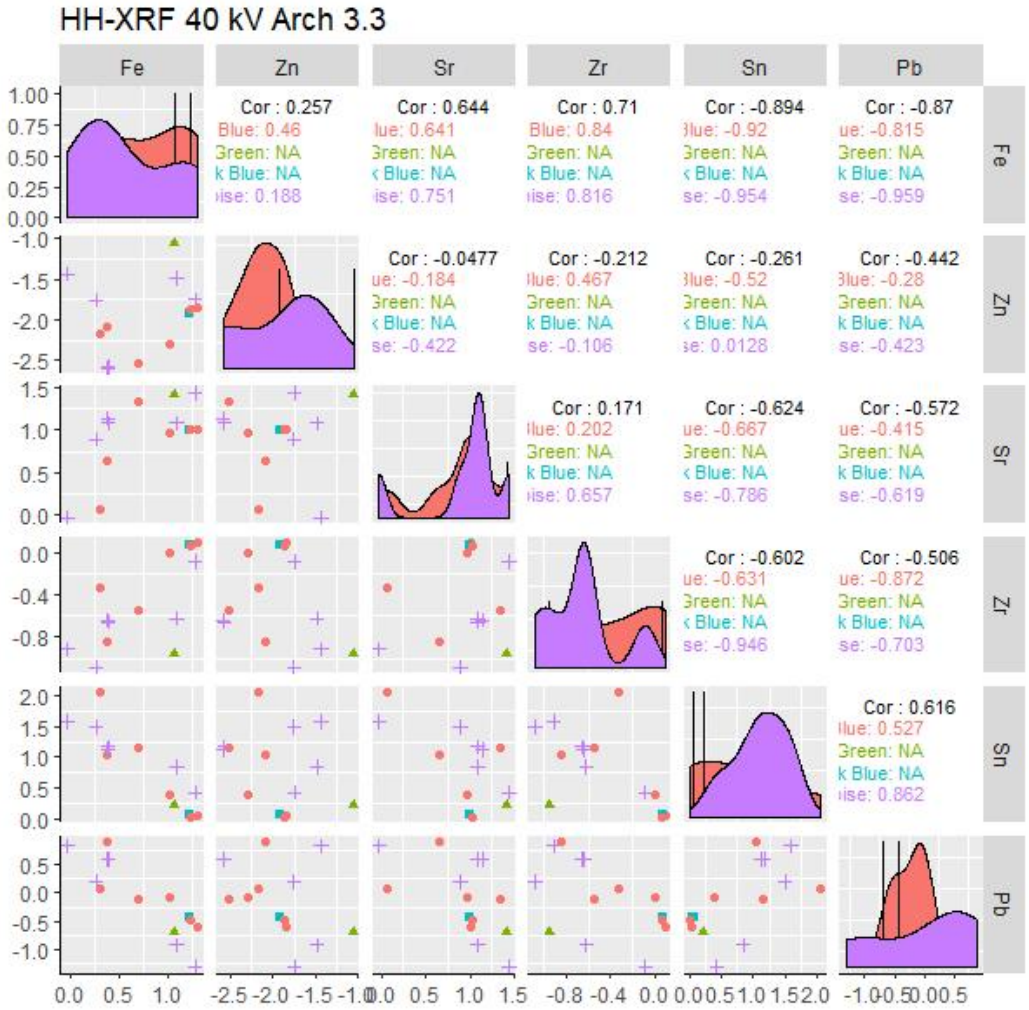

Fig. 10-51: Pairwise plot of dataset Arch 3.3R exhibiting bivariate plots, histogram and correlations of the variables.

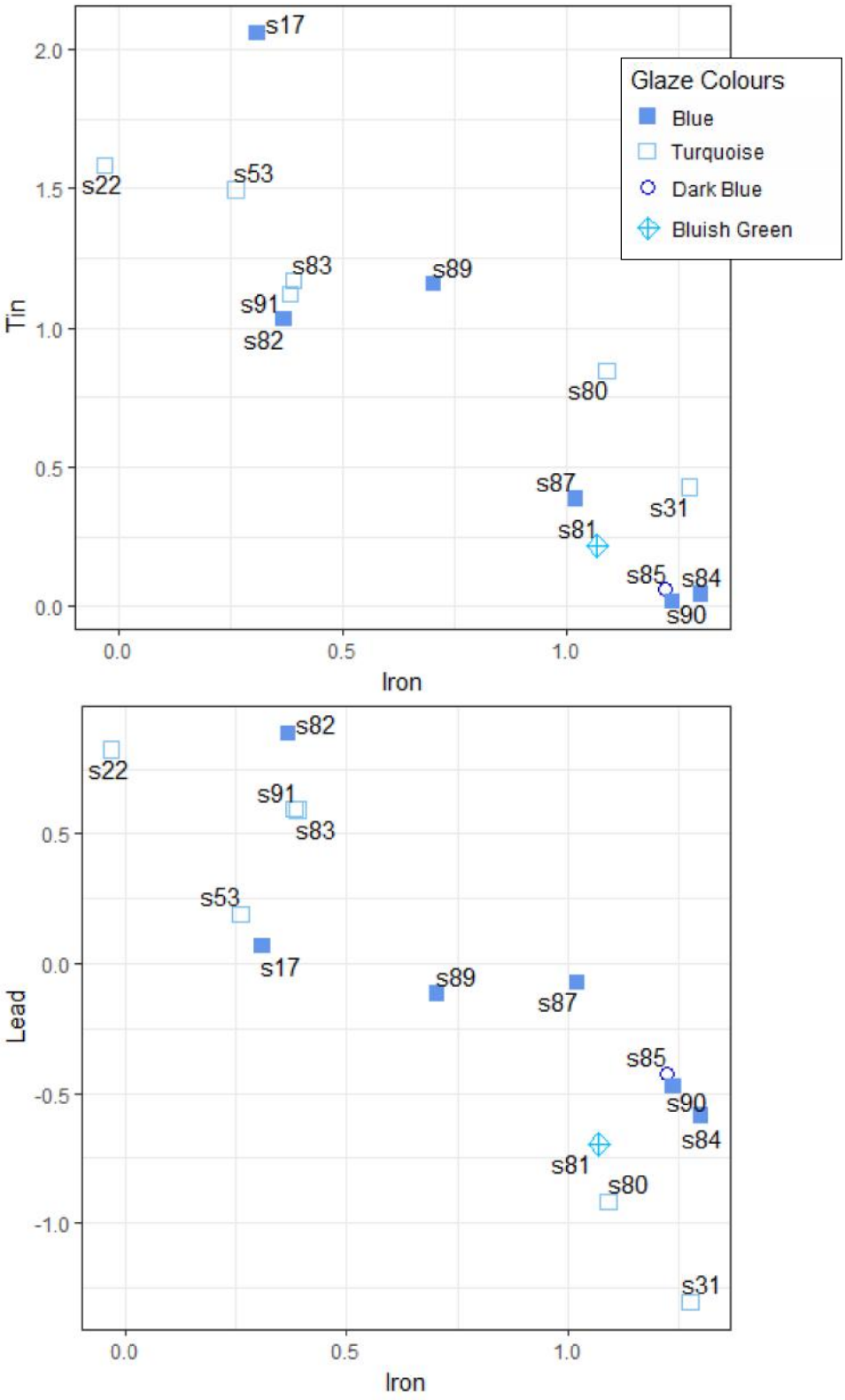

Fig. 10-52: Bivariate plots for iron/tin and iron/lead for dataset Arch 3.3R. These have the highest correlations (R2 = 0.89 and 0.87, respectively) of the dataset but fail to form distinct clusters.

The bivariate plots for iron/tin and iron/lead are good examples of the relationship.

The PCA biplot (Fig. 10-53) exhibits no distinct clustering with the exception of the S84, s85 and s90 relationship. The loadings (Table 10-21) exhibit the first PCA component variance defined by all the variables. The second component is defined by zinc. The Varimax rotated results indicate lead for component 1 and zinc for component 2. The two PCA components represent 81.88% of the total data variance.

The optimum number of clusters (k) based in gap statistics, average silhouette width and a scree plot is 2. The HCA (Ward's Method) dendrogram (Fig. 10-54) fails to reveal previously recognized clustering of samples but does exhibit the s84, s85 and s90 relationship found with the pairwise plots. The same is true for the K-means analysis (Fig. 10-55). The relationship between samples s84, s85 and s90 was not isolated until a k of 6 was introduced to the algorithm but this statistically forced sample pairs into clusters.

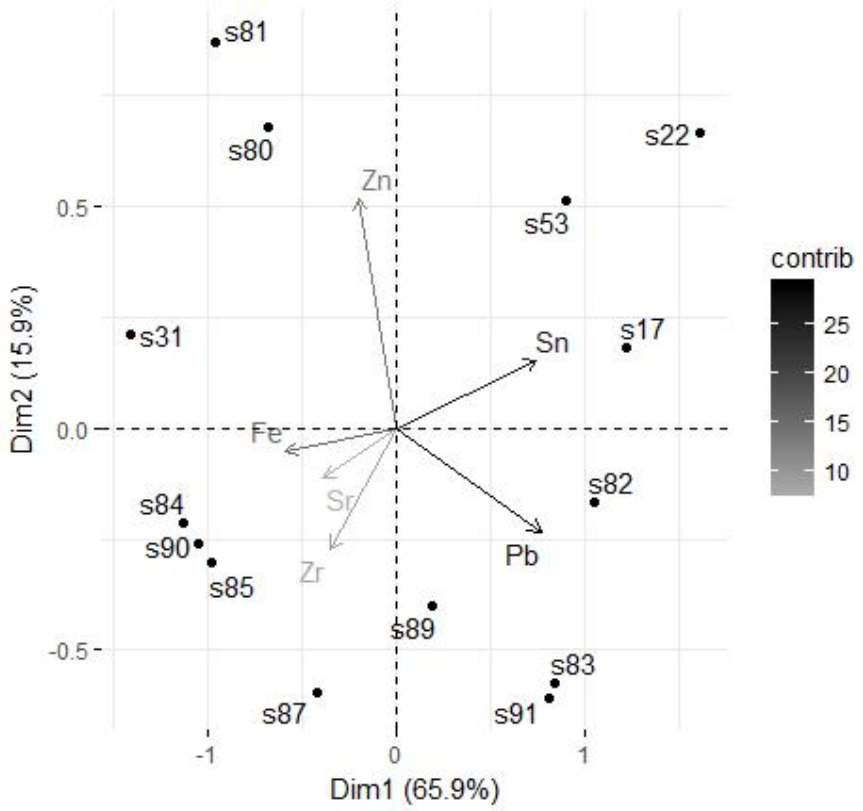

Fig. 10-53: PCA biplot for dataset Arch 3.3R.

Table 10-21: Loadings, Eigenvalues and Variance for dataset Arch 3.2.

Dataset Arch3.3R HH-XRF 40 kV PCA Loadings											
Non-Rotated Results						Varimax Rotated Results					
	Dim.1	Dim.2	Dim.3	Dim.4	Dim.5		Dim.1	Dim.2	Dim.3	Dim.4	Dim.5
Fe	-0.44	-0.08	0.08	-0.01	0.79	Fe	-0.12	-0.12	0.12	-0.12	0.88
Zn	-0.15	0.78	-0.01	-0.39	-0.22	Zn	-0.12	0.88	0.12	-0.12	-0.12
Sr	-0.29	-0.17	-0.69	0.39	-0.31	Sr	-0.12	-0.12	-0.88	-0.12	-0.12
Zr	-0.26	-0.41	0.62	-0.07	-0.46	Zr	-0.41	-0.41	0.41	-0.41	-0.41
Sn	0.56	0.23	0.26	0.63	0.10	Sn	-0.12	-0.12	0.12	0.88	-0.12
Pb	0.57	-0.35	-0.26	-0.55	0.09	Pb	0.88	-0.12	0.12	-0.12	-0.12

Dataset Arch3.3R Eigenvalues and Variance			
	Eigenvalue	Variance %	Cumulative Variance %
Dim.1	1.02	65.95	65.95
Dim.2	0.25	15.93	81.88
Dim.3	0.14	9.17	91.05
Dim.4	0.14	8.73	99.78
Dim.5	0.00	0.22	100.00
Dim.6	0.00	0.00	100.00

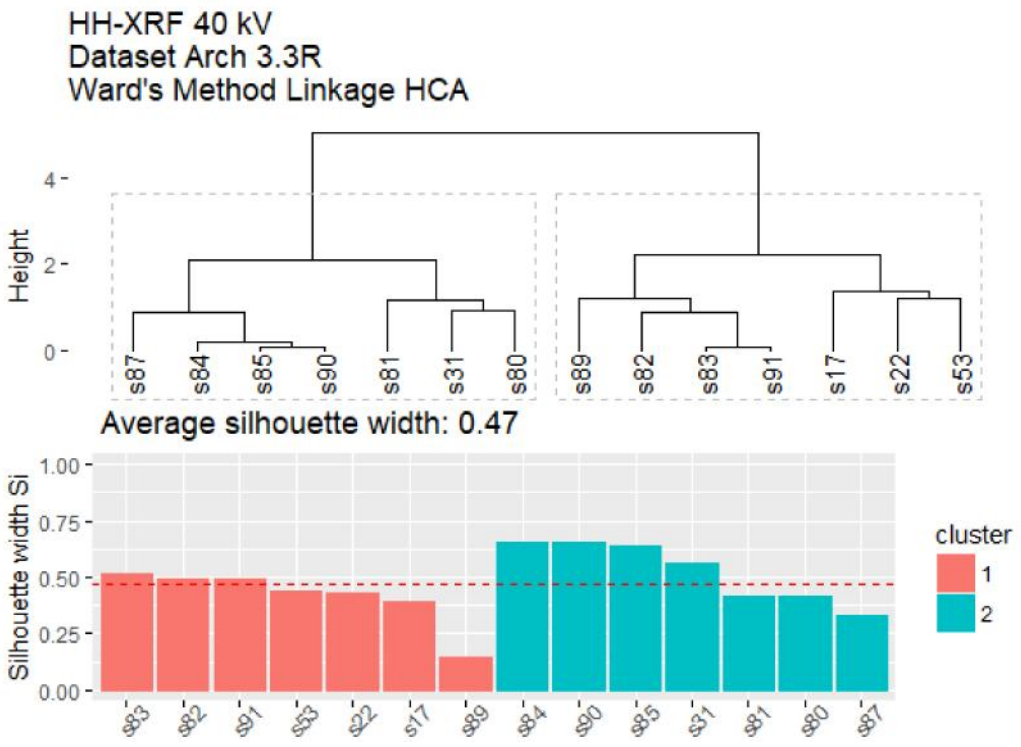

Fig. 10-54: The HCA (Ward's Method) dendrogram and silhouette graph for dataset Arch 3.3R. The relationship between samples s84, s85 and s90 is linked.

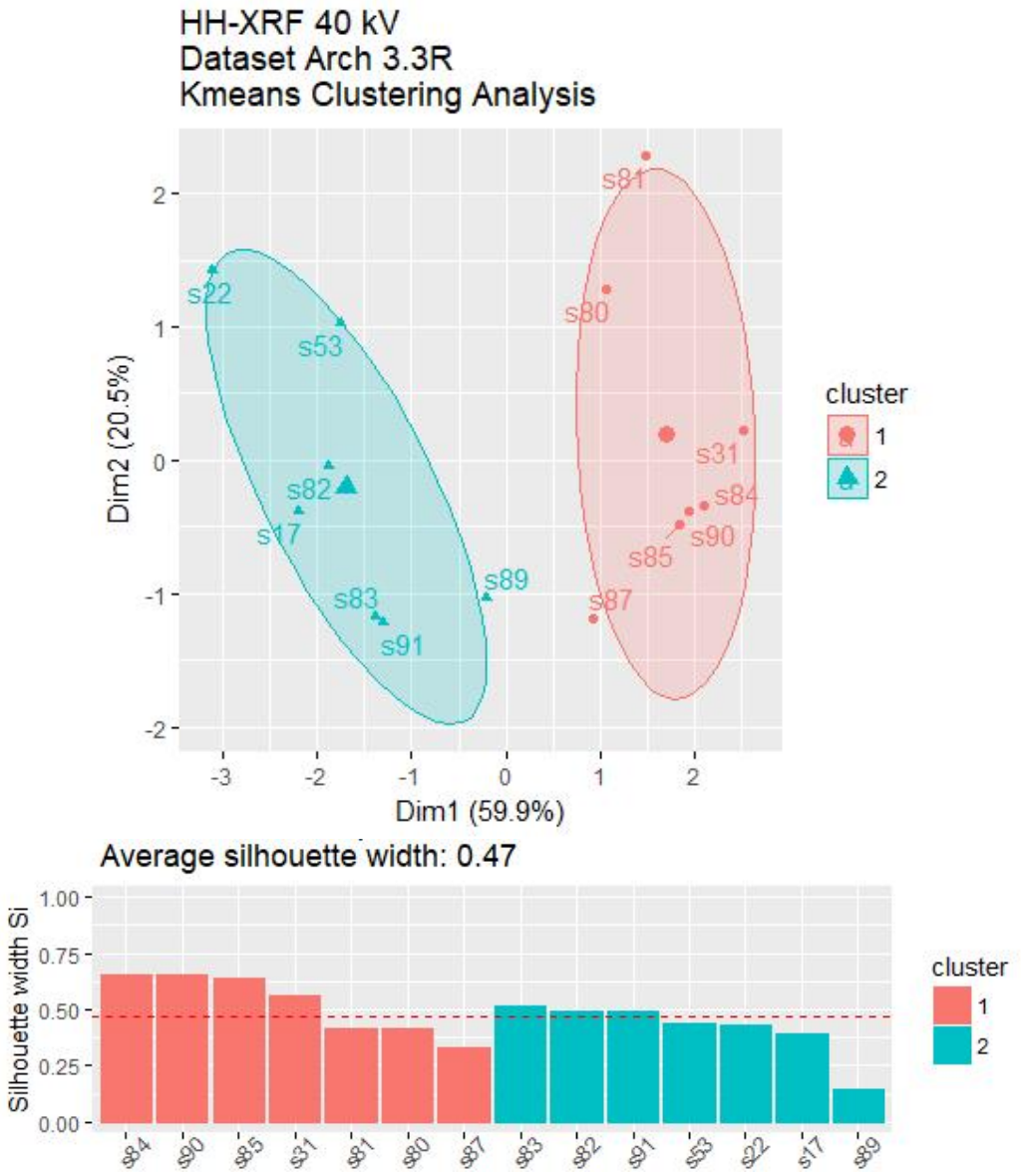

Fig. 10-55: The K-means biplot and silhouette graph for dataset Arch 3.3R. No distinct clustering with the exception of samples s84, s85 and s90.

10.5 Discussion

The MVS analysis of dataset Arch 1 assigned the samples into clusters generally based on glaze colour. The clusters have been designated into several groupings.

Group 1 is composed of sample s21 (purple). The purple glaze was distinct from the others by the manganese used to provide the violet to purple colour. This sample caused skewing with the MVS analysis and was removed before additional analysis of dataset 1.1R. It is considered its own cluster but was statistically an outlier. The element manganese is within the optimal range of the 15 kV HH-XRF settings and it was identified in every sample but in much lower proportions than s21.

Manganese is not a variable in datasets Arch 1.2 (SEM-EDS) and Arch 1.3R (40 kV HH-XRF). The Arch 1.2 MVS analysis failed to isolate manganese-heavy s21 but it did segregate it from the copper blue glazes and designate it as a part of a group (cluster 4) containing two cobalt blue and one yellow glaze best illustrated by HCA and K-means analysis (Fig. 10-16). Dataset Arch 1.3R MVS analysis has assigned s21 to the copper blue glaze clusters. Manganese is situated below the range of optimization for the 40 kV measurements. Group 1 illustrates the need for low and high kV measurements with HH-XRF; although not isolated with the higher kV settings, the lower kV settings are extremely compelling of the existence of this group based on manganese.

Group 2 is composed of the cobalt blue glazed sherds (s70, s72, s74 and s78). These glazes are visibly different from the other blue glazes because of their deep dark blue hue. This group can be subdivided into **Group 2a** consisting of dark purplish glazes (s72 and s74) and **Group 2b** consisting of ultra-marine blue glazes (s70 and s78). The aluminium content of these glazes is low which is consistent with the aluminium/cobalt relationship of post-New Kingdom cobalt glazes.

Dataset Arch 1.1R identifies the two groups based on the iron content. Group 2b is designated as a distinct cluster. Group 2a is a separate cluster and is associated with glazes s48 (dark blue) and s81 (blueish green). Glaze s48 contains more cobalt than the copper blue glazes and much less than the cobalt blue glazes. Glaze s48 contains more copper than most of the glazes and could be considered a copper/cobalt coloured glaze. Sample s81 contains average copper and cobalt amounts for the copper blue glazes. It contains the highest amount of zinc of all the samples in the assemblage. The next highest zinc containing glaze is sample s74 (Group 2a) and it may be this relationship that has combined these samples together in the cluster.

Dataset Arch 1.1 (full variable set based on criteria outlined in chapter 8) has clustered the cobalt glazes into a single cluster. Sample s81 was removed as an outlier because of high amounts of calcium (the highest of the assemblage) and s48 was clustered with the copper blue glazes.

Dataset Arch 1.2 MVS results reveal Group 2b as a distinct cluster. Group 2a is associated with samples s21 (purple) and s45 (yellow). All of these samples are distinct because of the iron oxide content as measured through SEM-EDS. Dataset Arch 1.3R has included the Group 2 sherds with the copper coloured glazes. This could be because the relationship is being masked by the presence of a distinct green and yellow glaze cluster based on lead which has, in effect, skewed the data results.

Groups 2a and 2b are found with dataset Arch 2.1R (15 kV HH-XRF) as well. The PCA biplot for Arch 2.1R (Fig. 10-24) reveals that the cobalt blue glazes and glaze s48 and s81 are consistently being clustered near each other based on the iron and zinc content in the glazes. The K-means analysis biplot (Fig. 10-27) exhibits the cobalt blue glazes as a distinct cluster but glazes s48 and s81 are still situated between the cobalt blue cluster and the copper cluster to which they have been assigned. The MVS analysis for datasets Arch 2.2 (SEM-EDS) and 2.3R (40 kV HH-XRF) exhibit cobalt glaze s72 as associated with one of the copper blue glaze clusters but the other three cobalt blue glazes (s70, s74 and s78) have been assigned to the same cluster.

Group 3 is composed of the green (s12, s20 and s42) and yellow (s45) coloured sherds. Sample s12 was visually identified on its own as a copper blue glaze with a greenish hue but instrumental analysis combined with MVS consistently associated it with the green glazes. The yellow and green glaze colours are a product of lead antimonate in the glaze batch. The 15 kV HH-XRF measurement did not include lead and antimony and the variable relationships of the remaining elements were not distinct enough to assigned the glazes to a separate cluster. As a result they were clustered with the copper blue glazes.

Dataset Arch 1.1 (full variable set) bivariate plots (see Fig. 10-8) did group the green glazes based on the aluminium content and isolate the yellow glaze based on copper and iron. The PCA biplot (see Fig. 10-9) exhibits a divergent yellow glaze based on manganese and K-means (see Fig. 10-11) exhibits the green glazes in one distinct cluster and the yellow glazes as the single occupant of a separate cluster.

Dataset Arch 1.2 clustered the green and yellow glazes with the copper blue glazes. Aluminium and manganese were not measured with this dataset due to Limit of detection. MVS analysis of Dataset Arch 1.3R did cluster the green and yellow glazes

together based on the lead content in the glaze. Dataset Arch 1.3 (full variable set) which only added copper as a variable exhibited the same clusters but separated s45 (yellow) from the green glazes within the same cluster.

The green and yellow glazes are designated as **Group 3a** (green) and **Group 3b** (yellow). These two groups are segregated by greater quantities of iron, aluminium, magnesium and manganese associated with the yellow glaze and copper associated with the green glazes.

Group 4 is composed of the copper blues glazes. These were subdivided into **Group 4a** and **Group 4b**. Group 4a is composed of samples s22, s53, s80 and s82. It contained s12 when this is not recognized as a green glaze because of selection of variables. Sample s17 is included with the 15 kV HH-XRF measurements (due to zinc and nickel being measured) but not with the SEM-EDS measurements. Samples s48 and s81 are included when not associated with other groups. Group 4a is identified by the presence of zinc and nickel with 15 kV HH-XRF and SiO_2 content with SEM-EDS. Samples s48 and s81 contain high amounts of zinc and this is responsible for the relationship between these samples and the others in Group 4a with the HH-XRF measurements. Group 4b contains the remainder of the copper blue sherds and is identified by the amount of titanium and aluminium with HH-XRF measurements and aluminium and magnesium oxides with the SEM-EDS measurements. Within this group, glazes s84, s85 and s90 are usually closely associated in the various analyses indicating a strong relationship between them that could potentially represent a workshop connection and certainly a raw material relationship. It is quite possible that they represent sherds of the same vessel. The sub groups 4a and 4b are only identified using 15 kV HH-XRF and SEM-EDS measurements. The inability of 40 kV 45HH-XRF analysis to identify these subgroups is based on titanium, zinc and nickel falling below the optimum range for the high kV analysis.

Glaze sample s17 represents its own group (**Group 5**) defined by high copper and magnesium content in the glaze. A review of the HH-XRF 15 kV NPA counts reveal sample s17 having the highest potassium (not used in the MVS analysis), copper, titanium and nickel content of the study assemblage. Although glaze s17 is blue, it is isolated by having higher amounts of copper, zinc and nickel in the glaze compared to the other blue glazes. This glaze is distinct by having the thinnest glaze (with minimal de-alkalization) and the smallest and most uniform body silica particle sizes of the glaze assemblage.

In conclusion, this analysis reveals that 15 and 40 kV HH-XRF analysis is useful to determine sherd groups based on elemental composition but variable selection is also important. Dataset Arch 1.1 exhibited greater clustering ability than dataset Arch 1.1R based on colourants. This is expected as colourants are included in the variable set and greatest variance in the data is certainly represented by the colourants used in the glaze. The added variables that produce these results may obscure information pertaining to raw materials and/or workshops that trace elements may help to identify. Removing the colourants from the datasets will allow the detection of other relationships obscured by the colourants, such as those based on trace elements, to be exposed.

Chapter 11: General Discussion

11.1 Project Review, Rationale and Methodology

The project was devised to evaluate the use of HH-XRF NPA on archaeological monochrome blue faience from the Late through Roman Periods in Egypt. The HH-XRF lack of a radiological source and portability make it a useful tool for places like Egypt where the exportation of archaeological materials for analysis is extremely difficult if not impossible (Law 117 2010).

Faience is a layered material consisting of a soda-lime-silica glaze covering a body substrate of similar elemental components. Egyptian faience has been recovered from several sites across Egypt and the HH-XRF analysis of these glazes in the field and laboratory is useful with on-going excavation strategies, and may prove beneficial for future provenance studies. Raw faience glaze material sources and usage changed over time due to geopolitical and other factors facilitating the attribution of glazes into a loose chronology based on presence/absence of elements (e.g. cobalt ores and use of lead in green glazes; see Chapter 2). Late through Roman Period faience and its glaze characteristics (in the form of replications) were examined. This period marked an ingress of Greek and later Roman pottery techniques and styles into the more traditional pharaonic faience realm. Faience from this time period is less examined in the literature.

Each of the parameters of HH-XRF (i.e. acquisition time, filters, voltage, current, use of vacuum, end window selection) were examined and tested using Corning Glass B as the analyte to determine optimal settings for the analysis of faience glazes. Optimal results for each parameter were based on a combination of greatest precision coupled with greatest signal-to-noise (SNR) ratio. The optimum levels of these characteristics often did not correspond so that the largest SNR usually had low precision and vice versa. The optimal settings were a balance between high precision and high SNR as determined through a bi-variant quotient (see Chapter 6).

Net peak analysis of the replicated and archaeological glazes using optimized HH-XRF parameter settings from the Corning Glass experiments produced MVS clusters. Clusters for replicated faience glazes discerned individual batches (two cobalt and one copper). Five clusters were identified for archaeological glazes and may represent raw

material sources and/or workshops[1]. The largest benefit of producing HH-XRF results in wt% is the ability to compare results across the literature. NPA cannot be compared unless all analysis was conducted on the same HH-XRF unit. However, clusters generated through MVS can be compared to those of other HH-XRF units or across the literature and will be similar regardless if NPA or wt% define them.

Egyptian faience is not ideal for HH-XRF analysis due to heterogeneity and glaze thickness. Anomalies due to heterogeneity can be averaged out by multiple assays across the glaze surface. Glaze thickness and depth of analysis is an issue because the origin (body or glaze) of the detected signals must be known to provide accurate characteristics of the glaze. Depth of analysis with HH-XRF is defined by several factors (see below; see Chapter 3) and is specific to each element in a glaze.

Faience replications were produced to help with the HH-XRF evaluation by providing a layered vitreous analyte with known composition. Three faience glaze batches, one copper colourant and two cobalt colourant, consisting of 30 replicate glazes were chosen over several produced that were based on previous reproduction studies and faience analyses (see Chapter 5). The two cobalt glazes shared the same elements with slight differences in element concentrations. Multivariate statistical analysis of HH-XRF and SEM-EDS results identified the three replicated glaze batches with HH-XRF NPA results revealing greater discernment (see Chapter 9). Afterwards a small assemblage of 24 archaeological glazes from Saqqara (housed at Cardiff University) were analysed with HH-XRF and SEM-EDS as a case study (see Chapter 10). Clusters produced through multivariate analysis of the HH-XRF and SEM-EDS results were similar.

Recording of analytical results for the replicate and archaeological glazes in NPA (HH-XRF) and wt% (SEM-EDS) permitted additional evaluations and interpretations based on the data (see Chapter 7). This includes the failure of SEM-EDS to reproduce known recipes, use of compositional profiles to determine glazing method, possible presence of clay in the bodies, cobalt element associations, alkali selection and copper colourant source.

[1] The attribution of faience to raw material sources and workshops is beyond the purview of this thesis. Much more analytical work needs to be conducted on raw materials and faience with known site/workshop provenance before attribution can occur.

11.2 Project Results and Implications for Practice

11.2.1 HH-XRF Parameter Settings Experiment

The HH-XRF parameter testing revealed optimized settings for the analysis of faience glazes. The range of elements found in the glazes had to be measured using a setting for the identification of low Z elements, and a second for high Z elements. Settings for low Z settings (sodium to iron) are as follows:

- Voltage: 15 kV
- Current: 50 µA
- Filter: None
- Air Purge: Vacuum or helium
- Acquisition Time: 180 seconds.

Setting for general bulk analysis and detection of higher Z elements (cobalt and higher Z elements) is a follows:

- Voltage: 40 kV
- Current: 30 µA
- Filter: 3 (12 mil aluminium, 1 mil titanium, 6 mil copper)
- Air Purge: None
- Acquisition Time: 180 seconds.

These settings are similar to those recommended by Kaiser and Wright (2008) and used by others in published reports (see Chapter 3, Tables 3-3 and 3-4). These settings were devised through the testing of various HH-XRF parameters using NPA and focusing on the best compromise between measurement precision (Cv) and SNR which do not always correspond. The results of this testing show a concurrence for parameter selection among most users of HH-XRF for glass and glaze studies with differences based on the questions addressing the analysis (e.g. choosing voltage or filter based on a select group of elements).

The voltage selection for low (15 kV) and high Z elements (40 kV) is common in studies of glass (natural and man-made) and glazes. It is based on physics and any analysis that takes physics into consideration and is analysing similar elements in a matrix with similar density will have similar voltages. Of the 30 articles reviewed in Chapter 3, only 6 reported a different kV for higher Z elements (Craig et al. 2007; De Viguerie et al. 2009; Domoney 2012; Fischer and Hsieh 2017; Pappalardo et al. 2004;

Scott et al. 2012b). Four of the 5 studies were restricted based on HH-XRF type and proprietary settings (De Viguerie et al. 2009; Domoney 2012; Fischer and Hsieh 2017; Pappalardo et al. 2004; Scott et al. 2012b). Four of the 5 studies were restricted to a single voltage for low and high Z elements (Craig et al. 2007; De Viguerie et al. 2009; Fischer and Hsieh 2017; Pappalardo et al. 2004).

A review of the same literature (12 studies discounting studies restricted to a single voltage for all elements) for HH-XRF parameters used for detection of low Z elements showed a single study that deviated from 15 kV. Kato et al. (2010) used 6 kV specifically for the detection of sodium to calcium in glass.

High voltage measurement required for the detection of higher Z elements will penetrate deeper into the glaze. Elements in the faience body may be detected depending on the thinness of the glazes. The depth of an archaeological glaze is usually unknown in the field and HH-XRF analysis of glazed ceramics is generally considered bulk analysis for this reason. However, if detection does penetrate through the glaze, clay bodies will introduce more elements into the analysis than faience bodies because the elemental composition of clay is completely different than the glaze. Faience bodies and glazes are mostly composed of the same elements with silica as the greatest contributor. Silica is usually not a diagnostic element for questions regarding faience. However, inclusions in the silica will contribute to the analysis if detected. They will also contribute to the final colour of the glaze and the faience workers were aware of this and tried to minimize this in colours that were susceptible to change (e.g. blue) by possibly using filtered sand, clean sand sources or crushed flint pebbles.

Voltage determines the elements that will be detected but also affects X-ray depth of penetration. The depth of analysis indicates the depth from which all but 1% of the X-ray signal is attenuated. The depth at which a major portion of the information is retrieved is much shallower than the depth of penetration. The mean depth for the 24 measured Saqqara glazes is 444 µm with the thinnest intact non-corroded glaze at 100 µm (s17). The depth of penetration for a 15 kV incident radiation with 1% energy returned for iron is 138 µm but 90% of the information is coming from a depth of <70 µm (see Table 7-16; Fig 7-30); for sodium its ~26 µm with 90% of the information coming from a depth of <13 µm. The depth of penetration for a 40 kV incident radiation with 1% energy returned for bismuth is ~728 µm but 90% of the information is coming from a depth of <365 µm; for cobalt its ~187 µm with 90% of the information coming from a depth of <94 µm. Anomalous inclusive elements from greater depths (e.g. from within the faience body) may be detected but their contribution will be small for most

elements of interest. However, elements that are detectable to very great depths should be suspect such as tin, antimony, barium, lead and bismuth. The Lα lines for tin, antimony and barium, and Mα lines for lead and bismuth can be used but these place the peaks in a convoluted area in the spectrum where trust has to be placed into the software's capabilities for deconvolution. This is not a warning against usage but of awareness.

The presence of a gel layer (weathering represented by a loss of alkali) will reduce accuracy of sodium, potassium and silicon HH-XRF measurement results. The current project addresses this by not using sodium, potassium and silica in the post-measurement HH-XRF MVS analysis and by using data from the center of the glaze profile when possible (i.e. SEM-EDS). Adlington and Freestone (2017:1793) address this concern and suggest looking at higher Z elements whose HH-XRF signal will originate deeper in the glaze (ibid. 1795).

The optimal current based on precision and SNR for the analysis of low Z elements (sodium to iron) in faience glazes using low voltage (15 kV) is 50 µA. The optimal current for the analysis of high Z elements in faience glazes using high voltage and a 12 mil aluminium, 1 mil titanium, 6 mil copper filter (filter 3; see below) while maintaining the life of the filament[2] is 30 µA. These are a compromise between precision (C_V) and SNR. All elements show greater SNR with higher current. Precision for each specific element is found at different currents. Scott's (2012:270-272) HH-XRF evaluation on Roman glass also found this to be the case with both low and higher voltage measurements.

The studies reviewed in Chapter 3 show much more variation in current selection than it did with voltage. Initially, the selection of current is based on the capabilities of the detector in the HH-XRF unit. The current can then be adjusted for specific elements or for bulk elements as previously discussed.

The use of filter 3 with 40 kV settings is a user defined parameter selected to optimize detection of elements between iron and molybdenum while still being useful for the detection of higher Z elements. A review of the chapter 3 studies shows that most studies did not report use of a filter with higher kV measurements. This is acceptable in that lack of filter will detect all elements (depending on selection of kV) but is optimized for none. Many of the studies did use filters and of these, filter 3 was the most selected

[2] Drake and Scott (pers. com.) both suggested that the wattage used should be <4 to prolong the life of the filament. A selection of 30 µa for high voltage measurements incorporates the wattage into the assessment while maintaining at least 75% SNR peak for all elements detected.

filter for the reasons explained above (Forster and Grave 2012, 2013; Jia et al. 2010; Nazaroff et al. 2010; Whisenant 2012).

Optimal acquisition time based on greatest SNR and precision is specific for each element. Generally, higher acquisition time results in higher SNR but with diminishing returns. This study found that 180 seconds for high and low kV measurements balances good precision and SNR against time. The increased SNR and precision between 120 and 180 seconds was considered significant while the increase between 180 and 240 seconds was not.

There was a range of acquisition times used in the Chapter 3 studies. Some of these times were fixed based on the instrument and the proprietary settings used (Adlington and Freestone 2017; Domoney 2012; Fischer and Hsieh 2017; Kennedy 2013; Milhauser et al. 2011; Milic 2014) and these were usually < 120 seconds. For those that could be manipulated, most were between 180 and 300 seconds per measurement. Only Gianoncelli et al. (2006) and Giumlia-Mair and Soles (2013) had higher acquisition times (900 seconds and 600-900 seconds per measurement, respectively). They do not provide a reasoning but it was presumably to retrieve more accurate data.

Two end windows are available for the Bruker Tracer III-SD. End window selection can adversely affect the detection of lower Z elements but was never reported in the HH-XRF studies consulted for this project (well beyond those reported in Chapter 3). One of the windows contains a sturdy grid that effectively doubles the thickness of the window thereby doubling the attenuation of the lower Z element (e.g. sodium and magnesium) characteristic X-rays but still affecting all elements at low and high kV settings. The window without a grid is for HH-XRF units that have a grid installed. The HH-XRF unit used in this study has a grid installed and requires the grid-less end window. Many people at Cardiff University and the National Museum of Wales have access to the instrument used in this study. Both windows have been installed on this instrument at different times without knowledge of the effects based on a general survey of the users.

A vacuum or helium flush was used with many of the studies consulted in chapter 3. The use of a vacuum with lower kV measurements are explained above. However, most reported uses of a vacuum are associated with 40 kV settings. Gianoncelli et al. (2009) used a helium flush to enhance the silicon Kα and lead Mα lines of glazed terracotta while using a single 40 kV setting for detection of all elements. Di Viguerie et al. (2009) uses a 35 kV single setting to measure all elements of a faience pendant

including low Z elements (i.e. sodium and magnesium) with use of a helium flush. Kato et al. (2009) and Tantrakarn et al. (2009) measured early Islamic and Roman glass, respectively, using a vacuum chamber and a single 40 kV setting for all elements including sodium. Kato et al. (2010) and Liu et al. (2012) continues this methodology on Islamic and Chinese glass, respectively, but used a vacuum with both low and high kV measurements. Liu et al. (2013) used high and low kV with vacuum on Chinese glass. Scott et al. (2012a) used a single setting of 40 kV and a vacuum on replicated Roman glass to reduce the number of variables and measure all elements, including low Z elements, for increased element detection while testing various currents. Scott et al. (2012b) measured Roman glass using a single 40 kV setting with vacuum to increase detection of low Z elements. Abe et al. (2012) and Whisenant (2012) both use a vacuum but provide no reasoning behind it.

Hardware factors consisting of instrument signature and instrument drift were addressed. The instrument signature for the specific Bruker Tracer III-SD used in the analysis consisted of 17 elements (see Table 6-2). The characteristic peaks for all signature elements are significantly smaller than the rhodium lines and the Compton peak indicating negligible effect on major and minor elements found in samples. However, these do present problems when looking at trace elements as the origin of the photons (HH-XRF or analyte) is uncertain.

Subtraction of the NPA produced from the instrument signature should only be undertaken when the blank is of a similar density to the analyte. A silicon wafer of appropriate thickness (i.e. 4 mm) would suffice for faience glazes but they are expensive and difficult to produce in a laboratory. Studies consulted in Chapter 3 did not report instrument signature with one exception; Domoney (2012:122-123) identified 9 elements introduced with the HH-XRF analyser: rhodium (Raleigh and Compton scatter), gold, chromium, nickel, copper, calcium, titanium and iron. Argon was also identified but attributed to the air column in the unit. Domoney subtracted the instrument signature contribution from the final results.

The HH-XRF unit was tested for machine drift by comparing NPA and SNR of measurements taken 2 hours, 2 days and 5 months apart. There is a 4% difference for durations of 2 days or longer (i.e. 5 months). The 2-hour drift evaluation produced a 2% difference indicating the need to check the HH-XRF against a known reference material at the beginning and end of an analysis session to confirm stability the HH-XRF unit. These %-difference figures are based on NPA cps which could number into the hundreds of thousands. Conversion of the %-difference figures into wt% will result in lower wt% drift figures. These small differences are acceptable for the relatively low

voltage generation of the HH-XRF. Drift management is not commonly cited in the studies. Only 5 studies of the 30 consulted in Chapter 3 indicate drift monitoring. Craig et al. (2007, obsidian), Domoney (2012, porcelain) Fischer and Hsieh (2017, porcelain) used standards to monitor drift by measuring before and after an HH-XRF session. Domoney also took a measurement in the middle of each session. Liu (2012, 2013) reported using standards for drift detection a number of times while measuring Chinese glass beads but does not specifically mention when it was conducted during a session.

Ideally there will be no air space between an object of study and the HH-XRF window. Object surface geometry will sometime result in small air spaces introduced between the object surface and the window of the HH-XRF unit. Various distances between the HH-XRF window and the object of study were examined to determine the effect on analytical results. A distance of 0 mm is optimum but distances up to 2 mm did not significantly affect the results.

Many studies indicate that the object was placed flat on the surface of the HH-XRF to maximize X-ray photon output and detection. Domoney (2012) conducted systematic experiments of source-to-distance (0-10 mm) and found that accuracy and precision for various glass standards were consistent between 0 and 3 mm but were more varied at distances greater than 3 mm.

11.2.2 Faience Replication Experiment

Application glazed replicated faience samples were prepared using recipes cited in the literature (see Chapter 2 and 5) for use as part of the HH-XRF evaluation. Preparation of bodies was required to provide a substrate for the glaze. Several faience batches for distinct bodies were produced and fired during the project but only one batch appeared similar to the archaeological material, was durable and did not fail upon minor stress and/or through time. This body was chosen for use as the substrate in a fired and unfired state for all reproduced glazes.

A glassy glaze was produced by prefritting and firing on both fired and unfired bodies. Raw material glazes (not fritted) failed to produce an enveloping glassy glaze. Glaze batch material was applied through immersion, painting and application of dry materials. Glazes with less porosity, less erupting bubbles and greater silica particle melt with complete coverage of the substrate were achieved by applying a prefritted glazing powder to the surface of the substrate through brush painting and firing to ~900 °C coupled with a 1-3+ hour kiln soak time. Immersing an unfired body into the glaze slurry often resulted in distorted bodies. Fired bodies could emerge with a glaze

layer that was too thick resulting in more bubbles when fired, or too thin resulting in glaze creep. These effects can also be a product of glaze slurry preparation (e.g. particles too large to remain suspended).

The final colour of the glaze can be affected by firing parameters (i.e. temperature ramp up, soaking time and temperature) and the type of body substrate (i.e. bisque or unfired). Longer firings and firings with quicker temperature ramp ups tended to produce a blue glaze with a slight greenish hue only visible under the microscope. Vandiver (2008:44) states that increase potassium in a glaze will result in a greener hue. It is possible that potassium may migrate from the body to the glaze with longer soak periods. However, reasons why faster temperature increase rates or low soak temperatures (with increased soak time) would result in a greener hue is unknown. Potassium in unfired bodies would be more free (not locked due to reaction) to migrate into the glaze to produce a green hue but these combinations result in a deeper blue hue, not green.

The faience replications are aesthetically and chemically similar but microstructurally different from the faience from antiquity. Generally, the archaeological material revealed thinner and less porous glazes. The silica particles in the body were smaller on average but had a greater range in size than the particles in the replicated bodies. Despite these differences, the glazes produced through replication are aesthetically similar and carry a similar weight (Pers. Com. Paul Nicholson and Anna Hodgkinson) to the archaeological material.

There were some surprises with the replication experiment. The application of glazing material is exothermic. The heat is a result of combining water with sodium carbonate which releases energy. The heat was not high enough to burn the skin but was definitely felt through nitrile gloves.

The size of the silica particles was relatively homogenous. A series of screen sieves with mesh sizes down to 180 µm were used for crushing silica sand. While the average size of the silica particles was lower than this, the size range and particle morphology were relatively similar when compared to the Saqqara material (see Chapter 7).

Fractionation and generation of CO_2 off-gassing was incomplete and lower than expected for the replicated materials (see Chapter 7). The result was the increased porosity of the replicated glazes compared to the Saqqara glazes. Longer and higher temperature kiln soak periods would increase the chemical reaction rate resulting in greater CO_2 generation, and the expulsion (i.e. rising bubbles) of the CO_2 from the glaze due to lower viscosity glaze melt.

A comparison of replicated glaze qualitative results with those in the literature proved difficult. A description of the qualitative characteristics (e.g. texture, sheen, presence of pores/bubbles) for fired glazes were not provided for many of the faience glaze replication studies. The focus was not on producing a glaze that had similar qualities as those from antiquity but instead to examine the microstructures (Tite and Bimson 1986; Vandiver 1998), composition (Binns et al. 1932; Griffin 2002; Kiefer and Allibert 1971; Vandiver 1998) and firing conditions (Eccelston 2008) associated with the replications which were produced in a similar fashion to those of antiquity. A direct comparison cannot be conducted with the replicated faience produced for this project but implications can be drawn from the figures and stated results in the literature.

Eccleston's (2008:35) replicated faience application glazing to show that small quantities of faience could be fired in typical bread ovens found in the houses at Amarna, Egypt. The replicated faience consisted of a clear glaze with copper colourant applied on top. The glaze mixture covered the bodies which in part contained 10 wt% ball clay and 5 wt% resin to facilitate formation. The oven peak soak was at ~800ºC for 1 hour. Four of the six replicates produced a blue glaze. The two that did not differed on two counts, they contained gum arabic produced on-site (by boiling acacia tree resin) and the applied colourant was composed of local bronze shavings.

Eccleston does not provide an in-depth description of the fired glazes but the photographs provided in the article (p.35) show glazes that look similar in texture to the raw glaze on a fired body in Fig. 5-7 of this report. Additionally, two of the successful Eccleston glazes share a similar colour to the same glazes in Fig. 5-7 while the other two are more similar in colour to the cobalt coloured glazes. There was a series of early failures during the current project where glazes produced a darker cobalt-like blue colour at a temperature of 800ºC with soak times of 1 and 3 hours, but a 3 hour soak at 950ºC produced the typical copper blue colour expected in copper blue faience (although texture for the glazes were rough and lacked glassiness). None of the glazes produced by Eccleston appear (in the photograph at least) smooth textured and glassy. This was also found in the current project where the glaze mixture was applied too thickly or in a raw unfired state (versus a prefritted glaze). A thicker glaze mixture can produce more CO_2 off-gassing which results in porous glazes with erupting surface bubbles unless the soak time and/or temperature is increased; this is true for both raw unfired and prefritted glazes.

Eccleston's failed glazes contained bronze scrap produced on-site and applied to the surface of the clear glaze prior to firing. Bronze powder remains from cutting bronze metal did produce a copper blue colour in some of the early replicated glazes

concocted for the current project. Bronze scrap, in general, should have produced some shade of blue indicating a glaze formation problem inherent in the recipe (e.g. resin combustion, elevated CO_2 off-gassing?).

It is hard to tell why the two Eccleston glazes failed to produce a glaze of any sort. All of the bodies contained clay and resin but only the failed glazes contained resin produced on-site during the Amarna project. Perhaps the resin was not refined to a required degree or too much was added and off-gassing and/or resin combustion interfered with the glaze formation processes.

Griffin (2003) replicated application glazed faience as a part of a larger project to characterize the faience collection at the Cleveland Museum of Art. Griffin tested faience body composition by including either ground sand, ground flint or a 1:1 combination. The various bodies also contained 0-18 wt% ball clay and 1-10 wt% lime in addition to silica, sodium and a colourant. All firings were at 915-923ºC for 8 hours.

Griffin describes how the variables affected the working properties of the faience replicated bodies but does not describe the resulting glazes. A photograph is provided (in black and white) but it represents efflorescent glazing technique. The glaze on one set of objects (moulded cats) appear to show a sheen possibly indicating a glassy glaze. The other pictured glazes resemble the raw glaze on a fired body in Fig. 5-7 of this report.

Griffin (ibid., p.333) reports that an increase in calcium translates into an increase in the strength of the dried unfired faience body enabling carving and filing. The calcium content of the glazes produced for the current project ranged between ~5 wt% and 7.5 wt%. There was no difference noted in the strength of the bodies but both could potentially be worked after drying.

Lucas and Harris (1962:175) suggested that clay may have been introduced to the faience body to facilitate body formation. Griffin (ibid., p.335) states that a faience body dries too quickly to produce detailed mouldings and that the addition of clay (≤6 wt%) provides a slower drying and malleable material capable of taking on moulding details. Clay was not used in the replications for the current project and the archaeological faience sherds revealed no clay in the bodies with the possible exception of one (s81) that appear to have a single 90 x 50 µm inclusion that showed high SEM-EDS peaks for aluminium and magnesium (see Fig. 7-36) but this is certainly not enough to impart any malleable properties to the prefired faience body.

There were similar results to Binns et al. (1932:272) when adding clay to a glaze. Binns et al. added ~3 wt% clay to an application glaze resulting in an ‘enriched’ colour.

Clay (~6 wt%) was added to a copper glaze in the current project which resulted in a Prussian blue colour (see GLZ04 in Fig. 5-5). While the colour was certainly enriched, it resembled a crayon more than a glaze. The material also slowly effloresced salts for months after production.

Griffin (ibid., p.328) found that an increase in alkali results in an increase in the IAL if using the same kiln soak temperature and time. An increase in alkali will lower the melting point of the silica producing a less viscous melt at the consistent kiln temperature used by Griffin. Similar changes in IAL thickness were also achieved in replications produced for this report by increasing the soak peak temperature and/or time to produce the same results at a consistent alkali wt%.

Application of a raw material slurry failed to produce a glassy glaze while application of prefritted material slurry resulted in a relatively thick glassy glaze layer in the current project. Tite and Bimson (1986) had similar results. SEM-BSE analysis of the replicated faience prefritted glaze profiles revealed glaze layers approximately 100 µm thicker than Tite and Bimson's glazes with a similar discrepancy in the IAL (see Table 7-5). These differences may be explained by application of a thicker glaze slurry on the body by the maker confirming Vandiver's (1998) findings that glaze characteristics are influenced by the way the glaze was applied and how the samples were processed. The IAL increased thickness may be the result of particle size which is approximately twice as big as the silica particles in Tite and Bimson's replicated faience bodies (see Fig. 7-8). A survey of silica particle sizes in the archaeological faience sherds from Saqqara (~70 µm) do reveal that they are smaller than the particles in the replicated faience sherds (~105 µm), but are larger on average than those examined by Tite and Bimson (~50 µm).

The replicated application glazes from these projects as well as the current project show that prefritted glazes more often than not produced a glassy glaze where raw material glazes did not. The off-gassing of CO_2 and other gases interfere with the glaze formation process. Some of the off-gassing has already occurred in prefritted glaze material allowing the glaze forming processes to occur. This has been shown in this project by the firing of faience glazes using the same composition and firing parameters of samples where the only difference was the state of the glazing material (raw and prefritted). Changes in other variables (i.e. kiln soak time and temperature) confirmed the findings of Vandiver (1998) and affected glaze porosity and the thickness of glaze and the IAL.

Changes in future replication studies might include the use of smaller particle size in the body and glaze as this will affect the amount of unreacted quartz in the glaze, the thickness of the IAL and the ability of the unfired body to take on greater decorative details. The use of crushed flint, as used by Griffin (2002) and Tite and Bimson (1986) is one possibility but the use of quartz pebbles as a firing bed (Eccelston 2008) for the faience will also allow them to be reduced to powder with minimal force. This is less strenuous than grinding sand. The resulting powder can be mixed with the other recipe ingredients to form the body and glaze batches.

Finally, reduction of carbonates introduced to the batches will reduce the amount of CO_2 off-gassing resulting in less porous glazes. The alkali salt component is potentially the largest contributor of carbonates in replicated faience. Use of sodium oxide or pre-firing sodium carbonate to ~800ºC (melting point: 851ºC) to release CO_2 may reduce the porosity and increase the melt of the glaze material.

11.2.3 Multivariate Statistics: Data Preparation and Faience Analysis

MVS was used to determine the outcome of NPA analysis of the replicated and archaeological faience samples. There is no system in place for the use of MVS in cultural heritage. Data preparation methods including selection of variables, data transformation methods and zero replacement strategies had to be evaluated to provide optimum statistical analysis of the SEM-EDS and HH-XRF analytical results. The faience replications were used for this evaluation and MVS data preparation was judged on how well it discerned the 3 replicate batches. Generally variables (i.e. elements/oxides) with a C_v <10 were selected for inclusion in the analyses but justifications were made for variables considered important while exhibiting a C_v >10. Choice in the C_v cut-off is based on user discretion with the caveat that higher C_v will result in lower accuracy and precision of the final MVS results.

Determination of outliers was conducted by comparing the results of boxplots, HCA (single linkage) and PCA. All can individually be interpreted incorrectly (e.g. boxplots indicating tailed data as outliers) showing a need for the redundant system (i.e. use of all three techniques). This major step which occurs early in data preparation will also show data transcription errors that may otherwise be unnoticed with subsequent MVS analysis.

Data transformations rescale the data for use in MVS. There are several transformation algorithms available for use but the study focused on the two most popular within cultural heritage, Centered logratios (CLR), standardizations and a combination of the two. Baxter (2016:55) and Drennan (2009:310) state that CLR and

standardizations should both be conducted to determine if either provides relevant information therefore requiring an evaluation of the techniques with the current project data.

Centered logratios worked well with the HH-XRF data by exaggerating the variance resulting in well-defined batch clusters. Centered logratios failed to work well with the SEM-EDS data and known faience replicate clusters were not represented in the results. However, standardization of the data did produce the known clusters with the SEM-EDS results.

The findings regarding CLR, standardization and a combination of the two contradict Baxter (1992; 2016:31) who writes that data transformation rarely is better than typical standardization methods. Baxter and Freestone (2006) found that logratio transformations tend to lose data structure relationships because of inclusion of elements (i.e. unintentional inclusions) not associated with the main glass and data structure. Beardah et al. (2003) found that PCA of logratios emphasized variables with high relative variation which obscured glass compositional relationships but that standardized data did interpret a known data structure.

The findings of this report indicate that standardization and CLR produce the same clustering but CLR slightly exaggerates the divisions making the clusters more clear on biplots and three-dimensional PCA scores plots. Standardization not involving logratios generally exhibits relationships between variables that are reflective of the original glaze recipes as concluded by Baxter and Freestone (2006). The use of standardization with the HH-XRF data may reveal results that reflect the glass and glaze recipes but these results make more sense when using wt% totals. This project is concerned with clustering the various samples based on element ratios using NPA and not wt%. In this sense, the recipe of the glaze is less important than the ability to discern clusters based on the element ratios.

Replicated faience glazes were analysed to evaluate HH-XRF prior to the analysis of a small archaeological sample set from Saqqara. HH-XRF analytical results of the faience replications reveal the capability of HH-XRF to discern the three glaze batches through the use of MVS (see Chapter 9). The copper coloured glaze batch was composed of the minimal number of oxides required to produce a glaze (i.e. silicon, sodium, potassium, copper and calcium). The two cobalt coloured glazes added to that other elements at minor and trace levels with small trace level differences between the batches (see Tables 5-1 and 5-2).

All the archaeological faience sherds were recovered from disturbed contexts at Saqqara and have been attributed to the Late 30th Dynasty (Late Period) and early Ptolemaic Period (Dayton 1981:135-136). The MVS results identify 5 groups with additional subgroups current case study (see Chapter 10). Most groups are defined by the colourant with manganese defining Group 1 (purple glazes), cobalt defining Group 2 (ultra-marine blue), lead antimonate defining Group 3 (yellow and green glazes) with the yellow glaze (s45) subdivided based on absence of copper, and copper defining Group 4 (blue). Group 5 is defined by a single sherd (s17) which represents an anomaly in the dataset by having the highest concentration of potassium, titanium, copper, zinc and nickel of the sherds. Additionally, the sherd has the thinnest uniform glaze and the smallest and most uniform average particle size (29 µm). The subgroups are defined by small variations in the major groups.

Three MVS clustering methods (HCA, K-means and PCA) provided useful information. MVS in the form of HCA (Ward's method) and K-means analysis proved invaluable for categorizing the samples based on chemical characteristics. PCA was useful in categorizing but more importantly revealing the relationships between the variables and in identifying elements defining established categories. Outliers were determined through boxplots, HCA (single linkage method) and PCA biplots. Outliers were retained or removed from further analysis based on justification in each specific case. All three methods were used because they provide different information and facilitate a system of results confirmation.

11.2.4 Other Findings

The HH-XRF and SEM (EDS and BSE) analysis facilitated the examination of various glaze technologies based on visual examination of back-scattered electron images, element presence/absence and ratios of examined replicate and archaeological glaze samples. While these questions were not the direct area of investigation, the opportunity was there to test on the glaze samples.

The analysis indicated that SEM-EDS (wt%) failed to accurately reproduce recipes[3] used for the replicate glaze batches based on analysis of 3 measurements taken from the glaze in a glaze/body profile (see Tables 7-17 and 7-18). Greatest accuracy was recorded for oxides in greatest abundance and for lead oxide but most other oxides were underrepresented while the oxides of copper and sodium are greatly

[3] The inability of SEM-EDS to reproduce known recipes has no bearing on its capability to accurately record presence/absence and wt% of elements identified in a sample. Changes occurred (i.e. fractionation) to the raw materials of the replicated faience glazes during firing and prior to SEM-EDS measurements.

overestimated. Changes (e.g. firing and fractionation) made to the glaze batches after mixing but before analysis account for the discrepancies.

Compositional profiles of oxides in the replicate and archaeological glazes exhibited results consistent with application glazing (see Chapter 7) in that there is no inward or outward migration of elements/oxides such a sodium and copper. These results meet expectations for the Saqqara material which consists of vessels. Application glazing would be expected to be used on such items with cementation reserved for small items like beads (Vandiver 1983:A35) and efflorescence best used on items that need complete contoured coverage but not exceeding 20-30 cm in size (Vandiver 2008:54).

Evidence for clay introduced into the archaeological faience body to facilitate formation of bodies (e.g. throwing on wheel, hand-forming) is non-existent. However, a small particle of what is probably clay based on aluminium and magnesium peaks was found in a single Saqqara sherd (s81) SEM-BSE image (see Fig. 7-36).

Cobalt element associations with other elements indicate Late Period or later sourcing for cobalt ores. Analysis of four cobalt coloured glazes (s70, s72, s74 and s78) reveal a relatively high iron content (1.71 - 4.22 wt%; see Table 7-16) that is similar to the range provided by Kaczmarczyk and Vandiver (2008:75) for cobalt ore used during the Late Period and after. Additionally, there is no relationships with aluminium, magnesium and manganese ruling out the cobalt ore source used prior to the Late Period.

The choice is alkali source (i.e. natron or plant ash) can be determined by examining the Na_2O/K_2O ratios where a ratio of ~2-6 indicates plant ash and >10 indicates natron (Kaczmarczyk and Vandiver 2008:66-67, 71; Shortland and Tite 2005:35). Natron has been indicated as the source for the alkali component for most of the Saqqara sherd glazes based on Na_2O/K_2O ratios of >10. This coincides with natron as the preferred alkali used during the Late through Roman Periods (Freestone 1991:40; Kaczmarczyk and Hedges 1983:280; Kaczmarczyk and Vandiver 2008:67). The sherd glazes that showed ratios <10 also revealed highly weathered glaze profiles upon SEM-BSE examination where the alkali component, and especially sodium, was most likely leached from these glazes.

Kaczmarczyk and Hedges (1983:280) suggest that Memphis faience workers may have preferred retaining the use of plant ash for the alkali component of their faience based on 1.6 wt% potassium levels. This would be interesting because it would indicate that the Saqqara material examined did not originate in Memphis, the closest major faience production workshop. Subsequent work by Shortland and Tite indicate

Na_2O/K_2O ratios of ~35 which does indicate natron contrary to Kaczmarczyk and Hedges (1983:280) suggest of plant ash. Additionally, Lilyquist and Brill (1993:56, Fig. 51) found plant ash use as an alkali is evinced by MgO and K_2O levels >2 wt% while natron is represented by <1.5%. Kaczmarczyk and Vandiver's tables 4.1a-e (2008:66-67) exhibit Memphis faience vessels containing ~0.5 wt% K_2O and ~1 wt% MgO suggesting use of natron at Memphis. Previous periods represented on the same table exhibit much greater K_2O and mixed MgO indicating plant ash.

SEM-EDS was used to determine if the tin/copper ratio in the archaeological glazes corresponded to the 4% to 10% tin used in contemporary bronze produced in Egypt after the New Kingdom Period (Kaczmarczyk and Hedges 1983: 83; Kaczmarczyk and Vandiver 2008: 74). The findings reveal that most of the blue glazes have a ratio between 0.04 and 0.15 (4% and 15%) indicating that contemporary bronze is likely the source of the copper colourant.

Lead antimonate is the colourant used for green glazes during the Late through Roman Periods, usually at a ratio of 5+:1 lead:antimony (Molina et al. 2014: 172). Testing to determine if lead antimonate was intentionally added to green faience glazes by examining the lead/antimony ratio will help to determine true green glazes from weathered blue glazes. This is a useful test in cases where there is uncertainty in the colourant used or when there is a possibility that weathering has transformed a copper blue glaze into green glaze. There is one bluish-green glaze (s12) that was first identified as a blue glaze. SEM-EDS, MVS and the lead-antimonate testing strongly indicate that it is a green glaze that contains more lead and less antimony than the other two green glazes in the study. Sherd s12 shared the high lead and low strontium/tin content as did the other green glazes in the 40 kV HH-XRF measurements. High aluminium content was a variable shared with the green glazes in the low voltage (15 kV) measurements. The use of the lead/antimony ratio with HH-XRF NPA results is a qualitative assessment of the NPA cps due to differing depths of detection for antimony and lead. The depth detection difference is small but it negates semi-quantitative HH-XRF analysis calculations.

The low (15 kV) and high (40 kV) voltage settings generally discerned the three replicated glaze batches using MVS analysis. Analysis of the Saqqara materials showed that the two voltages complimented one another with no contradictions in results. Low and high voltage settings, which detect different element groups, are combined to obtain as much information as possible from the analytes.

The low voltage measurements of the glaze can be regarded as glaze analysis because the theoretical depths of analysis will not penetrate into the body for most intact archaeological glazes (> 100 µm glaze thickness). They will, however, be susceptible to inaccuracies due to weathered glaze surfaces and the resultant alkali depletion. This can be reduced by removing the weathered surfaces but this is not highly favoured because it negates the non-destructive benefits of HH-XRF analysis.

The high voltage measurements of the glaze should be interpreted as bulk analysis. There is the possibility that elements in the body will be detected, especially with elements like tin and antimony, but most of the data will originate from the glaze including the data for tin and antimony.

11.3 Project Limitations

Scott (2012a) conducted extensive testing of HH-XRF using a set voltage (40 kV) and various currents and acquisition times for specific elements (aluminium, silicon, potassium, calcium, titantium, chromium, manganese, iron, nickel, copper, rhobidium, strontium and zirconium). The result showed the optimal current and acquisition times for each selected element at 40 kV. The current project could have examined the current and acquisition time to the same level but doing so with all expected elements at 10 measurements per element per variable would have extended the length of the final thesis beyond the word limit. Scott conducted the testing using a single measurement per variable change (see section 3.6.2 for Scott's results).

The body particles are all generally the same diameter and rather homogenous. It would be better to work with a combination of this size and smaller which will result in a better body (e.g. stronger and able to take better forms) for the faience glaze. The blue glazes were generally fine although could be improved with more experimentation on kiln control or through general experience over time. The cobalt blue glazes are more porous and could be bettered by more refined recipe with possibly less carbonates which result in the formation of CO_2 and pores within the glaze. Also, the bodies and the glazes are viscous within the kiln and do not tend to flow easily. Great care must be taken to reach the proper body shape and glaze thickness and not rely on the melt becoming less viscous during the firing.

Faience replication analysis worked well and little improvement can be made beyond the limitations covered on the production of the replicate material which could result in flatter surfaces and less porous glazes. These two improvements would results in less attenuation of the lighter Z elements. Production of up to two more glaze batches would be interesting from an MVS clustering perspective and further show the

capability of HH-XRF to discern between production batches and their resultant glazes. The replicate glazes do differ from the archaeological glazes in that there is little to no weathering nor surface detritus on the replicate glazes. The replicate glazes did show the capacity of HH-XRF to discern between the batches but archaeological glazes were required to show its capabilities in the field.

The analysis of the archaeological glazes worked well. The testing would have benefited from analysis of more archaeological samples. Linear discriminant analysis could have been employed with the cases numbering at 100+. Linear discriminant analysis is a better clustering tool than PCA, HCA and K-means analysis but requires larger ratio of cases to variables. In this way, MVS usage could have been improved as well.

11.4 Conclusion

The HH-XRF is capable of differentiating between the three replicated glaze batches using MVS cluster analysis of NPA results. The optimal HH-XRF parameter settings for faience glaze analysis, based on an evaluations of each setting using Corning Glass B as the analyte, are similar to those suggested by Kaiser and Wright (2008) for the Bruker Tracer III-SD and to those used by others in the analysis of glass and glazes. Low voltage setting (15 kV) detections are restricted to the glaze but may be affected by potential weathering and the loss of sodium in the glaze. High voltage setting (40 kV) detections are mostly restricted to the glaze but can extend into the faience body substrate depending on thickness of the glaze and the element of interest. The use of the 12 mil aluminium, 1 mil titanium, 6 mil copper filter (filter 3) was used to optimize analysis of the spectral region containing rubidium, strontium, zirconium, niobium and yttrium as these have been diagnostic elements in glass analysis. Researchers have the option of using no filter (good for detecting all elements but optimized for none) but selection of other filters should be justified.

The project expanded to include the HH-XRF analysis of 24 archaeological faience sherds from Saqqara. The analysis revealed 5 groups (2 with subgroups) differentiated by colour but based mostly on non-colourant elements. Group 5 is anomalous in that it contains a single copper coloured glazed sherd (s17) that has revealed compositional extremes relative to the sample set and microstructurally exhibits the smallest body particle size and the thinnest of the intact glazes.

Archaeological faience glazes excavated and analysed in the field have too many unknowns (glaze thickness, glaze weathering) for the measurement results to be completely trusted. While most fieldwork measurement results can be accepted, those

sherds/glazes that are anomalous to the sample set should be regarded with caution as the results may have been affected by weathering, surface deposits or detection of unintentional inclusions in the body. Glazes that have clustered due to MVS cluster analysis have shared compositional characteristics and it is most unlikely, although possible, that glazes affected by weathering or other unknowns will cluster. These are more likely to be classified as statistical outliers. Glaze surfaces can be cleaned with ethanol to help mitigate some of the issues (i.e. surface deposits). Field and laboratory NPA measurements are not comparable with results in the literature unless both datasets are treated to MVS cluster analysis. The clusters will be the same regardless if using wt% or NPA.

The replicated faience glazes produced as part of the HH-XRF evaluation are similar in colour and surface texture to the archaeological material. However, SEM-BSE revealed differences including homogenous and relatively large silica particle size in the body and greater porosity of the glazes. Microstructural glaze characteristics are affected by firing parameters and how the maker applied the glaze to the body (e.g. thick versus thin application).

Chapter 12: Conclusion

12.1 General Review of the Project

An evaluation of HH-XRF NPA was performed to determine if it was a useful technique for the analysis of faience glazes by field archaeologists and museum specialists. The project addressed Egyptian faience, what it is and how it was produced. Published literature on faience was investigated to provide greater insight into the raw materials used in its production and the elements to expect in its analysis. The principles and technology of HH-XRF were described, the benefits and limitations were addressed and case studies were provided involving the use of HH-XRF on vitreous materials. This information was used to formulate a methodology for determining the optimal HH-XRF parameters for the analysis of faience glazes. Replicated faience bodies and glazes were analysed using HH-XRF NPA. Multivariate statistics of the NPA results showed the capability of HH-XRF analysis to cluster the replicated samples based on known composition. The analytical procedure was used for the analysis of a small set of faience sherds from Saqqara which resulted in 5 glaze groups.

12.2 Research Questions Answered

The research study was composed of mixed methods including HH-XRF parameter evaluations, experimental archaeology, evaluation of MVS strategies and MVS practice. The objectives (indicated by •) and results are as follows:

- An assessment of HH-XRF analytical parameters using Corning Glass B as the analyte to determine an appropriate setup for the analysis of faience glazes using NPA.

Each of the parameters for HH-XRF were tested using Corning Glass B as the analyte. Best results are defined as a compromise between highest precision (C_v) and SNR. The results of the testing indicating the optimal HH-XRF parameters for use with faience glazes are similar to those suggested by Kaiser and Wright (2008) and used by others in the analysis of glass and glazes.

- The production of suitable faience replicates resembling Late through Roman Period blue monochrome faience for use with the HH-XRF evaluation.

Replicated glazes were produced using data from previous replication studies. The use of prefritted glazes resulted in glassy smooth textured glazes with colours resembling those of the archaeological material. The microstructure of the replicated material was slightly different than the archaeological material mainly in the size of the homogenized body silica particles and the porosity of the glazes.

- An assessment of the effect of replicate faience glaze characteristics (e.g. colourants and glaze thickness) on HH-XRF analysis of faience.

Qualitative analysis of HH-XRF spectra could readily discern between the two colourants (i.e. copper (blue), cobalt (dark blue)) used in the production of the replicate glazes. Semi-quantitative HH-XRF analysis (NPA) and MVS successfully clustered the batches into known groups even with the colourant excluded. Theoretical depths of detection (based on glaze thickness, glaze density and the physical characteristics of the elements of interest) indicated that the HH-XRF would not detect elements within the replicated faience bodies. In practical sessions the HH-XRF did not detect marker elements within the bodies confirming this.

- A comparison of HH-XRF and SEM-EDS analysis of applied faience glaze replicates and archaeological material.

The HH-XRF clusters produced through MVS were confirmed by similar analysis with SEM-EDS. The HH-XRF has a lower level of detection and the individual measurement points in the MVS clusters were more compact compared to their SEM-EDS counterparts.

- Determination of appropriate MVS parameters (e.g. outlier identifications, data transformations) for cluster analysis.

An evaluation of different MVS data transformations, zero replacement strategies and outlier identifications were performed on the replicated faience glaze analysis prior to the analysis on the archaeological material. Slightly different strategies had to be used for the SEM-EDS (wt%) data because it was confined to simplex space and HH-XRF (NPA) data that was in Euclidean space. Similar clusters were produced for both sets of data through PCA, HCA (Ward's Method) and K-means analysis despite the different strategies.

- Minor and trace element analysis of archaeological faience glazes to determine if groupings can be isolated.

MVS analysis using HH-XRF and SEM-EDS results indicated the Saqqara material was composed of sherds that could be placed into 5 categories differentiated by colour

but based on analysis mostly without colourants. Sub-groups were also defined for two of the main groups. Group 5 was composed of a single sherd (s17) which revealed extremes in element/oxide components relative to the sample set. Microstructural examination with SEM-BSE also revealed the smallest average silica particle size in the body and the thinnest intact glaze of the dataset.

12.3 Research Contribution

Net peak area HH-XRF analysis is a valid technique for examining faience glazes. Low voltage (15 kV – glaze analysis) and high voltage (40 kV – bulk analysis) measurements in combination with other parameters (e.g. time of acquisition, distance from object) complimented each other in obtaining as much information as feasible from replicated and archaeological faience glazes. Selection of elements that are archaeologically relevant, show relative precision across many measurements and are not considered outliers are paramount in data preparation for subsequent MVS analysis.

The Tracer III-SD parameter settings suggested by Kaiser and Wright (2008) and used by many for the analysis of glazes and glass were confirmed by the HH-XRF evaluation conducted during the study and covered in this report. The intention was not to confirm/deny but to conduct an evaluation to determine the optimum settings for the NPA analysis of faience glazes which resulted in similar parameters to Kaiser and Wright's initial setting recommendations.

Replicated faience bodies and glazes were produced for use in the HH-XRF evaluation. The results were similar to Tite and Bimson's (1986) where raw glazing (i.e. not prefritted) of bodies failed to produce glazes whereas prefritted glazing material resulted in glassy glazes. Fractionation of carbonates during firing results in CO_2 off-gassing which interferes with the glaze process. Sodium carbonate is the biggest contributor to off-gassing during firing.

Redundancy and the use of various MVS techniques (i.e. PCA, HCA, boxplots and k-means analysis) help to confirm outliers and faience glaze clusters. HCA (Ward's method) and K-means analysis are two different forms of cluster analysis that group the faience samples based on chemical characteristics. PCA is used for clustering but is also useful for revealing the relationships between the variables and in identifying cluster defining elements. Data preparation is dependent on the type of data being used (i.e. data in the simplex (wt%) or data in Euclidean space (NPA)). This information is not always conveyed in the archaeological literature but should be if the results are to be trusted.

12.4 Research Implications

Archaeological laboratory and field work in Egypt will benefit from the HH-XRF evaluation of blue faience glazes. Egypt has enforced a ban on the export of archaeological materials (Law 117:2010) and transportation of radiological sources for instrumental analysis is highly regulated (Radioactive Substances Act 1993; Ionizing Radiation Regulations 1999). The use of HH-XRF offers a solution that is not as constricted by regulation due to the X-ray tube which allows cessation of radiation emission by removal the power source (essentially by turning it off). Using the information presented in this report for HH-XRF analysis of faience glazes will facilitate decision-making processes in the field through immediate qualitative results and production of semi-quantitative results soon after measurements have been taken. Semi-quantitative results combined with MVS cluster analysis will form statistical faience groupings based on element composition that could relate to raw material source sites and/or faience workshop associations.

The scope of work for the project was conducted using tools accessible to the field archaeologist. The HH-XRF signature was determined using a filled water bottle as a blank per the suggestion of Lee Drake (pers. Com.) but verified using a pressed cellulose tablet. The MVS analysis was conducted using an open source software (R) freely available on the internet using libraries that are produced by statisticians and are rigidly controlled and the HH-XRF analysis was conducted using NPA which negated the use of glass standards, the number of which required is cost prohibitive for many.

12.5 Future Work

As early as 1912 (Burton 1912, cited in Lucas and Harris 1962:175), faience replication studies have entertained the addition of a binder for faience forming purposes. The body of literature has consistently returned to the hypothesis that clay or resin was intentionally added to the faience paste as a binder to facilitate forming (Vandiver 1983:A125) even though resin as a binder was discounted by Lucas (1933, cited in Aspinall et al. 1972:27) due to the lack of resin combustion carbon, and the evidence of the clay addition has not been proven, neither through elemental analysis (Kaczmarczyk and Hedges 1983:198) nor through observation (Nenna and Nicholson 2013:135). The suggested use of binders is particularly mentioned in association with increased Hellenization during the Late and Ptolemaic Periods and is associated with the possible use of the wheel (Kaczmarczyk and Vandiver 2008:60).

Further replication studies involving the systematic addition of a clay or resin binder coupled with elemental analysis and backscattered imagery may provide either a

positive or negative conclusion to the clay/resin binder hypothesis. Elevated levels of alumina and magnesia, when compared to typical Egyptian sands, could indicate the use of clay as a binder in faience bodies. SEM-BSE should show clay particles as they will have remained in the body after firing. Pores in association with carbonaceous material in the faience fabric could indicate use of a resin binder that subsequently burnt out during firing. These two materials could be compared to the systematic addition of calcium (1-10 wt%) suggested by Griffin 2002:332 and even natron suggested as a binder by Lucas (1933, cited in Aspinall et al. 1972:27).

This study is a proof of concept and illustrates that HH-XRF is capable of discerning replicated and archaeological glaze groups using NPA analysis. The archaeological case study was composed of a small assemblage of 24 archaeological faience glazed sherds from Saqqara. While the number of samples was adequate to exhibit a distinction of glaze groups based on elemental compositions, the survey population is too small for the analytical results to represent a general clustering tendency in faience. A larger sample population would facilitate this and allow the use of other MVS techniques to extract related information among samples and produce better defined clusters. Increasing the number of sherds to 100+ allows clearer groupings (if they exist) of glazes based on compositional analysis and enables the use of Mahalanobis distances (sample/variable ratio of 3 to 5 (Baxter and Jackson 2001:254)) and statistical analysis using linear discriminant analysis (LDA) which would be a useful addition to the other forms of MVS being used. In this study, PCA produced clusters that were diffused and indistinct in some cases possibly due to small sample size. LDA produces plots similar to PCA but the predictive methods provide a clearer distinction for existing groups in the data (Baxter 2016: 79-80). LDA is a better method than K-means analysis which requires the user to define the number of clusters before calculations are applied. The use should be aware that LDA will emphasize trace elements over the major and minor glass/glaze structural elements (ibid., pp.98-99). This is works well for trace element analysis but LDA may provide misleading results if the elements in question carry no archaeological significance.

I would suggest the HH-XRF analysis of 100+ monochromatic blue glazes from a variety of known workshops combined with samples of unknown origin and recently excavated material. Combining LDA, PCA, HCA and K-means with HH-XRF NPA results for archaeological faience glazes associated with known workshops would help to define workshop signatures based on elemental composition of the glazes while the unknown and recently excavated material could potentially be associated with a known workshop. This represents a step in establishing provenance based analysis of

faience. The final step is the analysis of raw materials from sources known to have been used in antiquity.

References

1993. Radioactive Substances Act 1993. In: https://www.legislation.gov.uk/ukpga/1993/12/contents ed. (Accessed on 18 July 2018).

1999. The Ionising Radiations Regulations 1999. In: http://www.legislation.gov.uk/uksi/1999/3232/introduction/made ed. (Accessed on 18 July 2018).

2010. Law 117 of 1983 as Amended by Law No. 3 of 2010 Promulgating the Antiquities' Protection Law In EGY OG of Febrary 14, 2010. Egypt: Ministry of Culture Supreme Council of Antiquities.

Abe, Y. and Harimoto, R. and Kikugawa, T. and Yazawa, K. and Nishisaka, A. and Kawai, N. and Yoshimura, S. and Nakai, I. 2012. Transition in the use of cobalt-blue colorant in the New Kingdom of Egypt. *Journal of Archaeological Science* 39(6), pp. 1793-1808.

ACS, C. o. E. I. 1980. Guidelines for Data Aquisition and Data Quality Evaluation in Environmental Chemistry. *Analytical Chemistry* 52, pp. 2242-2249.

Adlington, L. and Freestone, I. 2017. Using Handheld pXRF to Study Medieval Stained Glass: A Methodology Using Trace Elements. *Materials Issues in Art and Archaeology XI* 2(33-34), pp. 1785-1800.

Aitchison, J. 1982. The Analysis of Compositional Data. *Journal of the Royal Statistical Society, Series B (Methodological)* 44(2), pp. 139-177.

Aitchison, J. 1986. *The Statistical Analysis of Compositional Data*. London: Chapman and Hall.

Aitchison, J. and Barcelo-Vidal, C. and Pawlowsky-Glahn, V. 2002. Some Comments on Compositional Data Analysis in Archaeometry, in Particular the Fallacies in Tangri and Wright's Dismissal of Logratio Analysis. *Archaeometry* 44, pp. 295-304.

Aspinall, A. and Warren, S. E. and Crummet, J. G. and Newton, R. G. 1972. Neutron Activation Analysis of Faience Beads. *Archaeometry* 14(1), pp. 27-40.

Bandalos, D. L. and Boehm-Kaufman, M. R. 2008. Four Common Misconceptions in Exploratory Factor Analysis. In: Lance, C.E. and Vandenberg, R.J. eds. *Statistical and Methodological Myths and Urban Legends: Doctrine, Verity and Fable in the Organizational and Social Sciences.* Taylor and Francis, pp. 61-87.

Barone, G. and Crupi, V. and Longo, F. and Majolino, D. and Mazzoleni, P. and Spagnolo, G. and Venuti, V. and Aquilia, E. 2011. Potentiality of non-destructive XRF analysis for the determination of Corinthian B amphorae provenance. *X-Ray Spectrometry* 40(5), pp. 333-337.

Baxter, M. J. 1992. Statistical Analysis of Chemical Compositional Data and the Comparison of Analyses. *Archaeometry* 34, pp. 267-277.

Baxter, M. J. 1999. Detecting Multvariate Outliers in Artefact Compositional Data. *Archaeometry* 41(2), pp. 321-338.

Baxter, M. J. 2015. Notes on Quantitative Archaeology and R. Nottingham Trent University, Science and Technology.

Baxter, M. J. 2016. Multivariate Analysis of Archaeometric Data: An Introduction. Nottingham Trent University, Science and Technology.

Baxter, M. J. and Cool, H. E. M. 2016. Basic Statistical Graphics for Archaeology with R: Life Beyond Excel. Nottingham: Barbican Research Associates.

Baxter, M. J. and Freestone, I. 2006. Log-Ratio Compositional Data Analysis in Archaeometry. *Archaeometry* 48(3), pp. 511-531.

Baxter, M. J. and Jackson, C. 2001. Variable Selection in Artefact Compositional Studies. *Archaeometry* 43(2), pp. 253-268.

Beardah, C. C. and Baxter, M. J. and Cool, H. E. M. and Jackson, C. M. 2003. Compositional Data Analysis of Archaeological Glass: Problems and Possible Solutions.*CoDaWork03: Compositional Data Analysis Workshop*. Girona, Spain.

Beckoff, B. and Kanngiesser, B. and Langhoff, N. and Wedell, R. and Wolff, H. 2006. *Handbook of Practical X-Ray Fluorescence Analysis*. New York: Springer.

Berger, M. J. and Hubbell, J. H. and Seltzer, S. M. and Chang, J. and Coursey, J. S. and Sukumar, R. and Olsen, K. 2010. *XCOM: Photon Cross Sections Database (NIST Standard Reference Database 8 (XGAM))* [Online]. Gaithersburg, MD: National Institute of Standards and Technology (NIST): Available at: http://www.nist.gov/pml/data/xcom/ [Accessed: 25/01/2017].

Bergmann, M. and Heinzelmann, M. 2004. Schedia, Alexandria's Harbour on the Canopic Nile (Kom El Giza / Department of Beheira). Preliminary Report on the Second Season 2004. University of Gottingen and the University of Bern.

Berman, L. M. and Bohac, K. J. 1999. Catalogue of Egyptian Art. *The Cleveland Museum of Art*. New York: Hudson Hills Press.

Bertin, E. P. 1975. *Principles and practice of X-ray spectrometric analysis / Eugene P. Bertin*. New York: Plenum Press.

Bezur, A. and Casadio, F. 2012. The Analysis of Porcelain using handheld and portable X-ray fluorescence Spectrometers. In: Shugar, A.N. and Mass, J.L. eds. *Handheld XRF for Art and Archaeology*. Leuven: Leuven University Press, pp. 249-312.

Bianchi, R. S. 1998. Symbols and Meanings. In: Friedman, F.D. ed. *Gifts of the Nile: Ancient Egyptian Faience*. London: Thames and Hudson, pp. 22-31.

Binns, C. F. and Klem, M. and Mott, H. 1932. An Experiment in Egyptian Blue. *Journal of the American Ceramic Society* 15, pp. 271-272.

Bostock, J. 1855. *The Natural History of Pliny*. London: Henry G. Bohn.

Brand, N. W. and Brand, C. J. 2014. Performance Comparison of Portable XRF Instruments. *Geochemistry: Exploration, Environment, Analysis* 14(2), pp. 125-138.

Brill, R. H. 1970. The Chemical Interpretation of the Texts. In: Openheim, A.L. et al. eds. *Glass and Glassmaking in Ancient Mesopotamia*. New York: The Corning Museum of Glass, pp. 105-128.

Brill, R. H. 1971. A Chemical-Analytical Round-Robin on Four Synthetic Ancient Glasses. In: *IX Congrès International du Verre.* Versailles, 27 septembre–2 octobre 1971. Paris: L'Institut du Verre: Artistic and Historical Communications, pp. 93-110.

Brill, R. H. 1999a. *Chemical Analyses of Early Glasses Vol 1*. New York: The Corning Museum of Glass.

Brill, R. H. 1999b. *Chemical Analyses of Early Glasses Vol 2*. New York: The Corning Museum of Glass.

Bruker. 2010. *Tracer Series User Guide - PDA*. Bruker Corporation.

Bruker. 2016. *Handheld XRF: How it works* [Online]. Bruker. Available at: https://www.bruker.com/products/x-ray-diffraction-and-elemental-analysis/handheld-xrf/how-xrf-works.html [Accessed: February 5 2016].

Bruker. 2018. *XRF Data Differences: Quantitative, Semi-Quantitative and Qualitative Data* [Online]. Available at: https://www.bruker.com/products/x-ray-diffraction-and-elemental-analysis/handheld-xrf/xrf-data-primer-quantitative-semi-quantitative-qualitative.html [Accessed: 9/2/2018].

Castoldi, A. and Galimberti, A. and Guazzoni, C. and Rehak, P. and Hartmann, R. and Strüder, L. 2006. Multi-linear silicon drift detectors for X-ray and Compton imaging. *Nuclear Instruments and Methods in Physics Research Section A: Accelerators, Spectrometers, Detectors and Associated Equipment* 568(1), pp. 89-95.

Charlesworth, D. 1972. Tell El-Farain in Egypt: An Industrial Site in the Nile Delta. *Archaeology* 25, pp. 44-47.

Charrad, M. and Ghazzali, N. and Boiteau, V. and Niknafs, A. 2014. NbClust: An R Package for Determing the Relevant Numbers of Clusters in a Data Set. *Journal of Statistical Software* 61(6).

Color, M. 1994. *Munsell Soil Color Charts*. New Windsor, NY: Macbeth Division of Kollmorgen Instruments Corporation.

Color, M. 2010. *Munsell Book of Color: Matte Edition*. Grand Rapids, MI: Munsell Color.

Commision, O. S. a. O. O. P. f. A. 1976. Nomenclature, Symbols, Units and their Usage in Spectrochemical Analysis - II Data Interpretation. *Pure and Applied Chemistry* 45, pp. 99-103.

Cooper, F. G. 1929. *Munsell Manual of Color*. 3rd ed. Baltimore, MD: Munsell Color Company.

Cordella, C. 2012. PCA: The Basic Building Block of Chemometrics. In: Krull, I. ed. *Analytical Chemistry*. InTech. pp. 1-46.

Coulson, W. D. E. and Leonard, A. J. 1981. *Cities of the Delta, Part 1. Naukratis*. Malibu: Undena.

Craig, N. and Speakman, R. J. and Popelka-Filcoff, R. S. and Glascock, M. D. and Robertson, J. D. and Shackley, M. S. and Aldenderfer, M. S. 2007. Comparison of XRF and PXRF for analysis of archaeological obsidian from southern Perú. *Journal of Archaeological Science* 34(12), pp. 2012-2024.

Davies, N. 1902. *The Rock of Tombs of Deir El Gebrawi: Part I - Tomb of Aba and Smaller Tombs of the Southern Group*. London: The Egypt Exploration Fund.

Davison, S. 2003. *Conservation and Restoration of Glass*. Second Edition ed. Oxford: Butterworth-Heinemann.

Dayton, J. E. 1981. Faience. In: Martin, G.T. ed. *The Sacred Animal Necropolis at North Saqqara*. London: Egpyt Exploration Society, pp. 135-137.

De Francesco, A. M. and Bocci, M. and Crisci, G. M. 2011. Non-Destructive Applications of Wavelength XRF in Obsidian Studies. In: Shackley, M.S. ed. *X-Ray Fluorescence Spectrometry (XRF) in Geoarchaeology*. London: Springer, pp. 81-108.

De Francesco, A. M. and Crisci, G. M. and Bocci, M. 2008. Non-Destructive Analytic Method Using Xrf for Determination of Provenance of Archaeological Obsidians from the Mediterranean Area: A Comparison with Traditional Xrf Methods. *Archaeometry* 50(2), pp. 337-350.

de Viguerie, L. and Duran, A. and Bouquillon, A. and Sole, V. A. and Castaing, J. and Walter, P. 2009. Quantitative X-ray fluorescence analysis of an Egyptian faience pendant and comparison with PIXE. *Anal Bioanal Chem* 395(7), pp. 2219-2225.

Degryse, P. and Henderson, J. and Hodgins, G. 2009. *Isotopes in Vitreous Materials*. Leuven: Leuven University Press.

Demers, H. and Poirier-Demers, N. and de Jonge, N. and Drouin, D. 2011. Three-Dimensional Electron Microscopy Simulation with the CASINO Monte Carlo Software. *Microscopy and Microanalysis* 17(S2), pp. 612-613.

Dodson, A. 1995. *Monarchs of the Nile*. London: The Rubicon Press.

Domoney, K. 2012. *Non-Destructive Hand-Held X-Ray Fluorescence Analysis of Meissen and Vincennes-Sevres Porcelain: Characterisation, Dating and Attribution.* PhD Thesis, Cranfield University.

Drake, B. L. 2015. *Comparing Data obtained with Bruker Tracer III-V+ vs Tracer III-SD* [Online]. Available at: https://groups.google.com/forum/#!topic/pxrf/iWa37tVA8Z8 [Accessed: June 14].

Drake, B. L. and Nazaroff, A. J. and Prufer, K. M. 2009. Error Assessment of Portable X-Ray Florescence Spectometry in Geochemical Sourcing. *SAS Bulletin* 32(3), pp. 15-17.

Drennan, R. D. 2009. *Statistics for Archaeologists*. London: Springer.

Eccleston, M. 2008. Replicating Faience in a Bread Oven at Amarna. *Egyptian Archaeology* 32, pp. 33-35.

El Goresy, A. ed. 2000. *Polychromatic Wall Painting Decorations in Monuments of Pharaonic Egypt: Compositions, Chronology and Painting Techniques*. Proceedings of the First International Symposium: The Wall Paintings of Thera. Thera, Hellas, 1997.

Emmitt, J. J. and McAlister, A. J. and Phillipps, R. S. and Holdaway, S. J. 2018. Sourcing without sources: Measuring ceramic variability with pXRF. *Journal of Archaeological Science: Reports* 17, pp. 422-432.

Ernst, T. and Berman, T. and Buscaglia, J. and Eckert-Lumsdon, T. and Hanlon, C. and Olsson, K. and Palenik, C. and Ryland, S. and Trejos, T. and Valadez, M. and Almirall, J. R. 2014. Signal-to-noise ratios in forensic glass analysis by micro X-ray fluorescence spectrometry. *X-Ray Spectrometry* 43(1), pp. 13-21.

Escardino, A. and García-Ten, J. and Feliu, C. and Moreno, A. 2010. Calcium carbonate thermal decomposition in white-body wall tile during firing. I. Kinetic study. *Journal of the European Ceramic Society* 30(10), pp. 1989-2001.

Fischer, C. and Hsieh, E. 2017. Export Chinese blue-and-white porcelain: compositional analysis and sourcing using non-invasive portable XRF and reflectance spectroscopy. *Journal of Archaeological Science* 80, pp. 14-26.

Fitton, G. 2014. X-Ray Fluorescence Spectrometry. In: Gill, R. ed. *Modern Analytical Geochemistry: an introduction to quantitative chemical analysis techniques for Earth, environmental and materials scientists*

Oxon: Routledge, pp. 87-115.

Forster, N. and Grave, P. 2012. Non-destructive PXRF analysis of museum-curated obsidian from the Near East. *Journal of Archaeological Science* 39(3), pp. 728-736.

Forster, N. and Grave, P. 2013. Effects of elevated levels of lead in ceramics on provenancing studies using non-destructive PXRF: a case study in Byzantine Cypriot glazed ceramics. *X-Ray Spectrometry* 42(6), pp. 480-486.

Forster, N. and Grave, P. and Vickery, N. and Kealhofer, L. 2011. Non-destructive analysis using PXRF: methodology and application to archaeological ceramics. *X-Ray Spectrometry* 40(5), pp. 389-398.

Foster, H. E. and Jackson, C. M. 2009. The composition of 'naturally coloured' late Roman vessel glass from Britain and the implications for models of glass production and supply. *Journal of Archaeological Science* 36(2), pp. 189-204.

Foster, K. P. and Kaczmarczyk, A. 1982. X-RAY FLUORESCENCE ANALYSIS OF SOME MINOAN FAIENCE. *Archaeometry* 24(2), pp. 143-157.

Frahm, E. 2013. Validity of "off-the-shelf" handheld portable XRF for sourcing Near Eastern obsidian chip debris. *Journal of Archaeological Science* 40(2), pp. 1080-1092.

Frahm, E. and Doonan, R. and Kilikoglou, V. 2014a. Handheld Portable X-Ray Fluorescence of Aegean Obsidians. *Archaeometry* 56(2), pp. 228-260.

Frahm, E. and Schmidt, B. A. and Gasparyan, B. and Yeritsyan, B. and Karapetian, S. and Meliksetian, K. and Adler, D. S. 2014b. Ten seconds in the field: rapid Armenian obsidian sourcing with portable XRF to inform excavations and surveys. *Journal of Archaeological Science* 41, pp. 333-348.

Freestone, I. 1991. Looking Into Glass. In: Bowman, S. ed. *Science and the Past*. London: British Museum, pp. 37-56.

Freestone, I. and Leslie, K. A. and Thirlwall, M. and Gorin-Rosen, Y. 2003. Strontium Isotopes in the Investigation of Early Glass Production: Byzantine and Early Islaic Glass from the Near East. *Archaeometry* 45(1), pp. 19-32.

Freestone, I. C. 2005. The Provenance of Ancient Glass through Compositional Analysis. *MRS Proceedings* 852.

Friedman, F. D. 1998. *Gifts of the Nile: Ancient Egyptian Faience*. London: Thames and Hudson.

Gale, N. H. and Stos-Gale, Z. A. 1982. Bronze Age Copper Sources in the Mediterranean: A New Approach. *Science* 216, pp. 11-19.

Gianoncelli, A. and Castaing, J. and Bouquillon, A. and Polvorinos, A. and Walter, P. 2006. Quantitative elemental analysis of Della Robbia glazes with a portable XRF spectrometer and its comparison to PIXE methods. *X-Ray Spectrometry* 35(6), pp. 365-369.

Giumlia-Mair, A. R. G. and Soles, J. 2013. Egyptian faience and rose gold at Mochlos, Crete. *Surface Engineering* 29(2), pp. 114-120.

Goldstein, J. and Newbury, D. and Joy, D. and Lyman, C. and Echlin, P. and Lifshin, E. and Sawyer, L. and Michaels, J. 2003. *Scanning Electron Microscopy and X-Ray Microanalysis*. Third ed. New York: Kluwer Academic.

Goodale, N. and Bailey, D. G. and Jones, G. T. and Prescott, C. and Scholz, E. and Stagliano, N. and Lewis, C. 2012. pXRF: a study of inter-instrument performance. *Journal of Archaeological Science* 39(4), pp. 875-883.

Goodhew, J. and Humphreys, J. and Beanland, R. 2001. *Electron Miscroscopy and Analysis*. Third ed. London: Taylor and Francis.

Grave, P. and Attenbrow, V. and Sutherland, L. and Pogson, R. and Forster, N. 2012. Non-destructive pXRF of mafic stone tools. *Journal of Archaeological Science* 39(6), pp. 1674-1686.

Greene, K. 2007. Late Hellenistic and Early Roman Invention and Innovation The Case of Lead-Glazed Pottery. *American Journal of Archaeology* 111(4), pp. 653-671.

Griffin, P. 2002. Reconstructing the Materials and Technology of Egyptian Faience and Frit. In: Vandiver, P. et al. eds. *Materials Issues in Art and Archaeology VI*. Warrendale, Pennsylvania, pp. 323-355.

Guttman, L. 1954. Some Necessary Conditions for Common-Factor Analysis. *Psychometrika* 19, pp. 149-161.

Hall, M. E. 2016. X-Ray Fluorescence-Energy Dispersive (ED-XRF) and Wavelength Dispersive (WD-XRF) Spectrometry. In: Hunt, A. ed. *The Oxford Handbook of Archaeological Ceramic Analysis*. Oxford: Oxford University Press, pp. 342-362.

Hammerle, E. 2012. *Technological change or consistency? an investigation of faience produced from the Middle to the New Kingdom at Abydos, Egypt.* University of Liverpool.

Hatcher, H. and Henderson, J. and Kaczmarczyk, A. and Lakovara, P. and Vandiver, P. forthcoming. *Archaeological and Technical Studies of Faience and Faience Making from Kerma, Sudan*. Boston: Boston Museum of Fine Arts.

Hatton, G. D. 2005. *The Technology of Egyptian Blue.* University of Oxford.

Henderson, J. 2000. *The Science and Archaeology of Materials: An Investigation of Inorganic Materials*. London: Routledge.

Henderson, J. 2013. *Ancient glass: an interdisciplinary exploration*. CAmbridge: Cambridge University Press.

Henderson, J. and Evans, J. and Nikita, K. 2010. Isotopic Evidence for the Primary Production, Provenance and Trade of Late Bronze Age Glass in the Mediterranean. *Mediterranean Archaeology and Archaeometry* 10(1), pp. 1-24.

Henderson, J. and Evans, J. A. and Sloane, H. J. and Leng, M. J. and Doherty, C. 2005. The use of oxygen, strontium and lead isotopes to provenance ancient glasses in the Middle East. *Journal of Archaeological Science* 32(5), pp. 665-673.

Hodges, H. 1976. *Artifacts: An Introduction to Early Materials and Technology*. London: John Baker.

Hollingbery, L. A. and Hull, T. R. 2010. The Thermal Decomposition of Huntite and Hydromagnesite - A Review. *Thermochimica Acta* 509, pp. 1-11.

Homqvist, E. 2016. Handheld Portable Energy-Dispersive X-Ray Fluorescence Spectrometry (pXRF). In: Hunt, A. ed. *The Oxford Handbook of Archaeological Ceramic Analysis*. Oxford: Oxford University Press, pp. 363-381.

Hughes, R. E. 1984. Obsidian Sourcing Studies in the Great Basin: Problems and Prospects. In: Hughes, R.E. ed. *Obsidian Studies in the Great Basin*. 45 ed. Berkeley: Archaeological Research Facility, Department of Anthropology, pp. 1-20.

Hunt, A. M. W. and Speakman, R. J. 2015. Portable XRF analysis of archaeological sediments and ceramics. *Journal of Archaeological Science* 53, pp. 626-638.

Husson, F. and Josse, J. and Le, S. and Mazet, J. 2017. *Package 'FactoMineR'*. CRAN.

Jackson, C. M. and Baxter, M. J. 1999. Variable Selection in Archaeometry: The Statistical Analysis of Glass Compositional Data. In: Barcelo, J.A. et al. eds. *Computer Applications and Quantitative Methods in Archaeology 1998*. Oxford: Archaeopress, pp. 159-162.

Jackson, E. J. 2005. *A User's Guide to Principal Components*. John Wiley & Sons.

Janssens, K. 2013. X-Ray Based Methods of Analysis. In: Janssens, K. ed. *Modern Methods for Analysing Archaeological and Historical Glass*. Chichestor: Wiley, pp. 79-128.

Jenkins, R. 1999. *X-Ray Fluorescence Spectrometry*. New York: John Wiley and Sons.

Jia, P. W. and Doelman, T. and Chen, C. and Zhao, H. and Lin, S. and Torrence, R. and Glascock, M. D. 2010. Moving sources: A preliminary study of volcanic glass artifact distributions in northeast China using PXRF. *Journal of Archaeological Science* 37(7), pp. 1670-1677.

Johnson, J. 2014. Accurate Measurements of Low Z Elements in Sediments and Archaeological Ceramics Using Portable X-ray Fluorescence (PXRF). *Journal of Archaeological Method and Theory* 21(3), pp. 563-588.

Jones, L. H. P. and Handreck, K. A. 1967. Silica In Soils, Plants, and Animals. *Advances in Agronomy* 19, pp. 107-149.

Josse, J. and Husson, F. 2016. missMDA: A Package for Handling Missing Values in Multivariate Data Analysis. *Journal of Statistical Software* 70(1).

Kaczmarczyk, A. 1981. Personal Communication Reported by Vandiver in 1982.

Kaczmarczyk, A. 1986. The Source of Cobalt in Ancient Egyptian Pigments. In: Olin, J.S. and Blackman, M.J. eds. *Proceedings of the 24th International Archaeometry Symposium*. Washington, D.C.: Smithsonian Institution Press, pp. 369-376.

Kaczmarczyk, A. and Hedges, R. E. M. 1983. *Ancient Egyptian Faience: An Analytical Survey of Egyptian Faience from Predynastic to Roman Times*. Warministeer: Aris and Phillips.

Kaczmarczyk, A. and Vandiver, P. 2008. Faience Production in Egypt. In: Tite, M.S. and Shortland, A. eds. *Production Technology of Faience and Related Early Vitreous Materials*. Oxford: Oxford University School of Archaeology, pp. 57-91.

Kaiser, B. and Shugar, A. N. 2012. Glass Analysis Utilizing Handheld X-ray Fluorescence. In: Shugar, A.N. and Mass, J.L. eds. *Handheld XRF for Art and Archaeology*. Leuvan: Leuvan University Press, pp. 449-470.

Kaiser, B. and Wright, A. 2008. Draft Bruker XRF Spectroscopy User Guide: Spectral Interpretation and Sources of Interference. Bruker Corporation.

Kaiser, H. F. 1960. The Application of Electronic Computers to Factor Analysis. *Educational and Psychological Measurement* 20, pp. 141-151.

Kassambara, A. and Mundt, F. 2017. *Factoextra: Extract and Visualize the Results of Multivariate Data Analyses*. CRAN.

Kato, N. and Nakai, I. and Shindo, Y. 2009. Change in chemical composition of early Islamic glass excavated in Raya,Sinai Peninsula, Egypt: on-site analyses using a portable X-ray fluorescence spectrometer. *Journal of Archaeological Science* 36(8), pp. 1698-1707.

Kato, N. and Nakai, I. and Shindo, Y. 2010. Transitions in Islamic plant-ash glass vessels: on-site chemical analyses conducted at the Raya/al-Tur area on the Sinai Peninsula in Egypt. *Journal of Archaeological Science* 37(7), pp. 1381-1395.

Kaufman, L. and Rousseeuw, P. J. 1990. *Finding Groups in Data: An Introduction to Cluster Analysis.* New York: Wiley.

Keith, L. H. and Libby, R. A. and Crummett, W. and Taylor, J. K. and Deegan, J. J. and Wentler, G. 1983. Principles of Environmental Analysis. *Analytical Chemistry* 55, pp. 2210-2218.

Kennedy, C. J. and Murdoch, K. R. and Kirk, S. 2013. Characterization of Archaeological Andin Situscottish Window Glass. *Archaeometry* 55(3), pp. 465-478.

Kiefer, C. and Allibert, A. 1971. Pharaonic Blue Ceramics: The Process of Self-Glazing. *Archaeology* 24, pp. 107-117.

Koob, S. P. 2006. *Conservation and Care of Glass Objects*. London: Archetype.

Kregsamer, P. and Streli, C. and Wobrauschek, P. 2002. Total Reflection X-ray Fluorescence. In: Van Grieken, R.E. ed. *Handbook of X-Ray Spectromety*. New York: Marcel Dekker, Inc, pp. 555-598.

Kuhne, K. 1969. *Zur Kenntnis Silikatischer Werkstoffe und der Technologie ihrer herstellung im 2, Jahrtausend vor unserer zeitrechnung*. Berlin: Akademie-Verlag, .

La Delfa, S. and Formisano, V. and Ciliberto, E. 2008. Laboratory production of Egyptian faiences and their characterization. *Journal of Cultural Heritage* 9, pp. e113-e116.

Lawson, R. G. and Jurs, P. C. 1990. New Index for Cluster Tendency and its Application to Chemical Problems. *Journal of Chemical Information and Computer Sciences* 30(1), pp. 36-41.

Leonard, A. J. 1998a. Ancient Naukratis: Excavations at a Greek Emporium in Egypt Part 1.

Leonard, A. J. 1998b. Ancient Naukratis: Excavations at a Greek Emporium in Egypt. Part II: The Excavations at Kom Hadid. *The Annual of the American Schools of Oriental Research* 55, pp. iii-vii+ix-xvii+1-233+235-245+247+249-273.

Lilyquist, C. and Brill, R. H. 1993. *Studies in Early Egyptian Glass*. New York: The Metropolitan Museum of Art.

Liu, S. and Li, Q. H. and Fu, Q. and Gan, F. X. and Xiong, Z. M. 2013. Application of a portable XRF spectrometer for classification of potash glass beads unearthed from tombs of Han Dynasty in Guangxi, China. *X-Ray Spectrometry* 42(6), pp. 470-479.

Liu, S. and Li, Q. H. and Gan, F. and Zhang, P. and Lankton, J. W. 2012. Silk Road glass in Xinjiang, China: chemical compositional analysis and interpretation using a high-resolution portable XRF spectrometer. *Journal of Archaeological Science* 39(7), pp. 2128-2142.

Longoni, A. and Fiorini, C. 2006. X-Ray Detectors and Signal Processing. In: Beckoff, B. et al. eds. *Handbok of Practical X-Ray Fluorescence Analysis*. Berlin: Springer, pp. 204-262.

Lucas, A. and Harris, J. R. 1962. *Ancient Egyptian Materials and Industries*. 4 ed. London: Edward Arnold.

Mangone, A. and De Benedetto, G. E. and Fico, D. and Giannossa, L. C. and Laviano, R. and Sabbatini, L. and van der Werf, I. D. and Traini, A. 2011. A multianalytical study of archaeological faience from the Vesuvian area as a valid

tool to investigate provenance and technological features. *New Journal of Chemistry* 35(12), p. 2860.

Manti, P. 2004. *Analytical Investigation and Replication Studies on the Production of Ancient Egyptian Faience.* University of Oxford.

Manti, P. 2013. Analyses of Selected Faience Objects. In: Nicholson, P. ed. *Working in Memphis: The Production of Faience at Roman Period Kom Helul*. London: The Egypt Exploration Society, pp. 185-188.

Mao, Y. 2000. Lead-Alkaline Glazed Egyptian Faience: Preliminary Technical Investigation of Ptolemaic Period Faience Vessels in the Collection of the Walters Art Gallery. *Journal of the American Institute for Conservation* 39(2), pp. 185-204.

Mao, Y. 2001. A Technical Examination of three Ptolemaic Faience Vessels. *The Journal of the Walters Art Museum,* 59, pp. 17-22.

Markowicz, A. A. 2008. Quantification and Correction Procedures. In: Potts, P.J. and West, M. eds. *Portable X-ray Fluorescence Spectrometry: Capabilities for In Situ Analysis*. Cambridge: The Royal Society of Chemistry, pp. 13-38.

Martin-Fernandez, J. A. and Barcelo, J. A. and Pawlowsky-Glahn, V. 2003. Dealing With Zeros and Missing Values in Compostiional Data Sets Using Nonparametric Imputation. *Mathematical Geology* 35(3), pp. 253-278.

Matin, M. and Matin, M. 2012. Egyptian faience glazing by the cementation method part 1: an investigation of the glazing powder composition and glazing mechanism. *Journal of Archaeological Science* 39(3), pp. 763-776.

McGovern, P. and Fleming, S. and Swann, C. 1993. The Late Bronze Egyptian Garrison at Beth Shan_Glass and Faience Production and Importation in the Late New Kingdom. *Bulletin of the American Schools of Oriental Research* 290/291, pp. 1-27.

Mesbahinia, A. and Rashidi-Huyeh, M. and Shafiee Afarani, M. 2014. Persian turquoise glazed bodies: reproduction and optical properties. *Applied Physics A*.

Milić, M. 2014. PXRF characterisation of obsidian from central Anatolia, the Aegean and central Europe. *Journal of Archaeological Science* 41, pp. 285-296.

Millhauser, J. K. and Rodríguez-Alegría, E. and Glascock, M. D. 2011. Testing the accuracy of portable X-ray fluorescence to study Aztec and Colonial obsidian supply at Xaltocan, Mexico. *Journal of Archaeological Science* 38(11), pp. 3141-3152.

Mitchell, D. and Grave, P. and Maccheroni, M. and Gelman, E. 2012. Geochemical characterisation of north Asian glazed stonewares: a comparative analysis of NAA, ICP-OES and non-destructive pXRF. *Journal of Archaeological Science* 39(9), pp. 2921-2933.

Molina, G. and Odin, G. P. and Pradell, T. and Shortland, A. J. and Tite, M. S. 2014. Production technology and replication of lead antimonate yellow glass from New Kingdom Egypt and the Roman Empire. *Journal of Archaeological Science* 41, pp. 171-184.

Morey, G. W. 1964. Phase-Equilibrium Relations of the Common Rock-Forming Oxides Except Water. In: Fleischer, M. ed. *Data of Geochemistry*. Washington: United States Government Printing Office.

Morgan, M. M. 1914. *Vitruvius - The Ten Books on Architecture*. Cambridge: Harvard Univesity Press.

Morgenstein, M. and Redmount, C. A. 2005. Using portable energy dispersive X-ray fluorescence (EDXRF) analysis for on-site study of ceramic sherds at El Hibeh, Egypt. *Journal of Archaeological Science* 32(11), pp. 1613-1623.

Motzzfeldt, K. 1955. The Thermal Decomposition of Sodium Carbonate by the Effusion Method.

Mysliwiec, K. 1996. In the Ptolemaic Workshops of Athribis. *Egyptian Archaeology* 9, pp. 34-36.

NAPCOR. PET Basics: Features, Benefits and Information Resources. In: Resources, N.A.f.P.C. ed.

Nazaroff, A. J. and Prufer, K. M. and Drake, B. L. 2010. Assessing the applicability of portable X-ray fluorescence spectrometry for obsidian provenance research in the Maya lowlands. *Journal of Archaeological Science* 37(4), pp. 885-895.

Nazaroff, A. J. and Shackley, M. S. 2009. Testing the Size Dimension Limitation of Portable XRF Instrumentation for Obsidian Provenance. In: *Geological Society of America Annual Meeting.* Portland, OR.

Nenna, M. 2013. Faience Vessels and Objects. In: Nicholson, P. ed. *Working in Memphis: The Production of Faience at Roman Period Kom Helul*. London: Egypt Exploration Society, pp. 107-132.

Nenna, M. 2014. Description Archeologique des Objets Analyses. In: Empereur, J.-Y. ed. *Alexandrina 4*. Alexandria: Centre d'Etudes Alexandrines.

Nenna, M. and Nicholson, P. 2013. Faience Technology. In: Nicholson, P. ed. *Working in Memphis: The Production of Faience at Roman Period Kom Helul*. Vol. 105. The Egyptian Exploration Society, pp. 133-146.

Nenna, M. and Seif El-Din, M. 2000. La vaisselle en faience d'epoque greco-romaine. In: Orientale, I.F.D.a. ed. *Etudes Alexandrines 4*. Le Caire: Institut Francais D'Archeologie Oreintale.

Nenna, M. and Sief el-Din, M. 2014. La Vaisselle en Faience d'epoque Greco-Romaine au Musee Greco-Romain d'Alexandrie: Complente et Typologie. In: Empereur, J.-Y. ed. *Alexandrina 4*. Alexandria: Centre d'Etudes, pp. 213-294.

Newton, R. G. and Renfew, C. 1970. British Faience Beads Reconsidered. *Antiquity* 44(175), pp. 199-206.

Nicholas, M. 2015. *Metallurgy in the Gloaming: Non-Ferrous Metalwork from Three Early Anglo-Saxon Cemeteries at RAF Lakenheath, Suffolk.* PhD Thesis, Cardiff University.

Nicholas, M. and Manti, P. 2014. Testing the Applicability of Handheld Portable XRF to the Characterization of Copper Alloys. In: Bridgeland, J. ed. *ICOM-CC 17th Triennial Conference Preprints.* Melbourne, 15-19 September. Paris: International Council of Museums,

Nicholson, P. 2002. A New Furnace at Kom Helul, Memphis. *Egyptian Archaeology* 20, pp. 24-25.

Nicholson, P. 2007. *Brilliant Things for Akhenaten: The Production of Glass, Vitreous Materials and Pottery at Amarna Site O45.1*. Oxford: Oxbow Books.

Nicholson, P. and Jackson, C. 1998. "Kind of Blue": Glass of the Amarna Period Replicated. In: McCray, P. ed. *The Prehistory and History of Glassmaking Technology*. Westerville, Ohio: The American Ceramic Society, pp. 105-120.

Nicholson, P. and Jackson, C. 2013. GLASS OF AMENHOTEP II FROM TOMB KV55 IN THE VALLEY OF THE KINGS. *The Journal of Egyptian Archaeology* 99, pp. 85-100.

Nicholson, P. T. 1993. *Egyptian Faience and Glass*. Buckinghamshire: Shire Publications.

Nicholson, P. T. 1998. Materials and Technology. In: Friedman, F.D. ed. *Gifts of the Nile: Ancient Egyptian Faience*. London: Thames and Hudson.

Nicholson, P. T. 2009. Faience Technology. *UCLA Encyclopedia of Egyptology* [Online]. Available at: http://escholarship.org/uc/item/9cs9x41z.

Nicholson, P. T. 2013. *Working in Memphis: The Production of Faience at Roman Period Kom Helul*. The Egyptian Exploration Society.

Nickerson, D. 1976. The History of the Munsell Color Company. *Color Research and Application* 1(3), pp. 121-130.

NIST. 2016. *X-Ray Mass Attenuation Coefficients* [Online]. U.S. Department of Commerce. Available at: http://www.nist.gov/pml/data/xraycoef/index.cfm [Accessed: February 5 2016].

Noble, J. V. 1969. The Technique of Egyptian Faience. *American Journal of Archaeology* 73(4), pp. 435-439.

Nolte, B. 1969. Die GlassgefaBe im alten Agypten. *Munchner Agyptologische Studen* 14.

Otero, N. and Tolosana-Delgado, R. and Soler, A. and Pawlowsky-Glahn, V. and Canals, A. 2005. Relative vs. absolute statistical analysis of compositions: a comparative study of surface waters of a Mediterranean river. *Water Res* 39(7), pp. 1404-1414.

Palarea-Albaladejo, J. and Martín-Fernández, J. A. and Buccianti, A. 2014. Compositional methods for estimating elemental concentrations below the limit of detection in practice using R. *Journal of Geochemical Exploration* 141, pp. 71-77.

Palarea-Albaladejo, J. and Martin-Fernandez, J. A. and Gomez-Garcia, J. 2007. A Parametric Approach for Dealing with Compositional Rounded Zeros. *Mathematical Geology* 39(7), pp. 625-645.

Pappalardo, G. and Costa, E. and Marchetta, C. and Pappalardo, L. and Romano, F. P. and Zucchiatti, A. and Prati, P. and Mandò, P. A. and Migliori, A. and Palombo, L. and Vaccari, M. G. 2004. Non-destructive characterization of Della Robbia sculptures at the Bargello museum in Florence by the combined use of PIXE and XRF portable systems. *Journal of Cultural Heritage* 5(2), pp. 183-188.

Parodi, H. D. 1908. *La Verrerie en Egypte.* Université de Grenoble. Faculté des sciences: Le Caire : Imp. de l'école Khédiviale d'Arts.

Pearce, J. A. and Cann, J. R. 1973. Tectonic Setting of Basic Volcanic Rocks Determined Using Trace Element Analysis. *Earth and Planetary Science Letters* 19, pp. 290-300.

Pearce, N. J. G. and Bendall, C. A. and Westgate, J. A. 2008. Comment on "Some numerical considerations in the geochemical analysis of distal microtephra" by A.M. Pollard, S.P.E. Blockley and C.S. Lane. *Applied Geochemistry* 23(5), pp. 1353-1364.

Petrie, F. 1886. *Naukratis Part I., 1884-5*. London: Trubner and Company.

Petrie, F. 1909. *Memphis I*. London: School of Archaeology in Egypt, Unversity College Bernard Quaritch.

Petrie, F. 1911. The Pottery Kilns at Memphis. In: Knobel, E.B. et al. eds. *Historical Studies 1*. London: BSAE and Quaritch, pp. 34-37.

Petrie, F. and McKay, E. and Wainwright, G. 1910. *Meydum and Memphis (III)*. London: School of Archaeology in Egypt, Unversity College Bernard Quaritch.

Phillips, S. C. and Speakman, R. J. 2009. Initial source evaluation of archaeological obsidian from the Kuril Islands of the Russian Far East using portable XRF. *Journal of Archaeological Science* 36(6), pp. 1256-1263.

Pollard, A. M. and Batt, C. and Stern, B. and Young, S. 2007. *Analytical Chemistry in Archaeology*. Cambridge: Cambridge University Press.

Pollard, A. M. and Heron, C. 2008. *Archaeological Chemistry*. Second ed. Cambridge, UK: The Royal Society of Chemistry

Potts, P. J. 2008. Introduction, Analytical Instrumentation and Application Overview. In: Potts, P.J. and West, M. eds. *Portable X-ray Fluorescence Spectrometry: Capabilities for In Situ Analysis*. Cabridge: The Royal Society of Chemistry, pp. 1-12.

Potts, P. J. and West, M. 2008. *Portable X-Ray Fluorescence Spectrometry*. Cambridge: RSC Publishing.

R_Core_Team. 2016. *R: A Language and Environment for Statistical Computing* [Online]. Vienna: R Foundation for Statistical Computing. Available at: https://www.R-project.org/ [Accessed: 2016].

R_Studio_Team. 2016. *RStudio: Integrated Development for R* [Online]. Boston, MA: RStudio, Inc. Available at: http://www.rstudio.com/ [Accessed.

Rehak, P. and Chen, W. and Carini, G. and Chuang, H. and De Geronimo, G. and Dong, B. and Gaskin, J. and Keister, J. and Li, Z. and Ramsey, B. and Siddons, D. eds. 2009. *Comparison of Two Different Methods to Produce Thin-Window Silicon Drift Detectors*. 2009 IEEE Nuclear Science Symposium Conference.

Rehren, T. 2008. A review of factors affecting the composition of early Egyptian glasses and faience: alkali and alkali earth oxides. *Journal of Archaeological Science* 35(5), pp. 1345-1354.

Riccardelli, C. and Mass, J. L. and Thorton, J. 2002. Egyptian Faience Inlay Techniques: a process for obtaining detail and clarity by refiring. *Mat. Res. Soc. Symp. Proc.* 712, pp. 1-26.

Rodziewicz, M. 2005. *Elephatine XXVII: Early Roman Industries on Elephantine*. Mainz Am Rhein: Verlag Philipp Von Zabern.

Rousseau, R. M. 2001. Detection Limit and Estimate of Uncertainty of Analytical XRF Results. *The Rigaku Journal* 18(2), pp. 33-47.

Rousseeuw, P. 1987. Silhouettes: A Graphical Aid to the Interpretation and VAlidation of Cluster Analysis. *Journal of Computational and Applied Mathematics* 20, pp. 53-65.

Sandford, R. F. and Pierson, C. T. and Crovelli, R. A. 1993. An Objective Replacement Method for Censored Geochemical Data. *Mathematical Geology* 25(1), pp. 59-80.

Schiegl, S. and Weiner, K. L. and Gorsey, A. E. 1989. Discovery of copper chloride cancer in ancient Egyptian polychromic wall paintings and faience. *Natur Wissenschaften* 76, pp. 393-400.

Schindelin, J. and I., A.-C. and Frise, E. 2012. Fiji: an open-source platform for biological-image analysis. *Nature methods* 9(7), pp. 676-682.

Schneider, T. 2010. Foreigners in Egypt: Archaeological Evidence and Cultural Context. In: Wendrich, W. ed. *Egyptian Archaeology*. Chichester: Wiley-Blackwell, pp. 143-163.

Scott, R. and Braekmans, D. and Brems, D. and Degryse, P. eds. 2012a. *Danger! High Voltage! The Application of Handheld X-ray Fluorescence (HH-XRF) to Experimental Glass: Pitfalls and Potentials*. 39th International Symposium for Archaeometry. Leuven.

Scott, R. and Shortland, A. and Degryse, P. and Power, M. and Domoney, K. and Boyen, S. and Braekmans, D. 2012b. In Situ Analysis of Ancient Glass: 17th Century Painted Glass from Christ Church Cathedral, Oxford and Roman Glass Vessels. *Glass Technol,: Eur. J. Glass Sci. Technol. A* 53(2), pp. 65-73.

Sendova, M. and Kaiser, B. and Scalera, M. and Zhelyaskov, V. 2009. Della Robbia blue glaze: micro-Raman temperature study and X-ray fluorescence spectroscopy characterization. *Journal of Raman Spectroscopy*, pp. n/a-n/a.

Shackley, M. S. 1988. Sources of Archaeological Obsidian in the Southwest: An Archaeological, Petrological, and Geochemical Study. *American Antiquity* 53(4), pp. 752-772.

Shackley, M. S. 2010. Is There Reliability and Validity in Portable X-Ray Fluorescence Spectrometry (PXRF)? *The SAA Archaeological Record* 10(5), pp. 17-18, 20.

Shackley, M. S. 2011. An Introduction to X-Ray Fluorescence (XRF) Analysis in Archaeology. In: Shackley, M.S. ed. *X-Ray Fluorescence Spectrometry (XRF) in Geoarchaeology*. London: Springer, pp. 7-44.

Shapiro, S. and Wilk, M. 1965. An Analysis of Variance Test for Normality (Complete Samples). *Biometrika* 52(3/4), pp. 591-611.

Sharif, H. 2014. *Formation of Bromate in PET Bottle Water.* American University of Sharjah.

Sharp, Z. D. and Papike, J. J. and Durakiewicz, T. 2003. The Effect of Thermal Decarbonation on Stable Isotope Compositions of Carbonates. *American Mineralogist* 88, pp. 87-92.

Shortland, A. 2000. *Vitreous materials at Amarna*. Oxford.

Shortland, A. 2002. The Use and Origin of Antimonate Colorants in Early Egyptian Glass. *Archaeometry* 44(4), pp. 517-530.

Shortland, A. 2004. Evaporites of the Wadi Natrun: Seasonal and Annual Variation and Its Implication for Ancient Exploitation. *Archaeometry* 46(4), pp. 497-516.

Shortland, A. and Hatton, G. D. and Tite, M. 2007a. Scientific Examination of Vitreous Materials and Associated Ceramics. In: Nicholson, P. ed. *Brilliant Things for Akhenaten: The Production of Glass, Vitreous Materials and Pottery at Amarna Site 045.1*. London: The Egypt Exploration Society, pp. 183-188.

Shortland, A. and Rogers, N. and Eremin, K. 2007b. Trace element discriminants between Egyptian and Mesopotamian Late Bronze Age glasses. *Journal of Archaeological Science* 34(5), pp. 781-789.

Shortland, A. and Schachner, L. and Freestone, I. and Tite, M. 2006a. Natron as a flux in the early vitreous materials industry: sources, beginnings and reasons for decline. *Journal of Archaeological Science* 33(4), pp. 521-530.

Shortland, A. and Tite, M. S. 2005. Technological Study of Ptolemaic - Early Roman Faience from Memphis, Egypt. *Archaeometry* 47(1), pp. 31-46.

Shortland, A. and Tite, M. S. and Ewart, I. 2006b. Ancient Exploitation and use of cobalt alums from the western oases of Egypt. *Archaeometry* 48(1), pp. 153-168.

Shugar, A. N. 2013. Portable X-ray Fluorescence and Archaeology: Limitations of the Instrument and Suggested Methods To Achieve Desired Results. 1147, pp. 173-193.

Shugar, A. N. and Mass, J. L. 2012. Introduction. In: Shugar, A.N. and Mass, J.L. eds. *Handheld XRF for Art and Archaeology*. Leuven: Leuven University Press.

Shugar, A. N. and Sirois, P. J. 2012. Handheld XRF Used in the Identification of Heavy Metal Pesticides in Ethnographic Collections. In: Shugar, A.N. and Mass, J.L. eds. *Handheld XRF in Art and Archaeology*. pp. 313-348.

Singh, H. P. and Mahajan, P. and Kaur, S. and Batish, D. R. and Kohli, R. K. 2013. Chromium toxicity and tolerance in plants. *Environmental Chemistry Letters* 11(3), pp. 229-254.

Speakman, R. J. and Little, N. C. and Creel, D. and Miller, M. R. and Iñañez, J. G. 2011. Sourcing ceramics with portable XRF spectrometers? A comparison with INAA using Mimbres pottery from the American Southwest. *Journal of Archaeological Science* 38(12), pp. 3483-3496.

Speakman, R. J. and Steven Shackley, M. 2013. Silo science and portable XRF in archaeology: a response to Frahm. *Journal of Archaeological Science* 40(2), pp. 1435-1443.

Stocks, D. 1997. Derivation of Ancient Egyptian Faience Core and Glaze Materials. *Antiquity* 71, pp. 179-182.

Stone, J. F. S. and Thomas, L. C. 1956. The use and distribution of faience in the ancient east and prehistoric europe. In: *Proceedings of the Prehistoric Society 22.* pp. 37-84.

Susak-Pitzer, A. 2012. Chemical Analysis of Roman Glass from Karanis Using X-Ray Fluorescence Spectrometry Los Angeles: UCLA.

Tanasi, D. and Tykot, R. H. and Pirone, F. and McKendry, E. 2017. Provenance Study of Prehistoric Ceramics from Sicily: A Comparative Study between pXRF and XRF. *Open Archaeology* 3(1).

Tangri, D. and Wright, R. 1993. Multivariate analysis of compositional data: applied comparisons favour standard principal components analysis over Aitchison's loglinear contrast method. *Archaeometry* 35(1), pp. 103-112.

Tantrakarn, K. and Kato, N. and Hokura, A. and Nakai, I. and Fujii, Y. and Gluščević, S. 2009. Archaeological analysis of Roman glass excavated from Zadar, Croatia, by a newly developed portable XRF spectrometer for glass. *X-Ray Spectrometry* 38(2), pp. 121-127.

Templ, M. and Filzmoser, P. and Reimann, C. 2008. Cluster analysis applied to regional geochemical data: Problems and possibilities. *Applied Geochemistry* 23(8), pp. 2198-2213.

Thomas, R. I. and Villing, A. 2013. *Naukratis Revisited 2012: Integrating New Fieldwork and Old Research*.

Tite, M. S. 1987. Characterization of Early Vitreous Materials. *Archaeometry* 29(1), pp. 21-34.

Tite, M. S. 1991. Archaeological Science - Past Achievements and Future Prospects. *Archaeometry* 33(2), pp. 139-151.

Tite, M. S. 2009. The production technology of Italian maiolica: a reassessment. *Journal of Archaeological Science* 36(10), pp. 2065-2080.

Tite, M. S. and Bimson, M. 1986. Faience - An Investigation of the Microstructures Assocaited with the Different Methods of Glazing. *Archaeometry* 28(1), pp. 69-78.

Tite, M. S. and Freestone, I. and Bimson, M. 1983. Egyptian Faience - An Investigation of the Methods of Production. *Archaeometry* 25(1), pp. 17-27.

Tite, M. S. and Manti, P. and Shortland, A. J. 2007. A technological study of ancient faience from Egypt. *Journal of Archaeological Science* 34(10), pp. 1568-1583.

Tite, M. S. and Shortland, A. 2003. Production Technology for Copper and cobalt blue vitreous materials from the new kingdom site of amarna, a reappraisal. *Archaeometry* 45(2), pp. 285-312.

Tite, M. S. and Shortland, A. 2008. *Production Technology of Faience and Related Early Vitreous Materials*. Oxford: Oxford University.

Tite, M. S. and Shortland, A. and Maniatis, Y. and Kavoussanaki, D. and Harris, S. A. 2006. The composition of the soda-rich and mixed alkali plant ashes used in the production of glass. *Journal of Archaeological Science* 33(9), pp. 1284-1292.

Tite, M. S. and Shortland, A. and Nicholson, P. T. and Jackson, C. M. 1998. The Use of Copper and Cobalt colorants in vitreous Materials in Ancient Egypt. In: Colinart, S. and Menu, M. eds. *La Couleur dans la Peinture et l'emaillage de l'Egypte Ancienne*. Ravello: Edipuglia, pp. 111-120.

Toffolo, M. B. and Klein, E. and Elbaum, R. and Aja, A. J. and Master, D. M. and Boaretto, E. 2013. An early Iron Age assemblage of faience beads from Ashkelon, Israel: chemical composition and manufacturing process. *Journal of Archaeological Science* 40(10), pp. 3626-3635.

Turner, W. E. S. 1956. Studies in Ancient Glasses and Glassmaking Processes: Part V Raw Materials and Melting Processes. *Journal of the Society of Glass Technology* 40, pp. 277-300.

Vandiver, P. 1982. Technological Change in Egpytian Faience. In: Olin, J.S. and Franklin, A. eds. *Archaeological Ceramics*. Washington D.C.: Smithsonian Institute Press, pp. 167-179.

Vandiver, P. 1983. The Manufacture of Faience. In: Kaczmarczyk, A. and Hedges, R.E.M. eds. *Ancient Egyptian Faience: An Analytical Survey of Egyptian Faience from Predynastic to Roman Times*. Warministeer: Aris and Phillips, pp. A1-A137.

Vandiver, P. 1998. A review and proposal of new criteria for production technologies of egyptian faience. In: Colinart, S. and Menu, M. eds. *La couleur dans la peinture et I 'emaillage de I 'Egypte ancienne*. Bari: Edipuglia, pp. 121-139.

Vandiver, P. 2008. Raw Materials and Fabrication Methods Used in the Production of Faience. In: Tite, M.S. and Shortland, A. eds. *Production Technology of Faience and Related Early Vitreous Materials*. Oxford: Oxford University School of Archaeology, pp. 37-55.

Vandiver, P. and Kingery, W. D. 1986. Egyptain Faience: The first high tech ceramic. In: Kingery, W.D. ed. *High-Technology Ceramics: Past, Present, and Future*. Westerville, Ohio: The American Ceramic Society, pp. 19-34.

Vandiver, P. and Kingery, W. D. 1987. Manufacture of an Eighteenth Dynasty Egyptian Faience Chalice. In: Bimson, M. and Freestone, I. eds. *Early Vitreous Materials*. 56 ed. London: British Museum Press, pp. 79-90.

Vitruvius. 1914. *The Ten Books on Architecture*. Translated by M. Morgan, Cambridge: Harvard University Press.

Wagner, B. and Nowak, A. and Bulska, E. and Hametner, K. and Gunther, D. 2012. Critical assessment of the elemental composition of Corning archeological reference glasses by LA-ICP-MS. *Anal Bioanal Chem* 402(4), pp. 1667-1677.

Welc, F. 2011. Decorated Ptolemaic Faience Bowls from Athribis (Tell Atrib, Nile Delta). *ÉTUDES et TRAVAUX* 24, pp. 244-269.

Welc, F. 2013. Faience Workshop in Ptolemaic Athribis (Tell_Atrib). *ÉTUDES et TRAVAUX* 26, pp. 720-735.

Whisenant, L. A. 2012. *Exploring the Possibility of Low Temperature Glazing in Faience from the Djoser Step Pyramid through Compositional Analysis.* Thesis, Massachusetts Institute of Technology.

Wilson, A. L. 1978. Elemental Analysis of Pottery in the Study of its Provenance - A Review. *Journal of Archaeological Science* 5, pp. 219-236.

Wobrauschek, P. and Streli, C. and Lindgren, E. 2010. Energy Dispersive, X-Ray Fluorescence Analysis. In: Meyers, R.A. ed. *Encyclopedia of Analytical Chemistry*. Chichester: Wiley and Sons Ltd, pp. 1-17.

Wulff, H. E. and Wulff, H. S. and Koch, L. 1968. Egyptian Faience: A Possible Survival. *Archaeology* 21, pp. 98-107.

Zhao, H. X. and Li, Q. H. and Liu, S. and Li, L. and Gan, F. X. 2014. In situanalysis of stratified glass eye beads from the tomb of Marquis Yi of the Zeng State in Hubei Province, China using XRF and micro-Raman spectrometry. *X-Ray Spectrometry* 43(6), pp. 316-324.

Appendix A: Faience Glaze Replicates

Faience glaze replicates were produced from three batches (see Tables 5-1 and 5-2) to test the capabilities of HH-XRF in discerning known glazes (see Chapter 9) and of SEM-EDS to determine actual glaze recipes (see section 7.6.2). Macro- and microscopic glaze characteristics were collection including Munsell colour, surface texture, presences of pinholes, bubbles under the glaze surface, bubbles erupting through the glaze surface, glaze creep, and glaze profile using both SEM-BSE and optical microscopy (successful in differentiating the glaze, interaction layer (IAL) and body substrate). These characteristics are presented in this appendix.

Appendix A is divided into two sections. The first section is a descriptive table for the selected sherds. The second section dedicates a page for each selected sample showing SEM-BSE glaze profiles, OM glaze surface micrograph, OM sherd profile of broken edge and a photograph of the sample prior to firing to provide context. A caption for the figures is provided. Information regarding the production of the samples is found in Chapters 5; information regarding further descriptive information is provided in Chapter 7.

Replicated Blue Faience Glazes

Transparent Glaze Characteristics

Sample	Colour	Munsell Colour	Surface Texture	Pinholes	Bubbles	Erupting Bubbles	Crawling	Temp. Ramp Up ↑ (C/H)	Dwell Temp. ↕ (C)	Temp. Ramp Up ↑ (C/H)2	Temp. Peak (C)	Soak Time (Min)	Ramp Down ↓ (C/H)
R327	Blue	2.5PB 4/10	Smooth		x			200	400	100	850	360	200
R328	Blue	10B 5/10	Orange Peel		x			200	400	100	850	360	200
R340	Blue	10B 5/12	Smooth	x	x			200	400	100	850	180	200
R342	Blue	10B 5/10	Orange Peel		x			200	400	100	850	180	200
R349	Blue	2.5PB 4/10	Orange Peel		x			200	400	100	970	60	200

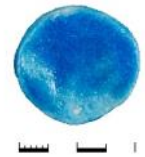

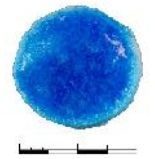

Replicated Blue Faience Glazes

Sample	Colour	Munsell Colour	Surface Texture	Pinholes	Bubbles	Erupting Bubbles	Crawling	Temp. Ramp Up ↑ (C/H)	Dwell Temp. 1 (C)	Temp. Ramp Up ↑ (C/H)2	. Peak (C)	Soak Time (Min)	Down ↓ (C/H)
		Transparent Glaze Characteristics											
R351	Blue	2.5PB 4/10	Orange Peel		x			200	400	100	970	60	200
R356	Blue	10B 4/8	Smooth		x		x	200	400	100	900	60	200
R359	Blue	2.5PB 4/10	Smooth		x	x		200	400	100	900	60	200
R360	Blue	10B 5/6	Smooth		x			200	400	100	800	60	200
R363	Blue	10B 5/6	Orange Peel		x	x		200	400	100	800	60	200

Replicated Blue Faience Glazes

Transparent Glaze Characteristics														
Sample	Colour	Munsell Colour	Surface Texture	Pinholes	Bubbles	Erupting Bubbles	Crawling	Temp. Ramp Up ↑ (C/H)	Dwell Temp. ↓ (C)	Temp. Ramp Up ↑ (C/H)2	. Peak (C)	Soak Time (Min)	Down ↓ (C/H)	
R364	Blue	10B 4/8	Smooth		x			999	850	999	850	60	200	
R367	Blue	10B 4/8	Smooth		x	x		999	850	999	850	60	200	
R383	Blue	10B 4/8	Smooth		x	x		200	400	200	850	60	200	
R384	Blue	10B 5/10	Smooth		x	x		200	400	200	850	60	200	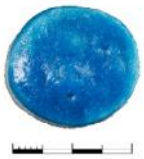
R386	Blue	10B 4/8	Smooth		x			200	400	100	850	60	200	

Replicated Blue Faience Glazes

Transparent Glaze Characteristics

Sample	Colour	Munsell Colour	Surface Texture	Pinholes	Bubbles	Erupting Bubbles	Crawling	Temp. Ramp Up ↑ (C/H)	Dwell Temp. ↓ (C)	Temp. Ramp Up ↑ (C/H)2	. Peak (C)	Soak Time (Min)	Down ↓ (C/H)
R388	Blue	10B 5/10	Smooth		x	x		200	400	100	850	60	200
R390	Blue	10B 4/8	Smooth		x			200	400	50	850	60	200
R392	Blue	10B 5/10	Orange Peel		x	x		200	400	50	850	60	200
R406	Dark Blue	5PB 3/8	Smooth		x	x		200	400	100	850	60	200
R408	Dark Blue	5PB 3/8	Orange Peel		x	x		200	400	100	850	60	200

Replicated Blue Faience Glazes

Transparent Glaze Characteristics

Sample	Colour	Munsell Colour	Surface Texture	Pinholes	Bubbles	Erupting Bubbles	Crawling	Temp. Ramp Up ↑ (C/H)	Dwell Temp. 1 (C)	Temp. Ramp Up ↑ (C/H)2	. Peak (C)	Soak Time (Min)	Down ↓ (C/H)
R411	Dark Blue	5PB 3/8	Smooth		x			200	400	100	900	60	200
R412	Dark Blue	5PB 3/8	Smooth		x			200	400	100	900	60	200
R415	Dark Blue	5PB 3/8	Smooth		x	x		200	400	100	970	60	200
R416	Dark Blue	5PB 3/8	Orange Peel		x	x		200	400	100	970	60	200
R418	Dark Blue	5PB 3/8	Orange Peel	x	x	x	x	200	400	100	850	60	200

Replicated Blue Faience Glazes

Transparent Glaze Characteristics

Sample	Colour	Munsell Colour	Surface Texture	Pinholes	Bubbles	Erupting Bubbles	Crawling	Temp. Ramp Up ↑ (C/H)	Dwell Temp. ↑ (C)	Temp. Ramp Up ↑ (C/H)2	. Peak (C)	Soak Time (Min)	Down ↓ (C/H)
R421	Dark Blue	5PB 3/8	Orange Peel		x	x		200	400	100	850	60	200
R423	Dark Blue	5PB 3/8	Smooth		x	x		200	400	100	900	60	200
R424	Dark Blue	5PB 3/8	Orange Peel	x	x	x		200	400	100	900	60	200
R426	Dark Blue	5PB 3/8	Smooth	x	x			200	400	100	970	60	200
R429	Dark Blue	5PB 3/8	Smooth		x	x		200	400	100	970	60	200





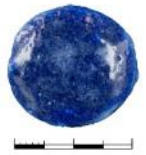

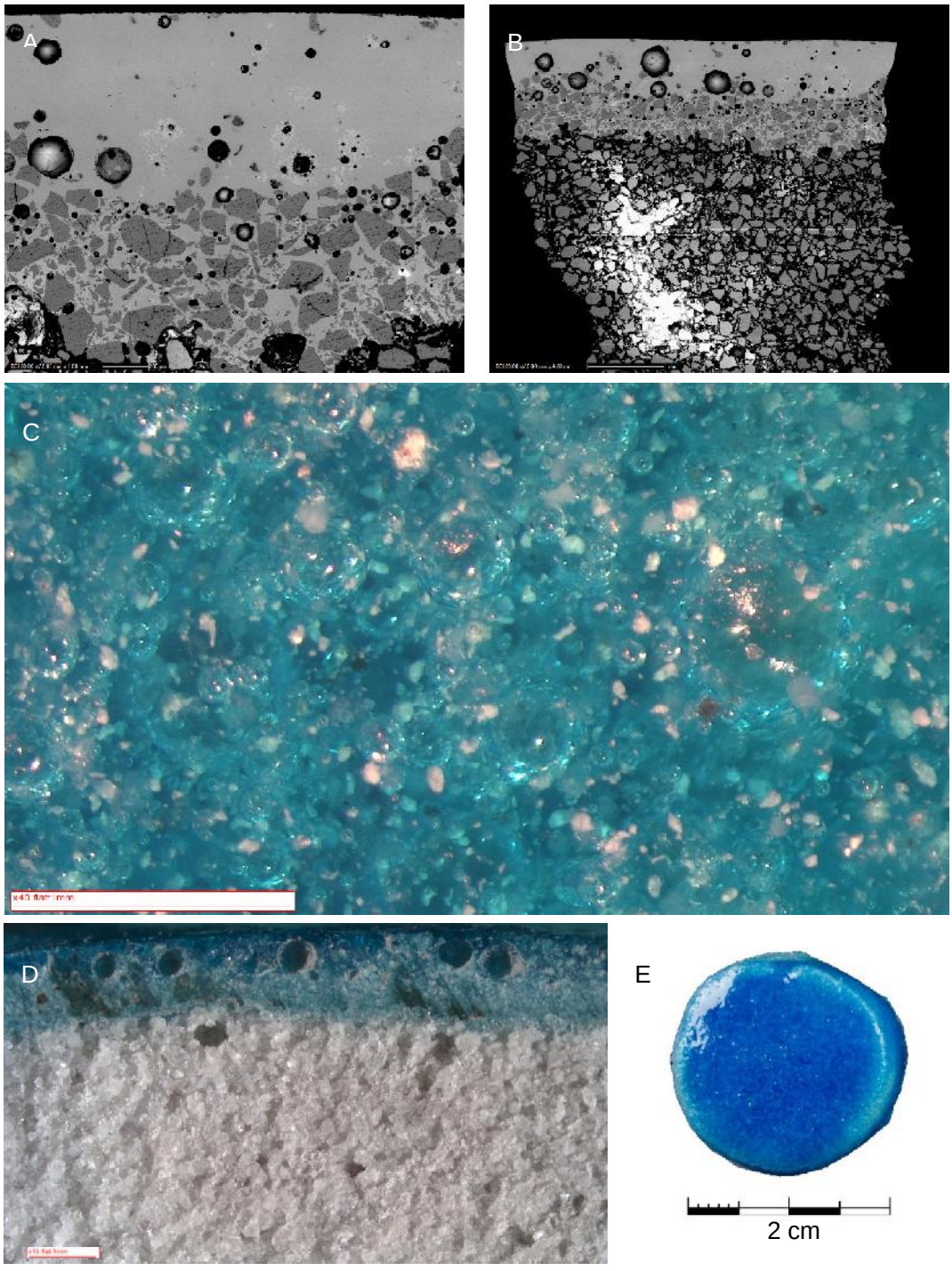

R327: SEM-BSE glaze profile (scale: 200 µm (A) and 1 mm (B)); OM glaze surface micrograph (C (scale: 1 mm)); OM glaze profile (D (scale: 1 mm)) and the replicate prior to sampling (E). BSE profile A shows a glaze layer with minimal unreacted quartz particles and bubbles. The IAL shows unreacted quartz and bubble formation. The charging areas in the replicate body (B) is due to lapping oil emerging from between the quartz grains in a vacuum. Figure C shows bubbles and unreacted quartz below the glaze surface. Center-top of the image reveals a single quartz particle that has broken the glaze surface. The OM profile (D) shows massed sintered quartz particles in the body.

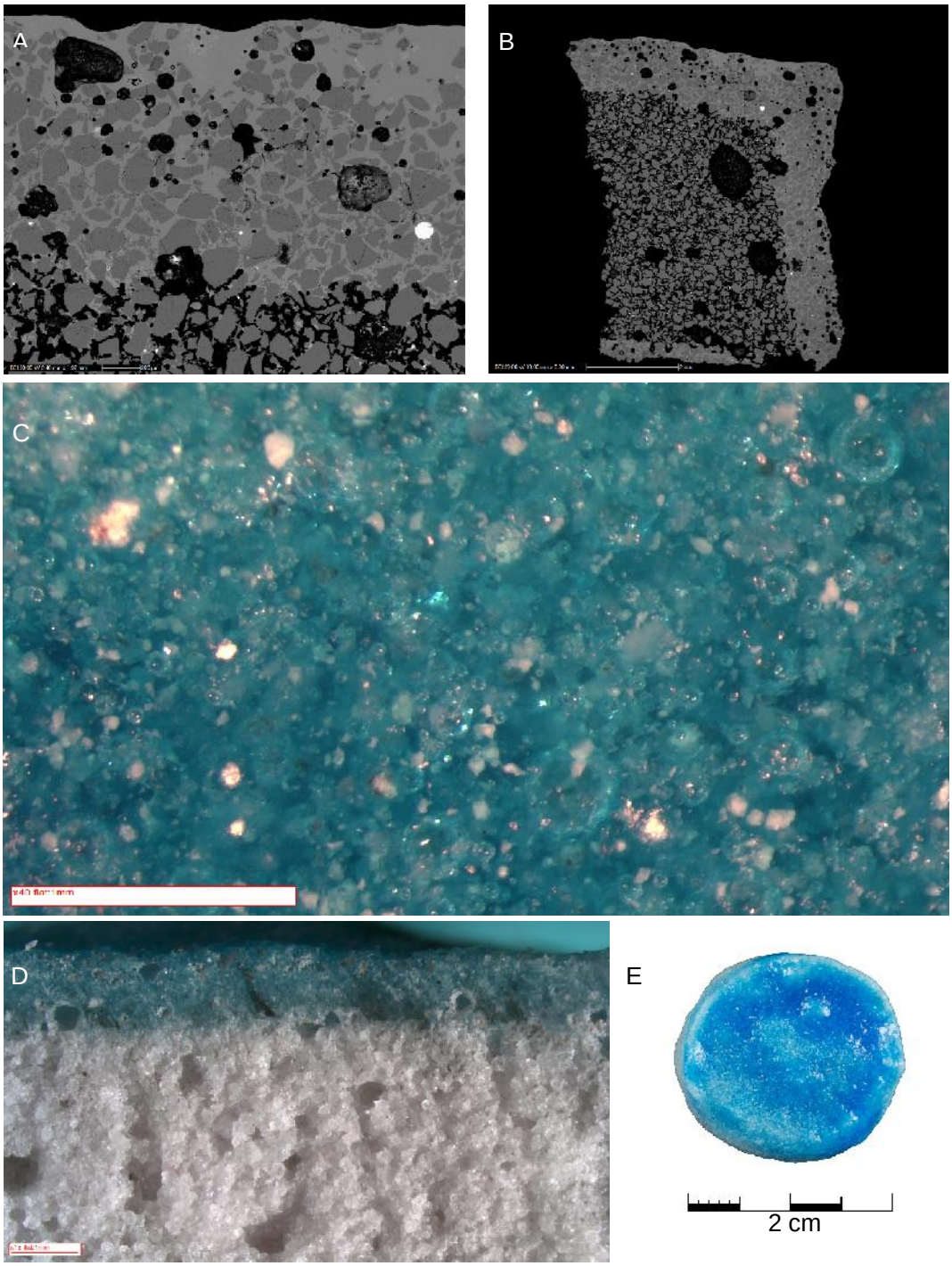

R328: SEM-BSE glaze profile (scale: 200 µm (A) and 2 mm (B)); OM glaze surface micrograph (C (scale: 1 mm)); OM glaze profile (D (scale: 1 mm)) and the replicate prior to sampling (E). BSE profile A shows a thin glaze layer with unreacted quartz particles and bubbles. The IAL shows unreacted quartz and bubble formation. Large pores are present in the body and most of the bubbles are restricted to the glaze layer (Figure B). Bubbles and unreacted quartz below the glaze surface are evident in Figure C. A large quartz particle has broken the glaze surface (top-left corner). The OM profile (D) shows massed sintered quartz particles in the body.

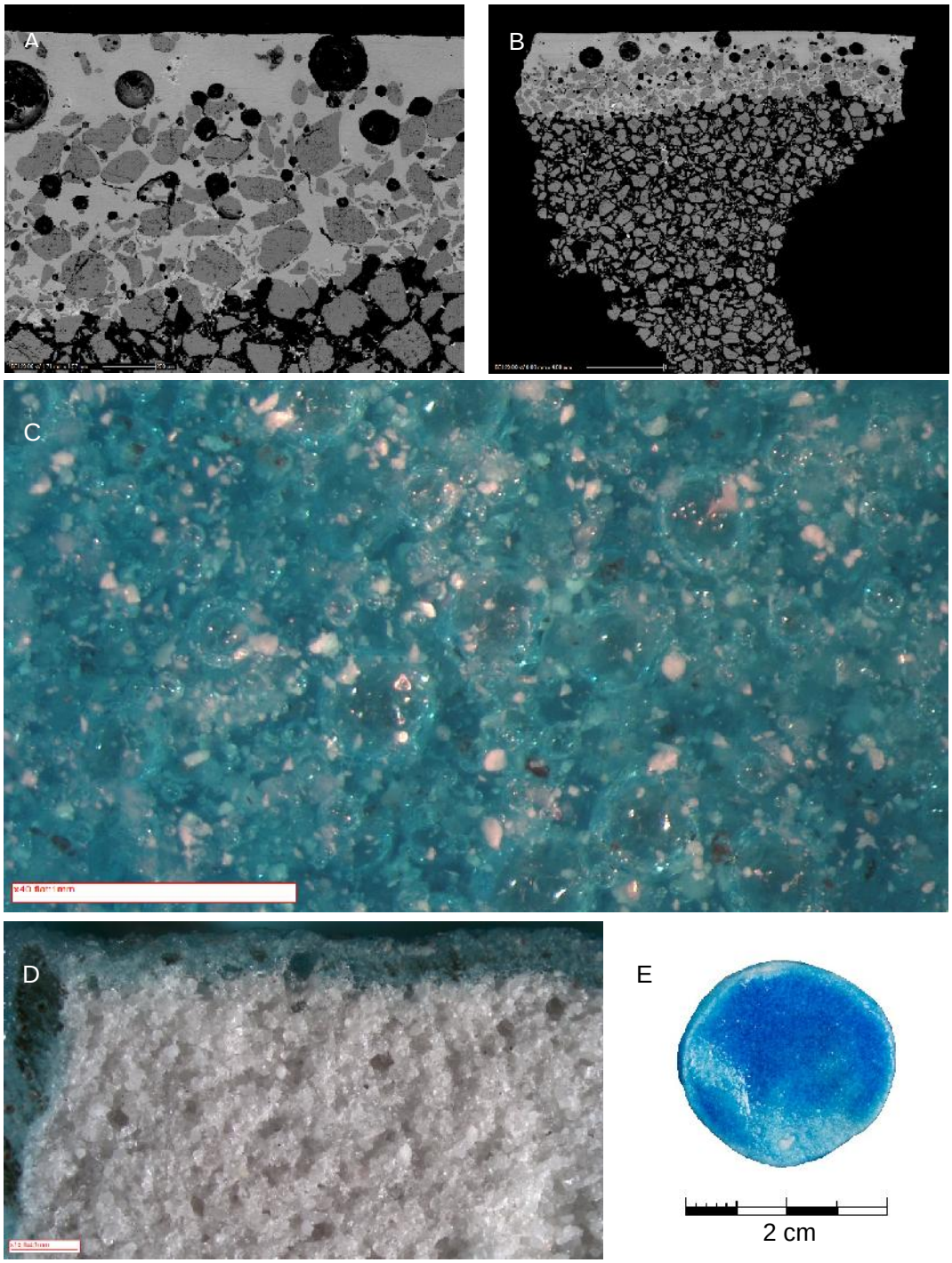

R340: SEM-BSE glaze profile (scale: 200 µm (A) and 1 mm (B)); OM glaze surface micrograph (C (scale: 1 mm)); OM glaze profile (D (scale: 1 mm)) and the replicate prior to sampling (E). BSE profile A shows a moderately thin glaze layer with unreacted quartz particles and bubbles. The IAL shows unreacted quartz and bubble formation. Pores are present in the body (Figure B). Bubbles and unreacted quartz below the glaze surface are evident in Figure C. The OM profile (D) shows massed sintered quartz particles in the body. A large pinhole revealing the body substrate is present in the glaze surface of the sample (E).

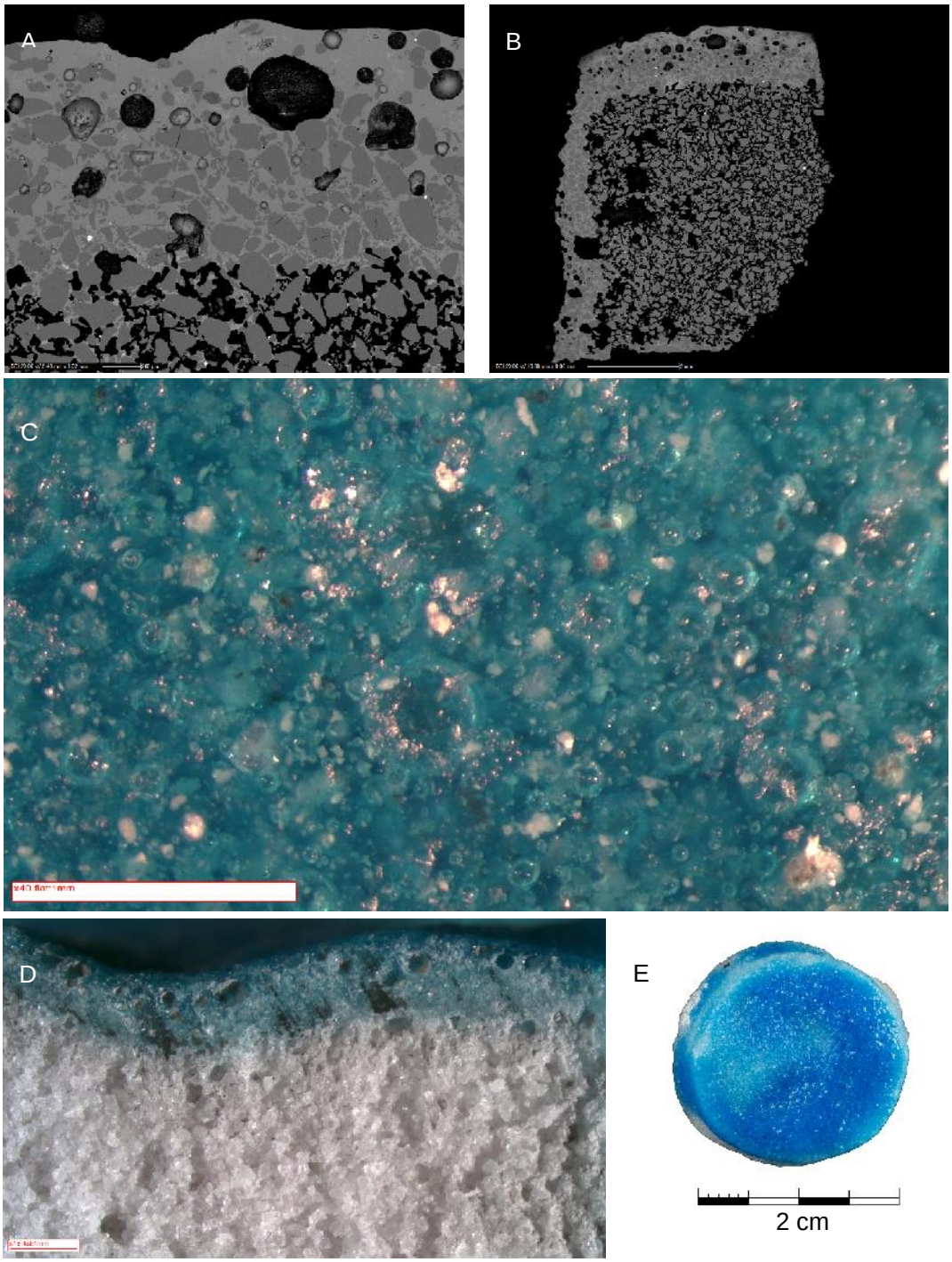

R342: SEM-BSE glaze profile (scale: 200 µm (A) and 2 mm (B)); OM glaze surface micrograph (C (scale: 1 mm)); OM glaze profile (D (scale: 1 mm)) and the replicate prior to sampling (E). The sample has a thin glaze layer (A) with unreacted quartz particles and bubbles. The IAL shows unreacted quartz and bubble formation. The body profile reveals relatively large pores and a thick IAL. Figure C shows bubbles and unreacted quartz below an uneven surface glaze. Some of the brighter quartz bodies have erupted through the glaze surface. The OM profile (D) shows massed sintered quartz particles in the body.

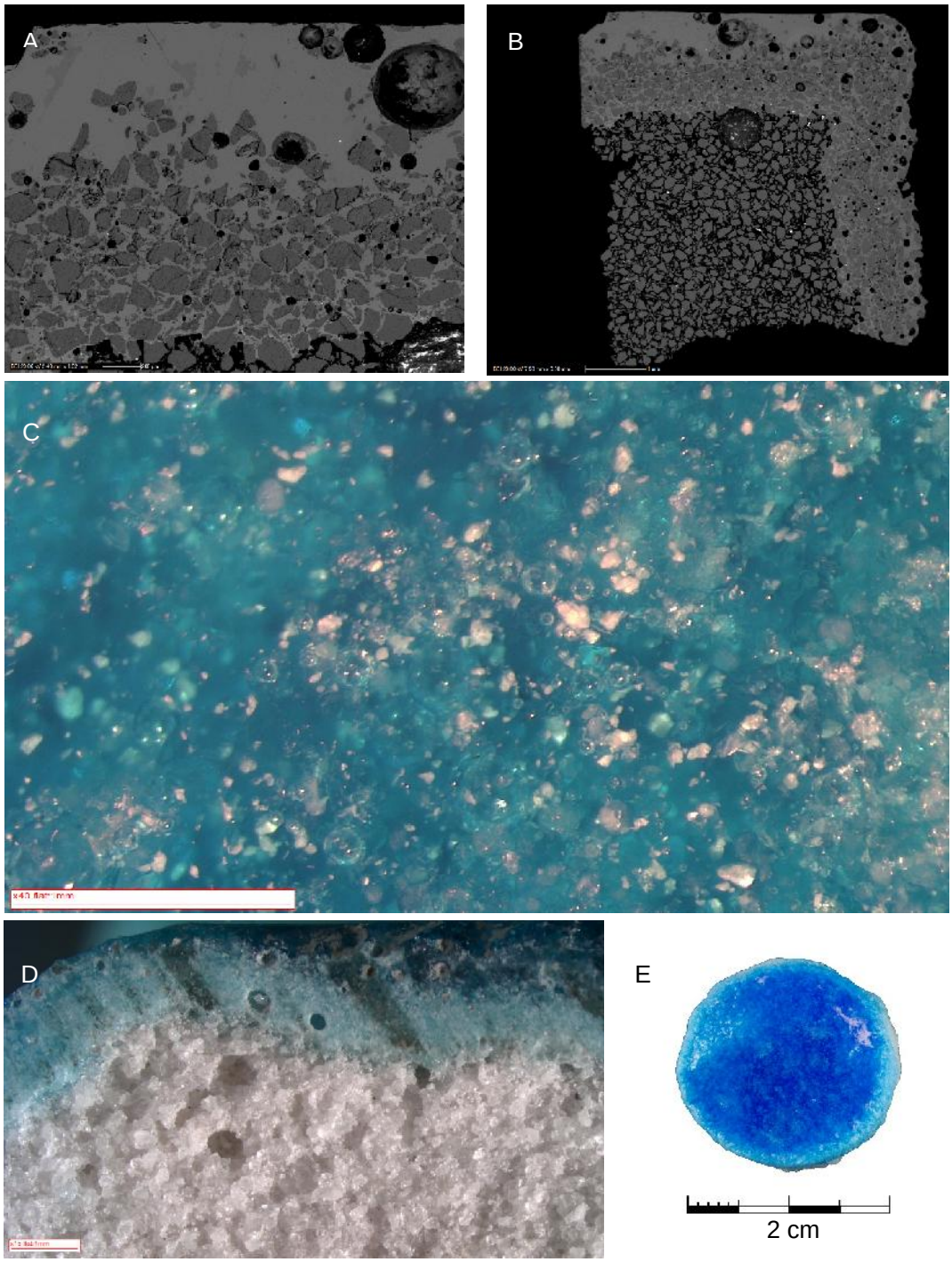

R349: SEM-BSE glaze profile (scale: 200 µm (A) and 1 mm (B)); OM glaze surface micrograph (C (scale: 1 mm)); OM glaze profile (D (scale: 1 mm)) and the replicate prior to sampling (E). BSE profile A shows a glaze layer with bubbles and minimal unreacted quartz particles. The relatively thick IAL shows unreacted quartz and bubble formation (B). There is a large rounded pore crossing the body/IAL boundary which is probably due to gas evolution. Figure C shows bubbles and unreacted quartz below the glaze surface. The frequency of bubbles is relatively low when compared to the other samples. The OM profile (D) shows massed sintered quartz particles in the body.

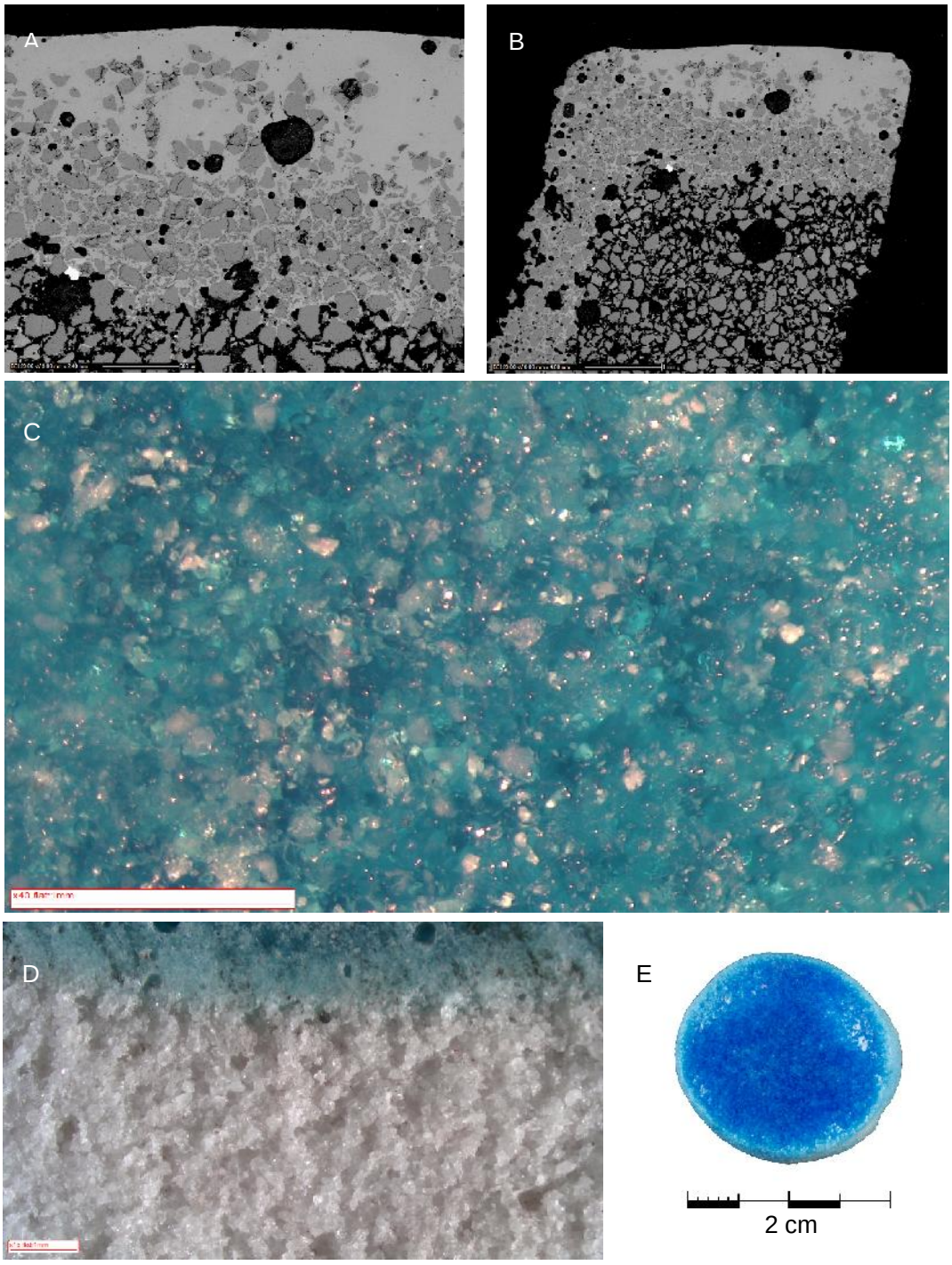

R351: SEM-BSE glaze profile (scale: 200 µm (A) and 1 mm (B)); OM glaze surface micrograph (C (scale: 1 mm)); OM glaze profile (D (scale: 1 mm)) and the replicate prior to sampling (E). BSE profile A shows a glaze layer with unreacted quartz particles and bubbles. The IAL shows unreacted quartz and bubble formation. There are large pores within the body substrate (B). Figure C shows bubbles and unreacted quartz below the glaze surface. The OM profile (D) shows massed sintered quartz particles in the body.

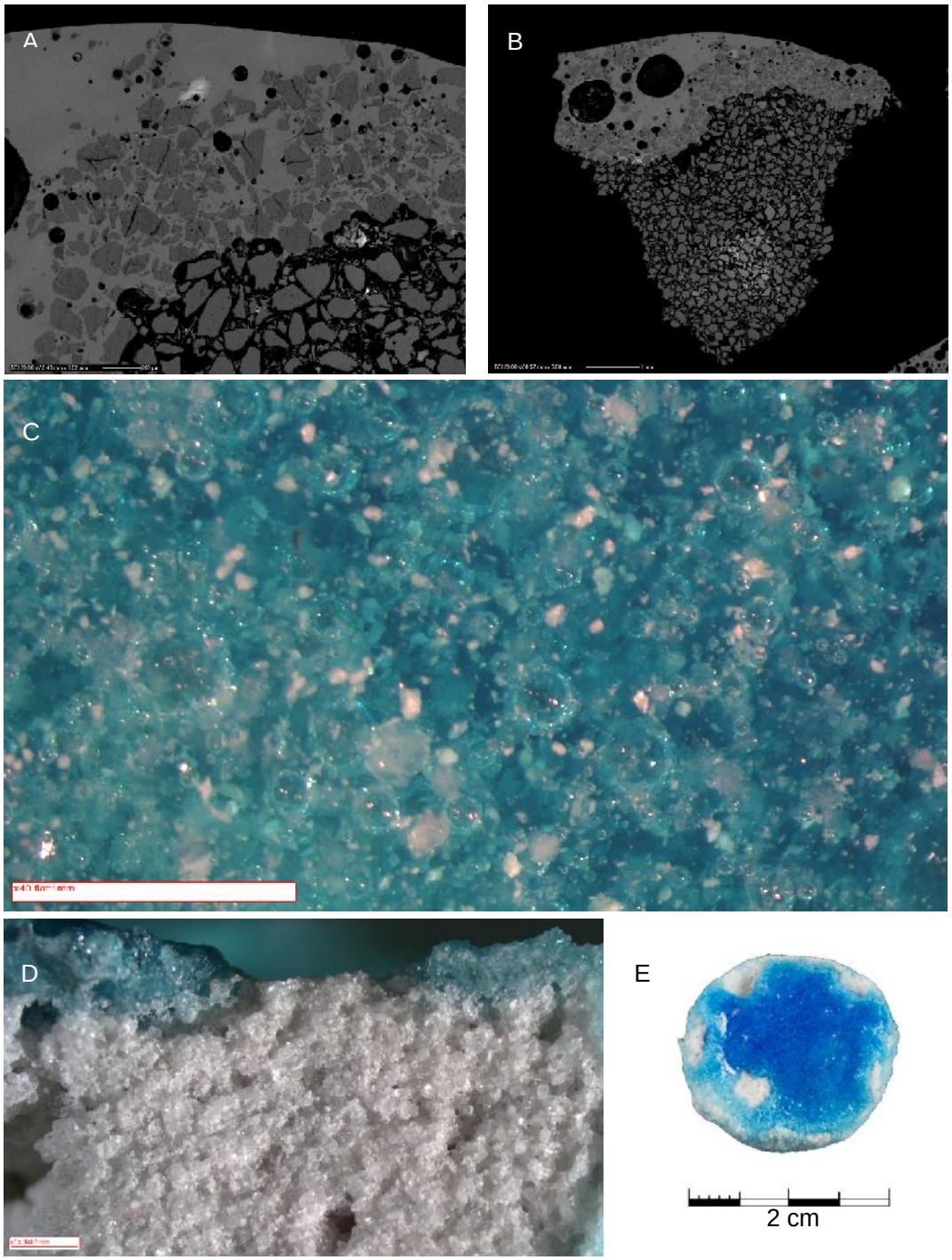

R356: SEM-BSE glaze profile (scale: 200 µm (A) and 1 mm (B)); OM glaze surface micrograph (C (scale: 1 mm)); OM glaze profile (D (scale: 1 mm)) and the replicate prior to sampling (E). The BSE profiles (A and B) reveal variability in the glaze thickness. Two large bubbles in the glaze have lifted unreacted quartz particle to near the surface (B). The unglazed sample surface was undulating as evinced by the IAL revealing a similar appearance. Charging in the BSE images is due to lapping oil emerging from micro-pores in the SEM vacuum. Bubbles and unreacted quartz are evident below the glaze surface (C) and the glaze has creeped to reveal the massed sintered ground quartz body substrate (D and E). Center-top of the image reveals a single quartz particle that has broken the glaze surface.

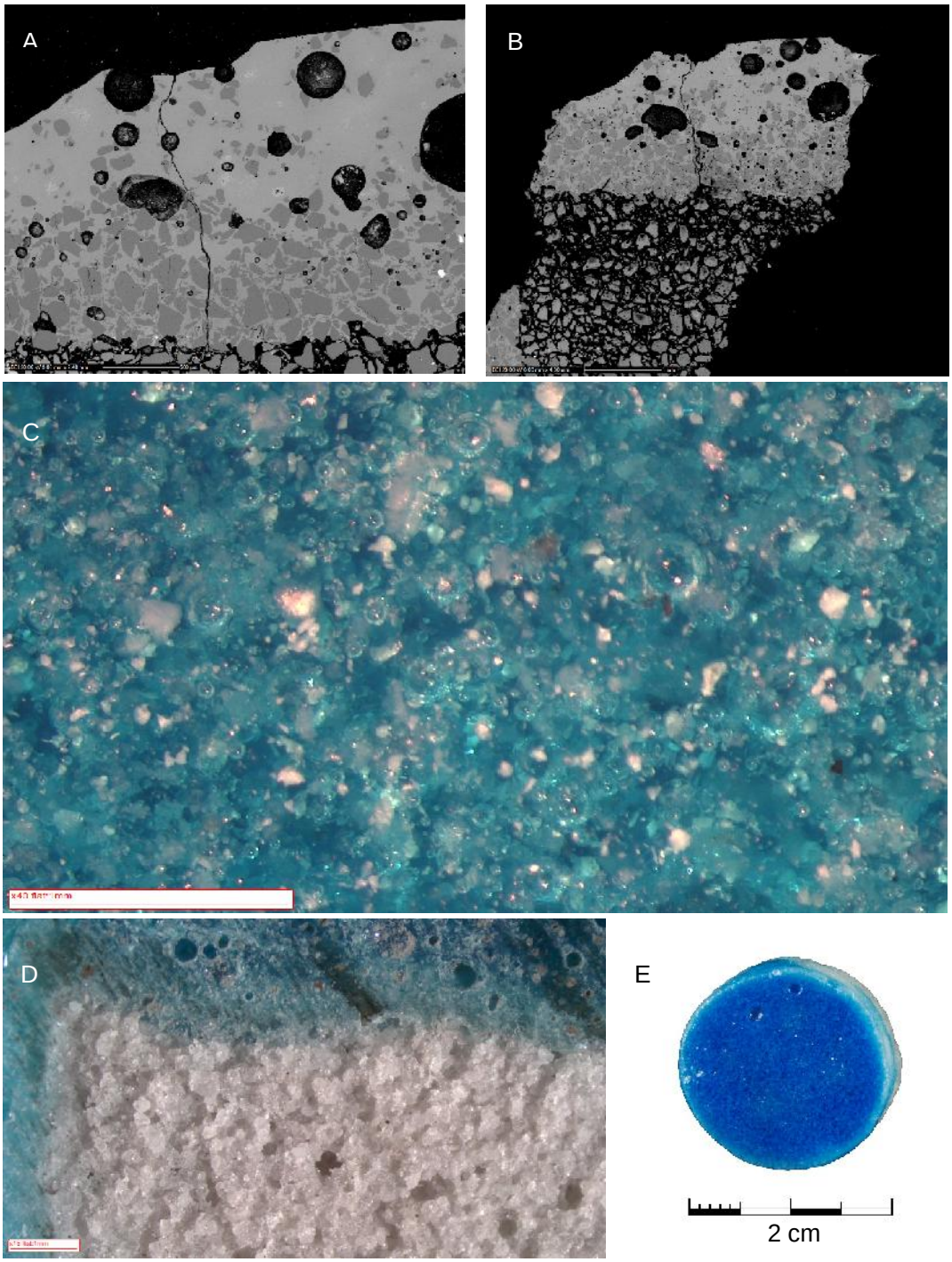

R359: SEM-BSE glaze profile (scale: 500 µm (A) and 1 mm (B)); OM glaze surface micrograph (C (scale: 1 mm)); OM glaze profile (D (scale: 1 mm)) and the replicate prior to sampling (E). The BSE profiles (A and B) reveal bubbles in the glaze with some minor unreacted quartz. Smaller bubbles are evolving in the IAL. A crack runs through the glaze and IAL. Bubbles and unreacted quartz are evident below the glaze surface (C). The OM profile (D) shows massed sintered quartz particles in the body. The replicate sample glaze surface (E) reveals two large erupting bubbles.

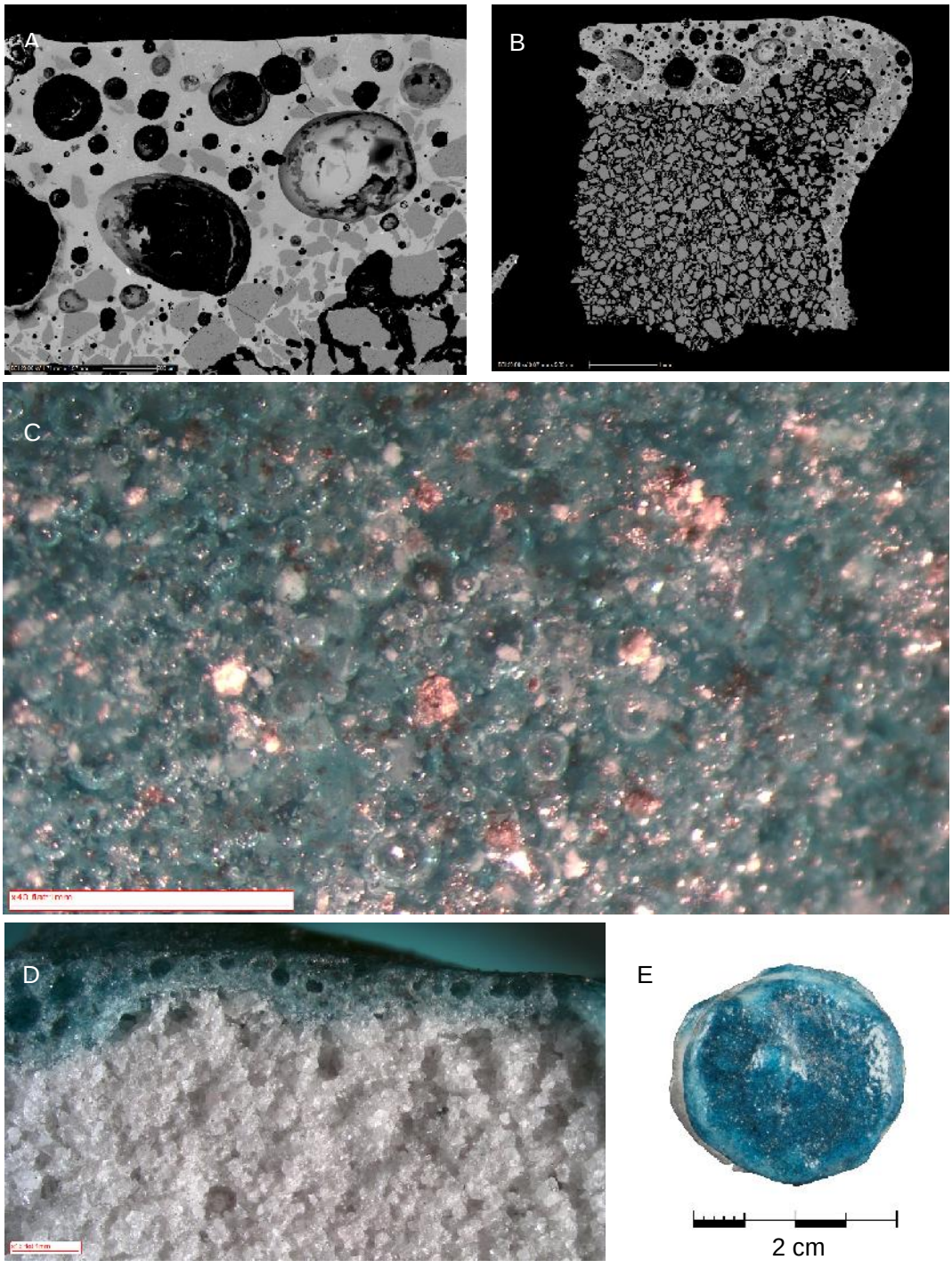

R360: SEM-BSE glaze profile (scale: 200 µm (A) and 1 mm (B)); OM glaze surface micrograph (C (scale: 1 mm)); OM glaze profile (D (scale: 1 mm)) and the replicate prior to sampling (E). The BSE profiles (A and B) reveal major bubbles and unreacted quartz in the glaze. The IAL is thin with smaller bubbles are evolving in-between the unreacted quartz. Bubbles and unreacted quartz are evident below the glaze surface (C). Several of the unreacted quartz particles has erupted through the glaze surface. The OM profile (D) shows massed sintered quartz particles in the body.

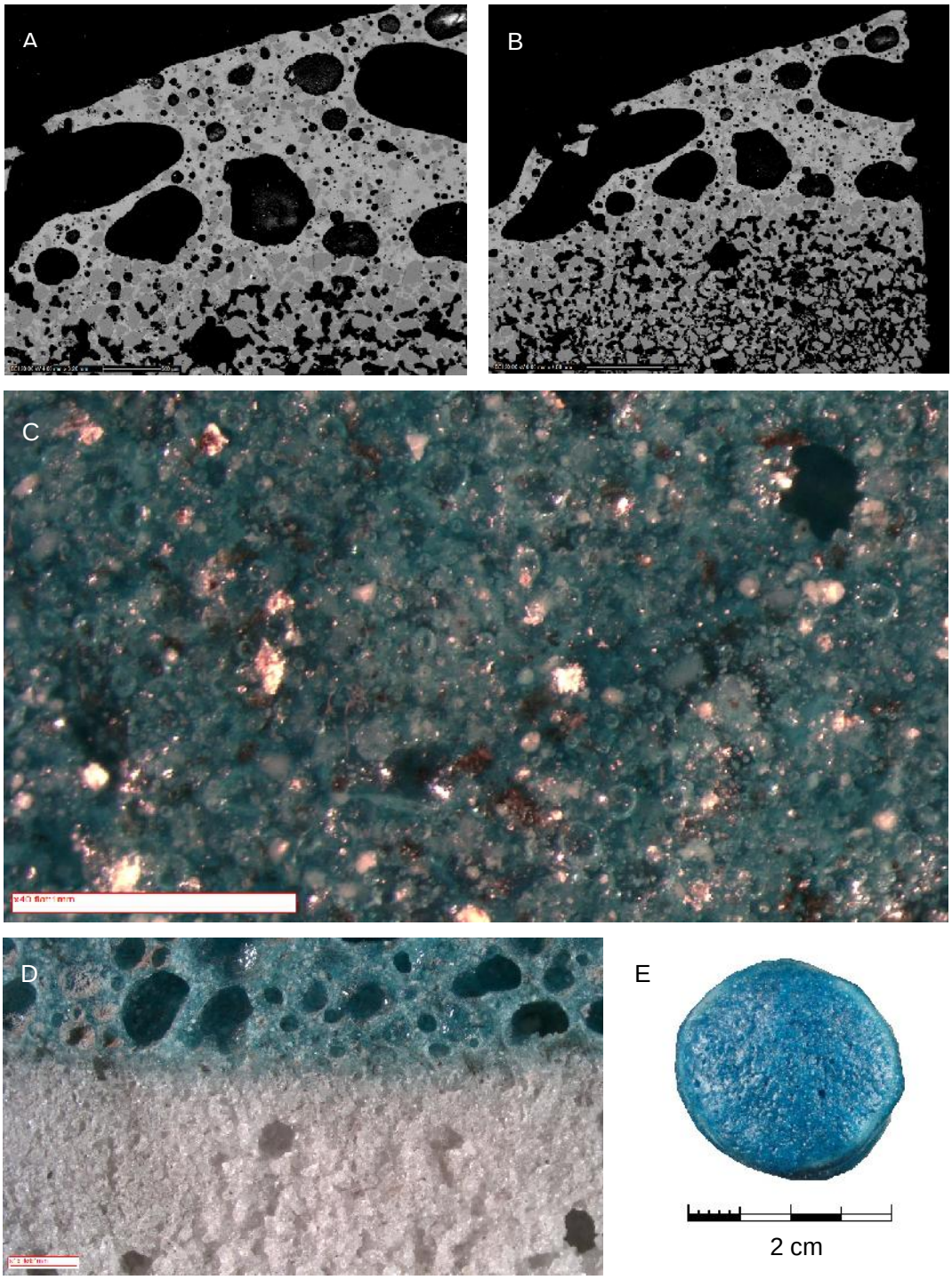

R363: SEM-BSE glaze profile (scale: 500 µm (A) and 1 mm (B)); OM glaze surface micrograph (C (scale: 1 mm)); OM glaze profile (D (scale: 1 mm)) and the replicate prior to sampling (E). The BSE profiles (A and B) reveal major bubbles and unreacted quartz in the glaze. The IAL is thin with smaller bubbles are evolving in-between the unreacted quartz. Bubbles and unreacted quartz are evident below the glaze surface (C). An erupting bubble is evident in the top right corner of the photomicrograph. The OM profile (D) shows massed sintered quartz particles in the body. The porosity of the body and glaze is evident. The faience replicate glaze surface (E) has an orange peel texture with erupting bubbles present.

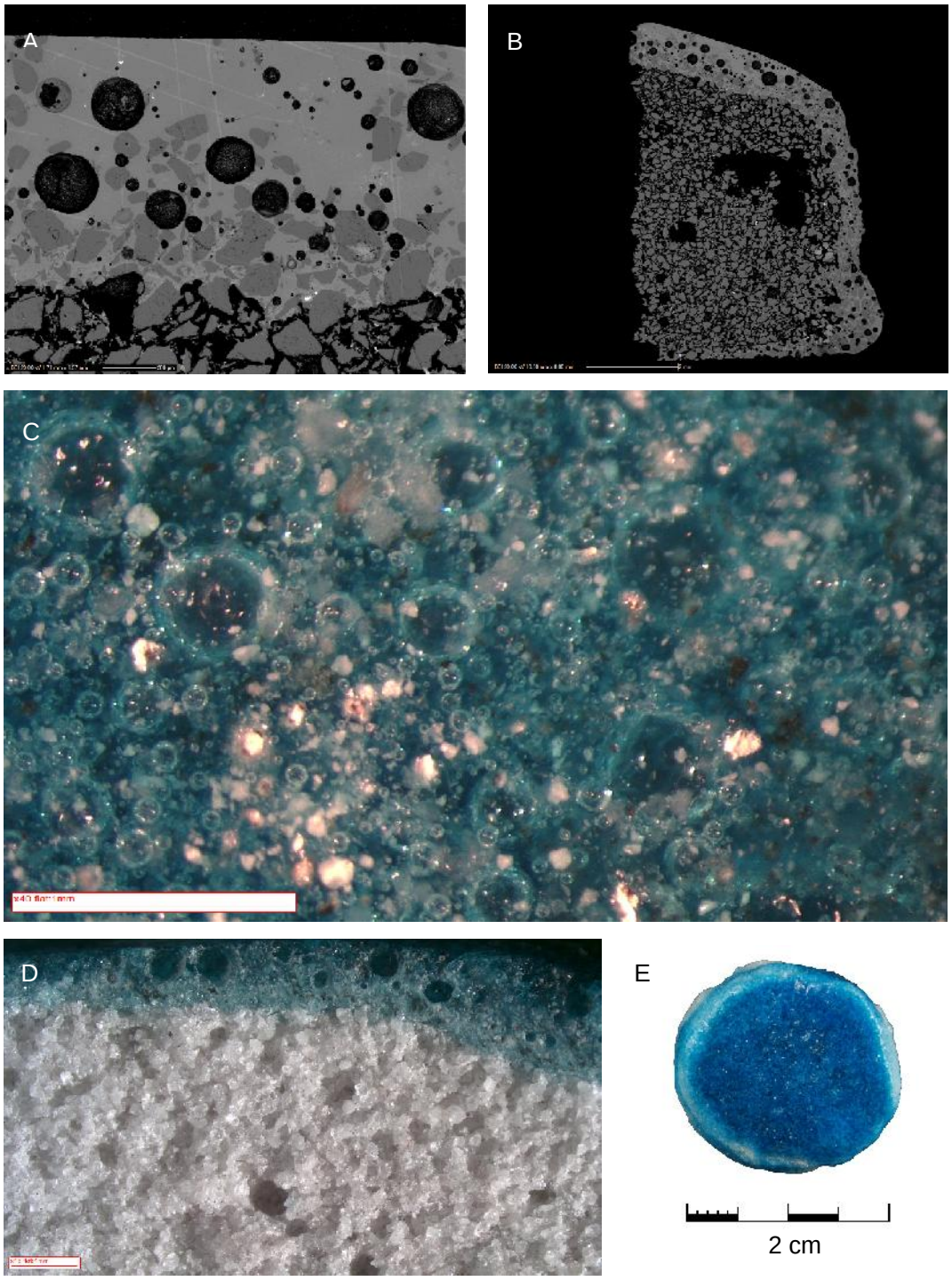

R364: SEM-BSE glaze profile (scale: 200 µm (A) and 2 mm (B)); OM glaze surface micrograph (C (scale: 1 mm)); OM glaze profile (D (scale: 1 mm)) and the replicate prior to sampling (E). The BSE profiles (A and B) reveal bubbles with some unreacted quartz in the glaze. The IAL is relatively thin with smaller bubbles evolving in-between the unreacted quartz. The cross-hatching in A is resultant of incomplete polishing of the resin sample block. Bubbles and unreacted quartz are evident below the glaze surface (C). Unreacted quartz has erupted through the glaze surface. The OM profile (D) shows massed sintered quartz particles in the body.

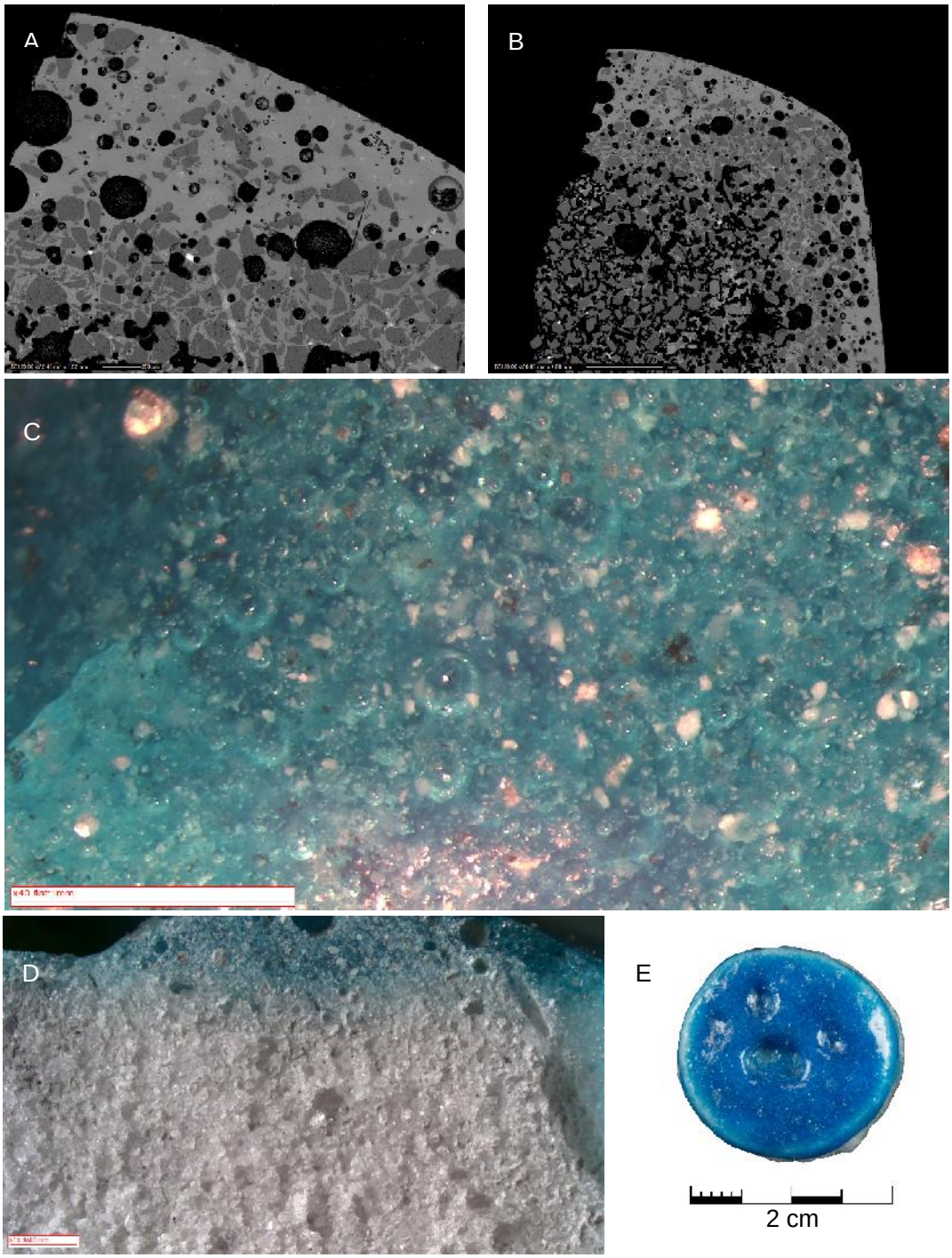

R367: SEM-BSE glaze profile (scale: 200 µm (A) and 1 mm (B)); OM glaze surface micrograph (C (scale: 1 mm)); OM glaze profile (D (scale: 1 mm)) and the replicate prior to sampling (E). The BSE profiles (A and B) reveal bubbles with some unreacted quartz in the glaze. The IAL is moderately thick with smaller bubbles evolving in-between the unreacted quartz. The straight black line center-right of A is probably carbon fibre from the carbon coating process. Bubbles and unreacted quartz are evident below the glaze surface (C). Some unreacted quartz has erupted through the glaze surface. The OM profile (D) shows massed sintered quartz particles in the body. Large erupting bubbles are evident on the faience replicate glaze surface (E).

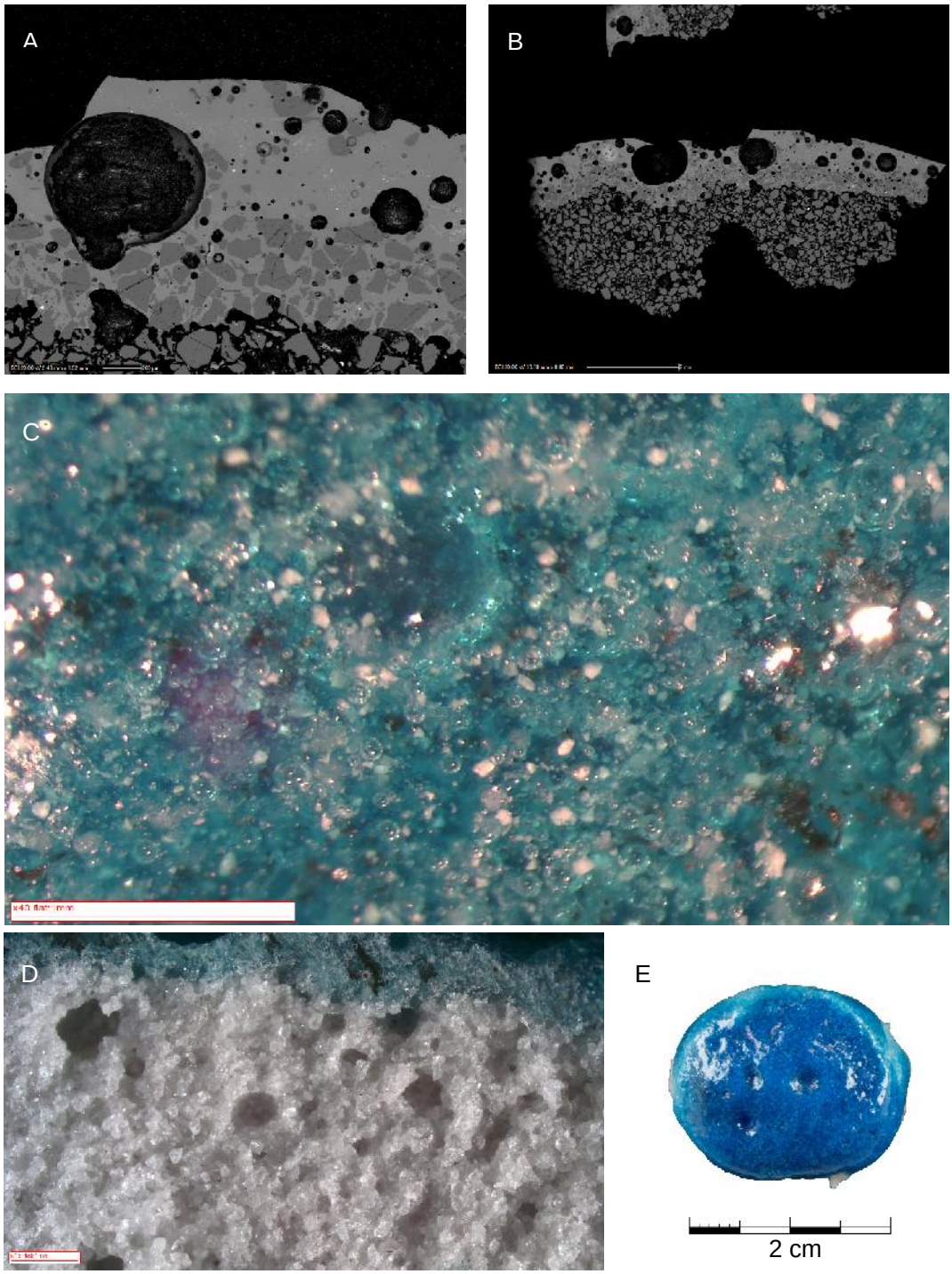

R383: SEM-BSE glaze profile (scale: 200 µm (A) and 2 mm (B)); OM glaze surface micrograph (C (scale: 1 mm)); OM glaze profile (D (scale: 1 mm)) and the replicate prior to sampling (E). The BSE profiles (A and B) reveal bubbles of various diameter with minor unreacted quartz in the glaze. The IAL is moderately thick with smaller bubbles evolving in-between the unreacted quartz. Bubbles and unreacted quartz are evident below the glaze surface (C). The OM profile (D) shows massed sintered quartz particles in the body. Large partially filled erupting bubbles are evident on the faience replicate glaze surface (E).

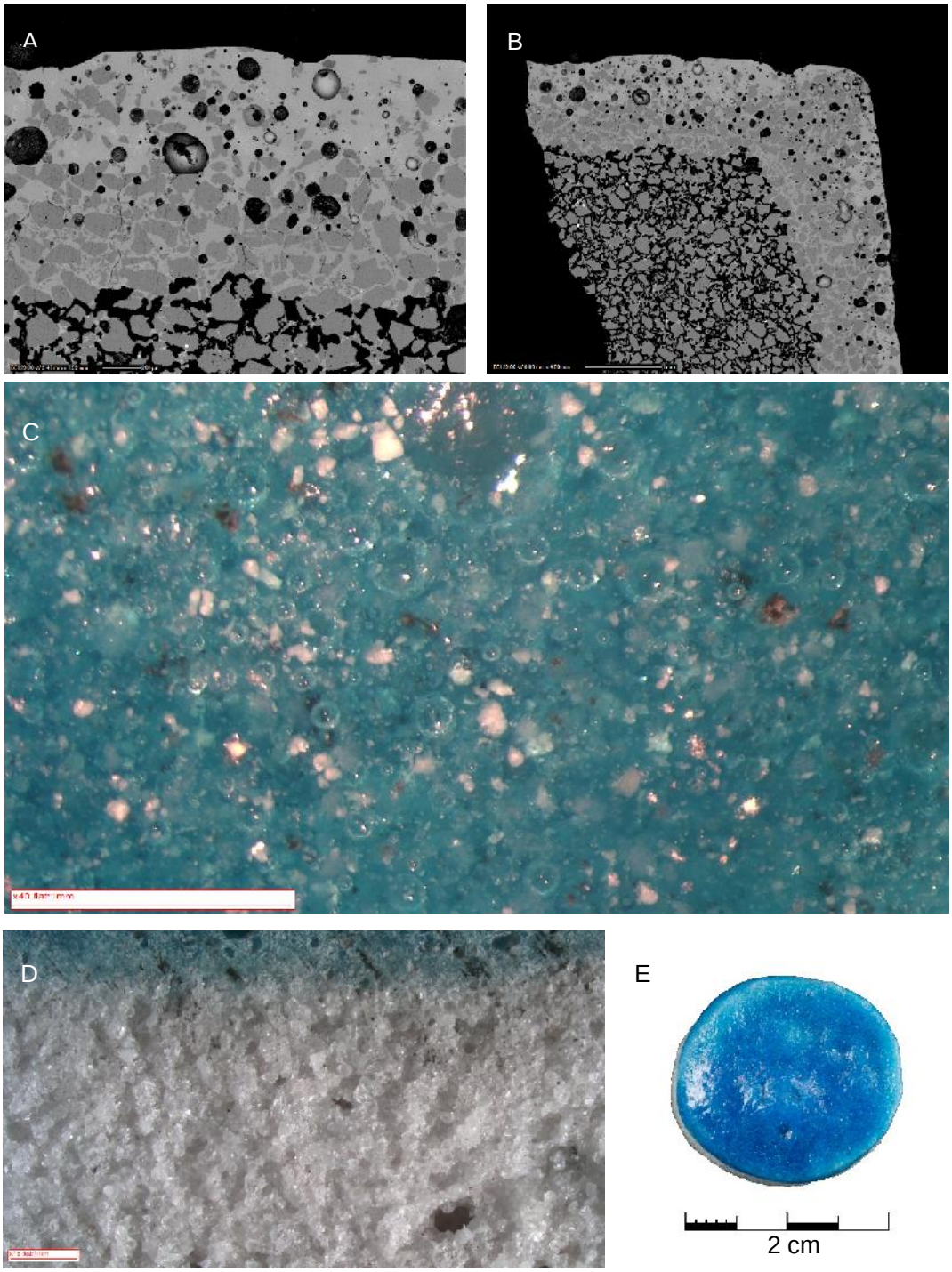

R384: SEM-BSE glaze profile (scale: 200 µm (A) and 1 mm (B)); OM glaze surface micrograph (C (scale: 1 mm)); OM glaze profile (D (scale: 1 mm)) and the replicate prior to sampling (E). The BSE profiles (A and B) reveal bubbles with unreacted quartz in the glaze. The IAL is moderately thick with smaller bubbles evolving in-between the unreacted quartz. Bubbles and unreacted quartz are evident below the glaze surface (C). The OM profile (D) shows massed sintered quartz particles in the body.

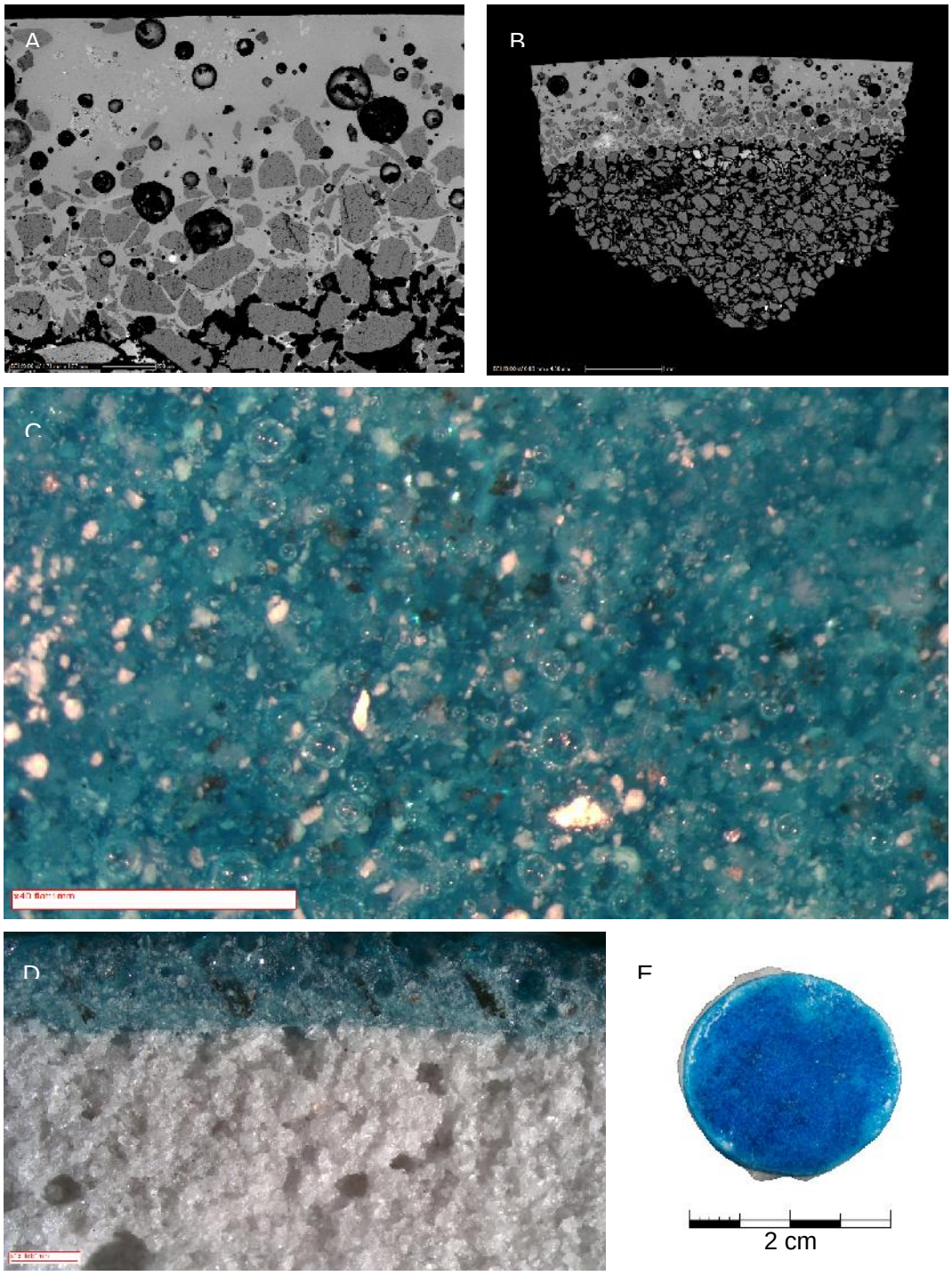

R386: SEM-BSE glaze profile (scale: 200 µm (A) and 1 mm (B)); OM glaze surface micrograph (C (scale: 1 mm)); OM glaze profile (D (scale: 1 mm)) and the replicate prior to sampling (E). The BSE profiles (A and B) reveal bubbles with unreacted quartz in the glaze. The IAL is moderately thick with smaller bubbles evolving in-between the unreacted quartz. The bright particles in the IAL are unreacted calcium particles confirmed through SEM-EDS spot analysis. Bubbles and unreacted quartz are evident below the glaze surface (C). Some unreacted quartz particles are erupting through the glaze surface. The OM profile (D) shows massed sintered quartz particles in the body.

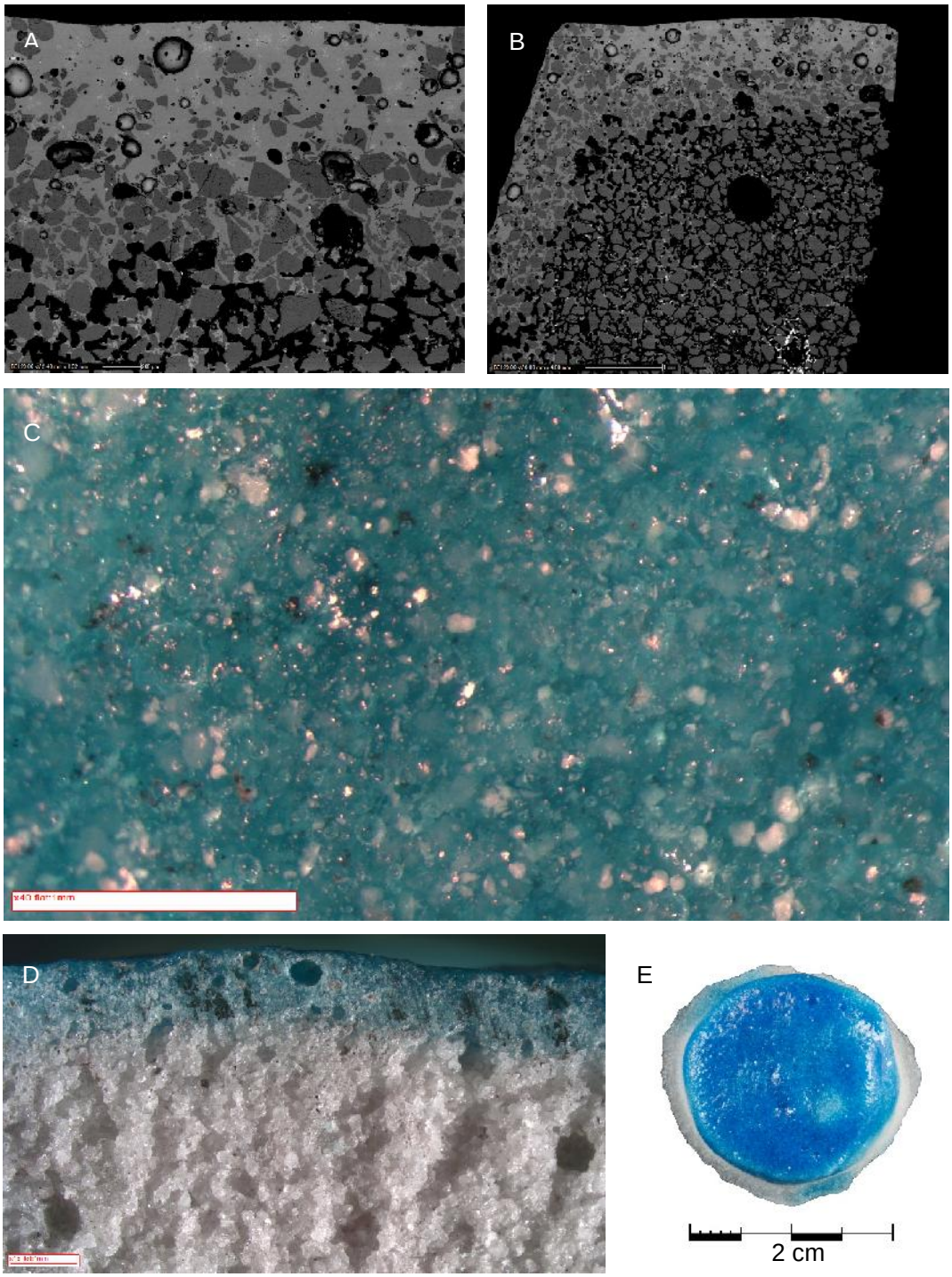

R388: SEM-BSE glaze profile (scale: 200 µm (A) and 1 mm (B)); OM glaze surface micrograph (C (scale: 1 mm)); OM glaze profile (D (scale: 1 mm)) and the replicate prior to sampling (E). The BSE profiles (A and B) reveal bubbles with unreacted quartz in the glaze. The IAL is moderately thick with smaller bubbles evolving in-between the unreacted quartz. Bubbles and unreacted quartz are evident below the glaze surface (C). The OM profile (D) shows massed sintered quartz particles in the body. The faience replicate glaze surface (E) reveals some partially filled erupted bubbles.

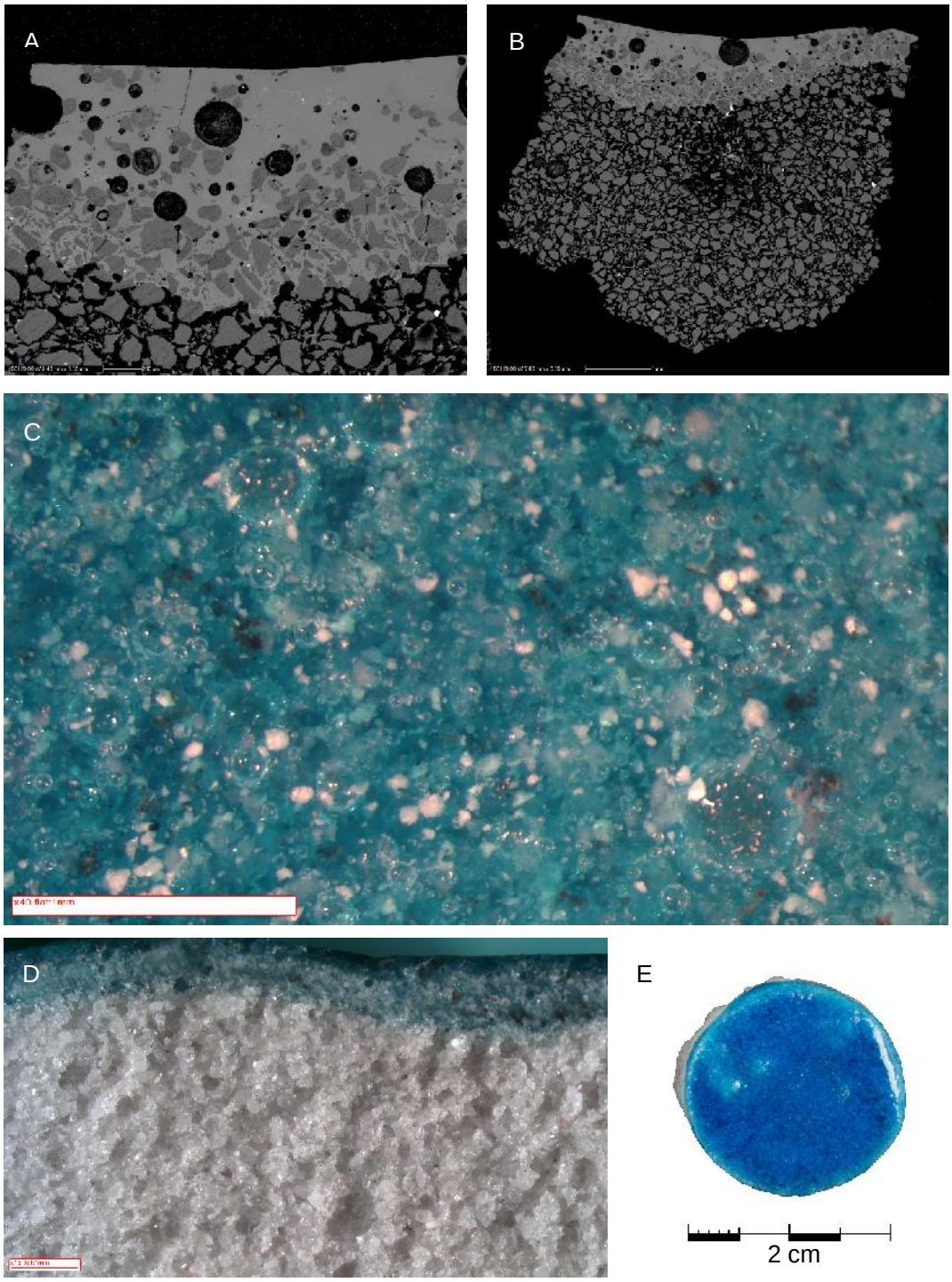

R390: SEM-BSE glaze profile (scale: 200 µm (A) and 1 mm (B)); OM glaze surface micrograph (C (scale: 1 mm)); OM glaze profile (D (scale: 1 mm)) and the replicate prior to sampling (E). The BSE profiles (A and B) reveal bubbles with minor unreacted quartz in the glaze. The IAL is moderately thick with smaller bubbles evolving in-between the unreacted quartz. Bubbles and unreacted quartz are evident below the glaze surface (C). The OM profile (D) shows massed sintered quartz particles in the body.

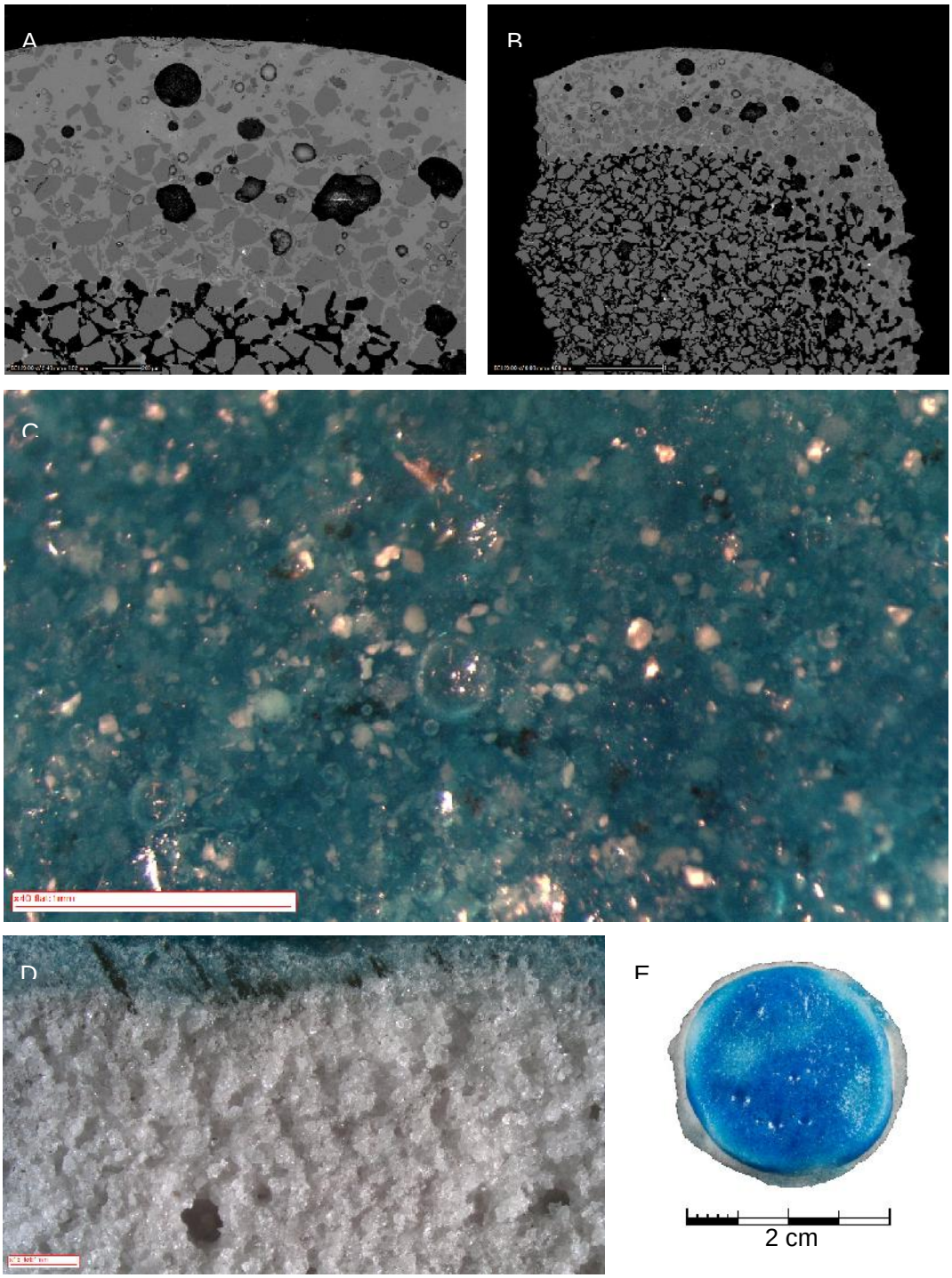

R392: SEM-BSE glaze profile (scale: 200 µm (A) and 1 mm (B)); OM glaze surface micrograph (C (scale: 1 mm)); OM glaze profile (D (scale: 1 mm)) and the replicate prior to sampling (E). The BSE profiles (A and B) reveal bubbles with moderate unreacted quartz in the glaze. The IAL is relatively thick with smaller bubbles evolving in-between the unreacted quartz. Bubbles and unreacted quartz are evident below the glaze surface (C). The OM profile (D) shows massed sintered quartz particles in the body. The faience replicate glaze surface (E) reveals some partially filled erupted bubbles.

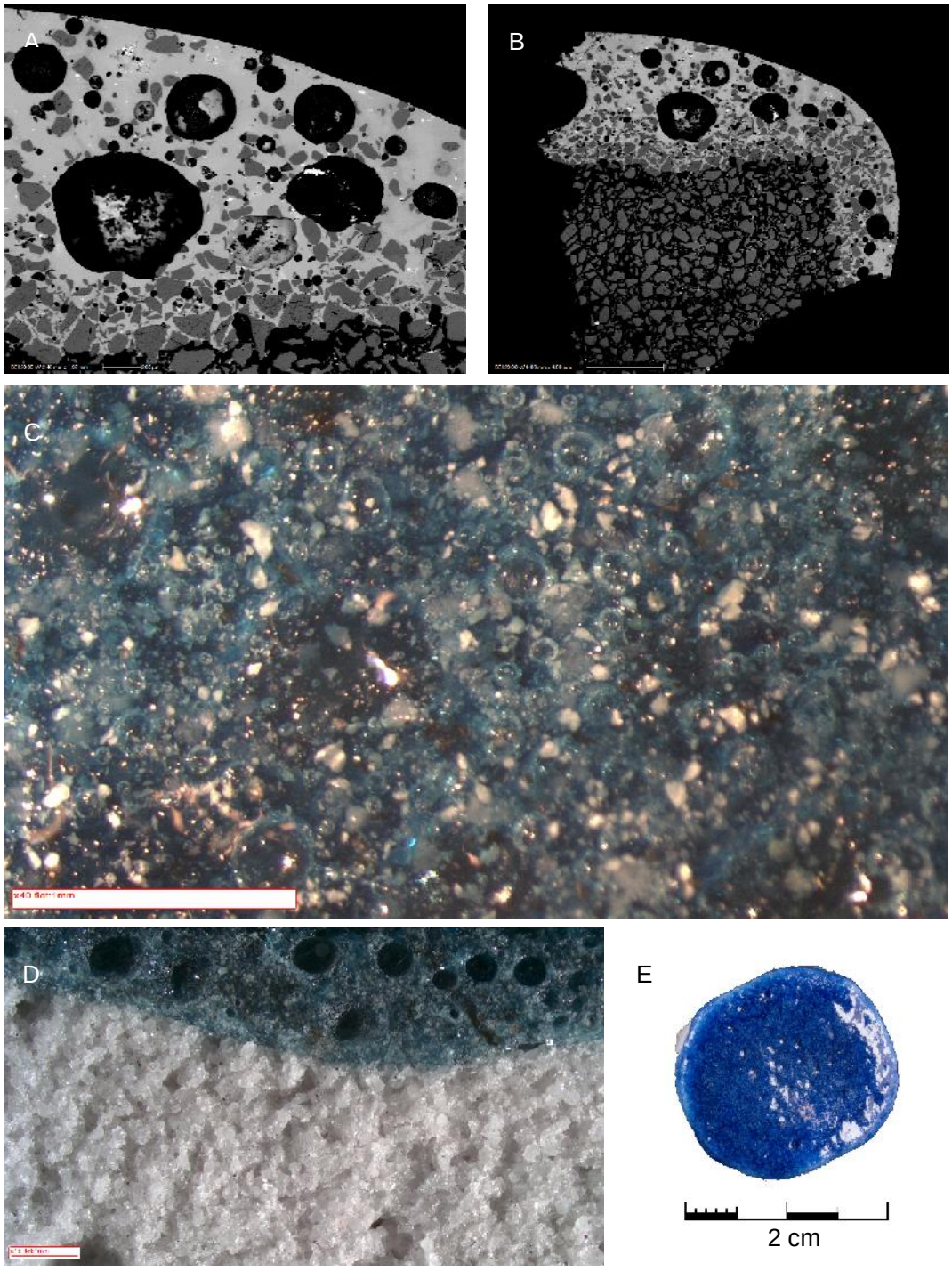

R406: SEM-BSE glaze profile (scale: 200 µm (A) and 1 mm (B)); OM glaze surface micrograph (C (scale: 1 mm)); OM glaze profile (D (scale: 1 mm)) and the replicate prior to sampling (E). The BSE profiles (A and B) reveal large bubble formation with unreacted quartz in the glaze. The IAL is thin with smaller bubbles evolving in-between the unreacted quartz. Bright spots in the glaze and body are tin particles confirmed through SEM-EDS spot analysis. Bubbles and unreacted quartz are evident below the glaze surface (C). The OM profile (D) shows massed sintered quartz particles in the body. The faience replicate glaze surface (E) reveals some partially filled erupted bubbles.

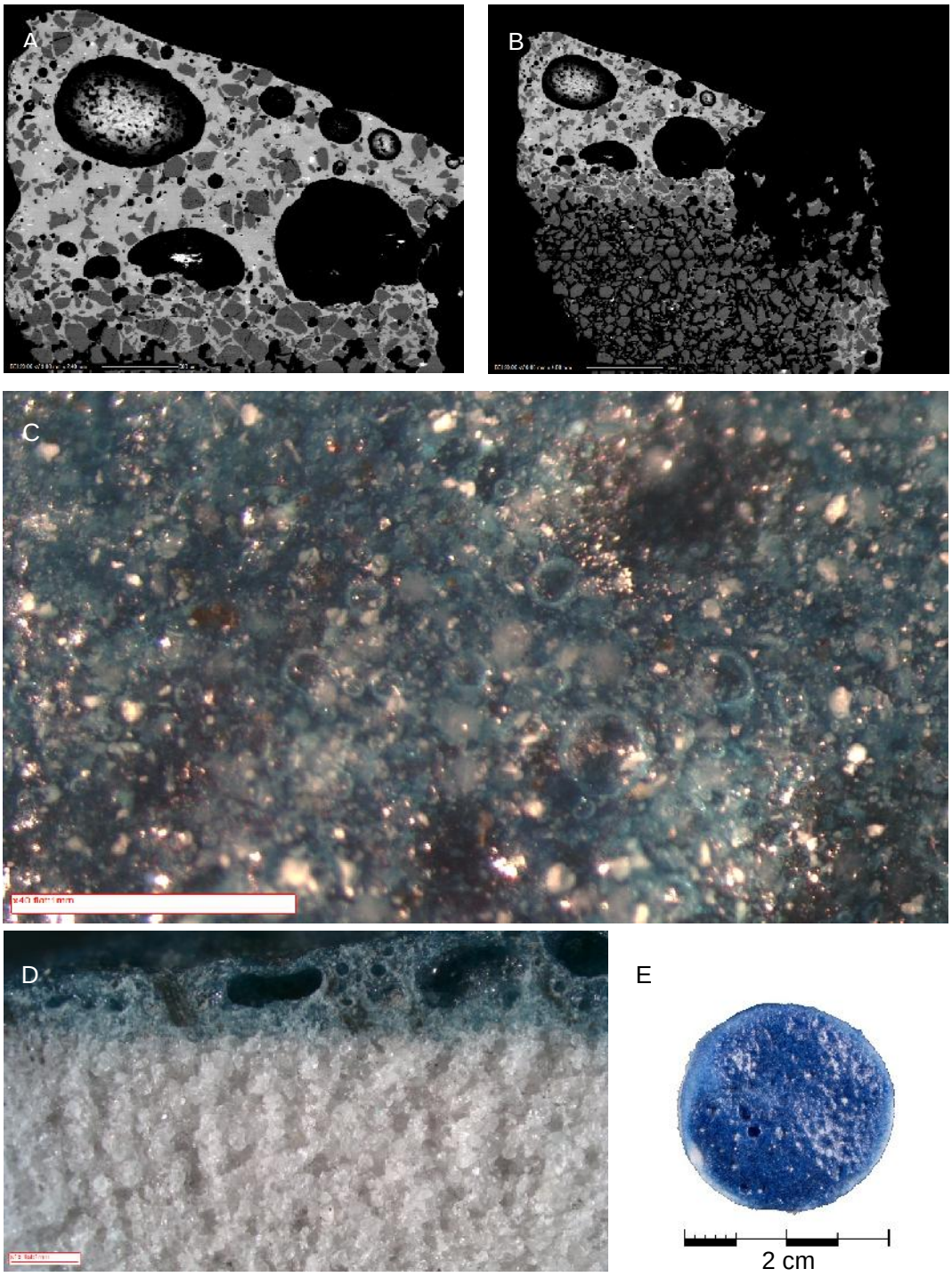

R408: SEM-BSE glaze profile (scale: 200 µm (A) and 1 mm (B)); OM glaze surface micrograph (C (scale: 1 mm)); OM glaze profile (D (scale: 1 mm)) and the replicate prior to sampling (E). The BSE profiles (A and B) reveal large bubble formation with unreacted quartz in the glaze. The IAL is thin with smaller bubbles evolving in-between the unreacted quartz. Bright spots in the glaze and body are tin particles confirmed through SEM-EDS spot analysis. Bubbles and unreacted quartz are evident below the glaze surface (C). The OM profile (D) shows massed sintered quartz particles in the body. The faience replicate glaze orange-peel textured surface (E) reveals partially filled erupted bubbles.

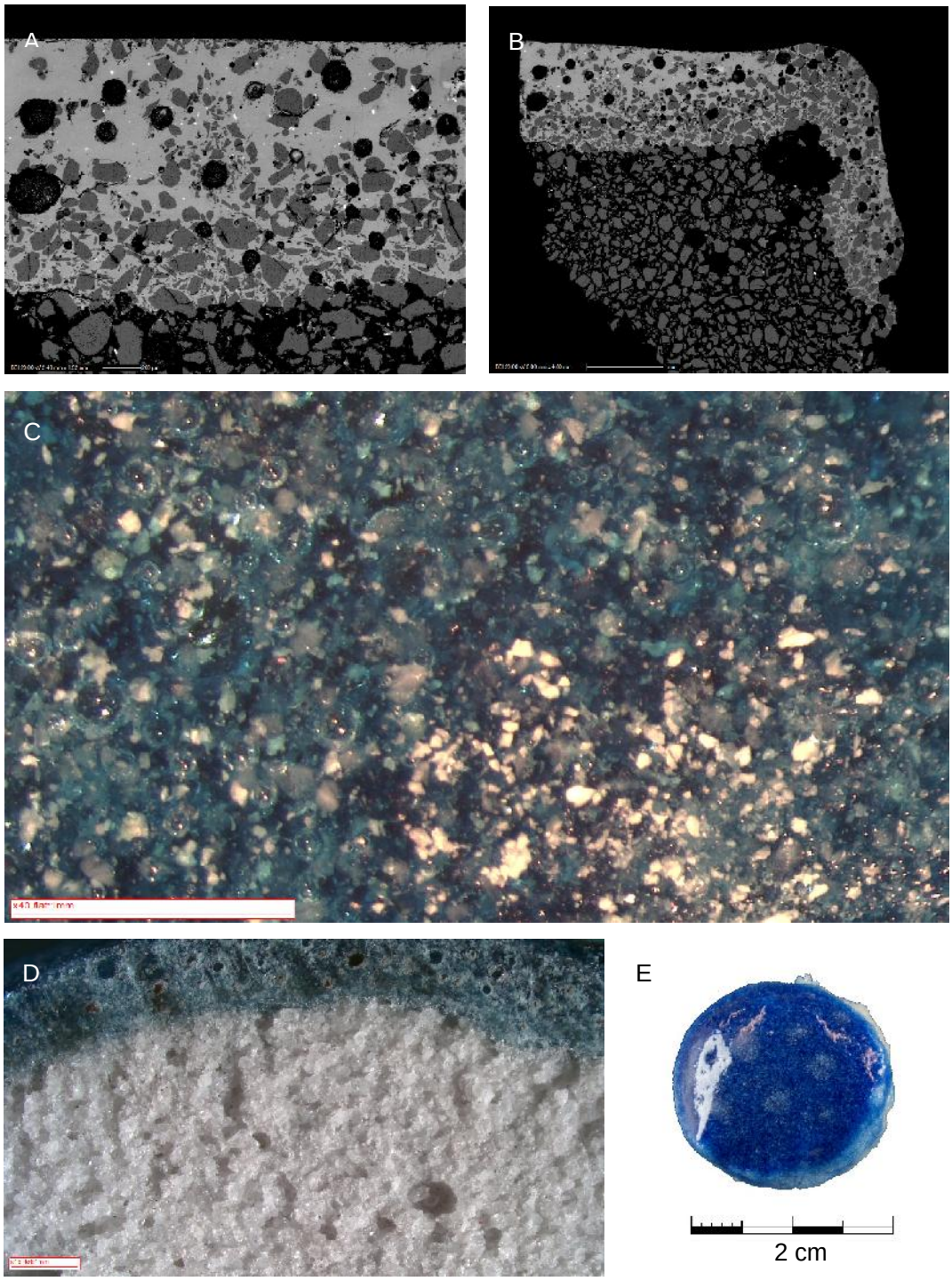

R411: SEM-BSE glaze profile (scale: 200 µm (A) and 1 mm (B)); OM glaze surface micrograph (C (scale: 1 mm)); OM glaze profile (D (scale: 1 mm)) and the replicate prior to sampling (E). The BSE profiles (A and B) reveal bubble formation with unreacted quartz in the glaze. The IAL is moderately thick with smaller bubbles evolving in-between the unreacted quartz. Bright spots in the glaze and body are tin particles confirmed through SEM-EDS spot analysis. Bubbles and unreacted quartz are evident below the glaze surface (C). The OM profile (D) shows massed sintered quartz particles in the body.

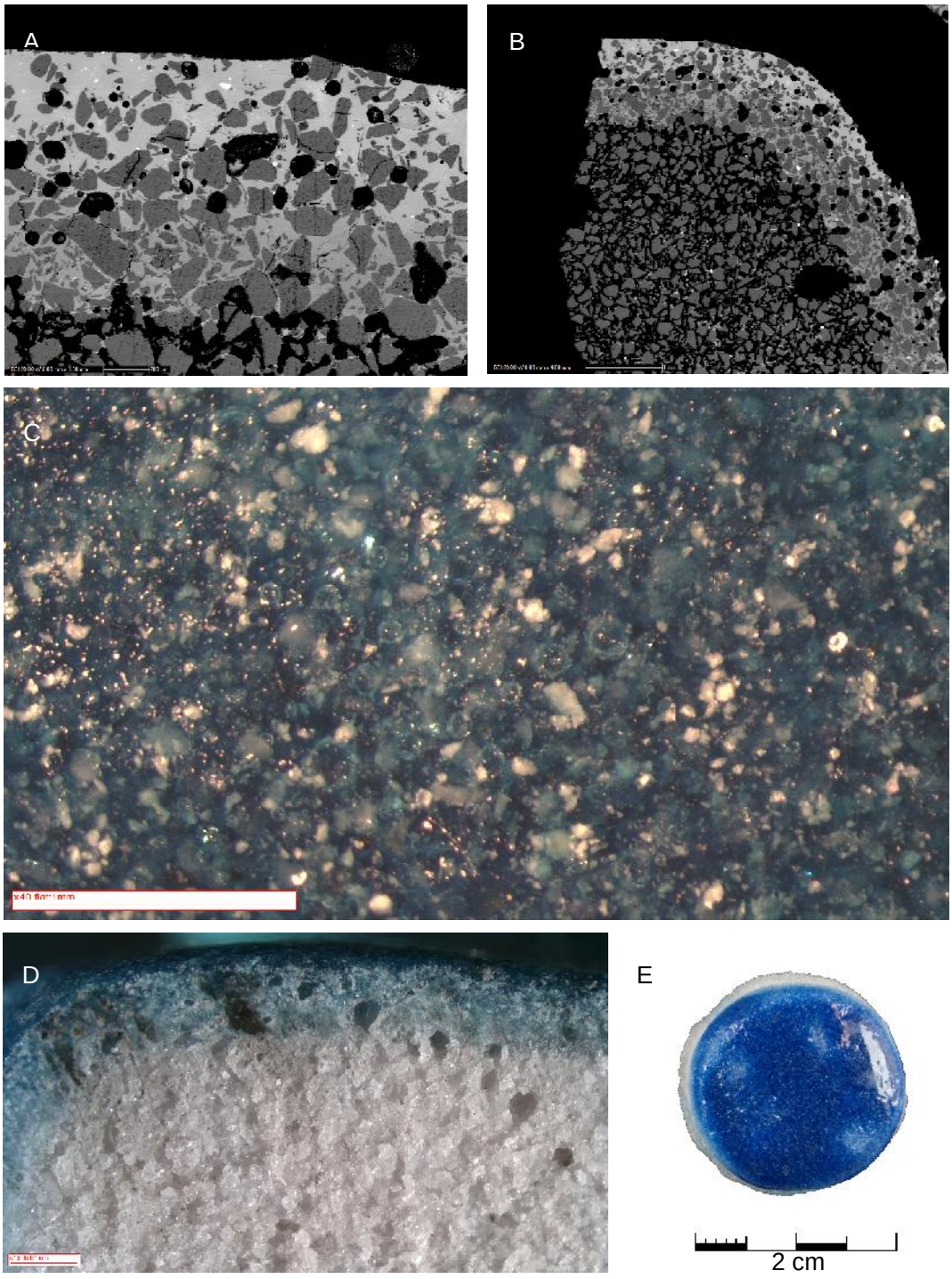

R412: SEM-BSE glaze profile (scale: 200 µm (A) and 1 mm (B)); OM glaze surface micrograph (C (scale: 1 mm)); OM glaze profile (D (scale: 1 mm)) and the replicate prior to sampling (E). The BSE profiles (A and B) reveal bubble formation with abundant unreacted quartz in the glaze. The IAL is relatively thick with smaller bubbles evolving in-between the unreacted quartz. Bright spots in the glaze and body are tin particles confirmed through SEM-EDS spot analysis. Bubbles and unreacted quartz are evident below the glaze surface (C). The OM profile (D) shows massed sintered quartz particles in the body.

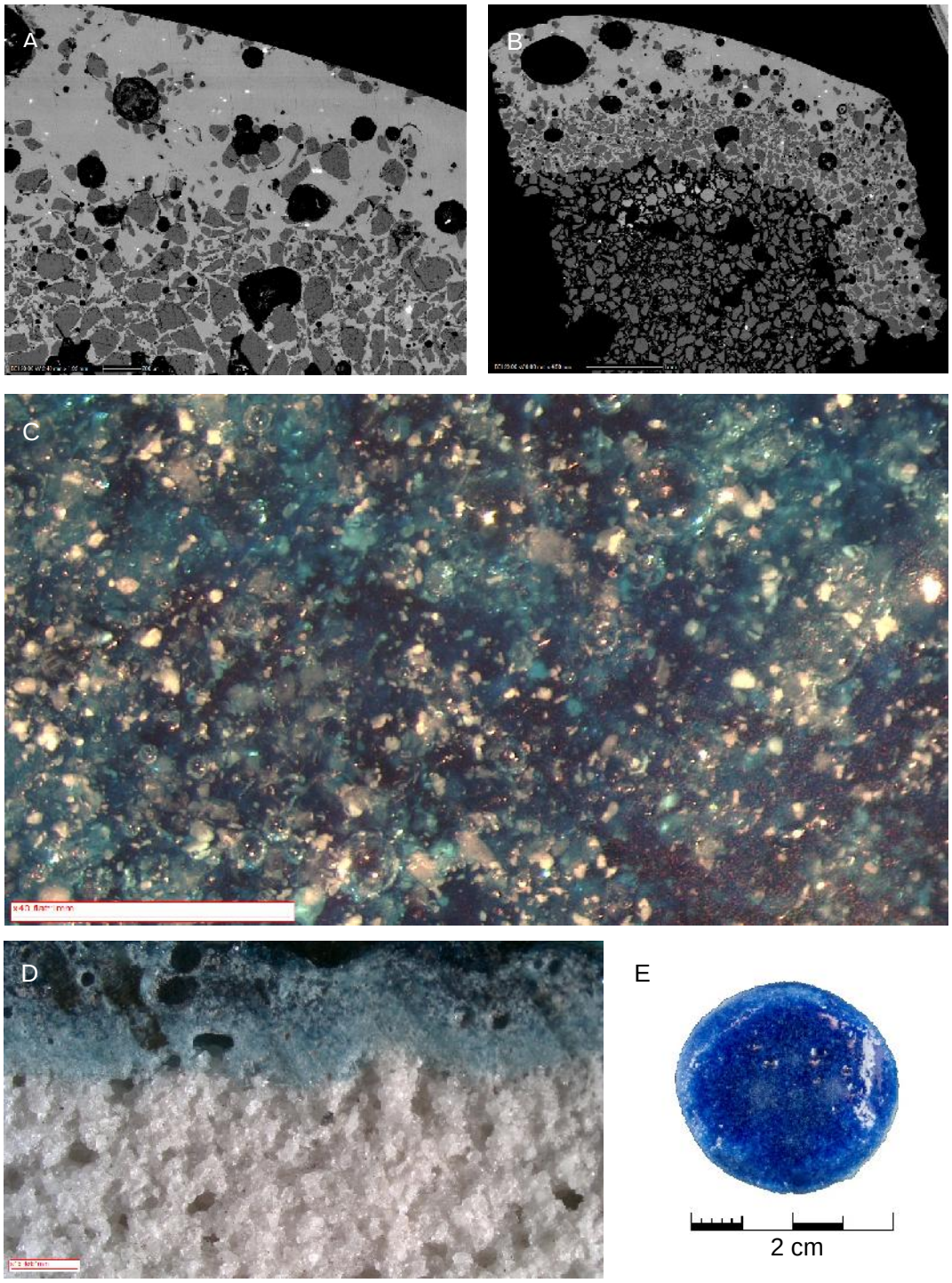

R415: SEM-BSE glaze profile (scale: 200 µm (A) and 1 mm (B)); OM glaze surface micrograph (C (scale: 1 mm)); OM glaze profile (D (scale: 1 mm)) and the replicate prior to sampling (E). The BSE profiles (A and B) reveal large bubble formation with unreacted quartz in the glaze. The IAL is moderately thick with smaller bubbles evolving in-between the unreacted quartz. Bright spots in the glaze and body are tin particles confirmed through SEM-EDS spot analysis. Bubbles and unreacted quartz are evident below the glaze surface (C). The OM profile (D) shows massed sintered quartz particles in the body. The faience replicate glaze surface (E) reveals partially filled erupted bubbles.

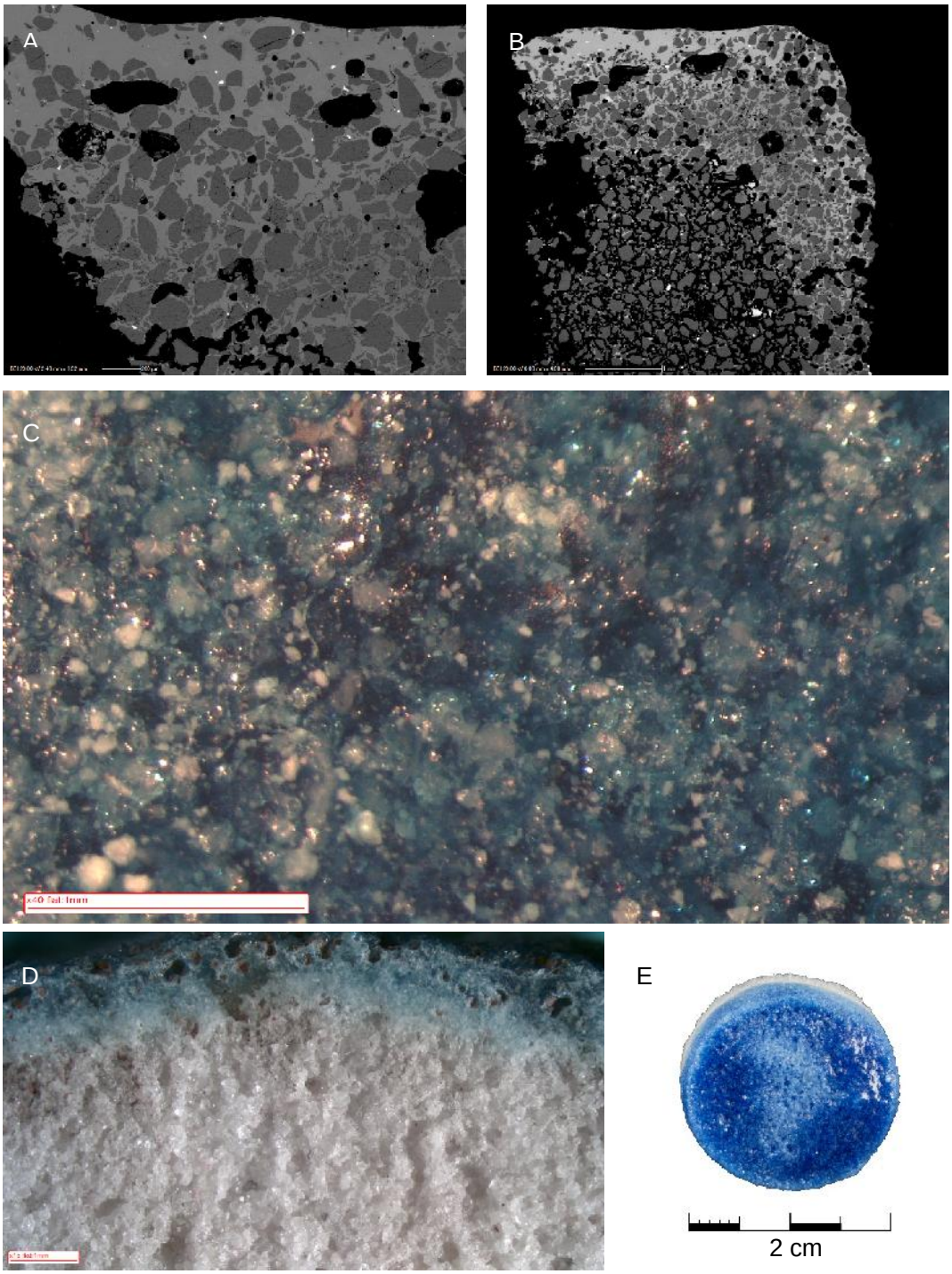

R416: SEM-BSE glaze profile (scale: 200 µm (A) and 1 mm (B)); OM glaze surface micrograph (C (scale: 1 mm)); OM glaze profile (D (scale: 1 mm)) and the replicate prior to sampling (E). The BSE profiles (A and B) reveal large bubble formation with unreacted quartz in the glaze. The IAL is thick with smaller bubbles evolving in-between the unreacted quartz. Bright spots in the glaze and body are tin particles confirmed through SEM-EDS spot analysis. Bubbles and unreacted quartz are evident below the glaze surface (C). The OM profile (D) shows massed sintered quartz particles in the body. The faience replicate glaze orange-peel textured surface (E) reveals partially filled erupted bubbles.

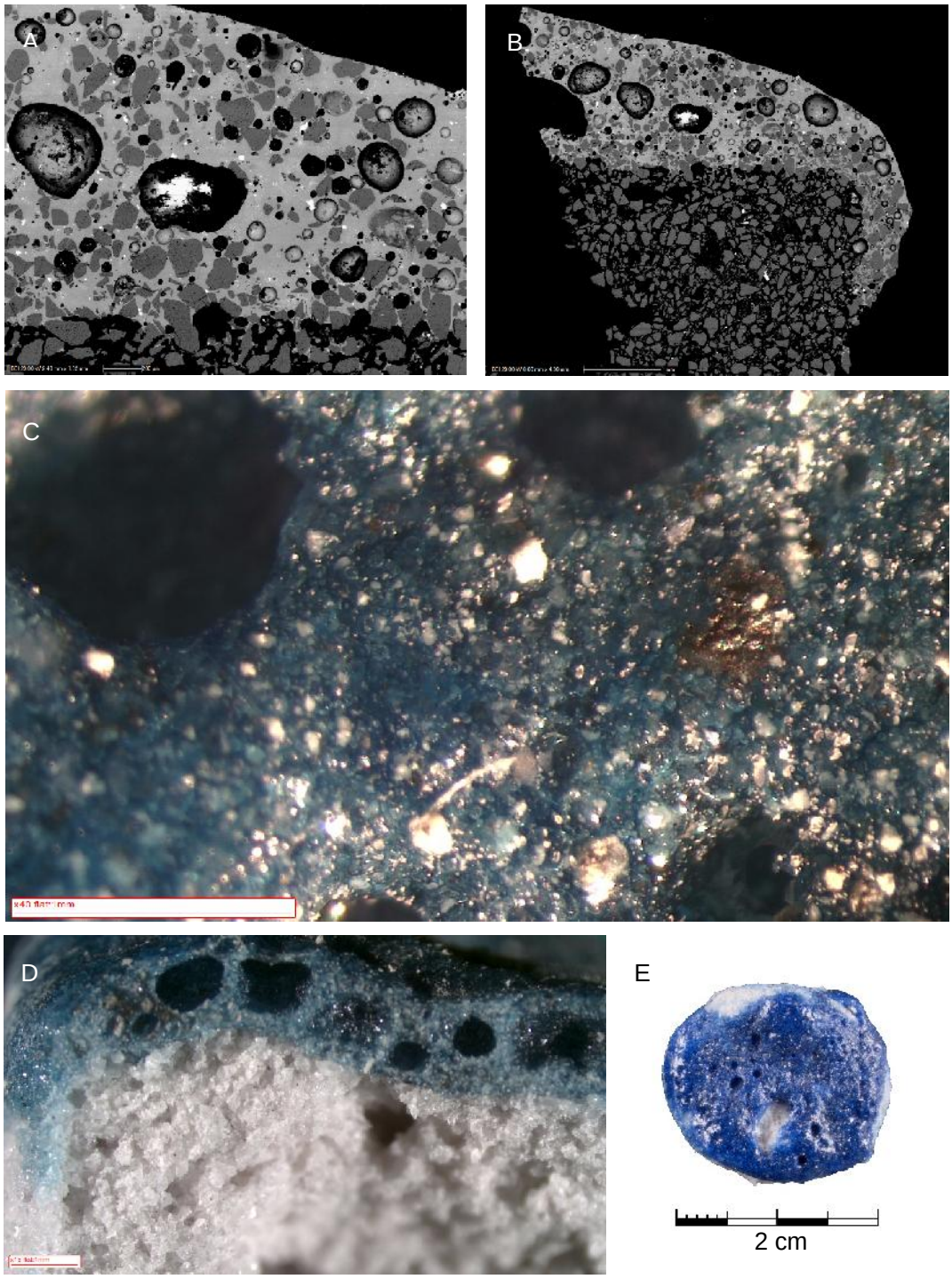

R418: SEM-BSE glaze profile (scale: 200 µm (A) and 1 mm (B)); OM glaze surface micrograph (C (scale: 1 mm)); OM glaze profile (D (scale: 1 mm)) and the replicate prior to sampling (E). The BSE profiles (A and B) reveal large bubble formation with abundant unreacted quartz in the glaze. The IAL is thin with smaller bubbles evolving in-between the unreacted quartz. Bright spots in the glaze and body are tin particles confirmed through SEM-EDS spot analysis. Bubbles and unreacted quartz are evident below the glaze surface (C). Erupting bubbles are also present. The OM profile (D) shows massed sintered quartz particles in the body. The faience replicate glaze orange-peel textured surface (E) reveals partially filled erupted bubbles. Glaze creep has also revealed the body substrate.

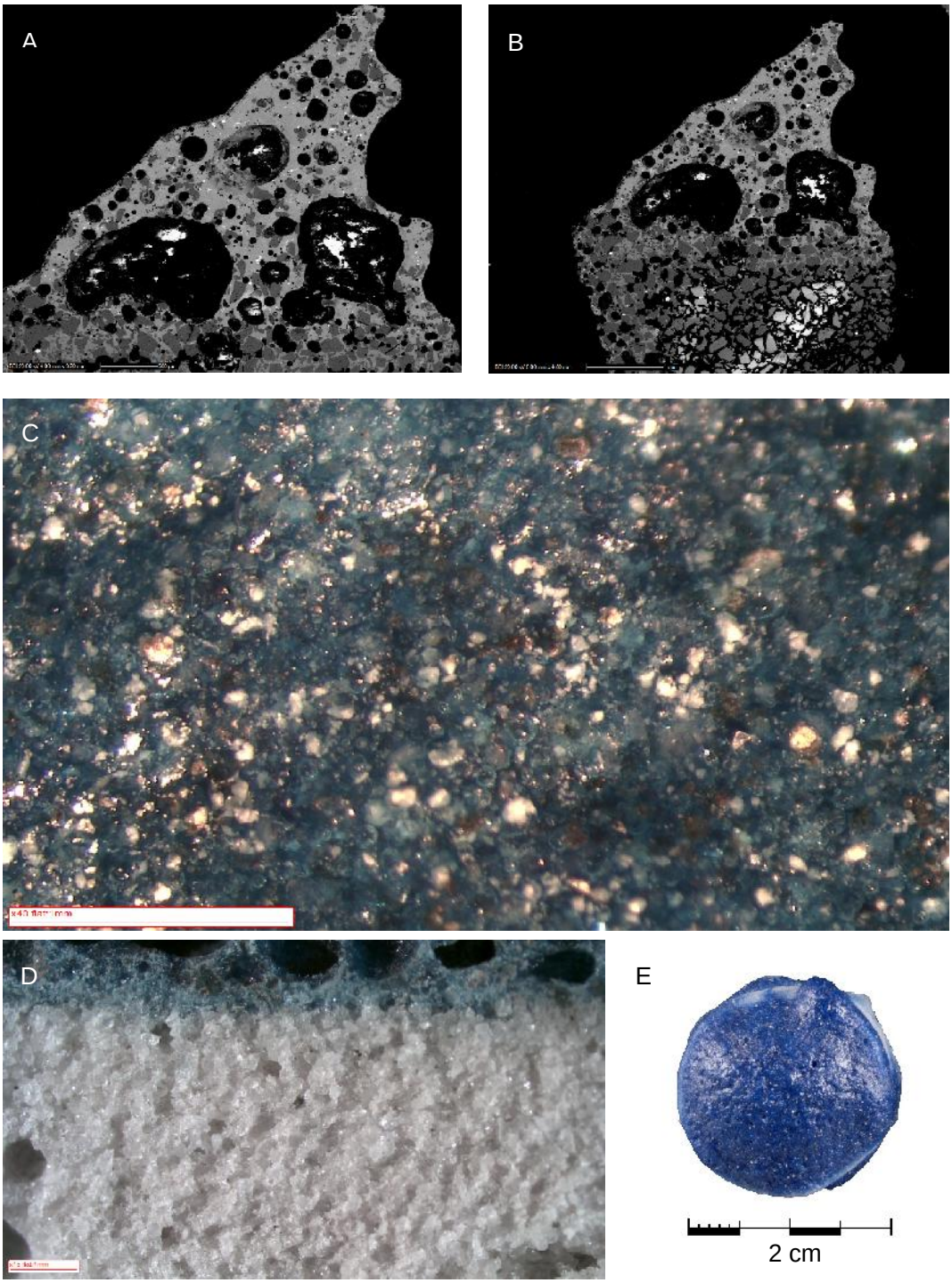

R421: SEM-BSE glaze profile (scale: 500 µm (A) and 1 mm (B)); OM glaze surface micrograph (C (scale: 1 mm)); OM glaze profile (D (scale: 1 mm)) and the replicate prior to sampling (E). The BSE profiles (A and B) reveal large bubble formation with abundant unreacted quartz in the glaze. The IAL is thin with smaller bubbles evolving in-between the unreacted quartz. Bright spots in the glaze and body are tin particles confirmed through SEM-EDS spot analysis. Bubbles and unreacted quartz are evident below the glaze surface (C). The OM profile (D) shows massed sintered quartz particles in the body. The faience replicate glaze orange-peel textured surface (E) reveals partially filled erupted bubbles.

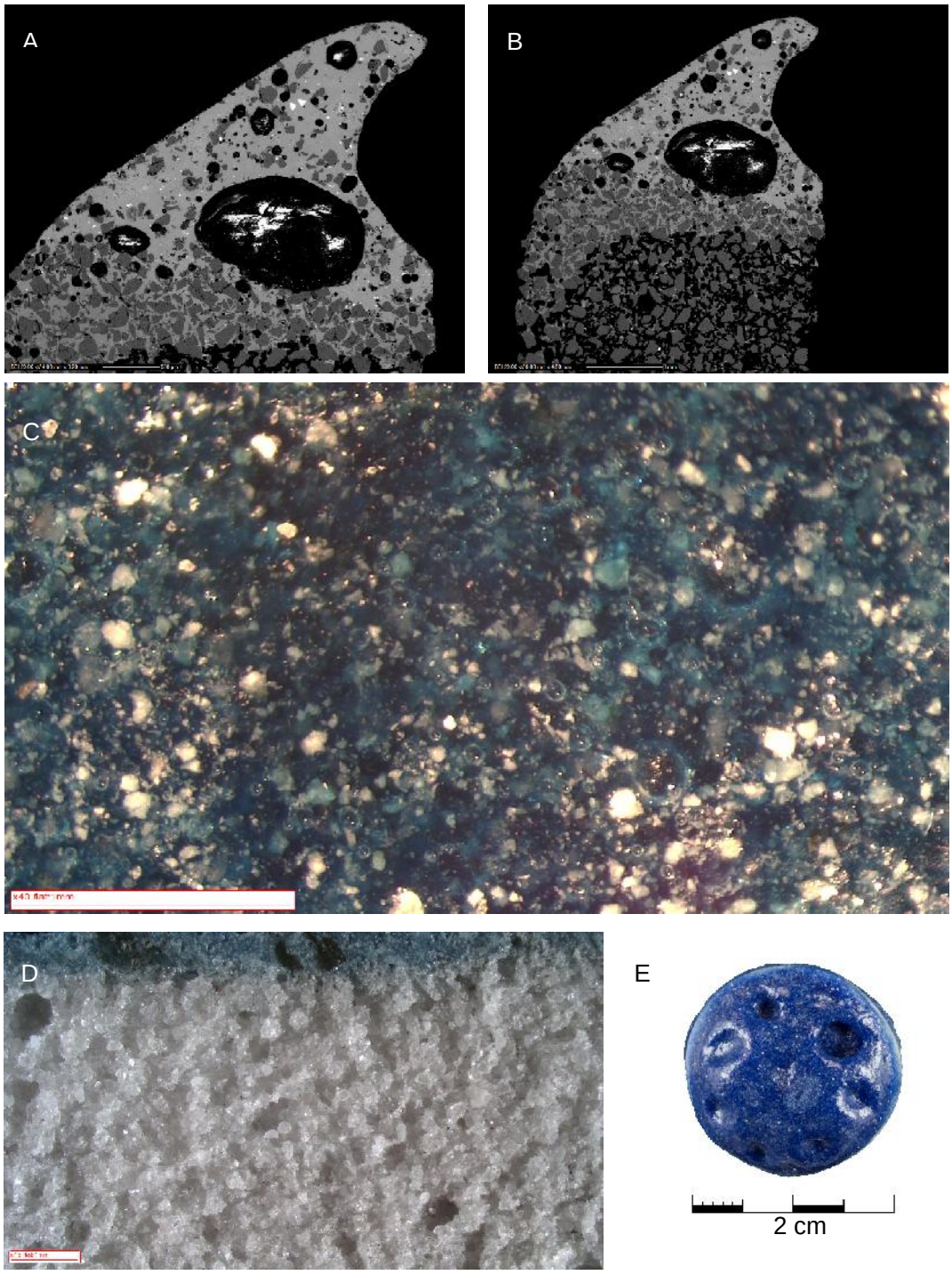

R423: SEM-BSE glaze profile (scale: 500 µm (A) and 1 mm (B)); OM glaze surface micrograph (C (scale: 1 mm)); OM glaze profile (D (scale: 1 mm)) and the replicate prior to sampling (E). The BSE profiles (A and B) reveal large bubble formation with abundant unreacted quartz in the glaze. The IAL is moderately thick with smaller bubbles evolving in-between the unreacted quartz. Bright spots in the glaze and body are tin particles confirmed through SEM-EDS spot analysis. Bubbles and unreacted quartz are evident below the glaze surface (C). Some unreacted quartz has erupted through the glaze surface. The OM profile (D) shows massed sintered quartz particles in the body. The faience replicate glaze surface (E) reveals large partially filled erupted bubbles.

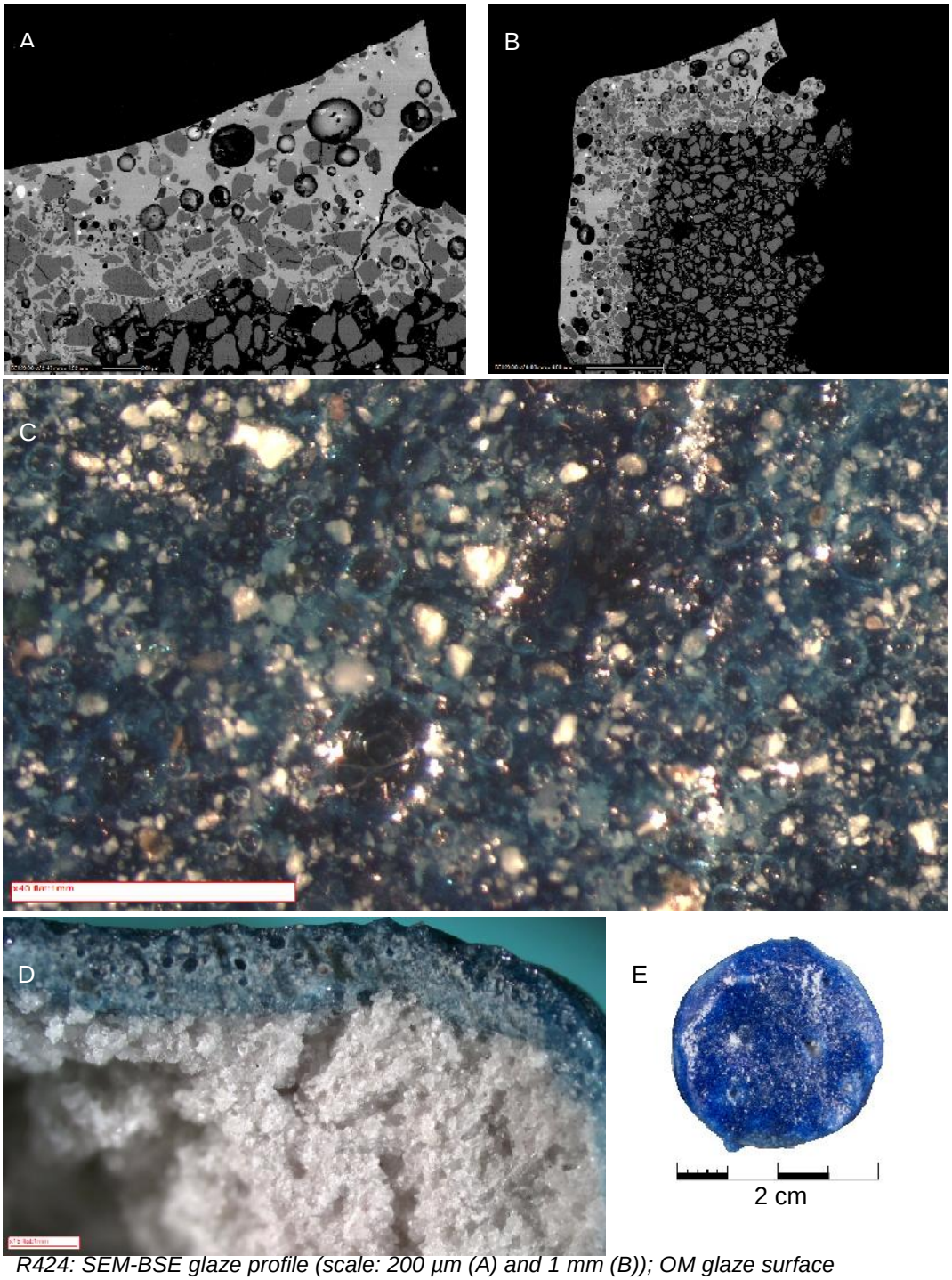

R424: SEM-BSE glaze profile (scale: 200 µm (A) and 1 mm (B)); OM glaze surface micrograph (C (scale: 1 mm)); OM glaze profile (D (scale: 1 mm)) and the replicate prior to sampling (E). The BSE profiles (A and B) reveal bubble formation with abundant unreacted quartz in the glaze. The IAL is thin with smaller bubbles evolving in-between the unreacted quartz. Bright spots in the glaze and body are tin particles confirmed through SEM-EDS spot analysis. Bubbles and unreacted quartz are evident below the glaze surface (C). Some unreacted quartz has erupted through the glaze surface. The OM profile (D) shows massed sintered quartz particles in the body. The faience replicate glaze orange-peel textured surface (E) reveals partially filled erupted bubbles. A large unfilled bubble crater has revealed the body substrate.

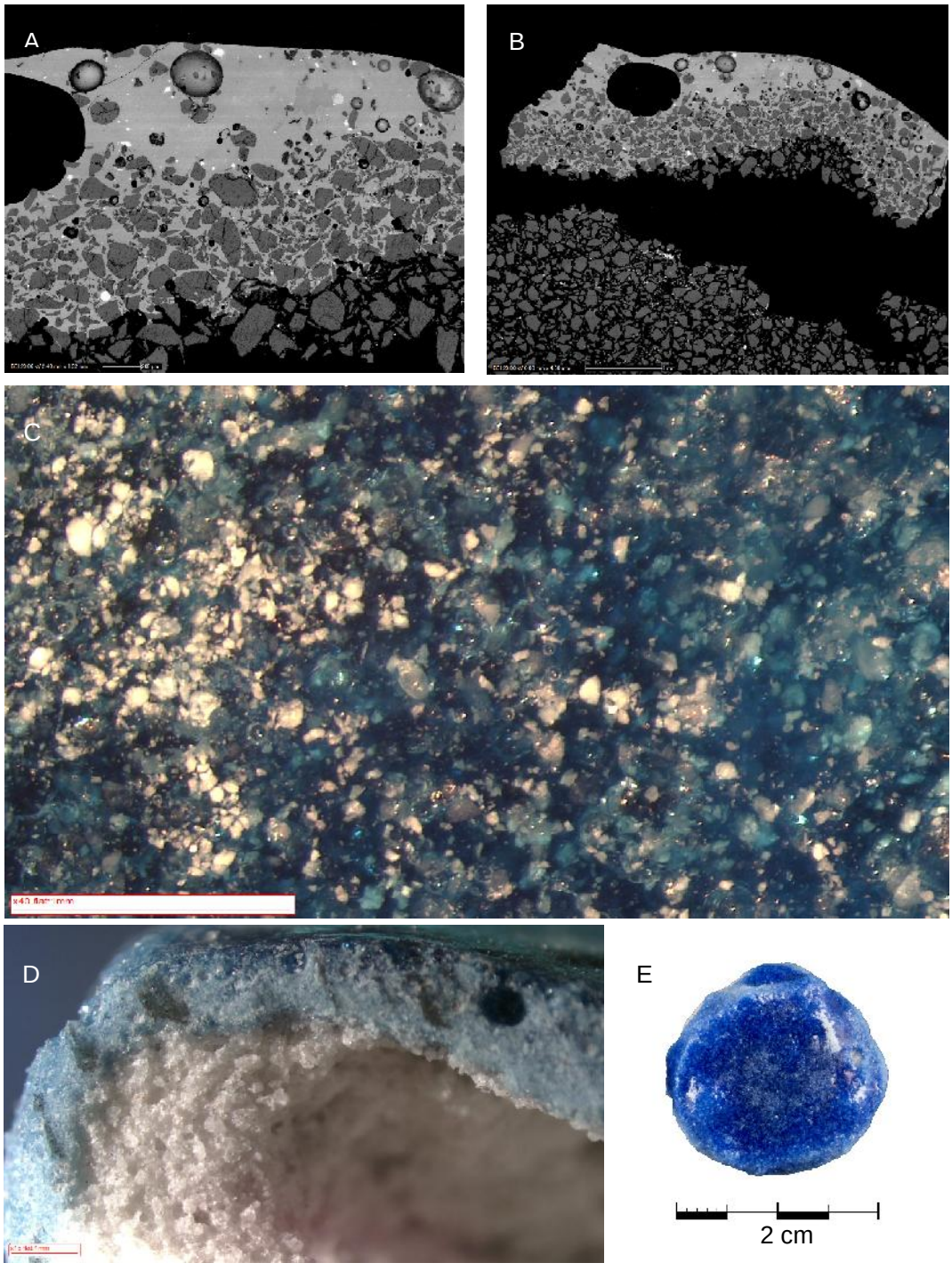

R426: SEM-BSE glaze profile (scale: 200 µm (A) and 1 mm (B)); OM glaze surface micrograph (C (scale: 1 mm)); OM glaze profile (D (scale: 1 mm)) and the replicate prior to sampling (E). The BSE profiles (A and B) reveal bubble formation with minor unreacted quartz in the glaze. The IAL is relatively thick with smaller bubbles evolving in-between the unreacted quartz. Bright spots in the glaze and body are tin particles confirmed through SEM-EDS spot analysis. Bubbles and unreacted quartz are evident below the glaze surface (C). The OM profile (D) shows massed sintered quartz particles in the body. The faience replicate glaze surface (E) reveals an unfilled bubble crater has revealed the body substrate.

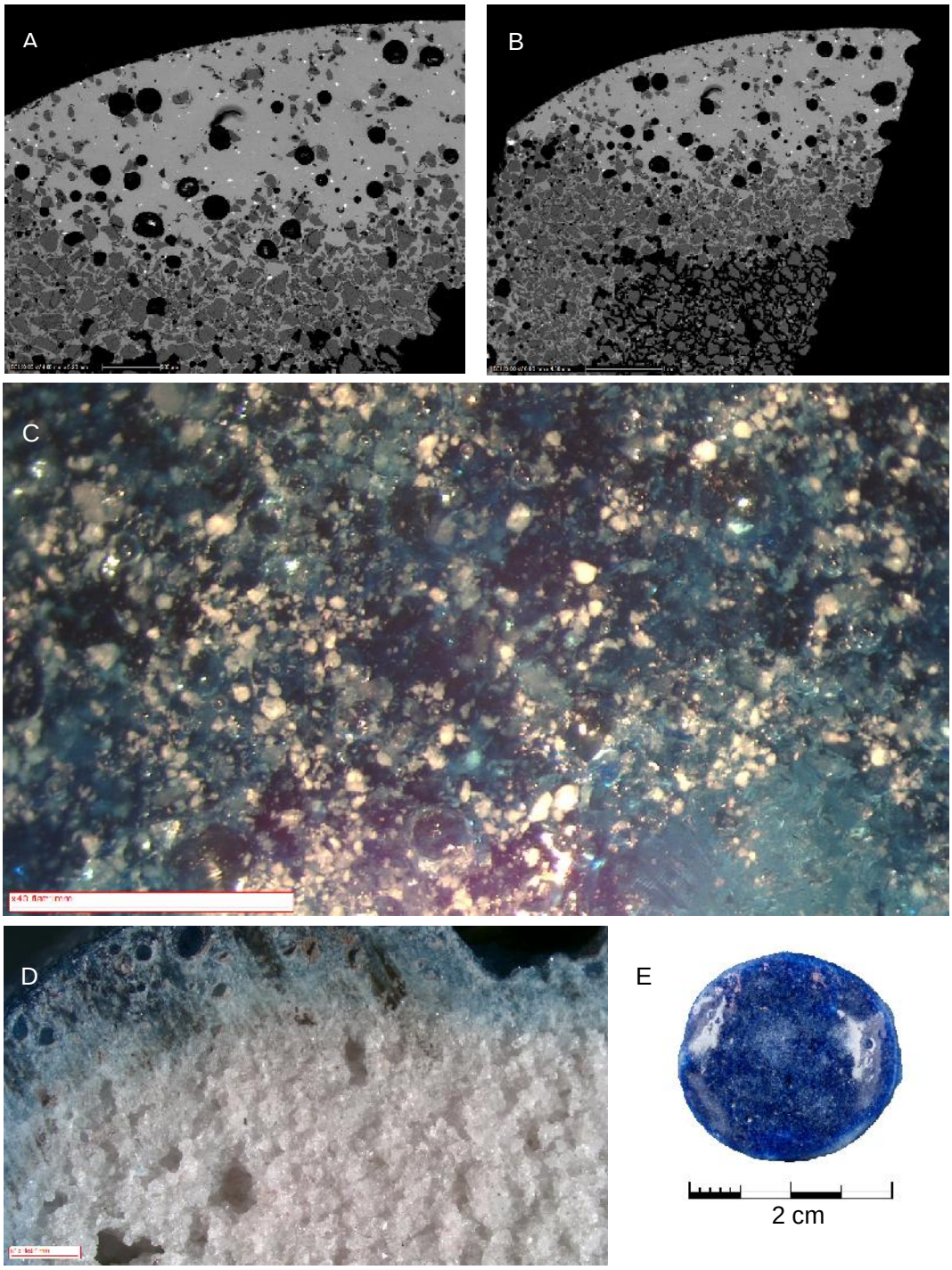

R429: SEM-BSE glaze profile (scale: 500 µm (A) and 1 mm (B)); OM glaze surface micrograph (C (scale: 1 mm)); OM glaze profile (D (scale: 1 mm)) and the replicate prior to sampling (E). The BSE profiles (A and B) reveal bubble formation with minor unreacted quartz in the glaze. The IAL is relatively thick with smaller bubbles evolving in-between the unreacted quartz. Bright spots in the glaze and body are tin particles confirmed through SEM-EDS spot analysis. Bubbles and unreacted quartz are evident below the glaze surface (C). Some unreacted quartz has erupted through the glaze surface. The OM profile (D) shows massed sintered quartz particles in the body. The faience replicate glaze surface (E) reveals partially filled erupted bubbles.

Appendix B: Archaeological Case Study Faience Sherds

Ninety-one faience sherds recovered from Saqqara excavations in the early 1970s are housed at Cardiff University. The sherds were retrieved from disturbed zones and on the surface in the south and west dumps of sector 7 at Saqqara (Dayton 1981:135). Dayton describes the sherds as belonging to the 30th dynasty (Late Period) or to the early Ptolemaic Period, c. 355 BC. The sherds are now a part of the Egyptian Exploration Society collection and have been kindly provided by Dr Paul Nicholson.

Twenty-four sherds were selected for analysis as a continued evaluation of the HH-XRF using the parameters chosen for the replicated faience samples and represent an archaeological case study. The case study consists of twenty blue glazed sherds. The other four sherds, representing purple, green, apple green and yellowish-green, were included to provide analytical contrast to the blue glazes. The case study glazes were chosen based on presence of a covering glaze and absence of soil or other surface deposits as detected with the stereomicroscope. Heavily weathered glazes were avoided but SEM-BSE revealed many of the sherds to have surface weathered glazes. Several of the sherds contain evidence of firing techniques such as clay setters and rough areas on the base indicating how they would have sat during the firing.

Appendix B is divided into three sections. The first section is a pictorial representation of the selected case study sherds. All rim sherds are associated with a silhouetted sherd profile. The second section is a descriptive table for the selected sherds. The third section dedicates a page for each selected sherd showing SEM-BSE glaze profiles, OM glaze surface micrograph, OM sherd profile of broken edge and a photograph of the sherd to provide context. A caption for the figures is provided. Additional descriptive information is provided in Chapter 7.

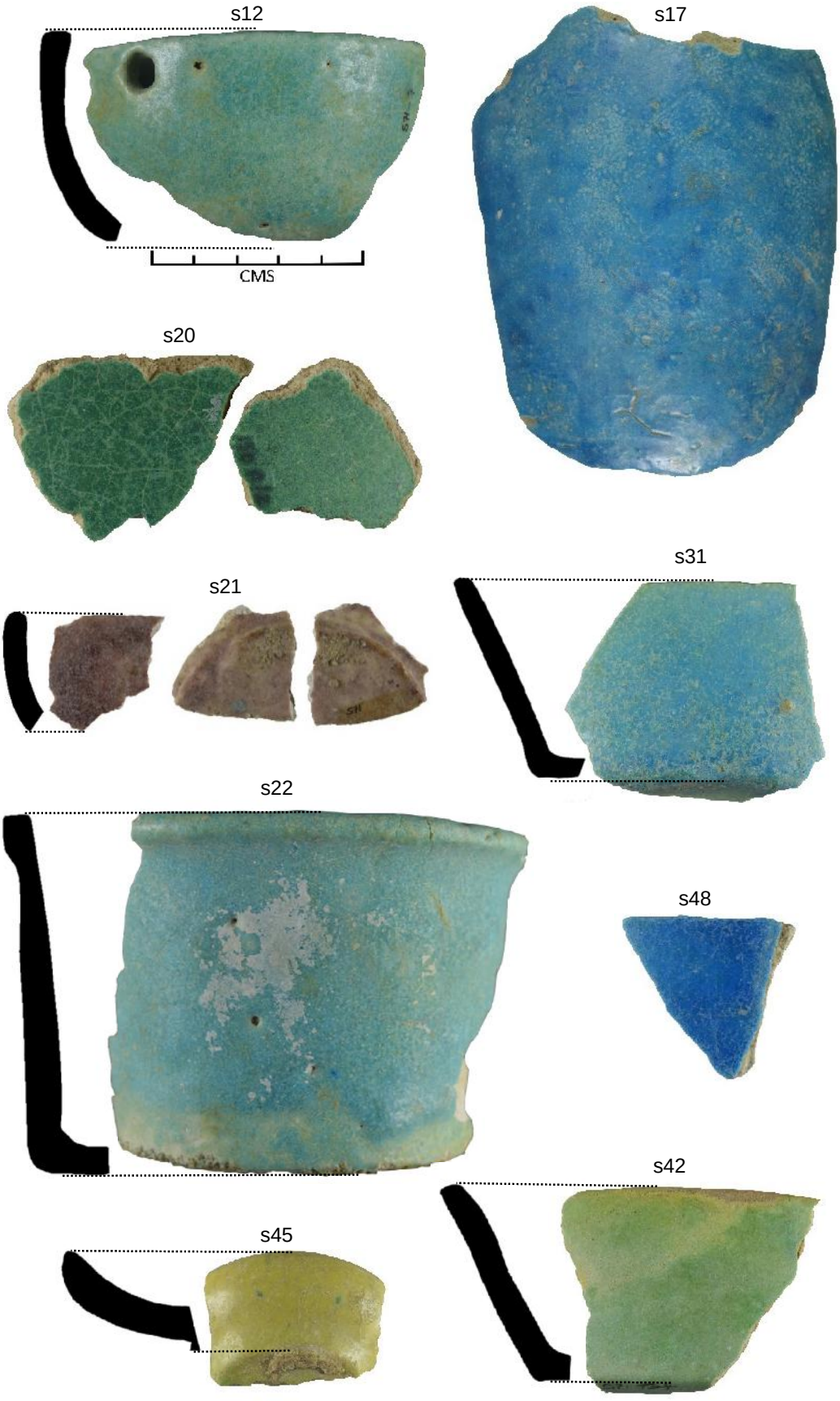
s12
CMS
s17
s20
s21
s31
s22
s48
s42
s45

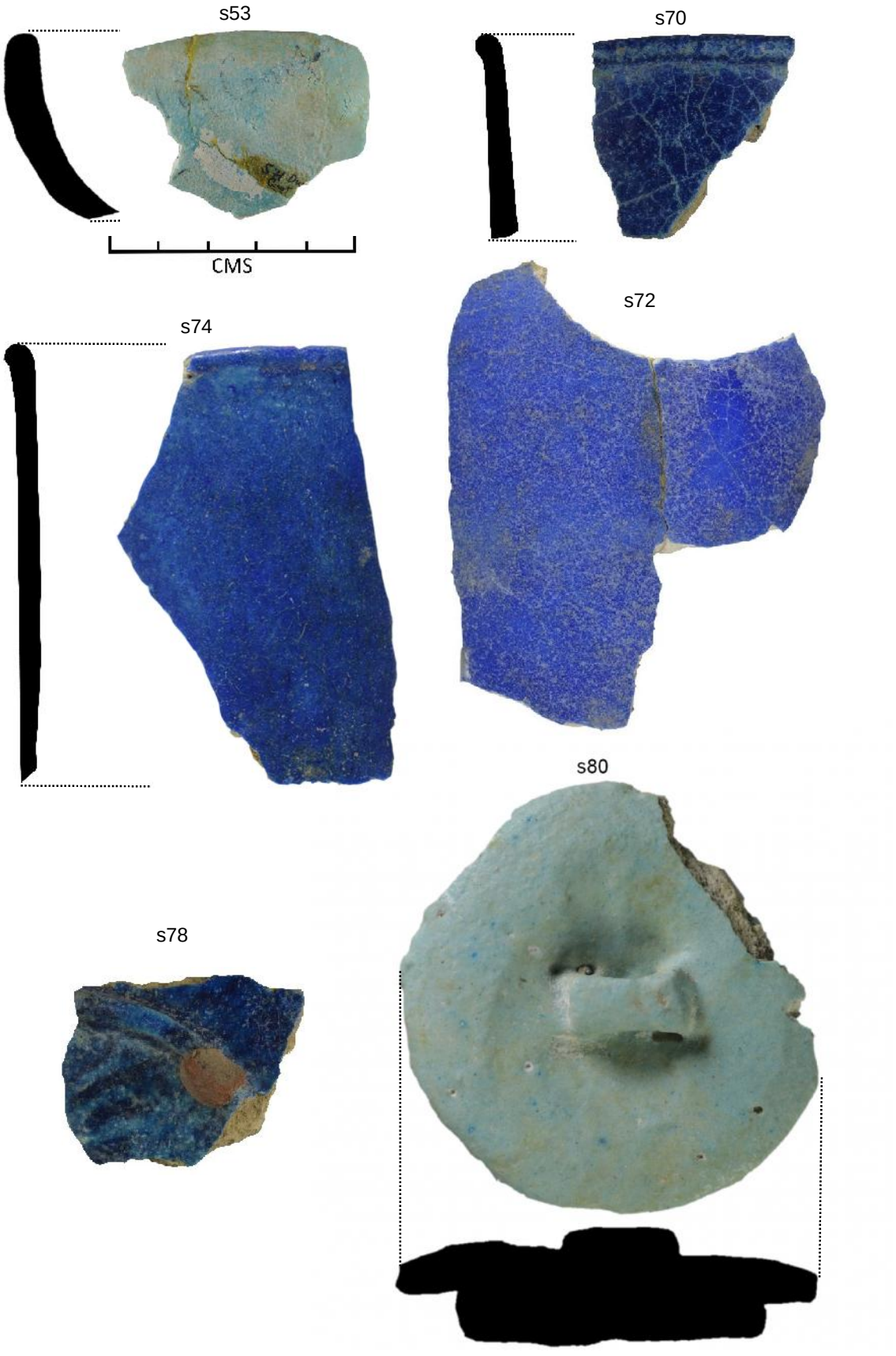
s53
CMS
s70
s72
s74
s80
s78

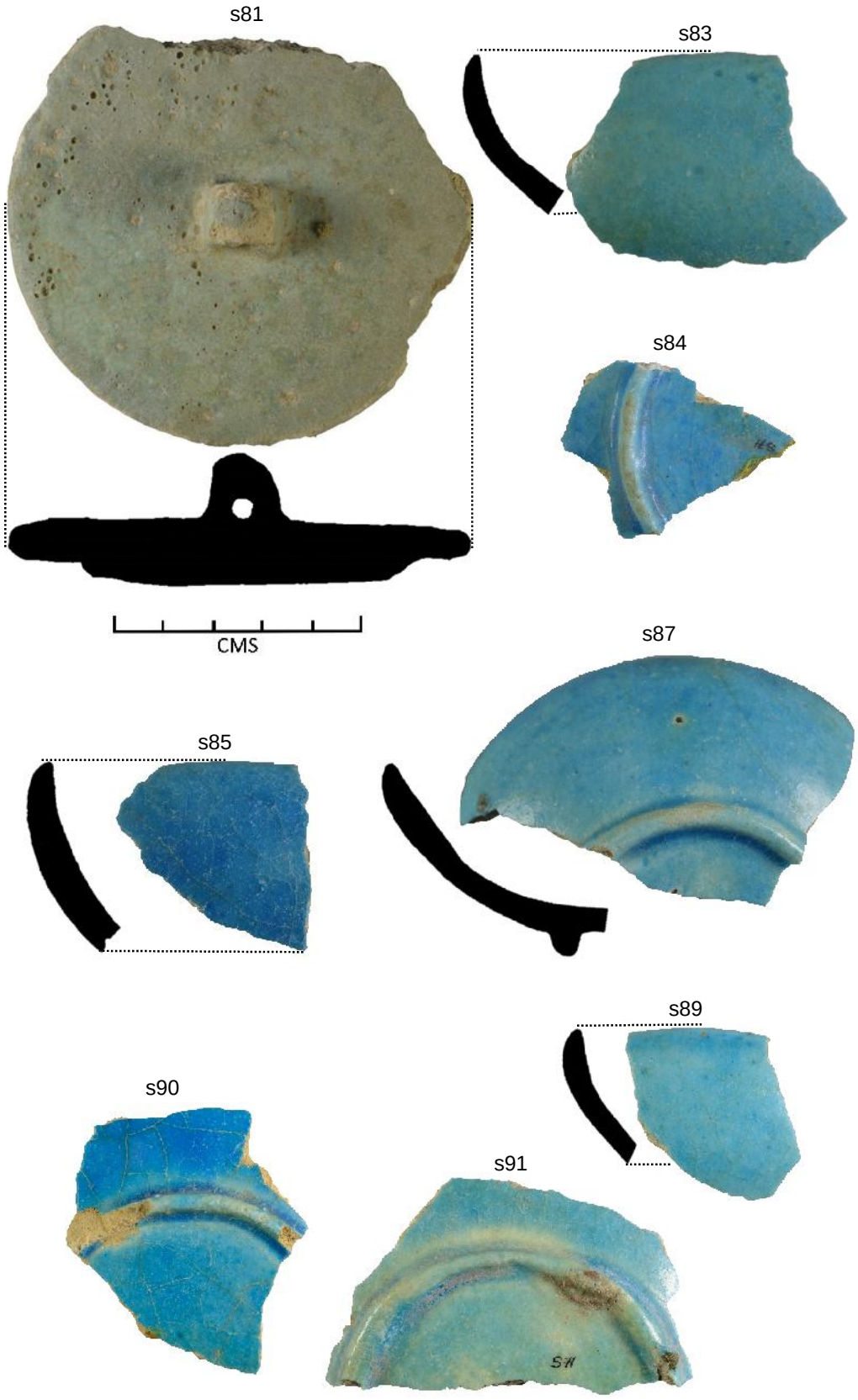
s81
s83
s84
CMS
s87
s85
s89
s90
s91

s82

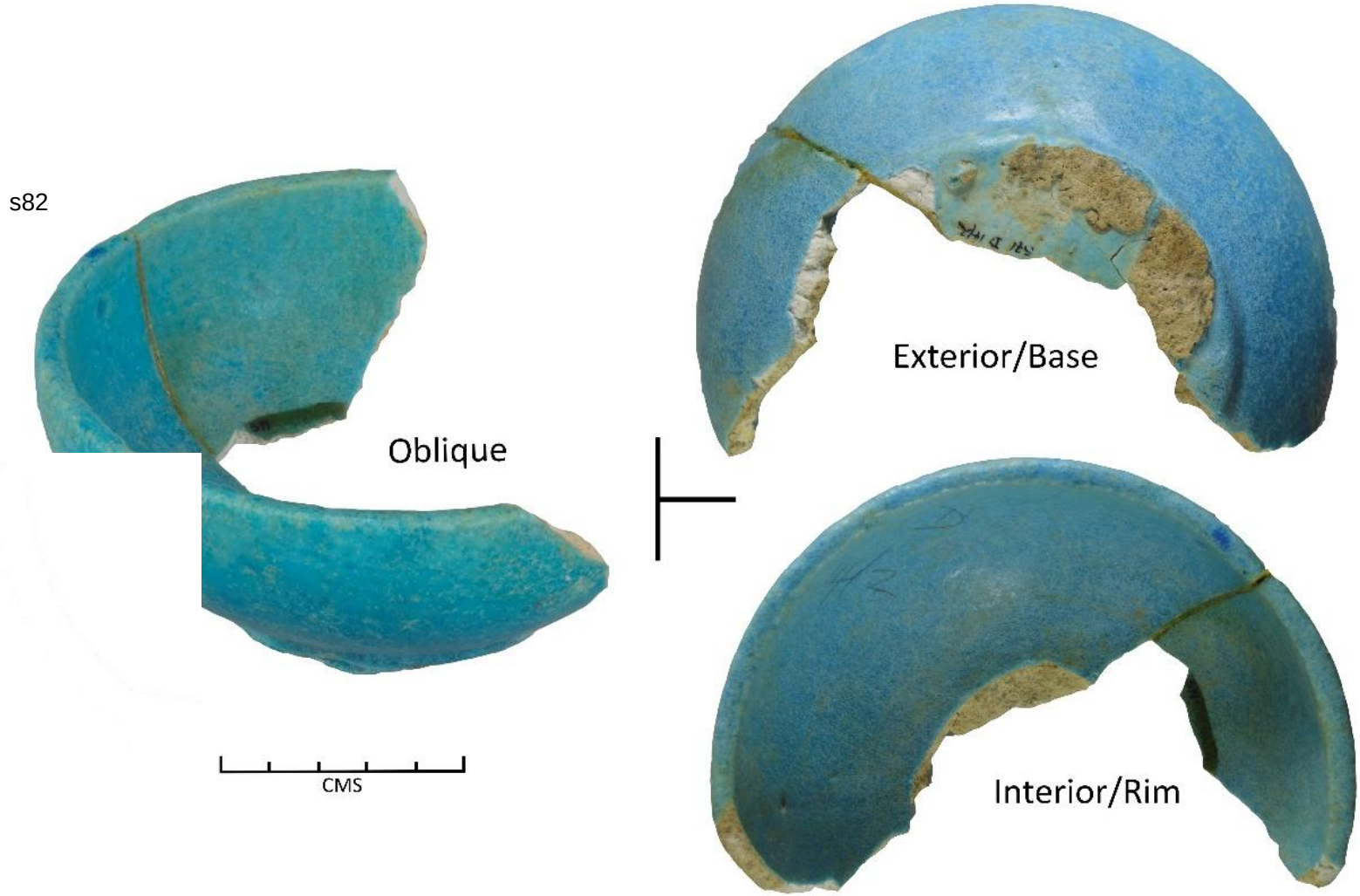

Sacred Animal Acropolis; North Saqqara

Sherd	Other Numbers	Object Description	Glaze Description	Typology	Photograph
s12	571-7	Flat lip rim sherd with one complete suspension hole and one partial hole along fracture line	Translucent crizzled bluish-green to green with pinholes, erupting bubbles and embedded material.		
s17		Deep vessel body sherd	Translucent crizzled blue with pinholes, erupting bubbles and embedded material.		
s20	571; 571 150 P/2	Two base sherds with attached foot ring and setter remnants	Translucent crizzled green with pinholes and erupting bubbles. Crusty white deposits on surface		
s21	571	Three sherds (two base; one rim). Flat base with setter remnants; rounded rim.	Translucent crizzled purple with pinholes, erupting bubbles and embedded material.		
s22	571-12	Flat based beaker; out-flaring rounded rim/lip; two adhered sherds; setter remnants on base.	Translucent crizzled/cracked turquoise with pinholes and erupting bubbles.	Dayton (747); Nenna (T6.4a)	
s31	571 East of T24, T27 7/2	Straight sided bowl with flat rim and base	Translucent crizzled turquoise with erupting bubbles and embedded material.	Dayton (1099); Nenna (T3.1d)	

Sacred Animal Acropolis; North Saqqara

Sherd	Other Numbers	Object Description	Glaze Description	Typology	Photograph
s42	571 T24	Bowl frament with flattened lip, flat base	Translucent crizzled green with pinholes, erupting bubbles and embedded material.	Dayton (1099); Nenna (T3.1d)	
s45	T32	Flat based vessel with tapered rim; setter remnants on base	Translucent crizzled yellowish-green with erupting bubbles.	Similar to: Dayton (375) Nenna (T12.1)	
s48	571	body sherd	Translucent crizzled dark blue with erupting bubbles and embedded material.		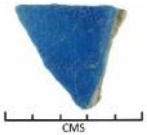
s53	571 DW Court	two adhered rounded rim sherds	Translucent turquoise crizzled orange peel textured and erupting bubbles. Crusty white deposits		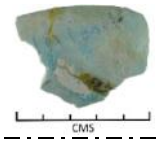
s70	571	rim sherd with out flaring rim; possible truncated beaker	Translucent crizzled ultra-marine blue with erupting bubbles.	Similar to: Nenna (T6.4a)	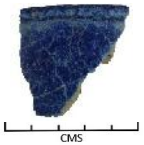
s72	571	two adhered body sherds	Translucent crizzled purplish blue with erupting bubbles and embedded material.		

Sacred Animal Acropolis; North Saqqara

Sherd	Other Numbers	Object Description	Glaze Description	Typology	Photograph
s74		Rim sherd: possible truncated beaker	Translucent crizzled purplish blue with erupting bubbles.	Similar to: Dayton (747) Nenna (T6.4a)	
s78	571	Base sherd with foot ring and attached clay setter	Translucent crizzled blue to ultra-marine blue with erupting bubbles. Star-like cystals on surface.		
s80	571 North of Court (5) 13/2	Vessel lid with small handle on top and rounded rim. Rough area on ventral side (firing evidence)	Translucent crizzled bluish-green to green with pinholes, erupting bubbles and embedded material.	Dayton (751)	
s81	571 T31 17/2	Vessel lid with small handle on top, rounded rim	Translucent bluish-green with pinholes and erupting bubbles.	Dayton (1103)	
s82	571 D 14/2	two adhered sherds; bowl with flat base and flat rim; rough area on base (firing evidence)	Translucent crizzled blue with pinholes.		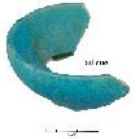
s83	571	Probable bowl with tapered rim	Translucent crizzled turquoise with erupting bubbles.		

Sacred Animal Acropolis; North Saqqara

Sherd	Other Numbers	Object Description	Glaze Description	Typology	Photograph
s84	571	Base with foot ring with pooled glaze around ring	Translucent crizzled blue with subsurface bubbles.		
s85	571	Rim sherd with tapered rim	Translucent crizzled dark blue with erupting bubbles		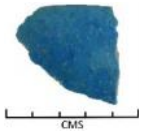
s87	T34 14/2	Bowl with tapered rim and foot ring; glaze pooled around foot ring	Translucent crizzled blue with pinholes, erupting bubbles and embedded material.	Dayton (749/750)	
s89	571-2	Rim sherd with tapered rim	Translucent crizzled blue with subsurface bubbles.		
s90		Basel Sherd with foot ring; glaze pooling around foot ring	Translucent crizzled blue with subsurface bubbles.		
s91	571	Basel Sherd with foot ring; glaze pooling around foot ring; setter remnants on interior and exterior	Translucent crizzled turquoise with subsurface bubbles.		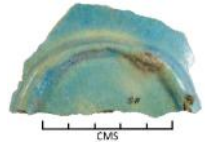

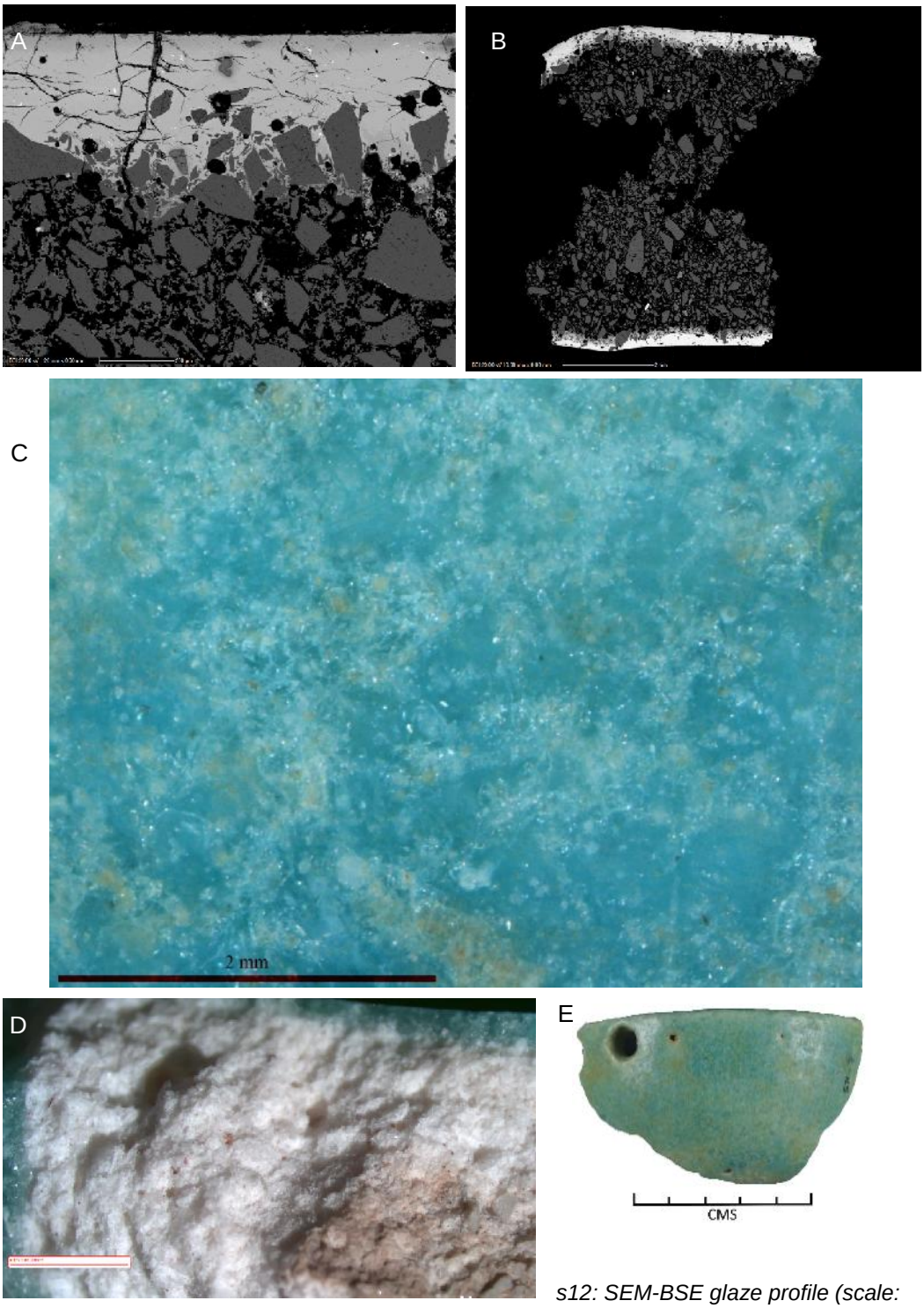

s12: SEM-BSE glaze profile (scale: 200 µm (A) and 2 mm (B)); OM glaze surface micrograph (C (scale: 2 mm)); OM glaze profile (D (scale: 2 mm)) and the sherd (E). The glaze has few bubbles (mostly restricted to the IAL) and minor unreacted quartz (A and B). The glaze is weathered as evinced by the cracks and a subtle change in contrast colour in the first 30 µm from surface. The IAL is thin and the sintered quartz in the body is heterogeneous in quartz particle size and shape. Bright specks in the body are iron (confirmed through SEM-EDS). The surface of the glaze is pocked and abraded by use and burial (C). The sherd paste (D) reveals a white body with red specks (iron).

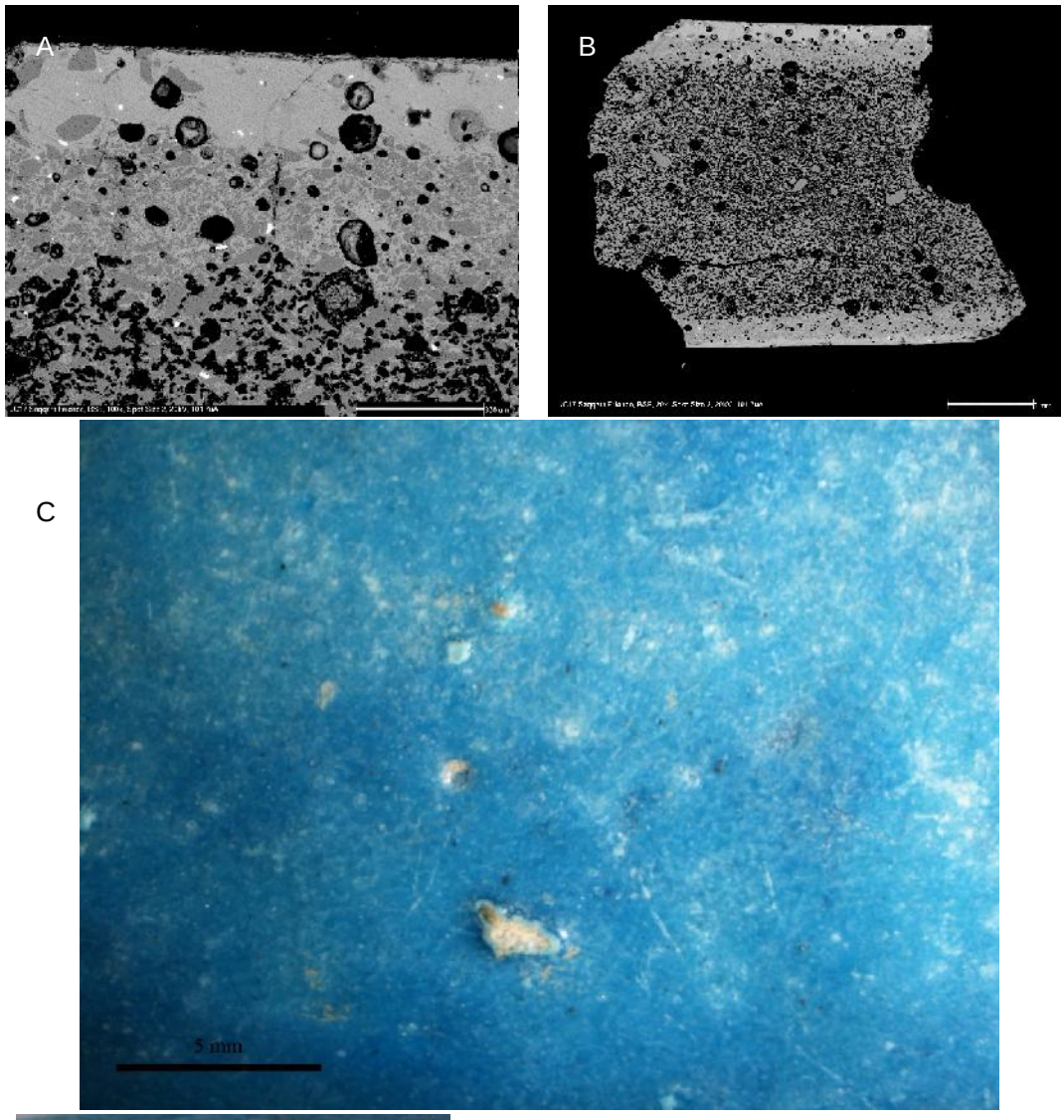

s17: SEM-BSE glaze profile (scale: 300 µm (A) and 1 mm (B)); OM glaze surface micrograph (C (scale: 2 mm)); OM glaze profile (D (scale: 1000 µm)) and the sherd (E). The glaze has few bubbles (mostly restricted to the IAL) and minor unreacted quartz (A and B). The IAL is relatively thick and the sintered quartz in the body is heterogeneous in quartz particle size and shape with extensive interparticle glass. Bright specks in the body are tin, antimony and copper (confirmed through SEM-EDS). The surface of the glaze is pocked and abraded by use and burial (C). Unreacted quartz particles are erupting through the surface. The sherd paste (D) reveals a coloured paste possibly resulting from the intentional addition of glaze material to the body to impart additional strength to the vessel.

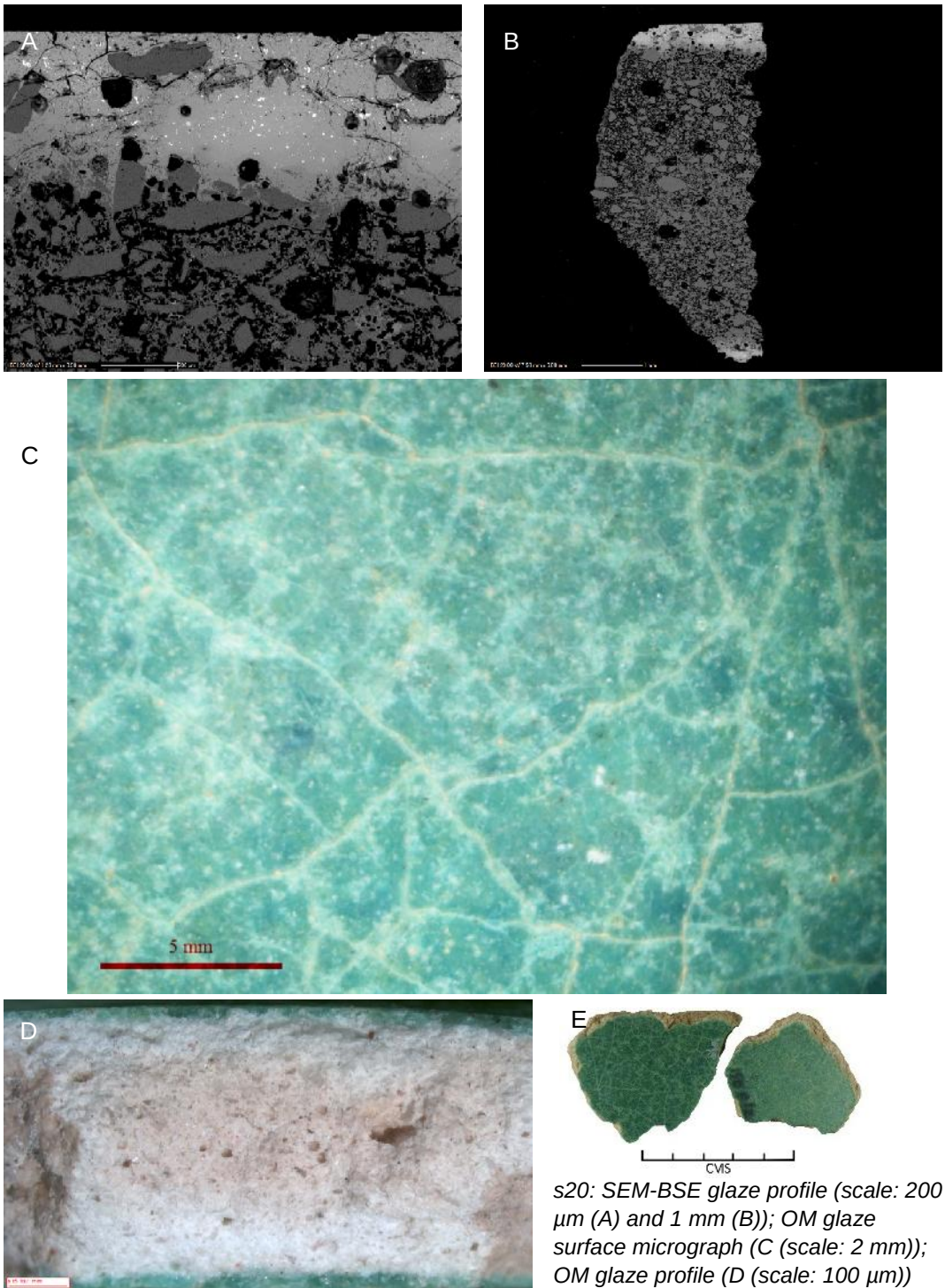

s20: SEM-BSE glaze profile (scale: 200 µm (A) and 1 mm (B)); OM glaze surface micrograph (C (scale: 2 mm)); OM glaze profile (D (scale: 100 µm)) and the sherd (E). The glaze has few bubbles (mostly restricted to the IAL) and minor unreacted quartz (A and B). The IAL is relatively thick and the sintered quartz in the body is heterogeneous in quartz particle size and shape with extensive interparticle glass. Bright specks in the body are tin, antimony and copper (confirmed through SEM-EDS). The surface of the glaze is pocked and abraded by use and burial (C). Unreacted quartz particles are erupting through the surface. The sherd paste (D) reveals a coloured paste possibly resulting from the intentional addition of glaze material to the body to impart additional strength to the vessel.

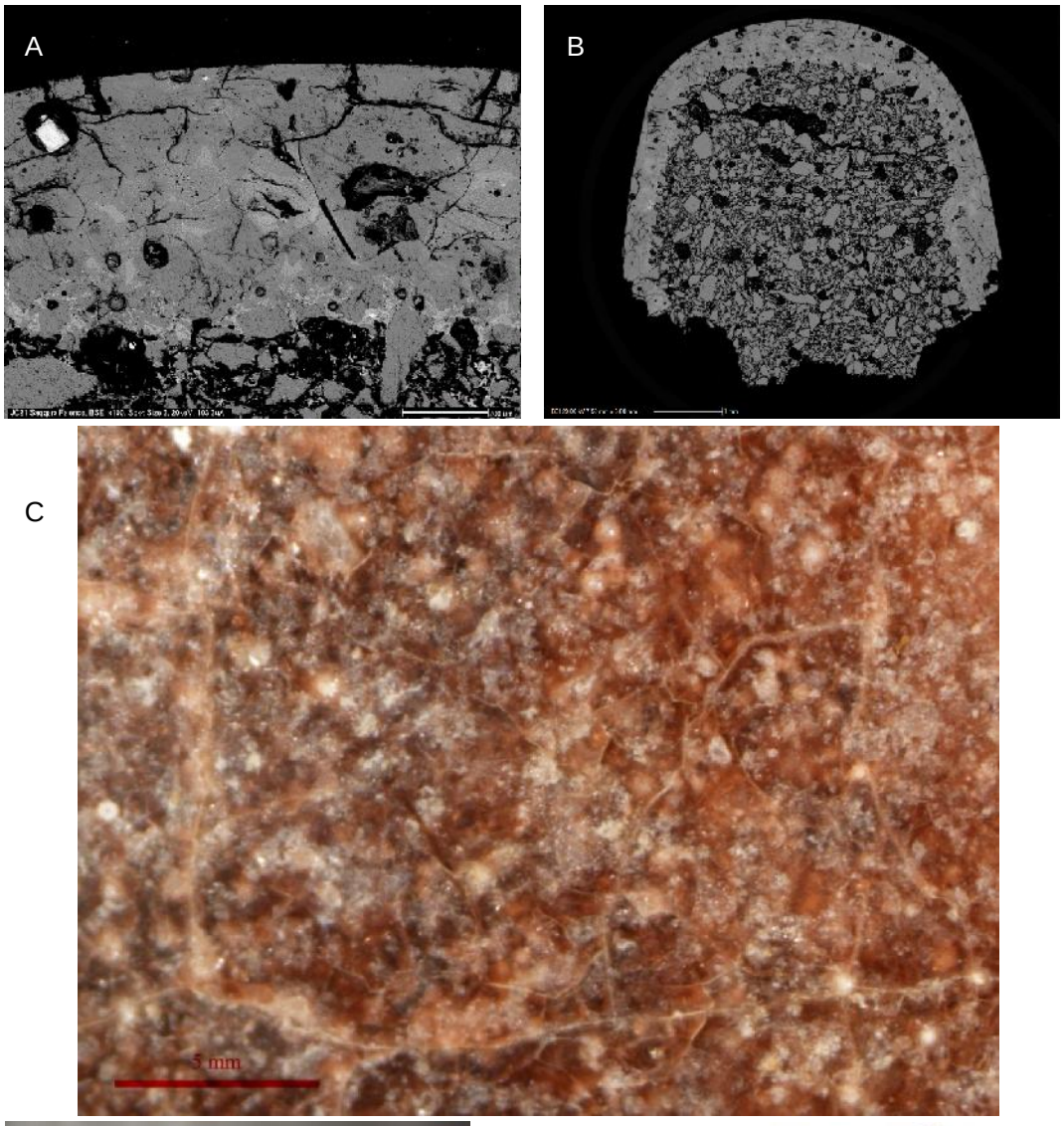

s21: SEM-BSE glaze profile (scale: 200 µm (A) and 1 mm (B)); OM glaze surface micrograph (C (scale: 5 mm)); OM glaze profile (D (scale: 2 mm)) and the sherd (E). The glaze has few bubbles and minor unreacted quartz (A and B). The glaze is heavily weathered with few areas of potentially low impacted glaze represented by slightly brighter glaze areas in-between the cracks. IAL is very thin and the sintered quartz in the body is heterogeneous in quartz particle size and shape. Bright specks in the body are titanium, iron, copper (confirmed through SEM-EDS). The bright square inclusion located in the bubble of A is a salt grain (NaCl). The surface of the glaze is pocked and abraded by use and burial (C). Glaze crizzling is evident by the network of tiny cracks running across the surface. The sherd paste (D) reveals a white body with red specks (iron).

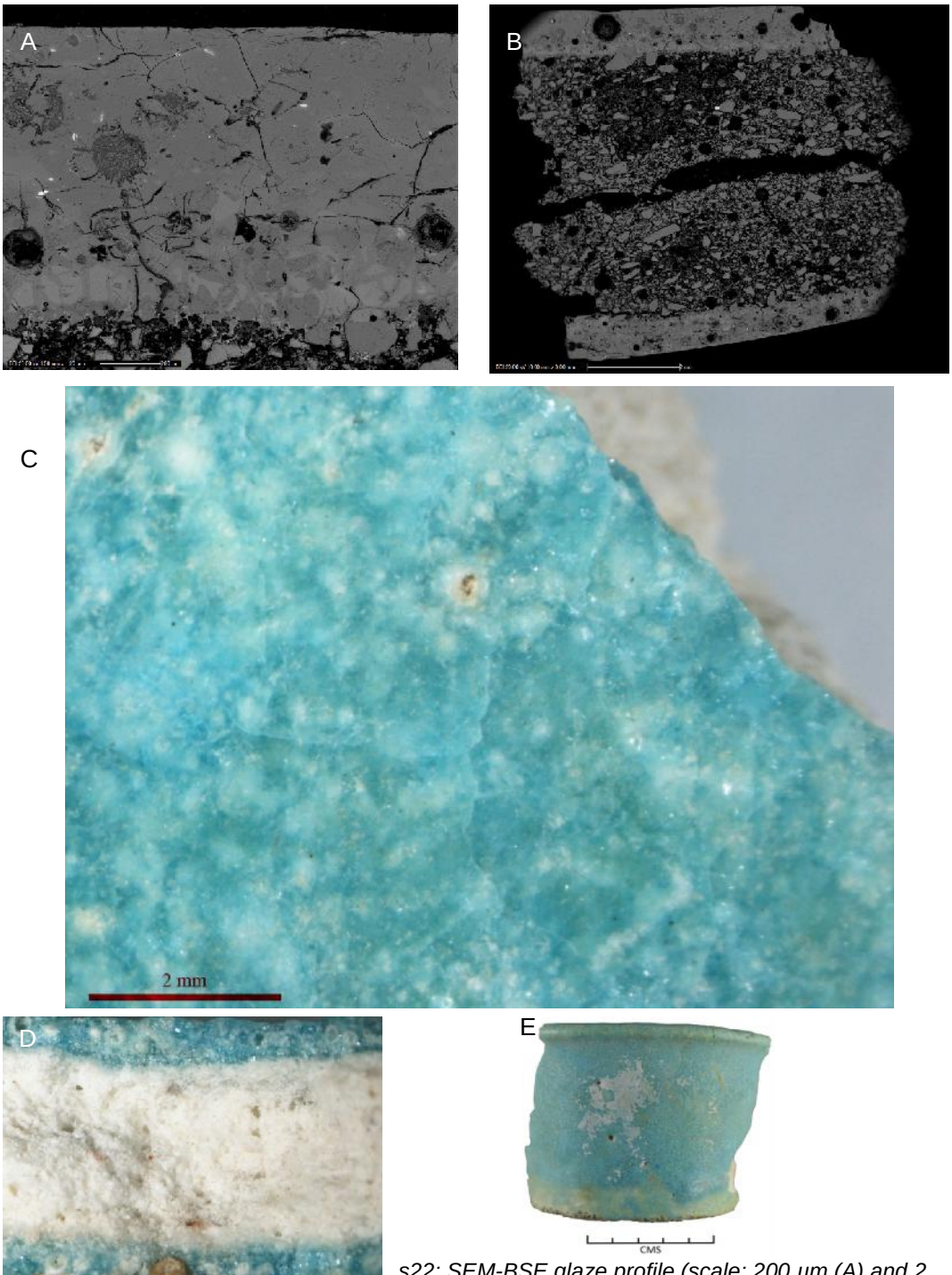

s22: SEM-BSE glaze profile (scale: 200 µm (A) and 2 mm (B)); OM glaze surface micrograph (C (scale: 2 mm)); OM glaze profile (D (scale: 2 mm)) and the sherd (E). The glaze has few bubbles and minor unreacted quartz (A and B). The glaze is heavily weathered with few areas of potentially low impacted glaze represented by slightly brighter glaze areas in-between the cracks. IAL is very thin and the sintered quartz in the body is heterogeneous in quartz particle size and shape. Bright specks in the body are titanium, tin and iron (confirmed through SEM-EDS). The surface of the glaze is pocked and abraded by use and burial (C). Glaze crizzling is evident by the faint network of tiny cracks running across the surface. The sherd paste (D) reveals a white body with red specks (iron). A pebble inclusion is present in the lower surface glaze.

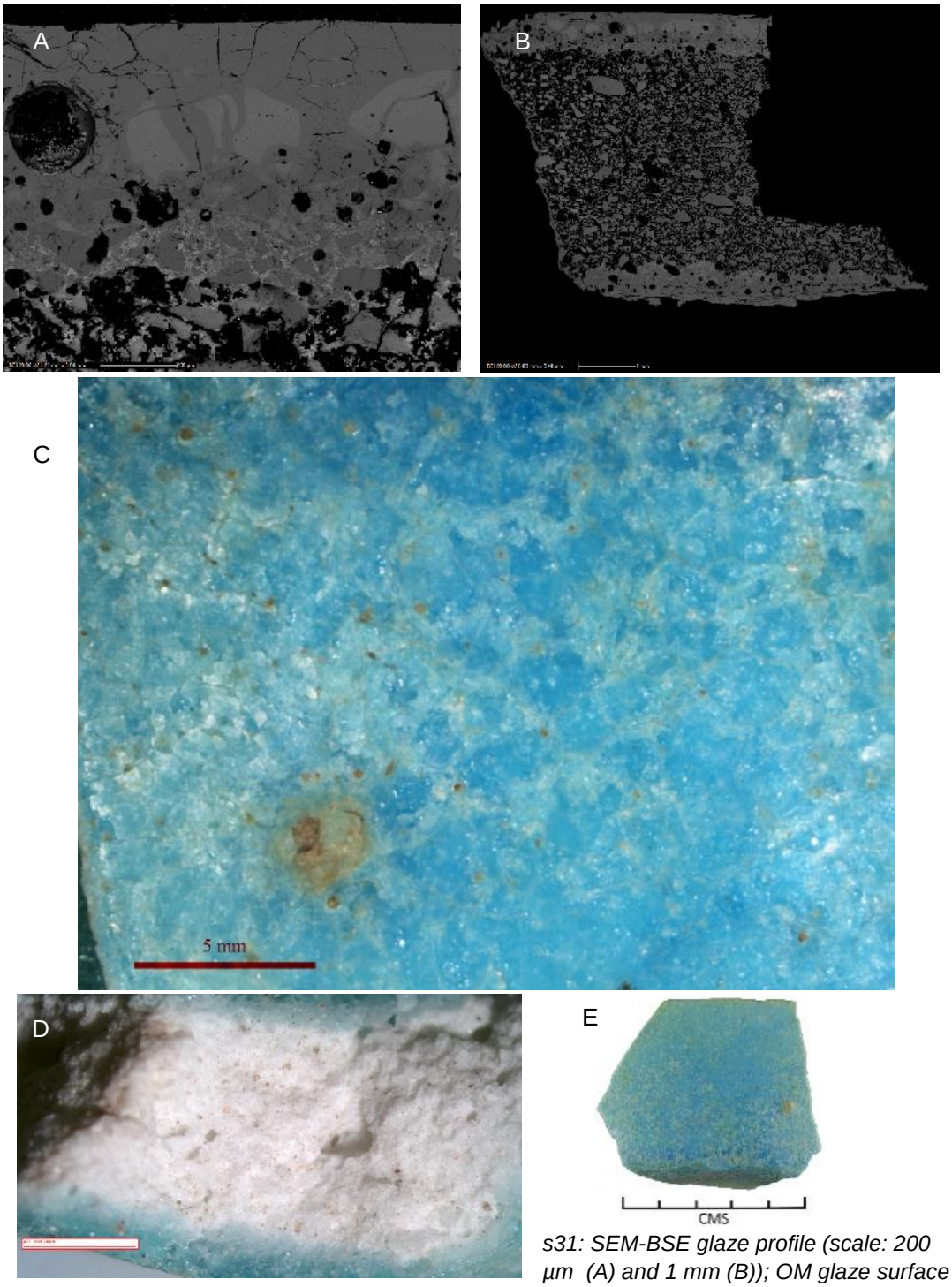

s31: SEM-BSE glaze profile (scale: 200 µm (A) and 1 mm (B)); OM glaze surface micrograph (C (scale: 5 mm)); OM glaze profile (D (scale: 2 mm)) and the sherd (E). The glaze has few bubbles and minor unreacted quartz (A and B). The glaze is heavily weathered with some areas of potentially low impacted glaze represented by slightly brighter glaze areas in-between the cracks. IAL is thin and the sintered quartz in the body is heterogeneous in quartz particle size and shape. The surface of the glaze is pocked and abraded by use and burial (C). Glaze crizzling is evident by the network of tiny cracks running across the surface. The glaze surface also reveals erupted bubbles that are possibly partially soil filled. The sherd paste (D) reveals a white body with red specks that possibly represent iron.

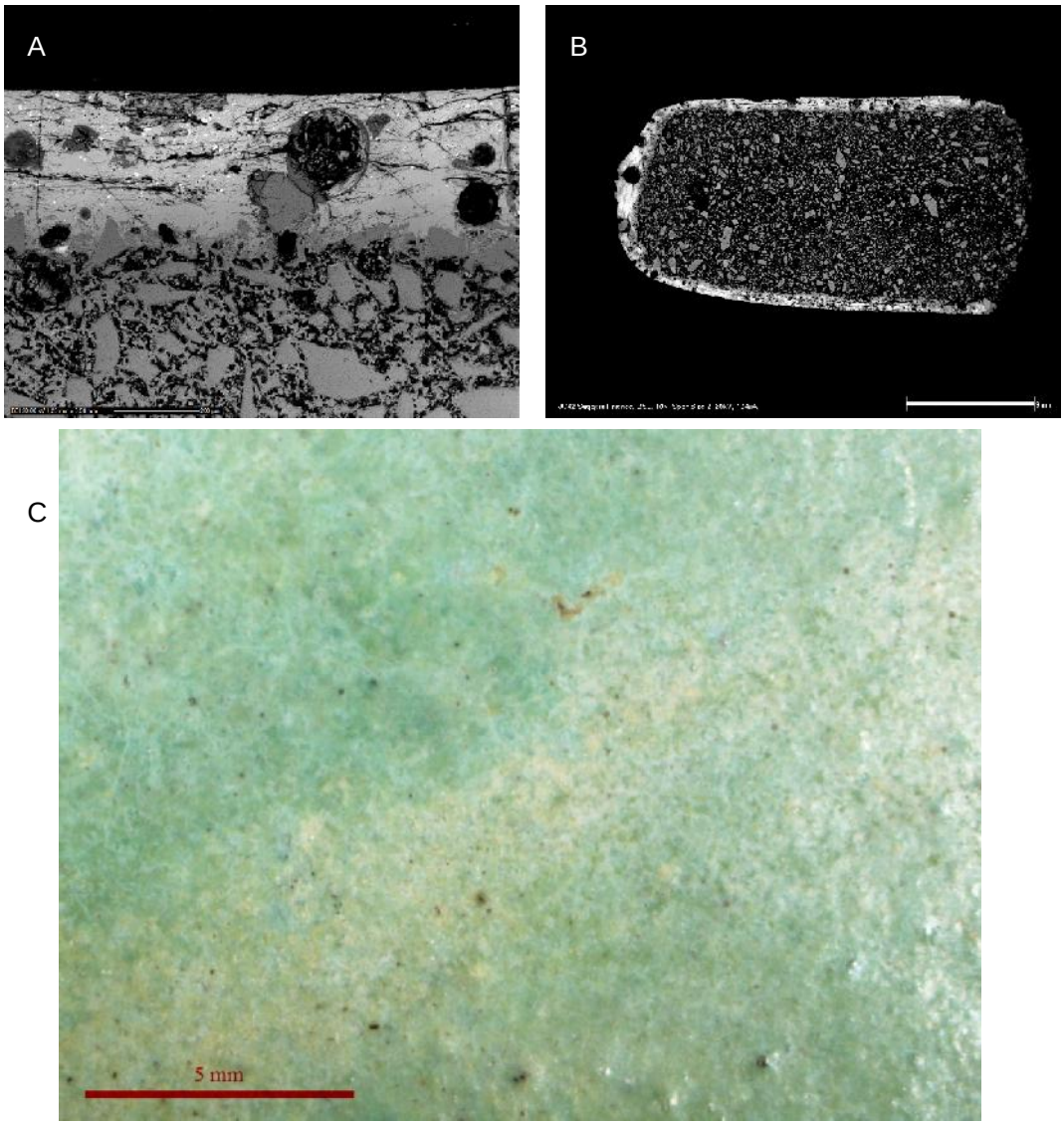

s42: SEM-BSE glaze profile (scale: 200 µm (A) and 3 mm (B)); OM glaze surface micrograph (C (scale: 5 mm)); OM glaze profile (D (scale: 1000 µm)) and the sherd (E). The glaze has a few large bubbles and minor unreacted quartz (A and B). The glaze is weathered as evinced by the large concentration of cracks. IAL is very thin and the sintered quartz in the body is heterogeneous in quartz particle size and shape. Bright specks in the glaze are lead antimonate (confirmed through SEM-EDS). The surface of the opaque glaze reveals dark inclusions (C). The sherd paste (D) reveals an off-white body with red specks (iron). The dark inclusions are present in the glaze near the lower left corner of the micrograph.

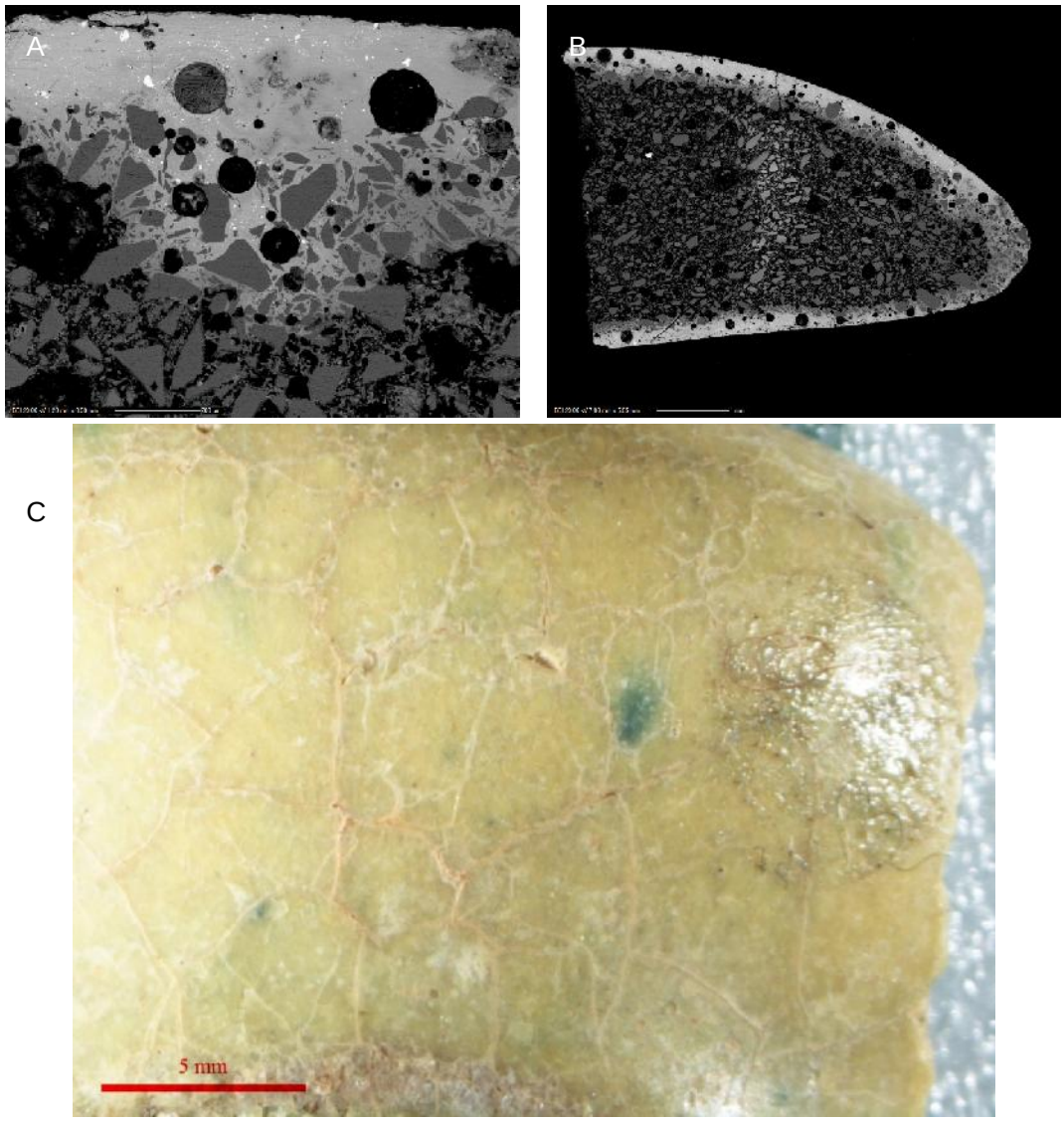

s45: SEM-BSE glaze profile (scale: 200 µm (A) and 1 mm (B)); OM glaze surface micrograph (C (scale: 5 mm)); OM glaze profile (D (scale: 1 mm)) and the sherd (E). The glaze has few bubbles and minor unreacted quartz (A and B). The IAL is thin with smaller bubble formation and the sintered quartz in the body is heterogeneous in quartz particle size and shape. Bright specks in the glaze are lead antimonate and the single bright speck in the body is zirconium (confirmed through SEM-EDS). Charging in the BSE image (B) is due to lapping oil emerging from micro-pores in the SEM vacuum. The surface of the glaze is opaque with surface crizzling as evident by the network of tiny cracks running across the surface (C). The green areas of the glaze are possible localized areas of higher copper concentration which will result in a green glaze. The rough area near the bottom of the micrograph is firing evidence representing where the vessel sat on gravel or where a setter was positioned during firing. The sherd paste (D) reveals a white body with reddish areas possibly due to presence of iron.

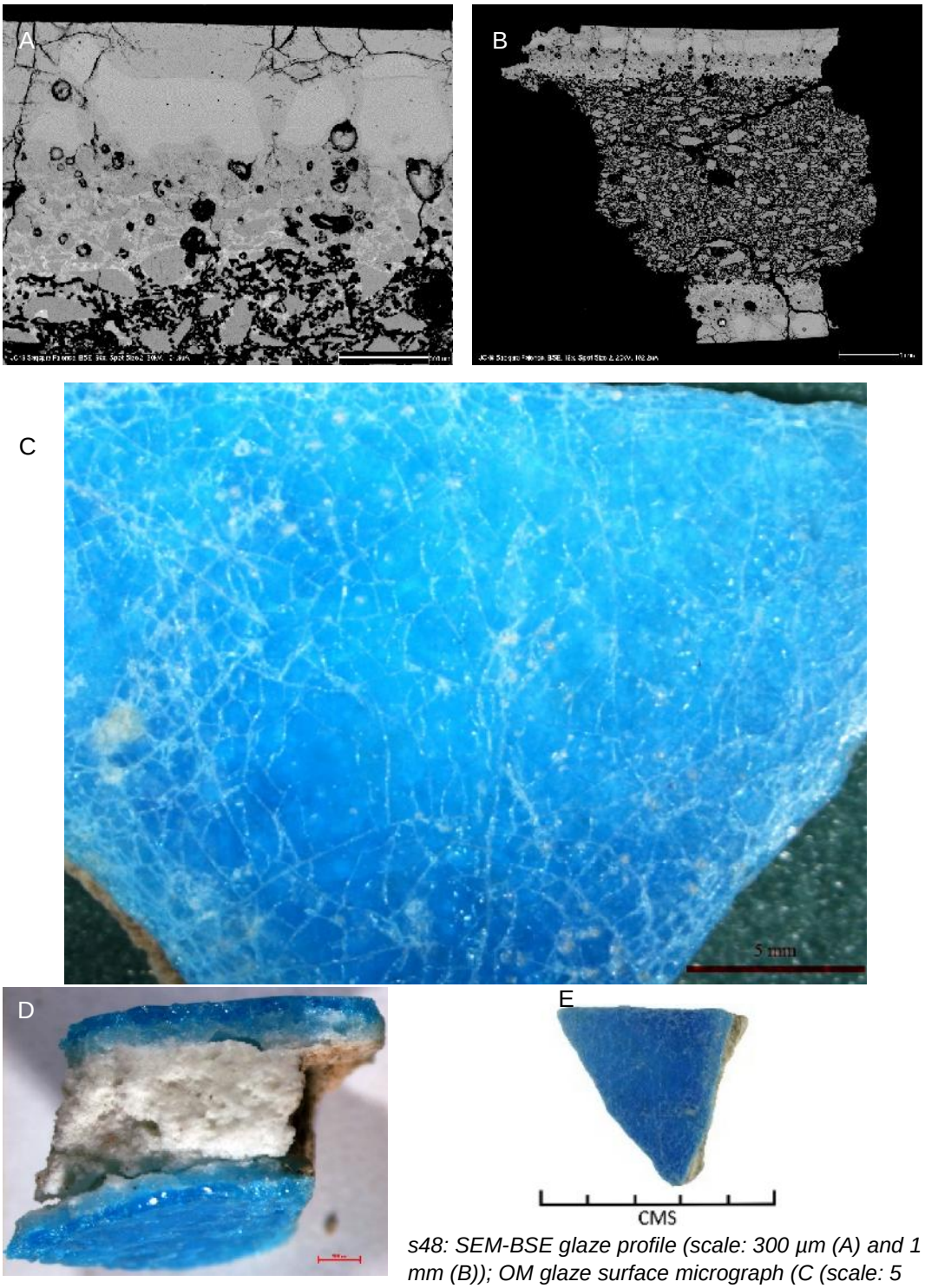

s48: SEM-BSE glaze profile (scale: 300 µm (A) and 1 mm (B)); OM glaze surface micrograph (C (scale: 5 mm)); OM glaze profile (D (scale: 1000 µm)) and the sherd (E). The glaze has few bubbles (mostly restricted to the IAL) and no identified unreacted quartz (A and B). The glaze is weathered with some areas of potentially low impacted glaze represented by slightly brighter glaze areas in-between the cracks. The IAL is moderately thick and the sintered quartz in the body is heterogeneous in quartz particle size and shape. Bright specks in the glaze are tin (confirmed through SEM-EDS). The surface of the glaze is pocked by use and burial (C). Glaze crizzling is evident by the network of tiny cracks running across the surface. The sherd paste (D) is white with few inclusions.

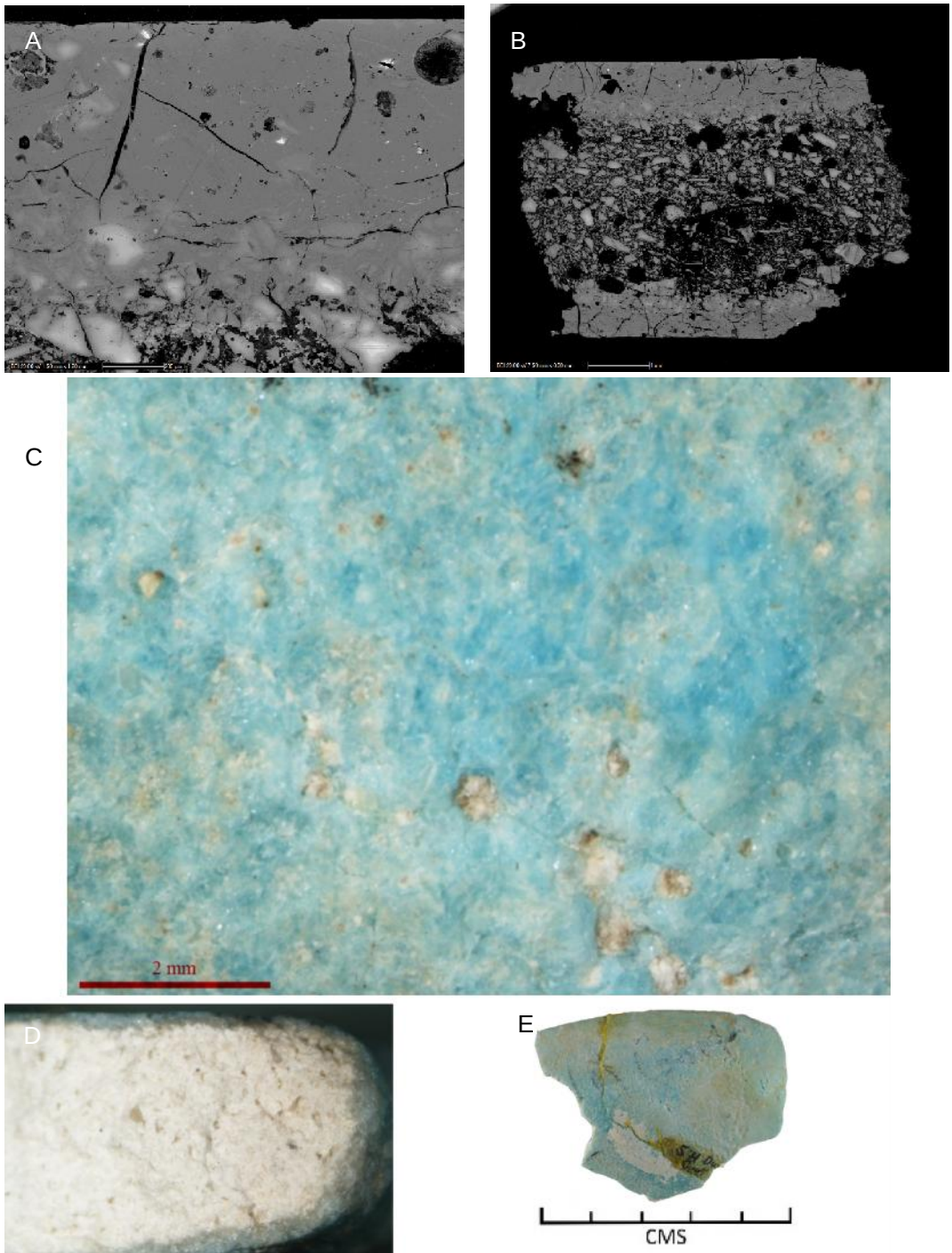

s53: SEM-BSE glaze profile (scale: 200 µm (A) and 1 mm (B)); OM glaze surface micrograph (C (scale: 2 mm)); OM glaze profile (D (scale: 2 mm)) and the sherd (E). The glaze has few bubbles and no identified unreacted quartz (A and B). The glaze is weathered with cracks running throughout. The IAL is thin and the sintered quartz in the body is heterogeneous in quartz particle size and shape. The surface of the glaze is pocked and abraded by use and burial (C). Glaze crizzling is faintly evident by the network of tiny cracks running across the surface. The sherd paste (D) is white with few inclusions. Modern provenience information is present in two types of writing on the surface of the glaze (F); ink directly on glaze surface and ink on a layer of adhesive. The adhesive has discoloured with age. A calcareous layer is also present on the sherd.

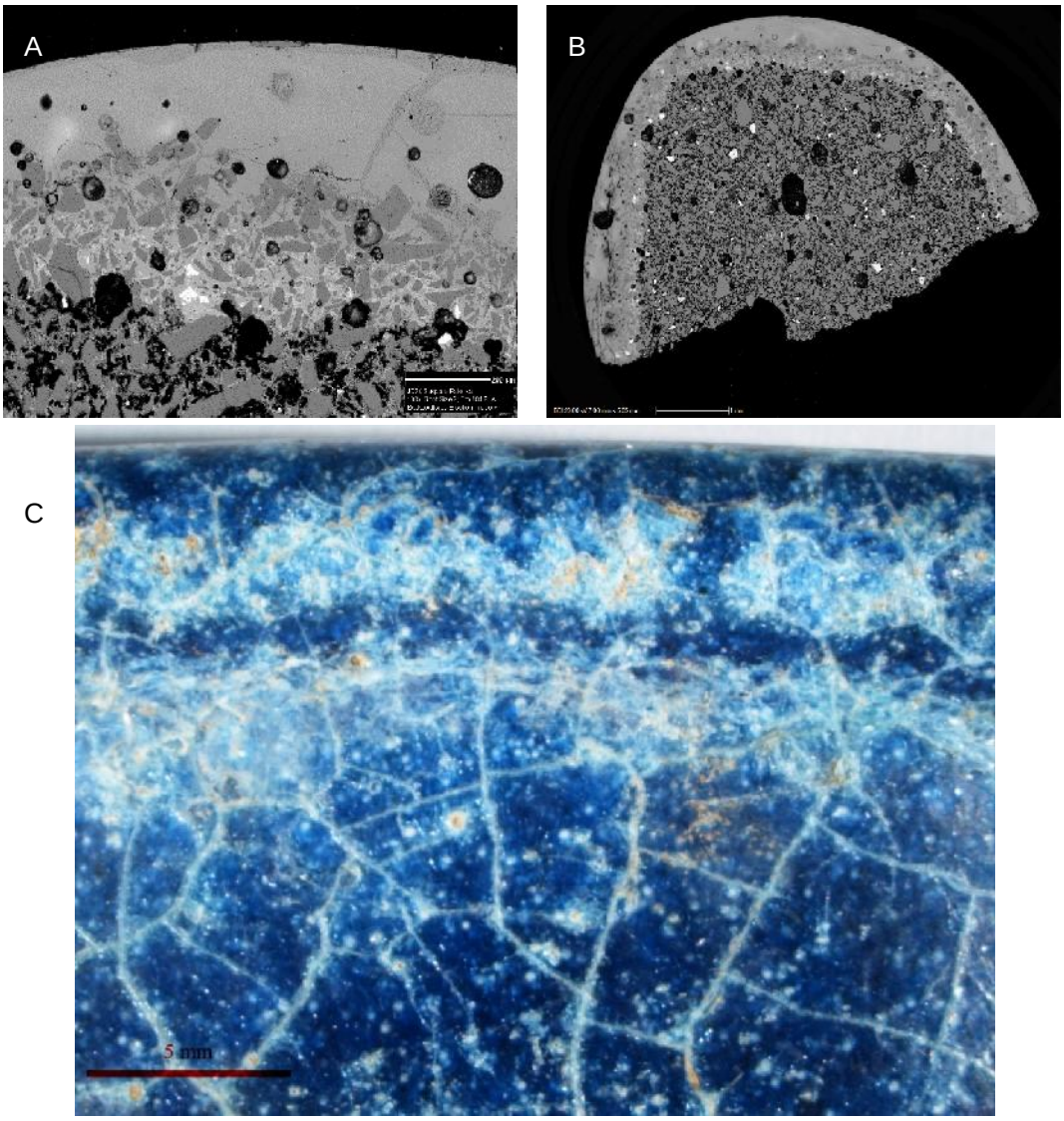

s70: SEM-BSE glaze profile (scale: 200 µm (A) and 1 mm (B)); OM glaze surface micrograph (C (scale: 5 mm)); OM glaze profile (D (scale: 1000 µm)) and the sherd (E). The glaze has few bubbles and minor unreacted quartz (A and B). The glaze is weathered with cracks and minor areas of alkali-depleted glaze as evinced by slightly darker glaze areas adjacent to cracks and the glaze surface. The IAL is moderately thick and the sintered quartz in the body is heterogeneous in quartz particle size and shape. The bright specks in the body and glaze are iron and cobalt to a lesser extent (confirmed through SEM-EDS). The surface of the glaze is pocked and abraded by use and burial (C). Glaze crizzling is evident by the network of cracks running across the surface. Bubbles are present below the glaze surface. The sherd paste (D) is grey with iron inclusions.

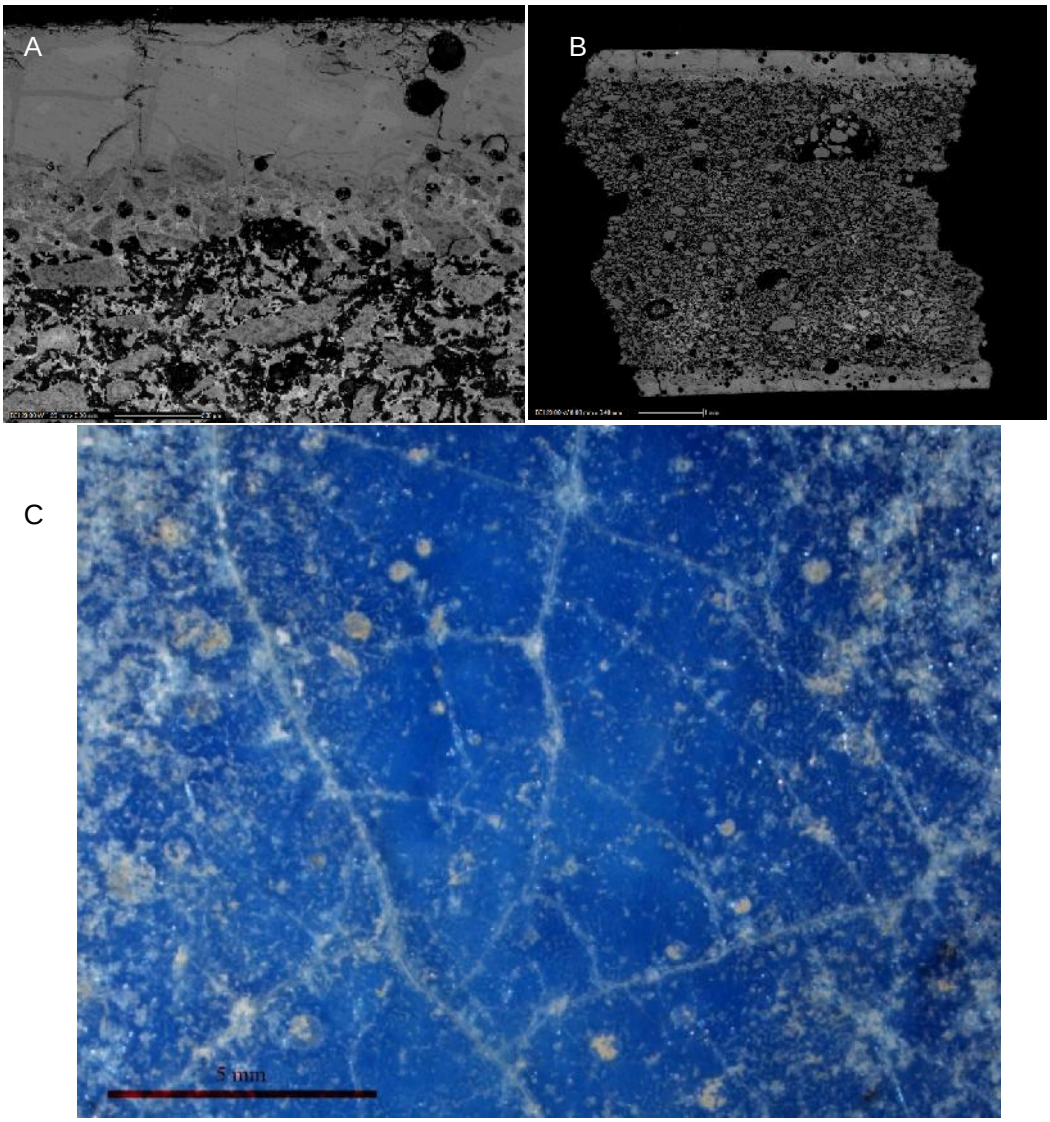

s72: SEM-BSE glaze profile (scale: 200 µm (A) and 1 mm (B)); OM glaze surface micrograph (C (scale: 5 mm)); OM glaze profile (D (scale: 2 mm)) and the sherd (E). The glaze has a few large bubbles and no identified unreacted quartz (A and B). The glaze is weathered with cracks and areas of alkali-depleted glaze as evinced by slightly darker glaze areas adjacent to cracks and the glaze surface. The IAL is thin and the sintered quartz in the body is heterogeneous in quartz particle size and shape. The bright specks in the glaze are iron with cobalt and copper to a lesser extent. The bright speck in the glaze (B) is composed of cerium, chloride and silver (confirmed through SEM-EDS). The surface of the glaze is pocked and abraded by use and burial (C). Glaze crizzling is evident by the network of cracks running across the surface. Bubbles are present below the glaze surface. The sherd paste (D) is off-white with iron inclusions.

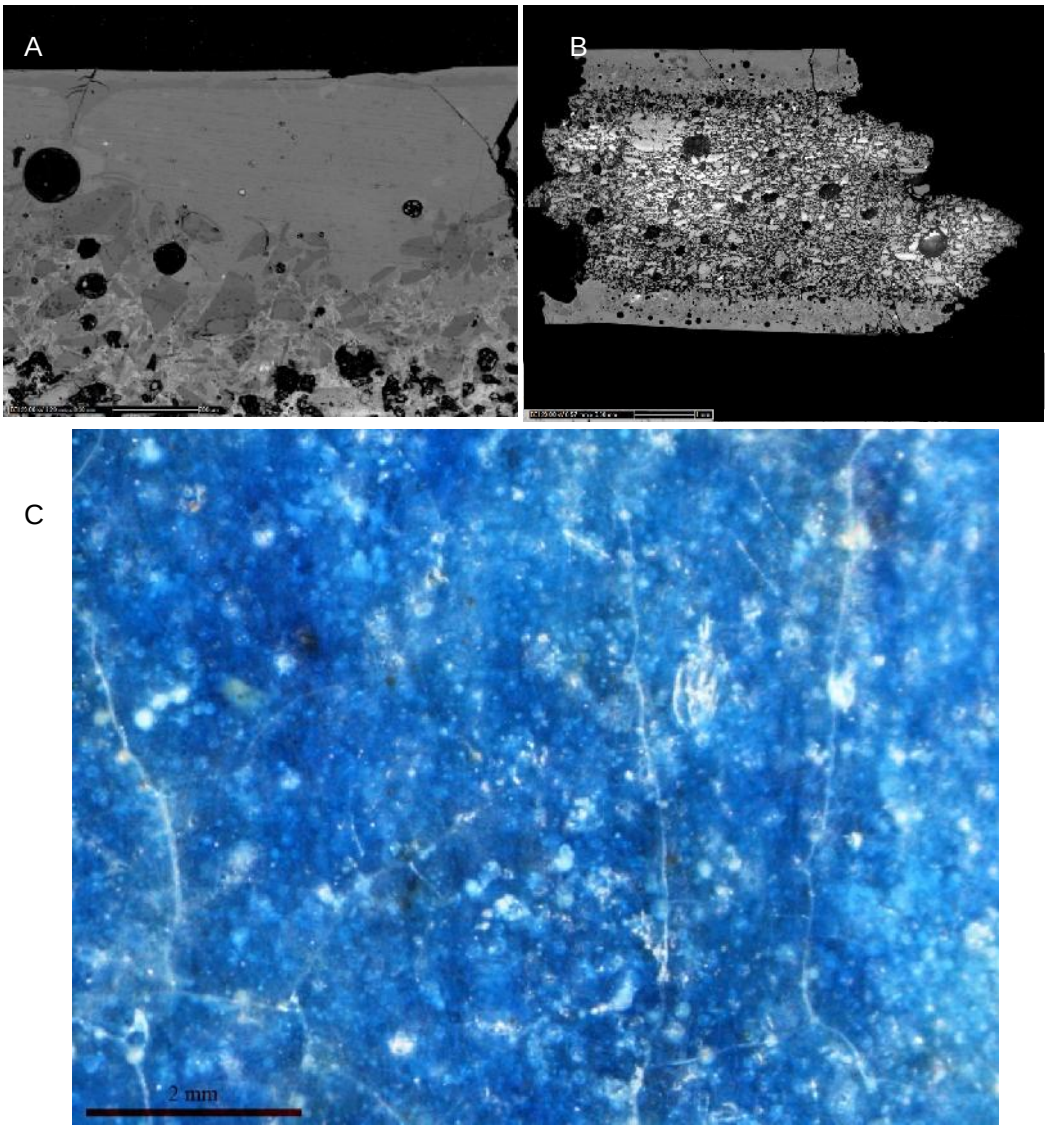

s74: SEM-BSE glaze profile (scale: 200 µm (A) and 1 mm (B)); OM glaze surface micrograph (C (scale: 2 mm)); OM glaze profile (D (scale: 2 mm)) and the sherd (E). The glaze has a few large bubbles and minor unreacted quartz (A and B). The glaze is weathered with areas of alkali-depleted glaze, as evinced by slightly darker glaze areas, adjacent to cracks and the glaze surface. The IAL is moderately thick and the sintered quartz in the body is heterogeneous in quartz particle size and shape. The bright specks in the glaze and body are iron and copper to a lesser extent. Charging in the BSE image (B) is due to lapping oil emerging from micro-pores in the SEM vacuum. The surface of the glaze is pocked and abraded by use and burial (C). Glaze crizzling is evident by the network of cracks running across the surface. Bubble and unreacted quartz are present below the glaze surface. The sherd paste (D) is off-white with iron inclusions.

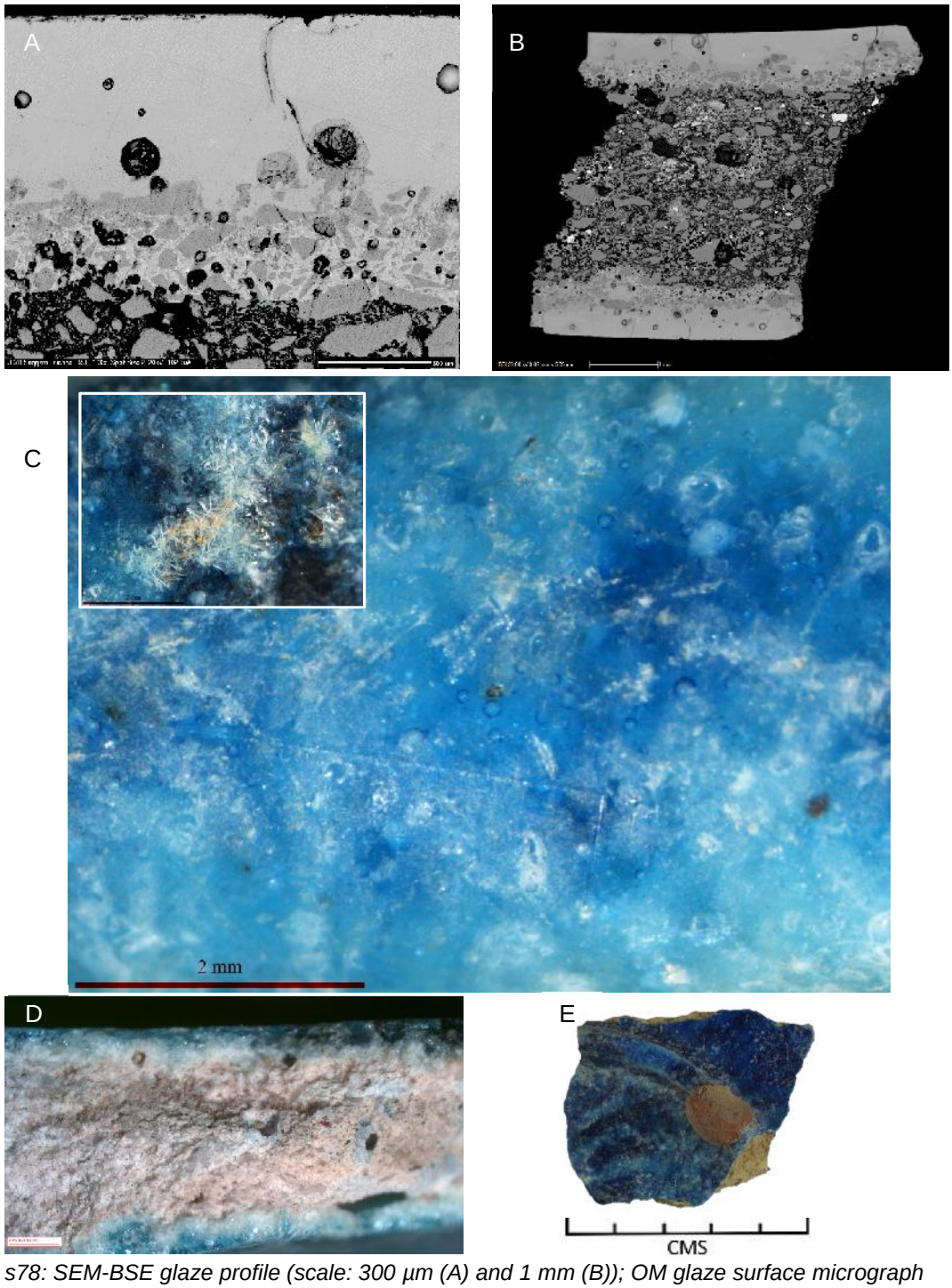

s78: SEM-BSE glaze profile (scale: 300 µm (A) and 1 mm (B)); OM glaze surface micrograph (C (scale: 2 mm)); OM glaze profile (D (scale: 2 mm)) and the sherd (E). The glaze has a few large bubbles and minor unreacted quartz (A and B). The glaze is weathered with areas of alkali-depleted glaze adjacent to cracks. The IAL is moderately thick and the sintered quartz in the body is heterogeneous in quartz particle size and shape. The bright specks in the glaze and body are iron and tin with copper, cobalt and aluminium to a lesser extent. The surface of the glaze is abraded by use and burial (C). Crystal are present on the exterior glaze (C inset; scale: 2 mm). Glaze crizzling is evident in the vessel interior. Bubble are present below the glaze surface. The sherd paste (D) is reddish-white with iron inclusions. A clay setter is present on the foot ring of the sherd (E).

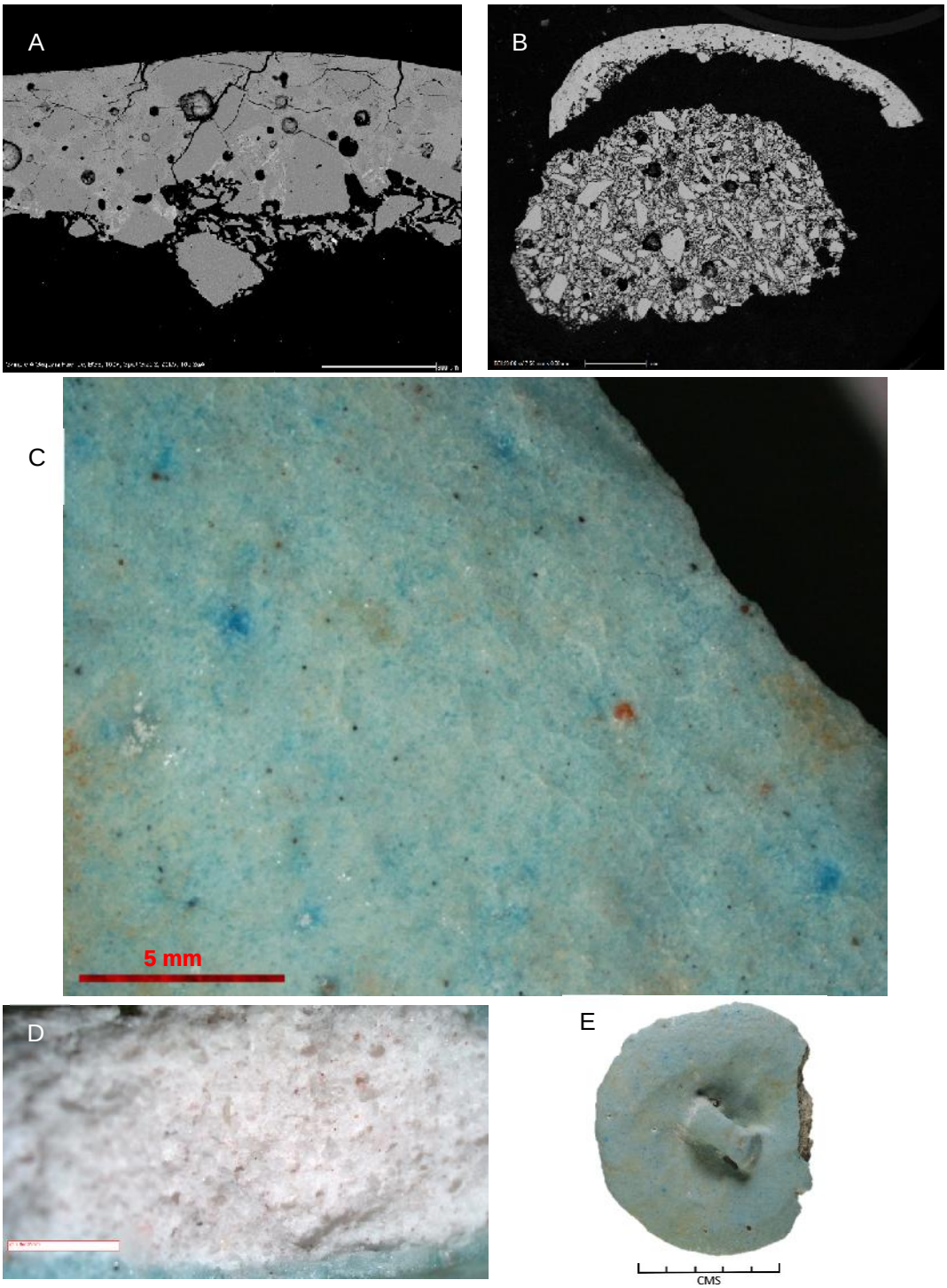

s80: SEM-BSE glaze profile (scale: 300 µm (A) and 1 mm (B)); OM glaze surface micrograph (C (scale: 5 mm)); OM glaze profile (D (scale: 2 mm)) and the sherd (E). The glaze has bubbles and unreacted quartz (A and B). The micrograph of the glaze reveals cracking. The IAL is thin which is partly responsible for the glaze/body separation during sampling. The sintered quartz in the body is heterogeneous in quartz particle size and shape. The surface of the glaze is crizzled as evident by the network of cracks running across the surface (C). Unreacted quartz has erupted through the glaze surface. The sherd paste (D) is off-white with probable iron inclusions.

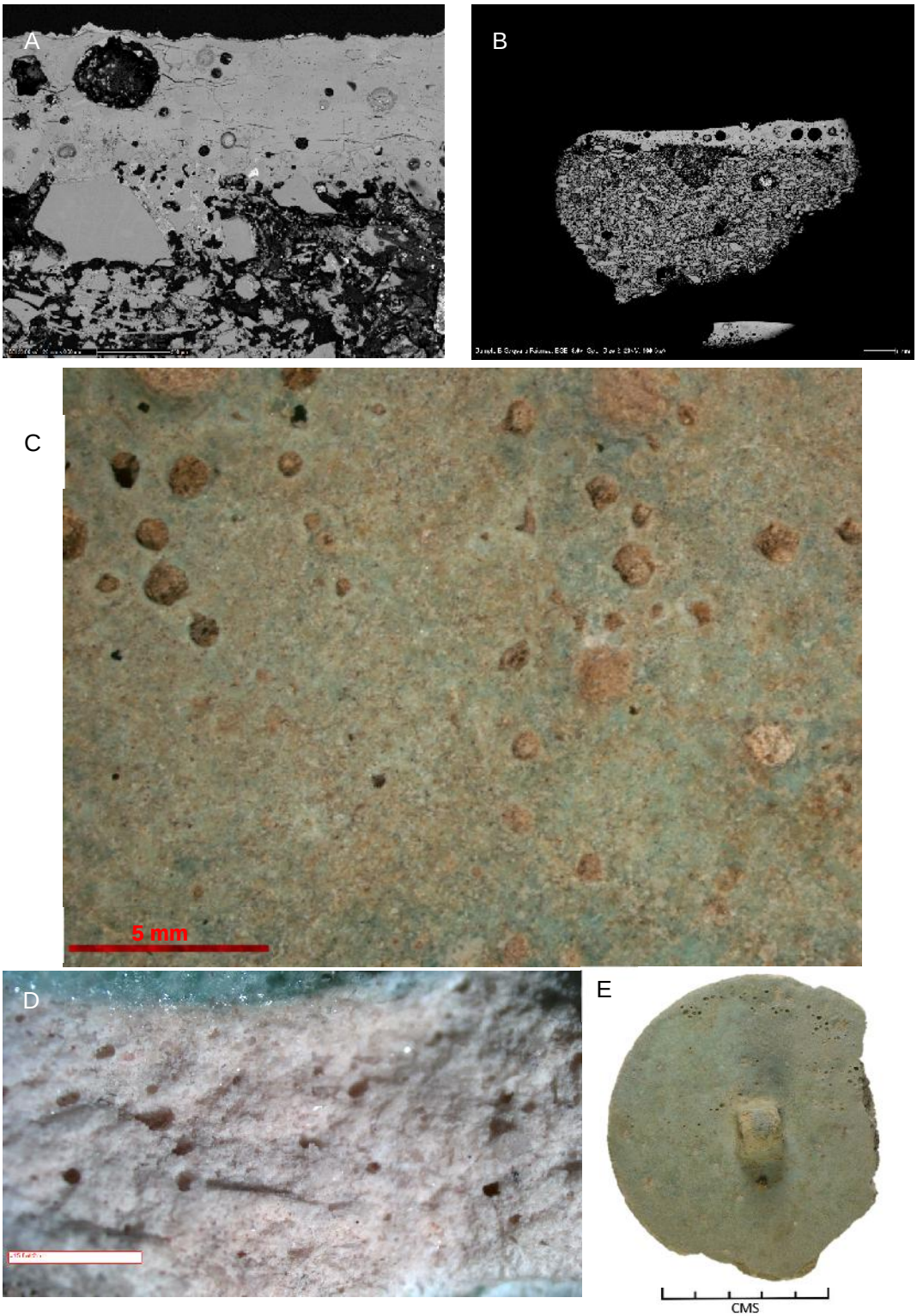

s81: SEM-BSE glaze profile (scale: 200 µm (A) and 1 mm (B)); OM glaze surface micrograph (C (scale: 5 mm)); OM glaze profile (D (scale: 2 mm)) and the sherd (E). The glaze has a few large bubbles and no identified unreacted quartz (A and B). There are cracks present in the glaze. The IAL is thin and the sintered quartz in the body is heterogeneous in quartz particle size and shape. The surface of the glaze is pocked and abraded by use and burial (C). The sherd paste (D) is reddish-white with probable iron inclusions.

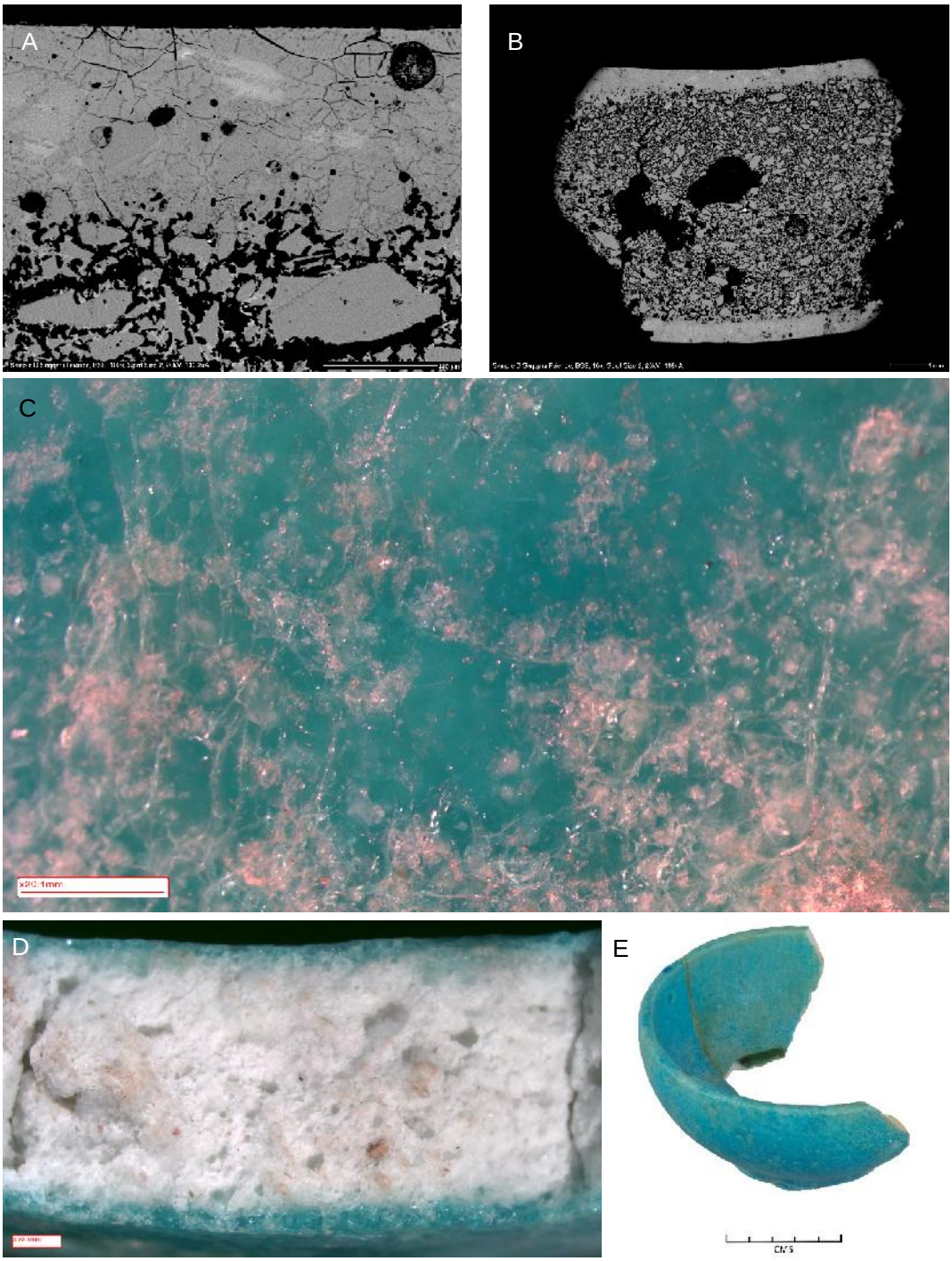

s82: SEM-BSE glaze profile (scale: 300 µm (A) and 1 mm (B); OM glaze surface micrograph (C (scale: 1 mm)); OM glaze profile (D (scale: 1 mm)) and the sherd (E). The glaze has bubbles and minor unreacted quartz (A and B). Cracks are present throughout the glaze. The IAL is thin and the sintered quartz in the body is heterogeneous in quartz particle size and shape. The bright specks in the glaze and body are iron and tin (confirmed through SEM-EDS). The surface of the glaze is abraded by use and burial (C). The surface of the glaze is crizzled as evident by the network of cracks running across the surface. Bubble are present below the glaze surface. The sherd paste (D) is white with iron inclusions. The adhesive used to adhere the individual sherds has discoloured (E).

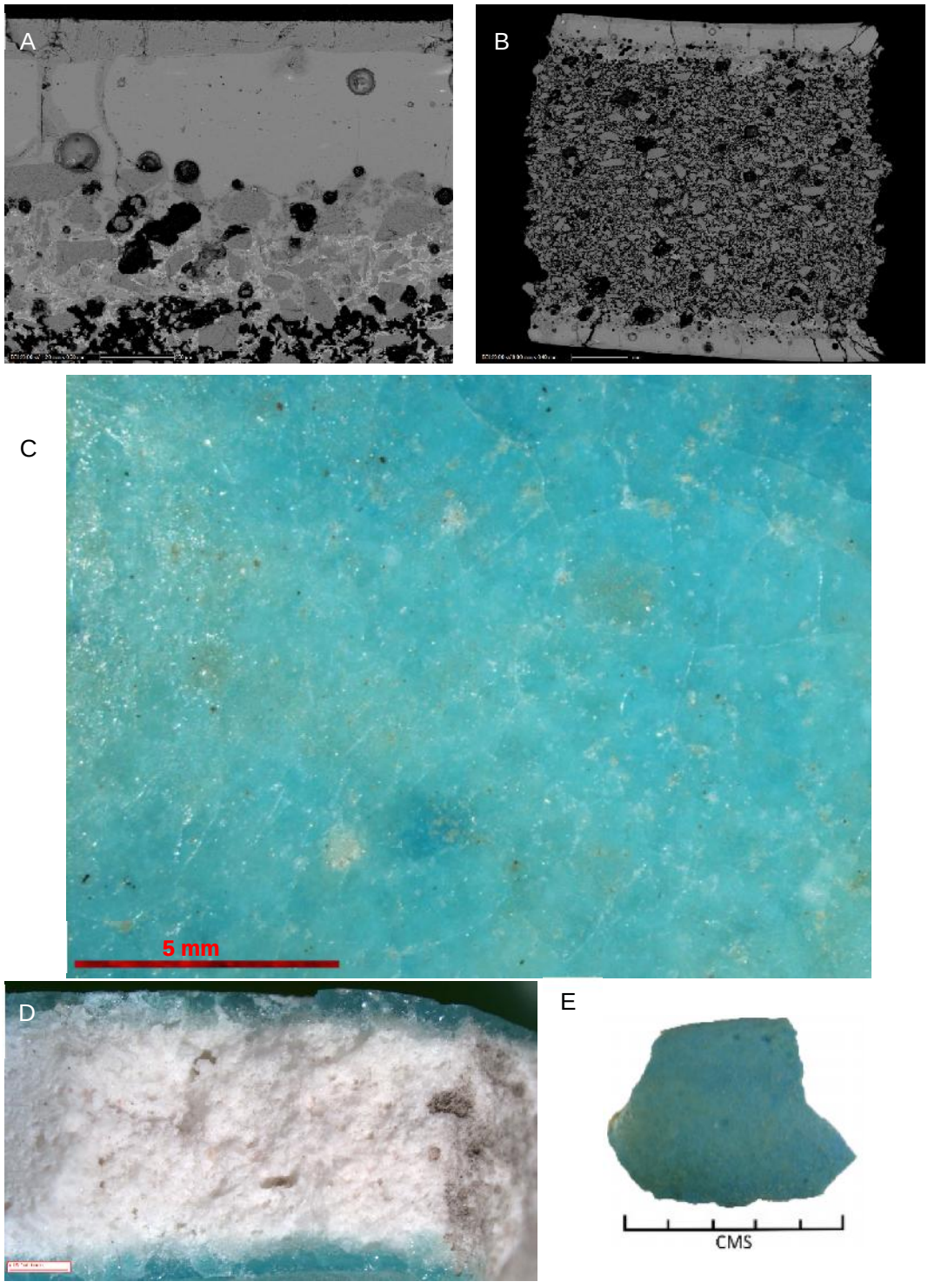

s83: SEM-BSE glaze profile (scale: 200 µm (A) and 1 mm (B)); OM glaze surface micrograph (C (scale: 5 mm)); OM glaze profile (D (scale: 1 mm)) and the sherd (E). The glaze has bubbles and minor unreacted quartz (A and B). The glaze is weathered with cracks and minor areas of alkali-depleted glaze as evinced by slightly darker glaze areas adjacent to cracks and the glaze surface. The IAL is moderately thick and the sintered quartz in the body is heterogeneous in quartz particle size and shape. The surface of the glaze is abraded by use and burial (C). The surface of the glaze is crizzled as evident by the network of cracks. The sherd paste (D) is white with iron inclusions.

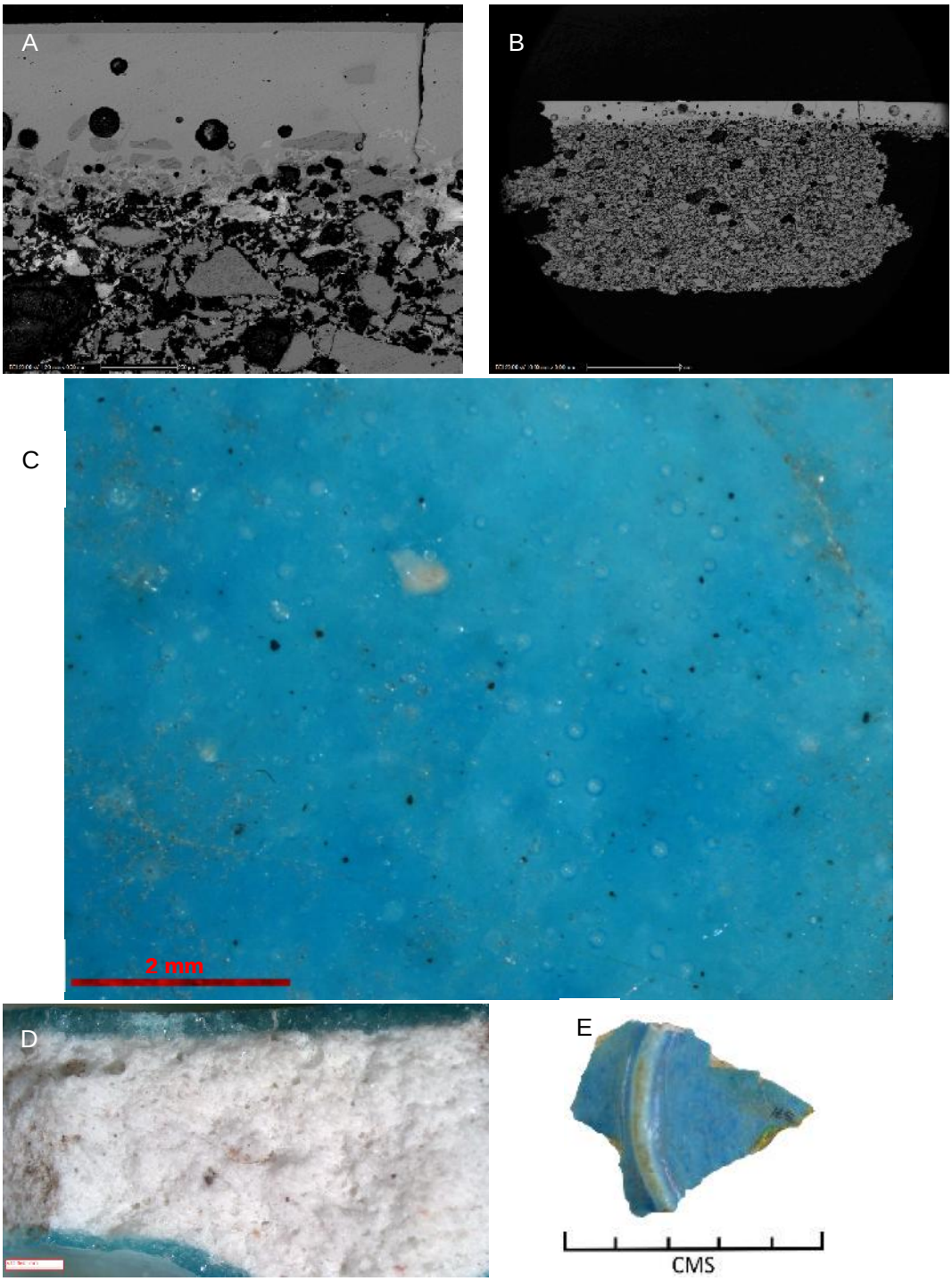

s84: SEM-BSE glaze profile (scale: 200 µm (A) and 2 mm (B)); OM glaze surface micrograph (C (scale: 2 mm)); OM glaze profile (D (scale: 1 mm)) and the sherd (E). The glaze has bubbles and minor unreacted quartz (A and B). The glaze is weathered with minor areas of alkali-depleted glaze as evinced by slightly darker glaze areas adjacent to cracks and the glaze surface. The IAL is thin and the sintered quartz in the body is heterogeneous in quartz particle size and shape. Bubbles and an erupted unreacted quartz particle are evident in the glaze (C). The sherd paste (D) is white with iron inclusions.

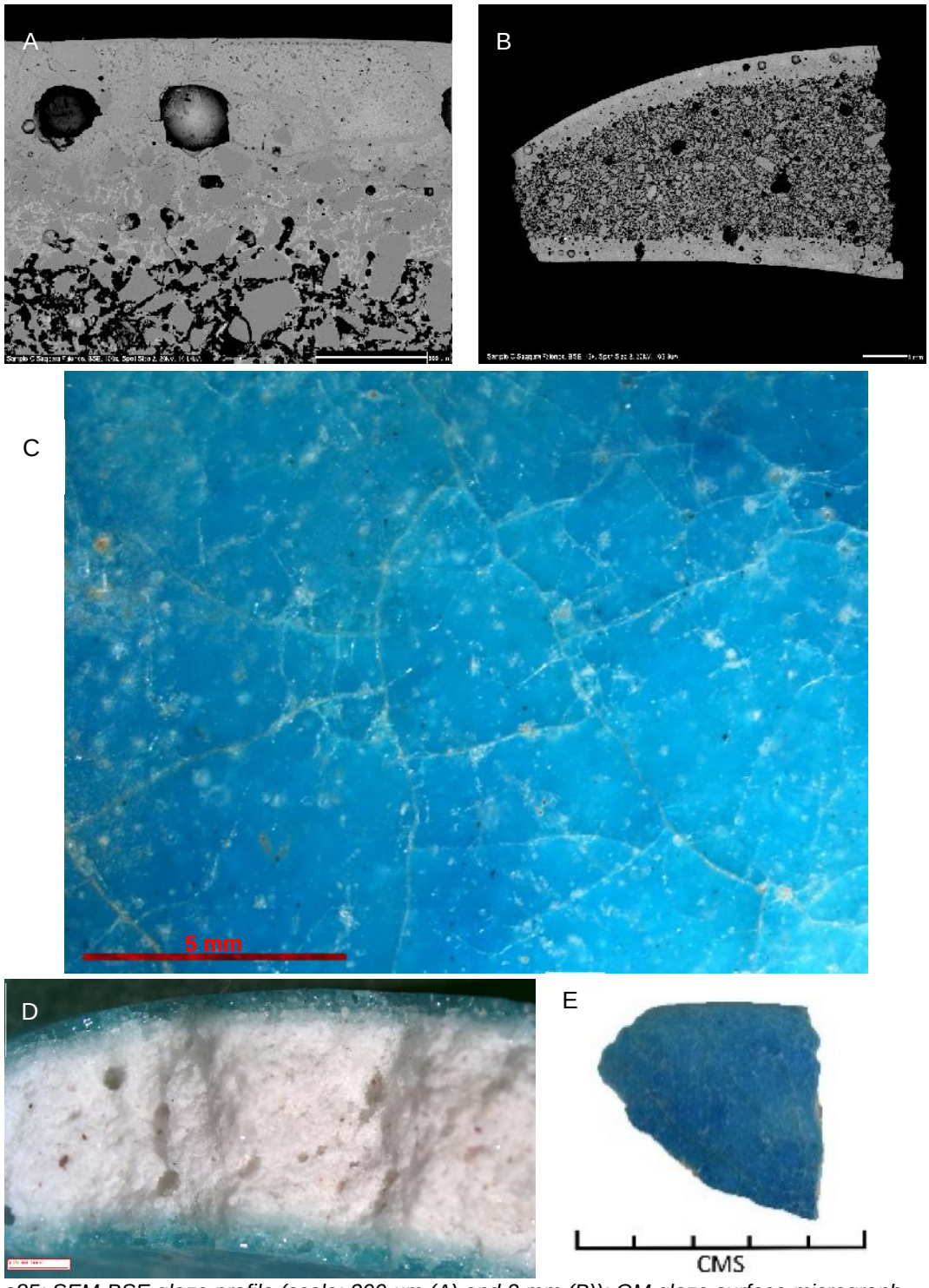

s85: SEM-BSE glaze profile (scale: 300 µm (A) and 2 mm (B)); OM glaze surface micrograph (C (scale: 5 mm)); OM glaze profile (D (scale: 1 mm)) and the sherd (E). The glaze has bubbles and minor unreacted quartz (A and B). The glaze is weathered with some areas of potentially low impacted glaze represented by slightly brighter glaze areas in-between the cracks. Iron and zirconium are identified as inclusions in the glaze and body (confirmed by SEM-EDS). The IAL is moderately thick and the sintered quartz in the body is heterogeneous in quartz particle size and shape. Bubbles are evident in the glaze (C). The surface of the glaze is crizzled as evident by the network of cracks. The sherd paste (D) is white with iron inclusions.

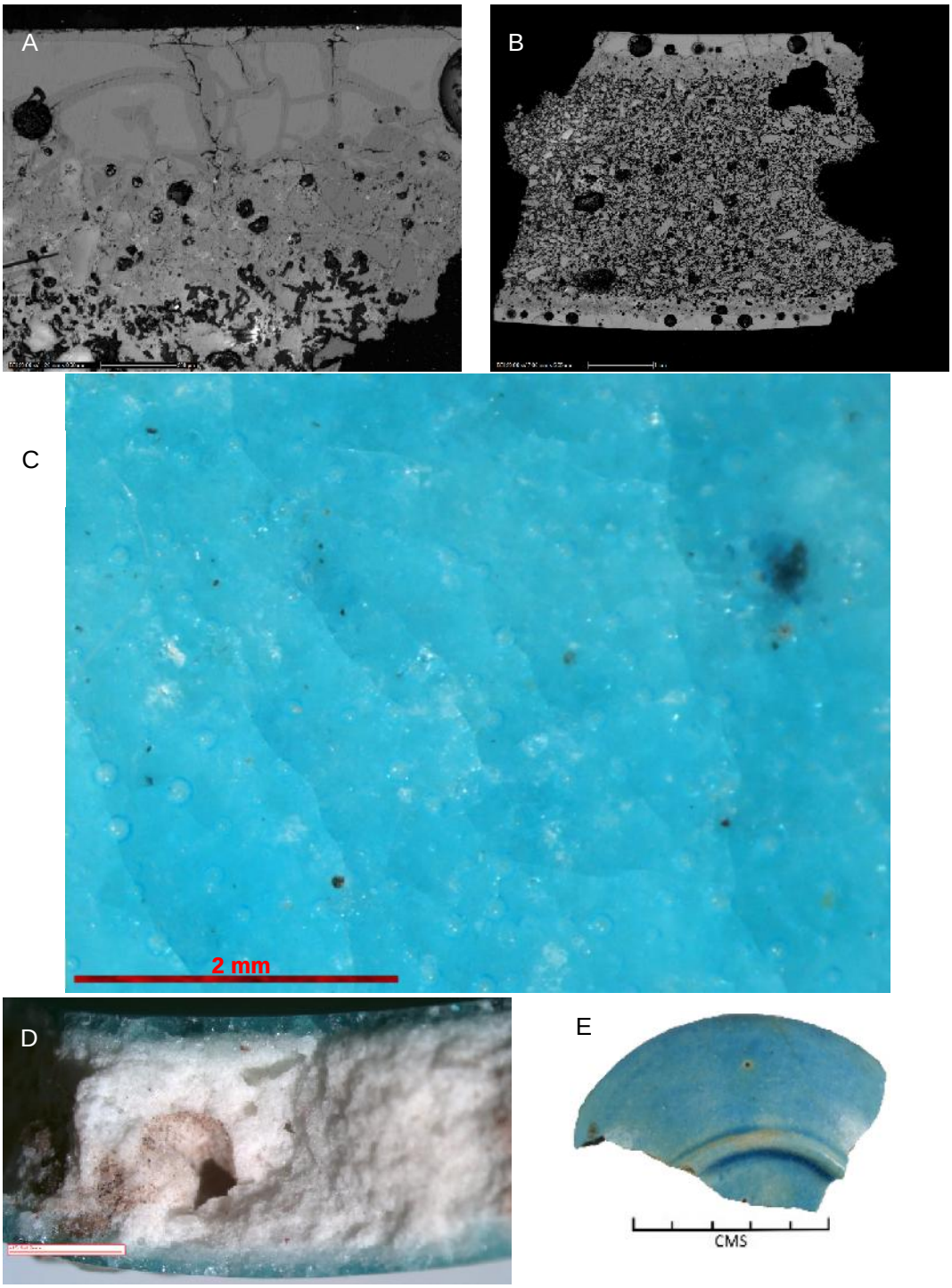

s87: SEM-BSE glaze profile (scale: 200 µm (A) and 1 mm (B)); OM glaze surface micrograph (C (scale: 2 mm)); OM glaze profile (D (scale: 2 mm)) and the sherd (E). The glaze has bubbles and no identified unreacted quartz (A and B). The glaze is weathered with some areas of potentially low impacted glaze represented by slightly brighter glaze areas in-between the cracks. The IAL is relatively thick and the sintered quartz in the body is heterogeneous in quartz particle size and shape. Bubbles are evident in the glaze (C). The surface of the glaze is crizzled as evident by the network of cracks. The sherd paste (D) is white.

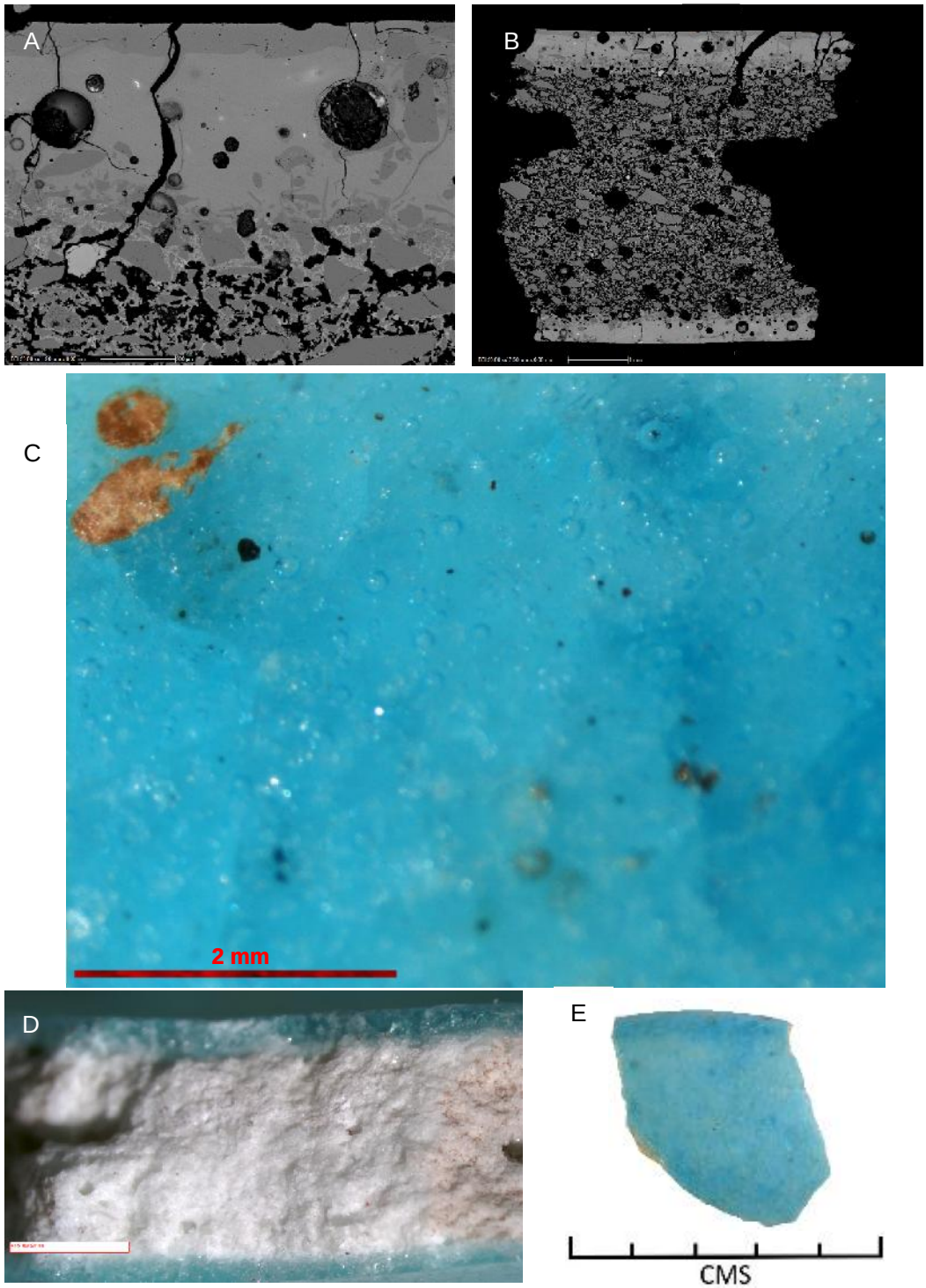

s89: SEM-BSE glaze profile (scale: 200 µm (A) and 1 mm (B)); OM glaze surface micrograph (C (scale: 2 mm)); OM glaze profile (D (scale: 2 mm)) and the sherd (E). The glaze has bubbles and unreacted quartz (A and B). The glaze is weathered with alkali depleted areas at the glaze surface as represented by slightly darker areas at the surface. The IAL is thin and the sintered quartz in the body is heterogeneous in quartz particle size and shape. Bubbles and embedded materials are evident in the glaze (C). The surface of the glaze is crizzled as evident by the faint network of cracks. A small area of soil coating the glaze is evident in the upper left corner of the micrograph. The sherd paste (D) is white.

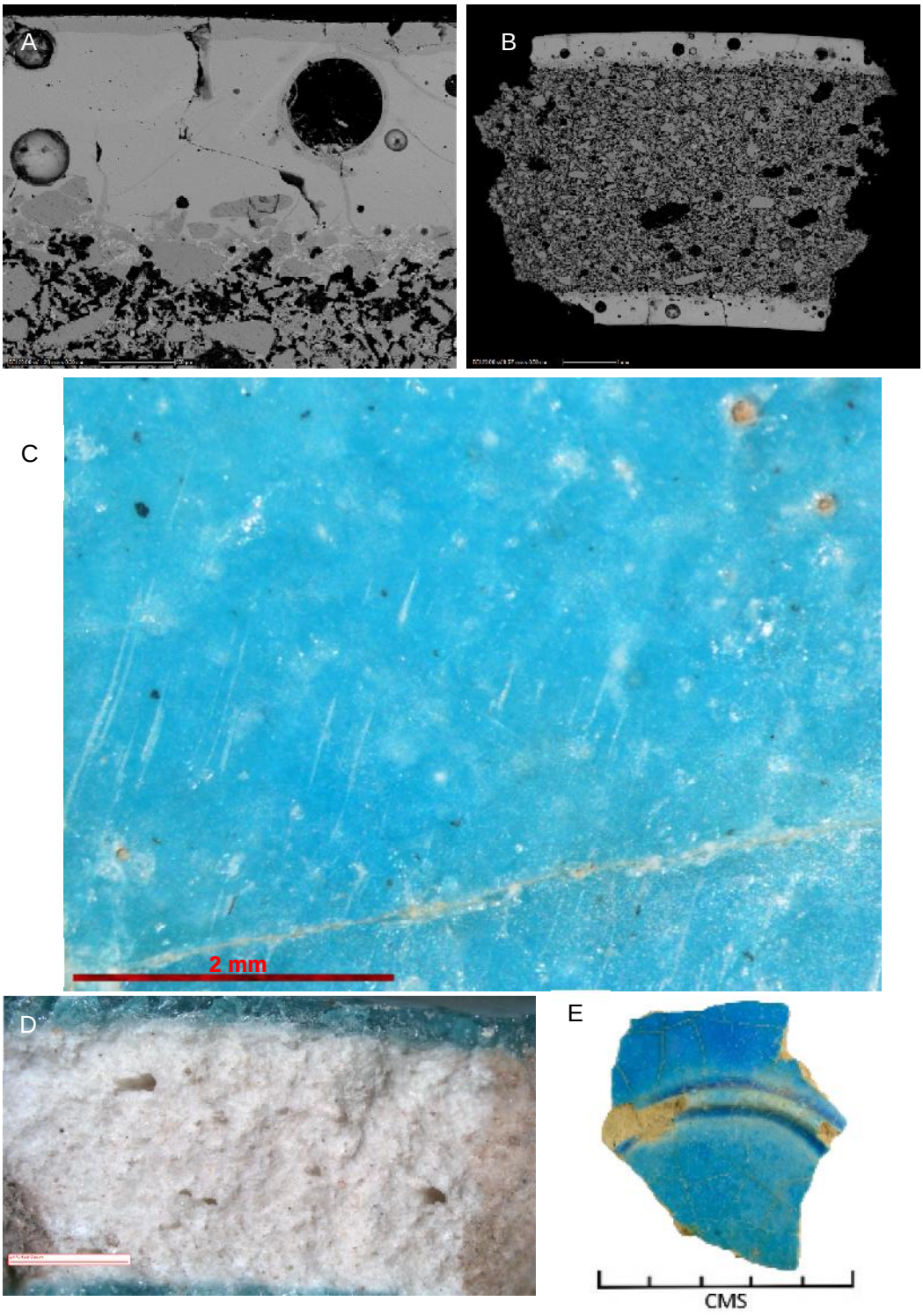

s90: SEM-BSE glaze profile (scale: 200 µm (A) and 1 mm (B)); OM glaze surface micrograph (C (scale: 2 mm)); OM glaze profile (D (scale: 2 mm)) and the sherd (E). The glaze has bubbles and minor unreacted quartz (A and B). The glaze is weathered with alkali depleted areas at the glaze surface as represented by slightly darker areas at the surface. The IAL is thin and the sintered quartz in the body is heterogeneous in quartz particle size and shape. The glaze surface is abraded through use and burial (C). Bubbles and cracks are evident in the glaze. The surface of the glaze is crizzled as evident by the network of cracks. The sherd paste (D) is white.

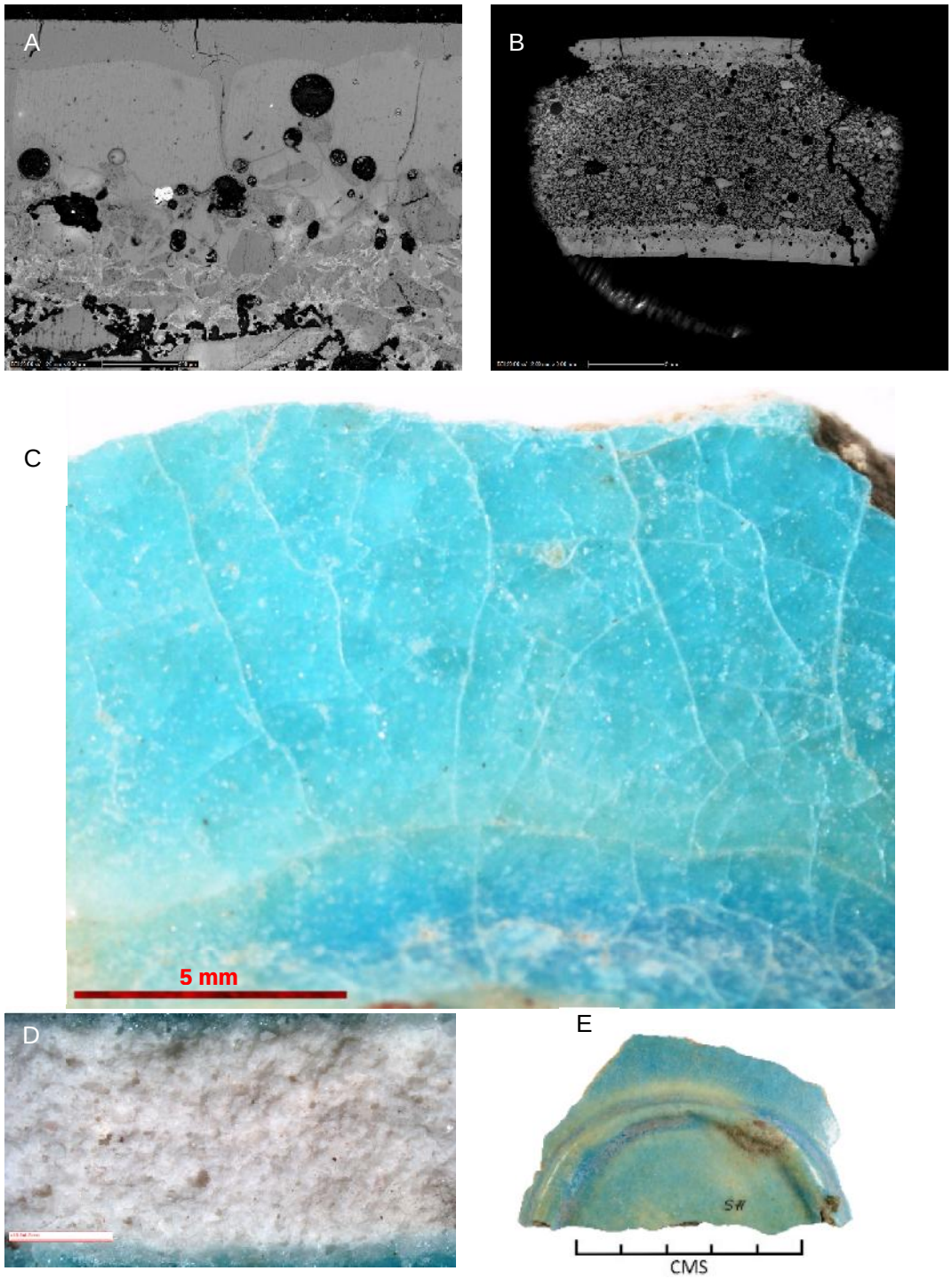

s91: SEM-BSE glaze profile (scale: 200 µm (A) and 2 mm (B)); OM glaze surface micrograph (C (scale: 5 mm)); OM glaze profile (D (scale: 2 mm)) and the sherd (E). The glaze has bubbles and minor unreacted quartz (A and B). The glaze is weathered with alkali depleted areas at the glaze surface as represented by slightly darker areas at the surface. The IAL is thin and the sintered quartz in the body is heterogeneous in quartz particle size and shape. The glaze surface is abraded through use and burial (C). Bubbles are evident in the glaze. The surface of the glaze is crizzled as evident by the network of cracks. The sherd paste (D) is white. Setter remnants are present on the foot ring (E).

Appendix C: Glass Standard Measurements

Elements: Aluminium to Manganese	Corning Glass A		Corning Glass B		NIST610		NIST612	
	Reference Composition	Theoretical Composition	Reference Composition	Theoretical Composition	Reference Composition		Reference Composition	
	Oxide Wt%	Oxide Wt%	Oxide Wt%	Oxide Wt%	ppm	Oxide Wt%	ppm	Oxide wt%
Aluminium (Al)	1.000	0.800	4.360	4.000	195000.00	1.9500	203000.00	2.0300
Antimony (Sb)	1.750	1.810	0.460	0.400	396.00	0.0396	34.70	0.0035
Arsenic (As)	--	--	--	--	325.00	0.0325	35.70	0.0036
Barium (Ba)	0.560	0.500	0.120	0.050	452.00	0.0452	39.30	0.0039
Beryillium (Be)	--	--	--	--	476.00	0.0476	37.50	0.0038
Bismuth (Bi)	--	0.001	--	0.005	384.00	0.0384	30.20	0.0030
Bromine (Br)	--	--	--		93.00	0.0093	0.00	0.0000
Boron (B)	--	0.200	--	0.020	350.00	0.0350	0.00	0.0000
Cadmium (Cd)	--	--	--		270.00	0.0270	28.10	0.0028
Calcium (Ca)	5.030	5.010	8.560	8.000	114000.00	11.4000	119000.00	11.9000
Cerium (Ce)	--	--	--	--	453.00	0.0453	38.40	0.0038
Chloride (Cl)	--	0.100	1.000	0.200	274.00	0.0274	142.00	0.0142
Chromium (Cr)	--	0.001	--	0.005	408.00	0.0408	36.40	0.0036
Cobalt (Co)	0.170	0.200	0.046	0.050	410.00	0.0410	35.50	0.0036
Cesium (Cs)	--	--	--	--	366.00	0.0366	42.70	0.0043
Copper (Cu)	1.170	1.200	2.660	3.000	441.00	0.0441	37.80	0.0038
Dysprosium (Dy)	--	--	--	--	437.00	0.0437	35.50	0.0036
Erbium (Er)	--	--	--	--	455.00	0.0455	38.00	0.0038
Europium (Eu)	--	--	--	--	447.00	0.0447	35.60	0.0036
Fluorine (F)	--	--	--	--	304.00	0.0304	80.00	0.0080
Gallium (Ga)	--	--	--	--	433.00	0.0433	36.90	0.0037
Gadolinium (Gd)	--	--	--	--	449.00	0.0449	37.30	0.0037
Germanium (Ge)	--	--	--	--	447.00	0.0447	36.10	0.0036
Gold (Au)	--	--	--	--	23.60	0.0024	0.00	0.0000
Hafnium (Hf)	--	--	--	--	435.00	0.0435	36.70	0.0037
Holmium (Ho)	--	--	--	--	449.00	0.0449	38.30	0.0038
Hydrogen (H)	--	--	--	--	15.00	0.0015	0.00	0.0000
Indium (In)	--	--	--	--	434.00	0.0434	38.90	0.0039
Iridium (Ir)	--	--	--	--	0.00	0.0000	0.00	0.0000
Iron (Fe)	1.090	1.100	0.340	0.300	458.00	0.0458	51.00	0.0051
Lanthanum (La)	--	--	--	--	440.00	0.0440	36.00	0.0036
Lead (Pb)	0.120	0.050	0.610	0.500	426.00	0.0426	38.57	0.0039
Lithium (Li)	--	0.010	--	0.001	468.00	0.0468	40.20	0.0040
Lutetium (Lu)	--	--	--	--	439.00	0.0439	37.00	0.0037
Magnesium (Mg)	2.660	3.010	1.030	0.800	432.00	0.0432	68.00	0.0068
Manganese (Mn)	1.000	1.220	0.250	0.250	444.00	0.0444	38.70	0.0039

Elements:	Corning Glass A		Corning Glass B		NIST610		NIST612	
Niobium to Zirconium	Reference Composition	Theoretical Composition	Reference Composition	Theoretical Composition	Reference Composition		Reference Composition	
	Oxide Wt%	Oxide Wt%	Oxide Wt%	Oxide Wt%	ppm	Oxide Wt%	ppm	Oxide wt%
Nickel (Ni)	--	0.02	0.099	0.1	458.7	0.0459	38.8	0.0039
Niobium (Nb)	--	--	--	--	485.90	0.0486	38.90	0.0039
Palladium (Pd)	--	--	--	--	3.12	0.0003	1.05	0.0001
Phosphorus (P)	0.130	0.100	0.820	0.600	413.00	0.0413	46.60	0.0046
Potassium (K)	2.870	3.010	1.000	0.300	464.00	0.0464	62.30	0.0062
Paseodymium (Pr)	--	--	--	--	448.00	0.0448	37.90	0.0038
Platinum (Pt)	--	--	--	--	3.12	0.0003	2.51	0.0003
Rhenium (Re)	--	--	--	--	49.90	0.0050	6.63	0.0007
Rhodium (Rh)	--	--	--	--	1.29	0.0001	0.91	0.0001
Rubidium (Rb)	--	0.010	--	0.001	425.70	0.0426	31.40	0.0031
Samarium (Sm)	--	--	--	--	453.00	0.0453	37.70	0.0038
Scandium (Sc)	--	--	--	--	455.00	0.0455	39.90	0.0040
Selenium (Se)	--	--	--	--	138.00	0.0138	16.30	0.0016
Silicon Oxide (Si)	66.560	65.830	61.550	62.030	697000.00	69.7000	721000.00	72.1000
Silver (Ag)	--	0.002	--	0.010	251.00	0.0251	22.00	0.0022
Sodium (Na)	14.300	14.540	17.000	18.510	134000.00	13.4000	134000.00	13.4000
Strontium (Sr)	0.100	0.100	0.019	0.010	515.50	0.0516	78.40	0.0078
Sulfer (S)	--	0.100	--	0.500	575.00	0.0575	377.00	0.0377
Tantalum (Ta)	--	--	--	--	446.00	0.0446	37.60	0.0038
Tellurium (Te)	--	--	--	--	302.00	0.0302	0.00	0.0000
Terbium (Tb)	--	--	--	--	437.00	0.0437	37.60	0.0038
Thallium (Tl)	--	--	--	--	59.60	0.0060	14.90	0.0015
Thorium (Th)	--	--	--	--	457.20	0.0457	37.79	0.0038
Thulium(Tm)	--	--	--	--	435.00	0.0435	36.80	0.0037
Tin (Sn)	0.190	0.200	0.040	0.020	430.00	0.0403	38.60	0.0039
Titanium (Ti)	0.790	0.800	0.089	0.080	452.00	0.0452	44.00	0.0044
Tungsten (W)	--	--	--	--	444.00	0.0444	38.00	0.0038
Uranium (U)	--	--	--	--	461.50	0.0462	37.38	0.0037
Vanadium (V)	--	0.006	0.036	0.030	450.00	0.0450	38.80	0.0039
Yttrium (Y)	--	--	--	--	462.00	0.0462	38.30	0.0038
Ytterbium (Yb)	--	--	--	--	450.00	0.0450	39.20	0.0039
Zinc (Zn)	0.044	0.040	0.190	0.200	460.00	0.0460	39.10	0.0039
Zirconium (Zr)	--	0.005	--	0.025	448.00	0.0448	37.90	0.0038

Replicated Faience:
Repeated Measurements of Corning Glass B
using SEM-EDS (Oxides wt%)

(122 CG-B Repeated Measurements)

Element of Oxide	EDS Average	Standard Deviation	Coefficent of Variance	Corning Glass B Reference Value (wt%)	Relative Error of Accuracy (%)
Na	**16.806**	0.192	0.011	**17.000**	-1.138
Mg	**1.009**	0.068	0.068	**1.030**	-2.023
Al	**4.188**	0.097	0.023	**4.360**	-3.951
Si	**61.998**	0.469	0.008	**61.550**	0.728
P	**0.862**	0.098	0.113	**0.820**	5.164
Cl*	**0.182**	0.039	0.215	**1.000**	-81.822
K	**1.079**	0.069	0.064	**1.000**	7.903
Ca	**8.634**	0.119	0.014	**8.560**	0.862
Ti	**0.099**	0.070	0.706	**0.089**	11.337
V	**0.034**	0.069	2.058	**0.036**	-6.462
Mn	**0.244**	0.075	0.309	**0.250**	-2.486
Fe	**0.314**	0.072	0.228	**0.340**	-7.625
Co	**0.044**	0.054	1.241	**0.046**	-5.420
Ni	**0.111**	0.065	0.582	**0.099**	12.219
Cu	**3.226**	0.138	0.043	**2.660**	21.279
Zn	**0.181**	0.078	0.433	**0.190**	-4.792
Sr	**0.084**	0.192	2.291	**0.019**	339.985
Sn	**0.031**	0.128	4.189	**0.040**	-23.316
Sb	**0.272**	0.213	0.784	**0.460**	-40.877
Ba	**0.069**	0.109	1.579	**0.120**	-42.326
Pb	**0.422**	0.146	0.347	**0.610**	-30.841

* No corresponding oxide

Saqqara Faience:
Repeated Measurements of Corning Glass B
using SEM-EDS (Oxides wt%)

(81 CG-B Repeated Measurements)

Element of Oxide	EDS Average	Standard Deviation	Coefficent of Variance	Corning Glass B Reference Value (wt%)	Relative Error of Accuracy (%)
Na	**16.531**	0.264	0.016	**17.000**	-2.760
Mg	**0.982**	0.062	0.064	**1.030**	-4.666
Al	**4.128**	0.101	0.025	**4.360**	-5.318
Si	**61.550**	0.329	0.005	**61.550**	-0.001
P	**0.941**	0.152	0.161	**0.820**	14.702
Cl*	**0.183**	0.033	0.180	**1.000**	-81.750
K	**1.047**	0.064	0.061	**1.000**	4.731
Ca	**8.672**	0.101	0.012	**8.560**	1.303
Ti	**0.088**	0.077	0.878	**0.089**	-0.957
V	**0.011**	0.061	5.301	**0.036**	-68.107
Mn	**0.248**	0.079	0.319	**0.250**	-0.778
Fe	**0.316**	0.065	0.207	**0.340**	-7.108
Co	**0.058**	0.048	0.819	**0.046**	26.409
Ni	**0.093**	0.070	0.757	**0.099**	-6.472
Cu	**3.360**	0.160	0.048	**2.660**	26.323
Zn	**0.188**	0.102	0.542	**0.190**	-0.975
Sr	**0.703**	0.361	0.514	**0.019**	3599.805
Sn	**-0.111**	0.251	-2.256	**0.040**	-377.778
Sb	**-0.116**	0.359	-3.111	**0.460**	-125.121
Ba	**0.080**	0.119	1.494	**0.120**	-33.642
Pb	**0.441**	0.117	0.265	**0.610**	-27.778

* No corresponding oxide

Replicate Corning Glass B Measurements with SEM-EDS (Compound wt% Normalized)

Group indicates association with replications (R) or Saqqara Sherds (S); Normalized totals = N. Totals; Analytical Totals = A. Totals; Shaded areas were not used due to poor results and/or poor settings

Group	Na	Mg	Al	Si	P	S	Cl	K	Ca	Ti	V	Cr	Mn	Fe	Co	Ni	Cu	Zn	As	Rb	Sr	Zr	Ag	Sn	Sb	Ba	Pb	Bi	N. Total	A. Total
R	16.44	1.1	4.16	62.59	1.07	0.49	0.15	1.07	8.66	-0.01	0.07	-0.02	0.2	0.26	0.07	0.08	3.35	0.19	0.15	-1.33	0.51	-0.29	0.24	0.1	0.35	0.21	0.47	-0.32	100	99.37
R	16.66	1.05	4.3	62.29	0.85	0.55	0.08	1.2	8.63	0.24	-0.1	0.02	0.27	0.4	-0.02	0.31	3.27	0.21	-0.01	-0.76	0.61	-0.02	-0.01	0.04	-0.18	-0.14	0.56	-0.28	100	99.1
R	16.78	1.03	4.32	61.79	1.05	0.72	0.29	1.1	8.58	-0.07	0.01	0.08	0.24	0.35	0.07	0.2	3.29	0.23	0.01	-0.95	0.73	-0.18	0.04	-0.12	-0.19	0.19	0.46	-0.04	100	101.3
R	17.07	0.96	4.16	62.46	0.94	0.73	0.14	1.05	8.6	0.13	0.03	0.14	0.21	0.37	-0.04	0.17	3.28	0.17	0.06	-0.79	0.09	-0.19	0.01	-0.06	0.04	-0.05	0.42	-0.11	99.99	99.51
R	17.25	0.87	4.33	62.26	0.87	0.58	0.17	1.01	8.58	0.07	0.06	0.08	0.28	0.28	0.11	0.2	3.02	0.21	0.02	-0.54	-0.05	-0.08	0.04	-0.16	0.16	0.05	0.62	-0.29	100	100.3
R	16.97	0.92	4.33	63.12	0.84	0.5	0.12	1.11	8.65	0.08	0.02	0.01	0.28	0.3	0.07	0.03	3.15	0.27	0.22	-0.95	0	-0.23	0.13	-0.19	0.19	-0.03	0.57	-0.48	100	99.02
R	16.66	1.11	4	62.48	0.83	0.77	0.18	1.06	8.68	0.27	-0.05	0.05	0.27	0.41	-0.11	0.18	3.05	0.25	0.05	-0.62	-0.21	-0.14	-0.03	0.02	0.44	-0.12	0.4	0.12	100	100.3
R	16.6	1.08	4.24	62.17	0.95	0.48	0.21	1.24	8.63	-0.03	0.09	0.01	0.23	0.35	-0.07	0.19	3.06	0.08	-0.08	-0.79	0.16	-0.33	0.01	0.08	0.48	0.41	0.71	-0.15	100	100.3
R	16.67	1.06	4.11	61.78	0.91	0.44	0.2	1.17	8.75	-0.03	0.15	-0.02	0.32	0.37	0.15	-0.04	3.16	0.16	0.13	-0.29	-0.02	0.26	-0.1	0.01	0.22	0.21	0.65	-0.39	99.99	99.81
R	16.73	1.05	4.19	61.57	0.58	0.73	0.22	1.15	8.76	0.16	0		0.27	0.27	0.04	0.11	3.14	0.38			-0.28			0.15	0.32	0.02	0.43		99.99	101.5
R	16.88	1.02	4.27	61.66	0.76	0.64	0.2	1.1	8.68	0.03	0		0.26	0.21	0.04	0.09	3.2	0.06			-0.07			-0.05	0.28	0.21	0.57		100	101.5
R	16.79	1.19	4.07	62.08	0.86	0.5	0.2	1.1	8.69	0.14	-0.03		0.23	0.36	0.04	0.12	3.21	0.18			0.01			-0.13	-0.01	0.02	0.41		100	102.2
R	16.94	1	4.15	61.09	0.89	0.6	0.18	1.15	8.44	0.16	0.02		0.21	0.29	0.1	0.16	3.09	0.28			0.05			0.16	0.35	0.03	0.62		99.96	92.11
R	16.83	1.08	3.92	61.58	0.82	0.67	0.19	1.1	8.53	0.1	-0.07		0.18	0.4	-0.09	0.1	3.3	0.19			0.22			0.08	0.33	0.11	0.4		99.97	91.45
R	17.03	0.94	4.17	61.7	0.88	0.62	0.22	1.11	8.63	0.02	0.12		0.3	0.25	0.01	0.09	3.06	0.18			0.41			-0.23	-0.2	0.13	0.53		99.97	90.38
R	16.93	1.03	4.11	61.28	0.82	0.8	0.14	1.17	8.56	0.06	0.16		0.2	0.38	0.06	0.19	2.9	0.17			0.01			-0.05	0.46	0.18	0.42		99.98	100.1
R	16.7	1.01	4.05	61.64	0.88	0.56	0.17	1.02	8.7	0.13	-0.05		0.4	0.27	0.03	0.17	3.03	0.03			0.17			0.08	0.61	-0.08	0.48		100	99.49
R	16.7	1.03	4.2	60.64	0.72	0.58	0.2	0.98	8.46	0.19	-0.02		0.23	0.4	0.01	0.16	3.4	0.32			0.37			0.22	0.82	0.05	0.34		100	101.6
R	16.7	1.12	3.95	61.21	0.82	0.65	0.15	1.1	8.51	0.04	0.15		0.18	0.21	0.15	0.17	3.21	0.29			0.12			0.28	0.4	0.15	0.45		100	100.4
R	17.08	1.06	4.11	61.94	0.84	0.73	0.17	1.08	8.57	0.18	0		0.22	0.36	0.06	0.17	3.25	0.26			-0.04			-0.28	-0.04	-0.01	0.29		100	98.51
R	16.47	1.1	4.23	61.63	0.87	0.62	0.15	1.09	8.57	0.15	0.02		0.26	0.26	0.02	0.12	3.26	0.33			-0.17			0.16	0.56	-0.06	0.36		100	99.53
R	16.45	1.06	4.17	62.27	0.87	0.58	0.19	1.07	8.73	0.2	-0.05		0.23	0.3	-0.05	0.1	3.27	0.21			-0.09			-0.01	0.17	0	0.33		100	98.29
R	16.6	1.04	4.13	61.31	0.82	0.62	0.21	1.07	8.52	0.11	0.08		0.26	0.35	0.07	-0.1	3.21	0.25			0.12			0.2	0.33	0.2	0.62		100	99.7
R	16.73	0.96	4.34	61.08	0.72	0.57	0.25	1.17	8.42	0.1	-0.03		0.32	0.28	0.09	0.16	3.33	0.13			-0.24			0.23	0.69	0.11	0.6		100	100.1
R	16.64	1.01	3.95	61.99	0.58	0.68	0.16	1.09	8.49	0.15	0.03		0.28	0.36	0.02	0.31	3.34	0.21			-0.34			0.08	0.21	0.12	0.64		100	99.28
R	17.08	1.07	4.15	60.92	0.82	0.65	0.19	1.2	8.52	0.09	0.1		0.17	0.29	0.09	0.2	3.27	0.19			-0.01			0.17	0.49	-0.01	0.35		99.99	100.5
R	16.99	1	4.13	60.86	1.01	0.42	0.23	1.19	8.81	0.17	0.08		0.25	0.23	-0.04	0.08	3.2	0.05			0			0.21	0.49	0.06	0.59		100	99.71
R	16.7	0.94	4.15	62.23	0.71	0.59	0.19	1.1	8.69	0.18	-0.04	0.01	0.17	0.39	0.1	0.11	3.37	0.21	0.11	-0.77	0.02	0.2	0.03	0.08	0.15	0.04	0.56	-0.22	100	99.27
R	16.83	0.98	4.17	62.58	0.89	0.5	0.1	1.16	8.64	0.07	0.24	-0.02	0.28	0.28	0.12	0.22	3.17	0.3	0.12	-1.01	0.28	-0.1	-0.03	-0.06	0.08	0.13	0.29	-0.23	99.98	99.89
R	16.85	1.06	4.24	63.07	0.76	0.62	0.14	1.19	8.59	0.02	0.15	0.02	0.26	0.34	0.09	0.1	3.18	-0.12	0.07	-0.73	0.19	0	-0.12	-0.03	-0.46	0.36	0.24	-0.1	99.98	99.37
R	16.99	0.87	4.11	61.44	1	0.68	0.2	1.17	8.59	0.2	-0.04	-0.03	0.3	0.29	0.05	0.01	3.06	0.3	0.22	-0.33	0.08	-0.08	0.02	0	0.41	-0.02	0.3	0.21	100	100.2
R	16.85	0.89	4.3	62.16	0.81	0.6	0.13	1.12	8.69	0.16	0	0.01	0.26	0.3	0.08	0.09	3.15	0.27	0.12	-1.09	-0.38	-0.04	-0.16	0.35	1.08	-0.05	0.49	-0.2	99.99	99.83
R	16.57	1.03	4.31	62.84	0.88	0.69	0.2	1.04	8.68	-0.02	0.16	0	0.16	0.26	0.03	0.14	3.09	0.18	0.13	-1.28	-0.02	0.18	-0.07	0.07	0.24	0.21	0.36	-0.08	99.98	98.41
R	16.83	0.99	4.17	61.63	0.78	0.86	0.23	1.1	8.7	0.09	0.06	0.01	0.17	0.37	0.05	0.22	3.21	0.13	0.13	-0.25	-0.24	-0.24	-0.1	0.1	0.42	0.05	0.43	0.12	100	99.64
R	16.98	0.96	4.38	62.35	0.96	0.47	0.14	1.09	8.53	0.1	-0.11	0.09	0.22	0.31	0.07	0.03	3.01	0.3	0.09	-0.85	0.21	-0.04	-0.05	0.15	0.31	0.18	0.53	-0.4	100	99.07
R	17.07	0.99	4.41	62.22	0.84	0.55	0.19	1.05	8.68	0.05	-0.05	-0.03	0.22	0.35	0	0.15	3.16	0.16	0.11	-0.3	0.06	-0.06	0.08	0.02	-0.23	0.05	0.45	-0.2	99.99	99.01
R	16.76	0.97	4.37	62.23	0.81	0.55	0.21	1.05	8.69	0.02	0.12	0.06	0.32	0.34	0.03	0.1	3.29	0.21	0.06	-0.87	-0.23	-0.08	-0.04	-0.03	0.28	0.16	0.62	0	100	99.79
R	17.06	1.06	4.21	61.61	0.9	0.49	0.19	1.19	8.66	0.11	-0.01	0.05	0.24	0.39	0.09	0.18	3.36	0.21	0.02	-0.58	-0.15	0.01	0	0.06	0.2	0.1	0.57	-0.24	99.98	100.6
R	16.91	1.13	4.33	63.28	0.87	0.42	0.17	0.94	8.6	0.12	-0.01	0.08	0.14	0.41	0.14	0.14	3.44	0.24	0.24	-1.64	-0.05	-0.01	0.04	-0.33	0	0.02	0.79	-0.39	100	99.5
R	16.81	1	4.18	61.49	0.98	0.91	0.24	0.97	8.7	0.27	0	0.05	0.21	0.27	0.02	0.16	3.04	0.17	0.01	-0.72	0.11	0.04	0.06	0.12	0.49	0	0.16	0.28	100	101.8
R	16.98	1.03	4.06	62.7	0.99	0.61	0.15	1.07	8.75	0.26	-0.01	0.07	0.3	0.41	-0.03	0.1	3.38	0.15	0.17	-1.36	-0.21	-0.09	0.12	-0.14	0.35	-0.13	0.32	0.02	100	100.6
R	16.78	0.98	4.23	62.02	1.02	0.62	0.2	1.02	8.39	0.07	0.06	0.06	0.32	0.26	0.05	0.17	3.36	0.09	-0.09	-0.68	0.08	-0.12	-0.05	-0.02	0.76	0.06	0.19	0.17	100	101.1
R	16.99	0.96	4.1	61.92	0.69	0.63	0.15	1.1	8.67	0.06	-0.04	0.02	0.3	0.4	0.11	0.18	3.25	0.09	0.22	-0.35	-0.1	-0.09	-0.05	0.13	0.45	0	0.36	-0.15	100	99.46
R	17.09	0.93	4.22	61.53	0.86	0.68	0.22	1.15	8.58	0.09	-0.03	-0.07	0.24	0.19	0.02	0.16	3.1	0.25	-0.05	-0.68	0.3	-0.13	-0.07	0.18	0.47	0.35	0.32	0.11	100	99.52
R	16.76	0.93	4.23	61.83	0.74	0.68	0.22	1.12	8.68	0.03	0.03	0.07	0.22	0.38	0.03	0.15	3.21	0.22	0.06	-0.81	0.08	0.13	0.13	-0.07	0.31	0.17	0.52	-0.05	100	98.37
R	16.81	1.08	4.09	62.85	0.83	0.57	0.24	1.03	8.64	0	0		0	0.41	0	0	3.44	0			0			0	0	0	0		99.99	100.1
R	16.64	1.08	4.15	62.52	0.81	0.51	0.25	1.1	8.56	0	0		0	0	0	0	3.52	0			0			0	0	0	0.87		100	102.2

Replicate Corning Glass B Measurements with SEM-EDS (Compound wt% Normalized)

Group indicates association with replications (R) or Saqqara Sherds (S); Normalized totals = N. Totals; Analytical Totals = A. Totals; Shaded areas were not used due to poor results and/or poor settings

Group	Na	Mg	Al	Si	P	S	Cl	K	Ca	Ti	V	Cr	Mn	Fe	Co	Ni	Cu	Zn	As	Rb	Sr	Zr	Ag	Sn	Sb	Ba	Pb	Bi	N. Total	A. Total
R	17.02	1.03	4.11	62.52	0.79	0.68	0.16	1.1	8.59	0	0		0.25	0.32	0	0	3.43	0			0			0	0	0	0		100	101.7
R	16.96	1.03	4.15	62.98	0.86	0.53	0.21	1.07	8.78	0	0		0.3	0	0	0	3.13	0			0			0	0	0	0		100	101.1
R	17.12	1.02	3.84	62.69	0.96	0.76	0.17	1	8.67	0	0		0.31	0.33	0	0	3.11	0			0			0	0	0	0		99.98	99.9
R	17.08	0.97	4.09	62.63	0.92	0.66	0.19	1	8.71	0	0		0.25	0.32	0	0	3.17	0			0			0	0	0	0		99.99	100.9
R	16.89	1.11	4.3	62.66	0.79	0.7	0.18	1.03	8.83	0	0		0.41	0	0	0	3.1	0			0			0	0	0	0		100	99.62
R	17.13	1.06	4.06	62.57	0.9	0.61	0.22	1.12	8.88	0	0		0	0.29	0	0	3.17	0			0			0	0	0	0		100	99.65
R	17.07	0.91	4.18	62.66	0.74	0.92	0.16	1.08	8.73	0	0		0	0.35	0	0	3.2	0			0			0	0	0	0		100	99.86
R	17.13	1.03	4.23	62.02	0.94	0.63	0.24	1.12	8.67	0	0		0.28	0.52	0	0	3.19	0			0			0	0	0	0		100	101.4
R	16.8	1.06	4.21	62.51	0.73	0.66	0.19	1.15	8.72	0	0		0.31	0.33	0	0	3.35	0			0			0	0	0	0		100	100.2
R	17.1	1.08	4.14	62.46	0.89	0.72	0.14	1.21	8.71	0	0		0	0.36	0	0	3.18	0			0			0	0	0	0		99.99	101.3
R	16.91	1.05	4.22	62.52	0.74	0.71	0.22	1.06	8.67	0	0		0	0.36	0	0	3.52	0			0			0	0	0	0		99.98	101.9
R	17.09	0.88	4.21	62.7	0.8	0.66	0.19	0.95	8.87	0	0		0	0.38	0	0	3.26	0			0			0	0	0	0		99.99	99.68
R	17.4	0.95	4.28	62.19	0.89	0.59	0.18	1.02	8.57	0	0		0.31	0.31	0	0	3.33	0			0			0	0	0	0		100	101.3
R	17.1	0.94	4.33	62.17	0.85	0.54	0.23	1.13	8.65	0	0		0.32	0.41	0	0	3.34	0			0			0	0	0	0		100	102.4
R	16.93	0.93	4.26	62.61	0.92	0.72	0.18	1.11	8.98	0	0		0.28	0	0	0	3.07	0			0			0	0	0	0		99.99	101.2
R	17.08	1.01	4.23	62.59	1.01	0.59	0.14	1.12	8.68	0	0		0	0.34	0	0	3.2	0			0			0	0	0	0		99.99	102.1
R	17.08	1.13	4.38	62.16	0.78	0.79	0.23	1.05	8.83	0	0		0.3	0	0	0	3.27	0			0			0	0	0	0		100	100.6
R	16.91	1.09	4.43	62.55	0.74	0.7	0.17	1.19	8.51	0	0		0	0.38	0	0	3.33	0			0			0	0	0	0		100	101
R	16.78	1.07	4.17	62.75	0.84	0.59	0.22	1.08	8.76	0	0		0	0.36	0	0	3.39	0			0			0	0	0	0		100	100.6
R	16.89	0.95	4.25	62.49	0.9	0.6	0.23	0.98	8.74	0	0		0.29	0.33	0	0	3.34	0			0			0	0	0	0		99.99	99.89
R	17.09	0.97	4.34	62.78	0.81	0.58	0.2	1.2	8.8	0	0		0	0	0	0	3.22	0			0			0	0	0	0		99.99	99.59
R	16.99	1	4.35	62.12	0.78	0.73	0.21	1.08	8.89	0	0		0.31	0.46	0	0	3.09	0			0			0	0	0	0		100	99.73
R	17.11	0.96	4.18	62.43	0.78	0.72	0.21	1.13	8.8	0	0		0.28	0.31	0	0	3.09	0			0			0	0	0	0		100	99.36
R	17.17	0.98	4.07	62.74	0.69	0.74	0.15	1.02	8.95	0	0		0	0.37	0	0	3.13	0			0			0	0	0	0		100	98.1
R	17.04	0.93	4.08	63.13	0.74	0.5	0.27	1.1	8.94	0	0		0	0	0	0	3.26	0			0			0	0	0	0		99.99	99.38
R	17.26	0.89	4.3	62.2	0.91	0.76	0.2	1.08	8.88	0	0		0	0.32	0	0	3.19	0			0			0	0	0	0		99.99	98.75
R	16.64	0.96	4.1	63.01	0.89	0.66	0.26	1.02	8.54	0	0		0.31	0.32	0	0	3.3	0			0			0	0	0	0		100	97.57
R	16.83	1	4.22	62.4	0.8	0.74	0.24	1.15	8.68	0	0		0.28	0.35	0	0	3.3	0			0			0	0	0	0		99.99	98.87
R	16.44	0.91	4.11	62.34	0.73	0.74	0.23	1.06	8.71	0.17	-0.06	0.18	0.27	0.31	0.04	0.14	3.43	0.14	0.21	-1.1	0.14	0.14	-0.13	0.01	0.4	-0.19	0.18	0.45	100	100.4
R	16.52	1.19	4.14	61.76	0.9	0.71	0.2	1.14	8.6	-0.03	0.11	0.11	0.27	0.4	0.09	0.04	3.46	0.29	0.01	-0.95	0.23	-0.23	0	0.27	0.25	0.2	0.5	-0.18	100	101.1
R	16.84	1.01	4.33	62.11	0.85	0.46	0.13	1.06	8.44	0.17	0	-0.02	0.26	0.34	0.11	0.21	3.48	0.37	-0.08	-1.16	0.5	-0.09	0.12	0.08	0.24	0.02	0.62	-0.38	100	101.4
R	16.7	0.98	4.45	62.85	0.91	0.31	0.14	1.12	8.61	0.15	0.08	0.03	0.17	0.33	0.08	0.22	3.22	0.11	-0.05	-1	0.41	-0.16	0.01	0.05	0.09	0.1	0.72	-0.61	100	98.5
R	16.66	0.91	4.26	61.77	0.81	0.81	0.19	0.99	8.55	0.2	-0.02	-0.03	0.31	0.29	0.09	0.12	3.35	0.27	0.1	-0.77	0.4	0.01	-0.07	-0.07	0.42	0.24	0.16	0.06	100	100.6
R	16.61	1.03	4.25	62.82	0.98	0.47	0.21	1.06	8.71	0.13	0.15	0.02	0.29	0.22	-0.04	0.12	3.37	0.16	0.09	-1	0.46	-0.18	-0.02	-0.25	-0.03	-0.06	0.69	-0.25	100	98.73
R	16.44	1.04	4.08	61.54	0.78	0.58	0.22	1.03	8.77	0.27	0.05	-0.01	0.33	0.28	0.04	0.15	3.21	0.2	0.19	-0.42	-0.03	0.03	0.08	0.15	0.35	-0.05	0.71	-0.01	100	99.91
R	16.82	0.92	4.39	62.09	0.88	0.82	0.21	1.02	8.64	0.24	0.01	-0.05	0.28	0.35	0.06	0.1	3.17	0.13	0.05	-0.49	0.15	0.06	-0.01	-0.05	-0.21	-0.04	0.41	0.07	100	99
R	17.2	1.08	4.13	62.35	0.75	0.75	0.21	1.04	8.62	0.15	-0.09	0.08	0.23	0.4	0	0.08	3.29	0.33	-0.22	-1.36	0.14	0.04	-0.12	0.08	0.32	0.06	0.59	-0.11	100	100.1
R	16.69	1.07	4.17	61.48	0.82	0.56	0.19	1.05	8.55	0.06	0.19	0.03	0.39	0.35	-0.01	0.11	3.02	0.28	-0.07	-0.63	0.02	0.12	0.01	0.11	0.83	0.26	0.39	-0.03	100	100.6
R	16.88	1.11	4.14	62.29	1.03	0.52	0.1	1.08	8.77	0.04	0.01	0.03	0.36	0.27	-0.08	0.08	3.41	0.32	-0.03	-0.65	-0.1	-0.43	-0.01	0.12	0.63	-0.1	0.41	-0.18	100	99.7
R	16.91	1.08	4.3	62.13	0.63	0.64	0.19	1.09	8.61	0.13	0.02	-0.04	0.33	0.3	0.09	0.2	3.31	-0.03	-0.18	-1.33	-0.06	0.17	0.14	-0.01	0.82	0.06	0.52	-0.04	99.98	100.5
R	16.95	0.94	4.4	61.74	0.76	0.94	0.2	1.08	8.72	0.01	0.08	0.01	0.22	0.21	0.06	0.25	2.92	0.2	-0.05	-0.73	-0.13	0.02	-0.14	-0.11	0.59	0.17	0.36	0.33	100	100.1
R	17.13	1.08	4.24	63.71	0.83	0.52	0.16	1.09	8.69	-0.02	-0.02	0.1	0.17	0.36	-0.01	0.09	3.28	-0.04	-0.01	-1.39	-0.29	0.01	-0.07	0	0.24	0.04	0.56	-0.45	100	97.69
R	16.74	0.95	4.21	61.88	1.12	0.32	0.17	1.09	8.61	0.13	0.01	0.02	0.34	0.35	0.1	0.09	3.12	-0.01	0.16	-0.74	0.19	-0.05	-0.09	0.1	0.64	0.04	0.79	-0.29	99.99	99.75
R	16.9	1.05	4.15	61.63	0.73	0.77	0.17	1.08	8.66	0.13	-0.05	0.01	0.28	0.43	0.12	0.05	3.33	0.23	0.06	-1	-0.26	-0.01	0.05	0.21	0.76	0.03	0.4	0.08	99.99	100.9
R	16.52	1.09	4.26	62.78	0.79	0.47	0.23	0.93	8.54	0.1	-0.01	0.03	0.29	0.42	0.06	0.11	3.42	0.19	0.03	-0.97	-0.22	0.14	-0.11	-0.31	0.7	0.11	0.73	-0.28	100	99.31
R	16.85	1.15	4.22	62.59	0.86	0.59	0.18	1.07	8.84	0.11	-0.01	-0.04	0.08	0.33	0.07	0.09	3.21	0.18	0.08	-0.81	0.01	-0.04	0.02	-0.24	0.36	0.02	0.7	-0.45	100	98.48
R	16.84	1	4.31	62.09	0.82	0.6	0.17	1.06	8.85	0.15	0.08	0.06	0.35	0.2	0.02	-0.02	3.29	0.44	0.06	-1.13	0.09	0.05	0.04	-0.03	0.35	0	0.41	-0.15	100	99.67

Replicate Corning Glass B Measurements with SEM-EDS (Compound wt% Normalized)

Group indicates association with replications (R) or Saqqara Sherds (S); Normalized totals = N. Totals; Analytical Totals = A. Totals; Shaded areas were not used due to poor results and/or poor settings

Group	Na	Mg	Al	Si	P	S	Cl	K	Ca	Ti	V	Cr	Mn	Fe	Co	Ni	Cu	Zn	As	Rb	Sr	Zr	Ag	Sn	Sb	Ba	Pb	Bi	N. Total	A. Total
R	16.77	1.17	4.01	61.04	0.89	0.7	0.19	1.1	8.62	0.17	0.03	0.03	0.23	0.34	0.11	0.24	3.18	0.25	-0.01	-0.79	0.27	-0.04	0.1	0.07	0.67	-0.02	0.51	0.18	100	100.2
R	16.84	0.95	4.17	62.49	0.93	0.58	0.18	1.04	8.55	0.11	0.03	-0.05	0.13	0.27	0.02	0.17	3.27	0.37	0.11	-1.22	0.86	-0.07	0	-0.1	0.26	-0.16	0.41	-0.14	100	98.52
R	16.82	1.04	4.16	63.45	0.84	0.66	0.13	1.06	8.86	0.08	-0.1	-0.05	0.19	0.29	-0.06	0.11	3.1	0.19	-0.01	-1.39	0.44	-0.08	0.13	-0.23	0.11	-0.08	0.52	-0.17	100	96.95
R	16.72	1.01	4.25	63.77	1.2	0.41	0.17	1.04	8.79	0.12	0.02	0.03	0.11	0.34	0.15	0.18	3.16	0.31	0.16	-1.88	0.78	-0.18	0.04	-0.57	-0.52	0.15	0.59	-0.36	99.99	96.75
R	16.9	1.05	4.23	63.02	0.83	0.39	0.18	1.14	8.57	0.01	0.17	-0.03	0.15	0.37	-0.03	0.16	3.24	0.16	-0.04	-0.94	0.08	-0.36	-0.06	0.11	-0.02	0.25	0.64	-0.19	99.98	97.89
R	16.36	0.79	4.15	61.71	0.9	0.47	0.22	1.19	8.74	0.06	0.16	0.04	0.15	0.36	0.01	0.09	3.5	0.13	0.19	-0.36	0.37	-0.16	0.05	0.15	0.15	0.1	0.48	-0.01	99.99	99.16
R	16.9	0.99	4.03	62.15	0.95	0.46	0.22	1.08	8.62	0.14	0	-0.04	0.34	0.29	0.14	0.17	3.14	0.18	0	-0.47	0.74	-0.2	-0.07	-0.27	-0.32	0.22	0.49	0.14	100	98.47
R	16.86	0.82	4.37	63.54	0.93	0.5	0.19	1.04	8.52	0.12	-0.06	-0.03	0.21	0.45	0	0.26	3.19	-0.12	0.23	-1.6	0.64	-0.11	0.03	0	-0.37	0.01	0.57	-0.24	99.95	86.93
R	16.76	1.18	4.26	63.25	0.74	0.76	0.2	1.12	8.65	0.07	-0.03	-0.05	0.14	0.38	0.04	0.29	3.4	0.33	-0.04	-1.69	0.46	0.04	-0.14	-0.32	-0.66	0.18	0.44	0.23	99.99	88.47
R	16.76	0.82	4.27	62.84	0.95	0.72	0.17	1.07	8.86	0.19	0.03	0.11	0.24	0.3	0.01	0.08	3.24	-0.02	0.07	-1.5	0.69	-0.16	-0.06	-0.25	-0.13	0.11	0.36	0.22	99.99	87.93
R	16.97	1.08	4.27	63.02	0.95	0.62	0.21	1.02	8.83	0.09	0.02	0.02	0.29	0.34	0.05	0.12	3.38	0.23	0.09	-1.98	0.87	0.05	0.01	-0.41	-0.61	0.09	0.52	-0.13	100	109.9
R	17.44	1.03	4.14	63.84	0.95	0.67	0.25	1.11	8.75	0.04	0.18	-0.04	0.21	0.41	0.1	0.21	3.16	0.26	-0.12	-2.66	0.72	0.14	0.1	-0.6	-0.64	0.11	0.37	-0.09	100	109.1
R	17.05	1.15	4.32	64.37	0.83	0.37	0.24	1.12	8.83	0.27	-0.16	0	0.26	0.37	-0.05	0.03	3.53	0.22	0.03	-2.91	0.83	0.08	0.02	-0.39	-0.54	-0.13	0.65	-0.37	100	108.4
R	16.6	1.01	4.25	61.47	0.76	0.67	0.27	1.16	8.68	0.09	0.06		0.35	0.42	0.01	0.02	3.16	0.33			0.26			-0.04	-0.04	0.12	0.41		100	102.1
R	16.81	1.09	3.88	61.04	0.9	0.59	0.21	1.07	8.6	0.2	-0.11		0.3	0.37	0.13	0.14	3.31	0.26			0.84			-0.11	0.06	-0.09	0.55		100	103.2
R	16.94	1.02	4.13	61.4	0.81	0.76	0.1	0.94	8.5	0.08	0.04		0.29	0.31	0.07	0.18	3.41	0.22			1.13			-0.4	-0.35	0.09	0.33		100	101.9
R	16.72	1.01	4.12	60.28	1	0.7	0.2	1.05	8.5	0.06	0		0.24	0.33	0.15	0.15	3.22	0.22			0.6			0.11	0.8	0.06	0.49		100	102
R	16.74	0.86	4.21	60.63	0.78	0.63	0.15	1.07	8.56	0.01	0.01		0.35	0.28	0.1	-0.06	3.16	0.32			0.92			0.05	0.48	0.19	0.54		99.98	101.5
R	16.96	1.05	4.17	61.02	0.96	0.69	0.19	1.02	8.6	0.02	-0.03		0.26	0.25	0.11	0.26	3.4	0.17			0.41			-0.09	-0.06	0.11	0.51		99.98	100.5
R	16.55	1.04	4.06	61.96	0.71	0.74	0.19	1.11	8.82	0.16	0.04		0.29	0.3	-0.06	0.04	3.3	0.06			-0.46			0.11	0.68	0	0.34		99.98	80.37
R	16.49	1.08	4.16	61.42	0.72	0.59	0.14	0.93	8.56	0.22	0.09		0.4	0.27	0.25	0.15	3.3	0.31			0.16			-0.23	0.24	0.15	0.57		99.97	80.94
R	16.73	0.95	4.41	61.11	0.95	0.44	0.18	1.14	8.65	0.11	0.01		0.23	0.36	0.01	0.08	3.3	0.1			0.4			0.08	0.18	0.03	0.5		99.95	81.31
R	16.31	1.03	4.05	61.92	1.04	0.44	0.18	1.13	8.44	0.08	0.04		0.2	0.3	-0.01	0.19	3.02	0.12			0.43			0.19	0.25	0.07	0.55		99.97	88.56
R	16.78	1.1	4.16	61.29	0.75	0.65	0.21	1.12	8.58	0.24	-0.03		0.22	0.26	-0.06	0.13	3.23	0.29			0.39			0.07	0.2	-0.17	0.54		99.95	89.11
R	16.81	1.01	4.03	61.67	0.95	0.73	0.18	0.93	8.6	0.11	-0.07		0.16	0.22	0.06	0.17	2.93	0.21			0.3			-0.2	0.51	0.09	0.57		99.97	88.68
R	17.09	1.09	4.22	61.99	0.8	0.53	0.16	0.9	8.72	0.12	-0.11		0.22	0.28	0.07	0.09	3	0.19			0.44			-0.44	0.01	0.07	0.56		100	108.5
R	16.82	0.95	4.21	61.6	0.93	0.57	0.33	1.05	8.51	0.15	-0.05		0.19	0.28	0.09	0.06	3.18	0.26			0.4			-0.09	-0.17	0.19	0.55		100	109.1
R	16.96	1.04	4.15	61.33	0.89	0.6	0.22	1.02	8.51	0.15	0.11		0.3	0.24	0.03	0.11	3.35	0.15			0.4			-0.12	0.1	0.04	0.43		100	110.3
R	16.64	0.93	4.08	61.66	0.93	0.58	0.15	1.03	8.78	0.13	0.03		0.22	0.25	0.13	0.11	3.21	0.18			0.09			0	0.41	0.03	0.43		100	100.2
R	16.93	1	4.12	61.35	0.78	0.68	0.2	1.1	8.42	0.14	0.1		0.35	0.21	0.14	0.03	3.43	0.15			-0.04			0.28	0.12	0.1	0.41		100	100.5
R	16.98	1.04	4.15	60.92	0.82	0.55	0.19	1.08	8.29	0.18	0.06		0.22	0.31	0.09	0.07	3.19	0.32			0.08			0.42	0.61	-0.03	0.46		100	100.4
R	16.78	1.01	4.01	60.36	1.05	0.69	0.16	0.93	8.48	0.31	0.05		0.23	0.35	0.01	0.16	3.52	0.28			0.23			0.17	0.71	0.04	0.49		100	102.4
R	16.77	0.83	4.13	61.33	0.77	0.58	0.16	0.99	8.78	0.19	0.18		0.17	0.34	0.01	0.16	3.27	0.14			-0.02			0.05	0.34	0.2	0.62		99.99	101.1
R	16.72	1.02	4.08	61.43	0.87	0.56	0.17	1	8.7	0.02	0.1		0.23	0.4	0.1	0.16	3.17	0.11			-0.06			0.03	0.44	0.21	0.54		100	100.7
R	16.79	0.96	4.15	61.73	0.86	0.7	0.13	1.08	8.8	0.22	-0.02		0.17	0.33	0.14	0.08	2.97	0.19			0.03			0.15	0.36	0.07	0.11		100	99.37
R	16.77	1.1	4.12	61.49	0.7	0.65	0.17	1.1	8.64	0.09	-0.04		0.21	0.29	0.03	0.16	3.13	0.32			0.01			0.04	0.29	0.1	0.63		100	100.9
R	16.78	0.97	4.13	62.51	0.79	0.58	0.25	1.03	8.63	0.33	-0.08		0.34	0.41	-0.06	0.16	3.2	0.14			-0.22			-0.16	-0.11	-0.09	0.46		99.99	99.21
R	16.59	0.99	4.11	62.45	0.78	0.69	0.23	1.11	8.67	0.2	0.11	0.02	0.41	0.34	0.13	0.01	3.12	0.11	0.02	-0.69	0.27	0.07	0.01	-0.05	-0.11	0	0.5	-0.07	100	99.47
R	16.35	0.99	4.13	62.25	0.97	0.69	0.16	1.07	8.7	0.1	0.1	-0.02	0.28	0.35	0.05	0.13	3.39	0.29	0.27	-0.94	0.6	-0.12	-0.18	-0.09	-0.01	0.12	0.48	-0.13	99.98	101.3
R	16.9	1	4.17	61.99	0.97	0.53	0.16	1.07	8.73	0.1	0	0.01	0.25	0.43	-0.01	0.12	3.08	0.14	0.06	-1.06	0.76	-0.1	0.15	0.08	0.17	-0.04	0.53	-0.21	99.98	101.9
R	16.31	1.03	4.1	61.26	0.85	0.66	0.21	0.86	8.57	0.01	0.06	-0.01	0.3	0.26	0.03	0.18	3.38	0.25	0.07	0.1	0.12	0.19	0.15	-0.19	0.29	0.38	0.3	0.28	100	101.8
R	16.93	1	4.13	62.19	0.77	0.54	0.08	1.15	8.66	0.11	0.09	-0.03	0.31	0.28	0.11	0.03	3.1	0.26	-0.14	-0.3	0.05	-0.04	0.1	0.11	0.21	0.05	0.62	-0.35	100	100.6
R	16.76	1.01	4.32	62.36	0.83	0.69	0.21	1.04	8.55	-0.01	0.11	0.03	0.13	0.33	0.04	0.26	3.15	0.18	0.1	-1.22	0.24	-0.01	0.03	0.01	0.16	0.32	0.33	0.08	100	101.8
R	16.54	1	4.21	61.66	0.86	0.7	0.19	1.14	9.04	0.01	-0.01	-0.08	0.35	0.26	0.06	0.03	3.08	0.28	0.14	0.21	0.14	-0.01	-0.07	-0.14	0.04	0.07	0.37	-0.05	100	99.36
R	16.92	1.07	4.02	62.19	0.96	0.35	0.18	1.1	8.54	-0.02	-0.04	0.07	0.15	0.25	0.08	0.07	3.28	0.2	-0.02	-0.29	0.1	-0.1	0.04	0.16	0.35	0.13	0.48	-0.2	100	100.7
R	16.92	0.99	4.16	62.29	0.91	0.65	0.21	1.01	8.43	0.11	0	-0.1	0.25	0.32	0.09	0.1	3.34	0.14	0.12	-0.75	0.08	-0.21	0.06	-0.25	0.34	0.3	0.6	-0.11	100	100.4
R	16.55	0.98	4.24	62.82	0.87	0.6	0.15	1.09	8.61	0.09	0.03	0.02	0.27	0.25	0.08	0.14	3.45	0.18	0.11	-1.16	-0.01	-0.01	0.1	0.02	0.17	0.08	0.57	-0.28	100	99.18

Replicate Corning Glass B Measurements with SEM-EDS (Compound wt% Normalized)

Group indicates association with replications (R) or Saqqara Sherds (S); Normalized totals = N. Totals; Analytical Totals = A. Totals; Shaded areas were not used due to poor results and/or poor settings

Group	Na	Mg	Al	Si	P	S	Cl	K	Ca	Ti	V	Cr	Mn	Fe	Co	Ni	Cu	Zn	As	Rb	Sr	Zr	Ag	Sn	Sb	Ba	Pb	Bi	N. Total	A. Total
R	17.05	1.16	4.16	62.17	0.98	0.67	0.19	1.04	8.57	0.13	0.16	-0.06	0.32	0.16	0.06	0.08	3.27	0.38	0.2	-1.03	0.14	-0.19	-0.05	-0.33	0.23	0	0.53	-0.02	99.97	100.2
R	16.52	0.99	4.34	62.2	0.91	0.71	0.2	1.04	8.58	0.03	0.12	-0.04	0.28	0.31	-0.04	0.12	3.39	0.2	0.14	-1.05	0.33	0.1	0.19	-0.14	0.02	0.17	0.52	-0.15	99.99	99.86
R	16.84	1.07	4.27	61.9	0.66	0.66	0.12	1.06	8.48	0.16	0.18	-0.03	0.33	0.29	0.03	0.09	3.29	0.27	-0.05	-0.61	-0.37	0.37	0.01	0.21	0.48	0.11	0.45	-0.28	99.99	100.9
R	16.59	0.87	4.39	62.11	0.94	0.66	0.19	1.1	8.44	0.23	-0.02	-0.04	0.31	0.32	-0.05	0.12	3.3	0.2	0.13	-1.13	0.16	0.05	0.14	0.09	0.41	-0.05	0.47	0.07	100	100.5
R	16.75	1.14	4.32	62.33	0.93	0.34	0.11	0.99	8.63	0.07	0.08	0.04	0.31	0.36	0.11	0.14	3.14	0.39	0.15	-0.93	0.23	-0.05	0.01	-0.1	0.1	0.19	0.68	-0.47	99.99	100.4
R	16.76	0.92	4.26	61.73	0.69	0.79	0.24	1.04	8.53	0.15	-0.04	0.01	0.24	0.29	-0.05	0.14	3.26	0.11	0.1	-0.47	-0.15	0.08	0.01	0.04	0.61	0.08	0.4	0.23	100	101.2
R	16.94	0.94	4.29	61.8	1.01	0.43	0.14	1.12	8.46	0.12	0.08	0	0.13	0.31	0.05	0.12	3.21	0.16	0.28	-0.65	0.13	-0.1	0.06	0.25	0.49	0.07	0.62	-0.46	100	101.8
R	16.86	0.98	4.21	62.02	0.94	0.82	0.22	1.04	8.54	0.05	0.14	0.05	0.27	0.33	0.21	0.15	3.28	0.31	0.05	-1.23	0.05	0.08	-0.2	0.06	0.18	0.12	0.2	0.27	100	101.8
R	16.84	1.12	4.35	61.28	1	0.61	0.18	1.04	8.47	0.06	-0.09	0.03	0.26	0.25	0.09	0.23	3.25	0.18	0	-0.53	0.26	-0.11	-0.08	0.16	0.6	0.21	0.52	-0.14	100	101.4
R	16.91	0.94	4.25	61.01	0.97	0.69	0.16	1.04	8.4	0.17	0.03	0.05	0.3	0.33	0.05	0.2	3.12	0.39	-0.02	-0.4	0.34	-0.12	-0.03	0.19	0.44	0.12	0.43	0.07	100	100.6
R	16.6	0.91	4.09	61.47	1.04	0.87	0.13	1.12	8.54	0.13	0.14	0.08	0.17	0.32	0.09	0.02	3.34	0.28	-0.02	-0.54	0.41	-0.04	0.01	0.17	0.59	-0.03	0.09	0.01	99.99	99.95
R	16.45	1.04	4.1	61.97	0.93	0.67	0.2	1.15	8.86	0.14	0.01	-0.1	0.26	0.34	-0.06	0.14	3	0.27	0.14	-0.64	0.02	-0.07	0	0.03	0.55	0	0.64	-0.05	99.99	99.83
R	17.07	0.93	4.14	62.09	0.78	0.66	0.23	1.26	8.65	0.07	0.01	0.02	0.23	0.36	0.04	0.1	3.22	0.25	-0.11	-0.7	-0.16	-0.02	-0.1	0.2	0.12	0.07	0.47	0.13	100	100.8
R	16.9	1.06	4.18	61.62	0.98	0.67	0.22	1.25	8.71	0.24	-0.16	-0.05	0.21	0.36	0.11	0	2.88	0.14	-0.03	0.04	0.21	-0.04	-0.13	0.13	0.25	-0.19	0.54	-0.1	100	98.95
S	16.54	1	4.07	61.31	0.6	0.7	0.17	1.14	8.62	-0.04	0.1		0.2	0.49	0.1	0.01	3.28	0.26			0.43			0.08	0.14	0.37	0.43		100	98.4
S	16.76	1.04	4.04	60.9	0.9	0.6	0.16	0.95	8.61	0.1	-0.02		0.23	0.26	0.1	0.17	3.4	0.4			1.01			-0.08	-0.07	0.01	0.51		99.98	98.66
S	17.13	1.04	4.19	61.36	0.8	0.46	0.14	0.94	8.46	0.27	-0.01		0.35	0.29	0.11	0.04	3.66	0.14			1.02			-0.36	-0.48	-0.16	0.62		100	98.9
S	16.72	0.96	4.01	60.83	0.98	0.43	0.18	1.12	8.62	-0.03	-0.08		0.38	0.28	0.07	0.08	3.33	0.31			0.41			0.12	0.46	0.31	0.52		100	101.6
S	17.03	1.17	3.96	60.58	0.77	0.55	0.23	1.09	8.71	0.11	0.04		0.2	0.29	0.15	0.13	3.87	0.3			0.44			-0.21	-0.01	0	0.59		99.99	102.1
S	16.89	1.04	4.3	61.37	0.99	0.64	0.21	0.99	8.7	0.01	0.02		0.18	0.3	0.07	0.06	3.6	0.26			0.81			-0.52	-0.4	0.11	0.36		99.99	101.6
S	15.96	0.99	4.12	61.63	0.83	0.77	0.2	1.2	8.9	0.18	-0.08		0.33	0.16	0.05	-0.02	3.36	0.04			0.31			0.4	0.31	-0.12	0.5		100	98.07
S	16.28	0.94	4.11	61.94	0.86	0.5	0.22	1.06	8.72	-0.01	0.05		0.27	0.35	0.17	0.15	3.46	0.32			0.07			-0.25	0.15	0.25	0.41		100	100.1
S	15.91	1.06	4.19	61.7	0.73	0.77	0.15	1.02	8.94	0.22	-0.08		0.26	0.35	0	0.14	3.06	0.29			0.84			0.01	-0.03	-0.01	0.46		99.98	97.89
S	16.64	0.93	4.32	61.24	0.83	0.58	0.14	1.16	8.52	0.16	0.04		0.21	0.35	0.11	0.07	3.34	0.01			0.5			0.29	0.17	0.11	0.29		100	101.4
S	16.35	0.87	4.39	61.2	1.11	0.63	0.19	1.05	8.58	0.08	0.08		0.34	0.26	-0.18	0.07	3.33	0.18			0.72			0.08	0.07	0.1	0.49		99.99	100
S	16.75	1.04	4.32	60.58	1.15	0.53	0.17	1.09	8.4	0.11	-0.11		0.25	0.26	0.19	0.17	3.12	0.14			0.52			0.26	0.38	0.2	0.48		100	102.8
S	17.04	0.96	4.24	61.67	0.85	0.62	0.2	0.94	8.56	-0.03	0.07		0.19	0.3	0.04	0.03	3.19	0.23			0.6			-0.27	-0.06	0.19	0.45		100	99.79
S	16.56	0.9	3.93	60.55	1.23	0.62	0.21	1.1	8.45	-0.05	0.03		0.17	0.4	0.07	0.13	3.25	0.24			1.61			0.22	-0.21	0.11	0.48		100	101.4
S	16.83	0.9	4.04	61.81	1.16	0.61	0.11	1.06	8.55	0.13	-0.02		0.23	0.34	-0.01	0.05	3.36	0.1			1.73			-0.28	-1.26	0.17	0.38		99.99	98.71
S	16.36	0.94	4.12	61.27	1.1	0.5	0.17	1.06	8.54	0.09	0.06		0.16	0.43	0.02	0.25	2.96	0.31			1.12			-0.15	-0.01	0.03	0.66		99.99	99.87
S	16.26	0.86	3.99	60.17	1.43	0.58	0.17	1.05	8.41	0.12	-0.04		0.3	0.38	0.07	0.27	3.3	0.26			2.28			0.04	-0.28	0.21	0.17		100	100.3
S	16.7	0.82	4.06	61.69	1.03	0.6	0.1	1.01	8.4	0.08	0.11		0.32	0.3	0.06	0.09	3.09	0.36			2.16			-0.37	-1.04	0.1	0.32		99.99	98.38
S	16.16	0.91	3.94	62.04	0.84	0.66	0.18	0.97	9.06	0.18	-0.07		0.31	0.27	0.06	-0.01	3.43	0.01			0.16			-0.13	0.4	0.15	0.49		100	99.68
S	16.35	1.01	3.9	61.92	0.83	0.59	0.2	1.02	8.88	0.07	0.04		0.23	0.24	0.02	0.18	3.44	0.23			0.58			-0.42	0.17	0.22	0.29		99.99	100.8
S	16.44	1.03	4.14	62.2	0.91	0.61	0.23	1.01	8.96	0.11	0.13		0.26	0.28	0.06	0.13	3.35	0.23			0.4			-0.46	-0.63	0.15	0.46		100	101.1
S	16.73	1.07	4.01	60.86	0.93	0.72	0.16	0.97	8.54	0.22	0.07		0.27	0.32	0.01	0.17	3.29	0.2			0.66			0.06	0.53	-0.13	0.34		100	102.5
S	16.59	1.05	3.95	61.23	1.18	0.79	0.22	1.02	8.72	0.09	0.08		0.24	0.4	0.04	0.04	3.26	0.2			1.11			-0.29	-0.36	0.12	0.32		100	101.4
S	16.73	0.97	3.99	61.68	0.98	0.66	0.21	1.08	8.55	0.25	0.01		0.19	0.22	0.03	0.15	3.16	0.11			1.19			-0.38	-0.34	0.05	0.52		100	102.7
S	16.09	0.88	4.18	61.69	0.95	0.51	0.21	1.06	8.66	0.14	0.09		0.27	0.36	0.06	0.06	3.21	0.19			0.78			0.19	-0.18	0.18	0.42		100	99.89
S	16.58	0.96	4.14	60.9	1.28	0.57	0.14	0.96	8.39	0.19	-0.01		0.34	0.38	0.04	0.05	3.45	0.31			1.57			-0.05	-0.77	0.12	0.43		99.97	100.9
S	16.86	0.93	4.17	61.77	1.36	0.68	0.12	0.91	8.44	0.04	-0.01		0.08	0.37	0.15	0.02	3.43	0.14			1.81			-0.62	-1.12	0.02	0.45		100	100.9
S	15.7	0.69	4.34	60.82	0.62	0.71	0.19	1.11	8.83	0.11	0.07		0.17	0.34	0.05	0.11	3.25	0.49			0.81			0.29	0.74	0.3	0.26		100	101.6
S	16.61	1.07	4.31	60.74	0.96	0.58	0.21	0.95	8.33	0.03	0.07		0.27	0.3	0.01	0.08	3	0.35			1			0.11	0.38	0.08	0.55		99.99	101.9
S	16.23	0.86	4.14	60.69	0.94	0.76	0.1	1	8.53	0.13	0.05		0.29	0.34	-0.02	0.14	3.13	0.3			1.11			0.39	0.5	0.13	0.26		100	102.3
S	16.01	0.72	4.4	60.73	0.52	0.94	0.15	1.11	8.46	0.07	0.06		0.24	0.44	0.13	0	3.33	0.07			0.49			0.78	0.7	0.41	0.24		100	101.8
S	15.41	1.12	4.54	61.45	0.38	0.74	0.08	1.16	8.51	0.13	0		0.2	0.41	0	0.07	3.37	0.25			0.74			0.33	0.89	-0.03	0.28		100	101.3
S	16.52	0.76	4.24	61.11	0.63	0.7	0.12	1	8.5	0.19	0.08		0.38	0.06	0.16	0.21	3.2	0.3			0.79			-0.08	0.55	0.04	0.54		100	99.83

Replicate Corning Glass B Measurements with SEM-EDS (Compound wt% Normalized)

Group indicates association with replications (R) or Saqqara Sherds (S); Normalized totals = N. Totals; Analytical Totals = A. Totals; Shaded areas were not used due to poor results and/or poor settings

Group	Na	Mg	Al	Si	P	S	Cl	K	Ca	Ti	V	Cr	Mn	Fe	Co	Ni	Cu	Zn	As	Rb	Sr	Zr	Ag	Sn	Sb	Ba	Pb	Bi	N. Total	A. Total
S	16.25	0.84	4.2	61.8	0.91	0.75	0.14	0.96	8.59	-0.03	0.12		0.23	0.25	-0.01	0.1	3.29	0.22			0.76			-0.03	0.23	0.2	0.22		99.99	100.4
S	16.33	0.85	4.28	60.37	1.01	0.73	0.22	1.1	8.5	0.15	-0.04		0.27	0.35	0	0.06	3.33	0.46			0.86			0.28	0.24	0.12	0.56		100	102.4
S	16.4	0.83	4.13	61.07	0.86	0.64	0.17	1.09	8.79	0.21	-0.07		0.15	0.33	0.11	0.12	3.38	0.14			0.39			0.52	0.34	-0.02	0.41		99.99	100.9
S	16.37	0.91	3.98	60.86	1.05	0.69	0.23	1.04	8.53	0.14	0.1		0.17	0.32	-0.1	0.12	3.21	0.31			0.75			0.17	0.74	-0.04	0.43		99.98	100.1
S	16.45	0.89	4.16	61.1	1.19	0.83	0.18	1.08	8.56	0.16	0		0.2	0.29	0.1	0.08	3.15	0.37			0.94			0.04	0.1	-0.02	0.15		100	99.94
S	16.58	1.04	4.38	59.92	0.76	0.61	0.23	1.05	8.36	0.12	0.1		0.32	0.31	0.09	0	3.26	0.17			0.87			0.39	1.12	-0.01	0.33		100	102.6
S	17.13	1.1	4.33	61.1	1.08	0.67	0.21	0.95	8.44	0.1	0.07		0.27	0.4	0.13	0	3.14	0.14			0.88			-0.36	-0.3	0.09	0.43		100	101
S	16.91	0.91	4.26	60.49	0.71	0.58	0.17	1.05	8.56	0.09	0.1		0.15	0.38	0.09	0.02	3.22	0.38			0.87			0.12	0.3	0.1	0.54		100	100.5
S	16.67	0.84	4.19	61.16	0.74	0.61	0.24	1	8.38	0.25	-0.06		0.3	0.41	0	-0.1	3.26	0.4			0.59			0.25	0.42	-0.14	0.6		100	100.2
S	16.68	0.89	4.22	60.82	0.88	0.49	0.19	1.12	8.5	0	0.04		0.22	0.32	-0.03	0.13	3.04	0.23			0.59			0.44	0.78	-0.07	0.53		100	101.3
S	16.87	0.89	4.14	60.57	1.02	0.67	0.1	1.06	8.39	0.12	0.04		0.33	0.42	0.07	0.14	3.13	0.46			1.02			0.14	0.45	-0.06	0.03		100	100.8
S	16.53	0.83	4.07	60.67	1.11	0.69	0.19	1.05	8.46	0.18	0.02		0.27	0.25	-0.04	0.03	3.14	0.18			1.11			0.02	0.78	0.06	0.38		99.98	99.95
S	16.59	1.02	4.18	60.9	1.1	0.76	0.28	1.15	8.42	-0.23	0.07		0.17	0.46	0.07	0.24	3.06	0.06			0.54			-0.08	0	0.66	0.58		100	101
S	16.3	0.97	4.29	61.15	0.83	0.74	0.22	1.22	8.49	0.08	0.06		0.28	0.49	-0.11	-0.11	3.12	0.14			0.15			0.19	1	0.01	0.48		99.99	101.4
S	16.5	0.84	4.14	60.6	1.19	0.48	0.19	1.17	8.48	0.02	0.16		0.19	0.27	0.14	0.02	2.97	0.3			0.61			0.32	0.79	0.18	0.43		99.99	102.1
S	17.01	0.79	4.35	60.23	0.91	0.75	0.14	1.11	8.45	0.13	-0.04		0.19	0.35	0.06	0.02	3.27	0.24			0.54			0.19	1.02	0.11	0.17		99.99	103.6
S	15.63	0.82	4.49	61.07	0.83	0.46	0.27	1.12	8.76	0.11	0.05		0.28	0.28	0.09	0.09	3.17	0.23			0.93			0.26	0.48	-0.03	0.6		99.99	100.8
S	16.13	0.81	4.49	60.94	1.02	0.46	0.18	1.17	8.61	0.3	-0.07		0.32	0.19	0.01	0.06	3.15	0.17			0.9			0.17	0.47	-0.2	0.71		99.99	102.6
S	17.01	0.93	4.3	62.12	0.88	0.52	0.23	1.04	8.5	0.23	0.06		0.2	0.26	0.11	0.2	3.18	0.14			0.24			-0.3	-0.47	0.02	0.59		99.99	98.55
S	16.82	0.86	4.23	60.46	0.91	0.44	0.23	1.07	8.48	0.14	-0.09		0.34	0.28	-0.01	0.11	3.28	0.18			0.75			0.34	0.75	-0.12	0.57		100	101.4
S	16.29	0.92	4.37	60.69	1.07	0.42	0.16	1.14	8.51	0.04	0.09		0.16	0.34	0.12	0.11	3.57	0.09			1.01			0.08	0.24	0.22	0.37		100	99.78
S	16.64	0.74	4.04	60.98	0.99	0.72	0.18	1.05	8.4	0.01	0.24		0.27	0.34	0.06	0.13	3.11	0.11			0.57			0.26	0.54	0.23	0.4		100	101.7
S	17.13	0.9	4.25	60.58	0.94	0.75	0.16	1.03	8.47	0.11	0.06		0.16	0.32	0.05	0.18	3.4	0.2			0.57			-0.08	0.49	-0.03	0.35		99.99	100.9
S	16.82	0.98	4.45	61.88	0.76	0.86	0.13	1.14	8.71	0.11	-0.04		0.31	0.3	0	0.16	3.05	0.18			0.06			-0.26	0.09	0.06	0.26		100	98.46
S	16.49	1.09	4.09	60.46	1.02	0.51	0.17	1.14	8.48	0.17	-0.05		0.13	0.38	0.1	0.03	3.15	0.09			0.54			0.61	1.18	-0.15	0.39		100	102.5
S	16.87	1.08	4.41	60.62	0.97	0.58	0.14	1.09	8.77	0.07	-0.07		0.31	0.31	0.02	0.24	3.08	0.09			0.4			-0.01	0.53	0.13	0.38		100	102.8
S	16.89	0.84	4.31	61.28	0.89	0.77	0.26	1.19	8.54	-0.02	-0.08		0.3	0.36	0.02	0.16	2.91	0.1			0.19			0.16	0.37	0.15	0.42		100	101.1
S	16.39	0.92	4.28	60.61	1.06	0.68	0.17	1.1	8.45	-0.01	0.11		0.19	0.45	0.01	0.19	3.01	0.09			1.15			0.11	0.44	0.32	0.27		99.99	100.4
S	16.42	0.97	4.23	60.59	0.87	0.81	0.17	1.19	8.47	0.04	0.25		0.23	0.23	0.13	0.1	3.29	0.21			0.38			0.23	0.75	0.15	0.29		100	100.9
S	16.88	0.84	4.13	60.42	1.27	0.56	0.2	1.05	8.39	-0.1	0.1		0.15	0.28	0.1	0.09	3.3	0.22			1.25			-0.01	0.33	0.23	0.32		100	100.6
S	16.86	1.05	4.42	60.55	1.08	0.68	0.18	1	8.45	0.11	0.18		0.16	0.33	0	0.02	3.32	0.38			1.22			-0.38	-0.26	0.26	0.41		100	100.7
S	16.96	0.92	4.09	61.06	1.17	0.54	0.17	1	8.49	0.23	-0.04		0.22	0.25	0.04	0.12	3.21	0.41			1.64			-0.33	-0.4	-0.06	0.31		100	101.6
S	16.55	0.94	4.43	61.7	1.22	0.55	0.2	1.01	8.43	-0.03	0.08		0.27	0.47	0.03	-0.12	3.22	0.23			1.56			-0.5	-0.82	0.19	0.38		99.99	99.78
S	16.34	0.84	4.21	61.56	1.06	0.71	0.21	1.13	8.64	0.08	-0.03		0.25	0.2	0.01	0.04	3.27	0.11			1.15			0.04	-0.36	0.19	0.35		100	100.6
S	16.35	0.94	4.16	61.11	1.13	0.64	0.22	1.06	8.6	0.12	0.04		0.15	0.41	-0.02	0.17	3.04	0.22			2.12			-0.19	-0.75	0.01	0.48		100	101
S	17.13	0.91	4.21	60.95	1.46	0.59	0.25	0.97	8.46	0.22	0.06		0.29	0.26	0	0.12	3.14	0.04			2.58			-0.51	-1.77	0.1	0.55		100	101.3
S	15.88	1.07	4.06	62.36	0.94	0.52	0.16	1.03	8.91	0.04	0.06		0.16	0.36	0.01	0.13	3.63	-0.04			0.41			-0.11	-0.26	0.1	0.58		100	98.8
S	16.13	1.12	3.91	62.26	0.74	0.68	0.18	1.05	8.68	0.14	-0.01		0.24	0.28	0.11	0.34	3.53	0.26			0.57			-0.23	-0.38	-0.12	0.53		100	99.32
S	16.49	1	4.07	62.16	1.16	0.52	0.24	1	8.73	0.11	-0.01		0.29	0.36	0.01	0.17	3.16	0.13			1.09			-0.58	-0.62	-0.1	0.62		100	98.98
S	16.9	1.08	4.22	62.3	1.07	0.61	0.2	1.1	8.6				0.27	0.28			3.38												100	102.1
S	16.88	0.88	4.03	61.62	1.26	0.56	0.17	1	8.44				0.32	0.36			3.1				1.37								99.99	102
S	16.95	0.95	4.1	62.79	1.09	0.64	0.18	1.01	8.77					0.28			3.25												100	101.4
S	16.91	0.99	4.27	62.12	0.83	0.67	0.22	1.2	8.7				0.31	0.41			3.37												100	103
S	16.81	0.98	4.1	62.01	0.91	0.49	0.21	1.04	8.82				0.32	0.36			3.32										0.63		100	101.3
S	16.77	1.01	4.22	62.31	0.91	0.76	0.19	0.98	8.77					0.28			3.37	0.43											100	102.3
S	16.9	0.99	4.24	61.8	0.86	0.69	0.19	1.07	8.84				0.31	0.33			3.24										0.55		100	100.9
S	16.63	0.94	4.18	62.49	1.21	0.68	0.2	1.1	8.65				0.23	0.36			3.33												100	100.9

Replicate Corning Glass B Measurements with SEM-EDS (Compound wt% Normalized)

Group indicates association with replications (R) or Saqqara Sherds (S); Normalized totals = N. Totals; Analytical Totals = A. Totals; Shaded areas were not used due to poor results and/or poor settings

Group	Na	Mg	Al	Si	P	S	Cl	K	Ca	Ti	V	Cr	Mn	Fe	Co	Ni	Cu	Zn	As	Rb	Sr	Zr	Ag	Sn	Sb	Ba	Pb	Bi	N. Total	A. Total
S	16.52	1.01	4.23	62.35	0.85	0.69	0.24	1.07	8.64					0.37			3.4										0.61		99.98	101.1
S	17.02	0.99	4.24	62.52	0.84	0.57	0.2	1.05	8.76				0.22	0.32			3.28												100	100
S	17.29	1.02	4.22	61.54	0.96	0.63	0.2	1.07	8.52				0.25	0.27			3.31										0.72		100	101.2
S	16.72	0.97	4.27	62.34	0.99	0.65	0.18	1.11	8.78				0.29	0.39			3.31												100	101
S	16.78	0.98	4.33	61.81	0.82	0.63	0.21	1.13	8.72				0.32	0.3			3.32										0.64		99.99	101.5
S	16.92	0.96	4.24	62.61	1	0.6	0.17	1.14	8.85					0.3			3.23												100	101.1
S	17.03	0.87	4.2	62.25	1.09	0.63	0.18	1.17	8.69				0.26	0.33			3.3												100	101.2
S	17.24	0.96	4.38	61.53	0.97	0.58	0.18	1.1	8.82				0.28	0.36			3.04										0.56		100	102.4
S	16.92	0.86	4.29	61.95	0.98	0.59	0.17	1.09	8.68				0.27	0.33			3.31										0.57		100	101.7
S	16.35	1.09	4.11	62.69	1.17	0.63	0.16	1.12	8.79				0.25	0.33			3.3												99.99	101
S	16.97	0.88	4.34	62.2	0.91	0.72	0.19	1.13	8.7				0.27	0.39			3.3												100	102.2
S	17.02	0.88	4.24	61.65	1.06	0.61	0.2	1.1	8.61				0.3	0.3			3.14	0.37									0.53		100	102.6
S	16.95	0.93	4.15	62.33	1.1	0.8	0.17	1.07	8.74				0.27	0.34			3.17												100	102.3
S	16.87	0.97	4.4	62.55	0.83	0.76	0.18	1.19	8.71				0.29				3.24												99.99	101
S	16.82	1.04	4.12	62.8	0.87	0.56	0.2	1.09	8.66				0.25	0.42			3.16												99.99	99.23
S	17.14	1.07	4.21	62.1	0.7	0.59	0.2	1.12	8.79				0.25				3.22										0.62		100	101.3
Replications																														
Mean	16.840	1.010	4.197	62.101	0.857	0.631	0.186	1.081	8.650	0.087	0.027	0.017	0.232	0.309	0.038	0.096	3.235	0.155	0.061	-0.785	0.063	-0.036	0.001	0.028	0.248	0.057	0.365			
Std. de	0.212	0.072	0.111	0.593	0.100	0.120	0.039	0.068	0.132	0.088	0.069	0.053	0.102	0.096	0.057	0.083	0.135	0.123	0.104	0.363	0.205	0.137	0.091	0.133	0.275	0.112	0.246			
Max.	17.4	1.19	4.45	63.71	1.12	0.94	0.29	1.26	9.04	0.33	0.24	0.18	0.41	0.52	0.21	0.31	3.52	0.44	0.28	0.21	0.76	0.37	0.24	0.42	1.08	0.41	0.87			
Min.	16.31	0.83	3.84	60.36	0.58	0.31	0.08	0.86	8.29	-0.07	-0.16	-0.1	0	0	-0.11	-0.1	2.88	-0.12	-0.22	-1.64	-0.38	-0.43	-0.2	-0.33	-0.46	-0.19	0			
Saqqara Sherds																														
Mean	16.580	0.940	4.206	61.287	0.955	0.631	0.185	1.069	8.589	0.096	0.032		0.245	0.327	0.050	0.096	3.260	0.218			0.863			0.010	0.117	0.094	0.437			
Std. de	0.376	0.102	0.150	0.574	0.205	0.112	0.043	0.072	0.163	0.092	0.076		0.067	0.078	0.067	0.086	0.179	0.117			0.533			0.303	0.595	0.150	0.135			
Max.	17.29	1.17	4.54	62.8	1.46	0.94	0.28	1.22	9.06	0.3	0.25		0.38	0.49	0.19	0.34	3.87	0.49			2.58			0.78	1.18	0.66	0.72			
Min.	15.41	0.69	3.9	59.92	0.38	0.42	0.08	0.91	8.33	-0.23	-0.11		0.08	0.06	-0.18	-0.12	2.91	-0.04			0.06			-0.62	-1.77	-0.2	0.03			

HH-XRF Spectrum of Corning Glass B; 40 kV, 30 µA, No Filter, 180 Second Acquisition Time

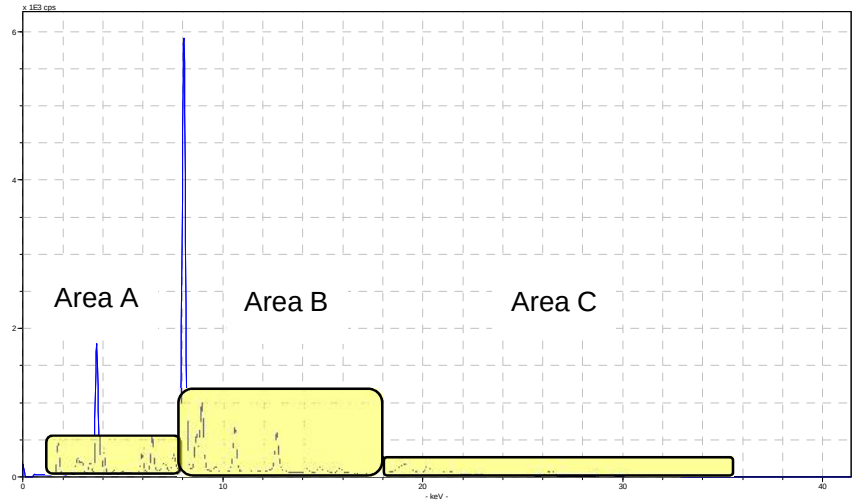

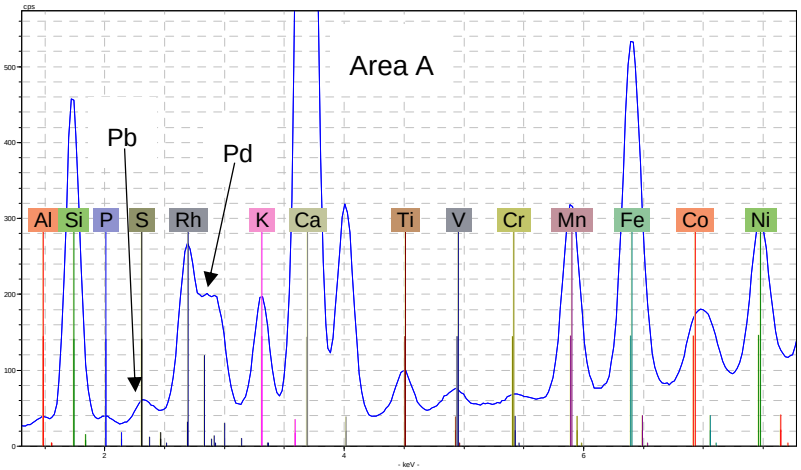

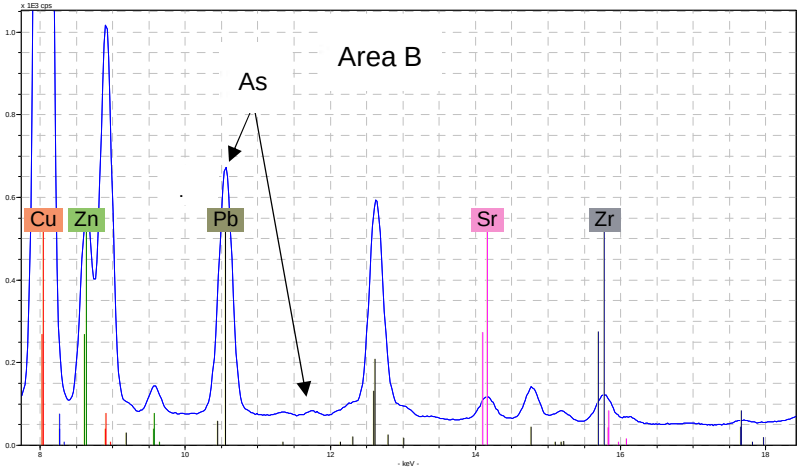

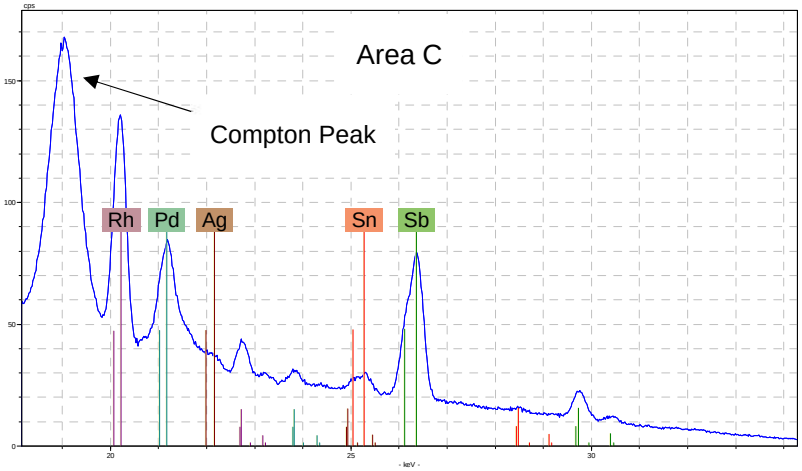

HH-XRF Spectrum of Corning Glass B; 40 kV, 30 µA, Filter 3, 180 Second Acquisition Time

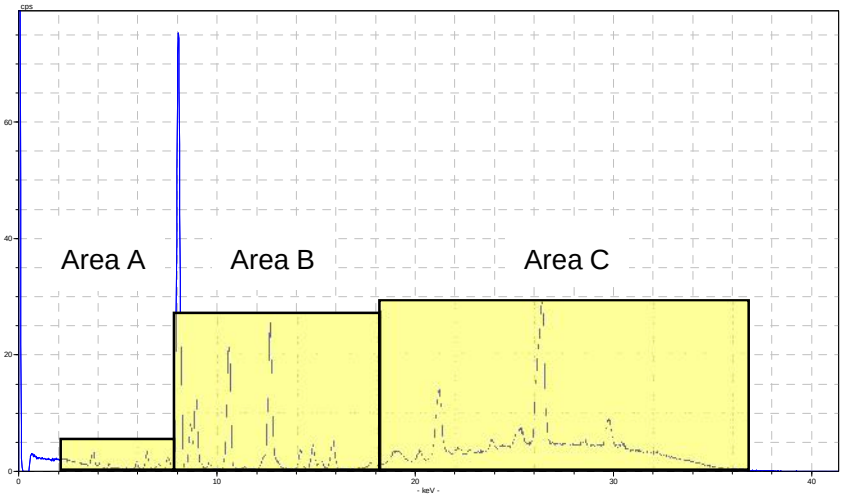

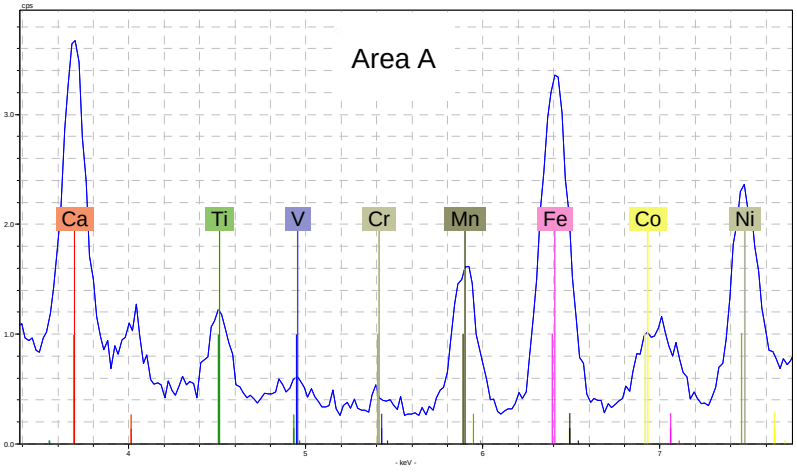

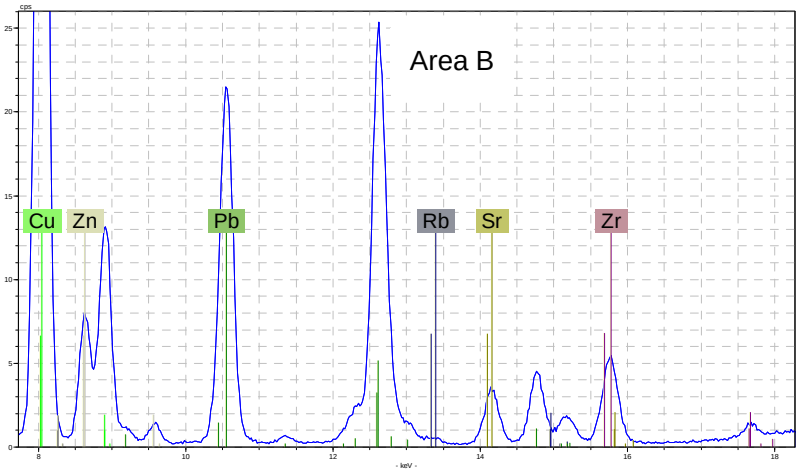

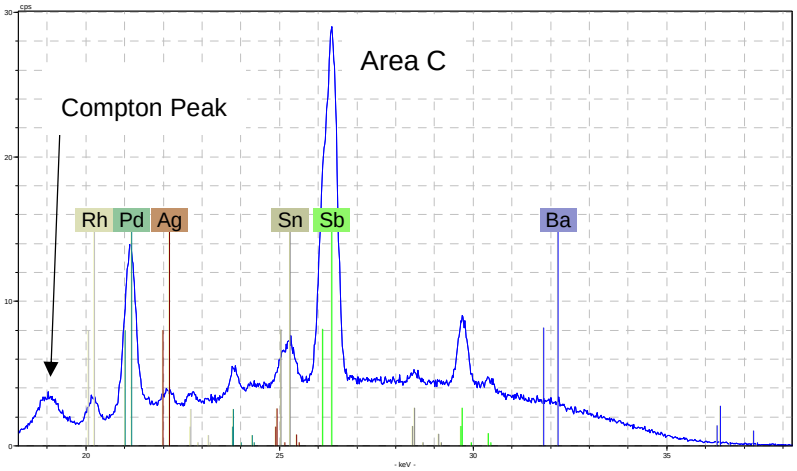

HH-XRF Spectrum of Corning Glass B; 15 kV, 50 µA, Filter 2, Vacuum, 180 Second Acquisition Time

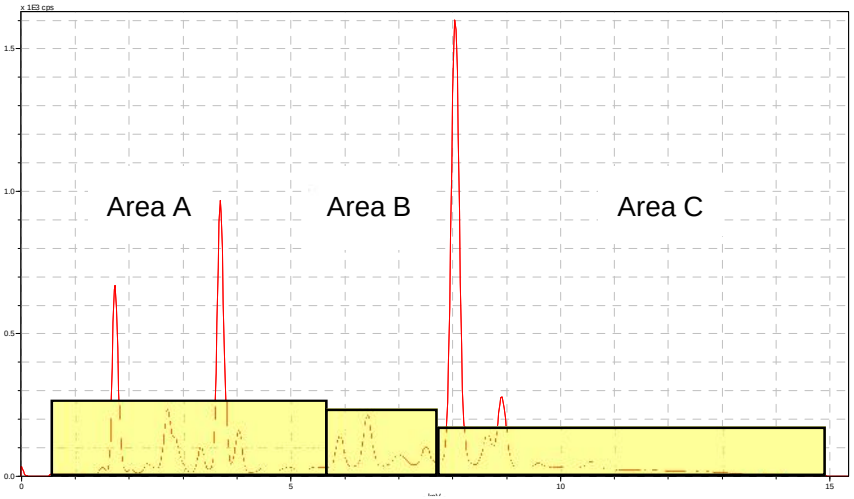

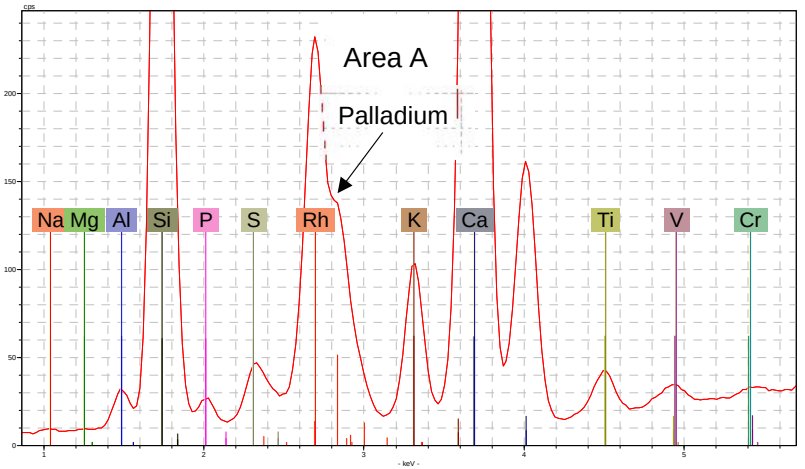

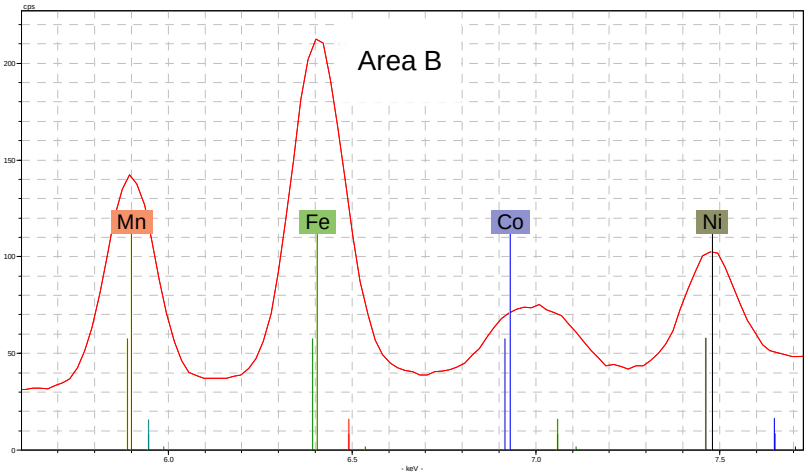

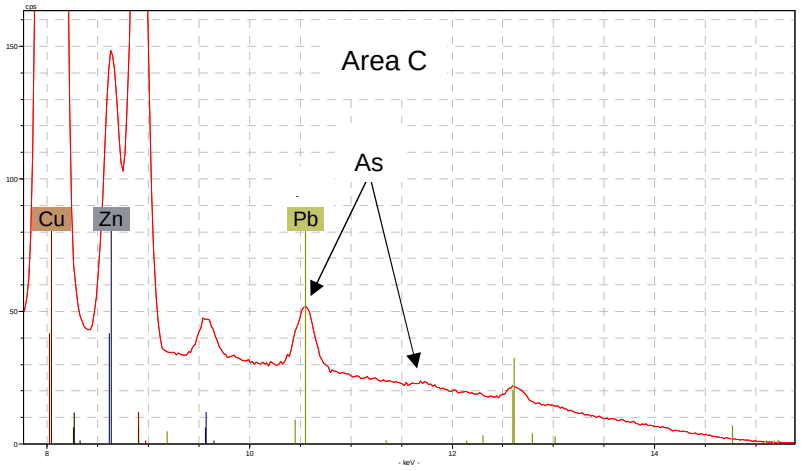

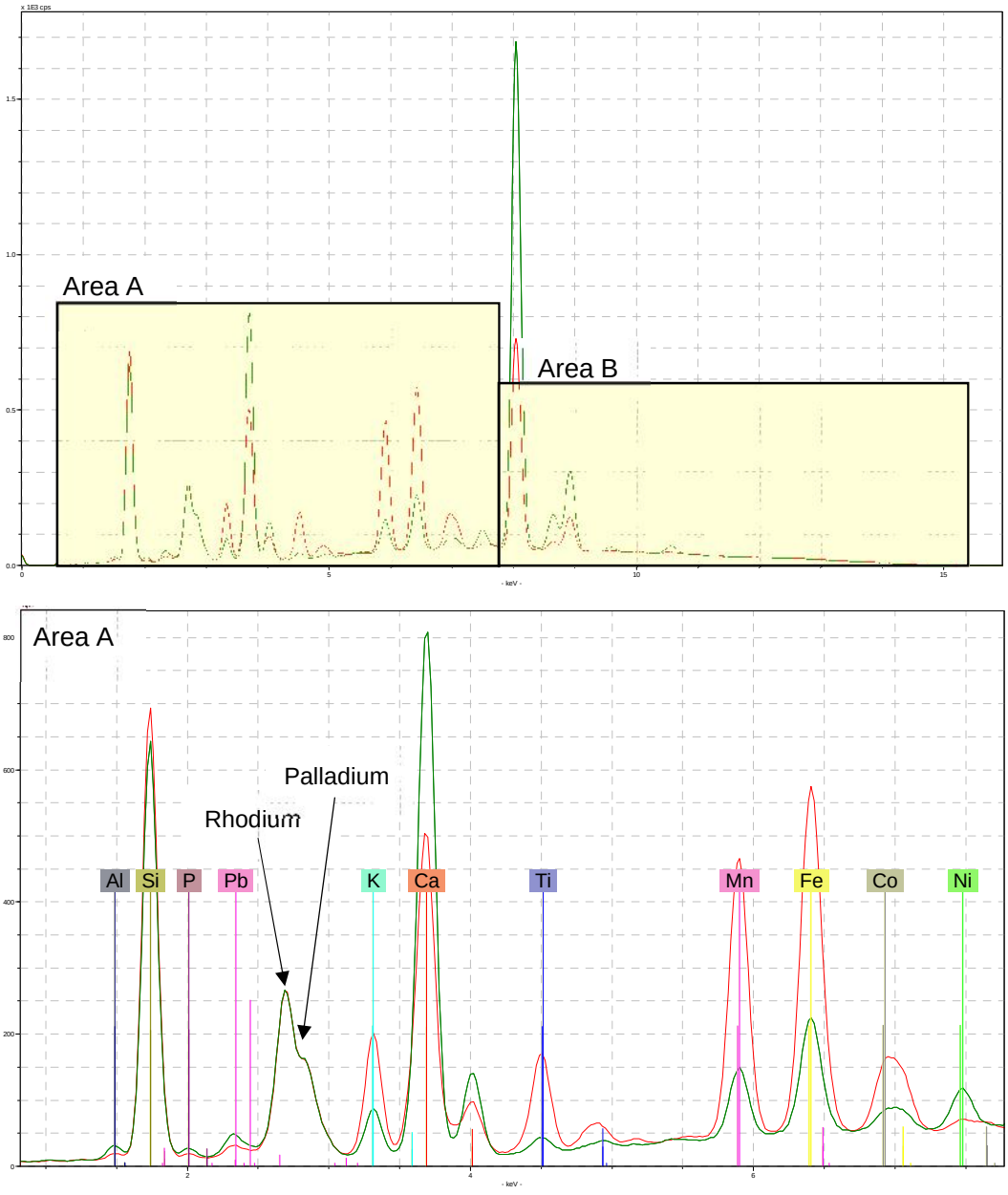

HH-XRF comparison spectra of Corning Glass A (red) and B (blue) using 15 kV, 55 µA, filter 2, and vacuum for 180 second acquisition time. The spectra show all elements identified within the glass standards but also show rhodium and palladium L-lines from the analyser unit.

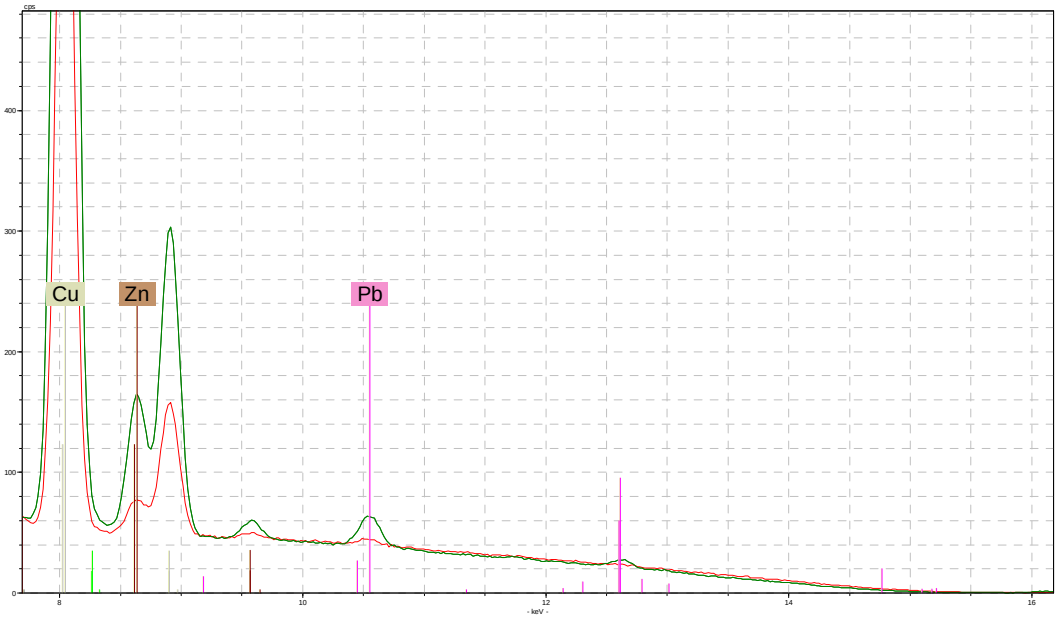

Continued: HH-XRF comparison spectra of Corning Glass A (red) and B (blue) using 15 kV, 55 µA, filter 2, and vacuum for 180 second acquisition time.

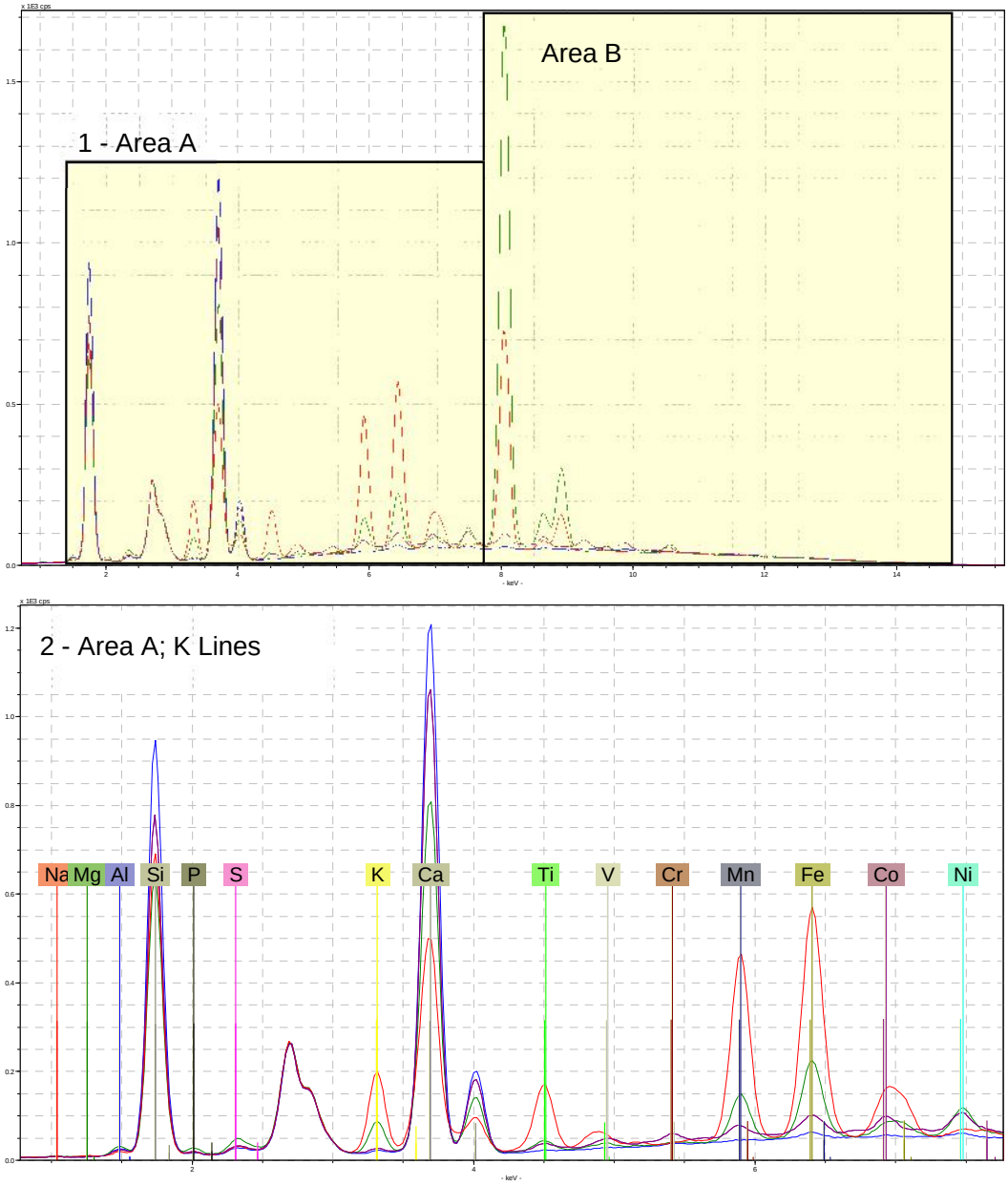

HH-XRF comparison spectra of Corning Glass A (red), B (green), NIST610 (purple) and NIST612 (blue) using 15 kV, 55 µA, filter 2, and vacuum for 180 second acquisition time. Frames 2 shows spectra with only the K lines and the L-Lines, respectively. The titanium Kβ1 line at 4.93 keV for Corning Glass A is slightly pulled toward a lower keV line due to the presence of barium (frame 3).

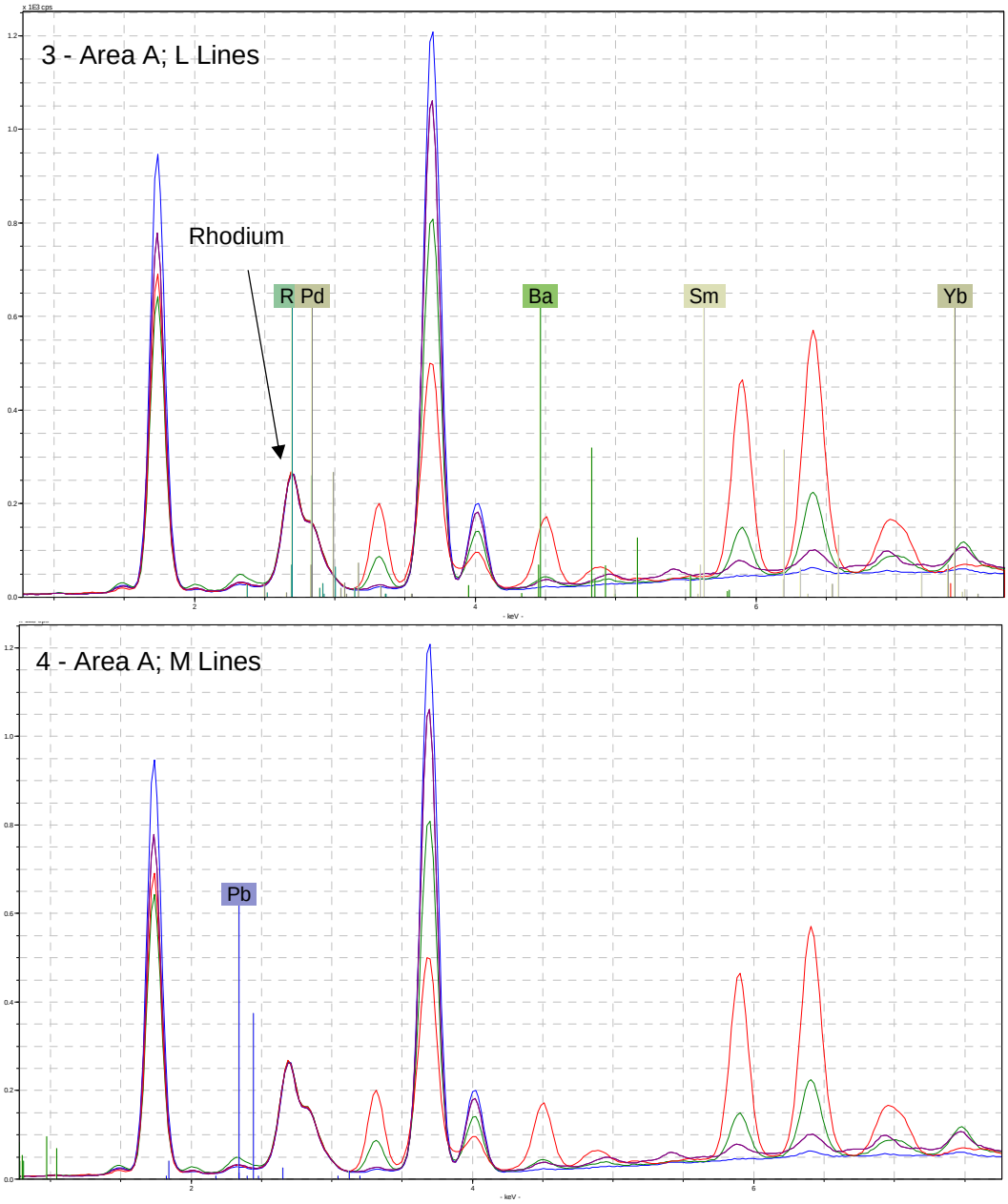

Continued: HH-XRF comparison spectra of Corning Glass A (red), B (green), NIST610 (purple) and NIST612 (blue) using 15 kV, 55 µA, filter 2, and vacuum for 180 second acquisition time. Frame 3 shows spectra with only the L-Lines. Ytterbium (7.41 keV), while present in the glass production batch, is less obviously present in the spectrum due to peak overlap with the nickel peak (7.48 keV). Frame 3 also shows the rhodium and palladium L-lines from the analyser unit. Frame 4 exhibits the M lines (Mα1 2.34 and Mβ1 2.44 keV) for lead.

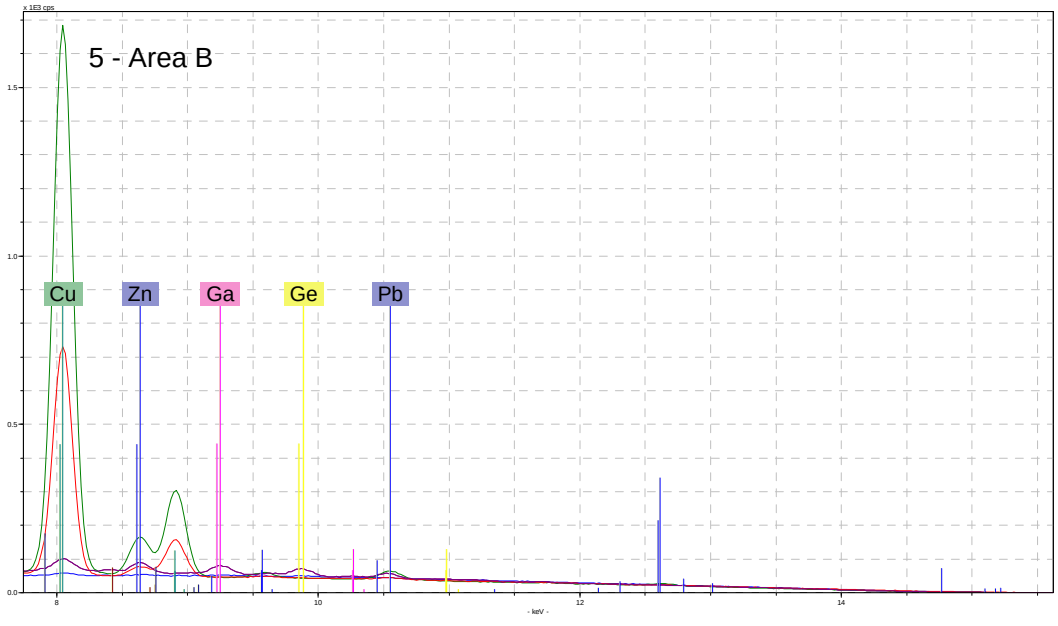

Continued: HH-XRF comparison spectra of Corning Glass A (red), B (green), NIST610 (purple) and NIST612 (blue) using 15 kV, 55 µA, filter 2, and vacuum for 180 second acquisition time. This frame shows both K and L lines for the exhibited elements.

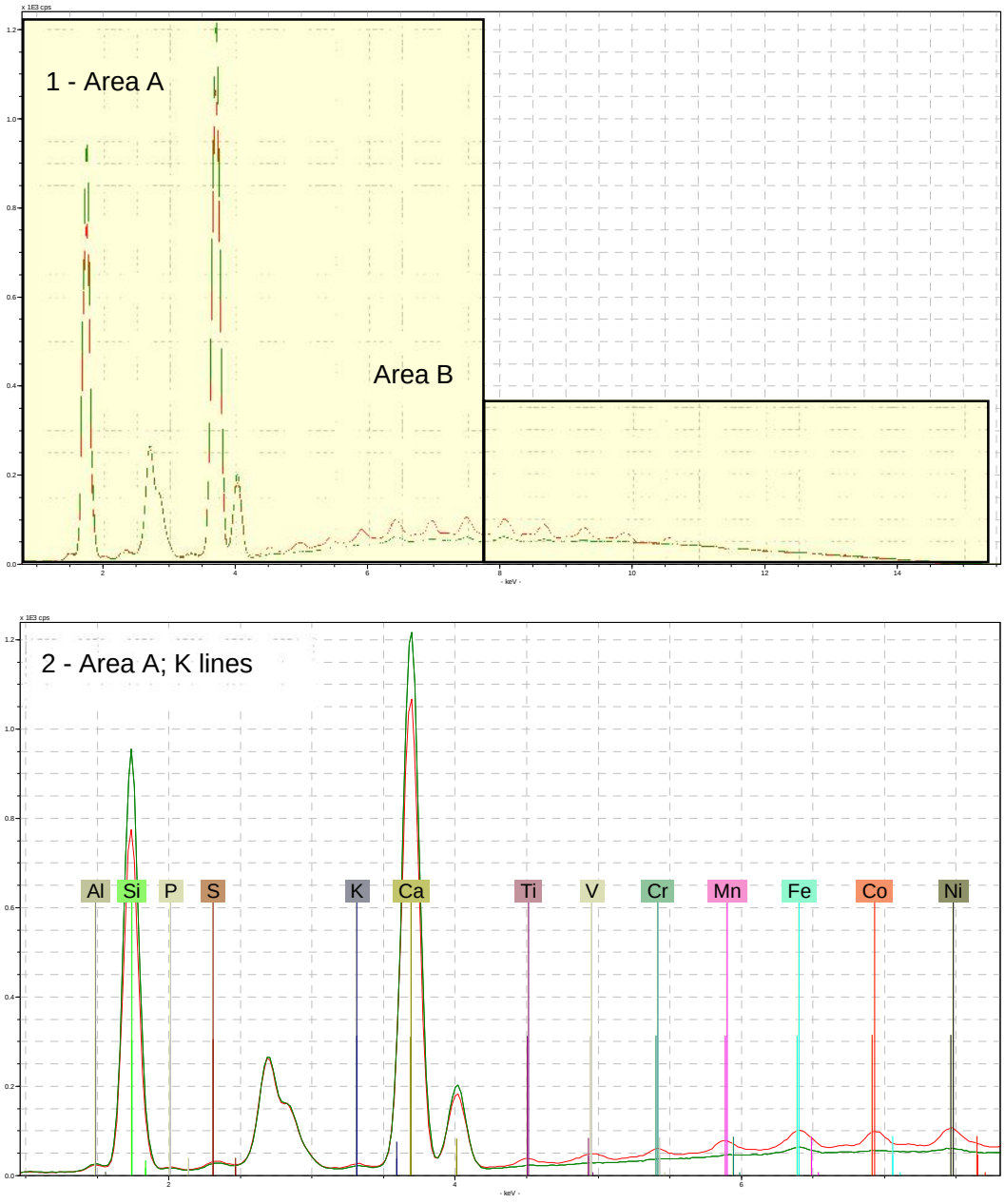

HH-XRF comparison spectra of NIST610 (red) and NIST612 (green) using 15 kV, 55 µA, filter 2, and vacuum for 180 second acquisition time. Frame 2 exhibits K lines of elements shown.

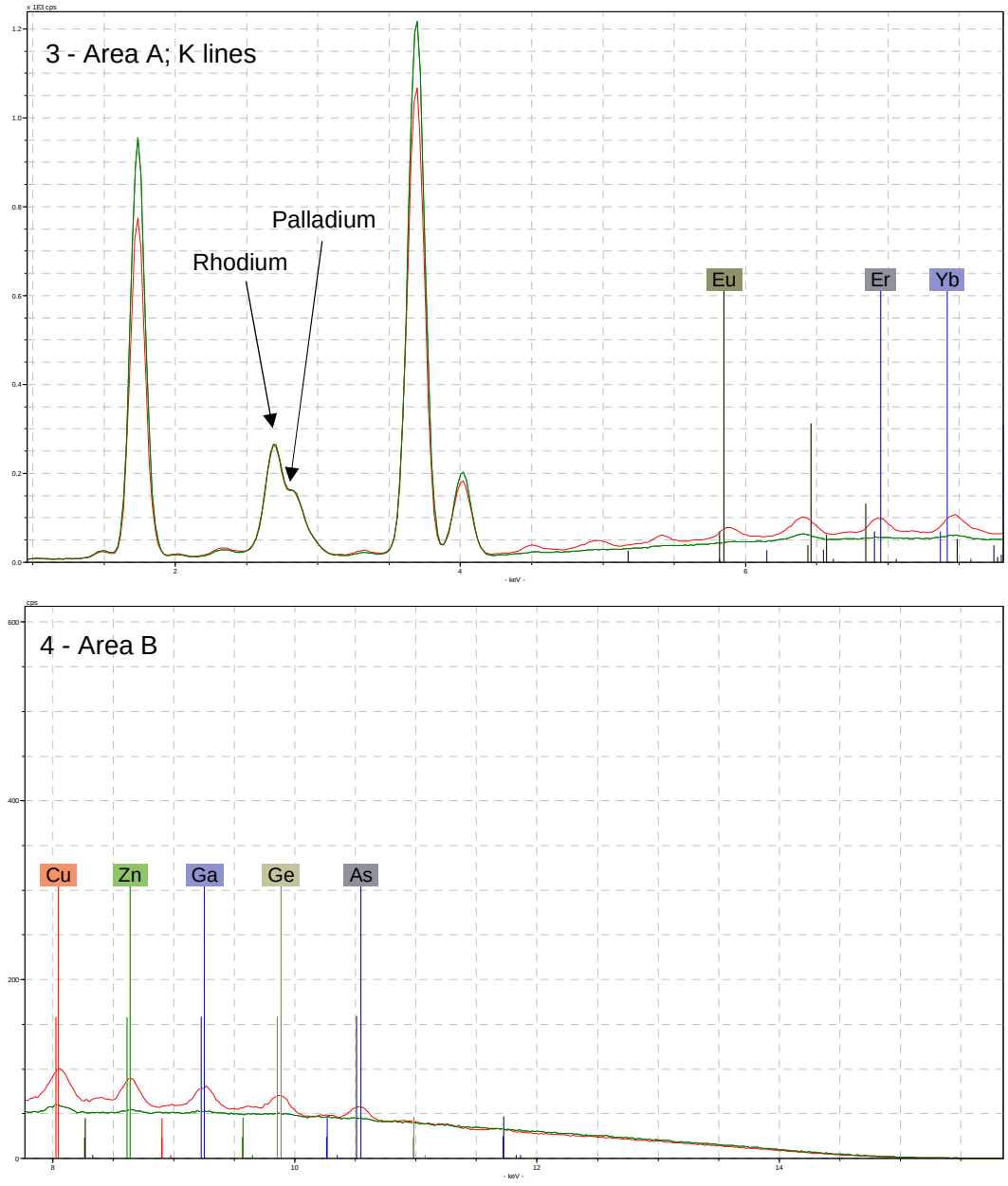

Continued: HH-XRF comparison spectra of NIST610 (red) and NIST612 (green) using 15 kV, 55 µA, filter 2, and vacuum for 180 second acquisition time. Frame 3 exhibits L lines of europium (Lα1 5.84 keV), erbium (Lα1 6.94 keV) and ytterbium (Lα1 7.41 keV). These elements are in the glass batches but the peaks for manganese (Kα1 5.90 keV), cobalt (Kα1 6.93 keV) and nickel (Kα1 7.48 keV) respectively overlap their peaks, and their presence is less obvious in the spectrum (see Frame 2). Frame 3 also shows the rhodium and palladium L-lines from the analyser unit. Frame 4 shows the K lines of the exhibited elements.

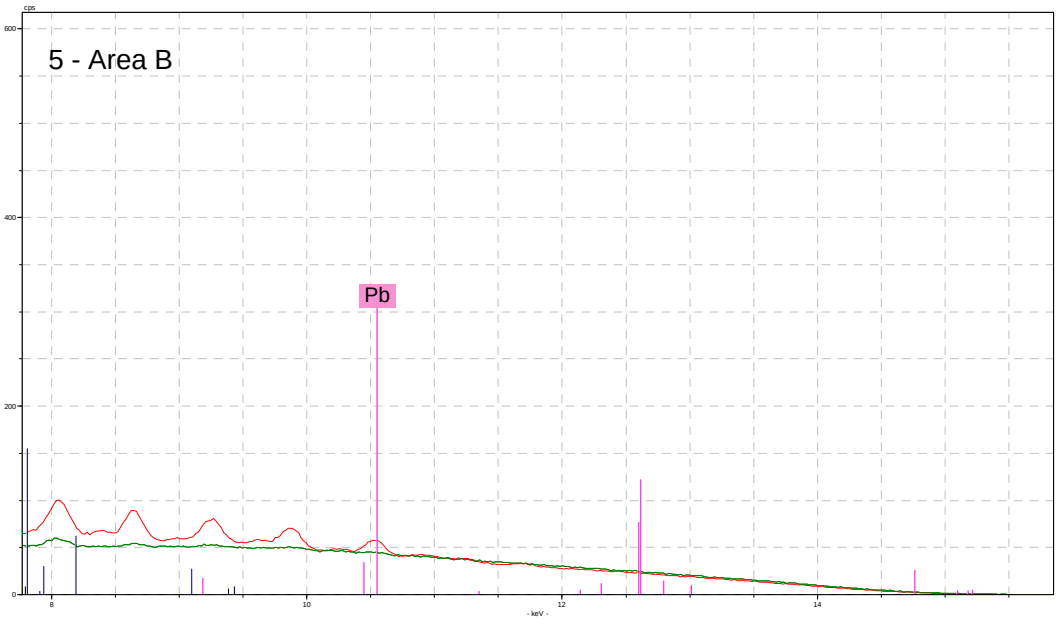

Continuation of the HH-XRF comparison spectra of NIST610 (red) and NIST612 (green) using 15 kV, 55 µA, filter 2, and vacuum for 180 second acquisition time. Frame 5 shows the Lα lines (Lα1 10.55 keV and Lα2 10.44 keV) for lead.

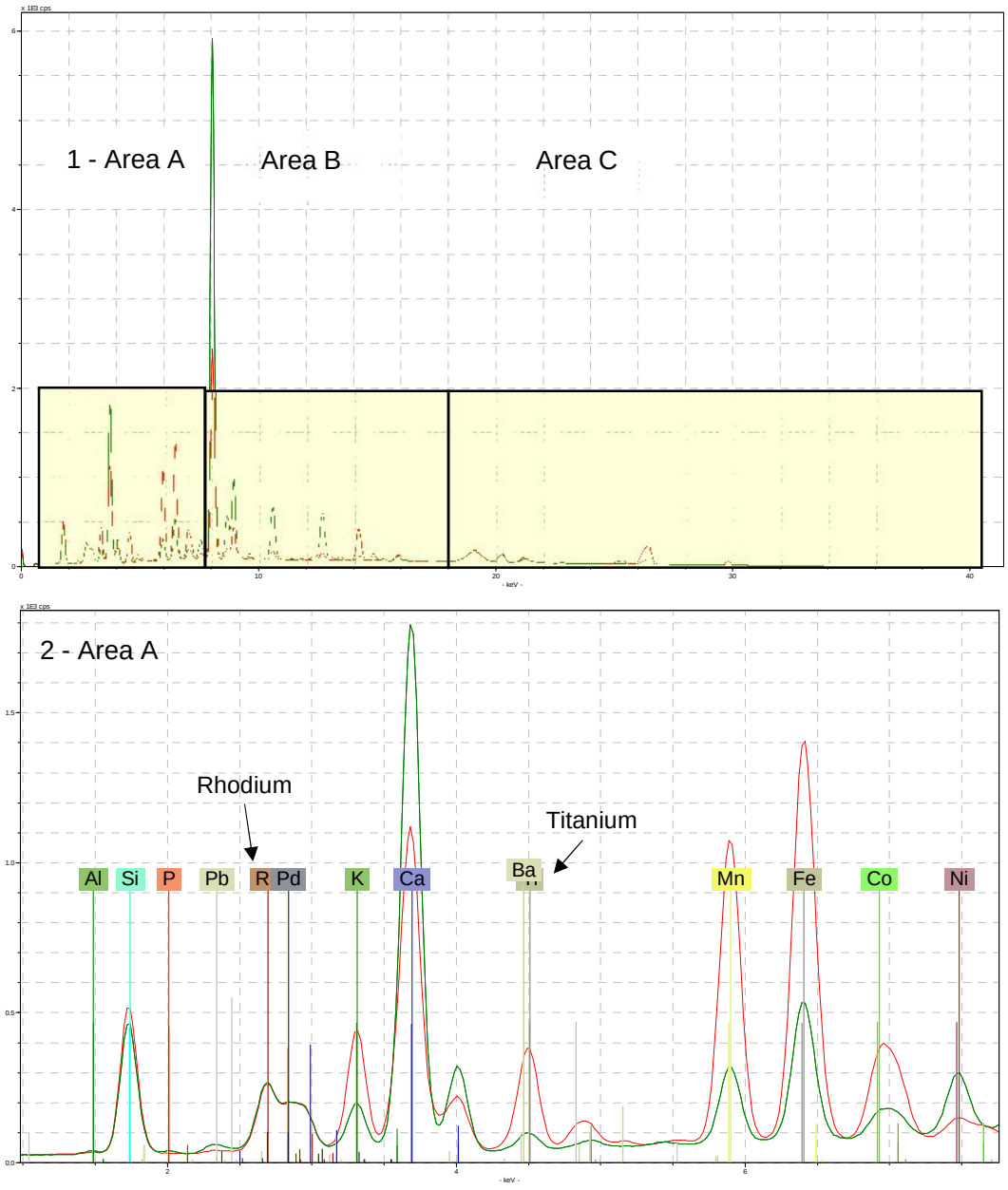

HH-XRF comparison spectra of NIST610 (red) and NIST612 (green) using 40 kV, 30 µA, filter 2, and vacuum for 180 second acquisition time.

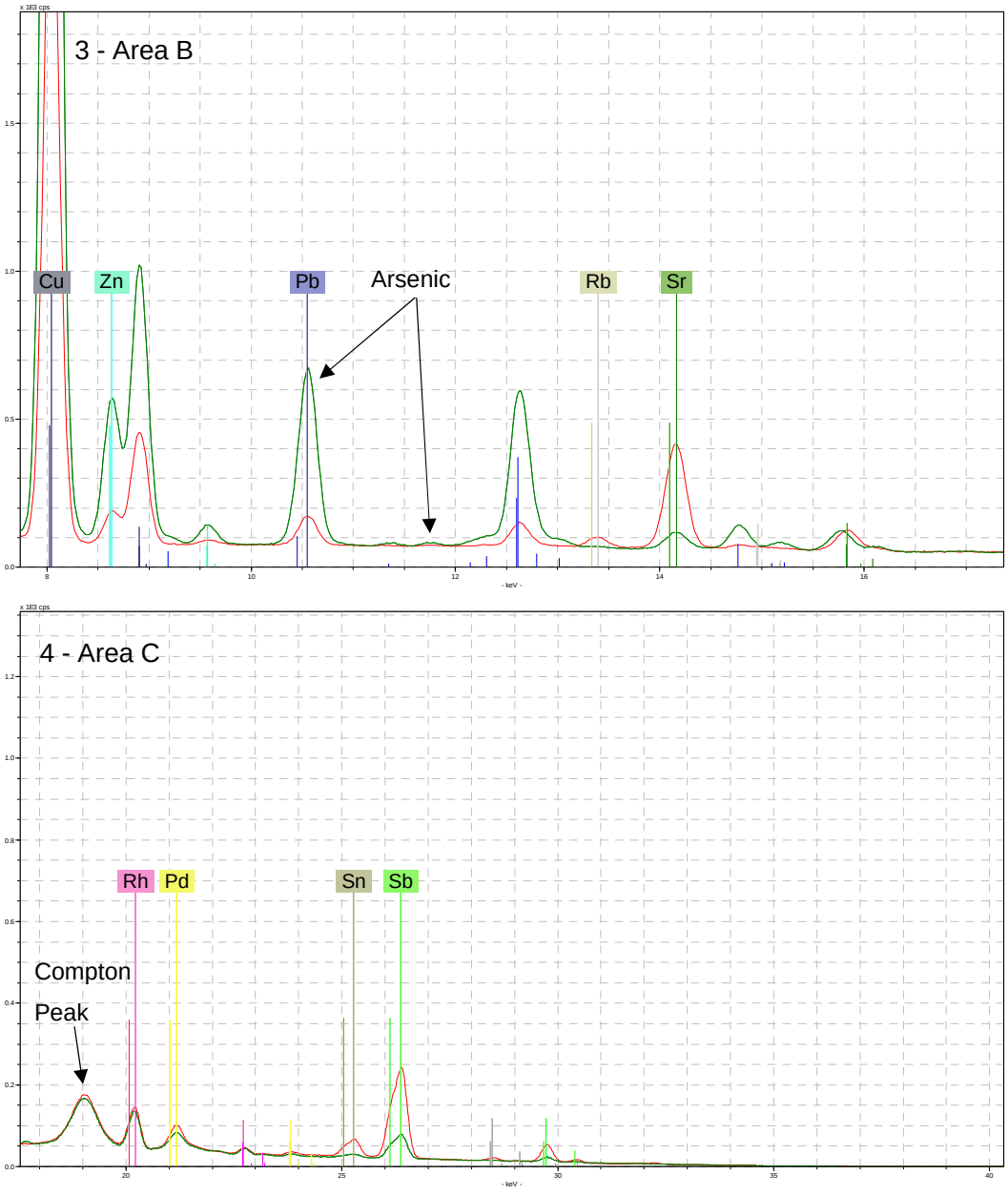

Continued: HH-XRF comparison spectra of NIST610 (red) and NIST612 (green) using 40 kV, 30 µA, filter 2, and vacuum for 180 second acquisition time. The Lα lines of lead at 10.55 keV overlap the arsenic Kα lines at 10.54 keV. Spectral evidence of arsenic are the Kβ peaks at 11.72 keV.

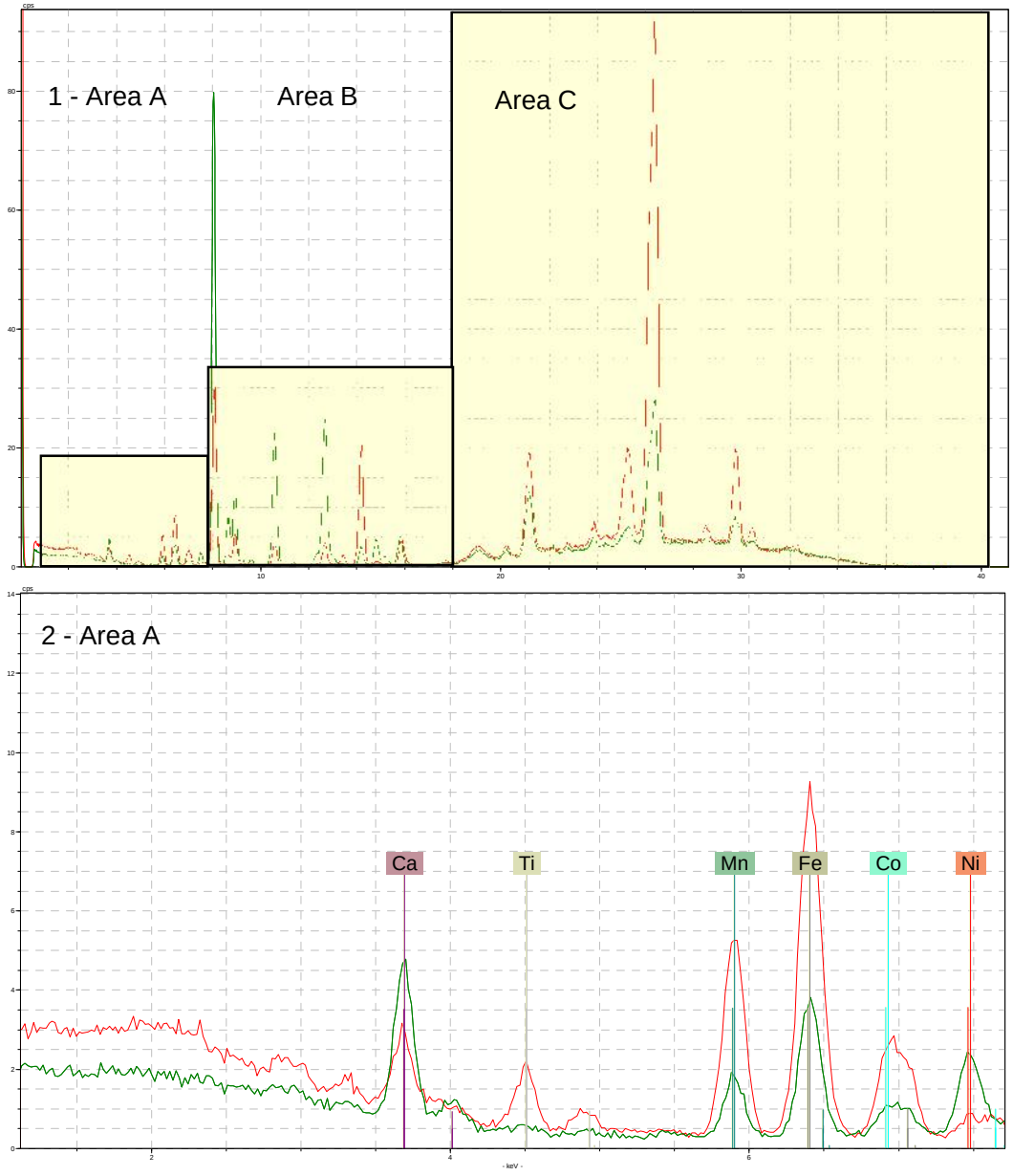

HH-XRF comparison spectra of Corning Glass A (red) and B (green) using 40 kV, 30 µA, filter 3, and vacuum for 180 second acquisition time.

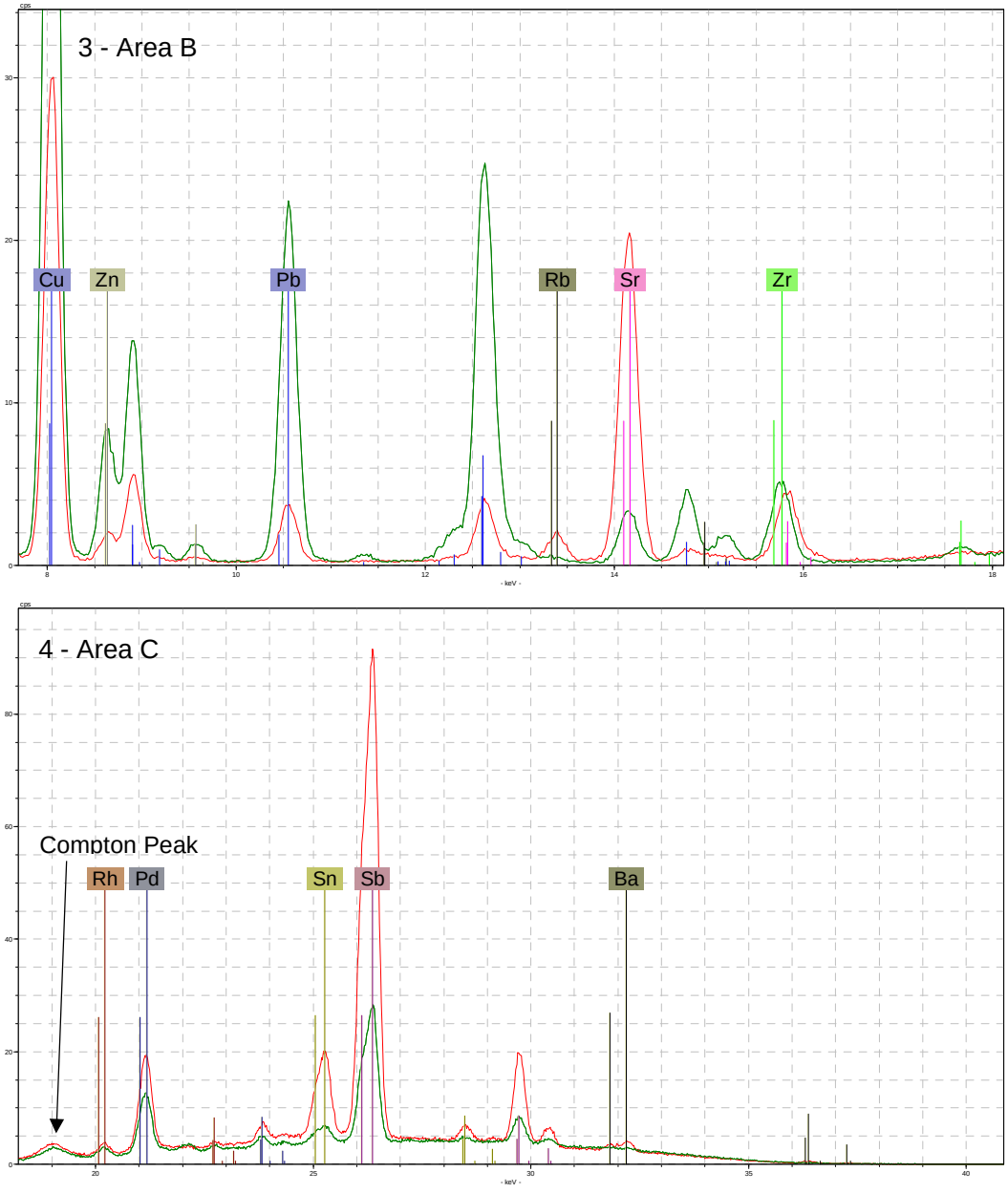

Continued: HH-XRF comparison spectra of Corning Glass A (red) and B (green) using 40 kV, 30 µA, filter 3, and vacuum for 180 second acquisition time.

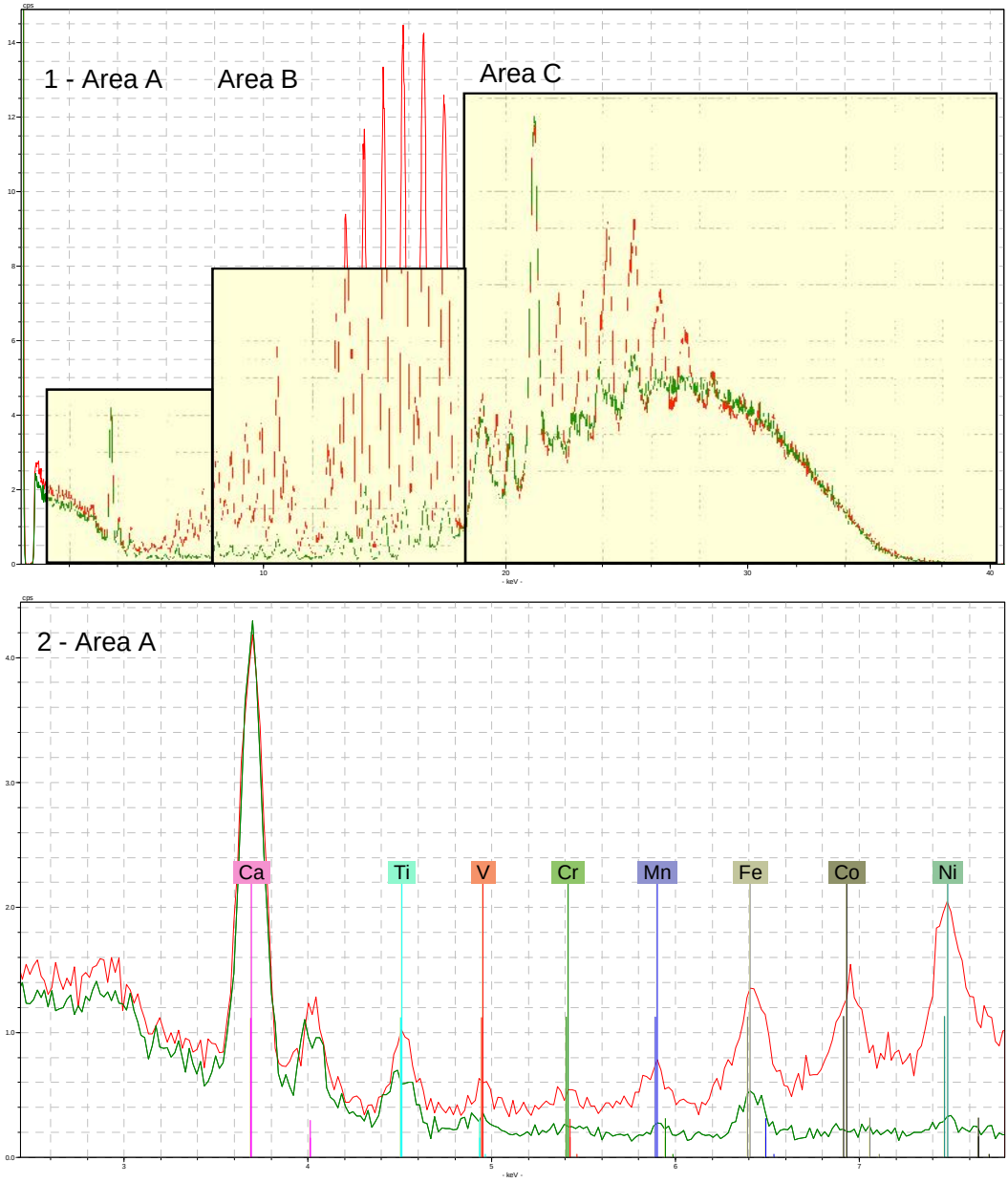

HH-XRF comparison spectra of NIST610 (red) NIST612 (green) using 40 kV, 30 µA, filter 3, and vacuum for 180 second acquisition time.

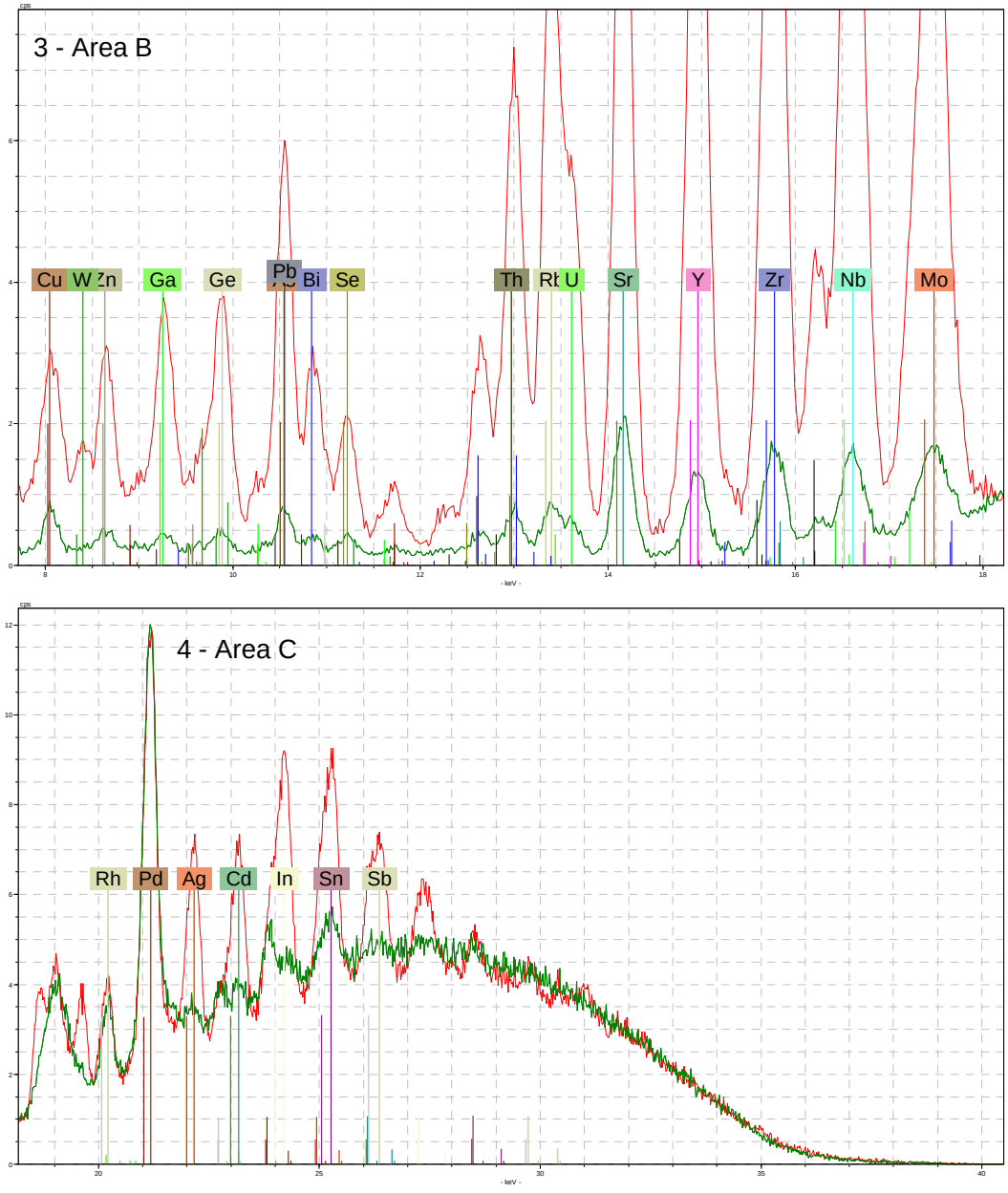

Continued: HH-XRF comparison spectra of NIST610 (red) NIST612 (green) using 40 kV, 30 µA, filter 3, and vacuum for 180 second acquisition time.

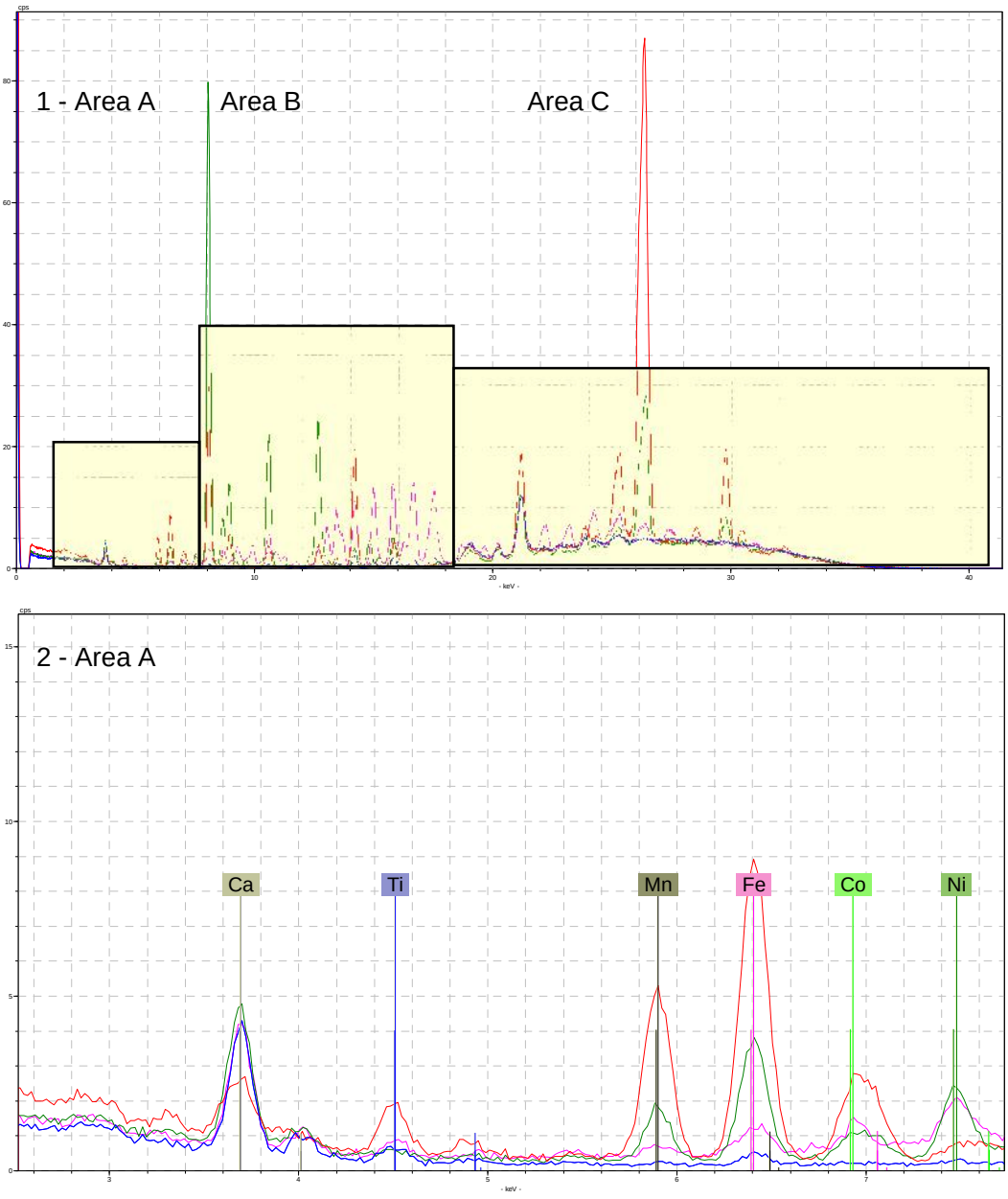

HH-XRF comparison spectra of Corning Glass A (red), Corning Glass B (green), NIST610 (purple) NIST612 (blue) using 40 kV, 30 µA, filter 3, and vacuum for 180 second acquisition time.

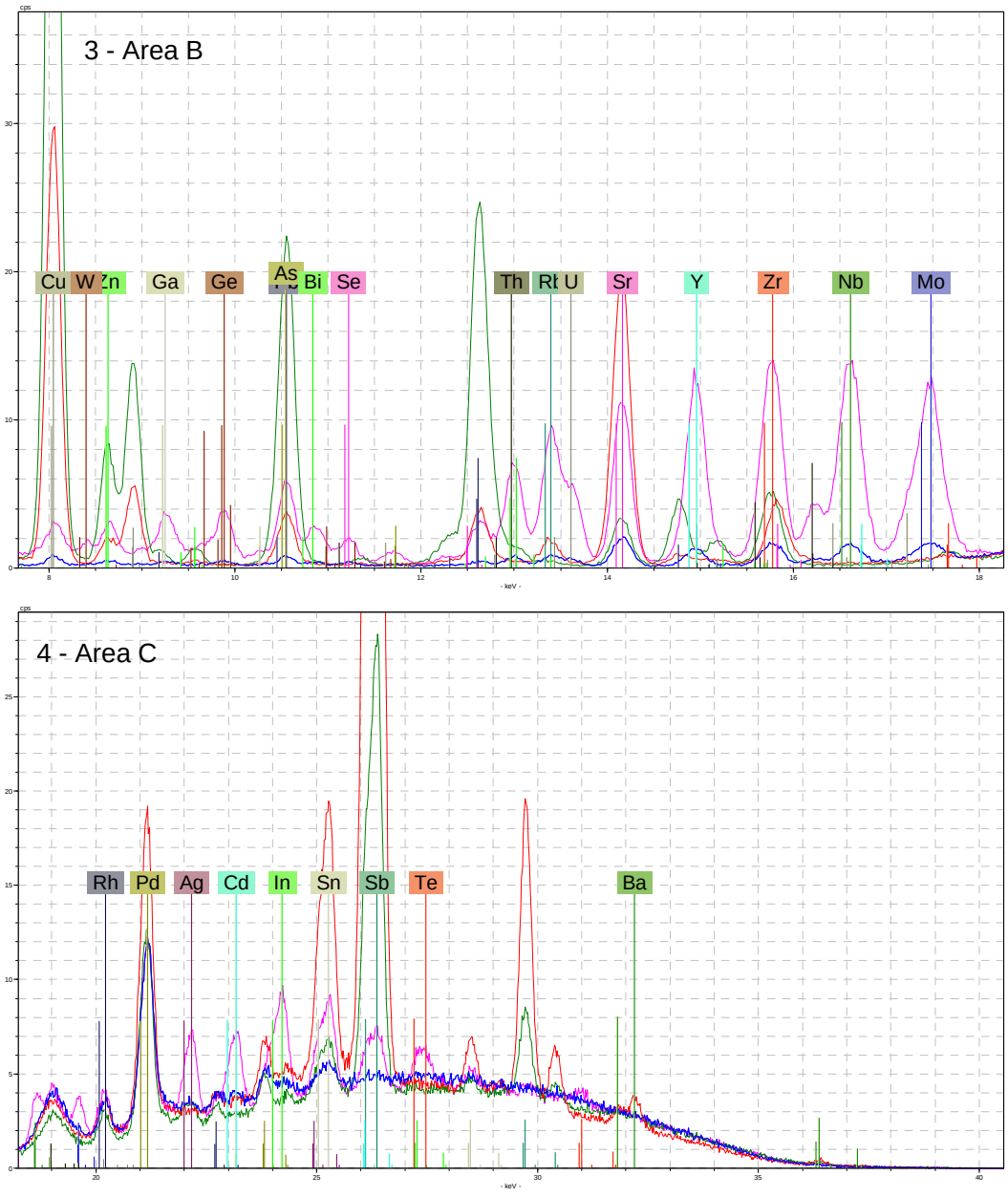

Continued: HH-XRF comparison spectra of Corning Glass A (red), Corning Glass B (green), NIST610 (purple) NIST612 (blue) using 40 kV, 30 µA, filter 3, and vacuum for 180 second acquisition time.

Glass Standards HH-XRF Measurements for Common Faience Elements: Settings 15 kV, 55 µA, Filter 2 and a Vacuum at 180 Seconds Acquisition Time																		
	Corning Glass A				Corning Glass B				NIST610				NIST612				Region of Interest	
		Peak Area				Peak Area				Peak Area				Peak Area				
Elements	**Oxide Wt%**	Gross	**Net**	Backgr.	**Oxide Wt%**	Gross	**Net**	Backgr.	**Oxide Wt%**	Gross	**Net**	Backgr.	**Oxide Wt%**	Gross	**Net**	Backgr.	Start/keV	End/keV
Sodium	**14.30**	5156	**-4453**	9610	**17.00**	6486	**-8190**	14676	**13.40**	4411	**-5088**	9499	**13.40**	5824	**-6944**	12768	1.00	1.08
Magnesium	**2.66**	11358	**-7448**	18806	**1.03**	12880	**-15558**	28438	**0.04**	10518	**-12609**	23127	**0.01**	13446	**-17112**	30557	1.16	1.329
Aluminium	**1.00**	20391	**371**	20019	**4.36**	34872	**5031**	29841	**1.95**	25921	**1495**	24427	**2.03**	35008	**3563**	31445	1.35	1.556
Silicon	**66.56**	558306	**525899**	32408	**61.55**	618222	**571291**	46931	**69.70**	680188	**641241**	38947	**72.10**	1022293	**974771**	47522	1.567	1.936
Phosphorus	**0.13**	21021	**3634**	17387	**0.82**	33402	**9125**	24277	**0.04**	23882	**3372**	20509	**0.00**	26641	**3307**	23334	1.942	2.141
Sulfur	**0.10**	50692	**19776**	30916	**0.50**	82462	**41883**	40579	**0.06**	57499	**22199**	35300	**0.04**	63848	**24252**	39596	2.143	2.484
Potassium	**2.87**	199834	**153668**	46166	**1.00**	117010	**68077**	48933	**0.05**	54330	**8851**	45480	**0.00**	58365	**9121**	49244	3.119	3.467
Calcium	**5.03**	543863	**489031**	54833	**8.56**	907150	**851366**	55784	**11.40**	1059247	**1006747**	52501	**11.90**	1481922	**1426261**	55661	3.475	3.877
Titanium	**0.79**	214261	**142738**	71523	**0.09**	98506	**24932**	73574	**0.05**	89059	**14993**	74066	**0.00**	80703	**4453**	76250	4.23	4.686
Vandium	**0.01**	118664	**43751**	74914	**0.04**	94024	**13371**	80654	**0.05**	109957	**20463**	89494	**0.00**	88147	**2338**	85808	4.702	5.1
Chromium	**0.00**	94013	**6118**	87895	**0.01**	105212	**6538**	98674	**0.04**	134715	**22623**	112091	**0.00**	113934	**8148**	105787	5.252	5.624
Manganese	**1.00**	557072	**423189**	133883	**0.25**	282342	**129743**	152599	**0.04**	206439	**41761**	164679	**0.00**	182709	**19431**	163278	5.651	6.135
Iron	**1.09**	749484	**576784**	172701	**0.34**	436770	**235532**	201237	**0.05**	289734	**74115**	215619	**0.01**	259204	**45588**	213616	6.137	6.705
Cobalt	**0.17**	364347	**181651**	182696	**0.05**	291517	**72102**	219415	**0.04**	285536	**61489**	224047	**0.00**	258619	**27739**	230880	6.717	7.269
Nickel	**0.02**	179178	**32738**	146440	**0.10**	269302	**88850**	180452	**0.05**	259829	**63181**	196648	**0.00**	210880	**21222**	189658	7.277	7.727
Copper	**1.17**	969000	**757245**	211755	**2.66**	2402892	**2138498**	264393	**0.04**	330273	**63031**	267241	**0.00**	291353	**16625**	274729	7.751	8.406
Zinc	**0.04**	148486	**34278**	114208	**0.19**	297912	**156571**	141341	**0.05**	188451	**39907**	148544	**0.00**	163744	**6979**	156765	8.393	8.757
Lead	**0.12**	97175	**8634**	88540	**0.61**	142499	**40416**	102082	**0.04**	131111	**18324**	112788	**0.00**	137359	**8097**	129262	10.36	10.735

Glass Standards HH-XRF Measurements for Common Faience Elements: Settings 40 kV, 30 µA, Filter 3 and a Vacuum at 180 Seconds Acquisition Time																		
	Corning Glass A				Corning Glass B				NIST610				NIST612				Region of Interest	
		Peak Area				Peak Area				Peak Area				Peak Area				
Elements	**Oxide Wt%**	Gross	**Net**	Backgr.	**Oxide Wt%**	Gross	**Net**	Backgr.	**Oxide Wt%**	Gross	**Net**	Backgr.	**Oxide Wt%**	Gross	**Net**	Backgr.	Start/keV	End/keV
Manganese	**1.00**	8848	**7306**	1542	**0.25**	3293	**2098**	1194	**0.04**	2117	**481**	1636	**0.00**	766	**81**	685	5.692	6.133
Iron	**1.09**	15360	**13567**	1793	**0.34**	6820	**5214**	1606	**0.05**	3864	**1338**	2526	**0.01**	1398	**561**	837	6.149	6.691
Cobalt	**0.17**	6871	**5300**	1570	**0.05**	3426	**1681**	1745	**0.04**	4394	**1107**	3287	**0.00**	1072	**229**	843	6.726	7.253
Nickel	**0.02**	2290	**1160**	1130	**0.10**	4796	**3191**	1604	**0.05**	5102	**2165**	2937	**0.00**	933	**244**	689	7.287	7.683
Copper	**1.17**	51107	**49198**	1908	**2.66**	131802	**128935**	2867	**0.04**	9991	**4671**	5320	**0.00**	2152	**928**	1223	7.742	8.371
Zinc	**0.04**	4405	**3224**	1181	**0.19**	15574	**13759**	1815	**0.05**	7562	**4078**	3484	**0.00**	1267	**451**	816	8.382	8.771
Arsenic	--	968	**-34**	1002	--	1114	**31**	1082	**0.03**	3013	**1284**	1729	**0.00**	721	**86**	636	11.491	11.929
Rubidium	**0.01**	5144	**3206**	1938	**0.00**	2049	**644**	1405	**0.04**	30359	**26245**	4114	**0.00**	3086	**1997**	1089	13.19	13.846
Strontium	**0.10**	42682	**41022**	1660	**0.02**	7960	**6605**	1355	**0.05**	25567	**22242**	3325	**0.01**	4918	**3967**	951	13.873	14.472
Zirconium	**0.01**	11396	**9483**	1913	**0.03**	12583	**10987**	1596	**0.04**	37021	**31341**	5679	**0.00**	4949	**3365**	1584	15.387	16.031
Tin	**0.19**	98848	**55279**	43569	**0.04**	47353	**11974**	35379	**0.04**	57518	**20235**	37282	**0.00**	45730	**6236**	39494	24.614	25.665
Antimony	**1.75**	358555	**311949**	46606	**0.46**	128812	**88866**	39946	**0.04**	55665	**14279**	41386	**0.00**	47752	**3405**	44346	25.71	26.821
Barium	**0.56**	10675	**3979**	6695	**0.12**	8613	**1014**	7599	**0.05**	8795	**654**	8141	**0.00**	9050	**447**	8603	32.036	32.383
Lead	**0.12**	7818	**6727**	1091	**0.61**	43036	**41843**	1193	**0.04**	14076	**10343**	3733	**0.00**	2116	**1087**	1029	10.213	10.756
Bismuth	**0.00**	855	**183**	673	**0.01**	2096	**1381**	715	**0.04**	6128	**4234**	1894	**0.00**	954	**416**	538	10.745	11.048

Appendix D: HH-XRF COSHH Risk Assessment

X

Risk Assessment Form

IMPORTANT: Before carrying out the assessment, please read the Guidance Notes

1.General Information

Department	SHARE	**Building**	John Percival	**Room No**	3.03 / Off-site
Name of Assessor	Johanna Thunberg	**Date of Original Assessment**	07/08/2017	**Assessment No**	

Status of Assessor: Supervisor ☐ Postgraduate ☐ , Undergraduate ☐ , Technician ☐ (Specify) , Other: Staff member

2. Brief Description of Procedure/Activity including its Location and Duration

XRF
Use of Bruker hand-held XRF Analyzer for analysis of objects, unit contains an x-ray generator.
Analysis to be carried out in room 3.03 Humanities Building, a controlled area while the XRF is connected to a power supply.
Analysis may be carried out off-site following a site risk assessment requiring temporary controlled area designation and using the principles below.

3. Persons at Risk Are they... Notes

Staff ☒ Students ☒ Visitor ☐ Contractor ☐	Trained ☒ Competent ☐ Inexperienced ☐ Disabled ☐	OPERATION OF THE XRF BY UNTRAINED STAFF/STUDENTS IS FORBIDDEN

4. Level of Supervision Notes

None ☒ Constant ☐ Periodic ☐ Training Required ☒	Once trained no supervision is necessary.

5. Will Protective Equipment Be Used? Please give ***specific*** details of PPE

Head ☐ Eye ☐ Ear ☐ Body ☐ Hand ☐ Foot ☐	

6. Is the Environment at Risk? Notes

Yes ☐ No ☒	

7. Will Waste be generated? If 'yes' please give details of disposal

Yes ☐ No ☒	

8. Hazards involved

Work Activity / Item of Equipment / Procedure / Physical Location	Hazard	Control Measures and Consequence of Failure	Likelihood (0 to 5)	× Severity (0 to 5)	= Level of Risk
X-radiography	External dose rate* hazard when power is supplied to the x-ray tube.	Unit requires a key for operation. The key should not be left in an unattended analyzer. Unit is password protected. Unit is shielded so x-rays are emitted from window only.	1	5	5

		Unit has infra red sample detection and x-ray backscatter detection which shuts the x-ray beam off if no sample is detected. An x-ray cabinet is available for analysis of small objects and should be used if possible. The cabinet door must be closed whilst x-ray exposures are underway. Where use of the x-ray shield is not possible, a radiation monitor will be used to set up a controlled area such that the dose rates at the boundary of the area are <7.5 µSv/h. If the user cannot guarantee access restriction to the area in front of the XRF, then shielding placed behind test objects should limit the controlled area to at least a 1m radius; shielding equivalent to 0.3mm lead (22 mm concrete) would be required. Alternatively 1mm lead will effectively attenuate all x-rays. A structural wall will also attenuate all x-rays. A free-standing radiation warning sign will be placed outside the room or, when in use in the field, adjacent to the designated area. No-one but the operator should be allowed closer than 1 metre to the analyzer when in use. No-one must walk in front of, or closer than 1m to the side of, the machine when in use. Local rules are provided with the unit. Users must be trained and follow the local rules provided with the unit. Users are able to obtain advice from their RPS and RPA. Report any irregularities in the operation during operation to a member of staff immediately. Women who are, or suspect they are, pregnant should be aware that improper handling or improper use of this device could result in radiation exposure which may be harmful to a developing foetus. In normal use, following the guidance above, dose rate experienced by operator (whole body and hand) is <1 µSv/h*. Misuse of the analyzer could result in localised exposures at dose rates of a few 100 mSv/h*. Exposure to ionising radiation is cumulative and damage depends on the x-ray strength and exposure time. The limits on effective dose (whole body) for employees aged 18 years or over are 6 mSv in a calendar year. *See dose assessment in local rules appendix.			

9. Chemical Safety (COSHH Assessment)

Hazard	Control Measures	Likelihood (0 to 5) ×	Severity (0 to 5) =	Level of Risk

Scoring Criteria for Likelihood (chance of the hazard causing a problem)
0 – Zero to extremely unlikely, 1 – Very Unlikely, 2 – Unlikely, 3 – Likely, 4 – Very Likely, 5 – Almost certain to happen

Scoring Criteria for Severity of injury (or illness) resulting from the hazard
0 – No injury, 1 – First Aid is adequate, 2 – Minor injury, 3 – "Three day" injury, 4 – Major injury, 5 – Fatality or disabling injury

10. Source(s) of information used to complete the above

OSHEU Guidance Documents RP0, RP1 RP3, RP6, RP7
User Manual S1 Turbo SD / LE Portable XRF Analyser, part number 485220-000 Revison D
TRACeR III-V User's Manual

11. Further Action

Highest Level of Risk Score	Action to be taken
0 to 5	No further action needed
6 to 11	Appropriate additional control measures should be implemented
12 to 25	Additional control measures **MUST** be implemented. Work **MUST NOT** commence until such measures are in place. If work has already started it must **STOP** until adequate control measures are in place.

12. Additional Control Measures – Likelihood and Severity are the values with the additional controls in place

Work Activity / Item of Equipment / Procedure / Physical Location	Hazard and Existing Control Measures	Additional Controls needed to Reduce Risk	Likelihood (0 to 5) ×	Severity (0 to 5) =	Level of Risk

After the implementation of new control measures the procedure/activity should be re-assessed to ensure that the level of risk has been reduced as required.

13. Action in the Event of an Accident or Emergency

Foreseeable scenarios include direct beam exposure due to failure to terminate a beam or of the IR sensor, deliberate misuse, unauthorised use or unauthorised entry into a controlled area. Raise the alarm and report the incident to a relevant member of staff or first aider. Note operating current/voltage where possible.

Report all accidents and faults/breakages. Inform the University RPA – Mike Sobanski – 75395, sobanski@cf.ac.uk

Out of hours contact the porter's lodge in the Humanities building entrance hall.

14. Arrangements for Monitoring the Effectiveness of Control

Radiation monitor to measure radiation dose rates during operation of analyzer. Initial survey results performed with a Berthold LB123 are found in the appendix to the local rules.

15. Review: This assessment must be reviewed by (1/8/20):

Name of Reviewer:		Date of Review:	
Have the Control measures been effective in controlling the risk?			

Have there been any changes in the procedure or in information available which affect the estimated level of risk?	
What changes to the Control Measures are required?	

16. Signatures for printed copies:

Assessor: Johanna Thunberg Date: 07/08/2017

Approved by: Date:

Reviewed by: Date:

Appendix E: HH-XRF Cardiff University Local Rules

CARDIFF UNIVERSITY

SCHOOL OF HISTORY, ARCHAEOLOGY AND RELIGION

LOCAL RULES/WRITTEN ARRANGEMENTS FOR USE OF HAND HELD X-RAY FLUORESCENCE (XRF) EQUIPMENT

Contents

Review date: 1 Feb 2013

1. INTRODUCTION

These Local Rules are produced in accordance with the requirements of the Ionising Radiations Regulations1999.

This document must be read in conjunction with the supplier's user manual (Ref. 1) and operators of the unit must be in possession of copies of both documents. All users shall be required to sign to the effect that they have read and understood the contents of the rules prior to their initial use of the XRF unit.

2. RADIATION PROTECTION SUPERVISOR (RPS)

The RPS appointed in accordance with IRR99 is:

David Watkinson

Tel. 029 20874249 (Office hours)

Any matter relating to radiation safety should, at first, be referred to the RPS.

The duties of the RPS, with respect to the XRF unit are as follows:-

2.1 The supervision of the day-to-day adherence with these local rules.

2.2 In the event of an emergency, to supervise the implementation of the Contingency Plans in Section 7 of these rules.

2.3 To act as a co-ordinator for contacts with the Health & Safety Executive and the Radiation Protection Adviser.

2.4 Normally, the equipment will be in the School for short periods of up to two weeks maximum. To check the location of the XRF equipment, when in storage in the School premises and to confirm that the location record for the equipment is being properly completed.

2.5 Periodic checks on the general condition of the XRF in accordance with manufacturers recommendations will be carried out by the principal owners, the National Museum of Wales.

2.6 To conduct checks of dose rates at the boundaries of the controlled area.

2.7 To ensure that operators use appropriate radiation monitors when using the equipment

2.8 To keep a record of the issue of the Local Rules to users.

3. DESIGNATED AREAS

3.1 During use of the XRF device samples should be placed in the x-ray shield where possible, including in the field. Two shields are available – a portable small specimen shield and a desktop cabinet housed in the department, room 3.03. Samples should be securely positioned before an exposure is initiated and manual adjustment is prohibited during emission. Objects under investigation must not be held in the hand during exposure.

3.2 Where samples are not able to fit in the x-ray shield a controlled area shall be set up such that the dose rates at the boundary of the controlled area are < 7.5⇑Sv/h. Further detail on requirements for designation are contained in the Appendix.

3.3 Access to the controlled area shall be restricted to non-classified workers working under these written arrangements.

3.4 On no occasion shall anyone enter the area in front of the analyser & within 1m to either side or rear whilst it is in use, apart from to initiate or stop an exposure using the XRF trigger. Where practicable this should be done via the dead-man's switch or the laptop PC to reduce the need to approach the controlled area.

3.5 The controlled area will continue to exist until the unit is disconnected from the battery pack/power supply.

4. STORAGE AND TRANSPORT OF THE XRF INSTRUMENT

4.1 When not in use the unit shall be stored in a locked case.

The unit shall not be left anywhere else when not in use.

4.2 When in the School, The PXRF unit will be stored in the Conservation Store.

The keys to the case, the detector and the PDA will be kept in the Conservation safe.

4.3 The controlled area for use of the unit will be in Room 3.03, on the bench between the X-radiography cabinet and the external wall. The unit will be used within its desk-top cabinet whenever possible. The cabinet door must be closed whilst x-ray exposures are underway. When the PXRF is removed from the lab it is essential that all points in

4.4, 4.5 & 4.6 below are adhered to. Users should also ensure they have a radiation monitor for checking x-ray emission (further detail is contained in the Appendix) and signs, barrier tape & measuring tape to establish the controlled area.

4.4 The person removing the XRF unit from the store (A&N X-ray room of the National Museum or Conservation Store of SHARE) must sign and date the appropriate log book to that effect, giving details of where the unit is to be taken. A second entry shall be made by the person returning the XRF unit to the store.

4.5 It is extremely important to avoid the possibility of theft of the XRF unit or of a vehicle containing it. The vehicle should never be left unattended with the unit inside. The machine should be treated as a museum object and only left unattended when in a secure locked environment.

4.6 The XRF unit is robust and is unlikely to be damaged if reasonable care is taken during handling. However if there is any reason to suspect that the unit has been damaged the emergency procedures in Section 7 must be implemented.

5. USE OF THE XRF UNIT ON SITE

5.1 Only authorised persons, trained in its use by a qualified operator and working under written arrangements may use the unit.

5.2 The supplier's operating instruction shall be adhered to when using the XRF unit.

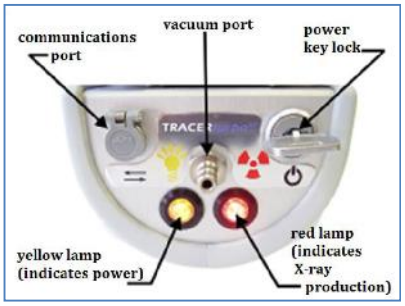

On the XRF probe;

- Yellow light indicates power
- Red light indicates x-ray emission

On the palm top PC;

- Red trefoil indicates x-ray emission

5.3 When out of its carrying case, care must be taken to avoid impact on the unit. If dropped the unit containing the X-ray tube may be damaged, resulting in a radiation hazard.

5.4 The unit should be used against a suitable backstop if possible.

Operators must be vigilant when the unit is placed against the sample. In particular the operator should always consider the possibility that persons may be present on the other side of the object being analysed and such persons should be physically excluded from the area. Wherever possible, the experimental configuration should be such that it is not possible to walk behind the sample. The sample should normally be in front of a structural wall. Studded walls should be avoided unless shielding is used or area is secure.

5.6 The radiation controlled area must be under constant visual supervision by the operator, who warns persons to stay away. If unauthorised persons disregard warnings and enter the controlled area, the operator should stop the measurement and ensure the unit X-rays are not on. If this is not possible then remove the battery pack.

5.7 The unit must **NEVER** be pointed at or held up against any person. KEEP YOUR FINGERS OR ANY PART OF YOUR BODY WELL AWAY FROM THE PROBE UNIT WHILST THE UNIT IS BEING USED. The dose rates close up to the opening on the base of the probe unit with the shutter open can be high (see user manual). Use the tripod support where practicable to reduce extended exposures to the hands.

6. MAINTENANCE OF THE XRF UNIT

Maintenance will be carried out when necessary by a Bruker qualified engineer, as arranged by National Museum staff.

7. CONTINGENCY PLANS FOR ACCIDENTS OR INCIDENTS INVOLING THE XRF

The following procedures must be initiated by the **unit operator** in the event of the following accidents:

(a) Exposure not terminating

Should the X-rays not turn off then (as indicated by warning light and/or environmental radiation meter) remove the battery pack/power source immediately, taking care to direct the beam towards a structural wall or shield. Consult the RPS and Radiation Protection Adviser immediately

(b) **Theft or Loss**

The Radiation Protection Supervisor must be consulted as soon as it is suspected that the unit has been lost or stolen and an immediate

search must be started. The Radiation Protection Adviser should also be informed.

(c) Damage Including Fire or Mechanical Damage

In the event of mechanical damage to the XRF instrument, X-rays may be emitted through the case of the unit. Place the unit in the case and remove the battery pack. Ensure unit is serviced/repaired by a suitably qualified engineer.

(d) Inadvertent exposure and/or Overexposures

The University has set a dose investigation level of 1mSv effective dose.

If unauthorised persons disregard warnings and enter the controlled area, the operator should stop the measurement and ensure the unit X-rays are not on. Note the details of the transgression (name, duration of exposure, distance to source, operating parameters) and report details to the RPS.

If it is suspected or known that an employee has received an overexposure to ionising radiation, then they must immediately inform the RPS who will carry out an investigation to ascertain whether an overexposure has occurred. The RPS will make a detailed record of that investigation and contact the Radiation Protection Adviser (Mike Sobanski – 75395, sobanski@cf.ac.uk) for further advice (confirmed doses may need to be reported externally).

REFERENCES

1. User Manual S1 Turbo SD / LE Portable XRF Analyser, part number 485220-000 Revison D
2. TRACeR III-V User's Manual

8. APPENDIX

(I) Dose assessment for the Bruker Tracer SD XRF operating at **40kV/20µA**;

In ***main beam*** [during thin sample analysis or where the proximity sensor fails]: 12.5mSv/h @ 10cm (from pg. 45 Bruker Manual at 10x the current) and 450mSv/h on skin contact with the examination window (applying ISL; the X-ray point source is ~2cm behind the front examination window; information from Bruker via MB). Note: Tracer IIIV & Sorter models have lower operating settings of 40kV/2µA.

To the ***hand at 10cm*** from any accessible surface:

Background radiation for thick samples which attenuate the beam (from pg. 53; Table 2; Bruker Manual):

(II) Dose assessment for the Bruker Tracer SD XRF operating at **15kV/60µA**;

To the ***hand at 10cm*** from any accessible surface:

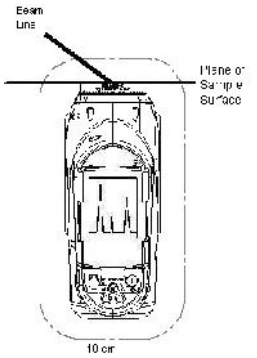

0.25µSv/h for thin samples which attenuate the beam (from pg. 53; Table 2; Bruker Manual):

Note: the beam is not aligned with the axis of the "gun barrel" but is emitted at an angle of 45⌈.

(III) Dose assessment for purposes of area designation;

An annual dose of 6mSv in a year is unlikely given expected usage. Assuming during-use exposures amount to 2h per day and the XRF is used twice a month. Dose to the hands = 48 x 0.25µSv/h = 12µSv/y; Dose to the body = 0. These are trivial doses and dosimeters (ADS issued) are not strictly required although might be issued for reassurance purposes.

If an accident leading to beam exposure occurred, direct skin contact would still be inadvertent, hence, only a fraction of the 2h work period, say 2 min. Skin dose = 450/60 x 2 = 15mSv dose, increasing the risk of localised cancers, but well within the legal limits for exposure of the extremities (150mSv/y). Even unauthorised use or deliberate misuse would require about 4h of direct skin contact to reach the threshold for erythema (note, only for the operating characteristics above!).

Brukers' RPA (Studsvik) identifies the controlled area as extending 3m in front of the beam aperture and 1m around all other surfaces during operation under

worst case scenario (poor sample attenuation, highest voltage/current combination).

Where beam enclosure is not possible, ***controlled areas*** should be maintained through display of controlled area notices at prominent locations and by ***continuous supervision*** by the operator who can verbally restrict access. The aim should be for the operator to have ***full control of the area*** e.g. through locking access doors, through working out of 'public' hours or by erecting barriers. For transient work, barriers are only necessary where the operator works unassisted and cannot see the entire controlled area.

- For areas of sufficient size to afford an unobscured view, establish a controlled area 1m to the sides and rear and 3m in the forward direction of the XRF.
- Where possible, aim the XRF toward a structural feature to act as a backstop e.g. a structural wall (brick or concrete block). 10cm concrete (or brick) is more than sufficient to reduce the direct beam dose rate (12.5mSv/h @ 10cm) by 2E-6 at 50kV (from BIR/IPEM guide) i.e. to 0.025µSv/h. In these circumstances, the controlled area only extends 1m to the sides and rear of the XRF.
- Do not fire the XRF against partition walls, stands or dividers where unrestricted access is possible within 3m of the x-ray aperture on the opposite side of the partition (the 3m forward direction is still necessary, plasterboard HVT is 18mm, hence typical partition walls [3x2" plus 1" plasterboard = 10cm total thickness] will only halve the dose rate). In these circumstances, the controlled area extends 1m to the sides and rear of the XRF and 3m into the adjacent room.
- Additional shielding could be employed. 1mm lead sheet placed 10cm away from the front of the XRF (e.g. on the opposite side of a typical partition wall) would effectively attenuate all radiation (code #3 commercially available flashing will do). For 12.5mSv/h @ 10cm, 1mm lead will reduce the dose rate 2E-6 at 50kV (from BIR/IPEM guide) i.e. to 0.025µSv/h (actually 11HVTs are enough hence 0.7mm lead will be sufficient to reduce <7.5µSv/h but code #3 easy to acquire).
- A suitable radiation monitor should be used to confirm emission and the extent of the controlled area boundary. A Mini-type D probe or Berthold LB1236 is available through the RPA. A Mini-type X probe can be acquired for dose estimation at exposures down to 10kV.

(IV) Practical dose measurement

Using a Berthold LB123 dose rate probe no readings above background were observed using the cabinet shield at 40kV/14µA (normal operation). Where thin samples are examined that do not attenuate radiation, at a 20cm radius around the aperture in the forward direction, unshielded, maximum readings were 50µSv/h at 40kV/14µA and 20µSv/h 15kV/55µA apart from in the main beam.

(V) Risk evaluation and conclusions

- In normal operation, dose rate experienced by operator (whole body and hand) is <1µSv/h.
- Misuse of the detector could result in localised exposures at doses rates of a few 100mSv/h.

Appendix F: Materials Used for Glaze Replication

Aluminium Hydroxide, Potclays Ltd.

Antimony Oxide, Acros Organics

Calcium Carbonate, Fisher

Cobalt Oxide, Acros Organics

Copper (II) Oxide, Alfa Aesar™

Iron Powder, BDH™

Lead Powder, Strand Glassfibre Ltd.

Magnesium Carbonate, Fisher

Manganese Oxide, Acros Organics

Potassium Carbonate, VWR™

Pure Sand, Acros Organics

Quartz Powder, Potclays, Ltd.

Sodium Carbonate, Alfa Aesar™

Tin Powder, BDH™

Appendix G: HH-XRF Signature Comparison: Water Bottle, Cellulose Tablet and Perspex

One measurement was conducted for the water bottle, cellulose tablet and Perspex blank for comparison (see Figs. a and b) using the high and low voltage settings as determined by the evaluation (Chapter 6). Perspex (also known as Plexiglas and Lucite) is a poly methyl methacrylate composed of carbon, hydrogen and oxygen atoms (undetectable by the HH-XRF) and has been used to determine HH-XRF instrument signatures (Shugar and Sirios 2012: 342), as a totally reflecting but non-contributing support for thin materials and residues (Kregsamer et al. 2001: 568) and as an X-ray scatterer in total reflection XRF (TXRF) (Wobrauschek et al 2010: 7). Perspex was measured to determine potential contributions of the other two blanks and its suitability as a blank. The Perspex was cut into a 10 x 15 cm rectangle approximately 1 cm thick. Descriptions for the water bottle and the cellulose pellet are included in chapter 6.

The cellulose pellet exhibited the highest Compton peak indicating lowest density while Perspex showed the highest density (low Compton peak). In all other regards the spectra were identical to the spectra (Fig. 8) using settings A and B. A change of 5 µA resulted in no qualitative difference between the recommended low voltage settings and setting A used during the evaluation of the HH-XRF except for a slightly higher baseline with setting A.

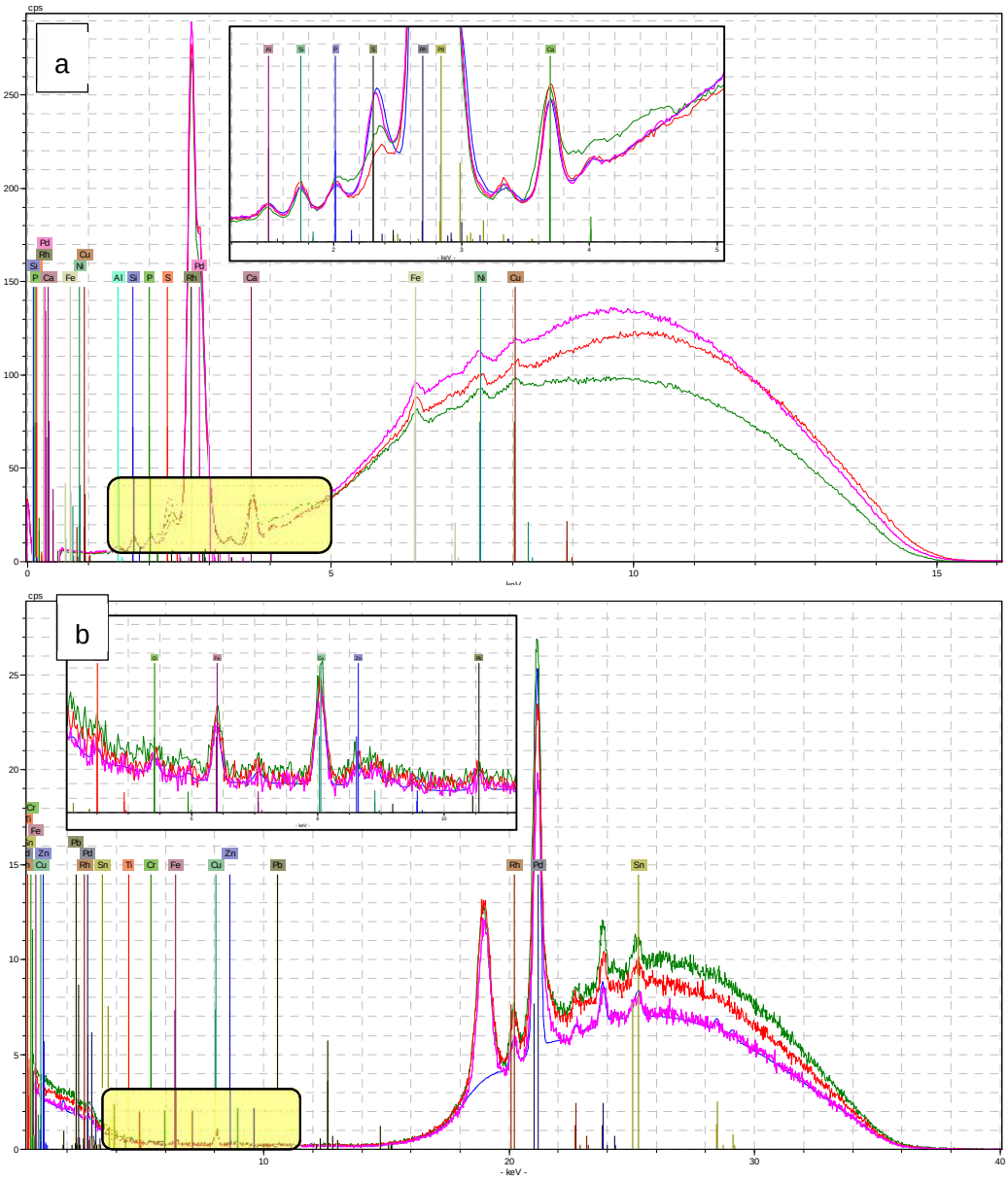

A comparison of deionized water filled bottle (green), cellulose pressed tablet (red) and 1 cm thick sheet of Perspex (purple) as blanks at 15 kV and 50 µA using a vacuum and no filter (Fig. a) and 40 kV and 30 µA using filter 3 and no vacuum (Fig. b). The inset in Fig. 9a is highlighting the area between 1.2 keV and 5 keV. This area exhibits a slight rise in the background for the water bottle near the titanium kα peak but with no definite characteristic peak. The inset in Fig. b is highlighting the area between 4 keV and 11 keV and exhibits the titanium, chromium, iron, copper zinc and lead instrument signature peaks. Thin blue line in the spectra is the Bayesian deconvolution line.

Appendix H: Statistics and Multivariate Analysis Sequences

Statistics Sequence

1. Data preparation: outliers, censored data
    a. Variables
        i. Variables should be restricted to half or less of the number of cases.
        ii. Variables should have values higher than the limit of detection and within the calibration range if compositional data is used (i.e. wt% or ppm).
        iii. Variables ideally will have a precision measurement of C_V<10% but this can be increased to 15% or 20% if it is essential to the analysis.
        iv. Variables can be dropped if the total missing values is >5-10% of the total data observations for a variable.
        v. Variables essential for glass forming should be included at least for the initial data mining.
        vi. Glass forming variables can be removed after initial data mining to reveal potentially masked relationships with lessor elements.
        vii. Choice in variables can be case specific but has to make archaeological sense (e.g. subset of variables can form same branch of a dendrogram or be related to a process).
    b. Censored Data and Zero Values
        i. Multiplicative simple replacement or the replacement of censored data with 50-75% the detection limit for the given element or oxide.
        ii. Mean of the qualified data for the given element or oxide.
        iii. Leave-one-out cross validation imputation method where replacement values are consistently recalculated until they provide a best fit along a PCA regression line.

iv. Multiplicative lognormal replacement which is dependent on detection limits for individual elements or oxides and avoids repetitive replacements.

c. Transformation of compositional data
    i. Logratio transformation retains element/oxide ratios but transforms the data so that it can be analysed in Euclidean space required by multivariate analysis.
    ii. Z-Transformations rescale the data in Euclidean space making data comparable while retaining ratios.
    iii. Logratios and Z-Transformations

d. Outliers
    i. Identification
        1. Hierarchical clustering analysis (single and average linkage)
        2. PCA
            a. Plots of first few components will represent single variable extremities
            b. Plots of the last few components may indicate other factors
        3. Draftsmen plots
        4. Boxplots
    ii. Action
        1. Omit if…
            a. Not an important aspect
            b. Fall into a single cluster
            c. Disrupt homogenous clusters
        2. Increase number of clusters in cluster analysis if outliers…
            a. Fall into a single cluster
            b. Disrupt homogenous clusters
        3. Include if they represent unexpected behaviour in a data environment

2. Shapiro-Wilk Normality Test for each variable - Histograms of elements to determine normality
3. Boxplots of elements included for analyses
4. Pairwise Correlation, can be retrieved from draftsman plot
5. Hopkins Statistics to determine clustering tendency
6. PCA… full dataset. see relationships, driving factors (first few components) and noise (last few components). See outliers.

7. Determine number of clusters for clustering analysis (i.e. HCA and K-Means).
8. Hierarchical… full dataset see relationships, group cases. Also group variables. This allows the restriction of variables (i.e. we look at one cluster of variables at a time). Single linkage will show outliers just as PCA may have. Single linkage and average linkage for outlier identification. Complete linkage or Ward D2 method better for actual clustering. This can be followed by silhouette validation methods.
9. K-means… clustering of group cases. This can be done separately for each cluster group found in hierarchical clustering in 2. This can be followed by silhouette validation methods.
10. Element Biplots… show relationships between elements (variables) after having seen them in other analysis forms (i.e. parts 6, 7 and 8).
11. Regression Analysis comparing results of SEM-EDS and HH-XRF.
12. Actions 2-10 can be run for each iteration of a dataset.

Multivariate Analysis Sequence

1. Data preparation: outliers, censored data and Transformations
    a. Statistical Testing on All variables that meet criteria (see Statistics Sequence Choices)
        i. Censored Data and Zero Values: Multiplicative Lognormal replacement imputation method for SEM-EDS; Leave one out (LOO) method for HH-XRF; Variables can be dropped if the total missing values is >5-10% of the total data observations for a variable.
        ii. For 15 kV HH-XRF Transformation: Centered Logratio-Transformations.

            For SEM-EDS and 40 kV HH-XRF Transformation: Z-Transformations

    b. Statistical Testing on underlying Variables
        i. Removal of major elements
        ii. Removal of colouring agents and major elements
        iii. Removal or addition of elements if needed (e.g. analyse one branch of the HCA dendrogram, a single cluster or a single colour)
2. Shapiro-Wilk Normality Test for each variable- Histograms of elements to determine normality (optional)

3. Outliers
    a. Identification
        i. Hierarchical clustering analysis (single linkage)
        ii. PCA
        iii. Draftsmen plots (bivariate plots)
    b. Action
        i. Omit
            1. Not an important aspect
            2. Fall into a single cluster
            3. Disrupt homogenous clusters
        ii. Increase number of clusters in cluster analysis if outliers…
            1. Fall into a single cluster
            2. Disrupt homogenous clusters
        iii. Include if they represent unexpected behaviour in a data environment
4. Boxplots of elements included for analyses
5. Pairwise Correlation, can be retrieved from draftsman plot
6. Hopkins Statistics to determine clustering tendency (optional)
7. PCA
8. Determine number of clusters for clustering analysis (i.e. HCA and K-Means).
9. HCA: Ward's Method with silhouette validation methods
10. K-means Clustering with silhouette validation methods
11. Element Biplots (selected from draftsman plots or for other reasons)
12. Regression Analysis comparing results of SEM-EDS and HH-XRF
13. Repeat actions 2-10 for each iteration of a dataset

Appendix I: R Statistical Analysis Coding Sequence

This coding is associated with the multivariate analysis (MVS) used in the study. This sequence is best understood in conjunction with the MVS chapter (Chapter 8). The coding is not explained in minute detail. Therefore, playing with the settings will provide the user with an idea of its function in the coding.

Uploading Data

Load data into R Studio. Loaded data is designated as “mydata” in the code. Any name can be used. Remove columns of the data if not part of the analysis (e.g. categorical data). This is accomplished in the following code which is used to create a new data frame (mydata1) based on the first 30 samples (1:30) and the third to thirteenth variables (3:13) of the mydata data frame.

```
mydata1 <- mydata[1:30, 3:13]
```

The new data frame contains only the information indicated in the code. The old data frame (mydata) still contains all the data and can be used as a source for other analyses. For the remaining codes, mydata will be retained for the data frame name.

Renaming Row Names for Data

Cases in MVS will be identified by the row name. Row names are automatically numbered numerically 1 through the number of cases in the dataset. However, row names can also be changed to more meaningful designators.

Rename the rows with the replicated faience glaze sample numbers

```
attr(mydata,"row.names") <- c("R327", "R328", "R340", "R342", "R349",
"R351", "R356", "R359", "R360", "R363", "R364", "R367", "R383",
"R384", "R386", "R388", "R390", "R392", "R406", "R408", "R411",
"R412", "R415", "R416", "R418", "R421", "R423", "R424", "R426",
"R429")
```

or for the Saqqara faience glazes.

```
attr(mydata,"row.names") <- c("s12", "s17", "s20", "s21", "s22",
"s31", "s42", "s45", "s48", "s53", "s70", "s72", "s74", "s78", "s80",
"s81", "s82", "s83", "s84", "s85", "s87", "s89", "s90", "s91")
```

To confirm the change has been made, type the following code

```
View(mydata)
```

or simply click off the data frame in the data frame window and re-click on it.

Categorical or other data can be added back into the manipulated data frame by the following code where ‘mydata 1’ is the manipulated data, ‘mydata’ is the original source data and ‘Colour’ is the variable to be added to the new data frame.

```
mydata1$Colour <- mydata$Colour
```

Loading Libraries

Load the required packages for running statistics required for the following data preparation and MVS.

```
library(chemometrics)
library(FactoMineR)
library(factoextra)
library(ggplot2)
library(ggrepel)
library(psych)
library(NbClust)
library(ClustOfVar)
library(zCompositions)
library(GGally)
library(beeswarm)
library(car)
library(rgl)
```

Beware… ggtern replaces some commands of ggplot. Might be best to load separately.

```
library(ggtern)
```

Replacement of Censored Data (Zeros, Below Detection)

Conduct Multiplicative Replacement for data that will be centered logratio transformed. This method will maintain ratios important to logratios. Replace “mydata” with file of interest. “dl” is the limits of detection for the variables (n=5).

The leave-one-out method of replacement requires a number of components to be selected. After processing “nb”, type nb, nbncp or $criterion for the number of components. Place this number after “ncp=” while conducting ‘imputePCA’. The last command displays the new data set.

Multiplicative Lognormal Replacement

```
dl <- c(2.24, 0.26, 1.4, 0.18, 0.22, 0.3)
mydata.LN<- multLN(mydata, label = 0, dl = dl)
```

Leave One Out Replacement

```
nb <- estim_ncpPCA(mydata,ncp.min=0,ncp.max=6)
$nb
nb$ncp
$criterion
res.impute <- imputePCA(mydata, ncp=2, seed = null, nb.init = 10,
maxiter = 1000)
res.impute$completeObs
```

Transforming Data

Conduct all three transforming techniques and they will be available for analysis by their assigned names (the name preceding the arrow).

Centered Logratio (clr)

```
mydataclr <- clr(mydata)
```

Z-Transformation (standardization)

```
mydatascale <- scale(mydata)
```

Z-Transformation with Centered Logratio

```
mydataclr <- clr(mydata)
mydataclrscale <- scale(mydataclr)
```

Center-logratioed data where row names were renamed to sherd number (e.g. s48) and the columns 'Glaze', 'Col' and 'ASN' had to be added from the source data frame after data transformation.

	Mg	Al	Ti	Mn	Fe	Zn	Glaze	Col	ASN
s48	-1.641993	0.0772165	0.19577531	0.14142672	3.845245	0.3385571	Dark Blue	mediumblue	s48
s70	-2.3053	-0.18484289	0.12684207	0.2850775	5.06528	-0.1516149	Ultra-Marine Blue	midnightblue	s70
s72	-1.991218	0.01361697	0.30834317	0.23844327	4.462153	0.5694193	Purplish Blue	darkblue	s72
s74	-1.726903	0.04335422	0.27004784	0.19127324	4.330088	0.4178354	Purplish Blue	darkblue	s74
s78	-1.912103	-0.0398321	0.05630831	0.03600187	4.968833	0.1600958	Ultra-Marine Blue	midnightblue	s78

Initial Exploratory Analysis

This initial analysis is to determine presence of outliers and other possible data preparation problems (e.g. 0s or blank data). If there are no problems this analysis can stand and does not need to be replicated below. HCA may need to be run again having changed the method to 'ward.D2'.

Hierarchical Cluster Analysis (HCA)

The following code will perform HCA clustering of the data and save it into a separate data frame. Inserting k=4 will designate 4 clusters. Omitting k designation will run boot-strap algorithm for cluster determination. Method is set for single linkage (i.e. "single") but can be switched to "complete" or "ward.D2" (Ward's Method) for final analysis. Replace 'mydata' with mydataclr, mydatascale, or mydataclrscale depending on which transformations you desire. The clip board scale works fine with 250:600.

```
res.hc <- eclust(mydata, "hclust", hc_method = "single", graph = FALSE)
```

```
fviz_dend(res.hc, rect = TRUE, k_colors = "black", type = "rectangle", horiz = T, cex = 0.8, main = "HH-XRF 15 kV SNR \nCentered Logratio Data \nSingle Linkage HCA")
```

Silhouette Validation of HCA

Visualize and validate the clusters using a silhouette plot. A negative result indicates the sample is in the wrong cluster while a result near 1 is confidently placed. A result near 0 indicates sample is probably between two clusters. Clip board scale is fine at 600:250.

```
fviz_silhouette(res.hc, label=T)
```

Optional: Clustering of the variables will provide information regarding relationships between variables on a dendrogram. Replace 'mydata' with mydataclr, mydatascale, or mydataclrscale depending on which transformations you desire. The number of variables are indicated by (,1:11). Change this to fit new data.

```
tree <- hclustvar(mydata[,1:11])
```

```
plot(tree, cex = 2, cex.lab = 2, main = "Title")
```

Principle Component Analysis (PCA)

Choose one of the transformations by replacing 'mydata' with mydataclr, mydatascale, or mydataclrscale and continue with steps below. Clip board is fine at 400:350.

```
res.pca <- PCA(mydata,  scale.unit=FALSE, graph = FALSE)
```

Run the following to completion before a new transformation is selected.

To retrieve Eigenvalues, type…

```
get_eig(res.pca)
```

To retrieve loadings, type…

```
sweep(res.pca$var$coord,2,sqrt(res.pca$eig[1:ncol(res.pca$var$coord),1
]),FUN="/")
```

or for varimax rotation

```
my.varimax<-
sweep(res.pca$var$coord,2,sqrt(res.pca$eig[1:ncol(res.pca$var$coord),1
]),FUN="/")
```

```
varimax(my.varimax)
```

To retrieve a complete summary, type…

```
summary(res.pca)
```

or, the following code will provide a list of variables that are most representative of the components…

```
dimdesc(res.pca)
```

or this code to retrieve the PCA scores…

```
res.pca$ind$coord
```

Optional: to produce a pairwise plot of the pca scores…

```
mydata <- res.pca$ind$coord
```

```
mydata <- as.data.frame(mydata)
```

add case designators to table matrix (number of designators should match number of cases)

```
mydata[["Glaze"]] <-
c("G3","G3","G3","G3","G3","G3","G3","G3","G3","G3","G3","G3","G3","G3
","G3","G3","G3","G3", "G7","G7","G7","G7","G7","G7","G5",
"G5","G5","G5","G5","G5")
```

Then…

```
ggpairs(mydata, columns = 1:5, axisLabels = "internal", title =
"mydata PCA Score Plots", aes(pch = Glaze, col = Glaze), upper =
“blank”) + theme(panel.grid.major = element_blank(), axis.line =
element_line(colour = "black"))
```

To plot a Scree Plot, type…

```
fviz_screeplot(res.pca, addlabels = TRUE, ylim = c(0, 50), main = "HH-XRF 15kV Co Blue 1")
```

To plot variable contributions, type the following. Default is components 1 and 2. To display components 1 and 3, add axes = c(1,3).

```
fviz_pca_var(res.pca, col.var="contrib", gradient.cols = c("grey69", "grey33", "grey0"), title = "Variable Contributions", repel = TRUE)
```

To plot PCA biplots, type the following. Default is components 1 and 2. For components 1 and 3, add axes = c(1,3).

```
fviz_pca_biplot(res.pca,  geom = c("point", "text"), repel=TRUE, title = "Biplots of ", col.var="contrib", gradient.cols = c("grey69", "grey33", "grey0"))
```

Optional: Plot PCA biplots without variables.

```
fviz_pca_ind(res.pca, repel = T, title = "Title")
```

Optional: To plot PCA biplots with coloured groupings, 'Habillage' points to a column in a data frame (not necessarily the same data frame) to use for grouping. The first code converts the specific column results in the source data frame from characters to a factors. This is required to make the code 'habillage' work.

```
mydata$Glaze <- as.factor(mydata$Glaze)
```

or

```
GC <- factor(mydata$Glaze)
```

Adding lines for ellipses (95%), colour, shape designations and removal of legend…

```
fviz_pca_biplot(res.pca,  col.var = "gray", geom = c("point", "text"), repel=TRUE, addEllipses = T, ellipse.level=.95,  habillage=GC, title = "HH-XRF 15 kV Dataset 1.1.2\nPCA Biplots") + geom_point(aes(shape = mydata$Glaze, colour= mydata$Glaze), size = 3) +
scale_colour_manual(name = "Faience Colours", breaks = colmapping$Glaze, values = colmapping$RColourName) +
scale_shape_manual(name = "Faience Colours", breaks = colmapping$Glaze, values = c(15, 16, 17)) + theme(legend.position = "none")
```

Colmapping is a 'key' data frame. 'RColourName' indicates desired colour to use.

A 'Key' data frame to designate colours attributed to specific glazes.

	Glaze	RColourName
1	GLZ03	cornflowerblue
2	GLZ07	blue
3	GLZ05	darkblue

Option: 3D PCA … May need to open rgl first.

```
pc <- princomp(Dataset.1.1.1[,1:5], cor=TRUE, scores=TRUE)
plot3d(pc$scores[,1:3], col=Dataset.1.1.1$Col)
text3d(pc$scores[,1:3],texts=rownames(Dataset.1.1.1 [,1:5]))
text3d(pc$loadings[,1:3], texts=rownames(pc$loadings), col="red")
coords <- NULL
for (i in 1:nrow(pc$loadings)) {
coords <- rbind(coords, rbind(c(0,0,0),pc$loadings[i,1:3]))
}
lines3d(coords, col="red", lwd=2)
```

…or Using data from PCA instead of princomp

```
plot3d(res.pca$ind$coord[,1:3], col=Datasetclr.1.1.1$Col, type = 's',
size = .5)
text3d(res.pca$ind$coord[,1:3],texts=rownames(Datasetclr.1.1.1
[,1:5]))
text3d(res.pca$var$coord[,1:3], texts=rownames(res.pca$var$coord),
col="red")
coords <- NULL
for (i in 1:nrow(res.pca$var$coord)) {coords <- rbind(coords,
rbind(c(0,0,0),res.pca$var$coord[i,1:3]))}
lines3d(coords, col="red", lwd=2)
```

Draftsman or Pairwise Plots

This produces all the bivariate plots based on the data frame. Replace ‘mydata’ with mydataclr, mydatascale, or mydataclrscale depending on which transformations you desire. The following code is best for single glazes or colours.

```
pairs.panels(mydata[,1:11], scale=FALSE, ellipses=F, lm=T, cex=1.6,
cex.labels=1.6, main="15 kV SNR")
```

Another code is best for multiple glazes or colours.

Add new column with R…

```
mydatascale[["Glaze"]] <-
c("G3","G3","G3","G3","G3","G3","G3","G3","G3","G3","G3","G3","G3","G3
","G3","G7","G7","G7","G7","G7","G7","G5", "G5","G5","G5","G5","G5")
```

Then the following code:

```
ggpairs(mydatascale, columns = 1:6, title = "HH-XRF 15 kV Centered
Logratio with Outliers Removed", aes(pch = Glaze, col = Glaze), upper
```

```
= list(continuous = wrap("cor", size = 3))) + theme(panel.grid.major =
element_blank(), axis.line = element_line(colour = "black"))
```

or this for Arch data with too many colour designated types. ‘GenCol’ is a variable showing general colours (e.g. all distinct hues of blue are indicated as ‘blue’ in the GenCol) instead of all colours so that the figure is less convoluted.

```
ggpairs(mydatascale, columns = 1:12, title = "HH-XRF 15 kV Arch
1.1.2", aes(pch = GenCol, col = GenCol), upper = list(continuous =
wrap("cor", size = 3))) + theme(panel.grid.major = element_blank(),
axis.line = element_line(colour = "black"))
```

Analysis

Prior to reaching this section, all data must be prepared with no problems identified in the previous section. Analysis can comprise all the data or data specific to a question or process (e.g. cobalt blue samples or sample on one branch of the HCA tree).

Hopkins Test

Hopkins Statistic is a spatial randomness test or a measure of clustering tendency of the data (Lawson and Jurs 1990). If number is closer to 0, the data is very clusterable, if number is 0.5 then the data is random and not clusterable although the various analyses can still force clustering on the random data. N is the number of samples. N-1 might work better (i.e. if 24 samples, n=23). Replace ‘mydata’ with mydataclr, mydatascale, or mydataclrscale depending on which transformations you desire.

```
get_clust_tendency(mydata, n=23, graph = TRUE, gradient = list(low =
"red", mid = "white", high = "blue"))
```

Determine the Number of Clusters (k)

Determine the number of clusters (k) in the data. Replace ‘mydata’ (only one instance in this code) with mydataclr, mydatascale, or mydataclrscale depending on which transformations you desire. This provides a table showing number of cluster results for various algorithms. Choose the highest occurring number.

```
lista.methods = c("kl", "ch", "hartigan","mcclain", "gamma", "gplus",
                  "tau", "dunn", "sdindex", "sdbw", "cindex",
"silhouette",
                  "ball","ptbiserial", "gap","frey")
lista.distance = c("metodo","euclidean", "maximum", "manhattan",
"canberra")
tabla = as.data.frame(matrix(ncol = length(lista.distance), nrow =
length(lista.methods)))
```

```
names(tabla) = lista.distance
for (j in 2:length(lista.distance)){
    for(i in 1:length(lista.methods)){

        nb = NbClust(mydata, distance = lista.distance[j],
                     min.nc = 2, max.nc = 10,
                     method = "ward.D2", index =lista.methods[i])
        tabla[i,j] = nb$Best.nc[1]
        tabla[i,1] = lista.methods[i]

    }}
tabla
```

Also can create a scree plot for the same function but only uses one algorithm. Replace ‘mydata’ with mydataclr, mydatascale, or mydataclrscale depending on which transformations you desire. Information after ‘#’ is not included in the function. Therefore, general notes can be included in the code by prefacing with ‘#’.

```
k.max <- 18 # Maximal number of clusters, could be columns
wss <- sapply(1:k.max,
              function(k){kmeans(mydata, k, nstart=10 )$tot.withinss})
plot(1:k.max, wss,
     type="b", pch = 19, frame = FALSE,
     xlab="Number of clusters K",
     ylab="Total within-clusters sum of squares")
```

or this one using gap stats ([,1:11] indicates all samples with variables one through eleven),

```
fviz_nbclust(mydata[,1:11], kmeans, method = "gap_stat")
```

or this one similar to scree plot ([,1:5] indicates all samples with variables one through five),

```
fviz_nbclust(mydata[,1:5], kmeans, method = "wss")
```

or this one using silhouette stats.

```
fviz_nbclust(mydata[,1:5], kmeans, method = "silhouette")
```

K-Means

This code produces clustering of data based on centroids. The number of clusters is determined above and placed into the code where ‘k = ’. It is set at 4 in the code below. Replace ‘mydata’ with mydataclr, mydatascale, or mydataclrscale depending on which transformations you desire. The number of samples is set at 30 (head(km.res$cluster, 30) and can be changed for other data sets. Clip board 400:350.

```
km.res <- eclust(mydata, "kmeans", k = 4, nstart = 25, graph = FALSE)
head(km.res$cluster, 30)
fviz_cluster(km.res,  ellipse.type = "norm", geom = c("point" , "text"), main = "SEM-EDS\nZ-Transformed / CLR Data\nKmeans Clustering Analysis", ellipse.level = 0.68, repel = T)
```

K-means validation using silhouette plot.

```
fviz_silhouette(km.res, label=T)
```

HKMeans (Hybrid HCA and K-Means Clustering)

Recall that, in k-means algorithm, a random set of observations are chosen as the initial centers. The final k-means clustering solution is very sensitive to this initial random selection of cluster centers. The result might be (slightly) different each time you compute k-means. To avoid this, a solution is to use a hybrid approach by combining the hierarchical clustering and the k-means methods. This process is named hybrid hierarchical k-means clustering (hkmeans).

Compute hierarchical clustering and cut the tree into k-clusters (k = number of clusters as determined above). Replace ‘mydata’ with mydataclr, mydatascale, or mydataclrscale depending on which transformations you desire.

```
res.hc <- eclust(mydata, "hclust", k = 4,
method = "ward.D2", graph = FALSE)
grp <- res.hc$cluster
```

Numerical representation of cluster centers are provided by the following code and are required for HKmeans. Replace ‘mydata’ with mydataclr, mydatascale, or mydataclrscale depending on which transformations you desire.

```
clus.centers <- aggregate(mydata, list(grp), mean)
clus.centers <- clus.centers[, -1]
clus.centers
```

The following code runs k-means analysis and silhouette validation. Replace ‘mydata’ with mydataclr, mydatascale, or mydataclrscale depending on which transformations you desire.

```
km.res2 <- eclust(mydata, "kmeans", k = clus.centers, graph = FALSE)
fviz_silhouette(km.res2)
```

The following code produces a table comparing ‘res.hc$cluster’ (clusters defined using hierarchical clustering) and ‘km.res2$cluster’ (clusters defined using k-means). Note that if positive integers are at a diagonal, the hybrid cluster analysis has not reordered any of the groups. Positive integers that are not on the diagonal indicate reordering of the groups.

```
table(km.res2$cluster, res.hc$cluster)
```

If the positive integers where not all on the diagonal then a dendrogram can be produced that shows the questionable sample in a colour different than the grouping colour.

```
fviz_dend(res.hc, k = 4, color_labels_by_k = TRUE, label_cols =
km.res$cluster[res.hc$order], cex = 0.8)
```

Element Biplots

Relationships between elements may have become evident based on the analysis above. These can be plotted in a biplots to indicate where the individual samples lie within the relationship. The original excel data set should have a categorical column representing glaze colour (can be labelled ‘Glaze’). Iron and zinc are being compared in the sample code below. The code assumes Fe and Zn are used as column labels and that there is a Glaze column indicating glaze colour and an RColourName column indicating specific R colours for the glaze in the data table. This coding can get out of hand rather quickly. The internet provides many examples of how to use ggplot to form bivariate plots and it is strongly recommended to help a new user of R. The clip board scale should be 550:400.

```
colmapping <- unique(mydata[c("Glaze", "RColourName")])
```

The assigned colours can be checked by typing the following.

```
colmapping
```

Plotting the biplots. Be sure to change all instance of Fe, Iron, Zn and Zinc with elements of choice. This code is for various glazes or sherd colours. 500/355 seems to work well.

```
ggplot(mydata, aes(x=CuO, y=CaO, label=T)) + geom_point(aes(shape =
mydata $Glaze[c(1:5, 7:13, 15, 17:30)], colour= mydata$Glaze[c(1:5,
7:13, 15, 17:30)]), size = 3) + scale_colour_manual(name = "Faience
Colours", breaks = colmapping$Glaze, values = colmapping$RColourName)
+ scale_shape_manual(name = "Faience Colours", breaks =
colmapping$Glaze, values = c(15, 16, 17)) + xlab("Copper Oxide") +
ylab("Calcium Oxide") + ggtitle("SEM-EDS of Faience Replicates") +
theme(plot.title = element_text(size = 15, face = "bold"),
axis.title=element_text(size=14)) +
theme(legend.text=element_text(size=12),
legend.title=element_text(size=12), legend.position="right")  +
theme_bw()
```

Add the following line to add labels

```
+  geom_text_repel(aes(label= mydata$X__1[c(1:5, 7:13, 15, 17:30)]))
```

The legend can be removed by replacing legend.position="right" with

```
+ theme(legend.position = "none")
```

This code is for biplots of the same glaze batch or colour.

```
ggplot(mydata, aes(x=SiO2, y=Al2O3))

+     geom_point(shape=15, color="blue", size=3) +
geom_text_repel(aes(label= mydata$X__1[c(1:5, 7:13, 15, 17:18)])) +
xlab("Silicon Oxide") + ylab("Aluminium Oxide") + ggtitle("SEM-EDS of
Faience Replicates: SiO2/Al2O3") + theme(plot.title =
element_text(size = 15, face = "bold"),
axis.title=element_text(size=14))
```

This code works with the archaeological samples…

```
ggplot(mydata, aes(x=Mn, y=Fe, label=T)) + geom_point(aes(shape =
mydata$Glaze, colour= mydata$Glaze), size = 3) +
scale_colour_manual(name = "Glaze Colours", breaks = mydata$Glaze,
values = ColMapping$RColourName) + scale_shape_manual(name = "Glaze
Colours", breaks = mydata$Glaze, values = c(15, 9, 1, 17, 8, 19, 0,
13, 14)) + xlab("Manganese") + ylab("Iron") + ggtitle("HH-XRF 15 kV
Saqqara Faience") + theme(plot.title = element_text(size = 15, face =
"bold"), axis.title=element_text(size=14)) +
theme(legend.text=element_text(size=12),
legend.title=element_text(size=12), legend.position="right")  +
theme_bw() +  geom_text_repel(aes(label= mydata$ASN))
```

For all arch colours with outliers removed. Will not work with no outliers removed.

```
ggplot(mydata, aes(x=Al, y=Ca, label=T)) + geom_point(aes(shape =
mydata$Glaze, colour= mydata$Glaze), size = 3) +
scale_colour_manual(name = "Glaze Colours", breaks = mydata$Glaze,
values = ArchColMapping$RColourName[c(1,3:9)]) +
```

```
scale_shape_manual(name = "Glaze Colours", breaks = mydata$Glaze,
values = c(15, 1, 17, 8, 19, 0, 13, 14)) + xlab("Sodium") +
ylab("Copper") + ggtitle("SEM-EDS Saqqara Faience") + theme(plot.title
= element_text(size = 15, face = "bold"),
axis.title=element_text(size=14)) +
theme(legend.text=element_text(size=12),
legend.title=element_text(size=12))  + theme_bw() +
geom_text_repel(aes(label= mydata$ASN)) + theme(legend.position =
"none")
```

For all blue arch…

```
ggplot(mydata, aes(x=Mg, y=Fe, label=T)) + geom_point(aes(shape =
mydata$Glaze, colour= mydata$Glaze), size = 3) +
scale_colour_manual(name = "Glaze Colours", breaks = mydata$Glaze,
values = ArchColMappingAllBlue$RColourName) + scale_shape_manual(name
= "Glaze Colours", breaks = mydata$Glaze, values = c(15, 9, 1, 16, 0,
13)) + xlab("Magnesium") + ylab("Iron") + ggtitle("HH-XRF 15 kV
Saqqara Faience") + theme(plot.title = element_text(size = 15, face =
"bold"), axis.title=element_text(size=14)) +
theme(legend.text=element_text(size=12),
legend.title=element_text(size=12), legend.position="right")  +
theme_bw() +  geom_text_repel(aes(label= mydata$ASN)) +
theme(legend.position = "none")
```

For all blue with outliers removed

```
ggplot(mydata, aes(x=Cu, y=Fe, label=T)) + geom_point(aes(shape =
mydata$Glaze, colour= mydata$Glaze), size = 3) +
scale_colour_manual(name = "Glaze Colours", breaks = mydata$Glaze,
values = ArchColMappingAllBlue.Routliers$RColourName) +
scale_shape_manual(name = "Glaze Colours", breaks = mydata$Glaze,
values = c(15, 1, 16, 0, 13)) + xlab("Copper") + ylab("Iron") +
ggtitle("HH-XRF 15 kV Saqqara Faience") + theme(plot.title =
element_text(size = 15, face = "bold"),
axis.title=element_text(size=14)) +
theme(legend.text=element_text(size=12),
legend.title=element_text(size=12), legend.position="right")  +
theme_bw() +  geom_text_repel(aes(label= mydata$ASN)) +
theme(legend.position = "none")
```

for Cu blues only

```
ggplot(mydata, aes(x=Mg, y=Fe, label=T)) + geom_point(aes(shape =
mydata$Glaze, colour= mydata$Glaze), size = 3) +
scale_colour_manual(name = "Glaze Colours", breaks = mydata$Glaze,
values = ArchColMappingCuBlue$RColourName) + scale_shape_manual(name =
"Glaze Colours", breaks = mydata$Glaze, values = c(15, 9, 1,0)) +
xlab("Magnesium") + ylab("Iron") + ggtitle("HH-XRF 15 kV Arch 3.1
```

```
Saqqara Faience") + theme(plot.title = element_text(size = 15, face =
"bold"), axis.title=element_text(size=14)) +
theme(legend.text=element_text(size=12),
legend.title=element_text(size=12), legend.position="right")  +
theme_bw() +  geom_text_repel(aes(label= mydata$ASN)) +
theme(legend.position = "none")
```

Element Box Plots

Errors can be caused by the quotes in the Arial font which R doesn't always recognize. Just erase them and retype while in R and it should work.

The box plot shows the distribution of the data with the lower line of the box being the 1st quartile, upper line of the box being the 3rd quartile, the line in the box being the median, the bottom whisker the minimum, and the top whisker being the maximum. The interquartile range (IQR) is the range between 1st and 3rd quartile. Suspected outliers lie at x1.5 IQR (above or below), known outliers are x3 IQR. Width of 300 or 250 or 230 is good.

```
boxplot(mydata$Na2O, main="Na2O", ylab="wt%")
```

```
beeswarm(mydata$Na2O, data=strip, add=TRUE, pwcol = mydata$Glaze,
labels = T, pwpch = c(1,2,0)[ mydata$Glaze], cex = 1.5)
```

…for some reason did does not work all the time. May have to type vector like the following…

```
Boxplot(mydata$Na2O, main="Na2O", ylab="wt%", id.method="y", labels =
mydata$RSN)
```

```
beeswarm(mydata$Na, data=strip, add=TRUE, pwcol = mydata$pch, labels =
T, pwpch =
c(1,1,1,1,1,1,1,1,1,1,1,1,1,1,1,1,1,2,2,2,2,2,2,0,0,0,0,0,0), cex =
1.5)
```

or…

```
Boxplot(mydata$Na, main="Na", ylab="NPA", id.method="y", labels =
mydata$RSN)
```

```
beeswarm(mydata$Na, data=strip, add=TRUE, pwcol = mydata$Col, labels =
T, pwpch =
c(1,1,1,1,1,1,1,1,1,1,1,1,1,1,1,1,1,2,2,2,2,2,2,0,0,0,0,0,0), cex =
1.5)
```

For arch all colours…

```
Boxplot(mydata$Mg, main="Mg", ylab="NPA (Centered Logratio)",
id.method="y", labels = mydata$ASN)
```

```
beeswarm(mydata$Mg, data=strip, add=TRUE, pwcol = mydata$Col, labels =
T, pwpch = c(17,15,
17,8,0,0,17,14,1,0,13,16,16,13,0,9,15,0,15,1,15,15,15,0), cex = 1.5)
```

to add outlier labels use the original boxplot command but use capitol B for Boxplot and add id.method="y" and add labels = mydata$RSN where RSN is a new column of sample numbers and $pch is colours (e.g. "black", "red", "green").

For all blue colours (arch)

```
Boxplot(mydata$Na, main="Na", ylab="NPA (Centered Logratio)",
id.method="y", labels = mydata$ASN)

beeswarm(mydata$Na, data=strip, add=TRUE, pwcol = mydata$Col, labels =
T, pwpch = c(15, 0,0,1,0,13, 16,16,13,0,9,15,0,15,1,15,15,15,0), cex =
1.5)
```

for Cu blue (arch)

```
Boxplot(mydata$Mg, main="Mg", ylab="NPA (Centered Logratio)",
id.method="y", labels = mydata$ASN)

beeswarm(mydata$Mg, data=strip, add=TRUE, pwcol = mydata$Col, labels =
T, pwpch = c(15, 0,0,0,0,9,15,0,15,1,15,15,15,0), cex = 1.5)
```

for Co blue (arch)

```
Boxplot(mydata$Mg, main="Mg", ylab="NPA (Centered Logratio)",
id.method="y", labels = mydata$ASN)

beeswarm(mydata$Mg, data=strip, add=TRUE, pwcol = mydata$Col, labels =
T, pwpch = c(1,13,16,16,13), cex = 1.5)
```

Ternary Plot

Data = mydata or the name of the data frame; x, y, z = variables in data. Fill = the discerning variable (e.g. glaze, Col). Only works for quantified data.

```
ggtern(data= mydata,aes(Cr,Fe,Zn,color=Glaze)) +
   theme_rgbw() + geom_point() +
   labs(x="Al",y="Fe",z="Zn",title="Title")
```

or for more pizazz…

```
ggtern(data= mydata,aes(Al2O3,CaO,FeO,color=GenCol)) +
geom_point(aes(shape = mydata$Glaze, colour= mydata$Glaze), size = 2)
+ scale_colour_manual(name = "Glaze Colours", breaks = mydata$Glaze,
values = ArchColMapping$RColourName) + scale_shape_manual(name =
"Glaze Colours", breaks = mydata$Glaze, values = c(15, 9, 1, 17, 8,
19, 0, 13, 14))
```

Appendix J: HH-XRF Standard Operating Procedure

The following parameters provide the greatest SNR and precision as well as the highest number of elements detected when measuring faience glazes using the Bruker Tracer III-SD. Users of other HH-XRF instruments can adapt these settings to their equipment but it is suggested that evaluation tests for their specific instrument be conducted.

- For low Z elements:
    - Voltage: 15 kV
    - Current: 50 µA
    - Filter: None
    - Air Purge: Vacuum or helium
    - Acquisition Time: 180 seconds.
- For general bulk analysis and detection of higher Z elements:
    - Voltage: 40 kV
    - Current: 30 µA
    - Filter: 3 (12 mil aluminium, 1 mil titanium, 6 mil copper)
    - Air Purge: None
    - Acquisition Time: 180 seconds.

Analysis of individual elements of interest may require different parameters based on the findings of this report. Filter 3 was used to optimize the detection of trace elements (e.g. Rb, Sr, Zr) that could help to determine raw material sources in the future. Filter 2 (no filter) can easily be substituted with the understanding that trace element detection will be reduced while most other elements will be enhanced. For safety concerns all measurements should be taken in a bench top stand or on the detachable stage with the X-ray shield in place. Only the user should handle the unit and all bystanders should be beyond a 3 m radius. The following workflow should be implemented after setup:

1. Objects of study should be free of dust, dirt and other surface contamination. Wipe the object with ethanol to remove any grease or stubborn grime.
2. Use XRayOps (version 1.2.15 or later) to optimize the beam according to the parameters chosen (e.g. kV, µA, filter, etc.). A pulse length of 200 ±2 shall be maintained by manipulating the beam properties (i.e. high voltage and current filament settings).
3. Use S1PXRF (version 3.8.30 or later) to collect data on the reference materials to check drift and monitor stability. Data will be saved as .pdz files.
4. Select measuring areas on the sample which are flat or convex to reduce/remove an air column between HH-XRF unit and sample which could attenuate lower Z photons. It is optimal if the HH-XRF unit is in contact with the object but it can be held a minimal distance away (~2mm) without much affect to the analysis.
5. Use S1PXRF to collect data on objects. Run several measurements per object: three, five or 10 per object. A greater number of measurements per object will increase the averaging power when anomalies are encountered. Use same number of measurements for all objects. Data will be saved as .pdz files.
6. Check window for contamination between measurements. Monitor pump readings to reveal punctures in the end window when using a vacuum.
7. Reference standards are measured at the beginning and end of each session to facilitate monitoring of drift and generally stability of the HH-XRF unit.
8. Spectra characteristic peaks can be identified while in S1PXRF but will have to be re-identified if importing in Artax Spectra. Note: Use of the Tracer III-SD negates the requirement of converting .pdf files into .txt (Artax) files (Pers. Comm. Bruce Kaiser).
9. Once imported into Artax Spectra (vers. 7.4 or later) the characteristic peaks will have to be identified again. Bayesian deconvolution can be used to determine presence of elements.

Spectra are analysed using a selected user-defined method (methods restrict the analysis to specific user determined variables) within Artax to produce NPA which can be exported to excel for further data mining. Confirm that the selected method has the full kV range desired (1-15 kV for 15 kV measurement and 1-40 for 40 kV measurements).